Redox Chemistry, Bimetallic Effects, and Ligand Design for Rhodium, Chromium, and Cerium Complexes

By
Julie Hopkins Leseberg
B.S., University of Saint Mary, Leavenworth, Kansas 2017

Submitted to the graduate degree program in Chemistry and the Graduate Faculty of the University of Kansas in partial fulfillment of the requirements for the degree Doctor of Philosophy.

Chair: Prof. James D. Blakemore

Prof. Mikhail V. Barybin

Prof. Cindy L. Berrie

Prof. Aaron J. Teator

Prof. Alan M. Allgeier

Date Defended: 29 March 2022

The dissertation committee for Julie Hopkins Leseberg certifies that this is the approved version of the following dissertation:

Redox Chemistry, Bimetallic Effects, and Ligand Design for Rhodium, Chromium, and Cerium Complexes

_____

Chair: Prof. James D. Blakemore

Date Approved: 06 April 2022

Abstract

Ligand derivatization and incorporation of secondary metals are established strategies for tuning the redox properties of inorganic and organometallic complexes, and these strategies have been leveraged in this dissertation to accomplish modulation of the properties of several novel classes of rhodium, chromium, and cerium complexes. Chapter 1 summarizes overarching themes and particular projects presented in this dissertation, while Chapter 2 reviews the foundational elements, methods, and techniques of organometallic electrochemistry that have been used in all of the projects composing the research in this dissertation. Chapters 3-6 describe research on [Cp*Rh] (Cp* = pentamethylcyclopentadienyl) complexes bearing bidentate ligand frameworks for modulation of reactivity and redox properties. Chapters 3 and 4 specifically discuss bidentate hybrid phosphine-imine ligand designs, the reactivity of hydride complexes, and dihydrogen evolution. Chapters 5 and 6 examine the influence of ligand substituents in a dipyridylmethane (dpma) ligand system on the kinetics of a redox-induced ligand rearrangement. Chapter 7 describes a series of electrochemical and spectroscopic studies of a family of chromium complexes that also bear bidentate hybrid phosphine-imine ligands; in this study, we utilized chemical reductants and aluminum reagents for mechanistic interrogation and assignment of the oxidation states accessible to chromium in the absence and presence of aluminum. Finally, Chapter 8 describes the modulation of cerium (IV)/cerium(III) redox chemistry with Lewis acidic secondary metals in a heteroditopic tripodal ligand scaffold developed in this work. The finding shows that installation of mono- and divalent cations near cerium enables systematic tuning of lanthanides for the first time. Taken together, the works described in this dissertation contribute to the areas of electrochemistry, organometallic chemistry, and *f*-element chemistry through the development of

ligand frameworks and utilization of bimetallic effects to modulate the redox chemistry of metal complexes.

Acknowledgements

First, I would like to thank my undergraduate professors that profoundly impacted my life by encouraging to pursue a research career. Professor Jemima Ingle not only taught me and encouraged me but inspired me with her profound and contagious love and enthusiasm for chemistry. She encouraged me to apply for Research Experience for Undergraduate (REU) programs that led me to the University of Kansas. Professor Ingle is the reason that I decided to get my PhD. Next, I would like to thank Professor Masa Watanabe whose kindness and patience is unmatched. He taught me so much during my time at the University of Saint Mary, and supported, encouraged, and helped me while I applied to graduate schools. I am forever thankful for you both being my first mentors and teachers.

I would like to thank my wonderful lab mates over my years at KU. I have had some of the best years of my life in graduate school, a big part of that is the friendships I have made in and out of my group during my time at KU. First, Amit Kumar and Wade Henke, I am so fortunate to have had you as my friends and support system for the last five years. Amit Kumar, or more affectionately known as Princess Amit Isobel Kumar; I will always treasure the late nights we spent in lab becoming friends, ordering too much pizza and teaching you how to say the word "code". I am so happy that you were my "bridesman" in my wedding and the many memories we made in our four years together in graduate school. Wade Henke, we have been friends since our first day of graduate school. I am very fortunate to have gone through graduate school with lab mate like you. I will never forget you dancing on a table at Sandbar or your and Amit's beautiful rendition of "Tequila" in honor of me passing my comprehensive exam. Thank you both for always supporting me.

Next, I would like to thank my other lab mates during my time at KU. Riddhi Golwankar, you are one of the sincerest and kindest people I have had the privilege of knowing. I am lucky to call you my friend and to have eaten all the wonderful Indian food that you made. Joe Karnes, thank you for always being a cheerful and goofy presence in our lab; I will never forget your ridiculous love of hot sauce. Emily Mikeska, thank you for your thoughtful heart and wiliness to always help others. Christian Nilles, I am truly amazed by your capacity for many hobbies, thank you for the many yummy baked goods and laughs. Davis Curry, I have enjoyed getting to know you during your time here, you never fail to make me laugh. To my former lab mates David Sconyers and Yun Peng: David, I enjoyed our many laughs together, I look forward to sending you the video of your fake Happy Birthday song in Iowa every year on your real birthday. Yun Peng, thank you for being my first mentor as an undergraduate student and showing me how to use the equipment in our lab.

I have had the privilege of working with some truly gifted undergraduate and postbaccalaureate students in the last five years in the Blakemore group. First, Jonah Stiel, I have enjoyed watching you grow as a scientist over the years and accomplish so much. I wish you the very best over your next years in graduate school. Claire Dopp, when I think of you, I think of a ray of sunshine. You are cheerful and uplifting to everyone around you. Be confident in yourself, you are more gifted than you realize. I will not be there to yell at you that you are great and that you can do whatever you set your mind to, so please remember that! To my former lab mate Will Moore, I will forever treasure the fond memories of joking with you, rolling my eyes at your many corny jokes and stories and laughing with you. I am very proud of you and all that you are accomplishing in graduate school. The former postbaccalaureate students in our group, Keaton Prather and Tyler Kerr, you both are part of my most fond memories as an undergraduate in the Blakemore group.

You are both wonderful people, I enjoyed laughing and teasing each other and Amit together. To the first undergrad that I "mentored" Emily Boyd, I put mentor in quotations because I feel that I less taught you, but rather we both learned from each other during our first years as researchers. You are such a gifted scientist; I can't wait to see the remarkable things you do in your career. I am very lucky to have had you as both a friend and a "mentee", I am very thankful for our time laughing and learning together. To my current undergraduate student, Emma Cosner, I am very happy that we listed each other as potential mentor/mentee so long ago at that WiSTEMM speed dating event and that fortuitus event led me to being your research mentor. I feel very privileged to have been your research mentor for the last few years. You are a truly remarkable young woman, and I cannot wait to see what you do next.

The last lab mate that I need to thank is Davide Lionetti, thank you for being my mentor, you taught me so much as a young graduate student. You inspired me with your incredible work ethic, knowledge and passion for chemistry, and determination. Thank you for teaching me, you are an incredibly gifted teacher and scientist. You have had a profound impact on my life and scientific career. I will always be thankful for getting to learn from you and laugh with you.

Next, I would be remiss to not mention Dr. Victor Day, without whom I would not have gotten 23 crystal structures during graduate school. I have immensely enjoyed my time learning and working with you. You are an incredibly gifted scientist and are a patient, wonderful person. I am so thankful for the time you invested in me (even when I was being relentlessly teased!) Your parties will forever be legendary in my memory, I will miss those parties and you dearly.

Thank you to my collaborator at Chevron Phillips Chemical, Orson Sydora. Working with you and Chevron Phillips has been one of the highlights of my graduate school career. Thank you for supporting my research for the last three years. This collaboration has given me invaluable

industrial experience during graduate school and the privilege to join a major industrial company following graduation.

Next, I would like to thank some of the friends I have made during my time at KU. Prasenjit, Ashely and Chase, I will miss you all very much. I am happy to have had such wonderful people in my year. Thank you for many potluck get togethers, game nights and cocktails. Prasenjit, I am very thankful to have a friend as thoughtful, supportive, and kind as you. I have many memories of graduate school with you that I will always cherish. Thank you for always being there for me, listening to me, and for always feeding me wonderful food and desserts. I can't wait to see the wonderful things that you do in the future.

First, to my long-term friend and short-term lab mate, Chelsea Comadoll. You were the first friend I made during GROW weekend; I am very happy that we were assigned as roommates that weekend, it is funny how God put you in my life five years ago. You are a truly gifted organic (and now organometallic!) chemist, you will be such a success in your future career. Thank you for always loving me so well. Thank you for being a part of my wedding, I am so happy I got to be a part of your legal ceremony so long ago when we barely knew each other. Ryley and I are so grateful for our friendship with you and Lucas, I will miss our game nights together. One last note to Lucas, I love you dearly, Justice Train forever – Choo choo!

To Ember Krech, I cannot describe how grateful I am for your friendship. We have been through so much together over the last years. I am so thankful to have a friend who understands me so well. There are too many memories between us to recount here, from trips to Arkansas, countless farmers market adventures, many John Brown Underground drinks and game nights. We have laughed, cried and prayed through so much together. You are such a gifted scientist and are

going to do truly remarkable things, I can't wait to see how God uses your gifts during your career. Ryley and I love you so much.

Thank you to my dissertation committee, I am thankful for your time and dedication to me and my dissertation. Thank you to Professor Misha Barybin, Professor Alan Allgeier, and Professor Cindy Berrie who have served in my comprehensive exam and dissertation defense. Thank you, Misha, for your support, advice, and exceptional teaching throughout my graduate career. Additionally, I would like to thank a few others who have impacted my time at KU. Thank you, Dr. Bala Subramaniam, for your guidance, support, and advice in my pursuit of an industrial career. Sarah Neuenswander, thank you for help with our NMR facilities any time I needed it and for being all around a wonderful person. Thank you, Dr. Justin Douglas for teaching me EPR spectroscopy and for your unwavering patience and kindness.

Lastly, thank you to my advisor and mentor Professor James Blakemore. I am grateful that so many years ago I was assigned to your lab the summer of my REU. That experience in your lab completely changed my life for the better. I remember sitting in your office so long ago, talking to you, trying to decide where to go to graduate school. You have helped me accomplish all my goals we discussed six years ago. Any success I have had in graduate school is because of that monumental conversation. It is remarkable how God put you in my life, and the profound impact that your mentorship has had on me as a researcher and person. You have inspired, challenged, encouraged, and taught me to be a better chemist. I feel so fortunate to have learned from you for the last six years, I could not have asked for a better mentor and teacher. I can never thank you enough for how you have positively impacted my life and career. We have worked together a long time, and I will miss working with you very much.

Dedication

I dedicate this dissertation to my family. To my sisters, Stephanie, and Rachael, thank you for being such loving sisters. Thank you for your love and support through graduate school and my whole life. I am thankful that you are my sisters. To my parents, John and Denise, you are both the reason I am here above anyone else. You have both loved and supported me so well. Thank you for your sacrifices and encouragement, every part of my success is a direct result of you both. To my husband, Ryley, thank you for being my best friend, my biggest supporter and comfort over the last few years. Thank you for always being there for me, during the good and bad, and for loving me selflessly. I love you all dearly.

Table of Contents

List of Figures

List of Tables

The unforgotten moments of my life are those rare ones which come after years of plodding work, when the veil over nature's secret seems suddenly to lift, and when what was dark and chaotic appears in a clear and beautiful light and pattern.

– Dr. Gerty Cori

3rd Woman to Win a Nobel Prize

Nobel Prize in Physiology or Medicine 1947

Chapter 1

Introduction to Redox Chemistry, Bimetallic Effects, and Ligand Design for Rhodium, Chromium, and Cerium Complexes

1.1 Introduction

The redox properties of metal complexes are important in a myriad of energy-relevant technologies and the field of molecular catalysis. The nature of ancillary ligands significantly influences the reactivity, structural, and redox properties of metal complexes.[1] Thus, targeted ligand design by varying steric electronic effects, denticity, and the identity of atoms in supporting ligand scaffolds is often necessary for tuning the properties of metal complexes. An alternative strategy to ligand-tuning of structural, reactivity, and redox properties of metal complexes is using bimetallic effects engendered by the placement of redox-inactive metals near redox-active metals.[2] The metal cooperativity provoked by the inclusion of a secondary metal engenders consequent tuning of reactivity and redox chemistry that is inaccessible to the isolated metal containing constructs.[3] Equally, an important approach to studying the redox properties of metal complexes is the combination of electrochemical and spectroscopic techniques, paired with the chemical preparation of spectroscopically and electrochemically observed complexes. As such, this dissertation focuses on the unifying themes of redox chemistry, ligand design, and bimetallic effects in transition metal and lanthanide complexes utilizing complementary electrochemical and chemical techniques to interrogate the properties of metal complexes.

Chapter 2 of this dissertation summarizes and reviews the diverse facets of electrochemistry in organometallic chemistry. Organometallic systems are typically redox-active and can access multiple oxidation states. Electrochemistry is a powerful tool for probing the properties inherent to unique oxidation states and redox interconversions of organometallic complexes. In this chapter, we explore the development of instrumentation, methods, and fundamental understanding relating to electrochemistry. The intent of this chapter is to provide the audience with an overview of experimental design for common electrochemical techniques. Electrochemistry of a variety of

molecular systems is explored to illustrate the power and versatility of electrochemical techniques for obtaining kinetic, mechanistic, and thermodynamic properties engendered by a changed oxidation state. Discussion of such electrochemical techniques is a unifying theme throughout the remaining chapters of this dissertation to understand the redox chemistry of rhodium, chromium, and cerium complexes.

Our group has extensively explored the reduction and protonation reactivity of a family of [Cp*Rh] complexes bearing bidentate nitrogen and phosphorus donors for the management of protons and electrons as in the contexts of electrocatalytic H_2 evolution.[4] This series of studies were inspired by the [Cp*Rh] workhorse catalyst reported by Kölle and Grätzel bearing the 2,2′-bipyridyl ligand.[5] The early proposed mechanism for H_2 evolution involves an initial reduction to a Rh(I) complex followed by two protonation events to generate a transient Rh(III)-hydride that is subsequently protonolyzed to generate H_2. However, reports from our group[6] and the Miller group[7] have shown that protonation of the Rh(I) results in protonation of the Cp* ring to form endo-η^4-pentamethylcyclopentadiene ([Cp*H]) complex. Although this system has been studied extensively, the mechanism is yet to be satisfactorily elucidated and the proposed, transient hydride species has not been fully characterized.[8] Due to the probable involvement of a transient hydride in this H_2 evolution mechanism we endeavored to synthesized stable [Cp*Rh] monohydrides; prior work with phosphine ligands provided precedence for isolation of a stable rhodium hydride suitable for chemical reactivity studies.[9] Thus, our group undertook the effort to synthesize diphosphine ligands for chelation to [Cp*Rh] frameworks. Employment of diphosphine ligand systems such as, (diphenylphosphino)benzene (dppb), bis(diphenylphosphino)methane (dppm), and 4,5-bis(diphenylphosphino)-9,9-dimethylxanthene (Xantphos), provided stable [Cp*Rh] monohydrides that proved to be inert to protonolysis.[10,11]

Inspired by work with [Cp*Rh] complexes bearing bidentate dimiine and diphosphine chelating ligands, we turned to the unexplored opportunity to probe the reactivity engendered by non-symmetric, hybrid ligand scaffolds to explore the electronic effects provoked by the inclusion of single imine and phosphine donors. Thus, chapter 3 describes the synthesis, characterization, and chemical properties of [Cp*Rh] (Cp* = pentamethylcyclopentadienyl) complexes supported by the bidentate 8-(diphenylphosphino)quinoline (PQN) ligand. In this study, we find that the PQN ligand engenders properties on the [Cp*Rh] that are, in many ways, a combination of those observed for the bpy and dppb systems. Electrochemical studies show that the Rh(III)/Rh(I) couple is like that observed for the bpy complex; however, protonation of the Rh(I) complex generates a formally Rh(III) monohydride similar to the hydride observed for the dppb framework. Detailed characterization of the family of [Cp*Rh(PQN)] complexes was accomplished with X-ray diffraction (XRD) studies, nuclear magnetic resonance (NMR) experiments, and cyclic voltammetry (CV). The ability of the rhodium hydride to catalytically evolve H_2 was interrogated utilizing both electrochemical and synthetic methods.[12]

Although the isolable $[Cp^*Rh(PQN)H]^+$ complex has a propensity to undergo protonolysis, reactivity studies of [Cp*Rh] complexes bearing hybrid phosphine imine ligands are limited. Thus, we were encouraged by the promising properties of the single phosphine and single imine donors for synthetic and reactivity studies. Chapter 4 describes a companion study to PQN with a hybrid [*P,N*] ligand to probe its reactivity properties to interrogate the utility of [*P,N*] scaffolds for H_2 evolution; this chapter describes the synthesis, electrochemistry, and chemical reactivity of a [Cp*Rh] complex bearing the [(diphenylphosphino)methyl]pyridine (PN) ligand. This bidentate chelating PN ligand is similar to that of PQN but bears an alkyldiarylphosphine donor and imine moiety bound to the Rh center. Characterization of a family of [Cp*Rh(PN)] complexes include

(XRD) studies, CV, and NMR experiments. ^{1}H NMR studies were utilized to identify the products formed upon chemical reduction of the Rh(III) complex.[13]

Effective metal redox catalysts are supported by ligands that can support multiple oxidation states. Catalyst stability over multiple oxidation states enables accessible catalytic intermediates that enable access to of redox cycles for multielectron processes. Non-innocent, redox-active ligands, such as bpy, are exceptionally well suited to stabilizing several metal oxidation states to help stabilize active catalyst intermediates. The π backbonding ability and readily accessible lowest unoccupied molecular orbital (LUMO) of the conjugated bpy ligand enable it to accept electron density and stabilize reduced metal centers.[14] Inspired by the characteristics of the bpy ligand, previous studies by the Blakemore group explored the synthetic chemistry of dimethyl-2,2′-dipyridylmethane (Me_2dpma). The ligand design of the Me_2dpma harnesses the accepting abilities of the bpy ligand but modulates the π backbonding ability of the framework by disrupting the inter-ring conjugation of the pyridyl rings resulting in less accessible π* orbitals to backbond into or accept electron density.[15] Prior studies from our group reveal that the bidentate Me_2dpma ligand is capable of stabilizing reduced metal centers; specifically, chemical reduction of the [Cp*Rh] complex bearing κ^2-Me_2dpma to the formally Rh(I) oxidation state engenders a ligand rearrangement in which a single pyridyl ring flips to facially bind to the Rh center in a η^2 manner.[15] Electrochemical studies of the Me_2dpma-ligated Rh(III) complex reveal an initial quasireversible reduction to a Rh(II) form followed by a second irreversible reduction to Rh(I) which indicates that a redox-induced chemical process occurs. This second reduction appears electrochemically irreversible a slow scan rates, but at faster scan rates this feature appears as quasireversible, the appearance of this voltammetry corresponds to an electrochemical-chemical (EC) process.[16]

Spectroscopic interrogation of molecular electrocatalysis that undergoes redox-induced chemical processes is challenging,[17] understanding of such chemical processes prompted by electron transfer is necessary for advancement in numerous areas of study.[18] Direct observation of active electrocatalytic species near the electrode surface is often difficult due to their transient nature and low concentration.[19] Therefore, the well-defined electrochemical processes engendered by the [Cp*Rh(Me_2dpma)] system make it an attractive model for understanding EC processes observed in molecular electrocatalysis that utilize non-innocent ligands. Thus, chapter 5 describes an in-depth electrochemical kinetic investigation of a family of [Cp*Rh] complexes bearing disubstituted dpma ligands. This study focuses on the role the steric influence of ligand substituents positioned on the methylene bridge play in the reactivity and kinetics of the well-defined EC process. The synthesis, characterization, XRD studies, and electrochemistry of a series of [Cp*Rh] complexes bearing dimethyl- (Me_2dpma)-, dibenzyl- (Bn_2dpma)-, methyl,methylpyrenyl- (MePyrdpma)-, and bis(methylpyrenyl)- (Pyr_2dpma)- substituted dpma ligand platform are described in this chapter. Electrochemical modeling and simulations of the experimental scan rate-dependent data in this study represent an uncommon situation in which a series of elementary rate constants for a well-defined ligand rearrangement could be reliably quantified; these rate constants could be useful for of interpretation of the electrochemical properties more complicated molecular systems in the future.[20]

Upon observation of the effects that substituents positioned on the methylene bridge have on the [Cp*Rh(R_2dpma)] system, we were interested in the implications that installation of substituents on the pyridyl motifs on the chemical reactivity of the dpma ligand. Desymmetrization of the ligand Me_2dpma scaffold and subsequent reduction of the Rh(III) complex presents an interesting situation in which the ligand has a choice to bind either the substituted or unsubstituted

pyridyl ring in an η^2 fashion to the formally Rh(I) center. Thus, we hypothesized that a non-symmetric analogue of the Me_2dpma ligand could greatly affect the chemical reactivity of the [Cp*Rh] chemistry. Chapter 6 describes the electrochemical and chemical implications resulting from desymmeterization of the Me_2dpma framework by the addition of electron-donating and -withdrawing substituents to a single pyridyl moiety. In this chapter, the synthesis, characterization, XRD studies and cyclic voltammetry studies of novel [Cp*Rh] complexes bearing dimethyl-2,2′-pyridyl(4-trifluoromethylpyridine)methane (Me_2dpma^{CF3}) and dimethyl-2,2′-pyridyl(4-methoxypyridinepyridine)methane (Me_2dpma^{OMe}) ligands are described. Investigations of such [Cp*Rh] complexes bearing non-symmetric ligands could provide chemical insights into charge stabilization processes observed in molecular metal complexes and/or catalysts.

Molecular metal catalysts for ethylene oligomerization represent another important class of complexes because of their application in industrial technologies for the synthesis of 1-alkenes or normal alpha olefins (NAO's). NAO's are ubiquitous in everyday applications such as synthetic motor oils, lubricants, surfactants, plasticizers, and polyethylene comonomers.[21] The NAO 1-hexene has been increasingly in demand in recent years, subsequently, recent work has focused on developing efficient and selective ethylene trimerization catalysts.[21] Chromium complexes, in particular, are notable for their higher selectivity, activity, and thermal stability for ethylene trimerization to produce 1-hexene.[21] Catalyst activation for chromium systems is typically achieved by mixing of a chromium source (i.e., chromium(III) acetylacetonate), a multidentate ligand, and an activator (e.g., methylaluminoxane or an alkylaluminum reagent(s)) prior to the addition of ethylene. Ethylene trimerization catalysts are significantly impacted by the nature of their ligand properties including steric bulk, denticity, and atom identity. Formation of intermediate species in ethylene trimerization has been shown to require a formal (n+2) oxidation

state change resulting from back donation of electron density from the metal d orbitals into the π* orbitals of the coordinated ethylene. The formation of metallacyclic intermediates is driven by the breaking of C-C π bonds of two ethylene molecules to form stronger M-C and C-C σ bonds. The ambiguity of the assignment of the Cr(III)/(I) or Cr(IV)/(II) cycle has sparked a long-running debate in the literature of the oxidation states accessible to Cr catalysts. Although experimental and theoretical findings support the Cr(III)/(I) mechanism, obtaining spectroscopic evidence in support of these claims is often challenging under catalytic conditions due to the low concentration of the active Cr species and unique spectroscopic challenges inherent to the observation of multiple Cr oxidation states. Thus, fundamental studies of the oxidation states accessible to such Cr-based systems could be useful for the future development of ethylene trimerization catalysis.

A notable ethylene trimerization catalyst system is based on a molecular chromium complex developed and commercialized by Chevron Phillips Chemical for 1-hexene production. In Chapter 7, we transition from rhodium chemistry across the periodic table to chromium to investigate a series of ethylene trimerization catalysts to understand the oxidation states accessible to chromium utilizing various spectroscopic and electrochemical techniques in collaboration with Chevron Phillips Chemical. In this chapter, we describe the redox chemistry of a series of novel Cr(III) complexes bearing bidentate *P*,*N* ligands. The redox reactivity of the Cr complexes is interrogated in the absence of ethylene and model substrates (i.e., hexyne). However, the oxidation states readily accessible to the Cr(III) complexes with aluminum-based reagents such as modified MAO and triethylaluminum ($AlEt_3$) by various electrochemical and spectroscopic methods including cyclic voltammetry, electrochemical quartz crystal microbalance (EQCM), electron paramagnetic resonance (EPR) spectroscopy, X-ray photoelectron (XP) spectroscopy, infrared (IR) spectroscopy, ultraviolet-visible (UV-vis) spectroscopy and XRD studies. Such methods are used

to interrogate the influence of bimetallic effects imposed by aluminum-based reagents on the redox chemistry accessible to the Cr(III) precatalysts.

Lastly, we transition across the periodic table again to the development of strategies to harness the chemistry of the lanthanide elements. Lanthanides primarily occur in the +III oxidation state, thus accessing more exotic oxidation states has developed as a strategy to advance lanthanide chemistry. Recent efforts by Evans have enabled synthetic accessibility of stable Ln(II) complexes;[22] similarly, works by Mazzanti[23] and La Pierre[24] have utilized strongly donating ligand scaffolds to access +IV oxidation states of praseodymium and terbium. An alternative to ligand-driven strategies[25] to tune the redox chemistry of metal complexes is the installation of Lewis acidic redox-inactive cations near redox-active metals as inspired by pioneering work from Agapie and co-workers regarding the tuning effects on the reduction potential of the Oxygen Evolving Complex (OEC) in Photosystem II.[26] This strategy involving redox-inactive metals has been extensively implemented for the tuning of redox properties of transition metals.[27] Recent efforts by Blakemore and co-workers have shown that this strategy is effective in the rational tuning of the uranium(VI/V) reduction potential and can be parameterized by the charge density effects engendered by the Lewis acidic cations.[28] However, the rational tuning of lanthanide elements in this context has received significantly less attention than it deserves, in that quantitative tuning of lanthanide elements, such as cerium, has not yet been achieved.[25,29] Parameterization of the tuning of lanthanides would provide significant insights into structural, electronic, and/or charge density that could contribute to developments of lanthanide-based clean energy technologies such as battery materials, catalysts, and magnets.

Encouraged by the effective tuning of the 5*f* metals (e.g., uranium) with redox-inactive metals, we endeavored to apply the same Lewis acidic metal-driven strategy to parameterize and rationally

tune the redox properties of lanthanides. In this effort, we anticipated that cerium's accessible +IV/+III redox couple would make it an attractive candidate for rational tuning in the under-explored area of 4*f* chemistry. Along this line, Chapter 8 describes the synthesis of a tripodal ligand that supports the divergent synthesis of a family of heterobimetallic cerium complexes that incorporates a range of redox-inactive Lewis acid metal cations (**M**; **M** = Li^{+}, K^{+}, Na^{+}, Ba^{2+}, Sr^{2+}, Ca^{2+}) for the systematic tuning of cerium. This chapter discusses the synthesis, characterization, XRD studies, UV-visible spectroscopy, X-ray absorption spectroscopy (XAS), and redox chemistry of the family of novel heterobimetallic cerium complexes. The results presented in Chapter 8 unveil the potential scope of rational tuning accessible to the lanthanide elements upon interaction with redox-inactive Lewis acidic metals for the first time.

1.2 References

[1] Lundgren, R. J.; Stradiotto, M., Key Concepts in Ligand Design. In *Ligand Design in Metal Chemistry*, 2016; pp 1-14.

[2] (a) Kanady, J. S.; Tsui, E. Y.; Day, M. W.; Agapie, T., A Synthetic Model of the Mn_3Ca Subsite of the Oxygen-Evolving Complex in Photosystem II. *Science* **2011,** *333*, 733-736. (b) Tsui, E. Y.; Tran, R.; Yano, J.; Agapie, T., Redox-inactive metals modulate the reduction potential in heterometallic manganese–oxido clusters. *Nat Chem.* **2013,** *5*, 293-299. (c) Kumar, A.; Lionetti, D.; Day, V. W.; Blakemore, J. D., Trivalent Lewis Acidic Cations Govern the Electronic Properties and Stability of Heterobimetallic Complexes of Nickel. *Chem. Eur. J.* **2018,** *24*, 141-149. (d) Reath, A. H.; Ziller, J. W.; Tsay, C.; Ryan, A. J.; Yang, J. Y., Redox Potential and Electronic Structure Effects of Proximal Nonredox Active Cations in Cobalt Schiff Base Complexes. *Inorg. Chem.* **2017,** *56*, 3713-3718. (e) Bang, S.; Lee, Y.-M.; Hong, S.; Cho, K.-B.; Nishida, Y.; Seo, M. S.; Sarangi, R.; Fukuzumi, S.; Nam, W., Redox-inactive metal ions modulate the reactivity and oxygen release of mononuclear non-haem iron(III)–peroxo complexes. *Nat Chem.* **2014,** *6*, 934-940. (f) Park, Y. J.; Ziller, J. W.; Borovik, A. S., The Effects of Redox-Inactive Metal Ions on the Activation of Dioxygen: Isolation and Characterization of a Heterobimetallic Complex Containing a Mn^{III}–(μ-OH)–Ca^{II} Core. *J. Am. Chem. Soc.* **2011,** *133*, 9258-9261. (g) Lacy, D. C.; Park, Y. J.; Ziller, J. W.; Yano, J.; Borovik, A. S., Assembly and Properties of Heterobimetallic CoII/III/CaII Complexes with Aquo and Hydroxo Ligands. *J. Am. Chem. Soc.* **2012,** *134*, 17526-17535. (h) Gupta, G.; Bera, M.; Paul, S.; Paria, S., Electrochemical Properties and Reactivity Study of [Mn^{V}(O)(μ-OR–Lewis Acid)] Cores. *Inorg. Chem.* **2021,** *60*, 18006-18016. (i) Kumar, A.; Lionetti, D.; Day, V. W.; Blakemore, J. D., Redox-Inactive Metal Cations Modulate the Reduction Potential of the Uranyl Ion in Macrocyclic Complexes. *J. Am. Chem. Soc.* **2020,** *142*, 3032-3041.

[3] Cooper, B. G.; Napoline, J. W.; Thomas, C. M., Catalytic Applications of Early/Late Heterobimetallic Complexes. *Cat. Rev.* **2012,** *54*, 1-40.

[4] (a) Comadoll, C. G.; Henke, W. C.; Hopkins Leseberg, J. A.; Douglas, J. T.; Oliver, A. G.; Day, V. W.; Blakemore, J. D., Examining the Modular Synthesis of [Cp*Rh] Monohydrides Supported by Chelating Diphosphine Ligands. *Organometallics* **2021,** *40*, 3808-3818. (b) Hopkins, J. A.; Lionetti, D.; Day, V. W.; Blakemore, J. D., Synthesis and reactivity studies of a [Cp∗Rh] complex supported by a methylene-bridged hybrid phosphine-imine ligand. *J. Organomet. Chem.* **2020,** *921*, 121294. (c) Hopkins, J. A.; Lionetti, D.; Day, V. W.; Blakemore, J. D., Chemical and Electrochemical Properties of [Cp*Rh] Complexes Supported by a Hybrid Phosphine-Imine Ligand. *Organometallics* **2019,** *38*, 1300-1310. (d) Boyd, E. A.; Lionetti, D.; Henke, W. C.; Day, V. W.; Blakemore, J. D., Preparation, Characterization, and Electrochemical Activation of a Model [Cp*Rh] Hydride. *Inorg. Chem.* **2019,** *58*, 3606-3615. (e) Peng, Y.; Ramos-Garcés, M. V.; Lionetti, D.; Blakemore, J. D., Structural and Electrochemical Consequences of [Cp*] Ligand Protonation. *Inorg. Chem.* **2017,** *56*, 10824-10831. (f) Henke, W. C.; Lionetti, D.; Moore, W. N. G.; Hopkins, J. A.; Day, V. W.; Blakemore, J. D., Ligand Substituents Govern the Efficiency and Mechanistic Path of Hydrogen Production with [Cp*Rh] Catalysts. *ChemSusChem* **2017,** *10*, 4589-4598. (g) Boyd, E. A.; Hopkins Leseberg, J. A.; Cosner, E. L.; Lionetti, D.; Henke, W. C.; Day, V. W.; Blakemore, J. D., Remote Oxidative Activation of a [Cp*Rh] Monohydride**. *Chem. Eur. J.* **2022,** *28*, e202104389.

[5] Kölle, U.; Grätzel, M., Metallorganische Rhodium(III)-Komplexe als Homogenkatalysatoren für die Photoreduktion von Protonen zu Wasserstoff an kolloidalem TiO_2. *Angew. Chem.* **1987,** *99*, 572-574.

[6] Quintana, L. M. A.; Johnson, S. I.; Corona, S. L.; Villatoro, W.; Goddard, W. A.; Takase, M. K.; VanderVelde, D. G.; Winkler, J. R.; Gray, H. B.; Blakemore, J. D., Proton–hydride tautomerism in hydrogen evolution catalysis. *PNAS* **2016,** *113*, 6409-6414.

[7] Pitman, C. L.; Finster, O. N. L.; Miller, A. J. M., Cyclopentadiene-mediated hydride transfer from rhodium complexes. *Chem. Commun.* **2016,** *52*, 9105-9108.

[8] (a) Kölle, U.; Kang, B.-S.; Infelta, P.; Comte, P.; Grätzel, M., Elektrochemische und pulsradiolytische Reduktion von (Pentamethylcyclopentadienyl)(polypyridyl)rhodium-Komplexen. *Chem. Ber.* **1989,** *122*, 1869-1880. (b) Steckhan, E.; Herrmann, S.; Ruppert, R.; Dietz, E.; Frede, M.; Spika, E., Analytical study of a series of substituted (2,2'-bipyridyl)(pentamethylcyclopentadienyl)rhodium and -iridium complexes with regard to their effectiveness as redox catalysts for the indirect electrochemical and chemical reduction of $NAD(P)^+$. *Organometallics* **1991,** *10*, 1568-1577. (c) Fukuzumi, S.; Kobayashi, T.; Suenobu, T., Efficient Catalytic Decomposition of Formic Acid for the Selective Generation of H_2 and H/D Exchange with a Water-Soluble Rhodium Complex in Aqueous Solution. *ChemSusChem* **2008,** *1*, 827-834.

[9] (a) Klingert, B.; Werner, H., Basische Metalle, XLII. Die Metall-Basizität der Komplexe $C_5Me_5Rh(PMe_3)_2$, $C_5Me_5Rh(C_2H_4PMe_3$ und $C_5Me_5Rh(C_2H_4)P_2Me_4$: Neue Pentamethyl-cyclopentadienylrhodium(I)- und -rhodium(III)-Verbindungen. *Chem. Ber.* **1983,** *116*, 1450-1462. (b) Faller, J. W.; D'Alliessi, D. G., Tunable Stereoselective Hydrosilylation of PhC∶CH Catalyzed by Cp*Rh Complexes. *Organometallics* **2002,** *21*, 1743-1746. (c) Faraone, F.; Bruno, G.; Schiavo, S. L.; Tresoldi, G.; Bombieri, G., η^5-Cyclopentadienylrhodium(I) complexes containing diphosphines and their reactions with the electrophiles H^+ and Me^+. Crystal and molecular structure of $[Rh(\eta\text{-}C_5H_5)(CO)(Ph_2PCH_2PPh_2)]$, a complex with a unidentate bis(diphenylphosphino)methane ligand. *J. Chem. Soc., Dalton Trans.* **1983**, 433-438.

[10] Boyd, E. A.; Lionetti, D.; Henke, W. C.; Day, V. W.; Blakemore, J. D., Preparation, Characterization, and Electrochemical Activation of a Model [Cp*Rh] Hydride. *Inorg. Chem.* **2019,** *58*, 3606-3615.

[11] Comadoll, C. G.; Henke, W. C.; Hopkins Leseberg, J. A.; Douglas, J. T.; Oliver, A. G.; Day, V. W.; Blakemore, J. D., Examining the Modular Synthesis of [Cp*Rh] Monohydrides Supported by Chelating Diphosphine Ligands. *Organometallics* **2021,** *40*, 3808-3818.

[12] Hopkins, J. A.; Lionetti, D.; Day, V. W.; Blakemore, J. D., Chemical and Electrochemical Properties of [Cp*Rh] Complexes Supported by a Hybrid Phosphine-Imine Ligand. *Organometallics* **2019,** *38*, 1300-1310.

[13] Hopkins, J. A.; Lionetti, D.; Day, V. W.; Blakemore, J. D., Synthesis and reactivity studies of a [Cp∗Rh] complex supported by a methylene-bridged hybrid phosphine-imine ligand. *J. Organomet. Chem.* **2020,** *921*, 121294.

[14] (a) Yasuo, T.; Takanori, Y.; Youkoh, K.; Shigetaka, M.; Hiroshi, K., Electronic Absorption Spectra of the Alkali Metal Complexes with Bipyridine. *Bull. Chem. Soc. Jpn.* **1969,** *42*, 2264-2267. (b) Ichiro, H.; Saburo, N., Electronic Structures of Tris(2,2′-bipyridyl) Complexes of Transition Metals in Lower Oxidation States. *Bull. Chem. Soc. Jpn.* **1971,** *44*, 2312-2321. (c) Bock, C. R.; Meyer, T. J.; Whitten, D. G., Electron transfer quenching of the luminescent excited state of tris(2,2'-bipyridine)ruthenium(II). Flash photolysis relaxation technique for measuring the rates of very rapid electron transfer reactions. *J. Am. Chem. Soc.* **1974,** *96*, 4710-4712. (d) Creutz, C., Bipyridine Radical Ions. *Comments Inorg. Chem.* **1982,** *1*, 293-311. (e) Kaim, W., The transition metal coordination chemistry of anion radicals. *Coord. Chem. Rev.* **1987,** *76*, 187-235.

[15] Lionetti, D.; Day, V. W.; Lassalle-Kaiser, B.; Blakemore, J. D., Multiple binding modes of an unconjugated bis(pyridine) ligand stabilize low-valent [Cp*Rh] complexes. *Chem. Commun.* **2018,** *54*, 1694-1697.

[16] (a) Nicholson, R. S.; Shain, I., Theory of Stationary Electrode Polarography. Single Scan and Cyclic Methods Applied to Reversible, Irreversible, and Kinetic Systems. *Anal. Chem.* **1964,** *36*, 706-723. (b)

Elements of Molecular and Biomolecular Electrochemistry An Electrochemical Approach to Electron Transfer Chemistry

[17] Gassman, P. G.; Macomber, D. W.; Willging, S. M., Isolation and characterization of reactive intermediates and active catalysts in homogeneous catalysis. *J. Am. Chem. Soc.* **1985,** *107*, 2380-2388.

[18] (a) Kumar, A.; Lionetti, D.; Day, V. W.; Blakemore, J. D., Redox-Inactive Metal Cations Modulate the Reduction Potential of the Uranyl Ion in Macrocyclic Complexes. *J. Am. Chem. Soc.* **2020,** *142*, 3032-3041. (b) Sconyers, D. J.; Blakemore, J. D., Distinguishing between homogeneous and heterogeneous hydrogen-evolution catalysis with molecular cobalt complexes. *Chem. Commun.* **2017,** *53*, 7286-7289.

[19] (a) Rakowski Dubois, M.; Dubois, D. L., Development of Molecular Electrocatalysts for CO2 Reduction and H_2 Production/Oxidation. *Acc. Chem. Res.* **2009,** *42*, 1974-1982. (b) Lewis, N. S.; Nocera, D. G., Powering the planet: Chemical challenges in solar energy utilization. *PNAS* **2006,** *103*, 15729-15735. (c) Qiao, J.; Liu, Y.; Hong, F.; Zhang, J., A review of catalysts for the electroreduction of carbon dioxide to produce low-carbon fuels. *Chem. Soc. Rev.* **2014,** *43*, 631-675.

[20] Hopkins Leseberg, J. A.; Lionetti, D.; Day, V. W.; Blakemore, J. D., Electrochemical Kinetic Study of [Cp*Rh] Complexes Supported by Bis(2-pyridyl)methane Ligands. *Organometallics* **2021,** *40*, 266-277.

[21] Sydora, O. L., Selective Ethylene Oligomerization. *Organometallics* **2019,** *38*, 997-1010.

[22] MacDonald, M. R.; Bates, J. E.; Ziller, J. W.; Furche, F.; Evans, W. J., Completing the Series of +2 Ions for the Lanthanide Elements: Synthesis of Molecular Complexes of Pr^{2+}, Gd^{2+}, Tb^{2+}, and Lu^{2+}. *J. Am. Chem. Soc.* **2013,** *135*, 9857-9868.

[23] (a) Palumbo, C. T.; Zivkovic, I.; Scopelliti, R.; Mazzanti, M., Molecular Complex of Tb in the +4 Oxidation State. *J. Am. Chem. Soc.* **2019,** *141*, 9827-9831. (b) Willauer, A. R.; Palumbo, C. T.; Fadaei-Tirani, F.; Zivkovic, I.; Douair, I.; Maron, L.; Mazzanti, M., Accessing the +IV Oxidation State in Molecular Complexes of Praseodymium. *J. Am. Chem. Soc.* **2020,** *142*, 5538-5542.

[24] Rice, N. T.; Popov, I. A.; Russo, D. R.; Bacsa, J.; Batista, E. R.; Yang, P.; Telser, J.; La Pierre, H. S., Design, Isolation, and Spectroscopic Analysis of a Tetravalent Terbium Complex. *J. Am. Chem. Soc.* **2019,** *141*, 13222-13233.

[25] Robinson, J. R.; Gordon, Z.; Booth, C. H.; Carroll, P. J.; Walsh, P. J.; Schelter, E. J., Tuning Reactivity and Electronic Properties through Ligand Reorganization within a Cerium Heterobimetallic Framework. *J. Am. Chem. Soc.* **2013,** *135*, 19016-19024.

[26] (a) McEvoy, J. P.; Brudvig, G. W., Water-Splitting Chemistry of Photosystem II. *Chem. Rev.* **2006,** *106*, 4455-4483. (b) Yano, J.; Yachandra, V., Mn4Ca Cluster in Photosynthesis: Where and How Water is Oxidized to Dioxygen. *Chem. Rev.* **2014,** *114*, 4175-4205.

[27] (a) Reath, A. H.; Ziller, J. W.; Tsay, C.; Ryan, A. J.; Yang, J. Y., Redox Potential and Electronic Structure Effects of Proximal Nonredox Active Cations in Cobalt Schiff Base Complexes. *Inorg. Chem.* **2017,** *56*, 3713-3718. (b) Bang, S.; Lee, Y.-M.; Hong, S.; Cho, K.-B.; Nishida, Y.; Seo, M. S.; Sarangi, R.; Fukuzumi, S.; Nam, W., Redox-inactive metal ions modulate the reactivity and oxygen release of mononuclear non-haem iron(III)–peroxo complexes. *Nat. Chem.* **2014,** *6*, 934-940. (c) Park, Y. J.; Ziller, J. W.; Borovik, A. S., The Effects of Redox-Inactive Metal Ions on the Activation of Dioxygen: Isolation and Characterization of a Heterobimetallic Complex Containing a Mn^{III}–(μ-OH)–Ca^{II} Core. *J. Am. Chem. Soc.* **2011,** *133*, 9258-9261. (d) Lacy, D. C.; Park, Y. J.; Ziller, J. W.; Yano, J.; Borovik, A. S., Assembly and Properties of Heterobimetallic $Co^{II/III}$/Ca^{II} Complexes with Aquo and Hydroxo Ligands. *J. Am. Chem. Soc.* **2012,** *134*, 17526-17535. (e) Gupta, G.; Bera, M.; Paul, S.; Paria, S., Electrochemical Properties and Reactivity Study of [Mn^{V}(O)(μ-OR–Lewis Acid)] Cores. *Inorg. Chem.* **2021,** *60*, 18006-18016.

[28] Kumar, A.; Lionetti, D.; Day, V. W.; Blakemore, J. D., Redox-Inactive Metal Cations Modulate the Reduction Potential of the Uranyl Ion in Macrocyclic Complexes. *J. Am. Chem. Soc.* **2020,** *142*, 3032-3041.

[29] (a) Rice, N. T.; Su, J.; Gompa, T. P.; Russo, D. R.; Telser, J.; Palatinus, L.; Bacsa, J.; Yang, P.; Batista, E. R.; La Pierre, H. S., Homoleptic Imidophosphorane Stabilization of Tetravalent Cerium. *Inorg. Chem.* **2019,** *58,* 5289-5304.

Chapter 2

Electrochemistry in Organometallic Chemistry

This chapter is adapted from a published manuscript:

Hopkins Leseberg, J.A,[#] Henke, W.C.,[#] and Blakemore, J.D.* "Electrochemistry in Organometallic Chemistry" in *Comprehensive Organometallic Chemistry IV*, Meyer, K. and Holland, P., Eds.; Elsevier: Amsterdam, forthcoming, 37 pages; *in press.*

2.1 Introduction

Many organometallic systems are redox active, featuring multiple accessible oxidation states that may each have their own unique properties. To study these redox-active systems, electrochemical techniques have been widely adopted by organometallic chemists to better understand the synthetic, kinetic, and thermodynamic properties that involve changes in oxidation state. Electrochemical research is typically complemented by study of reactions with chemical redox reagents and isolation of products. These parallel approaches to studying organometallic redox chemistry represent a truly powerful combination.

Organometallic electrochemistry emerged in the 1950s. Notably, soon after the synthesis of ferrocene by Kealy and Pauson,[1] studies on the redox chemistry of this species as well as the first polarographic investigation by Wilkinson, Rosenblum, Whiting, and Woodward enabled the correct assignment of the now famous "sandwich" structure of the compound.[2] Since these early days, studies of both aqueous and non-aqueous organometallic electrochemistry have flourished, enabled by the wide availability of potentiostats in laboratories.[3] Readers of this review may be unfamiliar with common electrochemical methods, and in this case, we suggest further reading in the wide variety of high quality books[4] and reviews[5,6,7] that are available to guide the reader through the fundamentals of workhorse electrochemical techniques such as cyclic voltammetry (CV) and controlled potential electrolysis (CPE). References throughout this review are cited to assist readers in identification of appropriate further resources.

The potentiostat, which readily enables the three-electrode cell configuration for electrochemical work wherein potentials can be measured with respect to a well-known reference electrode potential, can be thought of as a ready means of understanding free energy (ΔG) changes associated with organometallic redox reactions. Using the Nernst equation (2.1),[8] the reduction

potential (E) of a given compound (analyte) present in solution may be determined by consideration of the standard potential (E^o) of the compound and the concentrations of the oxidized and reduced forms of the analyte present in solution. Conversely, knowing the concentrations of these forms at the surface of the working electrode as well as the standard potential, one can readily calculate the effective potential of a given mixture. Thus, using the potentiostat to determine the reduction potential E of a given species or mixture, the free energy change ΔG associated with electron transfer to a second redox active species can be calculated from the difference in reduction potentials (ΔE) using equation (2.2).

$$E = E^o - \frac{RT}{nF} ln \frac{[ox]}{[red]} \tag{2.1}$$

$$\Delta G = -nF\Delta E \tag{2.2}$$

The values of E are best determined using a potentiostat during cyclic voltammetry (CV) experiments. Determination of E from cyclic voltammetry experiments is particularly illuminating for synthetic chemists interested in exploring the accessible oxidation states of their compounds, because such a determination allows for the selection of suitable chemical redox reagents for the oxidation, or reduction, of organometallic complexes. A list of suitable oxidants and reductants for chemical synthesis were tabulated for this purpose in a popular *Chemical Reviews* article by Connelly and Geiger.[9]

In addition to thermodynamic insights of the type described above, monitoring of redox reactions by voltammetry can often provide significant kinetic and mechanistic information about chemical reactivity that precedes or, more commonly, follows electron transfer from an electrode. Organometallic chemists can unite the study of chemical kinetics with electrochemical methods by leveraging the powerful concepts of electrochemical kinetic Zone Diagrams and methods like foot-of-the-wave analysis (FOWA) that were developed and popularized by Savéant, Costentin,

and others.[10,11] In such efforts, examining the shape of a redox 'wave' in a cyclic voltammogram and comparing it to those of standard waves organized into so-called Zone Diagrams can provide key insights into the kinetic regime and mechanism associated with the given redox process of an organometallic analyte. FOWA is an excellent companion method to such approaches, particularly when catalytic processes are involved, as it allows for the determination of observed rate constants under a variety of conditions, particularly those involving "fast" catalysts that may rapidly consume substrates or display product inhibition.

Information on the design of experiments with CV to interrogate (electro)catalysis are described in detail in Sections 1.5 and 1.6 of this chapter. Details that can be studied include quantification of key catalyst properties such as the overpotential required to achieve a given transformation with a certain catalyst.[12] Such electroanalytical work to interrogate catalysis is often also paired with bulk electrolysis efforts that are aimed at generation of isolable and/or useful quantities of electrocatalytically generated products; information on such efforts is also given at appropriate points in Sections 1.5 and 1.6. In these sections, examples are taken from areas of current interest in redox catalysis, including both small-molecule substrate activations of relevance to energy science as well as select electrosynthetic organic reactions.

In this chapter, our goal has been to weave together the elementary concepts needed to carry out and interpret results from electrochemical studies of organometallic compounds. The individual sections of the chapter have been organized to provide the reader with information on the diverse facets of the vibrant field of organometallic electrochemistry. Effort has been made to treat these facets in a balanced way, such that this chapter will provide both the key historical developments that underpin a given area as well as recount more recent developments that may be of use to researchers interested in applying electrochemical methods in their own work. We

highlight the usefulness of pairing chemical and electrochemical methods in order to understand, in a comprehensive manner, the redox chemistry of organometallic species. Specific examples are given to highlight both practical aspects and fundamental considerations for gaining insights into stoichiometric and catalytic chemistries. Our hope is that this primer inspires further growth and development in the field of organometallic electrochemistry.

2.2 Developments in Electrodes, Materials, and Methods

2.2.1 Early Electrochemical Studies

The foundational work that initiated the field of electrochemistry dates back to the late 18th century; these very early studies will not be reviewed here in detail.[13] Rapid development of the field as we know now it began with studies in the mid-20th century focused primarily on main-group organometallic compounds.[14,15] These studies, taking place before the synthesis and structural identification of ferrocene, largely focused on the reductive chemistry of Hg and Mg compounds with direct current (DC) polarography. DC polarography was the dominant electroanalytical method prior to the 1960s and utilized a mercury electrode (in the form of metallic Hg(0)) as the working surface for measurements. However, Hg(0) can undergo a thermodynamically accessible oxidation to Hg(I); this feature made studying many oxidation processes difficult via this method.[5]

The synthesis and determination of the sandwich structure of ferrocene marked a significant development in the field of organometallic chemistry, in that this compound displays chemically stable iron(II) form as well as a stable oxidized form containing iron(III), known as ferrocenium.[5,16] The first electrochemical characterization of ferrocene, which demonstrated the interconversion of these oxidation states, was a landmark study that heavily contributed to the development of modern organometallic electrochemistry. [2,3,5,17]

The first major studies of organometallic electrochemistry can be attributed to Raymond Dessy's research group.[5] The Dessy group published a series of papers in 1966 detailing their work in organometallic electrochemistry[18] using Hg electrodes to study cathodic processes as well as the use of polarography,[19] cyclic voltammetry, bulk cathodic electrolysis, and monitoring of solutions via voltammetry and "back electrolysis" to recover the compounds under study.[20] Building on these initial studies, systematic electrochemical investigations have become a key method for studying the redox chemistry of organometallic compounds.

2.2.2 Major Advances in Materials and Measurement

Following the foundational early studies, experimental work in electrochemistry was expanded significantly by two key advances: the use of solid electrodes and the operational-amplifier-based potentiostat. Solid electrodes with reproducible and reliable surface properties, features thought to be impossible to achieve in prior years, were developed by Ralph Adams at the University of Kansas; such electrodes enable facile electrochemical investigation of redox processes without the requirement of mercury or other challenging electrode materials.[21] The advent of solid electrodes expanded the accessible positive potential range and obviated the need for toxic Hg for electrodes. The second major advancement in technology in this period was the use of the operational-amplifier-based three-electrode potentiostat.[22,23,24,25,26] The employment of the three-electrode system, now universally applied in electroanalytical work, minimizes resistive errors especially in lower polarity solvents of relevance to organometallic chemistry carried out in solvents like tetrahydrofuran or acetonitrile. These technological advances have enabled the current popularity of studying non-aqueous redox processes of organometallic compounds.

Parallel to these improvements in experimental conditions, numerical approaches to solving the mathematical relationships underpinning diffusion and electron transfer kinetics enabled a once

qualitative technique to become a quantitative analytical tool for investigating organometallic redox processes. In 1964, Nicholson and Shain used a numerical integration approach to map the features encountered in cyclic voltammetry data arising in the cases of several common redox mechanisms. To this day, the relationships established in this work are bedrock features of the quantitative cyclic voltammetry analyses used in modern research with electrochemistry.[27]

Building on the redox mechanisms outlined by Nicholson and Shain, the work of Jean-Michel Savéant in "molecular electrochemistry" constitutes a major contribution to the systematic quantification of heterogeneous electron transfer chemistry and interpretation of data for cases where electron transfer at an electrode is coupled with follow-up chemical reactivity.[28] This work emphasizes the critical aspects of electron transfer and reaction kinetics, enabling study of complicated reaction schemes that involve short-lived electrochemically generated complexes that can be quantitatively investigated over periods of time that are readily interrogated with electrochemical methods.

Several helpful resources regarding the values of standard reduction potentials and the behavior of various elements under electrochemical conditions also appeared for the first time in the mid-twentieth century. Marcel Pourbaix introduced the use of potential-pH diagrams, now known as Pourbaix diagrams, which were first reported in 1945 to understand electrochemical reactions in aqueous media at an electrode. Pourbaix diagrams enable prediction of thermodynamic equilibrium states of reactions involving a specific element and its ions, and key solid, liquid, and gas phase compounds in aqueous media.[29] Similarly, in 1952, Wendell Latimer published potential diagrams that used the then-standard "oxidation potentials" to summarize thermodynamic data for inorganic compounds, including heat of formation, free energy of formation, entropies and equilibrium constants.[30] The eponymous Latimer diagrams summarize the key information needed

to predict the relative stability of oxidation states at a given pH, and represent electrochemical equilibria for compounds with multiple oxidation states. Bard, Parsons and Jordan expanded and modernized the work of Latimer in a noted volume published in 1985,[31] providing a thorough tabulation of standard reduction potentials in aqueous solution to assist in predictions of chemical reactions and behavior of metal-solution interfaces. Modern data available at the time was used in the updated volume and transitioned potential values to current notations and conventions used by IUPAC, particularly the standard reporting of half-reaction potentials as reductions.

2.2.3 Modern Electrochemical Methods and Techniques

Early developments in electrochemical methodology and technology have led to a plethora of modern techniques using electrochemistry. A compilation of modern electrochemical techniques can be found in Kissinger and Heineman's *Laboratory Techniques in Electroanalytical Chemistry*.[32]

The advent of gloveboxes with inert atmosphere has significantly advanced the facile study of air- and moisture-sensitive organometallic compounds. Accordingly, there is often interest among researchers to carry out electrochemical investigations inside the glovebox. There are two common configurations that enable this.

The first setup involves keeping both the potentiostat and electrochemical cell inside the glovebox, which requires either specialized USB feedthrough ports through the dry box wall to reach the operating computer or a wireless, WiFi-enabled potentiostat. The wireless potentiostat obviates the need for cables; the user can place the potentiostat in the glovebox and control it from a nearby computer.[33] However, in this configuration, it is advisable to exercise extreme caution and minimize exposure of the potentiostat to organic solvent vapors, as these can damage the electronics. Common sources of vibrations present near gloveboxes, like vacuum pumps and

refrigerator compressors, may also cause electronic noise and contribute to unexpected current flows by agitation of solutions under investigation.[34] Careful grounding of the potentiostat is another important consideration in this configuration; this can be done by grounding the instrument to the outside of the dry box. This approach can allow the glovebox to function as a Faraday cage, reducing electronic noise that originates from outside the glovebox that could impact electrochemical studies.

The second setup is the placement of the potentiostat outside the dry box, with connection of the electrochemical cell to the potentiostat through the glovebox wall using custom feedthroughs, or a more standard port with a KF-40 flange that can accommodate the needed cables. Alternatively, some gloveboxes come equipped with bulkhead connections built into side-panels, ready for wire-clips to be attached inside and outside for experiments. The longer cables needed for this cell-inside, potentiostat-outside configuration may be problematic for Electrochemical Impedance Spectroscopy (EIS) measurements, as they can introduce additional capacitance to the total electrochemical system.[34] The use of short, shielded cables with the fewest possible connections can minimize electrical noise as well as capacitance. In both configurations, electrical devices placed near the instrument or electrochemical cell may cause spurious signals arising from electrical or magnetic fields; for example, stir plates left on during voltammetry can induce significant noise or non-chemical contributions to the data. Finally, static electricity can also be present in gloveboxes; use of shielded cables minimizes this type of interference.

In potential step methods, the electrode potential is rapidly changed from a value at which no Faradaic current is flowing to a potential value at which the potential difference is sufficient to induce electron transfer. Potential step chronoamperometry measures the current passed at the working electrode at a fixed potential.[42] Using the Cottrell equation (2.3) this method can be used

to determine the number of electrons involved in an electron transfer reaction (n) and diffusion coefficient of the species undergoing electron transfer (typically, D_0). In a chronoamperometry measurement, an average value of current (i) is determined over a range of time at an electrode. From this measurement of the diffusion coefficient of electroactive species if the number of electrons transferred is known and vice versa. However, often D_0 and n are both unknown. D_0 can be estimated for most freely diffusing small-molecule/organometallic species to be on the order of 10^{-5} cm^2 s^{-1}. Alternatively, diffusion coefficients can be experimentally determined with hydrodynamic measurements using a rotating disk electrode to carry out Koutecký-Levich Analysis.[35,36] The number of electrons can be determined indirectly using chemical reduction with stoichiometric reductants[9] and characterization of chemically prepared reduced forms. Once either of the D_0 or n variables are known, the other variable can be calculated using the chronoamperometry measurement and the Cottrell equation.

$$i = \frac{nFAD_O^{1/2}C_O^*}{\pi^{1/2}t^{1/2}} \tag{2.3}$$

Potential step chronocoulometry enables measurement of the charge (Q) passed following a potential step versus time. Charge (Q) is often quantified directly in the instrument with this method, although integrating the current (i) flowing during the potential step can also return the total charge passed at a given time through mathematical means.[42] Chronoamperometry, the measurement of current passed during a potential step versus time, is advantageous when the goal is to monitor current as a function of time, while chronocoulometry is useful for monitoring the total charge passed as a function of time. Although chronocoulometry and chronoamperometry are similar and related because charge passed and current flow are related by calculus, the two techniques are especially useful for different purposes depending on context. Chronoamperometry is often utilized for investigation of catalytic processes because changes in current flow (changes

in the rate of a redox reaction), read out directly in chronoamperometry as current vs. time, are often straightforward to observe and interpret. For example, marked drop-off in current flow may suggest substrate consumption or catalyst decomposition during controlled potential electrolysis used for interrogating a molecular electrocatalyst. Chronocoulometry, on the other hand, reads out the total charge passed vs. time during a given experiment, making it useful for instantaneous determinations of expected product yields from redox reactions or calculation of predicted turnover numbers during a CPE investigation of a molecular electrocatalyst. However, as chronocoulometry records the total charge passed versus time, it can be more difficult to observe data trends that indicate changes in the chemical processes occurring during electrolysis. Chronocoulometry uses circuitry in the potentiostat to determine the number of electrons transferred, whereas chronoamperometry directly measures the current flow as a function of time, giving a mathematical (error-minimizing) benefit to use of chronoamperometry for measurements related to rates and chronocoulometry for measurements related to product yields.

Controlled potential electrolysis[37] (CPE) is an electrochemical technique in which the working electrode is held at a constant potential and monitored until completion of the redox reaction. Controlled potential methods such as bulk electrolysis requires a potentiostat that is capable of passing relatively large amounts of current and maintaining often substantial cell voltages. Additionally, placement of the working and counter electrodes is important in bulk electrolysis work to minimize uncompensated resistance; two-compartment cells are often useful for separation of the working and counter electrodes with a glass frit. Careful determination of the reduction potential of the target electroactive species by voltammetry is typically essential to ensure high current efficiency and complete conversion of the oxidized or reduced starting species.

Comparison of the number of Coulombs passed during an electrolysis to the amount of product formed is then used to determine the Faradaic efficiency of the system.

Potential sweep methods are techniques that apply a range of applied potentials over time, in which the resulting current passed at the working electrode is measured as a function of potential. The effective midpoint potential ($E^{0\prime}$) of a target species can be measured by varying the potential over a range to identify the potential associated with electron transfer. The most commonly used potential sweep methods are cyclic voltammetry (CV) and linear sweep voltammetry. Linear sweep voltammetry (LSV)[42] is a technique in which the potential is varied linearly with time and the current passed is measured. In LSV of an electroactive species, if the scan begins well positive of the $E^{0\prime}$, essentially only non-Faradaic current will flow and [ox]>[red]. However, once the potential sweeps to the reduction potential current starts to flow, [ox] and [red] are equal at $E^{0\prime}$. As the potential sweeps negative of $E^{0\prime}$, however, [ox]<[red] at the electrode surface.

CV is a method in which the potential is varied over a range like in LSV, but the potential scan is reversed after the $E^{0\prime}$ and towards the initial potential. The intricacies and powerful opportunities afforded by CV will be discussed here and in depth in later sections.[42] For those unfamiliar with running CV experiments, we direct the reader to several foundational books and articles which will provide practical guidance for organometallic chemists beginning to utilize electrochemistry. In particular, the books presented by Zoski,[38] Bard and Faulkner,[42] and Constentin and Savéant[28] can provide the reader with a comprehensive guide to the theory, instrumentation, and electrochemical techniques necessary for the investigation of organometallic complexes. Popular educational articles[7] and resources[39] are available that provide initial information on selecting solvents, electrolytes, electrodes, and use of electrochemical cells to perform a CV experiment.

Differential pulse voltammetry (DPV)[40] allows interrogation of a system via an approach similar to linear sweep voltammetry, but involving a more complex pulse sequence that minimizes non-Faradaic currents in the final data output. This technique, like CV and LSV, can be used for a variety of mechanistic and kinetic measurement applications.[41] DPV can be preferred over CV methods because the series of pulses applied at steadily changing potentials minimizes background from background charging of the electrode.[42]

Square wave voltammetry[41,43] is similar to DPV and utilizes a discontinuous potential change in which its current output is obtained as a symmetrical peak, unlike the current output obtained in linear sweep voltammetry that displays the direct influence of diffusion. Like DPV, square wave is a technique that is useful for detection of very low concentrations of analytes. The use of discontinuous potential in this technique allows measurement of Faradaic currents at the points in which current from double layer charging at the electrode is negligible.

Digital computer simulations of voltammetry data[32,44,45] can be employed as a complement to experimental cyclic voltammetry to help decipher and quantify coupled electron transfer reactions. Simulations of cyclic voltammograms can be performed by changing variables such as electrode area, solution concentration, scan rate and switching potential, in order to extract kinetic information from voltammograms. Mathematically derived differential equations can be applied to organometallic systems to describe the concentration of a species in solution as a function of time. Other variables that are described by these differential equations include diffusion, convection, and migration; however, understanding these variables can be complex due to heterogenous chemical processes occurring at the electrode surface and homogenous chemical reactions occurring in the bulk solution.[46] Some simulation packages available include:

ELSIM,[47,48,49,50] DigiSim,[51] DigiElch,[52] CVSIM[53] and CVPLOT.[53] An exhaustive list of packages and description can be found in *Digital Simulation in Electrochemistry.*[46]

Low temperature cyclic voltammetry[54] is an attractive technique for interrogating mechanistic pathways that create electrogenerated transient intermediate species. Additionally, this technique enables electrochemists to quantify thermodynamic parameters such as enthalpy change and kinetic parameters such as diffusion rate and heterogenous electron transfer rates of electron transfer reactions, and aids in the understanding of intricate coupled chemical reactions. Two cells are suitable for this technique, the *dip-type* cell that have an elongated cell body suitable for immersion in a coolant and *jacketed* cell that has a second outer jacket with feed throughs for coolants. Special care needs to be taken to choose an appropriate solvent and supporting electrolyte that can be used at low temperatures; a comprehensive list can be found in *Laboratory Techniques in Electroanalytical Chemistry.*[32] An additional challenge is that solution resistance increases at low temperatures; it is therefore often necessary to electronically compensate for the solution resistance.[32]

Spectroelectrochemistry[55] is a technique that allows for simultaneous electrochemical and spectroscopic interrogation of a compound. Spectroelectrochemistry enables the observation of spectral changes *in situ* to understand the reactions occurring at an electrode surface. These cells contain an optically transparent electrode (OTE) that are constructed of a conductive material such as platinum, gold, carbon, or a semiconductor material such as doped tin oxide on glass or quartz. Various spectroscopic techniques such as electronic absorption spectroscopy, infrared spectroscopy and Raman spectroscopy can be used in parallel with electrochemical methods.[42]

The use of chemically modified electrodes,[56] in which electrodes are purposefully modified via adsorption, coating or attachment of molecules to the electrode surface, is also a robust area of

inquiry relevant to numerous fields. Modified electrodes are studied for their interesting properties in applications such as electrocatalysis, display devices, analytical applications and photoelectrochemical applications.

Alternating current (AC) voltammetry is a small-amplitude method that involves the application of sinusoidal wave voltage to an electrochemical cell. This method enables deciphering of contributions to electrochemical behaviors of, separately, the analyte concentration, the identity of solution components, kinetics of charge transfer, and the nature of the double layer capacitance at the electrode/electrolyte interface. This technique can be used primarily for mechanistic studies and allows separation of Faradaic and non-Faradaic current responses.[32]

Modern electrochemical methods and techniques will be discussed in further detail in the context of organometallic electrochemistry throughout this chapter.

2.3 Chemical Reactivity at the Working Electrode Surface

2.3.1 Electrochemically and Chemically Reversible Electron Transfers

Electron transfer can be homogenous or heterogenous in nature. Homogenous electron transfer is the transfer of an electron from one solubilized molecule to another. The movement of an electron from the highest occupied molecular orbital (HOMO) of a donor molecule and the lowest unoccupied molecular orbital (LUMO) of a given acceptor should be thermodynamically favored to take place. The kinetics of homogeneous electron transfer are most commonly discussed in the context of Marcus Theory.[57] On the other hand, heterogenous electron transfer typically occurs in molecular electrochemistry, an electron being transferred from a solid electrode to a solubilized molecule in solution that is located near the electrode surface. This type of electron transfer is associated with electrochemical reduction/oxidation in which the driving force for electron transfer to a compound in solution is based on the potential applied to the electrode by the potentiostat.

Electron transfer reactions are ubiquitous in organometallic electrochemistry and it is therefore often important to understand how electron transfer to/from an electrode affects the structure and composition of organometallic complexes. Electron transfer reactions are broadly classified as either "reversible" or "irreversible" processes. However, these classifications should be more specific: electron transfer reactions can be classified as either *electrochemically (ir)reversible* and/or *chemically (ir)reversible*. *Chemical reversibility* refers to processes in which the electroactive species are stable and homogenous in their reduced and oxidized forms.[7] *Electrochemical reversibility* speaks to the rate of electron transfer kinetics between the electrode surface and the electroactive species, with fast rates of electron transfer giving rise to *electrochemically reversible* behavior. *Electrochemically reversible* systems are referred to as Nernstian, meaning that they obey the Nernst equation (2.1) by virtue of equilibrium concentrations being fully established at the electrode surface.[7,42] *Processes that are both electrochemically* and *chemically reversible* have a potential separation between cathodic and anodic peaks (ΔE_p) of 57 mV in cyclic voltammetry, a value derived first in the work of Nicholson and Shain for electron transfer rates at the fast limit. The term *quasi-reversible* refers to electron transfers that appear chemically reversible but have $\Delta E_p > 57$ mV, or for cases where the forward and backward rates are similar but not quite equal.

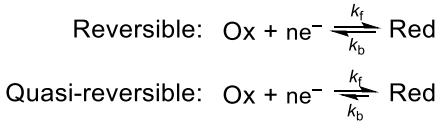

Scheme 2.1: Reversible electron transfer ($k_f = k_b$) and quasi-reversible electron transfer ($k_f \sim k_b$).

Reversible electron transfers can be described with the E mechanism notation used by Nicholson and Shain, referring to the involvement of a single electron transfer step.[27] The most well-known example of an organometallic complex that engenders an E mechanism upon

oxidation and reduction is ferrocene/ferrocenium; ferrocene is ubiquitous in organometallic electrochemistry in part due to its ability to undergo fast electron transfer with minimal redox-induced structural change. Cycling of the oxidation state of the ferrocenium/ferrocene couple results in very little structural distortion, giving rise to fast electron transfer and therefore it is typically electrochemically reversible.[58] This has led to the widespread adoption of ferrocenium/ferrocene ($Fc^{+/0}$) as an internal reference for the reporting of electrochemical potentials for redox events.[59] This is because the reversible behavior of the $Fc^{+/0}$ couple holds true for a range of solvents; there is little to no structural rearrangement upon electron transfer, and therefore there are no significant influences of solvent interactions that would otherwise affect the appearance of the voltammogram. Although ferrocene is traditionally viewed as highly stable and is therefore used as a standard for normalizing potential, readers should be aware that ferrocene can be oxidized to a dication[60] or reduced to an anion,[61] or degrade from reactions with electrogenerated species.

As the reader progresses ahead in this chapter toward the CV and CPE sections, please note that midpoint potentials ($E_{1/2}$ values) for redox processes may be reported, at various points, versus the ferrcenium/ferrocene couple ($Fc^{+/0}$) as well as versus SHE, the standard hydrogen electrode. This is because, in order to for a reported potential to be a standard reduction potential (E^0), the conditions of the measurement of the potential must satisfy the Nernst equation (see equation 2.2), wherein the temperature is 25 ºC, any gases involved are present at 1 atm, and the molarity of the analytes are 1 M.[62] These conditions are not always readily achievable or desireable in organometallic chemistry, and thus midpoint potentials measured for various redox processes are often simply reported as $E_{1/2}$ values vs. $Fc^{+/0}$ or other reference potentials. In order to convert between V vs SHE and V vs $Fc^{+/0}$, E^0 would need to be rigorously determined for ferrocene in

water. However, ferrocene is insoluble in water, limiting the ability to rigorously determine the E^0 of $Fc^{+/0}$ or other insoluble redox active species in terms of V vs $Fc^{+/0}$, limiting the precise and rigorous interconversion between V vs SHE and V vs $Fc^{+/0}$.

Thermodynamic half-cell potentials for processes like proton reduction, oxygen reduction, and water oxidation are typically discussed with referencing of V vs SHE instead of V vs $Fc^{+/0}$ because such small-molecule reactions often do not have well-defined standard potentials in non-aqueous solvents. We note, however, that the conversion between the two references (SHE and $Fc^{+/0}$) has been estimated to be $Fc^{+/0}$ = +400 mV vs SHE.[9]

Under non-aqueous conditions, the midpoint potential, $E_{1/2}$, measured using cyclic voltammetry of the $Fc^{+/0}$ couple can provide an estimate of the formal potential, $E^{0'}$, of the $Fc^{+/0}$ couple.[63] The midpoint potential and formal potential of the ferrocenium/ferrocene couple are virtually equivalent because of the electrochemically and chemically reversible nature of the redox chemistry of these species. Therefore, a traditional measurement to determine the standard reduction potential of ferrocenium/ferrocene (carried out so as to satisfy all the requirements of the Nernst equation) in which the potential of a half-cell prepared with a 1:1 mixture of ferrocenium and ferrocene would be compared to a reference potential can be reliably concluded to be comparable to that of the operationally much simpler measurement of the midpoint potential of the $Fc^{+/0}$ redox system via CV.

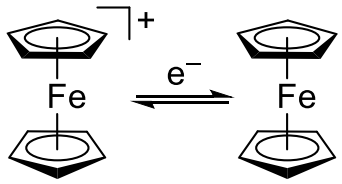

E: $A + e^- \rightleftharpoons B$

Scheme 2.2: One-electron reduction of ferrocenium/ferrocene. General E mechanism. Electrode electron transfer reaction.

2.3.2 Coupled Chemical Reactions

Chemical reactions are often coupled to electron transfer, because gain or loss of electrons by a metal complex can cause structural changes and/or changes in the frontier orbitals in the complex. An extensive review of examples of electrochemically induced redox chemistry is beyond the scope of this chapter, but a thorough list of examples is given in a review from Geiger.[5] Electronic changes often induce chemical processes due to the instability of formed intermediate species that result from electron transfer. *Irreversible* electron transfer processes involve a charge transfer that is rate limiting. A *non-reversible* electron transfer processes involve thermodynamically reversible process as well as a redox-induced chemical reaction.

Irreversible: $Ox + ne^- \underset{k_b}{\overset{k_f}{\rightleftharpoons}} Red$

Non-reversible: $Ox + ne^- \longrightarrow Red$

Scheme 2.3: Irreversible electron transfer ($k_f >> k_b$) and non-reversible electron transfer.

2.3.3 EC Mechanism

There are multiple mechanisms by which electron transfers and chemical processes can be coupled together at an electrode.[27] The simplest of these is the EC mechanism, in which an electron transfer is followed by a first-order or pseudo-first-order reaction that occurs in solution. If the

initial electron transfer is fast, the follow-up homogeneous chemical reaction often does not interfere with the electrochemical response in a kinetic sense. In the case of the EC mechanism, the redox-induced chemical reaction is the only rate limiting factor except for diffusion.[28]

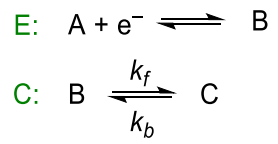

Scheme 2.4: General EC mechanism. Electrode electron transfer flowed by a first-order or pseudo-first-order homogenous reaction.

The zone diagrams developed by Savéant are helpful to understand redox reactions that engender a general EC mechanism. Zone diagrams serve to identify the relationship between the rate of diffusion, the kinetic properties of the reduction-induced reaction (as a function of equilibrium constant, K) and the ratio of the coupled chemical reaction rate and diffusion rate (quantified in a dimensionless parameter, λ). The scan rate at which the CV is measured is inversely proportional to λ. This inverse relationship means that as the scan rate is increased for a CV measurement, the λ parameter decreases. When scan rate is high in a reduction, λ is small, allowing less time for the reduced form of the organometallic complex to diffuse in solution, and therefore there is less time for the coupled chemical reaction to occur at the electrode surface and influence the electron transfer equilibrium that is measured as current. At faster scan rates, the anodic peak current associated with reoxidation increases until it appears to be quasi-reversible, indicating that the coupled chemical reaction has had insufficient time to occur. Conversely, at low scan rates the coupled chemical reaction appears as an irreversible process, because there is sufficient time for the coupled chemical reaction to occur at the electrode surface, and the back reaction is eliminated.[28] Two examples of kinetic zone diagrams are shown in Figure 2.1; for a complete set of the diagrams discussed in this chapter please refer to Savéant and Costentin's

Elements of Molecular and Biomolecular Electrochemistry: An Electrochemical Approach To Electron Transfer Chemistry.[28]

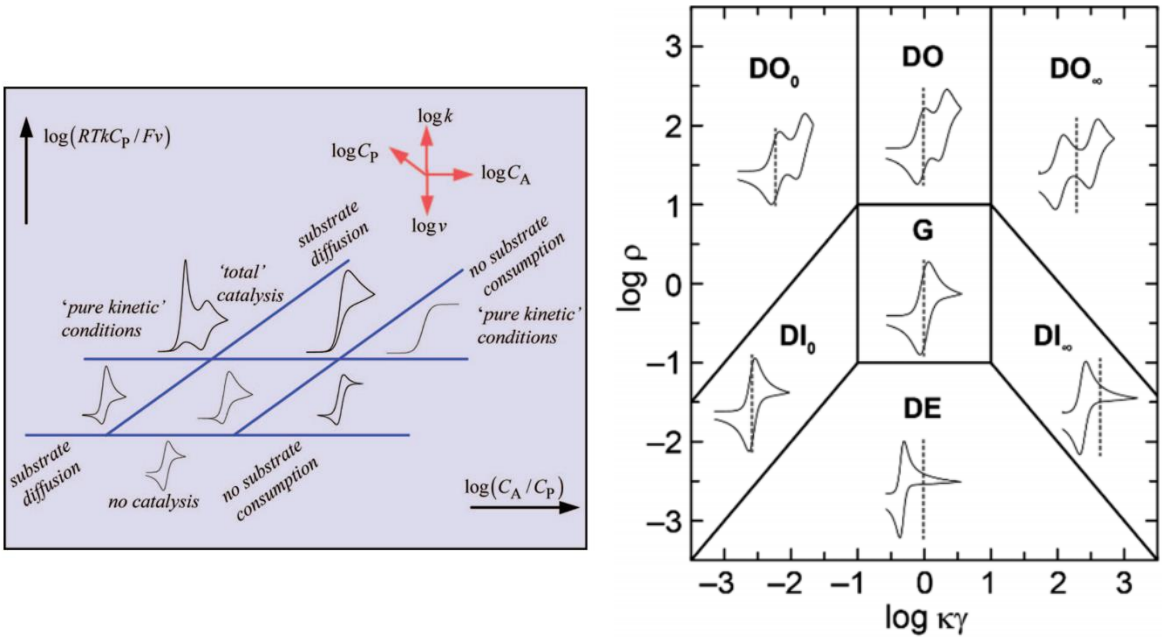

Figure 2.1: Examples of Zone diagrams. Left Panel: Kinetic zone diagram of expected shapes of CV response for a catalytic reaction first order in substrate (C_A) and catalyst (C_P). Reprinted (adapted) with permission from Savéant, J.-M., *Chem. Rev.* **2008,** *108* (7), 2348-2378. Copyright 2008, American Chemical Society. Right Panel: Kinetic zone diagram for the EC_rEC_i mechanism. Reprinted (adapted) with permission from Elias, J. S.; Costentin, C.; Nocera, D. G., *J. Am. Chem. Soc.* **2018,** *140* (42), 13711-13718. Copyright 2018, American Chemical Society.

A well-defined organometallic system that demonstrates this behavior with an EC mechanism is the series of [Cp*Rh] bis(2-pyridyl)methane complexes studied by our own group.[64,65] In this organometallic system, a $1e^-$ quasi-reversible reduction is followed by a second $1e^-$ reduction that is coupled to a rearrangement of the bis(2-pyridyl)methane ligand. Figure 2.2 shows the voltammograms of the benzyl (Bn) analog of **1** at 50, 1000, and 2500 mVs^{-1} (left panel) associated with the reduction-induced ligand rearrangement shown (right panel). The second reduction at E_{pc}

= −1.40 V vs $Fc^{+/0}$ exhibits characteristics of an EC mechanism in which there is an expected increase in cathodic current with increasing scan rate coupled with observation of the anodic process at only higher scan rates. As described by Savéant, λ is large at slower scan rates allowing ample time for the redox induced ligand rearrangement to occur. At higher scan rates the observation of the reoxidation event in the form of the anodic feature at leading to an electrochemically quasi-reversible process. At higher scan rates the relative increase in anodic current is a result of the small value of λ. In other words, the increased scan rate enables the rate of rate of the coupled chemical step to be overtaken, enabling direct observation of redox couple for the species that can otherwise be considered transient. As a complement to this experimental voltammetric study, digital simulations of the experimental data were performed using DigiElch in order to measure the first-order rate constant (k^+) for the ligand reorientation or "flip" chemical step. Multiple scan-rate dependent voltammograms were simulated to extract, from the behavior of the anodic feature, quantitative values of k^+.

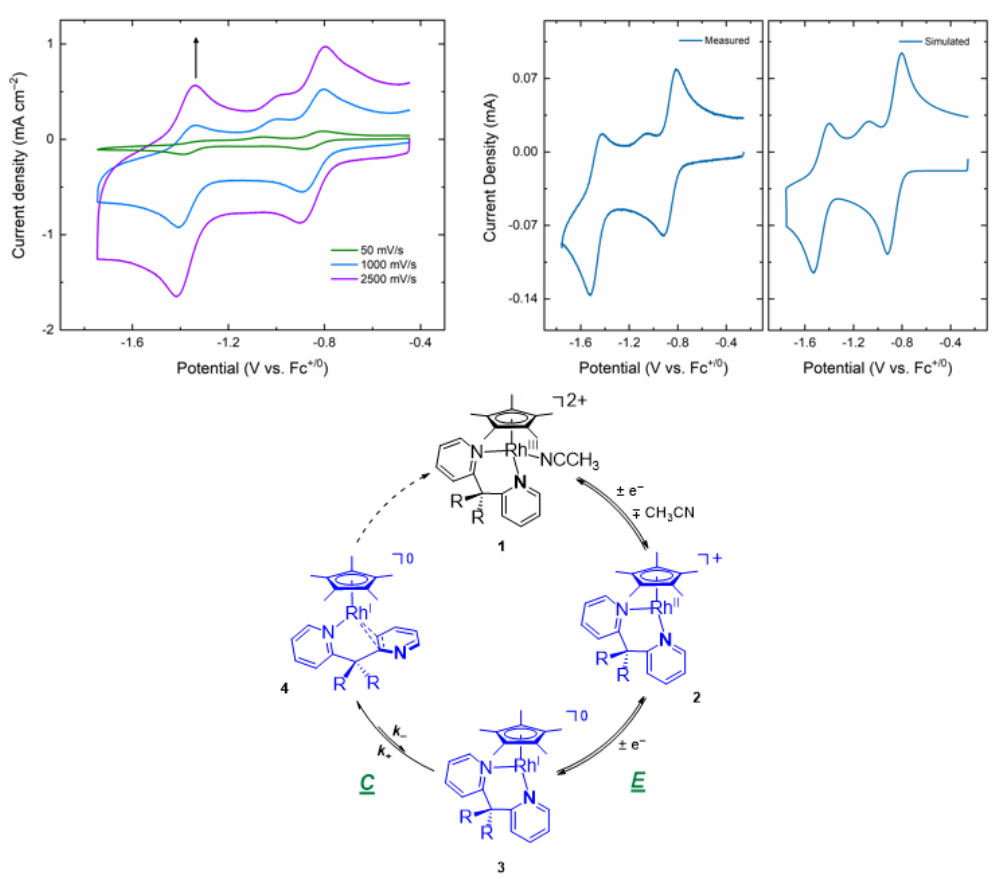

Figure 2.2: Top left panel: cyclic voltammetry of **1** (R = benzyl, Bn) at increasing scan rates. Conditions: electrolyte, 0.1 M $TBAPF_6$ in CH_3CN; working electrode, highly oriented pyrolytic graphite. Upper right panel: experimental and simulated voltammograms of **1** (R = methyl, Me). Lower scheme: electrochemical reduction pathway for **1**. Adapted from work described in citation 64. Copyright 2021, American Chemical Society.

2.3.4 ECC Mechanism

An electrochemical process that involving an electron transfer step followed by two sequential chemical reactions is referred to as an ECC mechanism. One of the most common ECC mechanistic scenarios results from the generation of an organometallic radical, followed by the loss of a ligand, and then dimerization to give the final product. This can occur by $1e^-$ oxidation or reduction of a substrate, which ultimately results in a ligand or metal centered radical. Radicals

are notoriously reactive species, and once generated electrochemically, often go on to react with another species present. A notable organometallic complex that undergoes $1e^-$ reduction to form a metal centered radical is $Mn(CO)_3Br(^Hbpy)$, a well-known CO_2 reduction catalyst. The electrochemical and electrocatalytic behavior of $Mn(CO)_3Br(^Hbpy)$ was first established by Deronzier, Chardon-Noblat, and co-workers using CV (see Figure 2.3).[66]

$$\text{E:}\quad A + e^- \rightleftharpoons B$$
$$\text{C:}\quad B \xrightarrow{k} C$$
$$\text{C:}\quad C \xrightarrow{k'} D$$

Scheme 2.5: General ECC mechanism. Electrode electron transfer followed by two first-order or pseudo-first-order homogenous reactions.

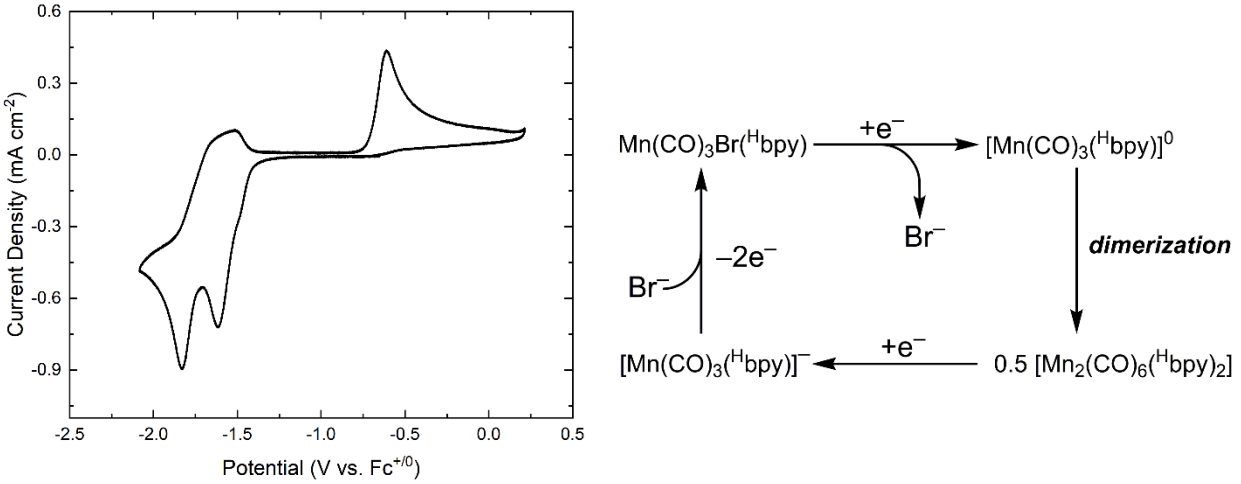

Figure 2.3: CV of $Mn(CO)_3Br(^Hbpy)$ in 0.1 M $TBAPF_6$/MeCN electrolyte at 100 mVs^{-1} (left). Accompanying chemical scheme for the sequential irreversible reductions and more positive oxidation associated with $Mn(CO)_3Br(^Hbpy)$ (right).

At first glance, the cyclic voltammogram of $Mn(CO)_3Br(^Hbpy)$ seems to be quite complicated; this is attributable to the multiple chemical reactions involved in the redox behavior of this complex. Scanning toward more negative potentials, two sequential and essentially irreversible

reductions are observed with cathodic peak potentials of –1.61 V vs $Fc^{+/0}$ and –1.83 V vs $Fc^{+/0}$, followed by an oxidation at more positive potentials with an anodic peak potential at –0.61 V vs $Fc^{+/0}$. Based on mechanistic work with this complex, the first irreversible reduction of $Mn(CO)_3Br(^{H}bpy)$ can be reliably assigned to result in a $19e^-$ complex.[67] This $19e^-$ complex then loses Br^- to generate a $17e^-$ species with a Mn-centered radical. Two of these Mn-centered radicals can recombine to dimerize and produce $Mn_2(CO)_6(^{H}bpy)_2$ (Mn–Mn dimer) in an overall ECC-type mechanism. The second reduction feature in the CV is attributed to the reduction of the Mn–Mn dimer, which cleaves the metal-metal bond to generate the 18 e^- complex, $[Mn(CO)_3(^{H}bpy)]^-$ in an overall EC process. Lastly, scanning to more positive potentials, $[Mn(CO)_3(^{H}bpy)]^-$ is re-oxidized to form the starting complex, $Mn(CO)_3Br(^{H}bpy)$.

2.3.5 CE Mechanism

The CE mechanism involves a rapid, reversible first-order or pseudo-first-order chemical reaction followed by an electron transfer. For CE mechanisms the electroactive starting material (A) is the product of chemical conversion of the starting material (species C in Scheme 2.6) in the chemical reaction labelled as step C.

$$\text{C:}\quad \mathrm{C} \underset{k_b}{\overset{k_f}{\rightleftharpoons}} \mathrm{A}$$

$$\text{E:}\quad \mathrm{A} + e^- \rightleftharpoons \mathrm{B}$$

Scheme 2.6: General CE mechanism. A first/pseudo first-order homogenous reaction preceding an electrode electron transfer.

CE mechanisms in which the pre-equilibrium is sufficiently fast to not influence the electrochemical response kinetically can be described using the equilibrium constant (K) and kinetic parameter λ.[28] In the case of one-electron reversible waves that engender a CE mechanism when the equilibrium constant is large, the couple appears reversible regardless of λ. However,

when K is small, the appearance of the CV becomes more complex and depends on the value of λ. The preceding reaction (C step) influences the electrochemical response (E step) when k_f is small. The CV response is controlled by the rate at which the species C is converted to the electroactive species A (k_f). The kinetics and thermodynamics of the conversion of C to A can influence the height and shape of the CV. As previously stated, the inverse relationship between scan rate and λ means that as the scan rate is increased for a CV measurement, the λ parameter decreases. The case of CE with a small λ engenders (fast scan rate and/or slow reaction) a reversible wave in which the height is influenced by the equilibrium constant. If the equilibrium constant is proportional to the peak heights of the CV, meaning for a CE case with a small K and small λ value there will be a reversible wave with small peak current. As λ increases as a result of slower scan rate the anodic wave takes the form of a plateauing wave which has a plateauing current independent of scan rate. An even slower scan rate and larger λ parameter results in a CV that gradually increases in reversibility until reaching a quasi-reversible wave.[28]

A distinct CE mechanism was observed in the titration of the solvent rhodium complex $[Cp^*Rh(PQN)NCCH_3]^{2+}$ (PQN) = (diphenylphosphino)quinoline) with tetrabutylammonium chloride (TBACl).[68] This titration was performed to understand the role of halide ligands in influencing the redox properties of [Cp*Rh] complexes supported by bidentate chelates. The CV of $[Cp^*Rh(PQN)NCCH_3]^{2+}$ reveals two distinct quasi-reversible one-electron couples ($Rh^{III/II}$ and $Rh^{II/I}$, –0.93 V and –1.16 V vs $Fc^{+/0}$ respectively). Increasing the concentration of TBACl to $[Cp^*Rh(PQN)NCCH_3]^{2+}$ clearly results in the diminution of the two original waves and gives rise to a new single $2e^-$ wave ($Rh^{III/II}$ = –1.19 V vs $Fc^{+/0}$) that corresponds to the electrochemical profile of $[Cp^*Rh(PQN)Cl]^+$; this was verified when this species was isolated through chemical synthesis and studied independently. This behavior confirms the rapid chemical conversion (C step) of

$[Cp^*Rh(PQN)NCCH_3]^{2+}$ to $[Cp^*Rh(PQN)Cl]^{+}$ by displacement of the ligated CH_3CN with chloride followed by an electron transfer to reduce the rhodium(III) complex (E step) giving rise to an EC mechanism observed in Figure 2.4.[69]

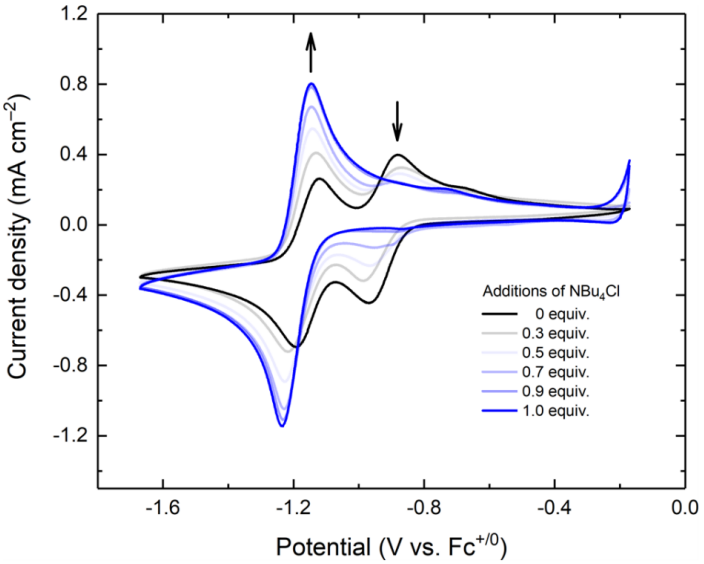

Figure 2.4: Electrochemical response of $[Cp^*Rh(PQN)NCCH_3]^{2+}$ in CH_3CN upon increasing additions of tetrabutylammonium chloride. Growth of the reduction process with $E_{1/2} = -1.19$ V indicates coordination of chloride to $[Cp^*Rh(PQN)NCCH_3]^{2+}$ by displacement of bound CH_3CN, generating $[Cp^*Rh(PQN)Cl]^{+}$. Reprinted (adapted) with permission from citation 68. Copyright 2019, American Chemical Society.

2.3.6 ECE Mechanism

The ECE mechanism is the case in which an electroactive species undergoes an electron transfer reaction followed by a coupled chemical reaction, like that of an EC reaction. However, the intermediate formed by the chemical step then undergoes a second electron transfer (Scheme 2.7). An ECE reduction occurs when the intermediate C formed has a standard reduction potential that is more positive than that of the standard reduction potential for the conversion of the initial electroactive species A to generate B. Each molecule of B is chemically converted to C, and

following the chemical conversion, C is instantaneously reduced by the electrode to generate the final species, D. This instantaneous reduction of C means that the ECE mechanism results in the appearance of a "$2e^-$ wave" which is often misinterpreted as arising from a truly simultaneous transfer of $2e^-$. However, virtually all ECE reductions actually involve two separate $1e^-$ reduction steps. Like many of the other mechanisms discussed here, the appearance of the CV can sometimes be influenced by varying the scan rate. In the ECE case, the λ kinetic parameter is interrelated with the rate of the chemical reaction that controls conversion of B to C. In the ECE case, at faster scan rates where λ is small, a quasi-reversible wave is predicted to be observed, corresponding to the one-electron process for reduction of A to B and re-oxidation of B to A. As the scan rate is decreased, however, λ increases, giving rise to irreversibility with respect to the original A/B wave and increase of the cathodic peak current, attributable to time being allowed for conversion of B to C and subsequent reduction of C to D. At slow scan rates the CV should then have the expected two-fold increase in the magnitude of the cathodic peak current. In certain systems which have appropriate kinetics of the chemical step associated with conversion of B to C, accumulation of the intermediate C at the electrode during scans can give rise to trace crossing; such behavior is attributable to the greater quantity of the intermediate C present at the surface during the reverse scan than the cathodic scan, giving rise to cathodic current during the anodic scan.[28] However, at typical electrodes and scan rates of relevance to molecular organometallic chemistry, this trace crossing associated with the ECE mechanism is not commonly observed and thus the absence of the behavior should not be taken as evidence against net $2e^-$, ECE-type behavior.

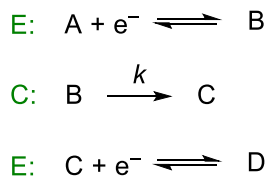

Scheme 2.7: General ECE mechanism (reduction shown). Electrode electron transfer flowed by a first/pseudo first-order homogenous reaction which undergoes a second electron transfer.

A well-defined family of Cp*Rh complexes illustrates the ECE mechanism engendering two sequential $1e^-$ reductions.[64,70,71,72,73] Electrochemical studies on the $[Cp^*Rh(PQN)L]^{n+}$ (PQN = 8-(diphenylphosphino)quinoline) complex exhibits interesting activity with substitution of the monodentate ligand (Figure 2.5). The $[Cp^*Rh^{III}(PQN)Cl]^+$ analog undergoes an initial $1e^-$ reduction generates a transient $[Cp^*Rh^{II}(PQN)Cl]^0$ following the initial E step, the Rh(II) complex undergoes a chemical loss of the monodentate Cl^- to form the intermediate $[Cp^*Rh^{II}(PQN)]^+$, which is immediately followed by a second $1e^-$ reduction to generate $[Cp^*Rh^{I}(PQN)]^0$. This ECE mechanism gives rise to a CV with the appearance of a quasi-reversible $2e^-$ reduction. In the absence of chloride, however, the reduction of the solvento species, $[Cp^*Rh^{III}(PQN)NCCH_3]^{2+}$ takes place at a potential more positive than that for $[Cp^*Rh^{III}(PQN)Cl]^+$ due to its dicationic nature. The shift in this potential is a result of the chemical reaction step (loss of CH_3CN rather than Cl^-) being insufficient to cause the transient $[Cp^*Rh^{II}(PQN)NCCH_3]^+$ complex to be reduced at a more positive potential compared to the $[Cp^*Rh^{III}(PQN)NCCH_3]^{2+}$ complex. Due to this phenomenon two discrete reductions are observable and results in the metastable $[Cp^*Rh^{II}(PQN)NCCH_3]^+$ complex generated near the electrode. The oxidation of the $[Cp^*Rh^{I}(PQN)]^0$ analog results in a very similar CV profile due to the generation of the $[Cp^*Rh^{III}(PQN)NCCH_3]^{2+}$ in CH_3CN solvent. The third reduction in each CV is attributed to the reduction of the PQN ligand.[72]

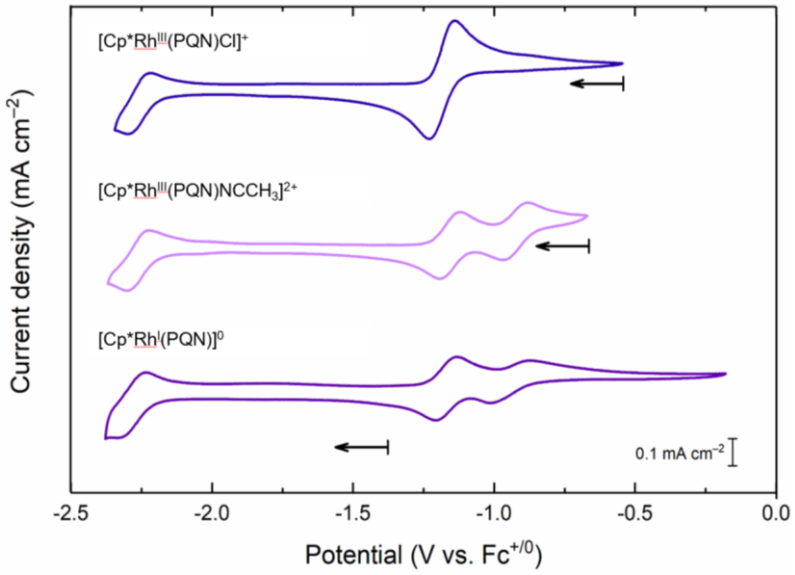

Figure 2.5: CV of $[Cp^*Rh^{III}(PQN)Cl]^+$ (upper panel) $[Cp^*Rh^{III}(PQN)NCCH_3]^{2+}$ (middle panel) and $[Cp^*Rh^{I}(PQN)]^0$ (lower panel). Reprinted (adapted) with permission from citation 68. Copyright 2019, American Chemical Society.

2.3.7 Substitution Mechanism

In inorganic and organometallic chemistry intermolecular substitution reactions typically occur by associative or dissociative mechanisms. In an associative mechanism, a ligand forms a bond to the metal center prior to the ejection of the exiting ligand. Conversely, in a dissociative mechanism, a ligand is initially expelled from the metal center to generate space for an incoming ligand to bind. Electrochemical oxidation or reduction has been shown to accelerate some intermolecular organometallic substitution reactions, and therefore gives useful mechanistic insights.

In an example from the work of Kochi and co-workers, organometallic intermolecular ligand substitution is enhanced and observed using electrochemical methods.[74] This series of reactions, monitored by CV, demonstrate that the acetonitrile ligand bound to $(\eta^5\text{-MeCp})Mn(CO)_2(NCMe)$ (Mn-NCMe) may be substituted with various alkyl and arylphosphines when an oxidative bias is

applied (see Figure 2.6). The initial CV of Mn-NCMe displays a well-behaved quasi-reversible 1e- redox couple at 0.22 V vs $Fc^{+/0}$. However, when 1 equiv. of triphenylphosphine (PPh_3) is added to the system, the quasi-reversibility of the initial redox couple ceases, but the $1e^-$ oxidation of Mn-NCMe to the $17e^-$ species $[Mn\text{-}NCMe]^+$ persists and a new redox couple begins to grow in at 0.55 V vs $Fc^{+/0}$. This behavior suggests that once [Mn-NCMe] is oxidized to $[Mn\text{-}NCMe]^+$, substitution of the NCMe for PPh_3 is facile and results in the rapid consumption of $[Mn\text{-}NCMe]^+$ to generate the intermolecular substitution product (η^5-MeCp)$Mn(CO)_2(PPh_3)$ (Mn-PPh_3). As increasing equivalents of PPh_3 are added to the electrochemical cell, $[Mn\text{-}NCMe]^+$ is consumed more rapidly until only the current corresponding to the substitution product is observed during CV. To confirm that it is indeed MeCp)$Mn(CO)_2(PPh_3)$ being generated, an authentic sample of (MeCp)$Mn(CO)_2(PPh_3)$ was found to be oxidized at the latter potential. This exemplifies a class of substitution reactions that take place when inner-sphere ligands become labile upon oxidation or reduction of different organometallic complexes.

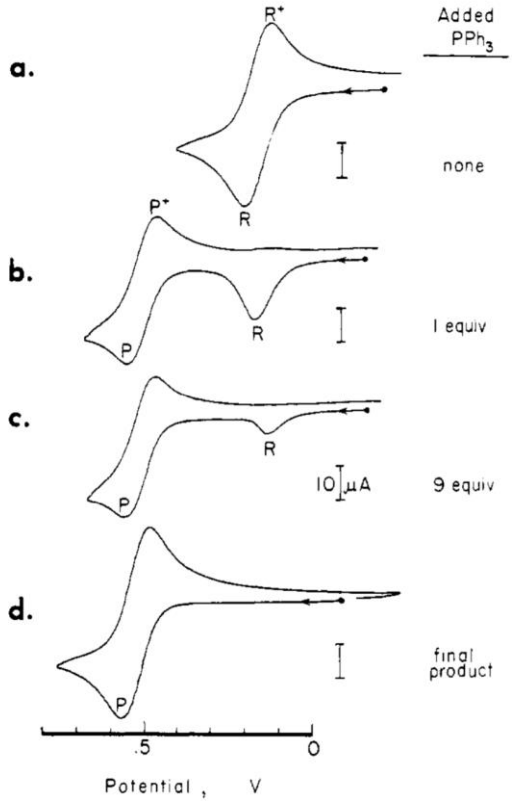

Figure 2.6: (**a**) Initial CV of (η^5-MeCp)$Mn(CO)_2$(NCMe). (**b** and **c**) Potentiometric titration of (η^5-MeCp)$Mn(CO)_2$(NCMe) (R) with PPh_3 to generate (η^5-MeCp)$Mn(CO)_2(PPh_3)$ (P) under electrochemical conditions. (**d**) CV of isolated (η^5-MeCp)$Mn(CO)_2(PPh_3)$. CVs are taken at 200 mVs^{-1} with MeCN solvent at 0.1 M TEAP electrolyte. Reprinted with permission from 74. Copyright 1983 American Chemical Society.

2.3.8 DISP Mechanism

The DISP mechanism, or disproportionation mechanism, is similar to that of the ECE mechanism previously discussed, but involves a second disproportionation pathway following the non-electrode-based generation of the intermediate C. For DISP mechanisms the second electron is transferred from B to C rather than from the electrode to C as in an ECE mechanism. In the ECE mechanism the $E^0_{C/D}$ is at a more positive potential than $E^0_{A/B}$, implying that the disproportionation reaction K_D is favorable. The two electron transfers engendered in the ECE mechanism are both

fast, therefore it is assumed that the thermodynamically favorable disproportionation reaction is fast. The chemical conversion of B to C is the rate determining step and λ behaves in the same manner as in ECE mechanism. As discussed for the ECE mechanism at faster scan rates λ is low, which gives rise to a quasi-reversible wave. As the scan rate is gradually decreased, λ increases giving rise to increasing irreversibility and increase of the cathodic peak current and slow scan rates the CV reaches complete irreversibility and has appearance of a $2e^-$ reduction in magnitude of the peak current. Under pure kinetic conditions the ECE and DISP mechanisms are indistinguishable by CV, but when pure kinetic conditions are not achieved it is possible to distinguish between ECE and DISP mechanisms. Non-pure kinetic conditions in DISP do not lead to crossing as seen in the ECE case discussed above. The absence of trace crossing in the DISP mechanism is due to the slow reaction of B to C, consequently the intermediate C is formed far from the electrode surface which allows ample time for the disproportionation to occur before C reaches the electrode. This prevents the accumulation of C at the electrode surface during scans, and therefore there is no possible contribution of cathodic current during the anodic scan as is possible during the ECE-type mechanism.[28]

$$A + e^- \rightleftharpoons B$$
$$B \xrightarrow{k} C$$
$$B + C \xrightarrow{k_D} A + D$$

Scheme 2.8: DISP mechanism. Electrode electron transfer followed by a first-order or pseudo-first-order homogenous reaction in which a second electron is transferred from species B to C.

An example of an organometallic system with an ECE-DISP mechanism is the series of substituted rhodium(III) porphyrin complexes studied by Savéant et al (Figure 2.7).[75] This rhodium(III) porphyrin family engenders chemical irreversibility that is attributed to the disproportionation of the rhodium(II) complexes caused by ligand exchange reactions. During

reduction $^{+}Rh(III)L_2$ is reduced by $1e^{-}$ to the corresponding $Rh(II)L_2$ followed by the loss of one L ligand. The loss of L generates a second Rh(II)L which is reduced at a more positive potential than the initial Rh(III) complex by $1e^{-}$. This electrochemical reduction thus involves a disproportionation step because the second electron step occurs concurrently with electrode reduction.

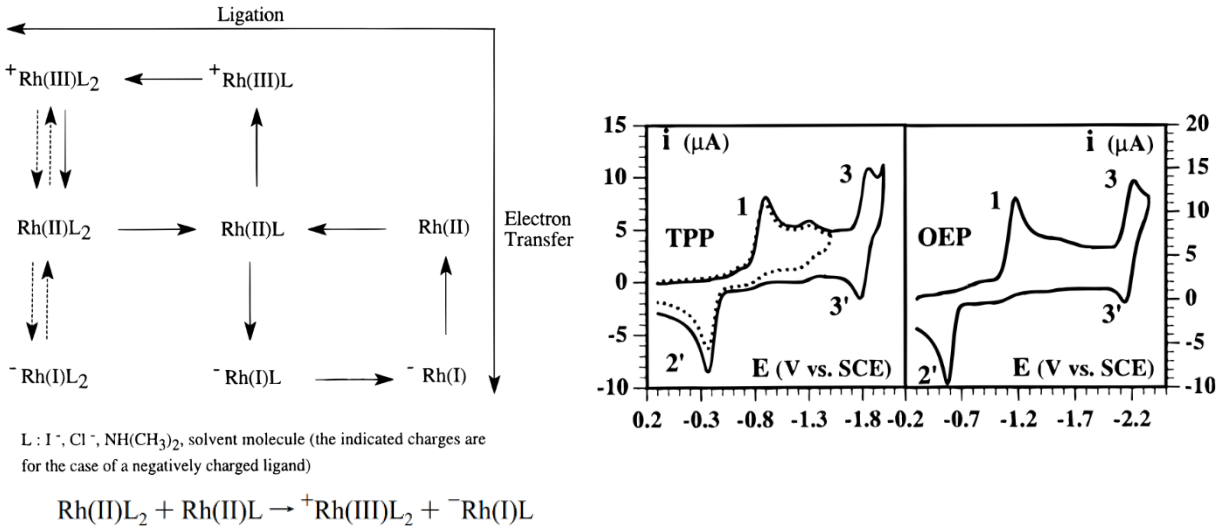

Figure 2.7: Reduction scheme of Rh(III) porphryin complexes in which disproportionation occurs with the reduction to $Rh(II)L_2$. Disproportionation scheme of $Rh(II)L_2$ shown below. (Left.) Cyclic voltammetry of rhodium(III) tetraphenylporphyrin (TPP) and rhodium(III) octaethylporphyrin (OEP) (Right.) Reprinted (adapted) with permission from citation 75. Copyright 1997, American Chemical Society.

2.4 Using Electrochemistry to Explore Chemical Reactivity with Stoichiometric Redox Reagents

2.4.1. Synthesis via Controlled Potential Electrolysis

Controlled potential electrolysis (CPE) is a well-established electrochemical method used for synthesis of electron transfer products.[9,76,77,78 79,80,81] There are advantages and disadvantages to this electrochemical synthetic method. CPE allows a wide range of precise potentials accessible for reduction/oxidation of organometallic compounds with minimal side reactivity that leads to byproducts. However, CPE can be problematic because of the need for a large amount of electrolyte salt in solution, which can be difficult to separate from the product.[9]

2.4.2. Synthesis via Chemical Redox Reagents

An alternative method for synthesis of electron transfer products is use of chemical redox reagents, chosen based on CV to determine the reduction potential of the electroactive species (Figure 2.8). The utilization of a homogeneous reductant/oxidant eliminates the necessity for a large excess of supporting electrolyte salt that must be separated. Another advantage of chemical methods is the fast time scale and large reaction scale compared to electrochemical methods. Chemical reduction and oxidation can be performed at low temperatures to reduce side reactivity and improve selectivity. Although it should be noted that low temperature electrolysis experiments are possible, it is necessary to be strategic when selecting the solvent and supporting electrolyte for work at low temperature. A list of appropriate solvents and electrolyte systems for work at reduced temperatures can be found in Kissinger and Heineman's *Laboratory Techniques in Electroanalytical Chemistry.*[82] Another notable difference between chemical and electrochemical synthetic methods is the former can be done in non-polar solvents. This may be advantageous for

precipitation of products, or for use of a non-coordinating solvent to prevent ligand exchange/displacement.[9]

However, the use of chemical redox reagents have notable disadvantages.[9] Chemical reagents have a fixed reduction/oxidation potential, which can be disadvantageous for target complexes for which there is no good match of a chemical redox agent with chemical compatibility and the correct potential, whereas electrochemical methods enable precise choice of potential. Chemical reagents also introduce a redox byproduct, which may give undesired reactivity. Particularly problematic are reagents that give inner-sphere electron transfer leading to installation of ligands such as NO when using the oxidant $[NO]^+$ or chloride derived from trityl chloride.[9,83] In choosing a redox reagent for chemical reduction or oxidation, one must take solubility into account as well as considering the reduction potential of the electroactive species and fixed potential of the redox reagent. It is important to note that for a Nernstian system (see section 1.3.1) a 99% reaction completion for a $1e^-$ transfer requires a reducing agent to have E^o 118 mV negative of the E^0 and an oxidizing agent to have $E°$ 118 mV positive of the E^0 (Figure 2.8).[9]

Table 2. Formal Potentials (V *vs* Fc) of Selected Oxidizing Agents

oxidant	solvent	$E^{0\prime}$	correction	ref
$[N(C_6H_2Br_3\text{-}2,4,6)_3]^+$	MeCN	1.36	*a*	228
Ce(IV)	$HClO_4$	1.30	*b*	*c*
	H_2O	0.88	*b*	*c*
$[N(C_6H_3Br_2\text{-}2,4)_3]^+$	MeCN	1.14	*a*	228
$[WCl_6]$	CH_2Cl_2	*ca.* 1.1	*d*	132
$[NO]^+$	CH_2Cl_2	1.00	none	195
$[Ru(phen)_3]^{3+}$	MeCN	0.87	*e*	108
$[NO]^+$	MeCN	0.87	none	195
[thianthrene]$^+$	MeCN	0.86	*f*	*g*
$[N(C_6H_4Br\text{-}4)_3]^+$	CH_2Cl_2	0.70	*d*	*h*
	MeCN	0.67	*i*	*j*
$[Fe(bipy)_3]^{3+}$	MeCN	0.66	*e*	111
Ag^+	CH_2Cl_2	0.65	*d*	63
$[Mo(tfd)_3]$	MeCN	0.55	*f*	*k*
$[IrCl_4(PMe_2Ph)_2]$	MeCN	*ca.* 0.5	*l*	123
$[Fe(\eta\text{-}C_5H_4COMe)_2]^+$	CH_2Cl_2	0.49	none	*h*
$[CuTf_2]$	MeCN	0.40	*f*	88
Ag^+	THF	0.41	*m*	63
$[Ni(tfd)_2]$	CH_2Cl_2	0.33	none	*h*
$[PtCl_6]^{2-}$	H_2O	0.31	*b*	*n*
$[Fe(\eta\text{-}C_5H_4COMe)Cp]^+$	CH_2Cl_2	0.27	none	*h*
Ag^+	acetone	0.18	*o*	63
Cl_2	MeCN	0.18	*b*	*p*
DDQ	MeCN	0.13	*i*	308
Br_2	MeCN	0.07	*b*	*p*
$[N_2C_6H_4NO_2\text{-}4]^+$	sulfolane	*ca.* 0.05	*f*	*q*
Ag^+	MeCN	0.04	*f*	63
$[C_3\{C(CN)_2\}_3]^-$	MeCN	0.03−0.06	*r*	304
$[FeCp_2]^+$		0.0		
$[N_2C_6H_4F\text{-}4]^+$	MeCN	−0.07	*f*	*q*
$[CPh_3]^+$	MeCN	−0.11	*f*	*s*
I_2	MeCN	−0.14	*f*	*t*
TCNE	MeCN	−0.27	*f*	*u*
TCNQ	MeCN	−0.30	*f*	*u*
$[FeCp^*_2]^+$	MeCN	−0.59	none	*h*
	CH_2Cl_2	−0.48	none	*h*
$[C_7H_7]^+$	MeCN	−0.65	*f*	*s*

[a] Use measured difference from potential of $[N(C_6H_4Br\text{-}4)_3]^+$ which is 0.70 V *vs* Fc. [b] Fc = 0.40 V *vs* NHE in H_2O. [c] Smith, G. F.; Getz, C. A. *Ind. Eng. Chem., Anal. Ed.* **1938**, *10*, 191. [d] Fc = 0.46 V *vs* SCE (CH_2Cl_2/$[NBu_4][PF_6]$). [e] Fc = 0.32 V *vs* sodium SCE. [f] Fc = 0.40 V *vs* SCE (MeCN/$[NBu_4][PF_6]$). [g] Hammerich, O.; Parker, V. D. *Electrochim. Acta* **1973**, *18*, 537. [h] Data from authors' laboratories. [i] Fc = 0.38 V *vs* SCE (MeCN/$[NEt_4][ClO_4]$). [j] Reynolds, R.; Line, L. L.; Nelson, R. F. *J. Am. Chem. Soc.* **1974**, *96*, 1087. [k] Davison, A.; Edelstein, N.; Holm, R. H.; Maki, A. H. *J. Am. Chem. Soc.* **1964**, *86*, 2799. [l] 0.9 V *vs* Ag/AgCl in MeCN/0.1 M $NaClO_4$; conversion to Fc approximate. [m] Fc = 0.56 V *vs* SCE (THF/$[NBu_4][PF_6]$). [n] Kravtsov, V. I.; Simakov, B. V. *Elektrokhimiya* **1966**, *2*, 646. [o] Fc = 0.48 V *vs* SCE (acetone/$[NBu_4][PF_6]$). [p] Parsons, R. *Handbook of Electrochemical Constants*; Butterworth: London, 1959; p 73. [q] Elofson, R. M.; Gadallah, F. F. *J. Org. Chem.* **1969**, *34*, 854. [r] Fc potential uncertain; no supporting electrolyte specified. [s] Volz, H.; Lotsch, W. *Tetrahedron Letts.* **1969**, 2275. [t] Nelson, I. V.; Iwamoto, R. T. *J. Electroanal. Chem.* **1964**, *7*, 218. [u] Gross-Lannert, R.; Kaim, W.; Olbrich-Deussner, B. *Inorg. Chem.* **1990**, *29*, 5046.

Table 3. Formal Potentials (V *vs* Fc) of Selected Reducing Agents

reductant	solvent	$E^{0\prime}$	correction	ref
$[C_{10}H_8]^-$	THF	−3.10	*a*	366b
	glyme	−3.05	*a*	366b
	DMF	−2.95	*b*	*c*
Na	THF, glyme	−3.04	*a*	*d*
Li	NH_3	−2.64	*e*	*f*
Li(Hg)	H_2O	−2.60	*e*	*g*
K	NH_3	−2.38	*e*	*f*
Na(Hg)	nonaqueous	−2.36	*e*	*h*
[anthracene]$^-$	glyme	−2.47	*i*	*j*
$[FeCp^*(\eta\text{-}C_6Me_6)]$	dmf	−2.30	*b*	437
Na	NH_3	−2.25	*e*	*f*
[benzophenone]$^-$	THF	−2.30	none	*k*
	DMF	−2.17	*b*	*l*
[acenaphthalene]$^-$	THF	−2.26	*a*	366b
	glyme	−2.17	*i*	*i*
$[FeCp(\eta\text{-}C_6Me_6)]$	glyme	−2.09	*m*	402
$[CoCp^*_2]$	CH_2Cl_2	−1.94	*n*	*o*
	MeCN	−1.91	*p*	*q*
$[Fe(CO)_2Cp]^-$	THF, MeCN	*ca.* −1.8 (irr)	*p*, *r*	448, 449
$[CoCp_2]$	CH_2Cl_2	−1.33	none	*k*
	glyme	−1.31	*m*	404a
$[Cr(\eta\text{-}C_6H_6)_2]$	CH_2Cl_2	−1.15	none	8
$[FeCp^*_2]$	CH_2Cl_2	−0.59	*n*	*q*
	MeCN	−0.48	*p*	*s*
hydrazine	DMSO	−0.41	*t*	357
$[FeCp_2]$		0.0		
NEt_3	MeCN	*ca.* 0.47	*u*	393

[a] $E^{0\prime}$ *vs* [biphenyl]$^{0/-}$; [biphenyl]$^{0/-}$ = −2.69 V *vs* SCE (DMF/$[NBu_4][ClO_4]$) (Grzeszczuk, M.; Smith, D. E. *J. Electroanal. Chem.* **1983**, *157*, 205); Fc = 0.45 *vs* SCE (DMF/$[NBu_4][ClO_4]$. [b] Fc = 0.45 V *vs* SCE (DMF/$[NBu_4][PF_6]$). [c] Aten, A. C; Buthker, C.; Hoijtink, G. J. *Trans. Faraday Soc.* **1959**, *55*, 324. [d] Hoijtink, G. J.; de Boer, E.; van der Meij, P. H.; Weijland, W. P. *Recl. Trav. Chim.* **1956**, *75*, 487. [e] Fc = 0.40 V *vs* NHE in H_2O. [f] Strehlow, H. *The Chemistry of Nonaqueous Solvents*; Lagowski, J. J., Ed.; Academic Press: New York, 1966. [g] Lebed, V. I.; Aleksandrov, V. V. *Russ. J. Phys. Chem.* **1964**, *38*, 1414. [h] Balej, J. *Electrochim. Acta* **1976**, *21*, 953. [i] $E^{0\prime}$ *vs* Ag^+/Ag; $[Cr(\eta\text{-}C_6H_6)_2]^{+/0}$ = −1.25 V *vs* Ag^+/Ag; Fc = 1.12 V *vs* $[Cr(\eta\text{-}C_6H_6)_2]^{+/0}$ (ref 8). [j] Dessy, R. E.; King, R. B.; Waldrop, M. *J. Am. Chem. Soc.* **1966**, *88*, 5112. [k] Data from authors' laboratories. [l] Jensen, B. S.; Parker, V. D. *J. Chem. Soc., Chem. Commun.* **1974**, 367. [m] Fc = 0.51 V *vs* SCE (glyme/$[NBu_4][PF_6]$). [n] Fc = 0.46 V *vs* SCE (CH_2Cl_2/$[NBu_4][PF_6]$). [o] Koelle, U.; Khouzami, F. *Angew. Chem., Int. Ed. Engl.* **1980**, *19*, 640. [p] Fc = 0.40 V *vs* SCE (MeCN/$[NBu_4][PF_6]$). [q] Gennett, T.; Milner, D. F.; Weaver, M. J. *J. Phys. Chem.* **1985**, *89*, 2787. [r] Fc = 0.56 V *vs* SCE (THF/$[NBu_4][PF_6]$). [s] Robbins, J. L.; Edelstein, N.; Spencer, B; Smart, J. C. *J. Am. Chem. Soc.* **1982**, *104*, 1882. [t] Fc = 0.43 V *vs* SCE (DMSO/$[NBu_4][PF_6]$). [u] Fc = 0.31 V *vs* SCE (MeCN/$Na[ClO_4]$).

Figure 2.8: List of chemical redox agents as summarized by Connelly and Geiger in 1996. Chemical oxidants (left) chemical reductants (right). Reprinted (adapted) with permission from 9. Copyright 1996 American Chemical Society.

2.4.3. Literature Examples of Combined Use of Cyclic Voltammetry and Chemical Redox Reagents

An example of utilizing chemical reducing agents as a supporting complement to cyclic voltammetry is a titanium polymerization catalyst with added $AlEt_3$.[84] This work features cyclic voltametric studies of the titanium catalyst **Ti-1** shown in Figure 2.9 in which the complex

undergoes a single irreversible 1e⁻ reduction at –2.12 V vs. $Fc^{+/0}$. The cyclic voltammogram of **Ti-1** in the presence of $AlEt_3$ changes the appearance to include an oxidative feature at E_{pa} at –1.32 V vs $Fc^{+/0}$. Chemical reduction of **Ti-1** in the presence of $AlEt_3$ yields bimetallic complex **Ti-2** (Figure 2.9). The anodic feature at E_{pa} at –1.32 V vs $Fc^{+/0}$ in the electrochemistry corresponds to the oxidation of **Ti-2.** This assignment is supported by matching spectral profiles of the spectroelectrochemical data of the parallel addition of $AlEt_3$ to **1** and the UV-vis data of the chemically prepared complex **Ti-1**.

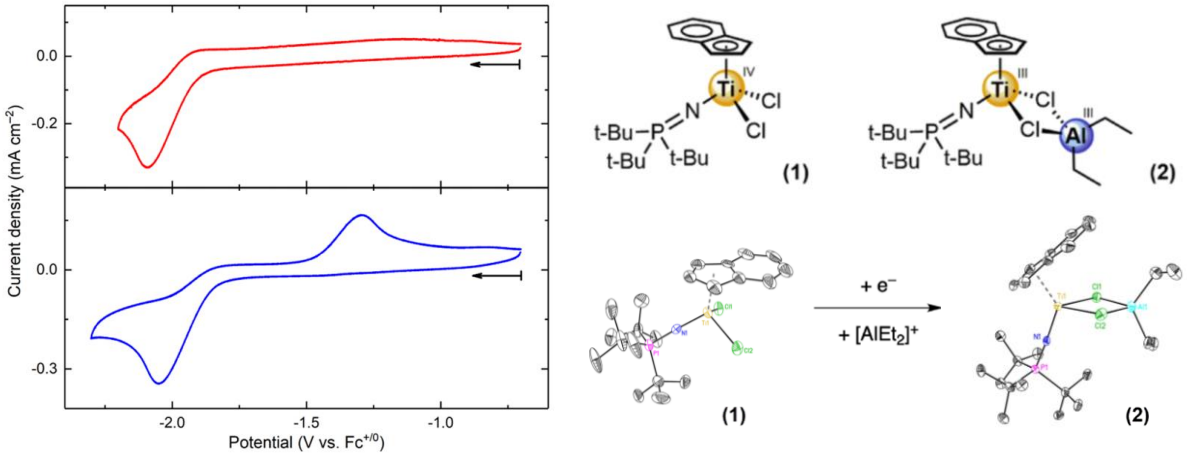

Figure 2.9: Cyclic voltammetry data for **Ti-1 (**red trace upper panel) and cyclic voltammetry of **Ti-1** with the addition of 6 equivalents of $AlEt_3$ (blue lower panel) (left panel.) Structures of compound **Ti-1** and **Ti-2** (top panel) and solid-state structures of complex **Ti-1** and **Ti-2**. Reprinted (adapted) with permission from citation 84. Copyright 2019, American Chemical Society.

Cyclic voltammetry published by Kubiak et al of a $Mn(bpy\text{-}tBu)(CO)_3Br$ complex exhibits two sequential, irreversible 1e⁻ reductions at –1.39 V and –1.57 V vs SCE. The first reduction is assigned to metal centered with concomitant loss of Br^- resulting in the formation of a Mn–Mn dimer[66] and the second reduction is attributed to formation of $[Mn(bpy\text{-}tBu)(CO)_3]^-$.[85] The feature at –0.30 V vs SCE is assigned to the oxidative cleavage of the Mn–Mn bond. The identity of the

second reduction at –1.57 V vs SCE was interrogated by reduction of Mn(bpy-tBu)$(CO)_3$Br by two equivalents of potassium graphite (KC_8, E^0 ~ –3.1 V vs. $Fc^{+/0}$ in THF)[9] in the presence of 18-crown-6 to yield the doubly reduced [Mn(bpy-tBu)$(CO)_3$][K(18-crown-6)(THF)] (Figure 2.10). Note the use of a much stronger reducing agent than formally needed for the reduction, which is common. The solid-state structure of the doubly reduced form was used to the assignment of the second 1e$^-$ reduction as the formation of [Mn(bpy-tBu)$(CO)_3$]$^-$.

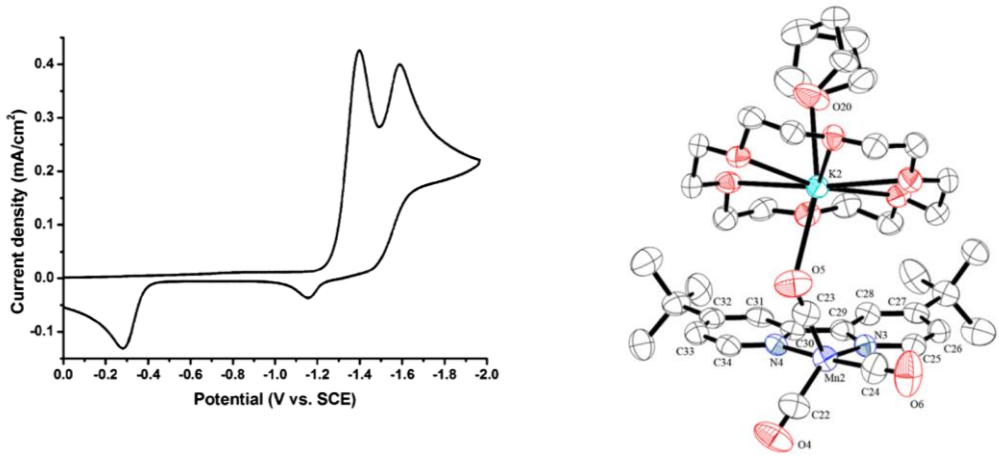

Figure 2.10: Cyclic voltammogram of Mn(bpy-tBu)$(CO)_3$Br (left) Solid state structure of chemically prepared doubly reduced [Mn(bpy-tBu)$(CO)_3$][K(18-crown$_6$)(THF)] (right.) Reprinted (adapted) with permission from citation 85. Copyright 2013, American Chemical Society.

Another literature example of combining cyclic voltammetry methods and chemical reductants comes from a study of dimeric tungsten species.[86] The CV of complex **W-1** in Figure 2.11 exhibits an irreversible oxidation at –2.21 V vs $Fc^{+/0}$ followed by a corresponding reduction feature indicating an EC process in which a new tungsten species is formed *in situ.* To interrogate the identity of this species formed the starting material **W-1** was chemically reduced by potassium graphite (KC_8, E^0 ~ –3.1 V vs. $Fc^{+/0}$ in THF)[9] and it was possible to isolate and crystallographically characterize **W-3**. The CV of isolated **W-3** reveals a quasi-reversible couple at –2.29 V vs. $Fc^{+/0}$

that matches the oxidation feature in the CV of **W-1**. The paper hypothesizes that the *in situ* formation of **W-3** is most likely a result of disproportionation reactions.

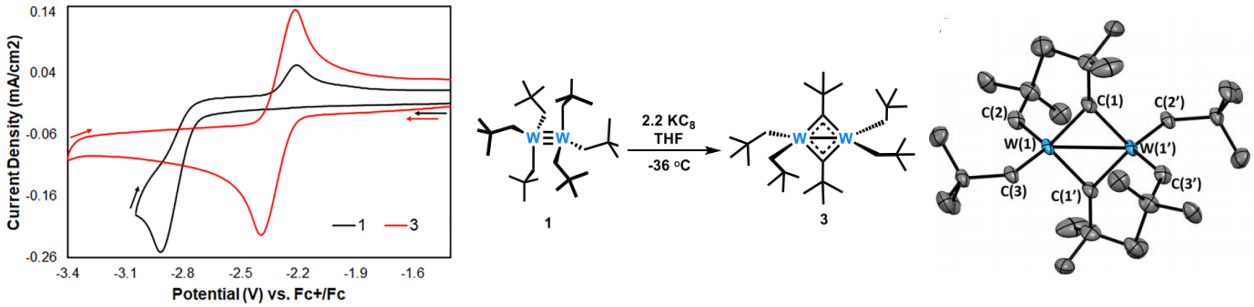

Figure 2.11: Cyclic voltammogram of **W-1** and **W-3** (left) chemical reduction of **W-1** with KC_8 to **W-3** (middle) solid state structure of **W-3** (right). Reprinted (adapted) with permission from citation 86. Copyright 2020, American Chemical Society.

A family of [Cp*Rh](Me$_2$dpma)] (Me$_2$dpma = dimethylbis(2-pyridyl)methane) complexes were studied for their redox properties as they relate to the [Cp*Rh(bpy)] system (Figure 2.12).[65] The cyclic voltammetry of **1-NCCH$_3$** displays an initial quasi-reversible 1e$^-$ reduction from Rh(III) to Rh(II) at –0.85 V vs $Fc^{+/0}$, and continuing to scan cathodically a second irreversible 1e$^-$ reduction occurs at –1.50 vs $Fc^{+/0}$. The irreversibility of this reduction suggests an EC process. To probe the identity of the species formed upon electrochemical reduction the **1-Cl** and **1-NCCH$_3$** complexes were treated with chemical reductants. Treatment of **1-Cl** with cobaltocene ($CoCp_2$, $E_{1/2}$ = –1.30 V vs $Fc^{+/0}$)[9] yielded the expected Rh(II) reduction product with minimal chemical change as indicated by the 1e$^-$ quasi-reversible couple. The **1-NCCH$_3$** complex was used to interrogate the EC process of the doubly reduced product to avoid side reactivity seen with the 2e$^-$ chemical reduction of **1-Cl**. Treatment of **1-NCCH$_3$** with a stronger reducing agent, sodium amalgam (Na(Hg), E^0 = –2.4 V vs $Fc^{+/0}$),[9] generated the doubly reduced Rh(I) product **3**. Upon the addition of the second electron there is a significant ligand rearrangement in which one pyridine

moiety “flips” on the bidentate Me_2dpma ligand. This assignment of the doubly reduced species identifies the chemical step upon the second reduction. The origin of this rearrangement is attributed to the ability of the Me_2dpma ligand to stabilize the low-valent Rh(I) center with strong π-backbonding by way of facial coordination of the pyridine moiety.

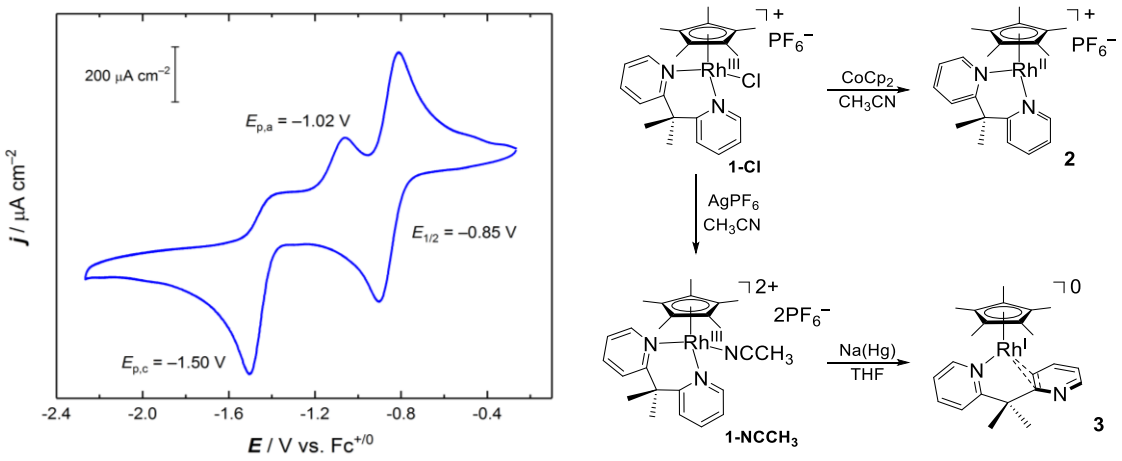

Figure 2.12: Cyclic voltammogram of **1-NCCH$_3$** (left) reduction scheme of **1-Cl** with $CoCp_2$ to **2** and **1-NCCH$_3$** with Na(Hg) to **3** (right).

2.5 Fundamental Concepts of Organometallic Electrocatalysis

2.5.1 Motivation for Studying Organometallic Electrocatalysts in the Context of Energy Science

Energy consumption is anticipated to continue increasing as the Earth’s population grows, motivating work to develop new renewable energy sources and technologies that can produce fuels and chemicals with renewable energy. The most abundant renewable energy source available is sunlight, which provides enough energy (1.2×10^{14} kWh) in 80 minutes to sustain the global power demand for over a year.[87,88,89] While there is plenty of potential energy available in the form of sunlight, utilizing this energy is challenging due to its intermittency, variable intensity, and uneven distribution across the surface of the Earth. Development of model molecular electrocatalysts capable of converting electrical energy into stored fuels and chemicals can provide fundamental

insights into how such catalysts convert energy. Considering that harnessing renewable energy sources is an important goal of contemporary chemistry, organometallic chemistry has been heavily utilized in recent years for development of new electrocatalysts. Electrocatalysts are typically classified as heterogeneous or homogeneous, and there are many relevant examples of studying both classes of catalysts using electrochemical techniques, particularly cyclic voltammetry (CV) and controlled potential electrolysis (CPE). In this section, priority will be given to discussion of homogeneous molecular catalysts because these are i) more relevant to organometallic chemistry and ii) mechanistic discussions are more certain for cases in which catalyst (or precatalyst) structures are well defined.

CV and CPE experiments are regularly used to interrogate candidate organometallic systems for oxidative or reductive electrocatalytic applications. This section will provide a brief overview of catalytic CV and CPE experiments to investigate organometallic complexes as potential electrocatalysts. CV techniques can also be employed to assist in distinguishing heterogeneous versus homogenous catalysis. CV and controlled potential electrolysis experiments are often used synergistically to extract important thermodynamic, kinetic, and mechanistic information about these electrocatalytic transformations. When these electrocatalytic experiments are combined with product detection, Faradaic efficiency (FE), turnover number (TON), and turnover frequency (TOF) parameters can be extracted. In this section, we will discuss some of the most popular areas of organometallic electrocatalysis, including literature examples that utilize organometallic complexes capable of electrocatalytic water (WO) and ammonia oxidation (AO), and proton (HER), carbon dioxide (CO_2R), dinitrogen reduction reactions (N_2RR), and electroorganic transformations (EOT).

2.5.2 Investigating Organometallic Electrocatalysis using CV

2.5.2.1 Electrocatalytic Parameters and Thermodynamic Overpotential Determined by CV

For catalytic CV experiments, the observations and parameters associated with the generation of a catalytic response are well detailed in the viewpoint provided by Appel and Helm.[12] Their work provides insight and information about the parameters gleaned from a set of catalytic CV experiments regarding electrocatalytic overpotential. Specifically, parameters associated with the electrocatalytic response such as peak catalytic current (i_{cat}), half the peak catalytic current ($i_{cat/2}$), and catalytic potential ($E_{cat/2}$) are used in this area to determine the thermodynamic overpotential of a molecular catalyst (see Figure 2.13). The i_{cat} is the maximum current that flows in a catalytic CV experiment; for a plateauing catalytic wave, this is assigned as the maximum current anywhere in the plateauing region of the wave, while for a non-plateauing wave, this is assigned as the absolute maximum current of the wave. $i_{cat/2}$ is defined as half the catalytic current, and the potential at which this current is observed is termed $E_{cat/2}$. Selection of $E_{cat/2}$ in this manner ensures that there is minimal variation in the catalytic rate when determining a catalytic potential.

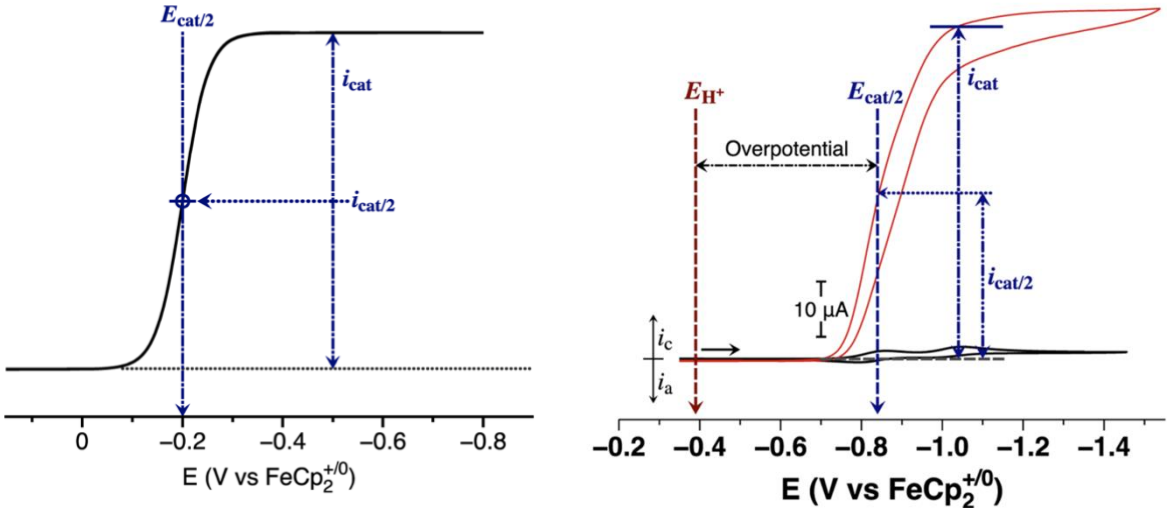

Figure 2.13: Simulated catalytic wave for a molecular catalyst showing the selection of i_{cat}, $i_{cat/2}$, and $E_{cat/2}$ (left). Experimental CV illustrating determination of $E_{cat/2}$ (and overpotential) for H_2

production (right). Reprinted with permission from 12. Copyright 2014 American Chemical Society.

The information provided by these CV experiments also provides essential information about the overpotential for a catalytic reaction, which is the driving force beyond the thermodynamic minimum needed to carry out a particular chemical transformation. The thermodynamic overpotential is most accurate when the Nernst equation is satisfied and can be determined using the following equations:

$$E_X = E_X^o + \frac{RT}{nF} \ln \frac{[HB^+]}{[B]} \quad (2.4)$$

$$E_X = E_X^o - 0.05916\, V \times pH \quad (2.5)$$

Notably, overpotential can be determined in aqueous or non-aqueous solvents, but the thermodynamic potential of a catalytic reaction at standard conditions (defined as the equilibrium potential (E^{o}_{X})), pH of the system, and the $E_{cat/2}$ must be defined. Acetonitrile is generally the preferred solvent because E^{o}_{X} can be determined[90] and there is well defined pK_a scale for this purpose.[91,92,93]

As an example, if the reader is interested in proton reduction to dihydrogen using an acid such as protonated dimethylformamide, $[DMFH]^+$, as the substrate, a series of cyclic voltammograms would be run at standard-state conditions, with a buffered solution of DMF/$[DMFH]^+$, and under 1 atm of H_2. Under these conditions, i_{cat}, $i_{cat/2}$, and $E_{cat/2}$ can be determined to calculate the thermodynamic overpotential. Though the observation of a catalytic response during a CV experiment does not depend on satisfying the Nernst equation for a particular transformation, an accurate calculation of the thermodynamic overpotential can only extracted when this is possible.

A relevant example uses the organometallic complex $[Cp^*RhCl(^{tBu}bpy)]^+$ (where Cp* is η^5-(1,2,3,4,5-pentamethylcyclopentadienyl) and ^{tBu}bpy is 4,4′-bis-*tert*butyl-2,2′-bipyridine) as a

proton reduction catalyst for the production of dihydrogen (see Figure 2.14).[71] In the absence of acid, the CV of [Cp*RhCl(^{tBu}bpy)]$^{+}$ exhibits a quasi-reversible redox event centered at -1.25 V vs. $Fc^{+/0}$ in MeCN. When acid is added, the quasi-reversible behavior of the Rh^{III} /Rh^{I} redox couple ceases, and a catalytic response is observed. The loss of reversibility here indicates that the acid is reacting with the reduced Rh^{I} species and the resulting current enhancement is consistent with catalytic behavior. The current enhancement results from the Rh^{III} starting material being reduced to Rh^{I}, which then interacts with the acid substrate, evolving dihydrogen, and subsequently regenerating the Rh^{III} starting complex. Since the potential at the electrode surface is still sufficiently reducing, this process continues as long as the potential of the electrode remains at values sufficient to drive the reduction processes involved in the chemistry. With these CVs in hand, the i_{cat} (–4.16 mA cm^{-2}), $i_{cat/2}$ (–2.08 16 mA cm^{-2}), $E_{cat/2}$ (–1.33 V), and overpotential (0.569 V) were determined for the catalytic process. Taking these parameters into account, the CPE experiments were carried out under identical conditions with polarization at –1.36 V vs $Fc^{+/0}$ over the course of 90 minutes. Other [Cp*RhCl(^{R}bpy)]$^{+}$ (R = 4,4-bis-substituted-2,2'-bipyridyl, H and CF_3) complexes have also shown this catalytic behavior in the presence of a proton source. These catalytic CV experiments are not limited to proton reduction and have been carried out in the exploration of catalytic applications involving WO, AO, HER, CO_2R, and N_2RR.

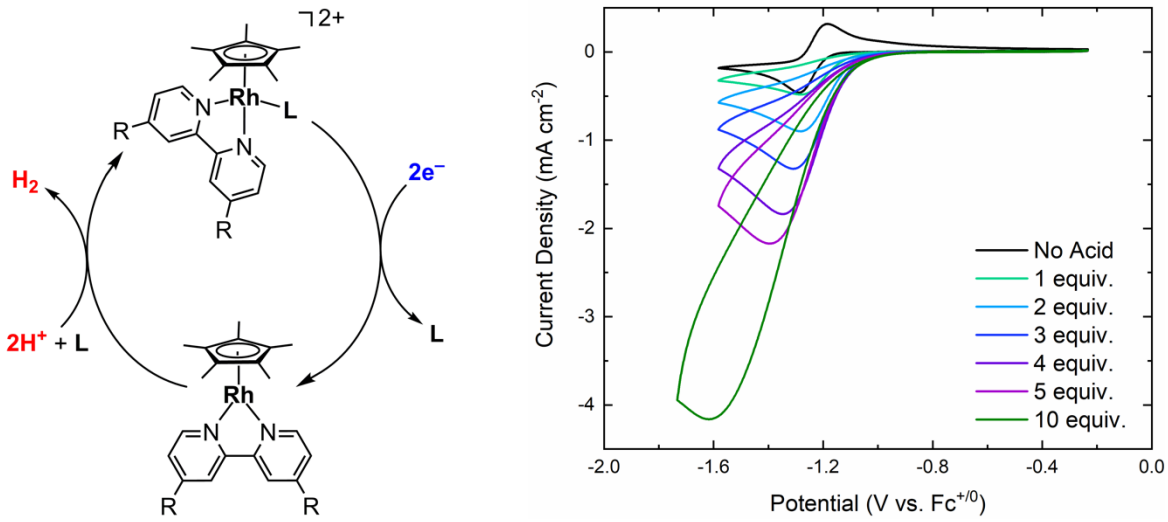

Figure 2.14: Pathway for HER using [Cp*Rh(^{R}bpy)] showing the energy loading and energy storage steps (left). Cyclic voltammograms with [Cp*RhCl(^{tBu}bpy)]$^{+}$, 1-5 equiv. of $PhNH_2$/[$PhNH_3$]OTf, and 1 atm of H_2 at a scan rate of 100 mVs^{-1} (right).

2.5.2.2 Kinetic Considerations in Electrocatalysis: Foot of the Wave Analysis

To extract kinetic and latent mechanistic information from CV experiments, one employs a method pioneered by Constentin, Savéant, and co-workers known as foot-of-the-wave analysis (FOWA).[94] This method simplifies the analysis because the earliest part of the catalytic wave inevitably has pseudo-first order kinetics because the substrate will be in vast excess compared to the catalyst.[95] FOWA minimizes the effects of secondary phenomena such as catalyst inhibition, decomposition, or saturation, and maximizes the information provided by the current that flows. Under ideal conditions, an observed rate constant can be computed using:

$$\frac{i_{cat}}{i_p} = \frac{2.24\,[\frac{RT}{Fv}2k_{obs}C_A]^{\frac{1}{2}}}{1+exp\,[\frac{F}{RT}(E-E^o)]} \qquad (2.6)$$

where i_{cat} is the peak catalytic current, i_p is the peak current of the redox process of the catalyst in the absence of substrate, R is the ideal gas constant, F is Faraday's constant, T is temperature, ν is the scan rate, k_{obs} is the observed rate constant, C_A is the initial concentration of substrate, *E* is the

present potential and $E^o = E_{cat/2}$ which is the thermodynamic potential for the catalytic wave. Plotting i_{cat}/i_p as a function of $1/\{1+\exp[(F/RT)(E–E^o)]\}$ produces a line with a slope equal to $2.24((RT/F\nu)2k_{obs}C_A)^{1/2}$, that can be used to extract the observed rate of catalysis (see Figure 2.15). These experiments can be repeated at various substrate concentrations, and at several different scan rates, to extract an average rate constant for the desired electrocatalytic reaction. The average k_{obs} is computed from a linear regression of the scan rate dependent data with a fixed slope of zero, since the intrinsic chemical kinetics should not depend on scan rate. This kinetic technique has become a recognized approach to determining substrate order and observed rates when mapping out the mechanistic details of electrocatalysts. FOWA has been used in various electrocatalytic kinetic studies for WO, [96] AO,[97] HER,[98] CO_2R, [99] and N_2RR.[100]

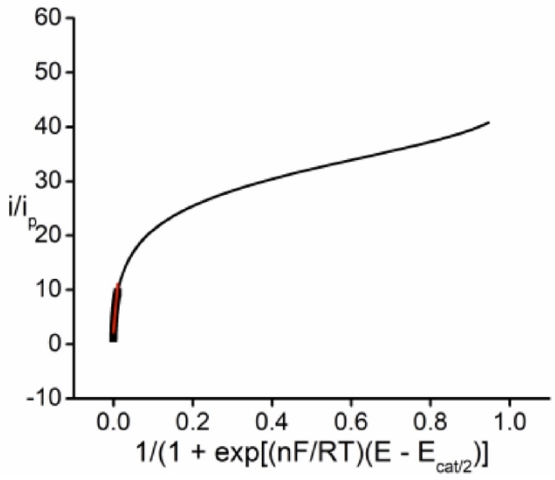

Figure 2.15: An example FOWA plot of i_{cat}/i_p as a function of $1/\{1+\exp[(F/RT)(E–E^o)]\}$. The pseudo-first order rate constant is extracted from the initial linear region of the plot. Reprinted with permission from 99. Copyright 2018 American Chemical Society.

2.5.2.3 Distinguishing Homogenous from Heterogeneous Catalysis with Electrochemical Methods

In organometallic catalysis, it is often desirable to confirm the identity or composition of a molecular catalyst. An important step in identifying the "true," or active, catalyst is distinguishing whether the materials in the electrochemical cell behaves as a homogenous or heterogeneous electrocatalyst. While there is an excellent precedent to explore heterogeneous materials in electrocatalysis because of their ease of separation from products, crucial structural, electronic, and mechanistic information is typically lost because traditional spectroscopic techniques such as NMR, IR, and electronic absorption spectroscopies are limited in the interrogation of these systems. However, there are several techniques and methods that may be used to investigate catalytic systems in an effort to distinguish homogenous from heterogeneous catalysts.[101] These methods include strategic catalyst poisoning, [102] X-ray photoelectron spectroscopy,[103] and transmission electron microscopy.[104] However, the *in situ* generation of new molecular species during electrocatalysis provides a unique challenge when there is a concern about distinguishing between homogeneous and heterogeneous catalysis. Distinguishing between homogeneous and heterogeneous electrocatalysts may be accomplished with electrochemical techniques such as a two-cell CV experiment, or by using an electrochemical quartz crystal microbalance (EQCM).[103]

In a two-cell CV experiment, homogeneous catalysis is distinguished from heterogeneous catalysis by running a series of CV scans under catalytic conditions. The first cell will contain the candidate catalyst, substrate, and electrolyte solution. When running this experiment, typical catalytic current enhancement should be observed. Following this series of scans, the working electrode is transferred to a second electrochemical cell which contains only substrate and electrolyte solution. A series of CVs identical to those run in the first cell are then run. If there is

still a large current enhancement observed, this suggests the deposition of heterogeneous material behaving as the catalyst at the surface of the electrode. If the current enhancement is absent in the fresh solution, this provides support for molecular homogeneous catalysis.

Another method for distinguishing heterogeneous from homogeneous catalysis is by using an electrochemical quartz crystal microbalance (EQCM).[103,105,106] This piezoelectric gravimetric technique can detect small mass changes at the surface of the working electrode as a function of scan rate during common electrochemical experiments, such as CV. In the case of formation of a heterogeneous catalyst, a change in mass at the surface of the electrode would be detectable during a catalytic CV experiment. Conversely, for a homogenous system, there would not be a detectable change in the mass at the working electrode surface. An example from our group highlights the possible distinction of heterogeneous catalysis from homogeneous catalysis in the analysis of a well-known molecular cobaloxime complex which catalyzes hydrogen production. The deposition of heterogeneous cobalt material on the surface of the working electrode could be detected during a CV experiment with an EQCM and is distinctive from an electrochemical blank containing only electrolyte solution (See Figure 2.16).

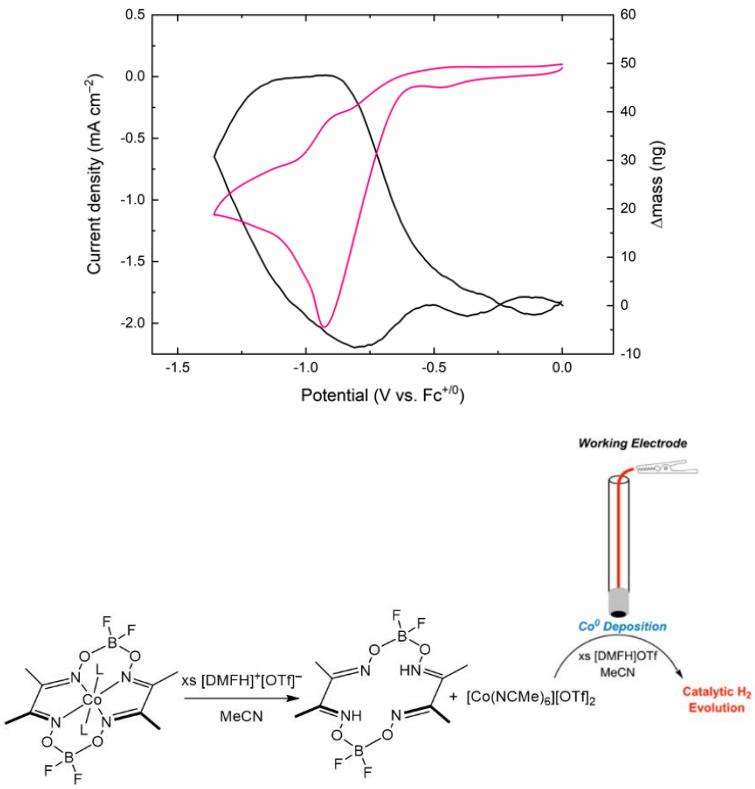

Figure 2.16: Upper panel: cyclic voltammetry data (pink trace) and gravimetry data (black trace) showing involvement of heterogeneous, electrodeposited material under potentials at which nominally molecular catalysis is indicated by CV data alone. See reference 103 for details. Lower scheme: After the addition of acid to a (bis-difluoroboryl)cobaloxime, spectral evidence from chemical work supports the presence of the demetallated, protonated macrocycle and cobalt(hexakis-acetonitrile) ($[Co(NCMe)_6]^{2+}$). When conducting a CV of (bis-difluoroboryl)cobaloxime in the presence of acid during an EQCM experiment, the observation of a catalytic wave is observed, as well as the deposition of cobalt metal on the surface of the working electrode. The cobalt metal is generated by reduction of $[Co(NCMe)_6]^{2+}$, a reaction that can be probed by independent electrochemical work with $[Co(NCMe)_6]^{2+}$.

2.5.3 Investigating Organometallic Electrocatalysis using Controlled Potential Electrolysis

To generate the product(s) associated with the current enhancement observed during electrocatalytic CV experiments, CPE experiments are commonly employed. For a detailed explanation of bulk and controlled potential electrolysis methods, Bard and Faulkner dedicate a chapter to the discussion of these techniques.[42] Briefly, a CPE is typically carried out in an electrochemical cell designed specifically for the product being analyzed (See Figure 2.17). Common design principles among the CPE cells include two separated compartments, with a known volume and headspace, capable of a gas-tight seal, and the ability to have headspace withdrawn after electrolysis is complete.

Using the first CPE cell as an example, a typical experiment is set up where the left compartment contains the candidate electrocatalyst, the substrate, electrolyte solution, a large surface area working electrode, and reference electrode, while the right compartment contains a sacrificial reductant (for reductive catalysis) or oxidant (oxidative catalysis), electrolyte solution, and the counter electrode. The experiment is set up to apply a bias, ideally at the determined $E_{cat/2}$ from the electrocatalytic CV experiments, for a fixed amount of time, typically ranging from 30 min., up to 24 hours. Once the experiment is complete, the amount of product produced may be quantified via various detection methods. Based on the amount of charge passed during the electrolysis, and the amount of product detected, the Faradaic efficiency, turnover number, and turnover frequency can also be calculated. The Faradaic efficiency is determined by converting the charge passed, into moles of electrons passed, and then into the theoretical amount of product that should be produced. The actual yield is then divided by this theoretical yield to obtain the FE. The TON is determined by computing the moles of product per moles of catalyst. Finally, the TOF is determined by dividing the amount of product produced over unit time.

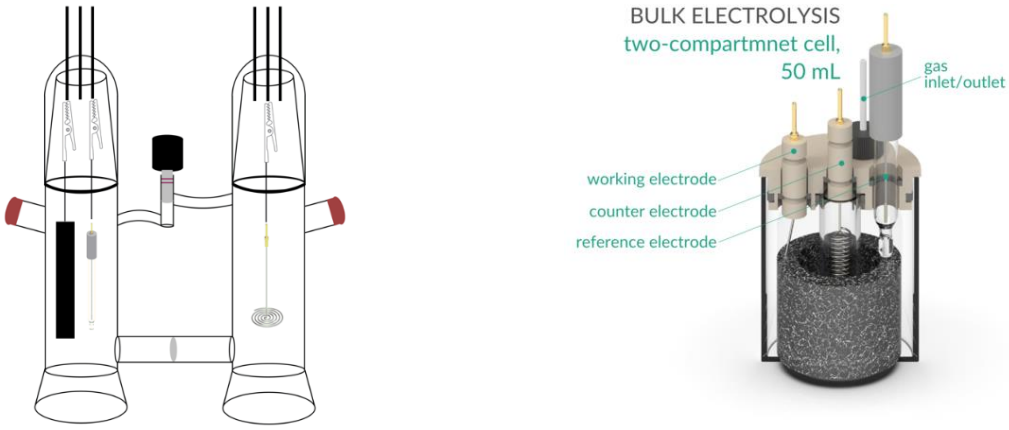

Figure 2.17: Example controlled potential electrolysis cells that can be used to conduct WO, AO, HER, CO_2R, N_2RR, or EOT reactions. Cells can be custom made to specialize in gaseous product detection (left[107]) or ordered directly from a supplier if the goal is complete liquid or solid isolation (right, from redoxme[108]).

2.5.4 Product Analysis in Organometallic Electrochemistry

To analyze the product(s) produced during organometallic electrocatalysis, quantitative methods of analysis are employed.[109] Products generated in electrocatalytic reactions may be gaseous, liquid, or solid. Common laboratory techniques and instruments such as gas chromatography (GC), liquid chromatography-mass spectrometry (LC-MS), nuclear magnetic resonance (NMR), electron paramagnetic resonance (EPR), UV-Vis, and gravimetry may be used to determine the amount of product generated during electrocatalytic experiments. For gaseous product detection and quantification of common electrocatalytic products such as O_2, N_2, H_2, and CO, gas chromatography is capable of rapid product detection and quantification when a calibration curve can be established for the particular product being examined. Likewise, when samples contain liquid or dissolved solids in solution, LC-MS techniques can be used to identify

and quantify products. Furthermore, solid and liquid samples that can be dissolved in deuterated solvents may also be examined via NMR and integrated in reference to a known standard, such as trimethoxybenzene, to quantify the product produced. For paramagnetic products, EPR can be used to quantify the amount of product produced by using spin quantitation.[110] Some electrolysis products, such as ammonia, can undergo a quantitative reaction that gives a product that can be quantitated colorimetrically, using UV-Vis since the molar absorptivity of the generated product is known. Lastly, for solid samples that cannot be reasonably dissolved, gravimetric methods may be used to weigh out the product produced from the CPE experiment.

2.6 Applications of Organometallic Electrocatalysis for Select Transformations

2.6.1 Electrocatalytic Water Oxidation

Solar fuel cells are one possible solution to the renewable energy storage challenge, and the basic design makes use of a solar photovoltaic assembly used in combination with an efficient WO electrocatalyst at the anode and a HER electrocatalyst at the cathode to generate H_2.[87] The allure of a clean energy future powered by sunlight and water continues to spark interest in electrocatalytic WO, which has been the topic of many reviews.[111,112,113,114] As inspiration, metalloenzymes found in nature often serve as role models for the development and investigation of organometallic electrocatalysts. For instance, the oxygen-evolving complex (OEC) in photosystem II is responsible for oxidizing water to dioxygen, with release of four protons and four electrons.[115] When written according to the standard of the IUPAC, the reduction potential for the interconversion of water and oxygen is +1.23 V vs SHE (see Table 2.1).[31,116] However, if you wish to discuss the potential for the oxidation, which may be useful in computing electrochemical cell potentials, the value will be -1.23 V; this is the minimum voltage needed to drive WO. For example, using a platinized platinum electrode as a cathode, the equilibrium

potential of the H_2/H^+ couple is set to 0 V vs SHE. At the anode, two equivalents of water is oxidized to dioxygen, four protons, and four electrons at +1.23 V vs SHE. Thus, using equation 1.2, the four electron oxidation of water to dioxygen and dihydrogen is shown to be endothermic by approximately 113 kcal/mol under aqueous conditions (see equations 2.7-2.10).[112]

Overall: $2H_2O \rightarrow O_2 + 2H_2$ (2.7)

Cathode: $2H^+ + 2e^- \rightarrow H_2$ (2.8)

Anode: $2H_2O \rightarrow O_2 + 4H^+ + 4e^-$ (2.9)

$$\Delta G = -nF\Delta E = -(4\ mol\ e^-)\left(96485\ \frac{C}{mol\ e^-}\right)(0 - 1.23\ V) = +475\ \frac{kJ}{mol} = +113\ \frac{kcal}{mol} \quad (2.10)$$

The calculation shown here is readily extended to other reactions too, but with the caveat that the reversible potentials for the reactions at the cathode and the anode must be known for a specific set of conditions that satisfy the Nernst equation. Partial oxidation of water is also possible, generating products such as hydroxyl radicals, hydrogen peroxide, and peroxyl radicals, along with the appropriate number of protons and electrons. The mechanisms for formation of these partial oxidation products are also important to understand, because they may be generated as undesired side products during WO.

Thermodynamic Half-Reactions	Potential, E^0 (V vs SHE)
$O_2 + 4H^+ + 4e^- \rightleftharpoons 2H_2O$	+1.23
$H_2O_2 + 2H^+ + 2e^- \rightleftharpoons 2H_2O$	+1.76
$HO\cdot + H^+ + e^- \rightleftharpoons H_2O$	+2.38
$HOO\cdot + 3H^+ + 3e^- \rightleftharpoons 2H_2O$	+1.65

Table 2.1: Standard thermodynamic electrochemical half-reaction potentials for water in aqueous solution.[31,42]

Heterogeneous metal oxides of manganese, ruthenium, and iridium have long been recognized as electrocatalysts for WO.[117,118] On the other hand, homogeneous catalysts were discovered much more recently; such homogeneous systems offer numerous advantages with regard to mechanistic studies, detection of reactive intermediates, and development of tunable catalysts. In 1982, Meyer and co-workers were the first to synthesize and characterize a molecular ruthenium electrocatalyst for water-oxidation.[119] Since then, other homogeneous and heterogeneous molecular catalysts of ruthenium,[120,121] iridium,[122,123,124] and other metals,[125,126] have allowed for more in-depth analysis of the steps involved in WO. For example, Brudvig, Crabtree, and co-workers,[127] Macchioni and co-workers[128] and several other groups have developed iridium-based catalyst precursors supported by Cp* or Cp rings along with a variety of other ligands, including diimines, halides, waters, carbonyls, and phosphines (see Figure 2.18 for some example complexes). Most of these complexes serve as precatalysts for water oxidation, in that initial electrochemical oxidation generates the active catalytic species that can then undergo further oxidation, triggering catalytic water oxidation. One notable example precatalyst, $[Cp^*Ir(H_2O)_3]^{2+}$, undergoes oxidation to form

a heterogeneous “blue layer” on the electrode surface that is readily observed by a variety of techniques, including cyclic voltammetry.[129] In other cases, catalyst activation leads to formation of homogeneous species that can catalyze water oxidation in solution (i.e., without formation of solids or particulate species). Distinguishing between homogeneous and heterogeneous catalysis, a recognized challenge in organometallic chemistry, is made especially challenging under these conditions for water oxidation catalysis driven by organometallic precatalysts. The electrochemical quartz crystal microbalance has been shown to be a useful tool for observing formation of insoluble heterogeneous species, both for oxidative reactions like water oxidation driven by organometallic precursors[130] as well as reductive reactions like hydrogen evolution and metal electrodeposition.[103,105,106] Along a similar line, dynamic light scattering is useful for formation of particulates or particles in solution. Application of specialized techniques like these, in concert with detailed electroanalytical and mechanistic/kinetic/chemical work, can strongly inform studies of water oxidation catalysis. Approaching molecular electrocatalytic systems from multiple viewpoints and with multiple chemical and electrochemical techniques can thus be an appealing strategy, especially when dealing with challenging reactions like water oxidation.

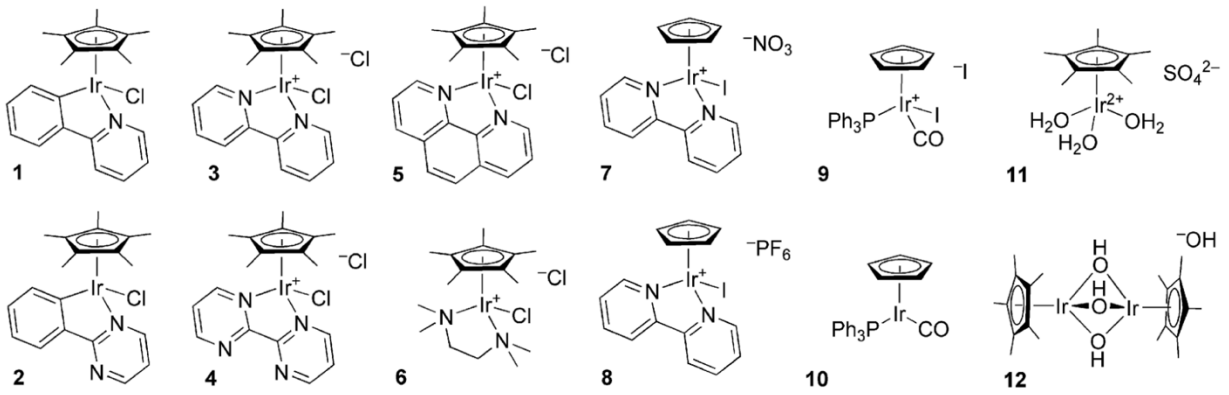

Figure 2.18: Select iridium(III) organometallic precatalysts for electrochemical WO. Reprinted with permission from reference 127. Copyright 2010, American Chemical Society.

2.6.2 Electrocatalytic Ammonia Oxidation

Electrocatalytic AO and WO are comparable in many ways; both reactions involve the removal of several electrons and protons, the formation of a new bond between heteroatoms, and the evolution of a gaseous product (N_2 or O_2). Likewise, electrocatalytic AO represents an alternative fuel cell design where AO would be carried out at an anode and proton reduction at a cathode to generate energy. However, unlike WO, electrocatalytic AO is still an emerging field and has been the topic of a recent review by Wu and co-workers[131] and perspective by Bullock and co-workers.[132] Complete ammonia oxidation is best summarized as a thermodynamic electrochemical half reaction where ammonia is converted into dinitrogen, six protons, and six electrons at –0.057 V vs SCE (see Table 2.2). Partial ammonia oxidation is also possible, generating other products such as hydrazine and hydroxylamine along with the relevant number of protons and electrons, on route to complete ammonia oxidation.

Thermodynamic Half-Reactions[24]	Potential E^0 (V vs SHE)
$N_2 + 6H^+ + 6e^- \rightleftharpoons 2NH_3$	– 0.06
$N_2 + 8H^+ + 6e^- \rightleftharpoons 2NH_4^+$	+0.28
$N_2 + 4H_2O + 4e^- \rightleftharpoons N_2H_4 + 4OH^-$	–1.16
$N_2 + 5H^+ + 4e^- \rightleftharpoons N_2H_5+$	–0.23
$3N_2 + 2e^- \rightleftharpoons 2N_3^-$	–3.40

Table 2.2: Standard thermodynamic electrochemical half-reaction potentials for dinitrogen in aqueous solution.[31,42]

Heterogeneous materials have been employed in electrocatalytic AO, but these instances rely heavily on precious metals and thus proposed mechanisms are not secure. The first report of a molecular electrocatalyst for AO was reported by Smith, Hamann, and co-workers, where they used a derivative of a Ru-based WO catalyst bearing an electron-donating ^{Me2N}bpy ligand.[133] Subsequently, other electrocatalysts for water oxidation have been repurposed for ammonia oxidation. Recent work from the Peters group makes use of a previously reported alkane oxidation catalyst.[134] The labile acetonitrile (MeCN) ligands of the starting complex are readily exchanged in the presence of ammonia, shown here in the solid-state structure of $[(bpyPy_2Me)Fe(MeCN)(NH_3)](OTf)_2$ (see Figure 2.19). Compared to $[(TPA)Fe(MeCN)_2](OTf)_2$ (TPA is tris(2-pyridylmethyl)amine),[97] a catalytic CV experiment shows a dramatic increase in a catalytic current for this newly reported complex and FOWA was performed to determine the observed rate of AO. The CPE cell was loaded with 0.05 mM [Fe] catalyst, 20 mM of NH_3, and 50 mM NH_4OTf in MeCN as the supporting electrolyte. After applying a bias of 0.85 V vs $Fc^{+/0}$ for 24 hours, product analysis revealed the formation of N_2 at the working electrode and H_2 at the

counter electrode in all instances, as well as the highest TON to date for a molecular AO electrocatalyst. Future work in the field of electrocatalytic AO requires probing the rational design, kinetics, and thermodynamics of molecular complexes.

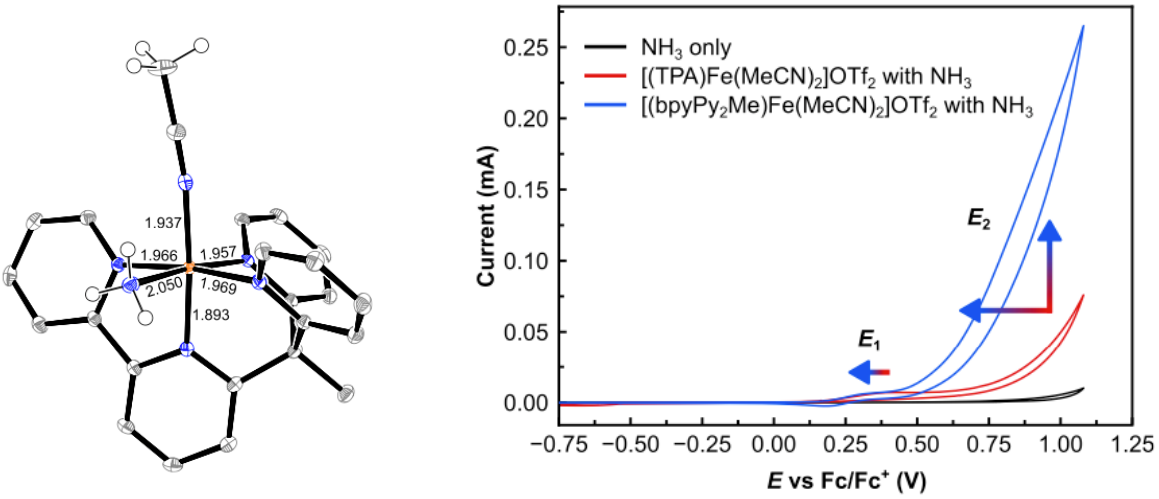

Figure 2.19: Solid-state structure of [(bpyPy$_2$Me)Fe(MeCN)(NH$_3$)](OTf)$_2$ (left). Displacement ellipsoids shown at 50% probability. Triflate and hydrogen atoms are omitted for clarity. CV of MeCN solutions containing 400 equiv. of NH$_3$, 0.05 M NH$_4$OTf, 0.5 M of [(bpyPy$_2$Me)Fe(MeCN)$_2$](OTf)$_2$ or [(TPA)Fe(MeCN)$_2$](OTf)$_2$. Reprinted with permission from reference 134. Copyright 2021, American Chemical Society.

2.6.3 Electrocatalytic Proton Reduction

In the electrocatalytic HER, two protons and two electrons are coupled with the help of a catalyst to generate dihydrogen. This is simpler than the multielectron N$_2$ and O$_2$ reactions, electrocatalytic HER has been the topic of significant work spanning decades. Electrocatalytic HER continues to draw major interest in the solar fuels community because understanding the elementary steps involved in this simple energy storage reaction could help in the rational design of future electrocatalysts.[135,136] Complete proton reduction to dihydrogen is represented by the

thermodynamic electrochemical half reaction where two protons and two electrons are coupled together to generate dihydrogen at 0.00 V vs SHE (see Table 2.3).[31]

Thermodynamic Half-Reaction	Potential E^0 (V vs SHE)
$2H^+ + 2e^- \rightleftharpoons H_2$	0.00

Table 2.3: Standard thermodynamic electrochemical half-reaction potentials for protons in aqueous solution.[31,42]

Gray, Winkler, Brunschwig and co-workers have discussed possible mechanisms for dihydrogen evolution,[135] as have other researchers in this vibrant area of electrocatalysis research. HER catalysis typically involves either a homolytic or heterolytic pathway to the production of dihydrogen. The heterolytic pathway involves a proton and a hydride reacting to generate dihydrogen, while the homolytic pathway involves homolytic cleavage of two hydride species which undergo recombination to produce dihydrogen. Heterogeneous noble metals, such as platinum, are prominent electrocatalysts for the reduction of protons to dihydrogen.[137] Other heterogeneous materials, such as metal nanoparticles, have also shown promise for the electrocatalytic production of dihydrogen.[138] Molecular cobaloxime complexes have also been shown to be highly active for the production of dihydrogen.[139] While these systems are competent and efficient HER electrocatalysts, they may generate Co nanoparticles in the presence of acid which generates ambiguity in the identity of the true electrocatalyst.[103] Thus, well-defined homogeneous model systems that show activity toward electrocatalytic HER have been desirable.

While many redox-active systems are capable of electrocatalytic HER, the homogeneous Rh-based electrocatalyst, $[Cp^*RhCl(^{H}bpy)]^+$, developed by Kölle and Grätzel is one of the most well-known.[140] CV of $[Cp^*RhCl(^{H}bpy)]^+$ reveals a quasi-reversible $2e^-$ redox couple centered at approximately –1.21 V vs $Fc^{+/0}$. Addition of two equivalents of acid to Cp*Rh(bpy) results in the quantitative production of dihydrogen, and further experiments confirm its catalytic ability. This led to a systematic examination of a series of $[Cp^*RhCl(^{R}bpy)]^+$ (^{R}bpy is 4,4´-disubstituted-2,2´-bipyridyl; R = H, tBu, and CF_3) complexes by Blakemore and co-workers in an effort to determine if electrocatalytic dihydrogen evolution could be modulated using substituents on the bpy ligand.[71] Initial catalytic CV experiments for these complexes were discussed in section 1.5.2.1. These experiments assisted in the determination of the parameters needed to carry out a series of CPE experiments. To systematically compare the catalytic ability of each complex, CPE experiment were conducted with identical conditions with 1 mM of [Rh] catalyst and 10 mM anilinium triflate in the WE portion of the cell, ferrocene was added to the CE portion of the cell as a sacrificial reductant, 0.1 M $TBAPF_6$ in MeCN was used as the supporting electrolyte, and a bias of –1.36 V vs $Fc^{+/0}$ was applied for 90 minutes.

Over the course of the experiment, steady current flow is observed for each complex over time (see Figure 2.20). Notably, each of the complexes has significantly more current flowing than the blank and the amount of current flowing is different based on the identity of the complex. When the experiment is first started, the first few seconds appears to show rapid consumption of acid, but this is actually the initial charging of the WE, and following this period, steady current flows over time. Upon completion of the experiment, the presence of dihydrogen was confirmed in all instances by GC. When the identity of the substituents was –tBu, –H, or $–CF_3$, the complexes

produced 2.6 mL, 3.5 mL, and 1.5 mL of dihydrogen, with corresponding TONs of 3.4, 4.4, and 2.7, respectively.

As an aside, keeping the bias at the same potential across the series of complexes results in what could be perceived as an "unfair" although uniformly direct comparison of these catalysts' abilities to produce dihydrogen. This is because from the perspective of the Nernst equation, when the potential is moved from $E_{cat/2}$ of a given individual complex, the amount of reduced species present at the electrode at any one point in time is changed. In other words, catalysis for each of these systems will be optimal when polarizing at $E_{cat/2}$, and thus comparing the kinetic performance of the catalysts at a common potential value that doesn't align with the value of $E_{cat/2}$ for all the catalysts introduces an additional concentration/potential dependence to this study. On the other hand, a common potential polarization for all the comparisons made here does satisfy a pratical aspect of testing and comparing these model catalysts under comparable conditions. Regardless of this potential ambiguity, however, based on the amount of charge transferred and the amount of dihydrogen detected, all three complexes were confirmed (in this study) to be electrocatalysts with FE exceeding 90% in all three systems. This study encapsulates the challenges and opportunities in comparing across a family of catalysts that may have unique redox chemistries.

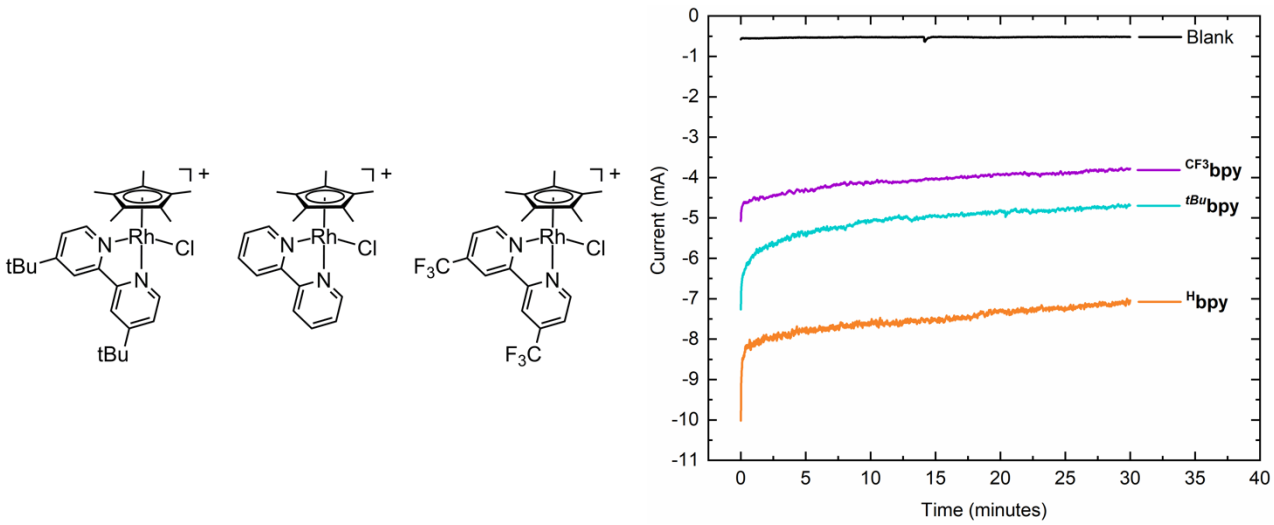

Figure 2.20: [Cp*RhCl(^{R}bpy)]$^{+}$ complexes with electron donating and withdrawing substituents (left). Comparison of CPE steady-state current as a function of time with an applied bias of –1.36 V vs $Fc^{+/0}$ with 10 mM anilinium triflate as the proton source (right).

2.6.4 Electrocatalytic Carbon Dioxide Reduction

Electrocatalytic CO_2 reduction continues to draw attention from the organometallic chemistry community because organometallic compounds are uniquely well-suited to understanding the bonding and activation of carbon-containing small molecules.[141] Use of CO_2 as input for preparation of useful chemicals could also decrease the environmental impact of chemical industry, motivating work in this area further. CO_2 has many potential reduction pathways and products, with one of the most common targets being carbon monoxide (CO) because of its use as an industrial synthon. More elaborate reactions could be used to produce carbon-based fuels or other chemicals. The thermodynamic electrochemical half-reaction for some key CO_2 reduction products involving two, four, six, or eight electron pathways are shown below (see Table 2.4).[31,142]

$$CO_2 + 2H^+ + 2e^- \xrightarrow{[catalyst]} CO + H_2O$$

Thermodynamic Half-Reactions	Potential E^0 (V vs SHE)
$CO_2 + 2H^+ + 2e^- \rightleftharpoons CO + H_2O$	–0.106
$CO_2 + 2H^+ + 2e^- \rightleftharpoons HCO_2H$	–0.199
$CO_2 + H_2O + 2e^- \rightleftharpoons HCO_2^- + OH^-$	–1.078
$CO_2 + 2H_2O + 2e^- \rightleftharpoons CO + 2OH^-$	–0.934
$CO_2 + 4H^+ + 4e^- \rightleftharpoons CH_2O + H_2O$	–0.070
$CO_2 + 3H_2O + 4e^- \rightleftharpoons CH_2O + 4OH^-$	–0.898
$CO_2 + 6H^+ + 6e^- \rightleftharpoons CH_3OH + H_2O$	+0.016
$CO_2 + 8H^+ + 8e^- \rightleftharpoons CH_4 + 2H_2O$	+0.169
$CO_2 + 5H_2O + 6e^- \rightleftharpoons CH_3OH + 6OH^-$	–0.812
$CO_2 + 6H_2O + 8e^- \rightleftharpoons CH_4 + 8OH^-$	–0.569
$2CO_2 + 2H^+ + 2e^- \rightleftharpoons C_2H_2O_4$	–0.475
$2CO_2 + 2e^- \rightleftharpoons C_2O_4^{2-}$	–0.590
$2CO_2 + 12H^+ + 12e^- \rightleftharpoons C_2H_4 + 4H_2O$	+0.064
$2CO_2 + 12H^+ + 12e^- \rightleftharpoons C_2H_6O + 3H_2O$	+0.084
$CO_2 + 4H^+ + 4e^- \rightleftharpoons C + 2H_2O$	+0.206
$CO_2 + 2H_2O + 4e^- \rightleftharpoons C + 4OH^-$	–0.627

Table 2.4: Standard thermodynamic electrochemical half-reaction potentials for CO_2 in aqueous solution.[31]

Heterogeneous electrode materials such as carbon, copper, and gold are capable of reducing CO_2 directly, but with various reaction pathways and significant overpotentials.[143] The use of these materials precludes the use of spectroscopic methods, making the development of future heterogeneous materials more difficult. Many homogeneous molecular complexes bearing first- and third-row transition metals have been synthesized with the goal of using them as CO_2 reduction catalysts. A notable example from Savéant and co-workers uses a molecular catalyst, tetraphenylporphyrin Fe(III) chloride (TPPFe(III)Cl), which undergoes three sequential one electron reductions to generate the active electrocatalyst for CO_2 reduction (see Figure 2.21).[144] In the presence of trifluoroacetic acid and CO_2, the reversible behavior in the CV of the Fe(TPP)

complex ceases and a substantial catalytic wave is observed at around -1.5 V vs. SCE. Preparative scale CPE results in the selective production of CO at 96% FE.

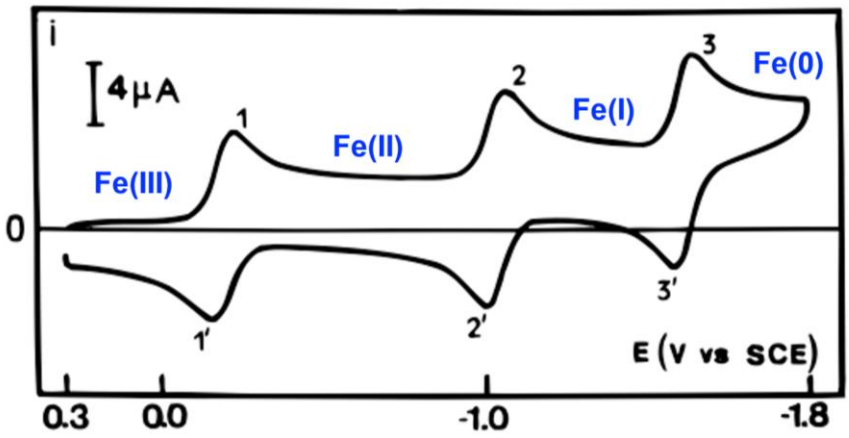

Figure 2.21: CV of TPPFe(III)Cl at 100 mVs^{-1} using 0.1 M $TEAClO_4$ in dimethylformamide as the supporting electrolyte and a glassy carbon working electrode. The sequential reductions of TPPFe(III)Cl at these negative potentials suggests that it was a prime candidate for electrocatalytic CO_2 reduction. Adapted with permission from 144. Copyright 1996 American Chemical Society.

However, the tricarbonyl complexes of the group 7 metals Re and Mn are perhaps the most famous CO_2 reduction electrocatalysts. The initial design of this class of homogeneous molecular CO_2 electrocatalysts began in the 1980s with the initial report of *fac*-$Re(CO)_3Cl(^{H}bpy)$ by Lehn and co-workers[145] and Meyer and co-workers.[146] Approximately thirty years later, Deronzier, Chardon-Noblat, and co-workers introduced the manganese analogue of the complex, *fac*-$Mn(CO)_3Br(^{H}bpy)$ as a significantly more Earth-abundant electrocatalyst for CO_2 reduction.[66] Both *fac*-$Re(CO)_3Cl(^{H}bpy)$ and *fac*-$Mn(CO)_3Br(^{H}bpy)$ are comparable and competent catalysts for the generation of CO from CO_2. Recent work in this area has focused on tuning the electron density at the [Re] and [Mn] metal centers by using 4,4´-disubstituted-bpy (^{R}bpy) ligands.[85,99,147]

The high cost of Re has resulted in an influx of reports on *fac*-$Mn(CO)_3Br(^{R}bpy)$ complexes. Some *fac*-$Mn(CO)_3Br(^{R}bpy)$ derivatives have been used to address potential shortcomings of

Mn(I) complexes, including the known visible-light photosensitivity and redox-induced dimerization of *fac*-$Mn(CO)_3Br(^{R}bpy)$ to form $Mn_2(CO)_6(^{R}bpy)_2$.[148,149] Kubiak and co-workers demonstrated that the dimerization of *fac*-$Mn(CO)_3Br(^{R}bpy)$ complexes can be impeded by utilizing bulky bipyridine ligands bearing mesityl groups in the 6 and 6´ positions of the bpy ligand (^{mes}bpy). CV of *fac*-$Mn(CO)_3(NCMe)(^{mes}bpy)$ reveals a quasi-reversible $2e^-$ redox couple centered at -1.55 V vs $Fc^{+/0}$ (see Figure 2.22).[150] In a catalytic CV experiment, *fac*-$Mn(CO)_3(NCMe)(^{mes}bpy)$ is reduced in the presence of methanol and CO_2. Interestingly, the onset of the catalytic wave does not occur at the initial $2e^-$ reduction, but rather, there is a kinetic potential shift that indicate the binding of CO_2, before being reduced again at -2.0 V to induce catalysis. Preparative CPE experiments reveal *fac*-$Mn(CO)_3(NCMe)(^{mes}bpy)$ is a competent CO_2 reduction electrocatalyst and selectively produces CO at 98% FE. Future work in the area of electrocatalytic CO_2 reduction will likely focus on kinetic, mechanistic, and thermodynamic studies in areas that extend beyond the common two-electron reduction products.

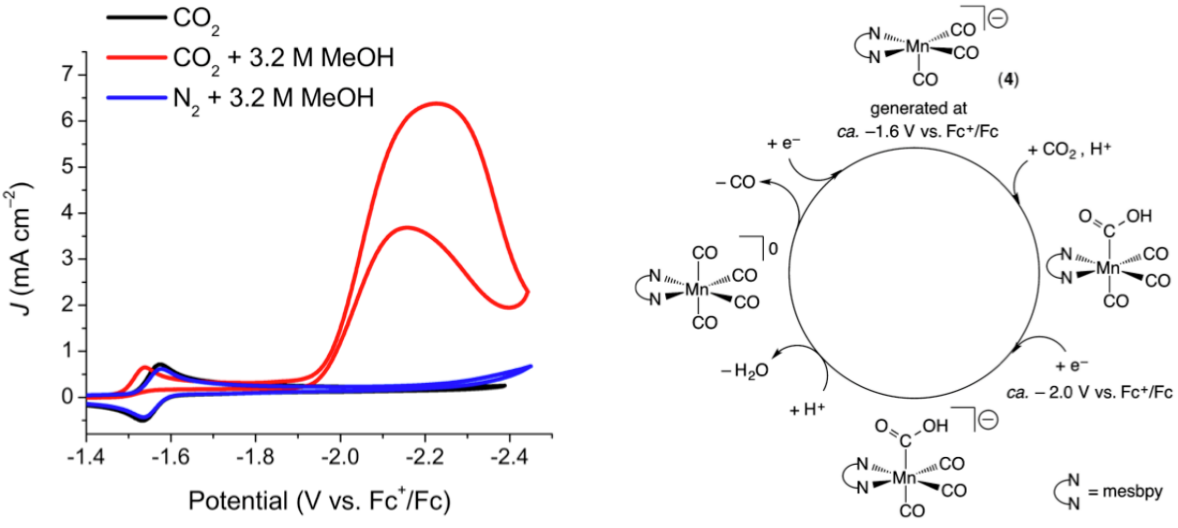

Figure 2.22: Catalytic CV experiment demonstrating that catalysis only occurs when *fac*-$Mn(CO)_3(NCMe)(^{mes}bpy)$ is in the presence of CO_2 and MeOH (left). A proposed catalytic cycle

for the electrocatalytic generation of CO using $Mn(CO)_3(NCMe)(^{mes}bpy)$ (right). Reprinted with permission from 150. Copyright 2014 American Chemical Society.

2.6.5 Electrocatalytic Dinitrogen Reduction

Functionalizing dinitrogen is a particularly challenging process, and this is manifested in its physicochemical characteristics.[151] However, since dinitrogen comprises more than 79% of the Earth's atmosphere, chemical or electrochemical generation of reduced nitrogen products, such as ammonia, could be a useful way to utilize this abundant resource. On an industrial scale, nitrogen fixation is accomplished using the Haber-Bosch process where dihydrogen (produced from the steam reformation of methane), dinitrogen (obtained from air), and a doped heterogeneous Fe-based catalyst are used to produce ammonia.[152] The Haber-Bosch process itself is quite efficient, converting >97% of the chemical inputs into ammonia, a fact made more incredible when considering that this reaction accounts for nearly half of the Earth's total ammonia production including both natural and artificial reactivity. However, the Haber-Bosch process as currently performed is the source of copious amounts of CO_2, and requires reaction temperatures exceeding 400 ^oC and pressures surpassing 200 atm. As a result, the redox process of reducing dinitrogen to ammonia has attracted increased interest from the electrocatalysis community; from this perspective, ammonia could either be used in fuel cells, producing only dinitrogen and water in an ideal scenario, or in its traditional role as a crop fertilizer. In nature, nitrogen fixation occurs by using the enzyme nitrogenase to reduce dinitrogen at room temperature and ambient pressure.[153] Toward this goal, the thermodynamic electrochemical half-reactions for some key dinitrogen reduction products involving, two, four, or six electrons are shown above (see Table 2.2 in AO).[31]

Figure 2.23: Reduction of dinitrogen using protons and electrons in combination with an electrocatalyst to generate ammonia.

While the electrocatalytic transformations (WO, HER, and CO_2R) discussed so far have many examples, electrocatalytic N_2RR with homogeneous catalysts is rare.[154] The first report of a true electrocatalytic N_2RR came from the Peters group in 2016 using $[(P_3^B)Fe]^+$ as a precatalyst and HBArF as an acid source.[155] Catalytic CV experiments revealed the onset of a catalytic wave at the $[(P_3^B)Fe]^+$ / $[(P_3^B)Fe(N_2)]$ couple at –1.5 V vs $Fc^{+/0}$, but greater enhancement was observed at the $[(P_3^B)Fe(N_2)]^{0/-1}$ couple at -2.2 V vs $Fc^{+/0}$. This potential is well within the range to observe HER as well as N_2RR. CPE of this complex revealed the presence of ammonia (2.3 equiv.) (as well as substantial amounts of H_2), confirming the catalytic ability of the complex. More recently, better kinetic control was achieved to improve the selectivity and turnover of this reaction by using a metallocene molecular mediator to facilitate the reduction of dinitrogen.[156,157] Improvement was achieved through the use of Cp^*_2Co as a mediator, resulting in a catalytic wave with onset at ~ -2.0 V vs. $Fc^{+/0}$. CPE of $[(P_3^B)Fe]^+$, with $[Ph_2NH_2]^+$ and a cocatalytic amount of Cp_2Co, at an applied bias of -2.1 V vs $Fc^{+/0}$ resulted in 4 equiv. of ammonia. Future work in this area depends on the synthesis of new heterogeneous or homogeneous electrocatalysts capable of N_2RR. This will be accomplished by developing systems and conditions that can operate negative enough to engender N_2RR, but at the same time disfavor the kinetics that prefers the HER.

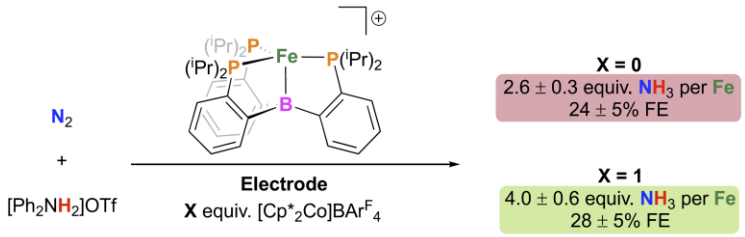

Figure 2.24: First molecular electrocatalyst for N_2RR in the presence of a cocatalytic amount of $[Cp^*_2Co]^+$. Reprinted with permission from reference 154. Copyright 2020, American Chemical Society.

2.6.6 Electrocatalytic Organic Transformations

Organometallic electrochemistry is typically associated with redox-induced small molecule activation where electrocatalysts are used to access and store energy. However, these techniques also are readily extended to electrocatalytic organic (electroorganic) transformations, which are rapidly gaining popularity.[158] Fortunately, organic chemists are beginning to think of electrochemistry as an essential method for driving synthetic processes. In this field, organometallic electrocatalysts typically behave as redox mediators, shuttling electrons from the surface of the working electrode to an organic substrate on the way to product generation.[156,159] In some instance, these electrocatalysts may also engender regio-, chemo-, and stereoselectivity in the products (see Figure 2.25).[160] In these reactions organic substrates are oxidized or reduced at a controlled potential, resulting in the generation of intermediate radical species that undergo further chemical reactivity before generating the product(s). To this end, electroorganic syntheses mediated by organometallic complexes have attracted the interest of commodity chemical and pharmaceutical industries because of the tunability, scalability, and potential energy control provided by electrochemical techniques. Indeed, selective manipulation and installation of functional groups on organic substrates with electrochemical methods offers a distinct new approach that is likely to continue surging in activity.

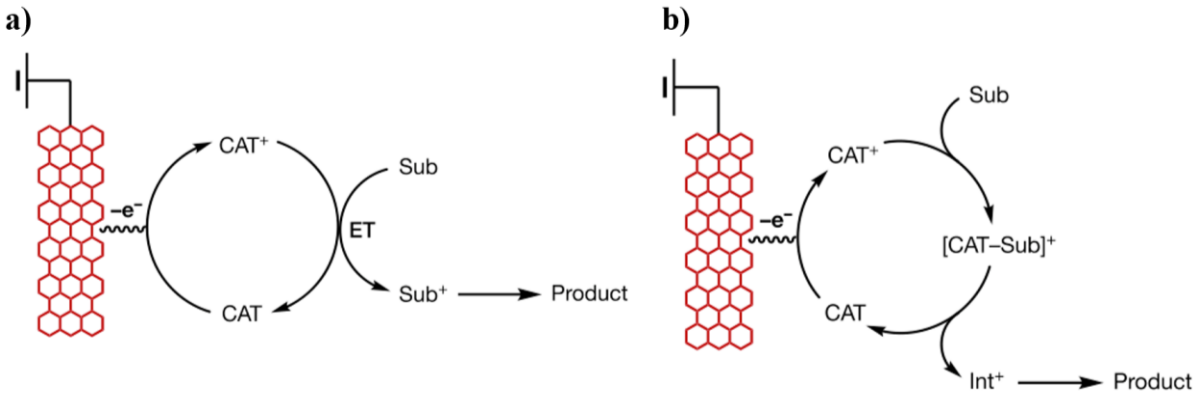

Figure 2.25: (**a**) a molecular mediator (CAT), in the context of oxidation, donating an electron to the working electrode, and later being reduced by the substrate (SUB) in route to product generation. (**b**) a molecular mediator, in the context of oxidation, donating an electron to the working electrode, stabilizing the substrate to form a catalyst–substrate complex, and then generating an intermediate on route to product generation. Figure adapted with permission from 160.

The earliest preparative scale electrochemical experiment was performed by Faraday in 1834, where an acetic acid solution was placed under anodic oxidative bias to generate ethane.[161] This experiment went on to inspire the Kolbe electrolysis in 1847, where abundant carboxylic acids were oxidized and used to produce alkyl radicals.[162] Around the same time, the first reductive preparative scale electroorganic experiment was also reported; this involved the reductive dehalogenation of trichlormethane sulfonic acid to methanesulfonic acid.[163] In the last twenty years, electrochemical methods have become more accessible to synthetic organic chemists due to the widespread availability of potentiostats and advancements in electrochemical techniques and methods, and this has resulted in an uptick in catalytic electroorganic synthesis literature reports.[164] Common functional groups such as aldehydes, ketones, esters, and olefins have been studied under electrocatalytic oxidative and reductive conditions with success. Hydrogenation of olefins and

alkynes has also been studied, taking advantage of reactive transition metal hydrides typically implicated in HER electrocatalysis.[165]

A common theme in organic electrocatalysis is the use of a redox mediator to drive a chemical transformation. In an example of organometallic electroorganic synthesis, Xu and co-workers have taken advantage of the reliable one-electron redox chemistry of ferrocene.[166] In their work, ferrocene is a mediator in the electrocatalytic C–H and N–H functionalization of functionalized (aza)indoles. A catalytic CV experiment shows that the addition of the model urea-based substrate in the presence of ferrocene does not result in any significant change to the appearance of the CV which displays the reversible oxidation of ferrocene to ferrocenium (see Figure 2.26). However, when sodium methoxide is added, a catalytic wave is observed and the return reduction has ceased, suggesting that the ferrocenium is consumed by the urea-based substrate. A possible mechanism involves a pre-equilibrium with deprotonation of the urea-based complex, resulting in a nitrogen-centered anion which then undergoes oxidation by intermolecular electron transfer with the electrogenerated ferrocenium. The oxidation generates a nitrogen centered radical that is capable of intramolecular cyclization with the neighboring alkyne which ultimately results in the formation of highly substituted indoles, while also regenerating ferrocene. Electrochemical methods for this redox-induced synthetic organic chemistry are advantageous because waste byproducts associated with the use of stoichiometric oxidants and reductants are eliminated. Future work in this area needs to focus on systematic studies of appropriate redox mediators capable of driving more complicated organic transformations. Important reactions, such as those involving the activation of aliphatic C-H bonds near amine and amide functionalities, is currently an active area in electroorganic synthesis.[167]

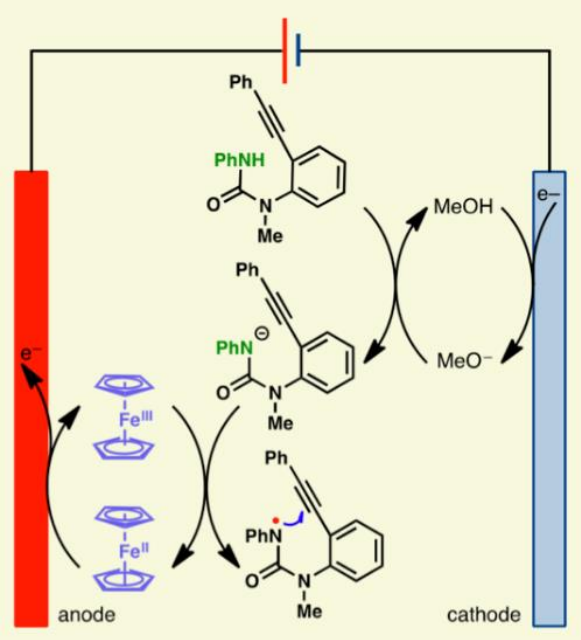

Figure 2.26: A proposed mechanism for the catalytic electrosynthesis of highly substituted indoles (right). Figure reprinted from reference 164 (right). Copyright 2017 American Chemical Society.

2.6.7 Analyses for Benchmarking Electrocatalysts

The significant increase in the production of new electrocatalysts over the years has contributed to the need for methods that can reliably benchmark in order to determine what is a "good" electrocatalyst. To this end, the derived Butler-Volmer[42] and Tafel[168] equations are two common analyses for benchmarking electrocatalysts, especially in the realm of heterogeneous catalysis. These methods are typically used to benchmark WO, HER, and CO_2RR catalysts, but can be performed for AO, N_2RR, and EOT reactions. Demonstrating high rates of activity and low overpotentials are the desired outcomes of catalyst benchmarking efforts. The main assessment methods are Butler-Volmer and Tafel analyses, and the reader may consult resources that give the full details.[42,169] Briefly, the Butler-Volmer equation describes the relationship between the current and potential between the surface of the electrode and the bulk sample for an elementary redox

reaction. However, at high overpotentials, the Butler-Volmer equations simplifies to the Tafel equation. The resulting Butler-Volmer and Tafel analyses provide kinetic and thermodynamic insight into systems by relating the rate of electrocatalysis to the overpotential.

In the realm of molecular electrocatalysis, alternative methods for benchmarking catalysts and understanding their kinetic behaviors are typically utilized. One such method is Foot-of-the-Wave (FOWA) analysis, a method developed by Savéant, Costentin, and co-workers.[11a] Summarizing this method, FOWA examines the "foot" of catalytic (and therefore irreversible) waves at points early in the onset of the catalytic current, in order to extract the instantaneous reaction rate from the voltammetric data.[170] One assumption that underlies typical FOWA is that the key redox-active intermediate involved in the rate-determining step of catalysis behaves in a Nernstian fashion, and thus its concentration can be considered directly controlled at the electrode surface by the applied potential. FOWA is distinguished as a very helpful method for extraction of rate information at short times, when catalyst deactivation, substrate consumption, and/or product inhibition are avoided. Notably, when voltammetric data is collected in such a way as to avoid these issues, other analyses based on Zone Diagrams and mathematical treatments are possible. The reader is encouraged to consult resources that give the full details on these methods.[28]

Significant work has also been accomplished in the last few years to better understand equilibrium potentials (E^{o}_{X}) of feedstocks capable of interconverting chemical and electrical energy in non-aqueous, organic solvents. These measurements establish a metric for evaluating and comparing different electrocatalysts for a given process in non-aqueous solvents. Work by Roberts and Bullock has provided an accurate determination of the H^{+}/H_2 equilibrium potential for various acids in MeCN (see Table 2.5).[90] These experiments use a Pt electrode, which is an excellent catalyst for reversible hydrogen reduction, even in organic solvents. In related work,

Mayer and Helm have also established E^{o}_{X} values (referenced to $Fc^{+/0}$ in acetonitrile and DMF) for electrocatalytic oxygen reduction and carbon dioxide reduction.[171] Determining these values in non-aqueous solvents has allowed the determination of accurate potentials for catalytic responses during electrocatalysis.

Half-Reactions	**Potential, E^0 (V vs $Fc^{+/0}$) MeCN**	**Potential, E^0 (V vs $Fc^{+/0}$) DMF**
$2H^+ + 2e^- \rightleftharpoons H_2$	-0.028	-0.662
$O_2 + 4H^+ + 4e^- \rightleftharpoons 2H_2O$	+1.29	+0.60
$CO_2 + 2H^+ + 2e^- \rightleftharpoons CO + H_2O$	-0.12	-0.73

Table 2.5: Thermodynamic equilibrium potentials for the reduction of protons, oxygen, and CO_2 in MeCN and DMF.[171]

2.7 Conclusion

The widespread availability of sensitive and robust potentiostats has led to substantial growth in the electrochemical investigation of redox processes in diverse compounds that are of interest to organometallic chemists. Modern electrochemical materials, methods and techniques have assisted in interpreting chemical reactivity that can be promoted at electrode surfaces. Cyclic voltammetry and controlled potential electrolysis experiments have provided important insights and continue to be workhorse methods in organometallic electrochemistry. Voltammetry experiments can reveal the potentials of redox events whose nature is then probed with stoichiometric redox reagents in chemical syntheses. The thermodynamic, kinetic, and mechanistic data provided by cyclic voltammetric experiments has informed design principles that can be used to generate organometallic complexes and catalysts with tailored properties. Further, the shapes of redox waves in cyclic voltammetry responses can provide crucial information about the nature of

electron transfer events and chemical reactions in solution, offering insights difficult to obtain by other techniques. This is particularly important in the field of electrocatalysis, in which efficiency and selectivity of a given catalyst can be investigated by coupling electrolysis methods to product analysis. Considering all the useful opportunities afforded by electrochemical methods, the future of organometallic electrochemistry is bright.

2.8 Acknowledgments

The authors thank the US National Science Foundation (OIA-1833087), the US Department of Energy, Office of Science, Office of Basic Energy Sciences, Early Career Research Program (DE-SC0019169), and the Kansas Academy of Science for funding different aspects of our group's work in redox chemistry and catalysis.

2.9 References

[1] Kealy, T. J.; Pauson, P. L., A New Type of Organo-Iron Compound. *Nature* **1951,** *168,* 1039-1040.

[2] Wilkinson, G.; Rosenblum, M.; Whiting, M. C.; Woodward, R. B., THE STRUCTURE OF IRON BIS-CYCLOPENTADIENYL. *J. Am. Chem. Soc.* **1952,** *74*, 2125-2126.

[3] Kuwana, T.; Bublitz, D. E.; Hoh, G., Chronopotentiometric Studies on the Oxidation of Ferrocene, Ruthenocene, Osmocene and Some of their Derivatives1. *J. Am. Chem. Soc.* **1960,** *82*, 5811-5817.

[4] Astruc, D., *Electron transfer and radical processes in transition metal chemistry*. New York : VCH: New York, 1995.

[5] Geiger, W. E., Organometallic Electrochemistry: Origins, Development, and Future. *Organometallics* **2007,** *26*, 5738-5765.

[6] Werlé, C.; Meyer, K., Organometallic Electrochemistry: Redox Catalysis Going the Smart Way. *Organometallics* **2019,** *38*, 1181-1185.

[7] Elgrishi, N.; Rountree, K. J.; McCarthy, B. D.; Rountree, E. S.; Eisenhart, T. T.; Dempsey, J. L., A Practical Beginner's Guide to Cyclic Voltammetry. *J. Chem. Educ.* **2018,** *95*, 197-206.

[8] Nernst, W., Über die Bildungswärme der Quecksilberverbindungen. *Z. Phys. Chem.* **1888,** *2U*, 23-28.

[9] Connelly, N. G.; Geiger, W. E., Chemical Redox Agents for Organometallic Chemistry. *Chem. Rev.* **1996,** *96*, 877-910.

[10] Savéant, J. M.; Su, K. B., Homogeneous redox catalysis of electrochemical reaction: Part VI. Zone diagram representation of the kinetic regimes. *J. Electroanal. Chem. Interf. Electrochem.* **1984,** *171*, 341-349.

[11] (a) Costentin, C.; Drouet, S.; Robert, M.; Savéant, J.-M., Turnover Numbers, Turnover Frequencies, and Overpotential in Molecular Catalysis of Electrochemical Reactions. Cyclic Voltammetry and Preparative-Scale Electrolysis. *J. Am. Chem. Soc.* **2012,** *134*, 11235-11242. (b) Costentin, C.; Savéant, J.-M., Multielectron, Multistep Molecular Catalysis of Electrochemical Reactions: Benchmarking of

Homogeneous Catalysts. *ChemElectroChem* **2014,** *1*, 1226-1236. (c) Costentin, C.; Drouet, S.; Robert, M.; Savéant, J.-M., A Local Proton Source Enhances CO_2 Electroreduction to CO by a Molecular Fe Catalyst. *Science* **2012,** *338*, 90-94.

[12] Appel, A. M.; Helm, M. L., Determining the Overpotential for a Molecular Electrocatalyst. *ACS Catalysis* **2014,** *4*, 630-633.

[13] Stock, J. T., *Electrochemistry in Retrospect. In Electrochemistry, Past and Present*, American Chemical Society: 1989; Vol. 390, pp 1-17.

[14] Mann, C. K.; Barnes, K. K. *Electrochemical Reactions in Nonaqueous Systems*; Marcel Dekker: New York, 1970; pp 403-418.

[15] Morris, M. D. *In Electroanalytical Chemistry*; Bard, A. J., Ed.; Marcel Dekker: New York, 1974; Vol. 7, pp 80-121.

[16] Kauffman, G. B., The discovery of ferrocene, the first sandwich compound. *J. Chem. Educ.* **1983,** *60*, 185.

[17] Page, J. A.; Wilkinson, G., The Polarographic Chemistry of Ferrocene, Ruthenocene and the Metal Hydrocarbon Ions. *J. Am. Chem. Soc.* **1952,** *74*, 6149-6150.

[18] (a) Dessy, R. E.; Kitching, W.; Chivers, T., Organometallic Electrochemistry. I. Derivatives of Group IV-B Elements. *J. Am. Chem. Soc.* **1966,** *88*, 453-459. (b) Dessy, R. E.; Kitching, W.; Psarras, T.; Salinger, R.; Chen, A.; Chivers, T., Organometallic Electrochemistry. II. Carbanion Stabilities. *J. Am. Chem. Soc.* **1966,** *88*, 460-467. (c) Dessy, R. E.; Chivers, T.; Kitching, W., Organometallic Electrochemistry. III. Organometallic Anions Derived from Group V Elements. *J. Am. Chem. Soc.* **1966,** *88*, 467-470. (d) Dessy, R. E.; Stary, F. E.; King, R. B.; Waldrop, M., Organometallic Electrochemistry. IV. The Transition Series. *J. Am. Chem. Soc.* **1966,** *88*, 471-476. (e) Dessy, R. E.; King, R. B.; Waldrop, M., Organometallic Electrochemistry. V. The Transition Series. *J. Am. Chem. Soc.* **1966,** *88*, 5112-5117. (f) Dessy, R. E.; Pohl, R. L.; King, R. B., Organometallic Electrochemistry.

VII.1 The Nucleophilicities of Metallic and Metalloidal Anions Derived from Metals of Groups IV, V, VI, VII, and VIII. *J. Am. Chem. Soc.* **1966,** *88*, 5121-5124. (g) Dessy, R. E.; Weissman, P. M., Organometallic Electrochemistry. VIII. The Formation of Metal-Metal Bonds. *J. Am. Chem. Soc.* **1966,** *88*, 5124-5129. (h) Dessy, R. E.; Weissman, P. M., Organometallic Electrochemistry. IX.1 Redistribution Reactions in Homo- and Heterodimetallic Compounds. *J. Am. Chem. Soc.* **1966,** *88*, 5129-5131. (i) Psarras, T.; Dessy, R. E., Organometallic Electrochemistry. X. Organomagnesium Reagents. *J. Am. Chem. Soc.* **1966,** *88*, 5132-5135. (j) Dessy, R. E.; Pohl, R. L., Organometallic electrochemistry. XI. Stable radical anions derived from acetylene-metal carbonyl complexes. *J. Am. Chem. Soc.* **1968,** *90*, 1995-2001. (k) Dessy, R. E.; Kornmann, R. L.; Smith, C.; Haytor, R., Organometallic electrochemistry. XII. Bridged bimetallic species. *J. Am. Chem. Soc.* **1968,** *90*, 2001-2004. (l) Dessy, R. E.; Wieczorek, L., Organometallic electrochemistry. XIV. Conversion of formal π acceptors to π donors. *J. Am. Chem. Soc.* **1969,** *91*, 4963-4974. (m) Dessy, R. E.; Charkoudian, J. C.; Abeles, T. P.; Rheingold, A. L., Organometallic electrochemistry. XVI. Electric charge distribution in organometallic compounds. Olefin-iron tetracarbonyls. *J. Am. Chem. Soc.* **1970,** *92*, 3947-3956. (n) Dessy, R. E.; Charkoudian, J. C.; Rheingold, A. L., Organometallic electrochemistry. XVII. Electric charge distribution organometallic compounds, tetrahedral derivatives of Co(CO)3(NO) and Fe(CO)2(NO)2. *J. Am. Chem. Soc.* **1972,** *94*, 738-745. (o) Dessy, R. E.; Rheingold, A. L.; Howard, G. D., Organometallic electrochemistry. XVIII. Effect of charge on geometry and activation paramenters for fluxional motion. *J. Am. Chem. Soc.* **1972,** *94*, 746-752. (p) Dessy, R. E.; Bares, L. A., Organometallic electrochemistry. *Acc. Chem. Res.* **1972,** *5*, 415-421.

[19] (a) Huebert, B. J.; Smith, D. E., Stereochemical effects in organic electrochemical kinetics: Part 1. D.C. and A.C. Polarographic study of cyclooctatetraene. *J. Electroanal. Chem. Interf. Electrochem.* **1971,** *31*, 333-348 For later work on the reduction of cyclooctatetraene see: Petersen, R. A.; Evans, D. H., Heterogeneous electron transfer kinetics for a variety of organic electrode reactions at the mercury-

acetonitrile interface using either tetraethylammonium perchlorate or tetraheptylammonium perchlorate electrolyte. *J. Electroanal. Chem. Interf. Electrochem.* **1987,** *222,* 129-150. (b) Smith, D. E. In Electroanalytical Chemistry; Bard, A. J., Ed.; Marcel Dekker Inc.: New York, 1966; Vol. 1, pp 102-110.

[20] (a) Gutmann, V.; Schöber, G., Polarographische Untersuchungen in wasserfreiem Äthylendiamin. *Monatsh. Chem. Verw. Teile Anderer Wiss* **1957,** *88,* 206-215. (b) Vlček, A. A., Relation between electronic structure and polarographic behaviour of inorganic depolarizers. XI. System cobaltocene-cobalticenium. *Collect. Czech. Chem. Commun*. **1965**, *30,* 952-960. (c) Mašek, J. Electrode and halogen oxidation of carbonyl triarsine complexes of zero-valent chromium, molybdenum and tungsten. *Collect. Czech. Chem. Commun.* **1965**, *30,* 4117-4126. (d) Denisovich, L. I.; Gubin, S. P.; Chapovskii, Y. A.; Ustynok, N. A., Polarography of π-cyclopentadienyltungstentricarbonyl compounds. *Bull. Acad. Sci. USSR, DiV. Chem. Sci.* **1968,** *17,* 891-892. (e) Piazza, G.; Paliani, G., Polarographic Behaviour of Transition Metal Nitrosyl Complexes in Nonaqueous Media. *Z. Phys. Chem.* **1970,** *71,* 91-101. (f) Mann, C. K.; Barnes, K. K. Electrochemical Reactions in Nonaqueous Systems; Marcel Dekker: New York, 1970; pp 403-418.

[21] Adams, R. N. Electrochemistry at Solid Electrodes; Marcel Dekker: New York, 1969

[22] Booman, G. L., Instrument for Controlled Potential Electrolysis Precision and Coulometric Integration. *Anal. Chem.* **1957,** *29,* 213-218.

[23] Smith, D. E. *In Electroanalytical Chemistry*; Bard, A. J., Ed.; Marcel Dekker Inc.: New York, 1966; Vol. 1, pp 102-110.

[24] DeFord, D. D. American Chemical Society 133rd Meeting, San Francisco, April 1958

[25] Smith, D. E., A.C. Polarography Employing Operational Amplifier Instrumentation. Evaluation of Instrument Performance and Application to Some New A.C. Polarographic Techniques. *Anal. Chem.* **1963,** *35,* 1811-1820.

[26] Schwarz, W. M.; Shain, I., Generalized Circuits for Electroanalytical Instrumentation. *Anal. Chem.* **1963,** *35*, 1770-1778.

[27] Nicholson, R. S.; Shain, I., Theory of Stationary Electrode Polarography. Single Scan and Cyclic Methods Applied to Reversible, Irreversible, and Kinetic Systems. *Anal. Chem.* **1964,** *36*, 706-723.

[28] Savéant, Jean-Michel; Costentin, C. *Elements of molecular and biomolecular electrochemistry: an electrochemical approach to electron transfer chemistry*, 2nd ed.; John Wiley & Sons: Hoboken, NJ, 2019.

[29] Pourbaix, M. *Atlas of Electrochemical Equilibria in Aqueous Solutions*, 2nd ed.; National Association of Corrosion Engineers: Houston, 1974.

[30] Latimer, W. M. *Oxidation potentials*, 2nd ed.; Prentice-Hall: New York, 1952.

[31] Bard, A. J.; Jordan, J.; Parsons, R. Standard potentials in aqueous solutions; Marcel Dekker: New York, 1985.

[32] Kissinger, P. T.; Heineman, W. R. *Laboratory techniques in electroanalytical chemistry*; Marcel Dekker: New York, 1984.

[33] https://pineresearch.com/shop/products/potentiostats/wavenow-series/wavenow-wireless/

[34]https://pineresearch.com/shop/kb/applications/general-electrochemistry/potentiostat-glovebox-installation/

[35] Treimer, S.; Tang, A.; Johnson, D. C., A Consideration of the Application of Koutecký-Levich Plots in the Diagnoses of Charge-Transfer Mechanisms at Rotated Disk Electrodes. *Electroanalysis* **2002,** *14*, 165-171.

[36] https://pineresearch.com/shop/kb/theory/hydrodynamic-electrochemistry/koutecky-levich-analysis/

[37] Gunasingham, H. In Electrochemistry, Past and Present; Stock, J. T., Orna, M. V., Eds.; ACS Symposium Series; American Chemical Society: Washington, DC, 1989; Vol. 390, Chapter 17.

[38] Zoski, C. G., Ed. *Handbook of Electrochemistry*; Elsevier: Amsterdam, The Netherlands, 2006.

[39] Graham, D. J. Standard Operating Procedures for Cyclic Voltammetry. https://sop4cv.com/index.html (accessed Jun 2021).

[40] Flato, J. B., Renaissance in polarographic and voltammetric analysis. *Anal. Chem.* **1972,** *44*, 75A-87a.

[41] Laborda, E.; González, J.; Molina, Á., Recent advances on the theory of pulse techniques: A mini review. *Electrochem. Commun.* **2014,** *43*, 25-30.

[42] Bard, A.J., Faulkner, L.R., *Electrochemical Methods: Fundamentals and Applications*, New York: Wiley, 2001, 2nd ed.

[43] Barker, G. C.; Jenkins, I. L., Square-wave polarography. *Analyst* **1952,** *77*, 685-696.

[44] Rudolph, M., Digital simulations on unequally spaced grids.: Part 2. Using the box method by discretisation on a transformed equally spaced grid. *J. Electroanal. Chem.* **2003,** *543*, 23-39.

[45] Feldberg, S. W., Theory of Controlled Potential Electrogeneration of Chemiluminescence1. *J. Am. Chem. Soc.* **1966,** *88*, 390-393.

[46] D. Britz, Jörg Strutwolf, *Digital simulation in electrochemistry*, Berlin New York : Springer, Berlin New York, **2016**.

[47] Bieniasz, L. K., ELSIM—A user-friendly PC program for electrochemical kinetic simulations. Version 1.0—Solution of integral equations for linear scan and cyclic voltammetry. *Comput. Chem.* **1992,** *16*, 11-14.

[48] Bieniasz, L. K., ELSIM—A PC program for electrochemical kinetic simulations. Version 2.0—solution of the sets of kinetic partial differential equations in one-dimensional geometry, using finite difference and orthogonal collocation methods. *Comput. Chem.* **1993,** *17*, 355-368.

[49] Bieniasz, L. K., ELSIM—a problem-solving environment for electrochemical kinetic simulations. Version 3.0-solution of governing equations associated with interfacial species, independent of spatial coordinates or in one-dimensional space geometry. *Comput. Chem.* **1997,** *21*, 1-12.

[50] https://home.cyf-kr.edu.pl/~nbbienia/elsim3ad.html

[51] Rudolph, M.; Reddy, D. P.; Feldberg, S. W., Anal. Chem. **1994,** 66 (10), 589A-600A.

[52] http://www.digielch.de/

[53] D. K. Gosser in *Cyclic voltammetry : simulation and analysis of reaction mechanisms*, Vol. New York, N.Y. : VCH, New York, N.Y., 1993.

[54] López, I.; Le Poul, N., Low-temperature electrochemistry and spectroelectrochemistry for coordination compounds. *Coord. Chem. Rev.* **2021,** *436*, 213823-21844.

[55] Kuwana, T.; Darlington, R. K.; Leedy, D. W., Electrochemical Studies Using Conducting Glass Indicator Electrodes. *Anal. Chem.* **1964,** *36*, 2023-2025.

[56] Bard, A. J., Chemical modification of electrodes. *J. Chem. Educ.* **1983,** *60*, 302.

[57] Marcus, R. A., On the Theory of Oxidation-Reduction Reactions Involving Electron Transfer. I. *J. Chem Phys* **1956,** *24*, 966-978.

[58] Johnson, M. D. Comprehensive Organometallic Chemistry; Wilkinson, G., Stone, F. G. A., Abel, E. W., Eds.; Pergammon Press: Oxford, 1982; Vol. 4, p 479.

[59] Gagne, R. R.; Koval, C. A.; Lisensky, G. C., Ferrocene as an internal standard for electrochemical measurements. *Inorg. Chem.* **1980,** *19*, 2854-2855.

[60] Malischewski, M.; Adelhardt, M.; Sutter, J.; Meyer, K.; Seppelt, K., Isolation and structural and electronic characterization of salts of the decamethylferrocene dication. *Science* **2016,** *353*, 678-682.

[61] Goodwin, C. A. P.; Giansiracusa, M. J.; Greer, S. M.; Nicholas, H. M.; Evans, P.; Vonci, M.; Hill, S.; Chilton, N. F.; Mills, D. P., Isolation and electronic structures of derivatized manganocene, ferrocene and cobaltocene anions. *Nat Chem* **2021,** *13*, 243-248.

[62] Bard, A.J., Faulkner, L.R., *Electrochemical Methods: Fundamentals and Applications*, New York: Wiley, 2001, 2nd ed. pp 49-51.

[63] Bard, A.J., Faulkner, L.R., *Electrochemical Methods: Fundamentals and Applications*, New York: Wiley, 2001, 2nd ed. pp 52-53.

[64] Hopkins Leseberg, J. A.; Lionetti, D.; Day, V. W.; Blakemore, J. D., Electrochemical Kinetic Study of [Cp*Rh] Complexes Supported by Bis(2-pyridyl)methane Ligands. *Organometallics* **2021,** *40*, 266-277.

[65] Lionetti, D.; Day, V. W.; Lassalle-Kaiser, B.; Blakemore, J. D., Multiple binding modes of an unconjugated bis(pyridine) ligand stabilize low-valent [Cp*Rh] complexes. *Chem. Commun.* **2018,** *54*, 1694-1697.

[66] Bourrez, M.; Molton, F.; Chardon-Noblat, S.; Deronzier, A., [Mn(bipyridyl)(CO)3Br]: An Abundant Metal Carbonyl Complex as Efficient Electrocatalyst for CO_2 Reduction. *Angew. Chem. Int. Ed.* **2011,** *50*, 9903-9906.

[67] Hartl, F.; Rossenaar, B. D.; Stor, G. J.; Stufkens, D. J., Role of an electron-transfer chain reaction in the unusual photochemical formation of five-coordinated anions $[Mn(CO)_3(\alpha\text{-diimine})]^-$ from fac-$[Mn(X)(CO)_3(\alpha\text{-diimine})]$ (X = halide) at low temperatures. *Recl. Trav. Chim. Pays-Bas* **1995,** *114*, 565-570.

[68] Hopkins, J. A.; Lionetti, D.; Day, V. W.; Blakemore, J. D., Chemical and Electrochemical Properties of [Cp*Rh] Complexes Supported by a Hybrid Phosphine-Imine Ligand. *Organometallics* **2019,** *38*, 1300-1310.

[69] See Appendix A Figure A48 of publication for electrochemical control experiment to confirm the absence of a chloride in TBAPF6/CH3CN electrolyte.

[70] Lionetti, D.; Day, V. W.; Blakemore, J. D., Noncovalent immobilization and surface characterization of lanthanide complexes on carbon electrodes. *Dalton Transactions* **2017,** *46*, 11779-11789.

[71] Henke, W. C.; Lionetti, D.; Moore, W. N. G.; Hopkins, J. A.; Day, V. W.; Blakemore, J. D., Ligand Substituents Govern the Efficiency and Mechanistic Path of Hydrogen Production with [Cp*Rh] Catalysts. *ChemSusChem* **2017,** *10*, 4589-4598.

[72] Hopkins, J. A.; Lionetti, D.; Day, V. W.; Blakemore, J. D., Synthesis and reactivity studies of a [Cp∗Rh] complex supported by a methylene-bridged hybrid phosphine-imine ligand. *J. Organomet. Chem.* **2020,** *921*, 121294.

[73] Boyd, E. A.; Lionetti, D.; Henke, W. C.; Day, V. W.; Blakemore, J. D., Preparation, Characterization, and Electrochemical Activation of a Model [Cp*Rh] Hydride. *Inorg. Chem.* **2019,** *58*, 3606-3615.

[74] Hershberger, J. W.; Klingler, R. J.; Kochi, J. K., Kinetics, thermodynamics, and mechanism of the radical-chain process for ligand substitution of metal carbonyls. *J. Am. Chem. Soc.* **1983,** *105*, 61-73.

[75] Grass, V.; Lexa, D.; Momenteau, M.; Savéant, J.-M., Reductive Electrochemistry of Rhodium Porphyrins. Disproportionation of Intermediary Oxidation States. *J. Am. Chem. Soc.* **1997,** *119*, 3536-3542.

[76] F. Goodridge and C. King, *Techniques of Electroorganic Synthesis*'(ed. NL Weinberg) John Wiley, New York **1974**.

[77] Harrar, J. E. *In Electroanalytical Chemistry*; Bard, A. J., Ed.; Marcel Dekker: New York, 1975; Vol. 8.

[78] A. J. Bard and C. G. Zoski, *Electroanalytical Chemistry: A Series of Advances*: Volume 23, CRC press, **2010**.

[79] Shōno, T., *Electroorganic synthesis*. Academic press 1991.

[80] Kyriacou, D. K. Basics of Electroorganic Synthesis; Wiley-Interscience: New York, 1981.

[81] Fry, A. J., *Synthetic organic electrochemistry*. John Wiley & Sons 1989.

[82] Heineman, W. R.; Kissinger, P. T., *Laboratory techniques in electroanalytical chemistry*. Dekker: New York, 1984; p. 504-506

[83] Robinson, J. R.; Gordon, Z.; Booth, C. H.; Carroll, P. J.; Walsh, P. J.; Schelter, E. J., Tuning Reactivity and Electronic Properties through Ligand Reorganization within a Cerium Heterobimetallic Framework. *J. Am. Chem. Soc.* **2013,** *135*, 19016-19024.

[84] Barr, J. L.; Kumar, A.; Lionetti, D.; Cruz, C. A.; Blakemore, J. D., Understanding the Roles of Triethylaluminum in Phosphinimide-Supported Titanium Catalyst Systems for Ethylene Polymerization. *Organometallics* **2019,** *38*, 2150-2155.

[85] Smieja, J. M.; Sampson, M. D.; Grice, K. A.; Benson, E. E.; Froehlich, J. D.; Kubiak, C. P., Manganese as a Substitute for Rhenium in CO_2 Reduction Catalysts: The Importance of Acids. *Inorg. Chem.* **2013,** *52*, 2484-2491.

[86] Chapovetsky, A.; Patel, P.; Liu, C.; Sattelberger, A. P.; Kaphan, D. M.; Delferro, M., Electrochemical Investigation of Low-Valent Multiply M≡M Bonded Group VI Dimers: A Standard Chemical Reduction Leads to an Unexpected Product. *Organometallics* **2020,** *39*, 4430-4436.

[87] Lewis, N. S.; Nocera, D. G., Powering the planet: Chemical challenges in solar energy utilization. *PNAS* **2006,** *103*, 15729-15735.

[88] International Energy Agency. Data and Statistics for World Electricity Generation by Source, 2018.

[89] International Energy Agency: World Energy Outlook, 2015.

[90] Roberts, J. A. S.; Bullock, R. M., Direct Determination of Equilibrium Potentials for Hydrogen Oxidation/Production by Open Circuit Potential Measurements in Acetonitrile. *Inorg. Chem.* **2013,** *52*, 3823-3835.

[91] Kütt, A.; Leito, I.; Kaljurand, I.; Sooväli, L.; Vlasov, V. M.; Yagupolskii, L. M.; Koppel, I. A., A Comprehensive Self-Consistent Spectrophotometric Acidity Scale of Neutral Brønsted Acids in Acetonitrile. *J Org Chem* **2006,** *71*, 2829-2838.

[92] Kaljurand, I.; Kütt, A.; Sooväli, L.; Rodima, T.; Mäemets, V.; Leito, I.; Koppel, I. A., Extension of the Self-Consistent Spectrophotometric Basicity Scale in Acetonitrile to a Full Span of 28 pKa Units: Unification of Different Basicity Scales. *J Org Chem* **2005,** *70*, 1019-1028.

[93] Schwesinger, R., Starke ungeladene Stickstoffbasen. *Nach. Chem. Tech. Lab.* **1990,** *38*, 1214-1226.

[94] Costentin, C.; Robert, M.; Savéant, J.-M.; Tatin, A., Efficient and selective molecular catalyst for the CO_2 to CO electrochemical conversion in water. *PNAS* **2015,** *112*, 6882-6886.

[95] Espenson, James H. *Chemical Kinetics and Reaction Mechanisms* / James H. Espenson. New York: McGraw-Hill, 1995.

[96] Matheu, R.; Neudeck, S.; Meyer, F.; Sala, X.; Llobet, A., Foot of the Wave Analysis for Mechanistic Elucidation and Benchmarking Applications in Molecular Water Oxidation Catalysis. *ChemSusChem* **2016,** *9*, 3361-3369.

[97] Zott, M. D.; Garrido-Barros, P.; Peters, J. C., Electrocatalytic Ammonia Oxidation Mediated by a Polypyridyl Iron Catalyst. *ACS Catalysis* **2019,** *9*, 10101-10108.

[98] Ahmad, E.; Rai, S.; Padhi, S. K., Proton reduction by a Ni(II) catalyst and foot-of-the wave analysis for H2 evolution. *Int. J. Hydrogen Energy* **2019,** *44*, 16467-16477.

[99] Clark, M. L.; Cheung, P. L.; Lessio, M.; Carter, E. A.; Kubiak, C. P., Kinetic and Mechanistic Effects of Bipyridine (bpy) Substituent, Labile Ligand, and Brønsted Acid on Electrocatalytic CO2 Reduction by Re(bpy) Complexes. *ACS Catal* **2018,** *8*, 2021-2029.

[100] Liu, X.; Li, F.-F.; Peng, P.; Licht, G.; Licht, S., Efficient Electrocatalytic Synthesis of Ammonia from Water and Air in a Membrane-Free Cell: Confining the Iron Oxide Catalyst to the Cathode. *Chem. Eur. J.* **2020,** *2020*, 1428-1436.

[101] Crabtree, R. H., Deactivation in Homogeneous Transition Metal Catalysis: Causes, Avoidance, and Cure. *Chem. Rev.* **2015,** *115*, 127-150.

[102] Whitesides, G. M.; Hackett, M.; Brainard, R. L.; Lavalleye, J. P. P. M.; Sowinski, A. F.; Izumi, A. N.; Moore, S. S.; Brown, D. W.; Staudt, E. M., Suppression of unwanted heterogeneous platinum(0)-catalyzed reactions by poisoning with mercury(0) in systems involving competing homogeneous reactions of soluble organoplatinum compounds: thermal decomposition of bis(triethylphosphine)-3,3,4,4-tetramethylplatinacyclopentane. *Organometallics* **1985,** *4*, 1819-1830.

[103] Sconyers, D. J.; Blakemore, J. D., Distinguishing between homogeneous and heterogeneous hydrogen-evolution catalysis with molecular cobalt complexes. *Chem. Commun.* **2017,** *53*, 7286-7289.

[104] Lin, Y.; Finke, R. G., A More General Approach to Distinguishing "Homogeneous" from "Heterogeneous" Catalysis: Discovery of Polyoxoanion- and Bu_4N^+-Stabilized, Isolable and Redissolvable, High-Reactivity Ir.apprx.190-450 Nanocluster Catalysts. *Inorg. Chem.* **1994,** *33*, 4891-4910.

[105] Sconyers, D. J.; Blakemore, J. D., Electrodeposition behavior of homoleptic transition metal acetonitrile complexes interrogated with piezoelectric gravimetry. *Analyst* **2020,** *145*, 466-477.

[106] Sconyers, D. J.; Blakemore, J. D., Distinguishing deposition, corrosion, and stripping of transient heterogeneous materials during molecular electrocatalysis. *Dalton Trans.* **2019,** *48*, 6372-6382.

[107] Nie, W.; Wang, Y.; Zheng, T.; Ibrahim, A.; Xu, Z.; McCrory, C. C. L., Electrocatalytic CO_2 Reduction by Cobalt Bis(pyridylmonoimine) Complexes: Effect of Ligand Flexibility on Catalytic Activity. *ACS Catal.* **2020,** *10*, 4942-4959.

[108] This bulk electrolysis cell may be available for purchase at redox.me; item: bulk electrolysis basic cell – 50 mL. https://redox.me/products/bulk-electrolysis-basic-cell-50-ml. Accesses June 2021.

[109] Harris, D. C. *Quantitative Chemical Analysis.* New York, NY: W.H. Freeman and Co, 2007. Print.

[110] Eaton, G. R.; Eaton, S. S.; Barr, D. P.; Weber, R. T. *Quantitative EPR*; Springer-Verlag: Vienna, 2010.

[111] Dau, H.; Limberg, C.; Reier, T.; Risch, M.; Roggan, S.; Strasser, P., The Mechanism of Water Oxidation: From Electrolysis via Homogeneous to Biological Catalysis. *ChemCatChem* **2010,** *2*, 724-761.

[112] Blakemore, J. D.; Crabtree, R. H.; Brudvig, G. W., Molecular Catalysts for Water Oxidation. *Chem. Rev.* **2015,** *115*, 12974-13005.

[113] Hunter, B. M.; Gray, H. B.; Müller, A. M., Earth-Abundant Heterogeneous Water Oxidation Catalysts. *Chem. Rev.* **2016,** *116*, 14120-14136.

[114] Yagi, M.; Kaneko, M., Molecular Catalysts for Water Oxidation. *Chem. Rev.* **2001,** *101*, 21-36.

[115] Meyer, T. J.; Huynh, M. H. V.; Thorp, H. H., The Possible Role of Proton-Coupled Electron Transfer (PCET) in Water Oxidation by Photosystem II. *Angew. Chem. Int. Ed.* **2007,** *46*, 5284-5304.

[116] Armstrong, D. A.; Huie, R. E.; Koppenol, W. H.; Lymar, S. V.; Merényi, G.; Neta, P.; Ruscic, B.; Stanbury, D. M.; Steenken, S.; Wardman, P., Standard electrode potentials involving radicals in aqueous solution: inorganic radicals (IUPAC Technical Report). *Pure Appl. Chem.* **2015,** *87*, 1139-1150.

[117] Harriman, A.; Richoux, M.-C.; Christensen, P. A.; Mosseri, S.; Neta, P., Redox reactions with colloidal metal oxides. Comparison of radiation-generated and chemically generated $RuO_2 \cdot 2H_2O$. *J. Chemi. Soc., Faraday Trans.* **1987,** *83*, 3001-3014.

[118] Najafpour, M. M.; Ehrenberg, T.; Wiechen, M.; Kurz, P., Calcium Manganese(III) Oxides ($CaMn_2O_4 \cdot x\ H_2O$) as Biomimetic Oxygen-Evolving Catalysts. *Angew. Chem. Int. Ed.* **2010,** *49*, 2233-2237.

[119] Gersten, S. W.; Samuels, G. J.; Meyer, T. J., Catalytic oxidation of water by an oxo-bridged ruthenium dimer. *J. Am. Chem. Soc.* **1982,** *104*, 4029-4030.

[120] Duan, L.; Bozoglian, F.; Mandal, S.; Stewart, B.; Privalov, T.; Llobet, A.; Sun, L., A molecular ruthenium catalyst with water-oxidation activity comparable to that of photosystem II. *Nat Chem* **2012,** *4*, 418-423.

[121] Schulze, M.; Kunz, V.; Frischmann, P. D.; Würthner, F., A supramolecular ruthenium macrocycle with high catalytic activity for water oxidation that mechanistically mimics photosystem II. *Nat Chem* **2016,** *8*, 576-583.

[122] McDaniel, N. D.; Coughlin, F. J.; Tinker, L. L.; Bernhard, S., Cyclometalated Iridium(III) Aquo Complexes: Efficient and Tunable Catalysts for the Homogeneous Oxidation of Water. *J. Am. Chem. Soc.* **2008,** *130*, 210-217.

[123] Hull, J. F.; Balcells, D.; Blakemore, J. D.; Incarvito, C. D.; Eisenstein, O.; Brudvig, G. W.; Crabtree, R. H., Highly Active and Robust Cp* Iridium Complexes for Catalytic Water Oxidation. *J. Am. Chem. Soc.* **2009,** *131*, 8730-8731.

[124] Zhao, Y.; Yang, K. R.; Wang, Z.; Yan, X.; Cao, S.; Ye, Y.; Dong, Q.; Zhang, X.; Thorne, J. E.; Jin, L.; Materna, K. L.; Trimpalis, A.; Bai, H.; Fakra, S. C.; Zhong, X.; Wang, P.; Pan, X.; Guo, J.; Flytzani-Stephanopoulos, M.; Brudvig, G. W.; Batista, V. S.; Wang, D., Stable iridium dinuclear heterogeneous catalysts supported on metal-oxide substrate for solar water oxidation. *PNAS* **2018,** *115*, 2902-2907.

[125] Najafpour, M. M.; Renger, G.; Hołyńska, M.; Moghaddam, A. N.; Aro, E.-M.; Carpentier, R.; Nishihara, H.; Eaton-Rye, J. J.; Shen, J.-R.; Allakhverdiev, S. I., Manganese Compounds as Water-Oxidizing Catalysts: From the Natural Water-Oxidizing Complex to Nanosized Manganese Oxide Structures. *Chem. Rev.* **2016,** *116*, 2886-2936.

[126] Singh, A.; Spiccia, L., Water oxidation catalysts based on abundant 1st row transition metals. *Coord. Chem. Rev.* **2013,** *257*, 2607-2622.

[127] Blakemore, J. D.; Schley, N. D.; Balcells, D.; Hull, J. F.; Olack, G. W.; Incarvito, C. D.; Eisenstein, O.; Brudvig, G. W.; Crabtree, R. H., Half-Sandwich Iridium Complexes for Homogeneous Water-Oxidation Catalysis. *J. Am. Chem. Soc.* **2010,** *132*, 16017-16029.

[128] Savini, A.; Bellachioma, G.; Ciancaleoni, G.; Zuccaccia, C.; Zuccaccia, D.; Macchioni, A., Iridium(iii) molecular catalysts for water oxidation: the simpler the faster. *Chem. Commun.* **2010,** *46*, 9218-9219.

[129] Blakemore, J. D.; Schley, N. D.; Olack, G. W.; Incarvito, C. D.; Brudvig, G. W.; Crabtree, R. H., Anodic deposition of a robust iridium-based water-oxidation catalyst from organometallic precursors. *Chem. Sci.* **2011,** *2*, 94-98.

[130] Schley, N. D.; Blakemore, J. D.; Subbaiyan, N. K.; Incarvito, C. D.; D'Souza, F.; Crabtree, R. H.; Brudvig, G. W., Distinguishing Homogeneous from Heterogeneous Catalysis in Electrode-Driven Water Oxidation with Molecular Iridium Complexes. *J. Am. Chem. Soc.* **2011,** *133*, 10473-10481.

[131] Adli, N. M.; Zhang, H.; Mukherjee, S.; Wu, G., Review—Ammonia Oxidation Electrocatalysis for Hydrogen Generation and Fuel Cells. *J. Electrochem. Soc.* **2018,** *165*, J3130-J3147.

[132] Dunn, P. L.; Cook, B. J.; Johnson, S. I.; Appel, A. M.; Bullock, R. M., Oxidation of Ammonia with Molecular Complexes. *J. Am. Chem. Soc.* **2020,** *142*, 17845-17858.

[133] Habibzadeh, F.; Miller, S. L.; Hamann, T. W.; Smith, M. R., Homogeneous electrocatalytic oxidation of ammonia to N_2 under mild conditions. *PNAS* **2019,** *116*, 2849-2853.

[134] Zott, M. D.; Peters, J. C., Enhanced Ammonia Oxidation Catalysis by a Low-Spin Iron Complex Featuring Cis Coordination Sites. *J. Am. Chem. Soc.* **2021,** *143*, 7612-7616.

[135] McKone, J. R.; Marinescu, S. C.; Brunschwig, B. S.; Winkler, J. R.; Gray, H. B., Earth-abundant hydrogen evolution electrocatalysts. *Chem Sci* **2014,** *5*, 865-878.

[136] Tong, L.; Duan, L.; Zhou, A.; Thummel, R. P., First-row transition metal polypyridine complexes that catalyze proton to hydrogen reduction. *Coord. Chem. Rev.* **2020,** *402*, 213079.

[137] Cheng, N.; Stambula, S.; Wang, D.; Banis, M. N.; Liu, J.; Riese, A.; Xiao, B.; Li, R.; Sham, T.-K.; Liu, L.-M.; Botton, G. A.; Sun, X., Platinum single-atom and cluster catalysis of the hydrogen evolution reaction. *Nat Comm* **2016,** *7*, 13638.

[138] Jaramillo, T. F.; Jørgensen, K. P.; Bonde, J.; Nielsen, J. H.; Horch, S.; Chorkendorff, I., Identification of Active Edge Sites for Electrochemical H_2 Evolution from MoS_2 Nanocatalysts. *Science* **2007,** *317*, 100-102.

[139] Valdez, C. N.; Dempsey, J. L.; Brunschwig, B. S.; Winkler, J. R.; Gray, H. B., Catalytic hydrogen evolution from a covalently linked dicobaloxime. *PNAS* **2012,** *109*, 15589-15593.

[140] Kölle, U.; Kang, B.-S.; Infelta, P.; Comte, P.; Grätzel, M., Elektrochemische und pulsradiolytische Reduktion von (Pentamethylcyclopentadienyl)(polypyridyl)rhodium-Komplexen. *Chem. Ber.* **1989,** *122*, 1869-1880.

[141] Francke, R.; Schille, B.; Roemelt, M., Homogeneously Catalyzed Electroreduction of Carbon Dioxide—Methods, Mechanisms, and Catalysts. *Chem. Rev.* **2018,** *118*, 4631-4701.

[142] Qiao, J.; Liu, Y.; Hong, F.; Zhang, J., A review of catalysts for the electroreduction of carbon dioxide to produce low-carbon fuels. *Chem. Soc. Rev.* **2014,** *43*, 631-675.

[143] Frese, K. W. *Electrochemical Reduction of carbon dioxide at solid electrodes. In Electrochemical and Electrocatalytic Reactions of Carbon Dioxide*; Sullivan, B. P., Krist, K., Guard, H. E., Eds.; Elsevier: Amsterdam, 2012; pp 145−216.

[144] Bhugun, I.; Lexa, D.; Savéant, J.-M., Catalysis of the Electrochemical Reduction of Carbon Dioxide by Iron(0) Porphyrins: Synergystic Effect of Weak Brönsted Acids. *J. Am. Chem. Soc.* **1996,** *118*, 1769-1776.

[145] Hawecker, J.; Lehn, J.-M.; Ziessel, R., Electrocatalytic reduction of carbon dioxide mediated by Re(bipy)$(CO)_3$Cl (bipy = 2,2′-bipyridine). *J. Chem. Soc., Chem. Commun.* **1984**, 328-330.

[146] Sullivan, B. P.; Bolinger, C. M.; Conrad, D.; Vining, W. J.; Meyer, T. J., One- and two-electron pathways in the electrocatalytic reduction of CO_2 by fac-Re(bpy)$(CO)_3$Cl (bpy = 2,2′-bipyridine). *J. Chem. Soc., Chem. Commun.* **1985**, 1414-1416.

[147] Tignor, S. E.; Kuo, H.-Y.; Lee, T. S.; Scholes, G. D.; Bocarsly, A. B., Manganese-Based Catalysts with Varying Ligand Substituents for the Electrochemical Reduction of CO_2 to CO. *Organometallics* **2019,** *38*, 1292-1299.

[148] Henke, W. C.; Otolski, C. J.; Moore, W. N. G.; Elles, C. G.; Blakemore, J. D., Ultrafast Spectroscopy of [Mn$(CO)_3$] Complexes: Tuning the Kinetics of Light-Driven CO Release and Solvent Binding. *Inorg. Chem.* **2020,** *59*, 2178-2187.

[149] Machan, C. W.; Sampson, M. D.; Chabolla, S. A.; Dang, T.; Kubiak, C. P., Developing a Mechanistic Understanding of Molecular Electrocatalysts for CO_2 Reduction using Infrared Spectroelectrochemistry. *Organometallics* **2014,** *33*, 4550-4559.

[150] Sampson, M. D.; Nguyen, A. D.; Grice, K. A.; Moore, C. E.; Rheingold, A. L.; Kubiak, C. P., Manganese Catalysts with Bulky Bipyridine Ligands for the Electrocatalytic Reduction of Carbon Dioxide: Eliminating Dimerization and Altering Catalysis. *J. Am. Chem. Soc.* **2014,** *136*, 5460-5471.

[151] Bazhenova, T. A.; Shilov, A. E., Nitrogen fixation in solution. *Coord. Chem. Rev.* **1995,** *144*, 69-145.

[152] Nishibayashi, Y., Recent Progress in Transition-Metal-Catalyzed Reduction of Molecular Dinitrogen under Ambient Reaction Conditions. *Inorg. Chem.* **2015,** *54*, 9234-9247.

[153] Fields, S., Global Nitrogen: Cycling out of Control. *Environ. Health Perspect.* **2004,** *112*, A556-A563.

[154] Chalkley, M. J.; Drover, M. W.; Peters, J. C., Catalytic N_2-to-NH_3 (or -N_2H_4) Conversion by Well-Defined Molecular Coordination Complexes. *Chem. Rev.* **2020,** *120*, 5582-5636.

[155] Del Castillo, T. J.; Thompson, N. B.; Peters, J. C., A Synthetic Single-Site Fe Nitrogenase: High Turnover, Freeze-Quench ^{57}Fe Mössbauer Data, and a Hydride Resting State. *J. Am. Chem. Soc.* **2016,** *138*, 5341-5350.

[156] Chalkley, M. J.; Garrido-Barros, P.; Peters, J. C., A molecular mediator for reductive concerted proton-electron transfers via electrocatalysis. *Science* **2020,** *369*, 850-854.

[157] Fajardo, J.; Peters, J. C., Catalytic Nitrogen-to-Ammonia Conversion by Osmium and Ruthenium Complexes. *J. Am. Chem. Soc.* **2017,** *139*, 16105-16108.

[158] Horn, E. J.; Rosen, B. R.; Baran, P. S., Synthetic Organic Electrochemistry: An Enabling and Innately Sustainable Method. *ACS Cent. Sci.* **2016,** *2*, 302-308.

[159] Francke, R.; Little, R. D., Redox catalysis in organic electrosynthesis: basic principles and recent developments. *Chem. Soc. Rev.* **2014,** *43*, 2492-2521.

[160] Siu, J. C.; Fu, N.; Lin, S., Catalyzing Electrosynthesis: A Homogeneous Electrocatalytic Approach to Reaction Discovery. *Acc. Chem. Res.* **2020,** *53*, 547-560.

[161] Faraday, M., Siebente Reihe von Experimental-Untersuchungen über Elektricität. *Annalen der Physik* **1834,** *109*, 481-520.

[162] Kolbe, H., Beobachtungen über die oxydirende Wirkung des Sauerstoffs, wenn derselbe mit Hülfe einer elektrischen Säule entwickelt wird. *J. Prakt. Chem* **1847,** *41*, 137-139.

[163] Schöenbein, ChF. *Liebigs Ann. Chem.*, **1845**, 54, 164.

[164] Yan, M.; Kawamata, Y.; Baran, P. S., Synthetic Organic Electrochemical Methods Since 2000: On the Verge of a Renaissance. *Chem. Rev.* **2017,** *117*, 13230-13319.

[165] Caix, C.; Chardon-Noblat, S.; Deronzier, A.; Moutet, J.-C.; Tingry, S., (Pentamethylcyclopentadienyl)(polypyridyl) rhodium and iridium complexes as electrocatalysts for the reduction of protons to dihydrogen and the hydrogenation of organics. *J. Organomet. Chem.* **1997,** *540*, 105-111.

[166] Hou, Z.-W.; Mao, Z.-Y.; Zhao, H.-B.; Melcamu, Y. Y.; Lu, X.; Song, J.; Xu, H.-C., Electrochemical C−H/N−H Functionalization for the Synthesis of Highly Functionalized (Aza)indoles. *Angew. Chem. Int. Ed.* **2016,** *55*, 9168-9172.

[167] Choi, G. J.; Zhu, Q.; Miller, D. C.; Gu, C. J.; Knowles, R. R., Catalytic alkylation of remote C–H bonds enabled by proton-coupled electron transfer. *Nature* **2016,** *539*, 268-271.

[168] Tafel, J., Über die Polarisation bei kathodischer Wasserstoffentwicklung. *Z. Phys. Chem.* **1905,** *50U*, 641-712.

[169] Li, D.; Lin, C.; Batchelor-McAuley, C.; Chen, L.; Compton, R. G., Tafel analysis in practice. *J. Electroanal. Chem.* **2018,** *826*, 117-124.

[170] Sconyers, D. J.; Shaughnessy, C. I.; Lee, H.-J.; Subramaniam, B.; Leonard, K. C.; Blakemore, J. D., Enhancing Molecular Electrocatalysis of CO2 Reduction with Pressure-Tunable CO_2-Expanded Electrolytes. *ChemSusChem* **2020,** *13*, 6338-6345.

[171] Pegis, M. L.; Roberts, J. A. S.; Wasylenko, D. J.; Mader, E. A.; Appel, A. M.; Mayer, J. M., Standard Reduction Potentials for Oxygen and Carbon Dioxide Couples in Acetonitrile and N,N-Dimethylformamide. *Inorg. Chem.* **2015,** *54*, 11883-11888.

Chapter 3

Chemical and Electrochemical Properties of [Cp*Rh] Complexes Supported by a Hybrid Phosphine-Imine Ligand

This chapter is adapted from a published manuscript:

Hopkins, J.A.; Lionetti D.; Day, V.W.; Blakemore, J.D. Chemical and Electrochemical Properties of [Cp*Rh] Complexes Supported by a Hybrid Phosphine-Imine Ligand. *Organometallics* **2019**, *38*, 1300-1310.

3.1 Introduction

Effective management of both protons (H^+) and reducing equivalents (e^-) can maximize efficiency in small-molecule activation processes, such as evolution of dihydrogen (H_2) and reduction of carbon dioxide (CO_2) to more useful chemicals.[1] Consequently, the study of metal complexes that can serve as catalysts or model compounds in such transformations is an area of robust activity within the field of energy science. Knowledge of the reactivity that metal complexes undergo when reduced and/or protonated is of especially high interest, since these reactions are nearly always involved in reductive, fuel-forming catalysis.

Reduction and protonation events are often metal-centered, and lead to formation of metal hydride complexes.[2] On the other hand, ligands may also be "non-innocent," and thus become intimately involved in reduction and protonation chemistry.[3] Understanding of these events can enable tuning of catalysis, and/or transfer of multiple H^+/e^- equivalents with modest energy penalties.[4] However, it remains difficult to predict and/or control transfer of electrons and protons to metal complexes. In systems that contain non-innocent ligands, understanding the nature of catalysis or the catalytic mechanism is especially challenging, as the locus of reduction or protonation may be metal- or ligand-centered.[5]

Recently, we have been working to understand reduction and protonation reactivity in a model family of organometallic rhodium complexes that can serve, in some cases, to couple H^+/e^- equivalents as molecular electrocatalysts for H_2 evolution. The complexes of interest are supported by the pentamethylcyclopentadienyl (Cp*) ligand, as well as an additional bidentate ligand; work to date has examined the properties of symmetric, bidentate chelates containing nitrogen or phosphorus donors (Chart 3.1, $^{\mathbf{R}}$**A** and **B**). The parent catalyst was reported by Grätzel and Kölle in 1987 to be an electrocatalyst for H_2 evolution, and bears the common 2,2´-bipyridyl ligand

(^{H}bpy).[6] Although several studies have examined this catalyst system, the full mechanism that guides H_2 generation has not been reported.[7] Original proposals involved reduction to form a rhodium(I) complex followed by two H^+ transfer events; the first protonation was expected to generate a Rh^{III}–hydride species, which would then be protonolyzed by the second H^+ equivalent to generate H_2. This system can also catalyze reactions involving transfer of [H^-] to other acceptor molecules, like NAD^+.[8] However, the putative [Cp*Rh–H] intermediates have only been observed under stringent conditions,[9] and have not yet been fully characterized.

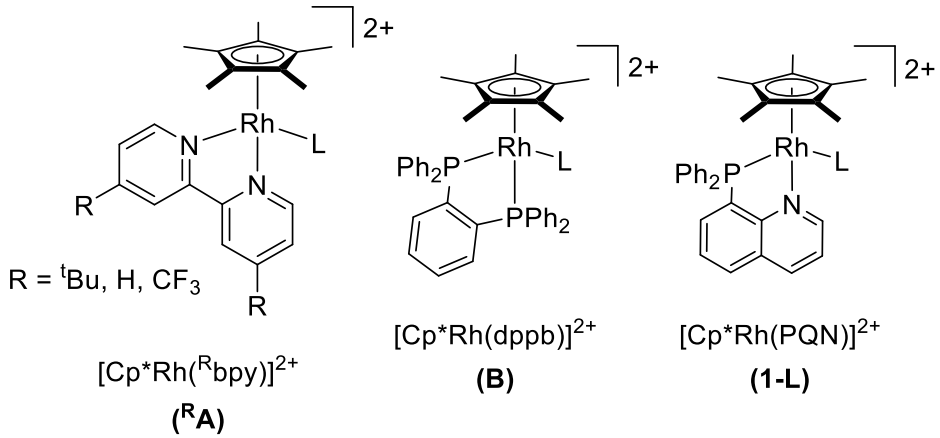

Chart 3.1. Half-sandwich Rh complexes supported by N- and P-containing bidentate ligands.

More recently, parallel reports from our group[10] and Miller's group[11] have shown that protonation of the isolable Rh(I) complex Cp*Rh(^{H}bpy) can result in clean transfer of the incoming H^+ equivalent to the [Cp*] ring. Spectroscopic (proton nuclear magnetic resonance, ^{1}H NMR) and structural (X-ray diffraction, XRD) studies reveal generation of an *endo*-η^4-pentamethylcyclopentadiene ([Cp*H]) species containing a formally Rh(I) center stabilized by π-backbonding interactions with the nascent diolefin ligand.[12] Such reactivity, in which a cyclopentadienyl ligand apparently acts as a pendant base, has been discussed and experimentally implicated in catalytic processes with a variety of organometallic species.[13,14,15] Because [Cp*] is ubiquitous in catalysis but is typically considered to be an innocent ancillary ligand, new

knowledge related to the phenomenon of reversible [Cp*] protonation could open new opportunities in catalyst design.

Building on our initial findings with half-sandwich complexes, we have found that [Cp*H] rhodium complexes can be supported by a variety of disubstituted bipyridyl ligands, independent of their electron-withdrawing or electron-donating nature. Complexes bearing ^{t}Bu– (^{tBu}bpy) or CF_3– (^{CF3}bpy) substituents are catalytically active for H_2 evolution, and generate [Cp*H] species *in situ* upon treatment of reduced precursors with appropriate H^+ sources.[16] Analogous behavior has also been observed for a complex supported by 1,10-phenanthroline (phen).[12]

Moreover, we have found that reduction of these [Cp*H] complexes by one additional e^- enables access to a new catalytic cycle leading to H_2 formation. Specifically, reduction of [Cp*H] complexes supported by ^{R}bpy ligands (R = H, CF_3) results in generation of unstable complexes that undergo net transfer of a hydrogen atom (H•), yielding the corresponding rhodium(I) complexes and H_2. In fact, electrochemical experiments on complex $^{\mathbf{CF3}}$**A** (Chart 3.1) indicate that this new catalytic pathway is responsible for the majority of the catalytic current enhancement, whereas the enhancement of the current corresponding to the rhodium(III/I) couple is less significant.[16] Based on the electrochemical potentials involved, and by comparison to other complexes, reduction of these [Cp*H] complexes is proposed to be centered on the ^{R}bpy ligand, whose redox non-innocence is well documented.[17] However, evidence is not yet available to distinguish between the possible homolytic (net release of H•) and heterolytic (protonolysis by an exogenous H^+ source) pathways that lead to H_2 evolution.[18]

Because of the likely involvement of transient hydride complexes in this chemistry, we have recently been investigating the synthesis and reactivity properties of [Cp*Rh] monohydrides. Prior work with such compounds,[19] and notable analogues,[20] suggested to us that phosphine ligands

would provoke formation of the Rh–H interaction. Indeed, we have recently shown that the 1,2-bis(diphenylphosphino)benzene ligand (dppb) drives formation of a rhodium(III) complex (**B**, Chart 3.1) that can be readily reduced and cleanly protonated to generate a stable rhodium(III)–hydride.[21] Unlike the tautomeric [Cp*H] species observed in ^{R}bpy-ligated systems, this [Rh–H] complex is remarkably resistant to further reactivity; the Rh–H bond does not undergo protonolysis even in the presence of strong acids in organic solvents. Furthermore, this hydride undergoes metal-centered reduction at a quite negative potential ($E_{1/2}(Rh^{III}/Rh^{II})$ = –2.25 vs. the ferrocenium/ferrocene couple, subsequently noted as $Fc^{+/0}$), precluding electrocatalytic studies. Thus, the ability to access [Cp*H]-type compounds appears essential for catalysis with [Cp*Rh] systems. However, only [Cp*Rh] complexes bearing diimine and diphosphine ligands have been explored so far in this chemistry. Thus, an opportunity lies in probing the reactivity profile engendered by less symmetric, hybrid ligands that could provide the electronic characteristics of both a single phosphine and a single imine.

Here, we report synthesis, characterization, and reactivity studies of [Cp*Rh] complexes supported by such a hybrid ligand, 8-(diphenylphosphino)quinoline (PQN). PQN presents a triarylphosphine donor and an imine donor with appropriate disposition for formation of an attractive five-membered metallacycle, complementing our prior work with dppb and 4,4´-disubstituted-2,2´-bipyridyls. The coordination chemistry of PQN ligands has been studied with several transition metals, including Pd,[22,23,24] Cu,[25] Ni,[26] Au,[27] Ru,[28] Zn,[29] Ir,[30] and Pt[23]; however, only two short reports regarding Rh complexes are available,[23,31] and no half-sandwich complexes have been investigated. We find that the PQN ligand engenders properties on [Cp*Rh] that are intermediate between those of systems supported by ^{R}bpy ligands and by the dppb scaffold: while the potential of the rhodium(III/I) couple of the $[Cp^*Rh(PQN)Cl]^+$ (**1-Cl**) complex is more similar

to that of the corresponding ^{R}bpy systems, protonation of the rhodium(I) complex **2** yields a rhodium(III)–hydride species (**3**), similarly to the dppb-supported complex. Importantly, we find that the PQN-supported hydride undergoes ligand-centered reduction, unlike the metal-centered reduction observed for the dppb-supported hydride. Based on chemical and electrochemical work carried out in the presence of acid, we find that **3** can only slowly generate H_2 in the presence of acid, and that electrochemical reduction of **3** leads to low yields of H_2 accompanying formation of multiple metal-containing products. Taken together, we conclude that use of the hybrid ligand PQN to enable formation of a hydride does not favor robust H_2 evolution, further underscoring the unique profile accessed by analogous [Cp*H] complexes.

3.2 Results

Synthesis and Electrochemical Characterization of [Cp*Rh] Complexes. The dimeric $[Cp^*RhCl_2]_2$ complex[32] is a useful precursor that can be utilized to prepare [Cp*Rh] complexes containing chelating bidentate ligands in a straightforward manner.[33] For the present [*P*,*N*] system, 2 equiv. of AgOTf were added to $[Cp^*RhCl_2]_2$, followed by 2.05 equiv. of free PQN (synthesized by the methods of Haftendorn[34]and Metzger[35]) to give the orange rhodium(III) complex **1-Cl** (Scheme 3.1).

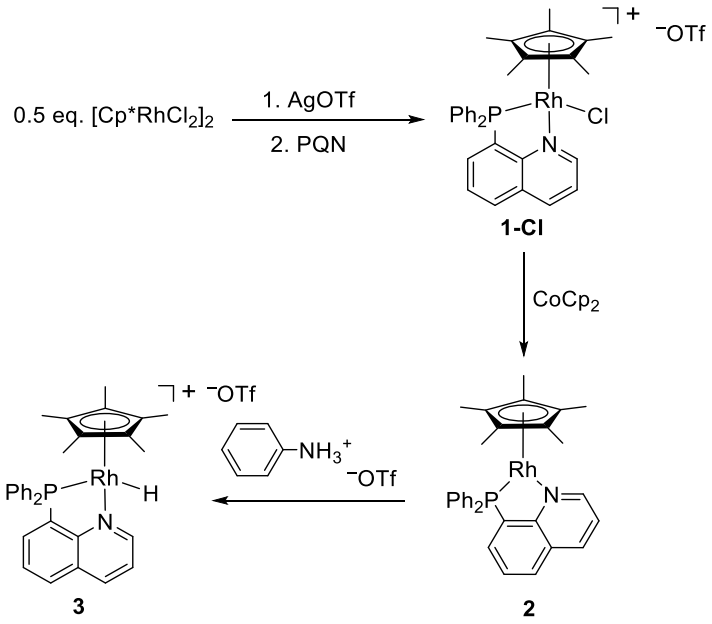

Scheme 3.1. Preparation of [Cp*Rh] complexes.

Characterization of this material by proton nuclear magnetic resonance (^{1}H NMR) reveals a signal at 1.54 ppm integrating to 15H that displays coupling to the NMR-active phosphorous nucleus ($^4J_{H,P} \approx 3.8$ Hz), and can therefore be assigned to the equivalent [Cp*] protons. (See Appendix A, Figure A4). In addition, a doublet ($^1J_{P,Rh} \approx 143.8$ Hz) was observed at 47.90 ppm in the ^{31}P{^{1}H} NMR spectrum of **1-Cl** corresponding to the Rh-bound phosphorus atom. Vapor diffusion of diethyl ether (Et_2O) into acetonitrile (CH_3CN) yielded orange crystals of **1-Cl** suitable for X-ray diffraction (XRD) studies. The resulting solid-state structure reveals the geometry of the formally Rh(III) metal center in **1-Cl** as *pseudo*-octahedral (Figure 3.1). The first coordination sphere around the metal contains the κ^2-[*P*,*N*]-PQN scaffold, a single bound chloride anion, and the [η^5-Cp*] ligand. The angle between the plane of the [Cp*] ligand the plane of the bidentate ligand (the plane defined by the Rh, N and P atoms) is ~81°, which is substantially larger than the analogous angle in the $[Cp^*Rh(bpy)Cl]^+$ system (~59°).[36] This difference in complexation angle

suggests that the steric bulk of the PQN ligand effects the geometry within the [Cp*Rh] and the bidentate framework.

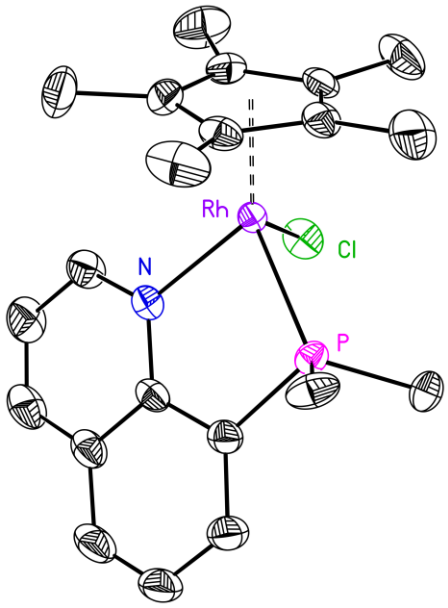

Figure 3.1. Solid-state structure of **1** (XRD); triflate counteranion and hydrogen atoms omitted for clarity. Phenyl groups truncated for clarity. Thermal ellipsoids shown at the 50% probability level.

Electrochemical studies were conducted to investigate the redox behavior engendered by the PQN ligand. Previously studied [Cp*Rh] systems bearing various 2,2´-bipyridyl (bpy) derivatives[6,16] undergo a single 2e$^-$ reduction from Rh(III) to Rh(I) via an ECE´-type mechanism[37] (E = electron transfer, C = chemical reaction) in which the monodentate ligand of the Rh(III) species is lost upon reduction. The cyclic voltammogram (CV) of **1-Cl** exhibits a similar appearance, with a first reduction event at –1.19 V vs. $Fc^{+/0}$ (Figure 3.2), which appears to be a quasireversible, 2e$^-$ process corresponding to reduction of Rh(III) to Rh(I) (*vide infra*). This behavior indicates that **1-Cl** undergoes a similar ECE´ process in relation to the previously reported bpy complexes: initial 1e$^-$ reduction of the chloride-bound Rh(III) species **1-Cl** generates a transient 19-electron complex (E). Loss of the Cl$^-$ ligand then results in formation of a 17-electron

species (C); the rhodium(II/I) reduction potential of this transient intermediate is very near to the rhodium(III/II) potential of **1-Cl**, resulting in immediate transfer of a second electron (E´).

During the ECE´ sequence, bpy-supported [Cp*Rh] complexes undergo a geometric rearrangement to a *pseudo*-square planar geometry, which improves overlap between empty π-symmetry orbitals on the bidentate framework and metal d orbitals, thereby activating π-backbonding to the bidentate ligand. These bpy complexes engage in π-backbonding by extensive delocalization of electron density into the ligand LUMO at the formally rhodium(I) oxidation state. As a result, the bpy bound to [Cp*Rh] appears to have significant reduced character as judged by crystallography,[38] as well as spectroscopic and theoretical methods.[17,39,40] In the case of the present system bearing [PQN], the bidentate ligand undergoes only a minor change in orientation upon reduction (vide infra), suggesting that its greater steric bulk (vs. bpy) affects its tendency to engage in π-backbonding.

Additionally, a third $1e^-$ reduction is observed for **1-Cl** centered at –2.26 V vs. $Fc^{+/0}$; an analogous reduction event has been reported in [Cp*Rh] complexes supported by bpy and 1,10-phenanthroline (phen), albeit at more negative potentials.[40,41] We note here that the metal-free PQN ligand can be redox active itself, and undergoes a more negative reduction event at –2.46 V (see Appendix A, Figure A54). Thus, the third reduction measured here cannot yet be reliably assigned as either ligand- or metal-centered. Further work with relevant model compounds could provide helpful comparisons in future work. However, we do note here that scan rate-dependent studies verify that all species present in the cyclic voltammetry of **1-Cl** are freely diffusing and soluble (see Appendix A, Figure A41 and A42).

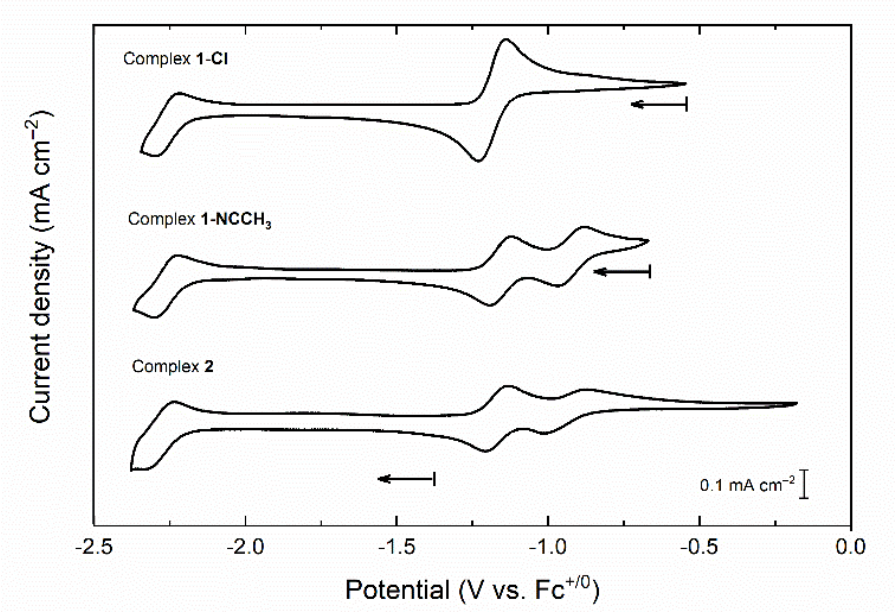

Figure 3.2. Cyclic voltammetry of **1-Cl** (upper), **1-NCCH$_3$** (middle), and **2** (lower). Electrolyte: 0.1 M $TBAPF_6$ in CH_3CN; Scan rate: 100 mV/s; Working electrode: highly oriented pyrolytic graphite (HOPG); [Rh] in each experiment was ca. 1 mM. Initial potentials (marked with the start line of each arrow): **1-Cl**, ca. –0.5 V ; **1-NCCH$_3$**, ca. –0.7 V; **2**, ca. –1.4 V.

Chloride is implicated to play a key role in the events governing the electrochemical reduction of **1-Cl**, because it serves as a ligand in the starting material and is lost upon the first one-electron reduction. To provide better support for assignment of this role for chloride, we turned to chemical preparation of the analogous acetonitrile-bound solvento species, **1-NCCH$_3$**. Specifically, 1 equiv. of **1-Cl** was treated with 1 equiv. of AgOTf in CH_3CN solvent. Filtration to remove the co-generated AgCl precipitate and removal of excess solvent *in vacuo* enabled isolation of the metastable solvento complex **1-NCCH$_3$**. Notably, the pure compound could be fully characterized by ^1H, $^{13}C\{^1H\}$, $^{31}P\{^1H\}$, and ^{19}F NMR, as well as ESI-MS (see Appendix A, Figures A28-A31). However, satisfactory elemental analysis could not be obtained due to association of a slight excess of solvent with the otherwise clean, isolated material. Upon extended drying to fully remove

CH_3CN, decomposition was encountered, likely driven by solvent loss. Similar observations have been made in prior synthetic work with solvento [Cp*Rh] and [Cp*Ir] complexes.[42]

In accord with the implicated role for chloride, the profile of cyclic voltammetry carried out with **1-NCCH$_3$** is distinct from that of **1-Cl**. Starting at positive potential, a negative-going scan reveals two sequential one-electron reduction events, in contrast to the single two-electron event measured for **1-Cl**. Specifically, we observe a first reduction of **1-NCCH$_3$** centered at –0.93 V, followed by a second reduction at –1.16 V. These events are quasi reversible, and correspond to the formal Rh(III/II) and Rh(II/I) couples, respectively. Both events are quasi-reversible, although the peak-to-peak separation (ΔE_p) for the first event (90 mV) is slightly greater than that of the second event (70 mV). These values are consistent with the expected loss of coordinated CH_3CN upon the first one-electron reduction (i.e., reduction results in generation of a transient 19e$^-$ Rh^{II} complex which undergoes loss of CH_3CN to form a metastable 17e$^-$ complex bearing only [Cp*] and [PQN]). This process is very similar to the reduction-induced loss of chloride implicated in the work with **1-Cl**. Finally, scan rate-dependent studies verify that all species present in the cyclic voltammetry of **1-NCCH$_3$** are freely diffusing and soluble (See Appendix A, Figure A44).

Within this model, the reduction of **1-NCCH$_3$** via two, sequential one-electron reductions and reduction of **1-Cl** in the two-electron event discussed above should produce an identical, formally rhodium(I) product. Consistent with this notion, the third one-electron reduction event centered at –2.26 V measured with **1-Cl** is observed at a virtually identical potential in the voltammetry with **1-NCCH$_3$**. Thus, we conclude that the reduction product is identical in these two cases; this product would be formulated as Cp*Rh(PQN) (**2**), produced by loss of chloride from **1-Cl** and loss of CH_3CN from **1-NCCH$_3$**.

With these electrochemical data in hand, we targeted chemical isolation of the reduced species **2**. Addition of cobaltocene (Cp_2Co, E^o = –1.31 V vs. $Fc^{+/0}$,[43] 1.9 equiv.) to **1-Cl** in a thawing mixture of tetrahydrofuran (THF) and CH_3CN results in a rapid, significant darkening of the reaction solution; removal of volatiles *in vacuo* and extraction with hexane yielded a dark red-orange solid. The ^{1}H NMR spectrum of this material displays a signal at 1.98 ppm ($^4J_{H,P} \approx 1.2$ Hz) corresponding to the [Cp*] protons (see Appendix A, Figure A12). In the $^{31}P\{^1H\}$ NMR spectrum, this material displays a doublet ($^1J_{P,Rh} \approx 246.3$ Hz) at 55.29 ppm; the downfield shift and substantial increase in coupling constant versus **1-Cl** (cf., 47.90 ppm, $^1J_{P,Rh} \approx 143.8$ Hz) are consistent with reduction of the metal center and activation of a stronger covalent interaction between P and Rh. Taken together, these data support chemical reduction of **1-Cl** to the formally Rh(I) complex **2** (see Scheme 3.1).

Dark-red single crystals of **2** suitable for XRD studies were obtained from slow evaporation of a solution of **2** in diethyl ether/toluene. The solid-state structure obtained confirms the reduction of the metal complex implicated by the NMR data. In **2**, the geometry of the formally Rh(I) metal center is distorted square-planar (Figure 3.3), resulting in a pseudo-C_S molecular geometry. The first coordination sphere around the metal contains both [η^5-Cp*] and [κ^2-PQN]. The angle between the plane defined by the [Cp*] ring and the plane containing Rh, N and P is 84°, indicating that the absence of the single bound chloride anion does not significantly affect this angle. This could be due to the steric bulk of the PQN ligand.

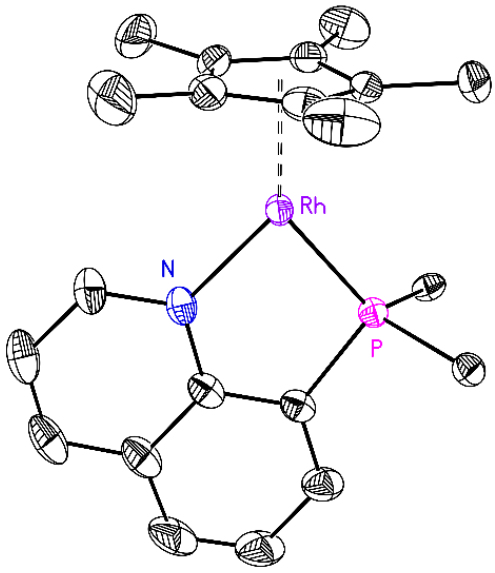

Figure 3.3. Solid-state structure of **2** (XRD); hydrogen atoms omitted for clarity. Phenyl groups truncated for clarity. Displacement ellipsoids shown at the 50% probability level.

The lowered formal oxidation state of the metal does not significantly alter the C–C bond lengths of the quinoline ligand framework in **2** when compared to the analogous bond lengths in **1** (see Appendix A, Table A2 for bond length comparisons). Thus, the quinoline moiety is likely not serving as a site for significant delocalization of electron density in the reduced complex **2**.[44] However, as there is a continuum between backbonding and formal ligand-centered reduction, both the phosphine and imine moieties are likely to assist in stabilization of the reduced metal center via π-backbonding. Consistent with this picture, the Rh–P, and Rh–N bond lengths contract substantially (by 0.1216 Å and 0.1106 Å, respectively) upon reduction of **1-Cl** to **2**.

To verify that the chemically reduced complex **2** is the product observed in electrochemical reduction of **1-Cl**, cyclic voltammetry data for **2** were collected. In a cathodic scan beginning at E = –1.38 V, the one-electron reduction at ca. –2.3 V is observed; however, the following anodic sweep shows two distinct oxidation waves ($E_{p,a}$= –1.13, –0.87 V vs. $Fc^{+/0}$), indicating two individual one-electron events. Two corresponding one-electron reductions are observed upon

scanning cathodically from the switching potential of ca. –0.25 V. As in the other cases discussed so far, scan rate dependent studies verify that all species present in CVs of **2** are freely diffusing and soluble (see Appendix A, Figure A46).

The two quasi-reversible couples measured for **2**, centered at –1.17 V and –0.95 V are assigned to the Rh^{II}/Rh^{I} and Rh^{III}/Rh^{II} reductions, respectively. Notably, these couples are virtually identical to the Rh^{II}/Rh^{I} and Rh^{III}/Rh^{II} reductions measured for **1-NCCH$_3$**; this observation is in accord with our model for the electrochemical behavior of these complexes. Specifically, we conclude that the two, sequential one-electron oxidations of chemically prepared **2** in acetonitrile containing tetrabutylammonium hexafluorophosphate supporting electrolyte lead to formation of $[Cp^*Rh(PQN)NCCH_3]^{2+}$ with hexafluorophosphate counteranions. As this complex is very similar to the chemically prepared analogue **1-NCCH$_3$**, $[Cp^*Rh(PQN)NCCH_3]^{2+}$ with triflate counteranions, these complexes display virtually identical profiles in cyclic voltammetry. This interpretation is corroborated by the peak-to-peak separation (ΔE_p) values measured for the two individual reduction events of **2**. ΔE_p is 140 mV for the more-positive reduction, and 70 mV for the more-negative event; this is consistent with a chemical reaction accompanying the first reduction (loss of the nascent CH_3CN ligand), while the second reduction is virtually reversible (cf. $\Delta E_p(Fc^{+/0})$ = 70 mV under our conditions), suggesting only rapid electron transfer.[45]

The changes in the CV profiles of **1-Cl** and **1-NCCH$_3$/2** are unique among the half-sandwich rhodium complexes that we have studied. Compounds in this class bearing bidentate ligands typically show a single, net $2e^-$ reduction from Rh(III) to Rh(I) without formation of a stable Rh(II) intermediate.[6,7b,16,] Reiterating the principles of our working model, the unique behavior of **1-NCCH$_3$** and **2** can be assigned to absence of a chloride ligand. One-electron reduction of **1-Cl** is followed by a chemical reaction that yields a transient Rh(II) complex with a more positive

reduction potential than **1-Cl** itself; immediate reduction of this species thus occurs, giving rise to the observed single two-electron wave. In the absence of chloride, however, electrochemical oxidation of **2** generates a different Rh(III) species, bearing a CH_3CN solvent molecule as monodentate ligand. Reduction of this solvento species, $[Cp^*Rh(PQN)(NCCH_3)]^{2+}$, takes place at a more positive potential than for **1-Cl** due to its dicationic nature; evidently, the shift in potential caused by the subsequent chemical reaction (in this case, loss of CH_3CN rather than chloride as in **1-Cl**) is insufficient to cause the transient Rh(II) species to be reduced at a more positive potential than the Rh(III) solvent complex. Thus, two distinct one-electron reductions are measurable, and a metastable rhodium(II) complex is formed near the electrode. These findings support the overall model for the electrochemical behavior of [Cp*Rh] complexes bearing bidentate ligands, and highlight a significant role for halide ligands in regulation of the electrochemical properties of the metal complexes. In accord with this viewpoint, anionic ligands, like halides, have long been known to decrease the reduction potentials of metal complexes, relative to analogues bearing neutral ligands.[46]

To further confirm the role for halide ligands in regulating the electrochemical properties of these [Cp*Rh] complexes, we titrated a sample of **1-NCCH$_3$** (in the electrochemical cell) with increasing quantities of tetrabutylammonium chloride. The two original reduction waves for **1-NCCH$_3$** are diminished upon chloride addition, while the single, two-electron wave for **1-Cl** centered at –1.19 V grows in intensity (See Figure 3.4). This confirms rapid conversion of **1-NCCH$_3$** to **1-Cl** by displacement of the ligated solvent with chloride and confirms that the presence/absence of chloride is responsible for the unique appearance of the voltammetric profiles of **1-NCCH$_3$** and **1-Cl**, as the other ligands to the rhodium center, [Cp*] and [PQN], are identical in the two cases.

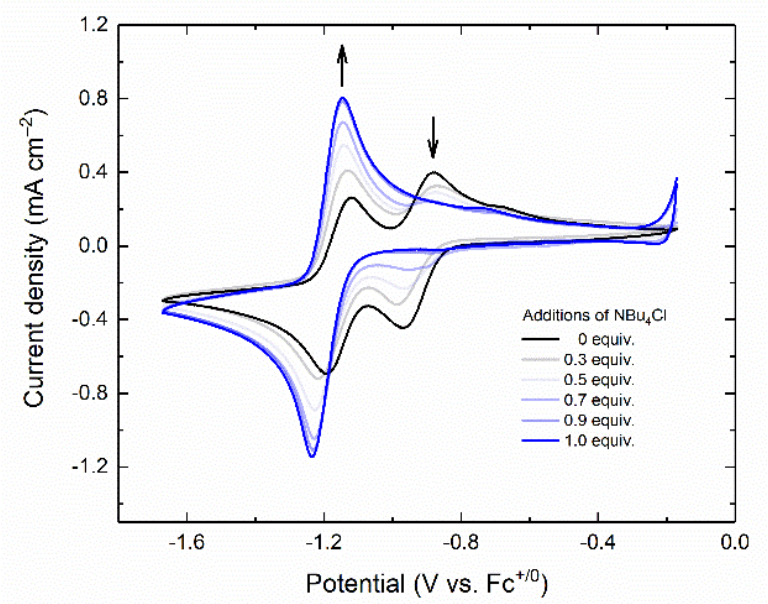

Figure 3.4. Electrochemical response of **1-NCCH$_3$** in CH_3CN upon addition of various amounts of tetrabutylammonium chloride. Growth of the reduction process with $E_{1/2}$ = –1.19 V indicates coordination of chloride to **1-NCCH$_3$** by displacement of bound CH_3CN, giving *in situ* generation of **1-Cl**.

As a complement to this electrochemical titration, we carried out a control electroanalytical study to confirm that chloride was not present as an adventitious impurity in our acetonitrile/tetrabutylammonium hexafluorophosphate electrolyte or isolated samples of **1-NCCH$_3$** and **2**. This was done by potential excursions to check for anodic oxidation of chloride, which is known to occur near +0.75 V vs. $Fc^{+/0}$ in CH_3CN (see Appendix A, Figure A48). We generated a standard curve (see Appendix A, Figure A49) with additions of NBu_4Cl, with the result of a linear relationship between [Cl^-] and peak currents measured near 0.75 V. This anodic process is absent in the initial CH_3CN solution containing 0.1 M NBu_4PF_6 supporting electrolyte, confirming a virtually zero baseline for chloride. Furthermore, anodic scans carried out with complexes **1-NCCH$_3$** and **2** do not reveal the presence of any free chloride, as judged by the absence of the key oxidation wave (see Appendix A, Figure A50 and A51). Thus, the

electrochemical behavior of the [Cp*Rh] complexes can be confidently ascribed to the model discussed above.

Preparation of a [Cp*Rh] Hydride. With **2** in hand, we next examined the possibility of producing a protonated species for comparison to other [Cp*Rh] complexes.[12,21] Upon addition of 1 equiv. of anilinium triflate (pK_a = 10.6 in CH_3CN[47]), a solution of **2** drastically lightens to yellow. Following evaporation of volatiles and washing with diethyl ether, a yellow solid is obtained. The ^{1}H NMR spectrum of this material displays an upfield peak at –9.9 ppm that is indicative of a metal hydride complex (see Appendix A, Figure A19). The hydride signal appears as a doublet of doublets due to H,Rh and H,P coupling ($J \approx 36.6, 19.9$ Hz). The signal for the [Cp*] protons appears at 1.67 ppm ($^4J_{H,P} \approx 3.1$ Hz; Figure A19). Consistent with the change in oxidation state from Rh(I) to Rh(III), a doublet with a smaller coupling constant ($^1J_{P,Rh} \approx 149.2$ Hz; Figure 3.5) than in the case of **2** ($^1J_{P,Rh} \approx 246.3$ Hz) is observed in the $^{31}P\{^1H\}$ NMR spectrum of **3**.

Vapor diffusion of Et_2O into a CH_3CN solution of **3** yielded yellow crystals suitable for XRD studies. The solid state structure of **3** (Figure 3.5) reveals a return of the Rh(III) center to a pseudo-octahedral geometry. The first coordination sphere around the metal contains the [κ^2-PQN] and [η^5-Cp*] ligands. Gratifyingly, the hydride ligand (H41) could be located in the Fourier difference map, and its position was freely refined. This confirms the direct Rh–H interaction, and identifies **3** as a metal-hydride species.[48] This structure complements another that we recently obtained for an analogous hydride complex supported by the bis(diphenylphosphino)benzene (dppb) ligand.[21]

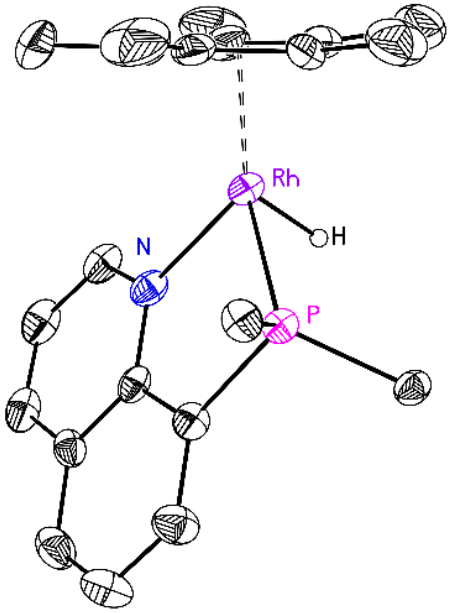

Figure 3.5. Crystal structure of **3**, triflate counteranion and hydrogen atoms (except for H41) omitted for clarity. Phenyl groups truncated for clarity. Displacement ellipsoids shown at the 50% probability level.

Chemical Reactivity of the [Cp*Rh] Hydride. As previously discussed, [(Cp*H)Rh] complexes generated from Cp*Rh(^{R}bpy) precursors have been isolated and are active for H_2 evolution catalysis.[6,10,11,12,16] The analogous [Cp*Rh–H] generated by protonation of Cp*Rh(dppb) does not react with further equiv. of acid to release H_2. [21] For comparison to these cases, we endeavored to assess the feasibility of release of H_2 from **3** via protonolysis. Treatment of **3** with 1 equiv. of $[DMFH]^+[OTf]^-$ (pK_a ≈ 6 in CH_3CN[49]) leads to slow consumption of the hydride complex **3** and generation of H_2 over 1 h; addition of 3 equiv. leads to complete conversion within 1 h. The metal-containing product of this reactivity is the expected **1-NCCH$_3$**; the disappearance of the upfield ^{1}H NMR signal corresponding to the hydride proton and significant shift of the diagnostic doublet in ^{31}P NMR signal to 50.28 ppm (Figure 3.6) support this assignment. On the other hand, addition of 10 equiv. of anilinium triflate (pK_a = 10.6 in CH_3CN[47]) does not lead to

any reactivity as judged by ^{1}H NMR over days, indicating that **3** is resistant to protonolysis by moderately strong acids.

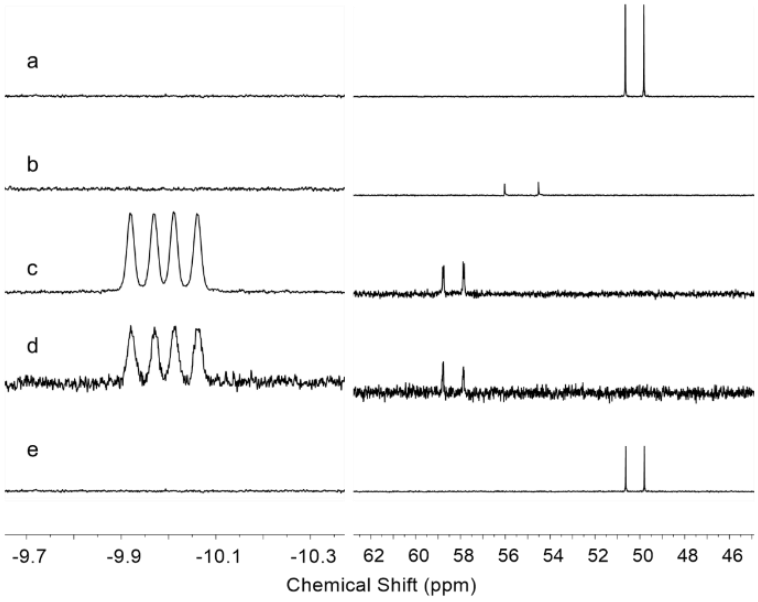

Figure 3.6. ^{1}H (left) and ^{31}P{^{1}H} (right) NMR spectra : (a) **1-NCCH$_3$**; (b) **2**; (c) **3**; (d) Addition of 10 equiv. anilinium triflate to **3**; (e) Addition of 3 equiv. [DMFH]$^{+}$[OTf]$^{-}$ to **3**.

Electrochemical Properties of the [Cp*Rh] Hydride Cyclic voltammetry experiments were carried out to investigate the electron transfer behavior of **3**. The first cathodic sweep of a CV beginning at –0.5 V reveals only an irreversible reduction corresponding to the reduction of the hydride ($E_{p,c}$= –1.75 V vs. $Fc^{+/0}$; see Figure 3.7). Further scanning to negative potentials reveals an additional reduction at a potential that closely aligns with that of the third reduction of the non-protonated species **2** ($E_{1/2}$ = –2.28 V vs. $Fc^{+/0}$). The returning anodic sweep features two oxidative events corresponding to the two 1e^{-} couples observed in the voltammogram of **2**. These data are consistent with a fast chemical reaction following 1e^{-} reduction of **3**, resulting in regeneration of a significant yield of **2**.

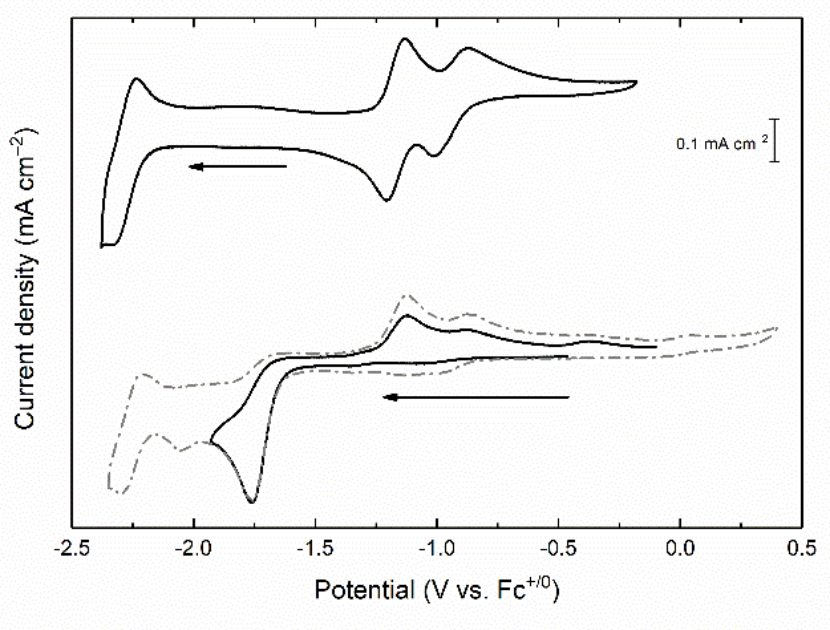

Figure 3.7. Cyclic voltammetry of **2** (upper panel, 1 mM) and **3** (lower panel, 1 mM). Electrolyte: 0.1 M $TBAPF_6$ in CH_3CN, scan rate: 100 mV/s, electrode: highly oriented pyrolytic graphite. The initial potential of the voltammogram of **2** (upper panel) is at ca. –1.38 V, and the initial potential of the voltammogram of **3** (lower panel) is at ca. –0.5 V.

In our recent work with [Cp*Rh] complexes supported by the 1,2-bis(diphenylphosphino)benzene (dppb) ligand, we found that the hydride $[Cp^*Rh(dppb)H]^+$ undergoes metal centered reduction at –2.34 V vs. $Fc^{+/0}$.[21] This quite negative potential contrasts with the more positive potentials (–1.45 and –1.73 V) encountered for reductions of [Cp*H] complexes supported by 2,2´-bipyridyl.[12] These reductions are centered on the bpy ligands, as a result of presence of low-lying, delocalized π* orbitals.[50] Similarly, in the case of hydride **3** supported by the PQN ligand, a significantly more positive reduction potential ($E_{p,c}$ = –1.75 V) is observed in comparison to that of the metal-centered reduction of $[Cp^*Rh(dppb)H]^+$. Thus, there is likely significant ligand involvement in the reduction measured for the hydride **3** at $E_{p,c}$ = –1.75 V.

For comparison, cyclic voltammetry collected with the metal-free PQN ligand revealed a quasireversible reduction at –2.46 V vs. $Fc^{+/0}$ (see Appendix A, Figure A54). A second oxidation wave was also observed at a more positive potential (–1.17 V vs. $Fc^{+/0}$) following reduction. These findings regarding reduction potentials are consistent with a shift of the ligand reduction to a significantly more positive value upon binding to the Lewis acidic Rh(III) center (cf. ligand-centered reduction of $[(Cp^*H)Rh(^{H}bpy)]^+$ at = –1.74 V vs. –2.57 V for free ^{H}bpy).[12,40] Confirming this assignment of ligand-centered reduction of **3**, prior work with PQN complexes of ruthenium has implicated ligand-centered reductions at similar potentials, through comparisons with diphosphine and diimine ligated complexes.[28a]

Electrochemical Generation of the [Cp*Rh] Hydride in the Presence of Acid. The observation that **2**, the product of two-electron reduction of **1-Cl**, can be readily protonated to prepare and isolate hydride **3** suggested to use that we might probe this hydride-forming reactivity under electrochemical conditions. Thus, we targeted an experiment in which **1-Cl** would be reduced electrochemically in the presence of a proton source, a situation that should lead to production of **3** *in situ*. However, a suitable organic acid must be carefully selected in such efforts. Anilinium triflate was used for synthesis of **3** in the preparative work, but this acid undergoes direct reduction at relatively positive potentials on carbon electrodes ($E_{p,c}$= –1.58 vs. $Fc^{+/0}$).[16] Such reactivity would interfere with observation of the reduction of **3** produced *in situ* ($E_{p,c}$= –1.75 V vs. $Fc^{+/0}$). Thus, triethylammonium triflate (pK_a = 18.8 in CH_3CN[47]) was chosen for this electrochemical study instead. Notably, we confirmed that treatment of **2** with excess triethylammonium does indeed lead to generation of **3** (as judged by ^1H NMR spectra), and thus this weaker acid is amenable to electrochemical studies.

Aliquots of a 1:1 mixture of $[Et_3NH]^+/Et_3N$ solution were added to **1-Cl** and cyclic voltammograms collected for each addition (Figure 3.8). As the acid solution was added, an increasingly irreversible response was recorded for the Rh(III)/Rh(I) couple previously measured for **1-Cl** (cf., Figure 3.2). The shape of the cathodic two-electron wave becomes distorted upon acid addition, likely due to activation of one or more coupled chemical reactions taking place between the reduced complex(es) and the added acid. Concurrently, a new irreversible reduction wave appears at –1.75 V. This reduction wave occurs at a virtually identical potential to that of the reduction wave measured for the chemically-prepared hydride **3** (cf., voltammetry data in Figure 3.7). Thus, we conclude that hydride **3** can be generated *in situ* by reduction of **1-Cl** and subsequent reaction with triethylammonium.

Upon further additions of the buffered acid, the current flow associated with reduction of **2** is modestly enhanced, slightly beyond the current associated with reduction of **3** alone. Enhancement is observed upon addition of up to 7 equiv. of $[Et_3NH]^+/Et_3N$ ($j_{cat}/(j_p/2) \approx 1.5$; Figure 3.8, inset).[51] We note that insignificant current is associated with background reduction of triethylammonium at these potentials (see Appendix A, Figure A56). The modest enhancement of the reductive current at –1.75 V suggested to us that conversion of H^+ to H_2 mediated by a reduced form of **3** might be occurring.

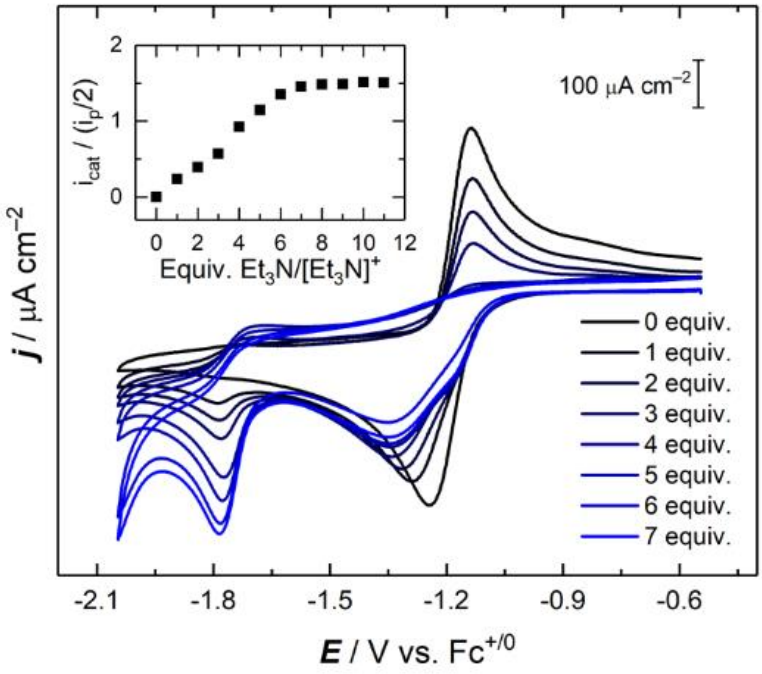

Figure 3.8. Cyclic voltammetry of 1 with 1 equv. of $[Et_3NH]^+$/Et3N in 50μL additions (CH_3CN, 0.1 M $[nBu_4N][PF_6]$, 100 mV/s). (Inset): Plot of $i_{cat}/(i_{p/2})$ vs equivalents (mMol) of $[Et_3NH]^+/Et_3N$ added.

Thus, we next moved to carry out bulk electrolysis experiments to assess the possibility of H_2 production. Controlled potential electrolysis (CPE) of **1-Cl** (see Appendix A, Figure A60 for chronoamperogram) in the presence of 10 equiv. of $[Et_3NH]^+$ was carried out for 1.5 h. at –1.75 V vs. $Fc^{+/0}$, resulting in the passage of 29.1 C of charge. Sampling of the headspace of the electrolysis cell by gas chromatography revealed generation of H_2 with a low 34% Faradaic efficiency. The total amount of H_2 evolved equates to a very low turnover number (TON; mol H_2 detected per mol [Rh]) of only 1.3, while the low Faradaic yield indicates involvement of unproductive side reactions under these conditions. A similar CPE experiment (see Appendix A, Figure A59) carried out with **1-NCCH3** under identical conditions reveals a similarly low Faradaic efficiency of 36%, confirming the poor H_2 evolving properties of these complexes, regardless of the presence of chloride or bound solvent ligands in the precatalysts. ^{1}H NMR spectra collected on the working

solution following electrolysis of **1-NCCH$_3$** or **1-Cl** with added acid show that the dominant Rh-containing component of the solution is the hydride **3**; however, there are also small new peaks in the aromatic region of the spectra (see Appendix A, Figures A33 and A34), suggesting formation of secondary side products during electrolysis. Likewise, electrolysis of isolated **3** for 1.5 h at –1.75 V vs. $Fc^{+/0}$ reveals no production of H_2 as judged by gas chromatography. However, a product of this electrolysis of **3** is **2**, as judged by UV-visible spectroscopy (see Appendix A for data, Figure A38), suggesting reactivity upon reduction that does not lead to H_2 production. Taken together, these results show that the reductive electrochemical reactivity of the hydride is not clean (whether chemically prepared or formed *in situ*) and does not lead to reliable H_2 generation.

To further probe this reactivity, we attempted chemical reduction of hydride **3** with decamethylcobaltocene (Cp^*_2Co, E = –1.94 V vs. $Fc^{+/0}$,[43] 1 equiv.). In line with conclusions drawn from the bulk electrolysis experiments, we observed null generation of H_2 by headspace analysis, and the presence of multiple P-containing by-products by $^{31}P\{^1H\}$ NMR (see Appendix A, Figure A32). No solids or heterogeneous material were visible. We also carried out a companion chemical reduction of **3** in the presence of both 1 equiv. of Cp^*_2Co and 1 equiv. of $[Et_3NH]^+$. This experiment revealed formation of null H_2 by GC, along with **3** and other byproducts by ^1H and $^{31}P\{^1H\}$ NMR (see Appendix A, Figures A35 and A36, respectively). Thus, we conclude that both in the presence and absence of exogeneous acid, and under both chemical and electrochemical conditions, hydride **3** is not effective for H_2 generation.

3.3 Conclusions

Introduction of the mixed [*P*,*N*]-donor ligand PQN engenders substantial changes in the properties of [Cp*Rh] complexes supported by this framework in comparison to those previously reported for [*P*,*P*]- and [*N*,*N*]-ligated systems. Modulation of the electrochemical properties of the

[Cp*Rh] fragment is perhaps the most striking change, as preparation of the solvento complex **1-NCCH$_3$** and related reduced complex **2** enable observation of two, sequential, quasi-reversible one-electron reductions. This behavior contrasts with the single two-electron reduction events measured most commonly for [Cp*Rh] complexes bearing diphosphine and diimine ligands. Treatment of Cp*Rh(PQN) (**2**) with acid results in generation of hydride complex **3**, which is resistant to protonolysis by the moderate acid anilinium triflate. Electrochemical studies show that **3** undergoes ligand-centered reduction at –1.75 V, inducing further reactivity. However, chemical and electrochemical reduction experiments show that this reactivity does not lead to effective H_2 generation. This contrasts with the robust and effective catalysis afforded by [Cp*Rh] complexes bearing diimine ligands and suggests that the [Cp*] ligand-centered protonation events associated with these diimine complexes may be crucial for effective H_2 generation in this broadly useful family of complexes.

3.4 Experimental Details

3.4.1 General Considerations

All manipulations were carried out in dry N_2-filled gloveboxes (Vacuum Atmospheres Co., Hawthorne, CA) or under N_2 atmosphere using standard Schlenk techniques unless otherwise noted. All solvents were of commercial grade and dried over activated alumina using a PPT Glass Contour (Nashua, NH) solvent purification system prior to use, and were stored over molecular sieves. All chemicals were from major commercial suppliers and used as received after extensive drying. $[Cp^*RhCl_2]_2$ was prepared according to literature procedure.[32] The PQN ligand was synthesized by the method of Haftendorn[34] and purified by the method of Metzger.[35] Deuterated NMR solvents were purchased from Cambridge Isotope Laboratories; CD_3CN was dried over molecular sieves and C_6D_6 was dried over sodium/benzophenone. ^1H, ^{13}C, ^{19}F, and ^{31}P NMR

spectra were collected on 400 or 500 MHz Bruker spectrometers and referenced to the residual protio-solvent signal[52] in the case of ^{1}H and ^{13}C. Heteronuclear NMR spectra were referenced to the appropriate external standard following the recommended scale based on ratios of absolute frequencies (Ξ).[53,54] ^{19}F NMR spectra are reported relative to CCl_3F, and ^{31}P NMR spectra are reported relative to H_3PO_4. Chemical shifts (δ) are reported in units of ppm and coupling constants (*J*) are reported in Hz. Electronic absorption spectra were collected with an Ocean Optics Flame spectrometer, in a 1-cm pathlength quartz cuvette. Elemental analyses were performed by Midwest Microlab, Inc. (Indianapolis, IN).

3.4.2 Synthesis

Synthesis of 1-Cl. To a suspension of $[Cp^*RhCl_2]_2$ in CH_3CN (0.4815 g, 0.0779. mmol) were added AgOTf (0.0552 g, 0.219 mmol, 2 equiv) in CH_3CN and PQN (0.5000 g, 0.319 mmol, 2.05 equiv) as a THF solution. The color of the reaction mixture rapidly changed from brick-red to orange, and a yellow precipitate formed. After 15 min, the suspension was filtered to remove the AgOTf byproduct, and the volume of the filtrate was reduced to ~1 mL. Addition of Et_2O (~80 mL) caused precipitation of a yellow solid, which was collected by filtration. Pure material was obtained via crystallization by vapor diffusion of Et_2O into a concentrated CH_3CN solution of the title compound (0.6807 g, 57.9%). The same strategy was employed to obtain single-crystals suitable for X-ray diffraction studies. ^{1}H NMR (500 MHz, CD_3CN) δ 9.10 (d, *J* = 5.2 Hz, 1H, *H1*), 8.68 (d, *J* = 8.4 Hz, 1H, *H3*), 8.30 (d, *J* = 8.2 Hz, 1H, *H5*), 8.27 – 8.22 (m, 1H, *H7*), 7.97 – 7.90 (m, 2H, *H11, H6*), 7.89 – 7.81 (m, 2H, *H2*), 7.67 (td, *J* = 7.2, 1.8 Hz, 1H, *H13*), 7.63 – 7.53 (m, 3H, *H12, H17*), 7.45 (td, *J* = 7.9, 2.6 Hz, 2H, *H16*), 7.18 – 7.11 (m, 2H, *H15*), 1.54 (d, *J* = 3.7 Hz, 15H, *H19*) ppm. $^{13}C\{^{1}H\}$ NMR (126 MHz, CD_3CN) δ 158.15 (s, *C1*), 151.64 (d, *J* = 21.37 Hz, *C9*), 140.31 (d, *J* = 2.2 Hz, *C3*), 138.81 (d, *J* = 2.7 Hz, *C7*), 135.05 (d, *J* = 11.2 Hz, *C11*), 133.27

(d, *J* = 2.6 Hz, *C5*), 132.78 (d, *J* = 10.8 Hz, *C15*), 132.15 (d, *J* = 3.3 Hz, *C13*), 131.94 (d, *J* = 48.7 Hz, *C14 or C8*), 131.15(d, *J* = 50.3 Hz, *C8 or C14*), 131.70 (d, *J* = 3.4 Hz, *C17*), 129.77 (d, *J* = 9.0 Hz *C4*), 128.89 (s, *C16*), 128.88 (d, *J* = 4.0 Hz *C6*), 128.80 (d, *J* = 11.4 Hz, *C12*), 124.83 (d, *J* = 55.4 Hz *C10*), 124.57 (s, *C2*), 101.77 (dd, *J* = 6.8 Hz, *J* = 3.0 Hz *C18*), 8.38 (m, *C19*) ppm. ^{19}F NMR (376 MHz, CD_3CN) δ –79.36 ppm. $^{31}P\{^1H\}$ NMR (162 MHz, CD_3CN) δ 47.90 (d, *J* = 143.8 Hz).ppm. Electronic absorption spectrum (CH_3CN): 366 nm (4323 M^{-1} cm^{-1}). ESI-MS (positive) *m/z*: 550.09 [**1-Cl** – Cl^- – OTf^-]$^+$, 586.07 [**1-Cl** – OTf^-]$^+$. Anal. Calcd. for $C_{40}H_{39}ClF_6P_3Rh$: C, 52.22; H, 4.25, N, 1.90. Found: C, 52.02; H, 4.31, N, 1.89.

Synthesis of 1-NCCH$_3$. A solution of **1** in CH_3CN (0. 0324 g, 0.0041 mmol) and a solution of AgOTf in CH_3CN (0. 0103 g, 0.0081 mmol) were combined and stirred for 1.5 hours, during which time the solution turned light yellow and a white precipitate formed. The of AgCl byproduct was removed by filtration over celite, and subsequent removal of volatiles *in vacuo* provides the title compound as a yellow solid (0.0324g, >99% yeild). ^{1}H NMR (500 MHz, CD_3CN) δ9.25 (d, *J* = 5.2 Hz, 1H), 8.90 (dt, *J* = 8.4, 1.7 Hz, 1H), 8.53 (dt, *J* = 8.2, 1.5 Hz, 1H), 8.31 (ddd, *J* = 10.2, 7.2, 1.3 Hz, 1H), 8.07 (ddd, *J* = 8.1, 7.2, 1.6 Hz, 2H), 8.02 (dd, *J* = 8.3, 5.2 Hz, 1H) 7.80 – 7.52 (m, 7H), 7.49 – 7.37 (m, 2H), 1.62 (d, *J* = 3.8 Hz, 15H) ppm. $^{13}C\{^1H\}$ NMR (126 MHz, CD_3CN) δ 159.21 (s), 152.97 (d, *J* = 20.7 Hz), 142.35 (s) 141.53 (s), 135.08 (d, *J* = 2.5 Hz), 134.19 (d, *J* = 10.9 Hz), 133.86 (d, *J* = 10.9 H), 133.64 (d, *J* = 3.5 Hz), 133.08 (d, *J* = 3.1 Hz), 131.34 (d, *J* = 9.1 Hz),130.20 (dd, *J* = 14.9, 11.4 Hz), 130.04 (s), 129.72 (s), 129.31 (s), 126.89 (d, *J* = 53.0 Hz), 126.07 (s), 125.93 (d, *J* = 52.6 Hz), 123.04 (s), 120.49 (s), 104.95 – 104.84 (m), 9.20 (s), ppm. ^{19}F NMR (376 MHz, CD_3CN) δ -79.30. $^{31}P\{^1H\}$ NMR (162 MHz, C_6D_6) δ 50.26 (d, *J* = 134.0 Hz) ppm. ESI-MS (positive) *m/z*: 550.09 [**1-NCCH$_3$** – CH_3CN – OTf^-]$^+$.

Synthesis of 2. A solution of **1** in a 1:1 mixture of THF/CH_3CN and a solution of Cp_2Co in THF (0.0491 g, 0.0178 mmol) was added to a 'thawing' solution of **1** (0. 1000 g, 0.0043 mmol) and stirred for 3 hours, during which time the yellow solution became a dark red. The volatiles removed *in vacuo*. Extraction with hexane and removal of the volatiles *in vacuo* provides the title compound as a dark red solid (00410g, 54.7%). Single-crystals suitable for X-ray diffraction studies were obtained by slow evaporation of Et_2O and toluene at -35°C. ^{1}H NMR (400 MHz, C_6D_6) δ 8.69 (d, *J* = 5.5 Hz, 1H, *H1*), 7.81 (dd, *J* = 10.5, 7.6 Hz , 4H, *H11*), 7.54 (t, *J* = 7.5 Hz, 1H, *H5*), 7.21 (d, *J* = 8.3 Hz, 1H, *H3*), 7.13 – 7.05 (m, 4H overlaps with solvent residual, *H12*), 7.09 (m, 2H, *H13*), 7.00 (d, *J* = 7.5 Hz, 1H, *H7*), 6.77 (t, *J* = 7.4 Hz, 1H, *H6*), 6.18 (dd, *J* = 8.1, 5.5 Hz, 1H, *H2*). 1.98 (d, *J* = 1.9 Hz, 15H) ppm. ^{13}C NMR (126 MHz, C_6D_6) δ 155.33 (d, *J* = 24.3 Hz, *C9*), 150.67 (s, *C1*), 139.74 (d, *J* = 35.74 Hz, *C10*), 139.30 (d, *J* = 26.3 Hz, *C8*), 133.07 (d, *J* = 13.6 Hz, *C11*), 132.90 (s, *C5*), 128.89 (s, *C4*), 128.75 (s, *C7*), 128.66 (s, *C13*), 127.26 (d, *J* = 4.5 Hz, *C6)*, 124.40 (s, *C2*), 123.40 (s, *C3*), (obscured by solvent peak, *C12*), 92.65 (s, *C14*), 10.93(s, *C15*), ppm. ^{31}P{^{1}H} NMR (162 MHz, C_6D_6) δ 55.29 (d, *J* = 245.0 Hz) ppm. Electronic absorption spectrum (CH_3CN): 478 nm (2,500 M^{-1} cm^{-1}).

Synthesis of 3. A solution of anilinium triflate CH_3CN (0.0185 g, 0.0035 mmol, 1 equiv) was added to a suspension of **2** in (0.0086g, 0.0071 mmol). The solution became light yellow immediately. Volatiles were removed *in vacuo*. Washing with hexanes followed by filtration removal of volatiles yielded the title compound as a light-yellow solid (0.0170g, 72.0%). Single-crystals suitable for X-ray diffraction studies were obtained by vapor diffusion of Et_2O into a CH_3CN solution of the title compound. ^{1}H NMR (400 MHz, CD_3CN) δ 8.90 (d, *J* = 5.1 Hz, 1H, *H1*), 8.55 (d, *J* = 8.4 Hz, 1H, *H3*), 8.29 (dd, *J* = 9.5, 7.5 Hz, 1H, *H7*), 8.23 – 8.13 (m, 3H, *H5, H12*), 7.86 – 7.78 (m, 1H, *H*6), 7.75 – 7.65 (m, 4H, *H2, H11, H13*), 7.55 (dt, *J* = 7.4, 4.1 Hz, 1H,

H17), 7.48 (dt, *J* = 7.5, 3.8 Hz, 2H, *H16*), 7.22 – 7.04 (m, 2H, H15), 1.70 (dd, *J* = 3.1, 1.4 Hz, 15H, *H19*), –9.9 (dd, *J* = 36.6, 19.9 Hz, 1H,), ppm. $^{13}C\{^{1}H\}$ NMR (126 MHz, CD_3CN) δ 157.53 (s, *C1*), 151.86 (s, *C9*), 138.98 (s, *C3*), 137.13 (s, *C7*), 135.79 (dd, *J* = 13.1, 2.0 Hz, *C10*) 134.3 (d, *J* = 49.05 Hz, *C8*), 132.79 (d, *J* = 48.76 Hz, *C14*), 132.42 (d, *J* = 2.9 Hz, *C5*), 132.38 (s, *C13*), 131.90 (d, *J* = 11.3 Hz, *C15*), 130.82 (s, *C17*), 129.74 (s, *C4*), 129.13 (d, *J* = 11.7 Hz, *C11*), 128.92 (s, *C6*), 128.80(s, *C12*), 128.76 (d, *J* = 1.8 Hz, *C16*), 123.99 (s, *C2*), 100.07 (dd, *J* = 5.4, 3.1 Hz), *C18*), 8.79 (s, *C19*) ppm. ^{19}F NMR (376 MHz, CD_3CN) δ –79.37 ppm. $^{31}P\{^{1}H\}$ NMR (162 MHz, CD_3CN) δ 57.49 (dd, *J* = 148.0, 8.2 Hz) ppm. Electronic absorption spectrum (CH_3CN): 404 nm (1,912 M^{-1} cm^{-1}). Anal. Calcd. for $C_{41}H_{40}O_3F_3P_2SRh$: C, 54.79; H, 4.60, N, 2.00. Found: C, 54.64; H, 4.52, N, 2.04.

3.4.3 X-ray crystallography

*Refinement Details for **1-Cl, 2** and **3.***

Sets of diffraction data [16617 (**1-Cl**), 25594 (**2**) and 17776 (**3**) reflections using 1º-wide ω- or ϕ-scan frames with scan times of 4-6 seconds (**1-Cl**), 5 seconds (**2**) or 4-6 seconds (**3**)] were collected[1] for single-domain crystals of **1-Cl**, **2**, and **3** using monochromated Cu Kα radiation (λ=1.54178 Å) on a Bruker Proteum Single Crystal Diffraction System with dual CCD detectors and associated Helios high-brilliance multilayer optics and a shared Bruker MicroSTAR microfocus Cu rotating anode x-ray source operating at 45 kV and 60 mA. Data for both compounds were collected with an Apex II CCD detector. The integrated data were corrected empirically for variable absorption effects using equivalent reflections.[2] The Bruker software package SHELXTL was used to solve both structures using "direct methods" techniques.[3] All stages of weighted full-matrix least-squares refinement were conducted using F_o^2 data using the

Olex software package[4] equipped with SHELXTL XL v2014.[5] Final crystallographic details are summarized in Table A1.

In the structure of **3**, the Rh-bound hydride ligand (H41) was located as residual electron density in the Fourier difference map; it was therefore included in the model as an isotropic atom and its position was freely refined.

3.4.4 Electrochemistry

Electrochemical experiments were carried out in a nitrogen-filled glove box. 0.10 M tetra(n-butylammonium)hexafluorophosphate (Sigma-Aldrich; electrochemical grade) in acetonitrile served as the supporting electrolyte. Measurements were made with a Gamry Reference 600 Plus Potentiostat/Galvanostat using a standard three-electrode configuration. The working electrode was the basal plane of highly oriented pyrolytic graphite (HOPG) (GraphiteStore.com, Buffalo Grove, IL.; surface area: 0.09 cm^2), the counter electrode was a platinum wire (Kurt J. Lesker, Jefferson Hills, PA; 99.99%, 0.5 mm diameter), and a silver wire immersed in electrolyte served as a pseudo-reference electrode (CH Instruments). The reference was separated from the working solution by a Vycor frit (Bioanalytical Systems, Inc.). Ferrocene (Sigma Aldrich; twice-sublimed) was added to the electrolyte solution at the conclusion of each experiment (~1 mM); the midpoint potential of the ferrocenium/ferrocene couple (denoted as $Fc^{+/0}$) served as an external standard for comparison of the recorded potentials. Concentrations of analyte for cyclic voltammetry were typically 1 mM. In most cases (except those involving acid additions), the second full sweep of voltammetry is shown.

3.5 Acknowledgements

The authors thank Dr. Justin Douglas and Sarah Neuenswander for assistance with NMR spectroscopy. This work was supported by the US National Science Foundation through award

OIA-1833087, and by the University of Kansas. Preliminary work on this project was supported by the US National Science Foundation through the NSF REU Program in Chemistry at the University of Kansas (CHE-1560279). Support for NMR instrumentation was provided by NIH Shared Instrumentation Grants S10OD016360 and S10RR024664, and by an NSF MRI grant CHE-1625923.

3.6 References

[1] (a) Rosenthal, J.; Nocera, D. G., Role of Proton-Coupled Electron Transfer in O–O Bond Activation. *Acc. Chem. Res.* **2007,** 40, 543-553. (b) Huynh, M. H. V.; Meyer, T. J., Proton-Coupled Electron Transfer. *Chem. Rev.* **2007,** 107, 5004-5064. (c) Roth, J. P.; Yoder, J. C.; Won, T.-J.; Mayer, J. M., Application of the Marcus Cross Relation to Hydrogen Atom Transfer Reactions. *Science* **2001,** 294, 2524-2526

[2] (a) Kaesz, H. D.; Saillant, R. B., Hydride complexes of the transition metals. *Chem. Rev*. **1972,** 72, 231-281. (b) Jordan, A. J.; Lalic, G.; Sadighi, J. P., Coinage Metal Hydrides: Synthesis, Characterization, and Reactivity. *Chem. Rev*. **2016,** 116, 8318-8372.

[3] Khusnutdinova, J. R.; Milstein, D., Metal-Ligand Cooperation. *Angew. Chem. Int. Ed.* **2015,** 54, 12236-12273.

[4] (a) Warren, J. J.; Tronic, T. A.; Mayer, J. M., Thermochemistry of Proton-Coupled Electron Transfer Reagents and its Implications. *Chem. Rev.* **2010,** 110, 6961-7001. (b) Huynh, M. H. V.; Meyer, T. J., Proton-Coupled Electron Transfer. *Chem. Rev*. **2007**, 107, 5004-5064. (c) Krishtalik, L. I., Energetics of multielectron reactions. Photosynthetic oxygen evolution. *Biochim. Biophys. Acta, Bioenerg.* **1986**, 849, 162-171. (d) Chirik, P. J.; Wieghardt, K., Radical Ligands Confer Nobility on Base-Metal Catalysts. *Science* **2010,** 327, 794-795.

[5] (a) Lyaskovskyy, V.; de Bruin, B., Redox Non-Innocent Ligands: Versatile New Tools to Control Catalytic Reactions. *ACS Catal.* **2012,** 2, 270-279. (b) Luca, O. R.; Crabtree, R. H., Redox-active ligands in catalysis. *Chem. Soc. Rev*. **2013,** 42, 1440-1459. (c) Chirik, P. J., Preface: Forum on Redox-Active Ligands. *Inorg. Chem.* **2011,** 50, 9737-974.

[6] (a) Kölle, U.; Grätzel, M., Metallorganische Rhodium(III)-Komplexe als Homogenkatalysatoren für die Photoreduktion von Protonen zu Wasserstoff an kolloidalem TiO_2. *Angew. Chem.* **1987,** *99*, 572-574. (b) Kölle, U.; Grützel, M., Organometallic Rhodium(III) Complexes as Catalysts for the Photoreduction

of Protons to Hydrogen on Colloidal TiO_2. *Angewandte Chemie International Edition in English* **1987,** *26*, 567-570.

[7] Kölle, U.; Kang, B. S.; Infelta, P.; Comte, P.; Grätzel, M., Electrochemical and Pulse-Radiolytic Reduction of (Pentamethylcyclopentadienyl)(Polypyridyl)Rhodium Complexes. *Chem. Ber*. **1989,** 122, 1869-1880.

[8] (a) Ruppert, R.; Herrmann, S.; Steckhan, E., Efficient Indirect Electrochemical Insitu Regeneration of Nadh - Electrochemically Driven Enzymatic Reduction of Pyruvate Catalyzed by D-LDH. *Tetrahedron Lett*. **1987,** 28, 6583-6586. (b) Lo, H. C.; Leiva, C.; Buriez, O.; Kerr, J. B.; Olmstead, M. M.; Fish, R. H., Bioorganometallic chemistry. 13. Regioselective reduction of NAD(+) models, 1-benzylnicotinamde triflate and beta-nicotinamide ribose-5 '-methyl phosphate, with in situ generated [CP*Rh(Bpy)H](+): Structure-activity relationships, kinetics, and mechanistic aspects in the formation of the 1,4-NADH derivatives. *Inorg. Chem.* **2001,** 40, 6705-6716.

[9] (a) Steckhan, E.; Herrmann, S.; Ruppert, R.; Dietz, E.; Frede, M.; Spika, E., Analytical Study of a Series of Substituted (2,2'-Bipyridyl)(Pentamethylcyclopentadienyl)Rhodium and Iridium Complexes with Regard to Their Effectiveness as Redox Catalysts for the Indirect Electrochemical and Chemical-Reduction of $Nad(P)^+$. *Organometallics* **1991,** 10, 1568-1577. (b) Fukuzumi, S.; Kobayashi, T.; Suenobu, T., Efficient Catalytic Decomposition of Formic Acid for the Selective Generation of H_2 and H/D Exchange with a Water-Soluble Rhodium Complex in Aqueous Solution. *ChemSusChem* **2008,** 1, 827-834.

[10] Quintana, L. M. A.; Johnson, S. I.; Corona, S. L.; Villatoro, W.; Goddard, W. A.; Takase, M. K.; VanderVelde, D. G.; Winkler, J. R.; Gray, H. B.; Blakemore, J. D., Proton-hydride tautomerism in hydrogen evolution catalysis. *PNAS.* USA **2016,** 113, 6409-6414.

[11] Pitman, C. L.; Finster, O. N. L.; Miller, A. J. M., Cyclopentadiene-mediated hydride transfer from rhodium complexes. *Chem. Commun.* **2016,** 52, 9105-9108.

[12] Peng, Y.; Ramos-Garces, M. V.; Lionetti, D.; Blakemore, J. D., Structural and Electrochemical Consequences of [Cp*] Ligand Protonation. *Inorg. Chem.* **2017,** 56, 10824-10831.

[13] (a) Kefalidis, C. E.; Perrin, L.; Burns, C. J.; Berg, D. J.; Maron, L.; Andersen, R. A., Can a pentamethylcyclopentadienyl ligand act as a proton-relay in f-element chemistry? Insights from a joint experimental/theoretical study. *Dalton Trans.* **2015,** 44, 2575-2587. (b) O, W. W. N.; Lough, A. J.; Morris, R. H., Bifunctional Mechanism with Unconventional Intermediates for the Hydrogenation of Ketones Catalyzed by an Iridium(III) Complex Containing an N-Heterocyclic Carbene with a Primary Amine Donor. *Organometallics* **2012,** 31, 2152-2165.

[14] (a) Chalkley, M. J.; Del Castillo, T. J.; Matson, B. D.; Roddy, J. P.; Peters, J. C., Catalytic N_2-to-NH_3 Conversion by Fe at Lower Driving Force: A Proposed Role for Metallocene-Mediated PCET. *ACS Central Science* **2017,** 3, 217-223. (b) Chalkley, M. J.; Del Castillo, T. J.; Matson, B. D.; Peters, J. C., Fe-Mediated Nitrogen Fixation with a Metallocene Mediator: Exploring pKa Effects and Demonstrating Electrocatalysis. *J. Am. Chem. Soc.* **2018,** 140, 6122-6129.

[15] Pal, S.; Kusumoto, S.; Nozaki, K., Dehydrogenation of Dimethylamine–Borane Catalyzed by Half-Sandwich Ir and Rh Complexes: Mechanism and the Role of Cp* Noninnocence. *Organometallics* **2018,** 37, 906-914.

[16] Henke, W. C.; Lionetti, D.; Moore, W. N. G.; Hopkins, J. A.; Day, V. W.; Blakemore, J. D., Ligand Substituents Govern the Efficiency and Mechanistic Path of Hydrogen Production with [Cp*Rh] Catalysts. *ChemSusChem* **2017,** 10, 4589-4598.

[17] Creutz, C., Bipyridine radical ions. *Comments Inorg. Chem*. **1982,** 1, 293-311.

[18] (a) Halpern, J.; Peters, E., Mechanism of the Catalytic Activation of Molecular Hydrogen by Metal Ions. *J. Chem. Phys.* **1955,** 23, 605-605. (b) Dempsey, J. L.; Winkler, J. R.; Gray, H. B., Mechanism of H2 Evolution from a Photogenerated Hydridocobaloxime. *J. Am. Chem. Soc.* **2010,** 132, 16774-16776.

[19] (a) Klingert, B.; Werner, H., Basische Metalle, XLII. Die Metall-Basizität der Komplexe $C_5Me_5Rh(PMe_3)_2$, $C_5Me_5Rh(C_2H_4PMe_3$ und $C_5Me_5Rh(C_2H_4)P_2Me_4$: Neue Pentamethyl-cyclopentadienylrhodium(I)- und -rhodium(III)-Verbindungen. *Chem. Ber.* **1983,** 116, 1450-1462. (b) Faller, J. W.; D'Alliessi, D. G., Tunable Stereoselective Hydrosilylation of PhC∶CH Catalyzed by Cp*Rh Complexes. *Organometallics* **2002,** 21, 1743-1746.

[20] Faraone, F.; Bruno, G.; Schiavo, S. L.; Tresoldi, G.; Bombieri, G., η^5-Cyclopentadienylrhodium(I) complexes containing diphosphines and their reactions with the electrophiles H^+ and Me^+. Crystal and molecular structure of $[Rh(\eta\text{-}C_5H_5)(CO)(Ph_2PCH_2PPh_2)]$, a complex with a unidentate bis(diphenylphosphino)methane ligand. *J. Chem. Soc., Dalton Trans.* **1983,** 433-438.

[21] Boyd, E. A.; Lionetti, D.; Henke, W. C.; Day, V. W.; Blakemore, J. D., Preparation, Characterization, and Electrochemical Activation of a Model [Cp*Rh] Hydride. *Inorg. Chem.* **2019,** *58*, 3606-3615.

[22] (a) Canovese, L.; Visentin, F.; Santo, C.; Chessa, G.; Bertolasi, V., Allyl Amination of Phosphinoquinoline Allyl Complexes of Palladium. Influence of the Allyl Hapticity on the Reaction Rate and Regiochemistry. *Organometallics* **2010,** 29, 3027-3038. (b) Suzuki, T., Crystal and Molecular Structures of Bis[8-(diphenylphosphino)quinoline]palladium(II) Complexes: $Pd(Ph_2Pqn)_2XY$ (XY = Cl_2, Br_2 or $ClBF_4$). *Bull. Chem. Soc. Jpn.* **2004,** 77, 1869-1876

[23] Wehman, P.; van Donge, H. M. A.; Hagos, A.; Kamer, P. C. J.; van Leeuwen, P. W. N. M., *J. Organomet. Chem.* **1997,** 535, 183-193.

[24] Suzuki, T.; Yamaguchi, H.; Fujiki, M.; Hashimoto, A.; Takagi, H. D., Crystal structures of dichloridopalladium(II), -platinum(II) and -rhodium(III) complexes containing 8-(diphenylphosphanyl)quinoline. *Acta Cryst. Sec. E* **2015,** 71, 447-451.

[25] (a) Suzuki, T.; Yamaguchi, H.; Hashimoto, A.; Nozaki, K.; Doi, M.; Inazumi, N.; Ikeda, N.; Kawata, S.; Kojima, M.; Takagi, H. D., Orange and Yellow Crystals of Copper(I) Complexes Bearing 8-(Diphenylphosphino)quinoline: A Pair of Distortion Isomers of an Intrinsic Tetrahedral Complex.

Inorg. Chem. **2011,** 50, 3981-3987. (b) Mondal, R.; Lozada, I. B.; Davis, R. L.; Williams, J. A. G.; Herbert, D. E., Site-Selective Benzannulation of N-Heterocycles in Bidentate Ligands Leads to Blue-Shifted Emission from $[(P\text{^}N)Cu]_2(\mu\text{-}X)_2$ Dimers. *Inorg. Chem.* **2018,** 57, 4966-4978.

[26] Akira, H.; Hiroshi, Y.; Takayoshi, S.; Kazuo, K.; Masaaki, K.; D., T. H., Preparation, Crystal Structures, and Spectroscopic and Redox Properties of Nickel(II) Complexes Containing Phosphane–(Amine or Quinoline)-Type Hybrid Ligands and a Nickel(I) Complex Bearing 8-(Diphenylphosphanyl)quinoline. *Eur. J. Inorg. Chem.* **2010,** 2010, 39-47.

[27] Huang, L.; Rominger, F.; Rudolph, M.; Hashmi, A. S. K., A general access to organogold(iii) complexes by oxidative addition of diazonium salts. *Chem. Commun*. **2016,** 52, 6435-6438.

[28] (a) Nakamura, G.; Okamura, M.; Yoshida, M.; Suzuki, T.; Takagi, H. D.; Kondo, M.; Masaoka, S., Electrochemical Behavior of Phosphine-Substituted Ruthenium(II) Polypyridine Complexes with a Single Labile Ligand. *Inorg. Chem*. **2014,** 53, 7214-7226. (b) Tao, C.; Yu, Y.; Wei-Wei, L.; Wen-Bing, Q.; Ting-Bin, W., Efficient endo Cycloisomerization of Terminal Alkynols Catalyzed by a New Ruthenium Complex with 8-(Diphenylphosphino)quinoline Ligand and Mechanistic Investigation. *Chem. Eur. J.* **2018,** 24, 1606-1618

[29] Tsukuda, T.; Nishigata, C.; Arai, K.; Tsubomura, T., Photophysical properties of copper(I) and zinc(II) complexes containing phosphinoquinoline ligands. *Polyhedron* **2009,** 28, 7-12.

[30] Suzuki, T.; Kotera, M.; Takayama, A.; Kojima, M., Crystal structures of (azido)(pentamethylcyclopentadienyl)iridium(III) complexes containing various types of bidentate ligands. *Polyhedron* **2009,** 28, 2287-2293.

[31] Kittaneh, I. M.; Hodali, H. A.; Tayim, H. A., Complexes of some mixed-donor ligands with Rh(I), Ir(I) and Ir(III). *Inorg. Chim. Acta.* **1982,** 60, 223-226.

[32] White, C.; Yates, A.; Maitlis, P. M., (η^5-Pentamethylcyclopentadienyl) Rhodium and -Iridium Compounds. *Inorg. Synth.* **1992,** 29, 228-234

[33] Nutton, A.; Bailey, P. M.; Maitlis, P. M. Pentamethylcyclopentadienylrhodium and -iridium complexes. Part 29. Syntheses and x-ray structure determinations of tri-micro -hydroxybis[(h-pentamethylcyclopentadienyl)rhodium] hydroxide undecahydrate and -iridium acetate tetradecahydrate and related complexes. *J. Chem. Soc., Dalton Trans*. **1981**, 1997-2002.

[34] Issleib, K.; Haftendorn, M., Alkali Phosphorus Compounds and Their Reactive Behavior .43. 8-Quinolylphosphines. *Z. Anorg. Allg. Chem.* **1970,** 376, 79-86

[35] Feltham, R. D.; Metzger, H. G., Synthesis of Vicinal Bis(Dimethylarsino) Compounds. *J. Organomet. Chem.* **1971,** 33, 347-86

[36] Dadci, L.; Elias, H.; Frey, U.; Hornig, A.; Koelle, U.; Merbach, A. E.; Paulus, H.; Schneider, J. S., Pi-Arene Aqua Complexes of Cobalt, Rhodium, Iridium, and Ruthenium - Preparation, Structure, and Kinetics of Water Exchange and Water Substitution. *Inorg. Chem.* **1995,** 34, 306-315

[37] Saveant, J.-M., *Elements of Molecular and Biomolecular Electrochemistry*. Wiley: Hoboken, NJ, 2006.

[38] (a) Blakemore, J. D.; Hernandez, E. S.; Sattler, W.; Hunter, B. M.; Henling, L. M.; Brunschwig, B. S.; Gray, H. B., Pentamethylcyclopentadienyl rhodium complexes. *Polyhedron* **2014,** 84, 14-18. (b) Nakai, H.; Jeong, K.; Matsumoto, T.; Ogo, S., Catalytic C-F Bond Hydrogenolysis of Fluoroaromatics by [(η5-C_5Me_5)Rh^{I}(2,2'-bipyridine)]. *Organometallics* **2014,** 33, 4349-4352.

[39] Johnson, S. I.; Gray, H. B.; Blakemore, J. D.; Goddard, W. A., Role of Ligand Protonation in Dihydrogen Evolution from a Pentamethylcyclopentadienyl Rhodium Catalyst. *Inorg. Chem.* **2017,** 56, 11375-11386.

[40] Kaim, W.; Reinhardt, R.; Waldhor, E.; Fiedler, J., Electron transfer and chloride ligand dissociation in complexes [(C_5Me_5)ClM(bpy)]$^{+}$/[(C_5Me_5)M(bpy)]^{n} (M=Co, Rh, Ir; n=2+,+,0,-): A combined electrochemical and spectroscopic investigation. *J. Organomet. Chem.* **1996,** 524, 195-202.

[41] Chardon-Noblat, S.; Cosnier, S.; Deronzier, A.; Vlachopoulos, N., Electrochemical Properties of [(C_5Me_5)Rh^{III}(L)Cl]$^{+}$ Complexes (L=2,2'-Bipyridine or 1,10-Phenanthroline Derivatives) in Solution

and in Related Polypyrrolic Films - Application to Electrocatalytic Hydrogen Generation. *J. Electroanal. Chem.* **1993,** 352, 213-228

[42] (a) White, C.; Thompson, S. J.; Maitlis, P. M., Pentamethylcyclopentadienyl-rhodium and -iridium complexes. Part XII. Tris(solvent) complexes and complexes of η^6-benzene, -naphthalene, -phenanthrene, -indene, -indole, and -fluorene and η^5-lndenyl and -indolyl. *J. Chem. Soc., Dalton Trans.* **1977,** 1654-1661. (b) Blakemore, J. D.; Schley, N. D.; Balcells, D.; Hull, J. F.; Olack, G. W.; Incarvito, C. D.; Eisenstein, O.; Brudvig, G. W.; Crabtree, R. H., Half-Sandwich Iridium Complexes for Homogeneous Water-Oxidation Catalysis. *J. Am. Chem. Soc.* **2010,** 132, 16017-16029.

[43] Connelly, N. G.; Geiger, W. E., Chemical Redox Agents for Organometallic Chemistry. *Chem. Rev.* **1996,** 96, 877-910.

[44] (a) By comparison, reduction of bpy-supported [Cp*Rh] complexes results in notable changes in the C–C bond lengths of the ligand scaffold (best observed in the contraction of the interpyridine C–C bond), as determined by single-crystal XRD. These observations have been taken as evidence of substantial delocalization of electron density into the π-system of the aromatic ligand. (b) Gore-Randall, E.; Irwin, M.; Denning, M. S.; Goicoechea, J. M., Synthesis and Characterization of Alkali-Metal Salts of 2,2′- and 2,4′-Bipyridyl Radicals and Dianions. *Inorg. Chem.* **2009,** 48, 8304-8316.

[45] Bard, A. J.; Faulkner, L. R., *Electrochemistry: Fundamentals and Applications*. 2nd ed.; John Wiley and Sons Inc.: Hoboken, 2001.

[46] Lever, A. B. P., Electrochemical parametrization of metal complex redox potentials, using the ruthenium(III)/ruthenium(II) couple to generate a ligand electrochemical series. *Inorg. Chem.* **1990,** 29, 1271-1285.

[47] Muckerman, J. T.; Skone, J. H.; Ning, M.; Wasada-Tsutsui, Y., Toward the accurate calculation of pKa values in water and acetonitrile. *Biochim. Biophys. Acta Bioenerg*. **2013,** 1827, 882-891.

[48] (a) The data provide an estimated Rh–H41 distance of 1.48(4) Å. However, the large amount of electron density associated with the rhodium center could lead to underestimation of this bond distance. See the following reference for more information: (b) Schmidtmann, M.; Coster, P.; Henry, P. F.; Ting, V. P.; Weller, M. T.; Wilson, C. C., Determining hydrogen positions in crystal engineered organic molecular complexes by joint neutron powder and single crystal X-ray diffraction. *CrystEngComm* **2014,** 16, 1232-1236.

[49] Appel, A. M.; Helm, M. L., Determining the Overpotential for a Molecular Electrocatalyst. *ACS Catal*. **2014,** 4, 630-633.

[50] Creutz, C., Bipyridine radical ions. *Comments Inorg. Chem.* **1982,** 1, 293-311.

[51] To report the ratio of enhancement, the peak current density associated with the reduction of **1-Cl** to **2** was divided by two to account for the two-electron nature of the wave.

[52] Fulmer, G. R.; Miller, A. J. M.; Sherden, N. H.; Gottlieb, H. E.; Nudelman, A.; Stoltz, B. M.; Bercaw, J. E.; Goldberg, K. I., NMR Chemical Shifts of Trace Impurities: Common Laboratory Solvents, Organics, and Gases in Deuterated Solvents Relevant to the Organometallic Chemist. *Organometallics* **2010,** 29, 2176-2179.

[53] Harris, R. K.; Becker, E. D.; Cabral De Menezes, S. M.; Goodfellow, R.; Granger, P., NMR nomenclature. Nuclear spin properties and conventions for chemical shifts (IUPAC recommendations 2001). *Pure Appl. Chem.* **2001,** 73, 1795-1818.

[54] Harris, R. K.; Becker, E. D.; Cabral De Menezes, S. M.; Granger, P.; Hoffman, R. E.; Zilm, K. W., Further conventions for NMR shielding and chemical shifts: (IUPAC recommendations 2008). *Pure Appl. Chem.* **2008,** 80, 59-84.

Chapter 4

Synthesis and Reactivity Studies of a [Cp*Rh] Complex Supported by a Methylene-Bridged Hybrid Phosphine-Imine Ligand

This chapter is adapted from a published manuscript:

Hopkins, J.A.; Lionetti D.; Day, V.W.; Blakemore, J.D. Synthesis and Reactivity Studies of a [Cp*Rh] Complex Supported by a Methylene-Bridged Hybrid Phosphine-Imine Ligand. *J. Organomet. Chem.* **2020**, *921*, 121294.

4.1 Introduction

Identification of ligand structure-function relationships is an important strategy for rational design of organometallic catalysts. In redox chemistry, substitution of one ligand for another often results in significant changes to the properties of the target metal complex, for example in shifted reduction potential, reactivity, or basicity.[1] Such shifts can often lead to marked changes in catalytic effectiveness, especially in molecular catalysis of small-molecule activation reactions requiring effective management of both protons (H^+) and reducing equivalents (e^-). Efforts to understand how ligands impact transfer of H^+/e^- form the basis of strategies aimed at tuning of catalysts and improving catalytic efficiencies.[2] However, these efforts remain challenging due to the propensity of both metal centers and ligands to become directly involved in reactivity.[3]

We have been working to understand the reactivity properties of a model family of organometallic rhodium complexes that can serve, in several cases, to couple H^+/e^- equivalents and catalyze production of H_2. The complexes are supported by the η^5-pentamethylcyclopentadienyl (Cp*) ligand, as well as an additional bidentate ligand. The parent catalyst in this family, $[Cp^*Rh(bpy)Cl]^+$ (A, Chart 4.1), is supported by the workhorse 2,2´-bipyridyl (bpy) ligand. This complex was reported in 1987 by Kölle and Grätzel as a catalyst for H_2 production,[4] and by other groups to serve as a catalyst for NAD^+ reduction to NADH.[5] For many years, this catalyst was presumed to operate via a rhodium(III) hydride intermediate, although such a species had not been isolated or fully characterized. New interest in this species was piqued by reports from our group[6] and others[7] showing that exposure of the reduced form of A, Cp*Rh(bpy), to weak proton sources results in generation of an isolable compound bearing the *endo*-η^4-pentamethylcyclopentadiene ligand (η^4-Cp*H), generated by transfer of H^+ to the Cp* ring.[8,9] (*n.b.*, the *endo* face of the ring is defined as the one facing the metal center). Related

reactivity studies have demonstrated that the exposure of the compound bearing (η^4-Cp*H) to a sufficiently strong acid results in quantitative generation of H_2 and regeneration of (η^5-Cp*). Inspired by this rather uncommon chemistry, we have been investigating synthesis and reactivity of other [Cp*Rh] complexes supported by various bidentate ligands.

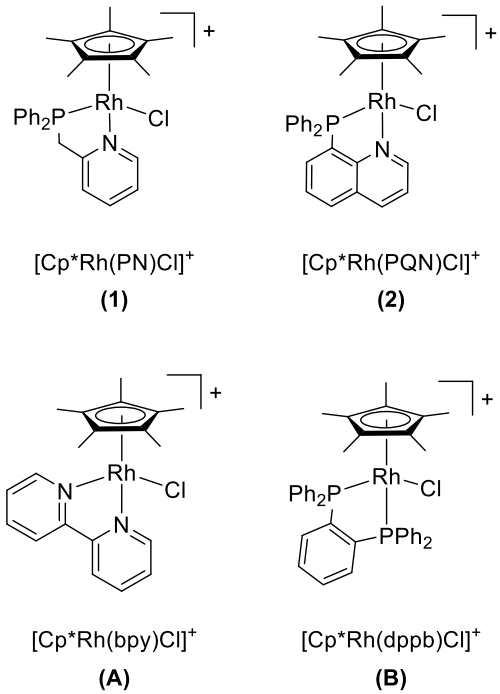

Chart 4.1. Series of half-sandwich rhodium complexes.

Along this line, we have shown that reduction and protonation of a [Cp*Rh] complex (**B**) bearing the 1,2-bis(diphenylphosphino)benzene (dppb) ligand affords access to a stable rhodium(III) hydride.[10] Unlike the [η^4-Cp*H] complexes mentioned above, this [Rh^{III}–H] complex is remarkably resistant to protonolysis.[6,7,11,12] This result agrees with the high apparent stability of other half-sandwich rhodium hydride complexes studied in different contexts,[13] as well as the reactivity properties of rhodium hydrides supported by other ligand sets.[14] However, the high stability of the dppb-supported hydride renders it somewhat less applicable to model studies of more reactive [Cp*Rh] hydrides.

More recently, we have reported the synthesis and reactivity of a [Cp*Rh] complex (**2**) supported by a hybrid ligand, 8-(diphenylphosphino)quinoline (PQN).[15] PQN presents a triarylphosphine donor and an imine donor with appropriate placement for binding to [Cp*Rh] in a five-membered metallacycle. Use of PQN engenders intriguing properties that are intermediary between those of systems bearing diimine ligands and dppb. In particular, use of PQN favors generation of an isolable [Rh^{III}–H] species that can, unlike its dppb analogue, undergo protonolysis and evolve H_2 (see Scheme 4.1). Moreover, **2** displays especially rich reductive electrochemistry, undergoing a two-electron reduction to form Cp*Rh(PQN) at –1.19 V vs. $Fc^{+/0}$ (all potentials referenced to ferrocenium/ferrocene, denoted hereafter as $Fc^{+/0}$) that can be further reduced by one electron at –2.26 V vs. $Fc^{+/0}$.

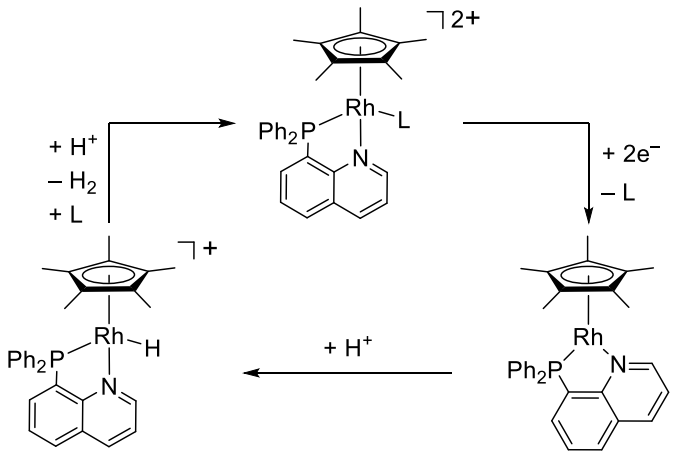

Scheme 4.1. H_2 evolution chemistry with the Cp*Rh(PQN) platform.

Despite these features, the only [Cp*Rh] system supported by a hybrid [*P*,*N*] chelating ligand that has been investigated for its reactivity properties is this example bearing PQN.[15] Because of the especially useful properties engendered by this donor set, we imagined that probing the synthesis and reactivity profile of [Cp*Rh] species supported by other hybrid [*P*,*N*] ligands could be a useful strategy for understanding the reactivity properties of this family of compounds. Along this line, our attention was drawn to the κ^2-[*P*,*N*]-2-[(diphenylphosphino)methyl]pyridine ligand,

commonly known as PN; this ligand is chelating, much like PQN, but presents an alkyldiarylphosphine donor and an imine donor for binding to a central metal. Importantly, although the coordination chemistry of PN ligands has been studied with a variety of transition metals,[16] only a few Rh complexes supported by PN are known.[17] In particular, we were pleased to find that structural data from X-ray diffraction (XRD) analysis was available in the Cambridge Structural Database[18] for [Cp*Rh(PN)Cl]PF_6 (**1**),[19] suggesting that this compound could be prepared. However, no information on the synthetic methods needed for preparation of **1** or information regarding its properties are available, encouraging further work to establish how its reactivity compares with other members of our family of complexes from previous studies.

Here, we report the synthetic procedures, characterization data, and reactivity studies of the [Cp*Rh] complex **1** supported by PN. New structural data for **1** from XRD are compared both to that previously available[19] as well as to our prior data for the PQN-ligated analogue **2**;[15] these analyses suggest that PN is a slightly more effective donor than PQN to Rh. Consistent with this structural data, **1** undergoes a net two-electron reduction near –1.28 V vs. $Fc^{+/0}$, a value that is significantly more negative than that of **2**, resulting in generation of a transient rhodium(I) complex (**3**) that is stable on the timescale of voltammetry. **3** displays no further reductions in our accessible solvent window. Chemical reduction of **1** with Na(Hg), however, does not yield **3** as an isolable compound; rather, a mixture of products forms as a result of further reactivity leading to generation of several observable compounds that has been studied by ^{1}H and $^{31}P\{^{1}H\}$ nuclear magnetic resonance (NMR). Taken together, the results suggest that the highly basic nature of **3** and the acidic backbone C–H bonds of PN engender unexpected reactivity upon chemical reduction of **1** that is unavailable in **2**, which lacks acidic backbone protons. Avoidance of acidic moieties in

supporting ligands is thus a strategy that can guide future work with highly basic [Cp*Rh] complexes intended for study of H^+/e^- management in catalysis.

4.2 Results and Discussion

4.2.1 Synthesis and characterization of 1

The dimeric complex, $[Cp^*RhCl_2]_2$,[29] is useful for straightforward synthesis of [Cp*Rh] complexes with chelating bidentate ligands.[20] For complex **1** addition of 2 equivalents of $AgPF_6$ to 1 equivalent of $[Cp^*RhCl_2]_2$, followed by 2.05 equivalents of free PN ligand results clean generation of complex **1** (Scheme 4.2).

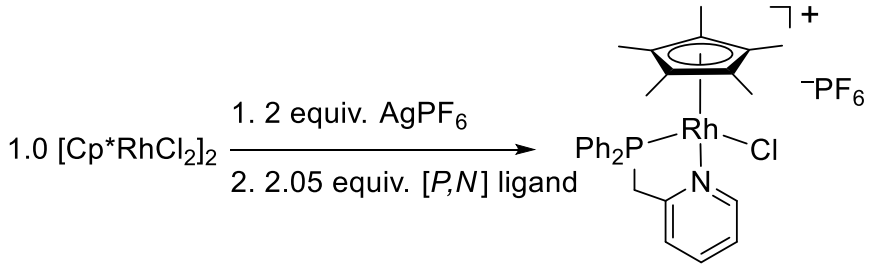

Scheme 4.2. Synthesis of **1.**

The characterization of **1** by proton nuclear magnetic resonance (^{1}H NMR) reveals a signal at 1.50 ppm (integrating to 15H) corresponding to the equivalent protons on [Cp*]; this resonance displays coupling to the phosphorous nucleus ($^4J_{H,P} \approx 3.9$ Hz) of the PN ligand. This coupling is assigned as H,P coupling due to the uniform absence of H,Rh coupling for the methyl groups in analogous [Cp*Rh] complexes bearing non-phosphorus-containing bidentate ligands.[11,12,15] Additionally, the ^{1}H NMR of **1** reveals two multiplets at 4.43 and 4.14 ppm (Figure 4.1, middle spectrum), each integrating to 1H and corresponding to the chemically inequivalent methylene protons on the bidentate [*P,N*] ligand. These multiplets exhibit geminal coupling to each other ($^2J_{H,H} \approx$ 17.4 Hz) as well as coupling to the phosphorus nucleus ($^2J_{H,P} \approx 14.5$ Hz and $^2J_{H,P} \approx$ 10.7 Hz, respectively) resulting in two doublets of doublets that display the expected "roofing"

behavior. For comparison, the $^{1}H\{^{31}P\}$ NMR spectrum displays only two doublets at 4.43 and 4.14 ppm ($J_{H,H} \approx 17.4$ Hz; see Figure 4.1, top spectrum). This result confirms the geminal coupling between the chemically inequivalent protons, through decoupling of phosphorus. The "roofing" appearance of the methylene peaks is expected considering that the difference in chemical shift between the chemically inequivalent protons is comparable in magnitude to their chemical coupling ($J_{H,H}$). The ^{1}H NMR spectrum of **2** does not display resonances near 4.25 ppm because the quinoline bridge of the PQN ligand lacks methylene protons.[15]

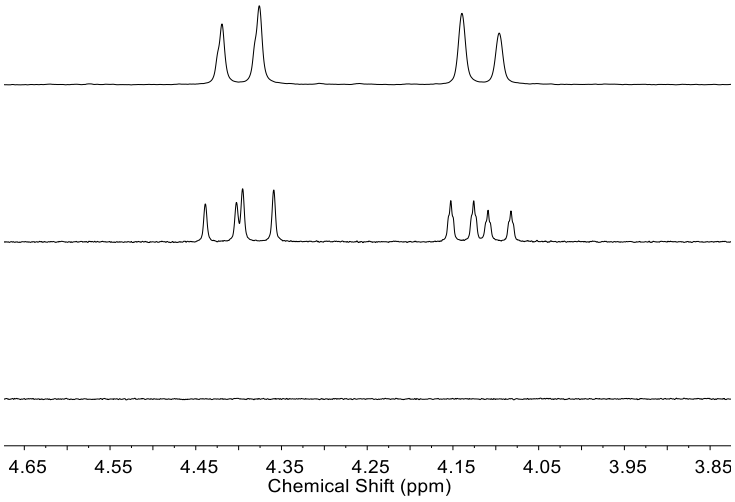

Figure 4.1. Characterization of **1** and **2**. Upper spectrum: $^{1}H\{^{31}P\}$ NMR of **1**; Middle spectrum: ^{1}H NMR of **1** (middle); Lower spectrum: ^{1}H NMR of **2**.

Further characterization of **1** with $^{31}P\{^{1}H\}$ NMR (Figure 4.2, upper spectrum) reveals a doublet at 51.57 ppm ($^{1}J_{P,Rh} \approx 140.3$ Hz), confirming direct bonding between rhodium and the phosphorus atom of PN. For comparison, the $^{31}P\{^{1}H\}$ NMR of **2** (Figure 4.2, lower spectrum) shows a doublet at 47.90 ppm ($^{1}J_{P,Rh} \approx 143.8$ Hz).[15] The more downfield position of the ^{31}P resonances in **1** is indicative of a more electron rich phosphorus atom, suggesting that PN behaves as a more strongly donating ligand in **1** than PQN in **2**.

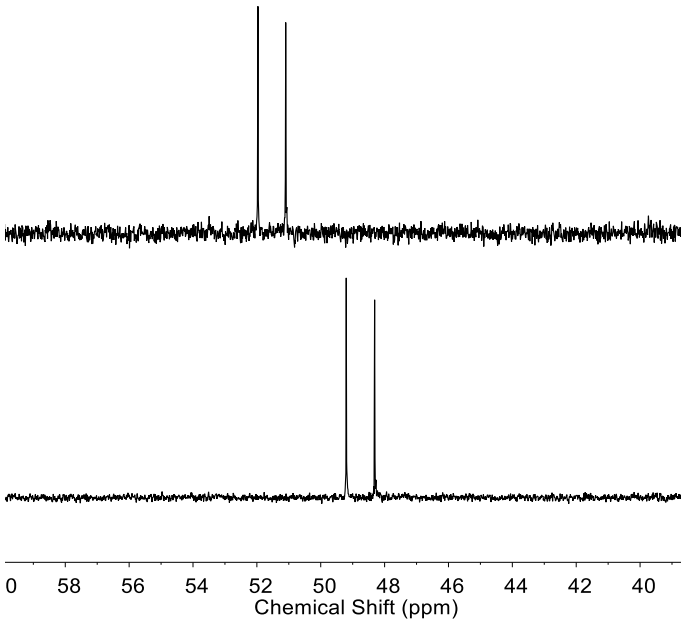

Figure 4.2. $^{31}P\{^{1}H\}$ NMR spectra: **1** (upper) and **2** (lower).

4.2.2 X-ray Diffraction Studies

As mentioned earlier, we were pleased to find that **1** was previously characterized by XRD analysis and reported to the Cambridge Structural Database as a Private Communication.[19] However, no description of the origin of the structure or the properties of **1** have been made available in prior work. Thus, we pursued further structural data to provide needed context for the work here, and to obtain information for comparison to the previously reported data.[19] Vapor diffusion of diethyl ether into acetonitrile yielded orange crystals of **1** suitable for X-ray diffraction studies. The resulting solid-state structure reveals the geometry of the formally Rh(III) metal center in **1** to be *pseudo*-octahedral (Figure 4.3). The first coordination sphere around the metal contains the κ^2-[*P*,*N*] scaffold, a single bound chloride anion, and the [η^5-Cp*] ligand. Notably, there is good agreement between the previously reported structural data and the data from our study; the bond lengths (and their estimated standard deviations, see Table 4.1) do not differ significantly

between the two data sets, confirming that these data are collectively suitable for interpretation here.

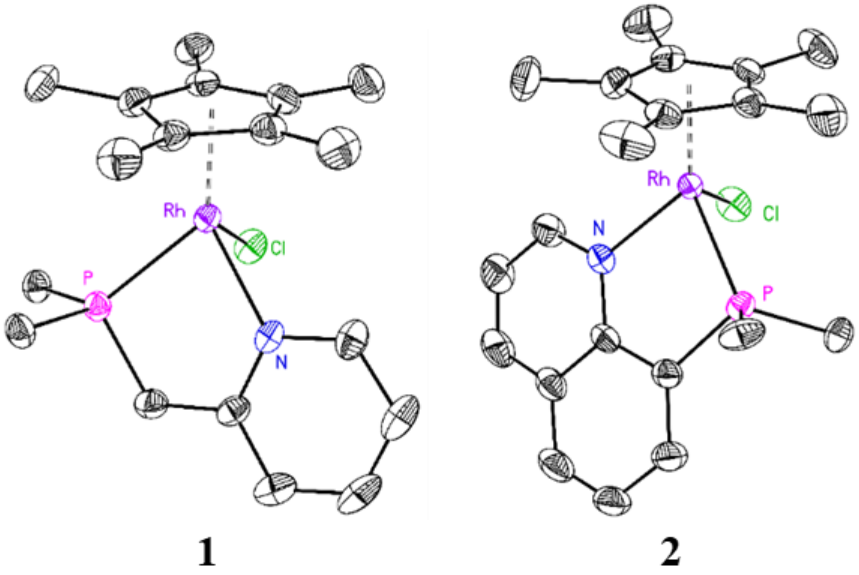

Figure 4.3. Comparison of the solid-state structures of **1** and **2**.[15] Outersphere hexafluorophosphate (**1**) and triflate (**2**) cournteranions and all hydrogen atoms are omitted for clarity. Phenyl groups are truncated for clarity. Displacement ellipsoids are shown at the 50% probability level.

	1 (new)	**1** (prior work)	**2**
CCDC entry	1973828	233218	1858635
Rh–Cl (Å)	2.416(2)	2.4176(6)	2.402(6)
Rh–P (Å)	2.2730(18)	2.2949(5)	2.3037(6)
Rh–N (Å)	2.119(3)	2.1275(15)	2.122(2)
Rh–Cp_{cent} (Å)	1.832	1.837	1.830
∠P–Rh–N (º)	81.14°	81.36°	82.20°
Reference	this work	Ref. 19	Ref. 15

Table 4.1. Comparison of bond lengths and angles for complexes **1** and **2**.

From inspection of our new structural data, the angle between the plane of the [Cp*] ligand and the plane of the bidentate PN ligand (the plane defined by the Rh, N and P atoms) is 60.5º, similar to the analogous angle (62.0º) in the structure of **2** supported by PQN.15 This similarity suggests that the increased flexibility of the PN ligand does not markedly influence the geometry

of the Rh center in **1**. In addition, the P–Rh–N bond angle does not differ significantly (<1º difference) between **1** and **2**, despite the greater rigidity enforced by the quinoline moiety within the PQN ligand of **2**. These similar structural features are consistent with the comparable Rh^{III}/Rh^{I} reduction potentials measured for **1** and **2** (*vide infra*).

However, comparison of the bond lengths of **1** and **2** reveal that the Rh–P bond in **1** is marginally shorter than that in **2**; the shorter bond length in **1** may again indicate that PN (at the P atom) is a stronger donor ligand and therefore engenders a more basic Rh center than that found in **2**. The more negative reduction potential of **1** versus **2** (*vide infra*) is also consistent with these structural findings.

4.2.3 Electrochemical studies

Past studies of [Cp*Rh] complexes supported by 2,2´-bipyridyl (bpy) derivatives4,[11,12] and dppb10 have shown that electrochemical reduction of the compounds proceeds through a net $2e^{-}$ reduction from Rh^{III} to Rh^{I} via an ECE´-type mechanism (E = electron transfer, C = chemical reaction).[21] In such studies, initial reduction (E) leads to ejection of the monodentate ligand (usually chloride or solvent) (C) and thus a positive shift in $E(Rh^{II}/Rh^{I})$ such that it is positive of the $E(Rh^{III}/Rh^{II})$ associated with the starting compound. In our prior work, **2** was found display a similar electrochemical profile, undergoing reduction from Rh^{III} to Rh^{I} at –1.19 V vs $Fc^{+/0}$ (Figure 4.4, lower panel).15 Unique to the PQN system, this $2e^{-}$ reduction is followed by a third reduction at –2.26 V vs. $Fc^{+/0}$, a feature that we have previously predicted to be PQN-ligand-centered on the basis of chemical reactivity.

We find that **1** displays similar electrochemical properties in comparison with these previously investigated systems. The cyclic voltammogram (CV) of **1** (Figure 4.4, upper panel) shows a single reduction event at –1.28 V vs $Fc^{+/0}$, consistent with a net $2e^{-}$ reduction from Rh^{III} to Rh^{I} *(vide*

infra). Evidently, the ECE´-type mechanism dominates the electrochemical behavior of **1** as it does with **2**, consistent with the similar chelating nature and structural features of PN and PQN, respectively.

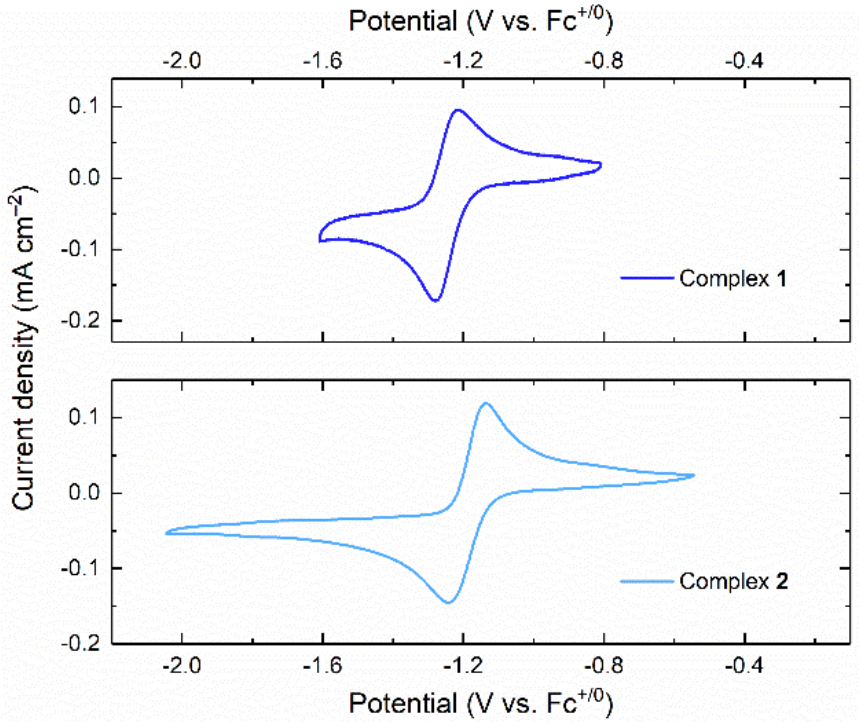

Figure 4.4. Cyclic voltammetry of **1** and **2**. Electrolyte: 0.1 M $TBAPF_6$ in acetonitrile; Scan rate: 100 mV/s; Working electrode: highly oriented pyrolytic graphite (HOPG); [Rh] in each experiment was ca. 1 mM. Initial potentials were ca. –0.8 V for **1** and ca. –0.6 V for **2**.

The CV profile of **1** is consistent with a sequence in which the chloride-bound Rh^{III} species undergoes $1e^-$ reduction to a transient 19-electron species. The expected subsequent loss of the Cl^- ligand (as occurs with **2**) would form a 17-electron complex that could undergo immediate transfer of a second electron, giving rise to a Rh^I product (**3**). We have assigned this sequence leading to generation of **3** on the basis of observed chemical reactivity (*vide infra*), along with the close similarity of the appearance of the electrochemical data for **1** with the prior systems we have studied in the [Cp*Rh] family. We also note that scan rate-dependent studies show that both **1** and

3 are freely diffusing in solution, consistent with their solubility in acetonitrile (see Appendix B, Figure B14).

As mentioned above, **2** undergoes a third, one-electron reduction at –2.26 V that we have tentatively assigned as a reduction associated with PQN ligand.[15] Consistent with this theory, no third reduction is observed in the CV data for **1** (Figure 4.5). The extended conjugation of PQN due to the presence of the quinoline moiety is expected to give rise to this notable difference in accessible oxidation states, as expected on the basis of the reduction potentials for quinoline and pyridine.[22]

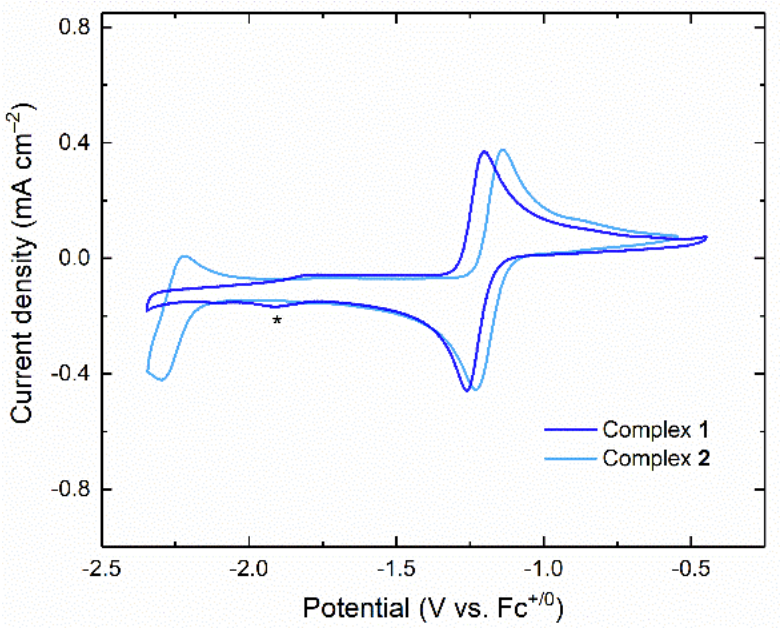

Figure 4.5. Comparison of CV data for **1** and **2**. Electrolyte: 0.1 M $TBAPF_6$ in acetonitrile; Scan rate: 100 mV/s; Working electrode: highly oriented pyrolytic graphite (HOPG); [Rh] in each experiment was ca. 1 mM. Initial potential: **1** and **2** ca. –0.5 V. * indicates reduction of a small impurity of $[Cp^*RhCl_2]_2$.[23]

Comparison of all the reduction potentials of the [Cp*Rh] complexes studied in our group to date reveals that **1** has the most negative Rh^{III}/Rh^{I} reduction potential yet accessed in our series.[10,

[11,12,15] Comparing the most closely related cases of **1** and **2**, this finding agrees with the available structural data implicating a greater donor strength for PN in comparison with PQN. More broadly, **3** can be anticipated from the electrochemical work to be rather basic in nature due to the rather negative potential at which this compound is generated. Indeed, we find that **3** is quite basic on the basis of chemical reactivity observed upon chemical reduction (*vide infra*).

4.2.4 Identification of the Product Mixture Resulting from Chemical Reduction of 1 Followed by Chemical Reactivity

The electrochemical data suggest that a Rh^{I} complex, **3**, is formed upon two-electron reduction of **1** and is stable at least on the timescale of seconds-to-minutes, as interrogated by CV. To further investigate the nature of **3** and/or further chemical reactivity of this species, we targeted chemical reduction of **1** by treatment with sodium amalgam (Na(Hg)). This reductant was selected for its rather negative reduction potential ($E^{o} \approx -2.36$), sufficiently negative for reduction of **1** on the basis of the CV results.[24] Addition of a solution containing **1** in tetrahydrofuran to a vial containing Na(Hg) results in a marked color change from orange to purple and eventually blue over the timescale of thirty minutes to an hour. From this rapid color change, we conclude that electron transfer from Na(Hg) to the starting compound **1** is relatively fast, a conclusion also supported by the chemically reversible voltammetry. Removal of THF solvent yields a dark blue solid that can be extracted and redissolved for characterization of products with ^{1}H NMR and $^{31}P\{^{1}H\}$ NMR.

Three rhodium species are detectable in the reaction mixture resulting from reduction of **1** with Na(Hg). ^{1}H NMR spectra shows two major sets of aromatic resonances in a 2:1 ratio (see Appendix B Figure B8). ^{1}H NMR also reveals accompanying aliphatic resonances corresponding to Cp* protons (relative to the aromatic protons, integrating to 30H and 15H, respectively) at 1.63 ppm ($J \approx 2.7$, 1.0 Hz) and 1.94 ppm ($J \approx 2.0$ Hz). These signals correspond to formation of two

diamagnetic species bearing intact [η^5-Cp*] ligands, one of which is **3** (see Scheme 4.3). The ^{1}H NMR spectrum also features a unique doublet at 3.02 ppm ($^2J_{H,P}$ = 10.4 Hz); on the basis of proper integration, this doublet is associated with the species giving the [η^5-Cp*] resonance at 1.94 ppm (the relative integration of the specific *ortho*-pyridyl proton, Cp* protons, and methylene protons in this species is 1:15:2 protons). The integration of this doublet as 2H is consistent with formation of **3**, as the methylene protons on the bridge of the PN ligand of **3** are spectroscopically equivalent; this compares well with the known C_{2v} symmetry of related formally Rh^I compounds bearing bidentate chelating ligands.[15,25] This assignment is further supported by findings from the two-dimensional ^{1}H–^{1}H NMR techniques NOESY and COSY that confirm the expected coupling network for **3** (see Appendix B, Figures B11 and B12). Furthermore, ^{31}P{^{1}H} NMR features a large doublet at 61.1 ppm associated with **3**; the significant increase in coupling constant for this set of resonances ($^1J_{P,Rh} \approx 244.7$ Hz) in comparison with those associated with **1** ($^1J_{P,Rh} \approx 140.7$ Hz) is consistent with reduction of the metal center upon formation of **3** from **1**.

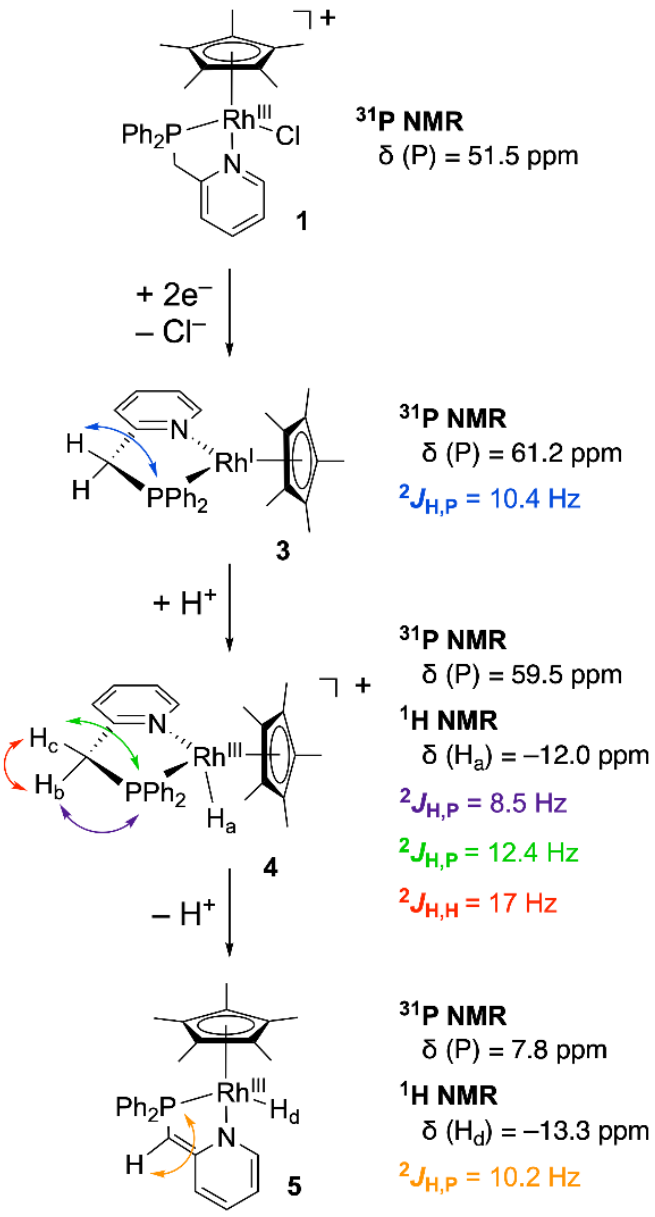

Scheme 4.3. Schematic reactivity of **1** upon reduction by Na(Hg).

The upfield region of the ^{1}H NMR collected on the mixture resulting from reduction of **1** with Na(Hg) features a doublet of doublets at –12.0 ppm that integrates as 1H with respect to the second full set of peaks associated with the [η^5-Cp*] signal at 1.63 ppm. This set of resonances indicates formation of the [Cp*Rh] hydride complex **4**; in particular, the distinctive doublet of doublets can be confidently ascribed to the hydride H-atom itself, as it displays the expected $^{1}J_{H,Rh}$ and $^{2}J_{H,P}$ couplings (40.8, 30.1 Hz). Also associated with **4**, two doublets of doublets of doublets appear in

the aliphatic region of the ^{1}H NMR spectrum at 4.18 ppm ($J \approx 17.6, 12.4, 2.3$ Hz) and 3.48 ppm ($J \approx 17.3, 8.5, 1.0$ Hz), integrating in a 2:1 ratio with the hydride peak at –12.0 ppm. These resonances are associated with the expected methylene protons of the PN ligand bound to **4**; due to the *pseudo*-octahedral geometry of **4**, the protons on the bridging methylene unit in PN are diastereotopic. This situation is similar to that encountered for the methylene protons in **1** (see Figure 4.1). Notably, the assignment of the formulation of **4** as a hydride bearing an unmodified PN ligand was confirmed by the two-dimensional NMR studies (see Appendix B, Figure B11 and B12). Consistent with this model, the ^{31}P{^{1}H} NMR spectrum shows a second major doublet centered at 59.5 ppm corresponding to **4** with $^{1}J_{P,Rh} \approx 148.5$ Hz.

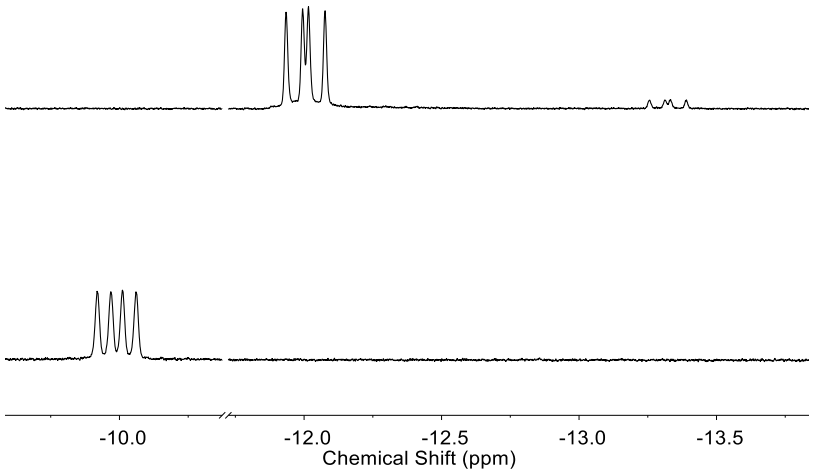

Figure 4.6. Upfield region of selected ^{1}H NMR spectra. Upper panel: chemical reduction of **1**; lower panel: $[Cp^*Rh(PQN)H]^{+}OTf^{-}$.

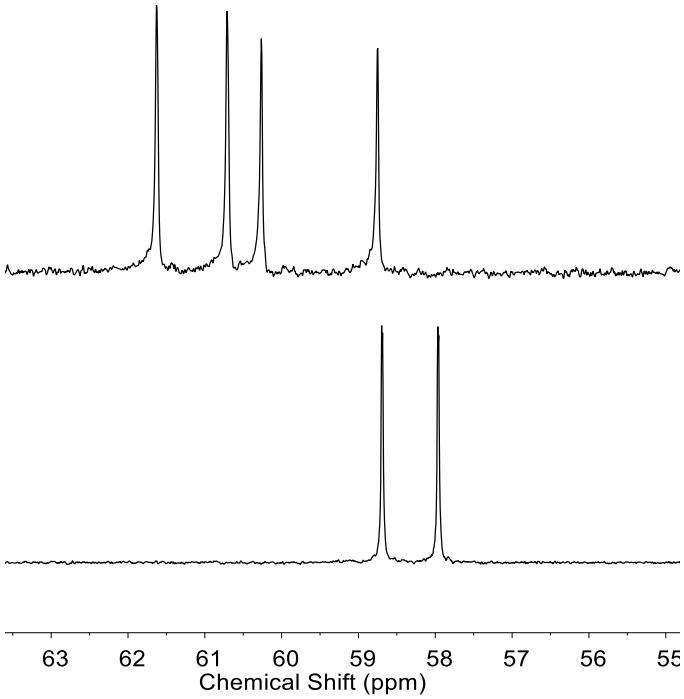

Figure 4.7. Partial $^{31}P\{^{1}H\}$ NMR spectra for the products of chemical reduction of **1** (upper) and [Cp*Rh(PQN)H]$^{+}$ OTf (lower).

In addition to the large signals associated with the major products of reduction being **3** and **4**, an additional doublet of doublets is observed by ^{1}H NMR at –13.3 ppm (J = 38.5, 28.4 Hz). This signal indicates generation of a second, minor [Rh^{III}–H] species, **5**. Indeed, re-inspection of the full ^{1}H NMR spectrum reveals an accompanying set of minor peaks in the aromatic region and a small [η^5-Cp*] peak at 1.39 ppm also associated with **5**. Most unique, a doublet appears at 3.84 ppm with $^{2}J_{H,P}$ = 10.2 Hz which integrates as 1H with respect to the hydride signal at –13.3 ppm; this doublet indicates that **5** bears an LX-type ligand derived from PN that is presumably generated by deprotonation of **4** by **3**. The $^{31}P\{^{1}H\}$ NMR spectrum of the mixture also displays an expected minor doublet associated with the hydride complex **5** at 7.81 ppm ($^{1}J_{P,Rh} \approx$ 195.4 Hz; see Figure B10). As in the other cases, two-dimensional NMR studies confirm the full assignment of the structure of **5** (see Appendix B, Figure B11 and B12). Notably, Norton and co-workers have

examined similar [Cp*Rh] hydride complexes to **5** bearing LX-chelate ligands like 2-phenylpyridine.[26]

The hydride resonances associated with **4** and **5** are reminiscent of those we have measured for the $[Cp^*Rh(PQN)H]^+$ species generated by two-electron reduction of **2** followed by addition of anilinium triflate (pK_a = 10.6 in CH_3CN) as an exogenous proton source.[27] The ^1H NMR of this species displays an upfield set of resonances at –9.9 ppm appearing as a doublet of doublets due to H,Rh and H,P coupling ($J \approx 36.6, 19.9$ Hz). This is notably similar to the resonances observed for the hydride ligands of **4** (δ = –12.0 ppm, $J \approx 40.8, 30.1$ Hz) and **5** (δ = –13.3 ppm, J = 38.5, 28.4 Hz).

The electrochemical data showing reduction of **1** and generation of **3** do not indicate that chemical reactivity to form **4** and **5** occurs on the timescale of cyclic voltammetry. Therefore, this reaction must be rather slow, taking place over the timescale of tens of minutes to an hour and therefore not observable on the electrochemical timescale. However, based on the appearance of the CV data as well as the rapid color change from orange to purple and then eventually blue observed upon treatment of **1** with Na(Hg), electron transfer can be assumed to be reasonably fast.

Based on the observed products, **3** is capable of deprotonation of other species in solution. The most likely species to undergo deprotonation are rhodium-containing species, as deprotonation of the tetrahydrofuran solvent is unlikely due to its high intrinsic pK_a value. The two most likely endogenous proton sources are either the Rh^{III} starting material, **1**, or a formally Rh^{II} species generated by reduction of **1**. Although the reduction of complex **1** is fast upon addition of Na(Hg), **1** has very poor solubility in tetrahydrofuran and becomes soluble only upon chemical reduction. This poor solubility could contribute to the simultaneous presence of both **3** and unreacted **1**, and enable **1** to serve as a proton source for generation of **4** from **3** in solution. The acidic protons of

the backbone C–H bonds of the PN ligands would be present in both **1** and its one-electron reduced species; either of these could lead to generation of the major hydride product **4**. Similarly, the minor hydride **5** could be generated by deprotonation of nascent **4** by **3**.

Notably, the NMR spectra suggest that a greater quantity of **4** than **5** is produced. This is reasonable, in that the initial solution contains mostly **1** at the start of exposure to Na(Hg), favoring possible deprotonation of **1** by nascent **3**. Additionally, there could be a difference in acidity of the backbone C–H bonds of the PN ligands in **1** and **4**. As the hydride ligand in **4** is a more effective donor than the chloride ligand in **1**, the effective pK_a of the C–H bonds of PN could be correspondingly higher for **4** than for **1**, making **1** more acidic and giving a higher driving force for proton donation. Notably, however, we do not observe the immediate products of deprotonation of the starting material **1** or the analogous Rh^{II} species. Thus, other Rh species bearing a deprotonated form of the PN ligand may be tentatively concluded to undergo further reactivity and/or decomposition under the conditions of reduction by Na(Hg).

4.3 Conclusions

We have described the synthesis, characterization, electrochemical properties, and chemical reactivity profile of a [Cp*Rh] complex (**1**) bearing a hybrid, methylene-bridged κ^2-[*P*,*N*]-2-[(diphenylphosphino)methyl]pyridine ligand (PN). Electrochemical studies of **1** reveal a quasi-reversible two-electron reduction at –1.28 V vs $Fc^{+/0}$. This negative reduction potential corresponds to generation of the Rh^{I} complex **3**, a rather basic compound that, on the basis of chemical reactivity, can be concluded to be capable of deprotonation of the methylene C–H bonds of PN. Multiple products arise from this reactivity over a timescale of hours; these include two observable Rh^{III} hydride compounds with [η^5-Cp*] ligands but, noticeably, no compounds bearing [η^4-Cp*H] ligands. As the reduction of **1** results in the deprotonation of the acidic methylene C–H

bonds and further speciation, this system is not amenable to further studies of H_2 generation during catalysis. Taken together, this work suggests that avoidance of acidic moieties in ancillary/supporting ligands[28] can be implicated as a winning strategy for improving the stability of complexes intended for study of H^+/e^- management during reductive catalysis.

4.4 Experimental Details

4.4.1 General Considerations

All manipulations were carried out in dry N_2-filled gloveboxes (Vacuum Atmospheres Co., Hawthorne, CA) or under N_2 atmosphere using standard Schlenk techniques unless otherwise noted. All solvents were of commercial grade and dried over activated alumina using a PPT Glass Contour (Nashua, NH) solvent purification system prior to use, and were stored over molecular sieves. All chemicals were from major commercial suppliers and used as received after extensive drying. $[Cp^*RhCl_2]_2$ was prepared according to literature procedure.[29] The PN ligand was synthesized by the method of Hung-Low.[30] Deuterated NMR solvents were purchased from Cambridge Isotope Laboratories; CD_3CN was dried over molecular sieves and C_6D_6 was dried over sodium/benzophenone. ^1H, ^{13}C, and ^{31}P NMR spectra were collected on 400 or 500 MHz Bruker spectrometers and referenced to the residual protio-solvent signal[31] in the case of ^1H and ^{13}C. Heteronuclear NMR spectra were referenced to the appropriate external standard following the recommended scale based on ratios of absolute frequencies (Ξ).[32]

4.4.2 Synthesis

4.4.2.1 Synthesis of 2-[(Diphenylphosphino)methyl]pyridine

PN was synthesized according to a modified literature procedure.[30] A solution of n-butyllithium in tetrahydrofuran (2.03 mL, 2.65 mmol, 1 equiv.) was added to a “thawing” sample of 2-picoline in tetrahydrofuran (0.500 g, 5.4 mmol, 1 equiv.) that had been previously frozen at

in a cold well in an inert atmosphere glovebox with liquid nitrogen (–196 °C). Allowing the sample to melt upon addition of the n-butyllithium solution over 20 min resulted in a bright orange solution. This solution containing n-butyllithium and 2-picoline was then refrozen in the same manner, and subsequently a solution of chlorodiphenylphosphine in tetrahydrofuran (1.185 g, 5.37 mmol, 1 equiv.) was added. Allowing the mixture to warm to room temperature and stir for 2 h yielded a bright yellow solution. The solution was filtered, and volatiles removed *in vacuo* to yield a dark orange solid. Direct extraction with hexane (without use of an acid/base extraction step as previously called for in ref. 30) and removal of the volatiles *in vacuo* yielded a useful quantity of an air-sensitive white solid. (Yield: 0.385 g, 26%) Spectroscopic data for the isolated material agreed with those previously reported for PN.[33]

4.4.2.2 Synthesis of 1

To a suspension of $[Cp^*RhCl_2]_2$ in acetonitrile (0.110 g, 0.177 mmol, 1.0 equiv.) were added $AgPF_6$ (0.180 g, 0.712 mol, 2 equiv.) and PN (0.097 g, 0.0348 mmol, 2.05 equiv.) as acetonitrile solutions. The color of the reaction mixture rapidly changed from brick-red to orange, and a yellow precipitate formed. After 15 min, the suspension was filtered to remove the AgCl byproduct, and the volume of the filtrate was reduced to ca. 1 mL. Addition of diethyl ether (ca. 20 mL) caused precipitation of a yellow solid, which was collected by filtration (0.0456 g, 38%). Vapor diffusion of diethyl ether into a concentrated acetonitrile solution of the product yielded single-crystals of 1 suitable for X-ray diffraction studies. ^{1}H NMR (500 MHz, CD_3CN) δ 8.61 (d, *J* = 5.7 Hz, 1H), 8.01 (t, *J* = 7.81 Hz, 1H), 7.78 (ddd, *J* = 11.8, 8.3, 1.4 Hz, 2H), 7.72 – 7.67 (m, 1H), 7.67 – 7.64 (m, 3H), 7.64 – 7.59 (m, 2H), 7.58 – 7.52 (m, 2H), 7.45 (ddd, *J* = 8.6, 5.3, 2.2 Hz, 2H), 4.43 (dd, *J* = 17.4, 14.5 Hz, 1H), 4.14 (dd, *J* = 17.4, 10.7 Hz, 1H), 1.50 (d, *J* = 3.8 Hz, 15H) ppm. $^{13}C\{^1H\}$ NMR (126 MHz, CD_3CN) δ 154.84 (s), 141.01 (s), 135.87 (d, *J* = 10.8 Hz), 133.68 (d, *J* = 2.84

Hz), 132.85 (d, J = 3.0 Hz), 130.19 (t, J = 9.8 Hz), 126.62 (s), 125.52 (d, J = 10.9 Hz), 102.47 (d, J = 3.0 Hz), 102.42 (d, J = 2.84 Hz), 43.31 (d, J = 34.5 Hz), 9.37 (s), ppm. $^{31}P\{^{1}H\}$ NMR (162 MHz, C_6D_6) δ 51.57 (d, J = 140.3 Hz), –144.65 (sep, J = 706.2 Hz) ppm. 1 was found to be acutely air-sensitive and satisfactory elemental analysis could not be obtained. In lieu of elemental analysis, ^{1}H NMR was used to confirm diamagnetic spectroscopic purity.

4.4.2.3 Chemical Reduction of 1

A suspension of 1 in tetrahydrofuran (0.5 g, 0.717 mmol) was stirred over freshly prepared sodium-mercury amalgam (1% Na in Hg; 0.049 g Na^0, 1.78 mmol, 10 equiv.) and stirred for 48 h, during which time the yellow suspension became a dark blue solution. The mixture was filtered, and the volatiles removed *in vacuo*. Further extraction with hexanes and removal of solvent *in vacuo* yielded a dark blue solid suitable for NMR studies in C_6D_6.

4.4.3 X-ray crystallography

A full hemisphere of diffracted intensities (560 5-second frames with an ω scan width of 1.00°) was measured for a single-domain crystal of **1** using graphite-monochromated Mo Kα radiation (λ = 0.71073 Å) on a Bruker SMART APEX CCD Single Crystal Diffraction System. X-rays were provided by a fine-focus sealed X-ray tube operated at 50 kV and 35 mA. Preliminary lattice constants were determined with the Bruker program SMART.[34] The Bruker program SAINT[35] was used to produce integrated reflection intensities from the frames and determine final lattice constants using 8486 peak centers. The data set was corrected empirically for variable absorption effects using equivalent reflections. The Bruker software package SHELXTL was used to solve the structure using "direct methods" techniques. All stages of weighted full-matrix least-squares refinement were conducted using Fo_2 data with the v2014.11-0 software package.[36] Relevant crystallographic and refinement data are given in Table B1in Appendix B.

The final structural model for **1** incorporated anisotropic thermal parameters for all nonhydrogen atoms and isotropic thermal parameters for all hydrogen atoms. All non-methyl hydrogen atoms were fixed at idealized riding model sp^2- or sp^3-hybridized positions with C-H bond lengths of 0.94 or 0.97 Å. All five [Cp*] methyl groups were incorporated into the structural model as sp^3-hybridized rigid groups with C-H bond lengths of 0.98 Å that were allowed to rotate freely about their C-C bonds in least-squares refinement cycles. The isotropic thermal parameters of all hydrogen atoms were fixed at values 1.2 (nonmethyl) or 1.5 (methyl) times the equivalent isotropic thermal parameter of the carbon atom to which they are covalently bonded.

4.4.4 Electrochemistry

Electrochemical experiments were carried out in a nitrogen-filled glove box. 0.10 M tetra(n-butylammonium)hexafluorophosphate (Sigma-Aldrich; electrochemical grade) in acetonitrile served as the supporting electrolyte. Measurements were made with a Gamry Reference 600 Plus Potentiostat/Galvanostat using a standard three-electrode configuration. The working electrode was the basal plane of highly oriented pyrolytic graphite (HOPG) (GraphiteStore.com, Buffalo Grove, IL.; surface area: 0.09 cm^2), the counter electrode was a platinum wire (Kurt J. Lesker, Jefferson Hills, PA; 99.99%, 0.5 mm diameter), and a silver wire immersed in electrolyte served as a pseudo-reference electrode (CH Instruments). The reference was separated from the working solution by a Vycor frit (Bioanalytical Systems, Inc.). Ferrocene (Sigma Aldrich; twice-sublimed) was added to the electrolyte solution at the conclusion of each experiment (~1 mM); the midpoint potential of the ferrocenium/ferrocene couple (denoted as $Fc^{+/0}$) served as an external standard for comparison of the recorded potentials. Concentrations of analyte for cyclic voltammetry were typically 1 mM.

4.5 Acknowledgements

The authors thank Dr. Justin Douglas and Sarah Neuenswander for assistance with NMR spectroscopy and Professor Kristin Bowman-James for helpful discussions. Synthesis and characterization of 1 was supported by the US National Science Foundation through the NSF REU Program in Chemistry at the University of Kansas (CHE-1560279). Reactivity studies were supported by the US National Science Foundation through award OIA-1833087. Support for NMR instrumentation was provided by NIH Shared Instrumentation Grants S10OD016360 and S10RR024664 and by the NSF MRI grant CHE-1625923.

This article is dedicated to Susan Teague, Bev Johnson, and Jan Akers in honor of their many years of distinguished service to the Department of Chemistry at the University of Kansas.

4.6 References

[1] Lever, A. B. P., Electrochemical parametrization of metal complex redox potentials, using the ruthenium(III)/ruthenium(II) couple to generate a ligand electrochemical series. *Inorg. Chem.* **1990,** *29*, 1271-1285.

[2] (a) Rakowski Dubois, M.; Dubois, D. L., Development of Molecular Electrocatalysts for CO_2 Reduction and H_2 Production/Oxidation. *Acc. Chem. Res.* **2009,** *42*, 1974-1982. b) Appel, A. M.; Helm, M. L., Determining the Overpotential for a Molecular Electrocatalyst. *ACS Catalysis* **2014,** *4*, 630-633.

[3] (a) Khusnutdinova, J. R.; Milstein, D., Metal–Ligand Cooperation. *Angew. Chem. Int. Ed.* **2015,** *54*, 12236-12273. (b) Kaim, W.; Schwederski, B., Non-innocent ligands in bioinorganic chemistry—An overview. *Coord. Chem. Rev.* **2010,** *254*, 1580-1588.

[4] (a) Kölle, U.; Grätzel, M., Metallorganische Rhodium(III)-Komplexe als Homogenkatalysatoren für die Photoreduktion von Protonen zu Wasserstoff an kolloidalem TiO_2. *Angew. Chem.* **1987,** *99*, 572-574. b) Kölle, U.; Kang, B.-S.; Infelta, P.; Comte, P.; Grätzel, M., Elektrochemische und pulsradiolytische Reduktion von (Pentamethylcyclopentadienyl)(polypyridyl)rhodium-Komplexen. *Chem. Ber.* **1989,** *122*, 1869-1880.

[5] (a) Ruppert, R.; Herrmann, S.; Steckhan, E., Efficient indirect electrochemical in-situ regeneration of nadh:electrochemically driven enzymatic reduction of pyruvate catalyzed by D-LDH. *Tetrahedron Lett.* **1987,** *28*, 6583-6586. (b) Ruppert, R.; Herrmann, S.; Steckhan, E., Very efficient reduction of $NAD(P)^+$ with formate catalysed by cationic rhodium complexes. *J. Chem. Soc., Chem. Commun.* **1988**, 1150-1151. (c) Steckhan, E.; Herrmann, S.; Ruppert, R.; Dietz, E.; Frede, M.; Spika, E., Analytical study of a series of substituted (2,2'-bipyridyl)(pentamethylcyclopentadienyl)rhodium and -iridium complexes with regard to their effectiveness as redox catalysts for the indirect electrochemical and chemical reduction of $NAD(P)^+$. *Organometallics* **1991,** *10*, 1568-1577. (d) Lo, H. C.; Leiva, C.; Buriez, O.; Kerr, J. B.; Olmstead, M. M.; Fish, R. H., Bioorganometallic Chemistry. 13. Regioselective

Reduction of NAD^+ Models, 1-Benzylnicotinamde Triflate and β-Nicotinamide Ribose-5'-methyl Phosphate, with in Situ Generated $[Cp^*Rh(Bpy)H]^+$: Structure−Activity Relationships, Kinetics, and Mechanistic Aspects in the Formation of the 1,4-NADH Derivatives. *Inorg. Chem.* **2001,** *40*, 6705-6716.

[6] Quintana, L. M. A.; Johnson, S. I.; Corona, S. L.; Villatoro, W.; Goddard, W. A.; Takase, M. K.; VanderVelde, D. G.; Winkler, J. R.; Gray, H. B.; Blakemore, J. D., Proton–hydride tautomerism in hydrogen evolution catalysis. *PNAS* **2016,** *113*, 6409-6414.

[7] Pitman, C. L.; Finster, O. N. L.; Miller, A. J. M., Cyclopentadiene-mediated hydride transfer from rhodium complexes. *Chem. Commun.* **2016,** *52*, 9105-9108.

[8] Johnson, S. I.; Gray, H. B.; Blakemore, J. D.; Goddard, W. A., Role of Ligand Protonation in Dihydrogen Evolution from a Pentamethylcyclopentadienyl Rhodium Catalyst. *Inorg. Chem.* **2017,** *56*, 11375-11386.

[9] Todorova, T. K.; Huan, T. N.; Wang, X.; Agarwala, H.; Fontecave, M., Controlling Hydrogen Evolution during Photoreduction of CO_2 to Formic Acid Using $[Rh(R\text{-}bpy)(Cp^*)Cl]^+$ Catalysts: A Structure–Activity Study. *Inorg. Chem.* **2019,** *58*, 6893-6903.

[10] Boyd, E. A.; Lionetti, D.; Henke, W. C.; Day, V. W.; Blakemore, J. D., Preparation, Characterization, and Electrochemical Activation of a Model [Cp*Rh] Hydride. *Inorg. Chem.* **2019,** *58*, 3606-3615.

[11] Peng, Y.; Ramos-Garcés, M. V.; Lionetti, D.; Blakemore, J. D., Structural and Electrochemical Consequences of [Cp*] Ligand Protonation. *Inorg. Chem.* **2017,** *56*, 10824-10831.

[12] Henke, W. C.; Lionetti, D.; Moore, W. N. G.; Hopkins, J. A.; Day, V. W.; Blakemore, J. D., Ligand Substituents Govern the Efficiency and Mechanistic Path of Hydrogen Production with [Cp*Rh] Catalysts. *ChemSusChem* **2017,** *10*, 4589-4598.

[13] (a) Klingert, B.; Werner, H., Basische Metalle, XLII. Die Metall-Basizität der Komplexe $C_5Me_5Rh(PMe_3)_2$, $C_5Me_5Rh(C_2H_4PMe_3$ und $C_5Me_5Rh(C_2H_4)P_2Me_4$: Neue Pentamethyl-

cyclopentadienylrhodium(I)- und -rhodium(III)-Verbindungen. *Chem. Ber.* **1983,** *116*, 1450-1462. (b) Faller, J. W.; D'Alliessi, D. G., Tunable Stereoselective Hydrosilylation of PhC∶CH Catalyzed by Cp*Rh Complexes. *Organometallics* **2002,** *21*, 1743-1746. (c) Faraone, F.; Bruno, G.; Schiavo, S. L.; Tresoldi, G.; Bombieri, G., η^5-Cyclopentadienylrhodium(I) complexes containing diphosphines and their reactions with the electrophiles H^+ and Me^+. Crystal and molecular structure of [Rh(η-C_5H_5)(CO)($Ph_2PCH_2PPh_2$)], a complex with a unidentate bis(diphenylphosphino)methane ligand. *J. Chem. Soc., Dalton Trans.* **1983**, 433-438.

[14] (a) Jones, W. D.; Kuykendall, V. L.; Selmeczy, A. D., Ring migration reactions of (C_5Me_5)Rh(PMe_3)H_2. Evidence for η^3 slippage and metal-to-ring hydride migration. *Organometallics* **1991,** *10*, 1577-1586. (b) Edelbach, B. L.; Jones, W. D., Mechanism of Carbon−Fluorine Bond Activation by (C_5Me_5)Rh(PMe_3)H_2. *J. Am. Chem. Soc.* **1997,** *119*, 7734-7742.

[15] Hopkins, J. A.; Lionetti, D.; Day, V. W.; Blakemore, J. D., Chemical and Electrochemical Properties of [Cp*Rh] Complexes Supported by a Hybrid Phosphine-Imine Ligand. *Organometallics* **2019,** *38*, 1300-1310.

[16] (a) Carlson, B.; Eichinger, B. E.; Kaminsky, W.; Phelan, G. D., Complexes of Osmium with the 2-[(Diphenylphosphanyl)-methyl]-pyridine Ligand. *J. Phys. Chem. C* **2008,** *112*, 7858-7865. (b) Wei, S.; Pedroni, J.; Meißner, A.; Lumbroso, A.; Drexler, H.-J.; Heller, D.; Breit, B., Development of an Improved Rhodium Catalyst for Z-Selective Anti-Markovnikov Addition of Carboxylic Acids to Terminal Alkynes. *Chem. Eur. J.* **2013,** *19*, 12067-12076. (c) de la Encarnación, E.; Pons, J.; Yáñez, R.; Ros, J., Diphenylphosphinopyridine (PPh_2Py) versus 2-(2-diphenylphosphinomethyl)pyridine (PPh_2CH_2Py) in the coordination to ruthenium centres: Study of the reaction of PPh_2Py containing formato-bridged dinuclear Ru(I) complexes and PPh_2CH_2Py containing mononuclear formato Ru(II) complexes with dithioles. *Inorg. Chim. Acta* **2006,** *359*, 745-752. (d) Essoun, E.; Wang, R.; Aquino, M. A. S., Disassembly of diruthenium(II,III) tetraacetate with P–N donor ligands. *Inorg. Chim. Acta*

2017, *454*, 97-106. (e) Murso, A.; Stalke, D., Electronic response of a (P,N)-based ligand on metal coordination. *Dalton Trans.* **2004**, 2563-2569. (f) Wei, D.; Bruneau-Voisine, A.; Chauvin, T.; Dorcet, V.; Roisnel, T.; Valyaev, D. A.; Lugan, N.; Sortais, J.-B., Hydrogenation of Carbonyl Derivatives Catalysed by Manganese Complexes Bearing Bidentate Pyridinyl-Phosphine Ligands. *Adv. Synth. Catal.* **2018,** *360*, 676-681. (g) Aakermark, B.; Krakenberger, B.; Hansson, S.; Vitagliano, A., Ligand effects and nucleophilic addition to (η^3-allyl)palladium complexes. A carbon-13 NMR study. *Organometallics* **1987,** *6*, 620-628. (h) Objartel, I.; Ott, H.; Stalke, D., Low-Temperature NMR and Crystal Structure Analyses of a Hemilabile Tin Complex. *Z. Anorg. Allg. Chem.* **2008,** *634*, 2373-2379. (i) Aguirre, P. A.; Lagos, C. A.; Moya, S. A.; Zúñiga, C.; Vera-Oyarce, C.; Sola, E.; Peris, G.; Bayón, J. C., Methoxycarbonylation of olefins catalyzed by palladium complexes bearing P,N-donor ligands. *Dalton Trans* **2007**, 5419-5426. (j) Kermagoret, A.; Braunstein, P., Mono- and Dinuclear Nickel Complexes with Phosphino-, Phosphinito-, and Phosphonitopyridine Ligands: Synthesis, Structures, and Catalytic Oligomerization of Ethylene. *Organometallics* **2008,** *27*, 88-99. (k) Dubs, C.; Yamamoto, T.; Inagaki, A.; Akita, M., A new method for the conversion of allyl alcohol into π-allyl species promoted by nucleophilic interaction with a CO ligand. *Chem. Commun.* **2006**, 1962-1964. (l) Flapper, J.; Kooijman, H.; Lutz, M.; Spek, A. L.; van Leeuwen, P. W. N. M.; Elsevier, C. J.; Kamer, P. C. J., Nickel and Palladium Complexes of Pyridine−Phosphine Ligands as Ethene Oligomerization Catalysts. *Organometallics* **2009,** *28*, 1180-1192. (m) Sharp, P. R.; Hoard, D. W.; Barnes, C. L., Rhodium(II) complex with a highly reactive rhodium-rhodium bond: insertion of dioxygen and nitrosobenzene. *J. Am. Chem. Soc.* **1990,** *112*, 2024-2026. (n) Hung-Low, F.; Klausmeyer, K. K., Silver coordination complexes of 2-(diphenylphosphinomethyl)pyridine and their bipyridine derivatives. *Inorg. Chim. Acta* **2008,** *361*, 1298-1310. (o) Mague, J. T.; Krinsky, J. L., Synthetic and Structural Studies of the Coordination Behavior of 2-Pyridylbis(diphenylphosphino)methane. *Inorg. Chem.* **2001,** *40*, 1962-1971. (p) Padron, D. A.; Klausmeyer, K. K., Syntheses and coordination studies of 2-

(diphenylphosphinomethyl)pyridine and its oxide towards mercury(II). *Polyhedron* **2012,** *34*, 215-220. (q) Ma, A.-F.; Seo, H.-J.; Jin, S.-H.; Ung, C.; Yoon, M.; Ho, H.; Kwon Kang, S.; Kim, Y.-I., Novel Cationic 2-Phenylpyridine-based Iridium (III) Complexes Bearing an Ancillary Phosphine Ligand: Synthesis, Photophysics and Crystal Structure. *Bull Korean Chem Soc* **2009,** *30*.

[17] (a) Wei, S.; Pedroni, J.; Meißner, A.; Lumbroso, A.; Drexler, H.-J.; Heller, D.; Breit, B., Development of an Improved Rhodium Catalyst for Z-Selective Anti-Markovnikov Addition of Carboxylic Acids to Terminal Alkynes. *Chem. Eur. J.* **2013,** *19*, 12067-12076. (b) Wei, S.; Moller, S.; Heller, D.; Drexler, H.-J., (η^2,η^2-Cycloocta-1,5-diene)[2-(diphenylphosphanylmethyl)pyridine-κ^2-N,P]rhodium(I) tetrafluoridoborate 1,2-dichloroethane monosolvate. *IUCrData* **2016,** *1*, x161318. (c) McNair, R. J.; Pignolet, L. H., Heterobimetallic complexes of rhodium with platinum, silver, and gold containing bridging 2-[bis(diphenylphosphino)methyl]pyridine (PNP) ligands. *Inorg. Chem.* **1986,** *25*, 4717-4723.

[18] Groom, C. R.; Bruno, I. J.; Lightfoot, M. P.; Ward, S. C., *Acta Cryst. Sec.* B **2016,** 72, 171-179.

[19] Brunner, H.; Kollnberger, A.; Mehmood, A.; Tsuno, T.; Zabel, M., *CSD Communication* **2009**, CCDC 233218, DOI: 10.5517/cc7tp5w

[20] Nutton, A.; Bailey, P. M.; Maitlis, P. M., Pentamethylcyclopentadienyl-rhodium and -iridium complexes. Part 29. Syntheses and X-ray structure determinations of $[\{Rh(C_5Me_5)\}_2(OH)_3]OH\cdot 11H_2O$ and $[\{lr(C_5Me_5)\}_2(OH)_3]O_2CMe\cdot 14H_2O$ and related complexes. *J. Chem. Soc., Dalton Trans.* **1981**, 1997-2002.

[21] Saveant, J.-M., *Elements of Molecular and Biomolecular Electrochemistry*. Wiley: Hoboken, NJ, 2006.

[22] Tabner, B. J.; Yandle, J. R., A correlation of half-wave reduction potentials with theoretical calculations for some nitrogen-containing heteromolecules in dimethylformamide. *J. Chem. Soc. A: Inorg. Phys. & Theor.* **1968**, 381-388.

[23] Lionetti, D.; Day, V. W.; Lassalle-Kaiser, B.; Blakemore, J. D., Multiple binding modes of an unconjugated bis(pyridine) ligand stabilize low-valent [Cp*Rh] complexes. *Chem. Commun.* **2018,** *54*, 1694-1697.

[24] Connelly, N. G.; Geiger, W. E., Chemical Redox Agents for Organometallic Chemistry. *Chem. Rev.* **1996,** *96*, 877-910.

[25] Blakemore, J. D.; Hernandez, E. S.; Sattler, W.; Hunter, B. M.; Henling, L. M.; Brunschwig, B. S.; Gray, H. B., Pentamethylcyclopentadienyl rhodium complexes. *Polyhedron* **2014,** *84*, 14-18.

[26] (a) Hu, Y.; Li, L.; Shaw, A. P.; Norton, J. R.; Sattler, W.; Rong, Y., Synthesis, Electrochemistry, and Reactivity of New Iridium(III) and Rhodium(III) Hydrides. *Organometallics* **2012,** *31*, 5058-5064. (b) Hu, Y.; Norton, J. R., Kinetics and Thermodynamics of $H^-/H^\bullet/H^+$ Transfer from a Rhodium(III) Hydride. *J. Am. Chem. Soc.* **2014,** *136*, 5938-5948.

[27] Muckerman, J. T.; Skone, J. H.; Ning, M.; Wasada-Tsutsui, Y., Toward the accurate calculation of pKa values in water and acetonitrile. *Biochim. Biophys. Acta Bioenerg.* **2013,** *1827*, 882-891.

[28] Lionetti, D.; Day, V. W.; Blakemore, J. D., Structural and chemical properties of half-sandwich rhodium complexes supported by the bis(2-pyridyl)methane ligand. *Dalton Trans.* **2019,** *48*, 12396-12406.

[29] (a) White, C.; Yates, A.; Maitlis, P. M., (η5-Pentamethylcyclopentadienyl) Rhodium and -Iridium Compounds. *Inorg. Synth.* **1992,** *29*, 228-234 (b) Mantell, M. A.; Kampf, J. W.; Sanford, M., Improved Synthesis of $[Cp^RRhCl_2]_2$ Complexes. *Organometallics* **2018,** *37*, 3240-3242.

[30] Hung-Low, F.; Klausmeyer, K. K., Silver coordination complexes of 2-(diphenylphosphinomethyl)pyridine and their bipyridine derivatives. *Inorg. Chim. Acta* **2008,** *361*, 1298-1310.

[31] Fulmer, G. R.; Miller, A. J. M.; Sherden, N. H.; Gottlieb, H. E.; Nudelman, A.; Stoltz, B. M.; Bercaw, J. E.; Goldberg, K. I., NMR Chemical Shifts of Trace Impurities: Common Laboratory Solvents,

Organics, and Gases in Deuterated Solvents Relevant to the Organometallic Chemist. *Organometallics* **2010,** *29*, 2176-2179.

[32] (a) Harris, R. K.; Becker, E. D.; Menezes, S. M. C. d.; Goodfellow, R.; Granger, P., NMR nomenclature. Nuclear spin properties and conventions for chemical shifts (IUPAC Recommendations 2001). *Pure Appl. Chem.* **2001,** *73*, 1795-1818. (b) Harris, R. K.; Becker, E. D.; Menezes, S. M. C. d.; Granger, P.; Hoffman, R. E.; Zilm, K. W., Further conventions for NMR shielding and chemical shifts (IUPAC Recommendations 2008). *Pure Appl. Chem.* **2008,** *80*, 59-84.

[33] Aakermark, B.; Krakenberger, B.; Hansson, S.; Vitagliano, A., Ligand effects and nucleophilic addition to (η^3-allyl)palladium complexes. A carbon-13 NMR study. *Organometallics* **1987,** *6*, 620-628.

[34] Data Collection: SMART Software in APEX2 v2014.11-0 Suite. Bruker-AXS, 5465 E. Cheryl Parkway, Madison, WI 53711-5373 USA.

[35] Data Reduction: SAINT Software in APEX2 v2014.11-0 Suite. Bruker-AXS, 5465 E. Cheryl Parkway, Madison, WI 53711-5373 USA.

[36] Refinement: SHELXTL Software in APEX2 v2014.11-0 Suite. Bruker-AXS, 5465 E. Cheryl Parkway, Madison, WI 53711-5373 USA.

Chapter 5

Electrochemical Kinetic Study of [Cp*Rh] Complexes Supported by Bis(2-pyridyl)methane Ligands

This chapter is adapted from a published manuscript:

Hopkins Leseberg, J.A.; Lionetti D.; Day, V.W.; Blakemore, J.D. Electrochemical Kinetic Study of [Cp*Rh] Complexes Supported by Bis(2-pyridyl)methane Ligands. *Organometallics* **2021**, *40*, 266-277.

5.1 Introduction

Electrochemical studies offer a promising way of studying the chemistry of many transformations involving redox reactions or redox catalysis. The active forms of catalysts are often formed upon reduction by two or more electrons, generating transient intermediates near the electrode that have virtually zero bulk concentration.[1,2] As conventional spectroscopic studies of molecular electrocatalysis are difficult,[3] progress in many fields depends upon understanding electron transfer-induced reactivity with electrochemical methods.[4]

Indeed, as a cascading series of reactions are often possible for compounds that undergo multiple reductions, information on individual elementary reactions steps can be obscured by the multiple pathways often accessible at a given potential. A related further complication arises when follow-up chemical reactivity results in potential inversion of sequential reductions (as in ECE-type reactions).[5,6] Scheme 5.1 shows a series of reactions in a model catalytic cycle to illustrate these points. In this scheme, a model pre-catalyst, $[Cat_A]^{2+}$ is reduced by $1e^-$ to $[Cat_B]^+$, and $[Cat_B]^+$ then undergoes a subsequent $1e^-$ reduction to generate an electron-rich complex $[Cat_C]^0$. The low-valent $[Cat_C]^0$ species is of particular interest to us, since many redox reactions of contemporary relevance (H^+ reduction to H_2, CO_2 reduction to CO or other products) involve transfer of at least $2e^-$. Due to its nascent electron-rich nature, $[Cat_C]^0$ in our scheme undergoes a chemical reaction to generate a more stable form, $[Cat_D]^0$. Compounds like $[Cat_D]^0$ are notable, in that their formation after loading with multiple reducing equivalents is directly relevant to multielectron catalysis under reducing conditions.

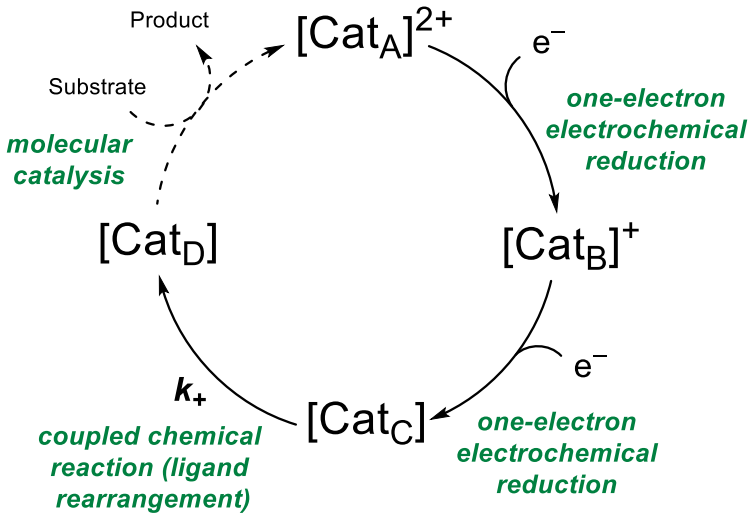

Scheme 5.1. General scheme for electrocatalysis

To serve as viable redox catalysts, metal complexes must bear ligands capable of supporting multiple metal/complex oxidation states. Non-innocent ligands that directly participate in redox chemistry are particularly noted for their ability to augment metal-based electron transfer and the resulting tendency to promote novel reactivity modes.[7] Ligands based upon the workhorse 2,2′-bipyridyl[8] (bpy) and pyridine-diimine[9] (PDI) cores are two such platforms, in which low-lying π* molecular orbitals help stabilize reduced metal complexes.[10] PDI-based ligands can undergo multiple reduction events, obviating the need for metal-centered ET processes.[11] Similarly, the conjugated bpy ligand can accept electron density through π-backbonding[12,13] as well as directly accept electrons to generate reduced forms.[14] Such redox-active ligands and their compounds are common in molecular catalysis precisely because their properties help stabilize the various charge states of intermediates. With stability supported across multiple oxidation states, catalytic intermediates become accessible and redox cycles can be constructed, even for complex multielectron reactions.

We have recently been exploring the synthetic chemistry of the dimethyl-2,2′-dipyridylmethane (Me_2dpma) ligand,[15] as we have found that Me_2dpma represents a notable

counterpoint to the more common and well-studied bpy. In particular, disruption of the inter-ring conjugation found in bpy with Me_2dpma results in π* orbitals that are less accessible for back-bonding or electron transfer as compared to those of bpy.[16] However, we have found that Me_2dpma is nonetheless capable of stabilizing reduced complexes. In particular, upon reduction of a model [Cp*Rh] complex (Cp* = η^5-pentamethylcyclopentadienyl) bearing κ^2-Me_2dpma to the formally Rh(I) oxidation state, one pyridyl ring of Me_2dpma rotates (flips) and facially coordinates to the Rh center in an η^2 fashion.[15] As demonstrated by crystallographic studies and complementary X-ray absorption spectroscopy, this rearrangement results in dearomatization of the flipped pyridyl ring and stabilization of the reduced metal center to a significant degree.[17]

[Cp*Rh(Me_2dpma)$NCCH_3$]$(PF_6)_2$ (**1**$^{\mathbf{LMe2}}$) is amenable to electrochemical studies of this redox chemistry; avoidance of halide(s) precludes formation of $[Cp^*RhCl]_2$ following $1e^-$ reduction and enables accurate electrochemical studies.[15] Cyclic voltammograms (CVs) collected with this complex reflect the chemical reactivity described above. CVs reveal two discrete $1e^-$ reductions; the first $1e^-$ reduction is electrochemically quasi-reversible and chemically reversible, occurs at –0.85 V vs ferrocenium/ferrocene (denoted hereafter as $Fc^{+/0}$), and leads to generation of an isolable Rh(II) complex.[15] A second $1e^-$ reduction leads to generation of the formally Rh^I form of the compound ($E_{p,c}$ = –1.50 V vs. $Fc^{+/0}$). However, the appearance of the CVs confirm involvement of the reduction-induced chemical reaction in which Me_2dpma flips to stabilize the low-valent complex via η^2-coordination of one pyridine ring; the process appears electrochemically irreversible at lower scan rates but shows improved reversibility at faster scan rates. Thus, an Electrochemical-Chemical (EC) process is taking place, as defined by Nicholson and Shain[18] and studied extensively by Savéant.[19]

The well-defined chemistry and electrochemistry of $\mathbf{1}^{\mathbf{LMe2}}$ make it an attractive model for studying metal complexes that undergo EC processes. However, our prior work with this system bearing Me_2dpma was primarily chemical in nature. As our work has also been restricted solely to Me_2dpma (and its unsubstituted analogue dpma[20]), the role of the ligand substituents in influencing the noted reactivity and kinetics remain unclear. However, such information would clarify the electrochemical reaction sequence and provide new insight into a ligand-promoted charge stabilization process like those often needed in molecular catalysis. The coordination chemistry of dpma-type ligands has been limited to only a few examples on Cu,[21] Hg,[22] Pt,[23] Pd,[24] and Rh.[15,20] Notably, Schley and co-workers recently reported use of aryl-substituted dpma ligands in iridium catalysis, highlighting the usefulness and powerful tunability of these platforms.[25]

Here, we report the synthesis and characterization of a family of novel R_2dpma ligands (**LR_2**, Chart 5.1) featuring substituents on the methylene "bridge" position and their [Cp*Rh^{III}] complexes ($\mathbf{1}^{\mathbf{LR2}}$, Scheme 5.2). We find the novel ligands **LBn_2**, **LMePyr**, and **$LPyr_2$** are readily synthesized by methods designed to tolerate the benzylic C–H bonds present in the new derivatives.[27] Electrochemical studies indicate that, for all these complexes, reduction from Rh(II) to Rh(I) results in ligand reorientation and binding of one pyridine ring in an η^2 fashion. In line with this interpretation, reduction of $\mathbf{1}^{\mathbf{LBn2}}$ with Na(Hg) results in ligand rearrangement as shown via isolation and full characterization of the corresponding Rh(I) complex $\mathbf{4}^{\mathbf{LBn2}}$, confirming that the reactivity upon reduction tolerates bulkier, aromatic substituents on the dpma core and that the Rh–arene interactions are restricted to the pyridine motifs on the dpma ligand. However, digital simulations of the experimental cyclic voltammograms with DigiElch[26] reveal that the bulkier ligands undergo kinetically slower ligand reorientation, showing that ligand derivatization impacts the kinetics of reduction-induced dpma reorganization. Taken together, our findings show that

disubstituted dpma ligands can stabilize multiple oxidation states and could thus be useful for developing new redox catalysts.

5.2 Results and Discussion

Synthesis and Characterization of Ligands and [Cp*Rh] Complexes. The new substituted dipyridylmethane (dpma) ligands were synthesized based on modified literature procedures.[27,28] In prior work, treatment of dpma with sequential additions of nBuLi and MeI resulted in double methylation of the bridging methylene carbon of dpma. Here, we expanded upon this effective strategy by substituting other alkyl halides in place of methyl iodide in order to install sterically bulkier groups (see Chart 5.1) at the central methylene carbon. In order to prepare **LBn$_2$**, the starting material bis(2-pyridyl)methane[29] was reacted with sequential additions of nBuLi and benzyl bromide. On the other hand, to prepare **LPyr$_2$**, additions of tBuOK and 1-(chloromethyl)pyrene[30] were utilized; use of tBuOK in particular enabled preparation of **LPyr$_2$** whose immediate precursor features a pyrene ring that is more susceptible to undesired reactivity with the more nucleophilic nBuLi. The mixed derivative, **LMePyr**, was prepared analogously from 2,2′-(ethane-1,1-diyl)dipyridine[23] by treatment with single additions of tBuOK and 1-(chloromethyl)pyrene. This synthetic approach highlights that dpma ligands can be prepared via modular synthetic methods; in the case of our substituted dpma ligands, varying steric bulk can be installed above and below the plane containing the pyridyl rings.

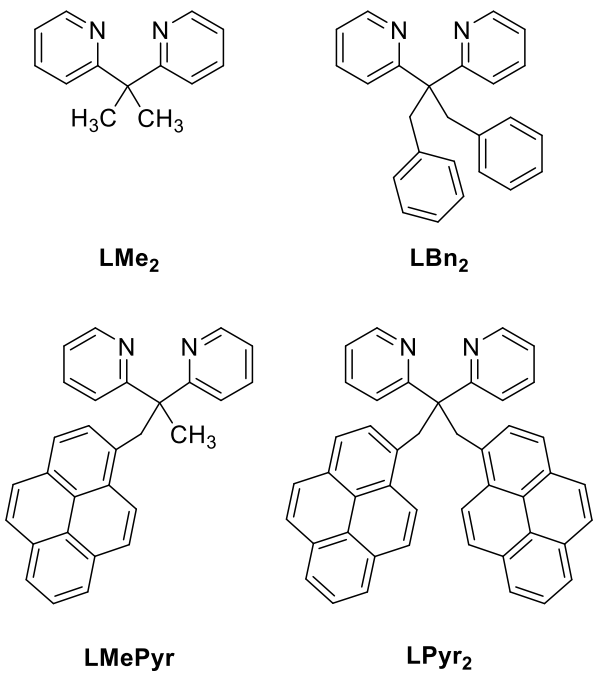

Chart 5.1. Substituted LR_2dpma ligands

The dimeric $[Cp^*RhCl_2]_2$ complex[31,32] is a generally useful precursor for the synthesis of [Cp*Rh] complexes bearing chelating bidentate ligands.[33] The family of $\mathbf{A^{LR2}}$ complexes (Scheme 5.2) were prepared by addition of 1.0 equivalent of $AgPF_6$ to 0.5 equivalents of $[Cp^*RhCl_2]_2$ followed by the addition of 1.05 equivalents of the desired $\mathbf{LR_2}$ ligand to yield rhodium(III) complexes as orange solids. The $\mathbf{A^{LR2}}$ compounds were very stable in our hands, and thus our initial characterization efforts focused on these derivatives. However, treatment of the $\mathbf{A^{LR2}}$ complexes with 1.0 equivalent of $AgPF_6$ in CH_3CN results in rapid formation of the corresponding yellow solvento complexes $\mathbf{1^{LR2}}$; while isolation of these species is challenging due to the lability of the bound solvent molecule, these solvento complexes lack a halide ligand, and were therefore utilized in the electrochemical studies to avoid electrochemically-induced generation of $[Cp^*RhCl]_2$ (*vide infra*).

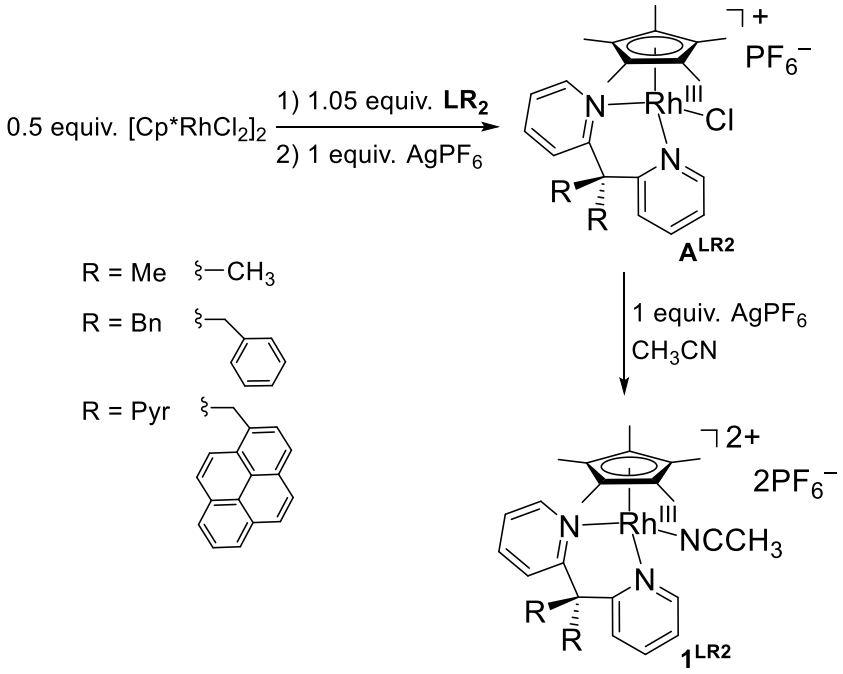

Scheme 5.2. Synthesis of series of $\mathbf{1}^{\mathbf{LR2}}$ Rh complexes.

Following isolation of the $\mathbf{A}^{\mathbf{LR2}}$ complexes, proton nuclear magnetic resonance (^{1}H NMR) was used to confirm chelation of the new disubstituted dpma ligands to rhodium. In the cases of all the new complexes, a strong singlet appears at ca. 1.60 ppm; this resonance is attributable to the fifteen equivalent protons associated with the freely rotating [Cp*] ligand and integrates to 15H with respect to the two *ortho*-pyridyl protons of the associated κ^2-$\mathbf{LR_2}$ ligand (see Appendix C, Figures C7, C12, C19). Additionally, the ^{31}P{^{1}H} NMR spectra of the complexes **A** reveal a septet attributable to the presence of the hexafluorophosphate counteranion ($^1J_{P,F} \approx 706$ Hz). The ^{1}H NMR spectrum for $\mathbf{A}^{\mathbf{LBn2}}$ reveals two unique singlets integrating to 2H each (3.85 and 3.67 ppm) corresponding to the chemically inequivalent methylene protons associated with each of the freely rotating benzyl substituents. These signals contrast with the single ^{1}H NMR resonance at 4.52 ppm (integrating to 4H) associated with the four equivalent methylene protons of the free $\mathbf{LBn_2}$ ligand.

On the other hand, the ^{1}H NMR spectrum of $\mathbf{A}^{\mathbf{LPyr2}}$ reveals a more complex case in which three unique resonances associated with the methylene protons of the methylpyrenyl substituents are

observed. One singlet at 4.66 ppm integrates to 2H, corresponding to one set of methylene protons associated with the methylpyrenyl substituent pointing away from [Cp*] which can freely rotate. Two further doublets are present at 6.28 and 6.59 ppm integrating to 1H each, corresponding to the two methylene protons on the methylpyrenyl substituent which points toward [Cp*]. These protons are chemically inequivalent, presumably due to hindered rotation of the upper methylpyrenyl substituent which would encounter steric clash if fully rotated upward, as can be estimated based on the solid-state structure of $\mathbf{A}^{\mathbf{LPyr2}}$ (vide infra). These methylene protons exhibit the expected geminal coupling to each other ($^2J_{H,H} \approx 8.1$ Hz) resulting in the measured doublet resonances.

The ^{1}H NMR spectrum for the non-symmetrically substituted free **LMePyr** ligand reveals a singlet integrating to 2H at 4.56 ppm that corresponds to the two equivalent methylene protons of the single methylpyrenyl substituent; another singlet at 1.63 ppm integrates to 3H and corresponds to the methyl substituent. In the spectrum of $\mathbf{A}^{\mathbf{LMePyr}}$, this singlet corresponding to the methyl substituent shifts to 1.73 ppm. The methylene protons for the methylpyrenyl substituent, however, are detected in this case as two broad singlets at 5.02 and 4.14 ppm; this is again indicative of hindered rotation of the methylpyrenyl substituent when **LMePyr** is bound to [Cp*Rh]. This stereochemical assignment, which predicts that the methylpyrenyl substituent is facing toward the [Cp*] ligand, is confirmed by the X-ray diffraction studies described below; it is also supported by detectable through-space coupling that occurs between the protons of the pyrenyl group and [Cp*] methyl groups in NOESY NMR of $\mathbf{A}^{\mathbf{LMePyr}}$ (see Appendix C, Figure C17). Taken together, the NMR data thus confirm the presence of the bidentate dpma ligands on the [Cp*Rh] for the new complexes.

Vapor diffusion of diethyl ether (Et_2O) into an acetonitrile (CH_3CN) solution containing $\mathbf{A^{LBn2}}$ or CH_2Cl_2 solutions of $\mathbf{A^{LMePyr}}$ and $\mathbf{A^{LPyr2}}$ afforded orange crystals suitable for X-ray diffraction (XRD) studies. The resulting solid-state structures (see Figure 5.1) reveal the geometries of the formally Rh(III) metal centers in all three complexes to be *pseudo*-octahedral. The first coordination sphere around each Rh center contains the appropriate κ^2-[*N*,*N*]-disubstituted dpma ligand, a single chloride anion, and the [η^5-Cp*] ligand. The bond metrics (Table 5.1) for the new structures reported here compare well with those for the previously investigated derivative $\mathbf{A^{Me2}}$, suggesting that the more sterically demanding ligands developed here do not markedly perturb the properties of the Rh(III) center. The N1-Rh-N2 chelate angles (Table 5.2) do not vary significantly, either, suggesting there only a subtle influence from the presence of the two more sterically demanding aromatic substituents in these cases. And, as mentioned above, the structure of $\mathbf{A^{LMePyr}}$ confirms that the methylpyrenyl substituent is oriented toward [Cp*] as predicted on the basis of NMR data (*vide supra*).

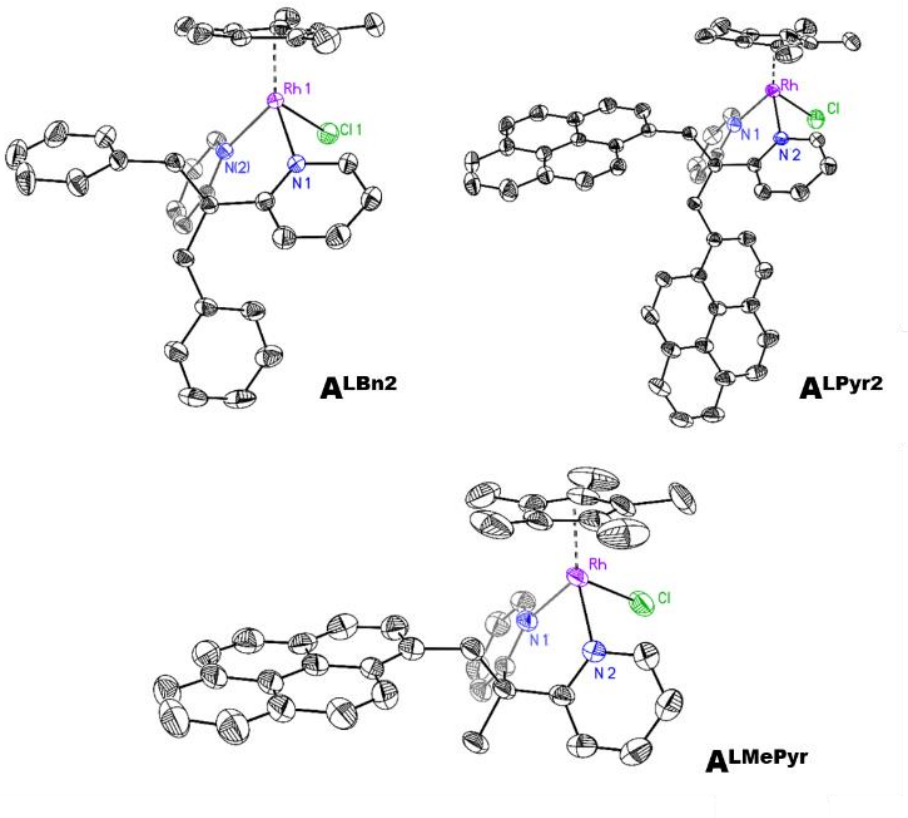

Figure 5.1. Solid-state structure of $\mathbf{A^{LBn2}}$, $\mathbf{A^{LPyr2}}$, and $\mathbf{A^{LMePyr}}$ (XRD). Hexafluorophosphate counteranion and hydrogen atoms are omitted for clarity. Displacement ellipsoids are shown at the 50% probability level.

The angle between the chelation plane of the bidentate ligand (a plane defined by the positions of the N1, N2, and Rh atoms) and the plane defined by the [η^5-Cp*] ligand is similar across the series (66.27–66.77°), except for the case of $\mathbf{A^{LPyr2}}$ which displays a narrower angle of 64.78°. The uniqueness of $\mathbf{A^{LPyr2}}$ is attributable to the steric bulk of the second methylpyrenyl substituent, which causes a marginally significant distortion of the first coordination sphere about Rh. Accordingly, all these angles are significantly greater than the analogous value for $[Cp^*Rh(bpy)Cl]^+$ (~59°)[34]; this is consistent with the greater out-of-plane steric bulk of all the κ^2-R_2dpma ligands here in comparison with κ^2-bpy ligand.

	Rh-N (Å)	Rh-Cp*(Å)	∠N1-Rh-N2	∠Cp*-dpma	Ref.
$\mathbf{A^{LMe2}}$	2.130(2), 2.133(2)	1.803	85.44(8)°	66.77°	Ref. 15
$\mathbf{A^{LBn2}}$	2.112(2), 2.122(2)	1.811	84.03(8)°	66.37°	This work
$\mathbf{A^{LMePyr}}$	2.125(3), 2.135(3)	1.809	85.30(2)°	66.27°	This work
$\mathbf{A^{LPyr2}}$	2.118(3), 2.120(3)	1.810	85.10(2)°	64.78°	This work

Table 5.1. Tabulated bond lengths and angles of $\mathbf{A^{LR2}}$ found from XRD.

Our previous studies have shown that [Cp*Rh(Me_2dpma)$NCCH_3$]$(PF_6)_2$ ($\mathbf{1^{LMe2}}$) has a unique electrochemical profile in which a distinct Electrochemical-Chemical (EC) process is observable upon reduction of the system from Rh(II) to Rh(I).[13,15] A similar profile was observed here for the new series of $\mathbf{1^{LR2}}$ complexes (Figure 5.2.) The $\mathbf{1^{LR2}}$ complexes, which are the acetonitrile solvento analogues of the chloride-bound $\mathbf{A^{LR2}}$ precursors described above, were used in the electrochemical studies to avoid a detrimental side reaction observed in the presence of chloride.[15] The $\mathbf{1^{LR2}}$ complexes could be cleanly generated in all cases with the addition of one equivalent of $AgPF_6$ (Scheme 5.2) to the corresponding $\mathbf{A^{LR2}}$ complexes. The $\mathbf{A^{LR2}}$ complexes were fully characterized by ^{1}H, ^{13}C{^{1}H}, ^{31}P{^{1}H} and ^{19}F NMR, elemental analysis and XRD, while the more sensitive $\mathbf{1^{LR2}}$ complexes, on the other hand, were characterized solely by ^{1}H NMR to confirm full conversion of $\mathbf{A^{LR2}}$ to $\mathbf{1^{LR2}}$ after *in situ* generation and isolation for immediate use in the electrochemical studies. The complexes $\mathbf{1^{LR2}}$ were studied as opposed to complexes $\mathbf{A^{LR2}}$ to avoid the formation [Cp*RhCl]$_2$ complex following 1e$^-$ reduction observed in electrochemical studies conducted in the presence of chloride/halide ligands that promote dimerization.

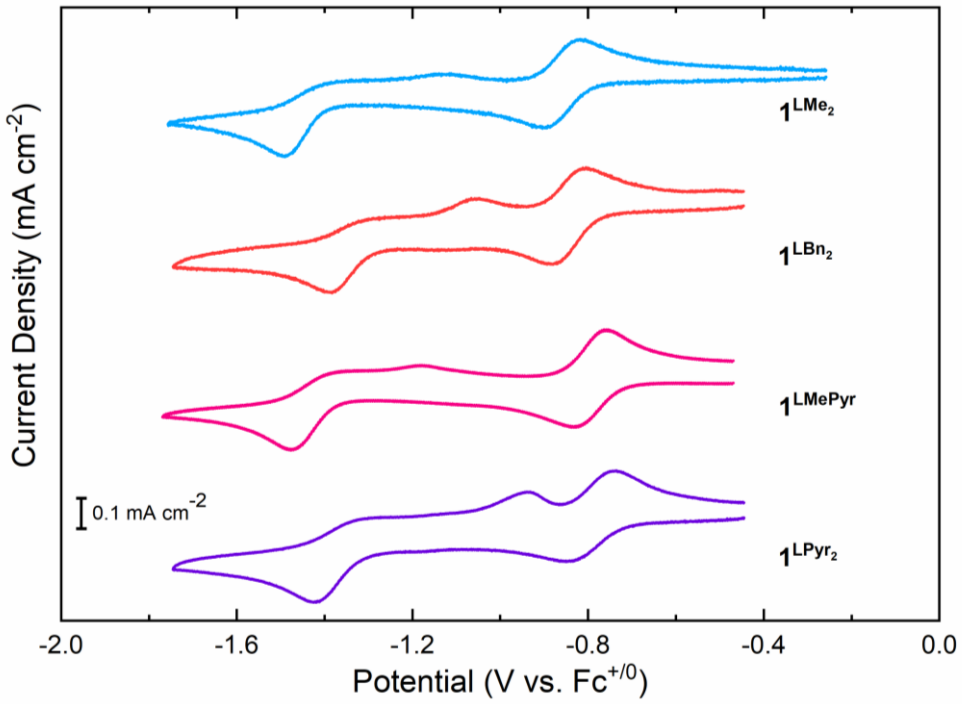

Figure 5.2. Cyclic voltammetry of $\mathbf{1}^{\mathbf{LMe2}}$ (blue), $\mathbf{1}^{\mathbf{LBn2}}$ (red), and $\mathbf{1}^{\mathbf{LMePyr}}$ (pink) and $\mathbf{1}^{\mathbf{LPyr2}}$ (purple). Conditions: Electrolyte, 0.1 M $TBAPF_6$ in CH_3CN; scan rate, 50 mV/s; working electrode, highly oriented pyrolytic graphite (HOPG); [Rh] in each experiment ca. 1 mM. Initial potentials $\mathbf{1}^{\mathbf{LMe2}}$, ca. − 0.5 V; $\mathbf{1}^{\mathbf{LR2}}$, ca. − 0.4 V.

Cyclic voltammetric studies of solutions containing the $\mathbf{1}^{\mathbf{LR2}}$ complexes reveal similar cathodic and anodic events in each case (Figure 5.2), in line with our initial chemical and electrochemical studies of $\mathbf{1}^{\mathbf{LMe2}}$. With a high degree of similarity to that of $\mathbf{1}^{\mathbf{LMe2}}$, the cyclic voltammogram of $\mathbf{1}^{\mathbf{LBn2}}$ reveals that initial quasi-reversible $1e^-$ reduction ($E_{1/2}$ (Rh^{III}/Rh^{II}) = –0.84 V) that leads to generation of $\mathbf{2}^{\mathbf{LBn2}}$ (Scheme 5.3). A second $1e^-$ reduction is observed at a more negative potential ($E_{pc}(Rh^{II}/Rh^{I})$= –1.40 V); this process appears fully irreversible at lower scan rates, implicating the relatively rapid conversion of the nascent $\mathbf{3}^{\mathbf{LBn2}}$ (a formally Rh(I) form bearing κ^2-Bn_2dpma) into $\mathbf{4}^{\mathbf{LBn2}}$ (bearing the flipped version of the ligand with an η^2 pyridine ring; see Scheme 5.3 for structures of all these compounds).[15] Consistent with stabilization of the reduced Rh center by the

rearrangement of the pyridine ring, the return anodic scan reveals a coupled irreversible oxidation ($E_{p,a}(Rh^{I} \rightarrow Rh^{II})$ = –1.05 V) that leads to regeneration of $\mathbf{2}^{\mathbf{LBn2}}$ via oxidation of $\mathbf{4}^{\mathbf{LBn2}}$ followed by reorientation of the Bn_2dpma ligand to the original κ^2 configuration. This model for the cyclic voltammetric response of $\mathbf{1}^{\mathbf{LBn2}}$ is consistent with the high degree of reversibility of the initial Rh^{III}/Rh^{II} couple, since $\mathbf{2}^{\mathbf{LBn2}}$ is cleanly regenerated by the proposed anodic reaction sequence. The model is also supported by the anodic electrochemical behavior of isolated $\mathbf{4}^{\mathbf{LBn2}}$ (*vide infra*), which shows two oxidation events (see Appendix C, Figures C35 and C36) that closely mirror those displayed in cyclic voltammetry experiments carried out with $\mathbf{1}^{\mathbf{LBn2}}$. The voltammetric responses of $\mathbf{1}^{\mathbf{LMePyr}}$ and $\mathbf{1}^{\mathbf{LPyr2}}$ closely mirror those of $\mathbf{1}^{\mathbf{LMe2}}$ and $\mathbf{1}^{\mathbf{LBn2}}$; a minor broadening of the cathodic and anodic waves for $\mathbf{1}^{\mathbf{LPyr2}}$, as well as a slight apparent increase in the diffusion coefficient for the pyrene-appended compounds (see Appendix C, Table C2), may implicate interactions between the carbon working electrode surface and the compound engendered by the extended aromatic π system of the pyrene groups. $\mathbf{1}^{\mathbf{LBn2}}$, $\mathbf{1}^{\mathbf{LMePyr}}$, and$\mathbf{1}^{\mathbf{LPyr2}}$ were all found to be freely diffusing on the basis of scan rate dependence cyclic voltammetry studies (see Appendix C, Figures C30, C33, C38, C41).

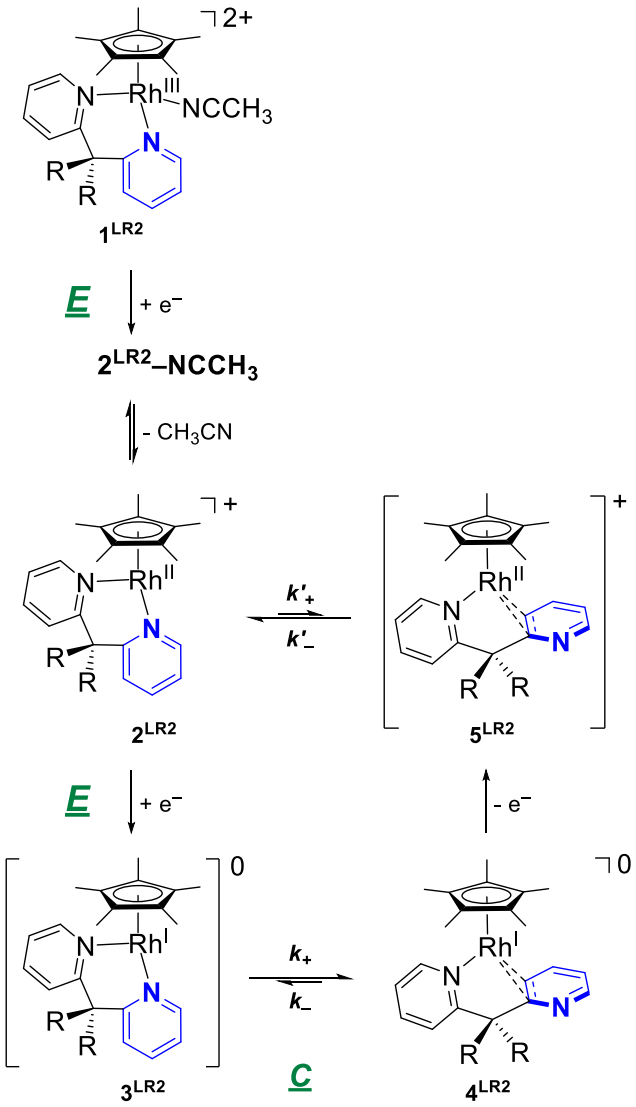

Scheme 5.3. Electrochemical reduction scheme for the family of $\mathbf{1}^{\mathbf{LR2}}$ complexes.

The values of the midpoint potential for the initial quasi-reversible Rh^{III}/Rh^{II} reduction among the series of $\mathbf{1}^{\mathbf{LR2}}$ complexes show that there is a slight electronic dependence based on the electron-donating or -withdrawing properties of the substituents appended to the LR_2 backbone (Table 5.2). $\mathbf{1}^{\mathbf{LMe2}}$, which features the most electron-donating substituents, two methyl groups, has the most negative Rh^{III}/Rh^{II} potential ($E_{1/2}$ = –0.86 V vs. $Fc^{+/0}$). $\mathbf{1}^{\mathbf{LBn2}}$ has the next more-positive reduction potential ($E_{1/2}$ = –0.84 V vs. $Fc^{+/0}$), consistent with the presence of the more electron-withdrawing aromatic benzyl substituents.[35] The most positive reduction potentials in the series

are associated with the methylpyrenyl substituted $\mathbf{1}^{\mathbf{LMePyr}}$ and $\mathbf{1}^{\mathbf{LPyr2}}$ complexes ($E_{1/2}$ = – 0.80 V vs. $Fc^{+/0}$). This is consistent with the presence of the large aromatic π-system in the pyrenyl functionalities, which can be expected to be the most electron-withdrawing. Notably, there is no significant trend among the E_{pa} and E_{pc} values associated with the Rh^{II}/Rh^{I} redox events in the series of complexes, suggesting that the electronic influence of the ligand substituents does not strongly affect the peak potentials associated with Rh^{II}/Rh^{I} interconversion.

	$E_{1/2}$ $Rh^{III/II}$	ΔE_p $Rh^{III/II}$	E_{pc} $Rh^{II/I}$	E_{pa} $Rh^{II/I}$
$\mathbf{1}^{\mathbf{LMe2}}$	–0.86 V	78 mV	–1.45 V	–1.02 V
$\mathbf{1}^{\mathbf{LBn2}}$	–0.84 V	79 mV	–1.40 V	–1.05 V
$\mathbf{1}^{\mathbf{LMePyr}}$	–0.80 V	72 mV	–1.48 V	–1.17 V
$\mathbf{1}^{\mathbf{LPyr2}}$	–0.80 V	109 mV	–1.43 V	–0.93 V

Table 5.2. Reduction potentials for series of $\mathbf{1}^{\mathbf{LR2}}$ complexes.

Further support for the reaction sequence outlined in Scheme 5.3 is provided by the chemical isolation (see Experimental Section) and structure of $\mathbf{4}^{\mathbf{LBn2}}$ obtained from XRD analysis (Figure 5.3). These data confirm that the structural rearrangement of the ligand that results in η^2 pyridine coordination upon reduction of the compound to the Rh^{I} oxidation state remains operative even when aryl substituents are appended to the ligand backbone that could alternatively interact with the metal center in the reduced form of the complex. Indeed, we find that one of the pyridine moieties of $\mathbf{4}^{\mathbf{LBn2}}$ binds to the Rh center in a closely similar fashion as in the $\mathbf{4}^{\mathbf{LMe2}}$ complex[15] in which the Rh center interacts with pyridine and effectively dearomatizes the ring. Analogous to the bonding metrics in $\mathbf{4}^{\mathbf{LMe2}}$, the Rh center is within bonding distance of C10 (C10–Rh: 2.065(2) Å) and C9 (C9–Rh 2.113(2) Å) attesting to the ligation of Rh to the C9–C10 olefin. Indicative of the bonding within the pyridine ring of $\mathbf{4}^{\mathbf{LBn2}}$, the C9–C10 bond elongates in comparison to the length found in $\mathbf{1}^{\mathbf{LBn2}}$ as a result of strong π-backbonding. Dearomatization of the heterocycle

results in localization of double bond character within the ring, comparable to the case of $\mathbf{4}^{\mathbf{LMe2}}$ in which alternating short/long C–C/C–N bond distances are observed (Figure 5.3). A remarkable feature observed in the $\mathbf{4}^{\mathbf{LBn2}}$ XRD structure is the significant pyramidalization of C10, consistent with the upfield shift in the ^{1}H NMR of H10 (see Appendix C, Figure C24) consistent with the anticipated sp^3-hybridization of C10 in both structures.[15] Notably, NMR studies corroborate the XRD finding that one of the pyridine motifs on the dpma framework is the only arene ligand interacting with Rh even in the presence of other aromatic fragments. Based on the bonding metrics measured for $\mathbf{4}^{\mathbf{LBn2}}$ and $\mathbf{4}^{\mathbf{LMe2}}$, we reason that the Rh center in $\mathbf{4}^{\mathbf{LBn2}}$ interacts with its olefinic ligand in a similar to manner to that in $\mathbf{4}^{\mathbf{LMe2}}$. Thus, metal-to-olefin backdonation within the context of the Dewar-Chatt-Duncanson[17] model stabilizes the formally Rh^{I} center in both cases.[15] Multiple attempts to isolate the $2e^{-}$ reduced forms of the $\mathbf{A}^{\mathbf{LMePyr}}$ and $\mathbf{A}^{\mathbf{LPyr2}}$ complexes were unsuccessful, due to cogeneration of side products with similar solubility profiles following chemical reduction.

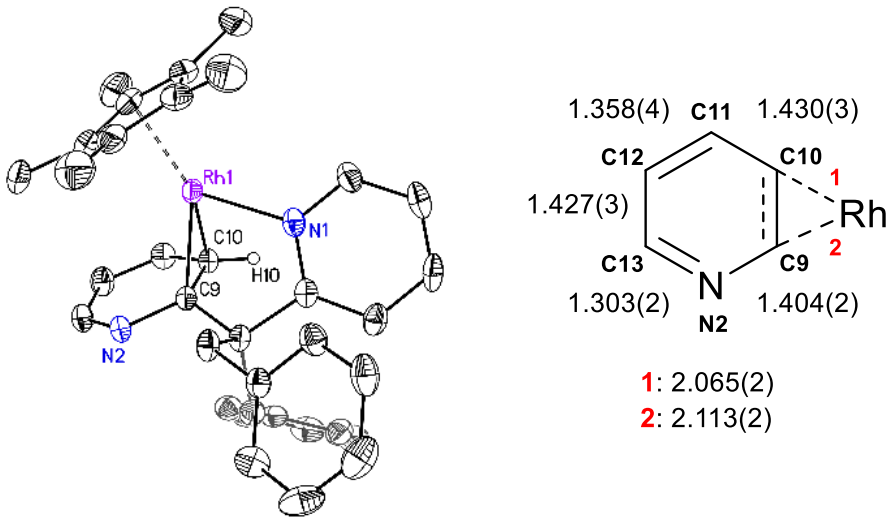

Figure 5.3. Solid-state structure of $\mathbf{4}^{\mathbf{LBn2}}$ (XRD) and selected bond metrics (Å). Hydrogen atoms (except H10) are omitted for clarity. Displacement ellipsoids are shown at the 50% probability level.

Upon observing the analogous EC processes for the various $\mathbf{1}^{\mathbf{LR2}}$ complexes resembling the process encountered in our prior studies with the $\mathbf{LMe_2}$-ligated complex, we next endeavored to quantify the rate of the redox-induced ligand rearrangement observed for conversion of $\mathbf{3}^{\mathbf{LR2}}$ to $\mathbf{4}^{\mathbf{LR2}}$ (Scheme 5.3). In cases where a redox process involves an EC mechanism, the current corresponding to re-oxidation of the reduced form of a given compound is negligible at slower scan rates, since the immediate product of reduction is consumed by the coupled chemical reaction before it can undergo reoxidation on the return anodic sweep. In order to understand this situation and analyze the rate of ligand rearrangement, we turned to the Zone Diagrams for electrochemical analysis developed by Savéant.[19] Savéant has used Zone Diagrams for general cases of the EC mechanism to understand the competition between the rate of diffusion, the properties of the redox induced chemical reaction (as a function of its equilibrium constant *K*) and a dimensionless parameter, λ, which describes the competition between the rate of the coupled chemical reaction and the rate of diffusion. The dimensionless parameter λ is inversely dependent upon the scan rate at which the cyclic voltammogram is measured. Therefore, as illustrated in the Zone Diagrams,[19] as the scan rate of the voltammetry is increased, the dimensionless parameter λ decreases. As λ decreases, the reduced form of the metal complex is allowed less time to diffuse in solution, and as a result, less time is allotted for the chemical process involved to occur. Thus, at the higher scan rates, the peak current associated with re-oxidation of the reduced form of the complex on the anodic sweep increases until it reaches a maximum value under conditions where the coupled chemical reaction has insufficient time to affect the appearance of the voltammetric data.

In order to provide the experimental data needed to quantify the rate of the ligand rearrangement of interest here, we performed cyclic voltammetry with each complex $\mathbf{1}^{\mathbf{LR2}}$ over a wide range of scan rates. Taking $\mathbf{1}^{\mathbf{LBn2}}$ as an example, Figure 5.4 shows selected voltammograms

of the compound taken at 50, 1000, and 2500 mV/s. The second reduction in the data exhibits the tell-tale characteristics of an EC mechanism; the expected increase in the cathodic peak current with increasing scan rate (increasing with a square root dependence per the Randles-Ševćik equation[36]) at E_{pc} = –1.40 V vs $Fc^{+/0}$ is associated with observation of a corresponding anodic process only at higher scan rates. At a slower scan rate, the dimensionless parameter λ is large, meaning that the system has ample time for the reduction-induced chemical reaction to occur. Conversely, at higher scan rates we observe the appearance of the re-oxidation coupled to the most negative reduction event, corresponding to the presence of a now electrochemically quasi-reversible process. This increase in anodic current is a direct result of the influence of the dimensionless parameter λ now having a smaller value, meaning at the faster scan rate we can overcome the rate of the diffusion and the rate of the chemical reaction to re-oxidize the reduced form of the compound. By this method we can measure the rate of the reduction-induced reaction observed by CV. Analogous scan rate dependent studies yielded similar behavior for each of the complexes $\mathbf{1}^{\mathbf{LR2}}$ in the series (see Appendix C, Figures C31, C34, C39, C42).

The rate constant for the chemical step in the EC process described above was taken as the target of our analysis. In order to measure this first-order rate constant (k_+) for the ligand reorientation/flip chemical step (see Scheme 5.3), we turned to digital simulation of our CVs since the well-resolved nature of the redox processes enable us to clearly model the data (Figure 5.5).[26] To examine the rate constant of the EC process, we focused on the anodic return wave that is a result of the oxidation of the doubly reduced complex outpacing the coupled chemical reaction. This anodic feature directly reports on the value of λ. In order to extract the value of k_+, we simulated our entire library of scan rate dependent cyclic voltammograms at which the anodic return wave was measurable, in order to capture the increasing chemical reversibility of the redox

process involving our chemical reaction of interest (see Scheme 5.3). Notably, within our model, the value of k_+ is independent of scan rate and concentration (at all scan rates, see Appendix C Figures C54 and C55) even though the value of λ does change at each scan rate, giving rise to the variable appearance of the data. The chemical properties of the system were thus interrogated at all of the scan rates for which a return wave is observable (**1**$^{\mathbf{LR2}}$: 300–2500 mV/s, **1**$^{\mathbf{LPyr2}}$: 250–2000 mV/s, see Appendix C Figure C44, C47-C53).

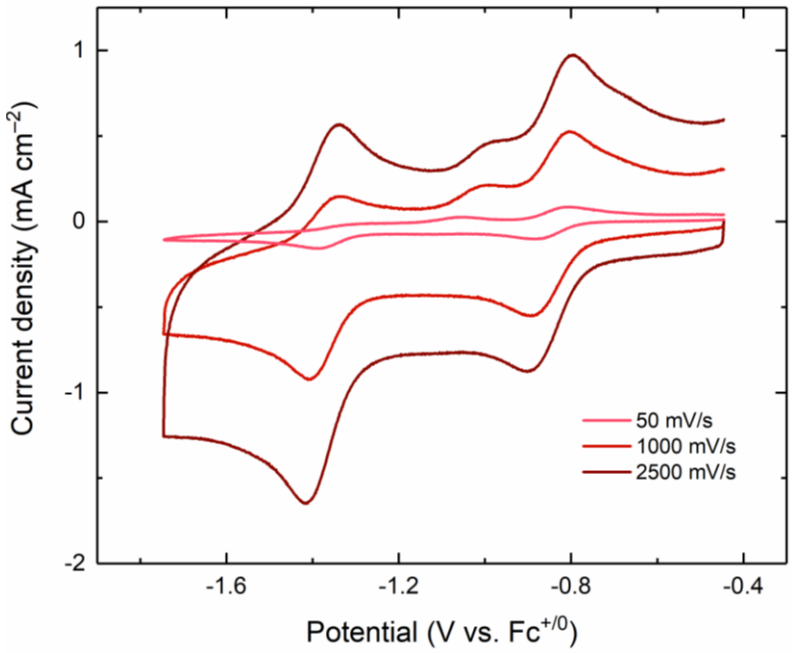

Figure 5.4. Cyclic voltammetry of **1**$^{\mathbf{LBn2}}$ at increasing scan rates. Conditions: Electrolyte, 0.1 M $TBAPF_6$ in CH_3CN; working electrode, highly oriented pyrolytic graphite (HOPG); [Rh] in each experiment ca. 1 mM.

To extract the kinetic information from the simulated data for our compounds, the reaction sequence given in Scheme 5.3 was programmed into DigiElch. Additionally, experimentally determined values for certain variables were added to the model as needed, including the following: the double layer capacitance of the highly oriented pyrolytic graphite (HOPG) working electrode (determined via scan rate dependence of electrode background currents in our 0.1 M

$TBAPF_6/CH_3CN$ electrolyte; 1.0 x 10^{-5} F) (see Appendix C, Figure C43); the solution resistance determined at several applied voltages (c.a. 110 −150 Ω); the area of the HOPG working electrode (0.09 mm^2); the temperature (298 K); and the concentration of the given $\mathbf{1}^{\mathbf{LR2}}$ compound in solution (ca. 10^{-3} M). Based on the appearance of the voltammetry, the initial value of the charge transfer coefficient, α, was set to 0.5 in all cases. The potentials shown in Table 5.2 ($E_{1/2}$, E_{pa}, E_{pc}), obtained from inspection of the initial voltammetric data were also input as starting points for the simulation software to fit the reduction potentials internally. Following optimization, the reduction potentials determined by DigiElch matched well with those determined manually by inspection of the data (see Appendix C, Figures C44, C47-C53). With this approach, we were able to determine the k_+ values for the target EC process (see Scheme 5.3 and Table 5.3). Reasonable values were also extracted for diffusion coefficients (cm^2/s) and heterogenous electron transfer rates (k°, cm/s) for each of the $\mathbf{1}^{\mathbf{LR2}}$ complexes (see Appendix C, Table C2).

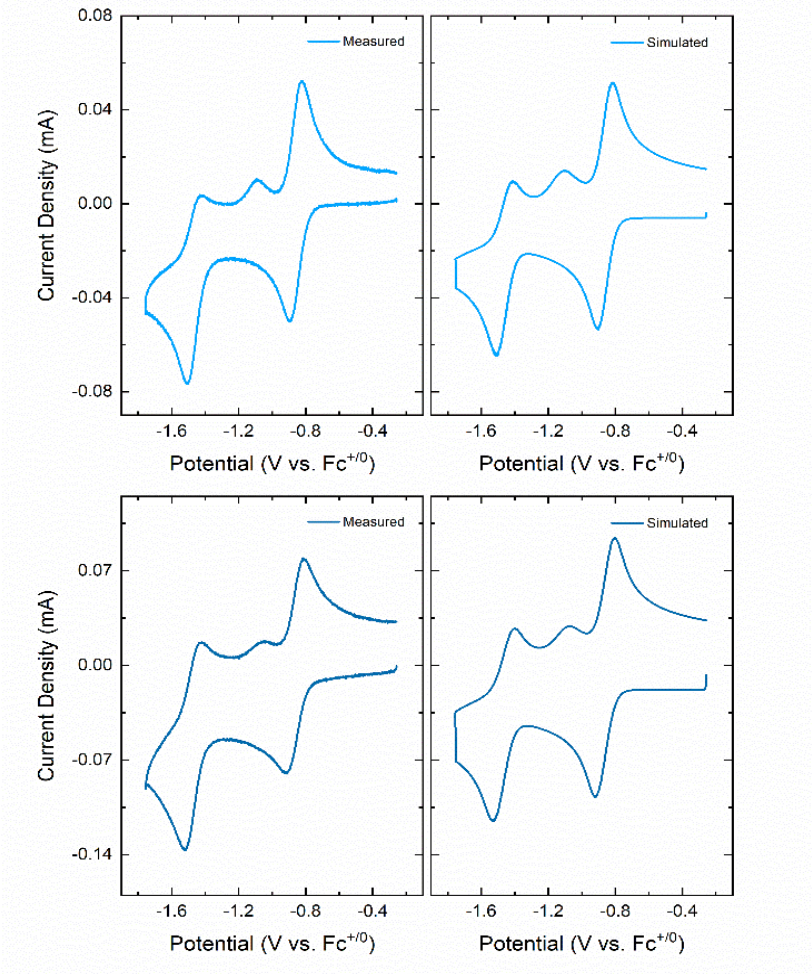

Figure 5.5. Measured (left) and simulated (right) CV of $\mathbf{1}^{\mathbf{LMe2}}$. Scan rates of 500 mV/s (upper), and 1500 mV/s (lower). Measured CV conditions: Electrolyte, 0.1 M TBAPF6 in CH_3CN; working electrode, highly oriented pyrolytic graphite (HOPG); [Rh] in each experiment ca. 1 mM. Initial potentials ca. −0.5 V. Simulated CV conditions: mechanism in shown in Scheme 5.3; reduction potentials (Table 5.2); double layer capacitance 1.0 x 10^{-5} F (see Appendix C, Figure C43); resistance c.a. 110 −150 Ω; working electrode area 0.09 cm^2; temperature 298 K; concentration c.a.1 mM.

Based on the results of the simulations, a distinct relationship between k_+ and the steric bulk of the substituents on the methylene bridge (Table 5.3) can be observed. We find that the least sterically bulky methyl substituents in $\mathbf{1}^{\mathbf{LMe2}}$ engender the fastest ligand rearrangement with k_+ =

1.65 ± 0.08 s^{-1}. The $\mathbf{1}^{\mathbf{LBn2}}$ complex, featuring the more sterically bulky benzyl substituents, has k_+ = 1.31 ± 0.19 s^{-1} which is slower. $\mathbf{1}^{\mathbf{LMePyr}}$ complex, featuring single methylpyrenyl and methyl moieties, displays a significantly slower rate of the ligand flip with k_+ = 0.60 ± 0.14 s^{-1}. The pyrene moiety features a considerably larger steric profile than the other substituents in this family of complexes, and as a result, the k_+ value associated with the EC process for $\mathbf{1}^{\mathbf{LMePyr}}$ is significantly slowed compared to the other derivatives. The value of k_+ for $\mathbf{1}^{\mathbf{LPyr2}}$ is even smaller at 0.16 ± 0.01 s^{-1}, supporting the notion that the steric bulk of the substituents appended to the methylene bridge of the **LR2** ligands influences the rate of the ligand flip giving rise to stabilization of the Rh^I oxidation state. The k_+ measured for the $\mathbf{1}^{\mathbf{LPyr2}}$ EC process is an entire order of magnitude slower than that observed for $\mathbf{1}^{\mathbf{LMe2}}$. Taken together, the simulations indicate that the substituents' steric bulk affects how long it takes to interconvert between intermediates upon reduction; greater steric bulk inhibits the rate of the ligand flip of the single pyridine moiety. Appealingly, the results show that the rates determined by digital simulation are significantly different from one another (see Appendix C Figure C55). Confirming the first-order nature of the ligand reorientation/flip step, the value of k_+ was found to be independent of the solution concentration of $\mathbf{1}^{\mathbf{LR2}}$ (see Appendix C, Figure C54).

	$\mathbf{1}^{\mathbf{LMe2}}$	$\mathbf{1}^{\mathbf{LBn2}}$	$\mathbf{1}^{\mathbf{LMePyr}}$	$\mathbf{1}^{\mathbf{LPyr2}}$
k_+ (s^{-1})	1.65 ± 0.08	1.31 ± 0.19	0.60 ± 0.14	0.16 ± 0.01

Table 5.3. First order rate constants (k_+) for the EC process observed for the family of complexes. Error bars are shown as ±1 σ and were determined by replicate measurements/simulations at the various scan rates given in the main text.

These findings are of potential relevance to the development of new ligand frameworks for use in molecular electrocatalysis, as (pre)catalysts prepared with sterically bulky substituents may be

prone to slow interconversion between intermediates. Use of bulky ligand substituents is especially likely in cases where a given catalyst is incorporated into elaborate supramolecular constructs; electrode surface attachment schemes and use of chromophore-catalyst assemblies are two examples of such situations. In these cases, the interconversion of intermediates could impact the expected catalysis, since simpler model compounds may not reflect the kinetic properties of highly functionalized analogues.[37,38] Along a similar line, the attachment of functionalities in the second coordination sphere (like acids or bases) via tethering groups could slow reactions following redox activation steps.[39] In particular, the kinetics of formation of the species $\mathbf{4^{LR2}}$ here that feature η^2-pyridyl ligands are of particular interest to us, since low-valent organometallic complexes are especially promiscuous in adopting a variety of coordination modes with carbon-based ligands.[40] Monitoring changes in coordination mode(s) and activation of substrates by electrochemical means offers interesting opportunities to develop new reaction schemes amenable to use in molecular electrocatalysis.

5.3 Conclusions

We find that transient Rh^I species bearing substituted κ^2-dpma ligands undergo a unique Electrochemical-Chemical (EC) process in cyclic voltammetry upon reduction from Rh(II) to Rh(I); transient electrogenerated Rh(I) species undergo a ligand rearrangement that results in facial η^2 coordination of one pyridine motif. Our studies indicate that the introduction of sterically bulky substituents engenders significant changes in the first-order rate constant associated with the chemical step of the noted EC process (k_+). We find that the steric bulk engendered by the $\mathbf{1^{LPyr2}}$ systems slows k_+ by an order of magnitude compared to the value measured with $\mathbf{1^{LMe2}}$. This study represents a relatively uncommon case where a series of elementary rate constants could be well quantified via modeling of scan rate-dependent electrochemistry data collected under readily

accessible conditions (Scheme 5.4). Thus, we anticipate that our findings could be of use in interpretation of results from other systems where more complex reactivity may preclude direct measurement of individual elementary rate constants, such as in systems where molecular electrocatalysis is taking place.

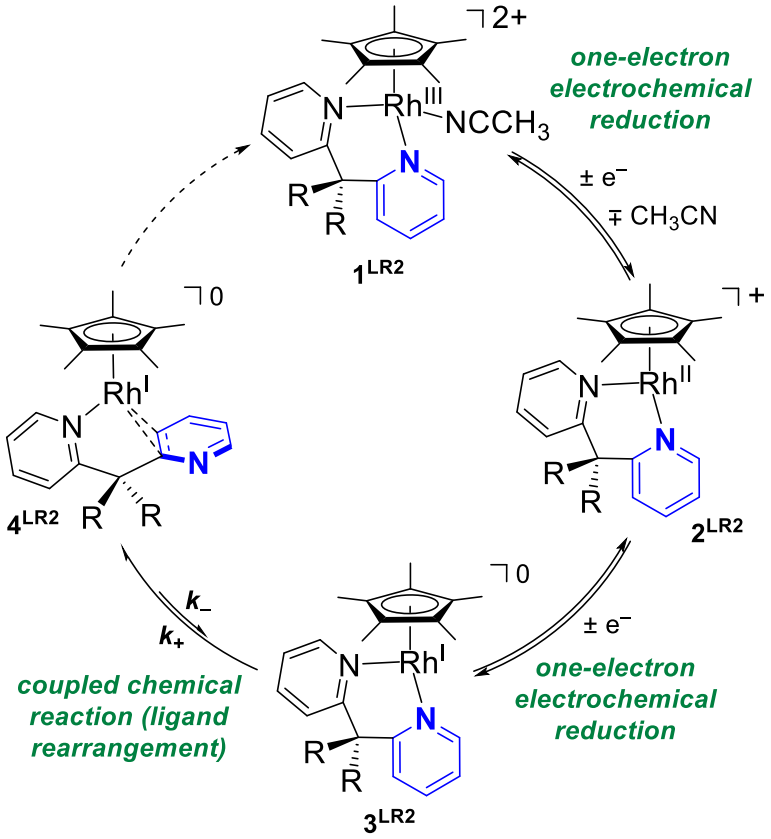

Scheme 5.4. Reactivity pathway measured for the family of [Cp*Rh] complexes.

5.4 Experimental Details

5.4.1 General Considerations

All manipulations were carried out in dry N_2-filled gloveboxes (Vacuum Atmospheres Co., Hawthorne, CA) or under N_2 atmosphere using standard Schlenk techniques unless otherwise noted. All solvents were of commercial grade and dried over activated alumina using a PPT Glass Contour (Nashua, NH) solvent purification system prior to use, and were stored over molecular

sieves. All chemicals were from major commercial suppliers and used as received after extensive drying. $[Cp^*RhCl_2]_2$ was prepared according to literature procedures.[31,32] The substituted dpma ligands were synthesized by the methods of Canty and Mohr.[27] Bis(2-pyridyl)methane, 2,2′-(ethane-1,1-diyl)dipyridine, and 1-(chloromethyl)pyrene were also prepared according to literature methods.[23,29 ,30]

Deuterated NMR solvents were purchased from Cambridge Isotope Laboratories; CD_3CN was dried over molecular sieves and C_6D_6 was dried over sodium/benzophenone. ^1H, ^{13}C, and ^{19}F NMR spectra were collected on 400 or 500 MHz Bruker spectrometers and referenced to the residual protio-solvent signal[41] in the case of ^1H and ^{13}C. Heteronuclear NMR spectra were referenced to the appropriate external standard following the recommended scale based on ratios of absolute frequencies (Ξ).[42] ^{19}F NMR spectra are reported relative to CCl_3F. Chemical shifts (δ) are reported in units of ppm and coupling constants (J) are reported in Hz. Electronic absorption spectra were collected with an Ocean Optics Flame spectrometer and 1-cm pathlength quartz cuvettes. Elemental analyses were performed by Midwest Microlab, Inc. (Indianapolis, IN).

5.4.2 Synthesis

Synthetic Procedures. Ligands were synthesized by modification of related procedures from the literature.[27,28]

Synthesis of **LBn$_2$.** A Schlenk flask with bis(2-pyridyl)methane (dpma; 0.6509 g, 3.82 mmol, 1.0 equiv.) was cooled to –78°C. A solution of nBuLi (1.67 mL, 4.59 mmol, 1.2 equiv.) was added dropwise and allowed to stir for 15 min then benzyl bromide (0.59 mL, 4.47 mmol, 1.3 equiv.) was added dropwise. The sequential addition of nBuLi (1.95 mL, 5.35 mmol, 1.4 equiv.) and benzyl bromide (0.68 mL, 5.74 mmol, 1.5 equiv.) was then repeated in the same manner. The resulting yellow solution was stirred with a saturated solution of sodium bicarbonate. The liquid

phase was separated by filtration and title ligand was then purified and obtained by a dichloromethane/water separation followed by a column with 50:50 dichloromethane:acetone column. (0.9889 g, 74% yield). ^{1}H NMR (500 MHz, C_6D_6): δ 8.51 – 8.46 (m, 2H), 6.99 – 6.93 (m, 7H), 6.90 – 6.80 (m, 7H), 6.69 (dd, *J* = 8.1, 1.2 Hz, 2H), 6.58 (ddd, J = 7.5, 4.8, 1.1 Hz, 2H), 4.01 (s, 4H) ppm. ^{13}C{^{1}H} NMR (126 MHz, C_6D_6): δ 165.26 (d, *J* = 5.2 Hz), 148.39 (d, *J* = 5.1 Hz), 139.47 (d, *J* = 5.2 Hz), 135.01 (d, *J* = 5.3 Hz), 131.21 (d, *J* = 5.3 Hz), 128.37, 127.77 (d, *J* = 5.1 Hz) 126.14 (d, *J* = 5.4 Hz), 124.75 (d, *J* = 5.4 Hz), 121.11 (d, *J* = 5.4 Hz), 59.21 (d, *J* = 5.3 Hz), 44.68 (d, *J* = 5.3 Hz) ppm.

Synthesis of **LMePyr.** A solution of tBuOK in THF (0.3005 g, 2.67 mmol, 1.2 equiv.) was added dropwise to a Schlenk flask charged with 2,2′-(ethane-1,1-diyl)dipyridine (0.4111 g, 2.23 mmol, 1.0 equiv.) at –78°C. The solution was stirred for 45 min and turned a light peach color. A solution of 1-chloromethylpyrene in THF (0.7274 g, 2.90 mmol, 1.3 equiv.) was added to the Schlenk, which was then allowed to warm to room temperature and refluxed overnight. Following reflux, the solution was cooled then stirred with a saturated solution of sodium bicarbonate and the liquid phase separated by filtration. Purification was accomplished by extraction of the product mixture with dichloromethane/water followed by column chromatography with chloroform as the initial eluent. However, the desired ligand was finally eluted from the column with methanol (0.4559 g, 51% yield). ^{1}H NMR (500 MHz, CD_2Cl_2): δ 8.66 – 8.61 (m, 2H), 8.25 – 8.09 (m, 3H), 8.06 – 7.90 (m, 4H), 7.85 (d, *J* = 7.9 Hz, 1H), 7.52 (td, *J* = 7.8, 1.9 Hz, 2H), 7.21 – 7.12 (m, 3H), 7.02 (dd, *J* = 8.0, 1.1 Hz, 2H), 4.56 (s, 2H), 1.64 (s, 3H) ppm. ^{13}C{^{1}H} NMR (126 MHz, CD_2Cl_2): δ 167.46, 149.12, 136.44, 134.38, 131.89, 131.27, 131.09, 130.27, 129.87, 127.94, 127.19, 126.99, 126.26, 125.32, 125.23, 125.04, 125.00, 124.42, 123.06, 121.75, 41.80, 25.87 ppm.

Synthesis of **$LPyr_2$.** A solution of tBuOK in THF (0.8587 g, 7.65 mmol, 2.5 equiv.) was added dropwise to a Schlenk flask charged with bis(2-pyridyl)methane (dpma; 0.5211 g, 3.06 mmol, 1 equiv.) at –78°C. The solution was stirred for 45 min and turned a light peach color. A solution of 1-chloromethylpyrene in THF (0.1.9952 g, 7.95 mmol, 2.6 equiv.) was added to the Schlenk then warmed to room temperature and refluxed overnight. Following reflux, the solution was first allowed to cool and then a stirred with a saturated solution of sodium bicarbonate; the liquid phase was then separated by filtration. The liquid phase was then extracted with dichloromethane/water and subjected to column chromatography with chloroform as the eluent. The desired ligand was eluted from the column with methanol (0.5504 g, 30% yield). ^{1}H NMR (500 MHz, $CDCl_3$): δ 8.71 (s, 2H), 8.10 (dd, *J* = 7.6, 1.2 Hz, 2H), 8.02 (d, *J* = 7.3 Hz, 2H), 7.99 – 7.89 (m, 7H), 7.86 (d, *J* = 8.0 Hz, 3H), 7.75 (d, *J* = 8.0 Hz, 2H), 7.70 (d, *J* = 9.4 Hz, 2H), 6.99 (s, 4H), 6.54 (s, 2H), 4.74 (s, 4H) ppm. ^{13}C{^{1}H} NMR (126 MHz, CD_3CN): δ 146.97, 131.35, 130.82, 130.69, 130.57, 130.23, 128.77, 127.43, 127.27, 125.96 (d, *J* = 4.2 Hz), 125.13, 124.98, 124.71 (d, *J* = 2.5 Hz), 124.20, 123.25, 100.12, 41.53 ppm.

Synthesis of **A^{LBn2}.** To a suspension of $[Cp^*RhCl_2]_2$ in CH_3CN (0.1717 g, 0.278 mmol, 0.5 equiv.) were added $AgPF_6$ (0.1405 g, 0.556 mmol, 1.0 equiv.) in CH_3CN and **L^{Bn2}** ligand (0.1947 g, 0.556 mmol, 1.05 etriquiv.) as a THF solution. The reaction mixture rapidly changed from brick red to orange, and a yellowish precipitate formed. After 15 min, the suspension was filtered to remove the AgCl byproduct, and the volume of the filtrate was reduced to ∼1 mL. Addition of Et_2O (∼80 mL) caused precipitation of a yellow solid, which was collected by filtration. Pure material was obtained via recrystallization with vapor diffusion of Et_2O into a concentrated CH_3CN solution of the title compound (0.1581 g, 37%). Vapor diffusion of Et_2O into a smaller concentrated CH_3CN solution was employed to obtain single crystals suitable for X-ray diffraction

studies.^{1}H NMR (500 MHz, CD_3CN): δ 9.00 (dd, *J* = 5.8, 1.7 Hz, 2H), 7.73 (ddd, *J* = 8.3, 7.4, 1.8 Hz, 2H), 7.52 (ddd, *J* = 7.4, 5.7, 1.4 Hz, 2H), 8.37 (d, *J* = 8.3 Hz, 2H), 7.35 – 7.16 (m, 4H), 7.03 – 6.99 (m, 4H), 6.60 – 6.50 (m, 2H), 6.49 – 6.44 (m, 2H), 3.85 (s, 2H), 3.67 (s, 2H), 1.59 (s, 15H) ppm. $^{13}C\{^{1}H\}$ NMR (126 MHz, CD_3CN): δ 161.15, 159.57, 157.97, 140.25, 139.11, 136.30, 135.26, 131.55, 131.32, 130.78, 129.34, 128.84, 128.58, 128.34, 128.01, 126.89, 126.77, 126.12, 125.28, 124.95, 99.14, 55.79, 49.06, 40.75, 9.55 ppm. ^{19}F NMR (376 MHz, CD_3CN): δ −73.80 (d, $^{1}J_{F,P}$ = 706 Hz) ppm. $^{31}P\{^{1}H\}$ NMR (162 MHz, CD_3CN): δ –145.50 (sept, $^{1}J_{P,F}$ = 706 Hz) ppm. Anal. Calcd for $C_{35}H_{37}ClF_6N_2PRh$: C, 54.67; H, 4.85, N, 3.64. Found: C, 54.70; H, 4.88, N, 4.97. Calcd for $C_{35}H_{37}ClF_6N_2PRh$ + $1CH_3CN$: C, 54.86; H, 4.98, N, 5.19. This analysis is consistent with observation of CH_3CN in the ^{1}H NMR spectra for $\mathbf{A}^{\mathbf{LBn2}}$ (see Appendix C).

Synthesis of $\mathbf{A}^{\mathbf{LMePyr}}$**.** To a suspension of $[Cp^*RhCl_2]_2$ in CH_3CN (0.0999 g, 0.162. mmol, 0.5 equiv.) were added $AgPF_6$ (0.0817 g, 0.323 mmol, 1.0 equiv.) in CH_3CN and $\mathbf{L}^{\mathbf{MePyr}}$ ligand (0.1320 g, 0.331 mmol, 1.05 equiv.) as a THF solution. The reaction mixture rapidly changed from brick red to orange, and a yellowish precipitate formed. After 15 min, the suspension was filtered to remove the AgCl byproduct, and the volume of the filtrate was reduced to ∼1 mL. Addition of Et_2O (∼80 mL) caused precipitation of a yellow solid, which was collected by filtration. Pure material was obtained via crystallization by vapor diffusion of Et_2O into a concentrated CH_2Cl_2 solution of the title compound (0.080 g, 30%). The same method was employed to obtain single crystals suitable for X-ray diffraction studies. ^{1}H NMR (500 MHz, CD_3CN): δ 9.05 (bs, 2H), 8.29 (d, *J* = 1.04 Hz, 3H), 8.23 – 8.12 (m, 5H), 8.12 – 8.05 (m, 3H), 7.93 (d, *J* = 7.9 Hz, 2H), 7.61 (t, *J* = 6.8 Hz, 2H), 6.52 (d, *J* = 7.9 Hz, 2H), 5.02 (broad s, 1H), 4.14 (broad s, 1H), 1.73 (s, 3H), 1.68 (s, 15H) ppm. $^{13}C\{^{1}H\}$ NMR (126 MHz, CD_3CN): δ 158.48, 141.44, 141.12, 132.29, 131.58, 131.44, 128.68, 128.54, 128.20, 128.03, 127.46, 126.52, 126.13, 125.82, 125.33, 124.62, 124.56,

99.20, 99.18, 52.26, 40.45, 23.81, 9.59 ppm. ^{19}F NMR (376 MHz, CD_3CN): δ −73.83 (d, $^1J_{F,P}$ = 706 Hz) ppm. $^{31}P\{^1H\}$ NMR (162 MHz, CD_3CN): δ –145.51 (sept, $^1J_{P,F}$ = 706 Hz) ppm. Satisfactory elemental analysis could not be obtained for $\mathbf{A^{LMePyr}}$, but NMR methods confirm the diamagnetic purity of the isolated material.

Synthesis of $\mathbf{A^{LPyr2}}$**.** To a suspension of $[Cp^*RhCl_2]_2$ in CH_3CN (0.0399 g, 0.0646 mmol, 0.5 equiv.) were added $AgPF_6$ (0.0326 g, 0.129 mmol, 1.0 equiv.) in CH_3CN and $\mathbf{L^{Pyr2}}$ ligand (0.0793 g, 0.132 mmol, 1.05 equiv.) as a THF solution. The reaction mixture rapidly changed from brick red to orange, and a yellowish precipitate formed. After 15 min, the suspension was filtered to remove the AgCl byproduct, and the volume of the filtrate was reduced to ∼1 mL. Addition of Et_2O (∼80 mL) caused precipitation of a yellow solid, which was collected by filtration. Pure material was obtained via crystallization by vapor diffusion of Et_2O into a concentrated CH_2Cl_2 solution of the title compound (0.0250 g, 26%). Vapor diffusion of Et_2O into a smaller concentrated CH_2Cl_2 solution was employed to obtain single crystals suitable for X-ray diffraction studies. ^{1}H NMR (500 MHz, CD_3CN): δ 9.16 (s, 2H), 8.74 (d, *J* = 9.3 Hz, 1H), 8.51 (dd, *J* = 8.5, 4.7 Hz, 2H), 8.37 (d, *J* = 7.6 Hz, 1H), 8.28 – 8.07 (m, 7H), 8.04 – 7.93 (m, 4H), 7.85 (dd, *J* = 13.6, 9.1 Hz, 3H), 7.74 (d, *J* = 9.3 Hz, 1H), 7.59 (d, *J* = 5.8 Hz, 3H), 7.54 (d, *J* = 8.1 Hz, 2H), 6.59 (d, *J* = 8.0 Hz, 1H), 6.28 (d, *J* = 8.1 Hz, 1H), 4.66 (s, 2H), 1.73 (s, 15H) ppm. $^{13}C\{^1H\}$ NMR (126 MHz, CD_3CN): δ 158.32, 140.34, 132.36, 132.13, 132.00, 131.91, 131.74, 131.34, 130.47, 130.43, 129.73, 129.27, 129.18, 129.11, 129.05, 128.82, 128.34, 128.29, 128.17, 127.94, 127.63, 127.29, 126.84, 126.57, 126.45, 126.39, 126.33, 126.02, 125.50, 125.32, 125.28, 124.84, 124.81, 123.96, 123.38, 99.37, 99.31, 57.27, 44.96, 39.08, 9.63. ppm. ^{19}F NMR (376 MHz, CD_3CN): δ −74.77 (d, $^1J_{F,P}$ = 706 Hz) ppm. $^{31}P\{^1H\}$ NMR (162 MHz, CD_3CN): δ –144.65 (sept, $^1J_{P,F}$ = 706 Hz) ppm. Anal. Calcd for $C_{55}H_{45}ClF_6N_2PRh$: C, 64.94; H, 4.46, N, 2.75. Found: C, 61.50; H, 4.65, N, 2.45.

Calcd for $C_{55}H_{45}ClF_6N_2PRh$ + $1CH_2Cl_2$: C, 61.02; H, 4.80, N, 2.61. This analysis is consistent with the single co-crystallized CH_2Cl_2 solvent molecule found in the solid-state structure of $\mathbf{A^{LPyr2}}$ (see Appendix C).

Synthesis of $\mathbf{1^{LBn2}}$**.** To an orange solution of $\mathbf{A^{LBn2}}$ in CH_3CN (0.0508 g, 0.064 mmol) was added $AgPF_6$ (0.0167 g, 0.066 mmol, 1 equiv.) in CH_3CN. The solution lightened to a pale-yellow color, and a colorless precipitate formed. The mixture was stirred for 3 hours; it was then filtered through Celite to remove AgCl and the volatiles removed *in vacuo*. $\mathbf{1^{LBn2}}$ ^{1}H NMR (500 MHz, CD_3CN): δ 8.99 (dd, *J* = 5.9, 1.7 Hz, 2H), 8.01 – 7.87 (m, 2H), 7.79 – 7.61 (m, 4H), 7.36 – 7.24 (m, 4H), 7.11 – 6.99 (m, 4H), 6.60 (d, *J* = 7.1 Hz, 2H), 6.44 (d, *J* = 7.3 Hz, 2H), 3.83 (s, 2H), 3.59 (s, 2H), 1.60 (s, 15H) ppm.

Synthesis of $\mathbf{1^{LMePyr}}$**.** To an orange solution of $\mathbf{A^{LMePyr}}$ in CH_3CN (0.0462 g, 0.047 mmol) was added $AgPF_6$ (0.0119 g, 0.443 mmol, 1 equiv.) in CH_3CN. The solution lightened to a pale-yellow color, and a colorless precipitate formed. The mixture was stirred for 3 hours; it was then filtered through Celite to remove AgCl and the volatiles removed *in vacuo*. $\mathbf{1^{LMePyr}}$ ^{1}H NMR (500 MHz, CD_3CN): δ 9.16 (s, 2H), 8.76 (d, *J* = 9.3 Hz, 1H), 8.53 (t, *J* = 8.1 Hz, 2H), 8.39 (d, *J* = 7.6 Hz, 1H), 8.28 – 8.17 (m, 4H), 8.15 – 8.07 (m, 2H), 8.05 – 7.96 (m, 4H), 7.87 (dd, *J* = 17.0, 9.2 Hz, 3H), 7.79 – 7.71 (m, 4H), 7.67 (d, *J* = 9.3 Hz, 1H), 7.59 (d, J = 8.1 Hz, 2H), 6.46 (d, *J* = 8.0 Hz, 1H), 6.40 (d, *J* = 8.2 Hz, 1H), 4.50 (s, 2H), 1.78 (s, 15H) ppm.

Synthesis of $\mathbf{1^{LPyr2}}$**.** To an orange solution of $\mathbf{A^{LPyr2}}$ in CH_3CN (0.0532 g, 0.053 mmol) was added $AgPF_6$ (0.0132 g, 0.052 mmol, 1 equiv.) in CH_3CN. The solution lightened to a pale-yellow color, and a colorless precipitate formed. The mixture was stirred for 3 hours; it was then filtered through Celite to remove AgCl and the volatiles removed *in vacuo*. $\mathbf{1^{LPyr2}}$ ^{1}H NMR (500 MHz, CD_3CN): δ 9.02 (broad s, 2H), 8.34 – 8.27 (m, 2H), 8.20 (d, *J* = 2.8 Hz, 2H), 8.17 (s, 1H), 8.15 (s,

1H), 8.13 – 8.06 (m, 4H), 7.93 (d, *J* = 8.0 Hz, 1H), 7.76 (t, *J* = 6.7 Hz, 3H), 6.45 (d, *J* = 8.0 Hz, 1H), 4.55 (broad s, 1H), 4.18 (broad s, 1H), 1.73 (s, 15H), 1.68 (s, 3H) ppm.

Synthesis of **4^{LBn2}.** A suspension of **A^{LBn2}** in THF (0.0698 g, 0.0759 mmol) was stirred over freshly prepared sodium-mercury amalgam (1% Na in Hg; 0.0175 g Na^0, 0.759 mmol, 10 equiv.) for 6 hours, during which time the yellow suspension became a dark red homogeneous solution. The mixture was filtered, and the volatiles removed in vacuo. Extraction with Et_2O and removal of the volatiles in vacuo provides the title compound as a dark red solid (0.0349 g, 77%). Extraction with hexanes can provide additional pure material, if the extracted solution is cooled to –35°C; these conditions provide additional pure and crystalline product. This strategy was employed using pure material to obtain single-crystals of the title compound suitable for X-ray diffraction studies.^{1}H NMR (400 MHz, C_6D_6) δ 8.42 (dd, *J* = 3.5, 1.8 Hz, 1H), 8.33 (d, *J* = 5.5 Hz, 1H), 7.10 – 7.02 (m, 4H), 6.93 – 6.83 (m, 3H), 6.74 – 6.68 (m, 2H), 6.57 (td, *J* = 7.7, 1.6 Hz, 1H), 6.51 (dd, *J* = 7.7, 1.9 Hz, 2H), 6.24 (d, *J* = 7.9 Hz, 1H), 6.17 (ddd, *J* = 7.2, 5.6, 1.4 Hz, 1H), 6.10 (dd, *J* = 8.5, 3.5 Hz, 1H), 4.85 (d, *J* = 13.4 Hz, 1H), 4.23 (d, *J* = 13.4 Hz, 1H), 3.38 (d, *J* = 13.7 Hz, 1H), 3.04 (d, *J* = 13.6 Hz, 1H), 1.50 (s, 15H). ^{13}C NMR (126 MHz, C_6D_6) δ 165.03, 151.77, 146.11, 145.17, 140.43, 139.16, 131.82, 131.10, 127.37, 126.17, 125.86, 125.67, 121.32, 111.63, 91.23 (d, *J* = 5.5 Hz), 88.55 (d, *J* = 16.9 Hz), 65.64, 53.03 (d, *J* = 12.7 Hz), 46.83, 41.89, 9.01 ppm. **4^{LBn2}** is acutely air sensitive and satisfactory elemental analysis results could not be obtained.

5.4.3 X-ray crystallography

*Refinement Details for **A^{LBn2}** (k90k), **A^{LMePyr}** (v12f), **A^{LPyr2}** (q54i), and **4^{LBn2}** (q35h)*

A single-domain crystal of **A^{LBn2}** (**k90k**) was mounted with Paratone N oil in a MiteGen nylon loop and placed in a cold nitrogen stream on a Bruker SMART APEX CCD Single Crystal Diffraction System at 200K. A complete set of diffraction data (560 1º-wide ω-scan frames with a

scan time of 5 seconds) was collected using graphite-monochromated Mo K_α radiation (λ = 0.71073 Å). X-rays were provided by a fine-focus sealed X-ray tube operated at 50 kV and 35 mA. Preliminary lattice constants were obtained with SMART in the Bruker Apex2 Software Suite.[43] Single domain crystals of $\mathbf{A^{LMePyr}}$ (**v12f**), $\mathbf{A^{LPyr2}}$ (**q54i**) and $\mathbf{4^{LBn2}}$ (**q35h**) were mounted with Paratone N oil in MiteGen nylon loops and placed in a cold nitrogen stream on a Bruker Proteum diffractometer equipped with two CCD detectors (Apex II and Platinum 135) sharing a common MicroStar microfocus Cu rotating anode generator running at 45 mA and 60 kV (Cu Kα = 1.54178 Å). Complete sets of low temperature (200 K) X-ray diffraction data were obtained for all three compounds using monochromated Cu radiation with the Apex II detector [($\mathbf{A^{LPyr2}}$, **q54i**) and ($\mathbf{4^{LBn2}}$, **q35h**)] positioned at 50.0 mm and equipped with Helios multilayer mirror optics or the Platinum 135 detector [$\mathbf{A^{LMePyr}}$**, v12f**] positioned at 80.0 mm and equipped with Helios high-brilliance multilayer mirror optics. Preliminary lattice constants were obtained for all three crystals with SMART in the Bruker Apex2 Software Suite.[1] Totals of 4882 ($\mathbf{A^{LMePyr}}$, **v12f**), 3039 ($\mathbf{A^{LPyr2}}$, **q54i**) and 3930 ($\mathbf{4^{LBn2}}$, **q35h**) 1.0°-wide ω- or ϕ-scan frames were collected with counting times of 4-6 seconds for all three crystals.

Final lattice constants and integrated reflection intensities for all four crystals were produced using SAINT in the Bruker Apex2 Software Suite.[1] Each data set was corrected empirically for variable absorption effects with SADABS[44] using equivalent reflections. The Bruker software package SHELXTL[45] was used to solve each structure using intrinsic direct methods phasing. Final stages of weighted full-matrix least-squares refinement were conducted using F_o^2 data with SHELXTL or the Olex software package[46] equipped with XL.[47] The relevant crystallographic and structure refinement data for all four structures are given in Table C-3.

The final structural model for each structure incorporated anisotropic thermal parameters for all nonhydrogen atoms. Isotropic thermal parameters were used for all hydrogen atoms. Two hydrogen atoms (H8A and H8B) for (**A**$^{\mathbf{LBn2}}$, **k90k**) and four hydrogen atoms (H22A, H22B, H23A and H23B) for (**A**$^{\mathbf{LPyr2}}$, **q54i**) were located from difference Fouriers and included in the structural models as independent isotropic atoms whose parameters were allowed to refine. The remaining ligand nonmethyl hydrogen atoms were fixed at idealized riding model sp^2- or sp^3-hybridized positions with C-H bond lengths of 0.95–0.99 Å. All methyl groups for the Cp* ligand in (**A**$^{\mathbf{LBn2}}$, **k90k**) were incorporated into the structural model as sp^3-hybridized riding-model rigid groups with an idealized "staggered" geometry and a C-H bond length of 0.98 Å. The methyl group for the MeOH solvent molecule of crystallization in (**A**$^{\mathbf{LBn2}}$, **k90k**) and the ligand methyl groups in the other three structures were refined as idealized riding model sp^3-hybridized rigid rotors (with a C-H bond length of 0.98 Å) that were allowed to rotate freely about their C–C bonds in least-squares refinement cycles.

The $[PF_6]^-$ anion in (**A**$^{\mathbf{LBn2}}$, **k90k**) is 53/47 disordered with two orientations about the linear F1–P–F2 linkage and parts of the hexane solvent molecule of crystallization in (**4**$^{\mathbf{LBn2}}$, **q35h**) are 52/48 disordered over two closely separated positions.

5.4.4 Electrochemistry

Electrochemical experiments were carried out in a nitrogen-filled glove box. 0.10 M tetra(n-butylammonium)hexafluorophosphate (Sigma-Aldrich; electrochemical grade) in acetonitrile served as the supporting electrolyte. Measurements were made with a Gamry Reference 600 Plus Potentiostat/Galvanostat using a standard three-electrode configuration. The working electrode was the basal plane of highly oriented pyrolytic graphite (HOPG) (GraphiteStore.com, Buffalo Grove, IL; surface area: 0.09 cm^2), the counter electrode was a platinum wire (Kurt J. Lesker,

Jefferson Hills, PA; 99.99%, 0.5 mm diameter), and a silver wire immersed in electrolyte served as a pseudo-reference electrode (CH Instruments). The reference was separated from the working solution by a Vycor frit (Bioanalytical Systems, Inc.). Ferrocene (Sigma Aldrich; twice-sublimed) was added to the electrolyte solution at the conclusion of each experiment (~1 mM); the midpoint potential of the ferrocenium/ferrocene couple (denoted as $Fc^{+/0}$) served as an external standard for comparison of the recorded potentials. Concentrations of analyte for cyclic voltammetry were typically 1 mM.

5.5 Acknowledgements

The authors thank Dr. Justin Douglas and Sarah Neuenswander for assistance with NMR spectroscopy. This work was supported by the US National Science Foundation through award OIA-1833087. Support for NMR instrumentation was provided by NIH Shared Instrumentation Grants S10OD016360 and S10RR024664 and by the NSF MRI grant CHE-1625923.

5.6 References

[1] Lewis, N. S.; Nocera, D. G., Powering the planet: Chemical challenges in solar energy utilization. *PNAS* U.S.A. **2006**, *103*, 15729-15735.

[2] (a) Rakowski Dubois, M.; Dubois, D. L., Development of Molecular Electrocatalysts for CO_2 Reduction and H2 Production/Oxidation. *Acc. Chem. Res.* **2009**, *42*, 1974-1982. (b) Qiao, J.; Liu, Y.; Hong, F.; Zhang, J., A review of catalysts for the electroreduction of carbon dioxide to produce low-carbon fuels. *Chem. Soc. Rev.* **2014**, *43*, 631-675.

[3] Gassman, P. G.; Macomber, D. W.; Willging, S. M., Isolation and characterization of reactive intermediates and active catalysts in homogeneous catalysis. *J. Am. Chem. Soc.* **1985**, *107*, 2380-2388.

[4] (a) Sconyers, D. J.; Blakemore, J. D., Distinguishing between homogeneous and heterogeneous hydrogen-evolution catalysis with molecular cobalt complexes. *Chem. Commun.* **2017,** *53*, 7286-7289. (b) Kumar, A.; Lionetti, D.; Day, V. W.; Blakemore, J. D., Redox-Inactive Metal Cations Modulate the Reduction Potential of the Uranyl Ion in Macrocyclic Complexes. *J. Am. Chem. Soc.* **2020,** *142*, 3032-3041.

[5] (a) Costentin, C.; Savéant, J.-M., Concepts and tools for mechanism and selectivity analysis in synthetic organic electrochemistry. *PNAS* U S A **2019**, *116*, 11147-11152. (b) Lexa, D.; Sayeant, J. M.; Zickler, J., Electrochemistry of vitamin B12. 5. Cyanocobalamins. *J. Am. Chem. Soc.* **1980**, *102*, 2654-2663. (c) Grass, V.; Lexa, D.; Momenteau, M.; Savéant, J.-M., Reductive Electrochemistry of Rhodium Porphyrins. Disproportionation of Intermediary Oxidation States. *J. Am. Chem. Soc.* **1997**, *119*, 3536-3542. (d) Amatore, C.; Gareil, M.; Savéant, J. M., Homogeneous vs. heterogeneous electron transfer in electrochemical reactions: Application to the electrohydrogenation of anthracene and related reactions. *J. Electroanal. Chem. Interfacial Electrochem.* **1983**, *147*, 1-38.

[6] (a) Boyd, E. A.; Lionetti, D.; Henke, W. C.; Day, V. W.; Blakemore, J. D., Preparation, Characterization, and Electrochemical Activation of a Model [Cp*Rh] Hydride. *Inorg. Chem.* **2018**, *58*, 3606-3615. (b)

Hopkins, J. A.; Lionetti, D.; Day, V. W.; Blakemore, J. D., Chemical and Electrochemical Properties of [Cp*Rh] Complexes Supported by a Hybrid Phosphine-Imine Ligand. *Organometallics* **2019**, *38*, 1300-1310.

[7] (a) Ward, M. D.; McCleverty, J. A., Non-innocent behaviour in mononuclear and polynuclear complexes: consequences for redox and electronic spectroscopic properties. *J. Chem. Soc., Dalton Trans.* **2002**, 275-288. (b) Chirik, P. J.; Wieghardt, K., Radical Ligands Confer Nobility on Base-Metal Catalysts. *Science* **2010**, *327*, 794-795. (c) Kaim, W.; Schwederski, B., Non-innocent ligands in bioinorganic chemistry—An overview. *Coord. Chem. Rev.* **2010**, *254*, 1580-1588. (d) Lyaskovskyy, V.; de Bruin, B., Redox Non-Innocent Ligands: Versatile New Tools to Control Catalytic Reactions. *ACS Catalysis* **2012**, *2*, 270-279. (e) Berben, L. A.; de Bruin, B.; Heyduk, A. F., Non-innocent ligands. *Chem. Commun*. **2015**, *51*, 1553-1554. (f) Zell, T.; Milstein, D., Hydrogenation and Dehydrogenation Iron Pincer Catalysts Capable of Metal–Ligand Cooperation by Aromatization/Dearomatization. *Acc. Chem. Res*. **2015**, *48*, 1979-1994.

[8] (a) Kaes, C.; Katz, A.; Hosseini, M. W., Bipyridine: The Most Widely Used Ligand. A Review of Molecules Comprising at Least Two 2,2‘-Bipyridine Units. *Chem. Rev.* **2000**, *100*, 3553-3590. (b) Kölle, U.; Grätzel, M., Metallorganische Rhodium(III)-Komplexe als Homogenkatalysatoren für die Photoreduktion von Protonen zu Wasserstoff an kolloidalem TiO_2. *Angew. Chem.* **1987**, *99*, 572–574. (c) Kölle, U.; Grätzel, M., Organometallic Rhodium(III) Complexes as Catalysts for the Photoreduction of Protons to Hydrogen on Colloidal TiO_2. *Angew. Chem. Int. Ed. Engl.* **1987**, *26*, 567 –570. (d) Wang, W.-H.; Hull, J. F.; Muckerman, J. T.; Fujita, E.; Himeda, Y., Second-coordination-sphere and electronic effects enhance iridium(III)-catalyzed homogeneous hydrogenation of carbon dioxide in water near ambient temperature and pressure. *Energy Environ. Sci*. **2012**, *5*, 7923-7926. (e) Chardon-Noblat, S.; Cosnier, S.; Deronzier, A.; Vlachopoulos, N., Electrochemical properties of $[(C_5Me_5)Rh^{III}(L)Cl]^+$ complexes (L = 2,2′-bipyridine or 1,10-phenanthroline derivatives) in solution in related polypyrrolic

films. Application to electrocatalytic hydrogen generation. *J. Electroanal. Chem.* **1993**, *352*, 213-228. (f) Caix, C.; Chardon-Noblat, S.; Deronzier, A.; Moutet, J.-C.; Tingry, S., (Pentamethylcyclopentadienyl)(polypyridyl) rhodium and iridium complexes as electrocatalysts for the reduction of protons to dihydrogen and the hydrogenation of organics. *J. Organomet. Chem.* **1997**, *540*, 105-111. (g) Blakemore, J. D.; Gupta, A.; Warren, J. J.; Brunschwig, B. S.; Gray, H. B., Noncovalent Immobilization of Electrocatalysts on Carbon Electrodes for Fuel Production. *J. Am. Chem. Soc.* **2013**, *135*, 18288-18291. (h) Brintzinger, H.; Bercaw, J. E., Bis(pentamethylcyclopentadienyl)titanium(II). Isolation and reactions with hydrogen, nitrogen, and carbon monoxide. *J. Am. Chem. Soc.* **1971**, *93*, 2045-2046.

[9] (a) Gibson, V. C.; Redshaw, C.; Solan, G. A., Bis(imino)pyridines: Surprisingly Reactive Ligands and a Gateway to New Families of Catalysts. *Chem. Rev.* **2007**, *107*, 1745-1776. (b) Small, B. L.; Brookhart, M., Iron-Based Catalysts with Exceptionally High Activities and Selectivities for Oligomerization of Ethylene to Linear α-Olefins. *J. Am. Chem. Soc.* **1998**, *120*, 7143-7144. (c) Bennett, A. M. A. Iron catalyst for the polymerization of olefins. US 6214761 B1, 2001. (d) J. P. Britovsek, G.; C. Gibson, V.; J. McTavish, S.; A. Solan, G.; J. P. White, A.; J. Williams, D.; J. P. Britovsek, G.; S. Kimberley, B.; J. Maddox, P., Novel olefin polymerization catalysts based on iron and cobalt. *Chem. Commun.* **1998**, 849-850. (e) Small, B. L., Discovery and Development of Pyridine-bis(imine) and Related Catalysts for Olefin Polymerization and Oligomerization. *Acc. Chem. Res.* **2015**, *48*, 2599-2611. (f) Chirik, P. J., Iron- and Cobalt-Catalyzed Alkene Hydrogenation: Catalysis with Both Redox-Active and Strong Field Ligands. *Acc. Chem. Res.* **2015**, *48*, 1687-1695. (g) Chirik, P. J., Carbon–Carbon Bond Formation in a Weak Ligand Field: Leveraging Open-Shell First-Row Transition-Metal Catalysts. *Angew. Chem. Int. Ed.* **2017**, *56*, 5170-5181.(h) Obligacion, J. V.; Chirik, P. J., Earth-abundant transition metal catalysts for alkene hydrosilylation and hydroboration. *Nat. Rev. Chem.* **2018**, *2*, 15-34. (i) Trovitch, R. J., The Emergence of Manganese-Based Carbonyl Hydrosilylation Catalysts. *Acc. Chem. Res.* **2017**, *50*, 2842-

2852. (j) Nückel, S.; Burger, P., Transition-Metal Complexes with Sterically Demanding Ligands: Facile Thermal Intermolecular C•H Bond Activation in a Square-Planar IrI Complex. *Angew. Chem. Int. Ed.* **2003**, *42*, 1632-1636. (k) Tang, J.; Gamez, P.; Reedijk, J., Efficient [bis(imino)pyridine-iron]-catalyzed oxidation of alkanes. *Dalton Trans.* **2007**, 4644-4646. (l) Britovsek, G. J. P.; England, J.; Spitzmesser, S. K.; White, A. J. P.; Williams, D. J., Synthesis of iron(ii), manganese(ii) cobalt(ii) and ruthenium(ii) complexes containing tridentate nitrogen ligands and their application in the catalytic oxidation of alkanes. *Dalton Trans.* **2005**, 945-955. (m) Cui, P.; Wang, Q.; McCollom, S. P.; Manor, B. C.; Carroll, P. J.; Tomson, N. C., Ring-Size-Modulated Reactivity of Putative Dicobalt-Bridging Nitrides: C−H Activation versus Phosphinimide Formation. *Angew. Chem. Int. Ed.* **2017**, *56*, 15979-15983. (n) Bart, S. C.; Lobkovsky, E.; Chirik, P. J., Preparation and Molecular and Electronic Structures of Iron(0) Dinitrogen and Silane Complexes and Their Application to Catalytic Hydrogenation and Hydrosilation. *J. Am. Chem. Soc.* **2004**, *126*, 13794-13807. (o) Margulieux, G. W.; Bezdek, M. J.; Turner, Z. R.; Chirik, P. J., Ammonia Activation, H2 Evolution and Nitride Formation from a Molybdenum Complex with a Chemically and Redox Noninnocent Ligand *J. Am. Chem. Soc.* **2017**, *139*, 6110-6113. (p) Manuel, T. D.; Rohde, J.-U., Reaction of a Redox-Active Ligand Complex of Nickel with Dioxygen Probes Ligand-Radical Character. *J. Am. Chem. Soc.* **2009**, *131*, 15582-15583. (q) Badiei, Y. M.; Siegler, M. A.; Goldberg, D. P., O2 Activation by Bis(imino)pyridine Iron(II)−Thiolate Complexes. *J. Am. Chem. Soc.* **2011**, *133*, 1274-1277. (r) Lau, K.-C.; Jordan, R. F., Reactivity of (Pyridine-Diimine)Fe Alkyl Complexes with Carbon Dioxide. *Organometallics* **2016**, *35*, 3658-3666. (s) Rummelt, S. M.; Zhong, H.; Korobkov, I.; Chirik, P. J., Iron-Mediated Coupling of Carbon Dioxide and Ethylene: Macrocyclic Metallalactones Enable Access to Various Carboxylates. *J. Am. Chem. Soc.* **2018**, *140*, 11589-11593.

[10] Bezdek, M. J.; Chirik, P. J., Pyridine(diimine) Chelate Hydrogenation in a Molybdenum Nitrido Ethylene Complex. *Organometallics* **2019**, *38*, 1682-1687.

[11] (a) Chirik, P. J.; Wieghardt, K., Radical Ligands Confer Nobility on Base-Metal Catalysts. *Science* **2010**, *327*, 794-795. (b) Chirik, P. J., Preface: Forum on Redox-Active Ligands. I*norg. Chem.* **2011**, *50*, 9737-9740. (e) Römelt, C.; Weyhermüller, T.; Wieghardt, K., Structural characteristics of redox-active pyridine-1,6-diimine complexes: Electronic structures and ligand oxidation levels. *Coord. Chem. Rev*. **2019**, *380*, 287-317.

[12] Kaim, W.; Reinhardt, R.; Waldhor, E.; Fiedler, J., Electron transfer and chloride ligand dissociation in complexes $[(C_5Me_5)ClM(bpy)]^+/[(C_5Me_5)M(bpy)]^n$ (M=Co, Rh, Ir; n=2+,+,0,-): A combined electrochemical and spectroscopic investigation. *J. Organomet. Chem.* **1996,** 524, 195-202

[13] Lionetti, D.; Day, V. W.; Blakemore, J. D., Synthesis and Electrochemical Properties of Half-Sandwich Rhodium and Iridium Methyl Complexes. *Organometallics* **2017**, *36*, 1897-1905.

[14] (a) Gore-Randall, E.; Irwin, M.; Denning, M. S.; Goicoechea, J. M., Synthesis and Characterization of Alkali-Metal Salts of 2,2′- and 2,4′-Bipyridyl Radicals and Dianions. *Inorg. Chem.* **2009**, *48*, 8304-8316. (b) Dallinger, R. F.; Woodruff, W. H., Time-resolved resonance Raman study of the lowest ($d\pi^*$,^{3}CT) excited state of tris(2,2'-bipyridine)ruthenium(II). *J. Am. Chem. Soc*. **1979**, *101*, 4391-4393. (c) Creutz, C., Bipyridine radical ions. *Comments Inorg. Chem.* **1982,** *1*, 293-311.

[15] Lionetti, D.; Day, V. W.; Lassalle-Kaiser, B.; Blakemore, J. D., Multiple binding modes of an unconjugated bis(pyridine) ligand stabilize low-valent [Cp*Rh] complexes. *Chem. Commun.* **2018**, *54*, 1694-1697.

[16] (a) Nakai, H.; Jeong, K.; Matsumoto, T.; Ogo, S., Catalytic C–F Bond Hydrogenolysis of Fluoroaromatics by $[(\eta^5\text{-}C_5Me_5)Rh^I(2,2'\text{-bipyridine})]$. *Organometallics* **2014**, *33*, 4349-4352. (b) Blakemore, J. D.; Hernandez, E. S.; Sattler, W.; Hunter, B. M.; Henling, L. M.; Brunschwig, B. S.; Gray, H. B., Pentamethylcyclopentadienyl rhodium complexes. *Polyhedron* **2014**, *84*, 14-18. (c) Lionetti, D.; Day, V. W.; Blakemore, J. D., Synthesis and Electrochemical Properties of Half-Sandwich Rhodium and Iridium Methyl Complexes. *Organometallics* **2017**, *36*, 1897-1905.

[17] (a) Dewar, M. J. S.; Ford, G. P., Relationship between olefinic .pi. complexes and three-membered rings. *J. Am. Chem. Soc.* **1979**, *101*, 783-791. (b) Chatt, J.; Duncanson, L. A., Olefin co-ordination compounds. Part III. Infrared spectra and structure: attempted preparation of acetylene complexes. *J. Chem. Soc.* **1953**, 2939-2947.

[18] Nicholson, R. S.; Shain, I., Theory of Stationary Electrode Polarography. Single Scan and Cyclic Methods Applied to Reversible, Irreversible, and Kinetic Systems. *Anal. Chem.* **1964**, *36*, 706-723.

[19] Saveant, J. Elements of Molecular and Biomolecular Electrochemistry, 1st ed.; Wiley, 2006.

[20] Lionetti, D.; Day, V. W.; Blakemore, J. D., Structural and chemical properties of half-sandwich rhodium complexes supported by the bis(2-pyridyl)methane ligand. *Dalton Trans.* **2019**, *48*, 12396-12406.

[21] (a) Sommerfeld, N. S.; Gülzow, J.; Roller, A.; Cseh, K.; Jakupec, M. A.; Grohmann, A.; Galanski, M.; Keppler, B. K., Antiproliferative Copper(II) and Platinum(II) Complexes with Bidentate N,N-Donor Ligands. *Chem. Eur. J.* **2017**, *2017*, 3115-3124. (b) Elie, M.; Weber, M. D.; Di Meo, F.; Sguerra, F.; Lohier, J.-F.; Pansu, R. B.; Renaud, J.-L.; Hamel, M.; Linares, M.; Costa, R. D.; Gail-lard, S., Role of the Bridging Group in Bis-Pyridyl Ligands: Enhancing Both the Photo- and Electroluminescent Features of Cationic (IPr)CuI Complexes. *Chem. Eur. J.* **2017**, *23*, 16328-16337. (c) Mohr, F.; Binfield, S. A.; Fettinger, J. C.; Vedernikov, A. N., A Practical, Fast, and High-Yielding Aziridination Procedure Using Simple Cu(II) Complexes Containing N-Donor Pyridine-Based Ligands. *J. Org. Chem.* **2005**, *70*, 4833-4839.

[22] Canty, A. J.; Chaichit, N.; Gatehouse, B. M.; George, E. E.; Hayhurst, G., Coordination chemistry of methylmercury(II). Synthesis, ^{1}H NMR, and crystallographic studies of cationic complexes of MeHg(II) with ambidentate and polydentate ligands containing pyridyl and N-substituted imidazolyl donors and involving unusual coordination geometries. *Inorg. Chem.* **1981**, *20*, 2414-2422.

[23] Sommerfeld, N. S.; Gülzow, J.; Roller, A.; Cseh, K.; Jakupec, M. A.; Grohmann, A.; Galanski, M.; Keppler, B. K., Antiproliferative Copper(II) and Platinum(II) Complexes with Bidentate N,N-Donor Ligands. *Chem. Eur. J.* **2017**, *2017*, 3115-3124.

[24] Byers, P. K.; Canty, A. J., Synthetic routes to methylpalladium(II) and dimethylpalladium(II) chemistry and the synthesis of new nitrogen donor ligand systems. *Organometallics* **1990**, *9*, 210-220.

[25] Jones, M. R.; Fast, C. D.; Schley, N. D., Iridium-Catalyzed sp^3 C–H Borylation in Hydrocarbon Solvent Enabled by 2,2′-Dipyridylarylmethane Ligands. *J. Am. Chem. Soc*. **2020,** *142*, 6488-6492.

[26] Rudolph, M., Digital simulations on unequally spaced grids.: Part 2. Using the box method by discretisation on a transformed equally spaced grid. *J. Electroanal. Chem.* **2003**, *543*, 23-39.

[27] (a) Canty, A. J.; Chaichit, N.; Gatehouse, B. M.; George, E . E.; Hayhurst, G., Coordination chemistry of methylmercury(II). Synthesis, ^{1}H NMR, and crystallographic studies of cationic complexes of MeHg(II) with ambidentate and polydentate ligands containing pyridyl and N-substituted imidazolyl donors and involving unusual coordination geometries. *Inorg. Chem.*, **1981**, *20*, 2414–2422. (b) Byers, P. K.; Canty, A. J., Synthetic routes to methylpalladium(II) and dimethylpalladium(II) chemistry and the synthesis of new nitrogen donor ligand systems. *Organometallics*, **1990**, *9*, 210–220. (c) Mohr, F.; Binfield, S. A.; Fettinger, J. C.; Vedernikov, A. N., A Practical, Fast, and High-Yielding Aziridination Procedure Using Simple Cu(II) Complexes Containing N-Donor Pyridine-Based Ligands. *J. Org. Chem.*, **2005**, *70*, 4833–4839.

[28] Vedernikov, N.; Miftakhov, R.; Borisoglebski, S. V.; Caulton, K. G.; Solomonov, B. N., Condensation of 2-Pyridylmethyllithium Nucleophiles and Pyridine Electrophiles as a Convenient Synthetic Route to Polydentate Chelating N-Donor Ligands. *Chem. Heterocycl. Compd.* **2002**, *38*, 406-416.

[29] Golden, J. H.; Facendola, J. W.; Sylvinson M. R, D.; Baez, C. Q.; Djurovich, P. I.; Thompson, M. E., Boron Dipyridylmethene (DIPYR) Dyes: Shedding Light on Pyridine-Based Chromophores. *J. Org. Chem.* **2017**, *82*, 7215-7222.

[30] Kumari, N.; Dey, N.; Jha, S.; Bhattacharya, S., Ratiometric, Reversible, and Parts per Billion Level Detection of Multiple Toxic Transition Metal Ions Using a Single Probe in Micellar Media. *ACS App. Mat. Interfaces* **2013**, *5*, 2438-2445.

[31] White, C.; Yates, A.; Maitlis, P. M., (η^5-Pentamethylcyclopentadienyl)Rhodium and -Iridium Compounds. *Inorg. Synth.* **1992**, *29*, 228−234

[32] Mantell, M. A.; Kampf, J. W.; Sanford, M., Improved Synthesis of $[Cp^RRhCl_2]_2$ Complexes. *Organometallics* **2018**, *37*, 3240-3242.

[33] Nutton, A.; Bailey, P. M.; Maitlis, P. M., Pentamethylcyclopentadienyl-rhodium and -iridium complexes. Part 29. Syntheses and X-ray structure determinations of $[\{Rh(C_5Me_5)\}_2(OH)_3]$ $OH\cdot 11H_2O$ and $[\{lr(C_5Me_5)\}_2(OH)_3]O_2CMe\cdot 14H_2O$ and related complexes. *J. Chem. Soc., Dalton Trans.* **1981**, 1997−2002.

[34] Dadci, L.; Elias, H.; Frey, U.; Hoernig, A.; Koelle, U.; Merbach, A. E.; Paulus, H.; Schneider, J. S., .pi.-Arene Aqua Complexes of Cobalt, Rhodium, Iridium, and Ruthenium: Preparation, Structure, and Kinetics of Water Exchange and Water Substitution. *Inorg. Chem.* **1995**, *34*, 306-315.

[35] Hammett, L. P., The Effect of Structure upon the Reactions of Organic Compounds. Benzene Derivatives. *J. Am. Chem. Soc.* **1937**, *59*, 96-103.

[36] (a) Ševčík, A., Oscillographic polarography with periodical triangular voltage. *Collect. Czech. Chem. Commun*. **1948**, *13*, 349-377 (b) Randles, J. E. B., A cathode ray polarograph. Part II.—The current-voltage curves. *Trans. Faraday Soc.* **1948**, *44*, 327-338.

[37] Ashford, D. L.; Gish, M. K.; Vannucci, A. K.; Brennaman, M. K.; Templeton, J. L.; Papanikolas, J. M.; Meyer, T. J., Molecular Chromophore–Catalyst Assemblies for Solar Fuel Applications. *Chem. Rev.* **2015**, *115*, 13006-13049.

[38] (a) Lewis, N. S.; Nocera, D. G., Powering the planet: Chemical challenges in solar energy utilization. *PNAS* U.S.A. **2006**, *103*, 15729-15735. (b) Young, K. J.; Martini, L. A.; Milot, R. L.; Snoeberger III,

R. C.; Batista, V. S.; Schmuttenmaer, C. A.; Crabtree, R. H.; Brudvig, G. W., Light-driven water oxidation for solar fuels. *Coord. Chem. Rev*. **2012**, *256*, 2503−2520.

[39] (a) Nichols, A. W.; Machan, C. W., Secondary-Sphere Effects in Molecular Electrocatalytic CO_2 Reduction. *Frontiers in Chemistry* **2019**, *7*. (b) Haviv, E.; Azaiza-Dabbah, D.; Carmieli, R.; Avram, L.; Martin, J. M. L.; Neumann, R., A Thiourea Tether in the Second Coordination Sphere as a Binding Site for CO2 and a Proton Donor Promotes the Electrochemical Reduction of CO_2 to CO Catalyzed by a Rhenium Bipyridine-Type Complex. *J. Am. Chem. Soc*. **2018**, *140*, 12451-12456. (c) Rotundo, L.; Garino, C.; Priola, E.; Sassone, D.; Rao, H.; Ma, B.; Robert, M.; Fiedler, J.; Gobetto, R.; Nervi, C., Electrochemical and Photochemical Reduction of CO_2 Catalyzed by Re(I) Complexes Carrying Local Proton Sources. *Organometallics* **2019**, *38*, 1351-1360.

[40] Geiger, W. E., Organometallic Electrochemistry: Origins, Development, and Future. *Organometallics* **2007**, *26*, 5738-5765.

[41] Fulmer, G. R.; Miller, A. J. M.; Sherden, N. H.; Gottlieb, H. E.; Nudelman, A.; Stoltz, B. M.; Bercaw, J. E.; Goldberg, K. I., NMR Chemical Shifts of Trace Impurities: Common Laboratory Solvents, Organics, and Gases in Deuterated Solvents Relevant to the Organometallic Chemist. *Organometallics* **2010**, *29*, 2176-2179.

[42] (a) Harris, R. K.; Becker, E. D.; Cabral De Menezes, S. M.; Goodfellow, R.; Granger, P., NMR nomenclature. Nuclear spin properties and conventions for chemical shifts (IUPAC Recommendations 2001) *Pure Appl. Chem.* **2001**, *73*, 1795– 1818. (b) Harris, R. K.; Becker, E. D.; Cabral De Menezes, S. M.; Granger, P.; Hoffman, R. E.; Zilm, K. W., Further conventions for NMR shielding and chemical shifts (IUPAC Recommendations 2008). *Pure Appl. Chem.* **2008**, *80*, 59−84.

[43] *APEX2, Version 2 User Manual, M86-E01078*. Bruker Analytical X-ray Systems: Madison, WI, June 2006.

[44] Sheldrick, G. M. SADABS (version 2008/1): Program for Absorption Correction for Data from Area Detector Frames, University of Göttingen2008.

[45] Sheldrick, G., SHELXT - Integrated space-group and crystal-structure determination. Acta Crystallogr., *Sect. A: Found. Crystallogr.* **2015,** *71*, 3-8.

[46] Dolomanov, O. V.; Bourhis, L. J.; Gildea, R. J.; Howard, J. A. K.; Puschmann, H., OLEX2: a complete structure solution, refinement and analysis program. *J. Appl. Crystallogr.* **2009,** 42, 339-341.

[47] Sheldrick, G., Crystal structure refinement with SHELXL. Acta Crystallogr., Sect. C: Cryst. *Struct. Commun.* **2015,** 71, 3-8.

Chapter 6

Electrochemical and Electrochemical Studies of [Cp*Rh] Complexes Supported by Monosubstituted bis(2-pyridyl)methane Ligands

6.1 Introduction

Half-sandwich rhodium complexes supported by pentamethylcyclopentadienyl (Cp*) as well as additional chelating bidentate ligands have proven attractive for the study of electron transfer and management of protons during redox transformations.[1] In particular, [Cp*Rh] (Cp* = pentamethylcyclopentadienyl) complexes have garnered attention of small molecule activation for dihydrogen (H_2) evolution[2] and hydrogenation of biological cofactors.[3] Understanding the redox chemistry of the met complexes involved in these transformation is of particular interest because such complexes are commonly used for reductive catalysis relevant to energy-relevant transformations. Consequently, our group has recently been exploring the chemical and electrochemical properties of a family of [Cp*Rh] complexes bearing a variety of κ^2-bidentate ligands; we have found that the identity of the bidentate ligand significantly affects the reactivity of the complexes.[4,5,6,7]

Non-innocent ligands such as 2,2′-bipyridyl (bpy) often promote unique reactivity upon reduction. The bpy ligand has readily accessible lowest unoccupied molecular orbital (LUMO) that can stabilize metal centers by accepting electron density[8] by π-backbonding or formal electron transfer to generate $bpy^{\bullet-}$ or bpy^{2-} species.[9] Reduction studies of [Cp*Rh] complexes bearing the κ^2-bidentate bpy ligand have shown that upon reduction of Rh(III) to the formally Rh(I) oxidation state, there is significant delocalization of electron density from Rh into the π system of bpy.[10] Inspired by this observation with [Cp*Rh] complexes bearing bpy, our group has also utilized a similar ligand framework, dimethyl-2,2′-dipyridylmethane (Me_2dpma), to modulate the π-backbonding characteristics of the pyridyl based frameworks while retaining the ability to stabilize low-valent metal centers.[4] The Me_2dpma ligand is closely related to the conjugated bpy ligand, but the dpma framework features two unconjugated pyridine donors linked by a methylene bridge.[4]

The disruption in conjugation introduced in the Me_2dpma ligand results in π* orbitals that are less readily accessible for electron transfer or π-backbonding in comparison to those i the analogous bpy scaffolds.

Previous studies from our group have interrogated the redox chemistry of the [Cp*Rh] complex bearing the κ^2-Me_2dpma ligand.[4] Chemical reduction of the [Cp*Rh] κ^2-Me_2dpma by one-electron indicated the possible stabilizing nature of the Me_2dpma framework that enabled isolation of a stable κ^2-Me_2dpma Rh(II) species. However, chemical preparation of the two-electron reduced species (to the formally Rh(I) oxidation state) promoted a chemical rearrangement in which one pyridyl ring flips to facially coordinate to the metal center in an η^2 mode.[4] Further electrochemical studies by our group with analogous dibenzyl (Bn_2dpma)-, methyl,methylpyrenyl- (MePyrdpma)-, and bis(methylpyrenyl) (Pyr_2dpma)-substituted dpma ligated [Cp*Rh] complexes have further illustrated the unique electrochemical properties of the dpma framework.[6] The cyclic voltammetry (CV) studies of these substituted complexes reveal similar electrochemical behaviour as observed for Me_2dpma in which there are two sequential one-electron transfers corresponding to the Rh(III)/Rh(II) and Rh(II)/Rh(I) cycling. The CV results and modelling of the voltammetry for these complexes enabled assignment of the unique electrochemical−chemical (EC) process observed as the transient electrogenerated Rh(I) κ^2-R_2dpma complex reacts to form a transient, formally Rh(I) species that rearranges to the form bearing the facially coordinated η^2 pyridine motif. Notably, we found that the steric bulk of the substituents in the R_2dpma system influenced first-order rate constants associated with the chemical step of the noted EC process (k^+) and that the bulkier ligands resulted in lower values of k^+. Those changes were marked as the value for all the derivatives span over one order of magnitude.

In this system, we can observe and assign the EC process as involving reorientation of the ligand, making it an attractive model for studying metal complexes that undergo redox-induced reactions. Our prior work with this system has interrogated the influence that the ligand substituents positioned on the methylene bridge play in the kinetics of the EC ligand rearrangement. However, we wondered what the influence the addition of substituents on the pyridyl motifs could have on the reactivity and electrochemical properties of this system. We hypothesized that the non-symmetric analogue of these R_2dpma ligand frameworks could result in unique the chemical reactivity, particularly with regards to the reactivity following $2e^-$ reduction. Desymmetrization of the Me_2dpma framework by the addition of a substituent on a single pyridyl moiety presents a situation in which the ligand would have the choice to rearrange (flip) to bind either the substituted or unsubstituted pyridyl ring in an η^2 fashion to stabilize the formally Rh(I) center. Thus, studies of the non-symmetric system would serve to probe the role that the addition of substituents, spanning electron-donating and -withdrawing natures, to a pyridyl motif have in tuning the structural and electrochemical properties of [Cp*Rh] complexes bearing the ligands. Investigation of non-symmetric dpma ligands could provide new insight into charge stabilization processes engendered by non-innocent ligand frameworks often observed in molecular catalysis.

Here, we report the synthesis and characterization of a two new **Me_2dpma^R** ligands featuring either an electron-donating or an elecron-withdrawing substituent on a single pyridyl moiety at the *para* position in the pyridine ring and their [Cp*Rh] complexes (Figure 6.1). We find that the novel ligands **Me_2dpma^{OMe}** and **Me_2dpma^{CF3}** can be readily synthesized and that the core Me_2dpma framework tolerates the addition of both an electron-donating and an electron-withdrawing substituent. Cyclic voltammetry studies indicate that **1^{OMe}** undergoes a reduction from Rh(II) to Rh(I) that results in a ligand rearrangement in which a single pyridyl moiety binds to the Rh center

in a η^2 fashion. Chemical reduction of $\mathbf{A^{OMe}}$ with Na(Hg) results in ligand rearrangement, as evidenced by the isolation and characterization of the formally Rh(I) complex, $\mathbf{3^{OMe}}$, confirms that the reactivity upon reduction is retained with the addition of an electron-donating substituent. Comparatively, the cyclic voltammetry of $\mathbf{1^{CF3}}$ displays two quasireversible couples, indicating that there is a lack of ligand rearrangement upon two-electron electrochemical reduction. However, the chemical reduction of $\mathbf{1^{CF3}}$ also engenders a ligand rearrangement confirmed by isolation and characterization of the formally Rh(I) complex, $\mathbf{3^{CF3}}$. Isolation of the two-electron reduced species confirms that the electron-withdrawing nature of the $-CF_3$ substituent promotes similar reactivity, but the ligand rearrangement, at least under synthetic condition at longer timescales, as is presumably too slow to observe on the cyclic voltammetry timescale. Solid-state structures and ^{1}H NMR characterization of $\mathbf{3^{OMe}}$ and $\mathbf{3^{CF3}}$ support that the substituted pyridyl ring in the non-symmetric $\mathbf{Me_2dpma^R}$ ligand flips preferentially to bind the substituted pyridyl moiety in a η^2-fashion. Taken together, our findings show that non-symmetric dpma ligands spanning a wide range of electron-donating and -withdrawing ability can stabilize multiple oxidation states and thus could be useful for the development of more complex catalytic systems.

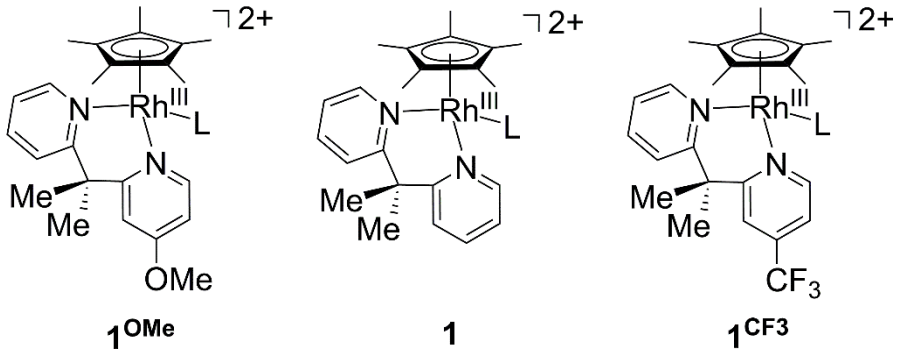

$\mathbf{1^{OMe}}$ $\mathbf{1}$ $\mathbf{1^{CF3}}$

Figure 6.1. Non-symmetric $\mathbf{1^R}$ and symmetric **1** complexes (L = $NCCH_3$).

6.2 Results and Discussion

The mono-substituted, non-symmetric dimethyldipyridylmethane (**Me$_2$dpma**) ligands were synthesized based on modified literature procedures[11] utilizing the bis(2-pyridyl)methane[12] (**dpma**) starting material. The **Me$_2$dpma^{CF3}** bidentate ligand was synthesized based on a modified literature procedure where we synthesized **dpma^{CF3}** by addition of nBuLi to 2-methylpyridine followed by addition of 2-fluoro-4-trifluoromethylpyridine and purified via column chromatography. Treatment of **dpma^{CF3}** with sequential additions of nBuLi and MeI and purification by vacuum distillation yields the doubly methylated **Me$_2$dpma^{CF3}** ligand. The **Me$_2$dpma^{OMe}** ligand was synthesized in an analogous manner apart from use of the 2-fluoro-4-methoxypyridine starting material.[13] This synthetic approach highlights that dpma ligands can be prepared via modular synthetic methods specifically, electron-donating and -withdrawing substituents can be installed on pyridyl rings to break the symmetry of previously studied **dpma** ligands.[11,12,14,15]

The dimeric [Cp*RhCl$_2$]$_2$ complex[21] is useful for the straightforward synthesis of [Cp*Rh] complexes with chelating bidentate ligands.[16] The complexes **A^R** (Scheme 6.1) were generated via the addition of 1.0 equivalent of $AgPF_6$ to 0.5 equivalents of [Cp*RhCl$_2$]$_2$ generating an orange reaction solution and AgCl precipitate. Following this reaction, 1.05 equivalent of the desired **Me$_2$dpma^R** chelating ligand was added to yield the [Cp*Rh] complexes **A^R** were obtained as stable orange solids suitable for characterization. Notably, complexation of the **Me$_2$dpma^{CF3}** ligand results in a mixture of non-isolable **A^{CF3}** and non-ligated ligand (see Appendix D, Figure D28). Purification attempts by crystallization of this solution yield a mixture of ligated and non-ligated products thus experimental work performed with the pure solvento complex, **1^{CF3}** (*vide infra*).

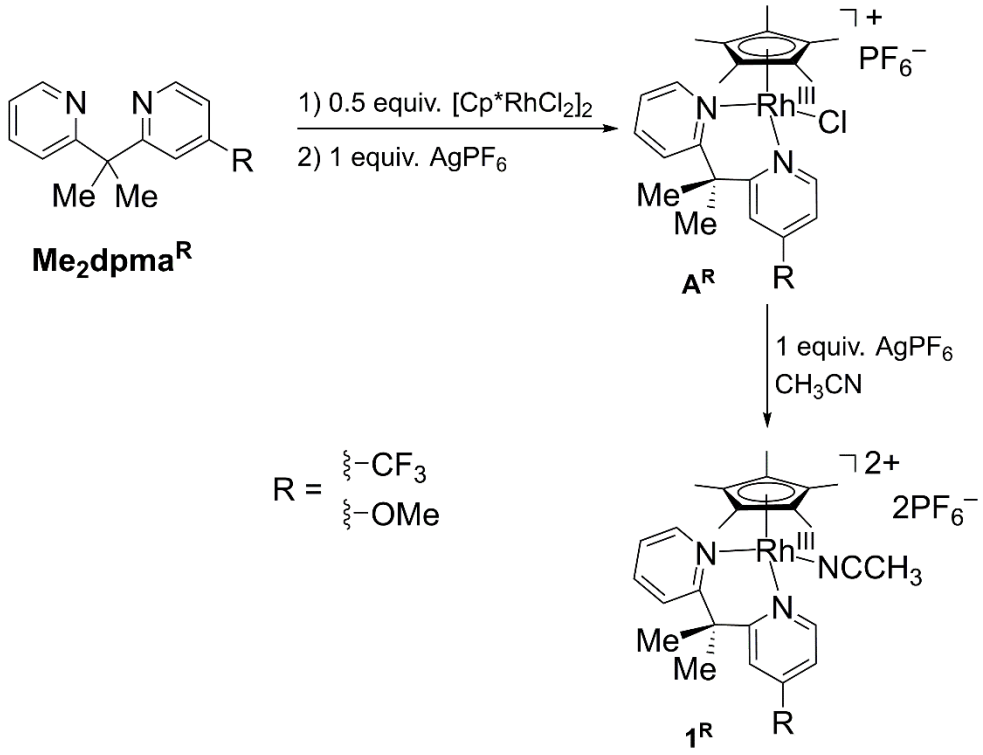

Scheme 6.1. Synthesis of $\mathbf{A^R}$ complexes.

Following isolation of the $\mathbf{A^R}$ complexes, characterization of $\mathbf{A^R}$ by proton nuclear magnetic resonance (^{1}H NMR) was used to confirm chelation of the non-symmetric dpma ligands to rhodium. The novel complexes $\mathbf{A^{OMe}}$ and $\mathbf{A^{CF3}}$ display a strong singlet at ca. 1.60 ppm associated with the freely rotating Cp* ligand. This resonance integrates to fifteen equivalent protons in respect to the ortho pyridyl protons corresponding to the κ^2-dpma ligand (see Appendix D, Figures D22 and D28). The ^{31}P NMR spectra of the complexes $\mathbf{A^R}$ reveal a septet indicating the presence of the hexafluorophosphate counteranion ($^1J_{P,F} \approx 706$ Hz). The ^{1}H NMR spectrum for $\mathbf{A^R}$ reveals two unique singlets integrating to 3H each ($\mathbf{A^{OMe}}$ at 2.02 and 1.87 ppm, $\mathbf{A^{CF3}}$ at 2.11 and 1.92 ppm) corresponding to the chemically inequivalent protons associated with the freely rotating methyl substituents. These inequivalent singlets contrast with the single ^{1}H NMR resonance for $\mathbf{A^{CF3}}$ and $\mathbf{A^{OMe}}$ at 1.84 ppm and 2.02 ppm respectively (integrating to 6H) associated methyl substituents on the free $\mathbf{Me_2dpma^R}$ ligands. The ^{1}H NMR spectrum for $\mathbf{A^{OMe}}$ reveals a unique singlet at 3.39 ppm

(integrates to 3H) associated with the methoxy substituent on the κ^2 ligand framework. The ^{1}H NMR of the free **Me$_2$dpma^{OMe}** ligand methoxy moiety appears at 3.04 ppm, which shifts downfield upon complexation. Taken together, these NMR data confirm the presence of the non-symmetric bidentate dpma ligands on the [Cp*Rh] for the new complexes.

Vapor diffusion of diethyl ether (Et_2O) into an acetonitrile (CH_3CN) solution containing **A^{OMe}** afforded orange crystals suitable for X-ray diffraction (XRD) studies. Similarly, a concentrated solution of Et_2O and CH_3CN containing **A^{CF3}** at – 34 °C afforded orange crystals suitable for XRD studies. The resulting solid-state structures (Figure 6.2) reveal the geometries of the formally Rh(III) center to be *pseudo*-octahedral for both complexes. The first coordination sphere surrounding the metal center contains the κ^2-[*N*,*N*]-non-symmetrically substituted Me_2dpma ligand, a freely rotating [η^5-Cp*] ligand, and a chloride anion. The bond metrics for **A^{OMe}** and **A^{CF3}** are very similar to those reported for the symmetric Me_2dpma complex suggesting that the addition of the non-symmetric electron-donating and -withdrawing group have little effect on the structural properties of the metal center.[14,15] The angle between the bidentate ligand plane (a plane defined by the positions of the N1, N2, and Rh atoms) and the plane defined by the [η^5-Cp*] ligand are similar are similar for **A^{OMe}** and **A^{CF3}**, 67.59° and 67.44° respectively, suggesting that the addition of the electron-donating/-withdrawing substituent does not significantly affect the first coordination sphere about Rh.

	Rh-N1 (Å)	Rh-N2 (Å)	∠N1-Rh-N2	∠Cp*-dpma
A^{OMe} *a*	2.134(2)	2.126(2)	85.83(9)°	67.59°
A (Ref. 4) *a*	2.123(3)	2.123(3)	85.51(8)°	67.07°
A^{CF3}	2.115(3)	2.136(3)	85.79(2)°	67.44°

Table 6.1. Tabulated bond lengths and angles of **A^{R}** found from XRD. *a* Values reflect averages for the two molecules in the unit cell.

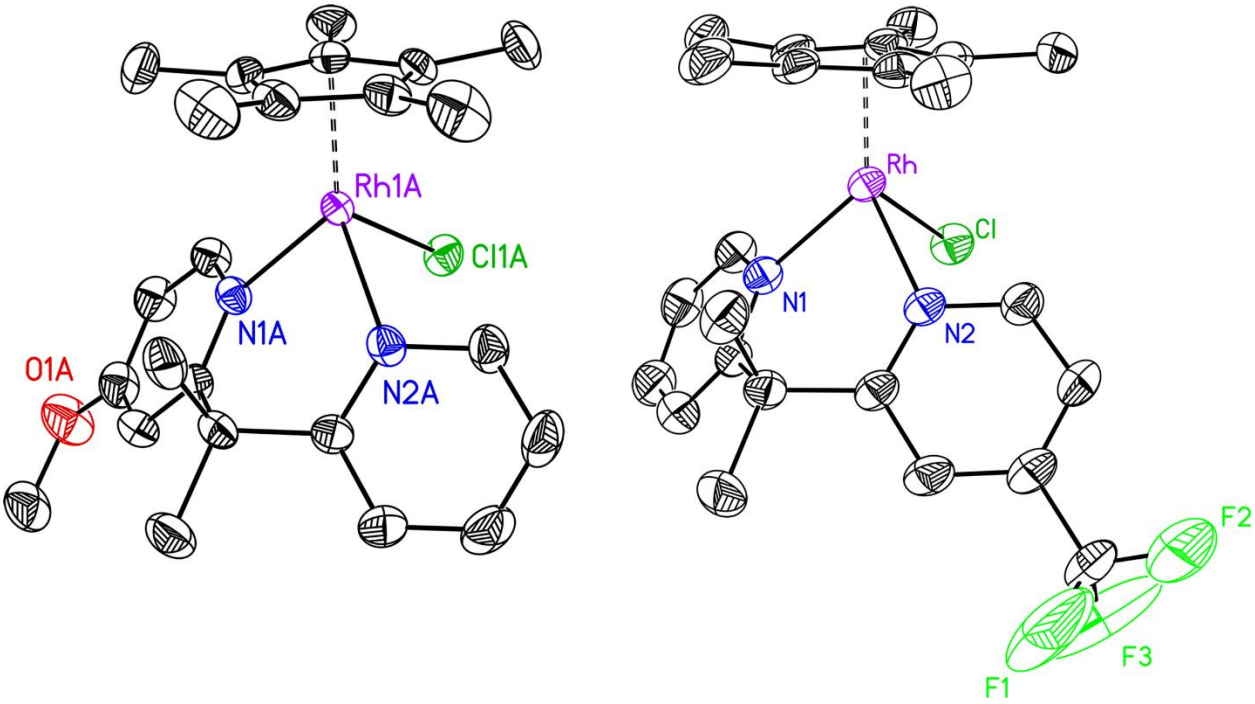

Figure 6.2. Solid-state structure (XRD) of $\mathbf{A^{OMe}}$ (left), and $\mathbf{A^{CF3}}$ (right). Hexafluorophosphate counteranion and hydrogen atoms are omitted for clarity. Displacement ellipsoids are shown at the 50% probability level.

Our previous work has shown that [Cp*Rh(dpma)] complexes have a unique CV profile in which a discrete redox-induced electrochemical-chemical process is observable upon reduction of Rh(II) to Rh(I).[14,15] The $\mathbf{1^R}$ complexes in this electrochemical study are acetonitrile solvent-bound analogs of the chloride-bound $\mathbf{A^R}$ precursors utilized to circumvent the formation of the side product $[Cp^*RhCl]_2$ observed in the presence of chloride.[15] The $\mathbf{1^R}$ complexes could be cleanly generated in both cases upon the addition of $AgPF_6$ (Scheme 6.1) to the $\mathbf{A^R}$ complexes. Additionally, elemental analysis confirms the purity of the recrystallized $\mathbf{1^{CF3}}$ material. The $\mathbf{A^{OMe}}$ was fully characterized by way of ^1H, $^{13}C\{^1H\}$, $^{31}P\{^1H\}$ and ^{19}F NMR, and XRD. The more sensitive $\mathbf{1^R}$ solvent complexes were characterized via ^1H NMR to confirm full conversion and were used immediately for electrochemical studies (see Appendix D, Figures D27 and D34).

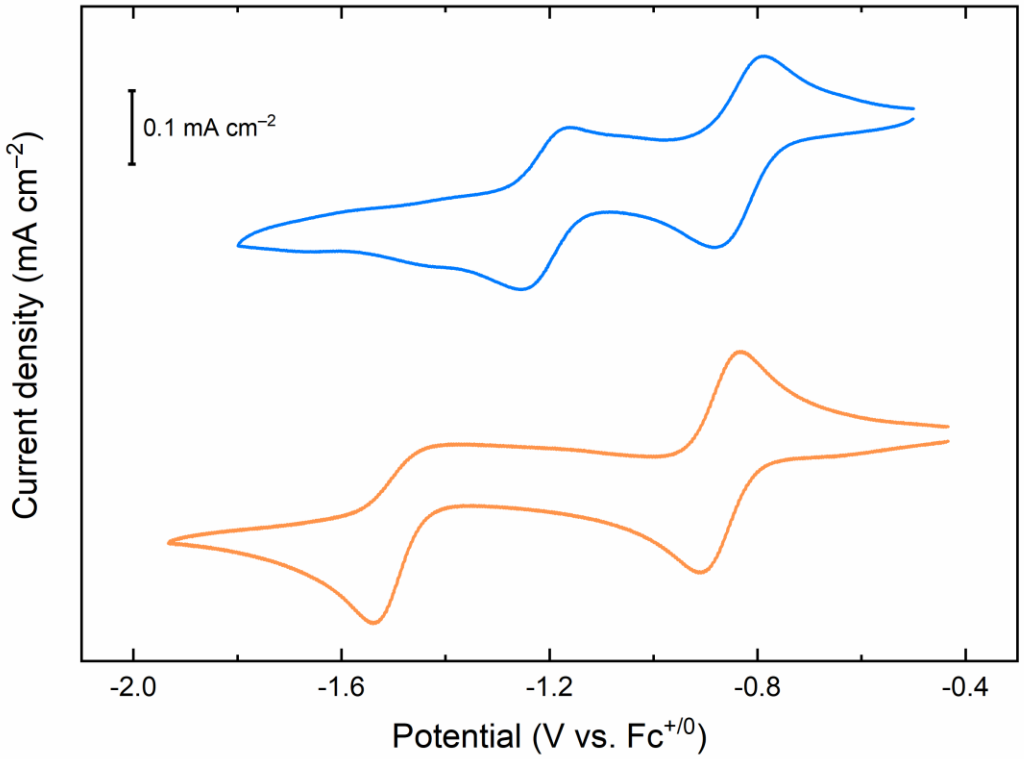

Figure 6.3. Cyclic voltammetry of $\mathbf{1}^{\mathbf{CF3}}$ (upper, blue) and $\mathbf{1}^{\mathbf{OMe}}$ (lower, orange). Conditions: Electrolyte, 0.1 M $TBAPF_6$ in CH_3CN; scan rate, 50 mV/s; working electrode, highly oriented pyrolytic graphite (HOPG); [Rh] in each experiment ca. 1 mM. Initial potentials $\mathbf{1}^{\mathbf{OMe}}$, ca. − 0.4 V; $\mathbf{1}^{\mathbf{CF3}}$, ca. − 0.4 V.

The cyclic voltammetry for $\mathbf{1}^{\mathbf{OMe}}$ is reminiscent of the analogous complexes previously studied,[14,15] electrochemical study reveals a quasi-reversible 1e$^-$ reduction ($E_{1/2}$ (Rh(III)/Rh(II)) = –0.87 V vs ferrocenium/ferrocene, hereafter denoted as Fc$^{+/0}$) to the predicted $\mathbf{2}^{\mathbf{OMe}}$ complex (Scheme 6.2, Figure 6.3 upper trace). A subsequent 1e$^-$ reduction is observed at a further negative potential ($E_{p,c}$(Rh(II)/Rh(I)) –1.53 V); this reduction appears fully irreversible at lower scan rates. The appearance of this data with an electrochemical-chemical (EC) profile suggests the rapid conversion of the doubly reduced, formally Rh(I) form bearing κ^2-$\mathbf{Me_2dpma}^{\mathbf{OMe}}$ ligand, $\mathbf{[3}^{\mathbf{OMe}}\mathbf{]}$, to

the [Cp*Rh] complex bearing the flipped version of the ligand with an η^2 pyridine ring, $\mathbf{3^{OMe}}$, reactivity observed previously for this family of complexes (see Appendix D, Figure D62).[14,15] Notably, $\mathbf{1^{OMe}}$ was found to be freely diffusing on the basis of scan rate dependence cyclic voltammetry studies (see Appendix D, Figures D61). However, the anodic feature observed at ca. –1.05 V vs $Fc^{+/0}$ for the previously reported similar complexes is not observed in the CV data of $\mathbf{1^{OMe}}$. The absent anodic feature $E_{p,a}$(Rh(I)→Rh(II)) corresponds to the regeneration of the $\mathbf{2^{OMe}}$ via reoxidation of $\mathbf{3^{OMe}}$ followed by reorientation of the κ^2-$\mathbf{Me_2dpma^{OMe}}$ ligand (**[2^{OMe}]** to $\mathbf{2^{OMe}}$). We hypothesize that the reversible feature at $E_{1/2}$ Rh(III)/Rh(II) = –0.87 V vs $Fc^{+/0}$ overlaps with anodic wave corresponding to reoxidation of the $1e^-$ species formed *in situ*. To summarize, on the CV of the $\mathbf{1^{OMe}}$ complex, we predict that the complex undergoes similar reductive processes as previously observed in complexes of this type (see Appendix D, Scheme D1).

Comparatively, electrochemical study of $\mathbf{1^{CF3}}$ reveals a quasi-reversible $1e^-$ reduction ($E_{1/2}$ ((Rh(III)/Rh(II))) = –0.83 V vs $Fc^{+/0}$) to generate $\mathbf{2^{CF3}}$ followed by an additional quasi-reversible $1e^-$ reduction ($E_{1/2}$ (Rh(II)/Rh(I))) = –1.21 V vs $Fc^{+/0}$) (Scheme 6.2). The quasireversible nature of the second reduction, even at low scan rates, indicates the lack of a redox-induced chemical reaction observed for the other [Cp*Rh(dpma)] complexes (see Appendix D, Figure D57). The more negative $1e^-$ reduction ($E_{1/2}$ = –1.21 V vs $Fc^{+/0}$) is indicative of formation of a formally Rh(I) form bearing κ^2-$\mathbf{Me_2dpma^{CF3}}$ ligand, **[3^{CF3}]**. The quasi-reversible nature of this reduction signifies the absence of the EC process to form the observed $\mathbf{3^R}$ species observed in other analogs in this family. The lack of an observable EC process in the CV of $\mathbf{1^{CF3}}$ indicates that the addition of the electron-withdrawing $–CF_3$ substituent precludes observation of the stable formally Rh(I) species $\mathbf{3^{CF3}}$ via the ligand rearrangement upon $2e^-$ reduction on the cyclic voltammetry timescale (see Appendix D, Scheme D2). Notably, $\mathbf{1^{CF3}}$ was found to be freely diffusing on the basis of scan rate

dependence cyclic voltammetry studies (see Appendix D, Figures D56); however, upon multiple scanning there is significant electrode fouling that is unique to $\mathbf{1^{CF3}}$ which gives rise to additional features in the CV at ca. –1.50 V vs $Fc^{+/0}$.

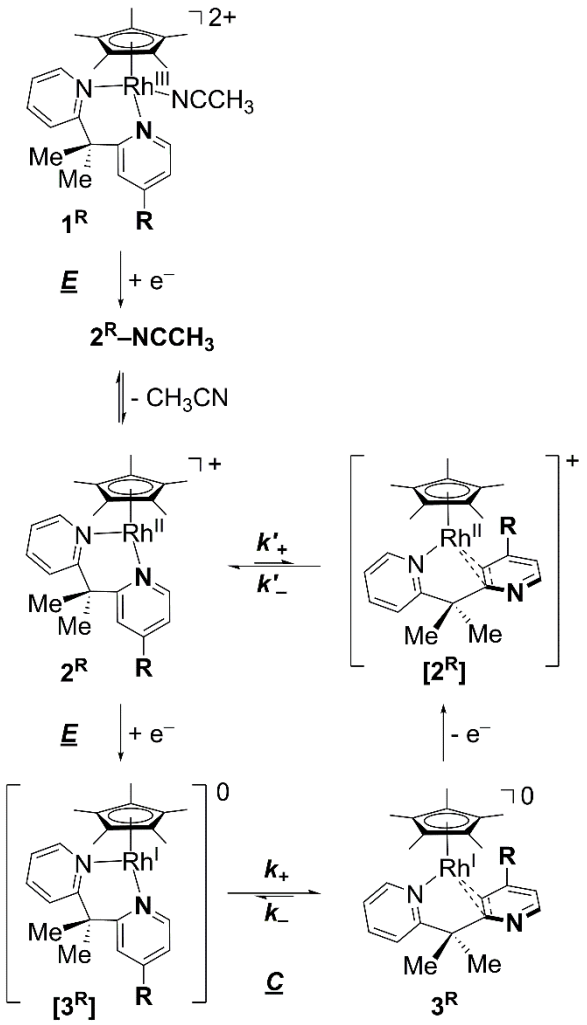

Scheme 6.2. Previously observed electrochemical reduction scheme for the [Cp*Rh] R_2dpma ligated complexes.

Additionally, the potentials measured for the sequential 1e⁻ reductions among the series of $\mathbf{1^R}$ show a direct dependence on the electron-donating and -withdrawing properties of the substituent on the single pyridine moiety (Table 6.2). The complex, $\mathbf{1^{OMe}}$, features the most electron-donating substituent that engenders the most negative Rh(III)/Rh(II) reduction potential ($E_{1/2}$ = –0.87 V vs

$Fc^{+/0}$) and Rh(II)/Rh(I) potential ($E_{p,c}$ = –1.53 V vs $Fc^{+/0}$). The previously reported complex, **1**, has the next more positive Rh(III)/Rh(II) potential ($E_{1/2}$ = –0.86 V vs $Fc^{+/0}$) and Rh(II)/Rh(I) ($E_{p,c}$ = –1.45 V vs $Fc^{+/0}$) consistent with the less electron-donating nature of the –H substituent. The complex bearing the most electron-withdrawing substituent, $\mathbf{1^{CF3}}$, engenders the most positive reduction potentials the for the Rh(III)/Rh(II) reduction potential ($E_{1/2}$ = –0.83 V vs $Fc^{+/0}$) and Rh(II)/Rh(I) potential ($E_{p,c}$ = –1.21 V vs $Fc^{+/0}$). The measured reduction potentials follow the expected trend in which the most electron-donating –OMe substituent produces the most reducing potential, the contrasting electron-withdrawing $–CF_3$ substituent provokes the most positive reduction potential. This observable trend suggests that there is a significant electronic influence of the substituents on the electron density of the rhodium center.

	$E_{1/2}$ (Rh(III)/Rh(II))	$E_{p,c}$
$\mathbf{1^{CF3}}$	–0.83 V	–1.21 V
1 (Ref. 4)	–0.86 V	–1.45 V
$\mathbf{1^{OMe}}$	–0.87 V	–1.53 V

Table 6.2. Reduction potentials for series of **1** and $\mathbf{1^R}$ complexes.

Chemical reduction of the Rh(III) complexes yields similar reactivity as that observed in other complexes bearing substituted dpma ligands.[14,15] Reduction studies of $\mathbf{1^{OMe}}$ and $\mathbf{1^{CF3}}$ were performed to investigate the nature of the $1e^-$ reduction product of $\mathbf{1^R}$. Treatment of $\mathbf{1^R}$ with 1 equivalent of cobaltocene in acetonitrile (Cp_2Co, $E_{1/2}$ = −1.34 V vs. $Fc^{+/0}$)[17] results in an immediate color change from yellow to dark purple. Attempts to isolate and obtain single crystals suitable for XRD of the presumed Rh(II) species ($\mathbf{2^R}$, Scheme 6.3), were not fruitful. Thus, we turned our attention to electron paramagnetic resonance (EPR) spectroscopy to interrogate the identity of the stochiometric, $1e^-$ reduction product of $\mathbf{1^R}$. EPR data for this material obtained at 10 K in acetonitrile reveal a signal for $\mathbf{1^{OMe}}$ and $\mathbf{1^{CF3}}$ at g_1 = 2.18, g_2 = 2.01 and g_1 = 2.17, g_2 = 2.03,

respectively (see Appendix D, Figures D65 and D66). The rhombic signal observed is consistent with a Rh-centered radical as predicted for the Rh(II) complex, $\mathbf{2^R}$. This broad feature is similar to that observed for previously reported Rh(II) complexes bearing κ^2-dpma.[15,18] Interestingly, there is a second narrow isotropic feature (g = 2.00 and g = 1.99 for $\mathbf{1^{OMe}}$ and $\mathbf{1^{CF3}}$, respectively) likely corresponds to an organic-based radical likely due to delocalized electron density on the **Me$_2$dpma^R** ligand. This feature is especially apparent in the spectra of $\mathbf{2^{CF3}}$, presumably due to the electron-withdrawing nature of the $–CF_3$ substituent. We note that here in the absence of structural data, the identity of $\mathbf{2^R}$ cannot be conclusively determined, however, on the basis of EPR data we conclude the 1e$^–$ reduction of $\mathbf{1^R}$ yields a Rh(II) species indicating that desymmetrization of the **Me$_2$dpma^R** ligands can support a Rh(II) center, even in the presence of electron-donating and -withdrawing moieties.[18]

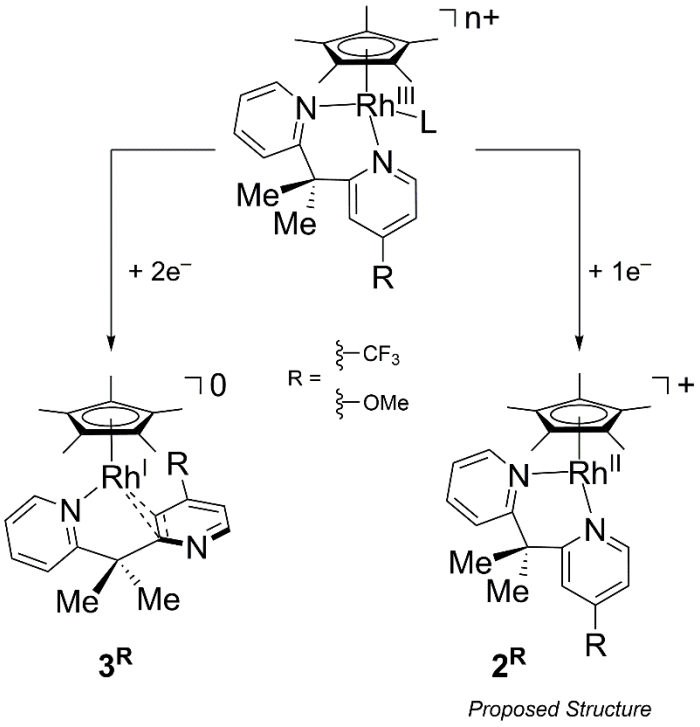

Scheme 6.3. Chemical reduction of Rh(III) complexes.

Similar structural rearrangement for $\mathbf{1^{R}}$ is observed upon $2e^-$ reduction as in previous [Cp*Rh] dpma complexes. Treatment of a suspension of $\mathbf{A^{OMe}}$ in THF with sodium-mercury amalgam (Na(Hg)[17]) resulted in a darkening of the reaction solution from yellow to a deep red homogenous solution. Similarly, the reduction of $\mathbf{1^{CF3}}$ with 2 equivalents of decamethylcobaltocene (Cp^*_2Co, $E_{1/2} = -1.91$ V vs. $Fc^{+/0}$, [17]) results in rapid darkening of the reaction mixture from yellow to dark red. Chemical isolation of the $2e^-$ reduced forms $\mathbf{3^{OMe}}$ and $\mathbf{3^{CF3}}$ (Scheme 6.3) is achieved by extraction with hexanes and subsequent crystallization. Cooling of a concentrated solution of extracted material in hexane yields single crystals of the Rh(I) material suitable for solid-state structures of $\mathbf{3^{OMe}}$ and $\mathbf{3^{CF3}}$ obtained from XRD analysis (Figure 6.4). These solid-state XRD data confirm the reduction induced ligand rearrangement in which the coordinated η^2 pyridine stabilizes the reduced rhodium center occurs even upon mono-substitution para to the N moiety. The electronic perturbation and non-symmetric nature introduced by instillation of the methoxy and trifluoromethyl groups does not result in differing reactivity upon reduction than observed in previous systems.

Interestingly, chemical reduction and X-ray diffraction studies (*vide infra*) provide evidence that $\mathbf{3^{CF3}}$ is the $2e^-$ reduction product of $\mathbf{1^{CF3}}$ (Scheme 6.3 and Figure 6.4). Taken together with the cyclic voltammetry, X-ray diffraction, and chemical reduction studies, it is evident that $\mathbf{1^{CF3}}$ does indeed undergo a redox-induced chemical process in which the formally Rh(I) is stabilized via the chemical flip of the pyridine moiety. However, presumably, the reaction is so slow that the chemical process is not observable on the electrochemical timescale (Figure 6.3). The model for $\mathbf{1^{CF3}}$ and $\mathbf{1^{OMe}}$ is also supported by the anodic electrochemical behavior of isolated $\mathbf{3^{OMe}}$ and $\mathbf{3^{CF3}}$ (*vide infra*), which shows two oxidation events (see Appendix D, Figures D59 and D63) that closely mirror those displayed in cyclic voltammetry experiments carried out with $\mathbf{1^{OMe}}$ and $\mathbf{1^{OMe}}$.

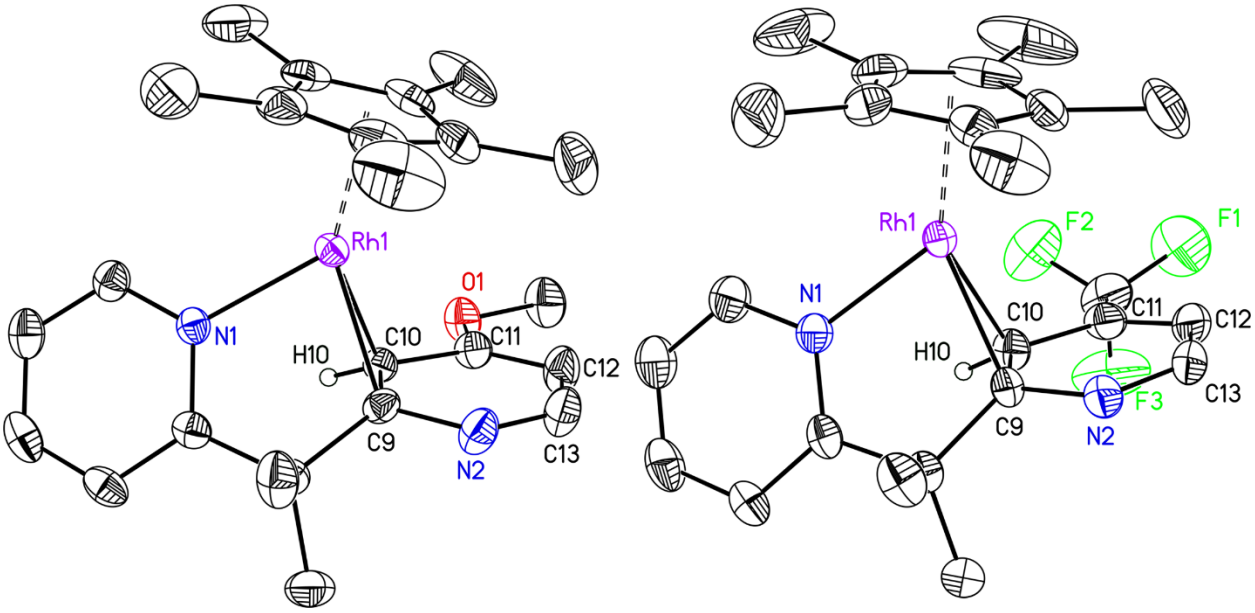

Figure 6.4. Solid-state structure (XRD) of $\mathbf{3^{OMe}}$ (left), and $\mathbf{3^{CF3}}$ (right). Hydrogen atoms (except H10) are omitted for clarity. Displacement ellipsoids are shown at the 50% probability level.

We find that the mono-substituted pyridine moiety of $\mathbf{3^{R}}$ binds to the rhodium center like that of the Me_2dpma complex in which the pyridine ring is dearomatized. As observed in similar complexes,[14,15] the C9–C10 bond of $\mathbf{3^{OMe}}$ and $\mathbf{3^{CF3}}$ elongates in comparison to the length of their Rh(III) analogs as a result of activation of strong π-backbonding. The dearomatization of $\mathbf{3^{OMe}}$ and $\mathbf{3^{CF3}}$ results in the previously observed phenomenon in which there is localization of double bond character within the ring giving rise to alternating short/long C–C/C–N bond distances (Figure D67). There is a slight trend with the electron-withdrawing and -donating nature of the substituent and the C9–C10 distances of the series. The electron-withdrawing nature of the $–CF_3$ moiety on the flipped pyridyl ring engenders the longest C9–C10 distance (1.476(5) Å) for $\mathbf{3^{CF3}}$. Complex **3** displays the intermediate C9–C10 distance (1.468(4) Å) followed by the shorted interbond distance promoted by the electron-donating nature of the –OMe substituted pyridyl ring (1.466(3) Å) of $\mathbf{3^{OMe}}$ (see Appendix D, Table D3 and Figure D67 for comparison of bond metrics). Notably,

the remaining inter-ring C–C/C–N distances do not significantly differ within ±3σ amongst the series of complexes.

Additionally, the solid-state structures of $\mathbf{3^{OMe}}$ and $\mathbf{3^{CF3}}$ indicate that there is significant pyramidalization of C10, as observed in previous studies. The ^{1}H NMR spectra of $\mathbf{3^{OMe}}$ and $\mathbf{3^{CF3}}$ are consistent with sp^3-hybridization of C10 in which there is an upfield shift of H10 resonance (Figure D35 and D46). The bond metrics measured for $\mathbf{3^{OMe}}$ and $\mathbf{3^{CF3}}$ indicate that the Rh centers interact in a similar fashion to its olefinic ligand as previously observed in for the Me_2dpma complex. The metal-olefin back donation within the context of the Dewar-Chatt-Duncanson[19] model stabilizes the formally Rh(I) center in both the $\mathbf{3^{OMe}}$ and $\mathbf{3^{CF3}}$ complexes.[15] Interestingly, two-dimensional ^{1}H NMR spectra of $\mathbf{3^{OMe}}$ and $\mathbf{3^{CF3}}$ agree with the solid-state data, in which the ligand rearrangement yields a single product in which the formally Rh(I) center facially coordinates in an η^2-fashion mono-substituted to the pyridine motif. (see Appendix D, Figures D39-D45 and D50-D54, respectively).[4]

These findings are potentially useful for the development of novel ligand frameworks for catalysis, the introduction of inductive effects, and desymmetrization to electrocatalytic scaffolds may engender significantly differing cyclic voltametric responses as well as affect the rate of interconversion of intermediates. These types of substituent effects could be observed in more complex systems as such photoactive dye constructs and electrode attachment assemblies. In these examples, the inductive effects engendered by electron-donating and -withdrawing ligands could affect the interconversion of intermediates and impact the capability of the electrocatalyst. The $\mathbf{3^{R}}$ species are of interest because they demonstrate the preference of the ligand framework to preferentially flip the mono-substituted pyridyl ring to bind in a η^2 manner. This is important because low valent complexes ligated with carbon-based frameworks tend to adopt a range of

coordination modes.[20] Understanding the consequences of inductive effects and desymmetrization on ligand scaffolds offers insight into the development of molecular electrocatalysis.

6.3 Conclusions

Here we find that the $\mathbf{1^{OMe}}$ system undergoes a unique EC process like observed in the other [Cp*Rh] complexes in this family. However, the cyclic voltammetry of $\mathbf{1^{CF3}}$ displays two quasireversible reductions implying a lack of ligand rearrangement of the transient Rh(I) species bearing substituted κ^2 -dpma ligand. Interestingly, the chemical reduction of both the κ^2 -dpma Rh(III) complexes and isolation of the formally Rh(I) compound demonstrates that both complexes undergo a chemical redox-induced ligand rearrangement. Thus, electrochemical reduction of $\mathbf{1^{CF3}}$ engenders a ligand rearrangement that is presumably too slow to observe on the cyclic voltammetry timescale. We find that isolation of the two-electron reduced η^2-dpma species results in preferential rearrangement of the substituted pyridyl ring in the non-symmetric $\mathbf{Me_2dpma^R}$ framework as evidenced by XRD and NMR studies. We, therefore, predict that these results could be useful for understanding more complex electrocatalytic systems bearing non-symmetric ligand frameworks or those influenced by inductive effects engendered by ligand substituents.

6.4 Experimental Details

6.4.1 General Considerations

All manipulations were carried out in dry N_2-filled gloveboxes (Vacuum Atmospheres Co., Hawthorne, CA) or under N_2 atmosphere using standard Schlenk techniques unless otherwise noted. All solvents were of commercial grade and dried over activated alumina using a PPT Glass Contour (Nashua, NH) solvent purification system prior to use, and were stored over molecular sieves. All chemicals were from ma*J*or commercial suppliers and used as received after extensive drying. $[Cp^*RhCl_2]_2$ was prepared according to literature procedure.[21] The 2-fluoro-4-

trifluoromethylpyridine was obtained from a commercial source. The 2-fluoro-4-methoxypyridine starting material was synthesized by the method of Hartwig.[22] The bis(2-pyridyl)methane ligands were synthesized by the method of Solomonov.[23] Deuterated NMR solvents were purchased from Cambridge Isotope Laboratories; CD_3CN was dried over molecular sieves and C_6D_6 was dried over sodium/benzophenone. ^1H, ^{13}C, and ^{31}P NMR spectra were collected on 400 or 500 MHz Bruker spectrometers and referenced to the residual protio-solvent signal[24] in the case of ^1H and ^{13}C. Heteronuclear NMR spectra were referenced to the appropriate external standard following the recommended scale based on ratios of absolute frequencies (Ξ).[25]

6.4.2 Synthesis

6.4.2.1 Synthesis of Me_2dpma^R ligands

Synthesis of **dpma^{OMe}**. A Schlenk flask with 2-pyridine (1.030 g, 11.05 mmol, 2.0 equiv.) was cooled to –78°C. A solution of nBuLi (4.0 mL, 11.05 mmol, 2.0 equiv.) was added dropwise and allowed to stir for 15 min then warmed to –15°C and 2-fluoro-4-methoxypyridine (0.7025 g, 5.53 mmol, 1.0 equiv.) was added and allowed to stir at reflux for 25 min. The resulting solution was stirred with a saturated solution of sodium bicarbonate. The liquid phase was separated by filtration and the title ligand was then purified and isolated by a dichloromethane/water separation, the organic layer dried over magnesium sulfate, followed by a column with 50:50 dichloromethane:acetone. (0.7466 g, 67% yield). ^1H NMR (500 MHz, C_6D_6): δ 8.45 (d, *J* = 4.2 Hz, 1H), 8.32 (d, *J* = 5.7 Hz, 1H), 7.18 (d, *J* = 7.7 Hz, 1H), 7.01 (td, *J* = 7.6, 1.9 Hz, 1H), 6.81 (d, *J* = 2.5 Hz, 1H), 6.57 (ddd, *J* = 7.5, 4.9, 1.2 Hz, 1H), 6.28 (dd, *J* = 5.7, 2.5 Hz, 1H), 4.40 (s, 2H), 3.04 (s, 3H) ppm. $^{13}C\{^1H\}$ NMR (126 MHz, C_6D_6): δ 166.21 (s), 161.97 (s), 160.42 (s), 150.88 (s), 149.60 (s), 136.02 (s), 123.75 (s), 121.31 (s), 109.39 (s), 108.25 (s), 54.34 (s), 48.06 (s) ppm

Synthesis of **Me$_2$dpma^{OMe}**. A Schlenk flask with **dmpa^{OMe}** (0.7466 g, 3.73 mmol, 1.0 equiv.) was cooled to –78°C. A solution of nBuLi (1.60 mL, 4.47 mmol, 1.2 equiv.) was added dropwise and allowed to stir for 15 min, then methyl iodide (0.30 mL, 4.85 mmol, 1.3 equiv.) was added dropwise. The sequential addition of nBuLi (1.90 mL, 5.22 mmol, 1.4 equiv.) and methyl iodide (0.35 mL, 5.59 mmol, 1.5 equiv.) was then repeated in the same manner. The resulting solution was stirred with a saturated solution of sodium bicarbonate. The liquid phase was separated by filtration and the title ligand was then purified and obtained by a dichloromethane/water separation, the organic layer dried over magnesium sulfate, the oily residue was purified by vacuum distillation. (0.6206 g, 73% yield). ^{1}H NMR (500 MHz, C_6D_6): δ 8.49 (dt, *J* = 4.6, 2.1 Hz, 1H), 8.37 (dd, *J* = 5.7, 2.3 Hz, 1H), 7.12 (dd, *J* = 8.1, 2.0 Hz, 1H), 7.04 (td, *J* = 7.7, 3.8 Hz, 1H), 6.85 (d, *J* = 2.5 Hz, 1H), 6.64 – 6.53 (m, 1H), 6.28 – 6.21 (m, 1H), 3.05 (d, *J* = 2.3 Hz, 3H), 2.03 (d, *J* = 2.3 Hz, 6H).ppm.^{13}C{^{1}H} NMR (126 MHz, C_6D_6): δ 169.98 (s), 168.23 (s), 166.14 (s), 150.26 (s), 148.82 (s), 135.75 (s), 121.62 (s), 120.85 (s), 107.89 (s), 107.18 (s), 54.26 (s), 28.77 (s). ppm

Synthesis of **dpma^{CF3}**. A Schlenk flask with 2-pyridine (1.360 g, 14.6 mmol, 2.0 equiv.) was cooled to –78°C. A solution of nBuLi (5.3 mL, 14.6 mmol, 2.0 equiv.) was added dropwise and allowed to stir for 15 min then warmed to –15°C and 2-fluoro-4-trifluoromethylpyridine (1.2051 g, 7.30 mmol, 1.0 equiv.) was added and allowed to stir at reflux for 25 min. The resulting solution was stirred with a saturated solution of sodium bicarbonate. The liquid phase was separated by filtration and the title ligand was then purified and obtained by a dichloromethane/water separation, the organic layer dried over magnesium sulfate, followed by a column with 50:50 dichloromethane:acetone. (1.1163 g, 64% yield). ^{1}H NMR (500 MHz, C_6D_6): δ 8.48 – 8.33 (m, 1H), 8.26 (d, *J* = 5.1 Hz, 1H), 7.41 (s, 1H), 6.97 (tt, *J* = 7.7, 1.5 Hz, 1H), 6.92 (d, *J* = 7.8 Hz, 1H),

6.69 (d, *J* = 5.0 Hz, 1H), 6.53 (dd, *J* = 7.2, 5.0 Hz, 1H), 4.23 (s, 2H) ppm. $^{13}C\{^{1}H\}$ NMR (126 MHz, C_6D_6): δ 161.77 (s), 159.18 (s), 150.52 (s), 149.86 (s), 138.21 (q, *J* = 33.6 Hz), 136.10 (s), 123.52 (s), 121.53 (s), 119.30 (q, *J* = 3.9 Hz), 116.91 (q, *J* = 3.9 Hz), 47.40 (s) ppm. ^{19}F NMR (376 MHz, C_6D_6): δ −64.56 (s) ppm.

Synthesis of **Me$_2$dpma^{CF3}**. A Schlenk flask with **dmpa^{CF3}** (0.5813 g, 2.44 mmol, 1.0 equiv.) was cooled to –78°C. A solution of nBuLi (1.17 mL, 2.92 mmol, 1.2 equiv.) was added dropwise and allowed to stir for 15 min then methyl iodide (0.20 mL, 3.17 mmol, 1.3 equiv.) was added dropwise. The sequential addition of nBuLi (1.36 mL, 3.40 mmol, 1.4 equiv.) and methyl iodide (0.23 mL, 3.66 mmol, 1.5 equiv.) was then repeated in the same manner. The resulting solution was stirred with a saturated solution of sodium bicarbonate. The liquid phase was separated by filtration and the title ligand was then purified and obtained by a dichloromethane/water separation, the organic layer dried over magnesium sulfate, the oily residue was purified by vacuum distillation. (0.425 g, 77% yield). ^{1}H NMR (500 MHz, C_6D_6): δ 8.47 – 8.34 (m, 1H), 8.30 (d, *J* = 5.1 Hz, 1H), 7.54 (s, 1H), 7.00 (td, *J* = 7.7, 1.8 Hz, 1H), 6.96 – 6.90 (m, 1H), 6.70 (d, *J* = 5.1 Hz, 1H), 6.52 (ddd, *J* = 7.2, 4.8, 1.1 Hz, 1H), 1.84 (s, 6H).ppm. $^{13}C\{^{1}H\}$ NMR (126 MHz, C_6D_6): δ 169.97 (s), 167.10 (s), 149.87 (s), 149.13 (s), 138.11 (q, *J* = 33.4 Hz), 136.01 (s), 121.14 (s), 120.86 (s), 116.92 (q, *J* = 4.2 Hz), 116.51 (t, *J* = 3.9 Hz), 28.40 (s) ppm. ^{19}F NMR (376 MHz, C_6D_6): δ −64.46 (s) ppm.

6.4.2.2 Synthesis of A^{R} complexes

Synthesis of **A^{OMe}**. To a suspension of $[Cp^*RhCl_2]_2$ in acetonitrile, (0.1209 g, 0.196 mmol, 0.95 equiv.) $AgPF_6$ (0.0989 g, 0.0.391 mmol, 1.9 equiv.) and **Me$_2$dpma^{OMe}** (0.0940 g, 0.412 mmol, 2.0 equiv.) were added as acetonitrile solutions. The color of the reaction mixture rapidly changed from brick-red to orange, and a yellow precipitate formed. After 15 min, the suspension

was filtered to remove the AgCl byproduct, and the volume of the filtrate was reduced to ca. 1 mL. The addition of diethyl ether (ca. 20 mL) caused precipitation of a yellow solid, which was collected by filtration (0.2087 g, 87%). Vapor diffusion of diethyl ether into a concentrated acetonitrile solution of the product yielded single-crystals of $\mathbf{A^{OMe}}$ suitable for X-ray diffraction studies. ^{1}H NMR (500 MHz, CD_3CN) δ 8.84 (d, *J* = 5.6 Hz, 1H), 8.61 (dd, *J* = 6.8, 1.9 Hz, 1H), 7.97 (t, *J* = 8.0 Hz, 1H), 7.76 (d, *J* = 8.2 Hz, 1H), 7.53 – 7.40 (m, 1H), 7.22 (d, *J* = 2.4 Hz, 1H), 6.99 (dd, *J* = 6.6, 2.8 Hz, 1H), 3.93 (d, *J* = 1.8 Hz, 3H), 2.02 (s, 2H), 1.87 (s, 2H), 1.65 – 1.53 (m, 15H) ppm. ^{13}C{^{1}H} NMR (126 MHz, CD_3CN) δ 169.22 (s), 164.92 (s), 163.99 (s), 158.81 (d, *J* = 1.8 Hz), 157.88 (d, *J* = 1.8 Hz), 141.15 (s), 125.37 (s), 123.76 (s), 110.99 (s), 110.71 (s), 98.52 (d, *J* = 8.5 Hz), 57.09 (s), 47.20 (d, *J* = 1.6 Hz), 28.87 (s), 27.59 (s), 9.46 (s) ppm. ^{31}P{^{1}H} NMR (162 MHz, CD_3CN) δ 51.57 (d, *J* = 140.3 Hz), – 145.49 (sep, *J* = 706.2 Hz) ppm. ^{19}F NMR (376 MHz, CD_3CN): –73.76 (d, *J* = 706.4 Hz) A satisfactory elemental analysis could not be obtained for $\mathbf{A^{OMe}}$, but NMR methods confirm the diamagnetic purity of the isolated material.

Synthesis of $\mathbf{A^{CF3}}$. To a suspension of $[Cp^*RhCl_2]_2$ in acetonitrile, (0.0948 g, 0.153 mmol, 1.0 equiv.) $AgPF_6$ (0.0776 g, 0.307 mmol, 2.0 equiv.) and $\mathbf{Me_2dpma^{CF3}}$ (0.0817 g, 0.307 mmol, 2.0 equiv.) were added as acetonitrile solutions. The color of the reaction mixture rapidly changed from brick-red to orange, and a yellow precipitate formed. After 15 min, the suspension was filtered to remove the AgCl byproduct, and the volume of the filtrate was reduced to ca. 1 mL. The addition of diethyl ether (ca. 20 mL) caused precipitation of a yellow solid, which was collected by filtration (0.187 g, 76%). Vapor diffusion of diethyl ether into a concentrated acetonitrile solution of the product yielded single-crystals of $\mathbf{A^{CF3}}$ suitable for X-ray diffraction studies. Crystallization, however, yields a mixture $\mathbf{A^{CF3}}$ as well as non-ligated $\mathbf{Me_2dpma^{CF3}}$ that is non-isolable, as is reflected in the NMR spectra in the Appendix D. Experimental work was performed

with the pure solvento complex, $\mathbf{1^{CF3}}$ (*vide infra*). NMR information is listed for the resonances corresponding to the $\mathbf{A^{CF3}}$ material. ^{1}H NMR (500 MHz, CD_3CN) δ 9.07 (d, *J* = 6.0 Hz, 1H), 8.83 (dd, *J* = 5.8, 1.7 Hz, 1H), 8.00 (ddd, *J* = 8.2, 7.4, 1.7 Hz, 1H), 7.98 (d, *J* = 1.9 Hz, 1H), 7.80 (dd, *J* = 8.3, 1.4 Hz, 1H), 7.72 (dd, *J* = 6.0, 1.9 Hz, 1H), 7.47 (ddd, *J* = 7.2, 5.7, 1.3 Hz, 1H), 2.12 (s, 3H), 1.93 (s, 3H), 1.61 (d, *J* = 0.9 Hz, 15H) ppm. $^{13}C\{^{1}H\}$ NMR (126 MHz, CD_3CN) δ 159.29 (s), 157.78 (s), 141.43 (s), 125.77 (s), 124.14 (s), 99.29 (d, *J* = 8.3 Hz), 27.59 (s), 9.55 (s) ppm. ^{31}P NMR (162 MHz, CD_3CN) δ –145.49 (septet, *J* = 706.5 Hz). ^{19}F NMR (376 MHz, C_6D_6): δ −73.80 (d, *J* = 706.5 Hz) ppm.

6.4.2.3 Preparation and Synthesis of 2^{R} and 3^{R} complexes

In situ generation of $\mathbf{2^{OMe}}$. For *in situ* EPR experiments a solution of Cp_2Co (0.0034 g, 0.178 mmol, 1 equiv) in acetonitrile was added to a thawing solution of $\mathbf{1^{OMe}}$ in acetonitrile (0.0116 g, 0.018 mmol, 1 equiv). The solution color changed immediately from yellow to dark purple which yielded material suitable for EPR studies at 10 K in acetonitrile.

In situ generation of $\mathbf{2^{CF3}}$. For *in situ* EPR experiments a solution of Cp_2Co (0.0038 g, 0.201 mmol, 1 equiv) in acetonitrile was added to a thawing solution of $\mathbf{1^{CF3}}$ in acetonitrile (0.0150 g, 0.020 mmol, 1 equiv). The solution color changed immediately from yellow to dark purple which yielded material suitable for EPR studies at 10 K in acetonitrile.

Synthesis of $\mathbf{3^{OMe}}$. A suspension of $\mathbf{A^{OMe}}$ in THF (0.0736 g, 0.114 mmol) was stirred over freshly prepared sodium-mercury amalgam (1% Na in Hg; 0.0262 g Na^0, 0.1.14 mmol, 10 equiv.) for 15 minutes, during which time the yellow suspension became a dark red homogeneous solution. The mixture was filtered, and the volatiles were removed in vacuo. Extraction with hexanes and removal of the volatiles in vacuo provides the title compound as a dark red solid (0.0487 g, 92%). If the extracted solution is cooled to –35°C; these conditions provide additional pure and

crystalline product. This strategy was employed using pure material to obtain single-crystals of the title compound suitable for X-ray diffraction studies. ^{1}H NMR (400 MHz, C_6D_6) δ 8.32 (d, *J* = 1.5 Hz, 1H), 8.30 (d, *J* = 4.4 Hz, 1H), 6.71 (td, *J* = 7.6, 1.6 Hz, 1H), 6.48 (dt, *J* = 8.0, 1.0 Hz, 1H), 6.22 (ddd, *J* = 7.3, 5.6, 1.5 Hz, 1H), 5.38 (dd, *J* = 4.4, 1.7 Hz, 1H), 3.37 (s, 3H), 2.25 (t, *J* = 1.8 Hz, 1H) 2.01 (s, 3H), 1.56 (s, 15H), 1.21 (s, 3H). ^{13}C NMR (126 MHz, C_6D_6) δ 175.97 (s), 172.07 (s), 151.59 (s), 146.24 (s), 133.42 (s), 121.70 (s), 121.02 (s), 91.11 (d, *J* = 6.1 Hz), 89.55 (s), 55.08 (s), 43.62 (d, *J* = 14.0 Hz), 28.48 (s), 26.35 (s), 8.87 (s). ppm. **3^{OMe}** is acutely air sensitive and satisfactory elemental analysis results could not be obtained.

Synthesis of **3^{CF3}**. A solution of decamethylcobaltocene (Cp^*_2Co, 0.0210g, 0.0639 mmol, 1.9 equiv.) in acetonitrile was added to a solution of **1^{CF3}** in CH_3CN (0.0267 g, 0.0336 mmol, 1.0 equiv.) and was allowed to stir for 2 hours, during which time the yellow suspension became a dark red homogeneous solution. The mixture was filtered, and the volatiles were removed in vacuo. Extraction with hexanes and removal of the volatiles in vacuo provides the title compound as a dark red solid. The extracted solution was cooled to –35°C; to provide pure and crystalline product (0.0138 g, 81%). This strategy was employed using pure material to obtain single-crystals of the title compound suitable for X-ray diffraction studies. ^{1}H NMR (400 MHz, C_6D_6) δ 8.34 – 8.25 (m, 1H), 8.19 (d, *J* = 3.6 Hz, 1H), 6.69 (td, *J* = 7.7, 1.6 Hz, 1H), 6.41 (dt, *J* = 7.9, 1.1 Hz, 1H), 6.35 (dt, *J* = 3.7, 1.2 Hz, 1H), 6.18 (ddd, *J* = 7.3, 5.6, 1.4 Hz, 1H), 2.34 (d, *J* = 1.8 Hz, 1H), 1.89 (s, 3H), 1.42 (s, 15H), 1.03 (s, 3H) ppm. ^{13}C NMR (126 MHz, C_6D_6) δ 171.54 (s), 151.43 (s), 145.31 (q, *J* = 30.8 Hz), 143.95 (s), 134.25 (s), 121.93 (d, *J* = 2.0 Hz), 121.29 (d, *J* = 1.9 Hz), 108.09 (d, *J* = 5.3 Hz), 91.63 (d, *J* = 6.3 Hz), 90.58 (d, *J* = 16.6 Hz) 54.89 (s), 41.40 (dd, *J* = 14.2, 3.0 Hz), 28.15 (s), 26.39 (s), 8.73 (s) ppm. ^{19}F NMR (376 MHz, C_6D_6): δ −66.22 (s) ppm. **3^{CF3}** is acutely air sensitive and satisfactory elemental analysis results could not be obtained.

6.4.3 X-ray crystallography

A single-domain crystal of $\mathbf{A}^{\mathbf{OMe}}$ (K87K_0M) was mounted with Paratone N oil in a MiteGen nylon loop and placed in a cold nitrogen stream on a Bruker SMART APEX CCD Single Crystal Diffraction System at 200K. A total of 17295 1.0°-wide ω- or ϕ-scan frames were collected with counting times of 5-8 seconds for all three crystals. was collected using graphite-monochromated Mo K_α radiation (λ = 0.71073 Å). X-rays were provided by a fine-focus sealed X-ray tube operated at 45 kV and 60 mA. The Platinum 135 detector was positioned at 80.0 mm and equipped with high-brilliance Helios multilayer mirror optics. Preliminary lattice constants were obtained with SMART in the Bruker Apex2 Software Suite.[26]

Single domain crystals of $\mathbf{A}^{\mathbf{CF3}}$ (v18f), $\mathbf{3}^{\mathbf{CF3}}$ (q73h), and $\mathbf{3}^{\mathbf{OMe}}$ (q40h) were mounted with Paratone N oil in MiteGen nylon loops and placed in a cold nitrogen stream on a Bruker Proteum diffractometer equipped with two CCD detectors (Apex II and Platinum 135) sharing a common MicroStar microfocus Cu rotating anode generator running at 45 mA and 60 kV (Cu Kα = 1.54178 Å). Complete sets of low temperature (200 K) X-ray diffraction data were obtained for all three compounds using monochromated Cu radiation with the Apex II detector [$\mathbf{A}^{\mathbf{CF3}}$ (v18f), $\mathbf{3}^{\mathbf{CF3}}$ (q73h), and $\mathbf{3}^{\mathbf{OMe}}$ (q40h)] positioned at 80.0 mm and equipped with Helios multilayer mirror optics. Preliminary lattice constants were obtained for all three crystals with SMART in the Bruker Apex2 Software Suite.[1] Totals of 4727 ($\mathbf{A}^{\mathbf{CF3}}$ (v18f)), 4058 ($\mathbf{3}^{\mathbf{CF3}}$ (q73h)) and 3939 ($\mathbf{3}^{\mathbf{OMe}}$ (q40h)) 1.0°-wide ω- or ϕ-scan frames were collected with counting times of 5-8 seconds for $\mathbf{A}^{\mathbf{CF3}}$ (v18f), and 4-6 seconds for $\mathbf{3}^{\mathbf{CF3}}$ (q73h), and $\mathbf{3}^{\mathbf{OMe}}$ (q40h).

Final lattice constants and integrated reflection intensities for all four crystals were produced using SAINT in the Bruker Apex2 Software Suite.[1] Each data set was corrected empirically for variable absorption effects with SADABS[27] using equivalent reflections. The Bruker software

package SHELXTL[28] was used to solve each structure using intrinsic direct methods phasing. Final stages of weighted full-matrix least-squares refinement were conducted using F_o^2 data with SHELXTL or the Olex software package[29] equipped with XL.[30] The relevant crystallographic and structure refinement data for all four structures are given in Table D1 and D2.

Unless otherwise stated in the special refinement section for each structure, the final structural model for each compound incorporated anisotropic thermal parameters for all non-hydrogen atoms and isotropic thermal parameters for all included hydrogen atoms**.** Non-methyl hydrogen atoms bonded to carbon in each complex were fixed at idealized riding model sp^2- or sp^3-hybridized positions with C–H bond lengths of 0.95 - 0.99 Å. Methyl groups were incorporated into the structural models either as sp^3-hybridized riding model groups with idealized "staggered" geometry and a C-H bond length of 0.98 Å or as idealized riding model rigid rotors (with a C–H bond length of 0.98 Å) that were allowed to rotate freely about their C–C bonds in least-squares refinement cycles. The isotropic thermal parameters of idealized hydrogen atoms in all nine structures were fixed at values 1.2 (non-methyl) or 1.5 (methyl) times the equivalent isotropic thermal parameter of the carbon atom to which they are covalently bonded.

6.4.4 Electrochemistry

Electrochemical experiments were carried out in a nitrogen-filled glove box. 0.10 M tetra(n-butylammonium)hexafluorophosphate (Sigma-Aldrich; electrochemical grade) in acetonitrile served as the supporting electrolyte. Measurements were made with a Gamry Reference 600 Plus Potentiostat/Galvanostat using a standard three-electrode configuration. The working electrode was the basal plane of highly oriented pyrolytic graphite (HOPG) (GraphiteStore.com, Buffalo Grove, IL; surface area: 0.09 cm^2), the counter electrode was a platinum wire (Kurt *J*. Lesker, *J*efferson Hills, PA; 99.99%, 0.5 mm diameter), and a silver wire immersed in electrolyte served

as a pseudo-reference electrode (CH Instruments). The reference was separated from the working solution by a Vycor frit (Bioanalytical Systems, Inc.). Ferrocene (Sigma Aldrich; twice-sublimed) was added to the electrolyte solution at the conclusion of each experiment (~1 mM); the midpoint potential of the ferrocenium/ferrocene couple (denoted as $Fc^{+/0}$) served as an external standard for comparison of the recorded potentials. Concentrations of analyte for cyclic voltammetry were typically 1 mM.

6.5 Acknowledgements

The authors thank Dr. Justin Douglas and Sarah Neuenswander for assistance with NMR and EPR spectroscopy. These studies were supported by the US National Science Foundation through award OIA-1833087. Support for NMR instrumentation was provided by NIH Shared Instrumentation Grants S10OD016360 and S10RR024664 and by the NSF MRI grant CHE-1625923.

6.6 References

[1] (a) Lewis, N. S.; Nocera, D. G., Powering the planet: Chemical challenges in solar energy utilization. *PNAS* **2006,** *103*, 15729-15735. (b) Eckenhoff, W. T.; Eisenberg, R., Molecular systems for light driven hydrogen production. *Dalton Trans.* **2012,** *41*, 13004-13021. (c) McKone, J. R.; Marinescu, S. C.; Brunschwig, B. S.; Winkler, J. R.; Gray, H. B., Earth-abundant hydrogen evolution electrocatalysts. *Chem. Sci*. **2014,** *5*, 865-878.

[2] (a) Kölle, U.; Grätzel, M., Metallorganische Rhodium(III)-Komplexe als Homogenkatalysatoren für die Photoreduktion von Protonen zu Wasserstoff an kolloidalem TiO_2. *Angew. Chem.* **1987,** *99*, 572-574. (b) Kölle, U.; Kang, B.-S.; Infelta, P.; Comte, P.; Grätzel, M., Elektrochemische und pulsradiolytische Reduktion von (Pentamethylcyclopentadienyl)(polypyridyl)rhodium-Komplexen. *Chem. Ber.* **1989,** *122*, 1869-1880.

[3] (a) Ruppert, R.; Herrmann, S.; Steckhan, E., Efficient indirect electrochemical in-situ regeneration of nadh:electrochemically driven enzymatic reduction of pyruvate catalyzed by D-LDH. *Tetrahedron Lett.* **1987,** *28*, 6583-6586. (b) Ruppert, R.; Herrmann, S.; Steckhan, E., Very efficient reduction of $NAD(P)^+$ with formate catalysed by cationic rhodium complexes. *J. Chem. Soc., Chem. Commun.* **1988**, 1150-1151. (c) Indirect Electrochemical Regeneration of NADH by a Bipyridinerhodium(I) Complex as Electron-Transfer Agent. *Angew. Chem., Int. Ed. Engl.*, **1982,** *21*, 782-783. (d) Hildebrand, F.; Kohlmann, C.; Franz, A.; Lütz, S., Synthesis, Characterization and Application of New Rhodium Complexes for Indirect Electrochemical Cofactor Regeneration. *Adv. Synth. Catal.* **2008,** *350*, 909-918.

[4] Lionetti, D.; Day, V. W.; Lassalle-Kaiser, B.; Blakemore, J. D., Multiple binding modes of an unconjugated bis(pyridine) ligand stabilize low-valent [Cp*Rh] complexes. *Chem. Commun.* **2018,** *54*, 1694-1697.

[5] Lionetti, D.; Day, V. W.; Blakemore, J. D., Structural and chemical properties of half-sandwich rhodium complexes supported by the bis(2-pyridyl)methane ligand. *Dalton Trans.* **2019,** *48*, 12396-12406.

[6] Hopkins Leseberg, J. A.; Lionetti, D.; Day, V. W.; Blakemore, J. D., Electrochemical Kinetic Study of [Cp*Rh] Complexes Supported by Bis(2-pyridyl)methane Ligands. *Organometallics* **2021,** *40*, 266-277.

[7] (a) Henke, W. C.; Lionetti, D.; Moore, W. N. G.; Hopkins, J. A.; Day, V. W.; Blakemore, J. D., Ligand Substituents Govern the Efficiency and Mechanistic Path of Hydrogen Production with [Cp*Rh] Catalysts. *ChemSusChem* **2017,** *10*, 4589-4598. (b) Boyd, E. A.; Lionetti, D.; Henke, W. C.; Day, V. W.; Blakemore, J. D., Preparation, Characterization, and Electrochemical Activation of a Model [Cp*Rh] Hydride. *Inorg. Chem.* **2019,** *58*, 3606-3615. (c) Hopkins, J. A.; Lionetti, D.; Day, V. W.; Blakemore, J. D., Chemical and Electrochemical Properties of [Cp*Rh] Complexes Supported by a Hybrid Phosphine-Imine Ligand. *Organometallics* **2019,** *38*, 1300-1310. (d) Hopkins, J. A.; Lionetti, D.; Day, V. W.; Blakemore, J. D., Synthesis and reactivity studies of a [Cp∗Rh] complex supported by a methylene-bridged hybrid phosphine-imine ligand. *J. Organomet. Chem.* **2020,** *921*, 121294. (e) Comadoll, C. G.; Henke, W. C.; Hopkins Leseberg, J. A.; Douglas, J. T.; Oliver, A. G.; Day, V. W.; Blakemore, J. D., Examining the Modular Synthesis of [Cp*Rh] Monohydrides Supported by Chelating Diphosphine Ligands. *Organometallics* **2021,** *40*, 3808-3818.

[8] (a) Yasuo, T.; Takanori, Y.; Youkoh, K.; Shigetaka, M.; Hiroshi, K., Electronic Absorption Spectra of the Alkali Metal Complexes with Bipyridine. *Bull. Chem. Soc. Jpn.* **1969,** *42*, 2264-2267. (b) Ichiro, H.; Saburo, N., Electronic Structures of Tris(2,2′-bipyridyl) Complexes of Transition Metals in Lower Oxidation States. *Bull. Chem. Soc. Jpn.* **1971,** *44*, 2312-2321. (c) Creutz, C., Bipyridine Radical Ions. *Comments Inorg. Chem.* **1982,** *1*, 293-311. (d) Kaim, W., The transition metal coordination chemistry of anion radicals. *Coord. Chem. Rev.* **1987,** *76*, 187-235. (e) Bock, C. R.; Meyer, T. J.; Whitten, D. G., Electron transfer quenching of the luminescent excited state of tris(2,2'-bipyridine)ruthenium(II). Flash photolysis relaxation technique for measuring the rates of very rapid electron transfer reactions. *J. Am. Chem. Soc.* **1974,** *96*, 4710-4712.

[9] (a) Gore-Randall, E.; Irwin, M.; Denning, M. S.; Goicoechea, J. M., Synthesis and Characterization of Alkali-Metal Salts of 2,2′- and 2,4′-Bipyridyl Radicals and Dianions. *Inorg. Chem.* **2009,** *48*, 8304-8316. (b) Dallinger, R. F.; Woodruff, W. H., Time-resolved resonance Raman study of the lowest ($d\pi^*$,^{3}CT) excited state of tris(2,2'-bipyridine)ruthenium(II). *J. Am. Chem. Soc.* **1979,** *101*, 4391-4393.

[10] (a) Lionetti, D.; Day, V. W.; Blakemore, J. D., Noncovalent immobilization and surface characterization of lanthanide complexes on carbon electrodes. *Dalton Trans.* **2017,** *46*, 11779-11789. (b) Blakemore, J. D.; Hernandez, E. S.; Sattler, W.; Hunter, B. M.; Henling, L. M.; Brunschwig, B. S.; Gray, H. B., Pentamethylcyclopentadienyl rhodium complexes. *Polyhedron* **2014,** *84*, 14-18. (c) Nakai, H.; Jeong, K.; Matsumoto, T.; Ogo, S., Catalytic C–F Bond Hydrogenolysis of Fluoroaromatics by [(η^5-C_5Me_5)Rh^I(2,2′-bipyridine)]. *Organometallics* **2014,** *33*, 4349-4352.

[11] (a) Canty, A. J.; Chaichit, N.; Gatehouse, B. M.; George, E. E.; Hayhurst, G., Coordination chemistry of methylmercury(II). Synthesis, ^{1}H NMR, and crystallographic studies of cationic complexes of MeHg(II) with ambidentate and polydentate ligands containing pyridyl and N-substituted imidazolyl donors and involving unusual coordination geometries. *Inorg. Chem.* **1981,** *20*, 2414-2422. (b) Byers, P. K.; Canty, A. J., Synthetic routes to methylpalladium(II) and dimethylpalladium(II) chemistry and the synthesis of new nitrogen donor ligand systems. *Organometallics* **1990,** *9*, 210-220. (c) Mohr, F.; Binfield, S. A.; Fettinger, J. C.; Vedernikov, A. N., A Practical, Fast, and High-Yielding Aziridination Procedure Using Simple Cu(II) Complexes Containing N-Donor Pyridine-Based Ligands. *J. Org. Chem.*, **2005,** *70*, 4833-4839. (d) Vedernikov, N.; Miftakhov, R.; Borisoglebski, S. V.; Caulton, K. G.; Solomonov, B. N., Condensation of 2-Pyridylmethyllithium Nucleophiles and Pyridine Electrophiles as a Convenient Synthetic Route to Polydentate Chelating N-Donor Ligands. *Chem. Heterocycl. Compd.*, **2002,** *38*, 406-416.

[12] Golden, J. H.; Facendola, J. W.; Sylvinson M. R, D.; Baez, C. Q.; Djurovich, P. I.; Thompson, M. E., Boron Dipyridylmethene (DIPYR) Dyes: Shedding Light on Pyridine-Based Chromophores. *J. Org. Chem.,* **2017,** *82*, 7215-7222.

[13] Fier, P. S.; Hartwig, J. F., Selective C-H Fluorination of Pyridines and Diazines Inspired by a Classic Amination Reaction. *Science* **2013,** *342*, 956-960.

[14] Hopkins Leseberg, J. A.; Lionetti, D.; Day, V. W.; Blakemore, J. D., Electrochemical Kinetic Study of [Cp*Rh] Complexes Supported by Bis(2-pyridyl)methane Ligands. *Organometallics* **2021,** *40*, 266-277.

[15] Lionetti, D.; Day, V. W.; Lassalle-Kaiser, B.; Blakemore, J. D., Multiple binding modes of an unconjugated bis(pyridine) ligand stabilize low-valent [Cp*Rh] complexes. *Chem. Commun.* **2018,** *54*, 1694-1697.

[16] Nutton, A.; Bailey, P. M.; Maitlis, P. M., Pentamethylcyclopentadienyl-rhodium and -iridium complexes. Part 29. Syntheses and X-ray structure determinations of $[\{Rh(C_5Me_5)\}_2(OH)_3]OH\cdot 11H_2O$ and $[\{lr(C_5Me_5)\}_2(OH)_3]O_2CMe\cdot 14H_2O$ and related complexes. *J. Chem. Soc., Dalton Trans.* **1981**, 1997-2002.

[17] Connelly, N. G.; Geiger, W. E., Chemical Redox Agents for Organometallic Chemistry. *Chem. Rev.* **1996,** *96*, 877-910.

[18] Lionetti, D.; Day, V. W.; Blakemore, J. D., Structural and chemical properties of half-sandwich rhodium complexes supported by the bis(2-pyridyl)methane ligand. *Dalton Trans.* **2019,** *48*, 12396-12406.

[19] (a) Nakai, H.; Jeong, K.; Matsumoto, T.; Ogo, S., Catalytic C–F Bond Hydrogenolysis of Fluoroaromatics by $[(\eta^5\text{-}C_5Me_5)Rh^I(2,2'\text{-bipyridine})]$. *Organometallics* **2014,** *33*, 4349-4352. (b) Blakemore, J. D.; Hernandez, E. S.; Sattler, W.; Hunter, B. M.; Henling, L. M.; Brunschwig, B. S.; Gray, H. B., Pentamethylcyclopentadienyl rhodium complexes. *Polyhedron* **2014,** *84*, 14-18. (c) Lionetti, D.; Day,

V. W.; Blakemore, J. D., Noncovalent immobilization and surface characterization of lanthanide complexes on carbon electrodes. *Dalton Trans.* **2017,** *46*, 11779-11789.

[20] Geiger, W. E., Organometallic Electrochemistry: Origins, Development, and Future. *Organometallics* **2007,** *26*, 5738-5765.

[21] (a) White, C.; Yates, A.; Maitlis, P. M., (η^5-Pentamethylcyclopentadienyl) Rhodium and -Iridium Compounds. Inorg. Synth. **1992,** 29, 228-234 (b) Mantell, M. A.; Kampf, J. W.; Sanford, M., Improved Synthesis of $[Cp^RRhCl_2]_2$ Complexes. *Organometallics* **2018,** *37*, 3240-3242.

[22] Fier, P. S.; Hartwig, J. F., Selective C-H Fluorination of Pyridines and Diazines Inspired by a Classic Amination Reaction. *Science* **2013,** *342*, 956-960.

[23] Vedernikov, N.; Miftakhov, R.; Borisoglebski, S. V.; Caulton, K. G.; Solomonov, B. N., Condensation of 2-Pyridylmethyllithium Nucleophiles and Pyridine Electrophiles as a Convenient Synthetic Route to Polydentate Chelating N-Donor Ligands. *Chem. Heterocycl. Compd.*, **2002,** *38*, 406-416.

[24] Fulmer, G. R.; Miller, A. J. M.; Sherden, N. H.; Gottlieb, H. E.; Nudelman, A.; Stoltz, B. M.; Bercaw, J. E.; Goldberg, K. I., NMR Chemical Shifts of Trace Impurities: Common Laboratory Solvents, Organics, and Gases in Deuterated Solvents Relevant to the Organometallic Chemist. *Organometallics* **2010,** *29*, 2176-2179.

[25] (a) Harris, R. K.; Becker, E. D.; Menezes, S. M. C. d.; Goodfellow, R.; Granger, P., NMR nomenclature. Nuclear spin properties and conventions for chemical shifts(IUPAC Recommendations 2001). *Pure Appl. Chem.* **2001,** *73*, 1795-1818. (b) Harris, R. K.; Becker, E. D.; Menezes, S. M. C. d.; Granger, P.; Hoffman, R. E.; Zilm, K. W., Further conventions for NMR shielding and chemical shifts (IUPAC Recommendations 2008). *Pure Appl. Chem.* **2008,** *80*, 59-84.

[26] *APEX2, Version 2 User Manual, M86-E01078*. Bruker Analytical X-ray Systems: Madison, WI, June 2006.

[27] Sheldrick, G. M. *SADABS (version 2008/1): Program for Absorption Correction for Data from Area Detector Frames*, University of Göttingen 2008.

[28] Sheldrick, G., Crystal structure refinement with SHELXL. *Acta Crystallogr., Sect. C: Cryst. Struct. Commun.* **2015,** *71*, 3-8.

[29] Dolomanov, O. V.; Bourhis, L. J.; Gildea, R. J.; Howard, J. A. K.; Puschmann, H., OLEX2: a complete structure solution, refinement and analysis program. *J. Appl. Crystallogr.* **2009,** 42, 339-341.

[30] Sheldrick, G., Crystal structure refinement with SHELXL. *Acta Crystallogr., Sect. C: Cryst. Struct. Commun.* **2015,** 71, 3-8.

Chapter 7

Spectroscopic Interrogation of the Reduction of Model Chromium Precatalysts for Olefin Oligomerization

This chapter is adapted from a submitted manuscript:

Hopkins Leseberg, J.A.; Henke, W.C.; Douglas, J.T.; Oliver, A.G.; Sydora, O.L.; Blakemore, J.D.

Spectroscopic Interrogation of the Reduction of Model Chromium Precatalysts for Olefin Oligomerization, *Submitted* **2022**.

7.1 Introduction

Ethylene oligomerization catalysts attract significant attention for their applications in commercial technologies for production of 1-alkenes known as linear α-olefins (LAO's) or normal α-olefins (NAO's) that are ubiquitous in everyday applications.[1] Early work in this field showed that simple alkyl aluminum reagents, such as triethylaluminum (TEA), are competent catalysts for ethylene oligomerization. Although effective, such catalyst systems for ethylene oligomerization require high pressures (>200 bar) to drive the reaction forward at acceptable rates.[2] The advent of transition metal catalysts (based on Zr and Ni complexes) to this field enabled catalysis of ethylene oligomerization at lower pressures.[3] Metal catalysts in the nickel-based Shell Higher Olefin Process (SHOP)[4], zirconium-based α-SABLIN (Sabic-Linde), and Idemitsu processes[3] enabled commercialization of LAO production at moderate temperatures. In recent years, there has been an increased demand for 1-hexene, resulting in a renewed focus on the development of efficient and selective ethylene trimerization catalysts.[3,5,6] Although there are multiple metals[7,8] utilized in ethylene trimerization catalysts for the production of 1-hexene, chromium-based systems have been observed to engender higher selectivity, activity, and thermal stability than other systems.[9,10,11,12,13] One such chromium catalyst is based upon a molecular Cr metal complex and was commercialized by Chevron Philips Chemical for use in a successful ethylene trimerization system for production of 1-hexene.[3,14]

Catalyst activation for chromium is typically accomplished by mixing a chromium source, ligand, and an activator, such as methylaluminoxane or an alkylaluminum reagent(s), before the addition of ethylene.[15] There are many ligand-related properties that affect the performance of ethylene trimerization catalysts such as steric bulk, backbone rigidity, atom identity, and denticity.[3,16] Notable examples of ligands utilized in ethylene trimerization include the Wass'

PNP^{OMe} ligand,[17] Wasserscheid's **SNS** ligand,[11] Exxon Mobil's **CNN** ligand,[18] Köhn's facially coordinated **NNN** ligand,[12] Chevron Phillip's bidentate **P,N**,[19] and Phillip's **DMP** that engenders catalysis with commercially-relevant selectivity (see Chart 7.1).[13] In such systems for ethylene trimerization, the formation of the key intermediate species requires a formal (*n* + 2) change in oxidation state, enabling backbonding with coordinated ethylene ligands from filled metal *d* orbitals into unoccupied ligand π* orbitals. Such reduced intermediates are involved in manifolds in which there is a cleavage of the weak C–C π-bonds of two ethylene molecules in order to form two stronger bonds (M–C σ and C–C σ), driving formation of the metallacycle forward.[3] Notably, the oxidation state of the metal redox couple has been highly debated for this process because of the many readily accessible oxidation states of Cr.[20,21] Although a significant body of experimental and theoretical findings support the importance of $Cr^{III/I}$ cycling,[22] limited spectroscopic evidence supporting such an assignment of the redox chemistry of Cr catalysts is available.[23] Obtaining evidence is challenging due to the presumed low concentration of the chromium-derived active species, measurements under catalytic conditions that involve multiple oxidation states, and the challenges inherent in measuring particular oxidation states of Cr, each of which present unique spectroscopic challenges.[24,25,26]

Chart 7.1. Notable ethylene trimerization ligands

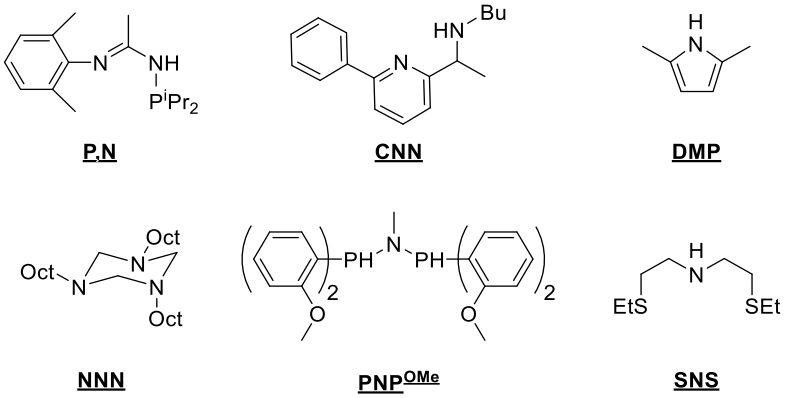

Here, we report the redox reactivity that is accessible to a family of novel Cr^{III} complexes supported by bidentate P,N ligands in the absence of substrates, such as ethylene or related models like hexyne (Chart 7.2). Electrochemical studies of the complexes reveal accessible quasi-reversible reductions at $E_{1/2}$ = ca. –1.5 V vs. ferrocenium/ferrocene (denoted hereafter as $Fc^{+/0}$) that appear to be dominated by slow heterogeneous electron transfer kinetics in all three cases. The electrochemical reductions appear to be significantly affected by chemical rearrangements that occur upon reduction, as evidenced by large peak-to-peak separations. In addition to these molecular features, an observable anodic stripping wave occurs at $E_{p,a}$ = ca. –0.1 V vs $Fc^{+/0}$, suggesting formation of surface-bound heterogeneous material upon reduction. Formation of the heterogenous material was quantified here by piezoelectric gravimetry and the material itself characterized by X-ray photoelectron spectroscopy; the material on the electrode appears to be Cr-based but the total amount formed corresponds to only a small fraction of the total complex undergoing reduction. EPR spectra collected at ca. 7 K reveal broad signals centered near g = 1.98 (with FWHM values of ca. 1000 G) for the paramagnetic Cr^{III} complexes, consistent with literature findings for related S = 3/2 Cr^{III} complexes. *In situ* reduction of the Cr^{III} complexes with the chemical reductants Cp^*_2Co, $AlEt_3$, and modified methylaluminoxane (MAO) reveal complete loss of signal for the Cr^{III} complex to form minor but observable signals at g = 1.98 that are sharper (FWHM of ca. 200 G) and correspond to S = 1/2 Cr^{I} species. Spin quantification with calibrated QEPR techniques reveal the Cr^{I} signals to correspond to very small yields with respect to the total predicted amount of *in situ* generated species.

Additionally, the Cr^{III} complexes were characterized using UV-visible spectroscopy, revealing similar absorption features for all of the complexes that correspond to low molar absorptivity values. UV-vis titrations with **1** and Cp^*_2Co revealed that in the absence of a source of aluminum,

the Cr^{III} complexes undergo clean conversion to one-electron reduced species. This is supported by the chemical preparation, isolation, and solid-state structure obtained on a Cr^{II} form of **1**. Contrasting with these results, we observe that multi-electron reduction of Cr^{III} is accessible in the presence of aluminum. Time-dependent UV-visible spectroscopic studies showed clean conversion of **1** to what we tentatively assign as an Al-bound Cr species upon addition of $AlEt_3$, possibly a doubly-reduced (Cr^{I}) species. Consequently, the presence of aluminum enables further reduction than what is accessible in its absence, consistent with the high Lewis acidity of Al^{3+}. Taken together, these studies show that Cr precatalysts for ethylene oligomerization can be readily reduced to Cr^{II} species, with only minor formation of heterogeneous materials under electrochemical conditions and minor generation of Cr^{I} under analogous chemical reduction conditions. Considering the presence of Al shifts this balance toward favoring Cr^{I} (or Cr^{0}) generation, we anticipate these results will inform future mechanistic studies of these systems in efforts to develop more active catalysts.

Chart 7.2. Chromium model catalysts (Ct = cyclopentyl)

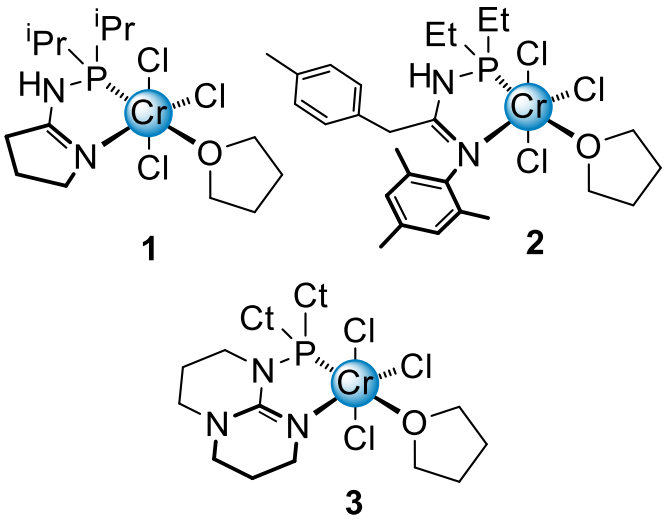

7.2 Results

7.2.1 Cyclic Voltammetry

Cyclic voltammetric studies of the Cr^{III} complexes **1**, **2**, and **3** reveal a quasireversible reduction in all cases that we assign as an accessible Cr^{III}/Cr^{II} reduction at ca. –1.5 V vs. $Fc^{+/0}$ in tetrahydrofuran-based electrolyte (see Figure 7.1). Reduction of **1** ($E_{1/2}$ = –1.41 V) occurs with $E_{p,c}$ = ca. –1.75 V and $E_{p,a}$ = ca. –1.06 V. The wide separation of these peaks (ΔE_p = 690 mV) suggests slow electron transfer; the relatively slow electron transfer kinetics (between the metal center and the electrode) dominate the appearance of the Cr^{III}/Cr^{II} system in each case. Similarly, complex **2** displays a $Cr^{III/II}$ couple at a slightly more positive potential, $E_{1/2}$ = –1.36 V, and an even larger peak-to-peak separation (ΔE_p = 960 mV). Comparatively, the voltammetry of **3** ($E_{1/2}$ = –1.36 V) appears have a more chemically reversible reduction than **1** and **2**; the reduction occurs with $E_{p,c}$ = ca. –1.53 V with reoxidation at $E_{p,a}$ = ca. –1.19 V (ΔE_p = 340 mV). Scan rate dependence of the redox process for **1**, **2**, and **3** and their reduced analogues show that all the species involved are soluble and freely diffusing (see Appendix E, Figures E2, E6, and E10).

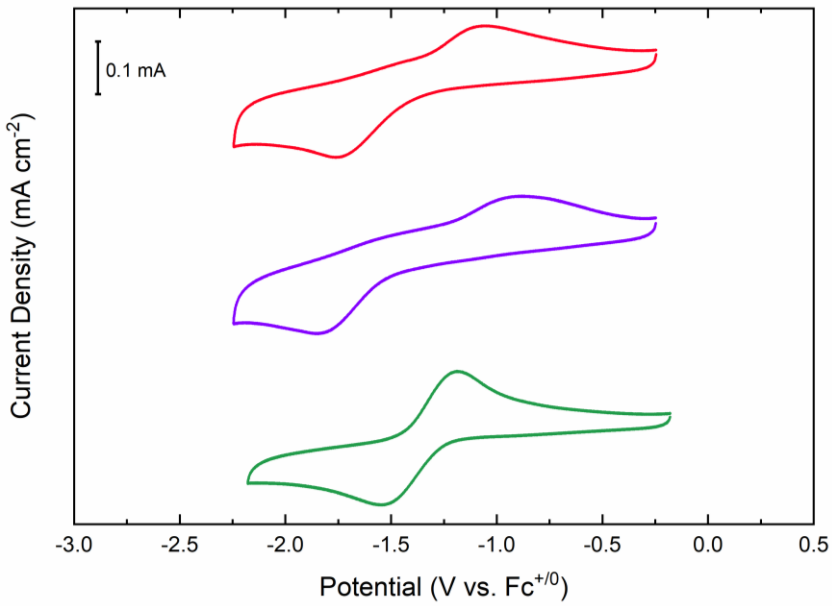

Figure 7.1. Cyclic voltammetry of **1** (red, upper), **2** (purple, middle), and **3** (green, lower). Conditions: electrolyte, 0.1 M $TBAPF_6$ in THF ; scan rate, 100 mV/s; working electrode, highly oriented pyrolytic graphite (HOPG); [Cr] in each experiment ca. 1.5 mM. Initial potentials ca. − 0.25 V.

Cyclic voltammetry (CV) of the Cr^{III} complexes with extended cathodic polarizations subsequently scanned to +0.5 V reveal a symmetric reoxidation event near –0.1 V. This symmetric oxidation indicates formation of heterogenous material on the electrode following reduction (see Figure 7.2 and Appendix E, Figures E3 and E11). Following constant polarization at –2.25 V for extended periods of time prior to scanning oxidatively results in increased anodic current in the symmetric anodic wave, indicating greater reductive accumulation of the material undergoing oxidation (see Figure 7.2). Notably, heterogenous material is not formed in the absence of the precursor. Thus, heterogenous material is anticipated to be formed by further follow up reactivity of the reduced molecular species.

In the case of **3**, the system appears to remain molecular in nature, undergoing a relatively "clean" reduction (see Appendix E, Figure E11). Reduction of **1** and **2**, on the other hand, results

in generation of significant quantities of heterogenous material at the electrode surface (observable in the anodic stripping waves at $E_{p,a}$ = ca. –0.1 V vs. $Fc^{+/0}$). There is a notably greater formation of heterogenous material upon reduction of **2** versus the case of reduction of **1** (see Figure 7.2 and Appendix E, Figure E3). The reduction of Cr^{III} to Cr^{II} thus appears to be accompanied by multiple significant chemical reactions in each case, and these depend upon the identity of the supporting [*P*,*N*] ligand.

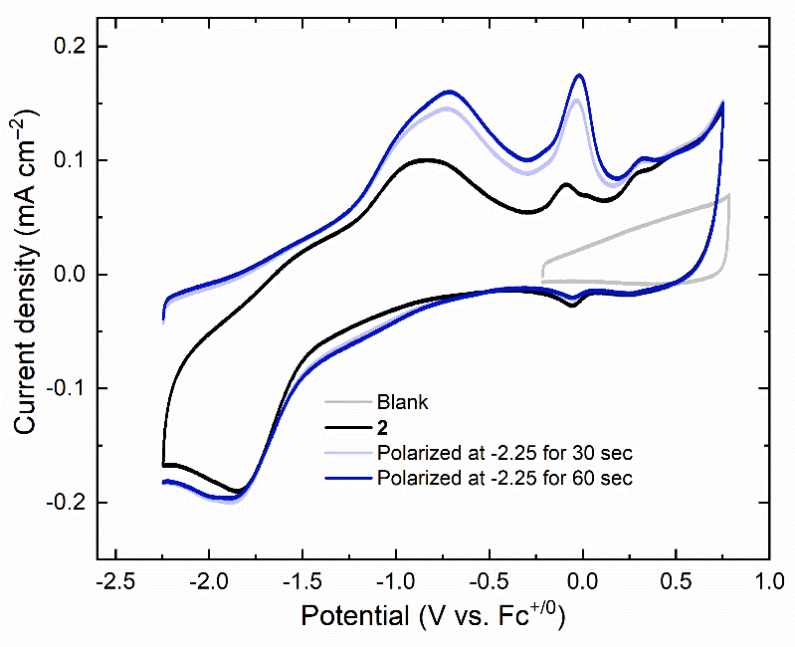

Figure 7.2. Extended cyclic voltammetry of **2** (black), **2** polarized for 30 seconds at –2.25 V (light blue), polarized for 30 seconds at –2.25 V (dark blue), Blank scan: 0.5 V to –0.2 V (gray). Conditions: Electrolyte, 0.1 M $TBAPF_6$ in THF ; scan rate, 100 mV/s; working electrode, highly oriented pyrolytic graphite (HOPG); [Cr] in experiment ca. 1.5 mM.

In addition to interrogation of accessible oxidation states available to the Cr^{III} complexes by cyclic voltammetry, we performed electrochemical titrations with **1**, **2,** and **3** with $AlEt_3$ to probe the identity and behavior of the reduced forms of the chromium precatalysts in the presence of $AlEt_3$. In each case, there is an observed positive shift of $E_{p,c}$ and $E_{p,a}$ in the presence of $AlEt_3$.

Titration of **1** results in a positive shift of $E_{p,c}$ by +33 mV while $E_{p,a}$ shifts by +327 mV. The significantly greater positive shift in $E_{p,a}$ versus $E_{p,c}$ is indicative of the electrogenerated Cr^{II} species interacting more significantly with $AlEt_3$. Prior work with $Ti^{IV/III}$ complexes has implicated that reduction of Ti induces reactivity with $AlEt_3$, a reactivity pattern that appears to be at work here as well.[27,28] Similarly, with **2** and **3**, there is an observed larger shift in $E_{p,a}$ than $E_{p,c}$ (**2**: $E_{p,c}$ = +45 mV, $E_{p,a}$ = +96 mV; **3**: $E_{p,a}$ = 642 mV, $E_{p,c}$ = 126 mV) indicating that there is a similar effect occurring with **2** and **3** upon addition of $AlEt_3$ (see Appendix E, Figures E13 and E14). This electrochemical behavior motivated us to study each of these complexes further with $AlEt_3$ to investigate the influence that the reagent has over the reactivity of these complexes under reductive conditions.

7.2.2 EQCM Quartz Crystal Microbalance

The heterogeneous material implicated by the voltammetric data to form on the electrode surface upon reduction of the Cr^{III} complexes in the absence of Al could be directly confirmed and quantified using the electrochemical quartz crystal microbalance (EQCM). The EQCM relies on the inverse piezoelectric effect to monitor the apparent mass change at a working electrode during electrochemical experiments.[29] The working electrode in an EQCM experiment serves as an electroactive surface that is in direct contact with the bulk solution, but in the specific case of EQCM studies, a working electrode consisting of an AT-cut quartz crystal sputtered with gold is used to enable monitoring of the mass of the electrode during electrochemistry experimentation. The vibrational frequency measured for the quartz disk can be converted to an apparent change of mass with the Sauerbrey equation (see Appendix E, Equation E1).[30] This highly sensitive technique, also known as piezoelectric gravimetry, is capable of consistent measurement of mass changes on the order of ±5 ng (±5 Hz) with our equipment.[31] Our previous studies have utilized

EQCM for measurement of heterogenous material deposited during molecular electrocatalysis.[32,33]

EQCM studies with concurrent CV studies confirm formation of significant heterogeneous material from reduction-induced decomposition of the Cr^{III} starting materials, even upon single voltammetric cycles (see Appendix E, Figures E15-E18, E20-E23, and E25-E27). In particular, **2** appears to be the least stable system upon reduction, as judged by the formation of the greatest amount of heterogeneous material upon reduction (see Figure 7.3). To quantify the amount of material deposited following constant polarization at a reducing potential, controlled potential electrolysis (E_{app} = –2.25 V) was carried out with EQCM-based mass monitoring. These studies confirm that **2** generates the most heterogenous material upon reduction, ca. 2000 ng over 15 minutes (Figure 7.3). The electrodeposited material generated from **2** is clearly visible on the surface of the quartz disk following reduction. Eimilar reduction of **1** generates heterogenous material to a lesser degree, ca. 200 ng over 15 minutes (see Appendix E, Figure E19). Comparatively between **1** and **2**, **3** undergoes the most chemically reversible reduction and deposits the least amount of heterogeneous material on the electrode surface, only ca. 20 ng over 15 minutes (see Appendix E, Figure E28). These findings underscore the utility of the EQCM in assaying the stability of precatalysts upon reduction, and indicate that there are indeed multiple chemical reactions taking place upon reduction of the Cr^{III} complexes. Some of these must lead to formation of heterogenous material; the reactivity is dependent upon the identity of the supporting bidentate ligand framework.

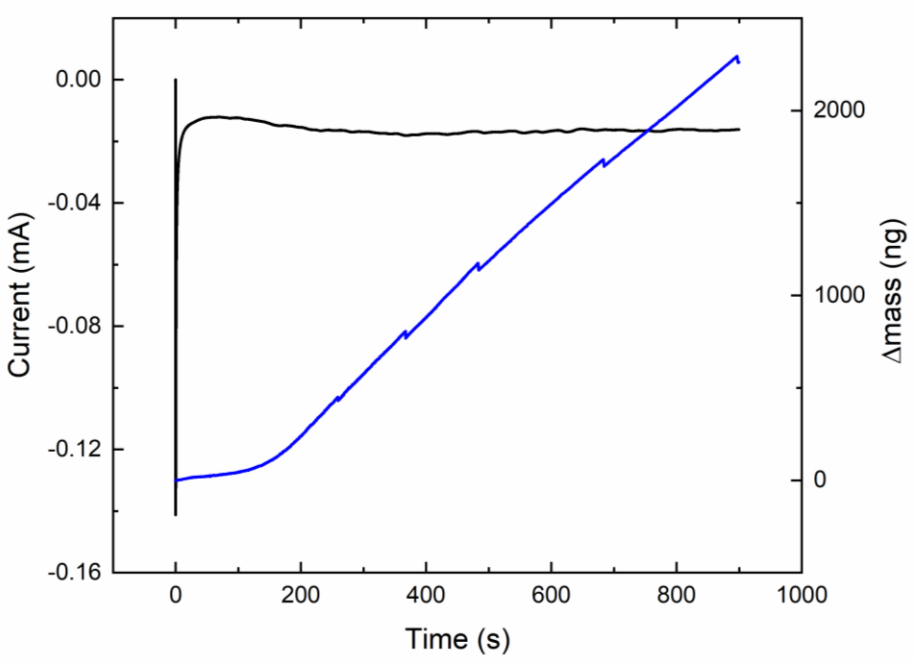

Figure 7.3. EQCM/bulk electrolysis studies **2**. Constant potential current (black line) and gravimetric mass data (blue line). Working electrode: gold-sputtered quartz disc. Pseudo-reference electrode: $Ag^{+/0}$. Counter electrode: platinum wire. Bulk electrolysis carried out in solution 0.1 M $TBAPF_6$ in THF where [Cr] = 1.5 mM.

7.2.3 X-ray Diffraction Studies

In parallel to electrochemical experiments, we performed chemical reduction experiments to elucidate the structural properties of the reduced species accessible to the Cr^{III} model catalysts. Reduction of **1** with one equivalent Cp^*_2Co ($E_{1/2}$ = ca. –1.9 V)[34] in THF yielded light blue crystals suitable for X-ray diffraction (XRD) studies that were obtained from slow cooling of a solution of the reaction mixture of **1** + 1 equivalent of Cp^*_2Co in THF. The resulting solid-state structure reveals the geometry of the formally Cr^{II} metal center to be square pyramidal in nature, with C_1 symmetry. The solid-state structure obtained confirms that one-electron reduction of the metal complex leaves the bidentate [*P*,*N*] ligand intact and bound inner-sphere along with two monodentate chloride ligands and a bound, disordered THF molecule (see Figure 7.4; reduced

complex denoted **1-R**). This crystal represents a unique case of a Cr^{II} center bearing a [*P*,*N*] ligand framework, and is a system that compares to related examples.[35,36] This result confirms that addition of one equivalent of Cp^*_2Co as a stoichiometric reductant to **1** results in one-electron reduction and confirms the overall interpretation of the redox processes observed in the electrochemical experiments (*vide supra).*

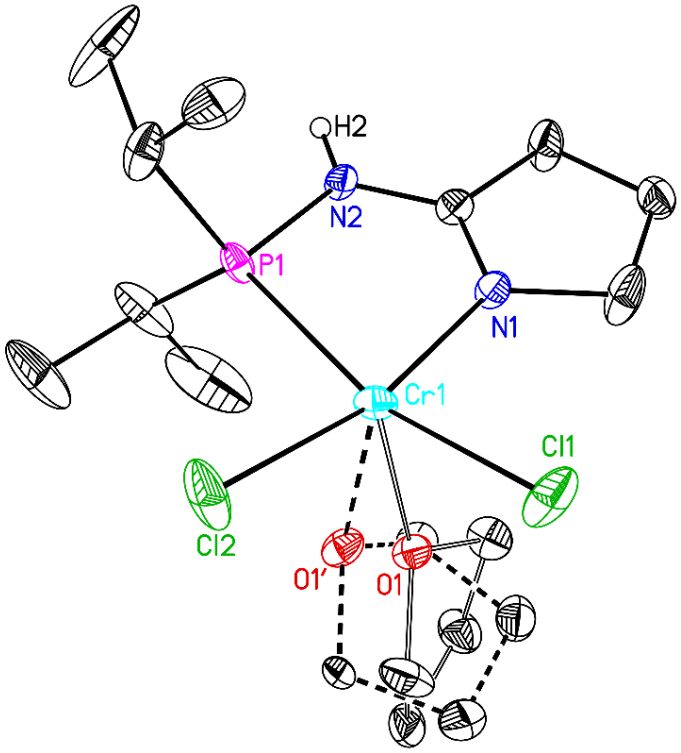

Figure 7.4. Solid-state structures of **1-R** (XRD). All hydrogens except H2 omitted for clarity. Displacement ellipsoids are shown at 50% probability level. Disorder for the THF ligand shown.

7.2.4 X-ray Photoelectron Spectroscopy

Next, we turned to X-ray photoelectron (XP) spectroscopy to investigate the nature of the electrodeposited material on the electrode surface.[37] XP studies were performed with **2**, as this complex was observed to generate the most heterogenous material upon reduction. Control studies interrogating the clean surface of basal-plane highly oriented pyrolytic graphite (HOPG) electrodes

revealed signals in the survey spectrum (Figure 7.5, upper panel) corresponding to carbon (C 1s photoelectron and C KLL Auger electron peaks) as well as more minor contributions from oxygen (O 1s photoelectron and O KLL Auger electron peaks); the signals corresponding to O are attributable to oxygen from adventitious water on the electrode surface as well as oxidized carbon species.[38]

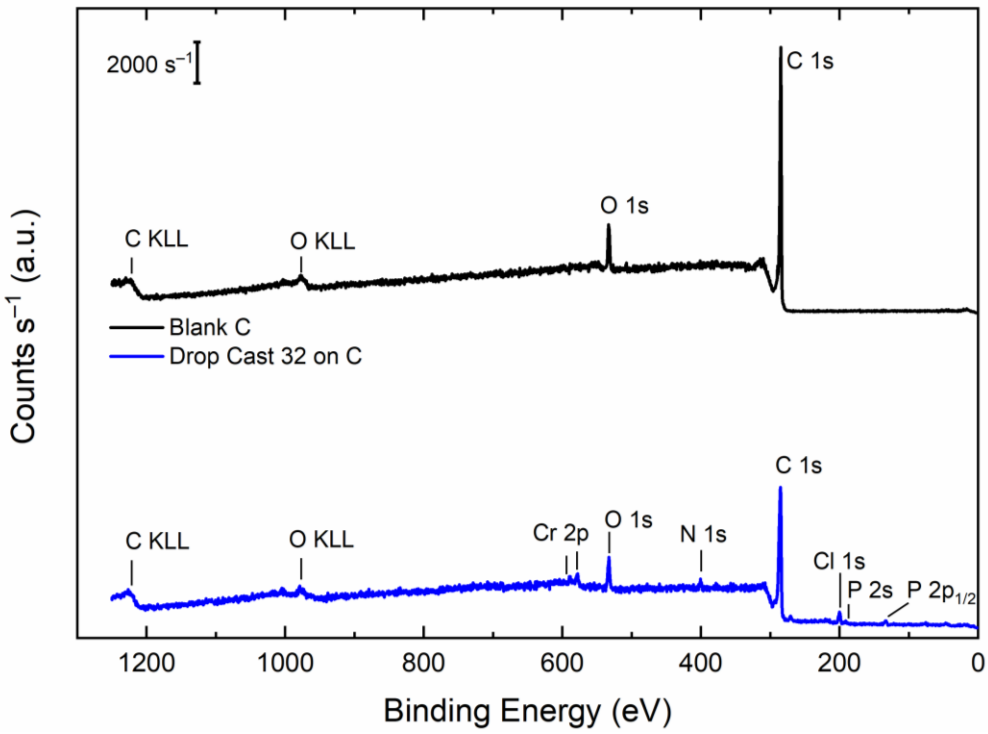

Figure 7.5. X-ray photoelectron spectra for a blank electrode (upper, black) and a drop casted electrode with **2** (lower, blue).

To interrogate the appearance of unreduced **2** in XP spectra, a sample was prepared by drop-casting a solution of **2** in THF onto the basal plane of a HOPG electrode. The survey spectrum of this electrode revealed new signals that correspond to chromium (Cr 2p), nitrogen (N 1s), chlorine (Cl 2p) and phosphorus (P 2p), in agreement with the anticipated composition of **2**. High resolution scans of the regions of interest (Cr 2d, N 1s, Cl 2p and P 2p) corroborate the formulation and stability of the complex and provided a suitable baseline for comparison to the electrogenerated

species on the electrode (Figure 7.5, lower panel). Analysis of the Cr 2p region (570 - 595 eV) displays the expected $2p_{3/2}$ and $2p_{1/2}$ doublet signal; the signals could be readily fitted with peaks in a 3:2 area ratio as theoretically expected (see Appendix E, Figures E31-E33).[39] The Cl 2p region (195 – 215 eV) could be reliably fit with three unique chlorine signals in a 1:1:1 ratio, in accord with the unique chemical environments of the chloride ions in **2**. Similarly, the N 1s region (390 – 410 eV) could be reliably fitted to two N signals in a 1:1 ratio; we assign the signal at 401.6 eV to the imine moiety and the signal at 400.6 eV to the amine nitrogen.[40]

With this baseline characterization of the starting material in hand, we next characterized the electrogenerated heterogenous material. In this work, the gold-sputtered quartz EQCM disks were tethered to the XP sample holder with carbon tape to ensure conductivity and mitigate charging issues inherent to XP spectroscopy on dielectric substrates.[38] The survey spectrum of the electroactive gold surface of a clean disk revealed the numerous typical signals corresponding to gold (Au 1s, 4p, 4d, 4f and 5p) with additional contributions from carbon (C 1s photoelectron and C KLL Auger electron peaks) as well as contributions from oxygen (O 1s photoelectron and O KLL Auger electron peaks; see Appendix E, Figure E34). The signals corresponding to O are attributable to oxygen from adventitious water on the electrode surface, as well as, perhaps, minor contributions from oxidized Au species.

The survey spectrum of a working-electrode EQCM disk prepared by electrolysis (E_{app} = –2.25 V) in the presence of **2** revealed signals that correspond to chromium (Cr 2p), nitrogen (N 1s), chlorine (Cl 2p) and phosphorus (P 2p). The Cr 2p region (570 - 595 eV) displays the expected $2p_{3/2}$ and $2p_{1/2}$ signals for this element; the signals could be fitted in a 3:2 area ratio as theoretically expected (see Figure 7.6 and Appendix E, Figure E36-E39) for a single Cr species on the electrode surface. The doublet signal is shifted to lower binding energies in comparison to the Cr^{III} signal

for **2**, this shift is consistent with a reduced form of Cr-based material present on the electrode surface. Similarly, the N 1s region (390 – 410 eV) could be fitted with two N species in a 1:1 ratio, attributable to the imine moiety (signal at 399.5 eV) and to the amine moiety (398 eV) of the bidentate ligand present in the starting material **2**. Notably, the N 1s signal arising from the tetrabutylammonium cation of the $TBAPF_6$ electrolyte would appear at a significantly more positive binding energy (401 - 403 eV); $TBAPF_6$ was washed away with THF prior to analysis.[37] The Cl 2p region (195 – 215 eV) could be satisfyingly fitted to three chlorine signals in a 1:1:1 ratio, as well. Variable contributions from oxygen (O 1s photoelectron and O KLL Auger electron peaks), however, could be attributed to oxygen from adventitious water on the electrode surface.

Examination of the fitted high-resolution data for the electrodeposited material reveals 1 type of Cr and 1 type each of N and Cl arising from the ligand-derived signals on the surface. However, these signals for the individual elements appear significantly different from those of the drop-cast, unreduced **2** on HOPG. Most importantly, the Cr doublet signal shifts to lower binding energy, consistent with reduction of the starting Cr^{III} species to a reduced Cr species. The shift of the ligand components, N and Cl, to lower binding energies indicates that they are in a less electron-rich environment, consistent with being unbound from Cr^{III} on the surface of the electrode (see Appendix E, Table E1 and E2 for relative binding energies of **2** on HOPG and the EQCM prepared electrode by electrolysis of **2**, respectively). Using the Scofield relative sensitivity factors (RSF values),[41] the amounts of Cr, N, and Cl on the surface could be determined (see Appendix E, Table E1 and E2 for ratios based on relative areas for **2** on HOPG and the EQCM prepared electrode by electrolysis of **2**, respectively). The ratio of Cr:N and Cr:Cl is much greater than expected/measured for **2** (ca. 14:1 and 14:1, respectively). Taken together, this data suggests that **2** can undergo decomposition to reduced Cr species and non-ligated organic components on the

electrode surface. However, based on the EQCM experiments this deposition represents only ca. 3% of the total 1.5 mM Cr^{III} solution that was electrolyzed, indicating this heterogenous material represents a minor reaction channel upon reduction of **2**. Collectively, these findings support the assertion that the major product of reduction is a homogenous Cr^{II} species under electrochemical conditions.

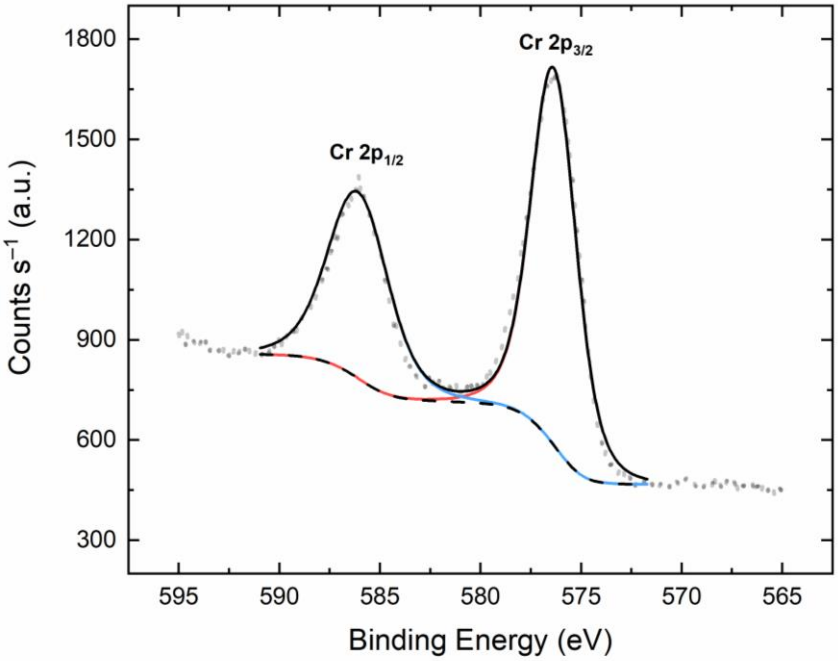

Figure 7.6. X-ray photoelectron spectrum in the Cr 2p regions for electrolyzed **2**. Cr $2p_{3/2}$ and $2p_{1/2}$ peaks are labelled. Legend: gray dots: data; dashed black line: fitting background; blue line: Cr $2p_{1/2}$ peak fit; red line: Cr $2p_{3/2}$ peak fit (constrained to 2/3 area with respect to Cr $2p_{3/2}$); continuous black line: overall fit.

7.2.5 Electron Paramagnetic Resonance Spectroscopy

Following investigation of the electrodeposited product observed upon electrochemical reduction, we were interested in confirming the oxidation state of the major reduction product(s) accessible from the Cr^{III} starting materials. X-band electron paramagnetic resonance (EPR) spectroscopy was utilized to investigate the intermediates formed upon reduction, as the Cr^{III}

starting materials are paramagnetic and the possible Cr^{II} and Cr^{I} products were anticipated to be paramagnetic in nature as well. Prior to chemical reduction, **1**, **2**, and **3** are EPR active with Cr^{III} centers having d^3 configurations and S = 3/2 ground states.[42] X-band EPR studies at ca. 7 K revealed broad absorptive-like features at g = ca. 4 and broad (FWHM values of ca. 1000 G) derivative-like features at g = ca. 2 for **1**, **2**, and **3** (see Figure 7.7, blue trace, and see Appendix E, Figure E40). These spectral features are consistent with S = 3/2 ground states and the formal Cr^{III} oxidation state, as well as an axial zero-field splitting parameter (D) much greater than the excitation microwave frequency (hν) of 9.6 GHz or 0.32 cm^{-1}.[43,44]

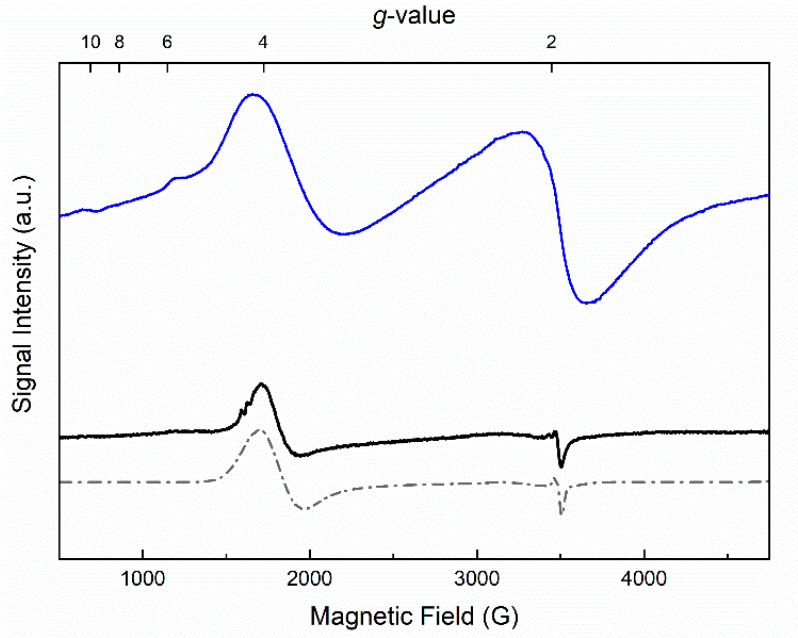

Figure 7.7. X-band continuous-wave EPR spectrum of 2 mM solution of **2** in DCM (blue trace). Conditions: T = ca. 7 K; modulation amplitude = 4.0 G; time constant = 5 ms. X-band continuous-wave EPR spectrum associated with *in-situ* reduction of **2** with Cp^*_2Co in THF (black trace). Conditions: T = ca. 7 K; modulation amplitude = 4.0 G; time constant = 5 ms. Simulated spectrum (gray dashed trace). EasySpin simulation parameters as follows: Cr^{I} component, S = 1/2, g = [1.97

2 2], nucleus: Cr, *g*-strain = [0.02 0.1], lw = 0; Cr^{III} component, *S* = 3/2, *g* = [1.98 1.98], nucleus: Cr, *D* = 18000 MHz, *E*/*D* = 0.0, *g*-strain = [0.3 0.15].

Treatment of **1**, **2**, and **3** with 1 equiv of Cp^*_2Co ($E_{1/2}$ = ca. –1.9 V)[34] results in attenuation of the axial Cr^{III} signals in all cases and the appearance of new species in the spectra that display isotropic symmetry and characteristic features at *g* = ca. 2 in all cases (see Experimental Section for details on sample preparation for the *in situ* reduction studies). The FWHM values of the new isotropic species are relatively small (ca. 200 - 250 G) at 7 K in THF (see Figure 7.7, black trace,43 and Appendix E, Figures E41-E44). These narrower signals can be assigned to d^5 Cr^I species with *S* = 1/2 in all three cases on the basis of spectral profiles for Cr^I systems in the literature.[45,46] Notably, the d^4 Cr^{II} species expected as the major reduction products would be difficult to observe with the EPR instrumentation used in these studies in perpendicular mode; this is due to the high likelihood of these Cr^{II} species having non-Kramers *S* = 2 ground states.[47] In the detectable Cr^I species, no significant hyperfine coupling to ligands in the secondary shell (e.g., phosphorus) was detected. We observe a similar signal for the chemical reduction of the Cr^{III} complexes with $AlEt_3$ and modified MAO (see Appendix E, Figures E45 and E46 for reduction with $AlEt_3$ and modified MAO, respectively). The similarity in the spectral profiles suggests that the reactivity following chemical reduction is similar when using aluminum-based chemical reductants as in the case of Cp^*_2Co.

The experimental EPR spectra of the *in situ* reduced species could be successfully modeled using the EasySpin software to confirm the qualitative interpretation of the data as given above. The spectral profile of the data corresponding to the *in situ* reduction of **2** with Cp^*_2Co was well-reproduced using a mixture of two components (see Figure 7.7, dashed gray trace). One component is a *S*=1/2 system which exhibits *g* values consistent with Cr^I species; the second component is a

single *S*=3/2 system with *g* values consistent with a Cr^{III} species. Notably, the *in situ* experimental data for **2** showed a small portion of unreacted Cr^{III} starting material; all other data for the *in situ* reductions appear to have nearly complete conversion resulting in loss of the signals associated with Cr^{III} (see Appendix E, Figures E41 and E43). Modeling of the Cr^{I} components for *in situ* reduction of **1** and **3** resulted in similarly good agreement with the experimental data (see Appendix E, Figure E44). Thus, we conclude that reduction of the Cr^{III} precatalysts proceeds relatively quickly with all the reductants tested under our conditions and that the reduced products are stable on the seconds to minutes timescale (see Appendix E, Figure E41-E43).

Complementing these general observations from the EPR data, we also carried out spin quantification to define the amounts of Cr^{I} generated *in situ* in order to better define the overall outcome of reduction of **1**, **2**, and **3**. Spin quantification via quantitative EPR (QEPR) is an assay that relies on normalizing for both i) instrument response using a paramagnetic external standard of known concentration and ii) the spectral acquisition parameters and instrumental variables.[48] Additionally, as the EPR spectra acquired in this study were recorded as the first derivative of absorption with respect to magnetic field, our QEPR study also relied on double integration of the raw data to obtain the integrated absorption spectrum that is proportional to concentration in QEPR methodology. [48,49,50]

In our QEPR assay, we developed one calibration curve using solutions of paramagnetic standards with well-known properties at fixed concentrations: TEMPOL (4-hydroxy-2,2,6,6-tetramethyl-piperidin-1-oxyl), $Cu(NO_3)_2$, and $MnCl_2$ (see Appendix E, Figures E50-E52 for EPR spectra and plotted double integrals). The calibration curve spans concentrations from ca. 10 to 700 μM and was prepared in a glassing solvent system of 1:0.25 H_2O/glycerol (see Appendix E, Figure E49 and Table E3 for the calibration curve and experimental conditions).[51] In our protocol,

EPR spectra were recorded under non-saturating conditions for each sample, the double integral was determined from the relevant experimental spectrum and the concentration of Cr^{I} in each sample was calculated using Equations E2 and E3.[52] This method was applied to the spectra associated with the series of *in situ* reduction experiments. The double integration of the signal at ca. $g = 2$ corresponding to Cr^{I} was used for the quantification of Cr^{I} generated upon reduction; the calibration curve associated with the paramagnetic standard compounds that relates the corrected double integral value with the known concentrations was used to determine the concentration of Cr^{I} associated with each of the relevant signals for each *in situ* reduction experiment (see Appendix E for experimental and calculation details). The standard measurements indicate that, in our hands, the QEPR assay can be used to estimate concentrations of paramagnetic species with limits of detection in the low micromolar range an average error of ca. 2% on the basis of the variance ($\pm 1\sigma$) in the slope of the best-fit standard line.

The collected EPR data for the *in-situ* chemical reductions were analyzed using the validated QEPR assay to determine the concentration of the Cr^{I} species[46,53] formed upon reduction (*vide supra*). Our findings show that reduction results in <1% conversion to the species assigned as Cr^{I} with respect to the concentration of the Cr^{III} starting material used in each case. Similarly, the chemical reductions of the Cr^{III} complexes with $AlEt_3$ and modified MAO resulted in <1% conversion to Cr^{I} species as well (see Appendix E, Table E4). These results illustrate that the signals observed in the EPR spectra are not associated with the major product of the *in-situ* reduction of these complexes.

Complementing these *in situ* reduction experiments, the EPR spectrum of the well-defined Cr^{II} complex denoted **1-R** (crystalline material, *vide supra*) was obtained. The EPR spectrum of **1-R** shows no observable signals (see Appendix E, Figure E47). This finding supports the assignment

of the signals in the prior EPR studies as Cr^{I} oxidation state species, as these appear quite distinctive in the data.[47] Together these results imply that the major reduction products using Cp^*_2Co and Al-based reductants are integer-spin, non-Kramers Cr^{II} (d^4, $S = 2$) species that are not directly observable in our cases by X-band EPR. We conclude that the small signal observed near g = 2, however, upon chemical reduction is a minor Cr^{I} product.[53,**Error! Bookmark not defined.**]

7.2.6 Electronic Absorption Spectroscopy

Electronic absorption (EA) spectra were collected for the isolated Cr^{III} materials, yielding similar absorption spectra for **1**, **2**, and **3** that feature two *d-d* absorption bands at ca. 450 and 650 nm. The compounds are characterized by low molar absorptivity values for these bands in the visible range (ca. 100 M^{-1} cm^{-1}; see Appendix E, Figures E54-E59). With this characterization of the isolated Cr^{III} species in hand, we focused on reactivity studies of **1** with Cp^*_2Co, $AlEt_3$, and modified MAO. In particular, titrations with UV-visible monitoring were carried out for **1** with these chemical reductants in order to understand the spectral changes upon reduction of the precatalysts.

Titration of a 19 μM solution of **1** in THF with Cp^*_2Co (Figure 7.8) resulted in a decrease in absorbance at λ = 247 nm, a significant increase in absorbance at λ = 298 nm and a slight increase in absorbance at λ = 350 nm. There are two isosbestic points at 237 nm and 276 nm, indicating clean conversion of the Cr^{III} starting material to a reduced Cr^{II} complex upon addition of one equivalent of reductant. However, further additions of Cp^*_2Co past one equivalent did not result in new isosbestic points; these further additions only yielded an increase in absorption across the spectral range (see Appendix E, Figure E69), consistent with single-electron reduction of **1** to a Cr^{II} species. This finding is supported by the solid-state structure obtained by bulk chemical reduction of **1** (*vide supra).*

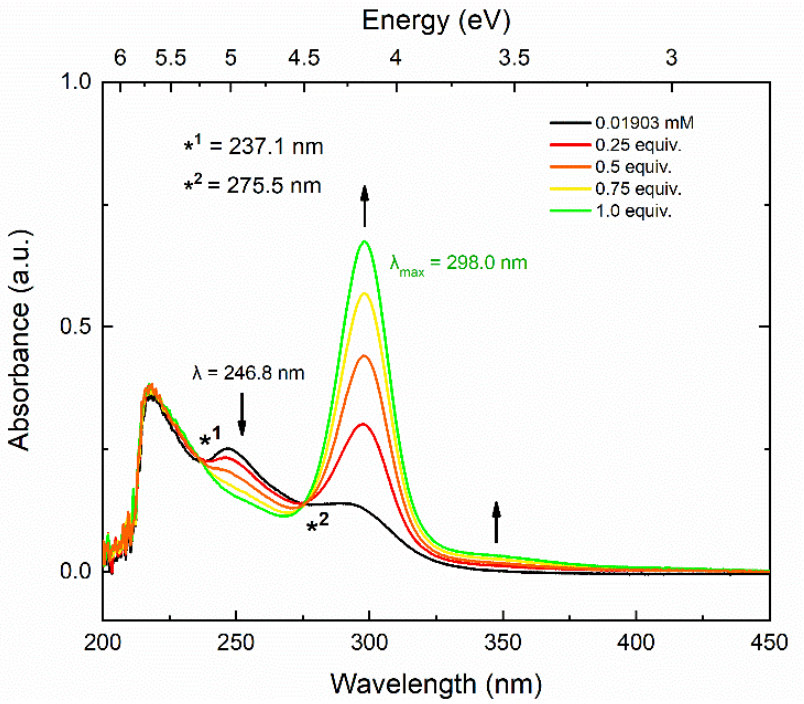

Figure 7.8. UV-Visible spectra of **1** in THF with increasing additions of Cp^*_2Co up to 1 equivalent.

Upon observation of the clean $1e^-$ reduction of **1** with Cp^*_2Co, we next probed the reactivity of **1** with $AlEt_3$. However, unlike in the case of the addition of Cp^*_2Co, spectral changes were not immediate with $AlEt_3$; thus, the spectral profile was monitored over time following addition of one equivalent of $AlEt_3$ to a 19 μM solution of **1** in THF. Collection of spectral data at two-minute intervals over a ten-minute time course (see Figure 7.9) revealed an increase in absorbance at λ = 227 nm, a decrease in absorbance at λ = 297 nm and an increase in absorbance at λ = 342 nm. The series of collected spectra display two isosbestic points at 244 and 310 nm, demonstrating clean conversion of **1** to a new species that we hypothesize be a reduced Cr species (formed by Al–C bond cleavage and subsequent radical reactivity) or an Al-bound Cr species (bridged by alkyl or chloride bridging ligands), among other possibilities.[27]

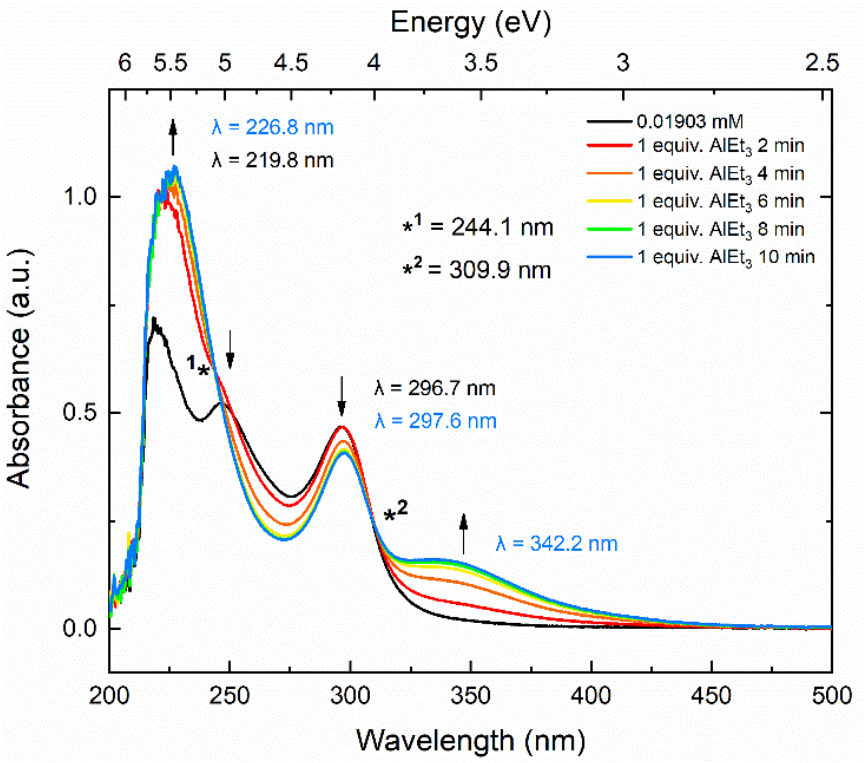

Figure 7.9. UV-Visible Spectra of **1** in THF. Time course study over 10 minutes of the addition of 1 equivalent of $AlEt_3$ to **1.** Spectra were collected at 2-minute time intervals.

Encouraged by our initial finding of clean reactivity between **1** and $AlEt_3$, we next titrated the resulting species with Cp^*_2Co to investigate possible further reduction chemistry accessible to the system. A solution of **1** in THF was thus mixed with $AlEt_3$ and allowed to stir for ten minutes; the mixture was then titrated with Cp^*_2Co in increasing increments of 0.25 equivalents (see Figure 7.10). Increasing equivalents of Cp^*_2Co yielded spectra in which there is a decrease in absorbance at λ = 221 nm, a significant increase in absorbance is observed at λ = 290 nm and a decrease in absorbance at λ = 358 nm. Titration with up to 1 equivalent of Cp^*_2Co gave rise to two isosbestic points at 254 and 323 nm, indicating clean conversion between the Al-treated intermediate complex to a further reduced species. This can be confidently inferred from the spectra in Figure 7.10 in light of the large increase in absorbance near 300 nm, corresponding to *in situ* generation of $[Cp^*_2Co]^+$ by electron transfer to Cr. However, addition further Cp^*_2Co reductant gives rise to

continued, identical isosbestic spectral changes, indicating that further reduction is accessible to this system.

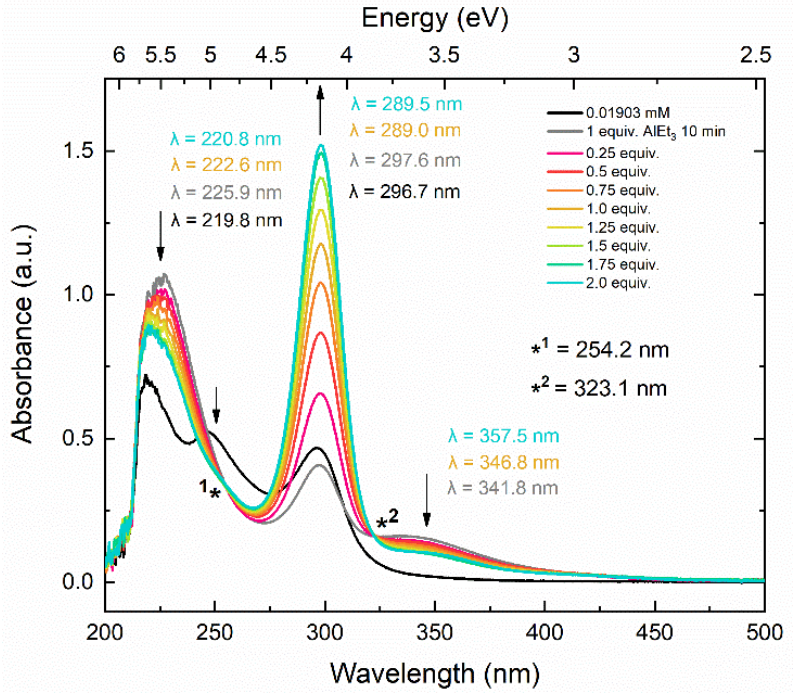

Figure 7.10. UV-Visible Spectra of **1** in THF. The addition of 1 equivalent of $AlEt_3$ to **1** with increasing additions of 0.25 equivalents up to 2 equivalents of Cp^*_2Co.

On the basis of the data and the appearance of a single set of isosbestic points across additions of up to 2 equivalents of Cp^*_2Co, we conclude that addition of $AlEt_3$ enables reduction of the generated species beyond Cr^{II}, a process not observed in the absence of $AlEt_3$. As the addition of up to a full third equivalent of Cp*Co results in no further isosbestic changes to the spectrum and general absorption increase instead (see Appendix E, Figure E75), an overall $2e^-$ reduction scheme becomes accessible for the Al^{III}-treated Cr system in this case. Thus, the presence of Al^{III} in solution with **1** appears to unlock a fundamentally different reductive reactivity manifold in comparison to that accessible to **1** in a monometallic context. Such shift in accessible oxidation state(s) in the presence of Al^{III} could impact catalysis, as the single set of isosbestic data suggest

that single electron reduction of the Al^{III}-treated **1** results in generation of a transient singly reduced species that undergoes disproportionation to yield a doubly reduced species that cannot undergo further reduction beyond $2e^-$. Although we cannot fully assign the formulation of the reduced species resulting from this manifold of reactivity at this time, it can be confidently concluded that the system becomes capable of accessing at least one oxidation state lower than +II upon treatment of **1** with $AlEt_3$.

7.3 Discussion

In this study, we endeavored to investigate the lower oxidation states accessible to a small set of Cr^{III} precatalysts for olefin oligomerization, as well as obtain structural information for any readily accessible reduced forms of the precatalysts. Electrochemical studies revealed the presence of a single quasi-reversible and one-electron reduction of all three Cr^{III} complexes at ca. –1.50 V vs $Fc^{+/0}$ in all cases; the observation of similar reduction potentials for **1**, **2**, and **3** is consistent with the similar donor properties of the [*P*,*N*] ligands supporting the complexes in all three cases. In line with this electrochemical data, *in-situ* X-band EPR spectroscopy studies of reduction of the complexes with Cp^*_2Co ($E_{1/2}$ = –1.# V vs. $Fc^{+/0}$) resulted in disappearance of the broad signal corresponding to the Cr^{III} starting materials in all cases; no signals ascribable to the resulting Cr^{II} were observed, however, due to the EPR-silent nature of these species. UV-visible spectroscopy coupled with titration experiments focusing on reduction of **1** with Cp^*_2Co gave rise to isosbestic points, however, confirming clean one-electron reduction of **1** to a Cr^{II} form. Bulk chemical reduction and isolation of the product coupled with data from single-crystal X-ray diffraction analysis confirmed the formation of a Cr^{II} species that retains the starting bidentate [*P*,*N*] ligand. Thus, the overall picture of the reduction chemistry accessible to **1** and its analogues is a $1e^-$ manifold with Cr^{III}/Cr^{II} redox cycling.

However, cyclic voltammetry studies with extensive polarization at negative voltage suggests that generation of further reduced and heterogenous material is possible as a side reaction under electrochemical conditions. Observation of an anodic stripping wave at $E_{p,a}$ = ca. –0.1 V vs. $Fc^{+/0}$ and related EQCM studies confirmed that heterogenous material is deposited on the surface of the working electrode; **2** generated the most heterogenous material upon reduction (ca. 2000 ng over 15 minutes). *Ex situ* XP studies of the heterogenous material revealed the electrodeposited material to be primarily composed of Cr^0 along with an organic ligand component in a ca. 10:1 ratio. At this stage, however, the formation of heterogeneous material under electrochemical conditions appears to be a minor side reaction. Similarly, under homogeneous conditions using Cp^*_2Co as a chemical reductant, QEPR studies showed that Cr^I represents a product of reduction that is formed in a yield of <1%, implying a high yield of the Cr^{II} oxidation state.

However, contrasting with all these findings implicating high yields of Cr^{II} under reductive conditions that lack a Lewis acidic additive, titration of **1** with $AlEt_3$ revealed the accessibility of a deeper reduction by $2e^-$; a single set of isosbestic points indicates that a reductive disproportionation can occur, chemistry that likely leads to generation of Cr^I or Cr^0 under mixed-metal conditions. As the $2e^-$-reduced product is not accessible in the absence of Al^{III}, a role for $AlEt_3$ in favoring access to a lower oxidation state of the precatalyst can be directly implicated from this work. As ethylene oligomerization is commonly practiced with Cr-based precatalysts and activating Al^{III} reagents, we anticipate that these findings could be of relevance to future mechanistic studies of ethylene oligomerization. The more highly reduced form of our model system **1** is not produced in large quantities in the absence of Al^{III}, but appears to be quite accessible via disproportionation reactivity when it is present.

On the basis of our findings, we conclude that $Cr^{IV/II}$ redox cycling in ethylene trimerization is unlikely to be a dominant redox manifold for catalysis, as the presence of Al^{III} favors deeper reduction of the system. Either $Cr^{III/I}$ or $Cr^{II/0}$ remain attractive possibilities, however, as Al^{III} enables ready access to lower oxidation states.[54] Looking forward, an area deserving of further attention in light of these results is investigation of the role of olefin coordination in modulating the redox chemistry of (pre)catalysts. As olefin coordination can significantly stabilizes reduced forms of metal complexes and can shift reduction potentials to more positive potentials,[55,56] olefinic substrates may have a role in both influencing catalyst activation via reduction (by making reduction/activation more favorable) as well as the oxidation states involved in the catalytic cycle itself.

7.4 Conclusions

We find that the Cr-based precatalysts **1**, **2**, and **3** can undergo quasi-reversible $1e^-$ reduction to Cr^{II} forms with $E_{1/2}$ values of ca. –1.5 V vs $Fc^{+/0}$ in all cases. Minor side reactions leading to generation of heterogenous material under electrochemical conditions were quantified via EQCM studies here, highlighting the usefulness of this technique for interrogating molecular catalysts of this type. X-band EPR and QEPR experiments revealed that the major reduction products are best formulated as a Cr^{II} species, confirming solid-state structural data from XRD analysis of a Cr^{II} analogue of **1**. UV-visible spectroscopy titrations of **1** reveal that in the absence of Al^{III} the Cr^{II} oxidation state is accessible as suggested by the cyclic voltammetry. However, in the presence of Al^{III}, **1** yields enables a further reduction. In light of all these, our future work will focus in part on reduction studies in the presence of model olefins to investigate the oxidations states accessible under conditions relevant to catalysis.

7.5 Experimental Details

7.5.1 General Considerations

All manipulations were carried out in dry N_2-filled gloveboxes (Vacuum Atmospheres Co., Hawthorne, CA) or under N_2 atmosphere using standard Schlenk techniques unless otherwise noted. All solvents were of commercial grade and dried over activated alumina and were stored over 4Å molecular sieves. All chemical reagents were purchased from Sigma-Aldrich and used as received. Electronic absorption spectra were collected with an Ocean Optics Flame spectrometer and 1-cm pathlength quartz cuvettes. Elemental analyses were performed by Atlantic Microlab, Inc. (Norcross, GA). Spectra were collected with a Shimadzu IRSpirit FTIR spectrometer equipped with a QATR-S single-reflection attenuated total reflectance (ATR) accessory and diamond prism plate.

7.5.2 Synthesis

The phosphine cyclic imine and phosphinoamidine ligands were prepared according to published methods as was $[Li(THF)_2][(PN)CrCl_4]$ where PN = 3,4-dihydro-2*H*-pyrrol-5-amine phosphine.[19,57]

*Synthesis of **1***. Blue solid $[Li(THF)_2][(PN)CrCl_4]$ (0.600g, 1.18 mmol), where PN = 3,4-dihydro-2*H*-pyrrol-5-amine phosphine, was added to dichloromethane (15 mL) resulting in a blue solution and insoluble blue solid. The mixture was filtered, and the solvent removed under vacuum resulting in a blue oil. The blue oil was readily dissolved in tetrahydrofuran (2 mL) and layered with n-pentane (10 mL) yielding a blue micro-crystalline solid (0.315g, 68%). $C_{14}H_{29}Cl_3CrN_2OP$ Calc. (Exp). C, 39.04 (38.67); H, 6.79 (7.00); N, 6.50 (5.85)

*Synthesis of **2**.* N'-(2,4,6-Trimethylphenyl)-N-(diethylphosphino)-2-*p*-tolylacetamidine (1.70g, 4.80 mmol) and $CrCl_3(THF)_3$ (1.70g, 4.54 mmol) were added to tetrahydrofuran (15 mL) and

stirred 18h. The solids were collected by filtration and dissolved in tetrahydrofuran (50 mL) followed by a second filtration to remove a small amount of purple solids. The product was crystallized by slow evaporation (1.21g, 43%). $C_{26}H_{39}Cl_3CrN_2OP$ Calc. (Exp). C, 53.39 (53.54); H, 6.72 (6.88); N, 4.79 (4.80)

*Synthesis of **3**.* Complex **3** was prepared according to the patented method.[58] Elemental analysis was consistent with a small amount of solvated THF (0.2 equiv./Cr) in addition to the single coordinated molecule. $C_{21.8}H_{39.6}Cl_3CrN_3O_{1.2}P$ Calc. (Exp). C, 47.41 (47.61); H, 7.24 (7.38); N, 7.61 (7.79)

7.5.3 X-ray crystallography

*Refinement Details for **1-R**.*

The sample was interrogated by X-ray diffraction analysis, crystals were mounted on a goniometer head using Paratone oil with MiTeGen MicroMounts and placed in a cold nitrogen stream. Complete sets of low-temperature (200 K) diffraction data frames were collected for crystal sample using 1.0°-wide w- and/or f-scans. X-rays for **1-R** were provided by a Bruker generator using a fine-focus Mo sealed tube running at 35 mA and 50 kV (Mo Kα = 0.71073.) and equipped with Bruker TRIUMPH curved-graphite optics. Data were collected with a Bruker PHOTON-II detector.

A total of 4178 scans were taken with 1.0°-wide wand/or f-scan frames with counting times of 4-6 seconds were collected on the Bruker PHOTON-II detector. All diffractometer manipulations, including data collection, integration and scaling were carried out using the SAINT in the Bruker Apex2 Software Suite.[59] The data was corrected empirically for variable absorption effects with SADABS[60] using equivalent reflections. Probable space groups were determined on the basis of systematic absences and intensity statistics and the structures were solved by direct methods using

The Bruker software package SHELXTL[61]. Final stages of weighted full-matrix least-squares refinement were conducted using F_o^2 data with SHELXTL or the Olex software package[62] equipped with XL[63]. The relevant crystallographic and structure refinement data for all four structures are given in Table E-3.

The final structural model for each structure incorporated anisotropic thermal parameters for all nonhydrogen atoms. Isotropic thermal parameters were used for all hydrogen atoms. The THF ligand is 55/45 disordered with two orientations about the Cr–O linkage.

7.5.4 Electrochemistry

Electrochemical experiments were carried out in a nitrogen-filled glove box. 0.10 M tetra(n-butylammonium)hexafluorophosphate (Sigma-Aldrich; electrochemical grade) in tetrahydrofuran served as the supporting electrolyte. Measurements were made with a Gamry Reference 600 Plus Potentiostat/Galvanostat using a standard three-electrode configuration. The working electrode was the basal plane of highly oriented pyrolytic graphite (HOPG) (Graph-iteStore.com, Buffalo Grove, IL.; surface area: 0.09 cm2), the counter electrode was a platinum wire (Kurt J. Lesker, Jefferson Hills, PA; 99.99%, 0.5 mm diameter), and a silver wire immersed in electrolyte served as a pseudo-reference electrode (CH Instruments). The reference was separated from the working solution by a Vycor frit (Bioanalytical Systems, Inc). Ferrocene (Sigma Aldrich; twice-sublimed) was added to the electrolyte solution at the conclusion of each experiment (~1 mM); the midpoint potential of the ferrocenium/ferrocene couple (denoted as $Fc^{+/0}$) served as an external standard for comparison of the recorded potentials. Concentrations of analyte for cyclic voltammetry were typically 1.5 mM.

Electrochemical quartz crystal microbalance (EQCM) experiments were likewise carried out in a N2-filled glovebox. 0.10 M tetra(n-butylammonium) hexafluorophosphate (Sigma-Aldrich;

electrochemical grade) in tetrahydrofuran served as the supporting electrolyte. Measurements were conducted with a Gamry eQCM 10M quartz crystal microbalance. Solutions were prepared in a static Teflon cell. An AT-cut quartz disc sputtered with gold and having a nominal resonant frequency of 10 MHz was used as the working electrode (Gamry Instruments; electroactive area ca. 0.205 cm^2). The counter electrode was a platinum wire (Kurt J. Lesker, Jefferson Hills, PA; 99.99%, 0.5 mm diameter), and a silver wire immersed in electrolyte served as a pseudo-reference electrode (CH Instruments). The reference was separated from the working solution by a Vycor frit (Bioanalytical Systems, Inc).

7.5.5 Spectroscopy

X-ray photoelectron spectra were collected using a Physical Electronics (Phi) VersaProbe II system. The sample chamber was kept at $<5 \times 10^{-9}$ torr and ejected electrons were collected at an angle of 45° from the surface normal. Survey scans were performed to identify the elements on the surface of carbon electrodes, while additional high-resolution spectra were obtained for details on specific elements. The XP Spectroscopy data were analyzed using the program Computer Aided Surface Analysis for X-ray Photoelectron Spectroscopy (CasaXPS; from Casa Software Ltd., Teignmouth, UK). All XP Spectroscopy signals reported here are binding energies and are reported in eV. Backgrounds were fit with standard Shirley or linear backgrounds. Element peaks were fit with a standard Gaussian-Lorentzian line shape. For the Co high-resolution spectra, the data were best fit with a single contribution in every case, and fits were constrained based only on peak area.

Electron paramagnetic resonance (EPR) spectra were collected on a Bruker EMXplus spectrometer equipped with an Oxford cryostat. The *in situ* reduction experiments were carried out by sequential layering of the starting Cr^{III} species and the reduction reagent of choice (Cp^*_2Co, $AlEt_3$, or modified MAO) in the EPR tube under an inert atmosphere followed by freezing in liquid

nitrogen. The layered sample was then allowed to melt and mix immediately before refreezing for collection of EPR data. This method was used in order to favor observation of transient and/or reactive species formed immediately upon reduction.

7.6 Acknowledgements

The authors thank Sarah Neuenswander for assistance with EPR and NMR spectroscopy, and Dr. Uriah J. Kilgore for initial discussions and synthetic support when he was employed by Chevron Phillips Chemical. This work was supported by Chevron Phillips Chemical. The authors also acknowledge the U.S. National Institutes of Health (S10OD016360, S10RR024664) and U.S. National Science Foundation (CHE-1625923, CHE-0946883) for support of the NMR and EPR instrumentation used in this study.

7.7 References

[1] Lappin, G. R.; Sauer, J. D.; Sauer, J. D., *Alpha Olefins Applications Handbook.* New York : M. Dekker: New York, 1989

[2] Ziegler, K. Aluminium Organische Synthese Im Bereich Olefinischer Kohlenwasserstoffe. *Angew. Chem.* **1952**, *64*, 323−329.

[3] Sydora, O. L., Selective Ethylene Oligomerization. *Organometallics* **2019**, *38*, 997-1010.

[4] Freitas, E. R.; Gum, C. R. Shell's Higher Olefins Process. *Chem. Eng. Prog.* **1979**, *75*, 73−76.

[5] Breuil, P.-A. R.; Magna, L.; Olivier Bourbigou, H. Role of Homogeneous Catalysis in Oligomerization of Olefins: Focus on Selected Examples Based on Group 4 to Group 10 Transition Metal Complexes. *Catal. Lett.* **2015**, *145*, 173−192.

[6] Deckers, P. J. W.; Hessen, B.; Teuben, J. H. Catalytic Trimerization of Ethene with Highly Active Cyclopentadienyl-Arene Titanium Catalysts. *Organometallics* **2002**, *21*, 5122−5135.

[7] Broene, R. D.; Brookhart, M.; Lamanna, W. M.; Volpe, A. F., Cobalt-Catalyzed Dimerization of α-Olefins to Give Linear α-Olefin Products. *J. Am. Chem. Soc.* **2005**, *127*, 17194-17195.

[8] Deckers, P. J. W.; Hessen, B.; Teuben, J. H., Switching a Catalyst System from Ethene Polymerization to Ethene Trimerization with a Hemilabile Ancillary Ligand. *Angew. Chem. Int. Ed.* **2001**, *40*, 2516-2519.

[9] Agapie, T.; Schofer, S. J.; Labinger, J. A.; Bercaw, J. E., Mechanistic Studies of the Ethylene Trimerization Reaction with Chromium−Diphosphine Catalysts: Experimental Evidence for a Mechanism Involving Metallacyclic Intermediates. *J. Am. Chem. Soc*. **2004**, *126*, 1304-1305.

[10] (a) Briggs, J. R., The Selective Trimerization of Ethylene to Hex-1-ene. *J. Chem. Soc., Chem. Commun*. **1989**, 674-675. (b) Carter, A.; Cohen, S. A.; Cooley, N. A.; Murphy, A.; Scutt, J.; Wass, D. F., High Activity Ethylene Trimerisation Catalysts Based on Diphosphine Ligands. *Chem. Commun*. **2002**, 858-859. (c) Wass, D. F. (British Petroleum). Patent WO 2002004119, 2002 (d) McGuinness, D. S.; Wasserscheid, P.; Keim, W.; Hu, C.; Englert, U.; Dixon, J. T.; Grove, C., Novel Cr-PNP Complexes as

Catalysts for the Trimerisation of Ethylene. *Chem. Commun.* **2003**, 334-335. (e) Wu, F.-J. (Amoco Corp.). Patent US 5,811, 618, 1998.

[11] McGuinness, D. S.; Wasserscheid, P.; Keim, W.; Morgan, D.; Dixon, J. T.; Bollmann, A.; Maumela, H.; Hess, F.; Englert, U., First Cr(III)−SNS Complexes and Their Use as Highly Efficient Catalysts for the Trimerization of Ethylene to 1-Hexene. *J. Am. Chem. Soc.* **2003**, *125*, 5272-5273.

[12] Köhn, R. D.; Haufe, M.; Kociok-Köhn, G.; Grimm, S.; Wasserscheid, P.; Keim, W., Selective Trimerization of α-Olefins with Triazacyclohexane Complexes of Chromium as Catalysts. *Angew. Chem. Int. Ed.* **2000**, *39*, 4337-4339.

[13] Reagen, W. K.; Pettijohn, T. M.; Freeman, J. W. Process of trimerizing and oligomerizing olefins using chromium compounds. US Patent 5,523,507 (Phillips Petroleum), 1996.

[14] http://www.cpchem.com/en-us/news/Pages/Chevron-Phillips-Chemical-Announces-Mechanical-Completion-and-Start-Up-of-World%27s-Largest-1-Hexene-Plant.aspx

[15] Overett, M. J.; Blann, K.; Bollmann, A.; de Villiers, R.; Dixon, J. T.; Killian, E.; Maumela, M. C.; Maumela, H.; McGuinness, D. S.; Morgan, D. H.; Rucklidge, A.; Slawin, A. M. Z., Carbon-Bridged Diphosphine Ligands for Chromium-Catalysed Ethylene Tetramerisation And Trimerisation Reactions. *J. Mol. Catal. A: Chem*. **2008**, *283*, 114-119.

[16] Boelter, S. D.; Davies, D. R.; Milbrandt, K. A.; Wilson, D. R.; Wiltzius, M.; Rosen, M. S.; Klosin, J., Evaluation of Bis(phosphine) Ligands for Ethylene Oligomerization: Discovery of Alkyl Phosphines as Effective Ligands for Ethylene Tri- and Tetramerization. *Organometallics* **2020**, *39*, 967-975.

[17] Carter, A.; Cohen, S. A.; Cooley, N. A.; Murphy, A.; Scutt, J.; Wass, D. F., High Activity Ethylene Trimerisation Catalysts Based on Diphosphine Ligands. *Chem. Commun.* **2002**, 858-859.

[18] Ackerman, L. J.; Bei, X.; Boussie, T. R.; Diamond, G. M.; Hall, K. A.; Lapointe, A. M.; Longmire, J. M.; Murphy, V. J.; Sun, P.; Verdugo, D.; Schofer, S.; Dias, E.; McConville, D. H.; Li, R. T.; Walzer,

J.; Rix, F.; Kuchta, M. Methods For Oligomerizing Olefins. WO Pat. Appl. 2006/096881 (ExxonMobil).

[19] Sydora, O. L.; Jones, T. C.; Small, B. L.; Nett, A. J.; Fischer, A. A.; Carney, M. J., Selective Ethylene Tri-/Tetramerization Catalysts. *ACS Catal.* **2012**, *2*, 2452-2455.

[20] McGuinness, D. S.; Brown, D. B.; Tooze, R. P.; Hess, F. M.; Dixon, J. T.; Slawin, A. M. Z., Ethylene Trimerization with Cr−PNP and Cr−SNS Complexes: Effect of Ligand Structure, Metal Oxidation State, and Role of Activator on Catalysis. *Organometallics* **2006**, *25*, 3605-3610.

[21] Jabri, A.; Temple, C.; Crewdson, P.; Gambarotta, S.; Korobkov, I.; Duchateau, R., Role of the Metal Oxidation State in the SNS−Cr Catalyst for Ethylene Trimerization: Isolation of Di- and Trivalent Cationic Intermediates. *J. Am. Chem. Soc*. **2006**, *128*, 9238-9247.

[22] Klemps, C.; Payet, E.; Magna, L.; Saussine, L.; Le Goff, X. F.; Le Floch, P., PCNCP Ligands in the Chromium-Catalyzed Oligomerization of Ethylene: Tri- versus Tetramerization. *Chem. Eur. J.* **2009**, *15*, 8259-8268.

[23] Venderbosch, B.; Wolzak, L. A.; Oudsen, J.-P. H.; de Bruin, B.; Korstanje, T. J.; Tromp, M., Role of The Ligand And Activator In Selective Cr–PNP Ethene Tri- And Tetramerization Catalysts – A Spectroscopic Study. *Catal. Sci. Tech.* **2020**, *10*, 6212-6222.

[24] Do, L. H.; Labinger, J. A.; Bercaw, J. E., Spectral Studies of a Cr(PNP)–MAO System for Selective Ethylene Trimerization Catalysis: Searching for the Active Species. *ACS Catal.* **2013**, *3*, 2582-2585.

[25] Rabeah, J.; Bauer, M.; Baumann, W.; McConnell, A. E. C.; Gabrielli, W. F.; Webb, P. B.; Selent, D.; Brückner, A., Formation, Operation and Deactivation of Cr Catalysts in Ethylene Tetramerization Directly Assessed by Operando EPR and XAS. *ACS Catal.* **2013**, *3*, 95-102.

[26] Grabow, K.; Bentrup, U., Homogeneous Catalytic Processes Monitored by Combined in Situ ATR-IR, UV–Vis, and Raman Spectroscopy. *ACS Catal.* **2014**, *4*, 2153-2164.

[27] Kumar, A.; Barr, J. L.; Cruz, C. A.; Blakemore, J. D., Heterobimetallic [Ti, Al] Complexes: Divergent Synthesis, Redox Properties, and Ethylene Polymerization Catalysis. *Organometallics* **2021**, *40*, 2139-2148.

[28] Barr, J. L.; Kumar, A.; Lionetti, D.; Cruz, C. A.; Blakemore, J. D., Understanding the Roles of Triethylaluminum in Phosphinimide-Supported Titanium Catalyst Systems for Ethylene Polymerization. *Organometallics* **2019**, *38*, 2150-2155.

[29] Buttry, D. A.; Ward, M. D., Measurement Of Interfacial Processes At Electrode Surfaces With The Electrochemical Quartz Crystal Microbalance. *Chem. Rev.* **1992**, *92*, 1355-1379.

[30] Sauerbrey, G., Verwendung Von Schwingquarzen Zur Wägung Dünner Schichten Und Zur Mikrowägung. *Z. Phys.* **1959**, *155*, 206-222.

[31] Sconyers, D. J.; Blakemore, J. D., Electrodeposition Behavior of Homoleptic Transition Metal Acetonitrile Complexes Interrogated With Piezoelectric Gravimetry. *Analyst* **2020**, *145*, 466-477.

[32] Sconyers, D. J.; Blakemore, J. D., Distinguishing Between Homogeneous and Heterogeneous Hydrogen-Evolution Catalysis With Molecular Cobalt Complexes. *Chem. Commun.* **2017**, *53*, 7286-7289.

[33] Sconyers, D. J.; Blakemore, J. D., Distinguishing Deposition, Corrosion, And Stripping of Transient Heterogeneous Materials During Molecular Electrocatalysis. *Dalton Trans.* **2019**, *48*, 6372-6382.

[34] Connelly, N. G.; Geiger, W. E., Chemical Redox Agents for Organometallic Chemistry. *Chem. Rev.* **1996**, *96*, 877-910.

[35] Liu, R.; Zhu, K.; Zhong, X.; Li, J.; Liu, Z.; Chen, S.; Zhu, H., Chromium Complexes Bearing Amidinato-Phosphino Ligand: Synthesis, Characterization, And Catalytic Properties of Ethylene Tri-/Tetramerization And Polymerization. *Dalton Trans.* **2016**, *45*, 17020-17029.

[36] Dobson, G. R.; Bernal, I.; Reisner, G. M.; Dobson, B.; Mansour, S. E., Solid-State Structure and Reactivity In Solution. 6. Flash Photolysis and Structural Investigations Of (1-(Diethylamino)-2-(Diphenylphosphino)Ethane)Tetracarbonylmolybdenum(0). *J. Am. Chem. Soc.* **1985**, *107*, 525-532.

[37] Grant, J. T., *Surface Analysis by Auger and X-ray Photoelectron Spectroscopy*, ed. Briggs, D., and Grant, J. T., IM Publications and Surface Spectra Ltd., Chichester, West Sussex, UK, 2003, pp. 31–56.

[38] Siegbahn, K., ESCA Applied to Free Molecules. North-Holland Publishing Co.: Amsterdam, 1969.

[39] Briggs, D., in Handbook of X-ray and Ultraviolet Photoelectron Spectroscopy, ed. D. Briggs, Heyden, London, 1977, pp. 153–182.

[40] Hendrickson, D. N.; Hollander, J. M.; Jolly, W. L., Nitrogen Ls Electron Binding Energies. Correlations With Molecular Orbital Calculated Nitrogen Charges. *Inorg. Chem.* **1969**, *8*, 2642-2647.

[41] Moulder, J. F.; Stickle, W. F.; Sobol, P. E.; Bomben, K. D. ; Handbook of X-Ray Photoelectron Spectroscopy, Perkin-Elmer Corp., 1992.

[42] Palmer, G., *Electron paramagnetic resonance of metalloproteins, in Physical Methods in Bioinorganic Chemistry, Spectroscopy and Magnetism*, ed. L. Que, Jr. University Science Books, Sausalito, CA, 2000.

[43] Uddin, K. M.; Alrawashdeh, A. I.; Debnath, T.; Aziz, M. A.; Poirier, R. A., Synthesis, Spectroscopic Characterization, And Theoretical Studies on The Substitution Reaction of Chromium(III) Picolinate. *J. Mol. Struct*. **2019**, *1189*, 28-39.

[44] López Plá, J. M.; Boudalis, A. K.; Telser, J.; Raptis, R. G., Chromium(III)-Pyrazole Complexes. X-Ray Crystal Structures, ^{1}H NMR Investigation Of Ligand Fluxional Behavior And EPR Studies. *Inorg. Chim. Acta* **2020**, *502*, 119299.

[45] Cummings, D. A.; McMaster, J.; Rieger, A. L.; Rieger, P. H., EPR Spectroscopic and Theoretical Study of Chromium(I) Carbonyl Phosphine and Phosphonite Complexes. *Organometallics* **1997**, *16*, 4362-4368

[46] Luckham, S. L. J.; Folli, A.; Platts, J. A.; Richards, E.; Murphy, D. M., Unravelling the Photochemical Transformations of Chromium(I) 1,3 Bis(diphenylphosphino), $[Cr(CO)_4(dppp)]^+$, by EPR Spectroscopy. *Organometallics* **2019** *38*, 2523-2529.

[47] (a) Telser, J.; Pardi, L. A.; Krzystek, J.; Brunel, L.-C., EPR Spectra from "EPR-Silent" Species: High-Field EPR Spectroscopy of Aqueous Chromium(II). Inorg. Chem. 1998, 37, 5769-5775. (b) Abragam, A.; Bleaney, B. *Electron Paramagnetic Resonance of Transition Ions*; Dover Publications: New York, 1986; pp 399, 434- 436, 679.

[48] Eaton, G. R.; Eaton, S. S.; Barr, D. P.; Weber, R. T.; Eaton, S. R., *Quantitative EPR*. Wien New York : Springer: Wien New York, 2010.

[49] Palmer, G., [94] *Electron Paramagnetic Resonance.* In Methods Enzymol., Academic Press 1967; Vol. 10, pp 594-609.

[50] Que, L., *Physical Methods in Bioinorganic Chemistry : Spectroscopy And Magnetism.* Sausalito, Calif. : University Science Books: Sausalito, Calif., 2000.

[51] Drago, R. S., *Physical Methods for Chemists.* 2nd ed. ed.; Drago, R. S., Ed. Ft. Worth : Saunders College Pub.: Ft. Worth, 1992.

[52] The noted equations correct the double integral to account for experimental variables including temperature (K), microwave power (W), modulation amplitude (B_m), quality factor (Q), average g-value (g_{ave}), Boltzman factor (n_b) and electron spin (S).

[53] Cummings, D. A.; McMaster, J.; Rieger, A. L.; Rieger, P. H., EPR Spectroscopic and Theoretical Study of Chromium(I) Carbonyl Phosphine and Phosphonite Complexes. *Organometallics* **1997**, *16*, 4362-4368

[54] Kelsey, S. R.; Kumar, A.; Oliver, A. G.; Day, V. W.; Blakemore, J. D., Promotion and Tuning of the Electrochemical Reduction of Hetero- and Homobimetallic Zinc Complexes. *ChemElectroChem* **2021**, *8*, 2792-2802.

[55] Lionetti, D.; Day, V. W.; Lassalle-Kaiser, B.; Blakemore, J. D., Multiple Binding Modes of an Unconjugated Bis(Pyridine) Ligand Stabilize Low-Valent [Cp*Rh] complexes. *Chem. Commun.* **2018**, *54*, 1694-1697.

[56] Hopkins Leseberg, J. A.; Lionetti, D.; Day, V. W.; Blakemore, J. D., Electrochemical Kinetic Study of [Cp*Rh] Complexes Supported by Bis(2-pyridyl)methane Ligands. *Organometallics* **2021**, *40*, 266-277.

[57] Kwon, D. -H.; Fuller III, J. T.; Kilgore, U. J.; Sydora, O. L.; Bischof, S. M.; Ess, D. H., Computational Transition-State Design Provides Experimentally Verified Cr(*P*,*N*) Catalysts for Control of Ethylene Trimerization and tetramerization, *ACS Catal*. **2018**, *8*, 1138-1142.

[58] Sydora, O. L.; Small, B. L.; Carney, M. J. Phosphinyl Guanidine Compounds, Metal Salt Complexes, Catalyst Systems, And Their Use To Oligomerize Or Polymerize Olefins. US Pat. #8,865,610 (Chevron Phillips Chemical Company LP).

[59] *APEX2, Version 2 User Manual, M86-E01078*. Bruker Analytical X-ray Systems: Madison, WI, June 2006.

[60] Sheldrick, G. M. *SADABS (version 2008/1): Program for Absorption Correction for Data from Area Detector Frames*, University of Göttingen 2008.

[61] Sheldrick, G., SHELXT - Integrated space-group and crystal-structure determination. *Acta Crystallogr., Sect. A: Found. Crystallogr.* **2015,** *71*, 3-8.

[62] Dolomanov, O. V.; Bourhis, L. J.; Gildea, R. J.; Howard, J. A. K.; Puschmann, H., OLEX2: a complete structure solution, refinement and analysis program. *J. Appl. Crystallogr.* **2009,** *42*, 339-341.

[63] Sheldrick, G., Crystal structure refinement with SHELXL. *Acta Crystallogr., Sect. C: Cryst. Struct. Commun.* **2015,** *71*, 3-8.

Chapter 8

Rational Tuning of Cerium Redox Chemistry with Redox-Inactive Metal Cations

This chapter is adapted from a manuscript in preparation:

Hopkins Leseberg, J.A.; Gompa, T.P; Oliver, A.G.; Day, V.W.;

La Pierre, H.S.; Blakemore, J.D.

Rational Tuning of Cerium Redox Chemistry with Redox-Inactive Metal Cations.

In Preparation.

8.1 Introduction

Development of strategies to harness the unique chemistry of heavier elements is an important goal in contemporary chemistry. The lanthanides (elements 57 to 71) are notable in this regard as their properties are strongly influenced by the core-like nature of their 4*f* valence orbitals. The progressive filling of these orbitals results in similar structural chemistry and reactivity properties across the series, a phenomenon often referred to as the "lanthanide contraction;" this progressive filling of core-like orbitals also engenders unique optical, magnetic, and redox properties for the individual lanthanides. Understanding and leveraging these properties has contributed to numerous important developments, particularly in the area of clean energy technologies (e.g., magnets, battery materials, and catalysts).

In the field of lanthanide chemistry, understanding and accessing key oxidation states has emerged as a central theme in enabling new chemistry. While the chemistry of most lanthanides is dominated by the +III oxidation state, recent work from Evans and co-workers has revealed[1] the accessibility of the +II oxidation state across the series in organometallic complexes, while Mazzanti and co-workers[2] and La Pierre and co-workers[3] have been able to access the +IV oxidation states of terbium and praseodymium with strongly donating ligand sets. These reports complement a wealth of knowledge available for the element cerium, which can commonly access both the +III and +IV oxidation states owing to the [Xe]4f^1 configuration of the +III state. Significant work has shown that ligand structure/environment influences the Ce(IV)/Ce(III) reduction potential, and that metal-ligand covalency increases substantially for the +IV oxidation state, providing key insights for design of new ligand-driven strategies for lanthanide redox tuning.

An alternative to ligand-driven tuning of redox chemistry and reactivity involves placement of redox-inactive cations in close proximity to redox-active metals of interest.[4] This approach is

inspired by the redox-inactive Ca^{2+} ion present in the Oxygen Evolving Complex (OEC) of Photosystem II,[5] which can be concluded on the basis of model work from Agapie and co-workers to play a key role in tuning the reduction potential of the OEC.[6] Use of redox-inactive cations to modulate the properties of transition metal complexes has been extensively explored, [7,8] particularly in the areas of metal-oxo chemistry and electrochemistry. More recently, some of us have shown that mono-, di-, and trivalent metal cations can be used to rationally tune the uranium(VI)/uranium(V) potential and electron transfer properties of the uranyl ion (UO_2^{2+}),[9] complementing prior scattered reports of shifted redox chemistry and reactivity modulation in the presence of secondary metals.[10] In our system, the reduction potentials varied linearly with the Lewis acidity of the incorporated redox-inactive metal ions, as judged by the pK_a values of the corresponding metal aqua complexes.[11]

In this context, the tuning of lanthanides through incorporation of secondary metal cations into multimetallic complexes has received significantly less attention than it deserves.[12] Early work in this area from Schelter and co-workers[4] revealed that formation of 3:1 M:Ce adducts (where M = Li, Na, K, and Cs) shifts the Ce(IV/III) reduction potential over a range of 400 mV. More recently, La Pierre and co-workers have used chemical redox reagents to estimate the Ce(IV/III) potential of complexes supported by imido-phosphorane ligands finding that, anomalously, a heterobimetallic derivative of Ce(III) with K^+ appears to be a stronger reductant than its monometallic Ce(IV) analogue (Chart 8.1).[13] Considering the relative lack of quantitative data on redox tuning of lanthanides by secondary metals, particularly for the unexplored divalent cations, we anticipated that use of a modular ligand supporting divergent synthesis could enable rapid access to heterobimetallic complexes for new systematic studies of redox tuning. Such studies

could provide details on the structural, electrostatic, and/or charge density factors that drive tuning of the lanthanides, which are distinguished for their generally core-like 4*f* valence orbitals.

Chart 8.1. Heterometallic f-element complexes.

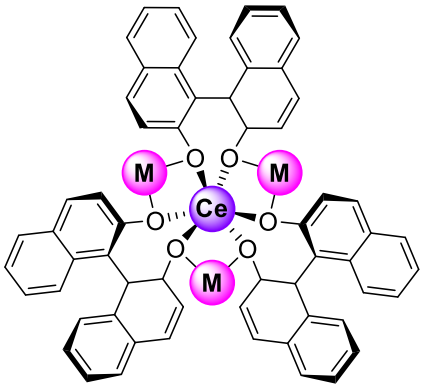

Schelter et al. 2013

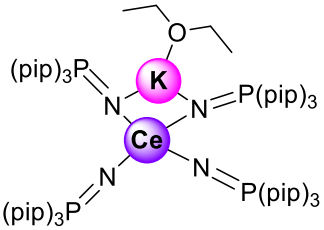

La Pierre et al 2019.

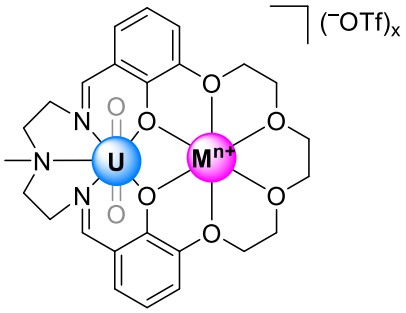

Blakemore et al. 2020

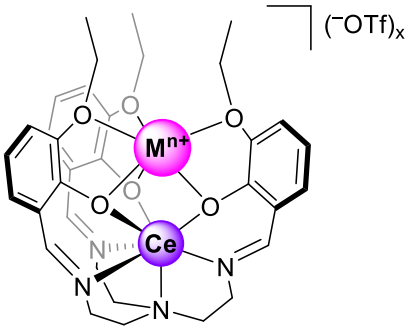

This Work

Here, we report the divergent synthesis and study of a series of well-defined heterobimetallic Ce(III) complexes supported by a heteroditopic ligand framework capable of incorporating a range of redox-inactive Lewis acidic metal cations (**M**; **M** = Li^+, K^+, Na^+, Ba^{2+}, Sr^{2+}, Ca^{2+}). The ligand ($\mathbf{L^{OEt}H_3}$) features a heptadentate binding site for cerium coordination and a hexadentate pocket for binding of the redox-inactive Lewis acids, which span nearly four orders of magnitude in estimated acidity. Solid-state X-ray diffraction data reveal that structural trends about the Lewis acids in the bimetallic complexes are best parametrized by the ionic radii of the redox-inactive metals; conversely, the structural properties about the cerium center are best described by the pK_a values

of the Lewis acidic metal cations, implying that the phenoxide moieties play a key role in mediating electrostatic communication of the secondary metals with the cerium center. Spectroscopic and electrochemical work confirm that the desired [Ce(μ -O_{Ar})$_3$**M**] cores are stable in solution enabling the Ce(IV/III) reduction potential to be investigated across the full series. The tuning observed in this series appears to be engendered by charge density effects that arise from interaction of the redox-inactive metals with the bridging aryl oxide ligands. The Ce(IV/III) potential shows a high sensitivity of –157 mV/pK_a unit to the Lewis acidity of the secondary metals, a value notably larger than in analogous d- and 5f-element species with only two bridging aryl oxide ligands. Taken together, these results show that heterobimetallic effects with mono- and di-valent secondary metals can be used to rationally tune the redox properties of cerium for the first time.

8.2 Results

8.2.1. Synthesis and Characterization of Monometallic and Heterobimetallic Complexes.

The heteroditopic ligand developed for this work, denoted **L^{OEt}H$_3$**, is based on a framework originally reported by Orvig[14] that features a Schiff-base-type heptadentate site for binding lanthanide ions (Ln = Pr, Nd, Gd, and Yb in previous studies). In our work, we modified this framework by appending ethoxy substituents to the ortho positions of each phenyl ring in the parent structure; we anticipated that upon coordination of cerium(III) to the heptadentate site, a second hexadentate binding site for additional metal cations would be formed. We have found that addition of the "upward" oriented ethoxy substituents enables both synthetic ease, as the precursor 3-ethoxysalicylaldehyde (ESA) is inexpensive, as well as advantageous solubility, as Ce(III) complexes of the simpler methoxy analogue were found to be insoluble in both acetonitrile (CH_3CN) and dichloromethane (CH_2Cl_2). In our modified literature procedure,[14,15] three

equivalents of ESA were added to one equivalent of tris(2-aminoethyl)amine (tren) in dry CH_2Cl_2 to yield the target tripodal ligand, $\mathbf{L^{OEt}H_3}$. Notably, scattered reports are available on the structure of this ligand[15] and monometallic complexes with lanthanides[16] (Ln = Tb, Dy, Nd, and Eu), but no work has systematically explored formation of heterobimetallic species of the type reported here.

Scheme 8.1. Synthesis of Heterobimetallic Cerium Complexes

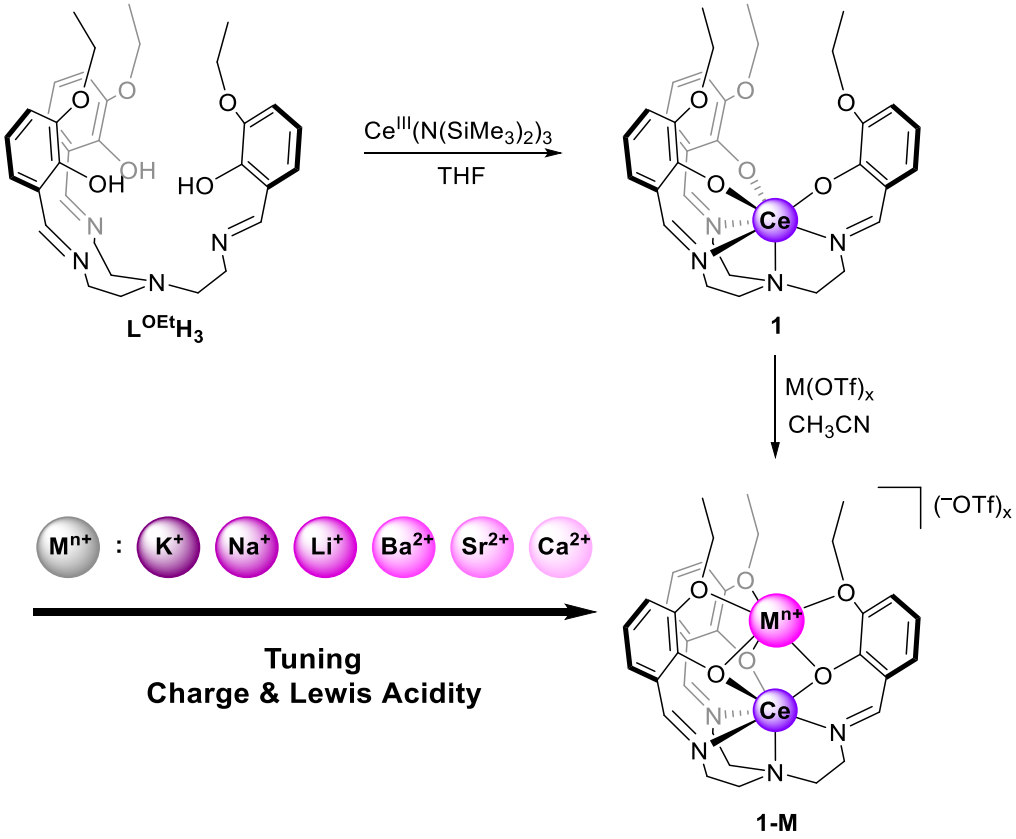

Characterization by ^{1}H nuclear magnetic resonance (NMR) spectroscopy confirms that $\mathbf{L^{OEt}H_3}$ displays C_3 symmetry in solution (see Appendix F, Figure F1) and is poised for formation of tripodal metal complexes. The monometallic complex **1** was prepared by combining tetrahydrofuran (THF) solutions of $\mathbf{L^{OEt}H_3}$ and $Ce(N(SiMe_3)_2)_3$,[17,18] resulting in precipitation of the orange monometallic cerium(III) complex **1** (see Scheme 8.1). Characterization of **1** with ^{1}H NMR reveals a single set of eight resonances spread over a wide range of chemical shift ($\Delta\delta$ =

25.05 ppm) values (see Appendix F, Figure F3), consistent with the anticipated *pseudo*-C_3 symmetric structure of the complex in solution and paramagnetism induced by the presence of the $4f^1$ Ce(III) ion.

The heterobimetallic cerium(III) complexes of the form **1-M** (see Scheme 8.1) were prepared by addition of acetonitrile (CH_3CN) solutions of the triflate salts of the desired secondary metal cations (**M**) to CH_3CN solutions of **1**.[7] In particular, we prepared derivatives containing Li^+, Na^+, K^+, Ba^{2+}, Sr^{2+}, and Ca^{2+} to access the **1-M** series. Characterization of the heterobimetallic complexes by ^{1}H NMR revealed a unique set of resonances in each case, consistent with incorporation of the secondary metal ions into the structures and implying stability of the desired complexes in solution. A wide range of chemical shift values was measured in each case, consistent with retention of paramagnetism and thus the Ce(III) oxidation state in all cases. Between seven and nine unique resonances were detected in each spectrum (see Appendix F, Figures F5, F8, F11, F14, F17, and F20), consistent with *pseudo*-C_3 symmetry that implicates binding of the secondary metals into the target hexadentate site composed of donor O-atoms from all three "arms" of the tripodal ligand. Notably, no diamagnetic metal-containing species or free ligand were detected in any case, suggesting that there is neither exchange of metal ions between the two intraligand binding sites nor scrambling of the mono- & divalent metals with the cerium(III) ions. This finding demonstrates that $\mathbf{L^{OEt}}$ supports orthogonal metalation and represents a platform for study of heterobimetallic effects in the lanthanide series.

Notably, we did attempt to synthesize heterobimetallic complexes pairing cerium(III) in the heptadentate site (as in **1**) with additional secondary trivalent metal cations for binding in the hexadentate site. However, ^{1}H NMR spectra collected on samples of **1** exposed to 1 eq. of $La(OTf)_3$ or $Lu(OTf)_3$ (see Appendix F, Figures F30 and F31) showed the formation of diamagnetic species

as well as sets of paramagnetically shifted resonances. These findings are consistent with speciation induced by exchange of trivalent ions between the two distinct binding sites of $\mathbf{L^{OEt}}$. The lack of any significant ligand field stabilization of Ce(III) could contribute to its ready exchange with other trivalent ions. These results with **1-M** differ from our prior work, however, on heterobimetallic Ni(II) and UO_2^{2+} complexes, in that these ions showed no exchange behavior when paired with trivalent ions in related heteroditopic ligands.[7,9]

8.2.2. X-Ray Diffraction Studies. Single crystals of **1** suitable for X-ray diffraction (XRD) analysis were grown, and the resulting structure confirms the presence of a bound cerium(III) ion in the heptadentate binding site as well as the formation of the nascent, hexadentate site primed for capture of secondary metal cations (see Figure 8.1). The geometry of $\mathbf{L^{OEt}}$ about the Ce(III) center can be described by the average "twist" angle of the structure (θ),[19,20] defined as the average dihedral angle of each of the ligand "arms"; this quantity is defined by the angle between the N atom, the center-of-gravity of the imine nitrogen plane, the center-of-gravity of the phenoxide oxygen plane, and phenoxide O atom for each arm. The twist angle (θ) in **1** is 43.2° (see Table 8.1 and Appendix F, Figure F123); thus, the geometry about cerium can be described as mono-capped pseudo-octahedral (a perfectly octahedral geometry would have θ = 60°).[21] The geometry of the upper hexadentate site can be measured in a similar manner, giving a twist angle (θ′) that is the average dihedral angle defined by the phenoxide O atom for each arm, the center-of-gravity of the phenoxide oxygen plane, the center-of-gravity of the aryl ether oxygen plane, and aryl ether O atom for each arm of the structure. The empty site in **1** has θ′ = 10.1° (see Table 8.1 and Appendix F, Figure F132), and thus this site can be described as pseudo-trigonal prismatic (for a perfect trigonal prism, θ′ = 0°).[21]

Table 8.1. Comparison of $[M(H_2O)_m]^{n+}$ and Shannon Ionic Radius. Selected Average Bond Lengths, Interatomic Distances, and Angles.

	1	**1-K**	**1-Na**[f]	**1-Ba**	**1-Sr**	**1-Ca**
pK_a of $[\mathbf{M}(H_2O)_m]^{n+}$	-	16.0	14.8	13.4	13.2	12.6
Shannon Ionic Radius of **M** (Å)[a]	-	1.46	1.02	1.47	1.21	1.12
Coordination Number of Ce	7	8	8	8	8	8
Coordination Number of **M**	-	7	6	9	8	8
θ (°)[b]	43.23	21.53	7.76	18.47	8.40	7.00
θ′ (°)[c]	10.10	14.75	14.09	17.67	9.10	9.97
Ce–N_{imine} (Å)	2.678(3)	2.667(2)	2.687(4)	2.644(1)	2.663(4)	2.654(2)
Ce–O_{Ar} (Å)	2.287(2)	2.323(1)	2.346(3)	2.366(1)	2.383(3)	2.380(1)
Ce–N4 (Å)	2.625(3)	2.699(2)	2.638(4)	2.657(1)	2.628(4)	2.599(2)
M–O_{Ar} (Å)	-	2.767(2)	2.374(4)	2.740(2)	2.563(3)	2.417(2)
M–O_{ether} (Å)	-	2.779(4)	2.550(4)	2.785(2)	2.661(4)	2.551(2)
Ce•••**M** (Å)	-	3.705	3.359	3.797	3.673	3.550
N_{imine} ••• N_{imine} (Å)[d]	4.111	3.930	4.077	4.003	4.060	4.051
O_{Ar} ••• O_{Ar} (Å)[e]	3.385	2.997	2.861	2.931	2.835	2.788
O_{Ar} ••• O_{ether} (Å) [e]	5.507	4.741	4.212	4.703	4.278	4.122

[a] Average radii observed for cation-anion distances in most oxide and fluoride crystal structures (Ref 22). [b] Average twist angle (θ) defined by the angle between the N atom, the center-of-gravity of the imine nitrogen plane, the center-of-gravity of the phenoxide oxygen plane, and phenoxide O atom for each arm. [c] Average twist angle (θ) the average dihedral angle defined by the phenoxide O atom, the center-of-gravity of the phenoxide oxygen plane, the center-of-gravity of the aryl ether oxygen plane, and aryl ether O atom for each arm. [d] Average distance between the N1, N2 and N3 atoms in the plane defined by the imine moieties. [e] Average distance between the O1, O2 and O3 atoms in the plane defined by the phenoxide moieties. [e] Average distance between the O4, O5 and O6 atoms in the plane defined by the aryl ether moieties. [f] Average bond lengths listed for molecule A of **1-Na** in unit cell. (Values for average and percent error are listed in the Appendix F Table F8)

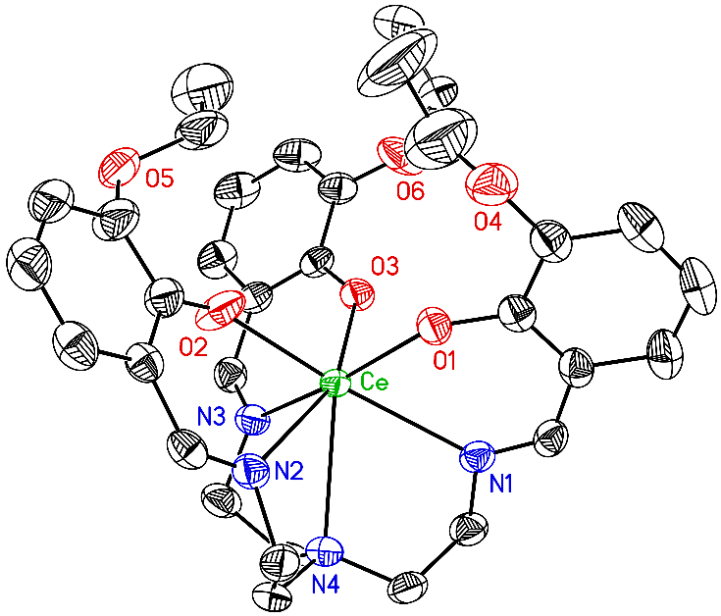

Figure 8.1. Solid-state structure of **1** (XRD). Hydrogen atoms are omitted for clarity. Displacement ellipsoids are shown at the 50% probability level.

Single crystals of the **1-M** complexes suitable for XRD studies confirm the binding of the Lewis acidic cations in the hexadentate site of the ligand framework in all cases. Notably, the structures reveal that an eighth ligand binds to the Ce center in each of the heterobimetallic complexes, in contrast to the seven-coordinate Ce center in monometallic **1** (see Table 8.1). Among the secondary metals, the larger ions (as judged by their Shannon ionic radii[22]) have higher coordination numbers than the smaller ones; K^+ in **1-K** has C.N. = 7 (see Figure 8.2) whereas Na^+ in **1-Na** has C.N. = 6 (see Figure 8.3). Similarly, Ba^{2+} in **1-Ba** has C.N. = 9 whereas Sr^{2+} and Ca^{2+} in **1-Sr** and **1-Ca** both have C.N. = 8 (see Figures 4 and 5). The hexadentate site provides six O-donors in each of these cases, with the additional ligands composed of triflates and bound solvent molecules, depending on the particular structure. Ce(III) remains fully coordinated to the heptadentate site of the tripodal ligand in all cases, with the additional ligand in each case being either κ^1-triflate (**1-Na** and **1-Ba**) or bound solvent (**1-K**, **1-Sr**, and **1-Ca**). The increased tendency for the Ce to interact with an eighth ligand in the heterobimetallic complexes can be attributed to the drawing together of the donor atoms of the hexadentate site upon secondary metal binding, in effect opening a site for exogeneous ligand binding to Ce (*vide infra*).

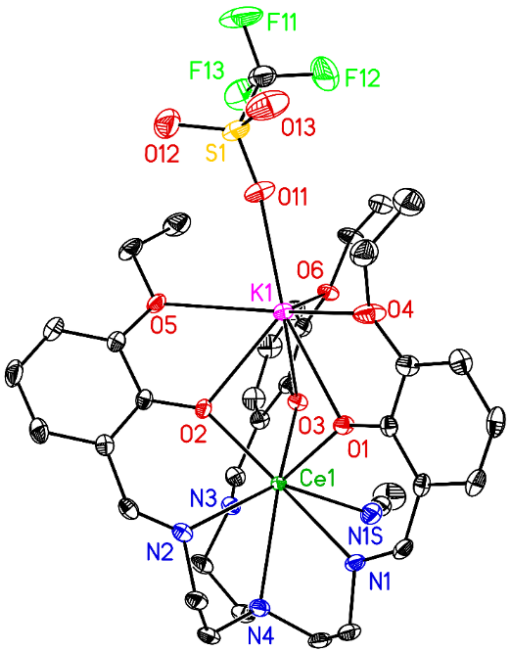

Figure 8.2. Solid-state structure of **1-K** (XRD). Hydrogen atoms and outer-sphere solvent molecules are omitted for clarity. Displacement ellipsoids are shown at the 50% probability level.

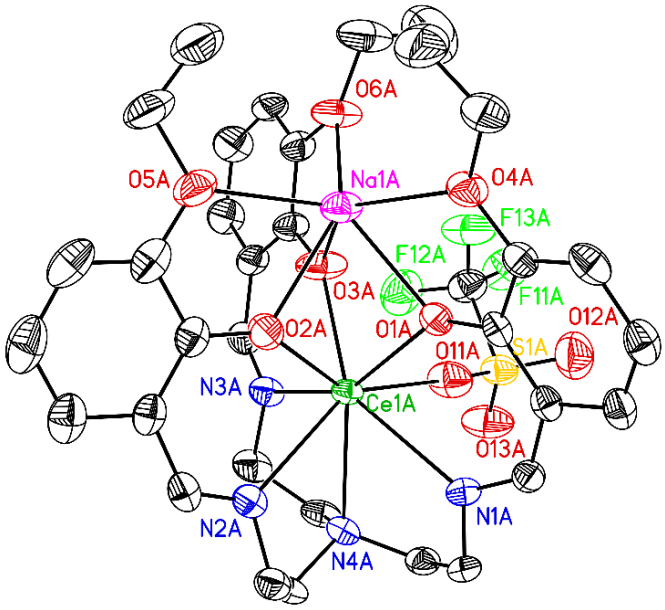

Figure 8.3. Solid-state structure of **1-Na** (XRD). Hydrogen atoms and outer-sphere solvent molecules are omitted for clarity. Displacement ellipsoids are shown at the 50% probability level.

In the **1-M** series, chelation of the secondary metals promotes a dramatic geometric change at the Ce site from the mono-capped pseudo-octahedral geometry observed for **1** (*vide supra*). Binding of the secondary ions induces a significant decrease in the average "twist" angle for each bimetallic complex and thus engenders a mono-capped pseudo-trigonal prismatic geometry about Ce (see Table 8.1, and Appendix F, Figures F125-F129). On the other hand, chelation of the secondary metals by the phenoxide and aryl ether moieties in each ligand arm does not significantly change the average twist angle of the upper binding site (*vide supra*) resulting in retention of pseudo-trigonal prismatic geometry of the hexadentate site, as was observed for **1** (see Table 8.1 and Appendix F, Figures F133-F137). The coordination geometry of the Ce site is also influenced by the steric profile of the additional eighth ligand; for the triflate-bound **1-Na** and **1-Ba**, there is a distinct elongation of the distance between the plane defined by the three imine N atoms (N1, N2, and N3) and the plane defined by the three phenoxide O atoms (O1, O2, and O3) in comparison to values measured for the other heterobimetallic complexes (see Appendix F, Table F5 and Figure F107).

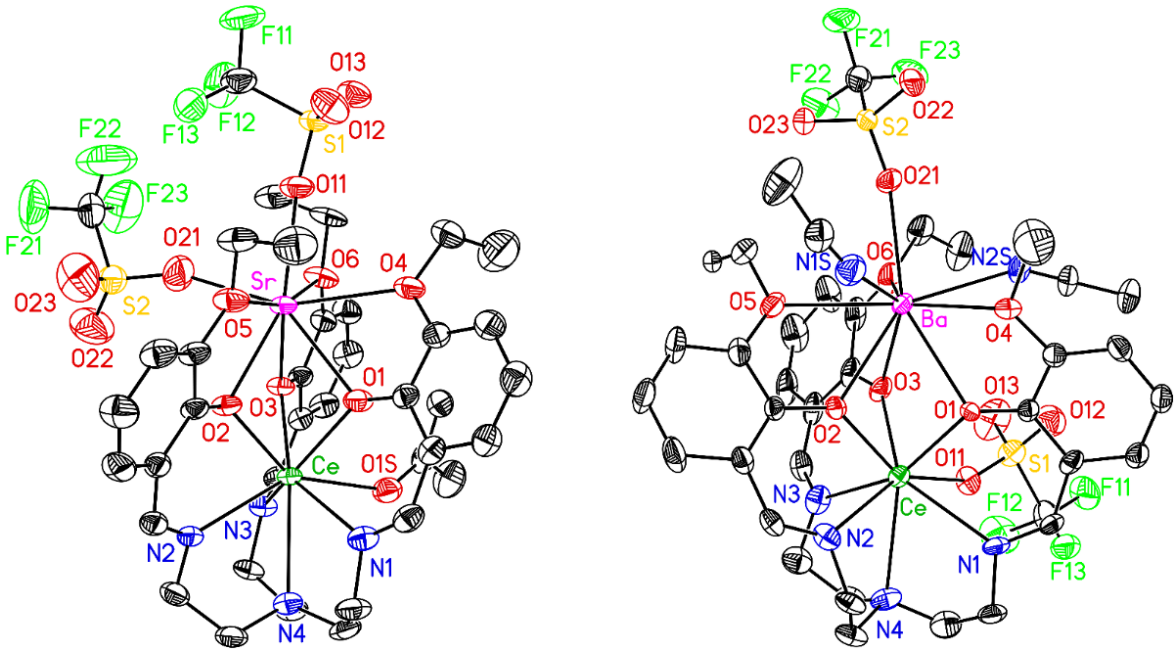

Figure 8.4. Solid-state structure of **1-Sr** (XRD) (left) **1-Ba** (XRD) (right). Hydrogen atoms and outer-sphere solvent molecules are omitted for clarity. Displacement ellipsoids are shown at the 50% and 20% probability level, respectively.

Beyond these general conclusions summarized above, we find that the structural data for the **1-M** series reveal significant trends in the properties of the complexes when judged as a function of the tabulated characteristics of the secondary metals, namely ionic radius and Lewis acidity. As a caveat, however, the C.N. (6 to 9) and identities of the external ligands to the secondary metal ions vary widely and thus could give rise to steric differences that muddle comparisons of structural properties across the full series. See Section F2.1 Appendix F for exposition on these considerations, including metrical parameters in Tables F5 and F6.

The $\mathbf{L}^{\mathbf{OEt}}$ ligand framework appears to be flexible, enabling it to accommodate all the secondary metal ions tested here along with Ce(III). The average distance (defined as d_1) between the aryl ether O-atoms (O4, O5, and O6) shortens upon binding of the secondary metals (d_1 = 5.51 Å for **1**, from 4.74 Å for **1-K** to 4.12 Å for **1-Ca**; see Table 8.1 and Appendix F, Figure F111**).**

Complexation similarly results in contraction of the average distance (d_2) between the phenoxide O atoms (O1, O2, and O3) as compared to **1** (d_2 = 3.39 Å for **1**, from 3.00 Å for **1-K** to 2.79 Å for **1-Ca**, see Table 8.1 and Appendix F, Figure F97). Both d_1 and d_2 trend linearly with Shannon ionic radius, consistent with the size of the ions dictating their positions in the hexadentate binding site. On the other hand, although the average distance (defined as d_3) between the imine N-atom donors (N1, N2, and N3) is larger for **1** (4.11 Å) than for all the heterobimetallic complexes, d_3 actually increases as the ionic radius of the secondary metal ion decreases (d_3 ranges from 3.93 Å for **1-K** to 4.07 Å for **1-Na**; see Table 8.1 and Appendix F, Figure F96). This trend is consistent with binding of the smaller, more demanding secondary ions coming at the expense of elongation of distances at the Ce center due to the presence of the shared, bridging phenoxides that, in effect, act as a fulcrum across the two binding sites. See Section F2.2 in Appendix F for exposition on the structural changes associated with the ligand framework across the series of heterobimetallic complexes.

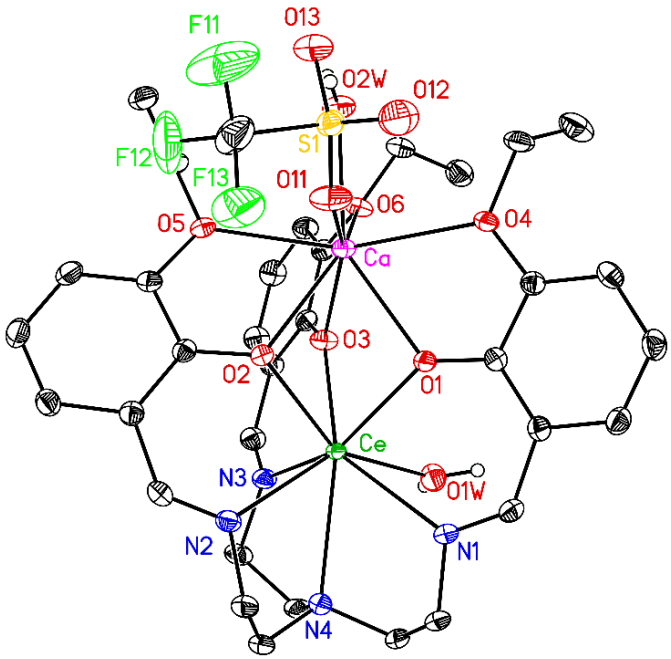

Figure 8.5. Solid-state structure of **1-Ca** (XRD). Hydrogen atoms and outer-sphere solvent molecules are omitted for clarity. Displacement ellipsoids are shown at the 50% probability level.

In accord with these findings, the Ce•••**M** distance was found to vary across the **1-M** series as a function of the Shannon ionic radii of the secondary metals; as the radius of **M** increases, there is a clear increase in the Ce•••**M** distance (see Table 8.1 and Appendix F, Figure F119). In the hexadentate site, the distance between **M** and a plane defined by the O-atoms of the phenoxide moieties (O1, O2 and O3) increases as a function of ionic radius (see Appendix F, Figure F117) while the distance between **M** and a plane defined by the O-atoms of the aryl ether moieties (O4, O5, and O6) decreases with increasing ionic radius (see Appendix F, Figure F118). These counterposed trends indicate that the sizes of the secondary metal ions determine their positions in the hexadentate site; the smaller ions can sit closer to the phenoxide groups, nestling into the site and positioning themselves at smaller Ce•••**M** distances. Ionic radius thus appears to be the major driver of the structural properties of the series **1-M**, at least in terms of the position of the secondary

metal ion relative to the Ce(III) center. See Section F2.3 in Appendix F for discussion of structural metrics for the secondary metals in the hexadentate site.

The structural properties of the heptadentate site contrast with these results, in that charge density considerations best describe the influence of the secondary metal ions on the Ce(III) center. These charge density effects have been quantified here by parametrizing the Lewis acidity of the secondary metal ions in terms of the pK_a values of the corresponding metal aqua complexes of these ions.[23] In particular, the average Ce–O_{Ar} (O1, O2, O3) distances increase linearly with the pK_a values of the incorporated secondary metal ions (see Table 8.1 and Appendix F, Figure F105). Thus, a stronger Lewis acid like Sr^{2+} (pK_a = 13.2) engenders a longer Ce–O_{Ar} average distance than a weaker Lewis acid like K^+ (pK_a = 16.0) (cf. 2.383(3) vs. 2.323(1) Å, respectively). This relationship can be rationalized by considering that the Lewis acidic metals polarize the electron density of the phenoxide groups toward themselves, decreasing the effective donor power of these ligands to Ce(III). Consistent with this proposal, an inverse trend of decreasing average Ce–N_{imine} (N1, N2, N3) distances is observed as the Lewis acidity of the secondary metal ions increases (see Appendix F, Figure F104); this indicates the decreased donor power of the phenoxide groups in the adducts with stronger Lewis acids drives the Ce center to more closely associate with the imine N-donors. See Section F2.4 in Appendix F for discussion of structural metrics related to the Ce(III) center in the heptadentate site. Taken together, these results show that the pK_a values can serve as a descriptor of the Ce(III) structural properties in the heterobimetallic complexes, and that electrostatic communication between the secondary metals **M** and Ce is mediated by the bridging phenoxide moieties.

The structure of **1-Li** from single-crystal XRD analysis reveals that this compound behaves differently in the solid state than the others in the series **1-M**. In the solid state, a dimeric molecular

species is formed that features two Li^+ ions, two Ce(III) centers, and two $\mathbf{L^{OEt}}$ ligands (see Appendix F, Figures F88). A [$Ce^{III}(\mu\text{-}O_{Ar})_2Ce^{III}$] diamond core lies at the center of the dimer, with the two separate phenoxide bridges provided by two independent $\mathbf{L^{OEt}}$ ligands. The small ionic radius of Li^+ no doubt drives formation of this unusual structure, as Li^+ has a C.N. of 5 in **1-Li**; the flexible nature of $\mathbf{L^{OEt}}$ enables binding of the small Li^+ ion,[22] apparently by accommodating slippage of Li^+ to one side of the tripodal structure of **1**. This results in loss of *pseudo*-C_3 symmetry and consequent formation of the dimeric species. The apparent mismatch between Li^+ and the size of the hexadentate binding site in **1** also appears to impact the solution behavior in that ^{1}H NMR data for **1-Li** are significantly broadened (see Appendix F, Figure F8) in comparison that for others in the series. In light of these differences in solution and solid-state behavior, we omitted **1-Li** from consideration in further studies (*vide infra*) in order to focus on the systems that display monomeric behavior. See Section F2.5 for detailed discussion of the structural properties of **1-Li**.

8.2.3. Electronic Absorption Spectroscopy Studies. Having observed the modular structural properties of the heterobimetallic complexes, we next interrogated the influence of the secondary metal ions on the electronic properties of **1-M**. The electronic absorption spectrum of **1** (see Figure 8.6, uppermost spectrum) displays a band with λ_{max} = 370 nm that can be assigned as a π-to-π* transition both on the basis of prior work with phenoxide-type ligands[13] as well as its high absorptivity ($\varepsilon \approx 10^4$ M^{-1} cm^{-1}). Two bands at higher energy (λ >300 nm) are also present and have larger absorptivity values ($\varepsilon \approx 10^5$ M^{-1} cm^{-1}); these are also attributable to intraligand π-to-π* transitions. Binding of the secondary metal ions and formation of the heterobimetallic complexes engenders a shift in the π-to-π* band originally observed at 370 nm for **1** to higher energies, similar to ligand-to-metal charge transfer events that we have measured in other complexes.[7,9,24,25] This

shift indicates that the π-to-π* highest occupied molecular orbital (HOMO) and lowest unoccupied molecular orbital (LUMO) gap widens as the Lewis acidity of the ion increases.

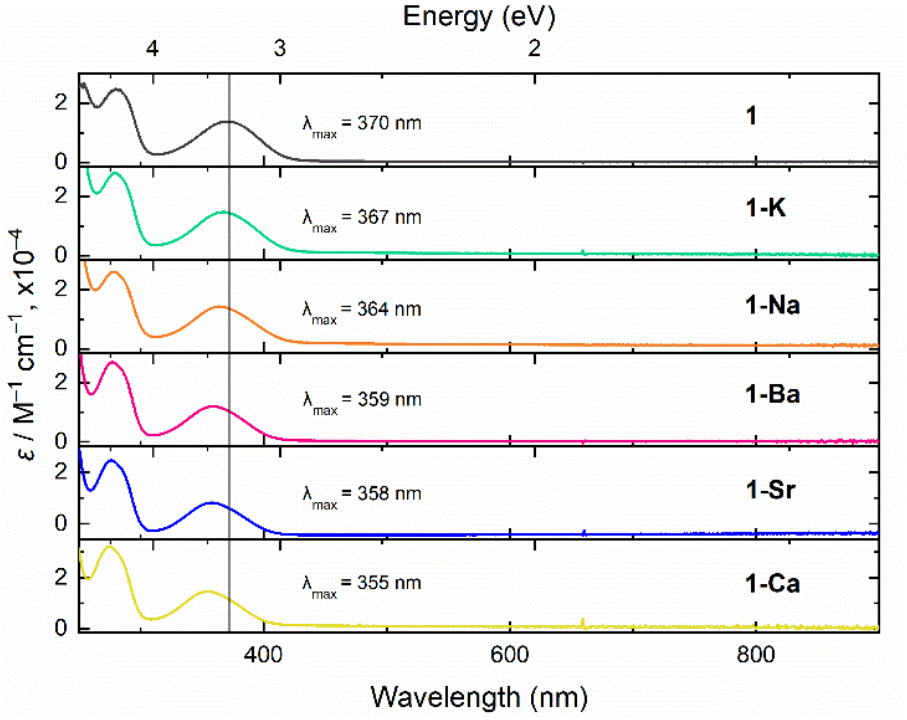

Figure 8.6. Stacked electronic absorption spectra of the **1** and **1-M** complexes.

Further analysis reveals that the energy of the π-to-π* band near 360 nm depends linearly on the pK_a value of **M**, with a sensitivity (slope) of –32 ± 2 meV/pK_a unit (Figure 8.7). This dependence indicates that the electronic properties of the **1-M** series can be parameterized according to charge density effects that are engendered by incorporation of secondary metal ions. Such observations have been made for transition metals and for complexes of the uranyl ion (UO_2^{2+}) in prior work, but to the best of our knowledge, the trend in this data represents the first observation of rational tuning of the electronic properties of a lanthanide species across a series incorporating mono- and di-valent secondary metals. Just as in prior work with complexes built around redox-active elements from other regions of the periodic table, divalent cations exert a stronger influence than monovalent cations (Figure 8.7) and the behavior across both valencies

can be parametrized through use of a common pK_a scale that serves as a descriptor for charge density considerations.

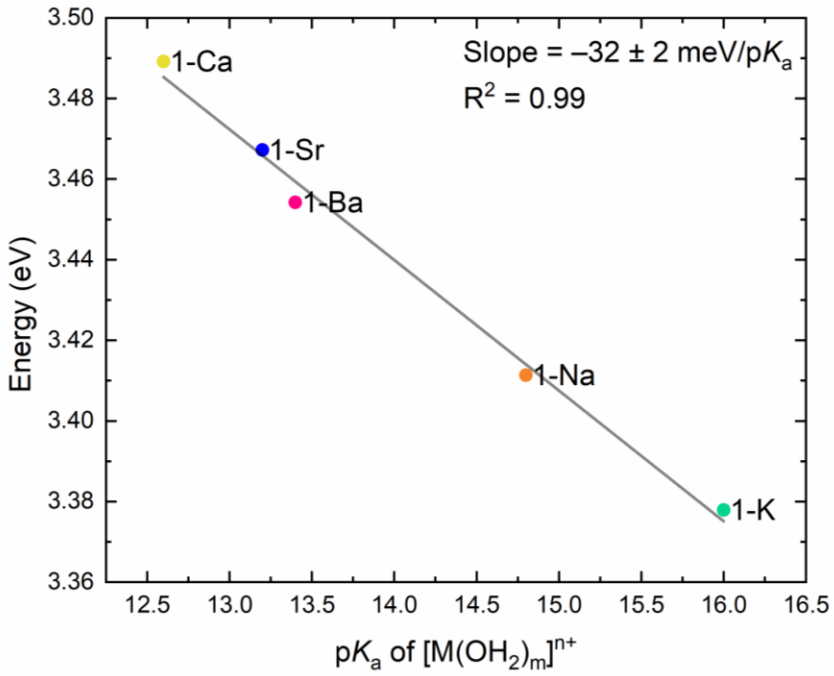

Figure 8.7. Dependence on π-to-π* band of the **1-M** complexes on the Lewis acidity (pK_a) of the corresponding **M** aqua complexes.

Electronic absorption spectroscopy was also used to confirm the 1:1 binding stoichiometry of the secondary metals with **1** in solution. To interrogate this, **1** was titrated with the triflate salts of K^+, Na^+, Ba^{2+}, Sr^{2+}, and Ca^{2+}; in each case, the λ_{max} value of the intraligand π-to-π* band near 370 nm shifted towards the values measured for the isolated complexes in the series **1-M** (see Figure 8.6). 1:1 binding was confirmed by the uniform changes in each set of spectra that occurred up to the addition of 1 eq. of metal triflate salt and by the cessation of any notable spectral changes upon additions of triflate salt beyond 1 eq. (see Appendix F, Figures F44-F55). These findings from the titrations confirm that our ligand framework prefers to tightly bind one mono- or di-valent metal cation in the hexadentate site in solution, as implied by the NMR and XRD discussed above.

8.2.4. Electrochemical Studies. With all of this data in hand, we next interrogated the electrochemical properties of the isolated Ce(III) complexes with cyclic voltammetry (CV). To begin, an anodic scan of a solution containing **1** beginning at ca. –0.8 V vs. ferrocenium/ferrocene (denoted hereafter as $Fc^{+/0}$) revealed a chemically reversible $1e^-$ oxidation of **1** at $E_{1/2}$ = –0.32 V vs. $Fc^{+/0}$, indicating facile generation of the corresponding Ce(IV) complex (denoted **2**; see Figure 8.8, black trace). The Ce(IV/III) couple displays a peak-to-peak separation (ΔE_p) of 88 mV (measured at a scan rate of 100 mV/s) indicating reasonably fast electron transfer (cf. ΔE_p of 76 mV for $Fc^{+/0}$ measured with the same electrode/conditions).[26] Scan rate dependent studies verified that both the isolated Ce(III) and Ce(IV) forms of **1** are freely diffusing and soluble (see Appendix F, Figure F58). Scanning to more positive potentials revealed that oxidation of $\mathbf{L^{OEt}}$ occurs at ca. +0.60 V vs. $Fc^{+/0}$ (see Appendix F, Figure F60); we find that oxidation of the ligand results in significant electrode fouling, and thus the data reported here correspond to electrochemical scans that do not involve potential excursions positive of +0.5 V vs. $Fc^{+/0}$.

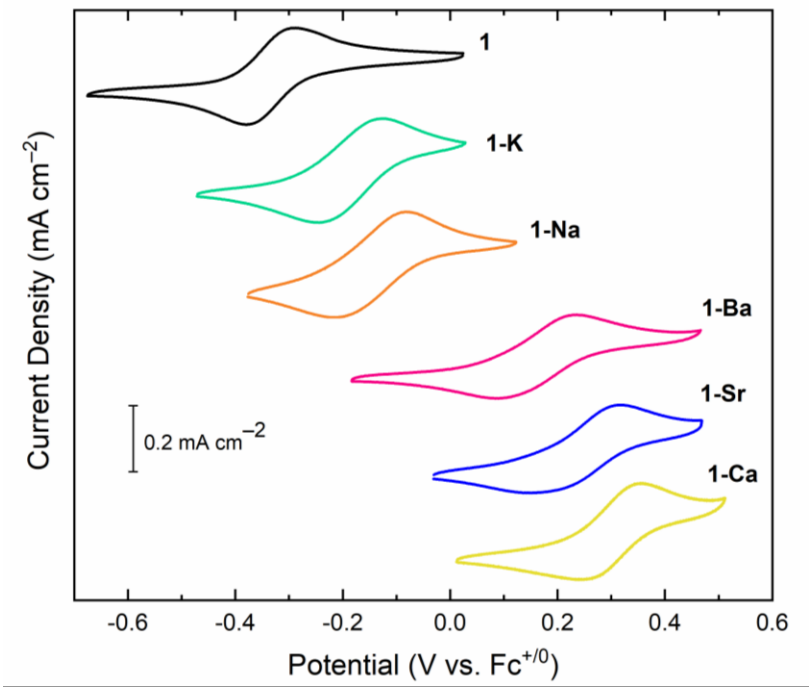

Figure 8.8. Cyclic voltammetry data for **1** and the complexes **1-M**. Conditions: electrolyte, 0.1 M $TBAPF_6$ in CH_3CN; scan rate, 100 mV/s; working electrode, highly oriented pyrolytic graphite (HOPG); in all cases, the [Ce] ≈ 1 mM.

Incorporation of the secondary metal ions results in significant shifts in the Ce(IV/III) reduction potentials (reported as $E_{1/2}$ values) in all cases studied here (Table 8.2). The reduction potentials of **1-K** and **1-Na** were measured at –0.19 V and –0.15 V vs. $Fc^{+/0}$, respectively. Na^+ thus drives a greater shift in the reduction potential than K^+. This trend continues for the heterobimetallic complexes **1-Ba**, **1-Sr** and **1-Ca**; these complexes displayed Ce(IV/III) reduction potentials of +0.16 V, +0.23 V, and +0.31 V vs. $Fc^{+/0}$ respectively. Across these two series of complexes, the cations with smaller ionic radii uniformly drive larger shifts in the $E_{1/2}$ values. The peak-to-peak separations (ΔE_p values) measured for **1-K** and **1-Na** are 116 mV and 131 mV, respectively, while the ΔE_p values measured for **1-Ba**, **1-Sr** and **1-Ca** were 140 mV, 148 mV and 106 mV, respectively; these values indicate slower heterogeneous electron transfer rates for the heterobimetallic complexes in comparison to monometallic **1**. However, we note that scan rate

dependent studies verified that both the reduced and oxidized forms of the complexes **1-M** are freely diffusing and soluble under the tested conditions (see Appendix F, Figures F56-F72). The $E_{1/2}$ values shifted to positive potentials measured for the heterobimetallic complexes **1-M** incorporating mono- and di-valent cations complement prior work from Robinson, Schelter, and co-workers that demonstrated potential shifts with monovalent cations only in a series of multimetallic cerium complexes.[4]

Table 8.2. Electrochemical data.

Complexes	$E_{1/2}$ Ce(IV/III)	$\Delta E_{1/2}$	ΔE_p
1	–0.32 V	-	88 mV
1-K	–0.19 V	130 mV	116 mV
1-Na	–0.15 V	170 mV	131 mV
1-Ba	+0.16 V	510 mV	140 mV
1-Sr	+0.23 V	550 mV	148 mV
1-Ca	+0.31 V	630 mV	106 mV

The chemically reversible Ce(IV/III) couple in the electrochemical data for **1** encouraged us to chemically prepare the 1e$^-$ oxidation product. To do this, the oxidant Ag^+ ($E_{1/2}(Ag^{+/0})$ = +0.04 V vs. $Fc^{+/0}$ in CH_3CN[27]) was added a CH_3CN solution of **1** in either the form of $AgPF_6$ or AgOTf (see Scheme 8.2). The reaction solution immediately darkened from orange to deep purple upon addition of either silver reagent, yielding the Ce(IV) products $\mathbf{2}^{PF6}$ and $\mathbf{2}^{\mathbf{OTf}}$, respectively. These monometallic complexes were characterized by ^{1}H NMR and were found to be diamagnetic in nature, in accord with the valence electron configuration of Ce(IV), and to display *pseudo*-C_3 symmetry as expected based on the properties of $\mathbf{L}^{\mathbf{OEt}}$ (see Appendix F, Figures F23 and F27). In the cases of both $\mathbf{2}^{\mathbf{PF6}}$ and $\mathbf{2}^{\mathbf{OTf}}$, cyclic voltammetry data (scanned cathodically from 0 V) revealed a chemically reversible 1e$^-$ reduction of the Ce(IV) complexes to Ce(III) at $E_{1/2}$ = –0.32 V vs. $Fc^{+/0}$ (see Appendix F, Figures F73-F76). These data match those obtained for **1** (*vide supra*), confirming that the 1e$^-$ oxidation product of **1** is a Ce(IV) complex. The electronic absorption

spectra of the isolated Ce(IV) complexes display similar π-to-π* features as **1** (*vide supra*) but also exhibit charge transfer bands at ca. 530 nm (see Appendix F, Figures F42 and F43) that can be assigned as ligand-to-metal charge transfer (LMCT) events; in line with prior work, such LMCT events involve electron transfer into empty f-orbitals on Ce^{IV}.[13] Single crystals of $\mathbf{2^{PF6}}$ and $\mathbf{2^{OTf}}$ suitable for XRD studies were grown, confirming the identities of the oxidized product and the presence of outer-sphere counter-anions in both cases (see Appendix F, Figures F91 and F94). See Section F2.6 in Appendix F for discussion of the structural data for the Ce(IV) complexes.

Scheme 8.2. One-electron Oxidation of 1 to Cerium(IV)

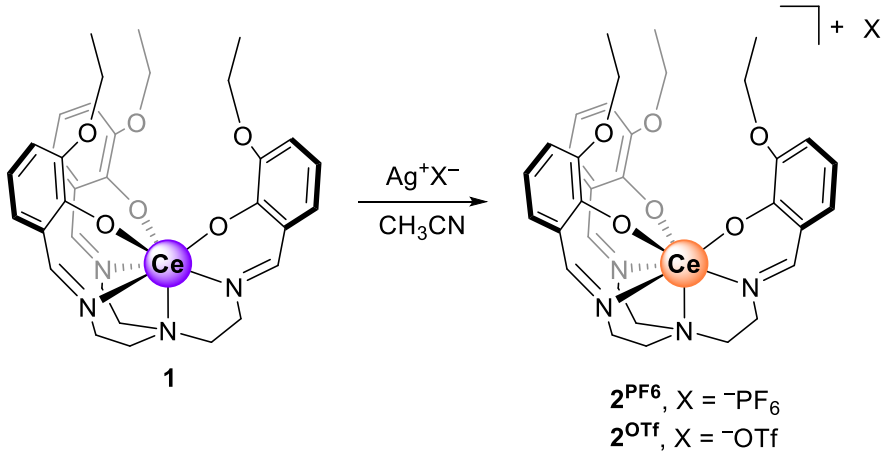

1

$\mathbf{2^{PF6}}$, X = $^{-}PF_6$
$\mathbf{2^{OTf}}$, X = ^{-}OTf

8.2.5. X-ray Absorption Spectroscopy Studies. To obtain further understanding of the electronic ground state behavior of the cerium complexes, cerium L_3-edge XANES was employed for **1**, **1-Na**, **1-Ca**, and $\mathbf{2^{PF6}}$. The L_3-edge probes electric-dipole-allowed transitions from Ce 2p orbitals to unoccupied states with Ce 5d character (i.e., $2p^6 4f^n 5d^0 \rightarrow 2p^5 4f^n 5d^1$, where n corresponds to the number of f electrons in the ground state). This transition is sensitive to both the ground state 4f occupation (oxidation state) and the effective nuclear charge on the cerium ion (i.e., differences in charge donation from the ligand field). The curve-fit analysis on the normalized and background subtracted data for **1**, **1-Na**, **1-Ca**, and $\mathbf{2^{PF6}}$ are shown in Figure 8.9. **1**, **1-Na**, and **1-Ca** all exhibit a singular white-line feature, typical for trivalent cerium ions.[28] For the

monometallic **1**, the inflection point of the rising edge is at 5723.3 eV. In comparison, the inflection point for the rising edge for both bimetallic complexes, **1-Na** and **1-Ca**, are both at 5724.4 eV. This difference in energy implies a increased effective nuclear charge for the cerium centers in the heterobimetallic complexes when compared to the monometallic system. See Section F3.1 for detailed discussion of the XANES analysis for **1**, **1-Na** and **1-Ca**.

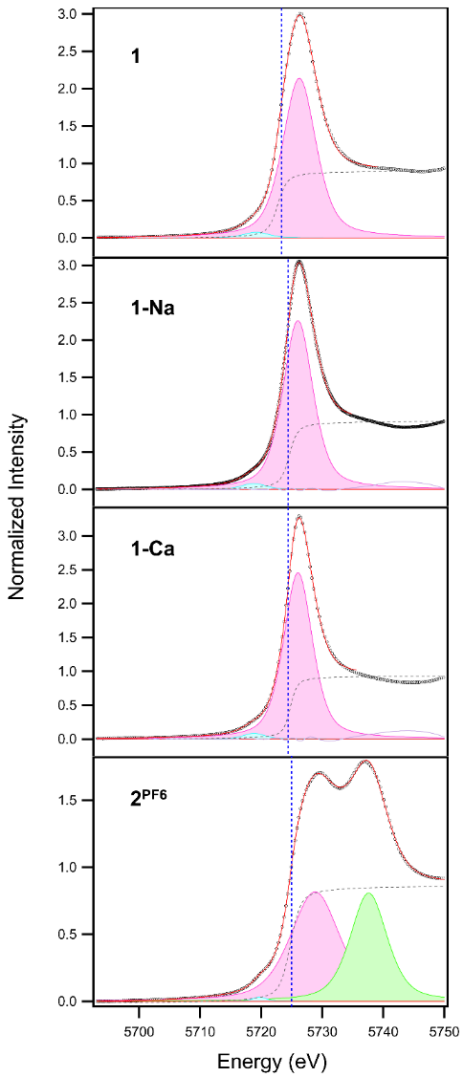

Figure 8.9. Ce L_3-edge XAS experimental data (black open circles) obtained for **1**, **1-Na**, **1-Ca**, and $\mathbf{2^{PF6}}$. The pseudo-Voigt (pink and green areas) and steplike functions (gray dashed lines) are also shown; these sum to generate the overall curve fit (red lines). The low-intensity pre-edge

feature observed near the edge onset is modeled with a single function (light blue area). The dark blue dashed line represents the energy of the first inflection point of the rising edge for each complex. All data were collected at 10 K.

The XANES behavior of the tetravalent **2^{PF6}** deviates from those of the trivalent cerium complexes, as expected, by the presence of a white-line doublet feature.[29] The inflection point at the rising edge for this compound is at 5724.9 eV. This value is 0.5 eV above the inflection points for both **1-Na** and **1-Ca**, and 1.6 eV above the inflection point for the monometallic cerium complex indicating an increase in formal oxidation state. The presence of the white-line doublet feature can be rationalized through the presence of a multiconfigurational ground state,[28] which consists of both a $4f^1$ open-shell singlet (Ce^{3+} character alongside a ligand hole, L) and a $4f^0$ closed-shell singlet (Ce^{4+} character).[30] See Section F3.1 for detailed discussion of XAS analysis of **2^{PF6}**.

8.3 Discussion

Incorporation of secondary, redox-inactive metals into redox-active complexes has emerged as a powerful strategy for tuning the properties of molecules and materials across the rows and groups of the periodic table. Metals used for the purpose of rational tuning in this approach span a significant range of sizes and coordination numbers, and are often chosen from among mono-, di-, and tri-valent ions; the wide-ranging properties of these metals can be used to reliably and widely tune the properties of the final multimetallic species, as shown by work from a variety of laboratories over the years. On the other hand, the vast majority of work examining incorporation of secondary redox-inactive cations as a tuning strategy has focused on the first-row metals of the transition series, leaving an open question as to the viability of this approach in the lanthanide and actinide series. In the present work, we were encouraged by findings from our group that have shown that the U(VI)/U(V) reduction potential of the uranyl ion (UO_2^{2+}) can be reliably tuned in

heterobimetallic complexes of K^+, Na^+, Ca^{2+}, Nd^{3+} and Y^{3+} over a range of ca. 600 mV. An appealing feature of using heterometallic effects to tune the electrochemical properties of compounds is that much work has found that the pK_a values of the corresponding aqua complexes of the redox-inactive metals used to accomplish the desired tuning can be used as a descriptor of Lewis acidity and can reliably predict & quantify the potential tuning engendered by a given ion.

Considering the numerous examples showing that reduction potentials depend linearly on the relevant pK_a values[7,8,11] of the incorporated redox-inactive metals in heterobimetallic species, we examined our data here in the same way. Following this strategy for the **1-M** series, we plotted the $E_{1/2}(Ce^{IV}/Ce^{III})$ values for each of the chemically reversible redox events, revealing a linear trend with a rather steep slope of –157 (±24) mV/pK_a unit (Figure 8.10). This trend in the $E_{1/2}$ values reveals that there is a clear relationship between the cerium(IV)/cerium(III) reduction potential and the identity of the incorporated Lewis acidic cations. The error on the linear slope of ±24 mV (reported as ±1σ) represents a quite modest estimated variance in the data of only 15%, a value that agrees well with prior variances that we have measured and confirms the reasonably tight relationship between $E_{1/2}$ and Lewis acidity. The most Lewis acidic metals in our series (Sr^{2+} and Ca^{2+}) engendered the largest shifts (550 mV and 630 mV, respectively), a finding that we initially hypothesized would be the case since these ions have the lowest pK_a values in the series tested (13.2 and 12.6, respectively).

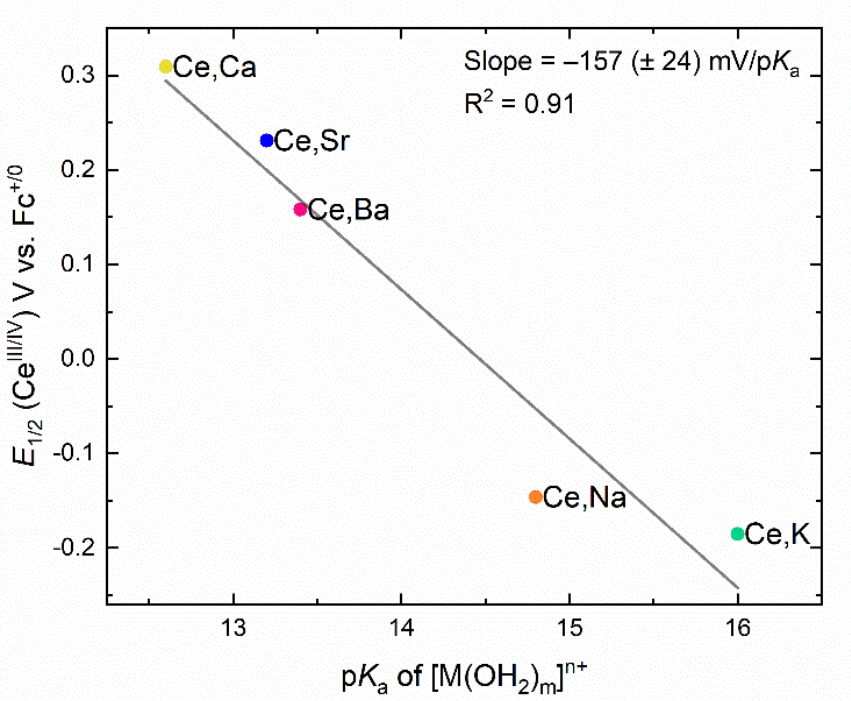

Figure 8.10. Plot of $E_{1/2}(Ce^{III/IV})$ vs. pK_a of $[\mathbf{M}(H_2O)_m]^{n+}$.

The slope, or tuning sensitivity, in our data is significantly larger in magnitude than those from our prior work with d-block (Ni, –70 (±12) mV/pK_a) and 5f-elements (UO_2^{2+}; –61 (±9) mV/pK_a). At this stage, we hypothesize that the greater magnitude of the tuning sensitivity achieved here for cerium arises from the presence of three bridging phenoxide donor ligands; based on the data, these groups mediate the electronic communication of the secondary metals with the redox-active cerium center. In our prior systems, only two bridging phenoxide donor moieties were present, providing weaker electrostatic coupling between the two metals. As a consequence of the greater magnitude of the slope in our complexes here, incorporation of Ca^{2+} (pK_a = 12.6) engenders a substantial $\Delta E_{1/2}$ of 630 mV, whereas this ion induces a shift of only 360 mV in our work with heterobimetallic uranyl complexes.

The XRD results provide a structural foundation for these interpretations on the basis of the Lewis acidity descriptor (i.e., charge density effects). Of particular note, the data show that the

$E_{1/2}(Ce^{IV}/Ce^{III})$ values trend linearly with the average Ce–O_{Ar} distance revealed by the solid-state XRD analysis of each complex (see Appendix F, Figure F77). This linear trend must result from the electrostatic influence of the secondary metals on the anionic phenoxide donor atoms, in that the cations distort the electron density such that it is less available for donation to the cerium center upon incorporation of the secondary metals. We re-emphasize here that the phenoxide moieties must mediate electronic communication between the Ce center and the secondary metal for this trend to emerge; comprehensive analysis of the structural data delineates aspects of the structural chemistry that are dictated by the ionic radii of the secondary metals in contrast to these dependent on charge density (Lewis acidity). All these effects can be quantified on the basis of the solid-state structures of the series of complexes **1-M** (*vide supra*, and see Appendix F).

In light of these observations, we feel that tuning the properties of lanthanide elements with heterometallic effects can be concluded to be a useful strategy worthy of future exploration for elements across the series. Additionally, $\mathbf{L^{OEt}}$ can be concluded to be a useful new platform for exploration of these effects, as it appears flexible enough to incorporate a wide range of secondary metals and presents the advantageous tripodal geometry which offers up to three phenoxide donors that can bridge between the two metals. Considering the high prevalence of the +III and +IV oxidation states in the later actinide elements (e.g., Bk(IV), Cf(III)), $\mathbf{L^{OEt}}$ could also be useful for encapsulation of these challenging transuranic elements in unexplored heterobimetallic environments.

The electrochemical tuning effect observed in this series of cerium complexes is best parameterized by a Lewis acidity descriptor; this descriptor, from our perspective, is a quantitative approach to estimating the charge density effect/shift that arises from incorporation of the redox-inactive metals. Consequently, this viewpoint can be used to interpret heterometallic effects

observed in prior work and in other coordination environments. Most notably, Robinson, Schelter, and co-workers reported shifts in $E_{1/2}(Ce^{IV}/Ce^{III})$ values by formation of 1:3 adducts of a Ce(binolate) core with Li^+, Na^+, K^+, and Cs^+. This work demonstrated the crucial nature of electrostatic interactions that modulate ligand donor properties, a finding that we could extend here to divalent metals as well. This extension seems especially powerful since the single descriptor of Lewis acidity (pK_a values) applies not only to monovalent ions but others as well.

More recently, La Pierre and co-workers have estimated the reduction potentials of a family of Ce(III) imidophosphorane complexes. Intriguingly, estimates of the reduction potentials for these complexes suggest a shift in $E_{1/2}(Ce^{IV}/Ce^{III})$ to a more negative value upon incorporation of an inner-sphere-bound K^+ ion into the imidophosphorane core of the complex. Inner sphere binding of K^+ was hypothesized in this work to contribute to this unorthodox shift.[13] Together with our findings here, these shifts underscore that the use of heterometallic effects to tune the properties and reactivity of lanthanide complexes has received far less attention than it deserves. A particularly attractive venue for future research would appear to be studies of the precise roles of bridging ligands in influencing the accessible scope of tuning with redox-active lanthanide systems, as only limited examples are available at present.

As accessing various oxidation states of the lanthanides has emerged as a central theme in enabling new chemistry with these important elements, we propose that strategic use of heterometallic effects and tuning could be an important tool for future development of lanthanide chemistry. The large body of work on Ce(IV/III) redox has shown that ligand coordination effects give rise to $E_{1/2}(Ce^{IV}/Ce^{III})$ values that vary by ca. 3.5 V, from –1.59 V to +1.87 V vs. the normal hydrogen electrode (NHE).[31] Even greater shifts may be possible when heterometallic tuning is considered as an additional handle beyond ligand re-design. Considering the importance of redox-

active cerium-based materials in catalysis[32] and other practical applications,[33] as well as the importance of understanding metal–ligand covalency in the heavier elements,[34,35] gaining ever better control over redox chemistry represents an exciting opportunity indeed.

8.4 Conclusions

Here, we have demonstrated that mono- and di-valent redox-inactive metals can effectively tune the electronic properties and reduction potential of cerium within a heteroditopic ligand framework. These findings were enabled by the development of a new tripodal ligand that can undergo divergent metalation to form a family of isolable heterobimetallic Ce(III) complexes. XRD analysis indicates that the structures of the bimetallic complexes are influenced by the ionic radii of the secondary metals, particularly with respect to the position of the secondary metals in their modular binding site. Conversely, we find that the electrostatic and structural properties about the cerium centers are best parameterized by the pK_a values of the incorporated secondary metal cations. We conclude that the phenoxide moieties mediate communication between cerium and the secondary metals; this electronic effect is further demonstrated by observation of uniformly shifted Ce(IV/III) reduction potentials varying by –157 mV/pK_a unit. The observed shifts in reduction potential are greater in magnitude than those reported for previously studied analogous d- and 5f-element complexes, a finding attributable to the tripodal nature of the ligand framework used here. Taken together, these results provide insights into the structural and charge density factors that can be used to drive tuning of cerium as well as reveal the wide scope of rational tuning possible with a lanthanide element by redox-inactive metals for the first time.

8.5 Experimental Details

8.5.1 General Considerations

All manipulations were carried out in dry N_2-filled gloveboxes (Vacuum Atmospheres Co., Hawthorne, CA) or under N_2 atmosphere using standard Schlenk techniques unless otherwise noted. All solvents were of commercial grade and dried over activated alumina using a PPT Glass Contour (Nashua, NH) solvent purification system prior to use, and were stored over molecular sieves. All chemicals were from major commercial suppliers and used as received. CD_3CN and CD_2Cl_2 was purchased from Cambridge Isotope Laboratories and dried over 3 Å molecular sieves and calcium hydride, respectively. ^1H, ^{13}C, and ^{19}F NMR spectra were collected on 400 and 500 MHz Bruker spectrometers and referenced to the residual protio-solvent signal[36] in the case of ^1H and ^{13}C. ^{19}F NMR spectra were referenced and reported relative to CCl_3F as an external standard following the recommended scale based on ratios of absolute frequencies (Ξ).[37,38] Chemical shifts (δ) are reported in units of ppm and coupling constants (*J*) are reported in Hz. NMR spectra are given in Appendix F (Figures F1 to F34). Electronic absorption spectra were collected with an Ocean Optics Flame spectrometer, in a 1-cm path length quartz cuvette. Infrared (IR) spectra were collected under an inert atmosphere in a dry N_2-filled glovebox (Vacuum Atmospheres Co., Hawthorne, CA). Spectra were collected with a Shimadzu IRSpirit FTIR spectrometer equipped with a QATR-S single-reflection attenuated total reflectance (ATR) accessory and diamond prism plate.

8.5.2 Synthesis

Synthetic Procedures. Ligands were synthesized by modification of related procedures to the literature.[14]

Synthesis of $\boldsymbol{L^{OEt}H_3}$*.* To a solution of 3-ethoxysalicylaldehyde (3.3594 g, 20.2 mmol, 3 equiv.) tren (Tris(2-aminoethyl)amine) (0.9862 g, 6.74 mmol, 1 equiv.) was added dropwise in dry dichloromethane and molecular sieves under a flow of nitrogen. The solution was allowed to stir for 2 h. Pure material was obtained via removal of volatiles in vacuo to yield a brow-yellow solid (3.9905 g, 99%). ^{1}H NMR (500 MHz, CD_3CN) δ 13.92 (s, 3H), 8.01 (s, 3H), 6.92 (dd, *J* = 8.0, 1.5 Hz, 3H), 6.58 (t, *J* = 7.9 Hz, 3H), 6.25 (dd, *J* = 7.5, 1.6 Hz, 3H), 4.03 (q, *J* = 7.0 Hz, 6H), 3.65 – 3.44 (m, 6H), 2.88 – 2.75 (m, 6H), 1.35 (t, *J* = 7.0 Hz, 9H). ppm. $^{13}C\{^{1}H\}$ NMR (126 MHz, CD_3CN) δ 167.31, 153.28, 148.52, 124.44, 119.62, 118.53, 116.76, 65.24, 58.25, 56.28, 15.26 ppm.

S*ynthesis of* ***1.*** A $Ce(N(SiMe_3)_2)_3$ (0.4345 g, 0.70 mmol) was added to a solution of $\mathbf{L^{OEt}H_3}$ (tris(((2-hydroxy-3-ethoxybenzyl)amino)ethyl)amine) in CH_3CN (0.4133 g, 0.70 mmol) was added in THF. The solution was allowed to stir overnight, and an orange precipitate formed and was filtered and washed with toluene to yield the title compound (0.4332 g, 85%) Single-crystals suitable for X-ray diffraction studies were obtained by vapor diffusion of Et_2O into a concentrated CD_2Cl_2 solution of the title compound.^{1}H NMR (500 MHz, CD_2Cl_2) δ 17.46 (s), 10.68 (d, *J* = 7.8 Hz), 8.17 (s), 7.97 (s), 1.87 (d, *J* = 6.9 Hz), 1.28 (s), -1.04 (s), -7.59 (s). ppm. $^{13}C\{^{1}H\}$ NMR (126 MHz, CD_2Cl_2) δ 184.02 – 177.69 (m), 174.20, 164.05 – 157.72 (m), 142.00 (d, *J* = 4.5 Hz), 130.95, 120.97, 64.26, 43.75 (q, *J* = 2.5 Hz), 13.29 ppm. Electronic absorption spectrum in CH_3CN (M^{-1} cm^{-1}): 250 (25329), 280 (24593), 371 (13783) nm.

Synthesis of ***1-M.*** To a solution of **1** the corresponding metal salt ($M^{n+}(OTf)_x$) was added in CH_3CN. The color of the reaction mixture rapidly lightened, and volatiles were removed in vacuo to yield the title **1-M** complex in >90% yield.

*Synthesis of **1-K.*** **1-K** was synthesized according to the above **1-M** procedure. Light orange single-crystals suitable for X-ray diffraction studies were obtained by vapor diffusion of Et_2O into a concentrated CH_3CN solution of the title compound. ^1H NMR (500 MHz, CD_2Cl_2) δ 14.95 (s), 8.69 (d, *J* = 7.9 Hz), 7.71 (d, *J* = 7.7 Hz), 7.18 (t, *J* = 7.7 Hz), 3.97 (dqd, *J* = 13.5, 6.6, 3.9, 3.3 Hz), 3.55 (d, *J* = 6.9 Hz), 1.91 (s), 0.52 (s), 0.05 (tdd, *J* = 13.2, 10.0, 8.8, 5.0 Hz). ppm. $^{13}C\{^1H\}$ NMR (126 MHz, CD_2Cl_2) δ 169.26 – 167.90 (m), 164.52 (d, *J* = 3.7 Hz), 157.84 – 157.14 (m), 132.39, 130.46 – 125.59 (m), 115.28 – 115.07 (m), 114.80, 63.74, 13.95, 1.56 ppm. ^{19}F NMR (376 MHz, CD_2Cl_2) δ –81.21 ppm. Electronic absorption spectrum in CH_3CN (M^{-1} cm^{-1}): 244 (55082), 279 (27868), 367 (14678) nm.

*Synthesis of **1-Li.*** **1-Li** was synthesized according to the above **1-M** procedure. Yellow single-crystals suitable for X-ray diffraction studies were obtained by cold concentrated solution of CH_3CN and Et_2O of the title compound. ^1H NMR (500 MHz, CD_3CN) δ 15.54 (s), 9.03 (s), 8.37 (s), 7.55 (s), 4.74 (s), 1.25 (d, *J* = 28.4 Hz), -1.83 (s) ppm. $^{13}C\{^1H\}$ NMR (126 MHz, CD_3CN) δ172.11, 159.79, 135.66, 129.63, 123.37, 120.82, 117.01, 66.33, 54.08, 47.19, 15.17 ppm. ^{19}F NMR (376 MHz, CD_3CN) δ –80.23 ppm. Electronic absorption spectrum in CH_3CN (M^{-1} cm^{-1}): 242 (49551), 279 (23794), 364 (11780) nm.

*Synthesis of **1-Na.*** **1-Na** was synthesized according to the above **1-M** procedure. Light orange single-crystals suitable for X-ray diffraction studies were obtained by vapor diffusion of Et_2O into a concentrated CH_2Cl_2 solution of the title compound. ^1H NMR (500 MHz, CD_2Cl_2) δ 12.09 (s), 7.79 (d, *J* = 7.5 Hz), 7.09 (s), 6.85 (d, *J* = 7.6 Hz), 6.47 (s), 4.73 (d, *J* = 7.0 Hz), 4.43 (s), 1.91 (s). ppm. $^{13}C\{^1H\}$ NMR (126 MHz, CD_2Cl_2) δ 160.15, 159.95, 158.38, 127.23, 126.25, 115.23, 114.34, 66.32, 58.82, 56.62, 15.86 ppm. ^{19}F NMR (376 MHz, CD_2Cl_2) δ –81.84 ppm. Electronic absorption spectrum in CH_3CN (M^{-1} cm^{-1}): 242 (51641), 279 (25915), 364 (14222) nm.

*Synthesis of **1-Ba.*** **1-Ba** was synthesized according to the above **1-M** procedure. Light orange single-crystals suitable for X-ray diffraction studies were obtained by vapor diffusion of Et_2O into a concentrated CH_3CN solution of the title compound. ^{1}H NMR (500 MHz, CD_3CN) δ 14.84 (s), 8.12 (d, *J* = 7.8 Hz), 7.62 (d, *J* = 7.8 Hz), 6.96 (t, *J* = 7.7 Hz), 6.41 (s), 4.28 (q, *J* = 7.0 Hz), 1.12 (t, *J* = 6.9 Hz), 0.63 (s). ppm. ^{13}C{^{1}H} NMR (126 MHz, CD_3CN) δ 168.78 (ddt, *J* = 15.2, 7.6, 3.1 Hz), 158.28, 131.21 (d, *J* = 2.6 Hz), 128.64, 123.04, 120.50, 117.02, 115.85, 64.58, 57.45, 50.99 (d, *J* = 6.7 Hz), 13.93 ppm. ^{19}F NMR (376 MHz, CD_3CN) δ –80.35 ppm. Electronic absorption spectrum in CH_3CN (M^{-1} cm^{-1}): 242 (49439), 277 (26940), 358 (11942) nm.

*Synthesis of **1-Sr.*** **1-Sr** was synthesized according to the above **1-M** procedure. Light orange single-crystals suitable for X-ray diffraction studies were obtained by vapor diffusion of Et_2O into a concentrated CH_2Cl_2 solution of the title compound. ^{1}H NMR (500 MHz, CD_3CN) δ 13.79 (s), 7.51 (d, *J* = 7.8 Hz), 7.40 (d, *J* = 7.7 Hz), 6.63 (t, *J* = 7.7 Hz), 4.73 (q, *J* = 7.0 Hz), 3.13 (s), 1.16 (t, *J* = 6.9 Hz), 1.13 (s).ppm. ^{13}C{^{1}H} NMR (126 MHz, CD_3CN) δ 165.74, 155.87, 155.14 (d, *J* = 3.9 Hz), 128.98, 127.86, 123.11, 120.57, 116.42, 115.87, 65.52, 58.14 (d, *J* = 3.2 Hz), 53.67 (t, *J* = 3.9 Hz), 13.93 ppm. ^{19}F NMR (376 MHz, CD_3CN) δ –80.19 ppm. Electronic absorption spectrum in CH_3CN (M^{-1} cm^{-1}): 242 (51276), 275 (28866), 358 (12426) nm.

*Synthesis of **1-Ca.*** **1-Ca** was synthesized according to the above **1-M** procedure. Light orange single-crystals suitable for X-ray diffraction studies were obtained by vapor diffusion of Et_2O into a concentrated CH_3CN solution of the title compound. ^{1}H NMR (500 MHz, CD_3CN) δ 12.80 (s), 7.43 (d, *J* = 7.8 Hz), 6.60 (d, *J* = 7.8 Hz), 6.25 (t, *J* = 7.7 Hz), 5.62 (s), 5.29 (d, *J* = 7.8 Hz), 1.23 (s) ppm. ^{13}C{^{1}H} NMR (126 MHz, CD_3CN) δ 161.44, 154.35, 150.96, 125.88, 125.66, 122.29, 119.74, 115.03, 114.82, 65.46, 57.76, 56.79 – 55.04 (m), 13.02 ppm. ^{19}F NMR (376 MHz,

CD_3CN) δ –80.14 ppm. Electronic absorption spectrum in CH_3CN (M^{-1} cm^{-1}): 240 (49583), 275 (32219), 354 (14581) nm.

Synthesis of $\boldsymbol{2^{PF6}.2^{PF6}}$ was synthesized by addition of $AgPF_6$ (0.163 g, 0.064 mmol) to a solution of **1** (0.0469 g, 0.064 mmol) in CH_3CN. The color of the reaction mixture rapidly darkened to purple, the solution was filtered to remove the Ag^0 biproduct and volatiles were removed in vacuo to yield the title complex Single-crystals suitable for X-ray diffraction studies were obtained by vapor diffusion of Et_2O into a concentrated CH_3CN solution of the title compound (0.0530 g, 94%). ^1H NMR (500 MHz, CD_3CN) δ 8.87 (s, 3H), 7.11 (d, *J* = 7.9 Hz, 6H), 6.69 (t, *J* = 7.8 Hz, 3H), 4.12 (t, *J* = 5.3 Hz, 6H), 3.92 (d, *J* = 7.0 Hz, 6H), 3.30 (t, *J* = 5.4 Hz, 6H), 1.02 (t, *J* = 7.0 Hz, 9H) ppm. $^{13}C\{^1H\}$ NMR (126 MHz, CD_3CN) δ 168.07, 159.64 (d, *J* = 4.0 Hz), 146.37, 127.22, 125.83, 121.86, 120.80 – 120.27 (m), 66.35, 61.48, 59.21, 15.23 ppm. ^{19}F NMR (376 MHz, CD_3CN) δ –73.71 (d, *J* = 706.6 Hz) ppm. $^{31}P\{^1H\}$(162 MHz, CD_3CN) δ –145.47 (sept, *J* = 706.6 Hz) ppm. Electronic absorption spectrum in CH_3CN (M^{-1} cm^{-1}): 249 (17624), 280 (20553), 347 (11102), 532 (2958) nm.

Synthesis of $\boldsymbol{2^{OTf}}$**.** $\mathbf{2^{OTf}}$ was synthesized by addition of AgOTf (0.0123 g, 0.48 mmol) to a solution of **1** (0.0349 g, 0.48 mmol) in CH_3CN. The color of the reaction mixture rapidly darkened to purple, the solution was filtered to remove the Ag^0 biproduct and volatiles were removed in vacuo to yield the title complex (0.0402 g, 95%). Single-crystals suitable for X-ray diffraction studies were obtained by vapor diffusion of Et_2O into a concentrated CH_2Cl solution of the title compound. ^1H NMR (500 MHz, CD_3CN) δ 8.85 (s, 3H), 7.09 (d, *J* = 7.9 Hz, 6H), 6.67 (t, *J* = 7.8 Hz, 3H), 4.13 (t, *J* = 5.4 Hz, 6H), 3.93 (q, *J* = 7.0 Hz, 6H), 3.31 (t, *J* = 5.6 Hz, 6H), 1.03 (t, *J* = 7.0 Hz, 9H) ppm. $^{13}C\{^1H\}$ NMR (126 MHz, CD_3CN) δ 168.00, 159.72, 146.40, 127.21, 125.83, 121.77 (d, *J* = 2.1 Hz), 120.40, 66.35, 61.50, 59.43, 15.25 ppm. ^{19}F NMR (376 MHz, CD_3CN) δ –

80.15 (s) ppm. Electronic absorption spectrum in CH_3CN (M^{-1} cm^{-1}): 241 (42052), 277 (28299), 352 (12704), 529 (3590) nm.

8.5.3 X-ray crystallography

*Refinement Details for **1-M and 2^X**.*

Crystals for all nine compounds were immersed in Paratone oil and scooped onto magnetic MiTeGen MicroMounts which were mounted on a goniometer head and placed in a cold nitrogen stream. Complete sets of low-temperature diffraction data frames were collected for crystals of all nine compounds using 1.0°-wide ω- and/or ϕ-scans.

X-rays for five (**[1]**, **[1-Na]**, **[1-Ba]**, **[1-Sr] and [2^{PF6}]**) of the eight compounds were provided by a Bruker MicroStar microfocus rotating anode generator running at 45 mA and 60 kV (Cu K_α = 1.54178 Å). Data for **[1] (q16l)**, **[1-Na] (27l)**, **[1-Ba] (q25l) and [2^{PF6}] (q21l)** were collected with a Bruker APEX II CCD detector positioned at 50.0 mm and equipped with Helios multilayer mirror optics; data for **[1-Sr] (v51f)** were collected with a Bruker Platinum 135 CCD detector positioned at 80.0 mm and equipped with Helios high-brilliance multilayer mirror optics.

X-rays for **[1-K] (JH3099)**, **[1-Ca] (JH3029)**, **[1-Li] (JH3100)** and **[2^{OTf}] (JH3145a)** were provided by a Bruker generator using a fine-focus Mo sealed tube running at 35 mA and 50 kV (Mo Kα = 0.71073 Å) and equipped with Bruker TRIUMPH curved-graphite optics. Data were collected with a Bruker PHOTON-II detector.

All diffractometer manipulations, including data collection, integration and scaling were carried out using the Bruker APEX2 or APEX3 software package.[39] The data for **[1]**, **[1-Na]**, **[1-Ba]** and **[2^{PF6}]**) were corrected empirically for variable absorption effects with SADABS[40] using equivalent reflections. A numerical face-indexed absorption correction was used for data sets of the other five structures. Probable space groups were determined on the basis of systematic

absences and intensity statistics and the structures were solved by direct methods using SIR2004[41] or XS[42] (incorporated into SHELXTL) and refined to convergence by weighted full-matrix least-squares on F_o^2 using the Olex2 software package equipped with XL[43] or with SHELXL that was incorporated into the APEX2 or APEX3 software package.

Unless otherwise stated in the special refinement section for each structure, the final structural model for each compound incorporated anisotropic thermal parameters for all non-hydrogen atoms and isotropic thermal parameters for all included hydrogen atoms**.** Non-methyl hydrogen atoms bonded to carbon in each complex were fixed at idealized riding model sp^2- or sp^3-hybridized positions with C–H bond lengths of 0.95 - 0.99 Å. Methyl groups were incorporated into the structural models either as sp^3-hybridized riding model groups with idealized "staggered" geometry and a C-H bond length of 0.98 Å or as idealized riding model rigid rotors (with a C–H bond length of 0.98 Å) that were allowed to rotate freely about their C–C bonds in least-squares refinement cycles. The isotropic thermal parameters of idealized hydrogen atoms in all nine structures were fixed at values 1.2 (non-methyl) or 1.5 (methyl) times the equivalent isotropic thermal parameter of the carbon atom to which they are covalently bonded.

The relevant crystallographic and structure refinement data for all nine compounds are given in Tables F3, F4,and F5.

8.5.4 Electrochemistry

Electrochemical experiments were carried out in a nitrogen-filled glove box. 0.10 M tetra(n-butylammonium) hexafluorophosphate (Sigma-Aldrich; electrochemical grade) in acetonitrile served as the supporting electrolyte. Measurements were made with a Gamry Reference 600 Plus Potentiostat/Galvanostat using a standard three-electrode configuration. The working electrode was the basal plane of highly oriented pyrolytic graphite (HOPG) (GraphiteStore.com, Buffalo

Grove, IL.; surface area: 0.09 cm^2), the counter electrode was a platinum wire (Kurt J. Lesker, Jefferson Hills, PA; 99.99%, 0.5 mm diameter), and a silver wire immersed in electrolyte served as a pseudo-reference electrode (CH Instruments). The reference was separated from the working solution by a Vycor frit (Bioanalytical Systems, Inc.). Ferrocene (Sigma Aldrich; twice-sublimed) was added to the electrolyte solution at the conclusion of each experiment (~1 mM); the midpoint potential of the ferrocenium/ferrocene couple (denoted as $Fc^{+/0}$) served as an external standard for comparison of the recorded potentials. Concentrations of analyte for cyclic voltammetry were typically 1 mM.

8.5.5 Spectroscopy

Cerium samples were prepared in an argon glovebox at Stanford Synchrotron Radiation Lightsource (SSRL) because both Ce^{4+} and Ce^{3+} complexes are air sensitive. A mixture of the analyte and boron nitride (BN) was weighed, such that the edge jump for the absorbing atom was calculated to be at one absorption length in transmission (~8−12 mg for the cerium samples). The samples were diluted with BN (~10 mg), which had been dried at elevated temperature (250 °C) under vacuum (1×10^{-3} Torr) for 24 h prior to use. Samples were ground with a mortar and pestle. Solid-state sample holders for the cerium samples consisted of an aluminum plate with a 3 × 15 mm oval window and screw holes. One side of the plate was covered with 0.5 mm Kapton tape, and the sample was evenly loaded in the window. The powder was then secured by covering the sample with a second piece of 0.5 mm Kapton tape. A second layer of the compound was painted onto a third piece of Kapton tape, which was subsequently fixed to the backside of the sample holder. The sample holder was then loaded onto a sample rod, taken out of the glovebox, and transported to the beamline while submerged within a liquid-nitrogen cooling bath. Once at the beam, the rod with the sample was placed at 45° inside the Oxford liquid helium cryostat, which

was precooled at 85 K and attached to the SSRL beamline 4-3 rail. When the cryostat was closed, the system was put under vacuum and flushed with helium three times. The valve was closed, and the measurements were performed in the cryostat at 10 K.

The cerium complexes were characterized by metal L_3- edge X-ray measurements. The XAS measurements were made at SSRL, under dedicated operating conditions (3.0 GeV, 5%, 500 mA using continuous top-off injections) on end station 11- 2. With the use of a liquid-nitrogen-cooled double-crystal Si(220) ($\varphi = 0$) monochromator that employed collimating and focusing mirrors, a single energy was selected from the incident white beam. For cerium measurements, the beam was fully tuned at 6023 eV, and harmonic rejection was achieved with Rh-coated mirror. The horizontal slit sizes were 8 mm, and vertical slit sizes were 1 mm in all measurements. The cryostat was attached to the beamline 11-2 XAS rail (SSRL), which was equipped with three ionization chambers, through which nitrogen gas was continually flowed. One chamber was positioned before the helium beam pass and the cryostat (10 cm) to monitor the incident radiation (I0). The second chamber was positioned after the cryostat (30 cm) so that sample transmission (I1) could be evaluated against I0 and so that the absorption coefficient (μ) could be calculated as ln(I0/I1). The third chamber (I2; 30 cm) was positioned downstream from I1 so that the XANES of a calibration foil could be measured against I1. A potential of 1100 V was applied in series to the ionization chambers. A Lytle detector under argon was placed on one side of the cryostat (4 cm) to detect the fluorescence from the samples. The cerium samples were calibrated in situ to the energy of the first inflection point of the K-edge of chromium foil (5989 eV). Data were acquired in triplicate and averaged. Background subtraction and normalization (at 5800 eV) were performed in Athena.4 Curve fitting was performed in IgorPro 7.0 using a modified version of EDG_FIT.5 Derivative spectra were used as guides to determine the number and positions of the peaks, and

edge features were modeled by pseudo-Voigt line shapes and an additional function consisting of arctangent and error function contributions, which was used to model the absorption threshold. Deconvoluted spectral models were performed over several energy ranges. The area under the (defined as the intensity) was calculated with the formula ph × fwhm × 1 /4($[\pi/\ln(2)]^{1/2} + \pi$), where ph = peak height (normalized intensity), fwhm = full-width at half-maximum height (eV), and the value 1 /4($[\pi/\ln(2)]^{1/2} + \pi$) ≈ 1.318 is a constant associated with the pseudo-Voigt function. The fits are shown in Figures F148-F151 and summarized in Tables F10-F13. Relative parameter error estimates are calculated from the covariance matrix assuming normally distributed variances in the data.

8.6 Acknowledgements

The authors thank Dr. Justin Douglas and Sarah Neuenswander for assistance with NMR spectroscopy. This work was supported by the US Department of Energy, Office of Science, Office of Basic Energy Sciences through the Early Career Research Program (DE-SC0019169).

8.7 References

[1] (a) MacDonald, M. R.; Bates, J. E.; Ziller, J. W.; Furche, F.; Evans, W. J., Completing the Series of +2 Ions for the Lanthanide Elements: Synthesis of Molecular Complexes of Pr^{2+}, Gd^{2+}, Tb^{2+}, and Lu^{2+}. *J. Am. Chem. Soc.* **2013,** *135*, 9857-9868. (b) MacDonald, M. R.; Ziller, J. W.; Evans, W. J., Synthesis of a Crystalline Molecular Complex of Y^{2+}, [(18-crown-6)K][$(C_5H_4SiMe_3)_3Y$]. *J. Am. Chem. Soc.* **2011,** *133*, 15914-15917.

[2] (a) Willauer, A. R.; Palumbo, C. T.; Fadaei-Tirani, F.; Zivkovic, I.; Douair, I.; Maron, L.; Mazzanti, M., Accessing the +IV Oxidation State in Molecular Complexes of Praseodymium. *J. Am. Chem. Soc.* **2020,** *142*, 5538-5542. (b) Palumbo, C. T.; Zivkovic, I.; Scopelliti, R.; Mazzanti, M., Molecular Complex of Tb in the +4 Oxidation State. *J. Am. Chem. Soc.* **2019,** *141*, 9827-9831. (c) Camp, C.; Guidal, V.; Biswas, B.; Pécaut, J.; Dubois, L.; Mazzanti, M., Multielectron redox chemistry of lanthanide Schiff-base complexes. *Chem. Sci.* **2012,** *3*, 2433-2448.

[3] Rice, N. T.; Popov, I. A.; Russo, D. R.; Bacsa, J.; Batista, E. R.; Yang, P.; Telser, J.; La Pierre, H. S., Design, Isolation, and Spectroscopic Analysis of a Tetravalent Terbium Complex. *J. Am. Chem. Soc.* **2019,** *141*, 13222-13233.

[4] Robinson, J. R.; Gordon, Z.; Booth, C. H.; Carroll, P. J.; Walsh, P. J.; Schelter, E. J., Tuning Reactivity and Electronic Properties through Ligand Reorganization within a Cerium Heterobimetallic Framework. *J. Am. Chem. Soc.* **2013,** *135*, 19016-19024.

[5] (a) McEvoy, J. P.; Brudvig, G. W., Water-Splitting Chemistry of Photosystem II. *Chem. Rev.* **2006,** *106* (11), 4455-4483. (b) Yano, J.; Yachandra, V., Mn_4Ca Cluster in Photosynthesis: Where and How Water is Oxidized to Dioxygen. *Chem. Rev.* **2014,** *114*, 4175-4205.

[6] (a) Kanady, J. S.; Tsui, E. Y.; Day, M. W.; Agapie, T., A Synthetic Model of the Mn_3Ca Subsite of the Oxygen-Evolving Complex in Photosystem II. *Science* **2011,** *333*, 733-736. (b) Tsui, E. Y.; Tran, R.;

Yano, J.; Agapie, T., Redox-inactive metals modulate the reduction potential in heterometallic manganese–oxido clusters. *Nat. Chem* **2013,** *5*, 293-299.

[7] Kumar, A.; Lionetti, D.; Day, V. W.; Blakemore, J. D., Trivalent Lewis Acidic Cations Govern the Electronic Properties and Stability of Heterobimetallic Complexes of Nickel. *Chem. Eur. J.* **2018,** *24*, 141-149.

[8] (a) Reath, A. H.; Ziller, J. W.; Tsay, C.; Ryan, A. J.; Yang, J. Y., Redox Potential and Electronic Structure Effects of Proximal Nonredox Active Cations in Cobalt Schiff Base Complexes. *Inorg. Chem.* **2017,** *56*, 3713-3718. (b) Bang, S.; Lee, Y.-M.; Hong, S.; Cho, K.-B.; Nishida, Y.; Seo, M. S.; Sarangi, R.; Fukuzumi, S.; Nam, W., Redox-inactive metal ions modulate the reactivity and oxygen release of mononuclear non-haem iron(III)–peroxo complexes. *Nat. Chem* **2014,** *6*, 934-940. (c) Park, Y. J.; Ziller, J. W.; Borovik, A. S., The Effects of Redox-Inactive Metal Ions on the Activation of Dioxygen: Isolation and Characterization of a Heterobimetallic Complex Containing a Mn^{III}–(μ-OH)–Ca^{II} Core. *J. Am. Chem. Soc.* **2011,** *133*, 9258-9261. (d) Lacy, D. C.; Park, Y. J.; Ziller, J. W.; Yano, J.; Borovik, A. S., Assembly and Properties of Heterobimetallic $Co^{II/III}$/Ca^{II} Complexes with Aquo and Hydroxo Ligands. *J. Am. Chem. Soc.* **2012,** *134*, 17526-17535. (e) Gupta, G.; Bera, M.; Paul, S.; Paria, S., Electrochemical Properties and Reactivity Study of [Mn^{V}(O)(μ-OR–Lewis Acid)] Cores. *Inorg. Chem.* **2021,** *60*, 18006-18016.

[9] Kumar, A.; Lionetti, D.; Day, V. W.; Blakemore, J. D., Redox-Inactive Metal Cations Modulate the Reduction Potential of the Uranyl Ion in Macrocyclic Complexes. *J. Am. Chem. Soc.* **2020,** *142*, 3032-3041.

[10] (a) Bell, N. L.; Shaw, B.; Arnold, P. L.; Love, J. B., Uranyl to Uranium(IV) Conversion through Manipulation of Axial and Equatorial Ligands. *J. Am. Chem. Soc.* **2018,** *140*, 3378-3384. (b) Arnold, P. L.; Pécharman, A.-F.; Hollis, E.; Yahia, A.; Maron, L.; Parsons, S.; Love, J. B., Uranyl oxo activation and functionalization by metal cation coordination. *Nat. Chem* **2010,** *2*, 1056-1061. (c) Zegke, M.;

Nichol, G. S.; Arnold, P. L.; Love, J. B., Catalytic one-electron reduction of uranyl(VI) to Group 1 uranyl(V) complexes via Al(III) coordination. *Chem. Commun.* **2015,** *51*, 5876-5879. (d) Faizova, R.; White, S.; Scopelliti, R.; Mazzanti, M., The effect of iron binding on uranyl(V) stability. *Chem. Sci.* **2018,** *9*, 7520-7527.

[11] Kumar, A.; Blakemore, J. D., On the Use of Aqueous Metal-Aqua pK_a Values as a Descriptor of Lewis Acidity. *Inorg. Chem.* **2021,** *60*, 1107-1115.

[12] Klamm, B. E.; Albrecht-Schmitt, T. E.; Baumbach, R. E.; Billow, B. S.; White, F. D.; Kozimor, S. A.; Scott, B. L.; Tondreau, A. M., Employing Lewis Acidity to Generate Bimetallic Lanthanide Complexes. *Inorg. Chem.* **2020,** *59*, 8642-8646.

[13] Rice, N. T.; Su, J.; Gompa, T. P.; Russo, D. R.; Telser, J.; Palatinus, L.; Bacsa, J.; Yang, P.; Batista, E. R.; La Pierre, H. S., Homoleptic Imidophosphorane Stabilization of Tetravalent Cerium. *Inorg. Chem.* **2019,** *58*, 5289-5304.

[14] Liu, S.; Yang, L. W.; Rettig, S. J.; Orvig, C., Bulky ortho 3-methoxy groups on N4O3 amine phenol ligands producing six-coordinate bis(ligand)lanthanide complex cations $[Ln(H_3L)_2]^{3+}$ (Ln = Pr, Gd; H_3L = tris(((2-hydroxy-3-methoxybenzyl)amino)ethyl)amine). *Inorg. Chem.* **1993,** *32*, 2773-2778.

[15] Ha, K., Crystal structure of tris(2-((3-ethoxysalicylidene)amino)ethyl)amine, $C_{33}H_{42}N_4O_6$. *Z Krist- New Cryst St.* **2010,** *225*, 697-698.

[16] (a) Kanesato, M.; Fujimoto, Y.; Wakayama, Y.; Kashiwada, A.; Matsuda, K.; Kikkawa, Y.; Sonoda, Y.; Goto, M., The Mutual Separation of Rare Earth Elements Utilizing the Reaction of Corresponding Complexes Coordinated by Tris(2-aminoethyl)amine with 3-Ethoxysalicylaldehyde. *Waste Biomass Valorization* **2012,** *3*, 451-458. (b) M.Kanesato, M.Goto CSD Communication(Private Communication) (2016) (c) M.Kanesato, M.Goto CSD Communication(Private Communication) (2016) (d) M.Kanesato, M.Goto CSD Communication(Private Communication) (2016)

[17] Bradley, D. C.; Ghotra, J. S.; Hart, F. A., Low co-ordination numbers in lanthanide and actinide compounds. Part I. The preparation and characterization of tris{bis(trimethylsilyl)-amido}lanthanides. *J. Chem. Soc., Dalton Trans.* **1973** 10, 1021-1023.

[18] Lionetti, D.; Day, M. W.; Agapie, T., Metal-templated ligand architectures for trinuclear chemistry: tricopper complexes and their O_2 reactivity. *Chem. Sci* **2013,** *4*, 785-790.

[19] Mizukami, S.; Houjou, H.; Kanesato, M.; Hiratani, K., Adjustment of Twist Angles in Pseudo-Helical Lanthanide Complexes by the Size of Metal Ions. *Chem. Eur. J.* **2003,** *9*, 1521-1528.

[20] Renaud, F.; Piguet, C.; Bernardinelli, G.; Bünzli, J.-C. G.; Hopfgartner, G., Nine-Coordinate Lanthanide Podates with Predetermined Structural and Electronic Properties: Facial Organization of Unsymmetrical Tridentate Binding Units by a Protonated Covalent Tripod. *J. Am. Chem. Soc.* **1999,** *121*, 9326-9342.

[21] (a) Alvarez, S.; Avnir, D.; Llunell, M.; Pinsky, M., Continuous symmetry maps and shape classification. The case of six-coordinated metal compounds. *New J. Chem.* **2002,** *26*, 996-1009. (b) Banerjee, S.; Ghosh, A.; Wu, B.; Lassahn, P.-G.; Janiak, C., Polymethylene spacer regulated structural divergence in cadmium complexes: Unusual trigonal prismatic and severely distorted octahedral coordination. *Polyhedron* **2005,** *24*, 593-599. (c) Alcock, L. J.; Cavigliasso, G.; Willis, A. C.; Stranger, R.; Ralph, S. F., Trigonal prismatic metal complexes: a not so rare coordination geometry? *Dalton Trans.* **2016,** *45*, 9036-9040. (d) Rare Earth Research, C., The rare earths in modern science and technology : volume 2 : [proceedings of the 14th Rare Earth Research Conference, held at North Dakota State University, Fargo, North Dakota, June 25-28, 1979]. McCarthy, G. J.; Rhyne, J. J.; Silber, H. B.; McCarthy, G. J.; Rhyne, J. J.; Rhyne, J. J.; Silber, H. B., Eds. New York : Plenum Press: New York, 1980.

[22] Shannon, R. D., Revised effective ionic radii and systematic studies of interatomic distances in halides and chalcogenides. *Acta Cryst. A.* **1976,** *32*, 751-767.

[23] Perrin, D. D. *Ionisation Constants of Inorganic Acids and Bases in Aqueous Solution*; Pergamon, 1982.

[24] Golwankar, R.; Kumar, A.; Day, V.; Blakemore, J. Revealing the Influence of Diverse Secondary Metal Cations on Redox-Active Palladium Complexes. *ChemRxiv* **2022**. This content is a preprint and has not been peer-reviewed.

[25] Kelsey, S. R.; Kumar, A.; Oliver, A. G.; Day, V. W.; Blakemore, J. D., Promotion and Tuning of the Electrochemical Reduction of Hetero- and Homobimetallic Zinc Complexes. *ChemElectroChem* **2021,** *8*, 2792-2802.

[26] Zanello, P.; Connelly, N. G. *Inorganic Electrochemistry: Theory, Practice and Application; Royal Society of Chemistry*: Cambridge, 2003; pp 55−58.

[27] Connelly, N. G.; Geiger, W. E., Chemical Redox Agents for Organometallic Chemistry. *Chem. Rev.* **1996,** *96*, 877-910.

[28] Sergentu, D.-C.; Booth, C. H.; Autschbach, J., Probing Multiconfigurational States by Spectroscopy: The Cerium XAS L_3-edge Puzzle. *Chem. Eur. J.* **2021**, *27*, 7188-7188.

[29] (a)Löble, M. W.; Keith, J. M.; Altman, A. B.; Stieber, S. C. E.; Batista, E. R.; Boland, K. S.; Conradson, S. D.; Clark, D. L.; Lezama Pacheco, J.; Kozimor, S. A.; Martin, R. L.; Minasian, S. G.; Olson, A. C.; Scott, B. L.; Shuh, D. K.; Tyliszczak, T.; Wilkerson, M. P.; Zehnder, R. A., Covalency in Lanthanides. An X-ray Absorption Spectroscopy and Density Functional Theory Study of $LnCl_6^{x-}$ (x = 3, 2). *J. Am. Chem. Soc.* **2015,** *137*, 2506-2523. (b) Bogart, J. A.; Lewis, A. J.; Medling, S. A.; Piro, N. A.; Carroll, P. J.; Booth, C. H.; Schelter, E. J., Homoleptic Cerium(III) and Cerium(IV) Nitroxide Complexes: Significant Stabilization of the 4+ Oxidation State. *Inorg. Chem.* **2013,** *52*, 11600-11607. (c) Halbach, R. L.; Nocton, G.; Booth, C. H.; Maron, L.; Andersen, R. A., Cerium Tetrakis(tropolonate) and Cerium Tetrakis(acetylacetonate) Are Not Diamagnetic but Temperature-Independent Paramagnets. *Inorg. Chem.* **2018,** *57*, 7290-7298. (d) Minasian, S. G.; Batista, E. R.; Booth, C. H.; Clark, D. L.; Keith, J. M.; Kozimor, S. A.; Lukens, W. W.; Martin, R. L.; Shuh, D. K.; Stieber, S. C. E.; Tylisczcak, T.; Wen, X.-d., Quantitative Evidence for Lanthanide-Oxygen Orbital Mixing in CeO_2, PrO_2, and TbO_2. *J. Am.*

Chem. Soc. **2017,** *139*, 18052-18064. (e) Aguirre Quintana, L. M.; Jiang, N.; Bacsa, J.; La Pierre, H. S., Homoleptic cerium tris(dialkylamido)imidophosphorane guanidinate complexes. *Dalton Trans.* **2020,** *49*, 14908-14913. (c) Kaul, S. N., Static critical phenomena in ferromagnets with quenched disorder. *J. Magn. Magn. Mater.* **1985,** *53*, 5-53. (f) Dexpert, H.; Karnatak, R. C.; Esteva, J. M.; Connerade, J. P.; Gasgnier, M.; Caro, P. E.; Albert, L., X-ray absorption studies of CeO_2, PrO_2, and TbO_2. II. Rare-earth valence state by LIII absorption edges. *Physical Review B* **1987,** *36*, 1750-1753.

[30] Gompa, T. P.; Ramanathan, A.; Rice, N. T.; La Pierre, H. S., The chemical and physical properties of tetravalent lanthanides: Pr, Nd, Tb, and Dy. *Dalton Trans.* **2020,** *49*, 15945-15987.

[31] (a)Piro, N. A.; Robinson, J. R.; Walsh, P. J.; Schelter, E. J., The electrochemical behavior of cerium(III/IV) complexes: Thermodynamics, kinetics and applications in synthesis. *Coord. Chem. Rev.* **2014,** *260*, 21-36. (b) Aspinall, H. C. *Chemistry of the f-block Elements*; Overseas Publishing Company: UK, 2001; Vol. 1. (b) Cotton, S. *Lanthanide and Actinide Chemistry*; John Wiley & Sons Ltd: West Sussex, England, 2006. (c) Schelter, E. J., Cerium under the lens. *Nat. Chem* **2013,** *5*, 348-348.

[32] (a) Trovarelli, A., Catalytic Properties of Ceria and CeO_2-Containing Materials. *Catalysis Reviews* **1996,** *38*, 439-520. (b) Murray, E. P.; Tsai, T.; Barnett, S. A., A direct-methane fuel cell with a ceria-based anode. *Nature* **1999,** *400*, 649-651. (b) Fu, Q.; Saltsburg, H.; Flytzani-Stephanopoulos, M., Active Nonmetallic Au and Pt Species on Ceria-Based Water-Gas Shift Catalysts. *Science* **2003,** *301*, 935-938. (c) Bunluesin, T.; Gorte, R. J.; Graham, G. W., Studies of the water-gas-shift reaction on ceria-supported Pt, Pd, and Rh: Implications for oxygen-storage properties. *Appl. Catal. B.* **1998,** *15*, 107-114.

[33] (a) Molander, G. A., Application of lanthanide reagents in organic synthesis. *Chem. Rev.* **1992,** *92*, 29-68. (b) Das, A. K., Kinetic and mechanistic aspects of metal ion catalysis in cerium(IV) oxidation. *Coord. Chem. Rev.* **2001,** *213*, 307-325. (c) Das, A. K., Kinetic and mechanistic aspects of metal ion catalysis in cerium(IV) oxidation. *Coord. Chem. Rev.* **2001,** *213*, 307-325

[34] Neidig, M. L.; Clark, D. L.; Martin, R. L., Covalency in f-element complexes. *Coord. Chem. Rev.* **2013,** *257*, 394-406.

[35] (a) Damon, P. L.; Wu, G.; Kaltsoyannis, N.; Hayton, T. W., Formation of a Ce(IV) Oxo Complex via Inner Sphere Nitrate Reduction. *J. Am. Chem. Soc.* **2016,** *138*, 12743-12746. (b) Löble, M. W.; Keith, J. M.; Altman, A. B.; Stieber, S. C. E.; Batista, E. R.; Boland, K. S.; Conradson, S. D.; Clark, D. L.; Lezama Pacheco, J.; Kozimor, S. A.; Martin, R. L.; Minasian, S. G.; Olson, A. C.; Scott, B. L.; Shuh, D. K.; Tyliszczak, T.; Wilkerson, M. P.; Zehnder, R. A., Covalency in Lanthanides. An X-ray Absorption Spectroscopy and Density Functional Theory Study of $LnCl_6^{x-}$ (x = 3, 2). *J. Am. Chem. Soc.* **2015,** *137*, 2506-2523.

[36] Fulmer, G. R.; Miller, A. J. M.; Sherden, N. H.; Gottlieb, H. E.; Nudelman, A.; Stoltz, B. M.; Bercaw, J. E.; Goldberg, K. I., NMR Chemical Shifts of Trace Impurities: Common Laboratory Solvents, Organics, and Gases in Deuterated Solvents Relevant to the Organometallic Chemist. *Organometallics* **2010,** 29, 2176-2179.

[37] Harris, R. K.; Becker, E. D.; Menezes, S. M. C. d.; Goodfellow, R.; Granger, P., NMR nomenclature. Nuclear spin properties and conventions for chemical shifts (IUPAC Recommendations 2001). *Pure Appl. Chem.* **2001,** *73*, 1795-1818.

[38] Harris, R. K.; Becker, E. D.; Menezes, S. M. C. d.; Granger, P.; Hoffman, R. E.; Zilm, K. W., Further conventions for NMR shielding and chemical shifts (IUPAC Recommendations 2008). *Pure Appl. Chem.* **2008,** *80*, 59-84.

[39] *SAINT. Ver. 8.34A.* Bruker Analytical X-ray Systems: Madison, WI, June 2014.

[40] *Sheldrick, G. M., SADABS (version 2008/1)*: Program for Absorption Correction for Data from Area Detector Frames, University of Göttingen, 2008.

[41] Sheldrick, G., SHELXT - Integrated space-group and crystal-structure determination. Acta Crystallogr., *Sect. A: Found. Crystallogr.* **2015,** *71*, 3-8.

[42] Sheldrick, G., Crystal structure refinement with SHELXL. Acta Crystallogr., Sect. C: Cryst. *Struct. Commun.* **2015,** 71, 3-8.

[43] Dolomanov, O. V.; Bourhis, L. J.; Gildea, R. J.; Howard, J. A. K.; Puschmann, H., OLEX2: a complete structure solution, refinement and analysis program. *J. Appl. Crystallogr.* **2009,** 42, 339-341.

Chapter 9

Summary and Future Outlook: Redox Chemistry, Bimetallic Effects, and Ligand Design for Rhodium, Chromium, and Cerium Complexes

9.1 Summary and Future Outlook

The results described in Chapters 2 through 8 demonstrate the importance of electrochemistry and chemical redox properties for the investigation of transition and lanthanide metal complexes. The work described in this dissertation illustrates the interwoven, unifying themes of redox chemistry, ligand design, and bimetallic effects for tuning of the properties of transition metal and lanthanide complexes. The development of novel metal complexes is critical to the advancement of multiple fields of energy-related technologies. For example, we showed that the ligand properties of [Cp*Rh] model catalysts significantly impact the reactivity and kinetics properties of model systems and the identity of intermediates formed. Similarly, we described a series of Cr-based olefin oligomerization catalysts for which the redox chemistry was significantly impacted by their supporting bidentate ligands. Additionally, we found that the redox chemistry of such oligomerization catalysts is considerably modulated by the addition of a Lewis acidic metal, aluminum. Lastly, we demonstrated that Lewis acidic metals can be employed to modulate the structural, electronic, and redox properties of cerium to reveal the wide scope of rational tuning with lanthanides with redox-inactive metals for the first time.

Chapter 2 included an extensive review of electrochemical fundamental concepts, methods, and notable advances in the field of organometallic electrochemistry. Many organometallic systems are cable of accessing many oxidation states that often feature unique properties. The purpose of this chapter was to inform readers of experimental design by review of common electrochemical techniques. The versatility of electrochemical techniques for kinetic, thermodynamic, and mechanistic understanding of redox-active organometallic systems were described. Examples such as kinetic, thermodynamic, and mechanistic studies were discussed to illustrate the interpretation of electrochemical data. In this chapter, complementing chemical

redox studies were described to accompany traditional electrochemical experiments; this parallel approach of chemical and electrochemical interrogation of organometallic complexes was a reoccurring theme throughout this dissertation.

In chapter 3 we discussed the investigation of the family of [Cp*Rh] complexes ligated with the bidentate 8-(diphenylphosphino)quinoline (PQN) ligand. Cyclic voltametric studies revealed that the Rh(III) complex is capable of a two-electron reduction followed by a sequential one-electron reduction engendered by the redox-active nature of the ligand. Chemical reduction of the Rh(III) complex enabled preparation and isolation of the Rh(I) analog bearing a κ^2-PQN. Protonation of the Rh(I) complex with an acid yielded a Cp*Rh monohydride complex. Chemical interrogation of the monohydride complex revealed that the presence of a single imine and phosphine donors enabled protonolysis of the hydride moiety; however, electrochemical studies revealed that the PQN ligand engenders a limited catalytic potential of the system as evidenced by low H_2 generation efficiency and side reactivity. The reactivity of the PQN ligand contrasts with the chemically inert [Cp*Rh] monohydride-based diphosphine systems as well as the robust and effective [Cp*H Rh] diimine based frameworks suggesting that the Cp* ligand protonation events associated with diimine systems may be central for the effective evolution of H_2.

Parallel studies of the [Cp*Rh] complex bearing the [(diphenylphosphino)methyl]pyridine (*P,N*) ligand were discussed in Chapter 4 of this dissertation. Synthesis and characterization of the *P,N* ligand for chelation to the modular [Cp*Rh] framework enabled isolation of an analogous Rh(III) complex to the PQN system. Cyclic voltametric data of the Rh(III) complex revealed a clean two-electron reduction to a Rh(I) that is stable on the CV time scale via an ECE′-type mechanism (E = electron transfer, C = chemical reaction) like that observed for other [Cp*Rh] complexes. However, parallel chemical preparation of the Rh(I) species observed via cyclic

voltammetry leads to unexpected side reactivity. This side reactivity is engendered by the electron-rich nature of the Rh center and the acidic benzylic methylene C–H bonds of the PN framework. The basic Rh(I) center is capable of subsequent deprotonation of the methylene protons to yield multiple monohydride complexes in the absence of an exogenous proton source; notably, there is no evidence of formation of [η^4-Cp*H] species. Speciation observed in this PN system is therefore not amenable to further chemical or electrochemical catalytic investigation for H_2 generation. Thus, this study suggests that avoidance of acidic moieties in supporting ligands is an attractive strategy for engendering stability for the management of protons and electrons during reductive catalysis.

Although the Blakemore group has extensively studied [Cp*Rh] complexes bearing bidentate frameworks for their proven ability to catalyze H_2 evolution, the use of new ligand frameworks could further illuminate the properties that engender effective H_2 catalysis. Our group has employed a diverse range of bidentate ligand frameworks to stabilize [Cp*Rh] monohydrides comprised of phosphine and imine moieties. Careful consideration of ligand design may enable preparation and isolation of more exotic [η^4-Cp*H] or monohydride rhodium complexes. One such promising ligand derivative is based on the fluorinated diphosphine ligand 1,2-Bis[di(pentafluorophenyl)phosphino]ethane.[1] Although this derivative is attractive for shifting the thermodynamics of the [Cp*Rh] complex, previous unpublished work by our group with the 1,2-Bis(diphenylphosphenyl)ethane (dppe) ligand has shown to yield undesirable dimerization due to the labile nature of the ethylene bridge. Thus, an attractive candidate for isolation of an [η^4-Cp*H] complex bearing diphosphine moieties could be the fluorinated derivative of the dppb ligand framework Bis[di(pentafluorophenyl)phosphino]benzene that features a rigid backbone to discourage dimerization and significantly electron-withdrawing substituents to promote a

substantial shift in thermodynamics to potentially stabilize a [η^4-Cp*H] rhodium diphosphine complex.

Chapters 5 described the kinetic properties of the redox chemistry of a series of [Cp*Rh] complexes bearing disubstituted dipyridylmethane (R_2dpma) ligands. Chapter 5 specifically discussed the kinetics and redox properties of a series of [Cp*Rh] complexes with κ^2-dpma ligands with varying substitution at the methylene position (dibenzyl (Bn_2dpma)-, methyl,methylpyrenyl-(MePyrdpma)-, and bis(methylpyrenyl) (Pyr_2dpma)-substituted dpma). The synthesis of the dpma ligand was shown to be modular and able to tolerate the installation of aromatic substituents. The cyclic voltammetry data measured for the novel aromatic dpma analogues are reminiscent of the previous dimethyl (Me_2dpma) substituted-dpma complex in which electrochemical reduction engenders an initial quasi-reversible reduction followed by a sequential irreversible reduction. The second reduction feature corresponds to an EC process in which the transient Rh(I) κ^2-dpma ligand undergoes a redox-induced ligand rearrangement to yield a formally Rh(I) complex with a facially η^2-coordination of one pyridyl ring. Scan rate dependent CV studies of this well-defined EC process were successfully modeled with electrochemical simulations using DigiElch software. Simulated CV data indicated that the introduction of sterically bulky substituents significantly impacts the first-order rate constant (k+) associated with the EC process. The steric bulk engendered by the Pyr_2dpma complex slows the k+ in comparison to the value measured for Me_2dpma by one order of magnitude. This work represents an unusual system that is suitable for quantification of an elementary rate constant of a well-defined EC process by simulation of CV data.

Similarly, Chapter 6 discussed the redox chemistry of a series of [Cp*Rh] complexes ligated with non-symmetric analogs of the Me_2dpma framework. Addition of electron-donating and -

withdrawing substituents to a single pyridyl moiety of Me_2dpma yielded the bidentate κ^2-dimethyl-2,2′-pyridyl(4-trifluoromethylpyridine)methane (Me_2dpma^{CF3}) and κ^2-dimethyl-2,2′-pyridyl(4-methoxypyridinepyridine)methane (Me_2dpma^{OMe}) ligands for coordination to the [Cp*Rh] framework. The CV data of the [Cp*Rh(Me_2dpma^{OMe})] complex resembles those of the Me_2dpma complex, as the CV features an EC process corresponding to rearrangement of the ligand scaffold. Two-electron reduction of the Rh(III) complex bearing Me_2dpma^{OMe} yields a facially η^2-coordination of the singly substituted pyridyl ring to the formally Rh(I) center. Comparatively, the CV of [Cp*Rh(Me_2dpma^{CF3})] complex differs from the Me_2dpma complex and features two quasi-reversible one-electron couples, thus there is a lack of evidence that a redox-induced chemical process occurs with the electron-withdrawing substituent. However, interestingly chemical preparation of the two-electron reduced species yields a formally Rh(I) complex bearing a facially η^2-coordinated singly substituted pyridyl moiety. Thus, the redox-induced ligand rearrangement is presumably too slow to observe on the cyclic voltammetry timescale. These findings could be useful for understanding more complex molecular electrocatalytic systems that utilize non-symmetric ligand frameworks and substituents that engender inductive effects.

The results presented in Chapter 7 consisted of work completed in collaboration with Chevron Phillips Chemical on a series of molecular chromium-based oligomerization catalysts ligated with mixed [*P*,*N*] ligands. In this chapter, we described the reactivity of a family of Cr(III) complexes in the absence of substrates or model substrates such as ethylene and 1-hexyne. Cyclic voltammetry data revealed an accessible quasi-reversible couple at $E_{1/2}$ = ca. –1.5 V vs $Fc^{+/0}$ dominated by the slow electron kinetics engendered by reduction of the Cr(III) complexes. Heterogenous material is formed upon reduction as evidenced by the appearance of an anodic stripping wave following reduction. Piezoelectric gravimetry confirmed that heterogeneous

material deposited formed upon reduction and quantified the amount deposited to be a very small side product of reduction of the bulk material. Characterization of the heterogeneous material done via X-ray photoelectron spectroscopy to revealed that the side product formed is primarily a reduced Cr-based species. X-band electron paramagnetic resonance (EPR) spectroscopy was utilized to characterize the Cr(III) precatalysts to reveal broad signals near g = 1.98 (with FWHM values of ca. 1000 G). *In situ* EPR studies were performed with chemical reductants to identify the oxidation state formed upon reduction. Chemical reduction with Cp^*_2Co, $AlEt_3$, and modified MAO (methylaluminoxane; MMAO) indicated the complete disappearance of the Cr(III) signal to yield a narrower signal at g = 1.98 (FWHM of ca. 200 G) that corresponds to a Cr(I) species. Quantitative EPR studies revealed that these signals correspond to a very small portion of the overall reduction product of the Cr(III) complexes. Thus, we employed a further spectroscopic technique to directly observe the predominant oxidation state accessible to the Cr complexes. UV-visible spectroscopy titrations of one of the Cr(III) precatalysts, **1**, with the chemical reductant Cp^*_2Co, revealed that the Cr(III) species can undergo clean conversion to a one-electron reduced Cr(II) species; this assignment is supported by chemical preparation, isolation and the solid-state structure obtained for the Cr(II) analog of **1**. Time-dependent UV-Visible studies with **1** revealed that upon addition of $AlEt_3$ there is a clean conversion to a new species that we assign as an Al-bound Cr species. Intriguingly, UV-visible spectroscopy titrations of **1** in the presence of $AlEt_3$ with Cp^*_2Co revealed that the Cr(III) complex is capable of a two-electron reduction. We observed that the presence of Al enables further a reduction that is not accessible in the absence of Al demonstrating the influence that secondary metals can have on unlocking access to lower oxidation states.

Although we have carried out a thorough study of the reactivity of Cr precatalysts utilizing multiple spectroscopic electrochemical techniques in this chapter, there are plentiful remaining opportunities to study the reactivity of these complexes in the presence of olefinic substrates. It is apparent, under the conditions studied, that a strong reductant is not produced in significant quantities to reach the Cr(I) oxidation state in the absence of Al. The favored Cr(III/I) ethylene oligomerization mechanism, however, could be based on the necessity of an olefinic substrate to facilitate a chemical step to reach a Cr(I) oxidation state or the binding of an olefin to engender an activation step that pushes the reduction sufficiently potential of the Cr(II/I) couple positive to enable facile access during trimerization of substrates via lower oxidation states. Therefore, experiments utilizing ethylene or 1-hexyne substrates are necessary to understand the mechanism of ethylene trimerization. Further EPR studies with 1-hexyne and MMAO would be attractive for identification of the oxidation states formed upon reduction to understand the influence of substrates for accessing the Cr(I) oxidation state. Quantitative EPR studies could be useful for studies under those new conditions for the quantification of oxidation states formed upon *in situ* activation of the Cr(III) precatalysts. Additional studies utilizing Stopped-Flow UV-visible spectroscopy could be attractive for probing the kinetics of catalyst activation with MMAO and substrate. Preliminary studies with MMAO reveal isosbestic behavior enabled us to deterimine an observed rate constant; these findings encourage further kinetic interrogation of precatalysts and MMAO as well as studies in the presence of ethylene and 1-hexyne to probe the influence that substrate has on the activation of trimerization catalysts. Further complementing work would be chemical preparation of the presumed Al-bound Cr species observed via UV-vis spectroscopy and characterization by solid-state XRD studies. Finally, further investigation and bulk synthesis of

the previously isolated and well-defined Cr(II) species would be attractive for studies in collaboration with Chevron Phillips Chemical.

Finally, Chapter 8 described the effective rational tuning of cerium's electronic properties and reduction potential through the incorporation of secondary metals. The complexes were built upon a heteroditopic tripodal framework that features a heptadentate cavity to accommodate the high coordination number of Ce as well as a second hexadentate site for coordination of the secondary metals. The divergent synthesis of the heterobimetallic complexes showed that this ligand construct can incorporate a range of Lewis acidic redox-inactive metal cations (M; M = Li^+, K^+, Na^+, Ba^{2+}, Sr^{2+}, Ca^{2+}). Spectroscopic, structural, and electronic studies revealed that there are significant effects driven by the inclusion of a secondary metal cation. Solid-state X-ray diffraction data reveal that the structural properties of the secondary metal of the heterobimetallic complexes are best parameterized by the ionic radii of the secondary metal. However, the structural properties about the Ce center are best described by the pK_a values of the incorporated metal cations. Comparatively, the tuning effect observed for the reduction potential is driven by the charge density effects arising from the Lewis acidic metals over a wide range of Lewis acidity 16.0 (K^+) to 12.6 (Ca^{2+}); the slope of ca. –160 mV/pK_a units is notably larger than those values observed for other transition metals or actinide metal complexes. Similarly, the electronic absorption data revealed that the addition of the Lewis acidic cations engenders a shift in the π to π^* feature associated with the ligand scaffold of –32 meV/pK_a units; indicating that there is significant electrostatic interaction with the secondary metal and the phenoxide donors in the ligand scaffold. Based on the structural and electronic influence on the cerium center we concluded that the phenoxide moieties have a key role in mediating electronic communication between the secondary metal and redox-active Ce center. Taken together, the findings in Chapter 8 allow us to conclude

that charge density effects and structural properties influence the tuning of 4*f* metals and revealed the possibilities of rational tuning of lanthanides with Lewis acidic redox-inactive cations for the first time.

Considering these promising results on the rational tuning of the properties of cerium, a wide new realm of possibilities has been opened by this dissertation for tuning the properties of other lanthanide metals. The lanthanides (elements 57 to 71) are strongly influenced by the uniquely core-like nature of their 4*f* valence orbitals. The gradual filling of these orbitals across the series results in similar structural and reactivity properties amongst the lanthanides. The nature of 4*f* metals have intrinsic magnetic, optical, and redox properties, investigation and harnessing of these properties have contributed to the development in clean energy technologies including magnets, catalysts, and battery materials. Thus, systematic tuning of lanthanides is of particular interest for enabling novel chemistry for advances in energy technology. Evans and co-workers have demonstrated that accessing lanthanides in the +II oxidation states often require remarkably strong reductants (Calculated $E_{1/2}$ ranging from (Eu^{3+}/Eu^{2+}) = –0.35 V vs Normal Hydrogen Electrode (NHE) to (Gd^{3+}/Gd^{2+}) = –3.90 V vs NHE)[2] to isolate stable Ln^{2+} species. The strategy of modulating the reduction potential of Ce outlined in Chapter 8 provides precedence for moving the Ln(III/II) potential to more positive potentials thus could provide an attractive method for facile synthetic preparation of lanthanides in the +II oxidation state.

Scattered reports of the heteroditopic framework with analogous terbium and dysprosium monometallic complexes give precedence for the potential usefulness of the heteroditopic scaffold for the study of lanthanides across the series. Furthermore, initial synthetic and electrochemical studies with europium and samarium in this heterobimetallic framework are currently underway in our group and demonstrates promise for a systematic tuning of the (+III/+II) reduction potential

of lanthanides. Following studies of europium and samarium, the another attractive lanthanide metal to interrogate would be ytterbium (aqueous $E_{1/2}$ for Yb(III/II) = −1.15 V vs NHE).[2] Based on the work presented in Chapter 8, installation of Ca^{2+} (pK_a = 12.6) would be the most promising strategy to engender the largest shift in redox potential as observed for the Ce system (ca. 600 mV shift positive for Ce(IV/III) reduction potential). Along this line, incorporation of thorium(IV) as a secondary metal in this framework is a novel attractive strategy for the significantly shifting the (+III/+II) reduction positive. The Th^{4+} ion is relatively comparable in size to Ca^{2+} (1.12 Å and 1.13 Å, respectively),[3] and thus can be predicted to effectively bind in the hexadentate site of the tripodal framework. The considerably Lewis acidic nature of Th^{4+} (pK_a = 3.9)[4] will presumably engender a substantial shift of $E_{1/2}$ Ln(III/II). Additionally, the +IV nature of this Th is attractive to avoid potential exchange between binding sites of Ln(III) ions with other tricationic secondary metals, as observed in Chapter 8. Thus, studies of this heterobimetallic framework have the potential to enable facile chemical preparation and electrochemical observation of stable lower valent oxidation states for a range of lanthanide metals utilizing secondary Lewis acidic metals. Lastly, the heteroditopic framework could be applicable for extending the study and tuning of 5*f* metals to compliment the Blakemore group's work rationally tuning the U(VI/V) redox couple. Thus, encapsulation and rational tuning of more challenging actinides in the +III and +IV oxidation states such as uranium(III), plutonium(III), berkelium(IV) and californium(III) could be achievable within this tripodal ligand framework. It is our hope that such studies, some of which could be quite challenging, will be fruitful in the years ahead.

9.2 References

[1] (a) Fairlie, D. P.; Bosnich, B., Homogeneous catalysis. Conversion of 4-pentenals to cyclopentanones by efficient rhodium-catalyzed hydroacylation. *Organometallics* **1988,** *7*, 936-945. (b) Chatt, J.; Hussain, W.; Leigh, G. J.; Ali, H. M.; Picket, C. J.; Rankin, D. A., The preparation and properties of some diphosphines $R_2PCH_2CH_2PR_2$(R = alkyl or aryl) and of their rhenium(I) dinitrogen derivatives. *J. Chem. Soc., Dalton Trans.* **1985**, 1131-1136. (c) Wu, H.-C.; Yu, J.-Q.; Spencer, J. B., Stereospecific Deoxygenation of Phosphine Oxides with Retention of Configuration Using Triphenylphosphine or Triethyl Phosphite as an Oxygen Acceptor. *Org. Lett.* **2004,** *6*, 4675-4678.

[2] MacDonald, M. R.; Bates, J. E.; Ziller, J. W.; Furche, F.; Evans, W. J., Completing the Series of +2 Ions for the Lanthanide Elements: Synthesis of Molecular Complexes of Pr^{2+}, Gd^{2+}, Tb^{2+}, and Lu^{2+}. *J. Am. Chem. Soc.* **2013,** *135*, 9857-9868.

[3] Shannon, R. D., Revised effective ionic radii and systematic studies of interatomic distances in halides and chalcogenides. *Acta Cryst. A.* **1976,** *32*, 751-767.

[4] Perrin, D. D. *Ionisation Constants of Inorganic Acids and Bases in Aqueous Solution*; Pergamon, 1982.

Appendices

Appendix A

Supplementary Information for Chapter 3

NMR Spectra

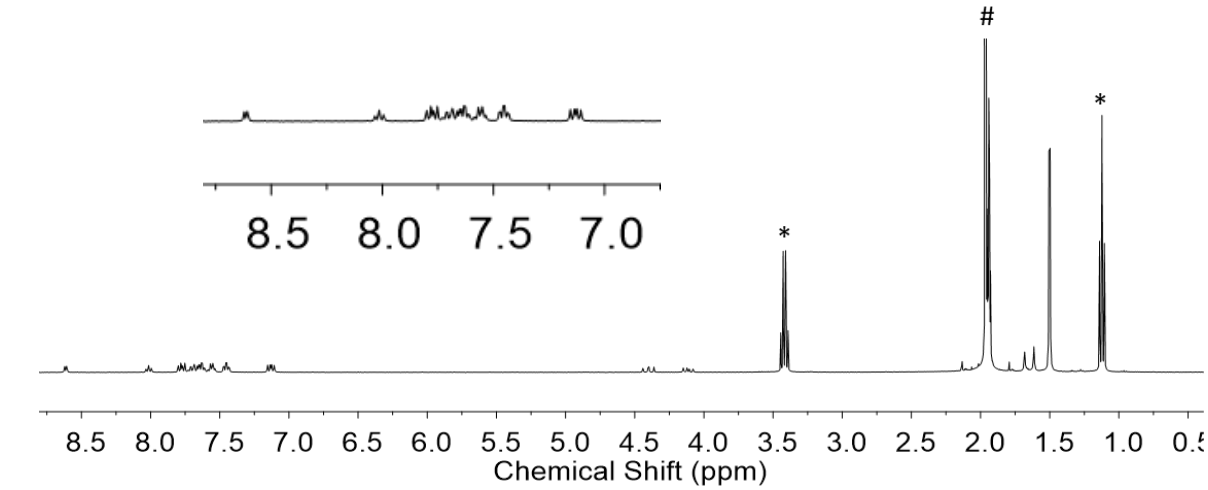

Figure A1. ^{1}H NMR spectrum (500 MHz, CD_3CN) of **1**. The signal indicated by # is associated with acetonitrile. The signal indicated by * is associated with diethyl ether.

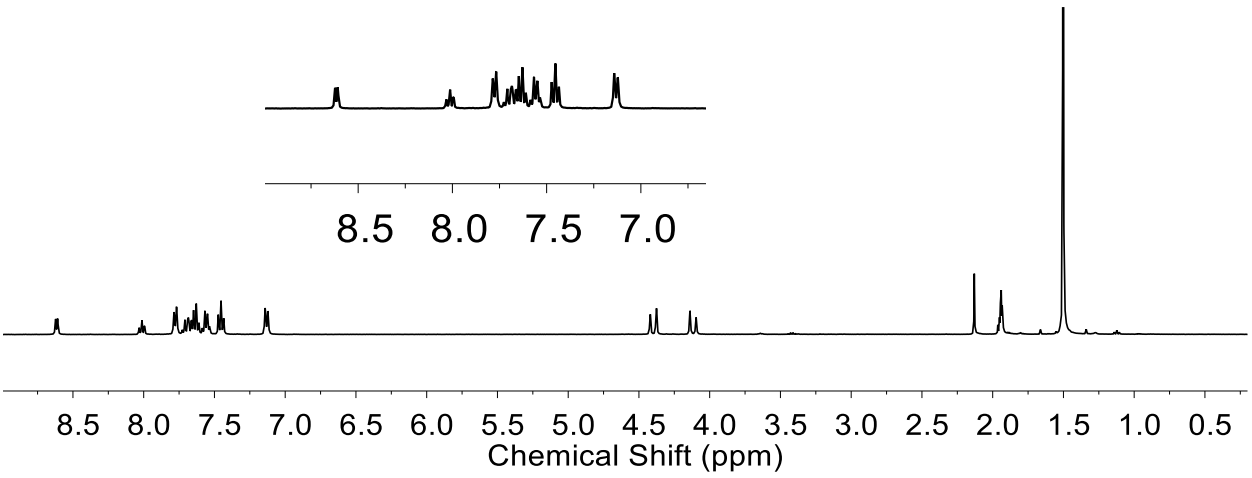

Figure A2. $^{1}H\{^{31}P\}$ NMR spectrum (500 MHz, CD_3CN) of **1**.

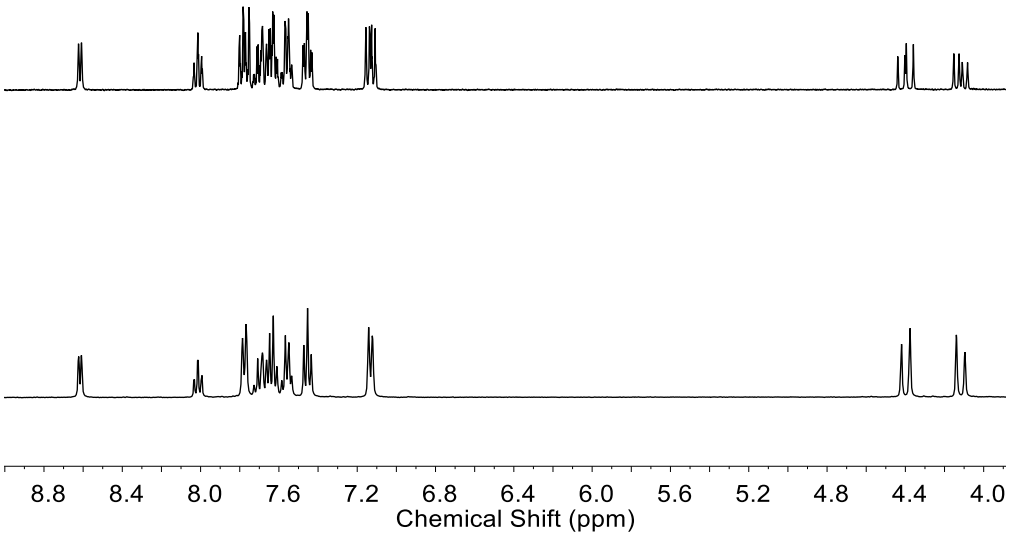

Figure A3. Stacked partial ^{1}H and $^{1}H\{^{31}P\}$ NMR spectrum (500 MHz, CD_3CN) of **1**.

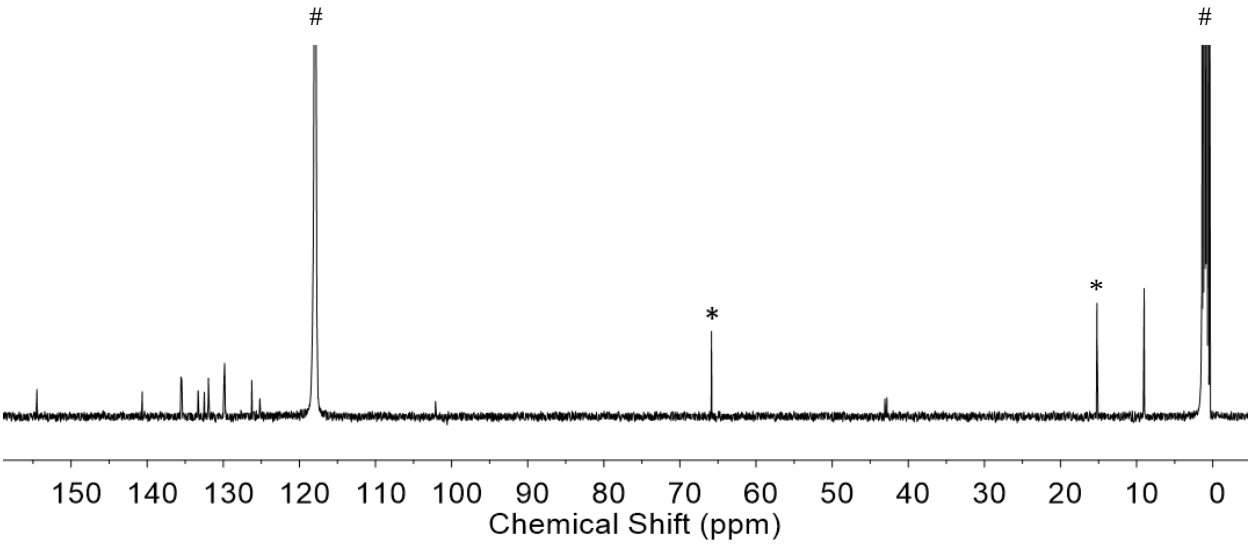

Figure A4. $^{13}C\{^{1}H\}$ NMR spectrum (126 MHz, CD_3CN) of **1**. The signal indicated by # is associated with acetonitrile solvent. The signal indicated by * is associated with diethyl ether solvent.

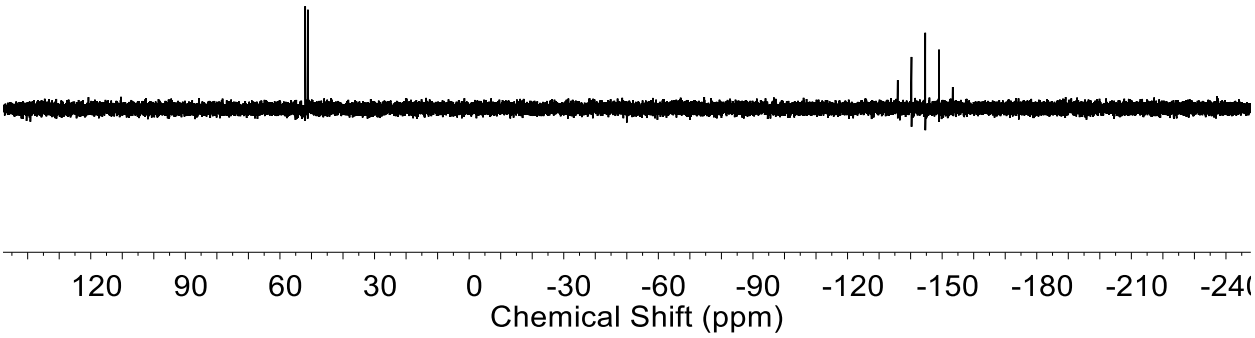

Figure A5. $^{31}P\{^{1}H\}$ NMR spectrum (162 MHz, CD_3CN) of **1**.

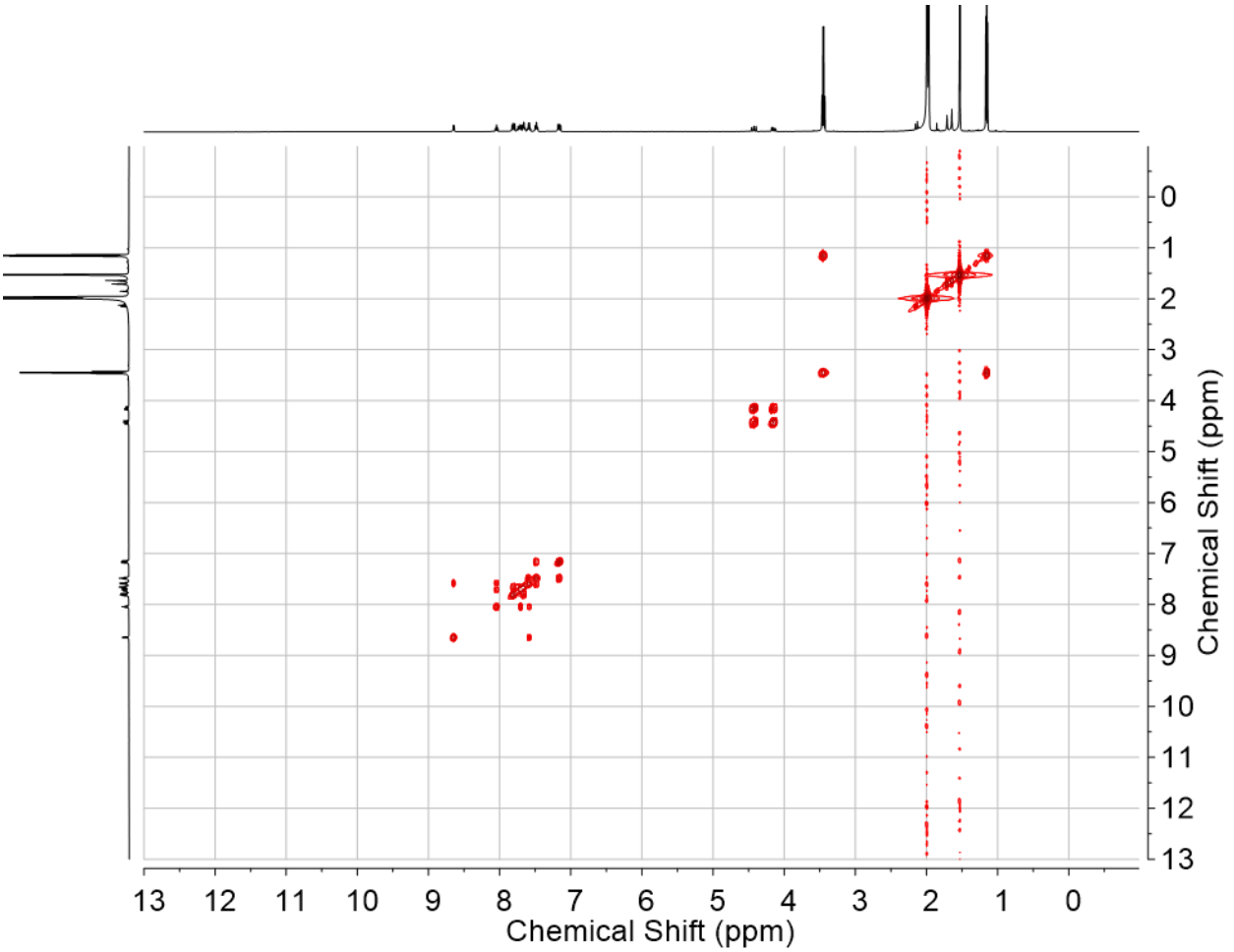

Figure A6. COSY NMR spectrum (162 MHz, CD_3CN) of **1**.

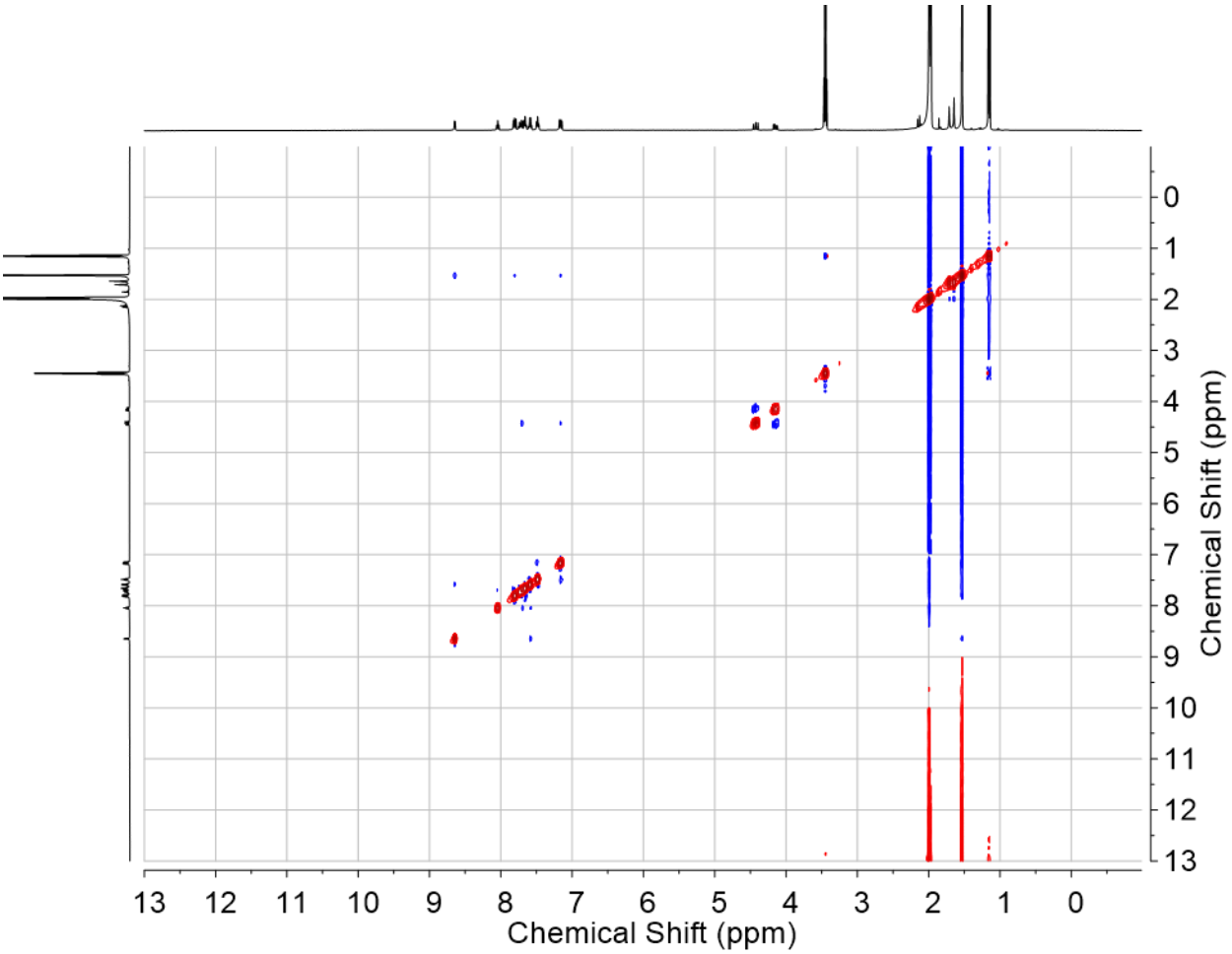

Figure A7. NOESY NMR spectrum (162 MHz, CD_3CN) of **1**.

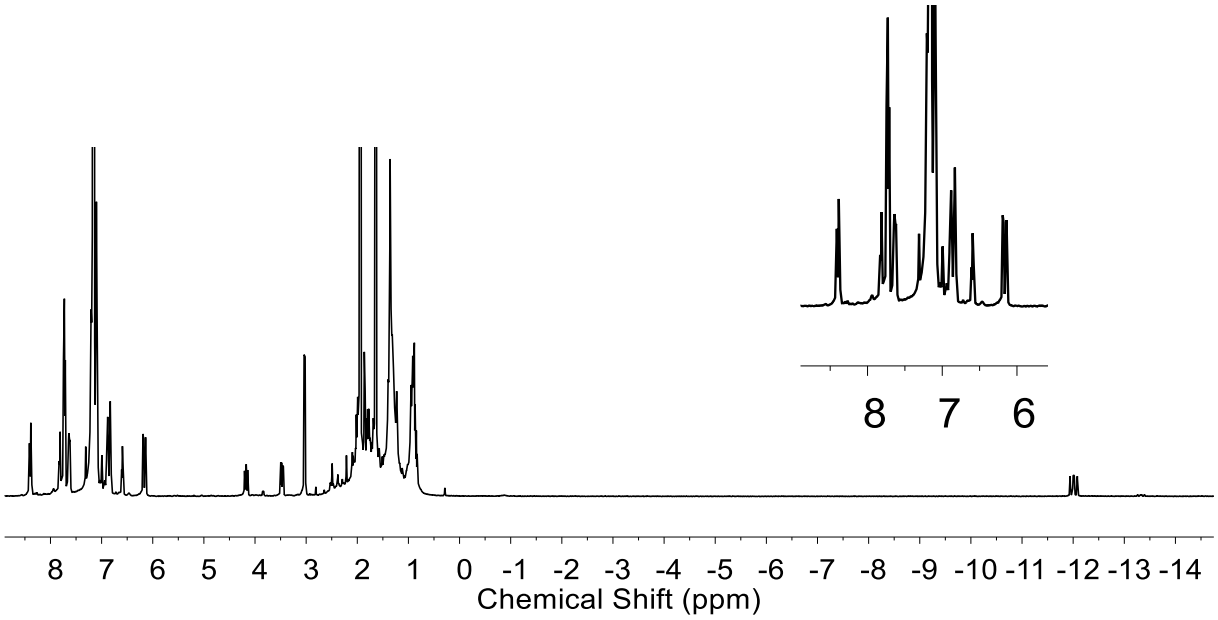

Figure A8. ^{1}H NMR spectrum (500 MHz, C_6D_6) of reduction of **1** with Na(Hg).

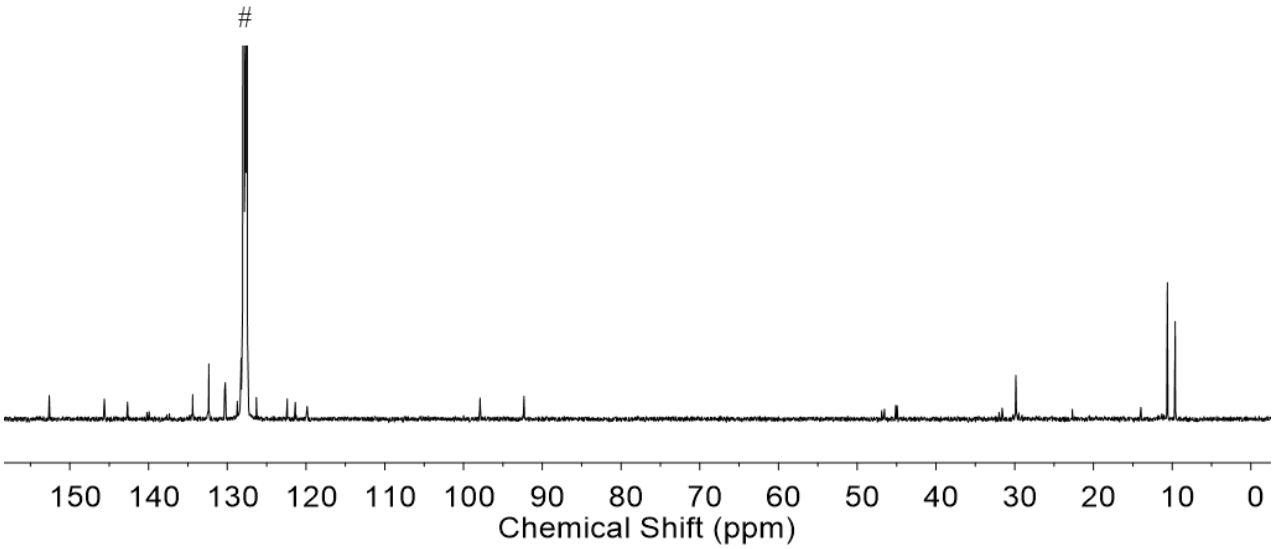

Figure A9. $^{13}C\{^{1}H\}$ NMR spectrum (126 MHz, C_6D_6) of reduction of **1** with Na(Hg). The signal indicated by # is associated with benzene solvent.

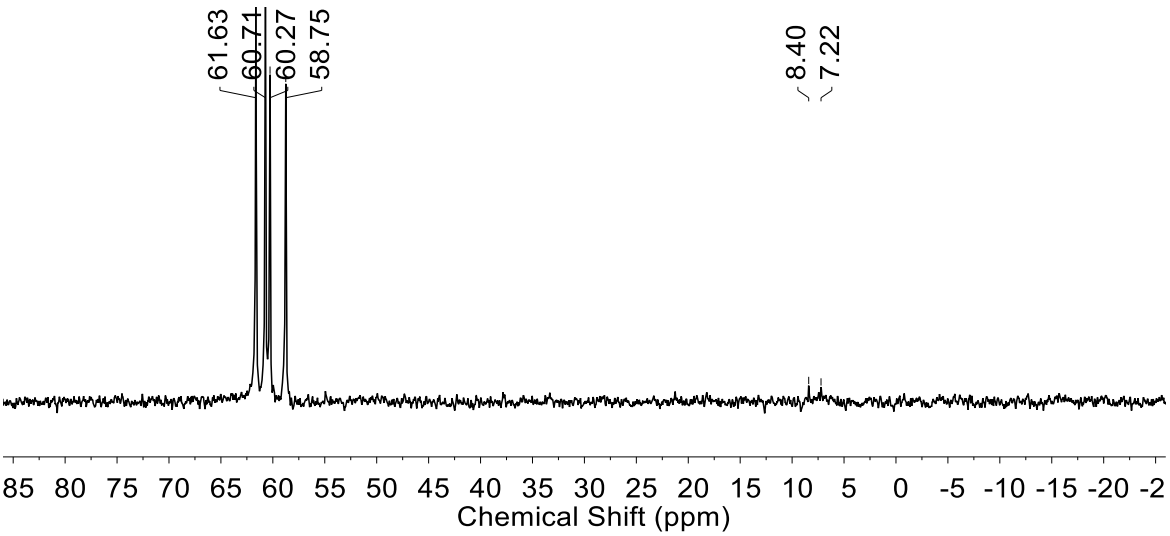

Figure A10. $^{31}P\{^{1}H\}$ NMR spectrum (162 MHz, C_6D_6) of reduction of **1** with Na(Hg).

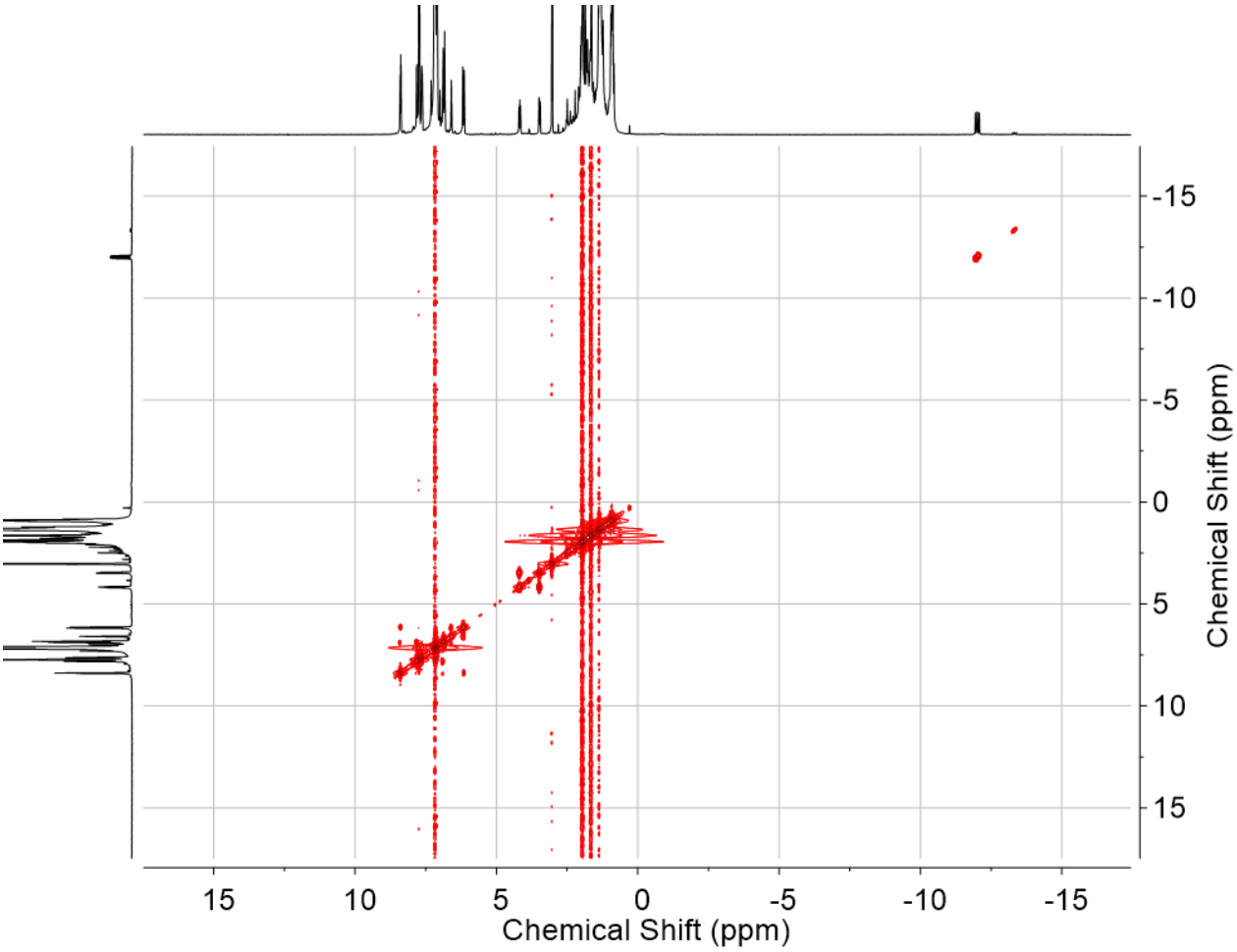

Figure A11. COSY NMR spectrum (162 MHz, CD_3CN) of reduction of **1** with Na(Hg).

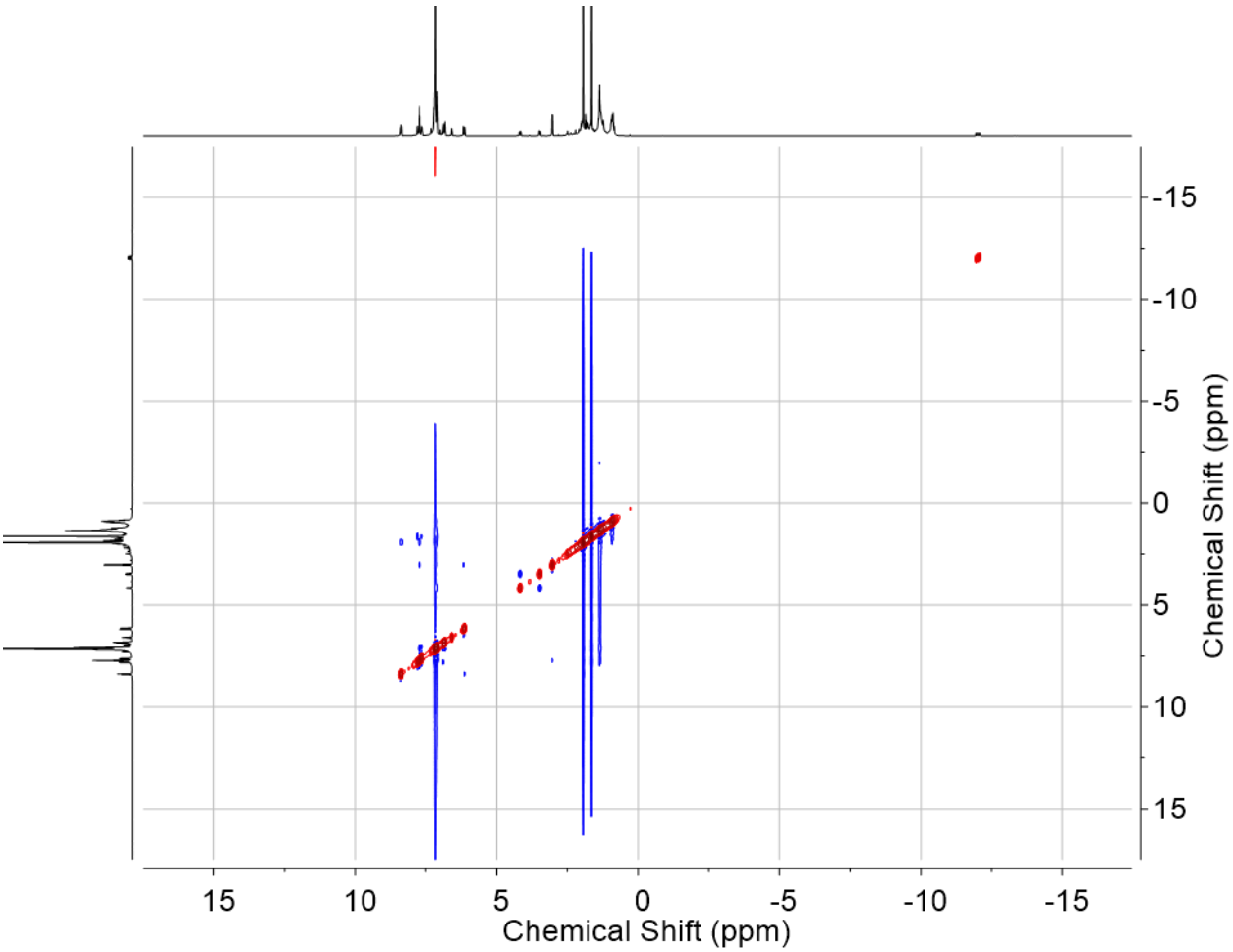

Figure A12. NOESY NMR spectrum (162 MHz, CD_3CN) of reduction of **1** with Na(Hg).

Electrochemistry

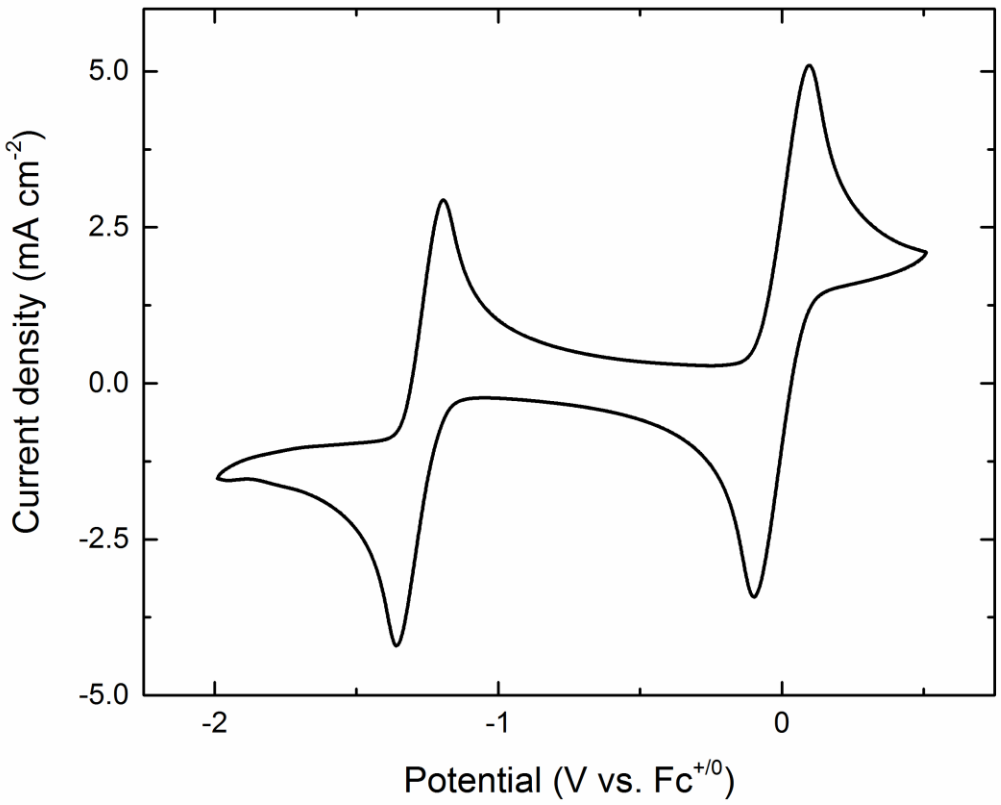

Figure A13. Cyclic voltammetry of **1** with a 1:2 ratio of ferrocene (CH_3CN, 0.1 M [$^nBu_4N$][PF_6], 100 mV/s)

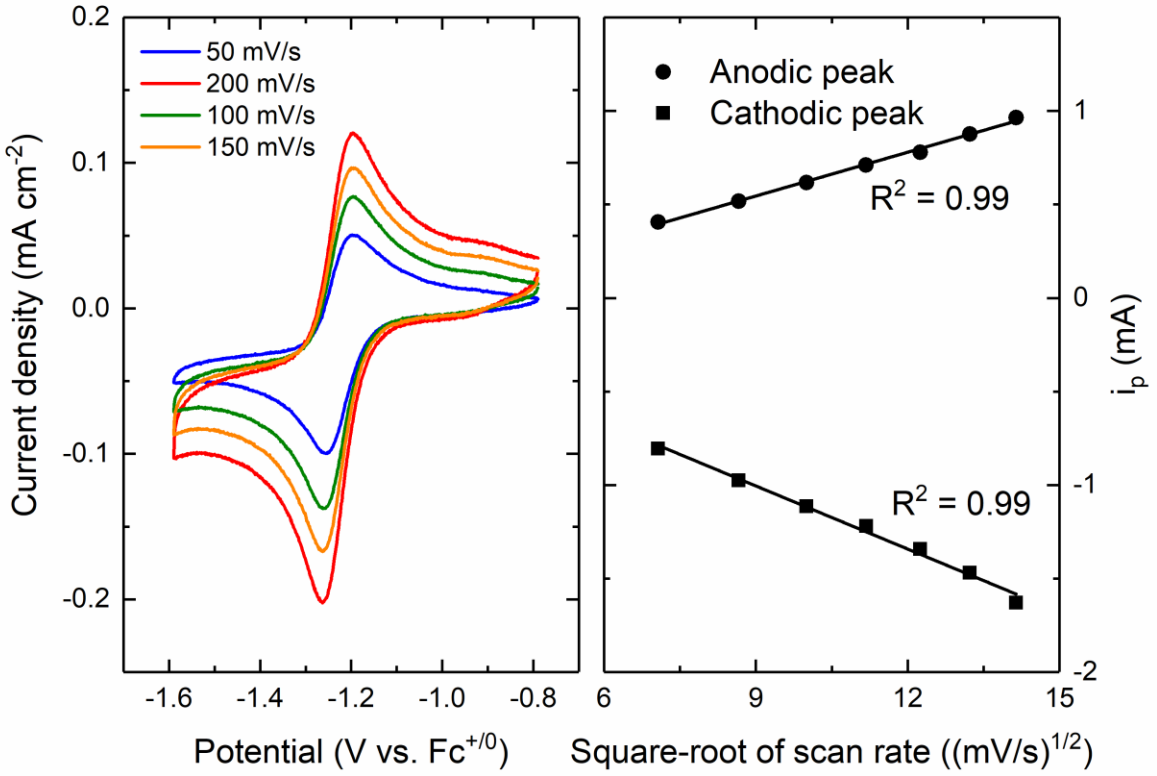

Figure A14. Cyclic voltammetry of first reduction event **1** at varying scan rate in CH_3CN (0.1 M [^{n}Bu$_4$N][PF_6]) (Left). Linear dependence of peak cathodic current on square root of scan rate with the y-intercept set to 0 (Right).

X-ray crystallography

Table A1. Crystal and Refinement Data for $[Cp^*Rh(PN)Cl]PF_6$

CCDC number	**1973828**
Empirical formula	$C_{56}H_{62}Cl_2F_{12}N_2P_4Rh_2$
Formula weight	1391.67
Temperature	225.15
Wavelength	0.71073
Crystal system	triclinic
Space group	P-1
a	8.886(9) Å
b	11.159(10) Å
c	14.851(15) Å
a	93.21(3)
β	96.03(2)
γ	93.050(18)
Volume	1459(2) $Å^3$
Z	1
Density (calculated)	1.583 g/cm^3
Absorption coefficient	0.844 mm^{-1}
F(000)	704.0
Crystal size	0.5 × 0.33 × 0.11 mm^3
Theta range	3.662 to 63.316
Index ranges	$-12 \leq h \leq 13$, $-16 \leq k \leq 16$, $-21 \leq l \leq 21$
Reflections collected	19133
Independent reflections	9484 [R_{int} = 0.0330, R_{sigma} = 0.0505]
Absorption correction	Multi-scan
Max. and min. transmission	0.7533 0.5664
Refinement method	Full-matrix least-squares on F^2
Data / restraints / parameters	9484/0/357
Goodness-of-fit on F^2	1.047
Final R indices [I>2σ(I)]	R_1 = 0.0399, wR_2 = 0.0866
R indices (all data)	R_1 = 0.0539, wR_2 = 0.0959
Largest diff. peak and hole	1.10 and -0.89 $e^-/Å^3$

[a] $R1 = \Sigma||F_o|-|F_c|| / \Sigma|F_o|$ [b] $wR2 = [\ \Sigma\ [w(F_o^2-F_c^2)^2] / \Sigma\ [w(F_o^2)^2]\ ]^{1/2}$

Table A2. Selected Bond Lengths for **1.**

Bond	**1** (Å)
Rh–Cl	2.416(2)
Rh–P	2.2730(18)
Rh–N	2.119(3)
Rh–Cp*$_{cent}$	1.832

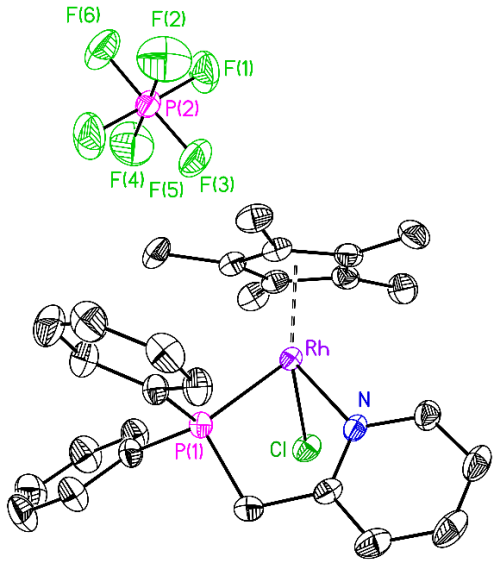

Figure A15. Full solid-state structure of **1**. Hydrogen atoms and associated solvent molecule omitted for clarity. Displacement ellipsoids shown at the 50% probability level.

Appendix B

Supplementary Information for Chapter 4

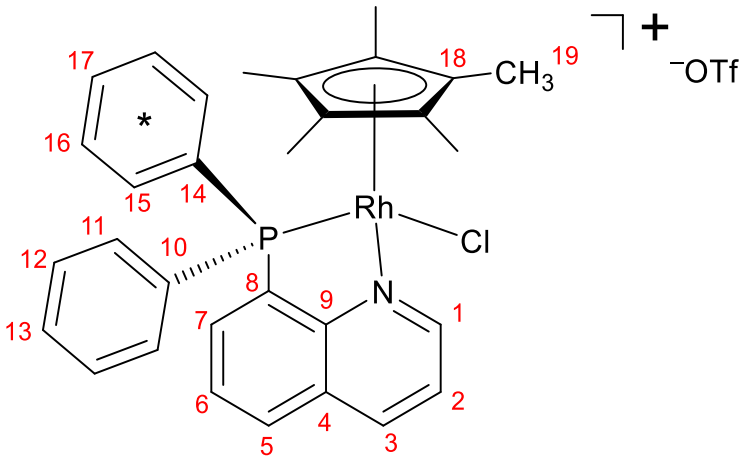

Figure B1. Numbering scheme for assignment of NMR data for complex **1-Cl** (* in ring denotes phenyl group closest to Cp* ring).

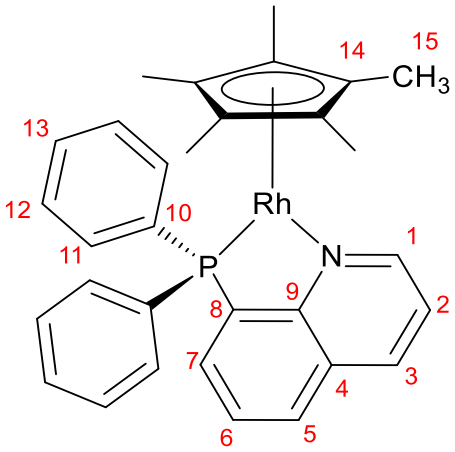

Figure B2. Numbering scheme for assignment of NMR data for complex **2**.

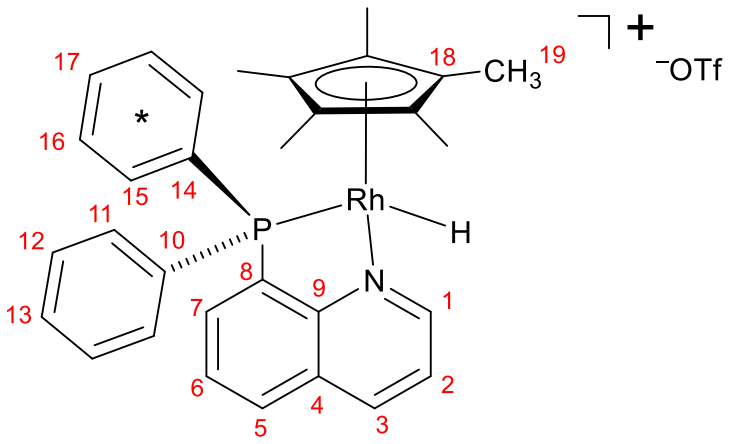

Figure B3. Numbering scheme for assignment of NMR data for complex **3** (* in ring denotes phenyl group closest to Cp* ring).

NMR Spectra

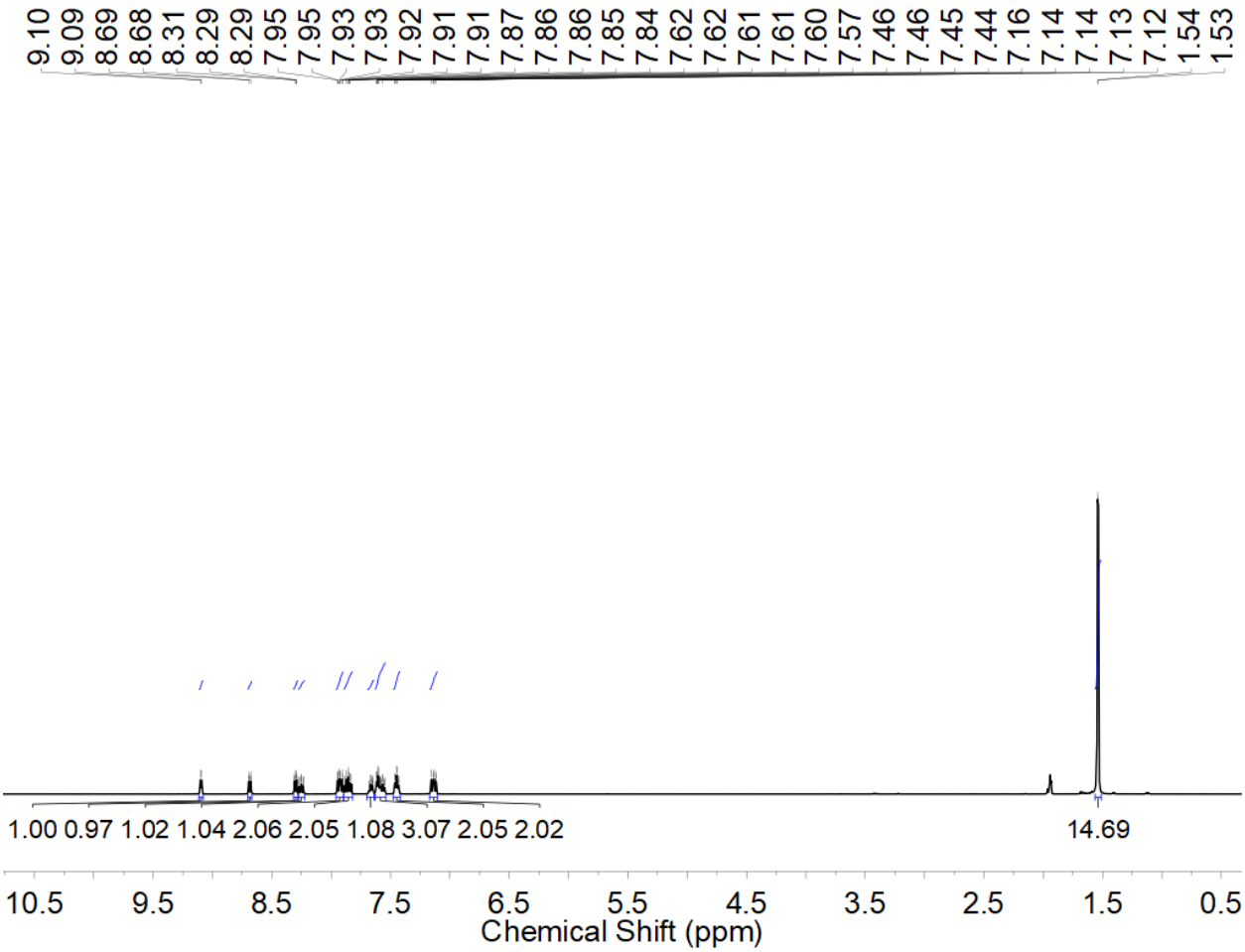

v

Figure B4. ^{1}H NMR spectrum (500 MHz, CD_3CN) of **1-Cl**.

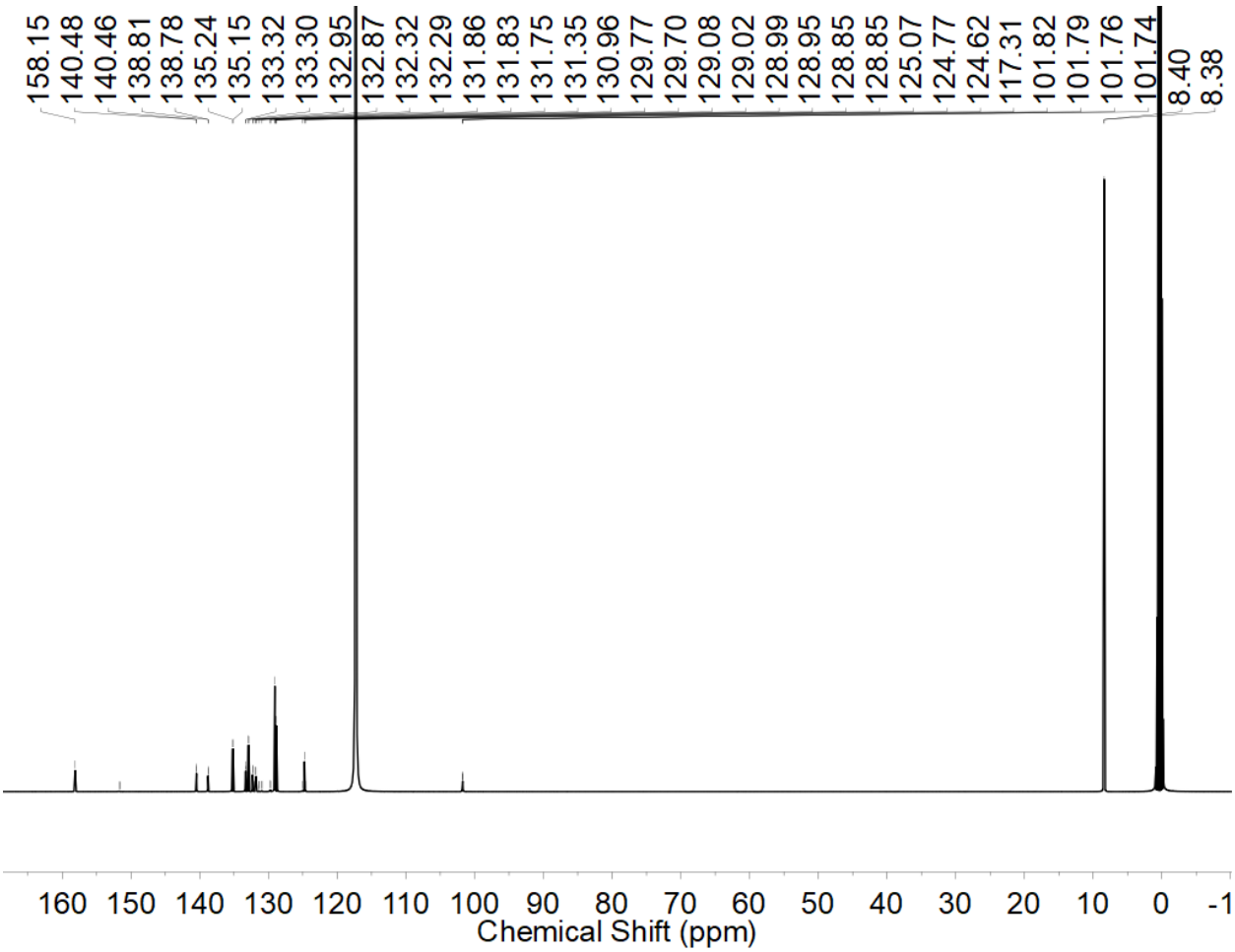

Figure B5. $^{13}C\{^{1}H\}$ NMR spectrum (126 MHz, CD_3CN) of **1-Cl**.

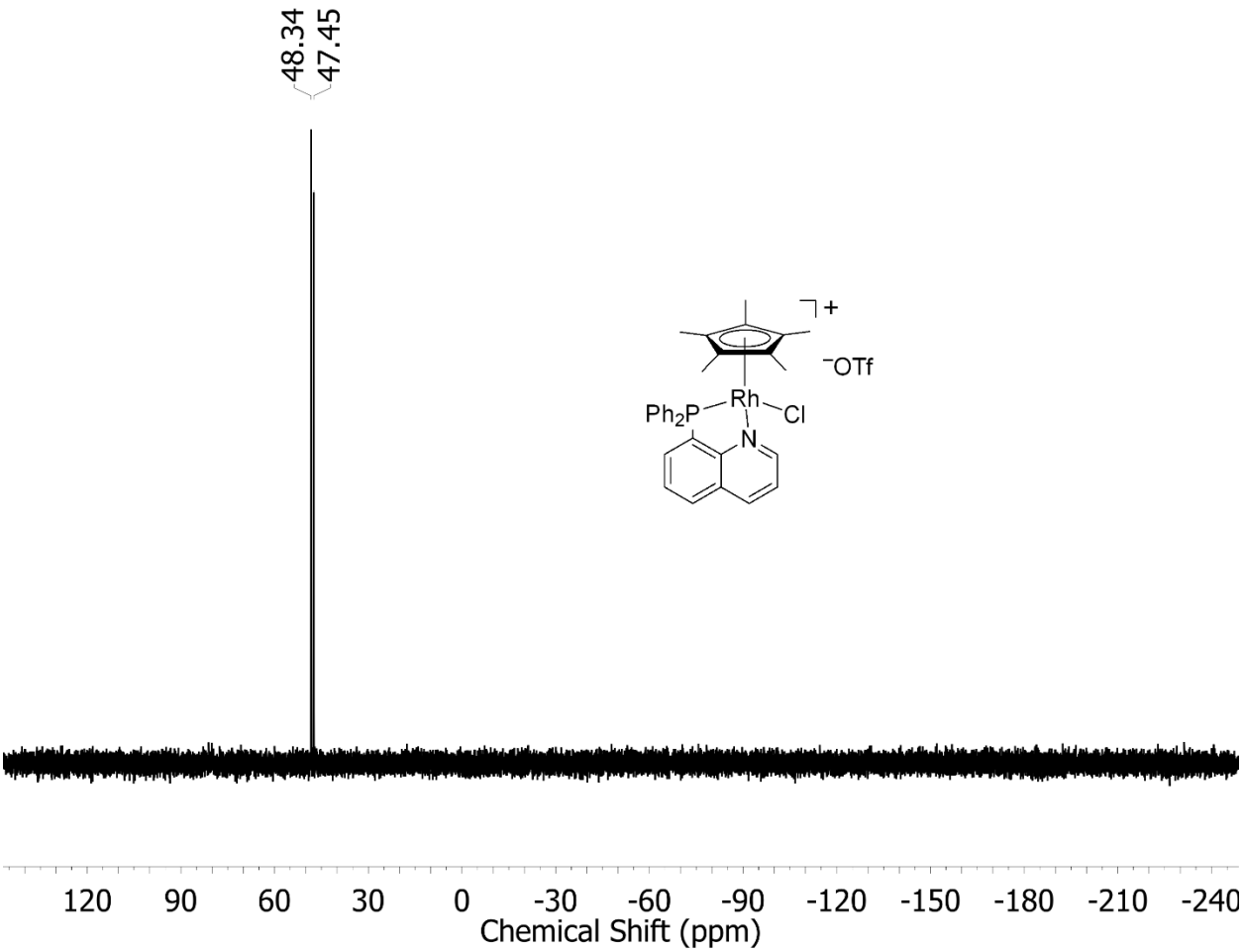

Figure B6. $^{31}P\{^{1}H\}$ NMR spectrum (162 MHz, CD_3CN) of **1-Cl**.

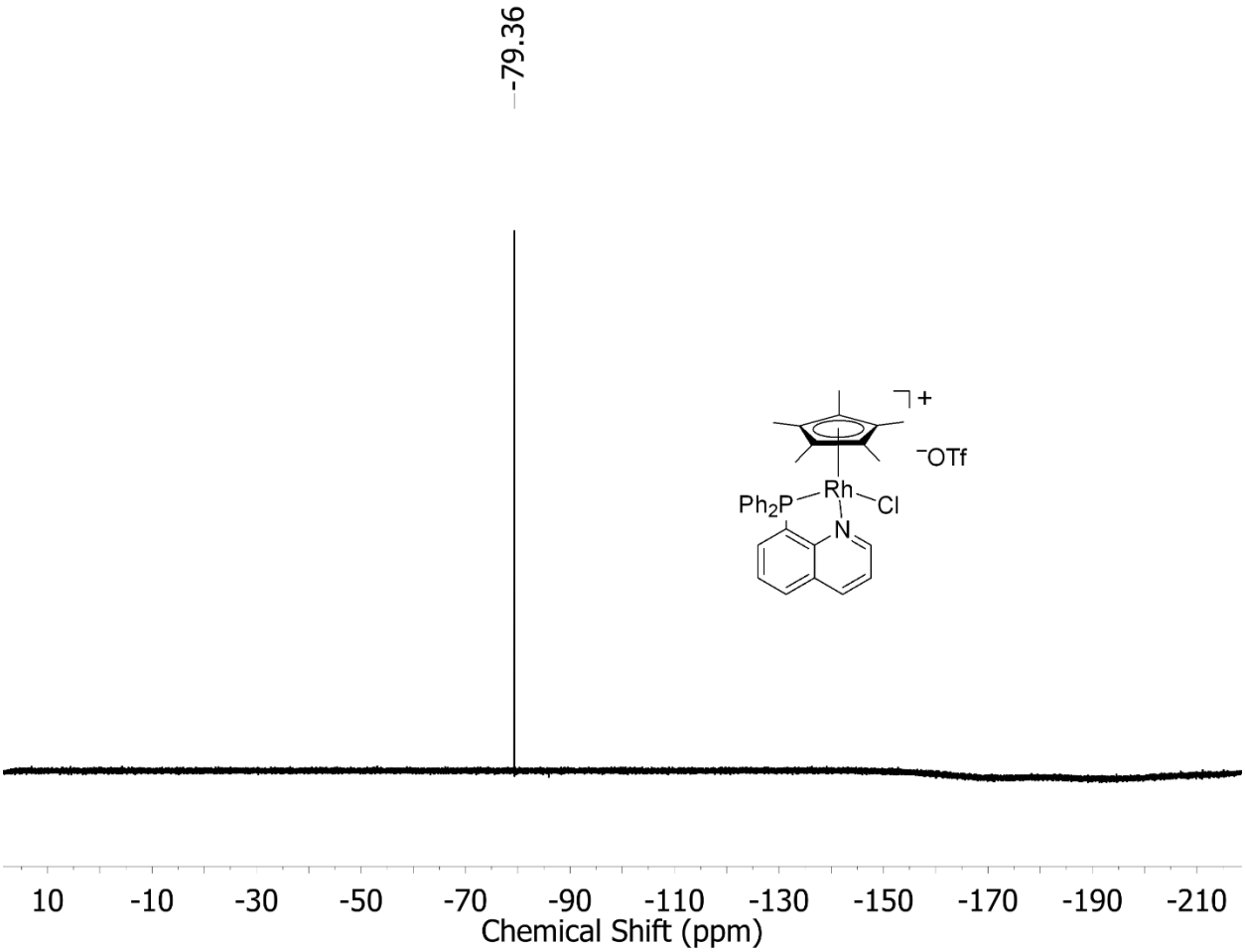

Figure B7. ^{19}F NMR spectrum (376 MHz, CD_3CN) of **1-Cl**.

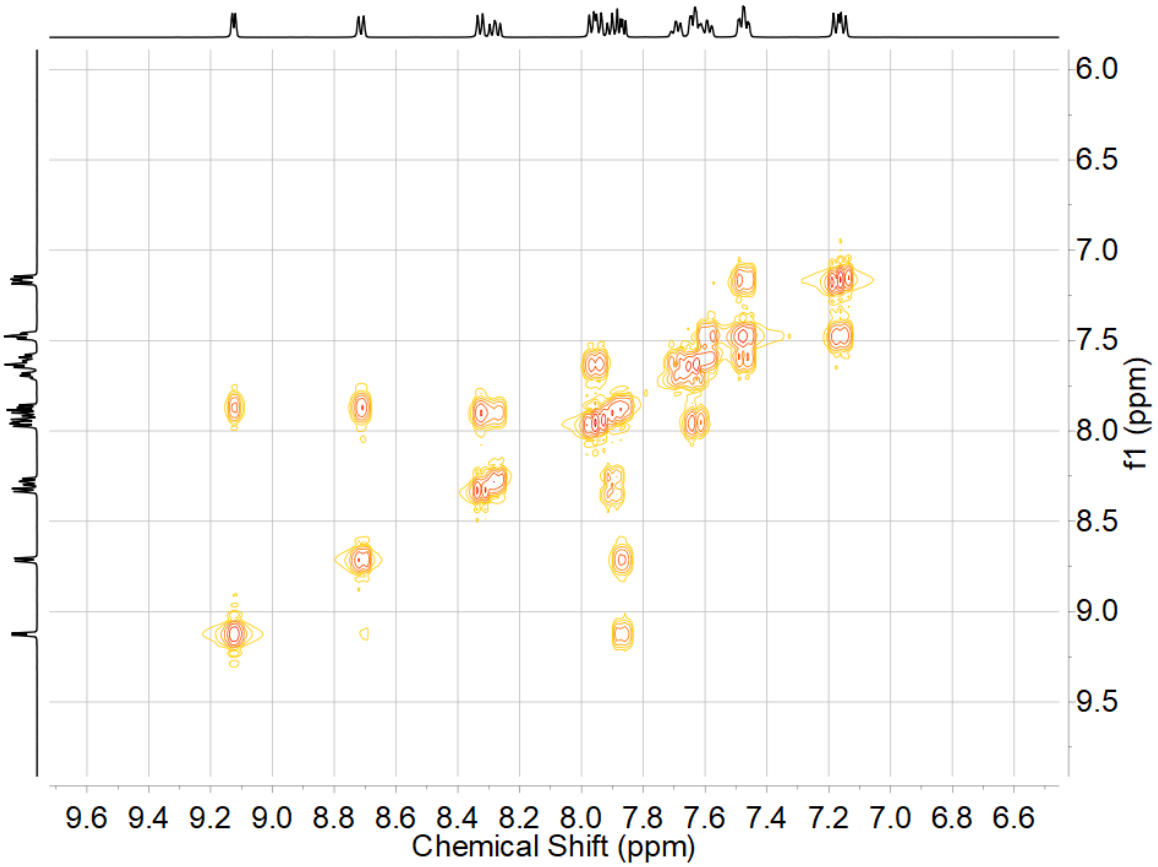

Figure B8. COSY NMR spectrum (CD_3CN) of **1-Cl**.

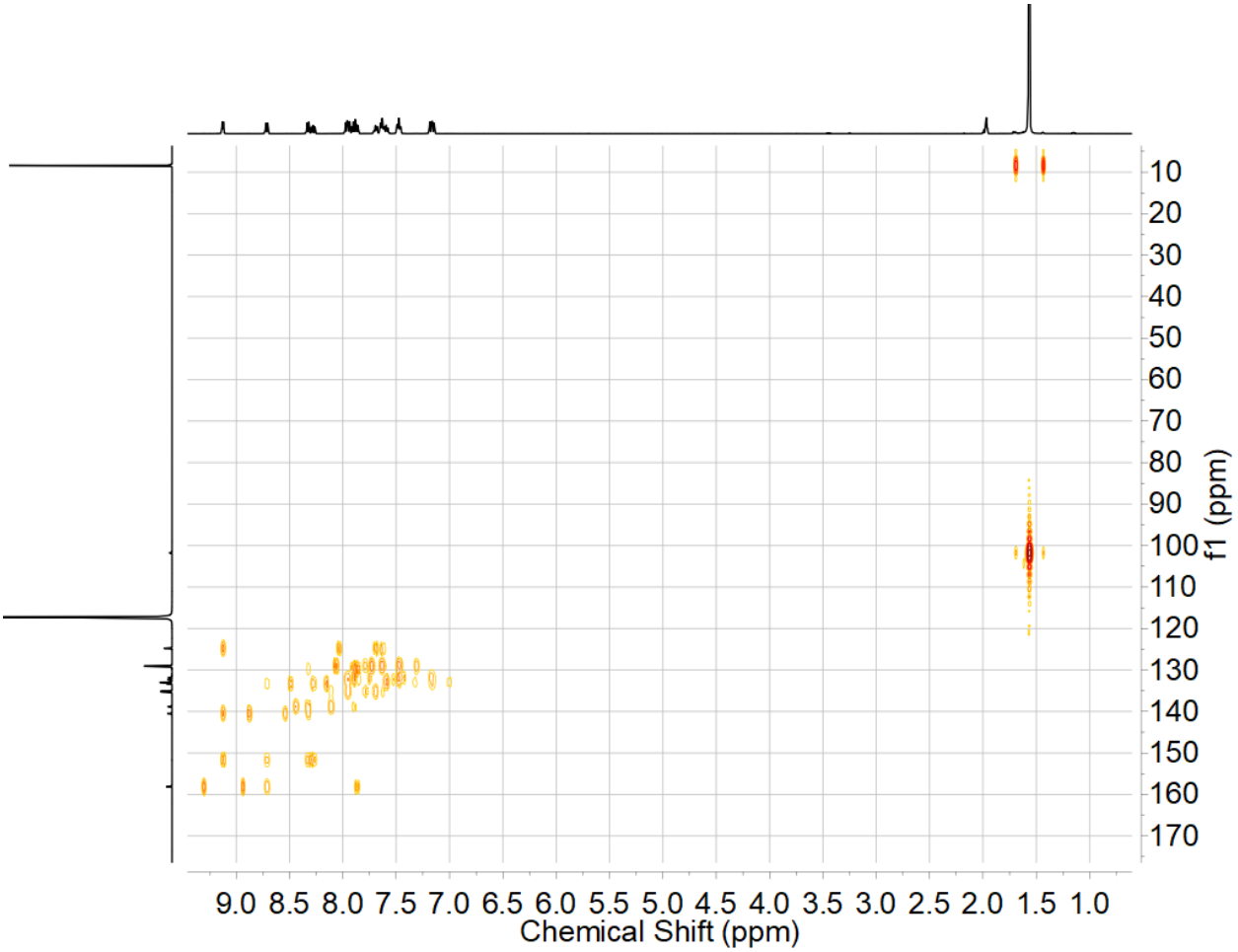

Figure B9. HMBC NMR spectrum (CD_3CN) of **1-Cl**.

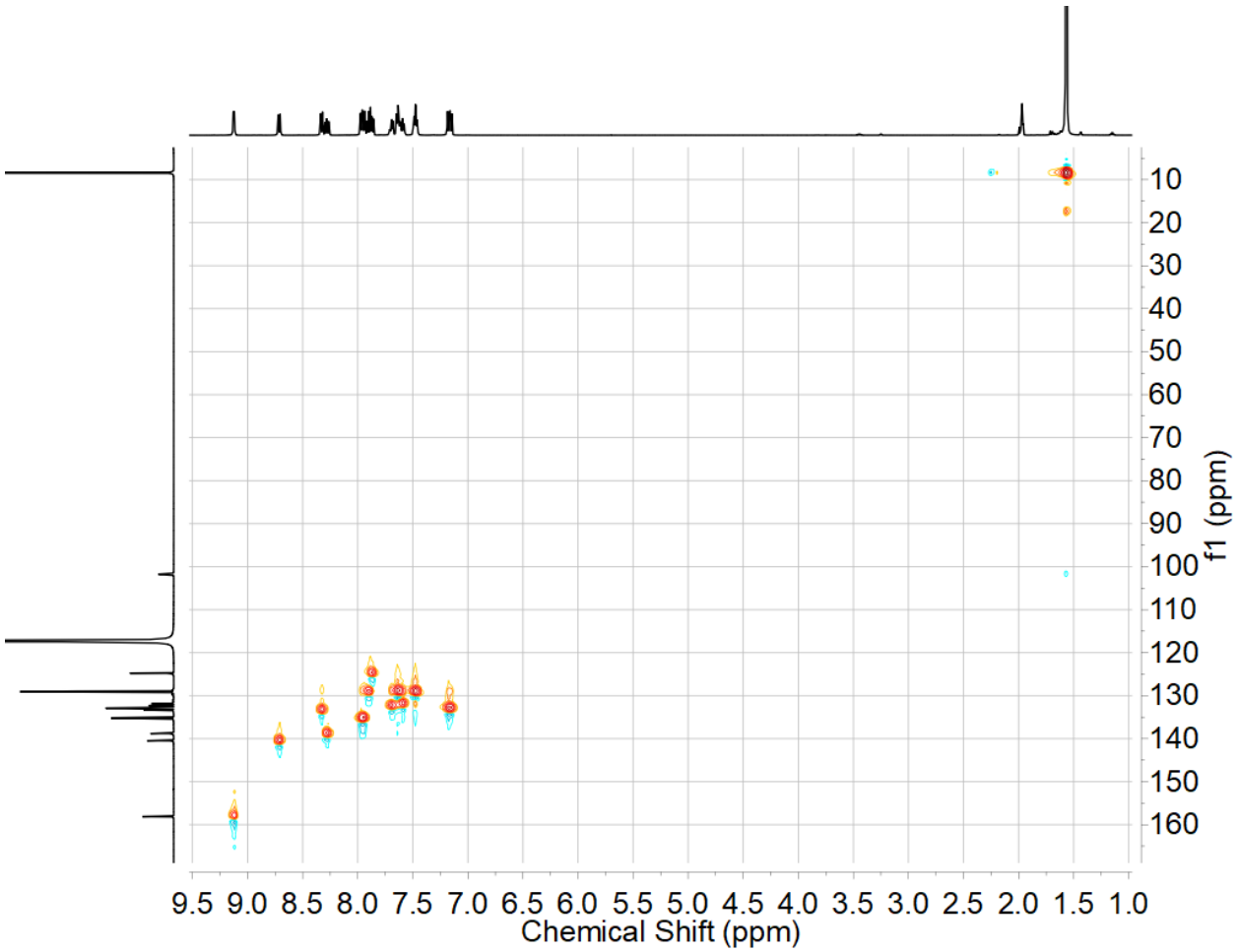

Figure B10. HSQC NMR spectrum (CD_3CN) of **1-Cl**.

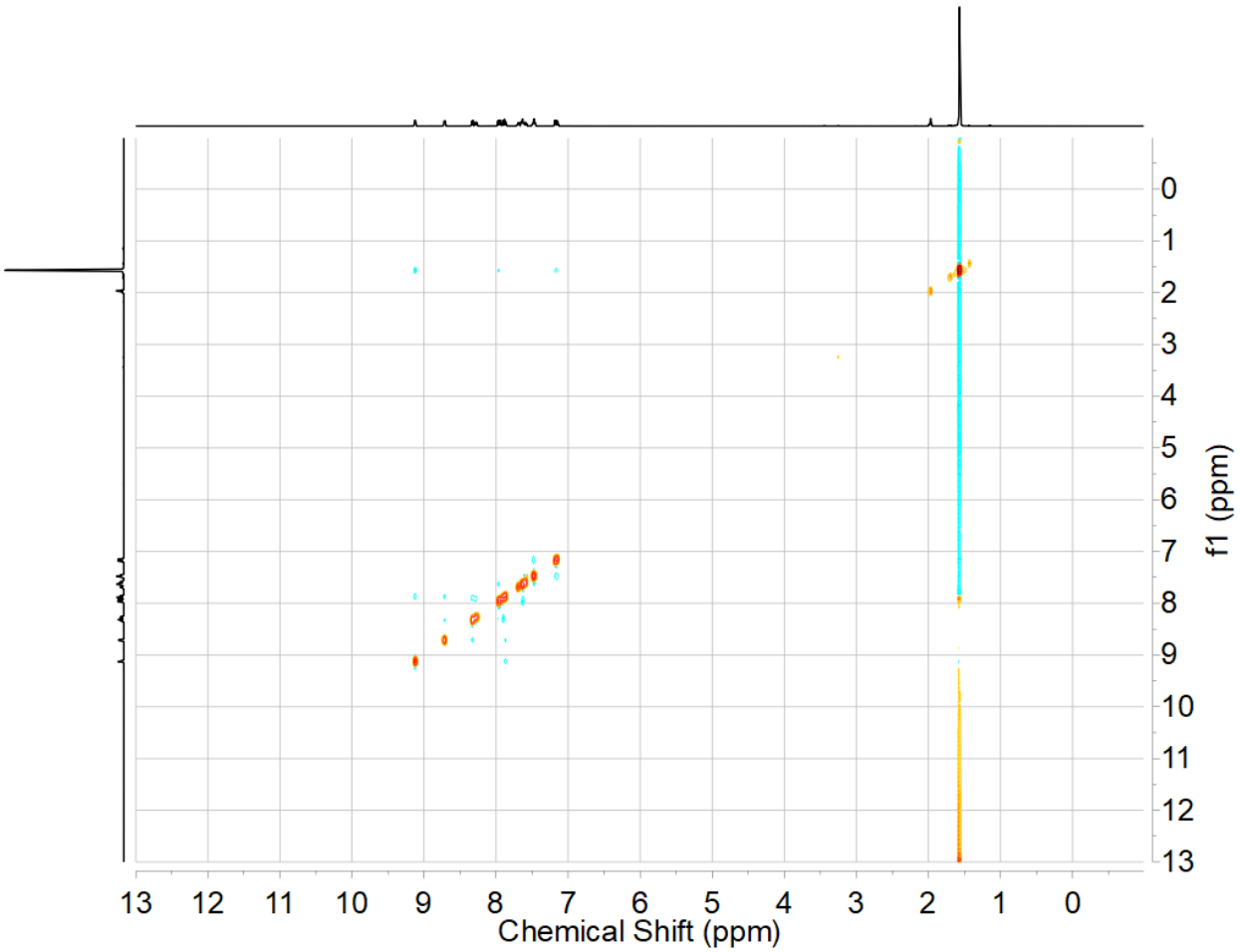

Figure B11. NOESY NMR spectrum (CD_3CN) of **1-Cl**.

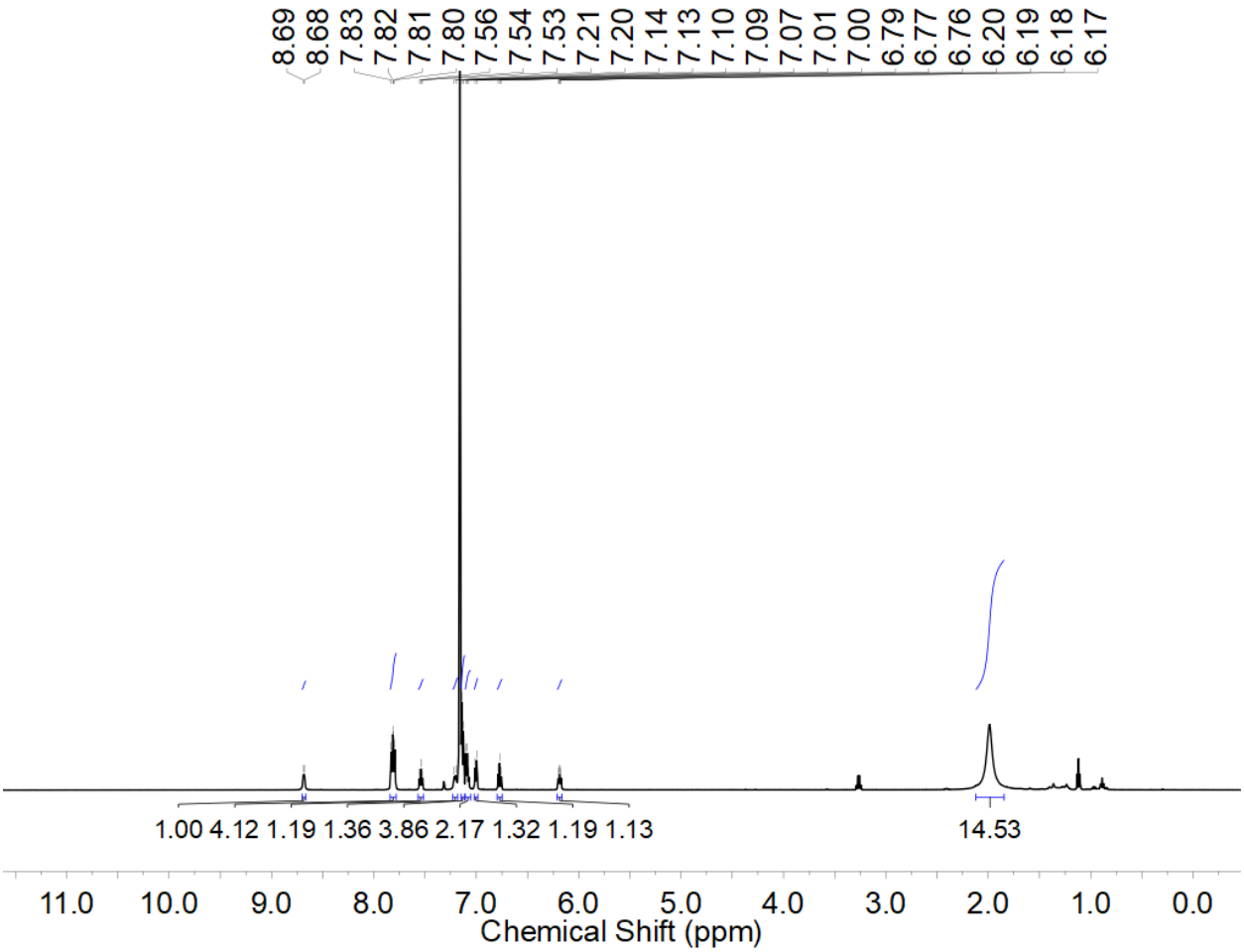

Figure B12. ^{1}H NMR spectrum (500 MHz, C_6D_6) of **2**.

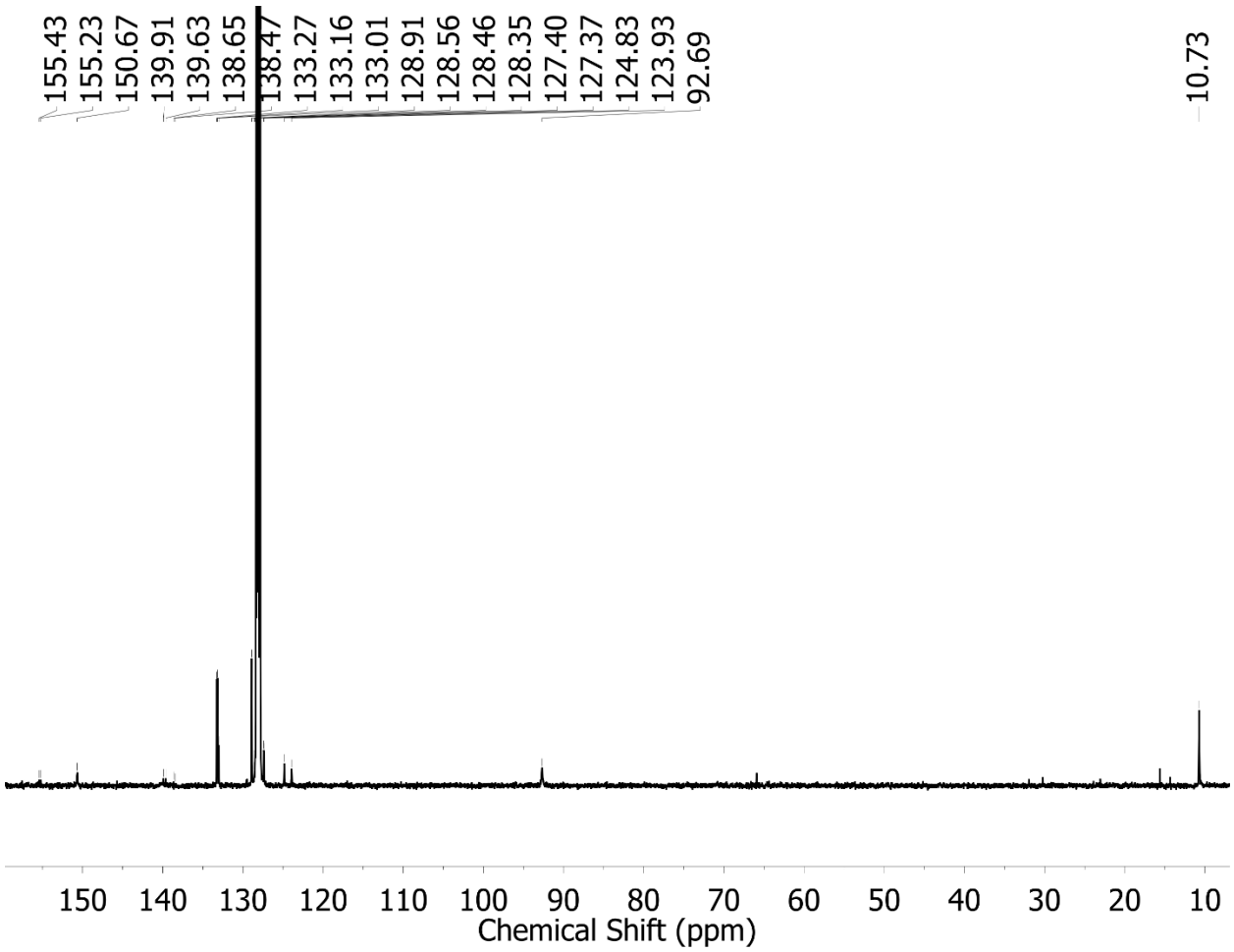

Figure B13. $^{13}C\{^{1}H\}$ NMR spectrum (126 MHz, C_6D_6) of **2**.

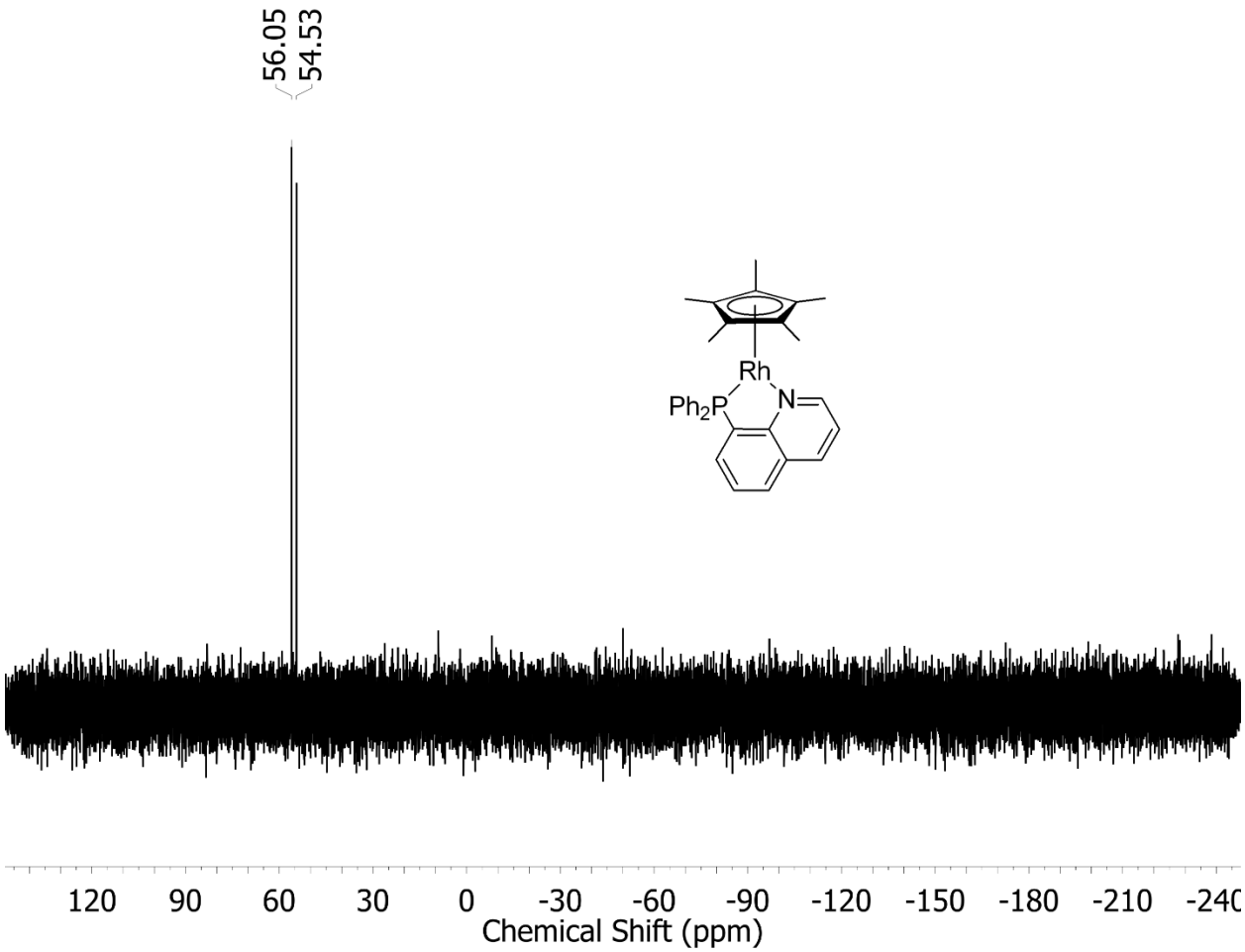

Figure B14. $^{31}P\{^{1}H\}$ NMR spectrum (162 MHz, C_6D_6) of **2**.

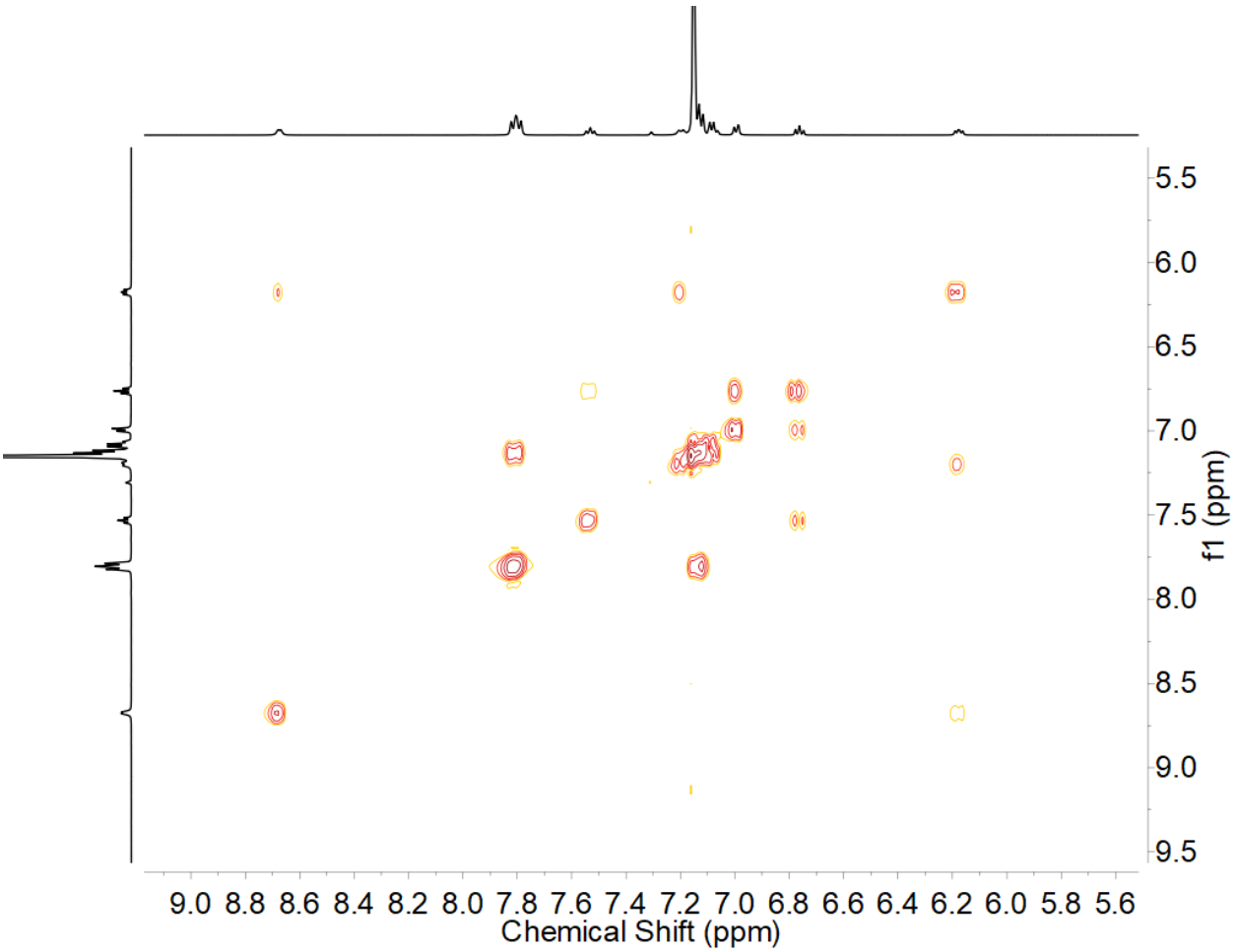

Figure B15. COSY NMR spectrum (C_6D_6) of **2**.

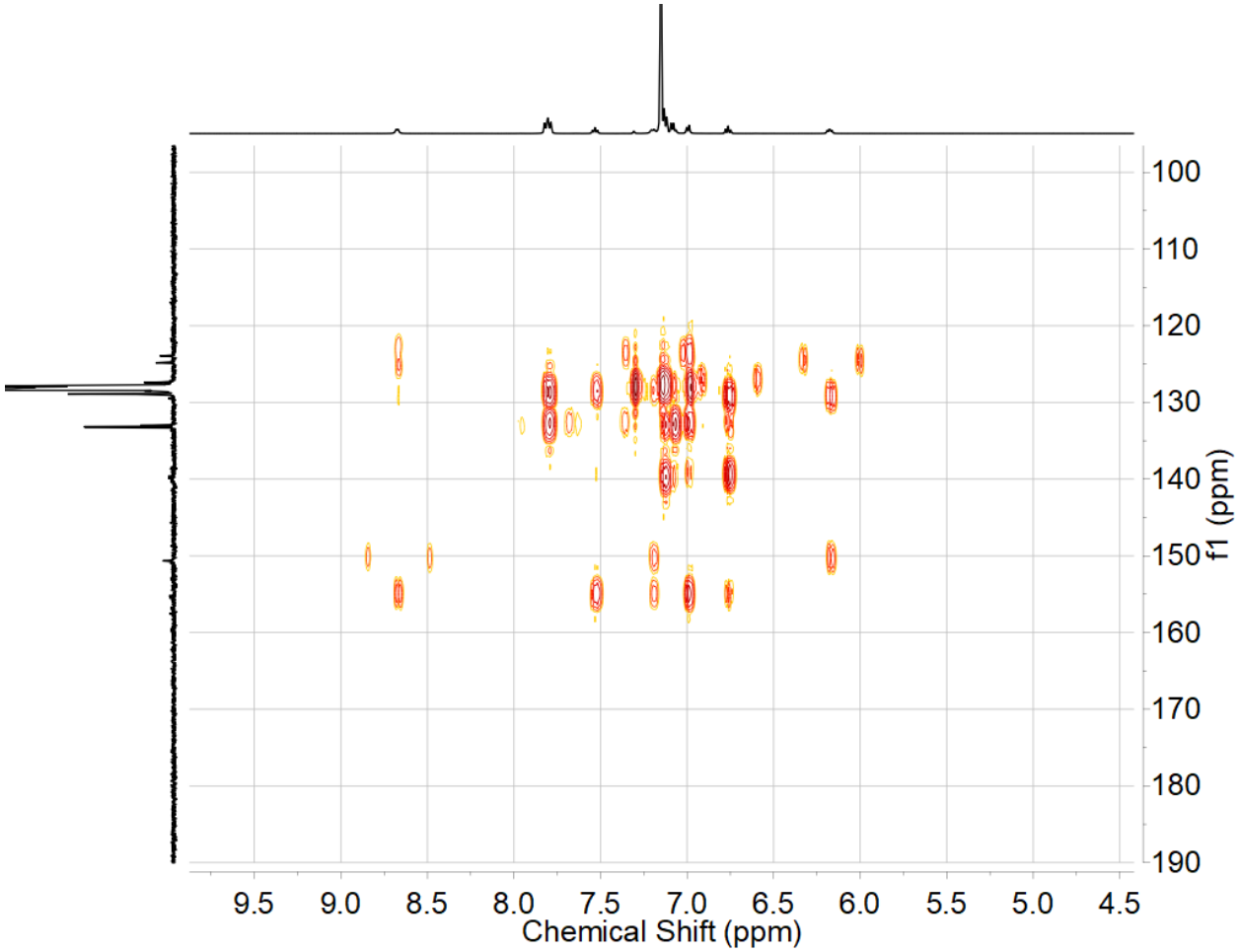

Figure B16. HMBC NMR spectrum (C_6D_6) of **2**.

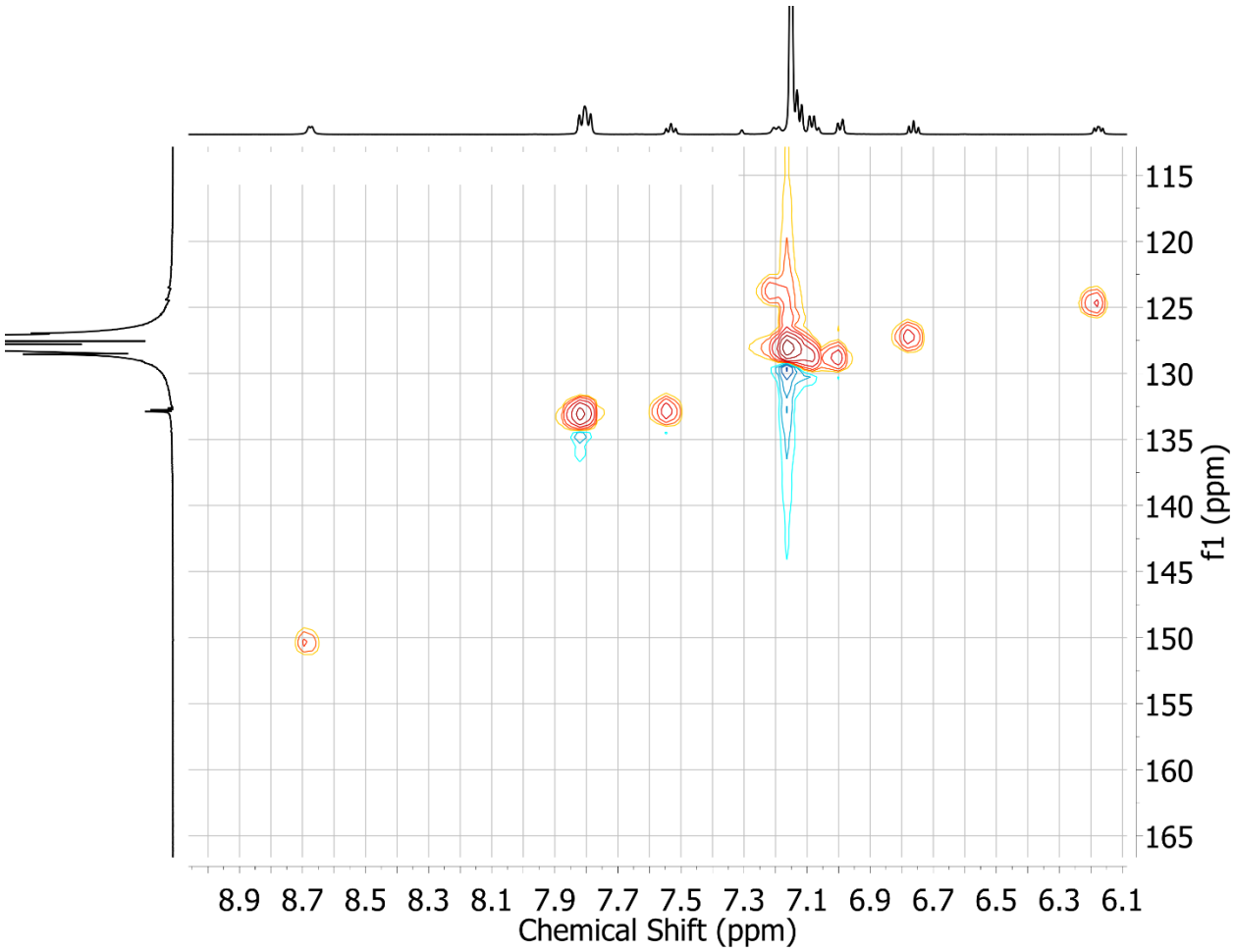

Figure B17. HSQC NMR spectrum (C_6D_6) of **2**.

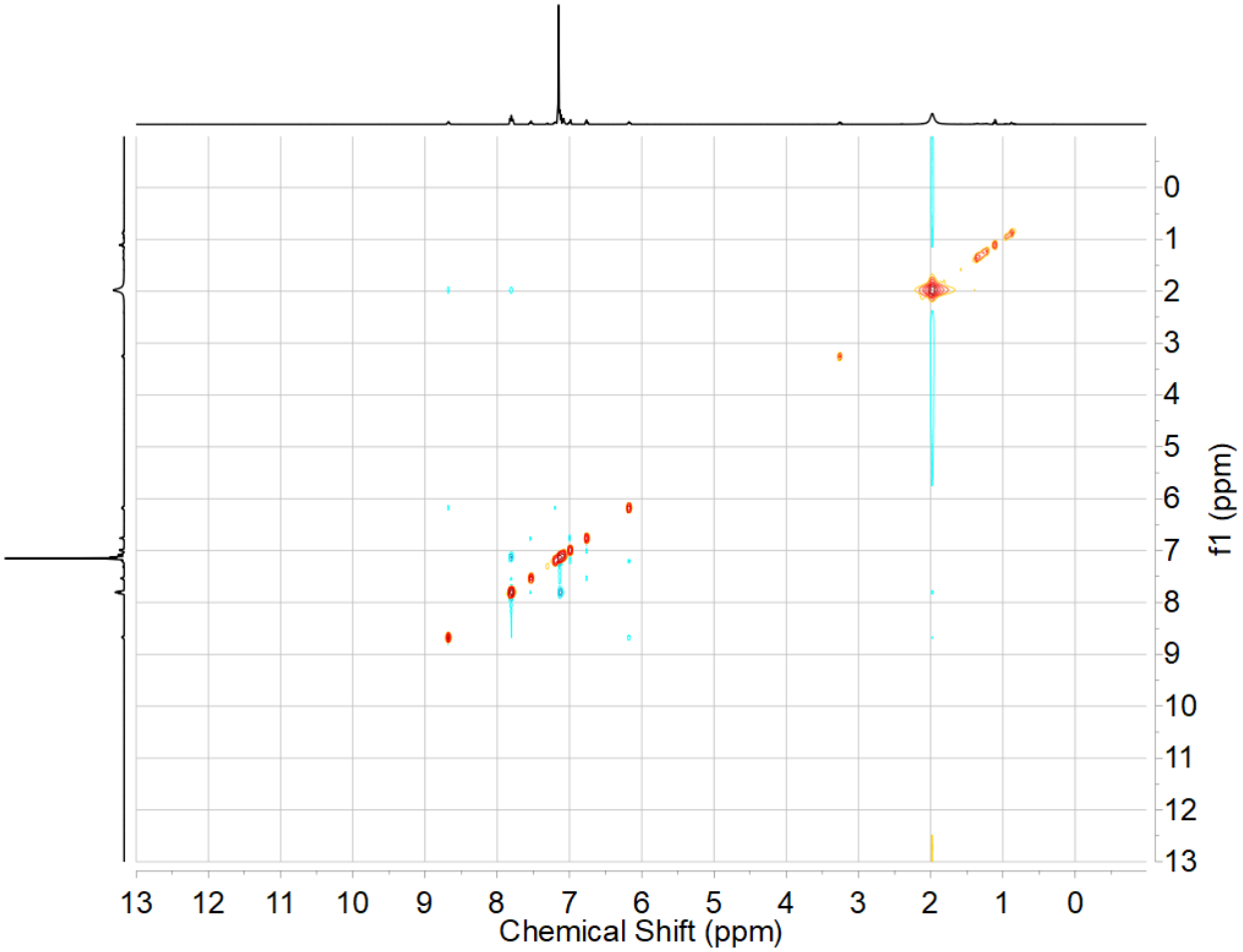

Figure B18. NOESY NMR spectrum (C_6D_6) of **2**.

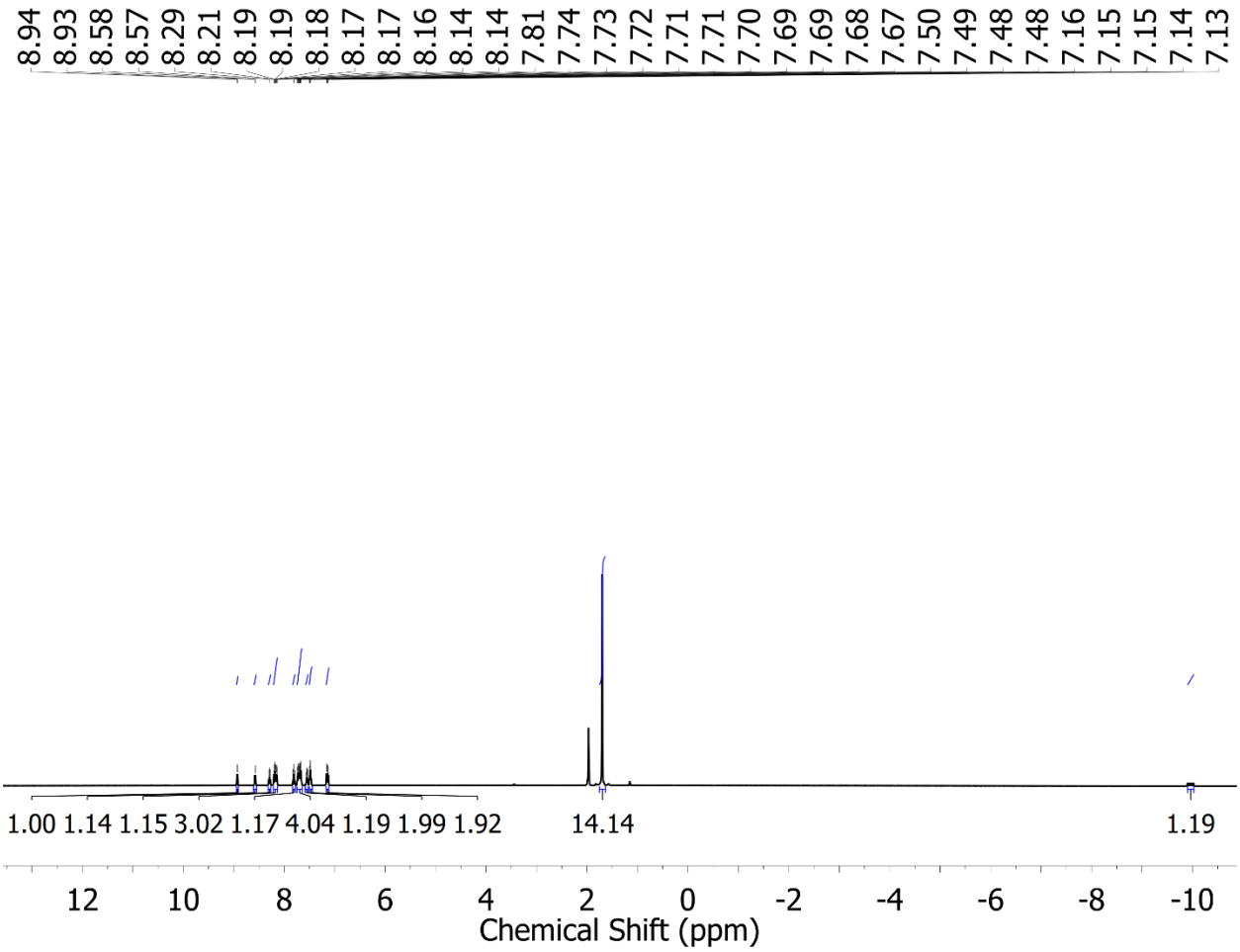

Figure B19. ^{1}H NMR spectrum (400 MHz, CD_3CN) of **3**.

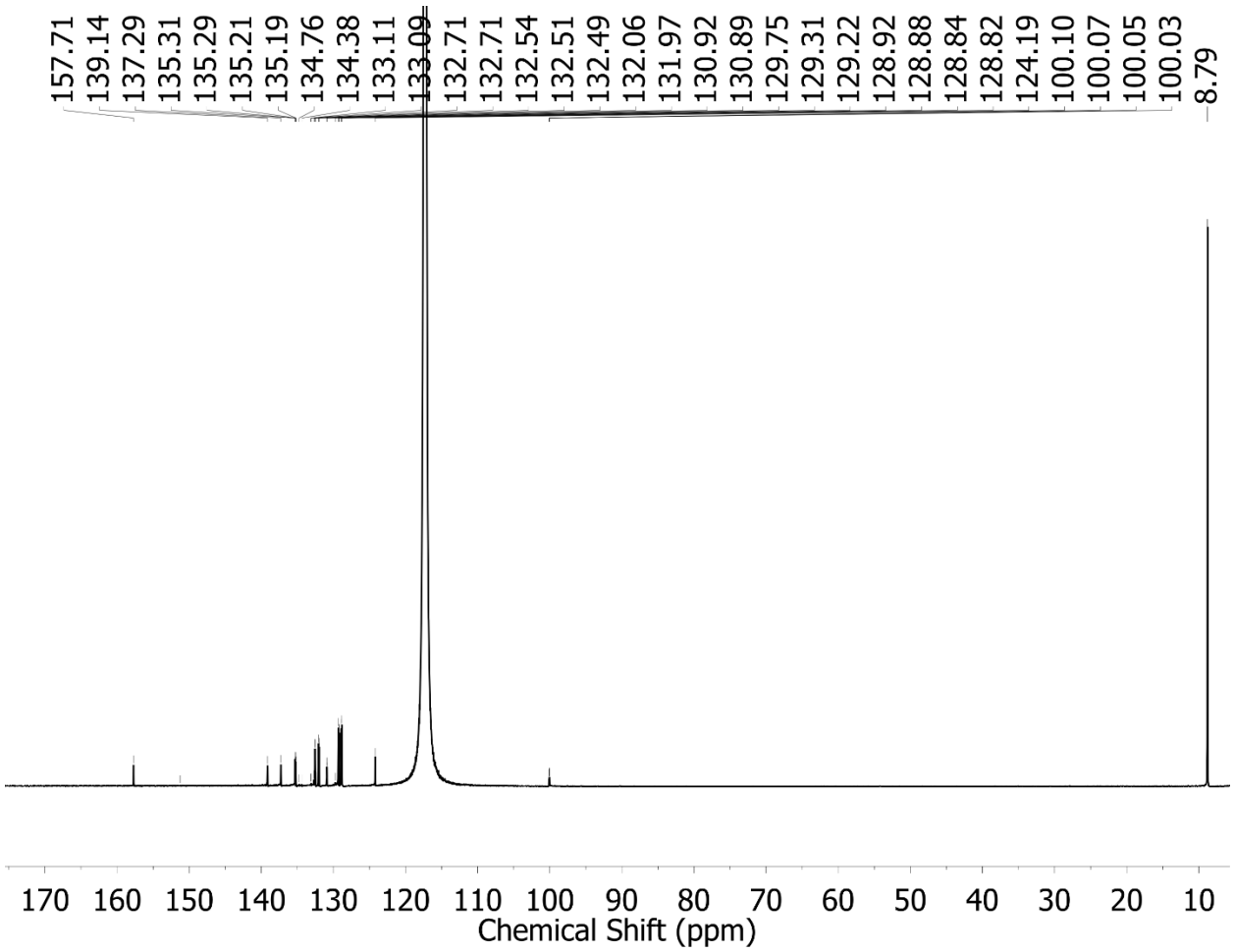

Figure B20. $^{13}C\{^{1}H\}$ NMR spectrum (126 MHz, CD_3CN) of **3**.

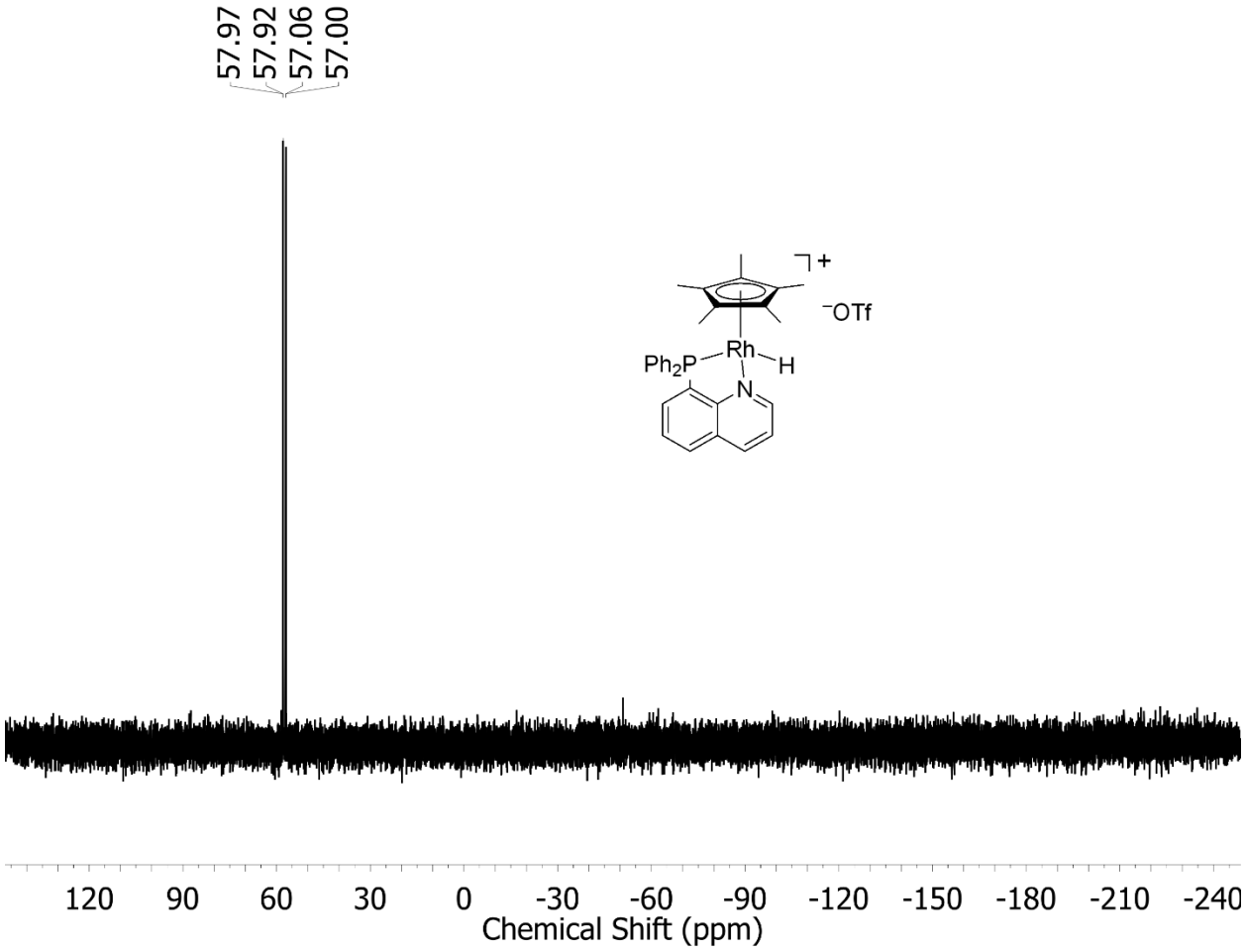

Figure B21. $^{31}P\{^{1}H\}$ NMR spectrum (162 MHz, CD_3CN) of **3**.

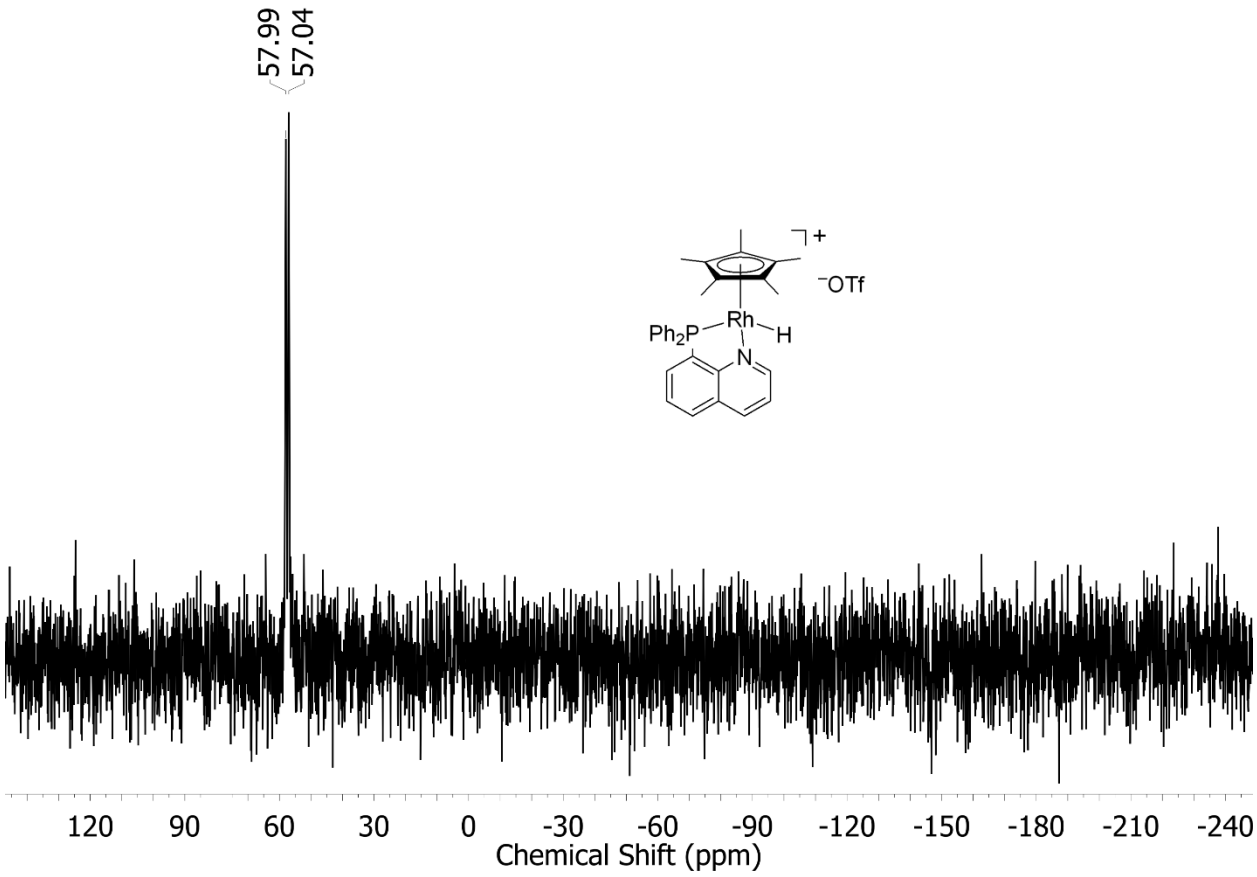

Figure B22. ^{31}P NMR spectrum (162 MHz, CD_3CN) of **3**. $^{2}J_{P,H}$ is not observed, while $^{1}J_{P,Rh}$ of 158 Hz is observed.

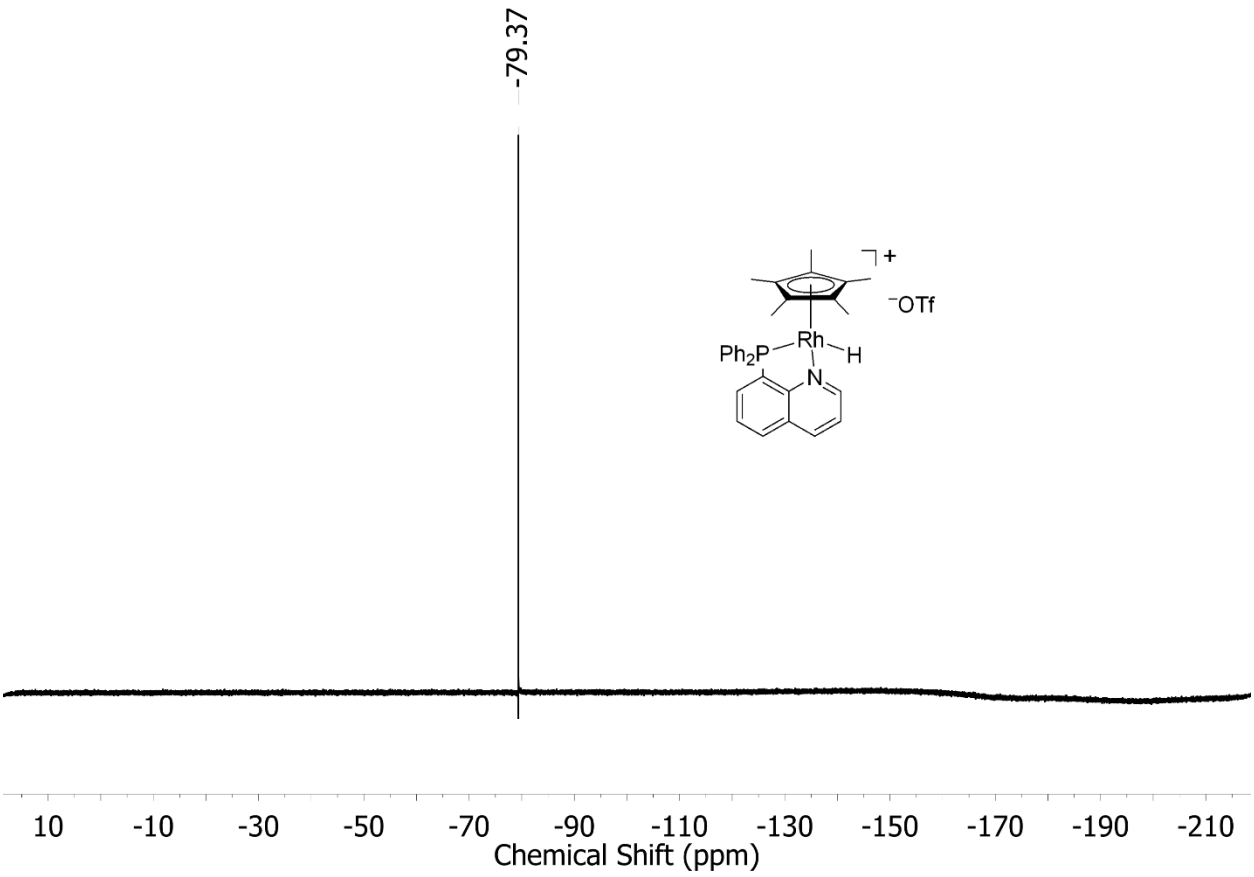

Figure B23. ^{19}F NMR spectrum (376 MHz, CD_3CN) of **3**.

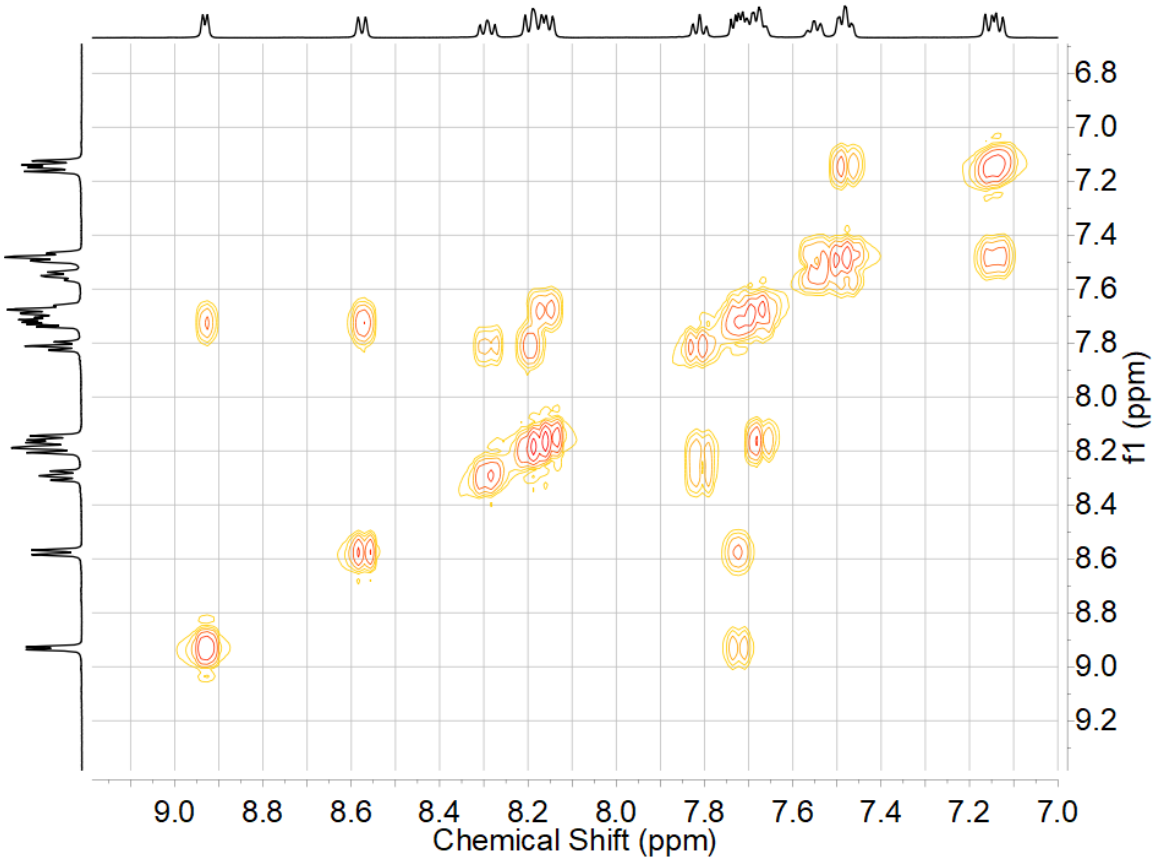

Figure B24. COSY NMR spectrum (CD_3CN) of **3**.

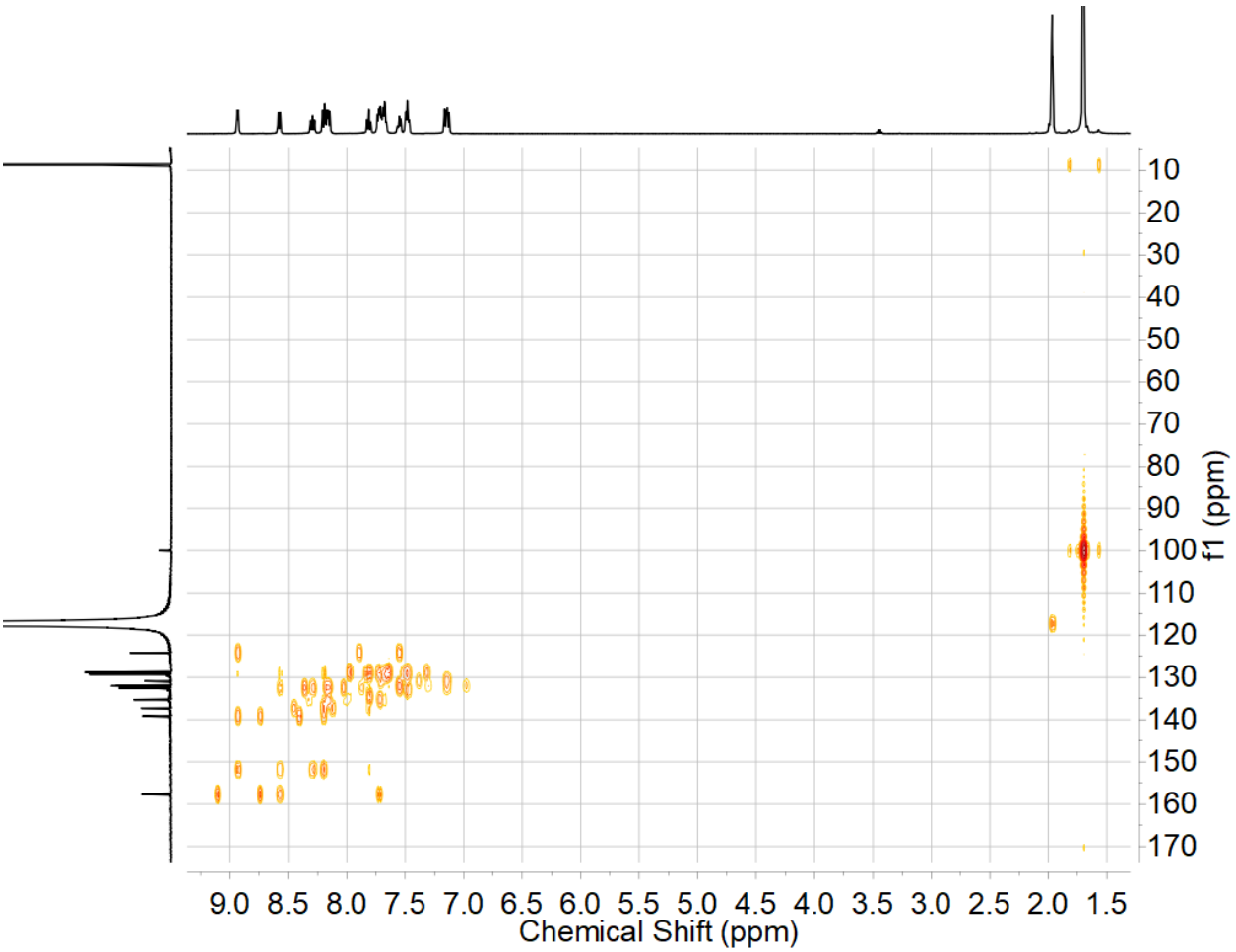

Figure B25. HMBC NMR spectrum (CD_3CN) of **3**.

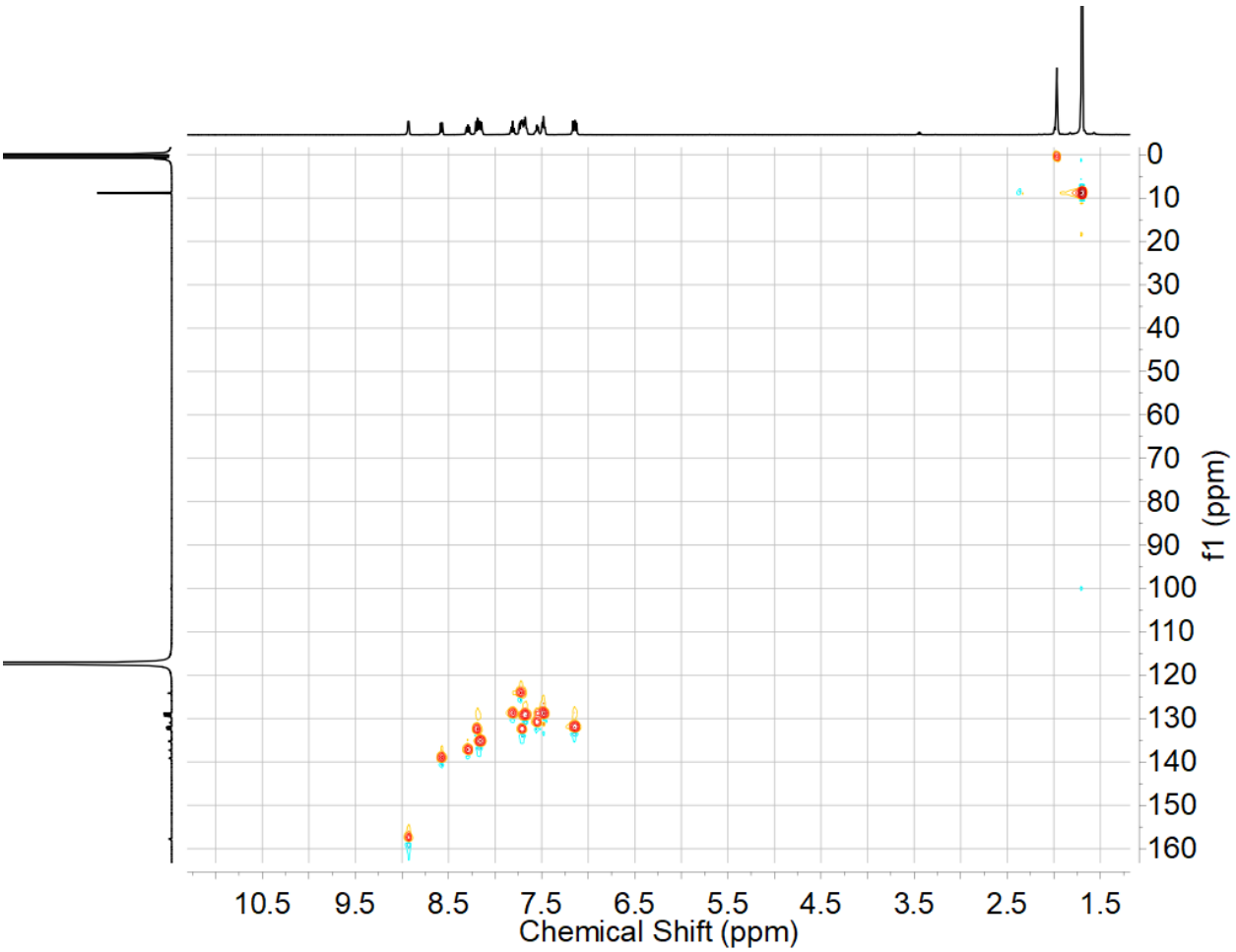

Figure B26. HSQC NMR spectrum (CD_3CN) of **3**.

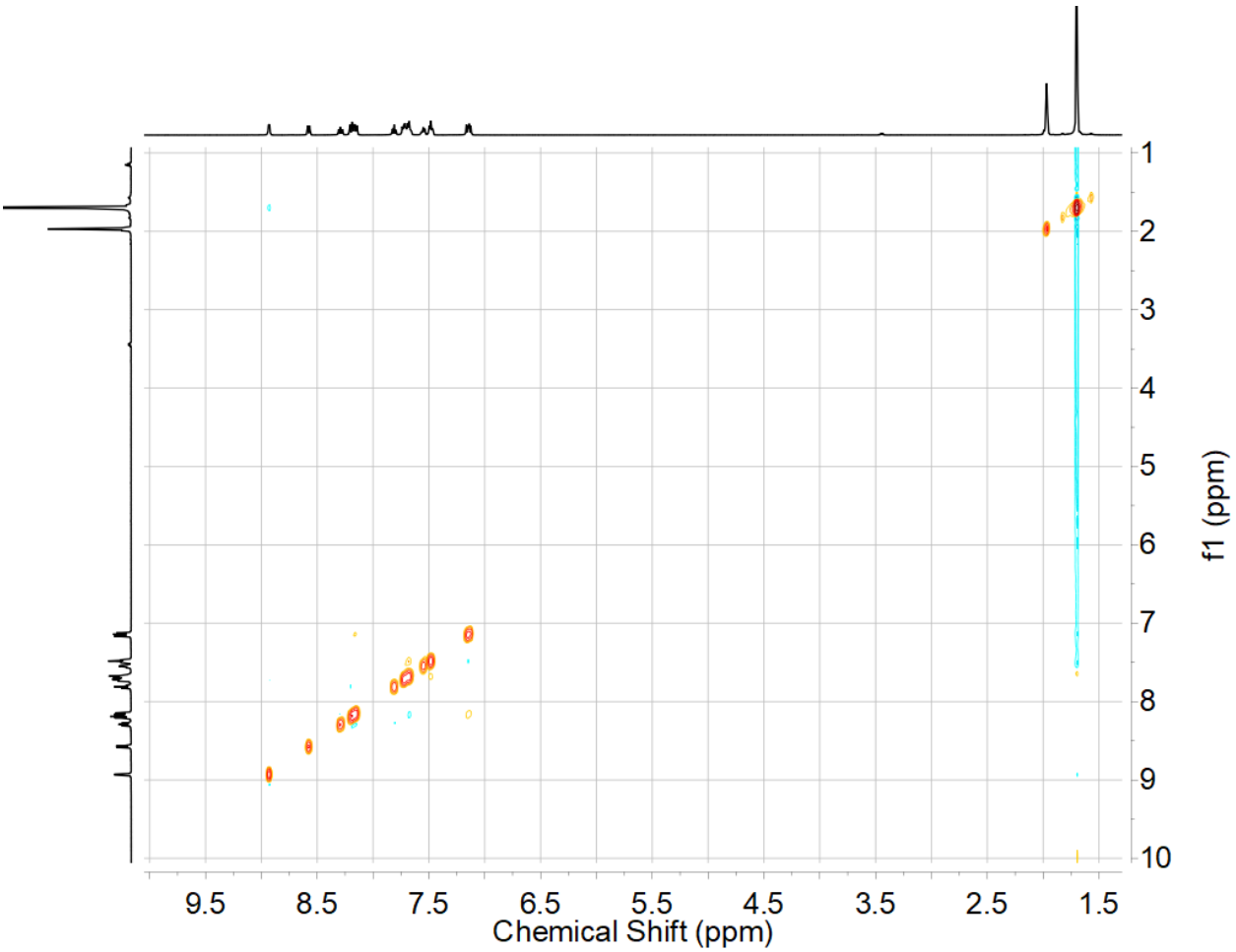

Figure B27. NOESY NMR spectrum (CD_3CN) of **3**.

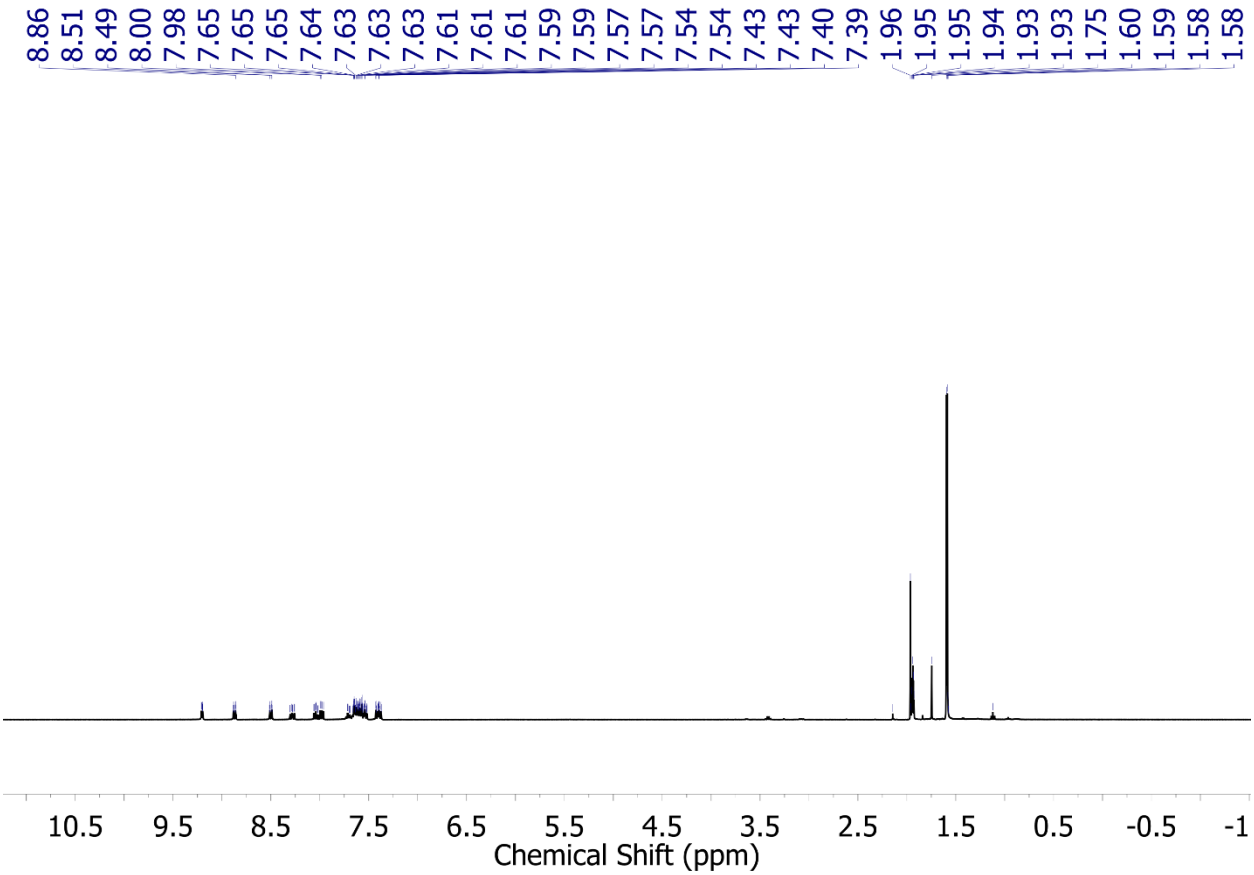

Figure B28. ^{1}H NMR spectrum (400 MHz, CD_3CN) of **1-NCCH$_3$**.

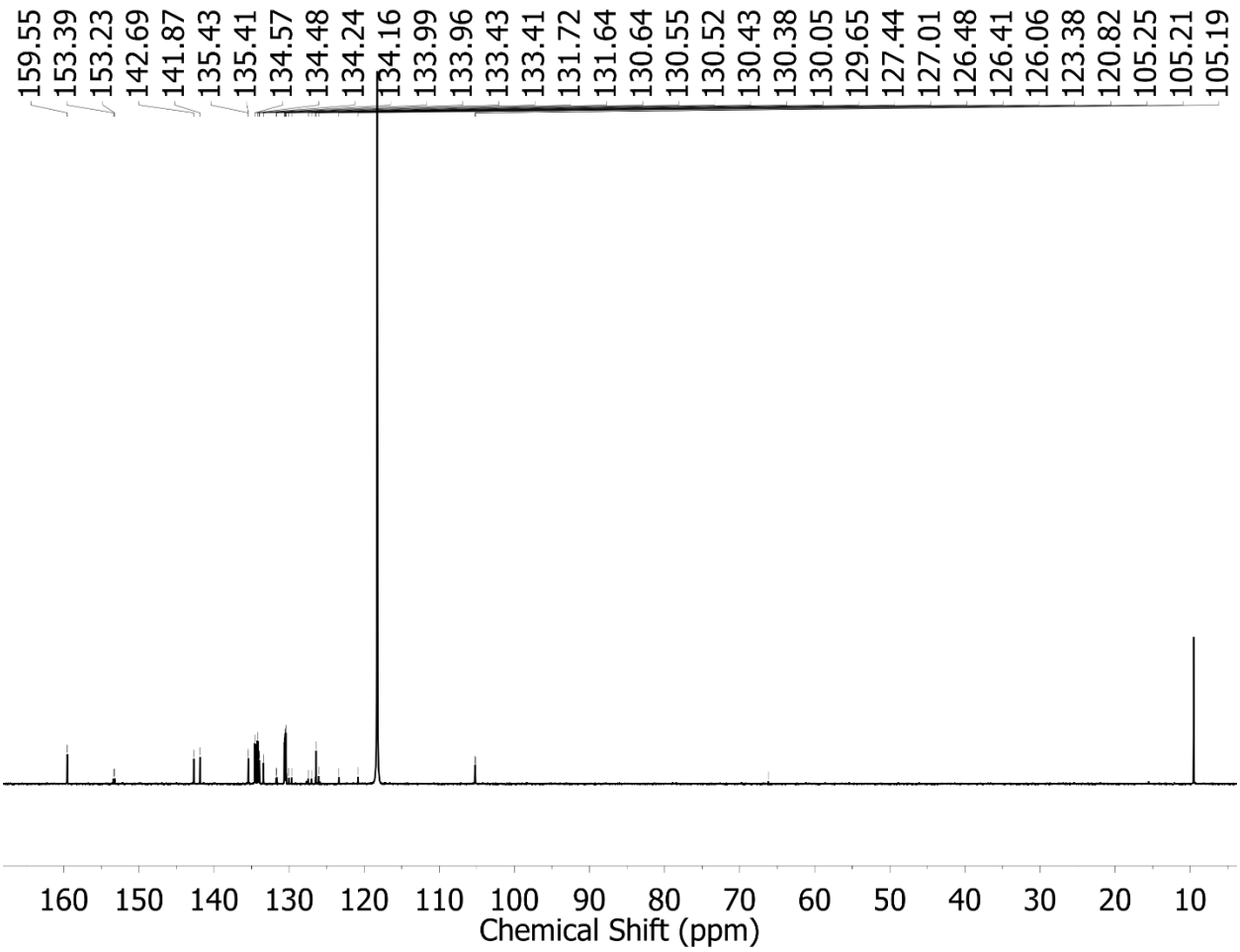

Figure B29. ^{13}C NMR spectrum (162 MHz, CD_3CN) of **1-NCCH$_3$**.

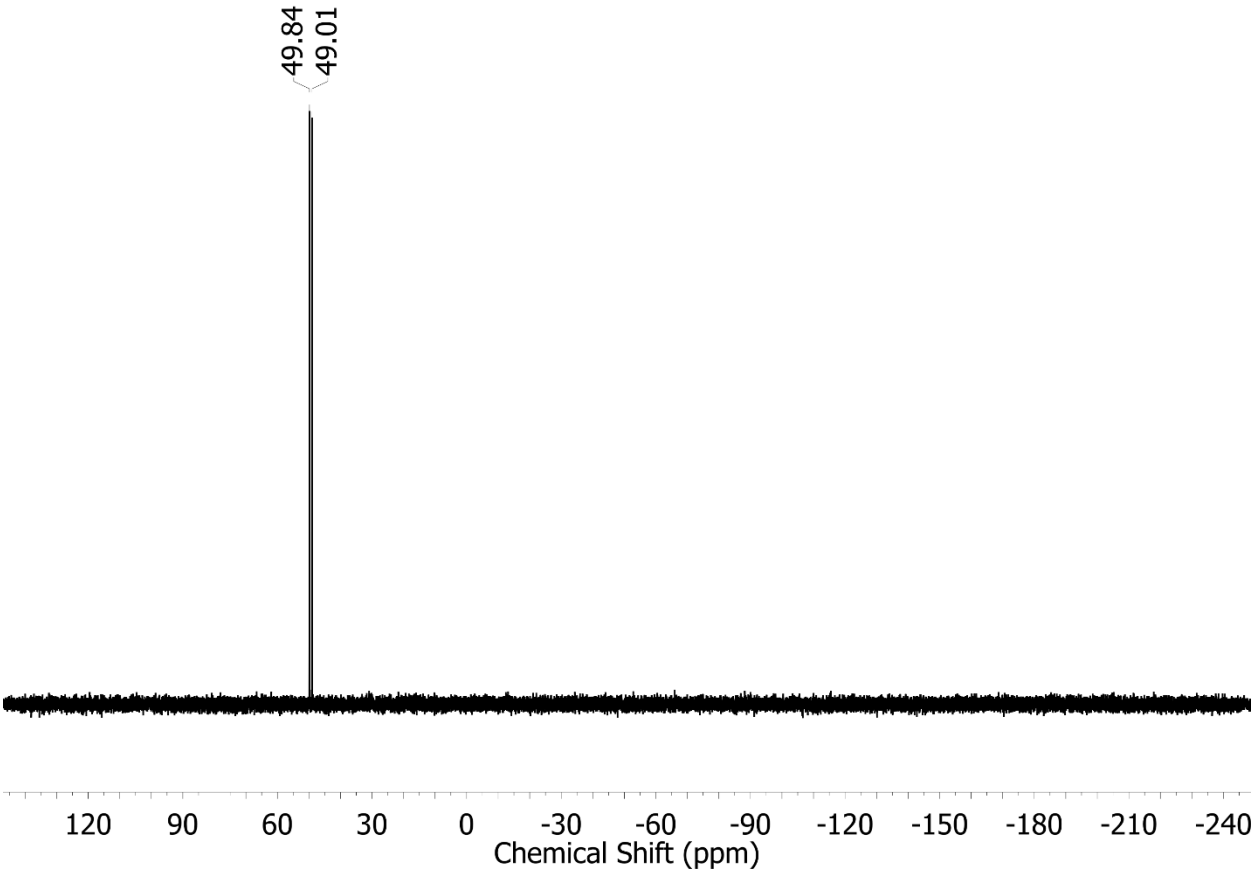

Figure B30. $^{31}P\{^{1}H\}$ NMR spectrum (162 MHz, CD_3CN) of **1-NCCH$_3$**.

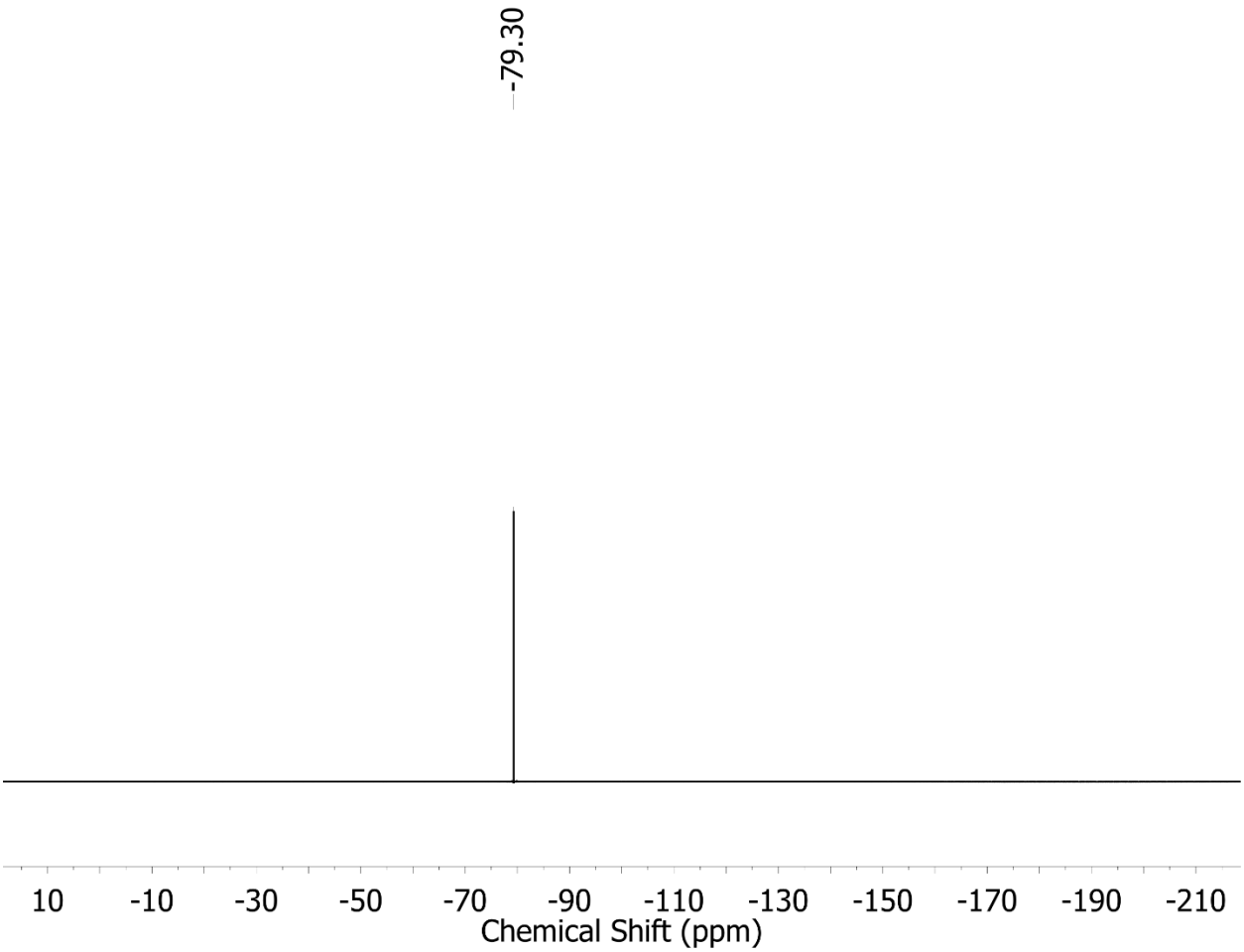

Figure B31. ^{19}F NMR spectrum (162 MHz, CD_3CN) of **1-NCCH$_3$**.

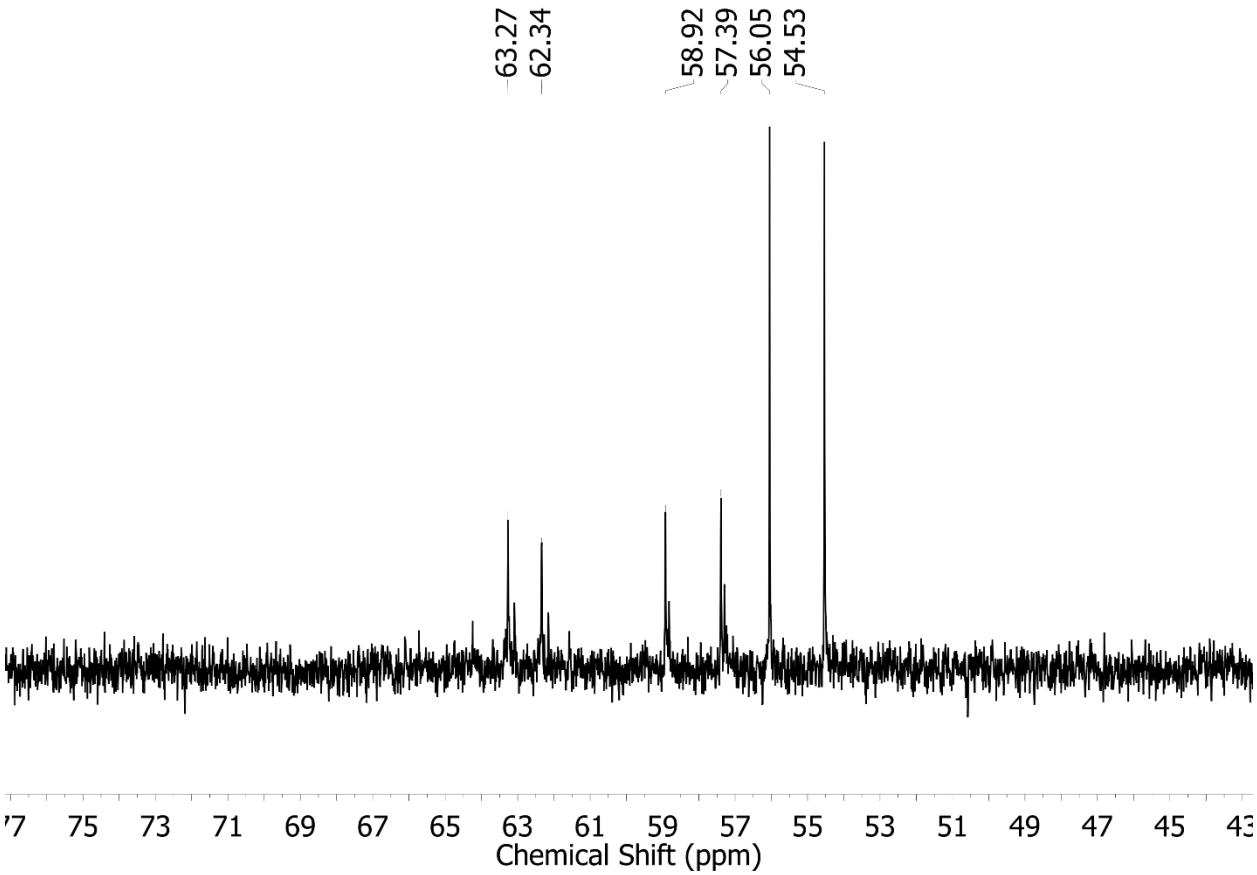

Figure B32. $^{31}P\{^{1}H\}$ NMR spectrum (162 MHz, C_6D_6) of aliquot from chemical reduction of **3** with decamethylcobalacene.

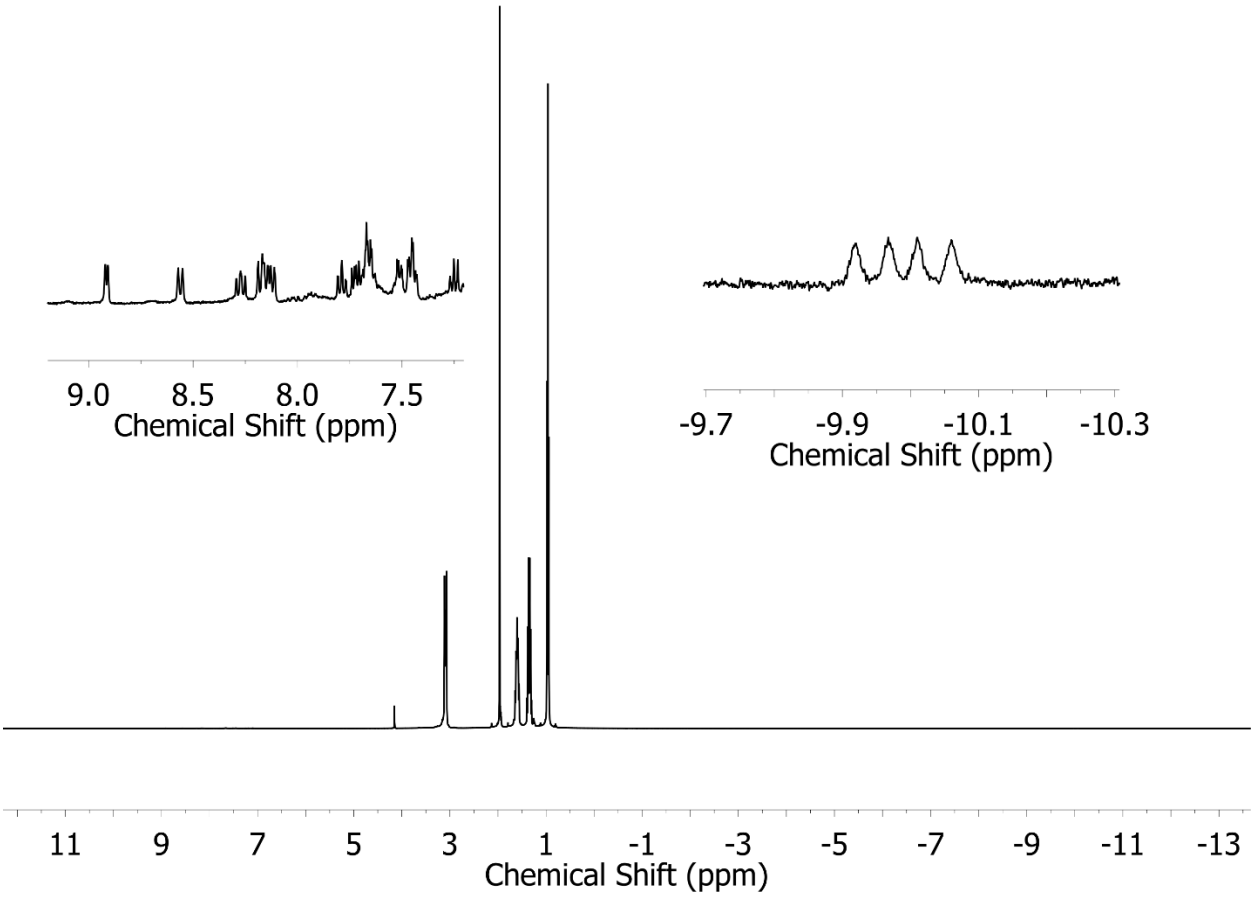

Figure B33. ^{1}H NMR spectrum (162 MHz, CD_3CN) of aliquot from bulk electrolysis of **1-NCCH$_3$** with 10 equiv. of $Et_3NH^+OTf^-$.

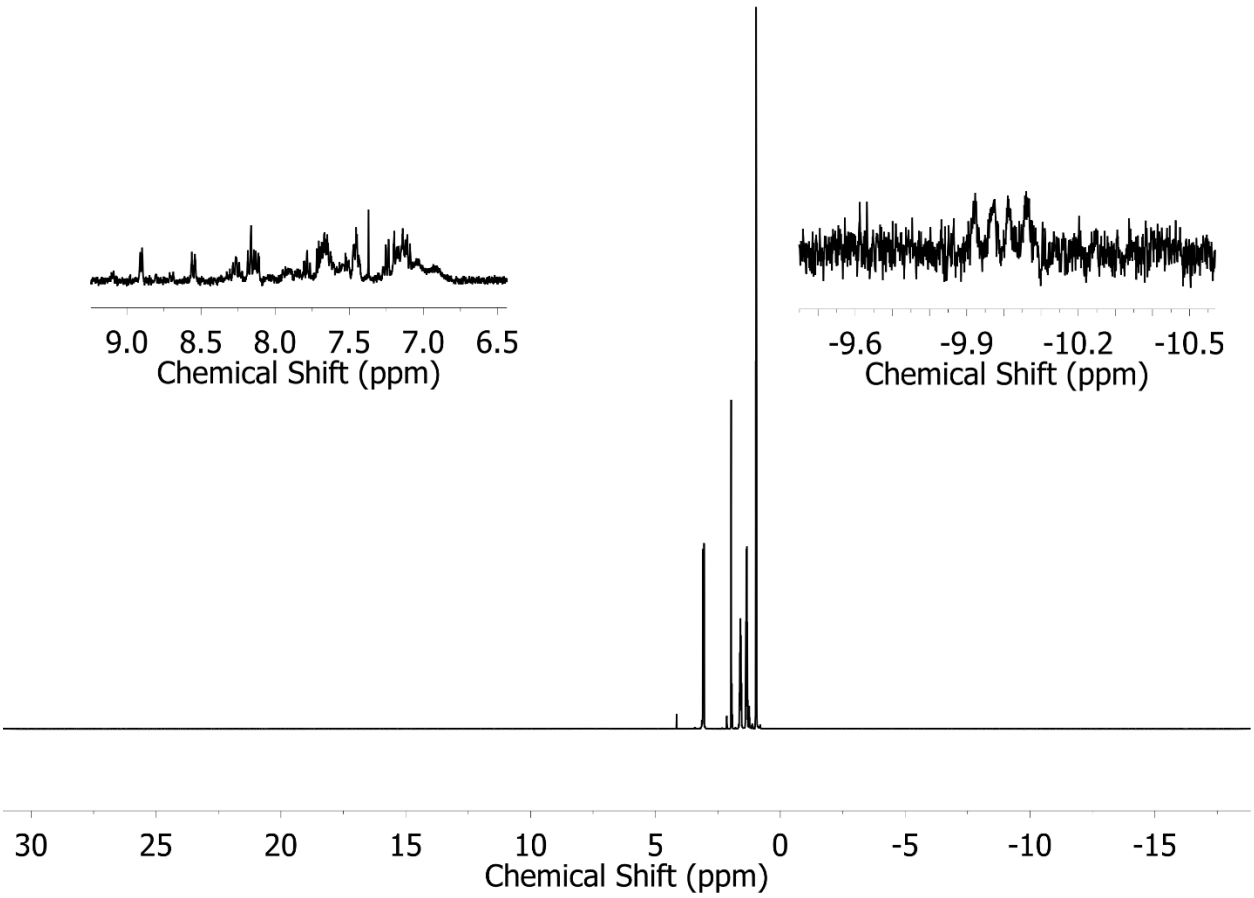

Figure B34. ^{1}H NMR spectrum (162 MHz, CD_3CN) of aliquot from bulk electrolysis of **1- Cl** with 10 equiv. of $Et_3NH^{+}OTf^{-}$.

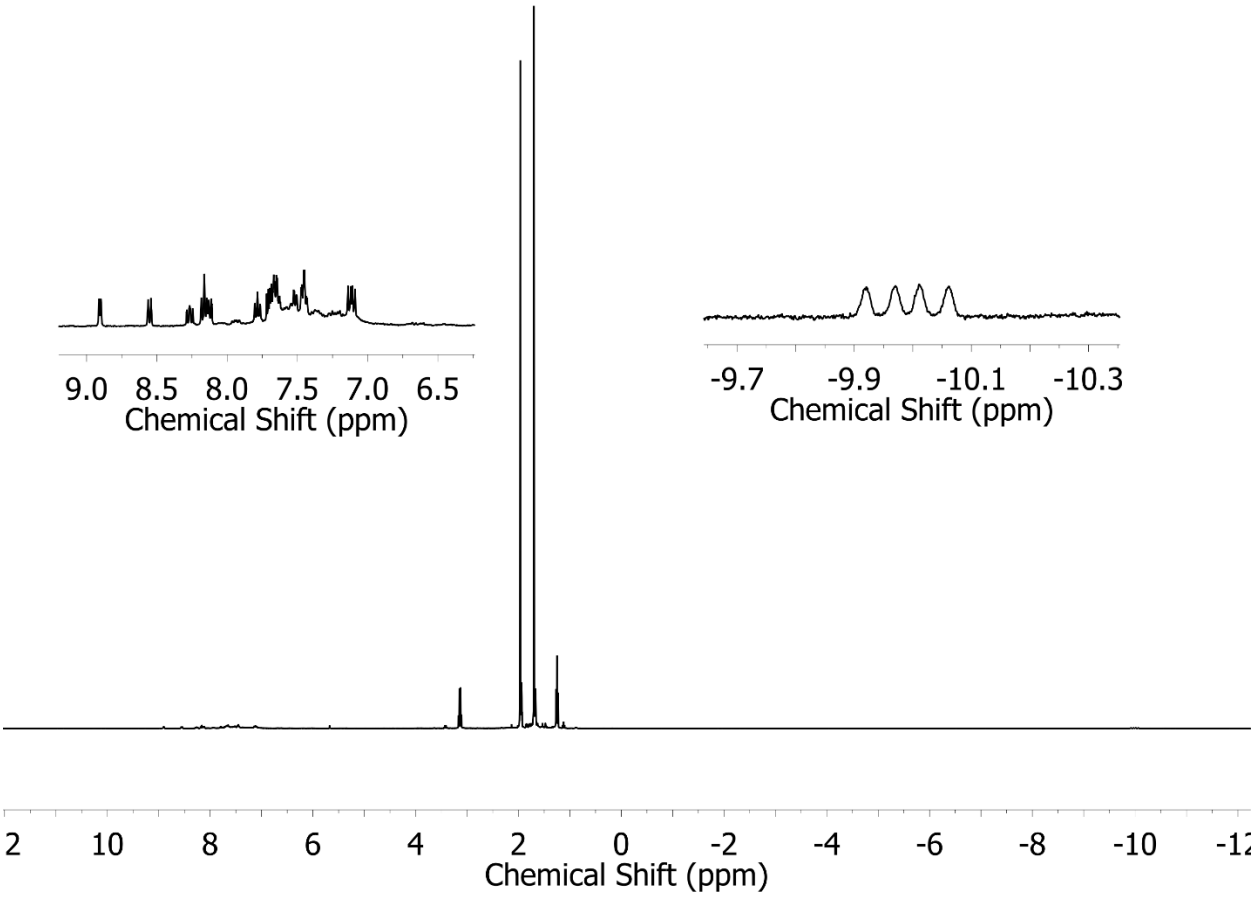

Figure B35. ^{1}H NMR spectrum (162 MHz, CD_3CN) of aliquot from chemical reduction of **3** with 1 equiv. of $Et_3NH^{+}OTf^{-}$ and decamethylcobaltacene.

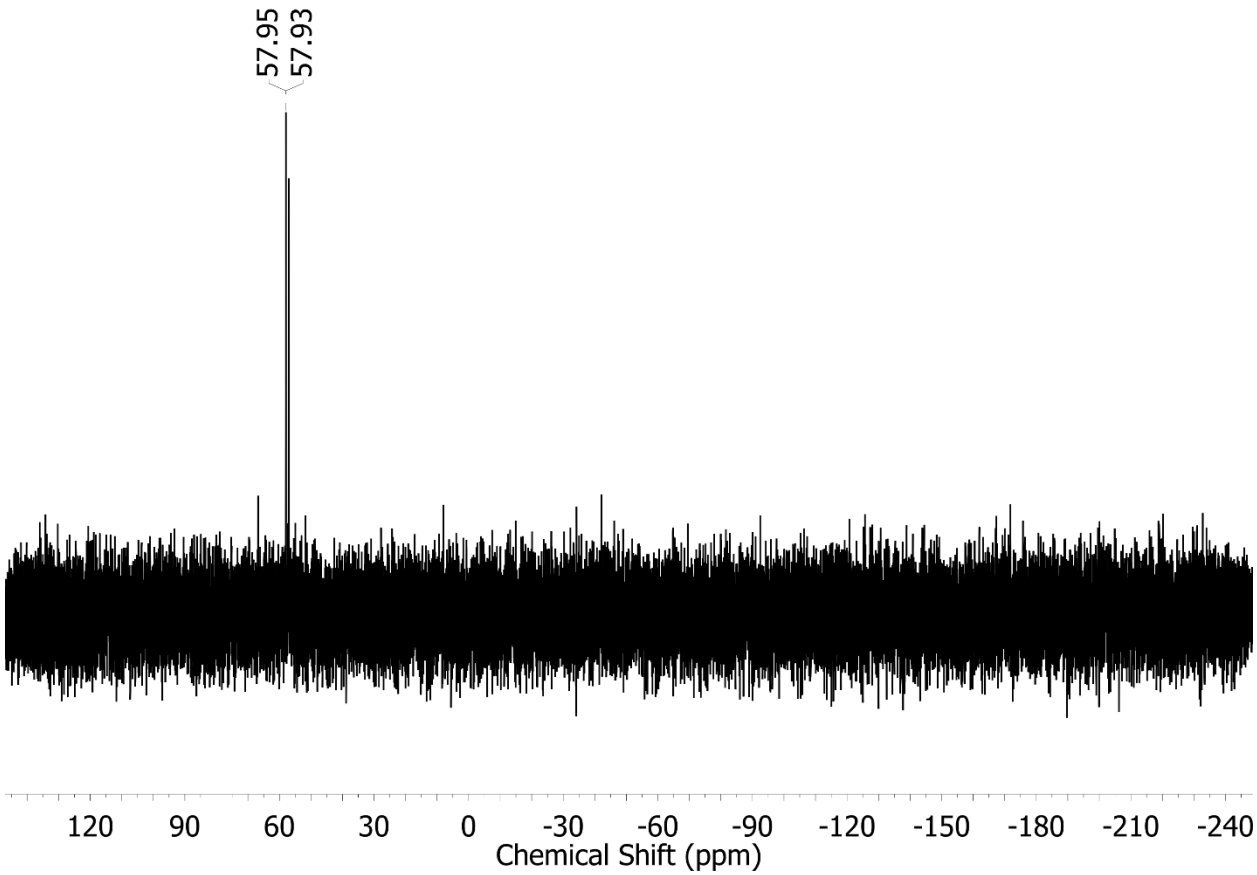

Figure B36. $^{31}P\{^{1}H\}$ NMR spectrum (162 MHz, CD_3CN) of aliquot from chemical reduction of **3** with 1 equiv. of $Et_3NH^+OTf^-$ and decamethylcobaltacene.

UV-Vis

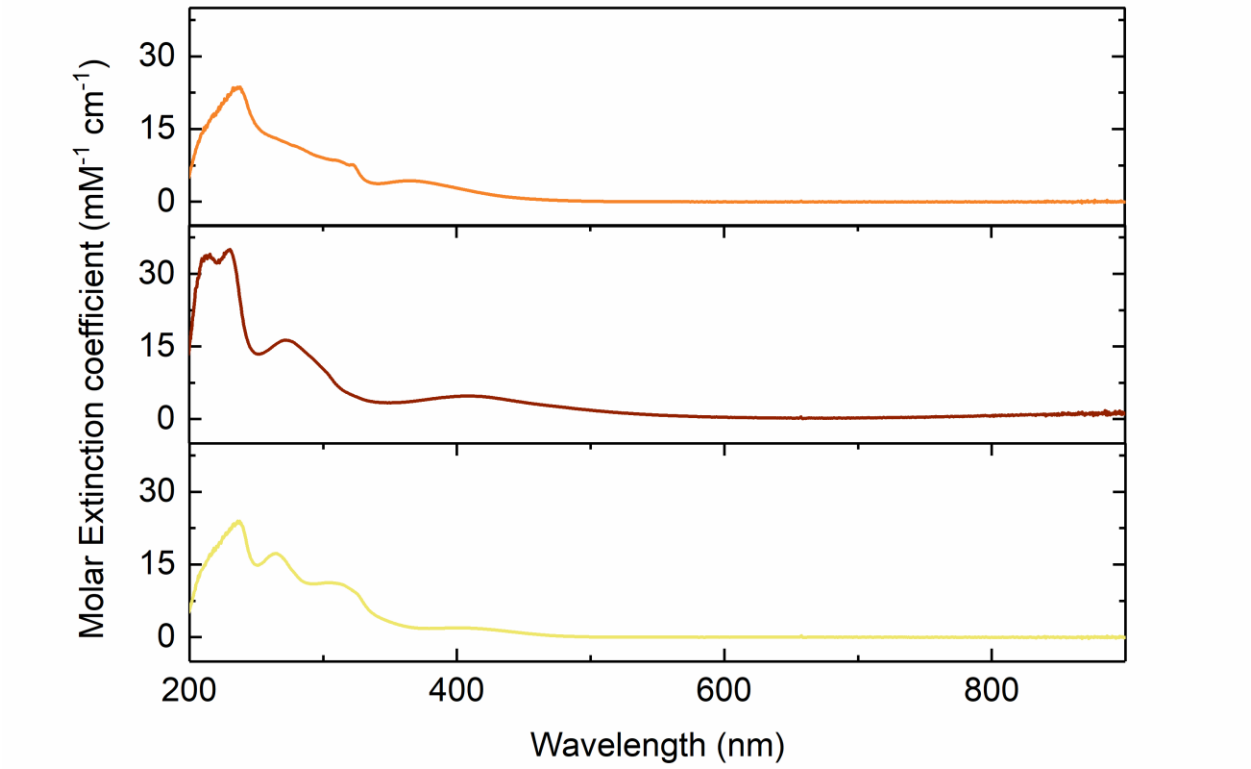

Figure B37. Electronic absorption spectra of **1-Cl** (upper panel), **2** (middle panel), and **3** (lower panel) in CH_3CN.

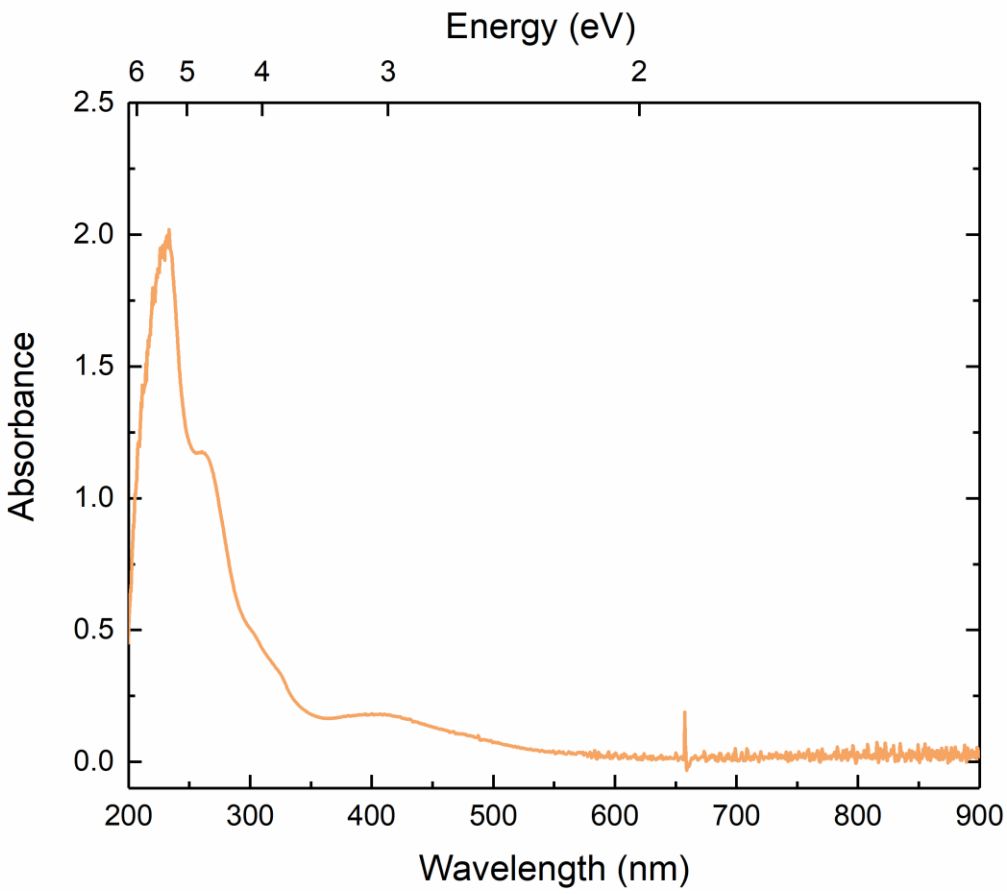

Figure B38. Electronic absorption spectrum of aliquot (CH_3CN) from bulk electrolysis of **3**.

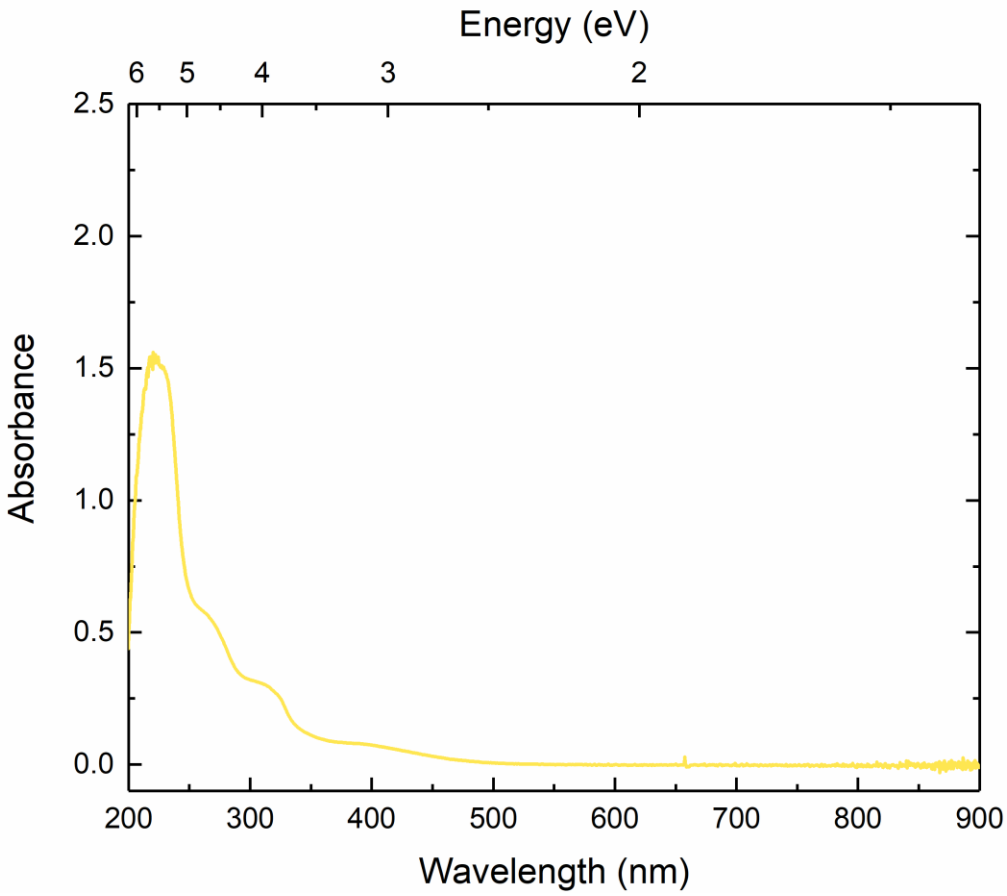

Figure B39. Electronic absorption spectrum of aliquot (CH_3CN) from bulk electrolysis of for **1-NCCH$_3$** with 10 equiv. of $Et_3NH^+OTf^-$.

Electrochemistry

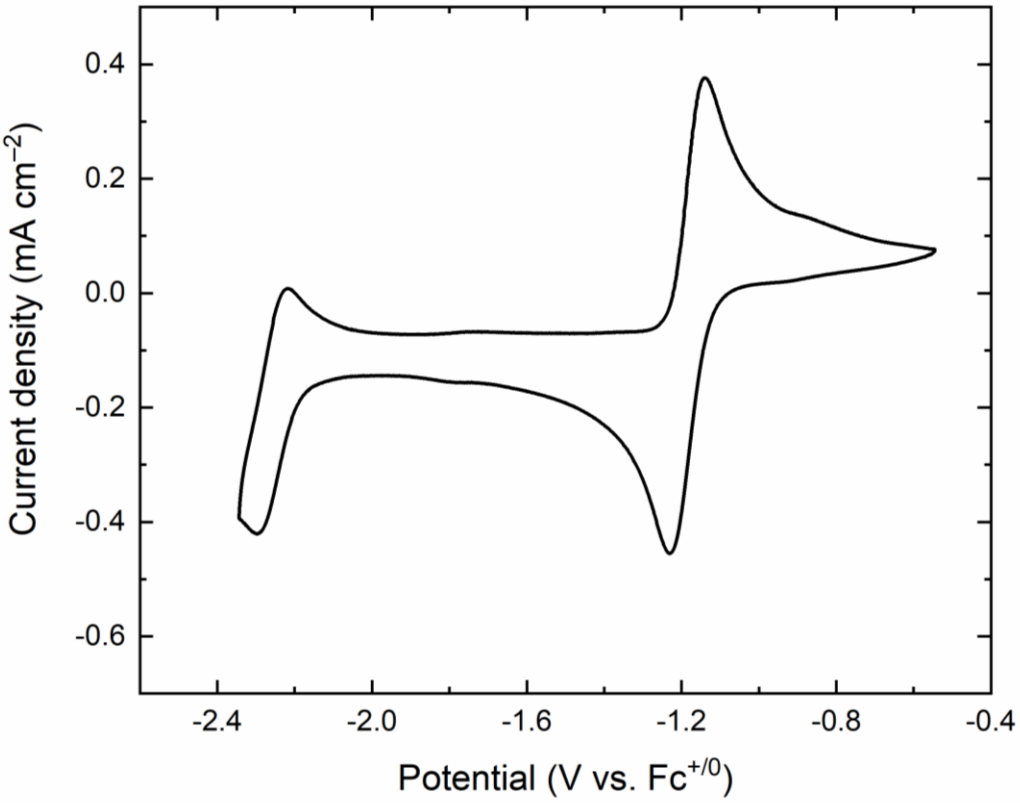

Figure B40. Cyclic voltammetry of **1-Cl** (CH_3CN, 0.1 M [$^nBu_4N$][PF_6], 100 mV/s)

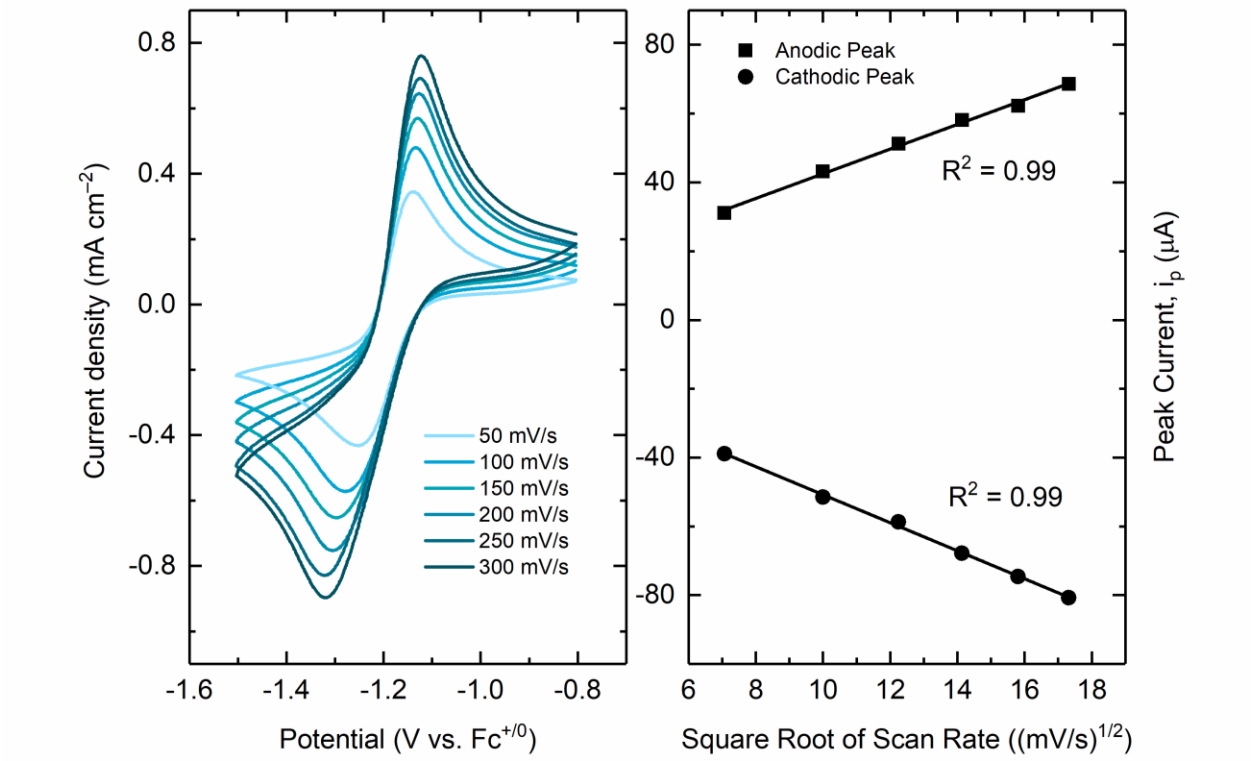

Figure B41. Left: cyclic voltammetry of first reduction event **1-Cl** at varying scan rate in CH_3CN (0.1 M [^{n}Bu$_4$N][PF_6]). Right: linear dependence of peak cathodic current on square root of scan rate with the y-intercept set to 0.

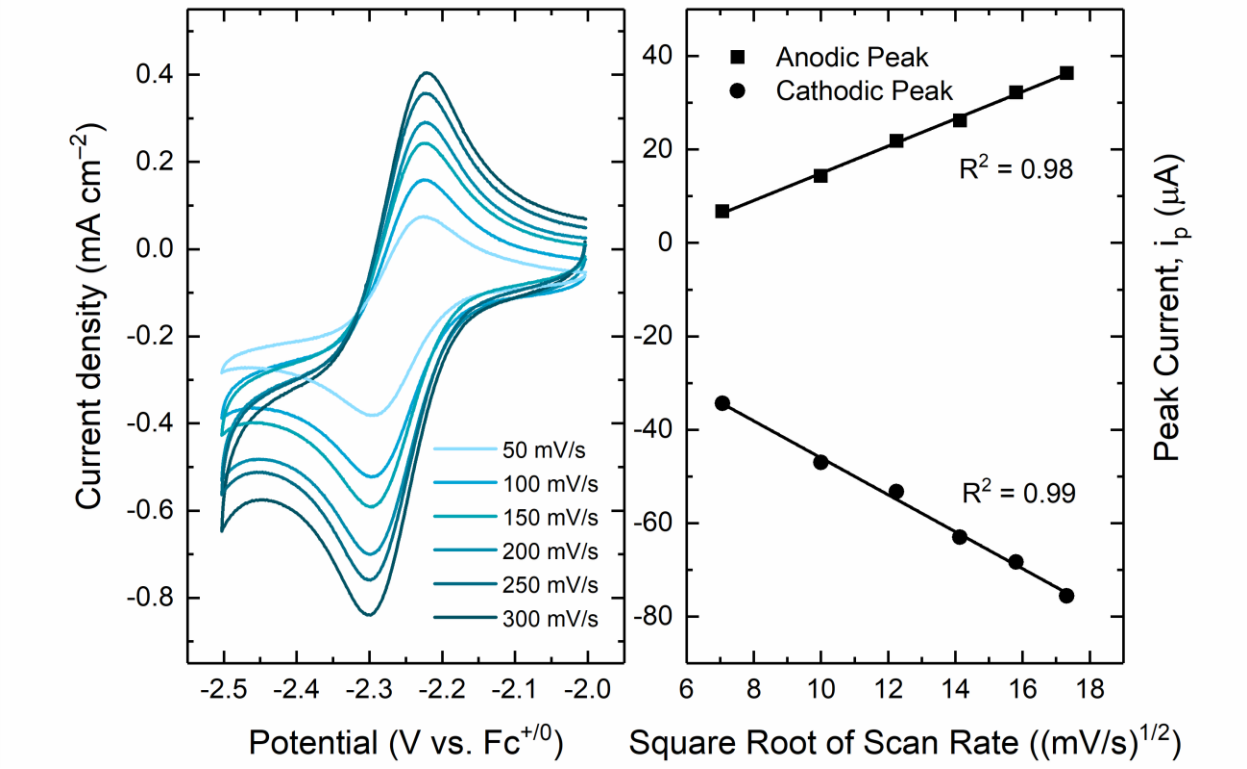

Figure B42. Left: cyclic voltammetry of second reduction event **1-Cl** at varying scan rate in CH_3CN (0.1 M [^{n}Bu$_4$N][PF_6]). Right: linear dependence of peak cathodic current on square root of scan rate.

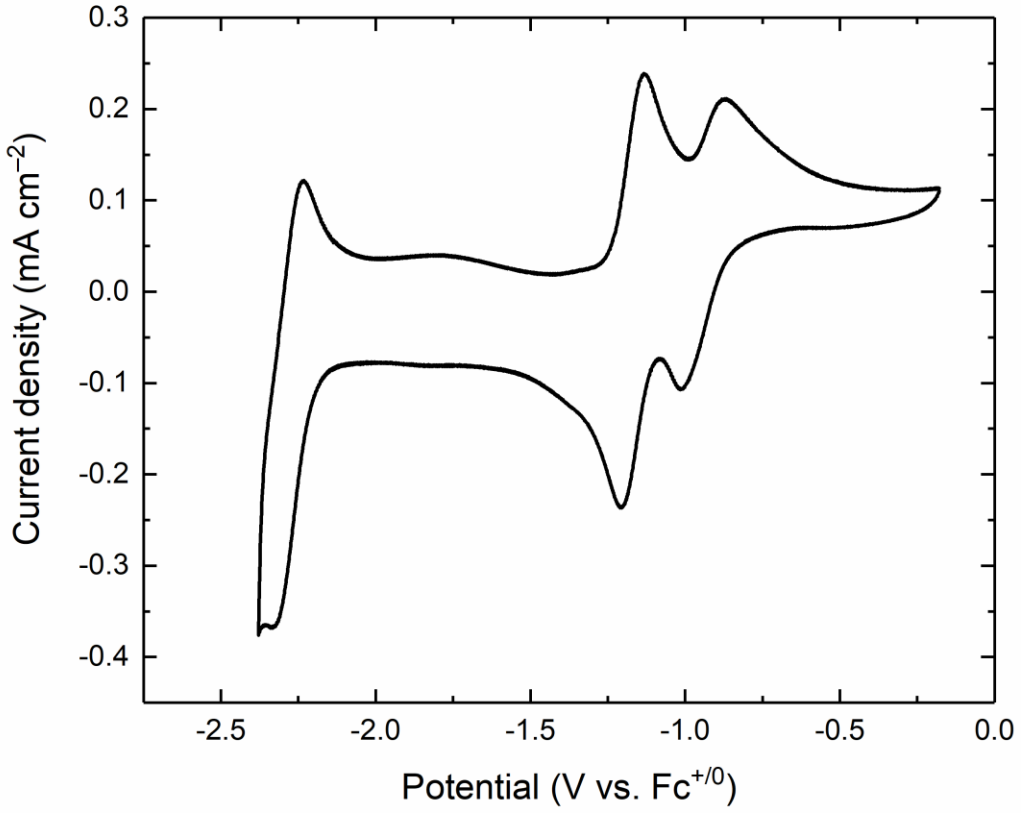

Figure B43. Cyclic voltammetry of **1-NCCH$_3$** (CH_3CN, 0.1 M [$^nBu_4N$][PF_6], 100 mV/s).

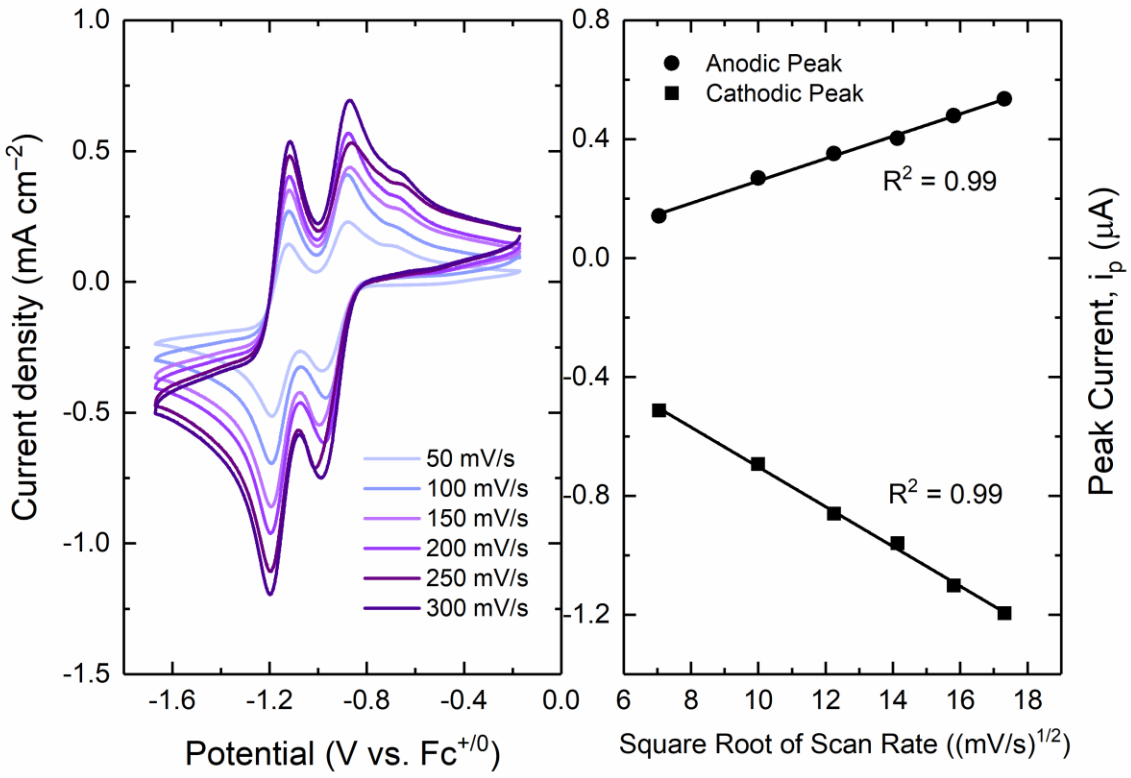

Figure B44. Left: cyclic voltammetry of second reduction event **1-NCCH$_3$** at varying scan rate in CH_3CN (0.1 M [^{n}Bu$_4$N][PF$_6$]). Right: linear dependence of peak cathodic current on square root of scan rate.

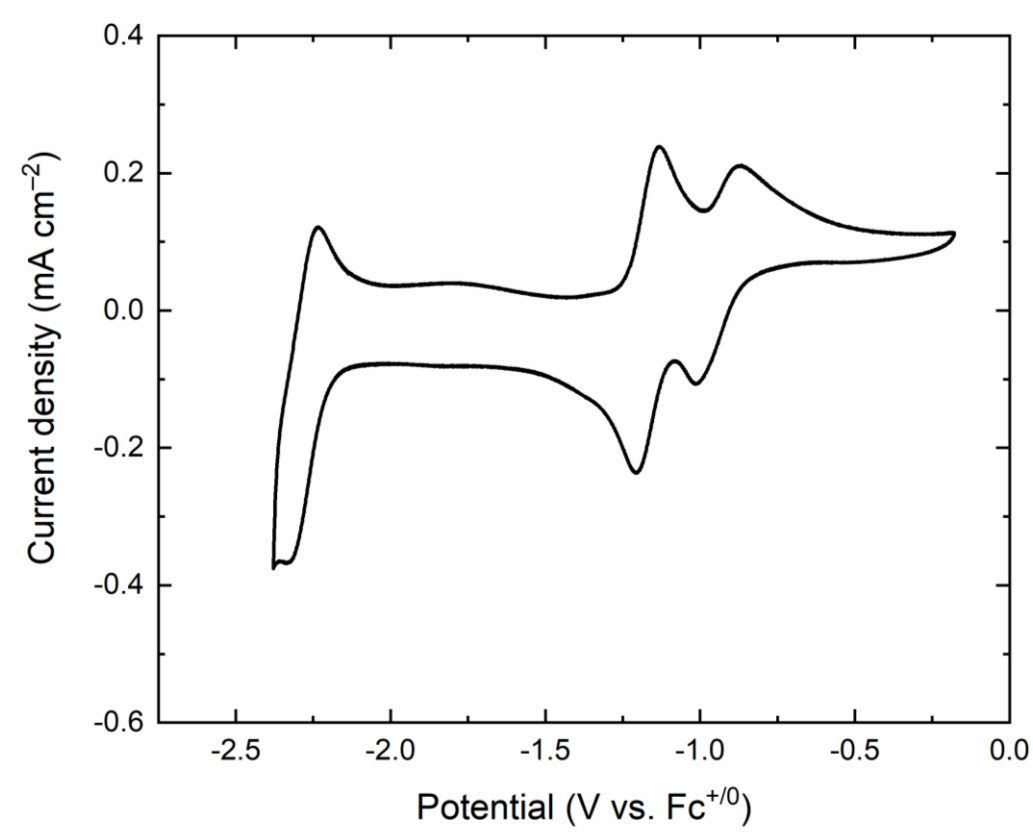

Figure B45. Cyclic voltammetry of **2** (CH_3CN, 0.1 M [$^nBu_4N$][PF_6], 100 mV/s)

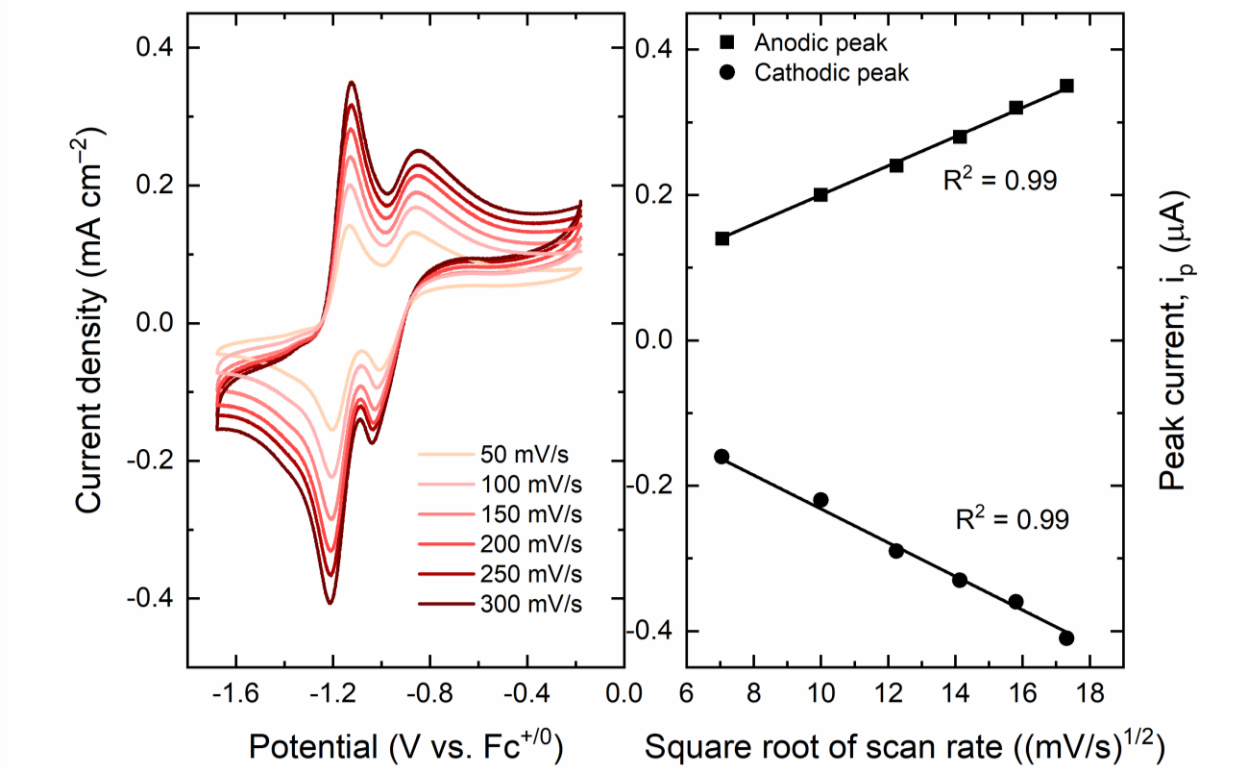

Figure B46. Left: cyclic voltammetry of **2** at varying scan rate in CH_3CN (0.1 M [^{n}Bu$_4$N][PF_6]). Right: linear dependence of peak cathodic current on square root of scan rate with the y-intercept set to 0.

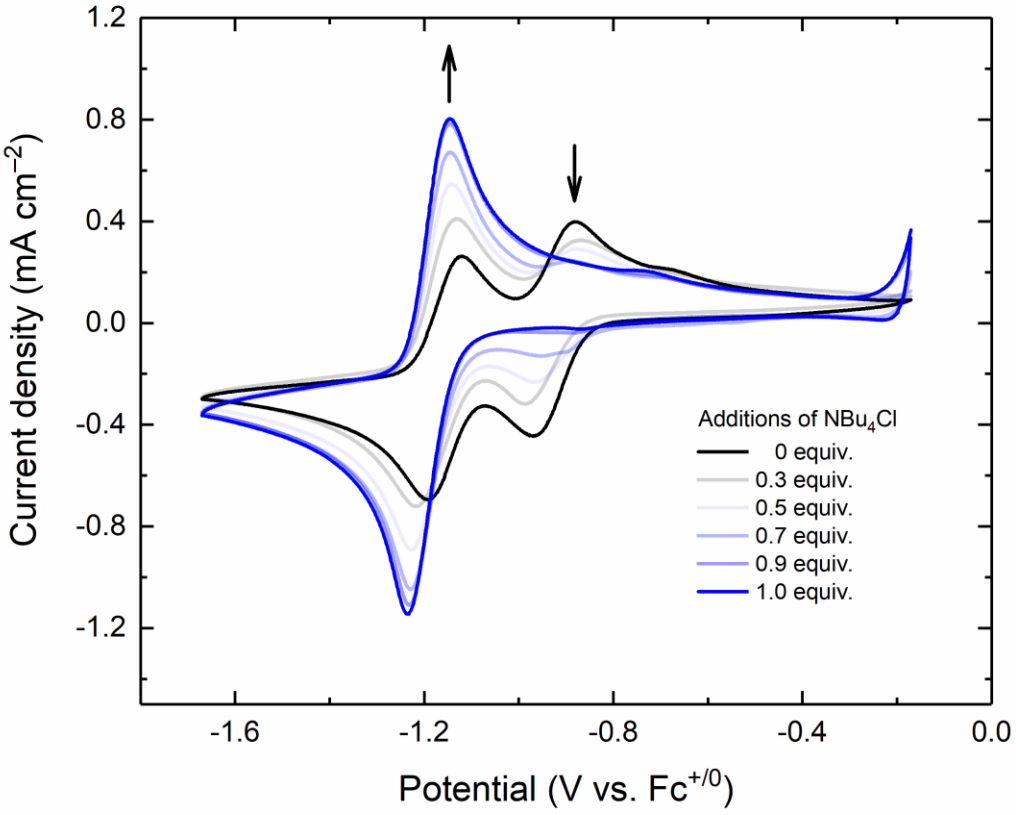

Figure B47. Titration of **1-NCCH$_3$** [^{n}Bu$_4$N][PF$_6$] solution with increasing equivalents of [^{n}Bu$_4$N][Cl] (CH$_3$CN, 0.1 M [^{n}Bu$_4$N][PF$_6$], 100 mV/s).

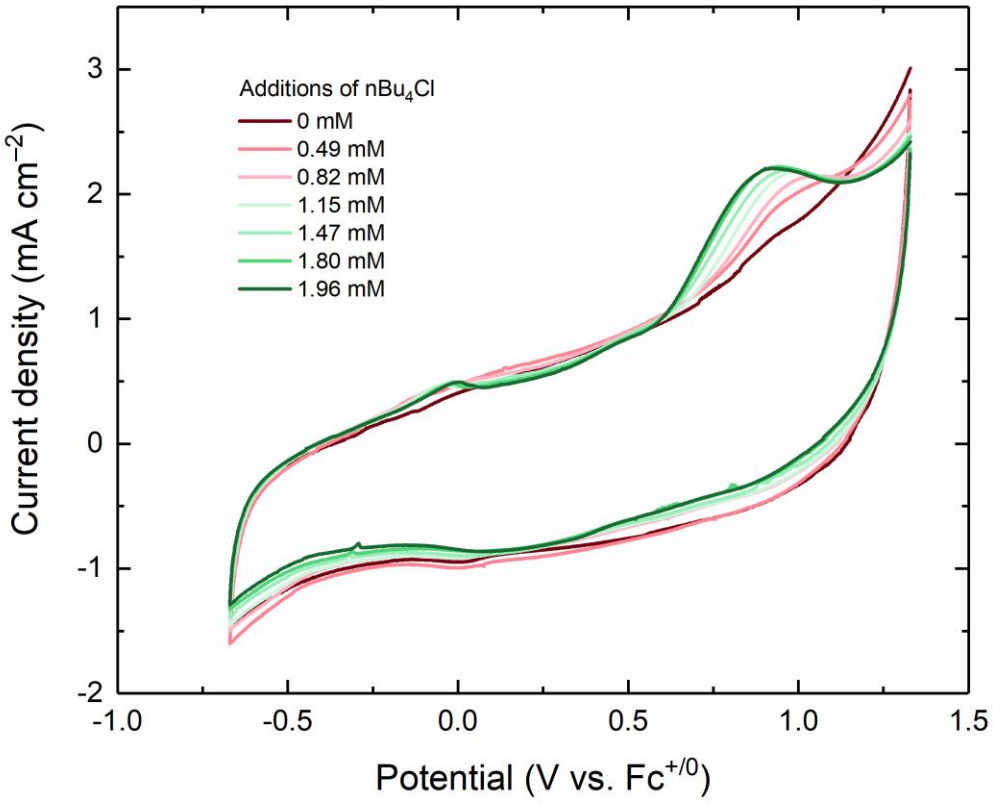

Figure B48. Titration of blank 0.1M [^{n}Bu$_4$N][PF$_6$] solution with increasing equivalents of [^{n}Bu$_4$N][Cl] (CH$_3$CN, 0.1 M [^{n}Bu$_4$N][PF$_6$], 100 mV/s).

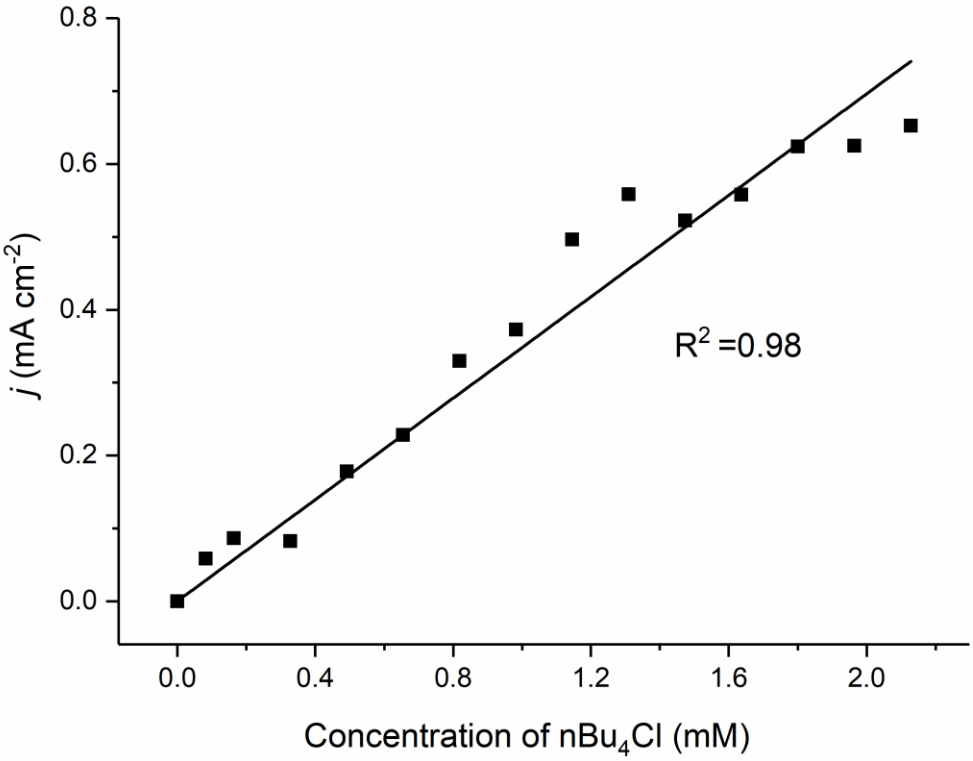

Figure B49. Linear regression of i_{pa} vs. concentration of [^{n}Bu$_4$N][Cl]. Titration of blank 0.1M [^{n}Bu$_4$N][PF$_6$] solution with increasing equivalents of [^{n}Bu$_4$N][Cl] (CH$_3$CN, 0.1 M [^{n}Bu$_4$N][PF$_6$], 100 mV/s).

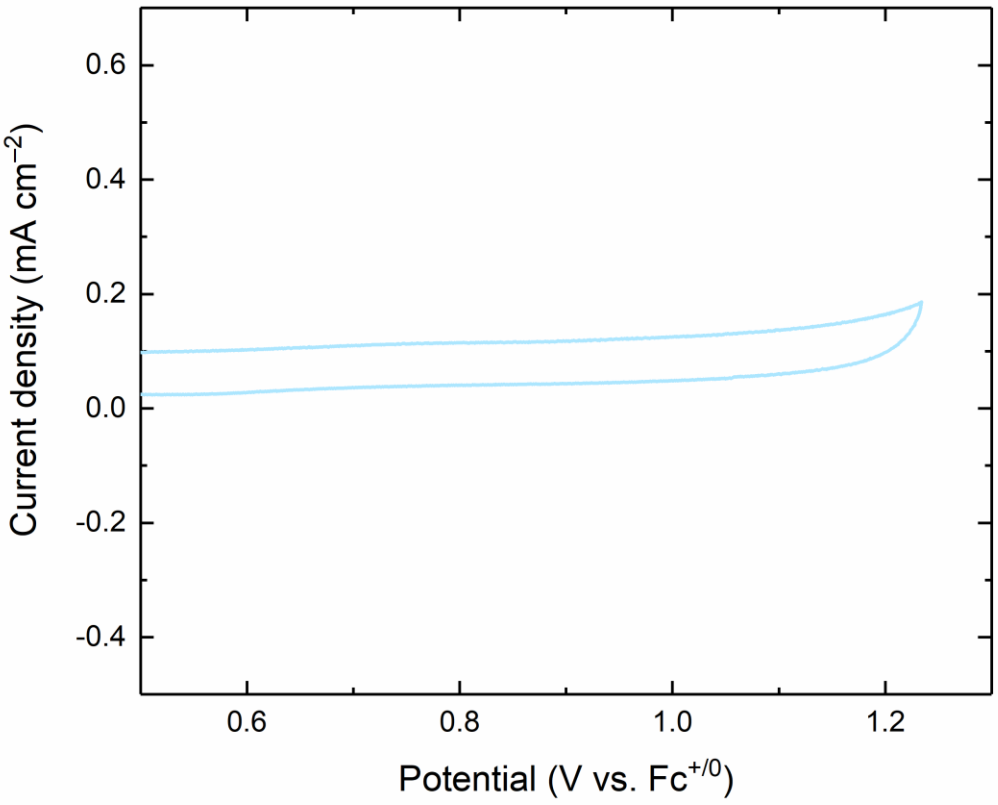

Figure B50. CV of chloride oxidation region of **2** (CH_3CN, 0.1 M [$^nBu_4N$][PF_6], 100 mV/s).

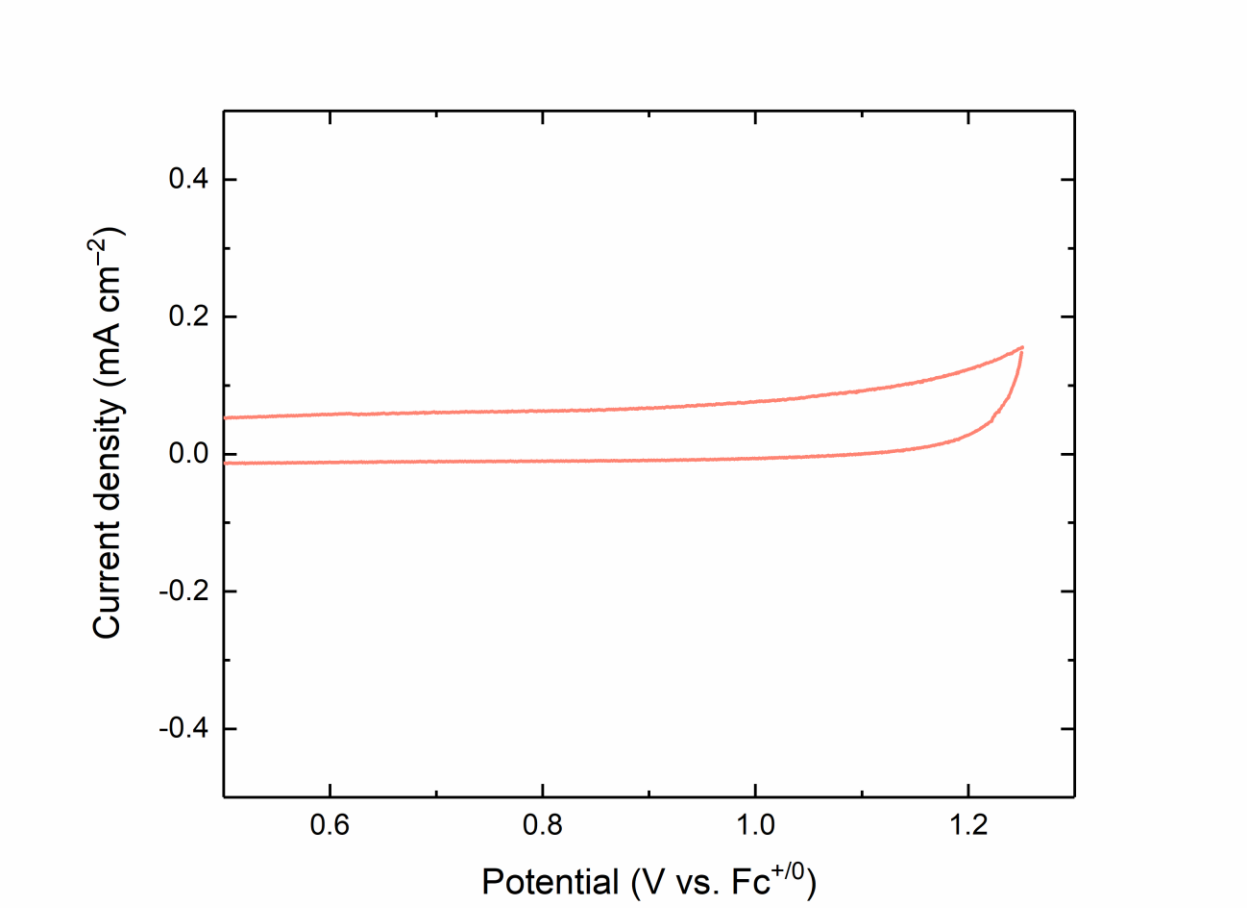

Figure B51. CV of chloride oxidation region of **1-NCCH$_3$** (CH_3CN, 0.1 M [^{n}Bu$_4$N][PF_6], 100 mV/s).

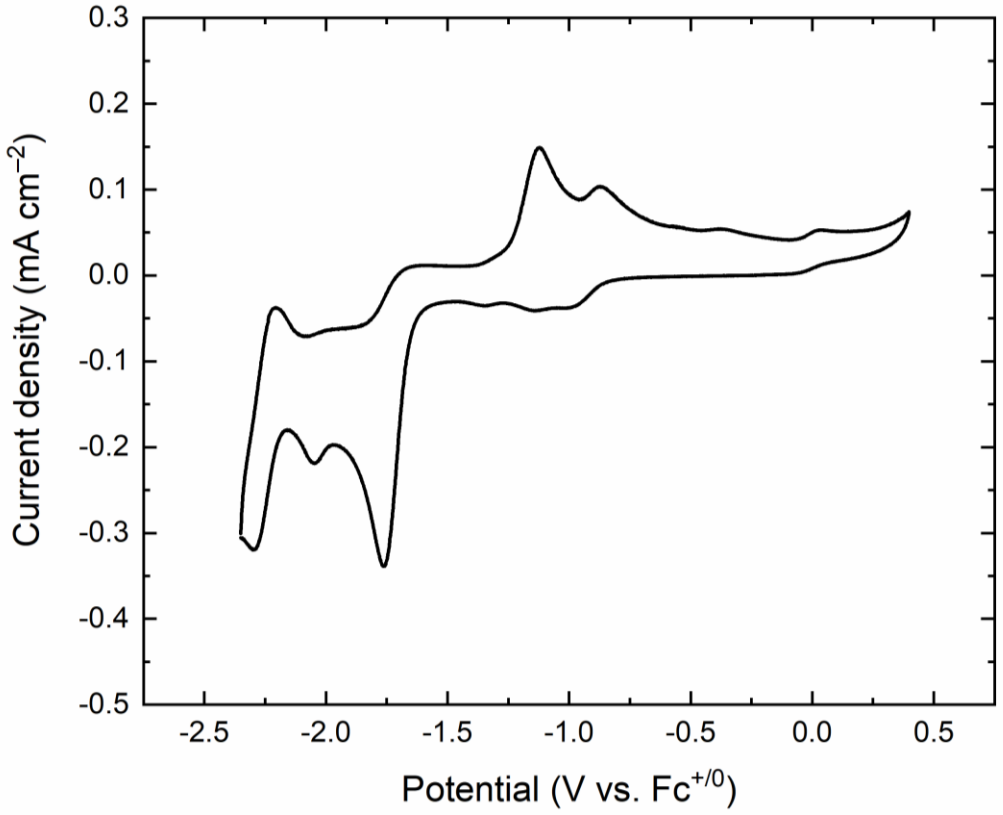

Figure B52. Cyclic voltammetry of **3** (CH_3CN, 0.1 M [$^nBu_4N$][PF_6], 100 mV/s)

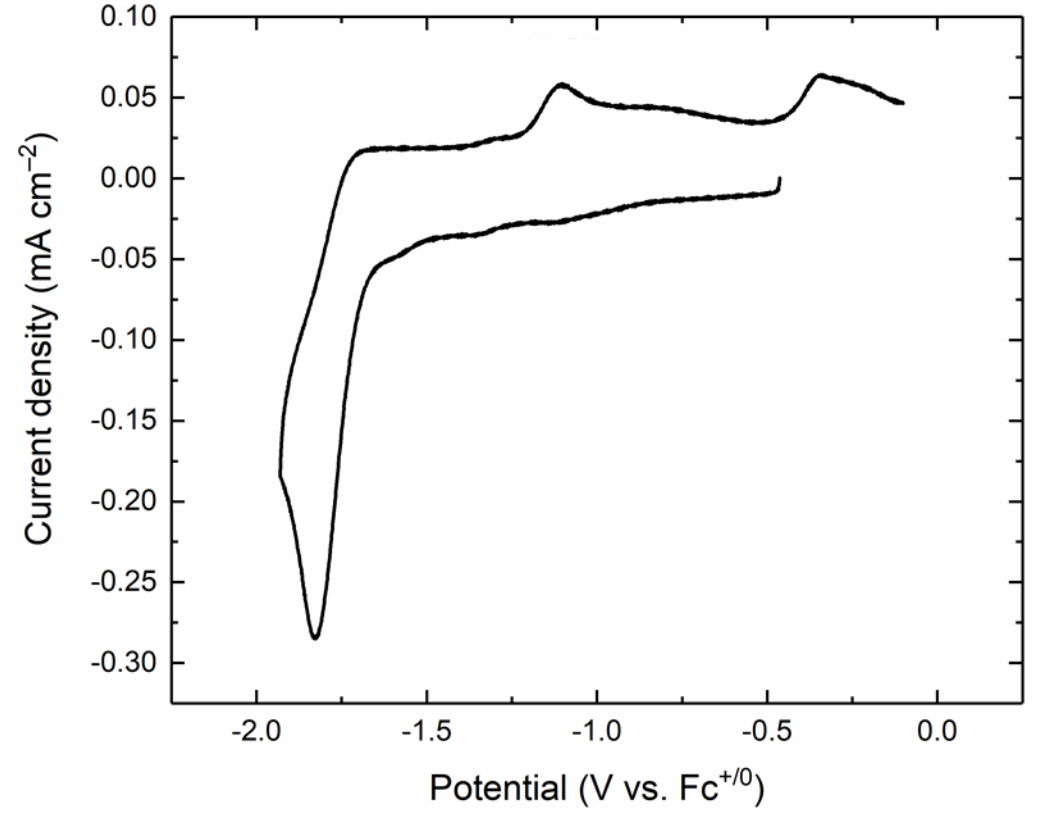

Figure B53. Cyclic voltammetry of **3** (CH_3CN, 0.1 M [$^nBu_4N$][PF_6], 4000 mV/s).

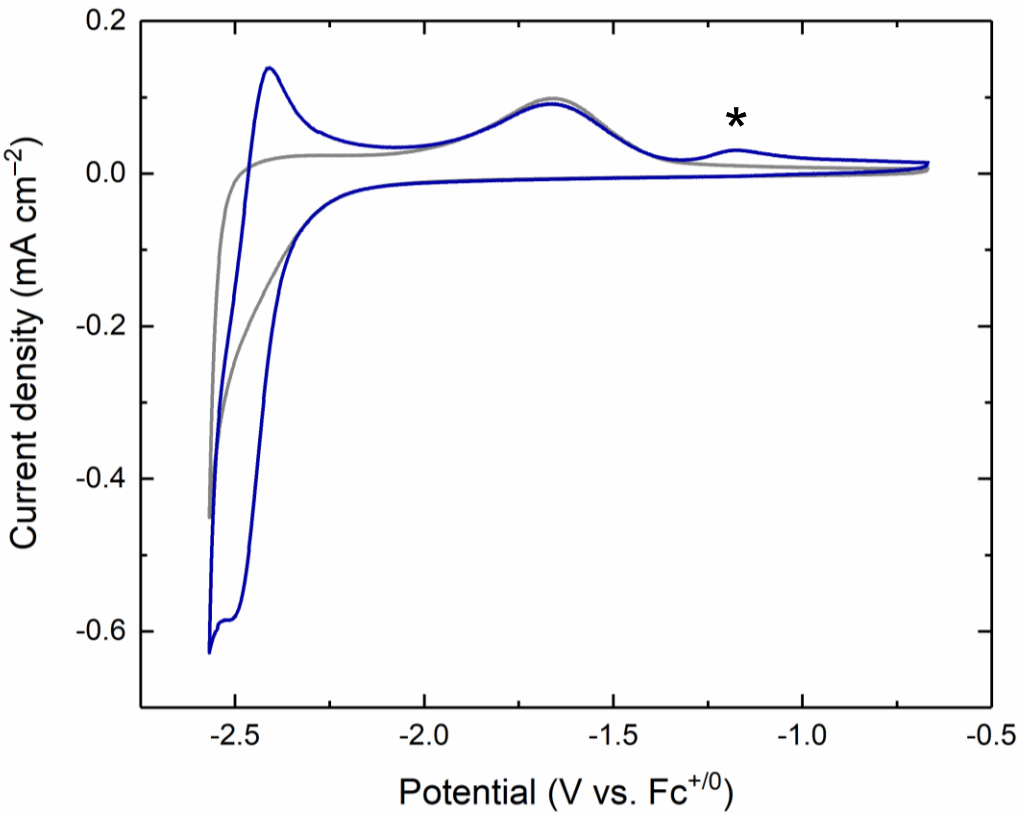

Figure B54. Cyclic voltammetry of PQN (CH_3CN, 0.1 M [$^nBu_4N$][PF_6], 100 mV/s) (*) denotes an anodic, electrode-based process resulting from cathodic scanning to rather negative potentials.

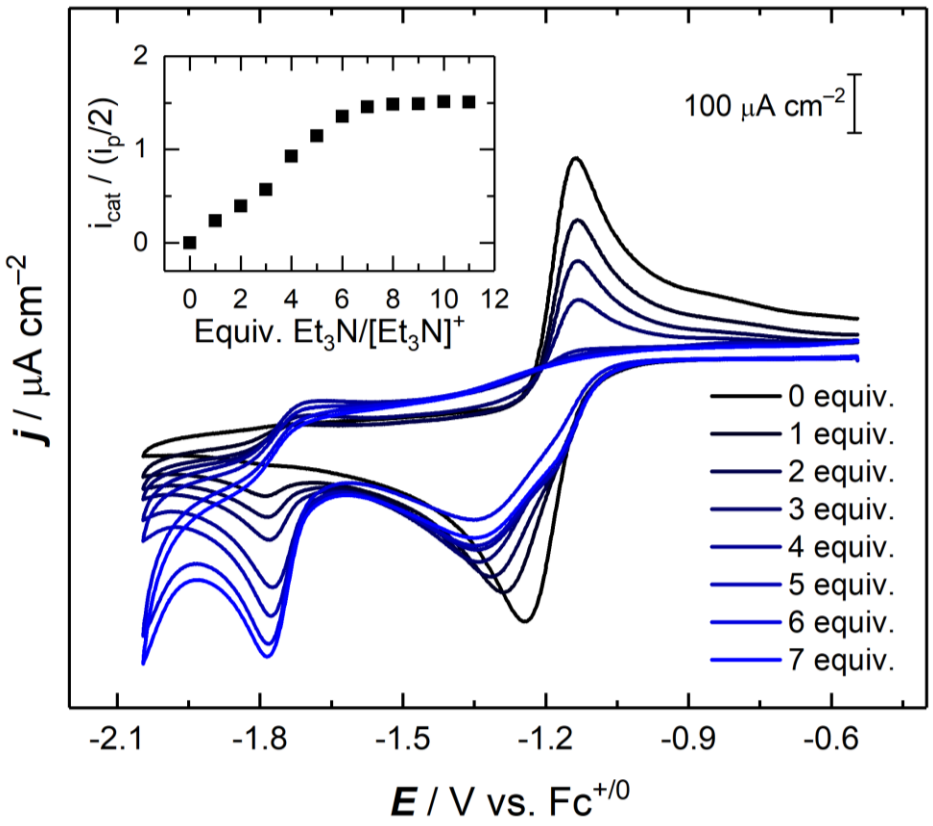

Figure B55. Cyclic voltammetry of **1-Cl** with 1 equv. of $[Et_3NH]^+/Et_3N$ in 50μL additions (CH_3CN, 0.1 M $[^nBu_4N][PF_6]$, 100 mV/s). (Inset): Plot of $i_{cat}/(i_{p/2})$ vs equivalents (mMol) of $[Et_3NH]^+/Et_3N$ added.

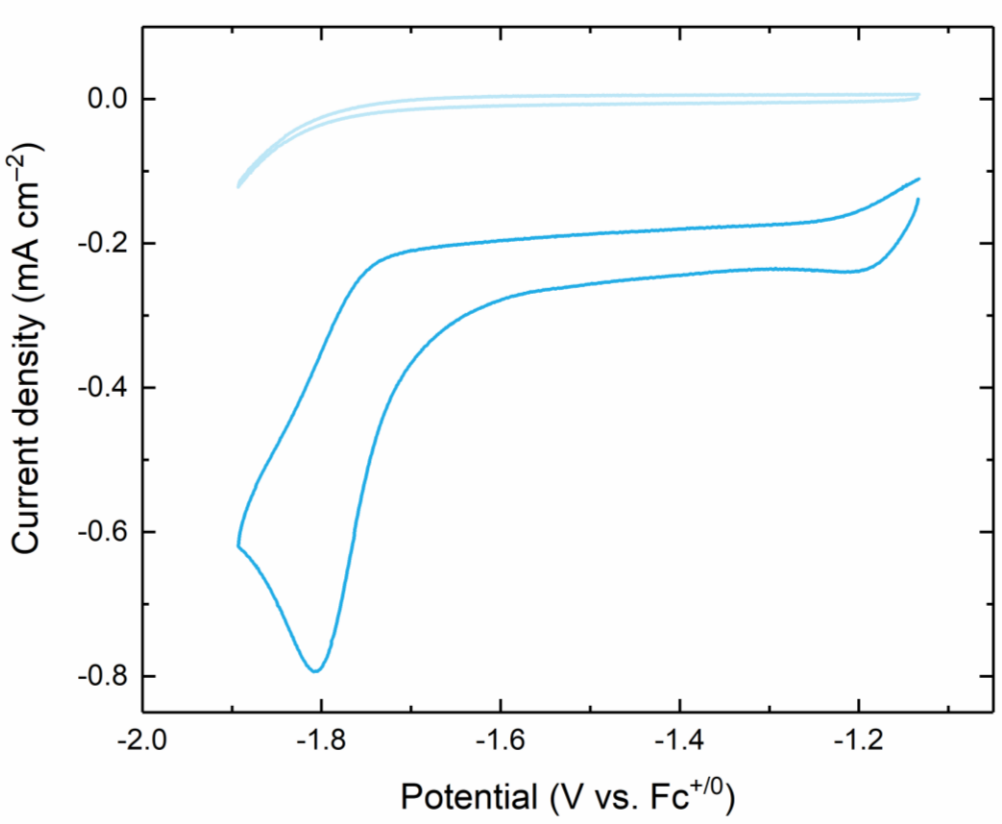

Figure B56. Cyclic voltammetry of $Et_3NH^+OTf^-$ (top); **1-Cl** and 1 equiv. of $Et_3NH^+OTf^-$ (bottom) (CH_3CN, 0.1 M [$^nBu_4N$][PF_6], 100 mV/s).

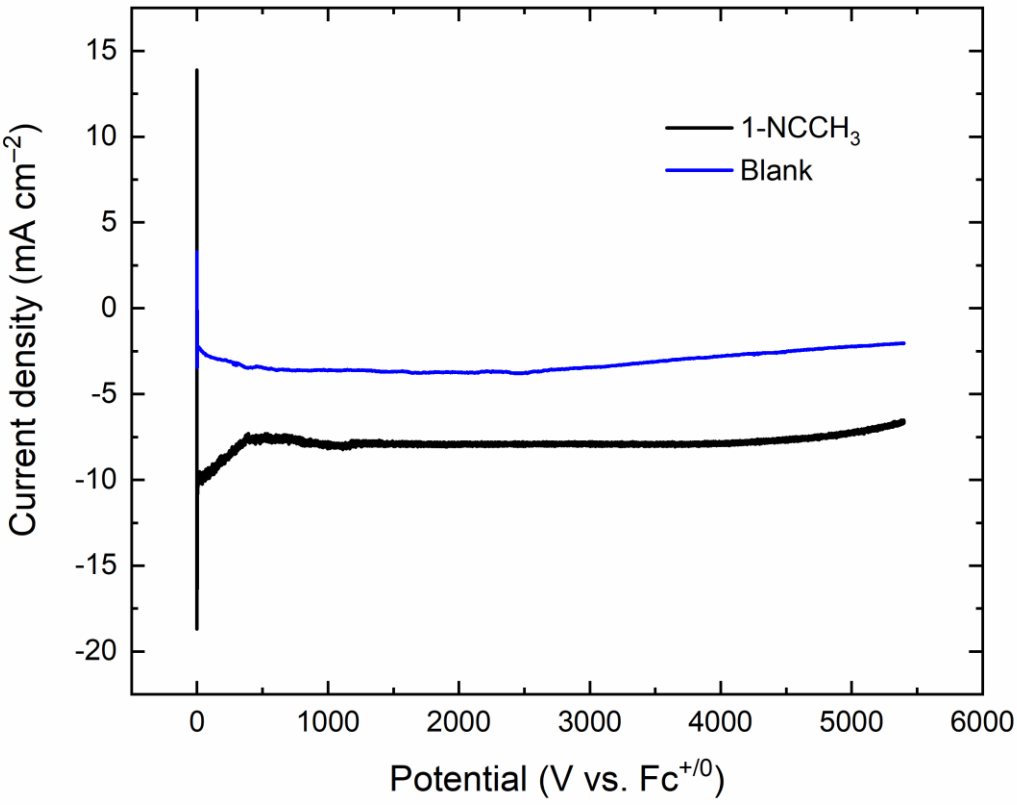

Figure B57. Chronoamperometry experiments conducted during bulk electrolyses with 1 mM **1-NCCH$_3$** plus acid (black line) and an acid-only blank (blue line). Polarization at −1.75 V vs $Fc^{+/0}$. Ten equivalents of ferrocene included as sacrificial reductant, and 10 equivalents of $[Et_3NH]Br$ added as the acid. Supporting electrolyte was 0.1 M $[^nBu_4N][PF_6]$ in each case.

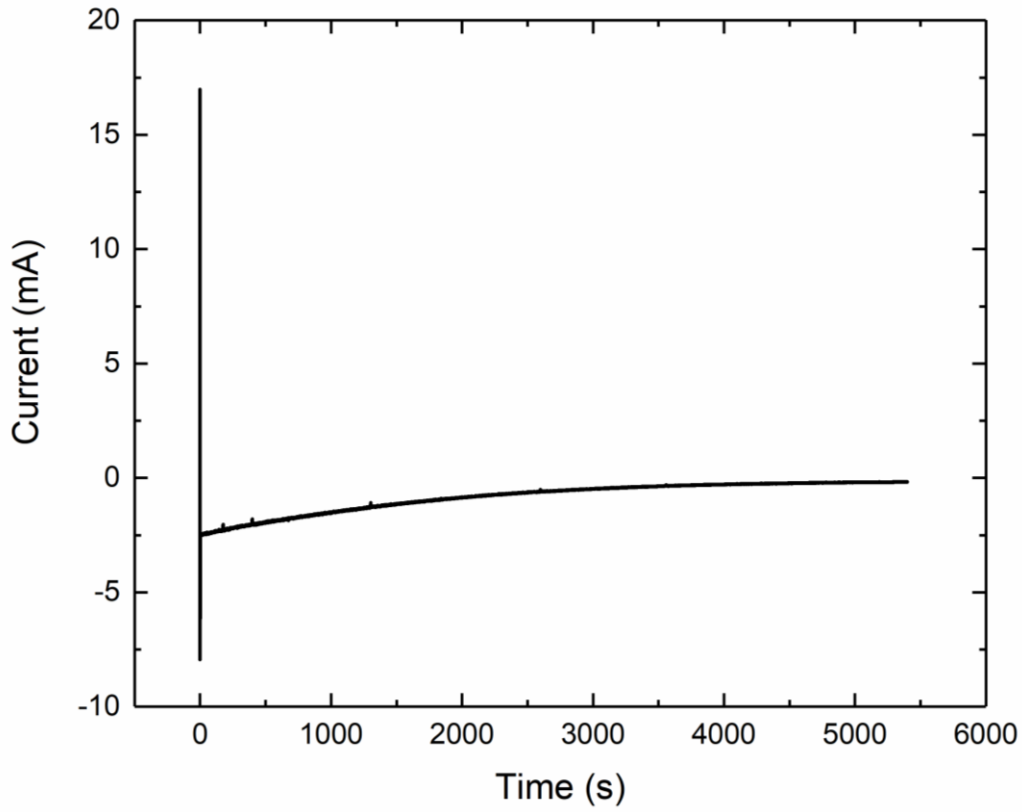

Figure B58. Bulk electrolysis data for **3** polarized at –1.75 V (CH_3CN, 0.1 M [$^nBu_4N$][PF_6]).

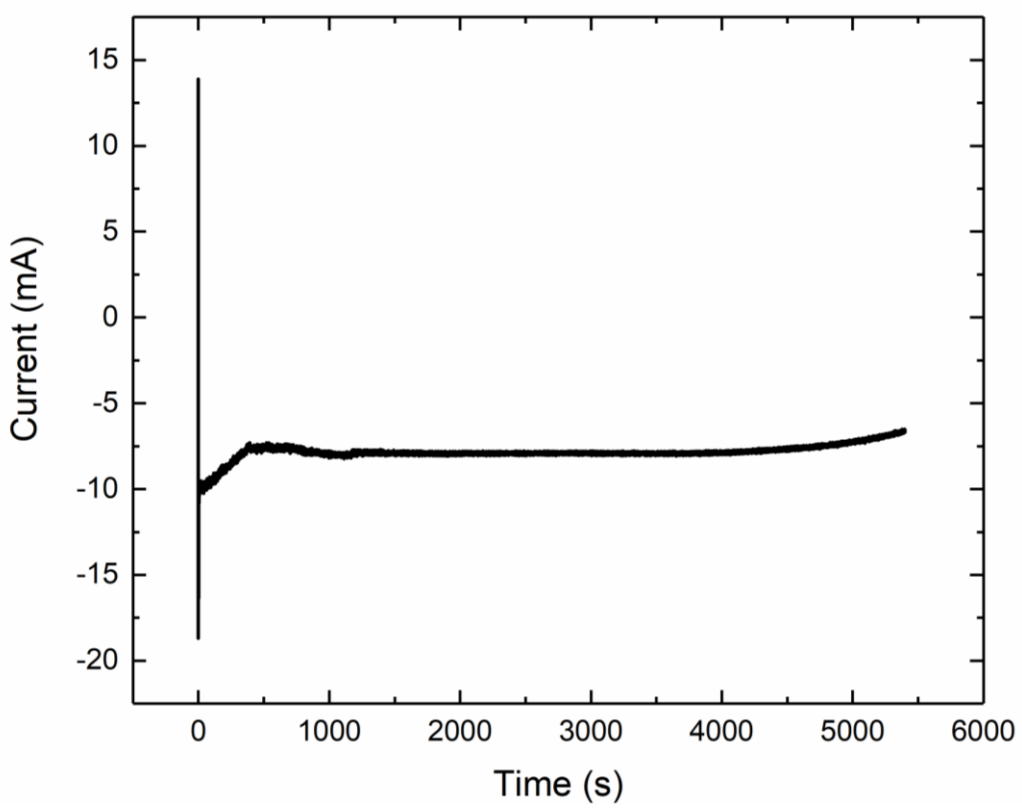

Figure B59. Bulk electrolysis data for **1-NCCH$_3$** with 10 equiv. of $Et_3NH^+OTf^-$ polarized at –1.75 V (CH_3CN, 0.1 M [$^nBu_4N$][PF_6], 100 mV/s).

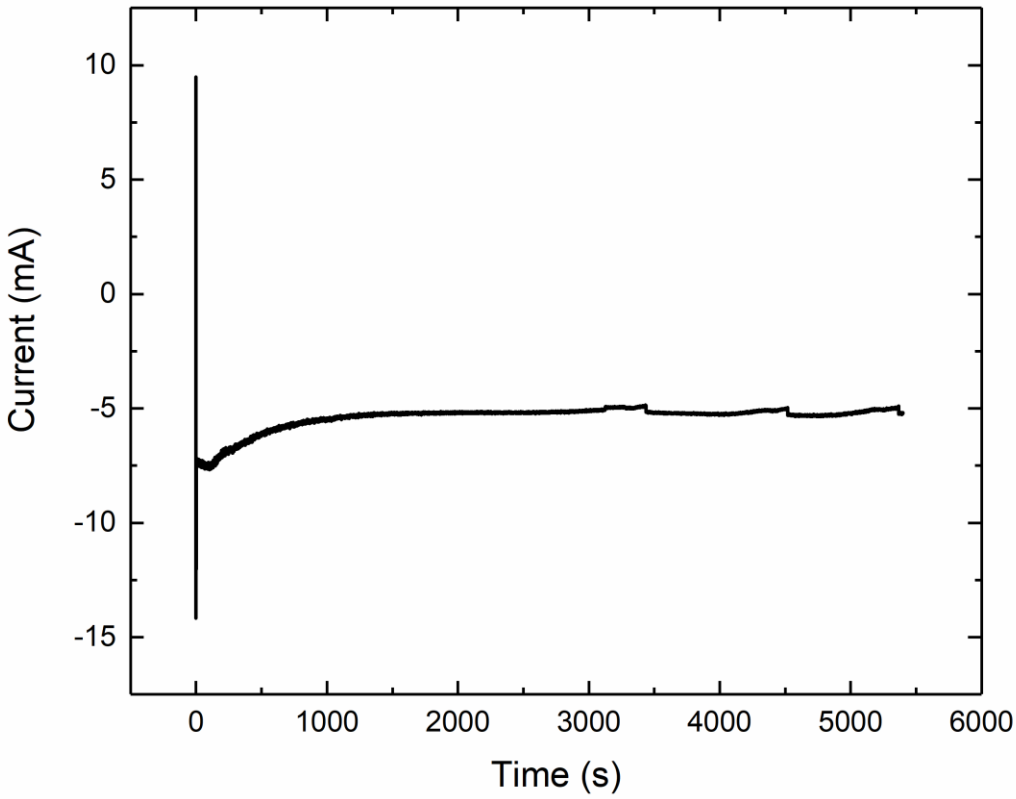

Figure B60. Bulk electrolysis data for **1-Cl** with 10 equiv. of $Et_3NH^+OTf^-$ polarized at –1.75 V (CH_3CN, 0.1 M [$^nBu_4N$][PF_6], 100 mV/s).

Table B1. Crystal and Refinement Data for [Cp*Rh(QPN)(Cl)]$^+$ [OTf] (**1-Cl**), [Cp*Rh(QPN)] (**2**) and [Cp*Rh(QPN)(H)]$^+$ [OTf] (**3**).

	1-Cl	**2**	**3**
CCDC number	1858635	1858633	1858634
Empirical formula	$C_{32}H_{31}ClF_3NO_3PRhS$	$C_{31}H_{31}NPRh$	$C_{32}H_{32}F_3NO_3PRhS$
Formula weight	735.97	551.45	701.52
Temperature	199.99	296.15	199.99
Wavelength	1.54178	1.54178	0.71073
Crystal system	monoclinic	monoclinic	triclinic
Space group	$P2_1/n$	$P2_1/n$	P-1
a	12.9399(2) Å	9.0754(2) Å	10.5485(9) Å
b	15.7672(3) Å	17.3941(4) Å	10.5301(9) Å
c	15.3994(3) Å	16.7425(4) Å	14.8517(12) Å
α	90	90	70.4770(10)
β	94.0144(6)	101.7270(10)	76.8720(10)
γ	90	90	82.9990(10)
Volume	3134.17(10) Å^3	2587.78(10) Å^3	1512.3(2) Å^3
Z	4	4	2
Density (calculated)	1.560 g/cm^3	1.415 g/cm^3	1.541 g/cm^3
Absorption coefficient	6.747 mm^{-1}	6.053 mm^{-1}	0.739 mm^{-1}
F(000)	1496.0	1136.0	716.0
Crystal size	0.14 × 0.085 × 0.045 mm^3	0.17 × 0.085 × 0.03 mm^3	0.24 × 0.23 × 0.08 mm^3
Theta range	8.036 to 140.37	7.41 to 140.456	3.97 to 61.508
Index ranges	$-14 \le h \le 15$, $-18 \le k \le 18$, $-15 \le l \le 18$	$-10 \le h \le 8$, $-20 \le k \le 21$, $-20 \le l \le 18$	$-14 \le h \le 15$, $-14 \le k \le 15$, $-21 \le l \le 21$
Reflections collected	16617	25594	17776
Independent reflections	5720 [R_{int} = 0.0311, R_{sigma} = 0.0311]	4692 [R_{int} = 0.0276, R_{sigma} = 0.0208]	8957 [R_{int} = 0.0380, R_{sigma} = 0.0681]
Absorption correction	Multi-scan	Multi-scan	Multi-scan
Max. and min. transmission	0.7533, 0.5664	0.839, 0.426	0.943, 0.842
Refinement method	Full-matrix least-squares on F^2	Full-matrix least-squares on F^2	Full-matrix least-squares on F^2
Data / restraints / parameters	5720/0/393	4692/0/313	8957/0/452
Goodness-of-fit on F^2	1.072	1.094	0.914
Final R indices [I>2σ(I)]	R_1 = 0.0325, wR_2 = 0.0837	R_1 = 0.0212, wR_2 = 0.0536	R_1 = 0.0466, wR_2 = 0.1251
R indices (all data)	R_1 = 0.0342, wR_2 = 0.0852	R_1 = 0.0217, wR_2 = 0.0539	R_1 = 0.0728, wR_2 = 0.1485
Largest diff. peak and hole	1.24 and -0.76 e$^-$/Å^3	0.30 and -0.41 e$^-$/Å^3	1.35/-0.98 e$^-$/Å^3

[a] R1 $\Sigma||F_o|-|F_c|| / \Sigma|F_o|$ [b] wR2 = $[\ \Sigma\ [w(F_o^2-F_c^2)^2] / \Sigma\ [w(F_o^2)^2]\ ]^{1/2}$

Table B2. Selected Bond Lengths for **1-Cl, 2 and 3**.

Bond	**1-Cl**	**2**	**3**
Rh–Cl	2.3784(9)	—	—
Rh–P	2.260(9)	2.1744(4)	2.2486(8)
Rh–N	2.140(3)	2.0294(13)	2.093(3)
Rh–Cp*	1.830	1.917	1.862
Rh–H41	—	—	1.48(4)

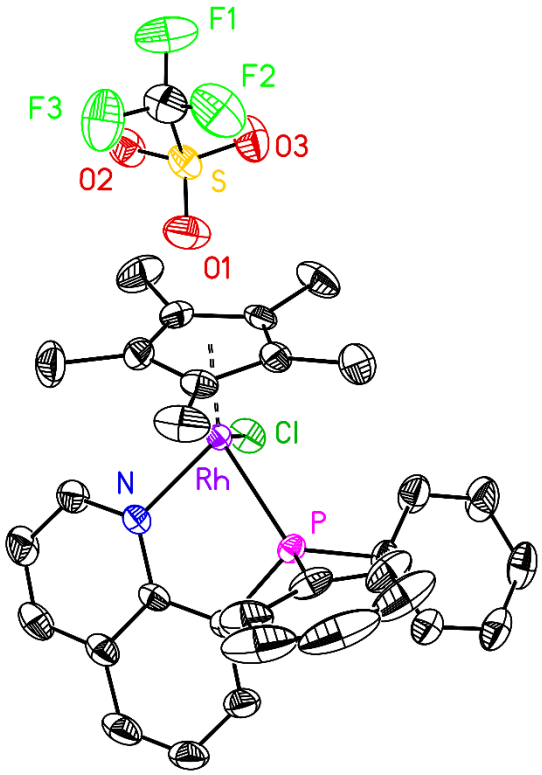

Figure B61. Full solid-state structure of **1-Cl**. Hydrogen atoms omitted for clarity. Displacement ellipsoids shown at the 50% probability level.

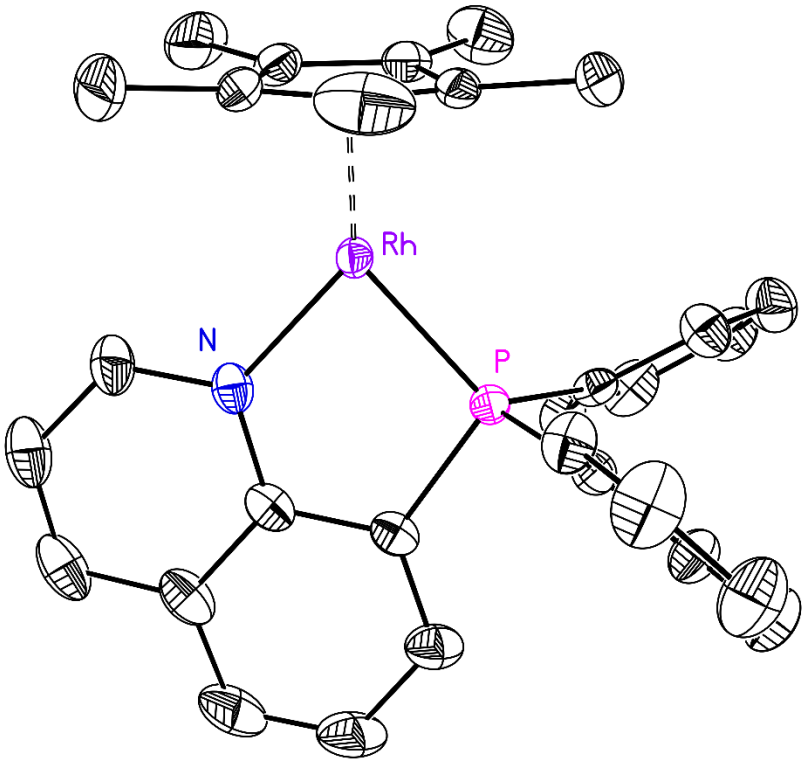

Figure B62. Full solid-state structure of **2**. Hydrogen atoms omitted for clarity. Displacement ellipsoids shown at the 50% probability level.

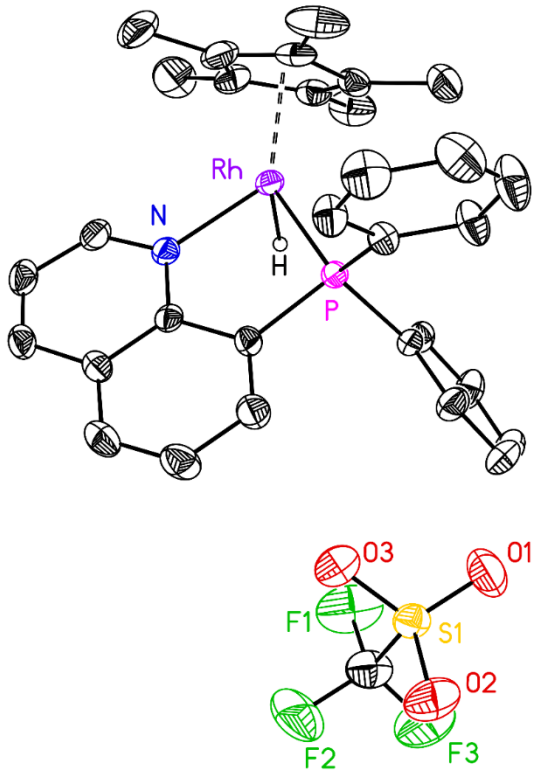

Figure B63. Full solid-state structure of **3**. Hydrogen atoms except for H41 omitted for clarity. Displacement ellipsoids shown at the 50% probability level.

Appendix C

Supplementary Information for Chapter 5

NMR Spectra

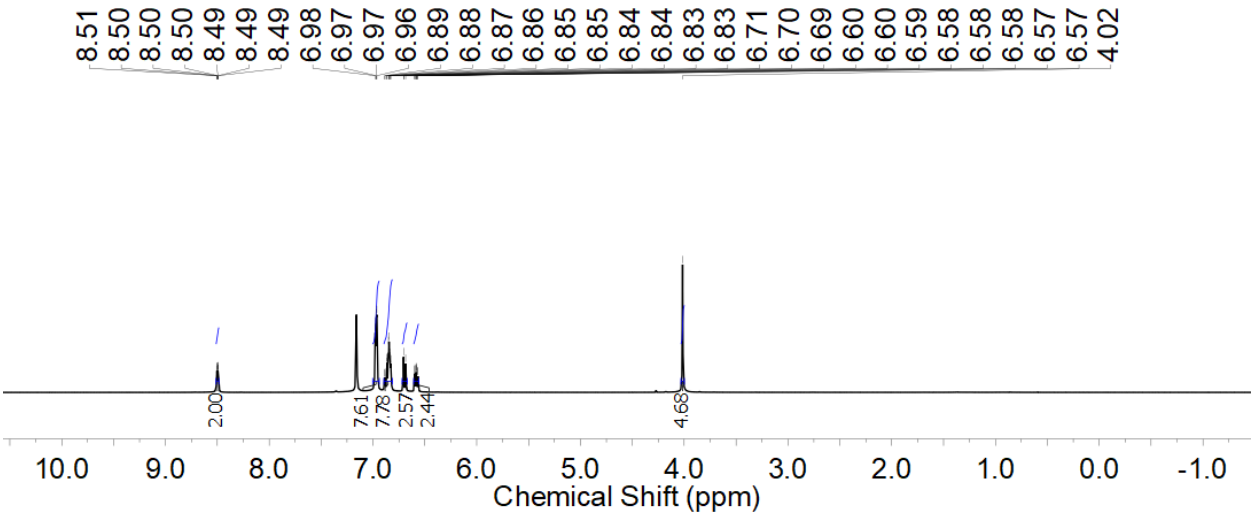

Figure C1. ^{1}H NMR spectrum (500 MHz, C_6D_6) of $\mathbf{L^{Bn2}}$.

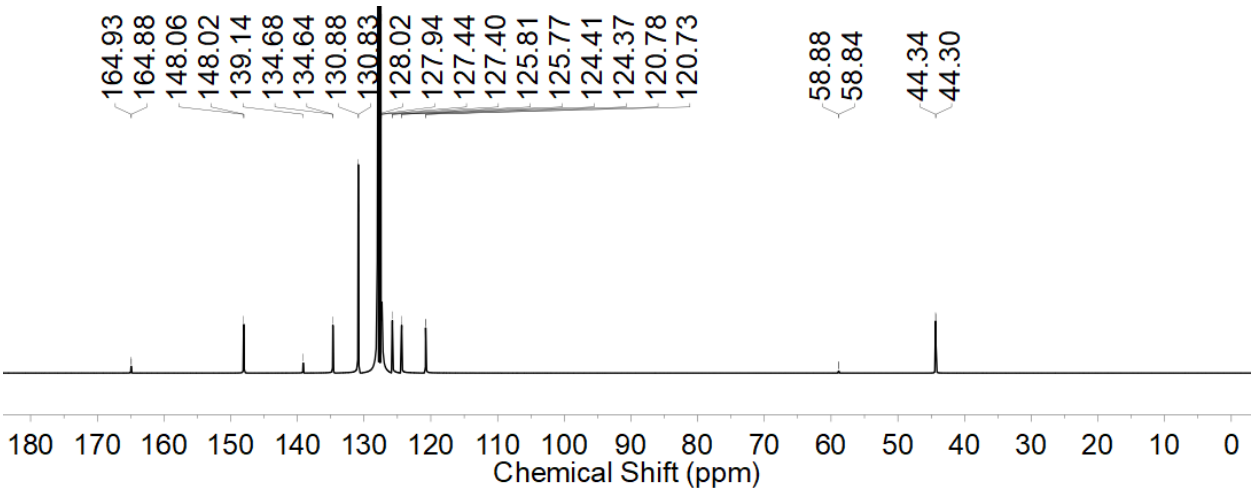

Figure C2. ^{13}C NMR spectrum (126 MHz, C_6D_6) of $\mathbf{L^{Bn2}}$.

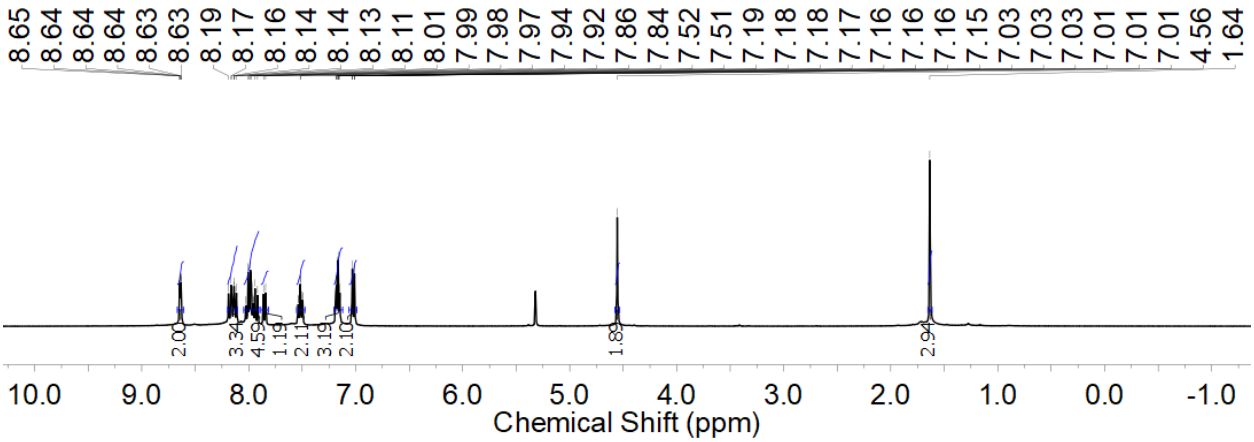

Figure C3. ^{1}H NMR spectrum (500 MHz, CD_2Cl_2) of $\mathbf{L^{MePyr}}$.

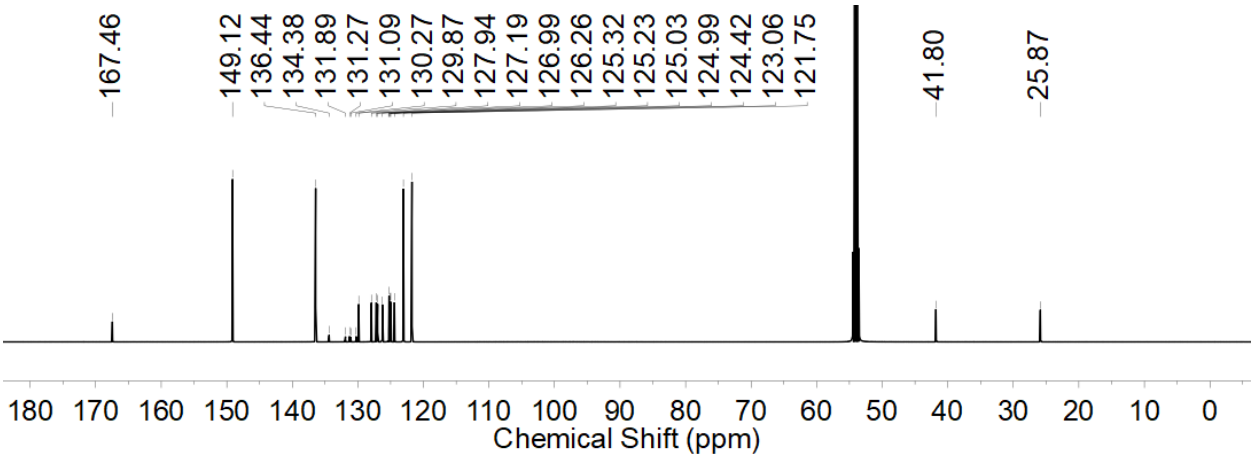

Figure C4. $^{13}C\{^{1}H\}$ NMR spectrum (126 MHz, CD_2Cl_2) of $\mathbf{L^{MePyr}}$.

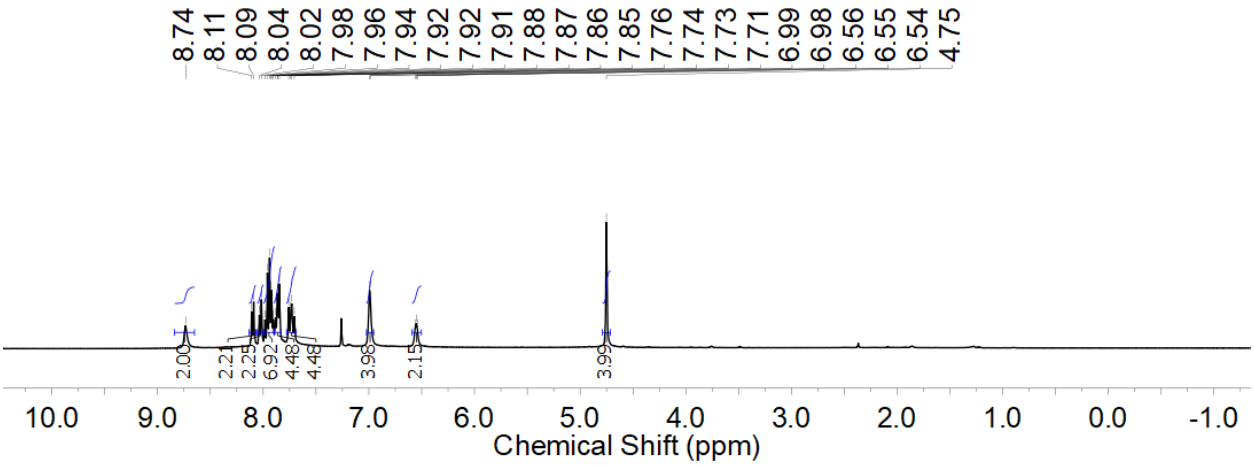

Figure C5. ^{1}H NMR spectrum (400 MHz, $CDCl_3$) of $\mathbf{L^{Pyr2}}$.

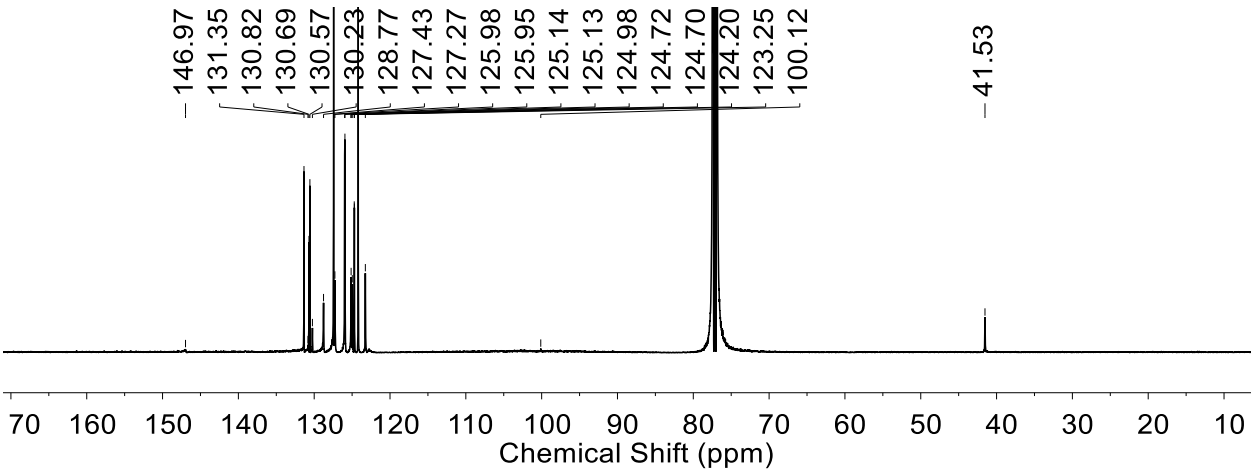

Figure C6. $^{13}C\{^{1}H\}$ NMR spectrum (126 MHz, $CDCl_3$) of $\mathbf{L^{Pyr2}}$.

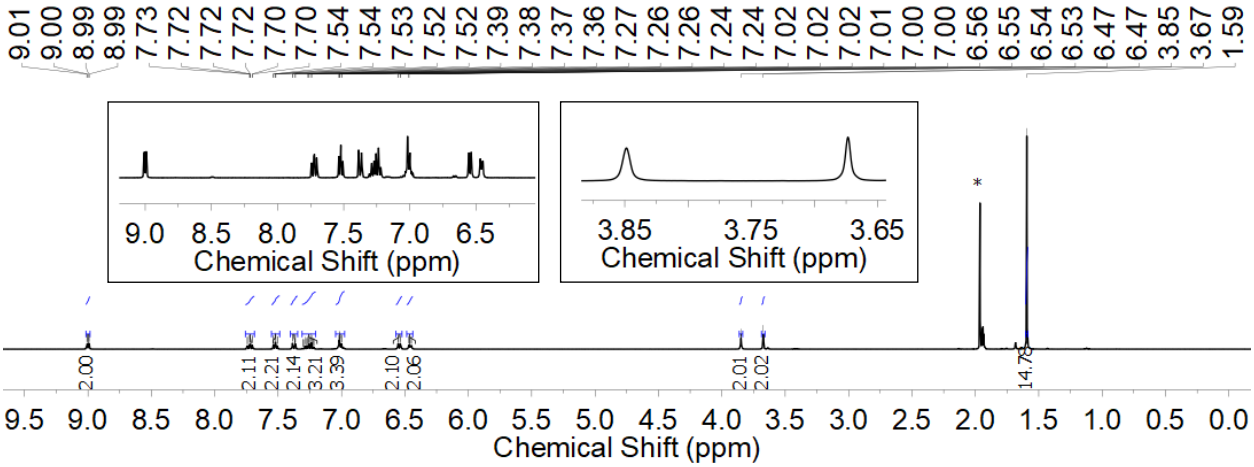

Figure C7. ^{1}H NMR spectrum (400 MHz, CD_3CN) of $\mathbf{A^{LBn2}}$. Adventitious CH_3CN (marked with *) was found to be present in the CD3CN solvent.

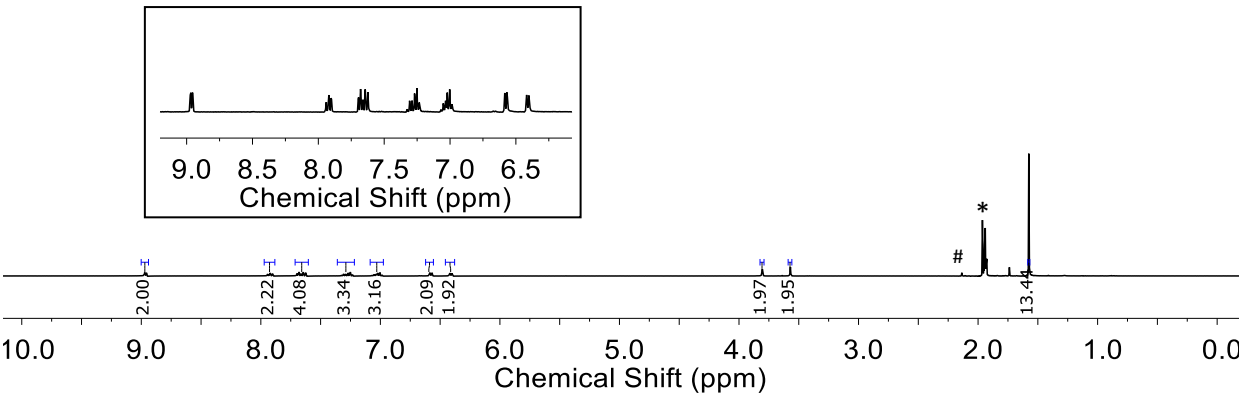

Figure C8. ^{1}H NMR spectrum (400 MHz, CD_3CN) of **1**$^{\mathbf{LBn2}}$. CH_3CN present, extensive drying of solvento complexes causes decomposition of complexes. Adventitious CH_3CN and small amount of H_2O (marked with * and #, respectively) were found to be present in the CD_3CN solvent.

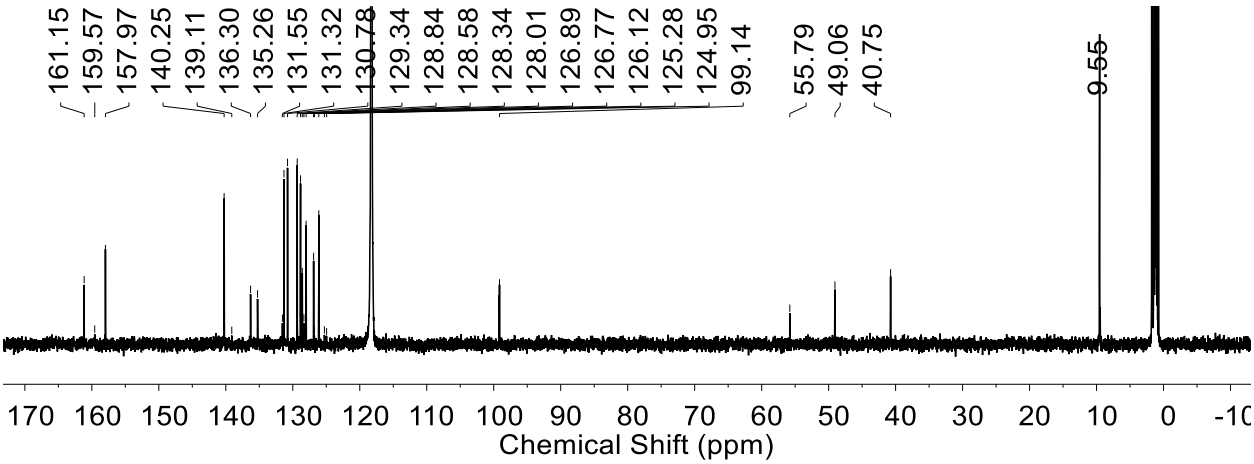

Figure C9. $^{13}C\{^{1}H\}$ NMR spectrum (126 MHz, CD_3CN) of **A**$^{\mathbf{LBn2}}$.

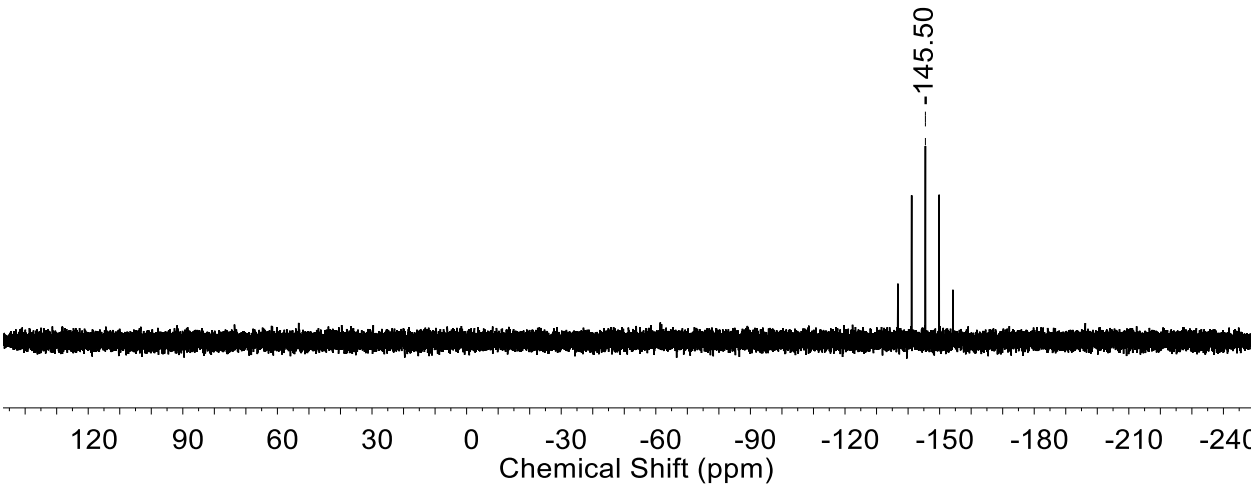

Figure C10. $^{31}P\{^{1}H\}$ NMR spectrum (162 MHz, CD_3CN) of $\mathbf{A}^{\mathbf{LBn2}}$.

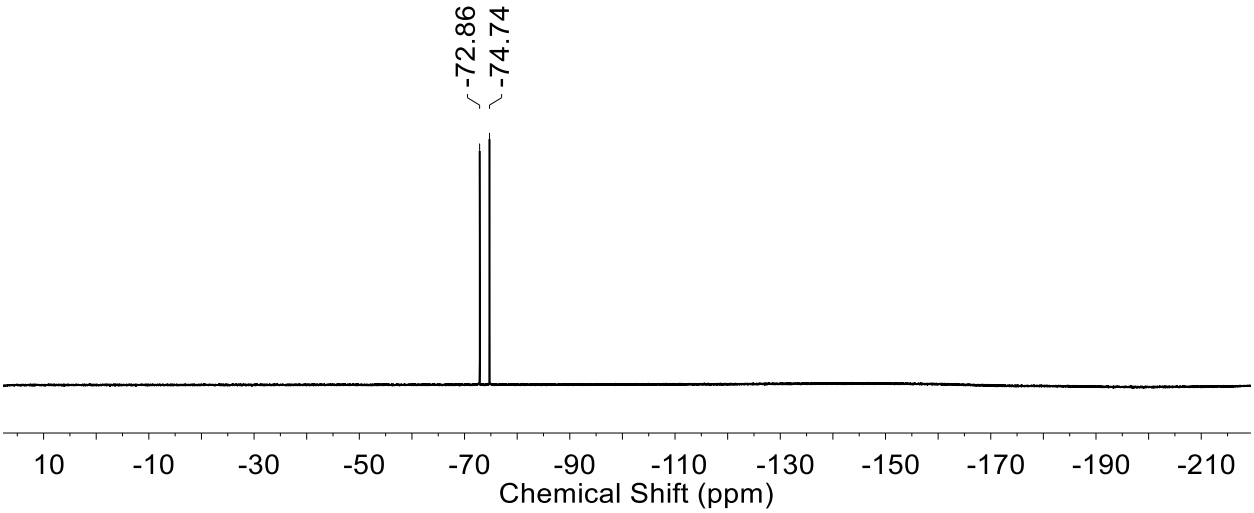

Figure C11. ^{19}F NMR spectrum (376 MHz, CD_3CN) of $\mathbf{A}^{\mathbf{LBn2}}$.

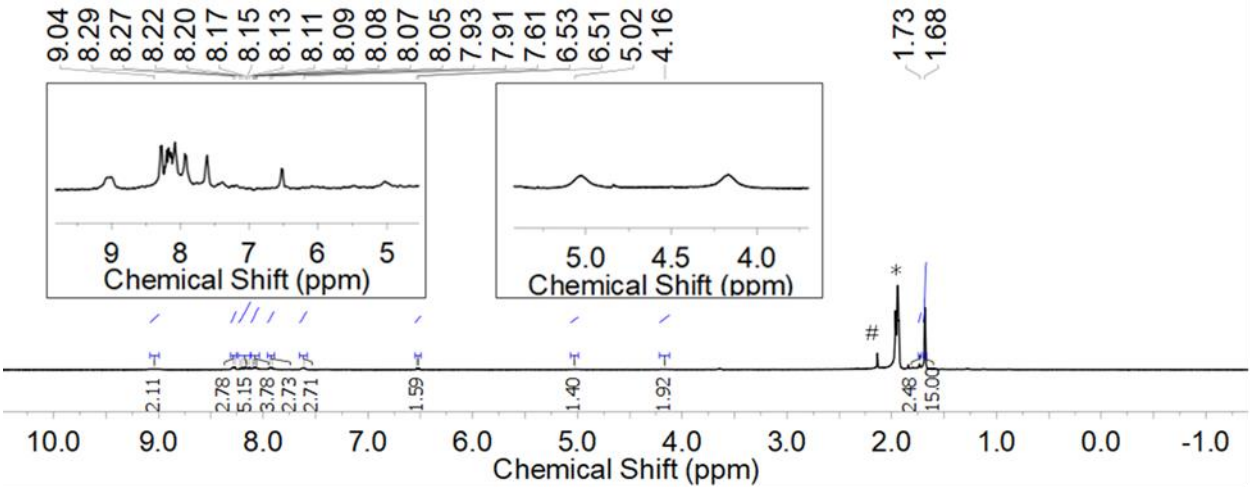

Figure C12. ^{1}H NMR spectrum (400 MHz, CD_3CN) of $\mathbf{A}^{\mathbf{LMePyr}}$. Adventitious CH_3CN and small amount of H_2O (marked with * and #, respectively) was found to be present in the CD_3CN solvent.

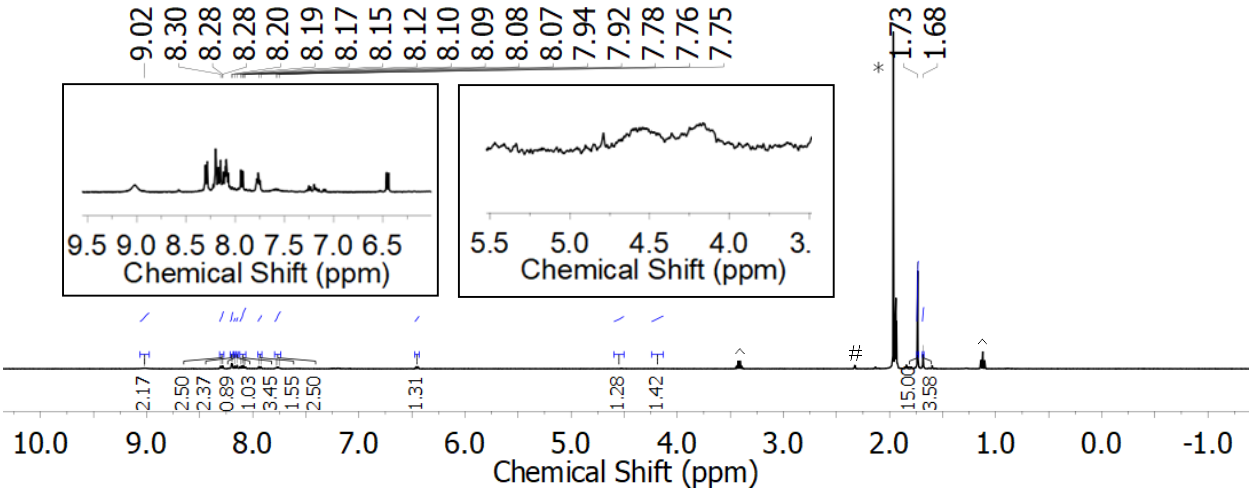

Figure C13. ^{1}H NMR spectrum (400 MHz, CD_3CN) of $\mathbf{1}^{\mathbf{LMePyr}}$. Some incidental Et_2O present (marked with ^) and CH_3CN present, extensive drying of solvento complexes causes decomposition of complexes. Adventitious CH_3CN and small amount of H_2O (marked with * and #, respectively) was found to be present in the CD_3CN solvent.

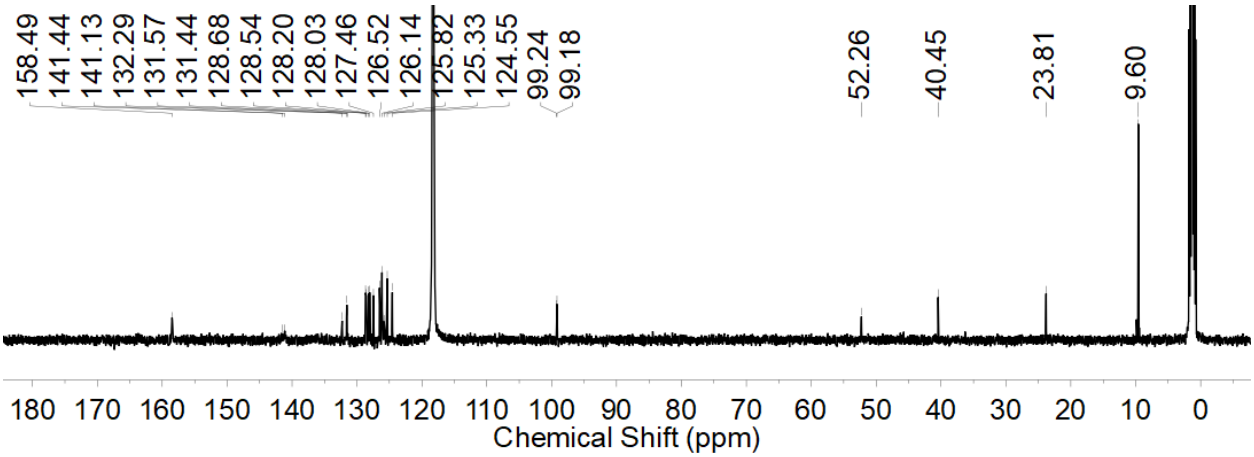

Figure C14. $^{13}C\{^{1}H\}$ NMR spectrum (126 MHz, CD_3CN) of $\mathbf{A}^{\mathbf{LMePyr}}$.

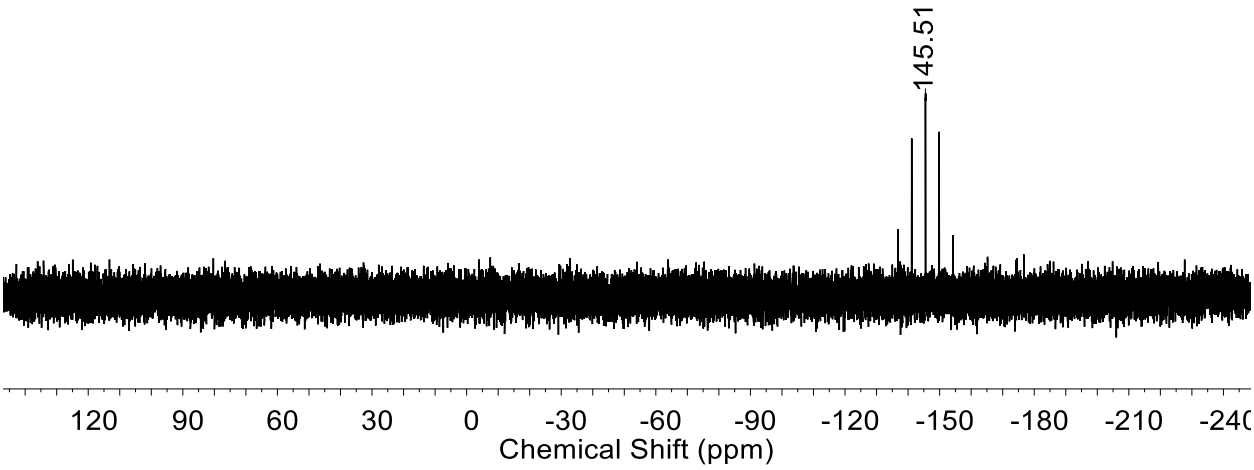

Figure C15. $^{31}P\{^{1}H\}$ NMR spectrum (162 MHz, CD_3CN) of $\mathbf{A}^{\mathbf{LMePyr}}$.

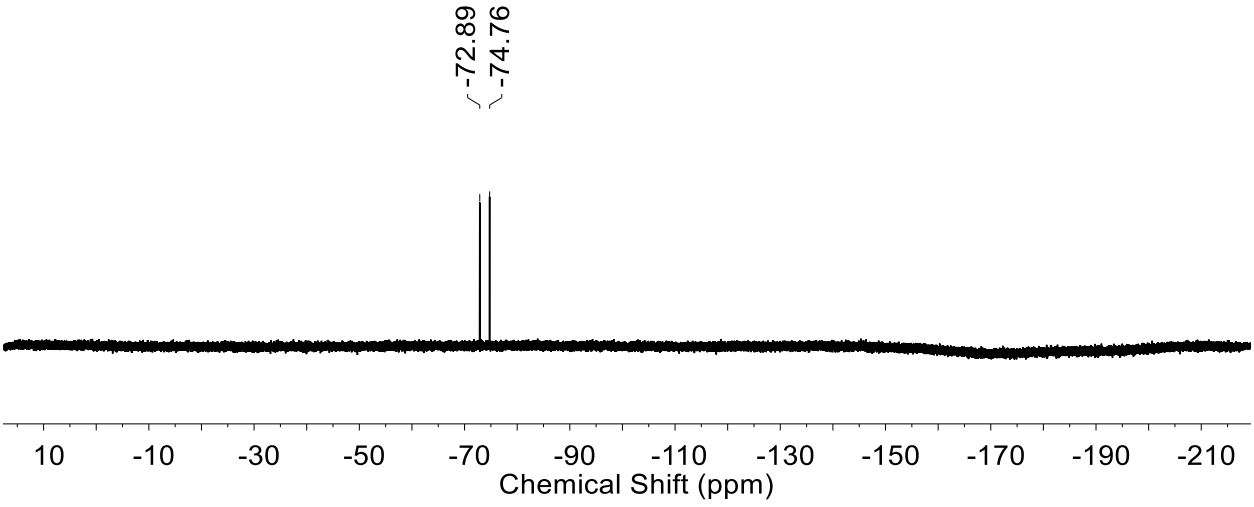

Figure C16. ^{19}F NMR spectrum (376 MHz, CD_3CN) of $\mathbf{A}^{\mathbf{LMePyr}}$.

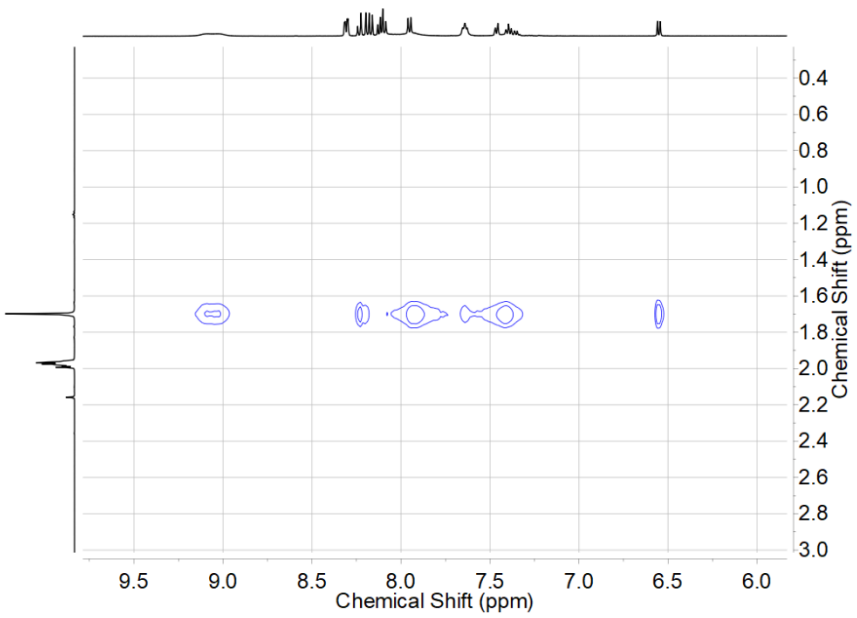

Figure C17. Aromatic region NOESY NMR spectrum of $\mathbf{A}^{\mathbf{LMePyr}}$.

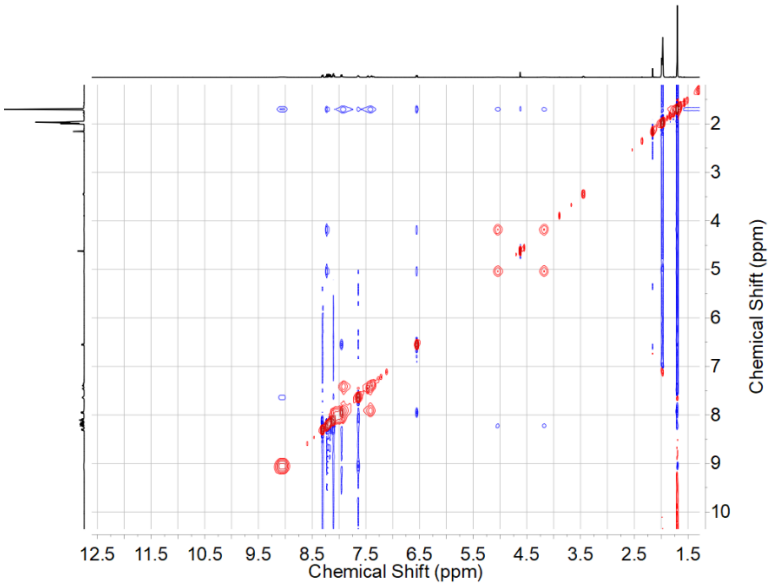

Figure C18. NOESY NMR spectrum of $\mathbf{A}^{\mathbf{LMePyr}}$.

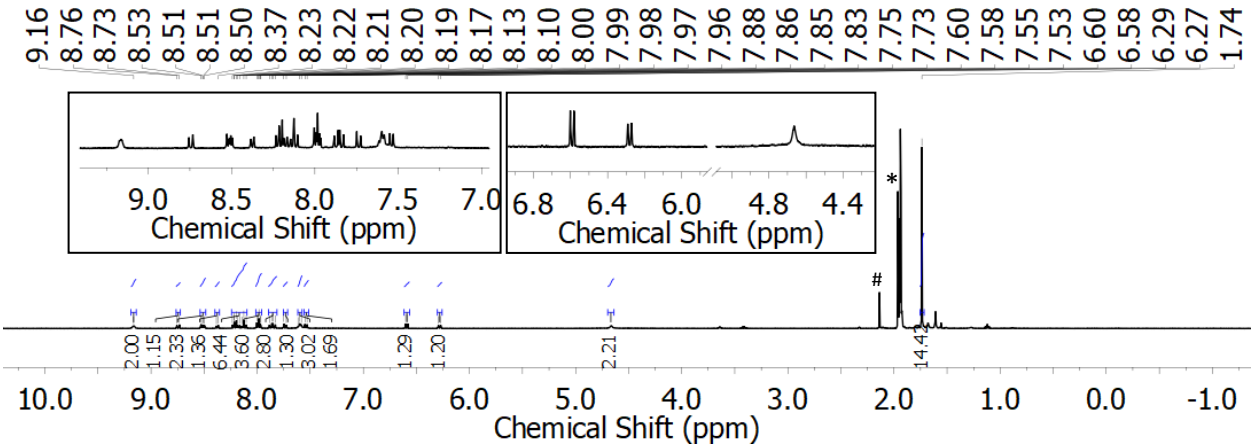

Figure C19. ^{1}H NMR spectrum (400 MHz, CD_3CN) of $\mathbf{A^{LPyr2}}$. CH_3CN and small H_2O peak present due to solvent impurity in CD_3CN. Adventitious CH_3CN and small amount of H_2O (marked with * and #, respectively) was found to be present in the CD_3CN solvent.

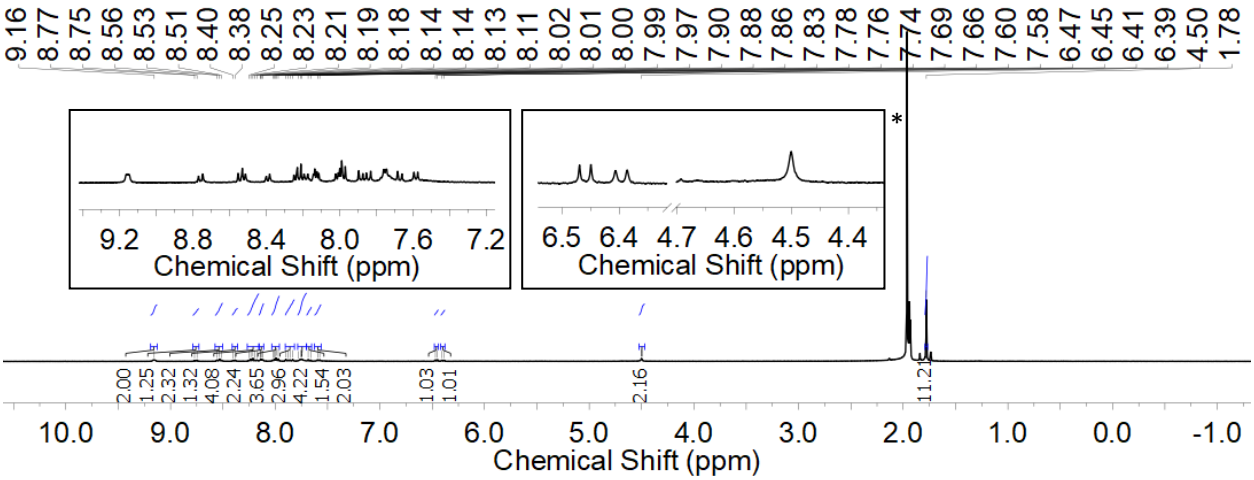

Figure C20. ^{1}H NMR spectrum (400 MHz, CD_3CN) of $\mathbf{1^{LPyr2}}$. CH_3CN present (marked with *), extensive drying of solvento complexes causes decomposition of complexes.

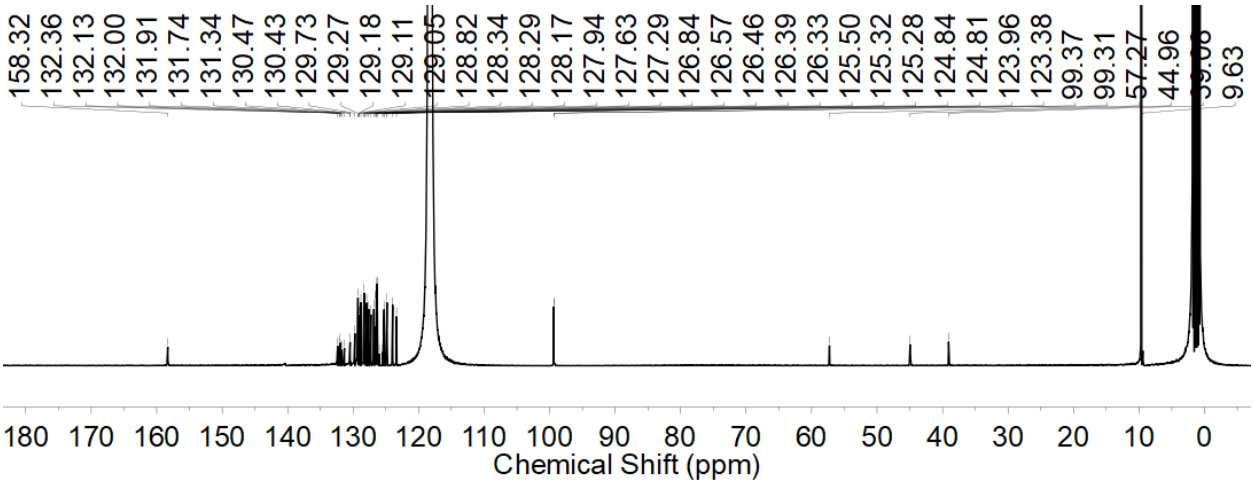

Figure C21. $^{13}C\{^{1}H\}$ NMR spectrum (126 MHz, CD_3CN) of $\mathbf{A}^{\mathbf{LPyr2}}$.

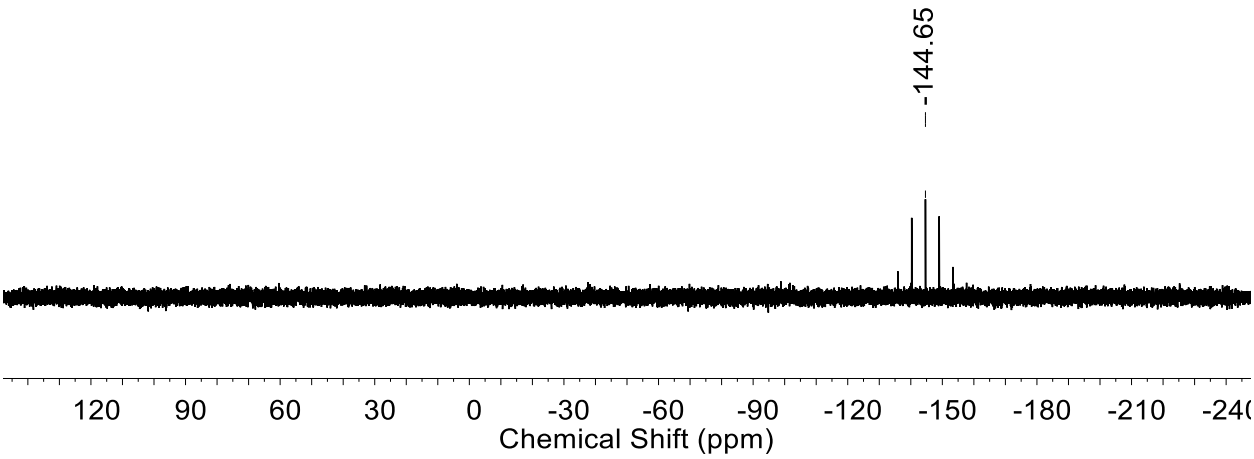

Figure C22. $^{31}P\{^{1}H\}$ NMR spectrum (162 MHz, CD_3CN) of $\mathbf{A}^{\mathbf{LPyr2}}$.

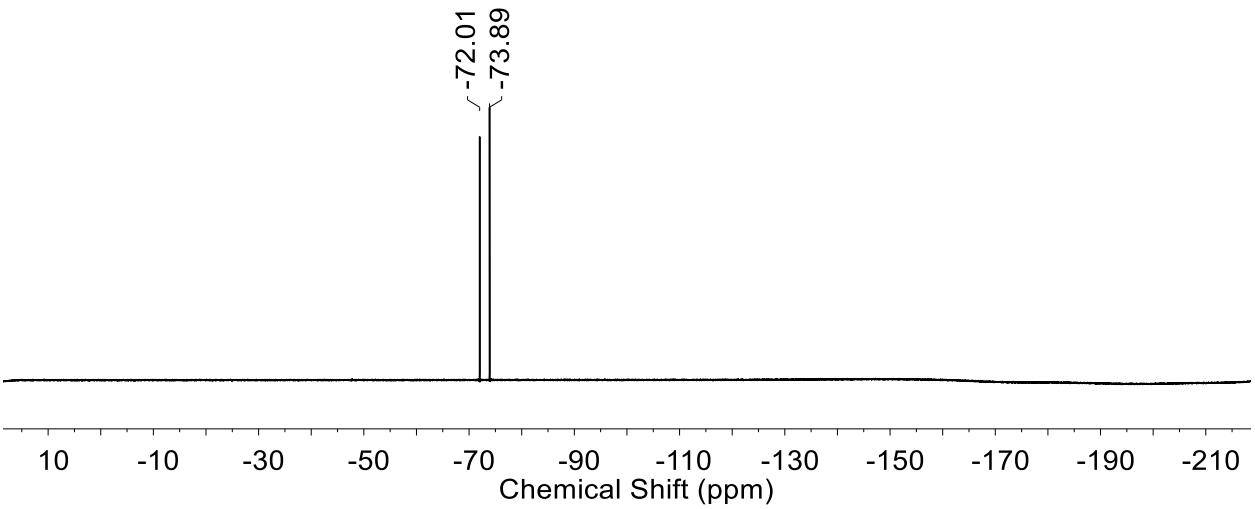

Figure C23. ^{19}F NMR spectrum (376 MHz, CD_3CN) of $\mathbf{A}^{\mathbf{LPyr2}}$.

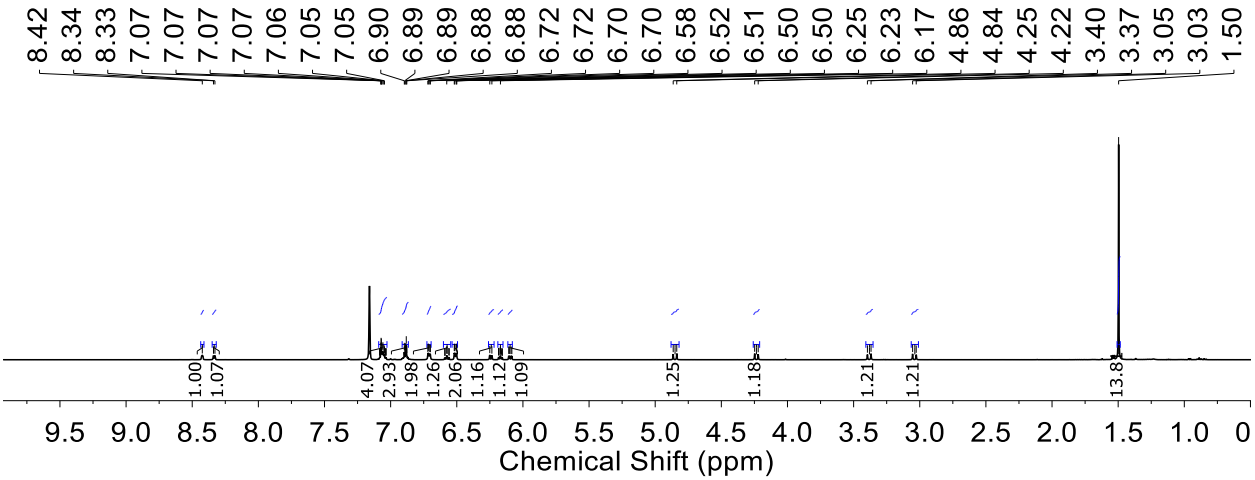

Figure C24. ^{1}H NMR spectrum (400 MHz, C_6D_6) of $\mathbf{4}^{\mathbf{LBn2}}$.

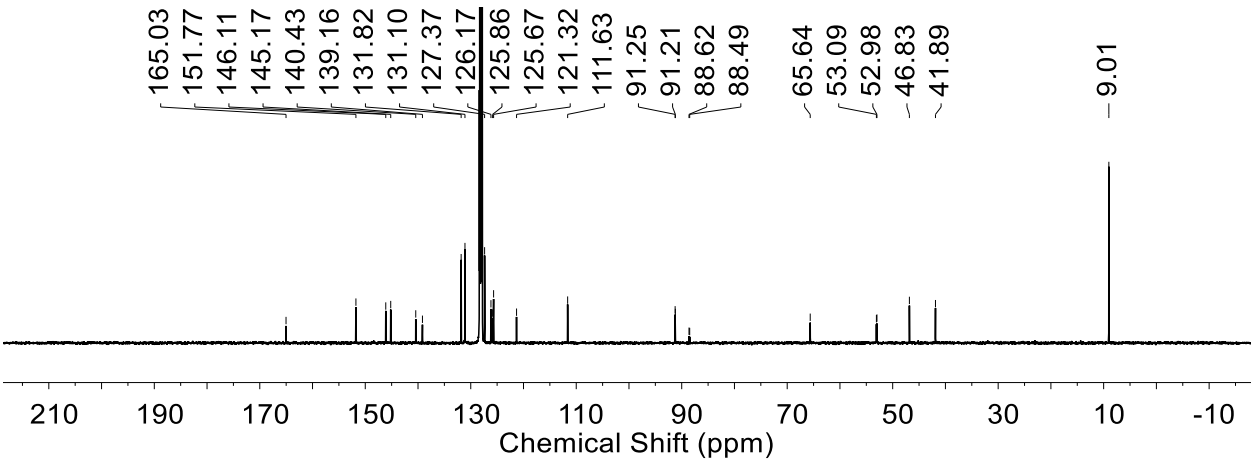

Figure C25. $^{13}C\{^{1}H\}$ NMR spectrum (126 MHz, C_6D_6) of $\mathbf{4^{LBn2}}$.

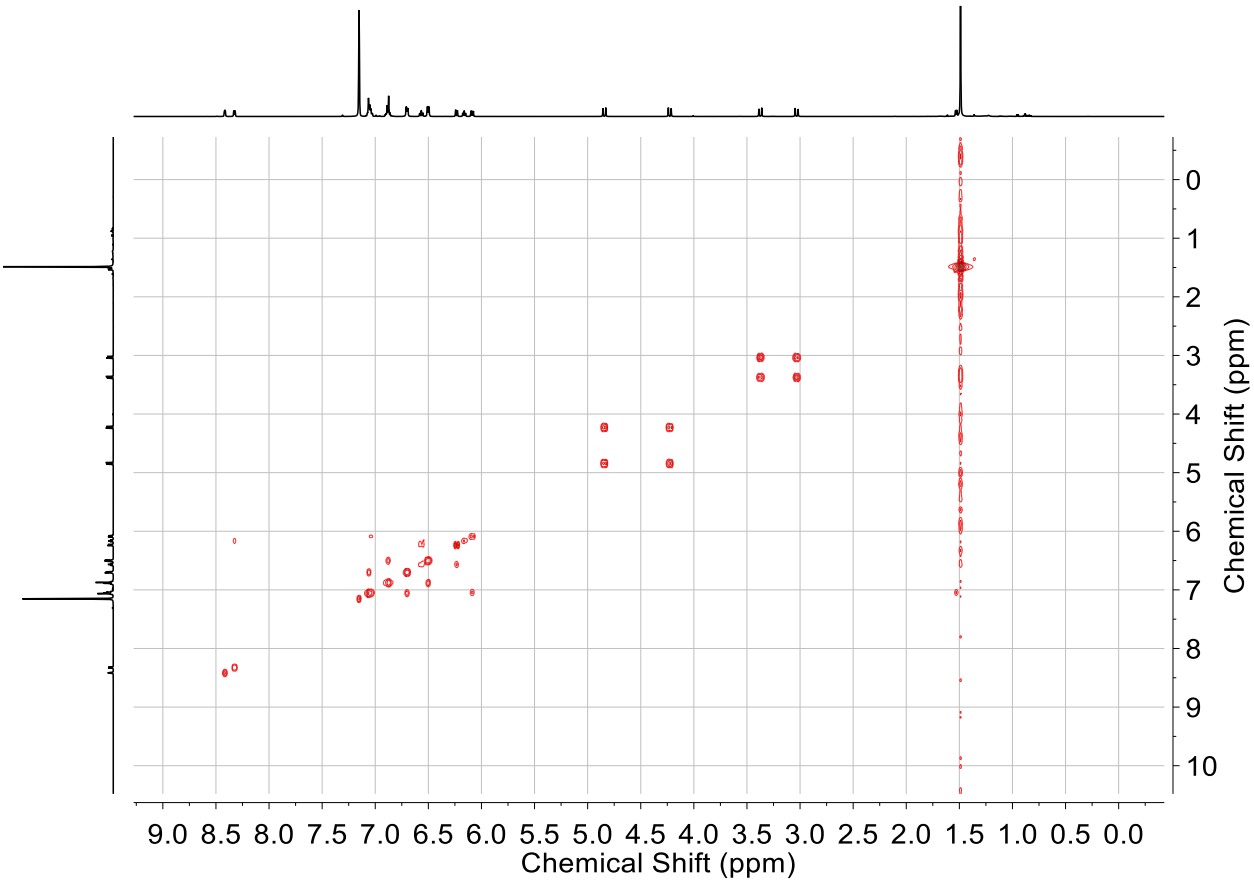

Figure C26. COSY NMR spectrum (C_6D_6) of $\mathbf{4^{LBn2}}$.

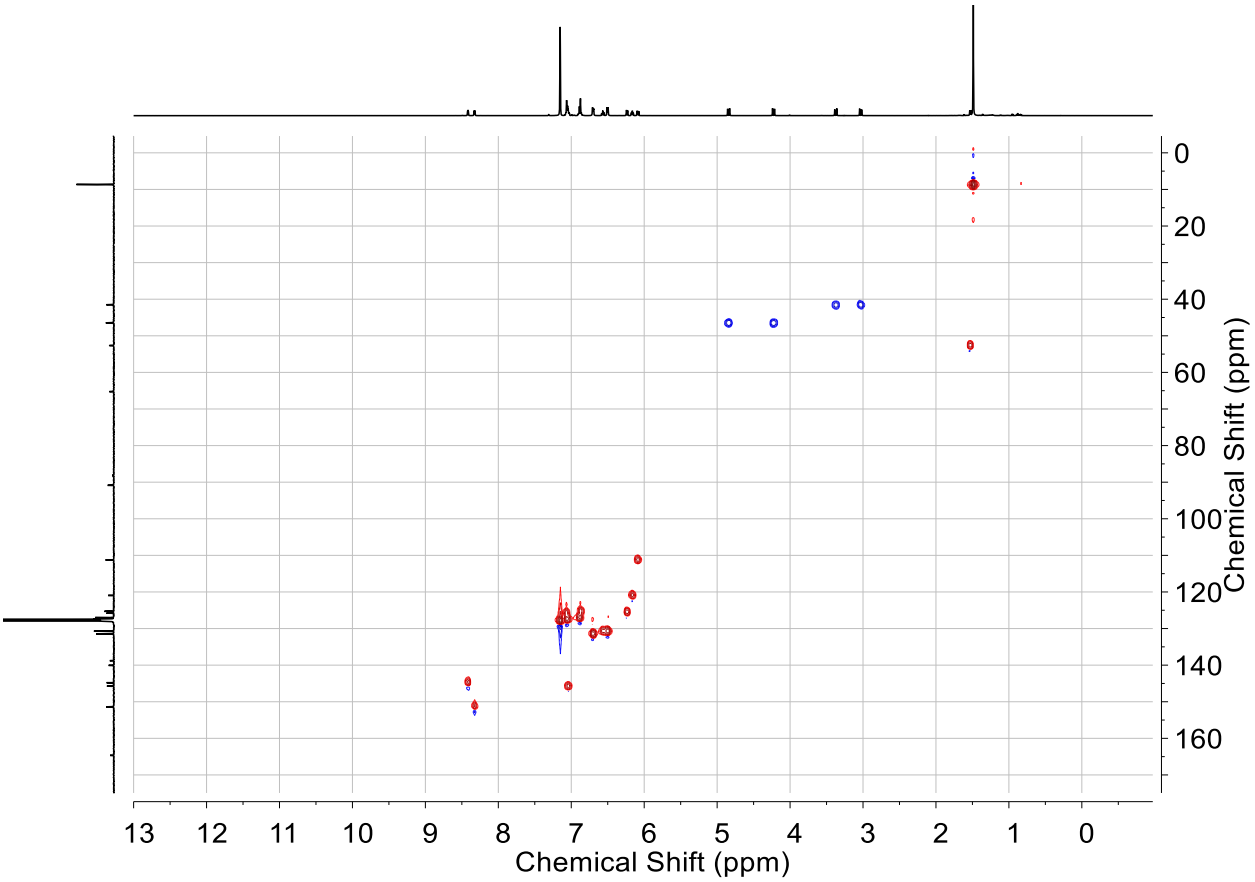

Figure C27. HSQC NMR spectrum (C_6D_6) of $\mathbf{4^{LBn2}}$.

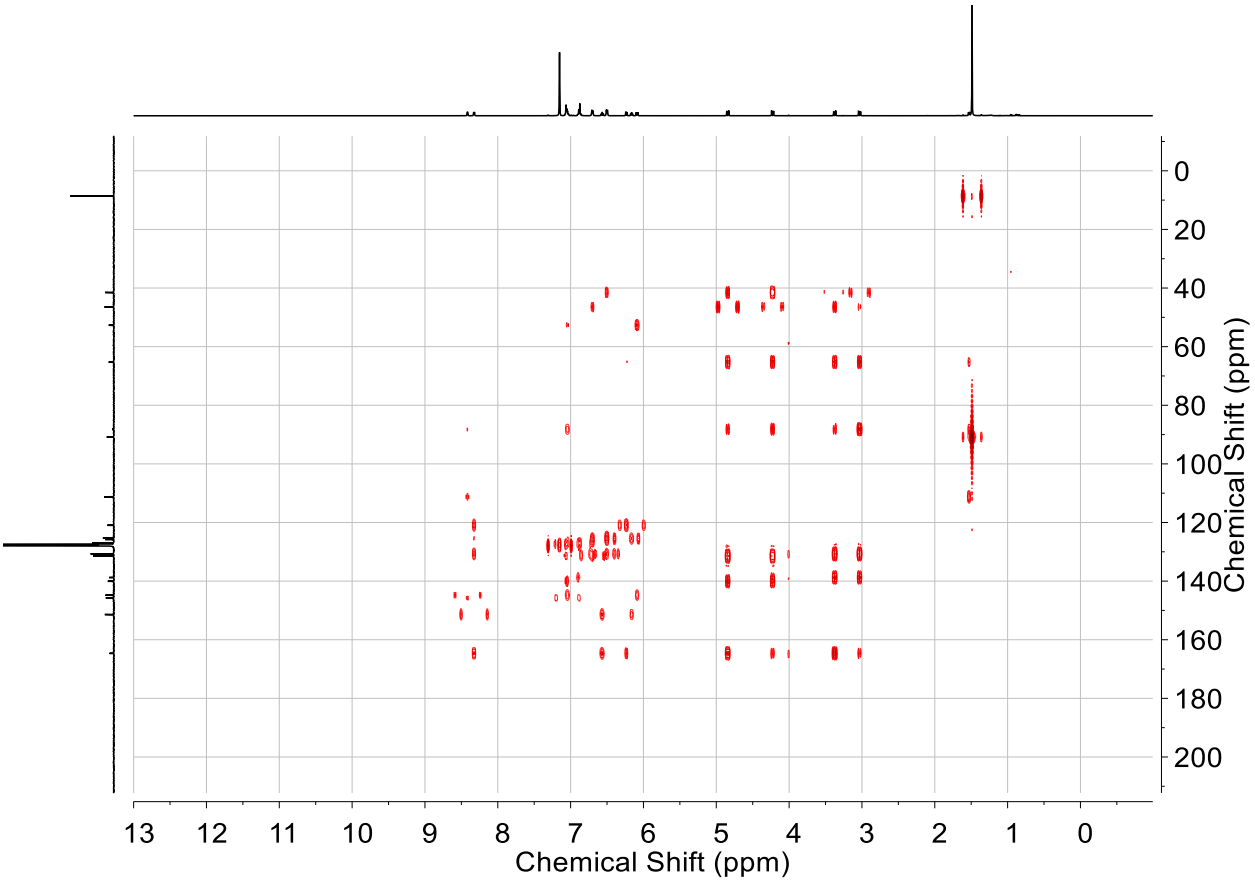

Figure C28. HMBC NMR spectrum (C_6D_6) of $\mathbf{4^{LBn2}}$.

Electrochemistry

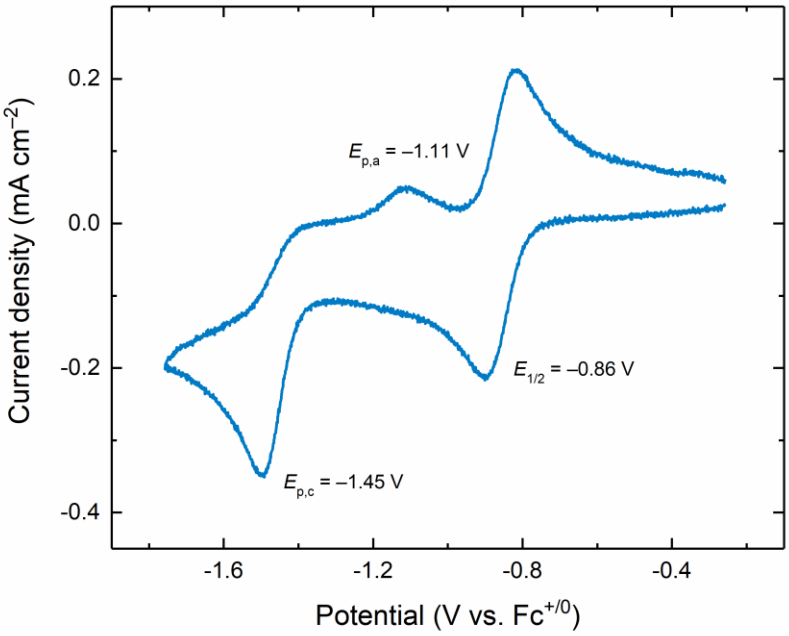

Figure C29. Cyclic voltammetry of **1**$^{\mathbf{LMe2}}$ (CH_3CN, 0.1 M [$^nBu_4N$][PF_6], 100 mV/s)

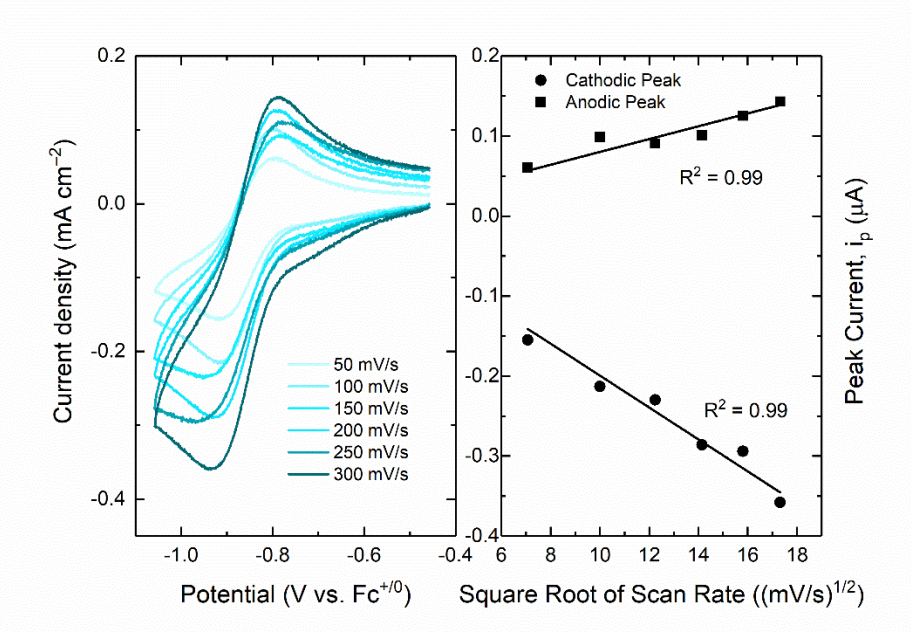

Figure C30. Left: cyclic voltammetry of first reduction event $\mathbf{1}^{\mathbf{LMe2}}$ at varying scan rate in CH_3CN (0.1 M $[^nBu_4N][PF_6]$). Right: linear dependence of peak cathodic current on square root of scan rate with the y-intercept set to 0.

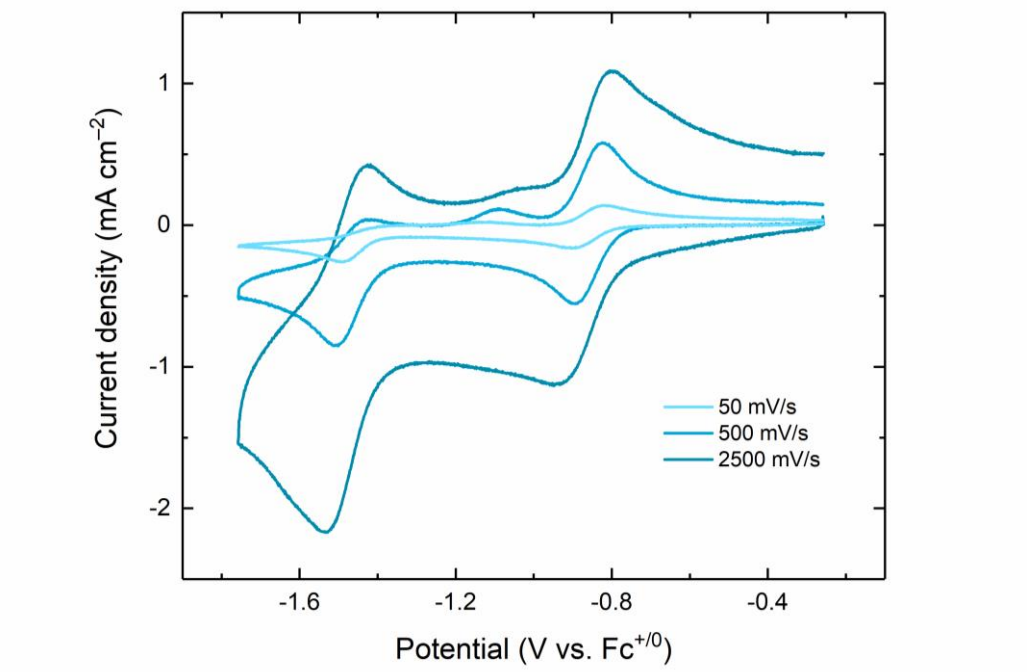

Figure C31. Cyclic voltammetry of **1**$^{\mathbf{LMe2}}$ at increasing scan rates (50 mV/s, 500 mV/s, and 2500 mV/s). Conditions: Electrolyte, 0.1 M $TBAPF_6$ in CH_3CN; working electrode, highly oriented pyrolytic graphite (HOPG); [Rh] in each experiment ca. 1 mM.

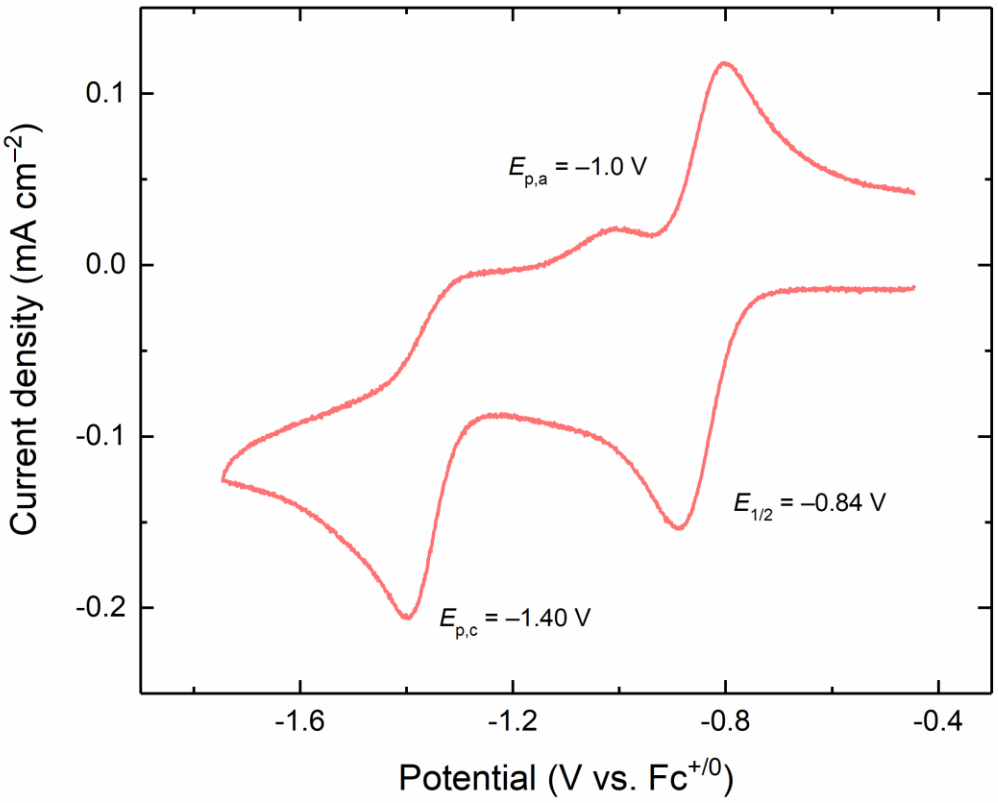

Figure C32. Cyclic voltammetry of $\mathbf{1}^{\mathbf{LBn2}}$ (CH_3CN, 0.1 M [$^nBu_4N$][PF_6], 100 mV/s)

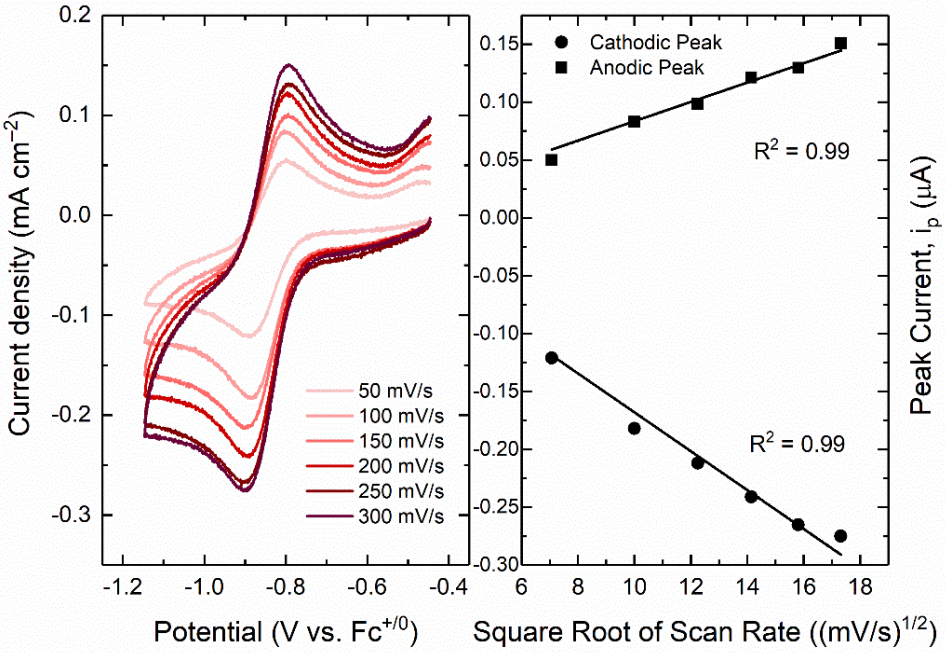

Figure C33. Left: cyclic voltammetry of $\mathbf{1}^{\mathbf{LBn2}}$ at varying scan rate in CH_3CN (0.1 M $[^nBu_4N][PF_6]$). Right: linear dependence of peak cathodic current on square root of scan rate with the y-intercept set to 0.

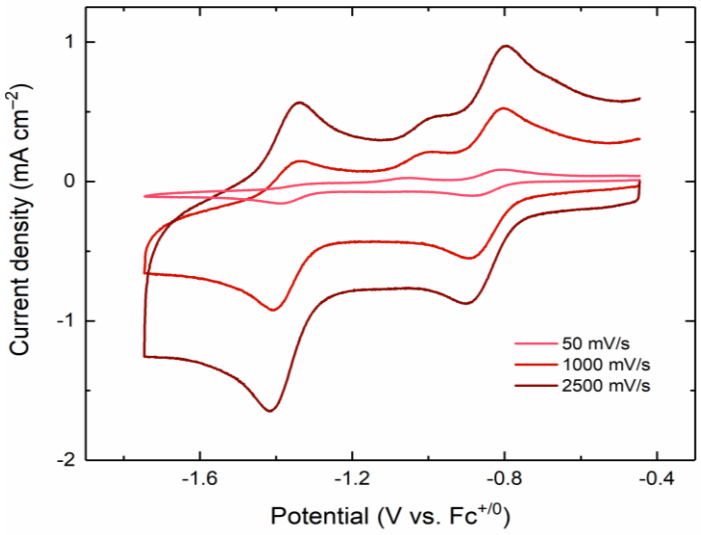

Figure C34. Cyclic voltammetry of **1**$^{\mathbf{LBn2}}$ at increasing scan rates (50 mV/s, 1000 mV/s, and 2500 mV/s). Conditions: Electrolyte, 0.1 M $TBAPF_6$ in CH_3CN; working electrode, highly oriented pyrolytic graphite (HOPG); [Rh] in each experiment ca. 1 mM.

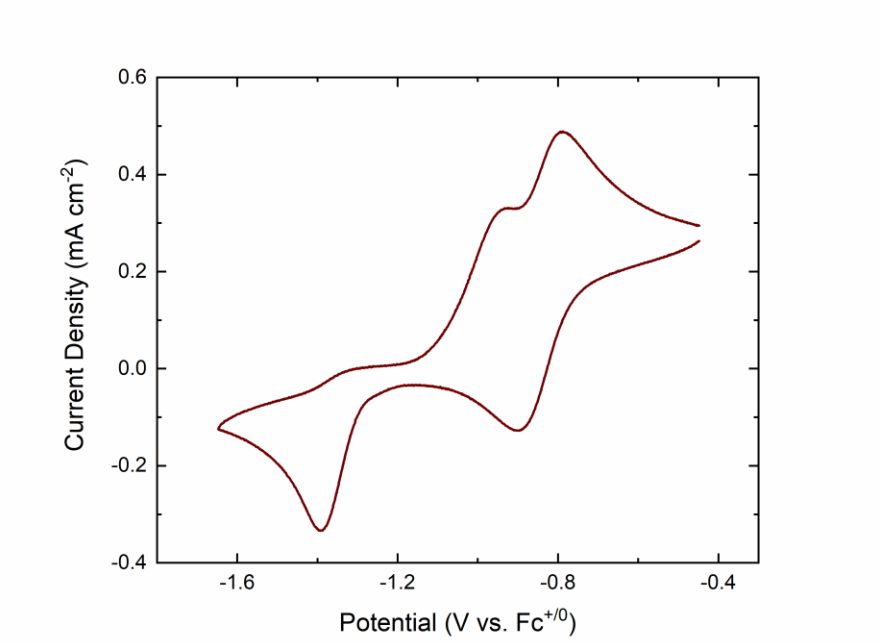

Figure C35. Cyclic voltammetry of $\mathbf{4^{LBn2}}$ (CH_3CN, 0.1 M [$^nBu_4N$][PF_6], 100 mV/s)

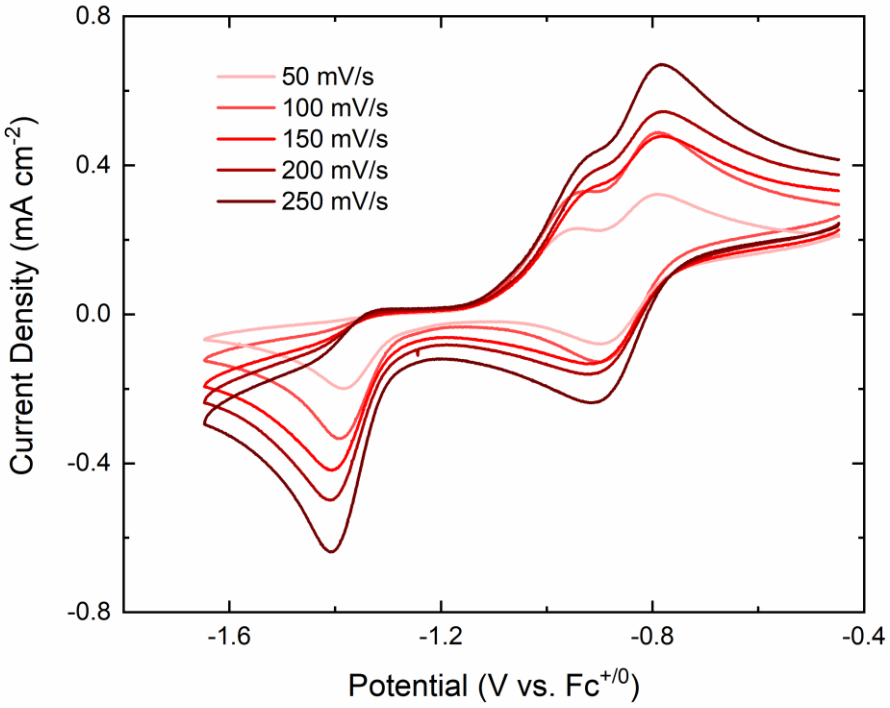

Figure C36. Cyclic voltammetry of $\mathbf{4}^{\mathbf{LBn2}}$ at increasing scan rates (50 mV/s, 100 mV/s, 150 mV/s, 200 mV/s, and 250 mV/s). Conditions: Electrolyte, 0.1 M $TBAPF_6$ in CH_3CN; working electrode, highly oriented pyrolytic graphite (HOPG); [Rh] in each experiment ca. 1 mM.

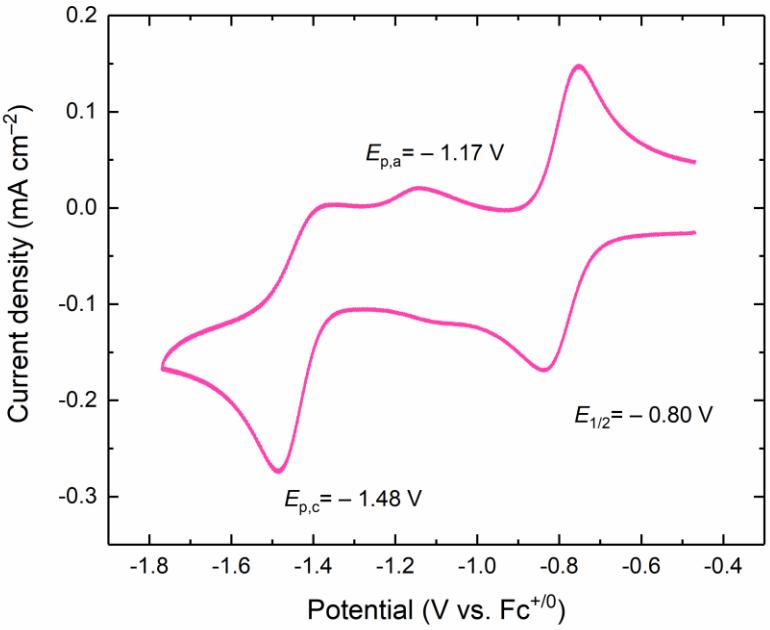

Figure C37. Cyclic voltammetry of **1**$^{\mathbf{LMePyr}}$ (CH_3CN, 0.1 M [$^nBu_4N$][PF_6], 100 mV/s)

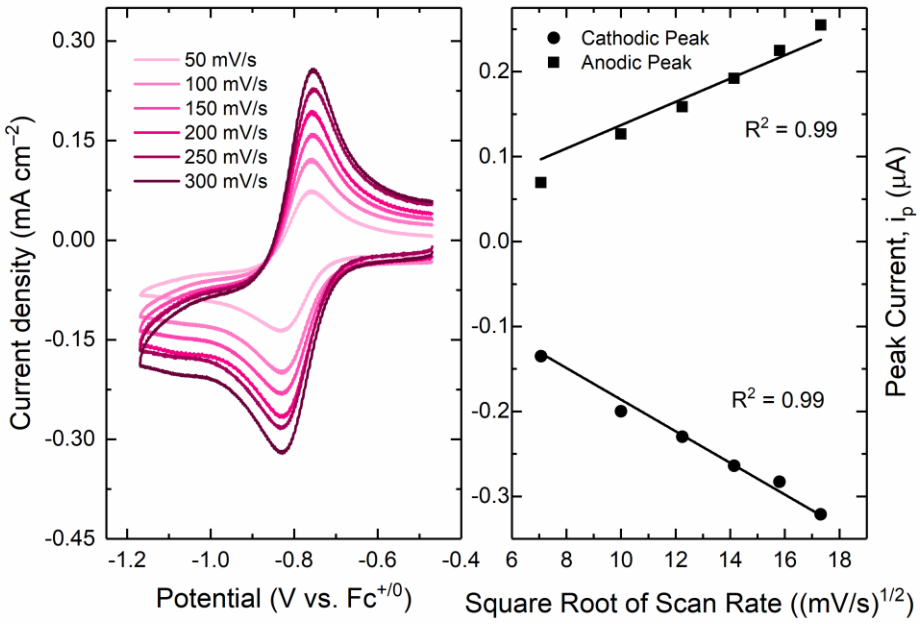

Figure C38. Left: cyclic voltammetry of **1**$^{\mathbf{LMePyr}}$ at varying scan rate in CH_3CN (0.1 M $[^nBu_4N][PF_6]$). Right: linear dependence of peak cathodic current on square root of scan rate with the y-intercept set to 0.

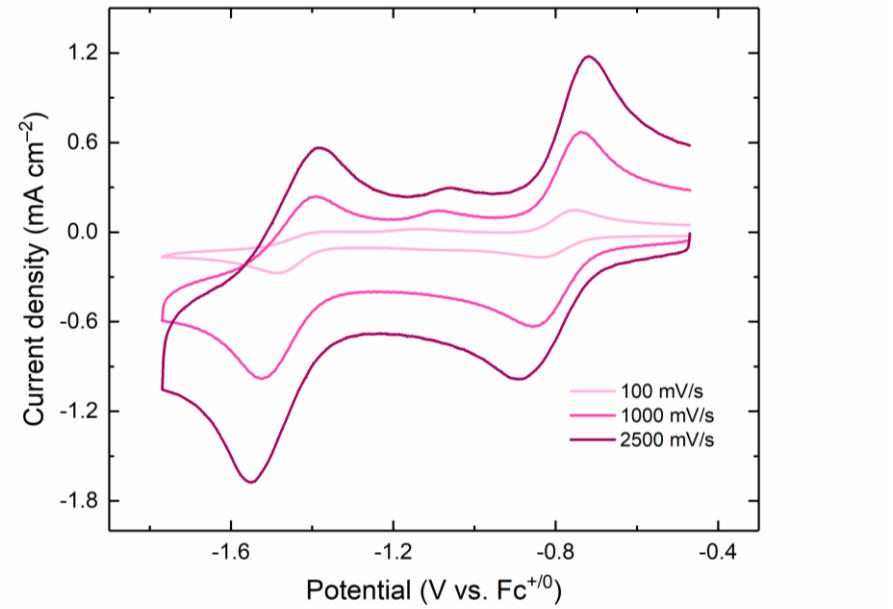

Figure C39. Cyclic voltammetry of $\mathbf{1}^{\mathbf{LMePyr}}$ at increasing scan rates (100 mV/s, 1000 mV/s, and 2500 mV/s). Conditions: Electrolyte, 0.1 M $TBAPF_6$ in CH_3CN; working electrode, highly oriented pyrolytic graphite (HOPG); [Rh] in each experiment ca. 1 mM.

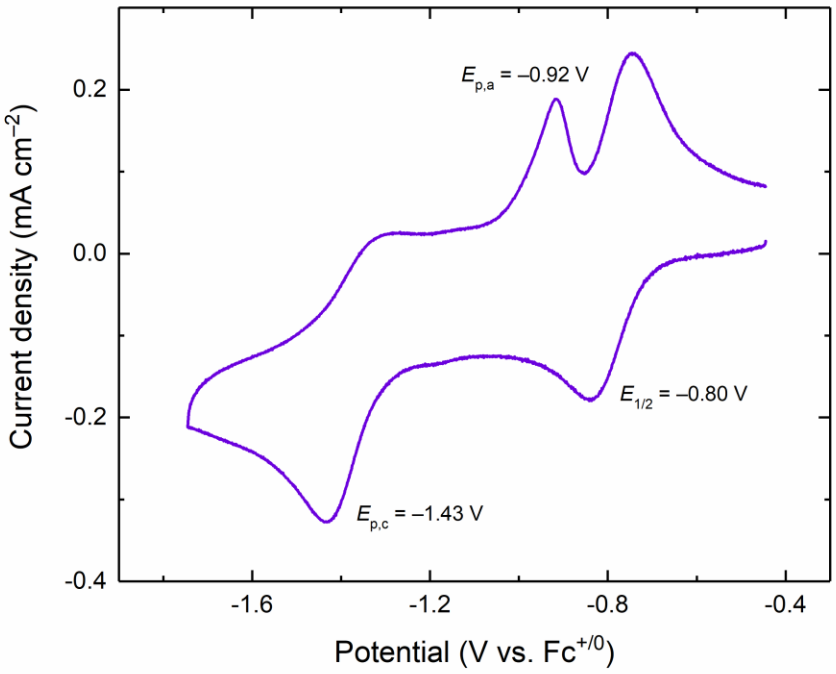

Figure C40. Cyclic voltammetry of $\mathbf{1}^{\mathbf{LPyr2}}$ (CH_3CN, 0.1 M [$^nBu_4N$][PF_6], 100 mV/s)

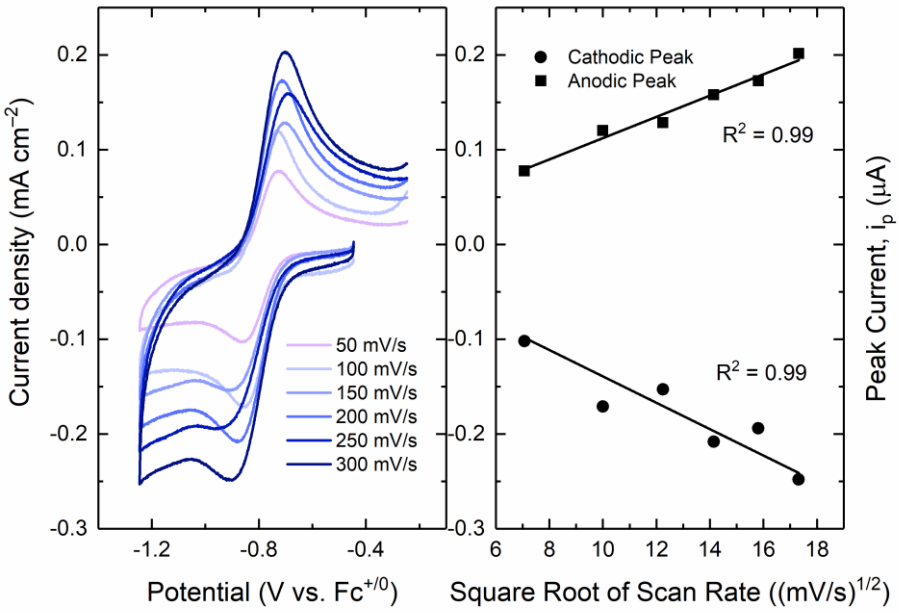

Figure C41. Left: cyclic voltammetry of $\mathbf{1}^{\mathbf{LPyr2}}$ at varying scan rate in CH_3CN (0.1 M $[^nBu_4N][PF_6]$). Right: linear dependence of peak cathodic current on square root of scan rate with the y-intercept set to 0.

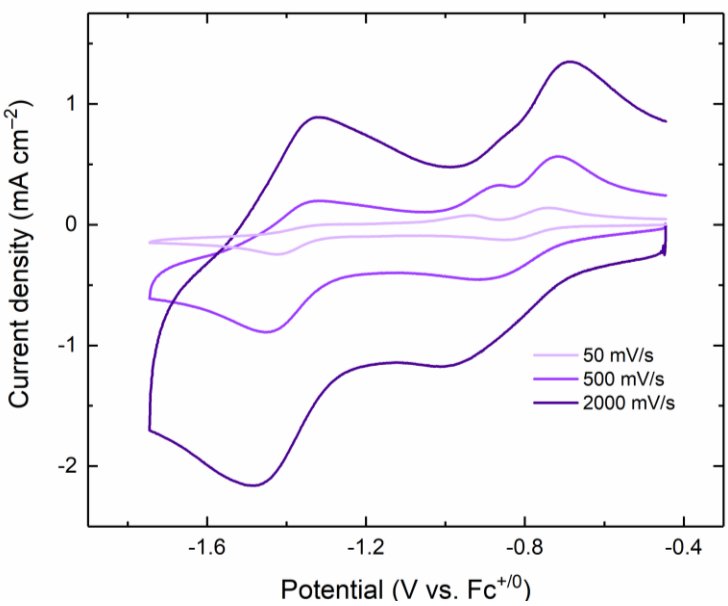

Figure C42. Cyclic voltammetry of **1**$^{\mathbf{LPyr2}}$ at increasing scan rates (50 mV/s, 500 mV/s, and 2000 mV/s). Conditions: Electrolyte, 0.1 M $TBAPF_6$ in CH_3CN; working electrode, highly oriented pyrolytic graphite (HOPG); [Rh] in each experiment ca. 1 mM.

Simulations

Table C1. Experimental Input and Calculated Output Parameters.

Experimental Inputs	Calculated Outputs
Mechanism	Rate of Chemical Rearrangement (k_+)
Reduction Potentials ($E_{1/2}$, E_{pc}, E_{pa})	Heterogenous Electron Transfer Rate (k^0)
Double Layer Capacitance (F)	Diffusion Coefficient (cm^2/s)
Resistance (Ω)	
Electrode Area ($0.09mm^2$)	
Temperature (K)	
Concentration (mM)	

Table C2: Calculated Outputs:

Complexes	Heterogenous Electron Transfer Rate (k^0) (cm/s)	Diffusion Coefficient (cm^2/s)
	$Rh^{III/II}$	
1^{LMe2}	0.009	9.85×10^{-6}
1^{LBn2}	0.013	1.05×10^{-5}
1^{LMePyr}	0.007	1.30×10^{-5}
1^{LPyr2}	0.005	2.81×10^{-5}

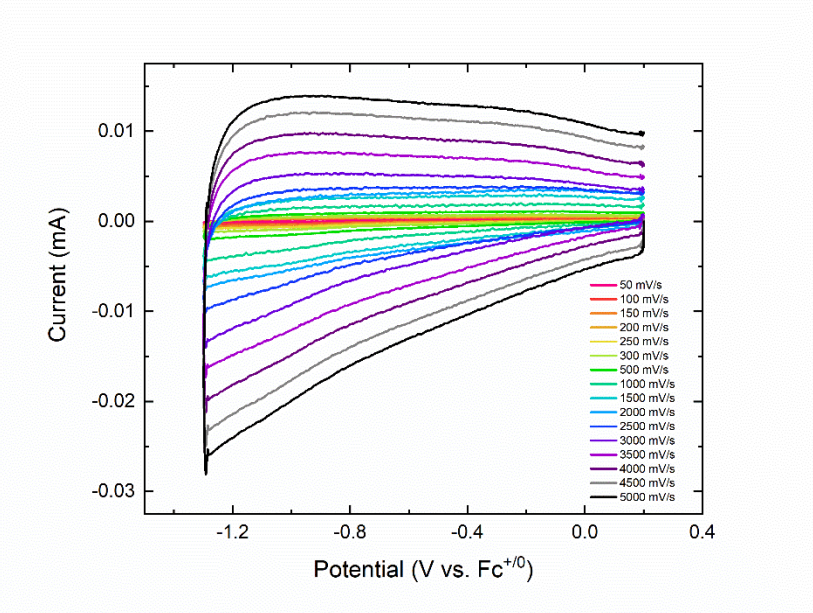

Figure C43. CV HOPG working electrode at varying scan rates 50 mV/s – 5000 mV/s (CH_3CN, 0.1 M [$^nBu_4N$][PF_6]).

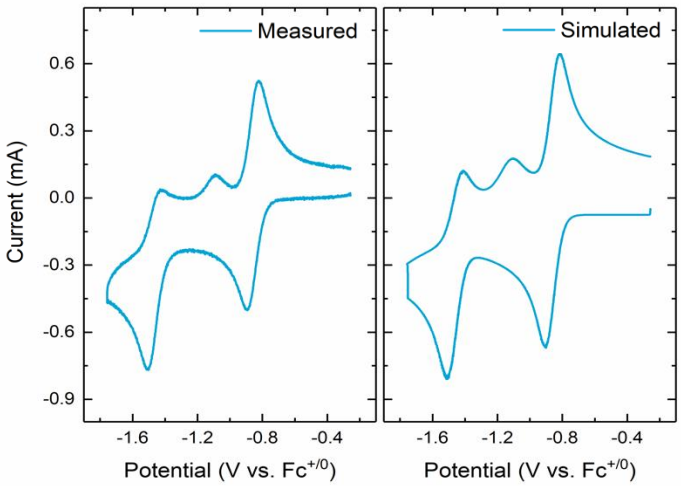

Figure C44. Experimental CV of $\mathbf{1}^{\mathbf{LMe2}}$ data (left) and simulated CV data with DigiElch (right) (CH_3CN, 0.1 M [$^nBu_4N$][PF_6], 500 mv/s).

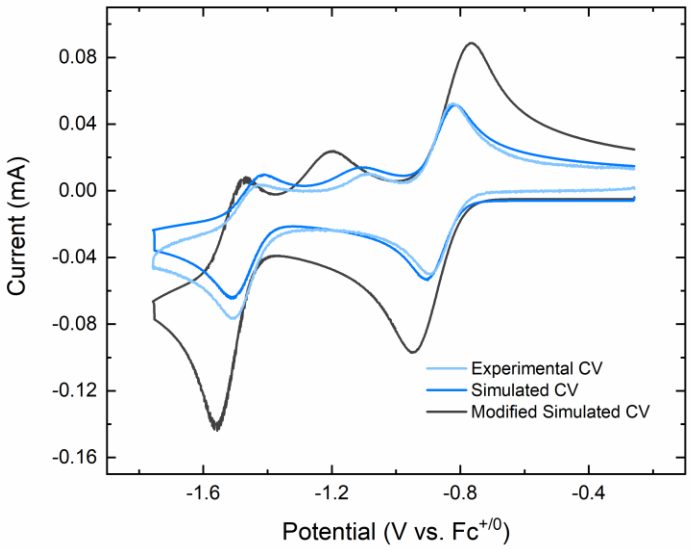

Figure C45. Experimental CV of $\mathbf{1}^{\mathbf{LMe2}}$ data (light blue) and simulated CV data (diffusion coefficient = 9.85 x 10^{-6} cm^2/s) with DigiElch (blue) and modified simulated CV (dark gray) to illustrate the change in simulation in comparison with an arbitrary input diffusion coefficient (2.81 x 10^{-5} cm^2/s). Best value of k_+ was found to be 1.02 s^{-1} for the simulation with a modified (incorrect) diffusion coefficient (CH_3CN, 0.1 M [$^nBu_4N$][PF_6], 500 mv/s).

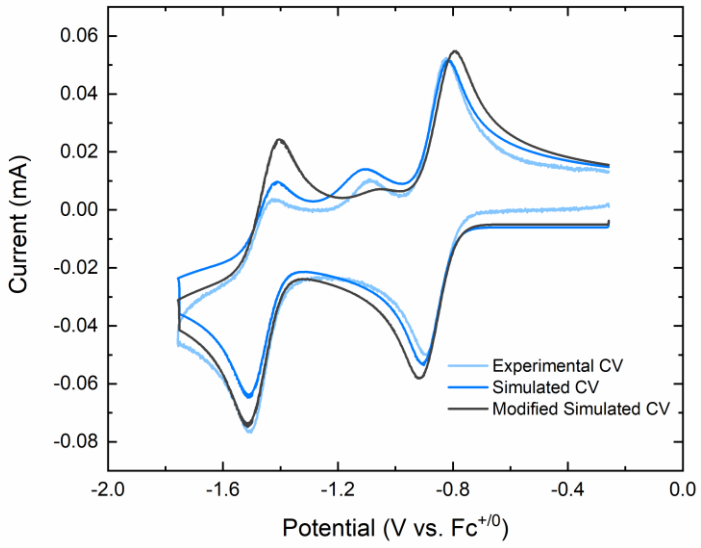

Figure C46. Experimental CV of $\mathbf{1}^{\mathbf{LMe2}}$ data (light blue) and simulated CV data (k_+ = 1.65 s^{-1}) with DigiElch (blue) and modified simulated CV (dark gray) to illustrate the change in simulation in comparison with an arbitrary input of rate of chemical rearrangement (k_+) of 0.16 s^{-1}. The different values for k_+ illustrate the drastic affect of k_+ on the appearance of the CV. The value of k_+ for the modified simulation (dark gray) is clearly smaller than that of the original simulated data (blue) as the $Rh^{II/I}$ couple appears to have a greater degree of chemical reversibility than actual couple in the experimental data (light blue). (CH_3CN, 0.1 M [$^nBu_4N$][PF_6], 500 mv/s).

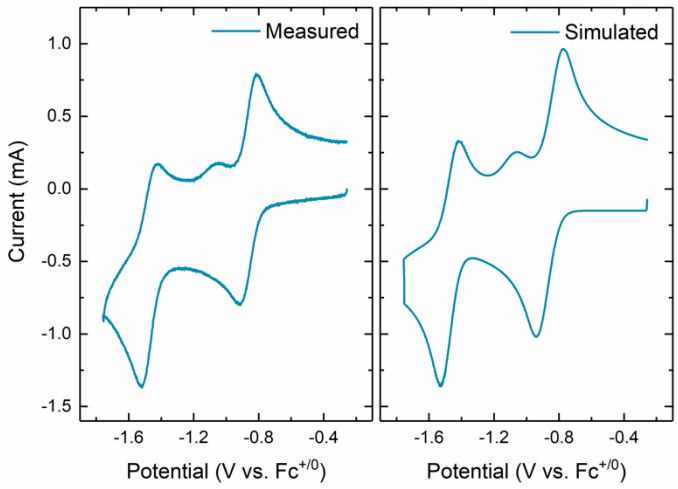

Figure C47. Experimental CV of $\mathbf{1}^{\mathbf{LMe2}}$ data (left) and simulated CV data with DigiElch (right) (CH_3CN, 0.1 M [$^nBu_4N$][PF_6], 1500 mv/s).

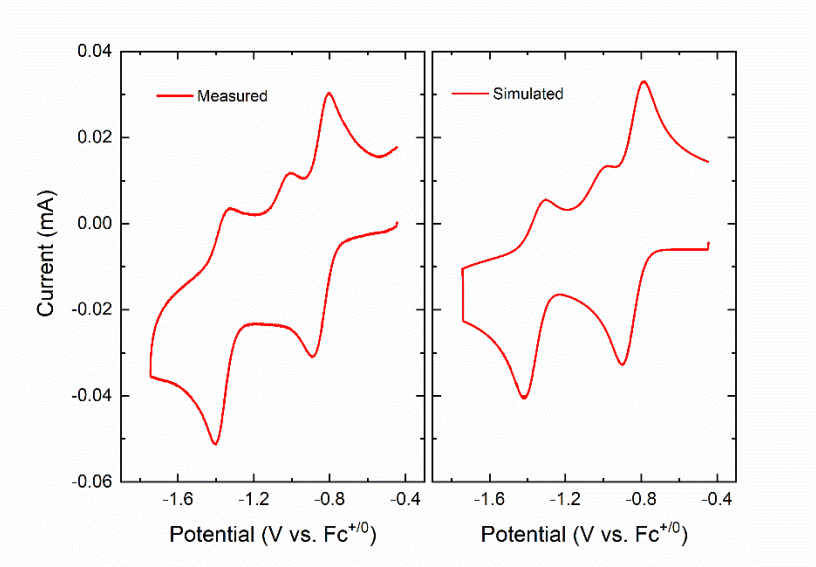

Figure C48. Experimental CV of $\mathbf{1}^{\mathbf{LBn2}}$ data (left) and simulated CV data with DigiElch (right) (CH_3CN, 0.1 M [$^nBu_4N$][PF_6], 500 mv/s).

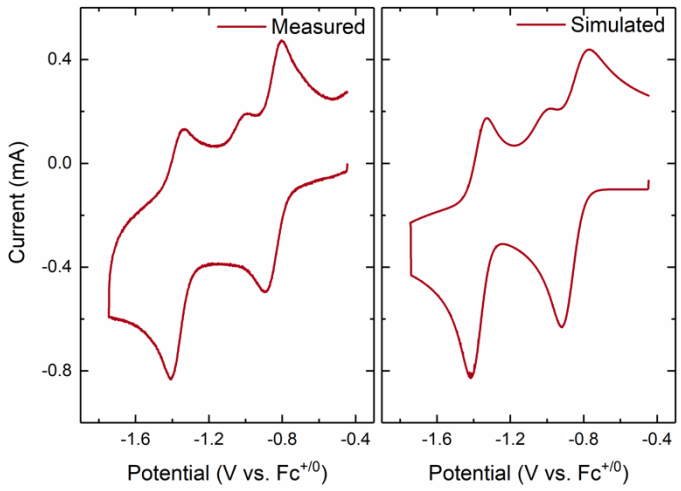

Figure C49. Experimental CV of $\mathbf{1}^{\mathbf{LBn2}}$ data (left) and simulated CV data with DigiElch (right) (CH_3CN, 0.1 M [$^nBu_4N$][PF_6], 1000 mv/s).

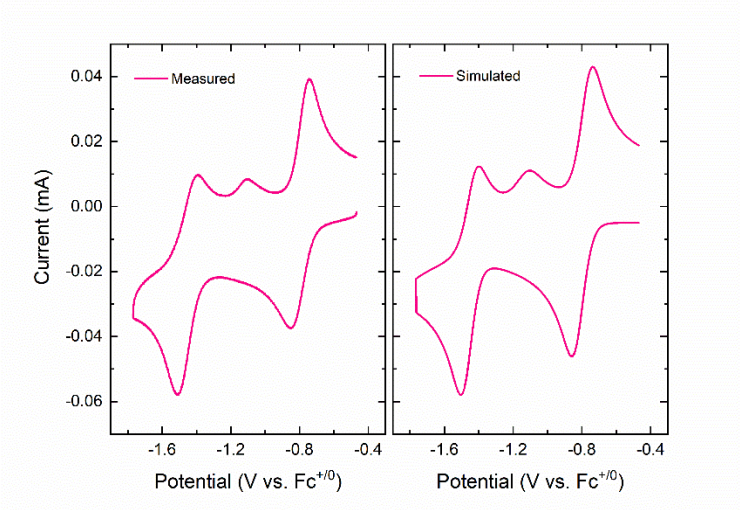

Figure C50. Experimental CV of $\mathbf{1}^{\mathbf{LMePyr}}$ data (left) and simulated CV data with DigiElch (right) (CH_3CN, 0.1 M [$^nBu_4N$][PF_6], 500 mv/s).

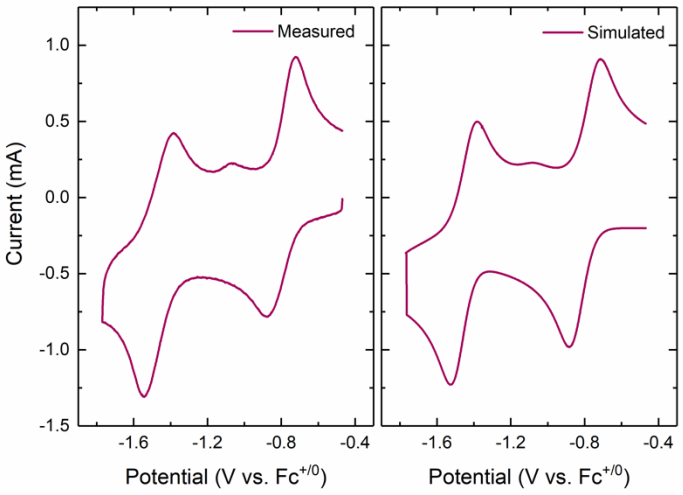

Figure C51. Experimental CV of $\mathbf{1}^{\mathbf{LMePyr}}$ data (left) and simulated CV data with DigiElch (right) (CH_3CN, 0.1 M [$^nBu_4N$][PF_6], 2500 mv/s).

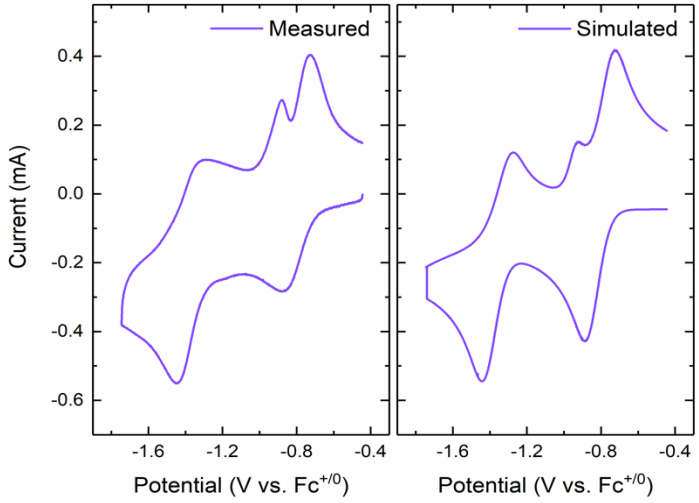

Figure C52. Experimental CV of $\mathbf{1}^{\mathbf{LPyr2}}$ data (left) and simulated CV data with DigiElch (right) (CH_3CN, 0.1 M [$^nBu_4N$][PF_6], 300 mv/s).

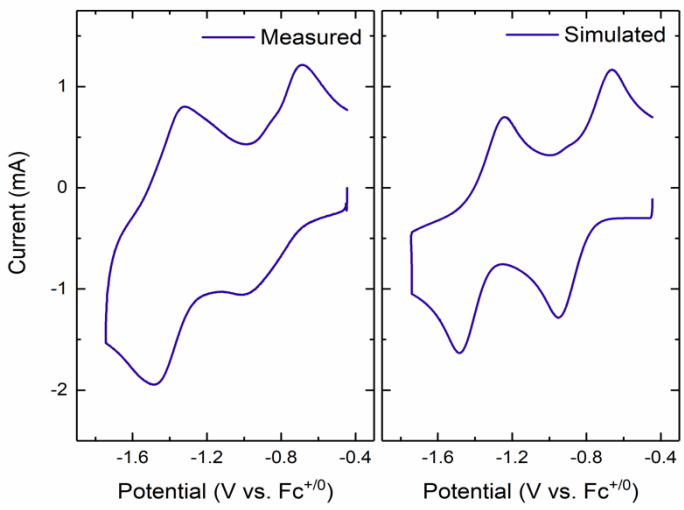

Figure C53. Experimental CV of $\mathbf{1}^{\mathbf{LPyr2}}$ data (left) and simulated CV data with DigiElch (right) (CH_3CN, 0.1 M [$^nBu_4N$][PF_6], 2000 mv/s).

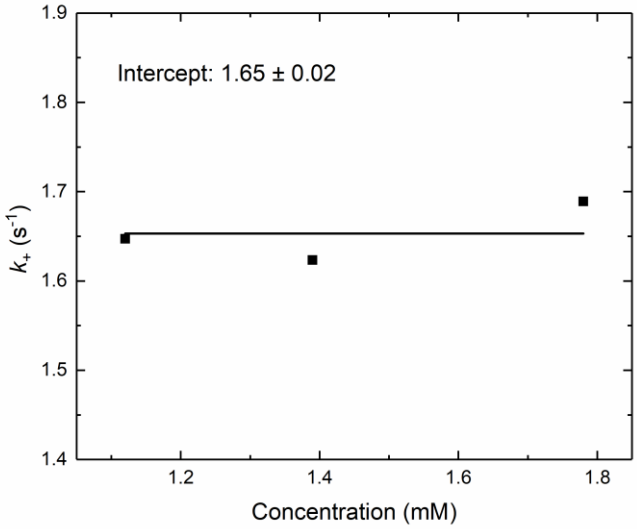

Figure C54. Simulated rate of ligand rearrangement (k_+) of $\mathbf{1}^{\mathbf{LMe2}}$ with differing concentrations (1.12 mM, 1.39 mM, 1.78 mM)

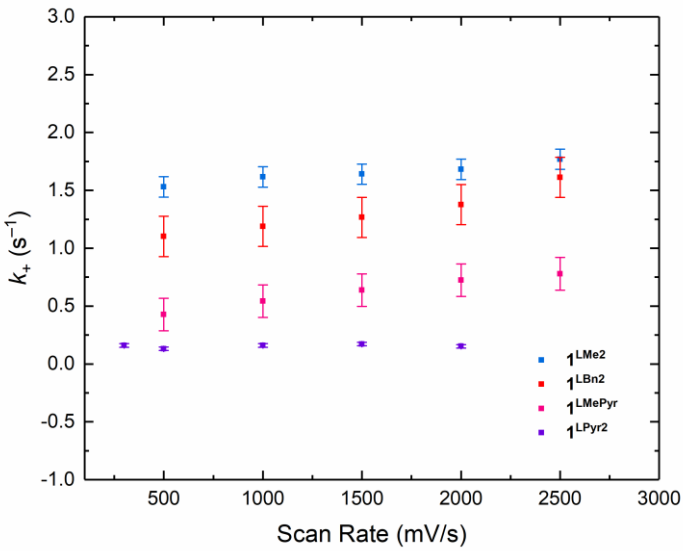

Figure C55. Simulated rate of ligand rearrangement (k_+) of $\mathbf{1}^{\mathbf{LR2}}$ at increasing scan rates with error bars.

Table C3. Crystal and Refinement Data for [Cp*Rh(Bn$_2$dpma)(Cl)][PF$_6$] (**A^{LBn2}**), [Cp*Rh(MePyrdpma)(Cl)][PF$_6$] (**A^{LMePyr}**), [Cp*Rh(Pyr$_2$dpma)(Cl)][PF$_6$] (**A^{LPyr2}**) and [Cp*Rh(Bn$_2$dpma)] (**4^{LBn2}**).

	A^{LBn2}	**A^{LMePyr}**	**A^{LPyr2}**	**4^{LBn2}**
CCDC number	2041687	2033846	2033845	2033848
KU Code	k90k	v12f	q54i	q35h
Empirical formula	$C_{36}H_{40}ClF_6N_2OPRh$	$C_{43}H_{47}ClF_6N_2OPRh$	$C_{56}H_{47}ClF_6N_2O_2PRh$	$C_{38}H_{44}N_2Rh$
Formula weight	801.04	891.15	1102.18	631.66
Temperature	200.00	200.00	200.00	200.00
Wavelength	0.71073	1.54178	1.54178	1.54178
Crystal system	monoclinic	triclinic	triclinic	monoclinic
Space group	$P2_1/n$	P-1	P-1	$P2_1/a$
a	11.500(3) Å	12.3953(6) Å	11.5173(3) Å	11.9716(2) Å
b	14.259(4) Å	13.0453(6) Å	13.9040(3) Å	12.2372(3) Å
c	21.944(6)Å	14.5552(7) Å	16.3949(4) Å	21.9936(5) Å
α	90	114.0135(10)	103.0330(10)	90
β	99.448(4)	105.8742(12)	103.4950(10)	96.3083(8)
γ	90	99.9498(11)	99.7720(10)	90
Volume	3549.6(18) Å^3	1956.80(16) Å^3	2417.69(10) Å^3	3202.53(12) Å^3
Z	4	2	2	4
Density (calculated)	1.499 g/cm^3	1.512 g/cm^3	1.514 g/cm^3	1.310 g/cm^3
Absorption coefficient	0.665 mm^{-1}	5.106 mm^{-1}	5.236 mm^{-1}	4.508 mm^{-1}
F(000)	1640	916	1124	1324
Crystal size	0.52 × 0.45 × 0.26 mm^3	0.14 × 0.32 × 0.3 mm^3	0.11 × 0.08 × 0.08 mm^3	0.12 × 0.11 × 0.01mm^3
2-Theta range(°)	3.42 to 63.10	7.19 to 136.76	5.77 to 14077	4.04 to 140.54
Index ranges	$-16 \le h \le 16$, $-20 \le k \le 20$, $-31 \le l \le 32$	$-12 \le h \le 14$, $-15 \le k \le 15$, $-17 \le l \le 16$	$-13 \le h \le 13$, $-16 \le k \le 16$, $-19 \le l \le 18$	$-14 \le h \le 14$, $-12 \le k \le 14$, $-26 \le l \le 26$
Reflections collected	44803	22934	28653	40524
Independent reflections	11777 [R_{int} = 0.049, R_{sig} = 0.049]	6954 [R_{int} = 0.036, R_{sig} = 0.034]	8461 [R_{int} = 0.027, R_{sig} = 0.027]	5871 [R_{int} = 0.040, R_{sig} = 0.023]
Completeness(%)/ θ°	100.0/25.24°	96.9/66.00°	94.0/66.00°	98.4/66.00°
Absorption correction	Multi-scan	Multi-scan	Multi-scan	Multi-scan
Max. and min. transmission	0.777 to 1.000	0.567 to 1.000	0.864 to 1.000	0.740 to 1.000
Refinement method	Full-matrix least-squares on F^2	Full-matrix least-squares on F^2	Full-matrix least-squares on F^2	Full-matrix least-squares on F^2
Data / restraints / parameters	11777/0/479	6954/0/502	8461/0/643	5871/0/474
Goodness-of-fit on F^2	1.021	1.038	1.088	1.093
Final R indices [I>2σ(I)]	R_1 = 0.045, wR_2 = 0.095	R_1 = 0.050, wR_2 = 0.135	R_1 = 0.044, wR_2 = 0.119	R_1 = 0.027, wR_2 = 0.069
R indices (all data)	R_1 = 0.073, wR_2 = 0.109	R_1 = 0.052, wR_2 = 0.137	R_1 = 0.047, wR_2 = 0.122	R_1 = 0.028, wR_2 = 0.070
Largest diff. peak and hole	0.80 and -0.77e$^-$/Å^3	1.72 and -0.83e$^-$/Å^3	1.37 and-1.25e$^-$/Å^3	0.76 and -0.87 e$^-$/Å^3

[a] $R1\ \Sigma||F_o|-|F_c|| / \Sigma|F_o|$ [b] $wR2 = [\ \Sigma\ [w(F_o^2-F_c^2)^2] / \Sigma\ [w(F_o^2)^2]\ ]^{1/2}$

Table C4. Selected Bond Lengths for $\mathbf{A}^{\mathbf{LBn2}}$, $\mathbf{A}^{\mathbf{LMePyr}}$, $\mathbf{A}^{\mathbf{LPyr2}}$, and $\mathbf{4}^{\mathbf{LBn2}}$.

Bond	$\mathbf{A}^{\mathbf{LBn2}}$ (Å)	$\mathbf{A}^{\mathbf{LMePyr}}$ (Å)	$\mathbf{A}^{\mathbf{LPyr2}}$ (Å)	$\mathbf{4}^{\mathbf{LBn2}}$
Rh–Cl	2.4110(8)	2.4134(10)	2.4095(9)	—
Rh–N1	2.112(2)	2.135(3)	2.118(3)	2.0646(15)
Rh–N2	2.122(2)	2.125(3)	2.120(3)	—
Rh–Cp*	1.811	1.809	1.810	1.892
Rh–C9	—	—	—	2.1133(19)
Rh–C10	—	—	—	2.1311(18)

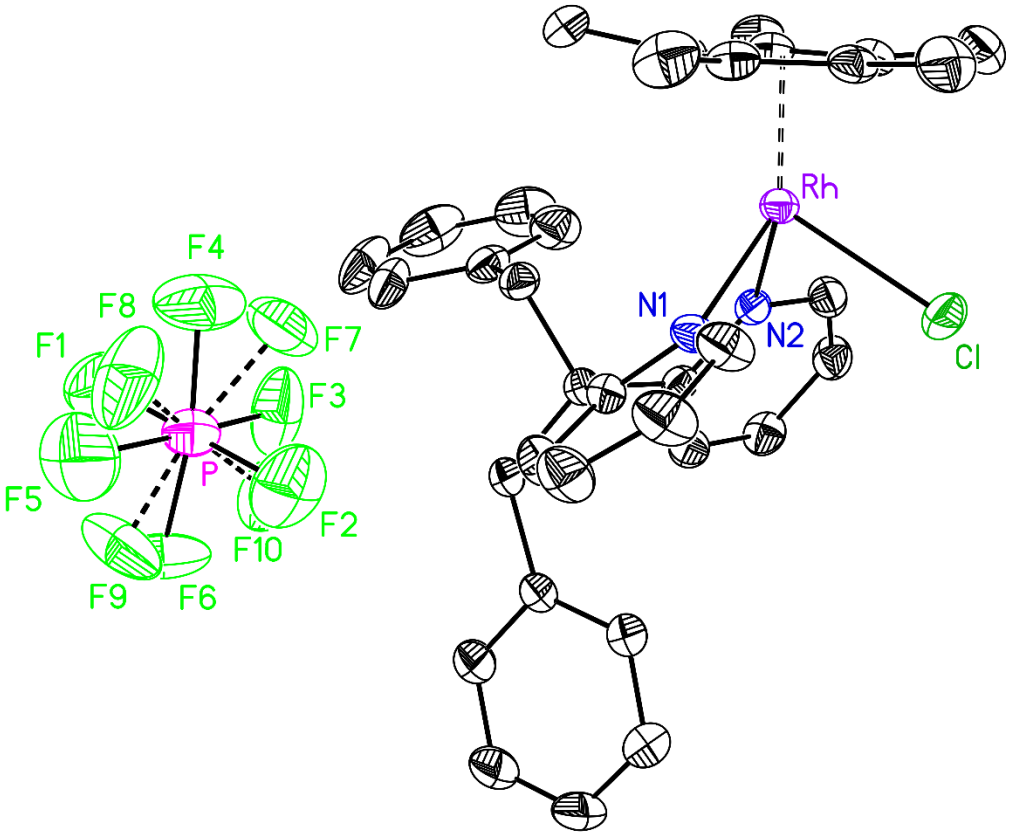

Figure C56. Solid-state structure of $\mathbf{A}^{\mathbf{LBn2}}$. Hydrogen atoms and associated solvent molecule omitted for clarity. Displacement ellipsoids shown at the 50% probability level.

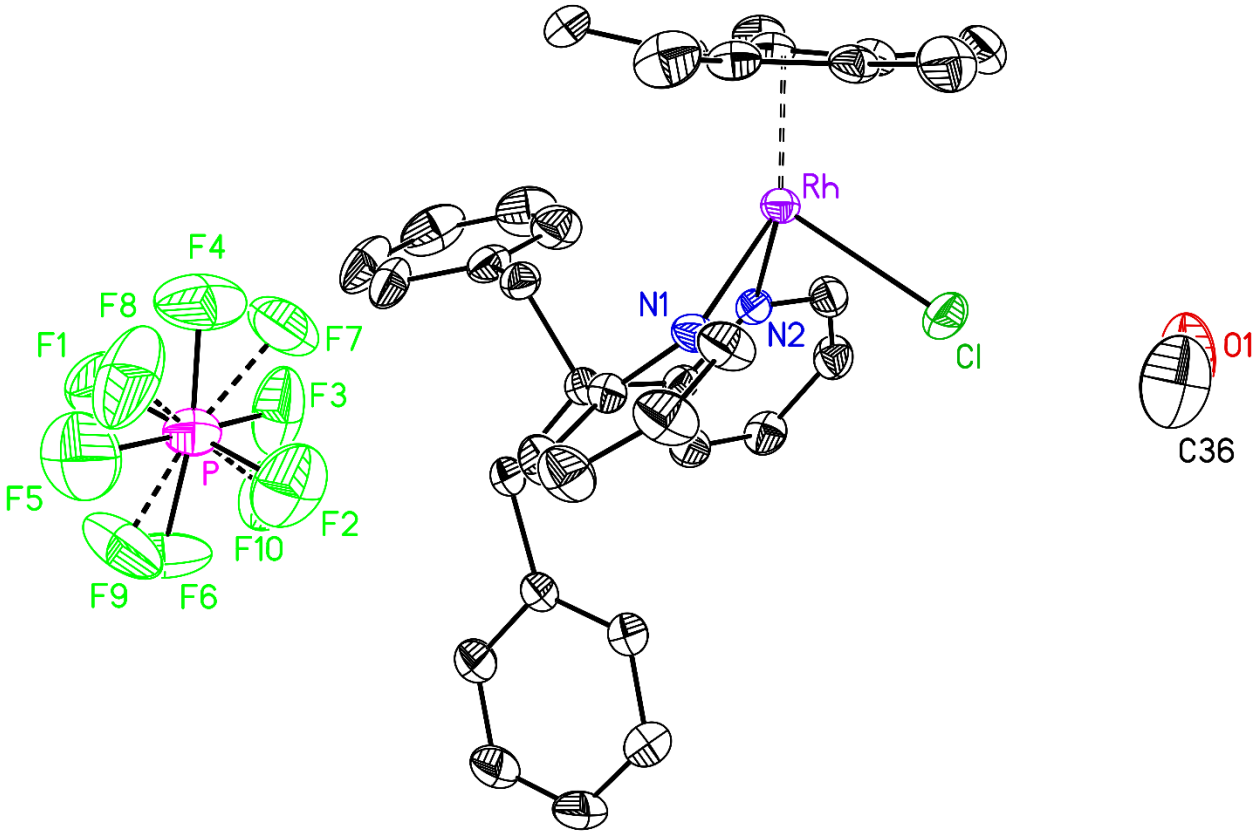

Figure C57. Solid-state structure of $\mathbf{A}^{\mathbf{LBn2}}$ asymmetric unit. Hydrogen atoms omitted for clarity. Displacement ellipsoids shown at the 50% probability level.

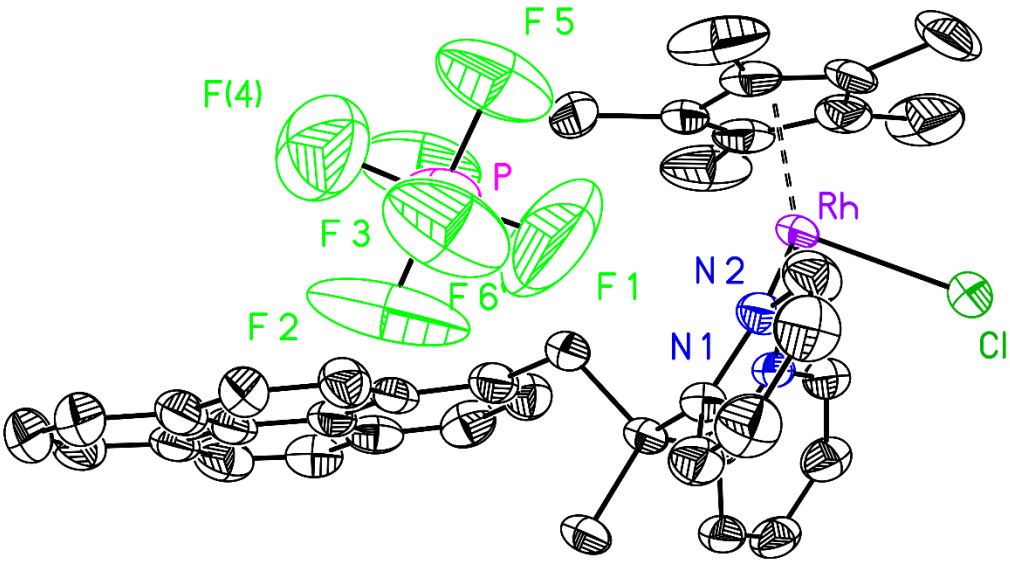

Figure C58. Solid-state structure of $\mathbf{A}^{\mathbf{LMePyr}}$. Hydrogen atoms and associated solvent molecule omitted for clarity. Displacement ellipsoids shown at the 50% probability level.

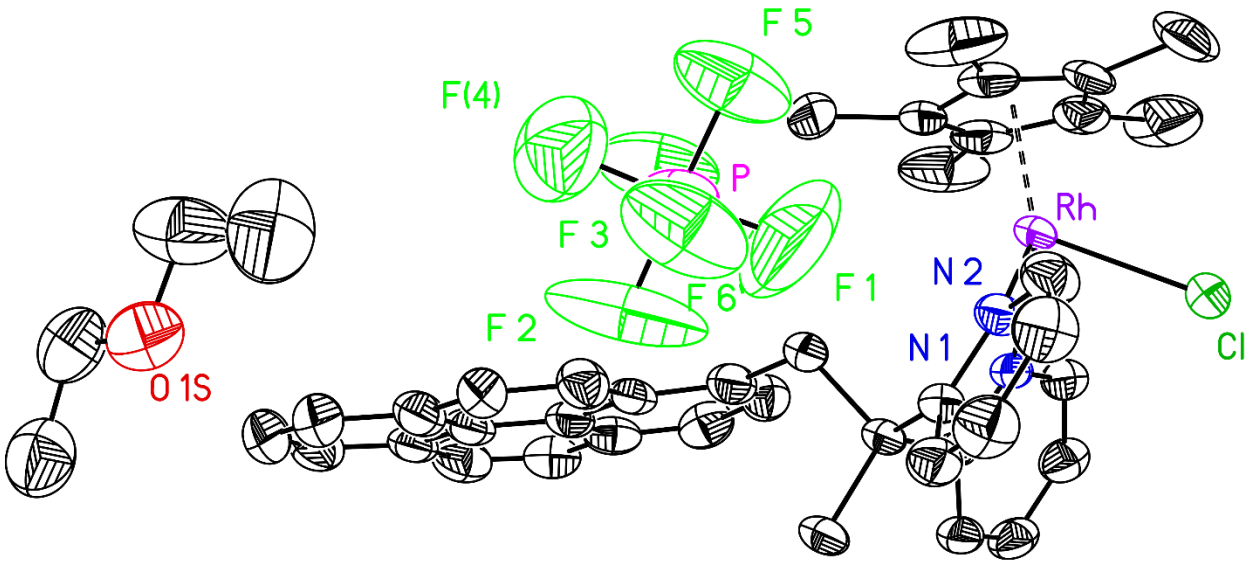

Figure C59. Solid-state structure of $\mathbf{A}^{\mathbf{LMePyr}}$ asymmetric unit. Hydrogen atoms omitted for clarity. Displacement ellipsoids shown at the 50% probability level.

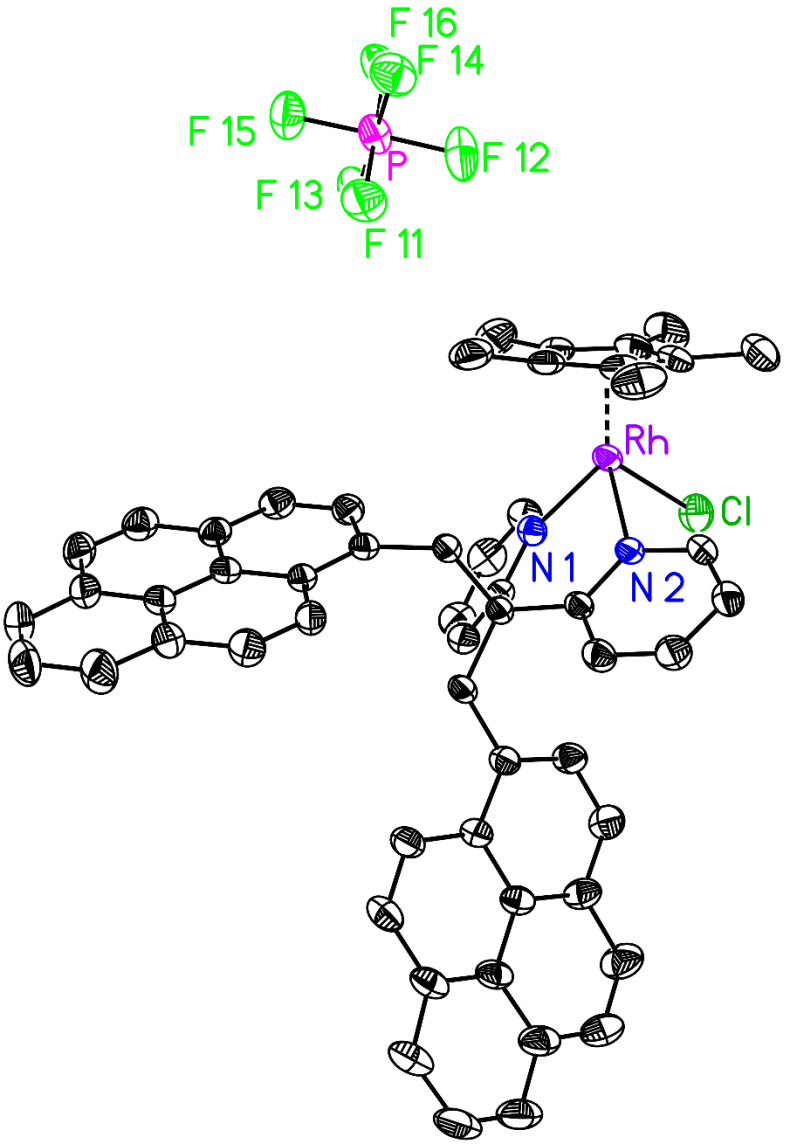

Figure C60. Solid-state structure of $\mathbf{A}^{\mathbf{LPyr2}}$. Hydrogen atoms and associated solvent molecule omitted for clarity. Displacement ellipsoids shown at the 50% probability level.

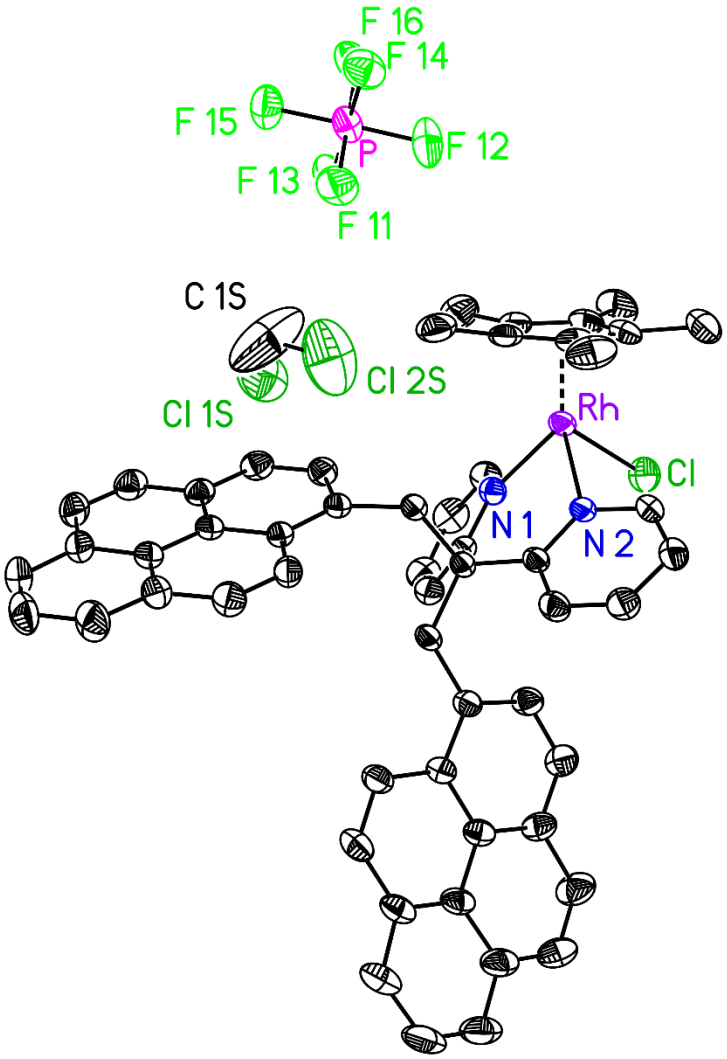

Figure C61. Solid-state structure of $\mathbf{A}^{\mathbf{LPyr2}}$ asymmetric unit. Hydrogen atoms omitted for clarity. Displacement ellipsoids shown at the 50% probability level.

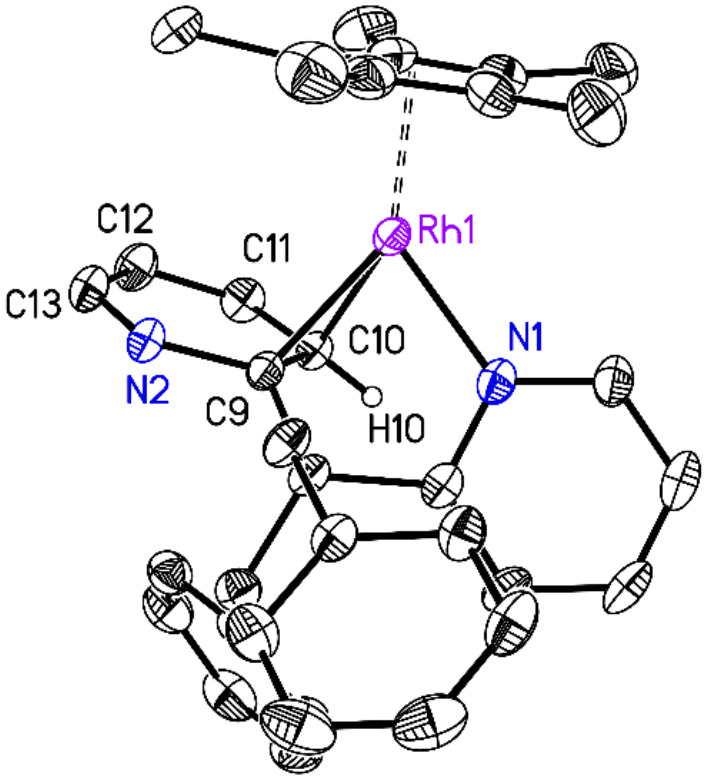

Figure C62. Solid-state structure of $\mathbf{4}^{\mathbf{LBn2}}$. Hydrogen atoms and associated solvent molecule omitted for clarity. Displacement ellipsoids shown at the 50% probability level.

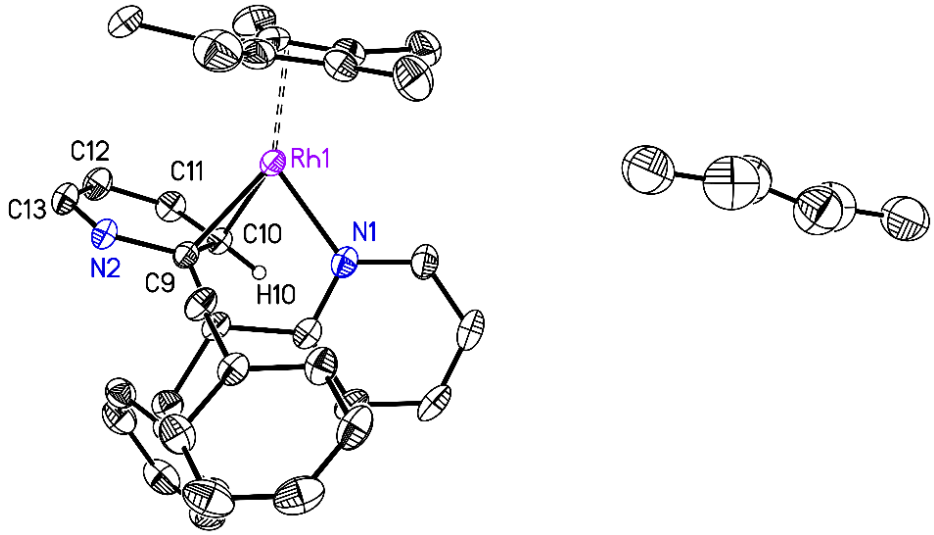

Figure C63. Solid-state structure of $\mathbf{4}^{\mathbf{LBn2}}$ asymmetric unit Hydrogen atoms omitted for clarity. Displacement ellipsoids shown at the 50% probability level.

Appendix D

Supplementary Information for Chapter 6

NMR Spectra

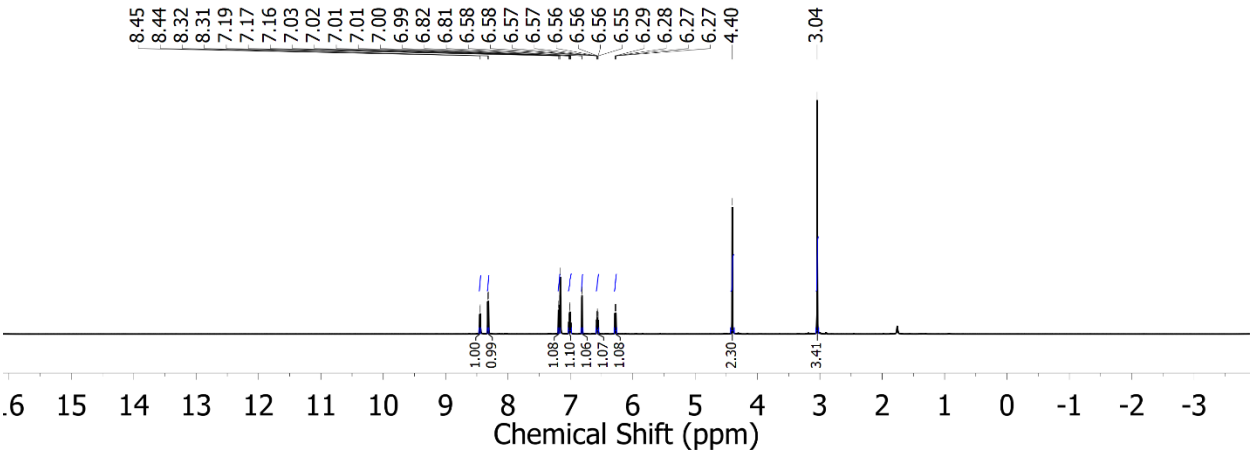

Figure D1. ^{1}H NMR spectrum (500 MHz, C_6D_6) of **dpma^{OMe}**.

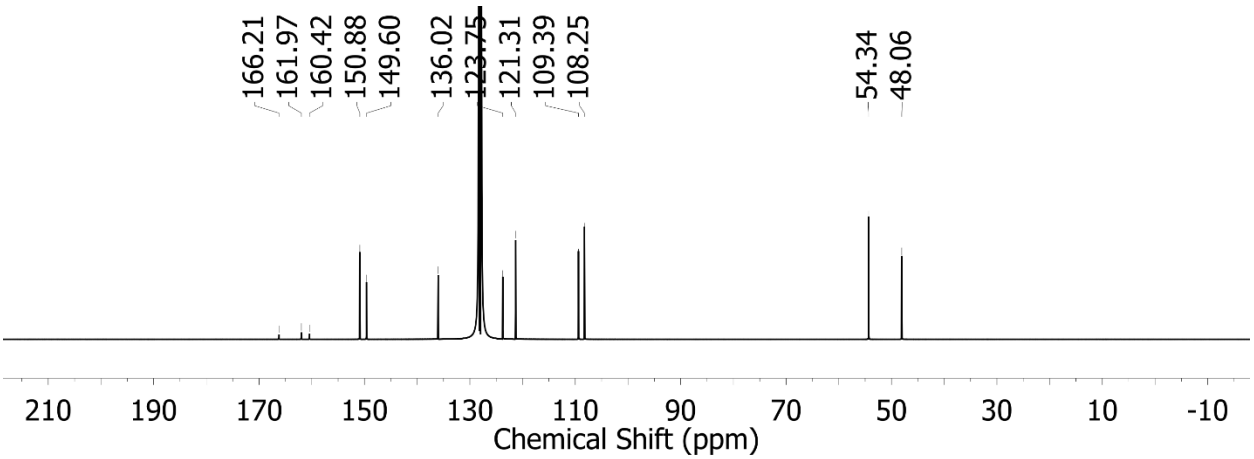

Figure D2. $^{13}C\{^{1}H\}$ NMR spectrum (126 MHz, C_6D_6) of **dpma^{OMe}**.

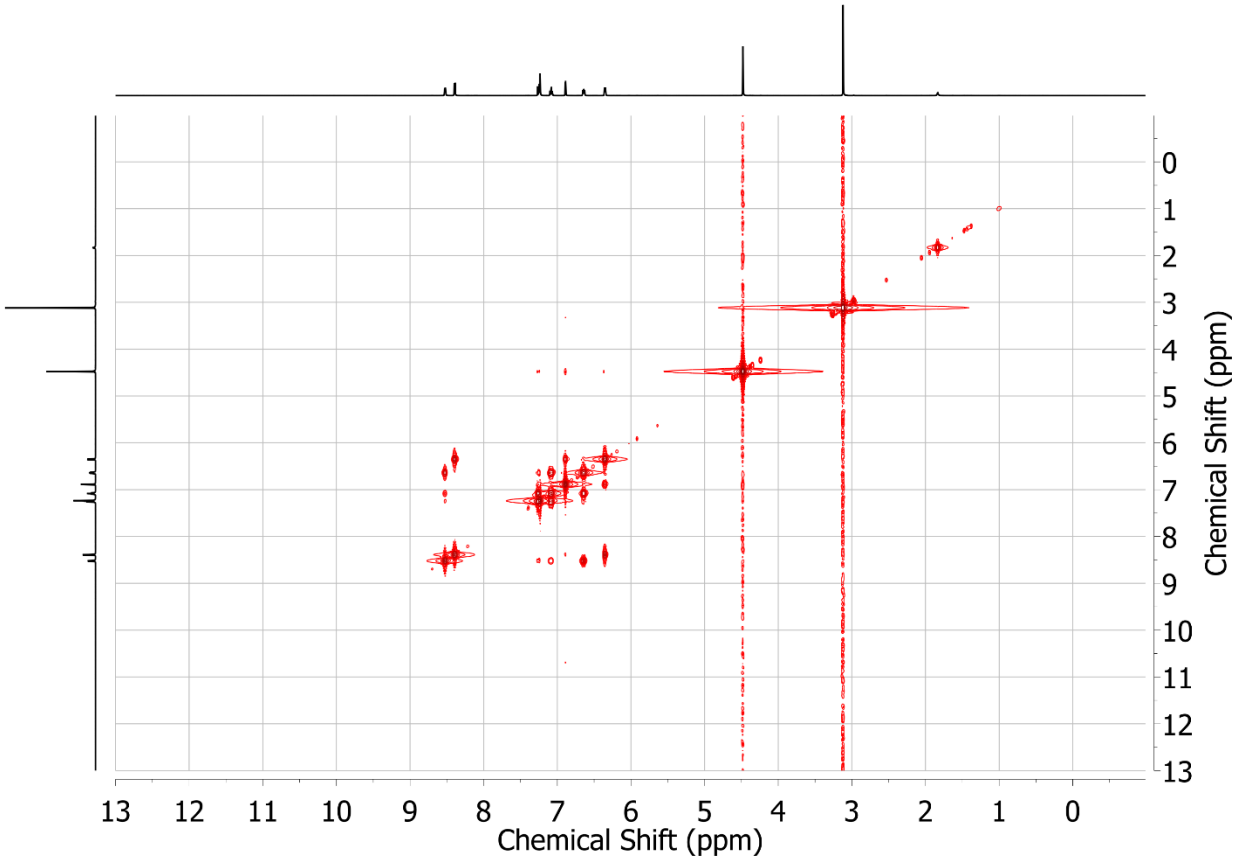

Figure D3. COSY NMR spectrum (162 MHz, C_6D_6) of **dpma^{OMe}**.

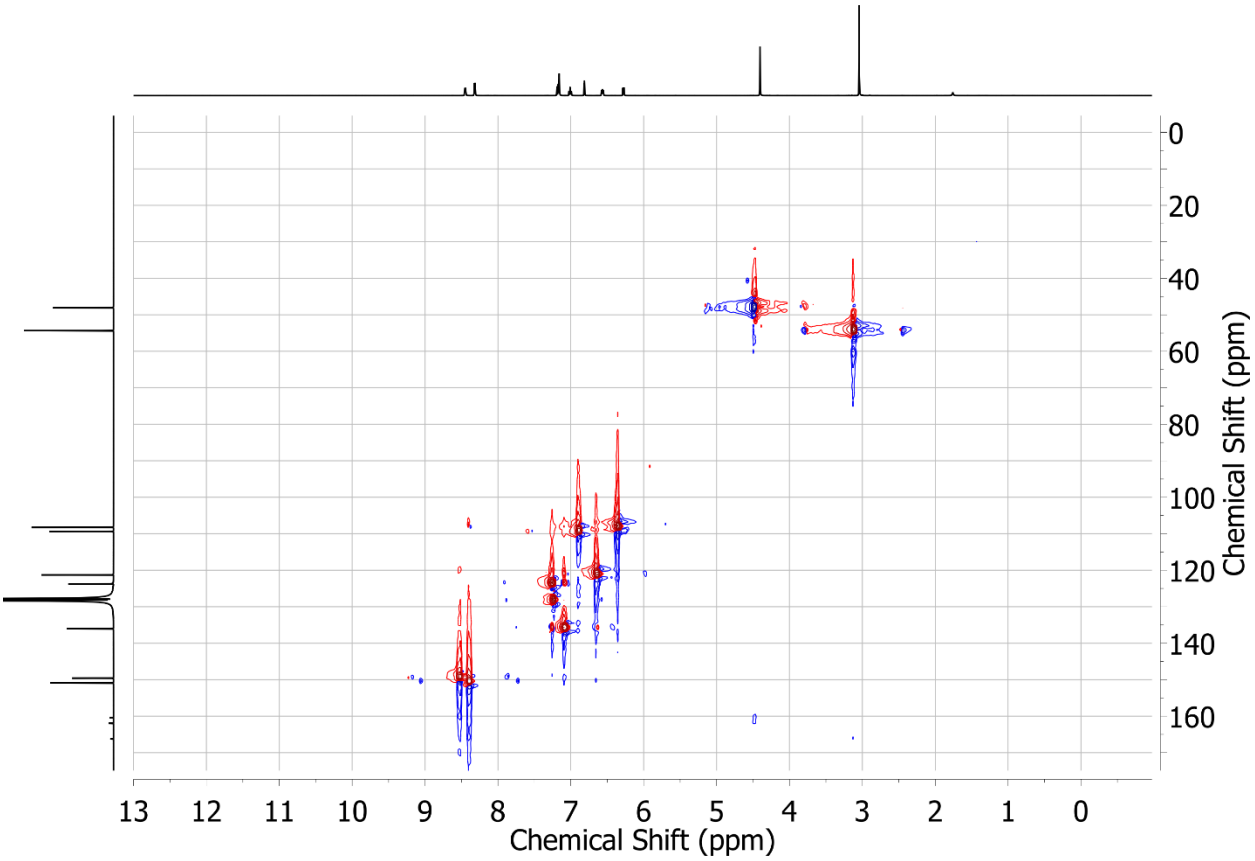

Figure D4. HSQC NMR spectrum (162 MHz, C_6D_6) of **dpma^{OMe}**.

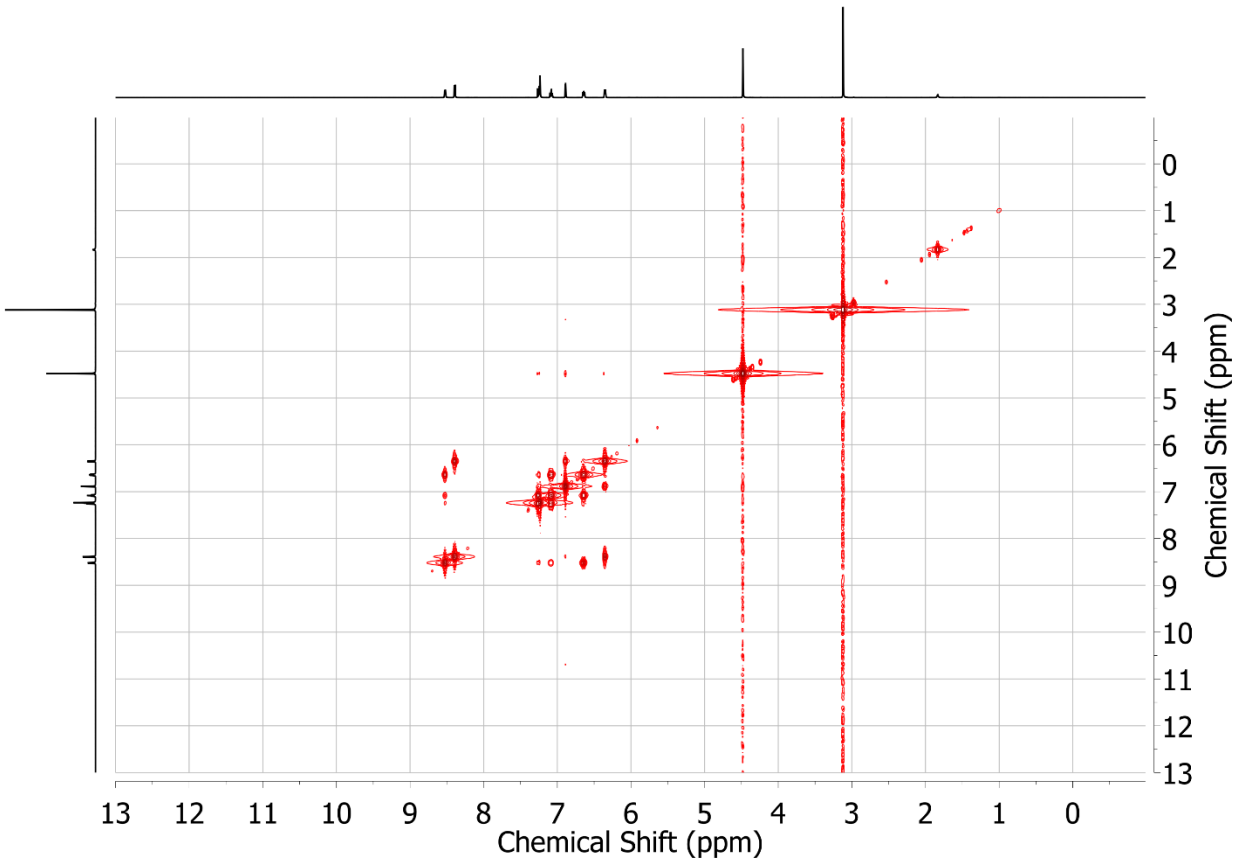

Figure D5. HMBC NMR spectrum (162 MHz, C_6D_6) of **dpma^{OMe}**.

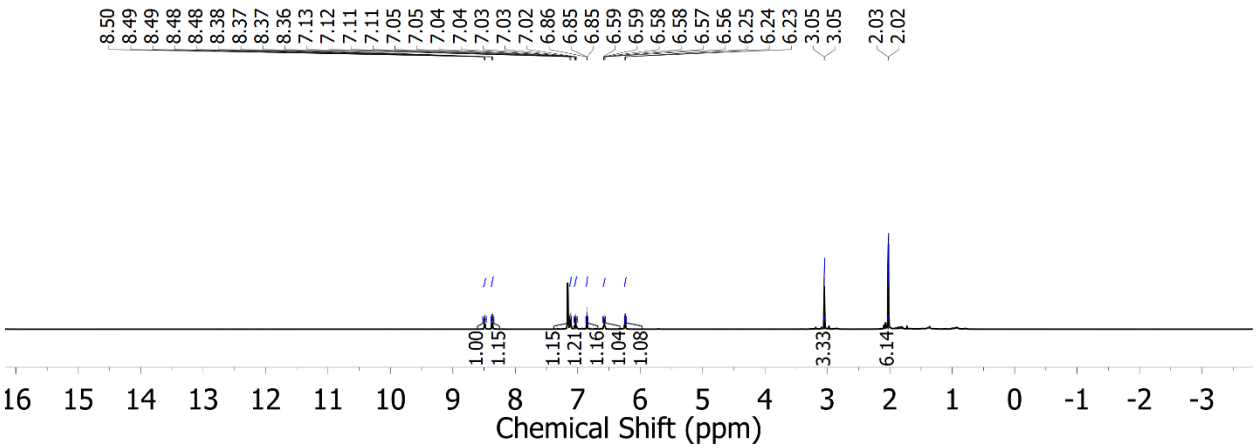

Figure D6. ^{1}H NMR spectrum (500 MHz, C_6D_6) of **Me$_2$dpma^{OMe}**.

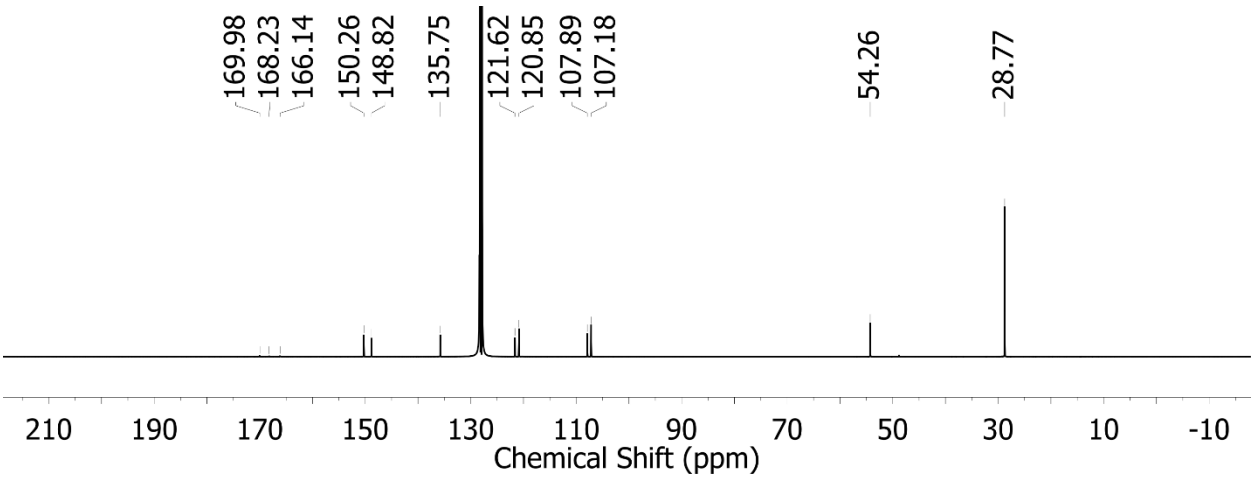

Figure D7. $^{13}C\{^{1}H\}$ NMR spectrum (126 MHz, C_6D_6) of **Me$_2$dpma^{OMe}**.

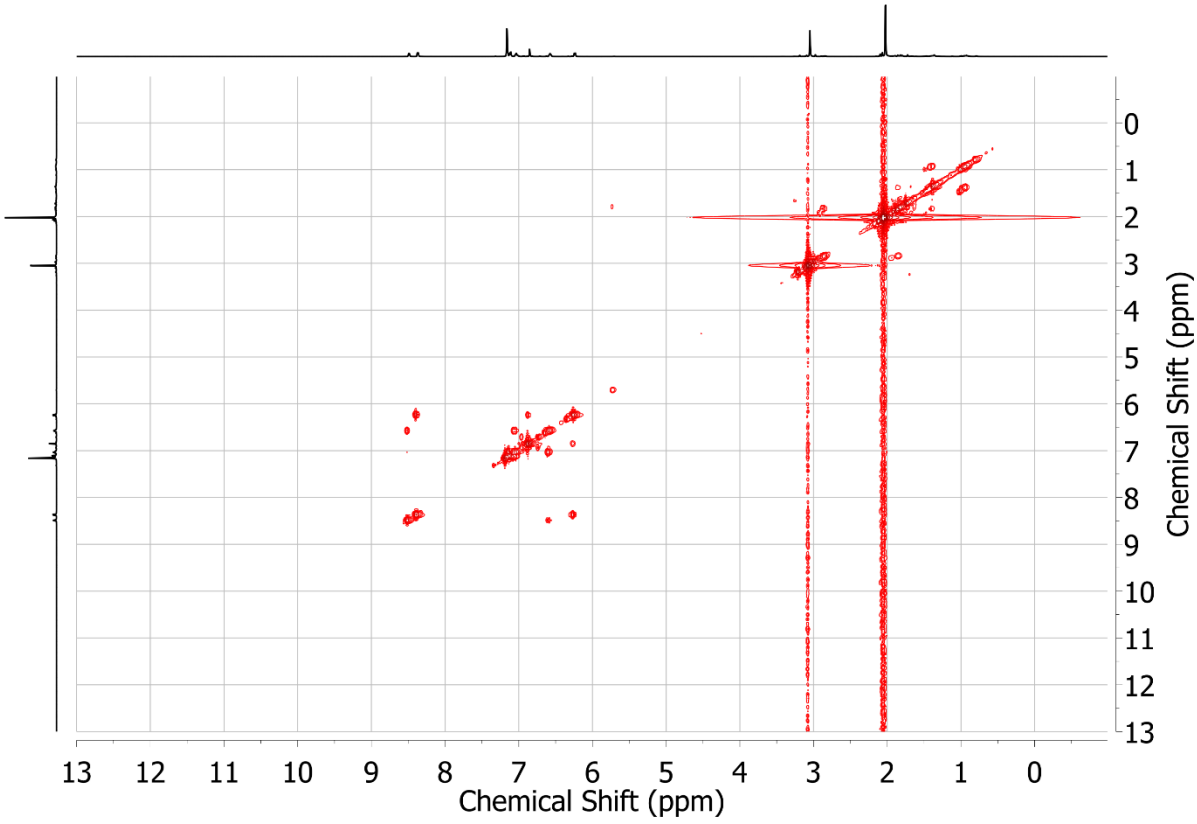

Figure D8. COSY NMR spectrum (126 MHz, C_6D_6) of **Me$_2$dpma^{OMe}**.

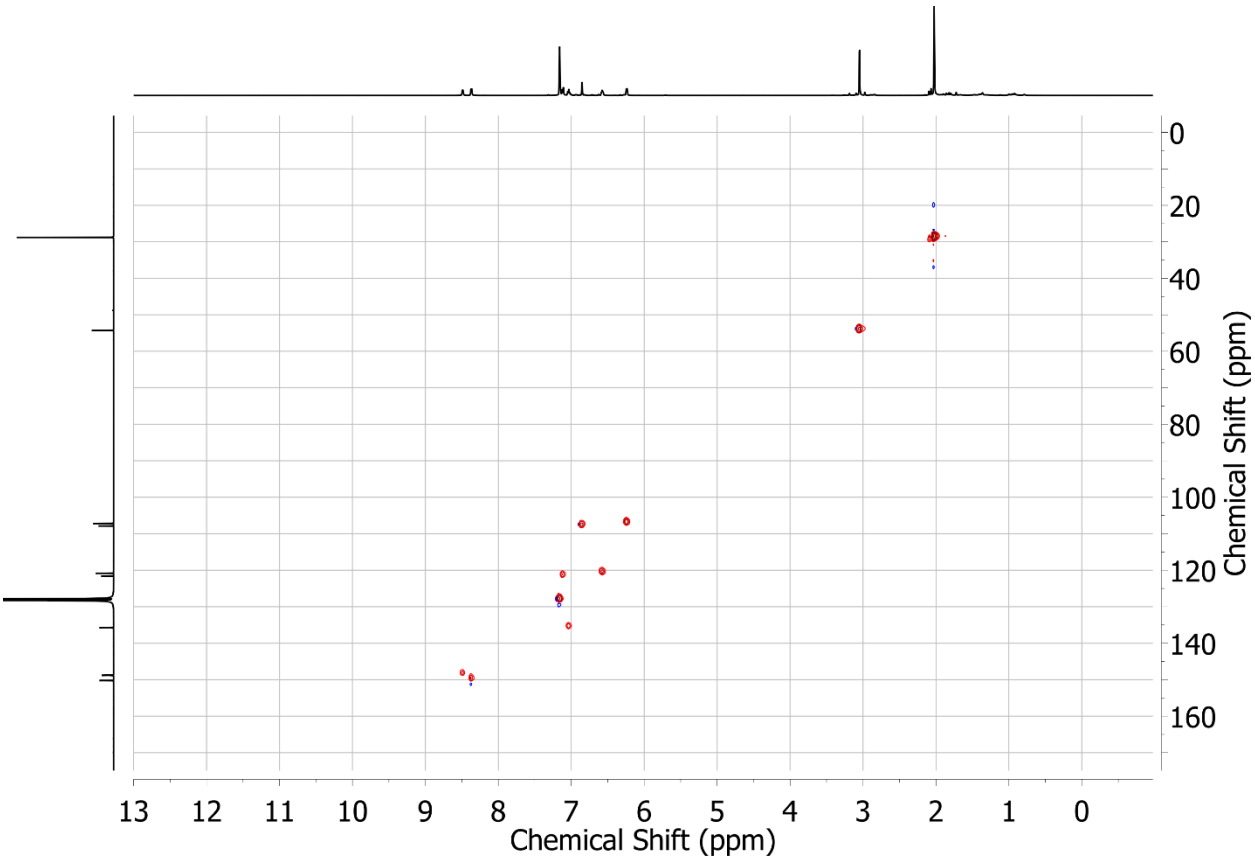

Figure D9. HSQC NMR spectrum (126 MHz, C_6D_6) of **Me$_2$dpma^{OMe}**.

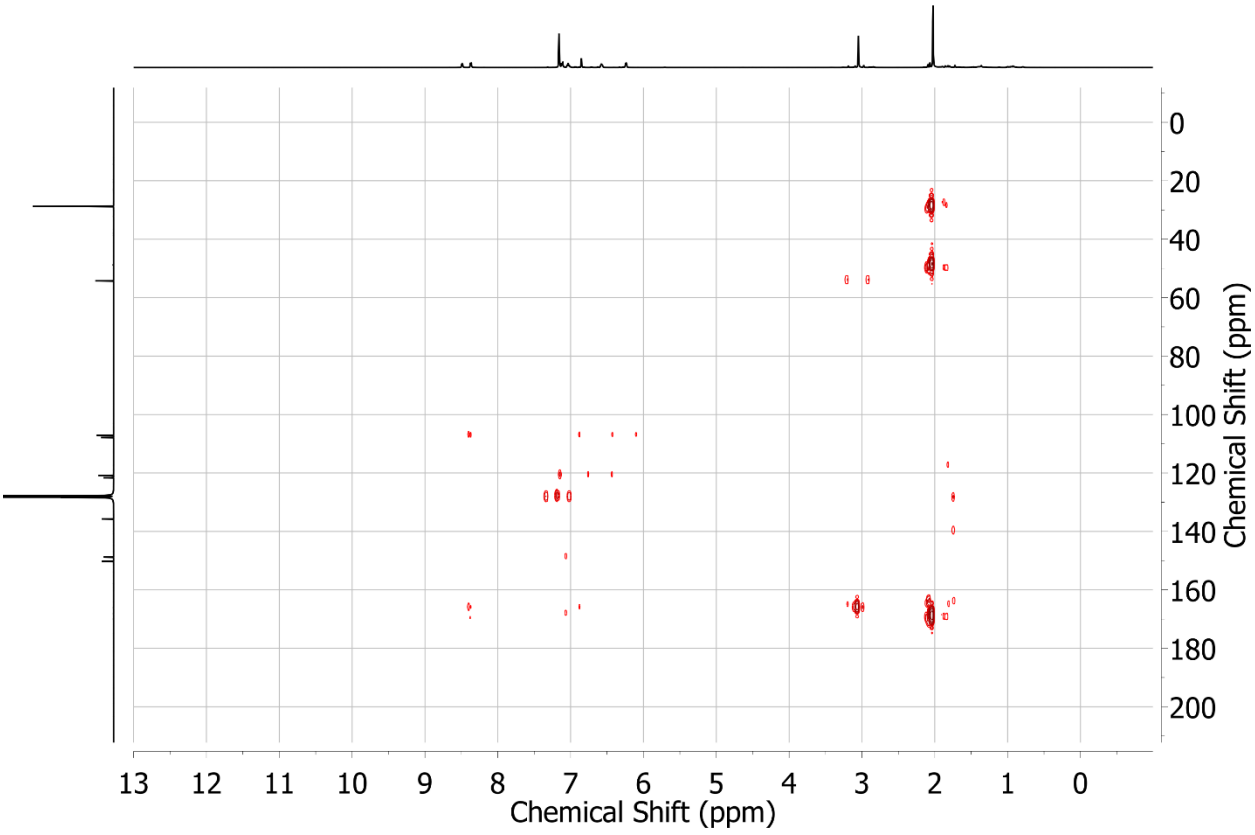

Figure D10. HMBC NMR spectrum (126 MHz, C_6D_6) of **Me$_2$dpma^{OMe}**.

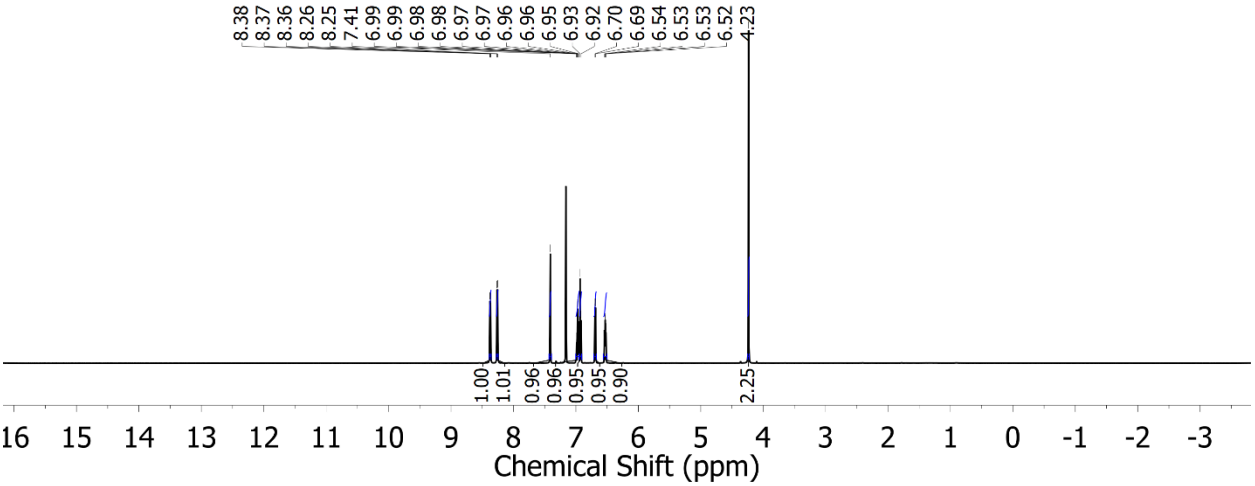

Figure D11. ^{1}H NMR spectrum (500 MHz, C_6D_6) of **dpma^{CF3}**.

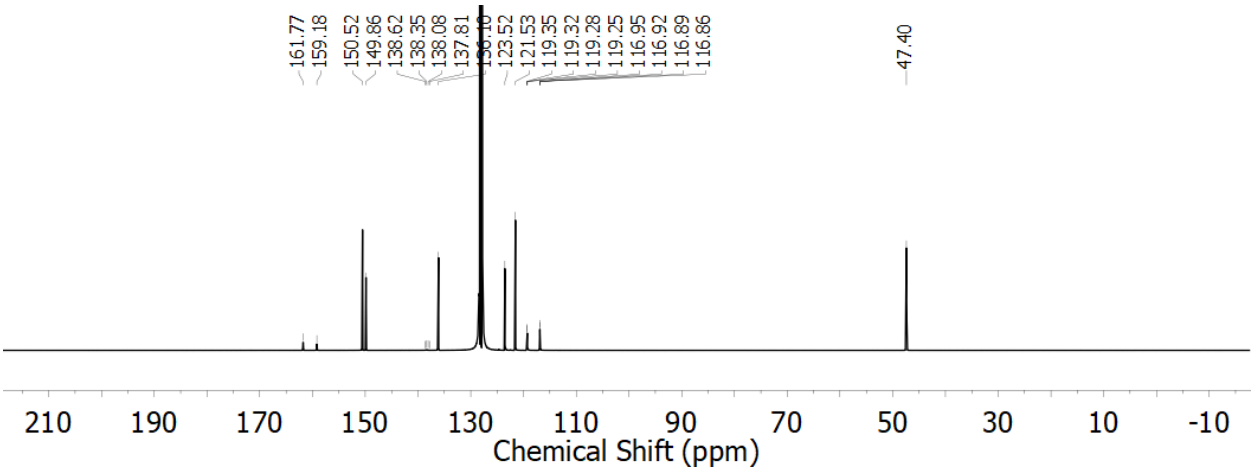

Figure D12. $^{13}C\{^{1}H\}$ NMR spectrum (126 MHz, C_6D_6) of **dpma^{CF3}**.

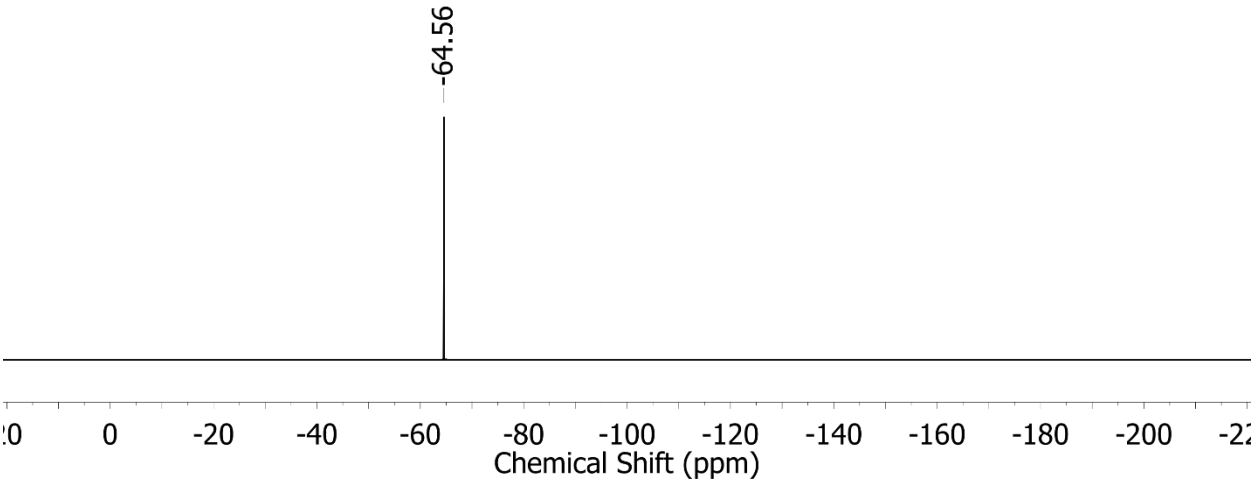

Figure D13. ^{13}F NMR spectrum (376 MHz, C_6D_6) of **dpma^{CF3}**.

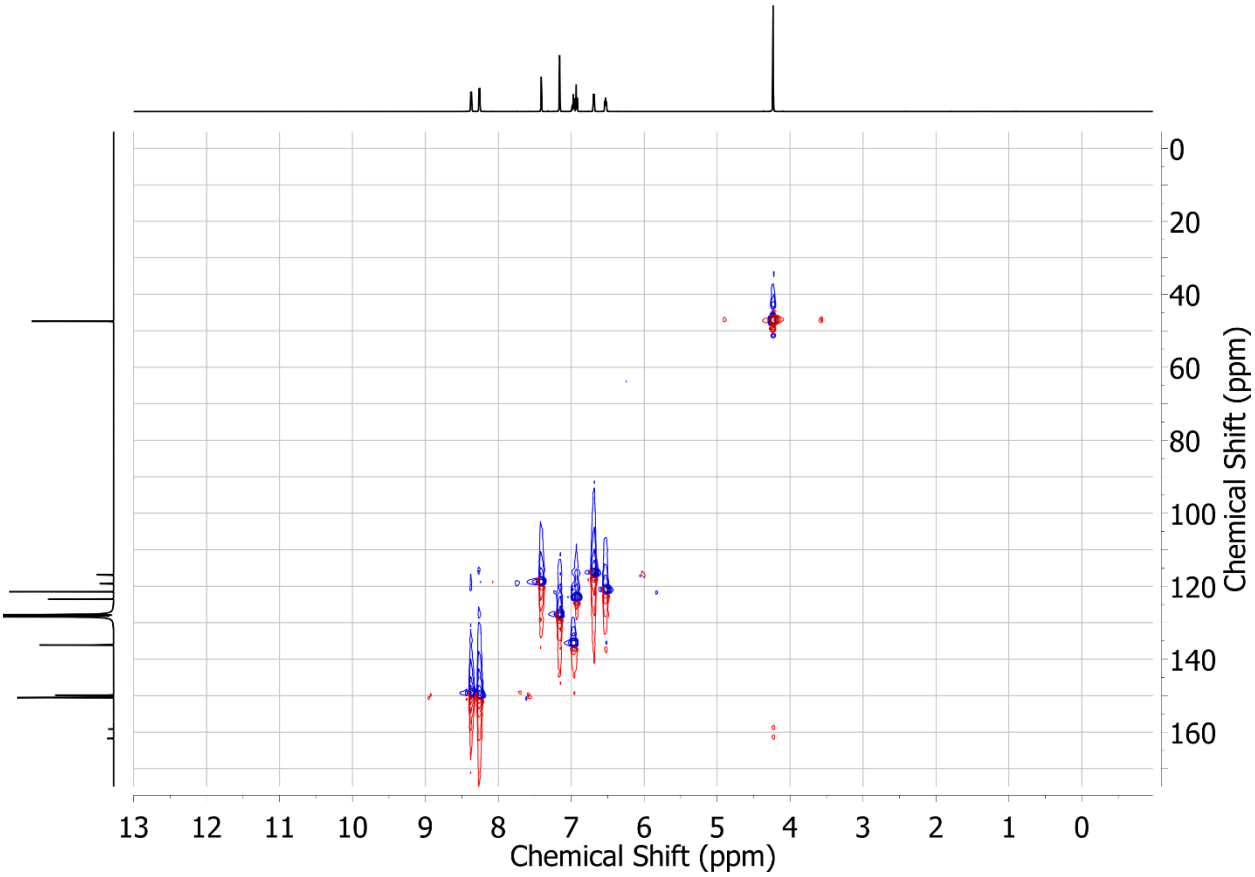

Figure D14. HSQC NMR spectrum (376 MHz, C_6D_6) of **dpma^{CF3}**.

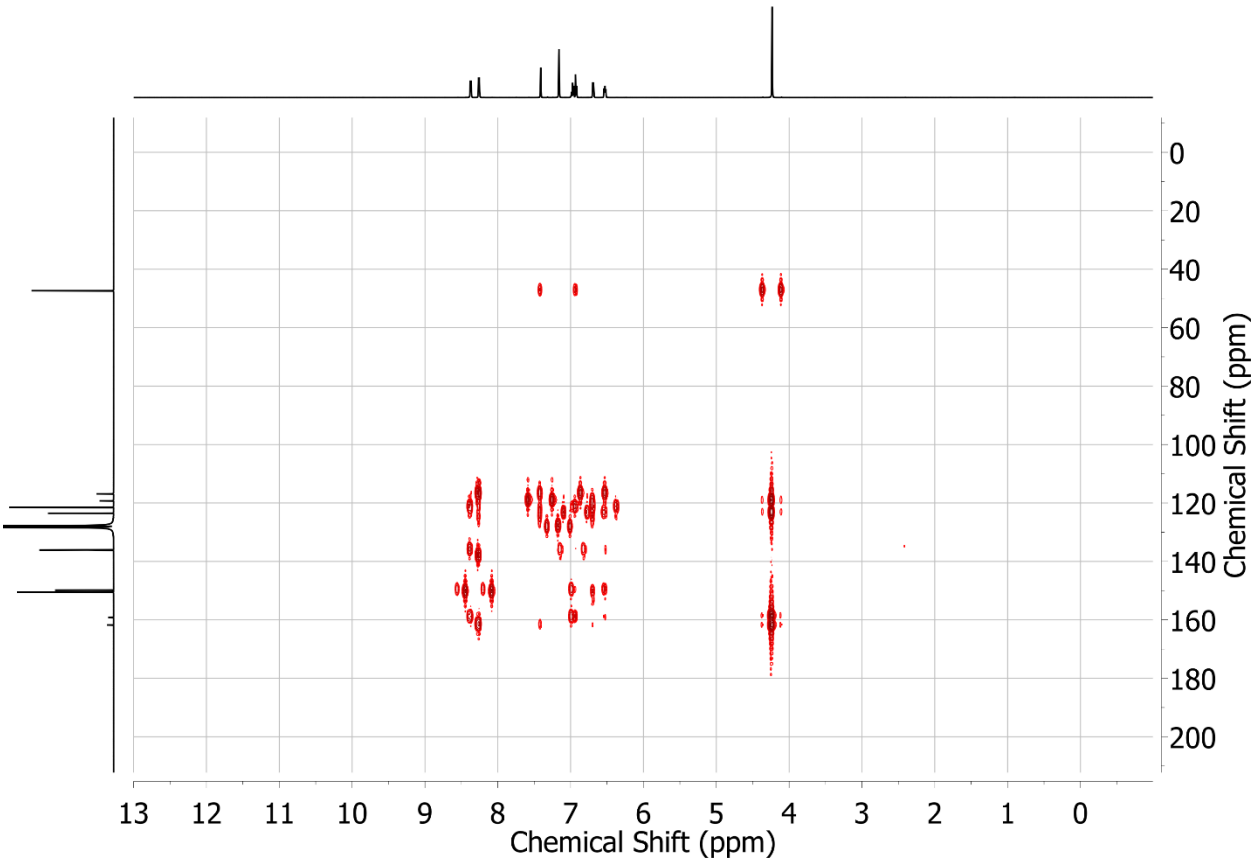

Figure D15. HMBC NMR spectrum (376 MHz, C_6D_6) of **dpma^{CF3}**.

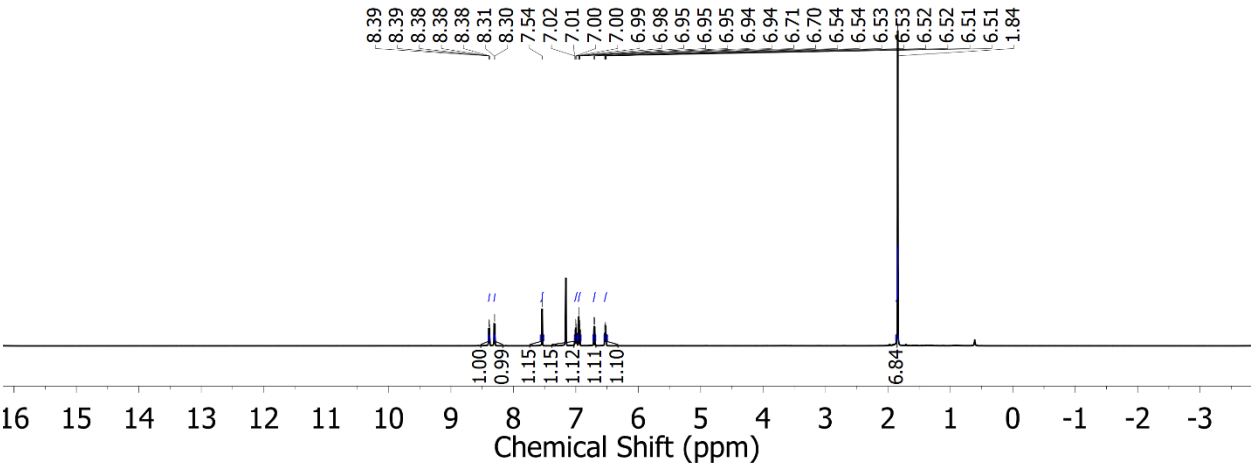

Figure D16. ^{1}H NMR spectrum (500 MHz, C_6D_6) of **Me$_2$dpma^{CF3}**.

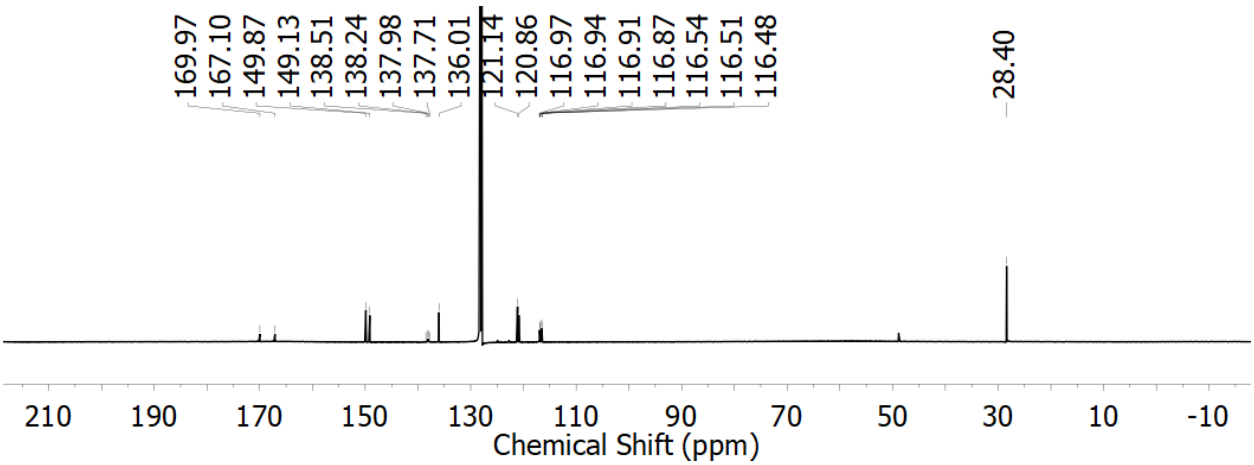

Figure D17. $^{13}C\{^{1}H\}$ NMR spectrum (126 MHz, C_6D_6) of **Me$_2$dpma^{CF3}**.

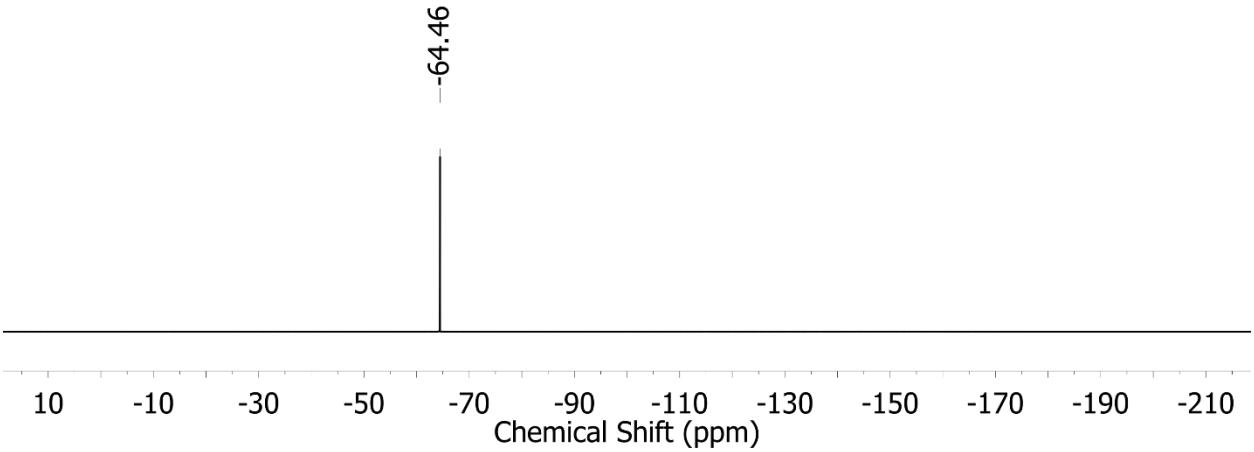

Figure D18. ^{13}F NMR spectrum (376 MHz, C_6D_6) of **Me$_2$dpma^{CF3}**.

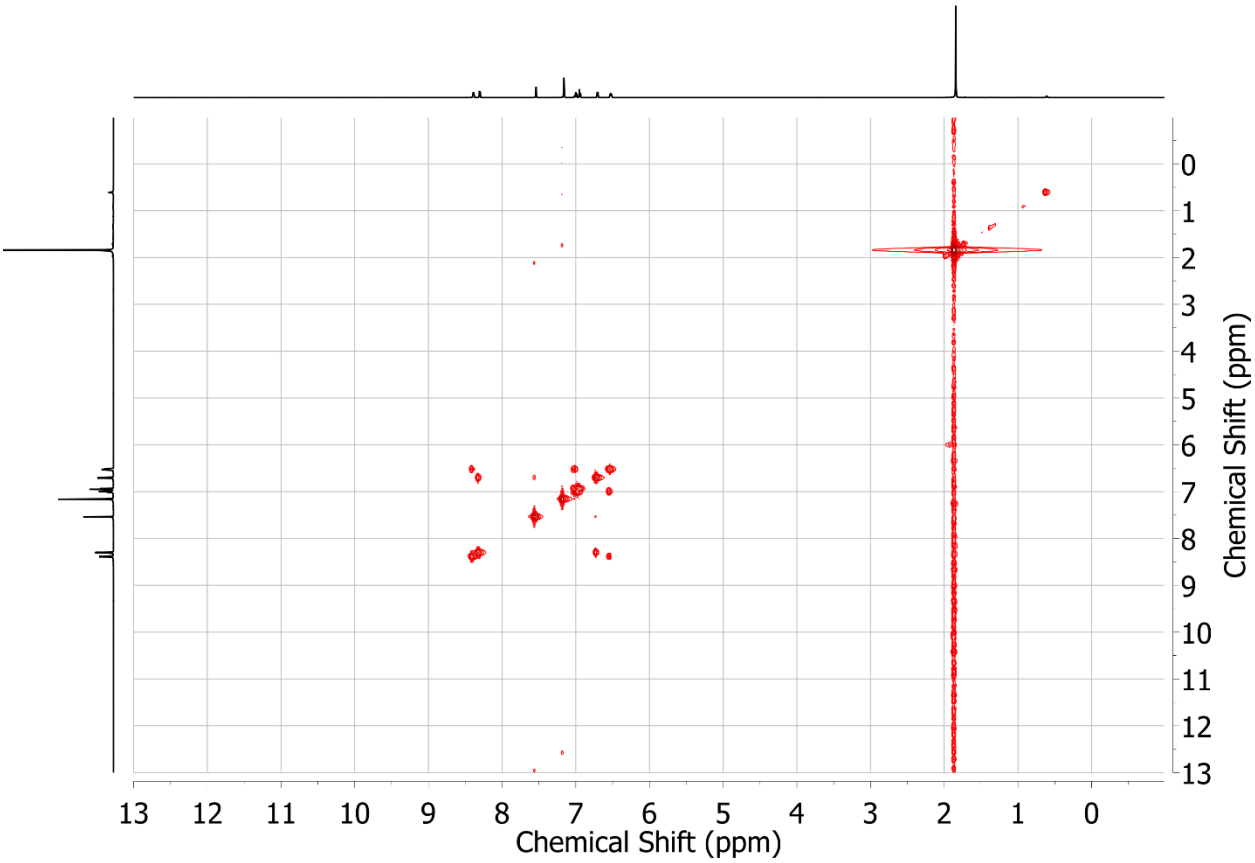

Figure D19. COSY NMR spectrum (126 MHz, C_6D_6) of **Me$_2$dpma^{CF3}**.

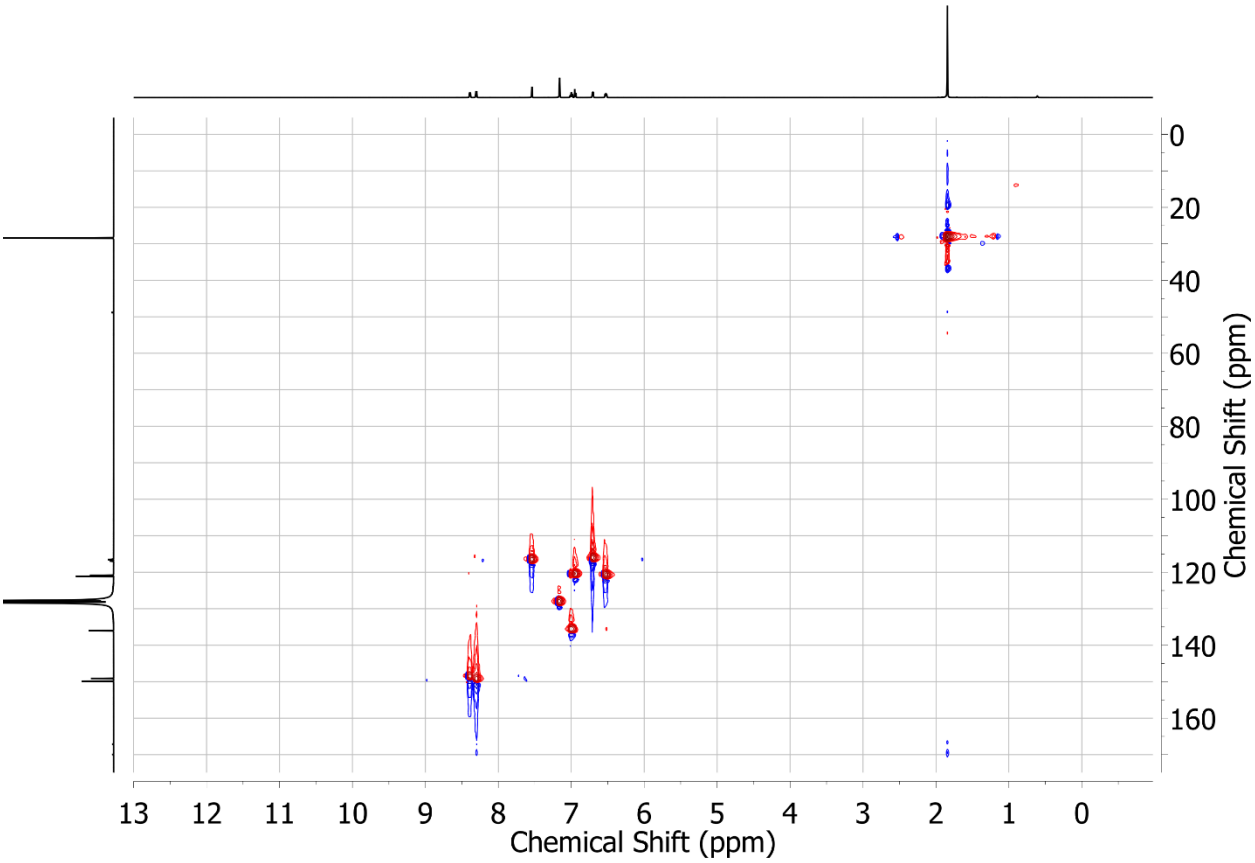

Figure D20. HSQC NMR spectrum (126 MHz, C_6D_6) of **Me$_2$dpma^{CF3}**.

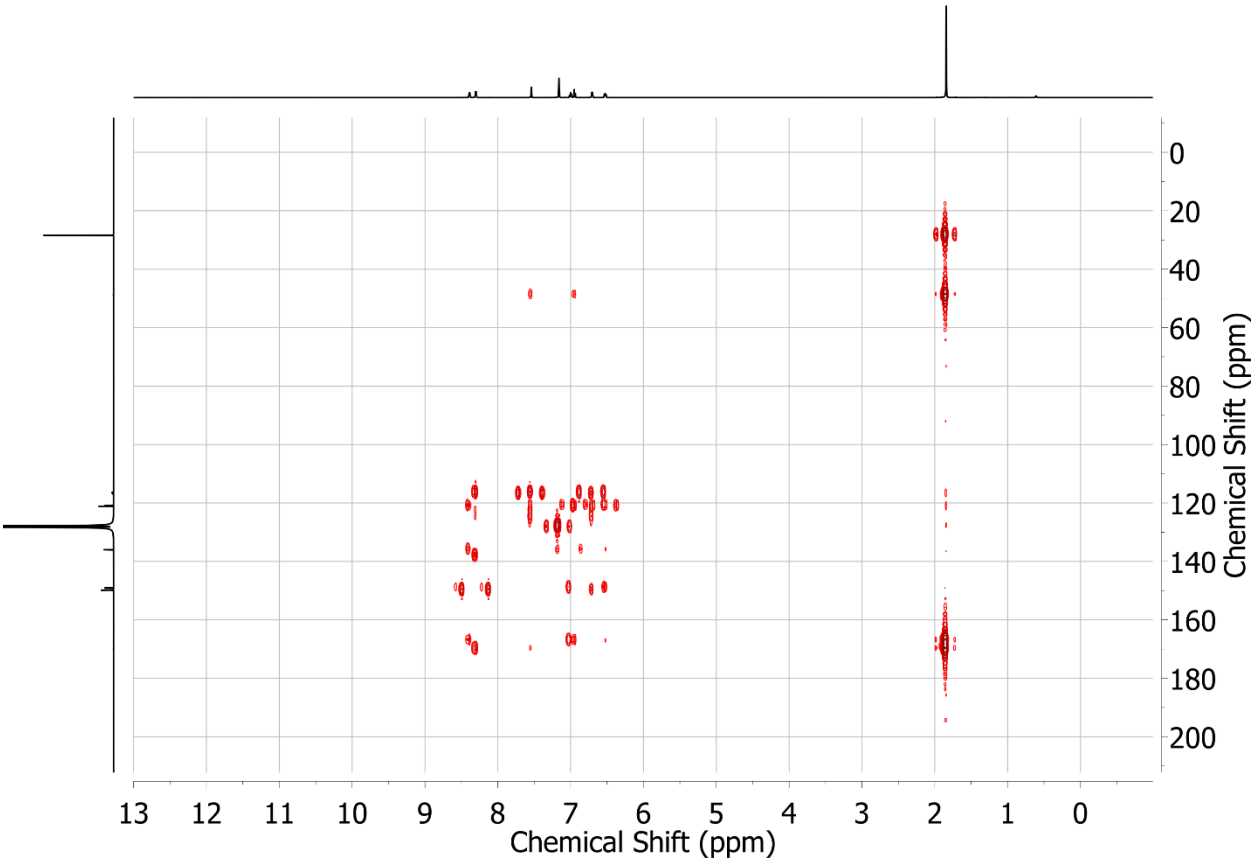

Figure D21. HMBC NMR spectrum (126 MHz, C_6D_6) of **Me$_2$dpma^{CF3}**.

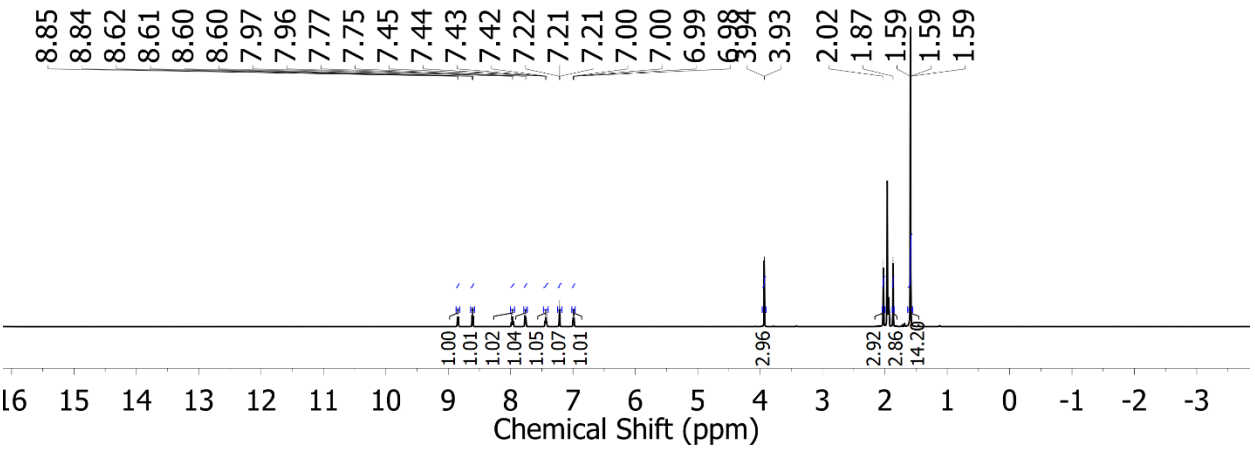

Figure D22. ^{1}H NMR spectrum (500 MHz, CD_3CN) of **A^{OMe}**.

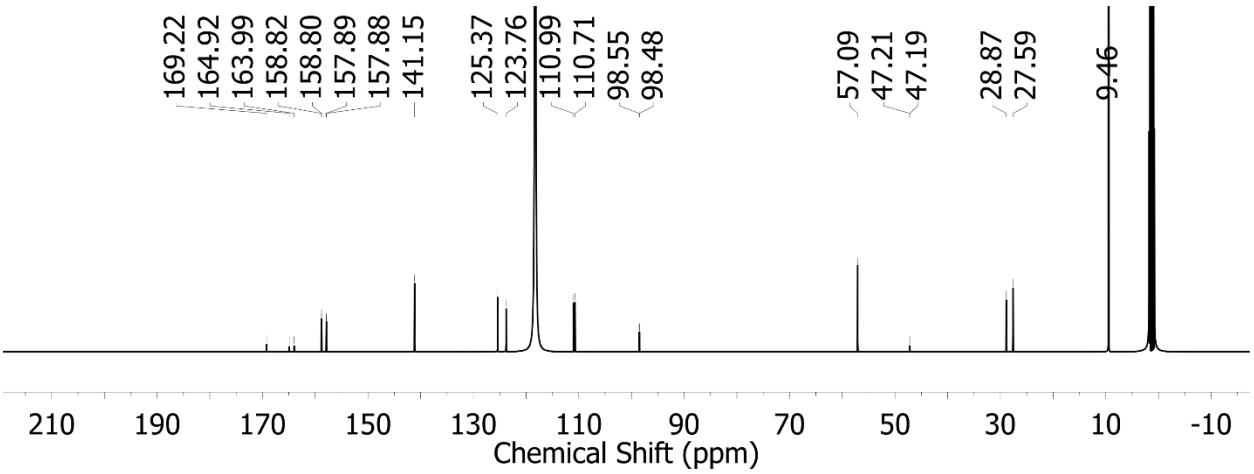

Figure D23. $^{13}C\{^{1}H\}$ NMR spectrum (126 MHz, CD_3CN) of $\mathbf{A^{OMe}}$.

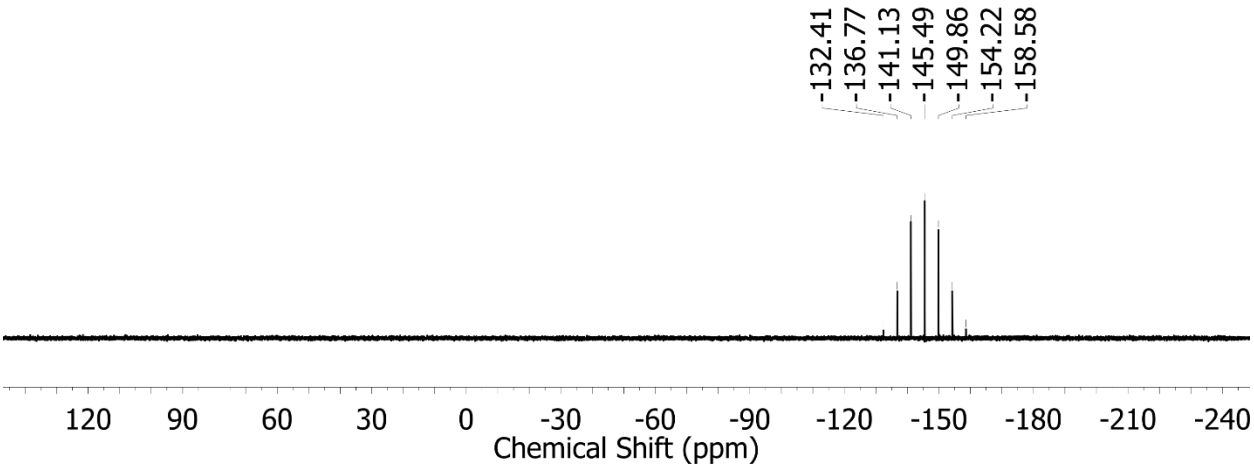

Figure D24. ^{31}P NMR spectrum (162 MHz, CD_3CN) of $\mathbf{A^{OMe}}$.

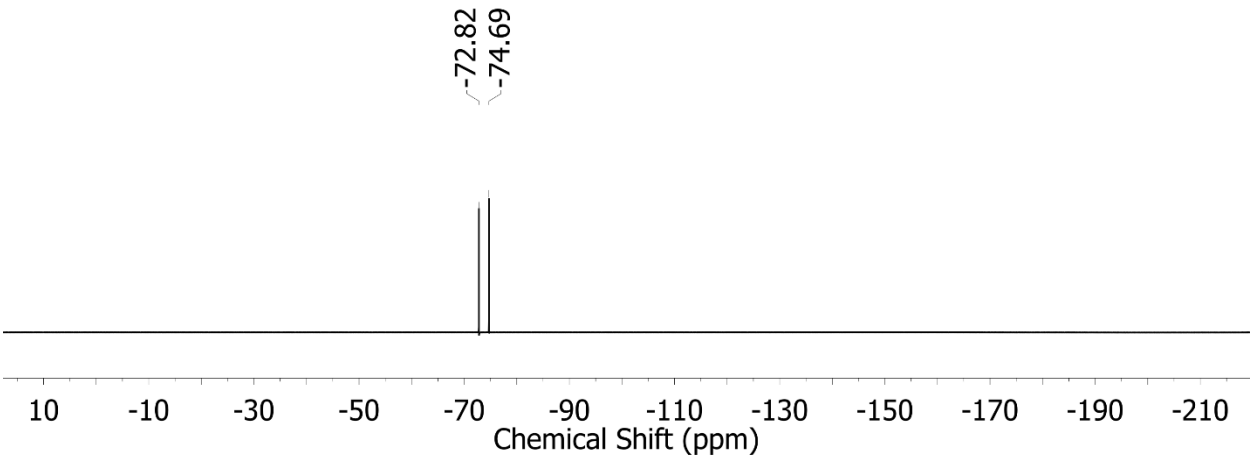

Figure D25. ^{19}F NMR spectrum (162 MHz, CD_3CN) of $\mathbf{A^{OMe}}$.

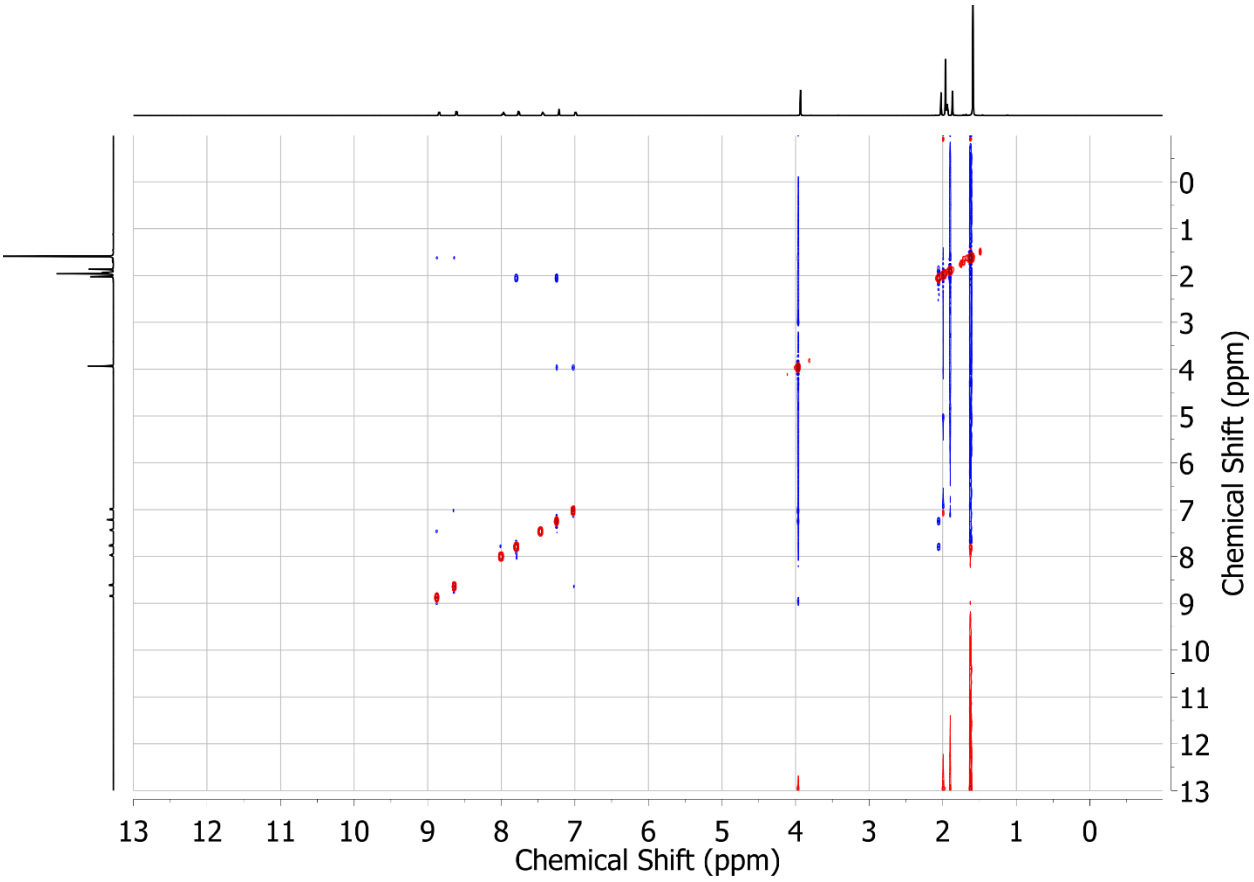

Figure D26. NOESY NMR spectrum (126 MHz, C_6D_6) of $\mathbf{A^{OMe}}$.

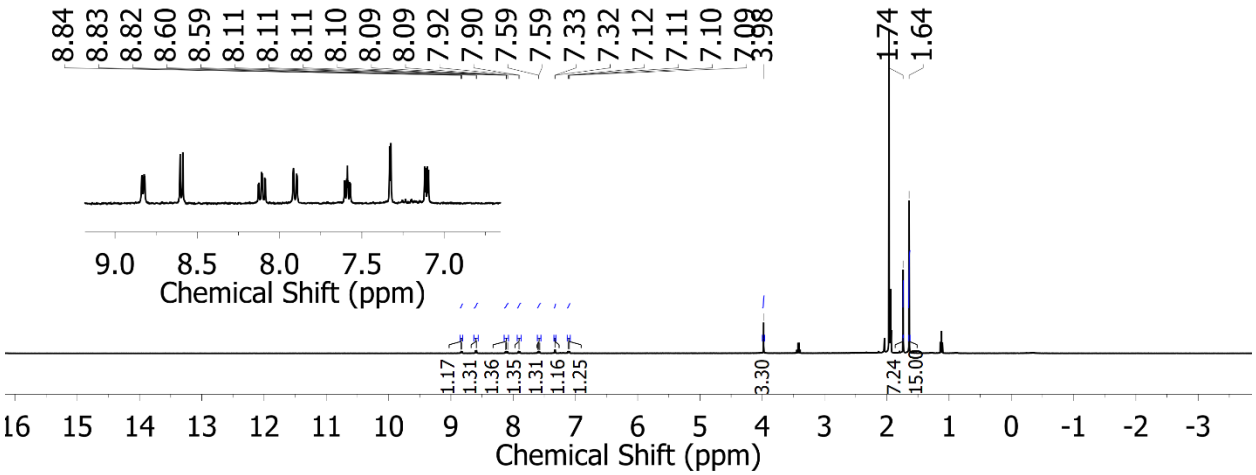

Figure D27. ^{1}H NMR spectrum (500 MHz, CD_3CN) of $\mathbf{1^{OMe}}$.

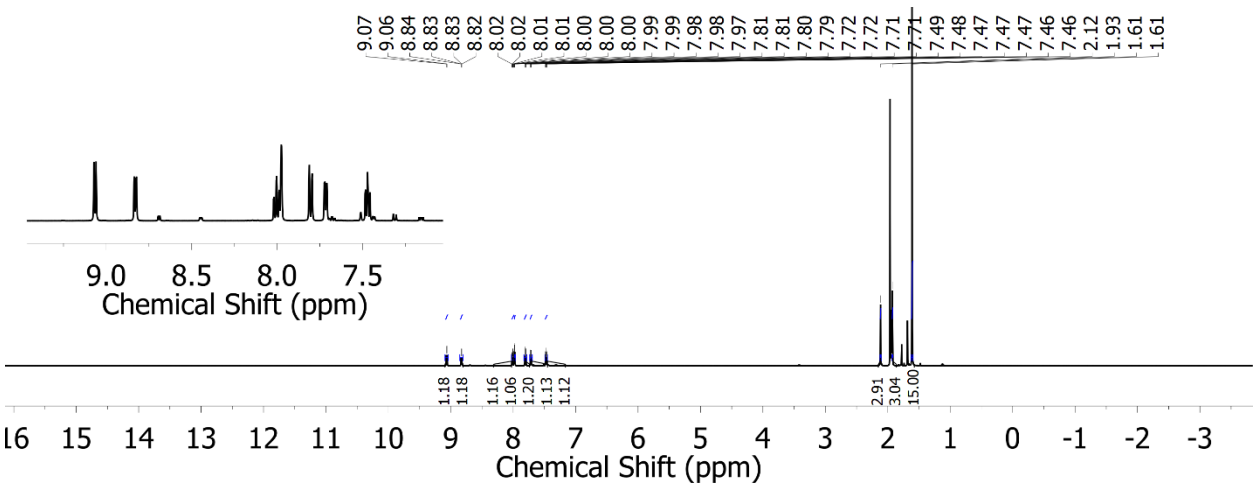

Figure D28. ^{1}H NMR spectrum (500 MHz, CD_3CN) of $\mathbf{A^{CF3}}$. Small aromatic resonances from 8.5 to 7.0 ppm corresponds to $\mathbf{Me_2dpma^{CF3}}$ ligand impurity.

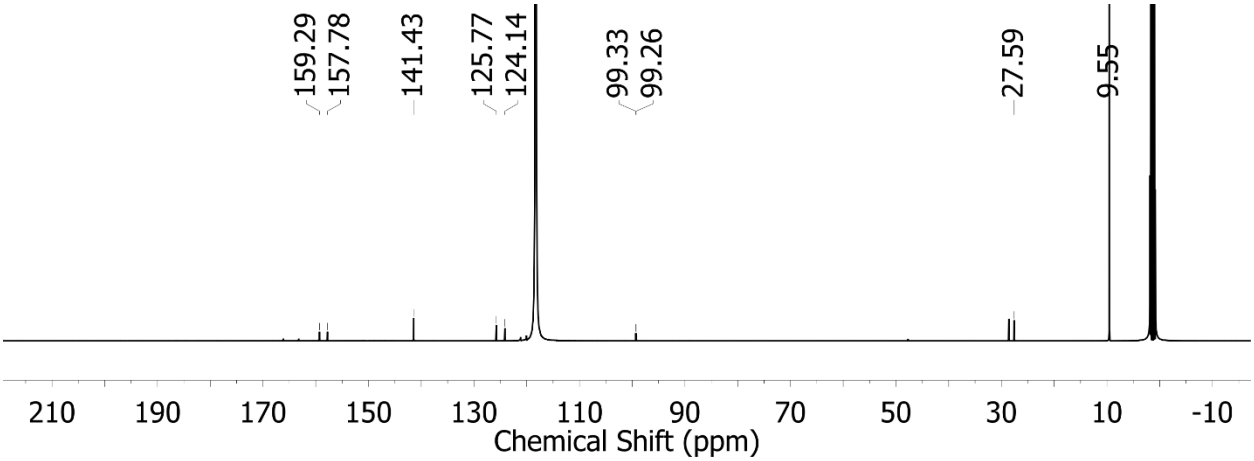

Figure D29. $^{13}C\{^{1}H\}$ NMR spectrum (126 MHz, CD_3CN) of $\mathbf{A^{CF3}}$. Additional resonances correspond to $\mathbf{Me_2dpma^{CF3}}$ ligand impurity.

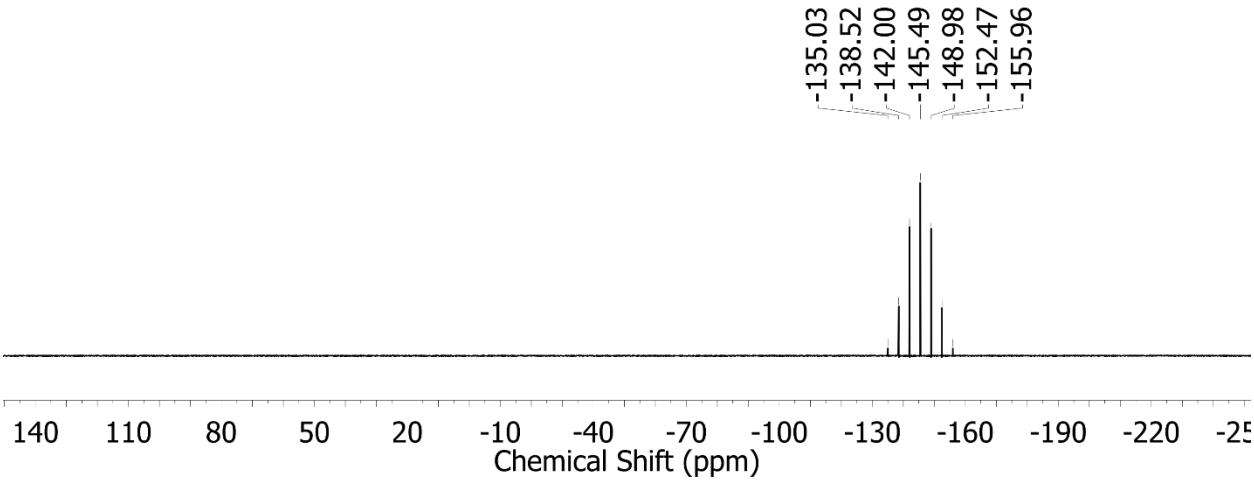

Figure D30. ^{31}P NMR spectrum (162 MHz, CD_3CN) of $\mathbf{A^{CF3}}$.

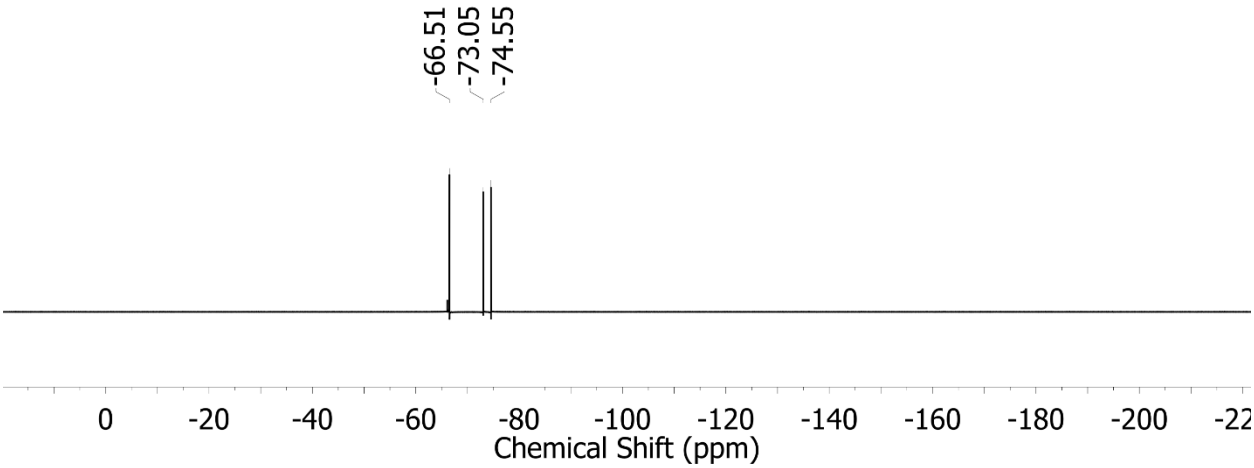

Figure D31. ^{19}F NMR spectrum (162 MHz, CD_3CN) of $\mathbf{A}^{\mathbf{CF3}}$. Singlet at –66.51 ppm corresponds to $\mathbf{Me_2dpma}^{\mathbf{CF3}}$ ligand impurity.

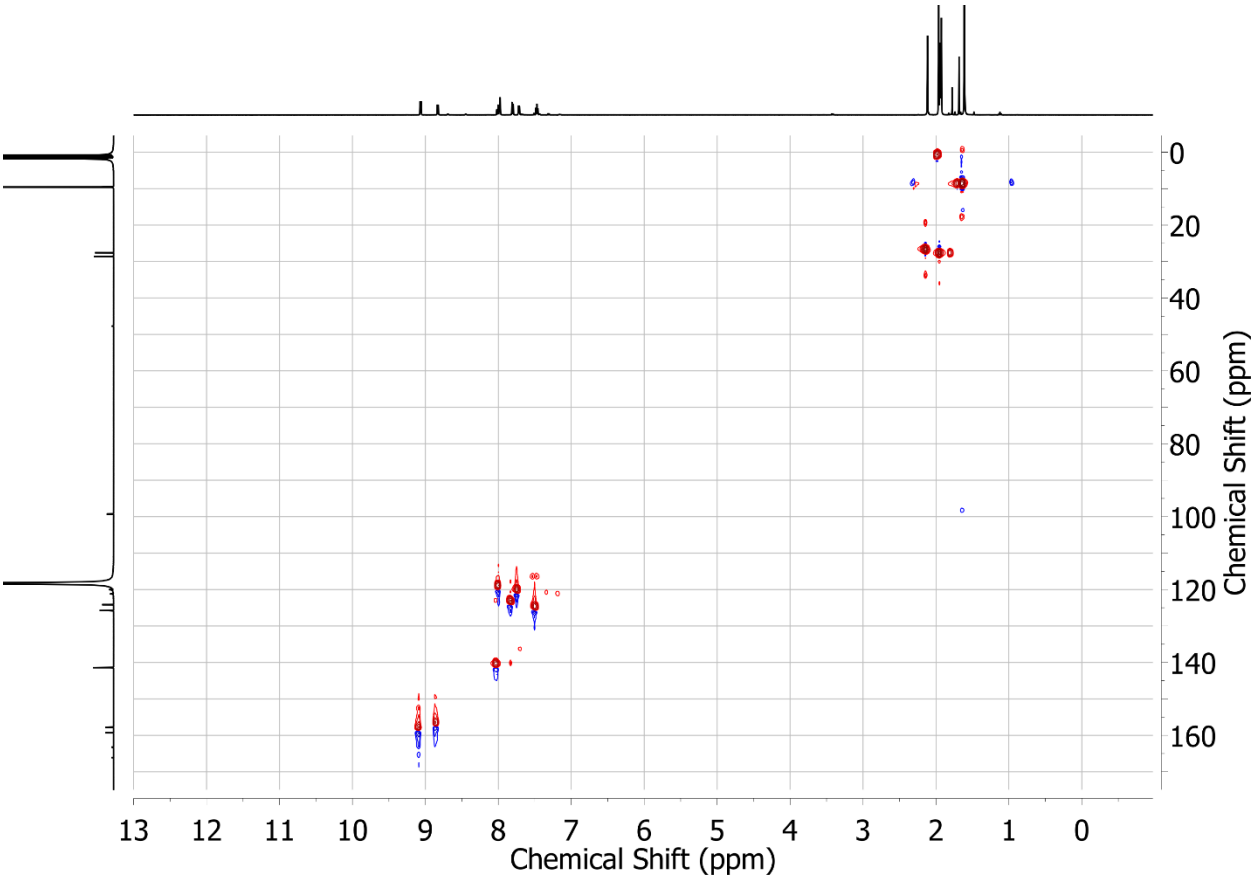

Figure D32. HSQC NMR spectrum (126 MHz, C_6D_6) of $\mathbf{A}^{\mathbf{CF3}}$.

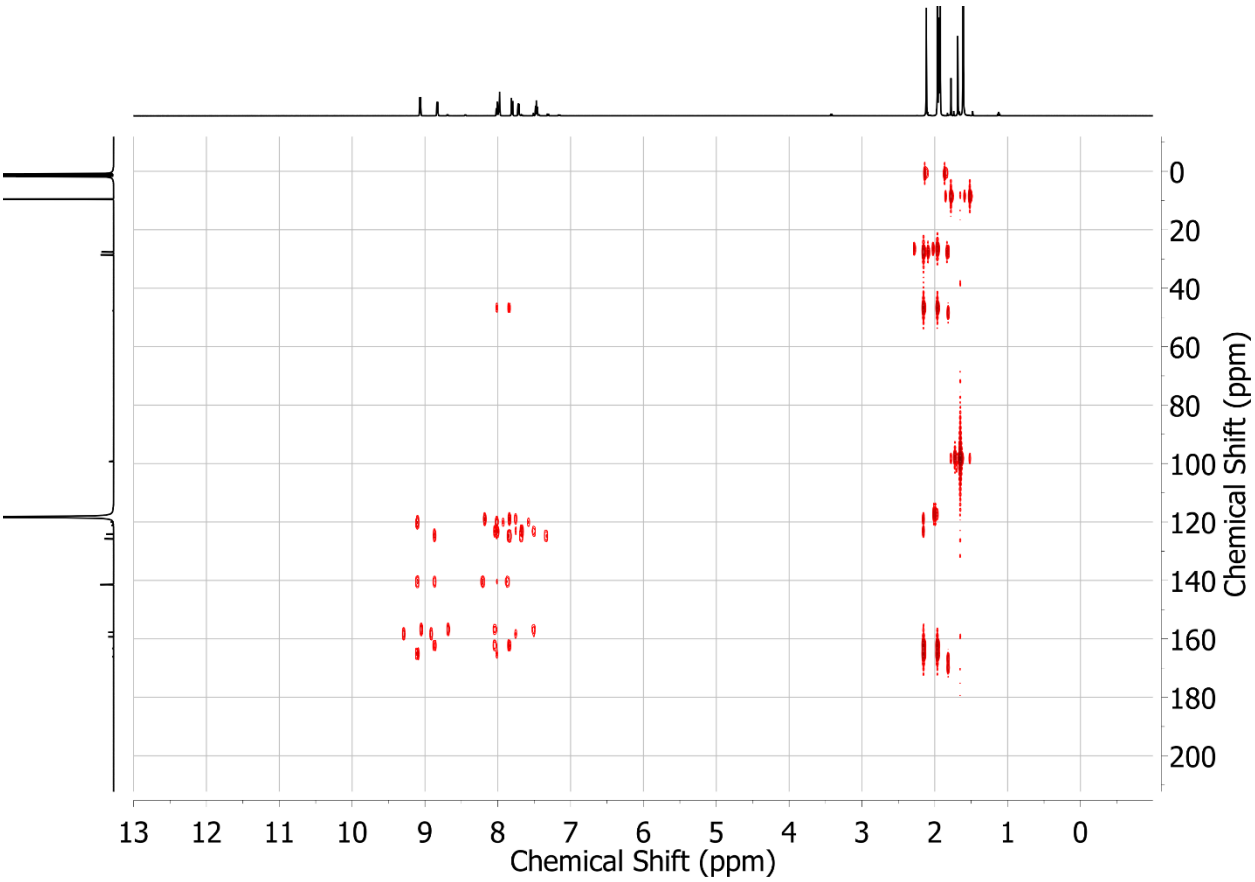

Figure D33. HMBC NMR spectrum (126 MHz, C_6D_6) of $\mathbf{A}^{\mathbf{CF3}}$.

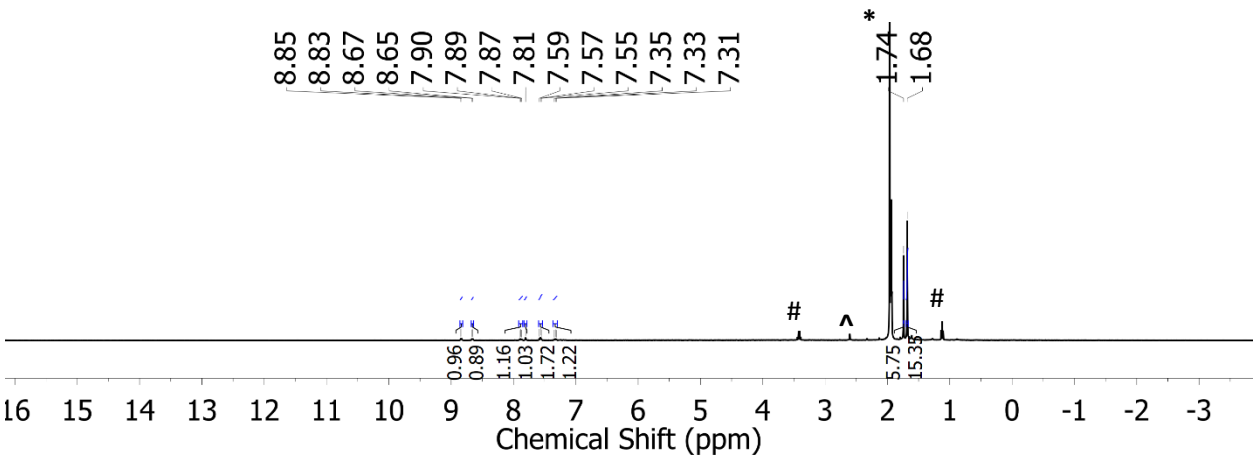

Figure D34. ^{1}H NMR spectrum (500 MHz, CD_3CN) of $\mathbf{1^{CF3}}$. #,^, and * indicate diethyl ether, water and CH_3CN respectively. Solvents are present due to inability to dry crystalline material extensively due to risk of desolvation and decomposition of solvento material.

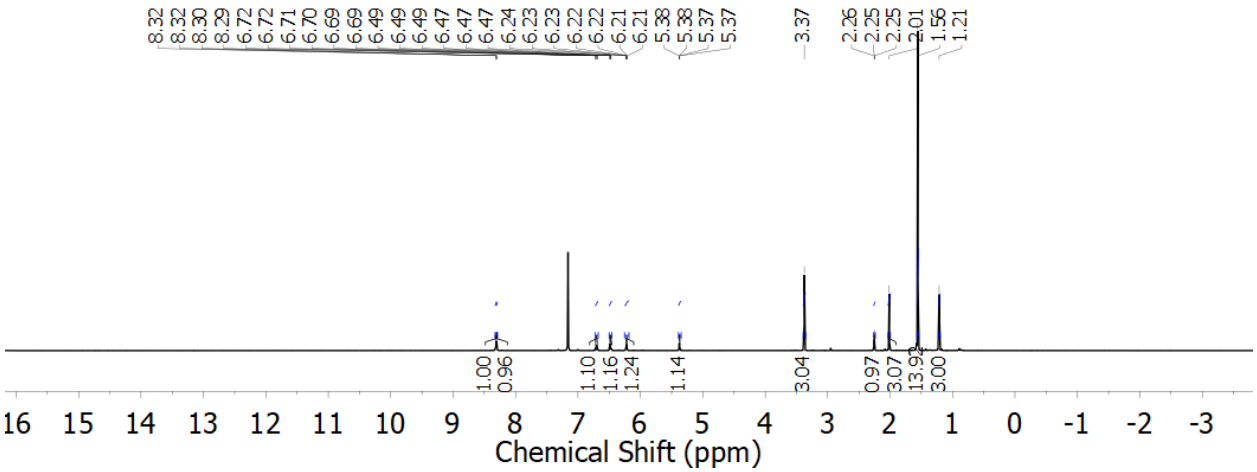

Figure D35. ^{1}H NMR spectrum (500 MHz, CD_3CN) of $\mathbf{3^{OMe}}$.

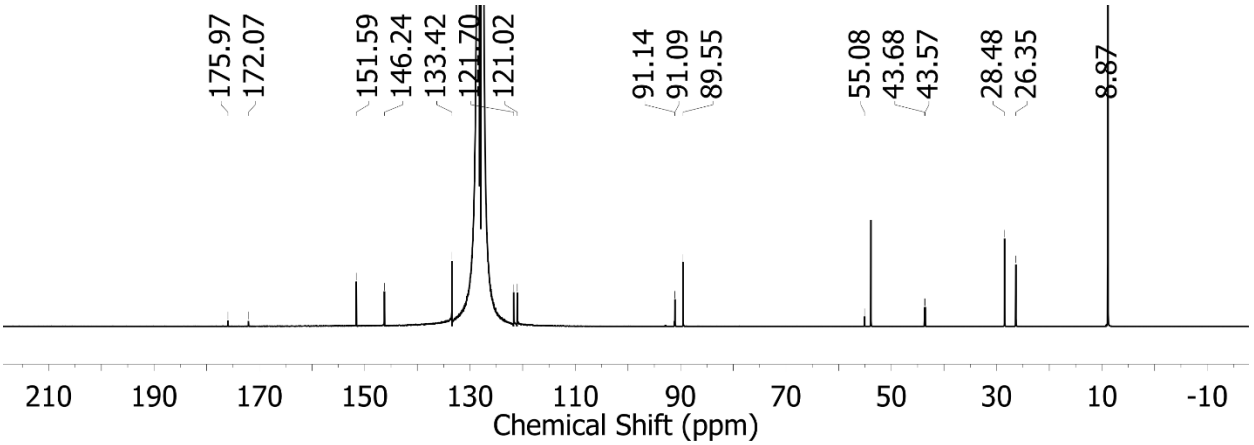

Figure D36. $^{13}C\{^{1}H\}$ NMR spectrum (126 MHz, CD_3CN) of **3^{OMe}**.

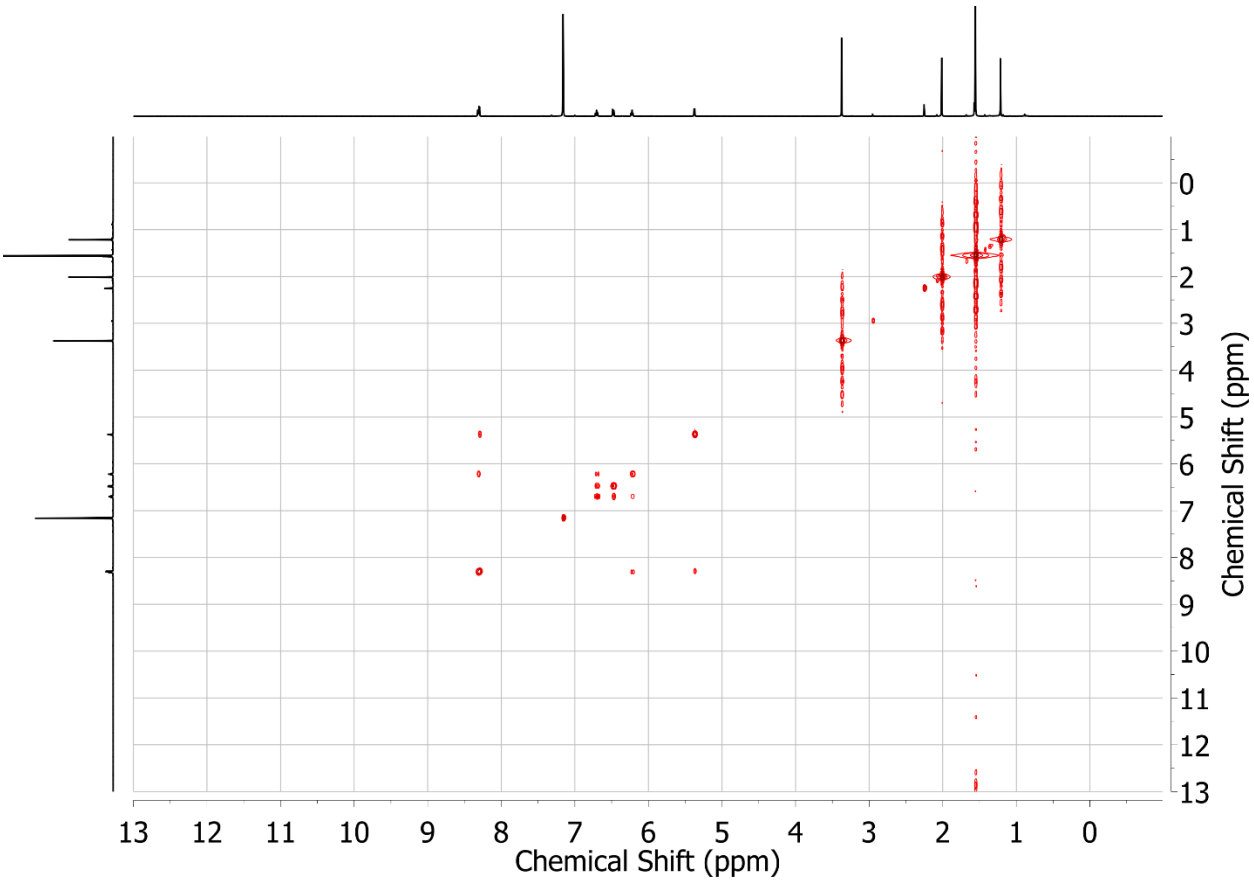

Figure D37. COSY NMR spectrum (126 MHz, C_6D_6) of **3^{OMe}**.

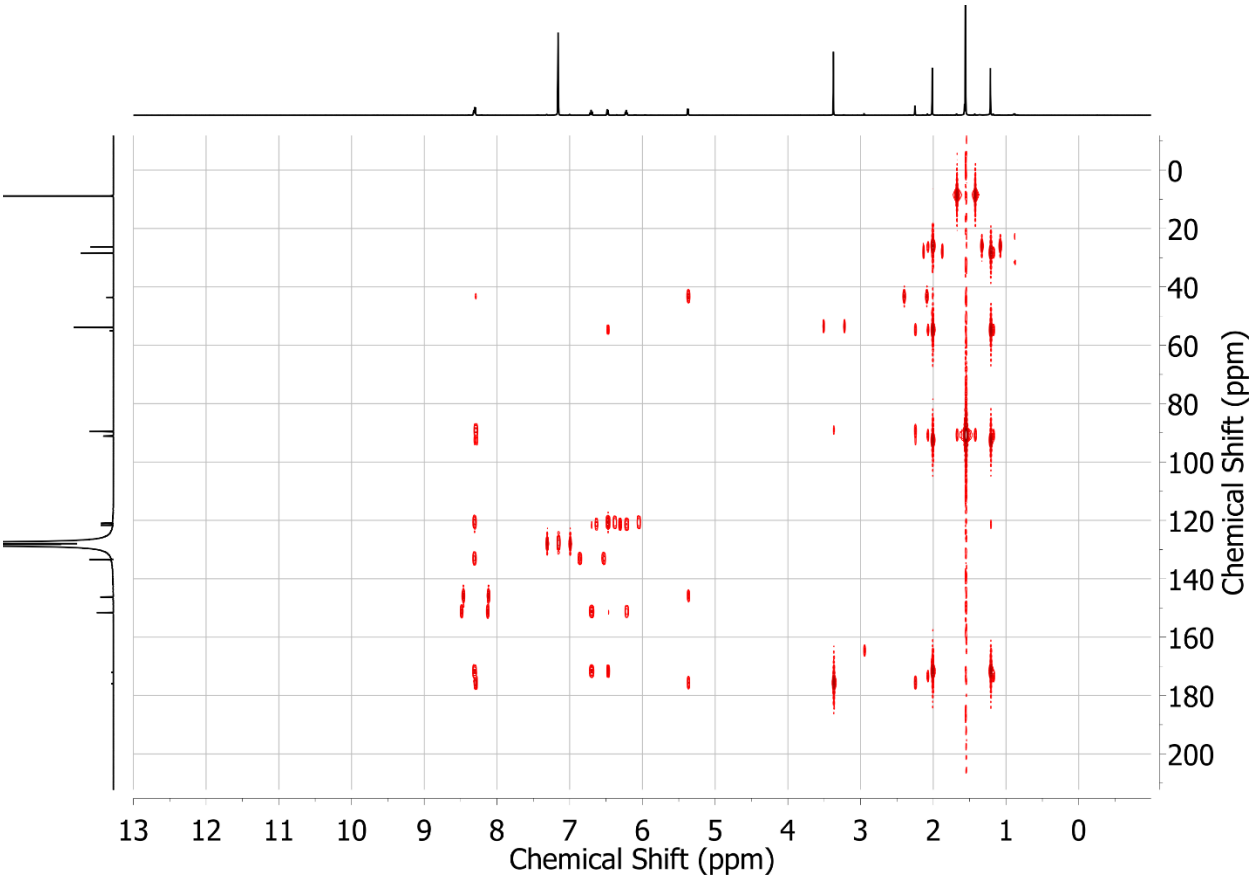

Figure D38. HSQC NMR spectrum (126 MHz, C_6D_6) of $\mathbf{3^{OMe}}$.

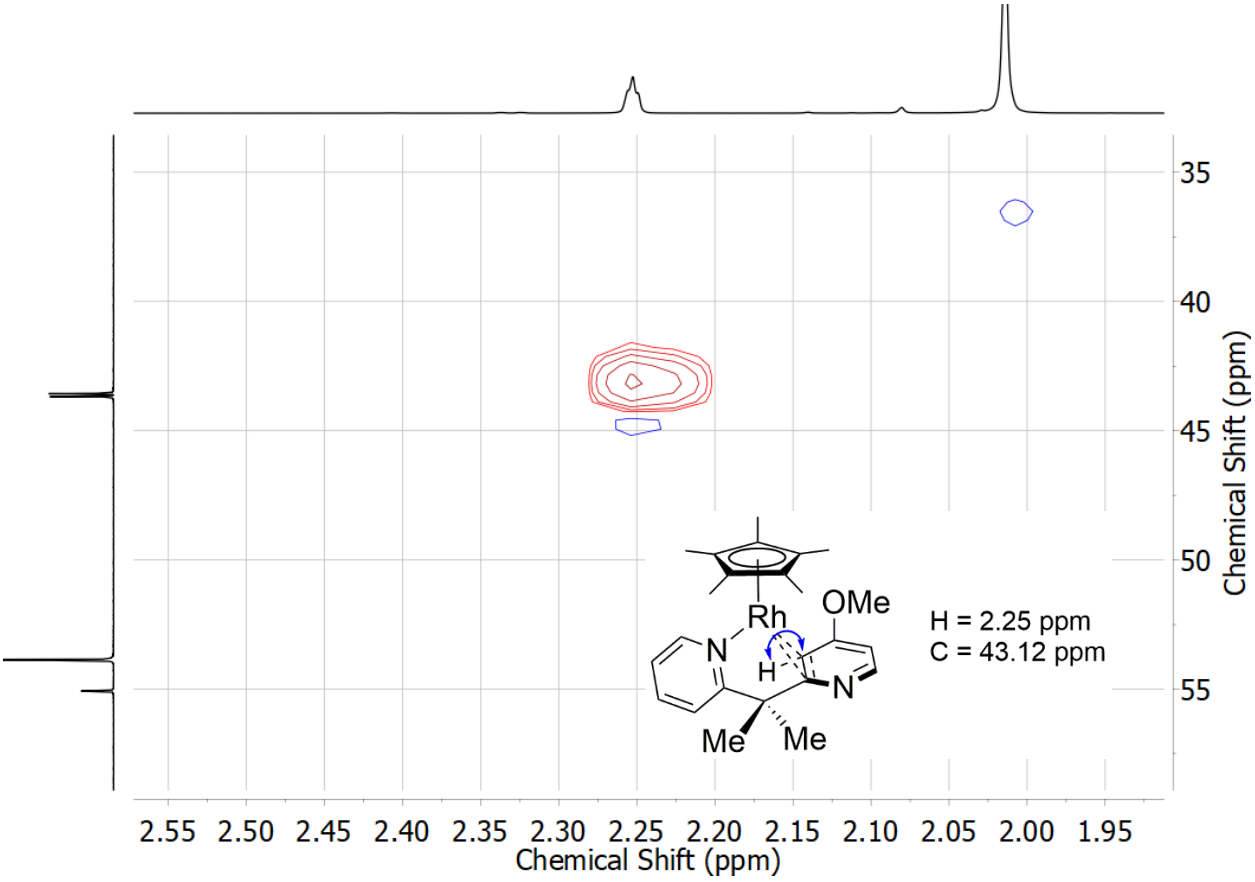

Figure D39. Zoomed in HSQC NMR spectrum (126 MHz, C_6D_6) of **3^{OMe}**. The ^{1}H NMR resonance at 2.25 ppm corresponding to H10 and $^{13}C\{^{1}H\}$ NMR resonance at 43.12 ppm corresponding to the pyramidalized C10 are interacting through bond coupling as indicated by the blue arrow.

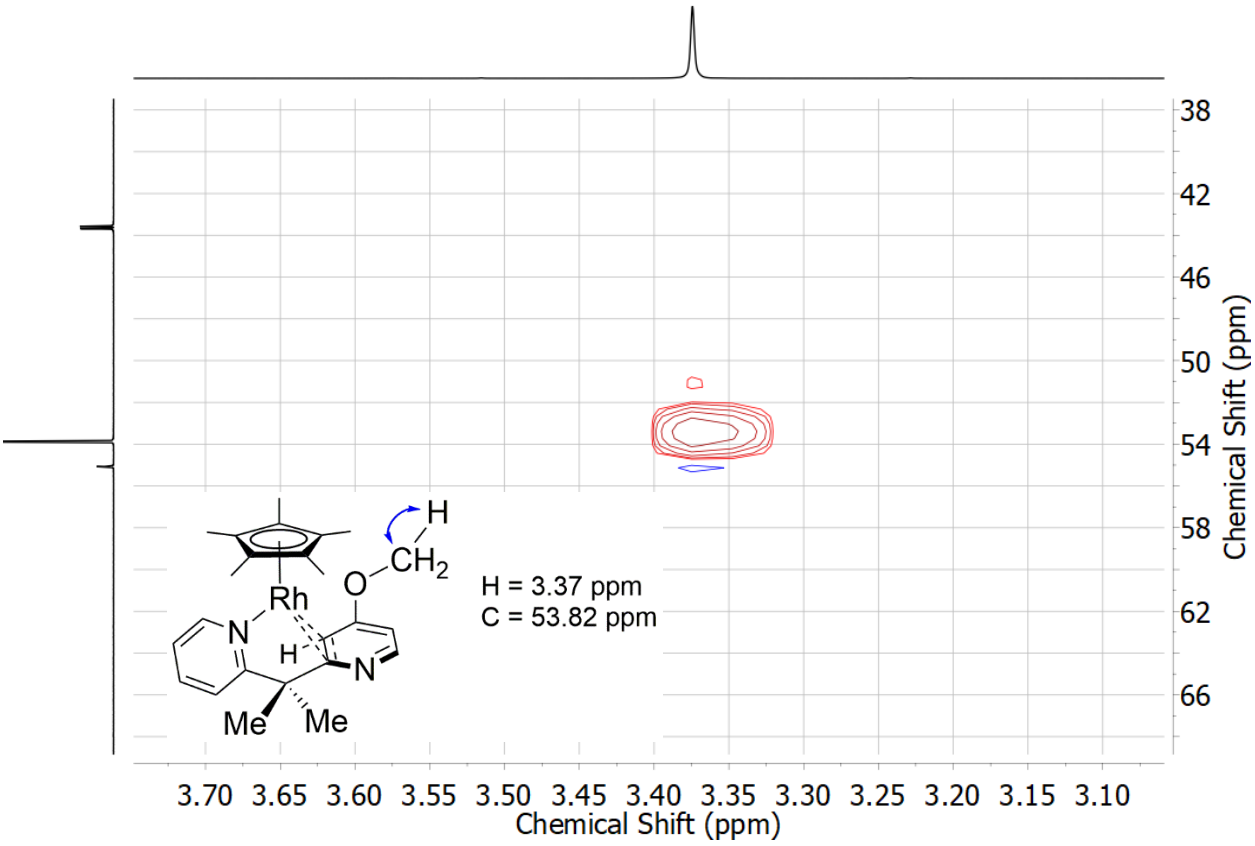

Figure D40. Zoomed in HSQC NMR spectrum (126 MHz, C_6D_6) of **3^{OMe}**. The ^{1}H NMR resonance at 3.37 ppm corresponding to the methoxy proton and $^{13}C\{^{1}H\}$ NMR resonance at 53.82 ppm corresponding to the methoxy carbon are interacting through bond coupling as indicated by the blue arrow.

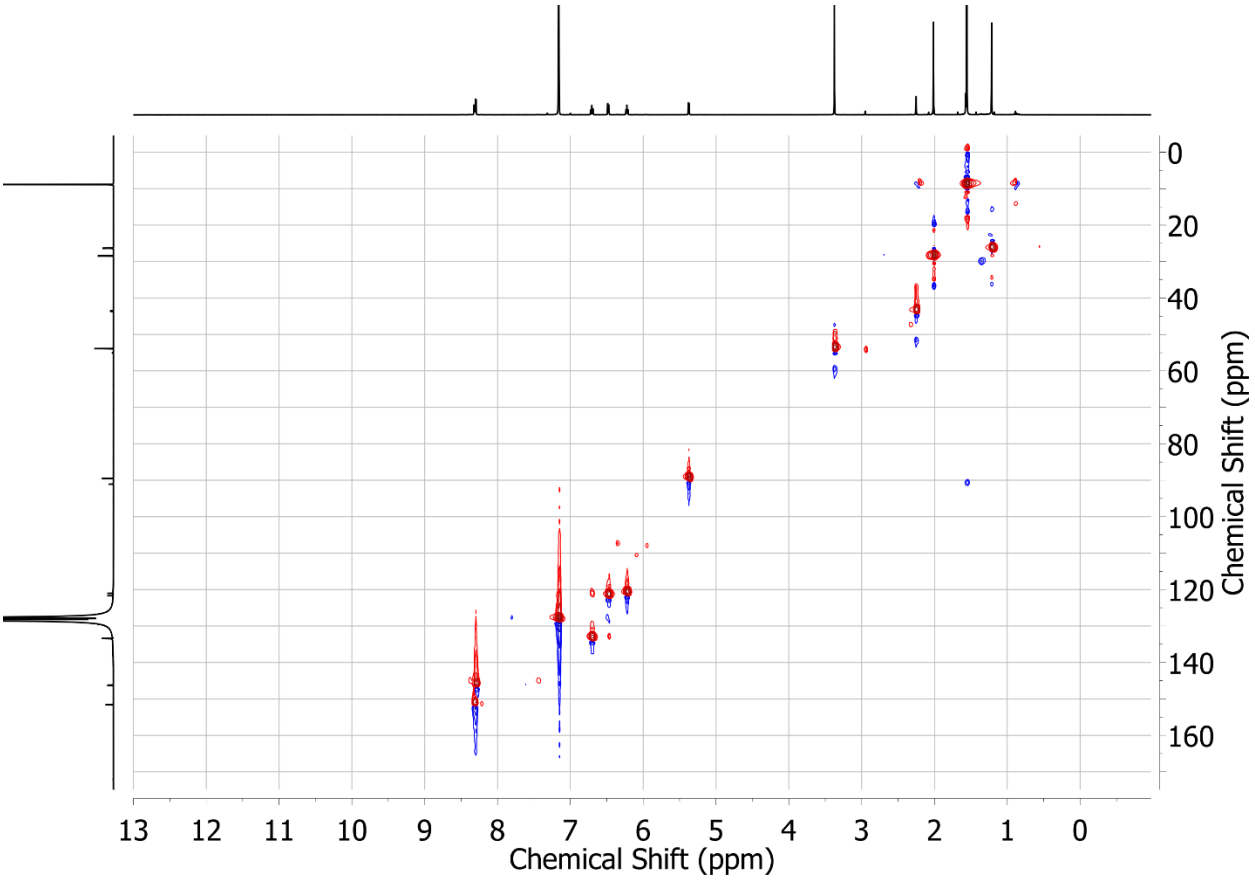

Figure D41. HMBC NMR spectrum (126 MHz, C_6D_6) of $\mathbf{3^{OMe}}$.

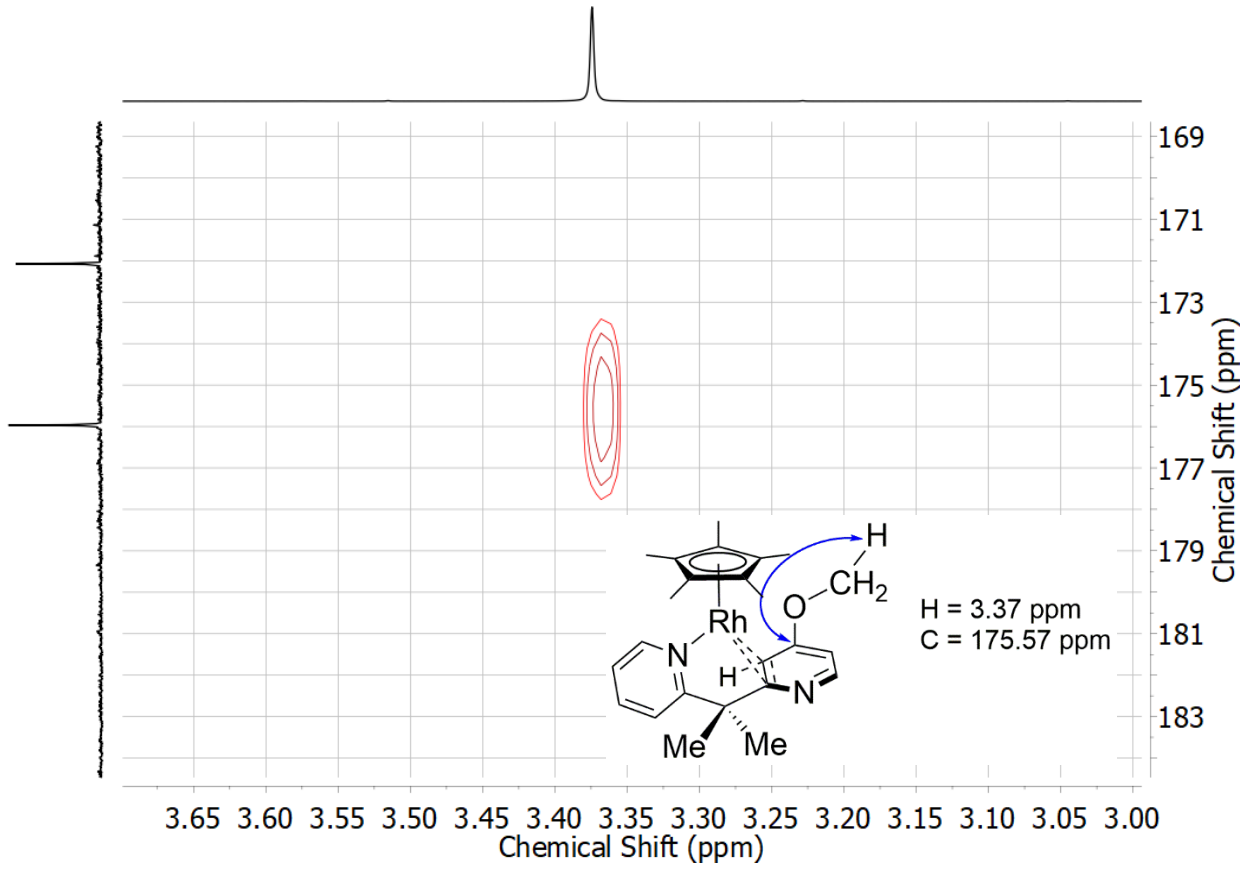

Figure D42. Zoomed in HMBC NMR spectrum (126 MHz, C_6D_6) of $\mathbf{3^{OMe}}$. The ^{1}H NMR resonance at 3.37 ppm corresponding to the methoxy proton and $^{13}C\{^{1}H\}$ NMR resonance at 175.57 ppm corresponding to the tertiary carbon on the pyridyl ring are interacting through multi-bond coupling as indicated by the blue arrow.

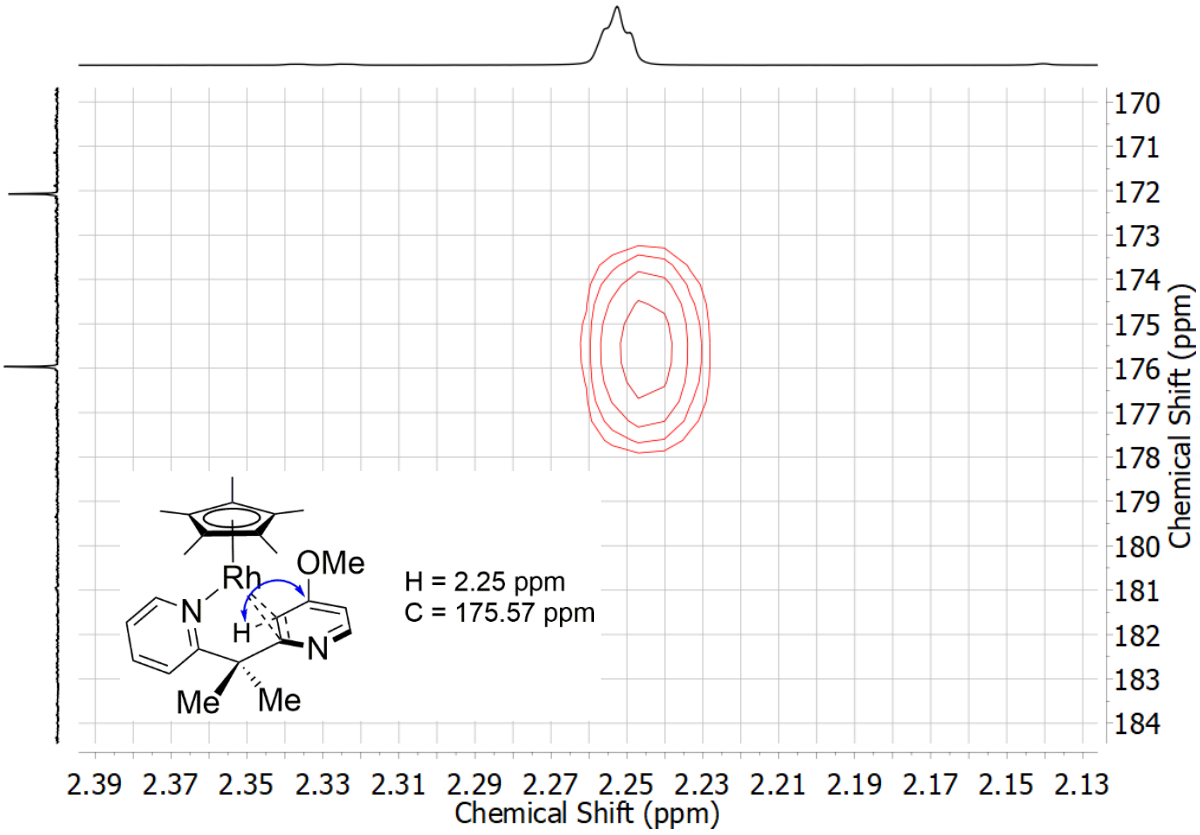

Figure D43. Zoomed in HMBC NMR spectrum (126 MHz, C_6D_6) of **3^{OMe}**. The ^{1}H NMR resonance at 2.25 ppm corresponding to H10 and $^{13}C\{^{1}H\}$ NMR resonance at 53.82 ppm corresponding to the methoxy carbon are interacting through bond coupling as indicated by the blue arrow.

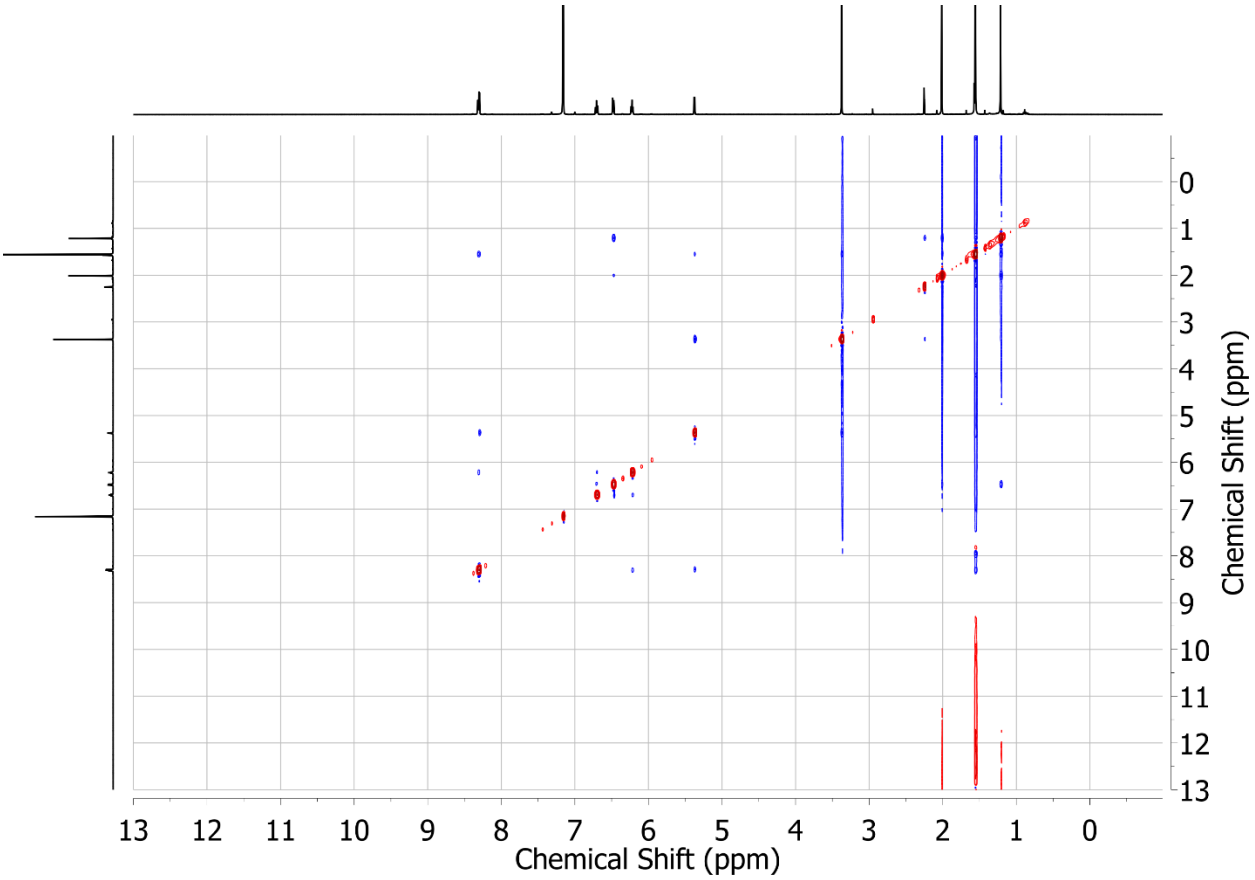

Figure D44. NOESY NMR spectrum (126 MHz, C_6D_6) of $\mathbf{3^{OMe}}$.

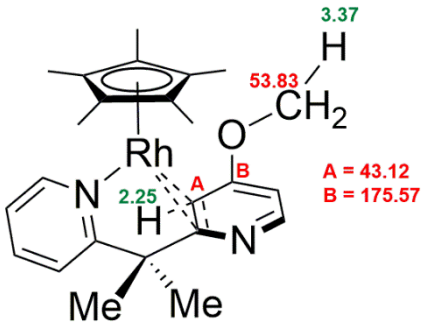

Figure D45. Numbering scheme for select atoms on flipped pyridyl ring assignment of NMR data for complex $\mathbf{3^{OMe}}$.

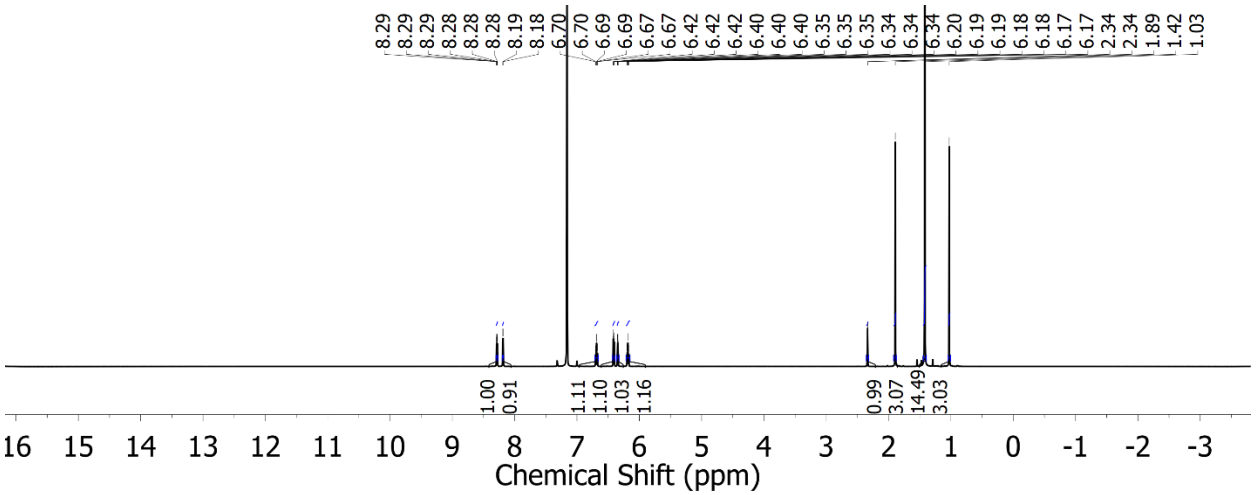

Figure D46. ^{1}H NMR spectrum (500 MHz, CD_3CN) of **3**$^{\mathbf{CF3}}$.

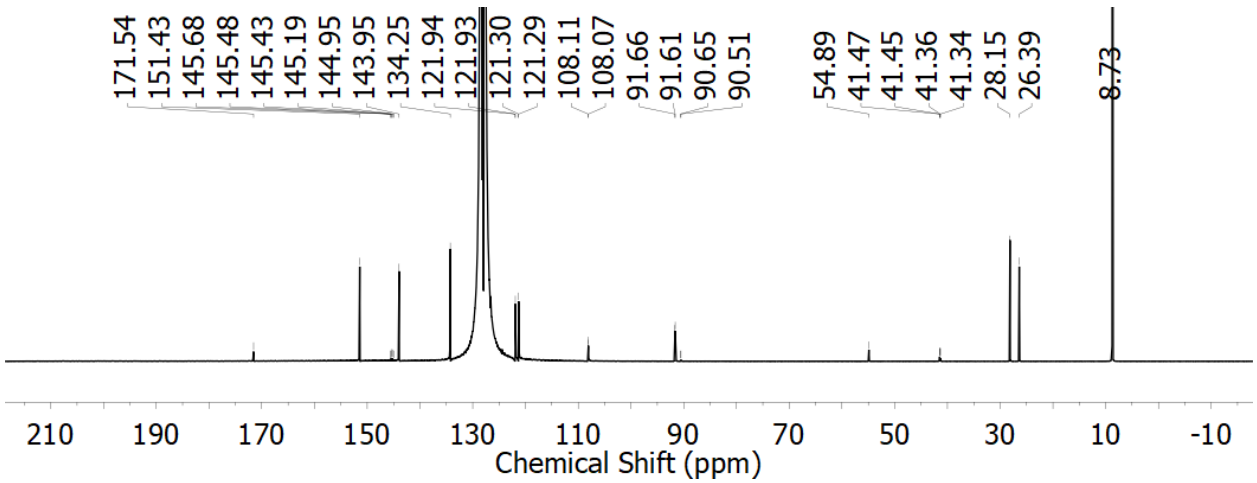

Figure D47. $^{13}C\{^{1}H\}$ NMR spectrum (126 MHz, CD_3CN) of **3**$^{\mathbf{CF3}}$.

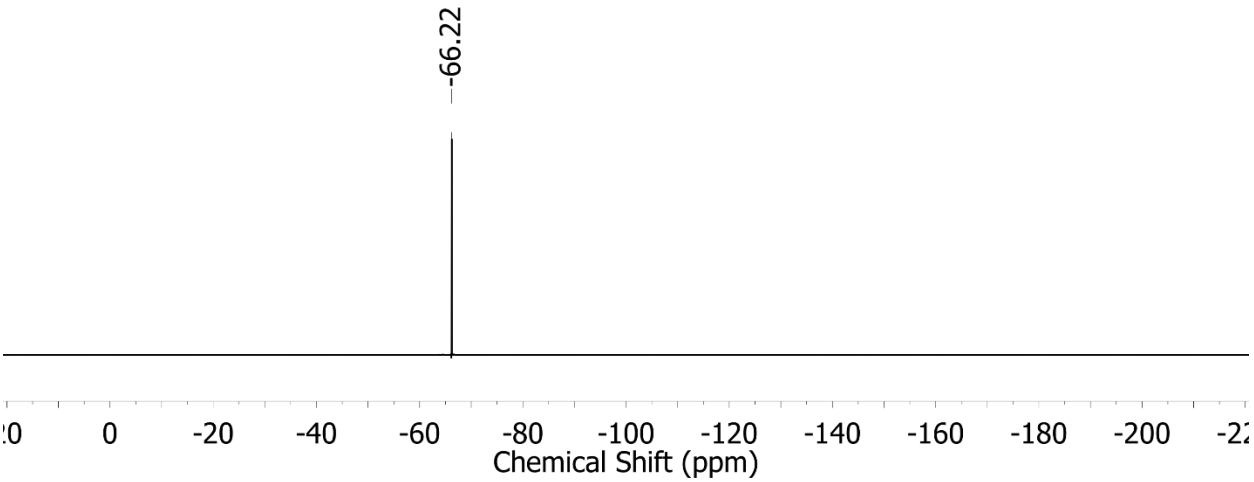

Figure D48. ^{19}F NMR spectrum (162 MHz, CD_3CN) of $\mathbf{3^{CF3}}$.

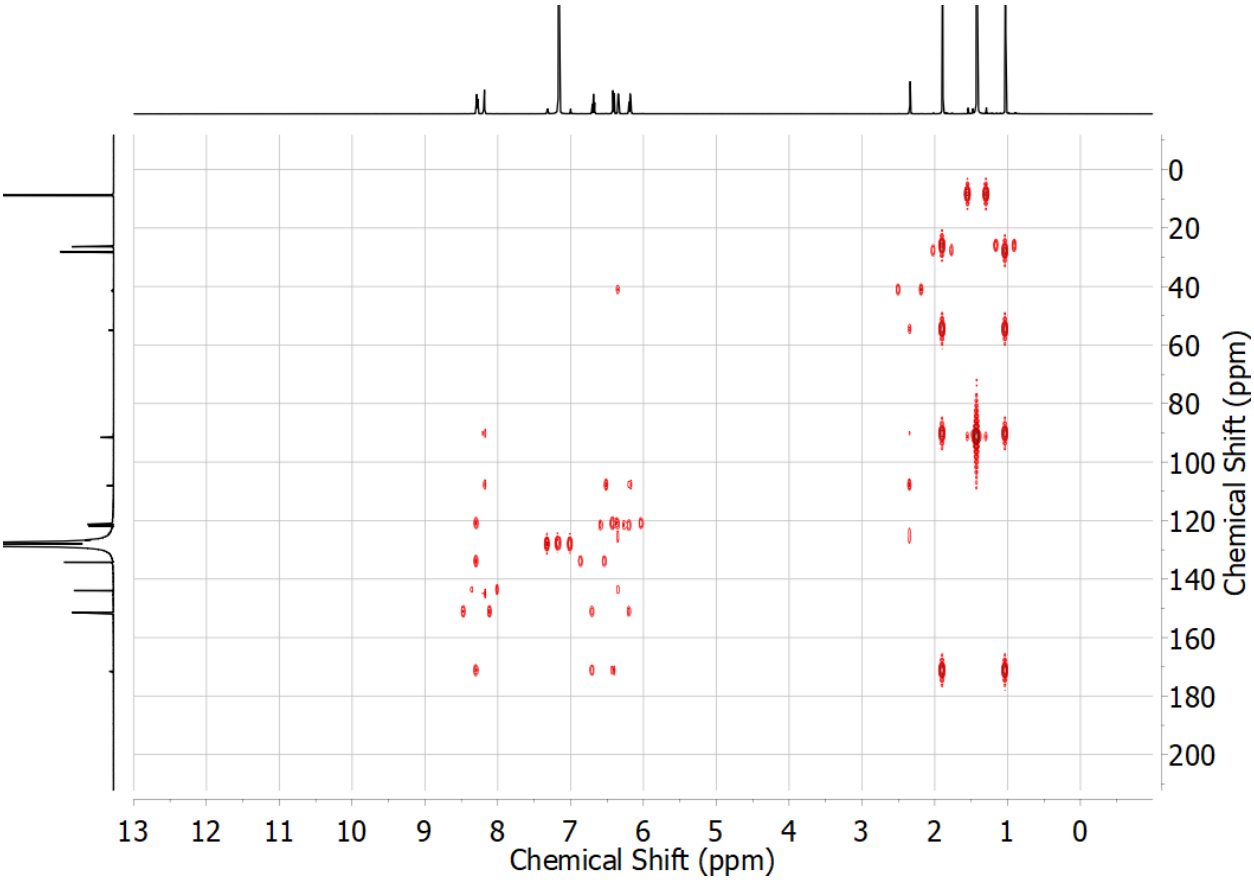

Figure D49. HSQC NMR spectrum (126 MHz, C_6D_6) of $\mathbf{3^{CF3}}$.

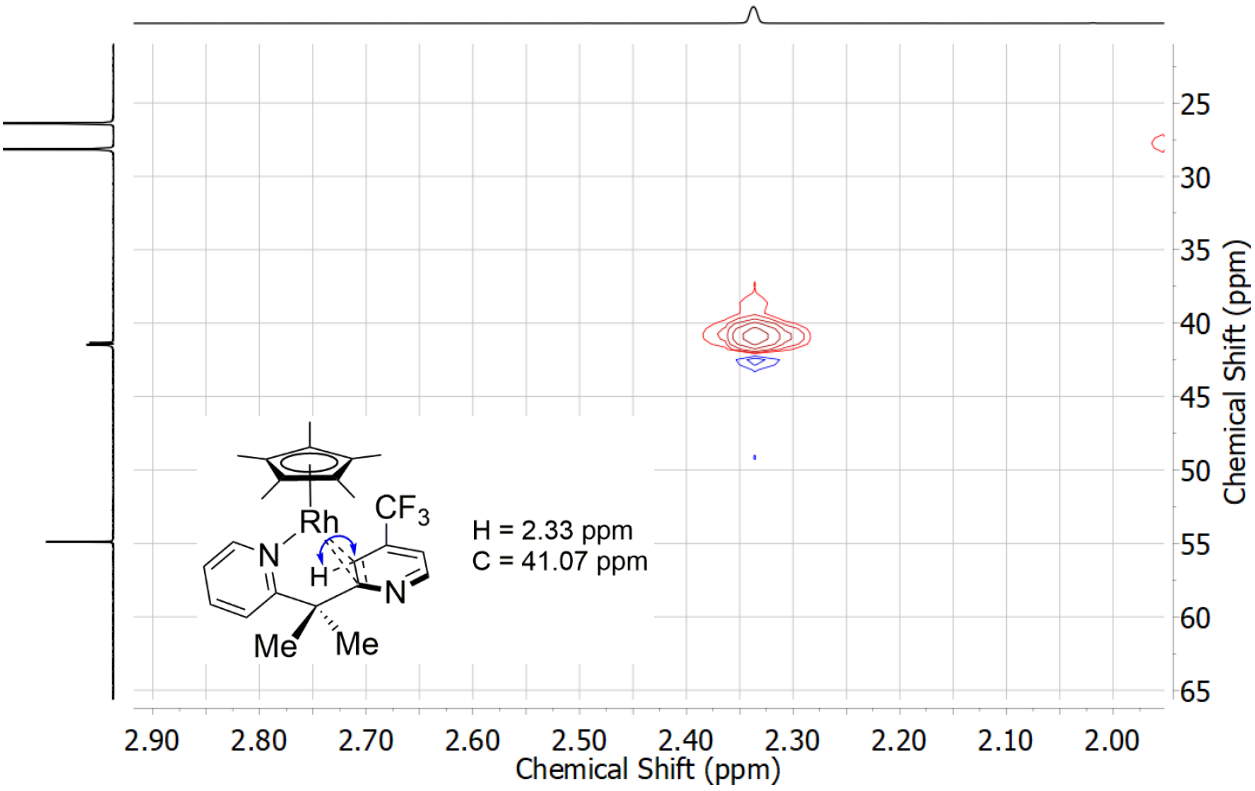

Figure D50. Zoomed in HSQC NMR spectrum (126 MHz, C_6D_6) of **3**$^{\mathbf{CF3}}$. The ^{1}H NMR resonance at 2.33 ppm corresponding to H10 and ^{13}C{^{1}H} NMR resonance at 41.07 ppm corresponding to the pyramidalized C10 are interacting through bond coupling as indicated by the blue arrow.

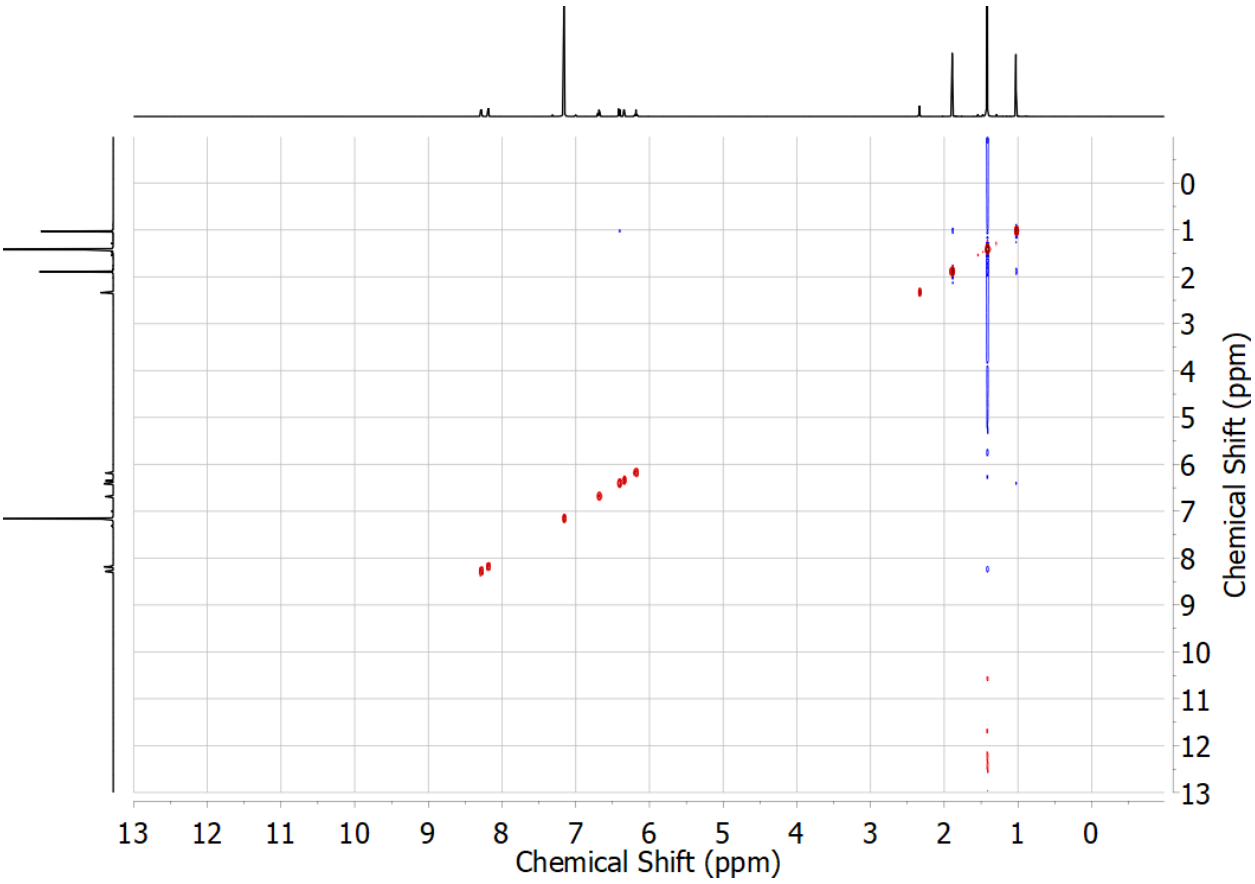

Figure D51. HMBC NMR spectrum (126 MHz, C_6D_6) of $\mathbf{3}^{\mathbf{CF3}}$.

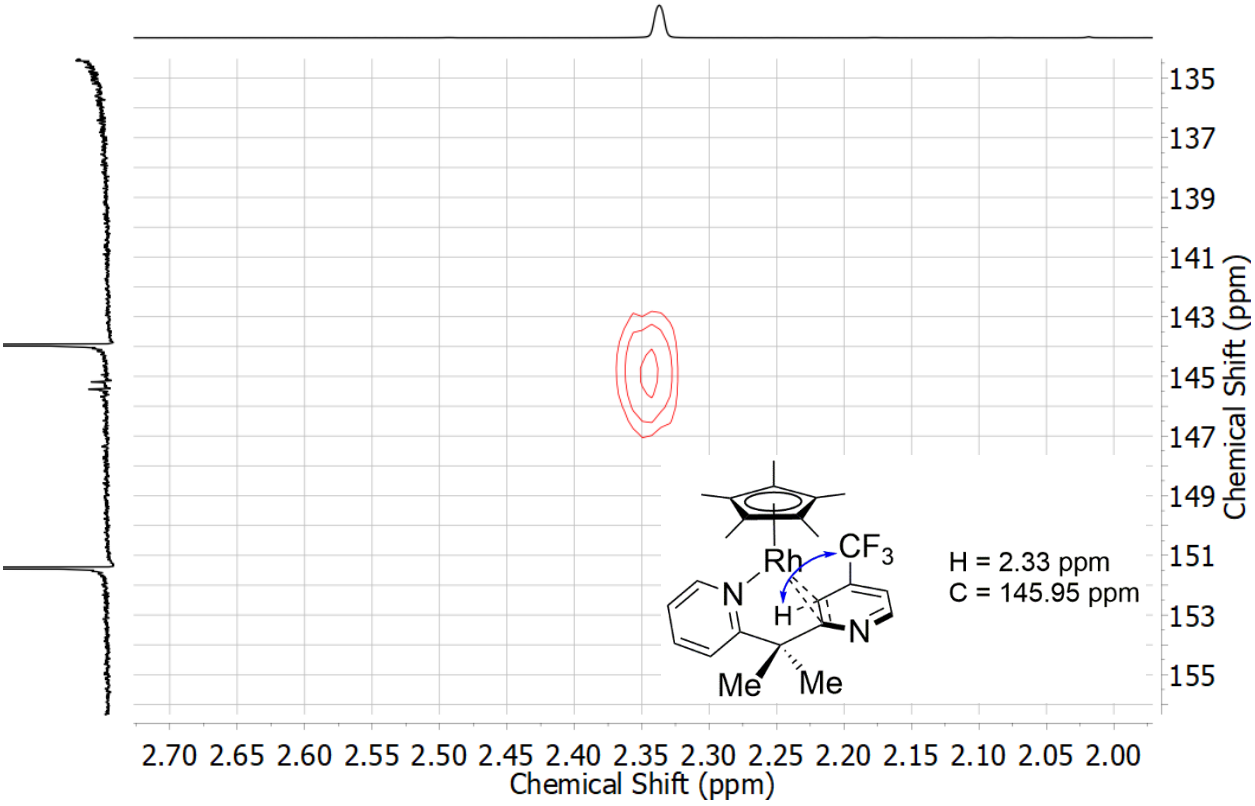

Figure D52. Zoomed in HMBC NMR spectrum (126 MHz, C_6D_6) of **3**^{CF3}. The ^{1}H NMR resonance at 2.33 ppm corresponding to H10 and ^{13}C{^{1}H} NMR the low intensity quartet (J=30.8 Hz) resonance at 145.95 ppm corresponding to the tertiary carbon on the trifluoromethyl substituen are interacting through multi-bond coupling as indicated by the blue arrow.

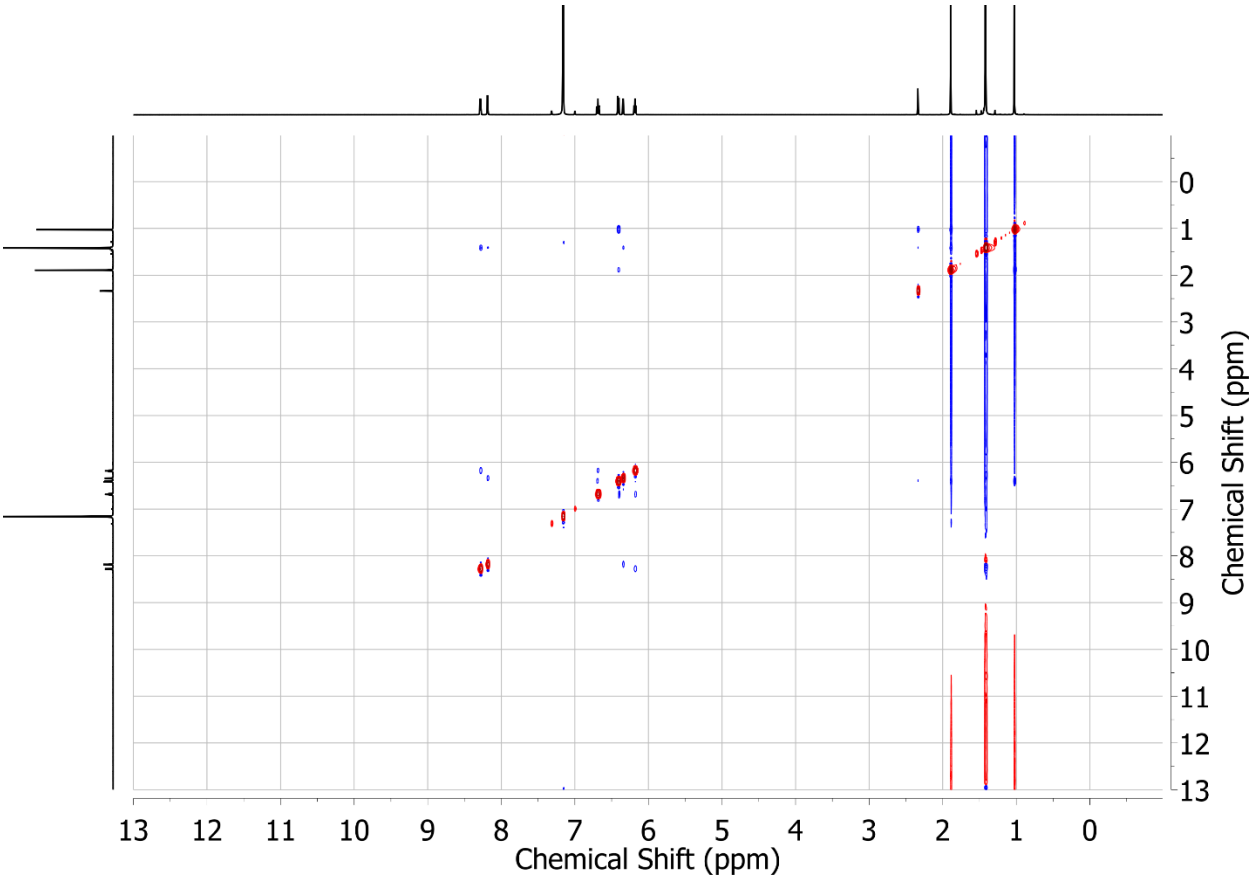

Figure D53. NOESY NMR spectrum (126 MHz, C_6D_6) of $\mathbf{3}^{\mathbf{CF3}}$.

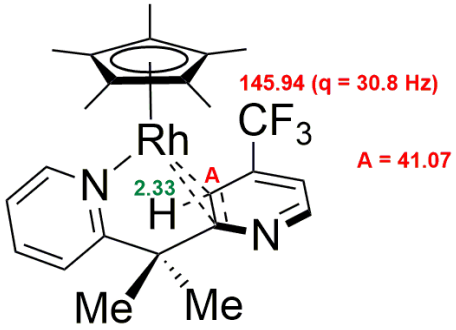

Figure D54. Numbering scheme for select atoms on flipped pyridyl ring assignment of NMR data for complex $\mathbf{3}^{\mathbf{CF3}}$.

Electrochemistry

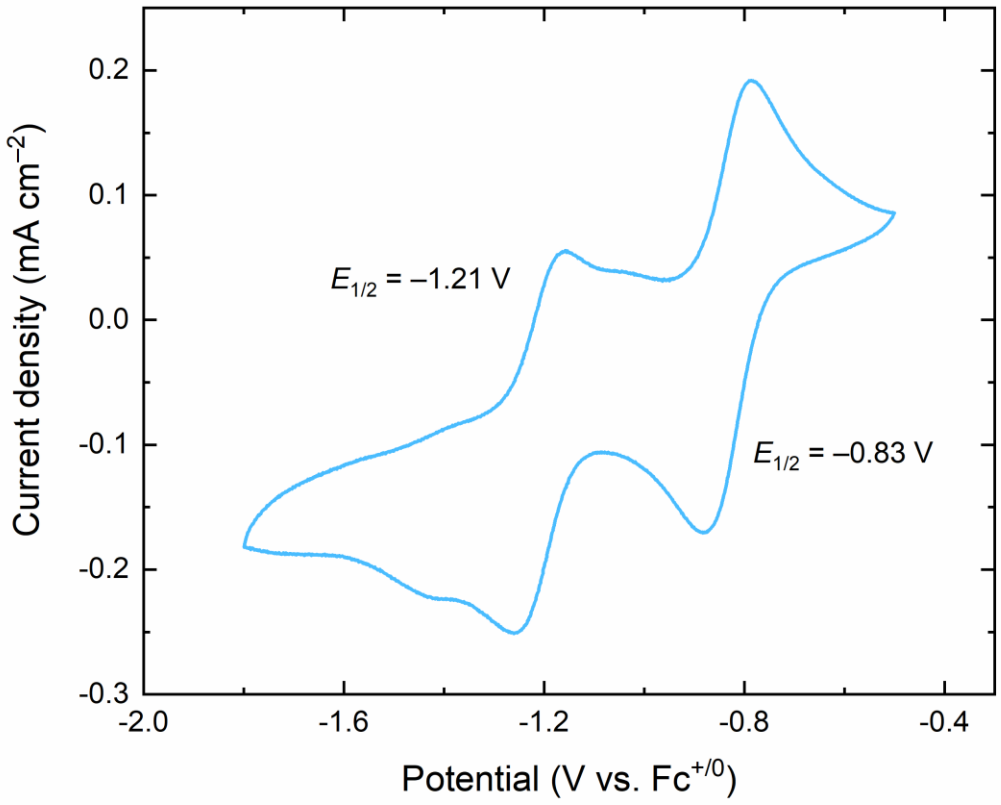

Figure D55. Cyclic voltammetry of **1**$^{\mathbf{CF3}}$ (CH_3CN (0.1 M [^{n}Bu$_4$N][PF_6], 100 mV/s).

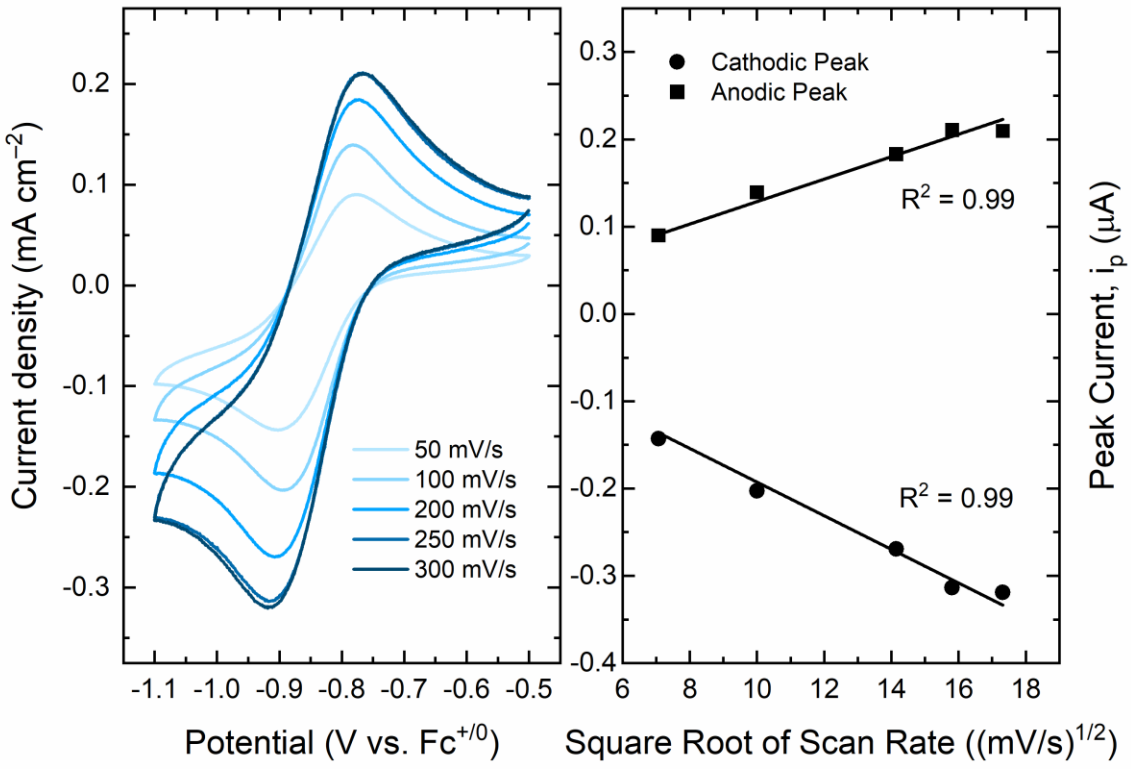

Figure D56. Left: cyclic voltammetry of **1**$^{\mathbf{CF3}}$ at varying scan rate in CH_3CN (0.1 M [nBu4N][PF6]). Right: linear dependence of peak cathodic current on square root of scan rate with the y-intercept set to 0.

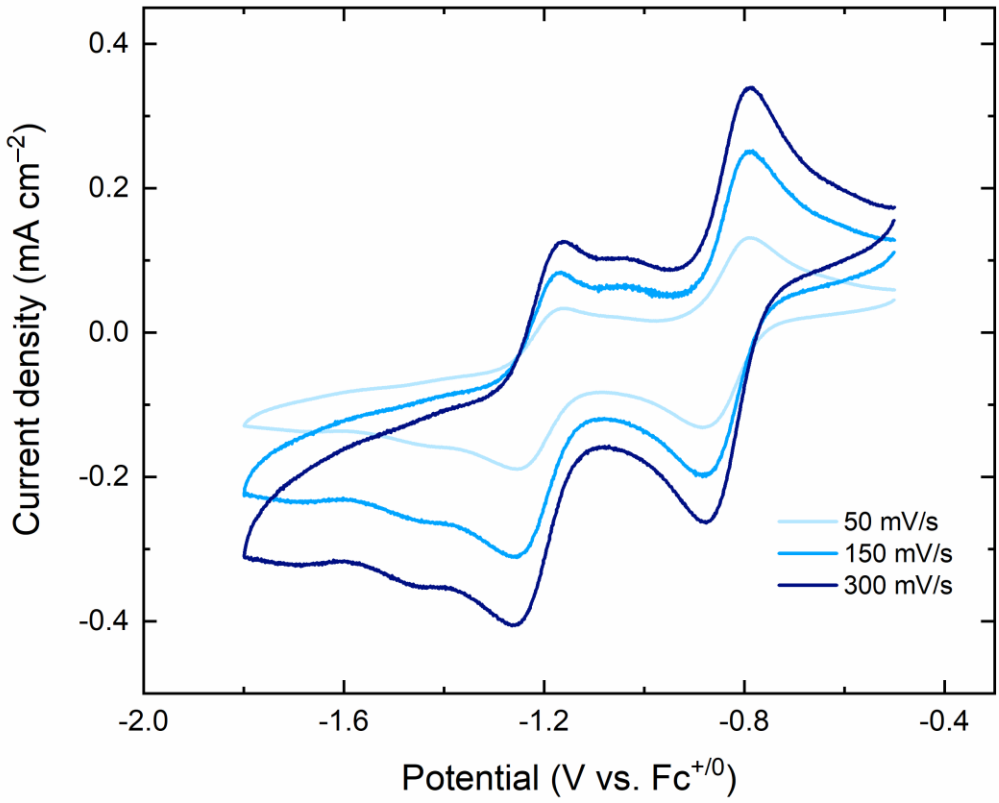

Figure D57. Cyclic voltammetry of **1**^{CF3} at increasing scan rates (50 mV/s, 150 mV/s, and 300 mV/s). Conditions: Electrolyte, 0.1 M TBAPF6 in CH_3CN; working electrode, highly oriented pyrolytic graphite (HOPG); [Rh] in each experiment ca. 1 mM.

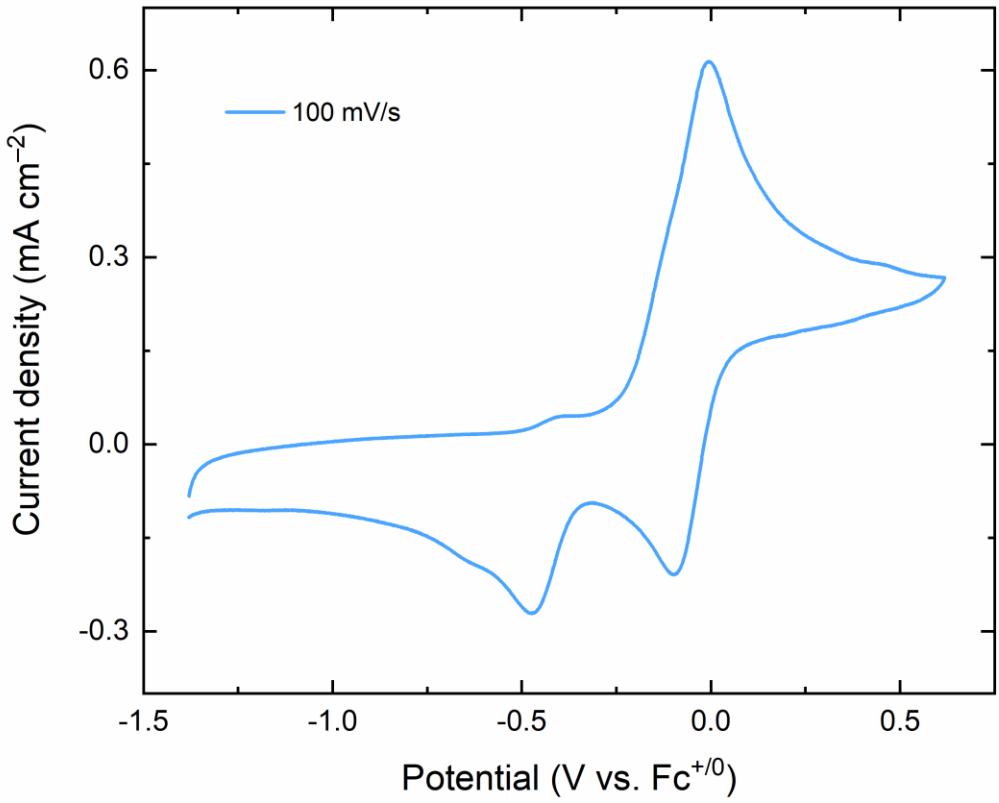

Figure D58. Cyclic voltammetry of **3^{CF3}** (CH_3CN (0.1 M [^{n}Bu$_4$N][PF_6], 100 mV/s).

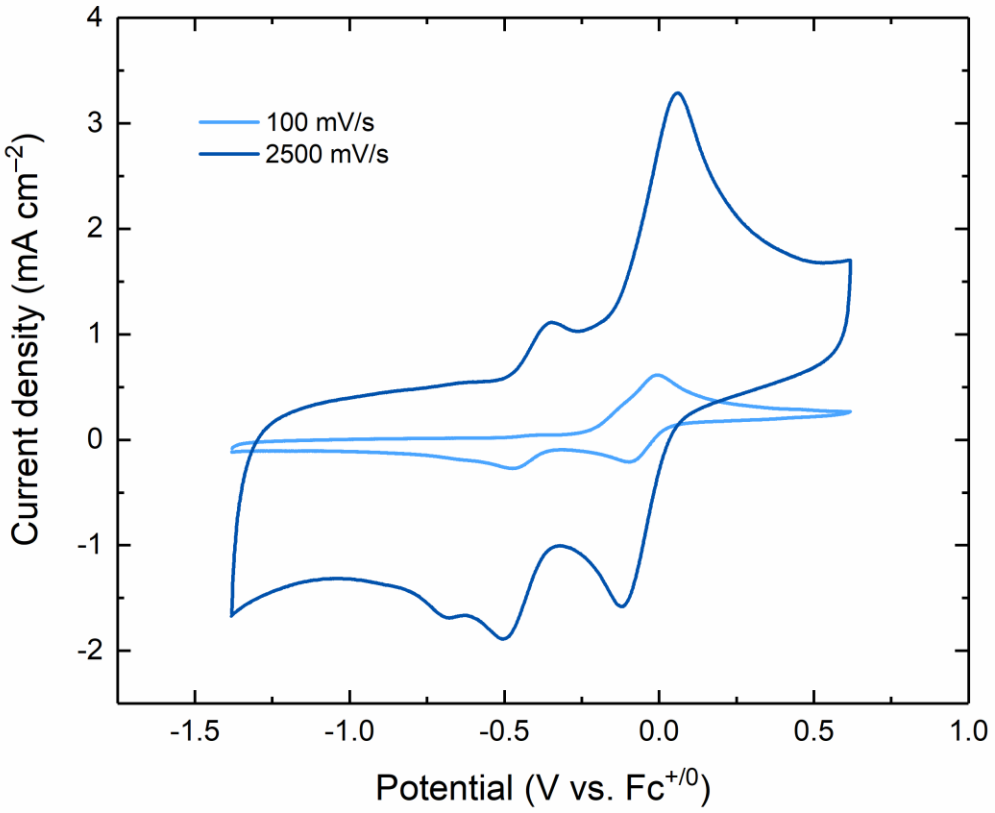

Figure D59. Cyclic voltammetry of **3**^{CF3} at increased scan rates (100 mV/s and 2500 mV/s). Conditions: Electrolyte, 0.1 M TBAPF6 in CH_3CN; working electrode, highly oriented pyrolytic graphite (HOPG); [Rh] in each experiment ca. 1 mM.

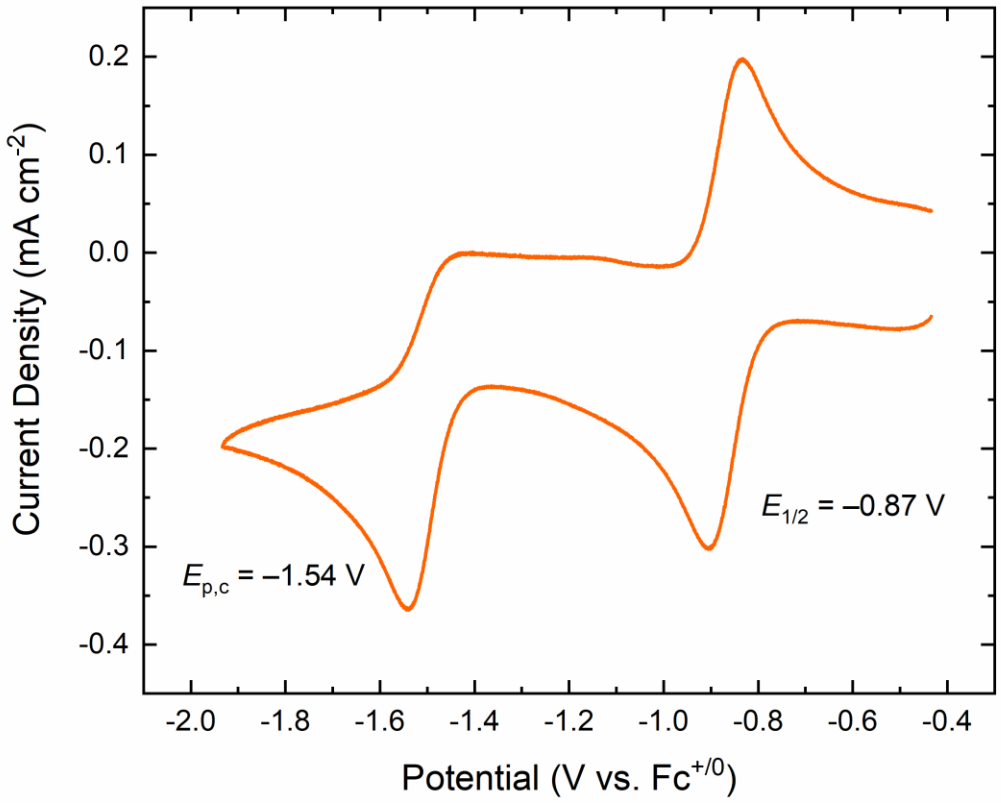

Figure D60. Cyclic voltammetry of **1^{OMe}** (CH_3CN (0.1 M [$^{n}Bu_4N$][PF_6], 100 mV/s).

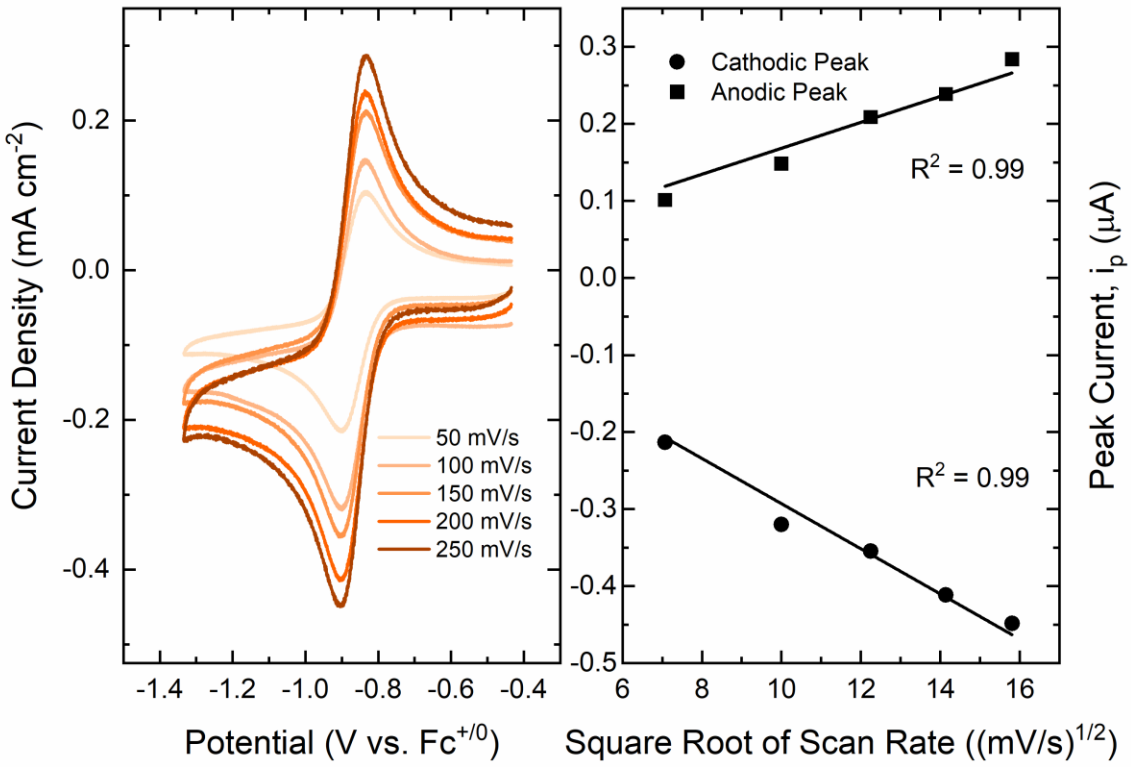

Figure D61. Left: cyclic voltammetry of $\mathbf{1^{OMe}}$ at varying scan rate in CH_3CN (0.1 M [nBu4N][PF6]). Right: linear dependence of peak cathodic current on square root of scan rate with the y-intercept set to 0.

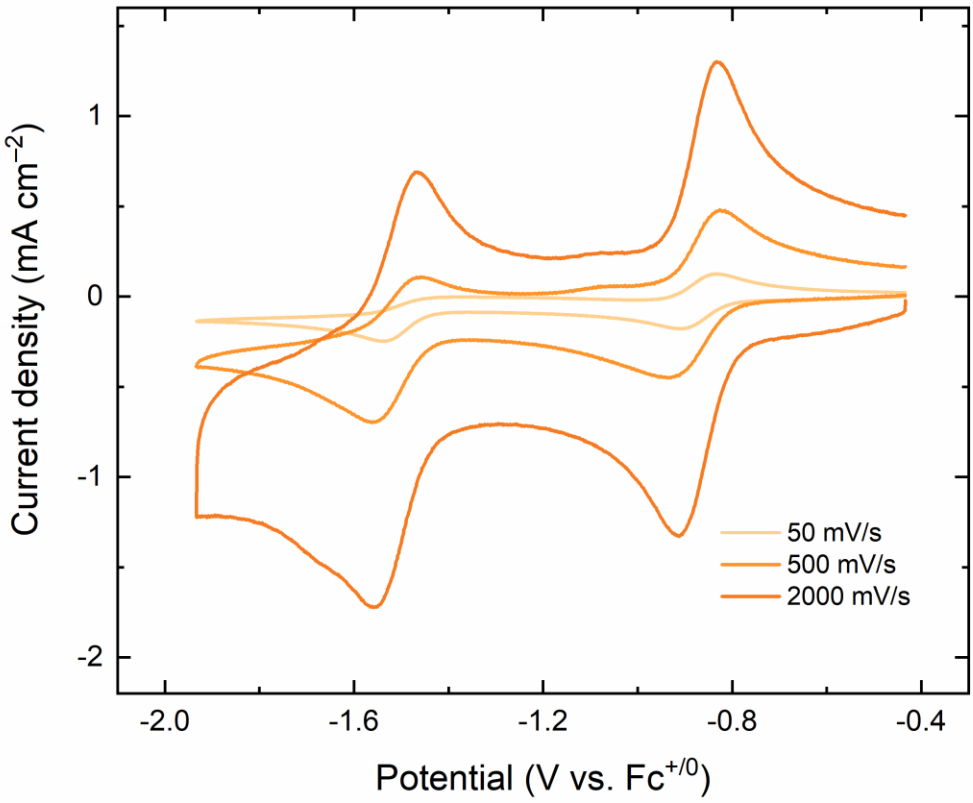

Figure D62. Cyclic voltammetry of $\mathbf{1^{OMe}}$ at increasing scan rates (50 mV/s, 500 mV/s, and 2000 mV/s). Conditions: Electrolyte, 0.1 M TBAPF6 in CH_3CN; working electrode, highly oriented pyrolytic graphite (HOPG); [Rh] in each experiment ca. 1 mM.

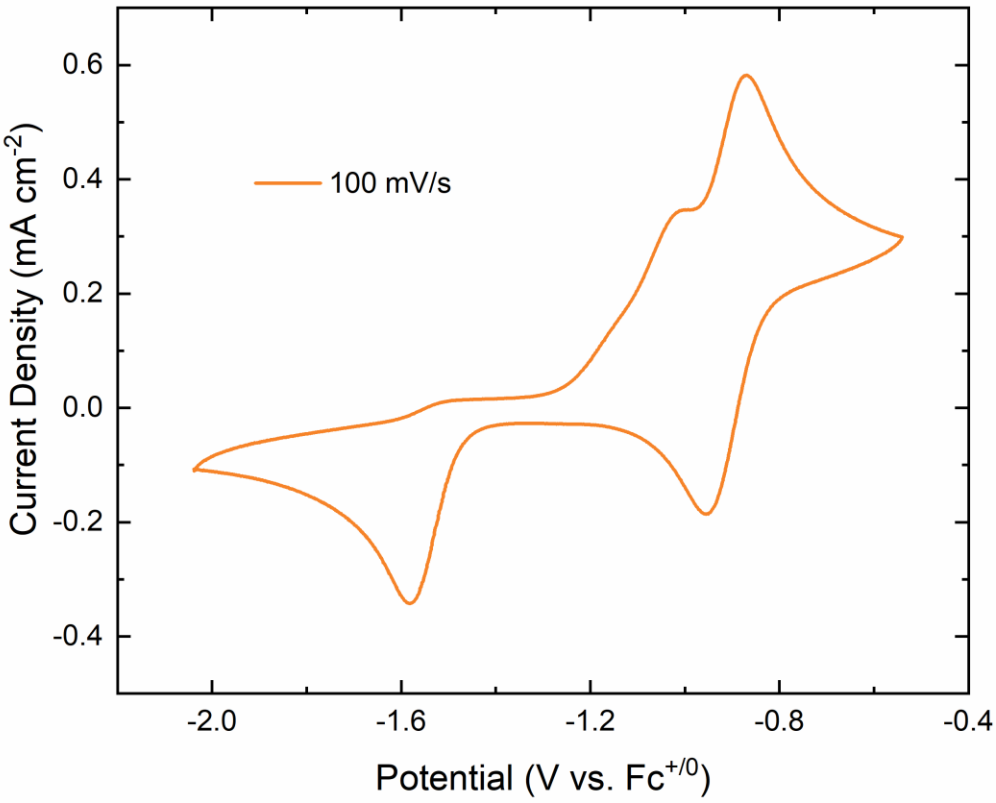

Figure D63. Cyclic voltammetry of **3^{OMe}** (CH_3CN (0.1 M [^{n}Bu$_4$N][PF_6], 100 mV/s).

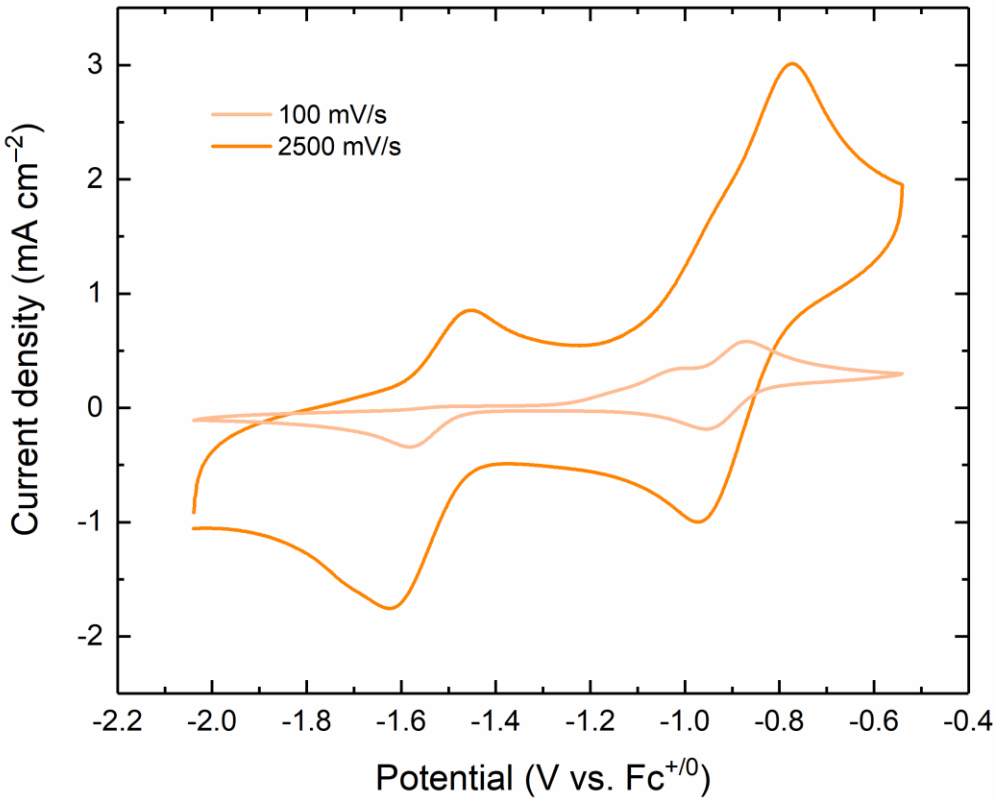

Figure D64. Cyclic voltammetry of **3^{OMe}** at increased scan rates (100 mV/s and 2500 mV/s). Conditions: Electrolyte, 0.1 M TBAPF6 in CH_3CN; working electrode, highly oriented pyrolytic graphite (HOPG); [Rh] in each experiment ca. 1 mM.

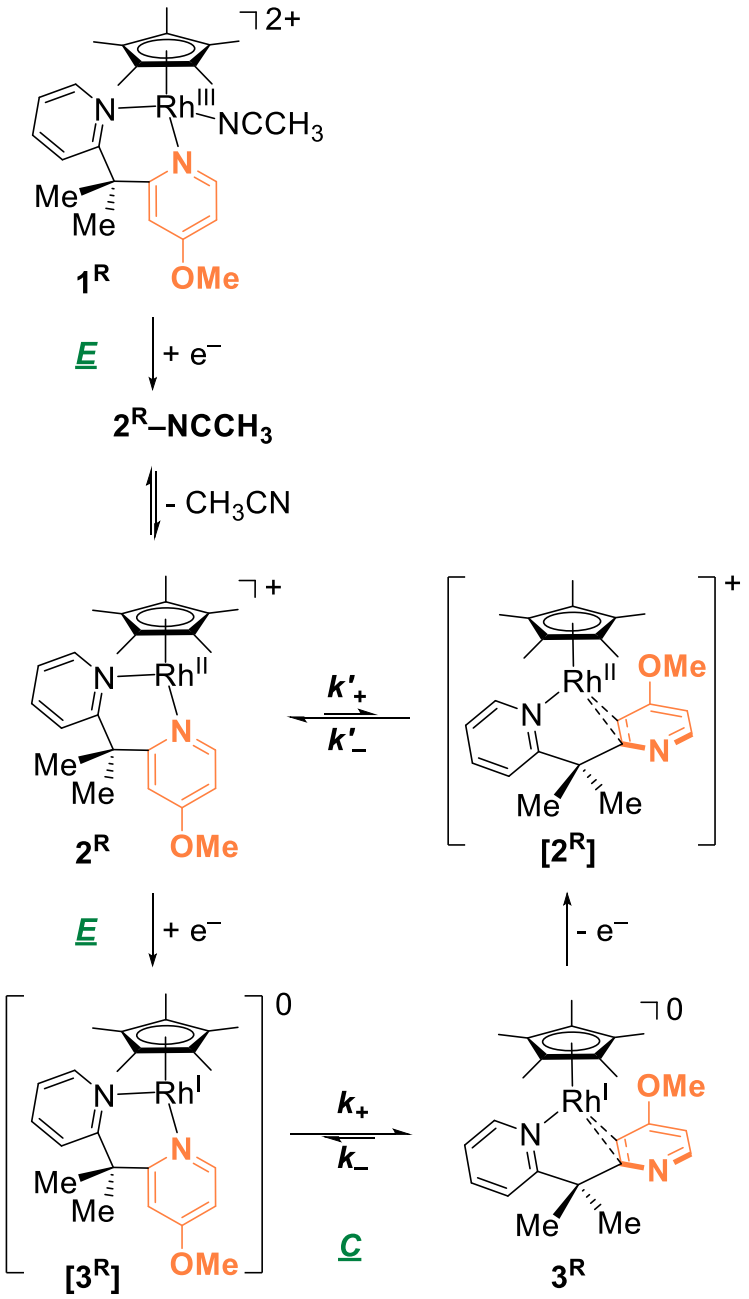

Scheme D1. Proposed Electrochemical Reduction Scheme for $\mathbf{1^{OMe}}$.

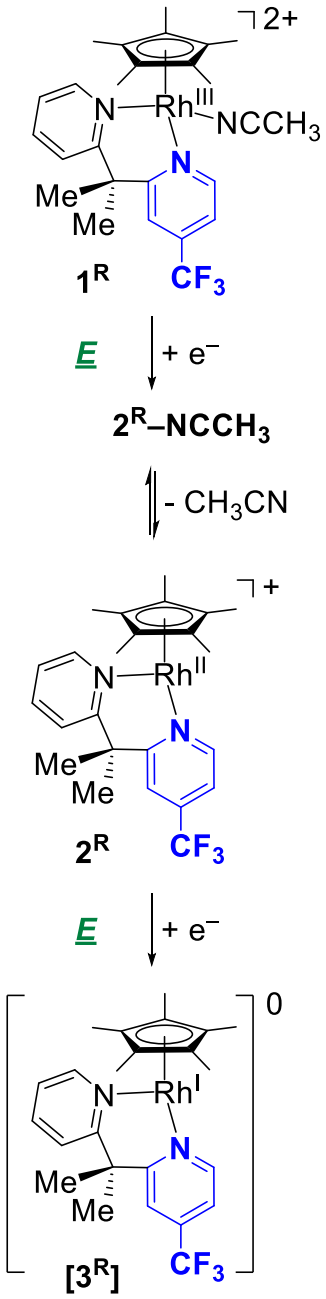

Scheme D2. Proposed Electrochemical Reduction Scheme for $\mathbf{1}^{\mathbf{CF3}}$. EC process indicitive of ligand rearagment is not observed in the CV of $\mathbf{1}^{\mathbf{CF3}}$.

Electron Paramagnetic Spectroscopy

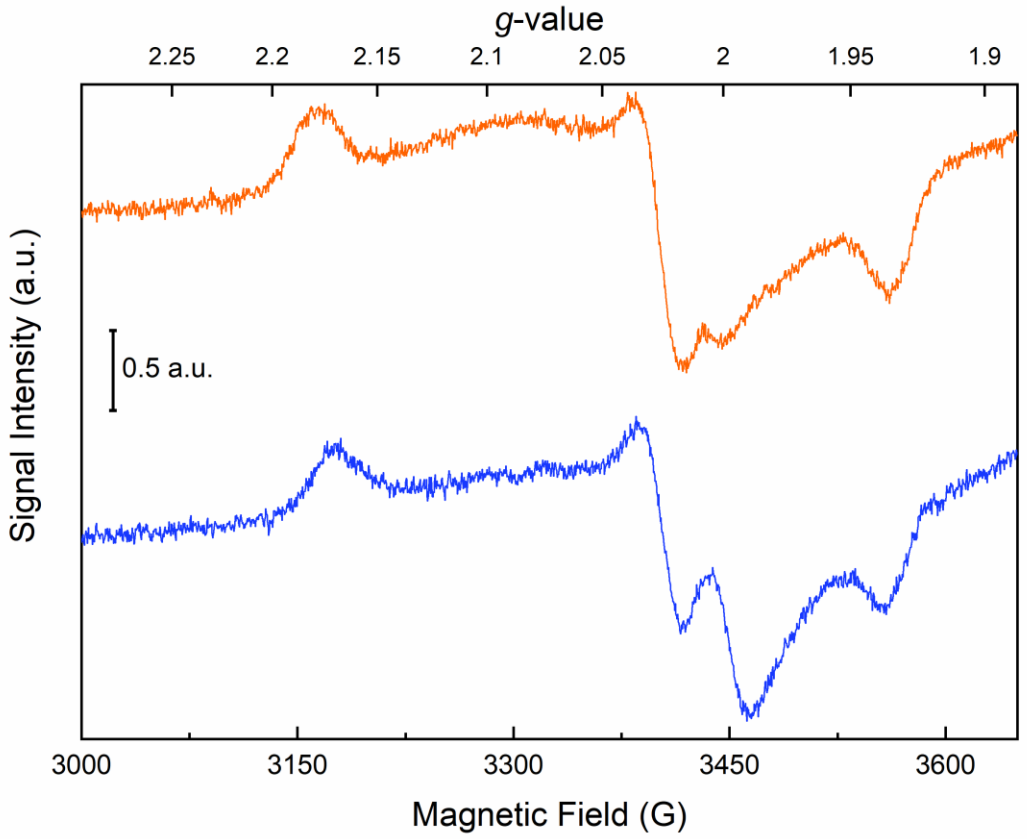

Figure D65. Zoomed in X-band EPR spectrum of in situ reduction of $\mathbf{1}^{\mathbf{OMe}}$ (upper panel) and $\mathbf{1}^{\mathbf{CF3}}$ (lower panel) in CH_3CN (T = 10 K, modulation amplitude = 4.0 G, time constant = 2.56 ms).

The spectrum $\mathbf{1}^{\mathbf{OMe}}$ of (upper panel) shows axial symmetry (g_1 = 2.18, g_2 = 2.01), and isotropic symmetry (g = 2.00), but no observable hyperfine coupling. The signal with isotropic symmetry presumably corresponds to ligand centered electron density.

The spectrum $\mathbf{1}^{\mathbf{CF3}}$ of (lower panel) shows axial symmetry (g_1 = 2.17, g_2 = 2.03) and isotropic symmetry (g = 1.99), but no observable hyperfine coupling. The signal with isotropic symmetry presumably corresponds to ligand centered electron density.

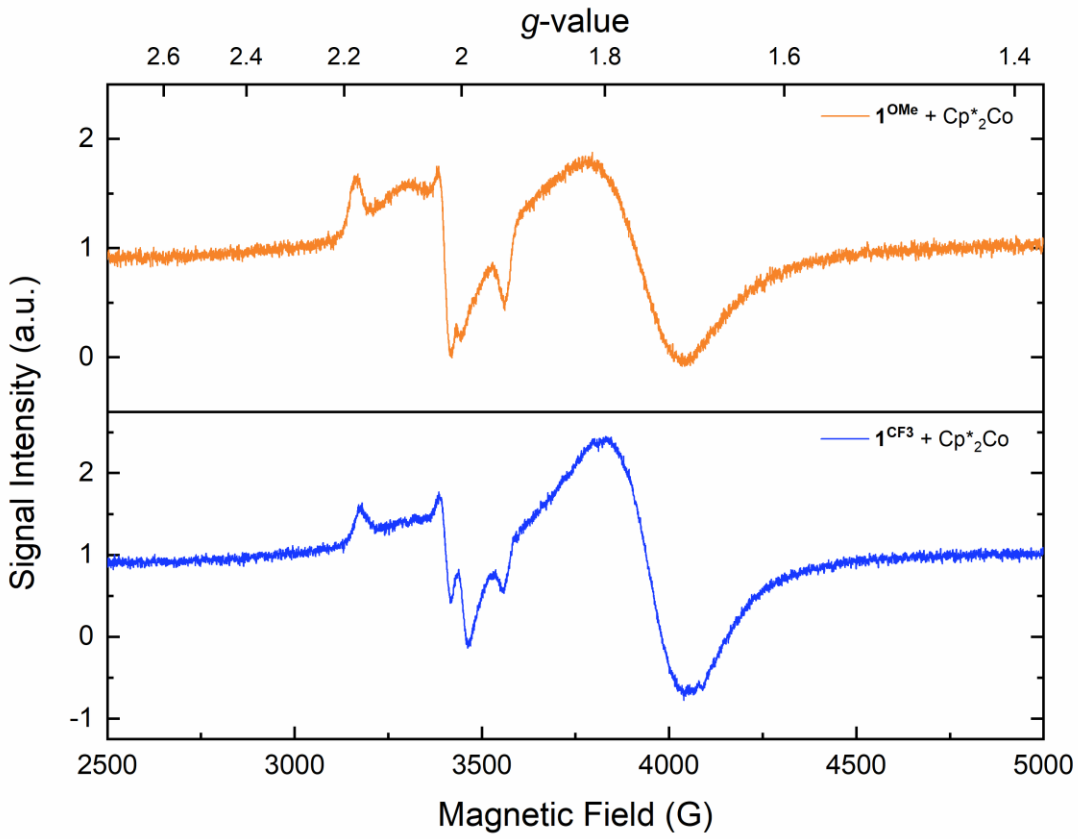

Figure D66. Full X-band EPR spectrum of in situ reduction of $\mathbf{1}^{\mathbf{OMe}}$ (upper panel) and $\mathbf{1}^{\mathbf{CF3}}$ with cobaltocene (lower panel) in CH_3CN (T = 10 K, modulation amplitude = 4.0 G, time constant = 2.56 ms).

The spectrum $\mathbf{1}^{\mathbf{OMe}}$ of (upper panel) shows axial symmetry (g_1 = 2.18, g_2 = 2.01), and isotropic symmetry (g = 2.00), but no observable hyperfine coupling. The additional signal with isotropic symmetry (g = 1.75) corresponds to unreacted cobaltocene.

The spectrum $\mathbf{1}^{\mathbf{CF3}}$ of (lower panel) shows axial symmetry (g_1 = 2.17, g_2 = 2.03) and isotropic symmetry (g = 1.99), but no observable hyperfine coupling. The additional signal with isotropic symmetry (g = 1.75) corresponds to unreacted cobaltocene.

Table D1. Crystal and Refinement Data for $\mathbf{A^{OMe}}$, and $\mathbf{A^{CF3}}$.

	$\mathbf{A^{OMe}}$ **(K87K_0M)**	$\mathbf{A^{CF3}}$ **(v18f)**
CCDC number	##	##
Empirical formula	$C_{50}H_{65}Cl_2F_{12}N_5O_2P_2Rh_2$	$C_{24}H_{28}ClF_9N_2PRh$
Formula weight	1334.73	684.81
Temperature	199.99	199.99
Wavelength	0.71073	1.54178
Crystal system	monoclinic	monoclinic
Space group	P21/c	$P2_1/n$
a	24.811(4) Å	17.7334(8) Å
b	14.382(2) Å	8.4947(4) Å
c	15.707(2) Å	18.4045(8) Å
α	90	90
β	90.675(2)	106.7777(12)
γ	90	90
Volume	5604.5(15) $Å^3$	2654.4(2)$Å^3$
Z	4	4
Density (calculated)	1.583 g/cm^3	1.714 g/cm^3
Absorption coefficient	0.825 mm^{-1}	7.448 mm^{-1}
F(000)	2712.0	1376.0
Crystal size	0.61 × 0.41 × 0.14 mm^3	0.17 × 0.07 × 0.055mm^3
Theta range	3.84 to 61.326	6.098 to 136.572
Index ranges	$-35 \le h \le 34$, $-20 \le k \le 20$, $-22 \le l \le 22$	$-21 \le h \le 21$, $-10 \le k \le 9$, $-19 \le l \le 22$
Reflections collected	68745	19439
Independent reflections	17295 [R_{int} = 0.0447, R_{sigma} = 0.0414]	4727 [Rint = 0.0312, Rsigma = 0.0275]
Absorption correction	Multi-scan	Multi-scan
Max. and min. transmission	0.6146 0.7461	0.5416 0.7531
Refinement method	Full-matrix least-squares on F^2	Full-matrix least-squares on F^2
Data / restraints / parameters	17295/0/925	4727/0/350
Goodness-of-fit on F^2	1.057	1.027
Final R indices [I>2σ(I)]	R_1 = 0.0438, wR_2 = 0.0963	R_1 = 0.0428, wR_2 = 0.1102
R indices (all data)	R_1 = 0.0666, wR_2 = 0.1105	R1 = 0.0457, wR2 = 0.1125
Largest diff. peak and hole	1.70 and -0.73 $e^-/Å^3$	1.37 and -0.77 $e^-/Å^3$

[a] $R1 = \Sigma||F_o|-|F_c|| / \Sigma|F_o|$ [b] $wR2 = [\ \Sigma\ [w(F_o^2-F_c^2)^2] / \Sigma\ [w(F_o^2)^2]\ ]^{1/2}$

Table D2. Crystal and Refinement Data for $\mathbf{3^{OMe}}$, and $\mathbf{3^{CF3}}$.

	$\mathbf{3^{OMe}}$ **(q40h)**	$\mathbf{3^{CF3}}$ **(q73h)**
CCDC number	##	##
Empirical formula	$C_{24}H_{31}N_2ORh$	$C_{24}H_{28}F_3N_2Rh$
Formula weight	466.42	504.39
Temperature	199.99	199.99
Wavelength	1.54178	1.54178
Crystal system	triclinic	monoclinic
Space group	P-1	$P2_1/c$
a	8.8792(2) Å	13.6639(5) Å
b	10.2439(2) Å	8.6438(3) Å
c	12.2589(2) Å	18.9646(7) Å
α	91.0375(5)	90
β	92.6241(7)	91.0266(10)
γ	93.6648(6)	90
Volume	1111.35(4) $Å^3$	2239.51(14) $Å^3$
Z	2	4
Density (calculated)	1.394 g/cm^3	1.496 g/cm^3
Absorption coefficient	6.322 mm^{-1}	6.486 mm^{-1}
F(000)	484.0	1032.0
Crystal size	0.11 × 0.075 × 0.035 mm^3	0.28 × 0.16 × 0.04 mm^3
Theta range	7.22 to 140.57	9.328 to 140.258
Index ranges	$-9 \le h \le 10$, $-12 \le k \le 12$, $-14 \le l \le 14$	$-15 \le h \le 16$, $-10 \le k \le 9$, $-22 \le l \le 17$
Reflections collected	16440	10784
Independent reflections	3939 [R_{int} = 0.0245, R_{sigma} = 0.0228]	4058 [R_{int} = 0.0469, R_{sigma} = 0.0564]
Absorption correction	Multi-scan	Multi-scan
Max. and min. transmission	0.6051 0.7533	0.4053 0.7533
Refinement method	Full-matrix least-squares on F^2	Full-matrix least-squares on F^2
Data / restraints / parameters	3939/0/265	4058/0/282
Goodness-of-fit on F^2	1.095	1.037
Final R indices [I>2σ(I)]	R_1 = 0.0240, wR_2 = 0.0585	R_1 = 0.0607, wR_2 = 0.1682
R indices (all data)	R_1 = 0.0243, wR_2 = 0.0588	R_1 = 0.0615, wR_2 = 0.1711
Largest diff. peak and hole	1.42 and -0.69 $e^-/Å^3$	1.03 and -2.15 $e^-/Å^3$

[a] $R1 = \Sigma||F_o|-|F_c|| / \Sigma|F_o|$ [b] $wR2 = [\ \Sigma\ [w(F_o^2-F_c^2)^2] / \Sigma\ [w(F_o^2)^2]\ ]^{1/2}$

Table D3. Selected Bond Lengths for $\mathbf{A}^{CF3}$, $\mathbf{A}^{OMe}$, $\mathbf{3}^{CF3}$, $\mathbf{3}^{OMe}$.

Bond	$\mathbf{A}^{CF3,a}$	$\mathbf{A}^{OMe}$ (Å)		$\mathbf{3}^{CF3}$ (Å)	$\mathbf{3}^{OMe}$ (Å)
		Molecule A	Molecule B		
Rh–Cp*,[b]	1.803 Å	1.800 Å	1.803 Å	1.893 Å	1.886 Å
Rh–N1	2.115(3) Å	2.129(2) Å	2.139(2) Å	2.069(3) Å	2.068(2) Å
Rh–N2	2.136(3) Å	2.122(2) Å	2.130(2) Å	-	-
Rh–C9	-	-	-	2.083(3) Å	2.099(2) Å
Rh–C10	-	-	-	2.152(6) Å	2.128(2) Å
C9–C10	1.392(6) Å	1.408(4) Å	1.383(4) Å	1.476(5) Å	1.466(3) Å
Rh–Cl	2.414(1) Å	2.413(7) Å	2.389(8) Å	-	-
∠(N1–Rh–N2)	85.79(1)°	85.66(9)°	86.00(9)°	-	-

[a] two independent molecules observed in the asymmetric unit cell; [b] distance between the Rh center and the calculated centroid of the Cp* ring.

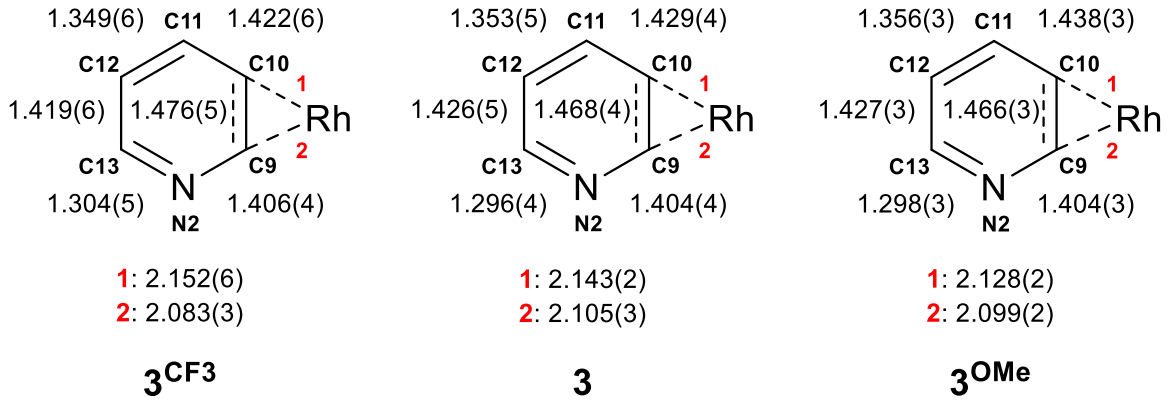

Figure 67. Select bond metrics for flipped pyridine moiety **3** and $\mathbf{3}^{R}$ (Left panel $\mathbf{3}^{CF3}$, Middle panel **2**, Right panel $\mathbf{3}^{OMe}$).

Special Refinement Details for A^{CF3}

No special refinement was required.

Solid-State Structure of A^{CF3}

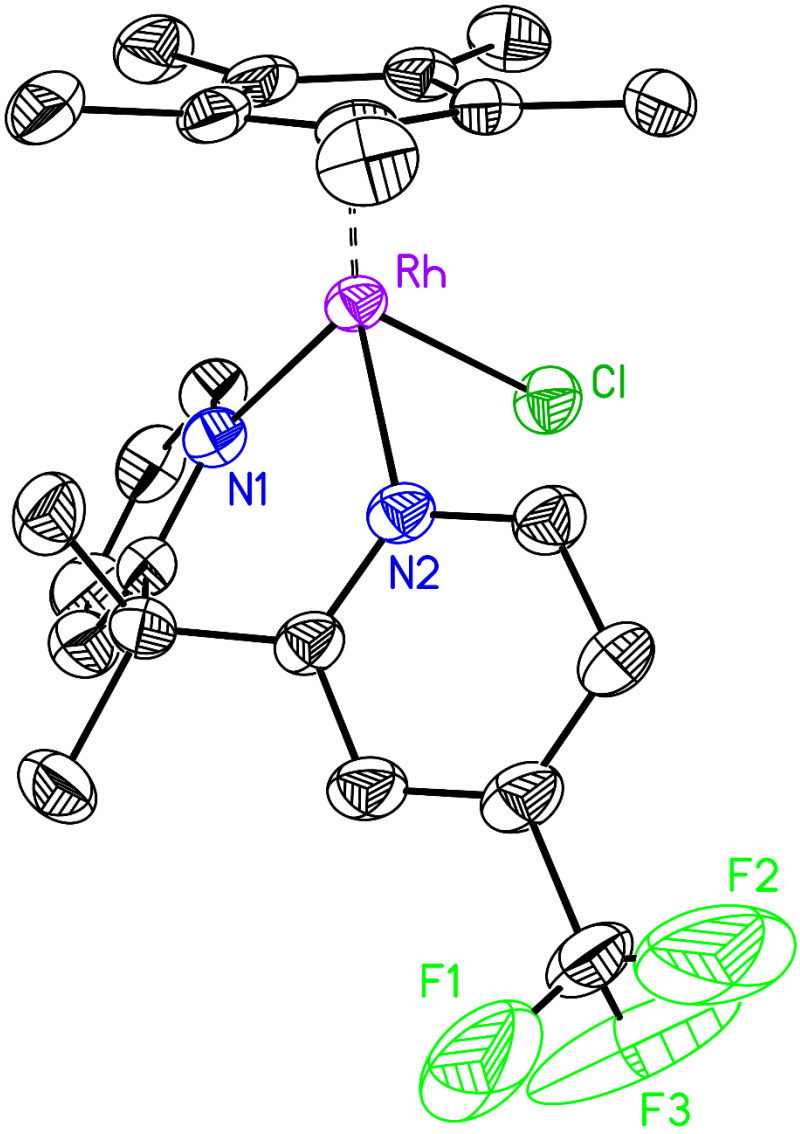

Figure D68. Full solid-state structure of A^{CF3}. Hydrogen atoms and associated counteranion molecule omitted for clarity. Displacement ellipsoids shown at the 50% probability level.

Full Solid-State Structure of A^{CF3}

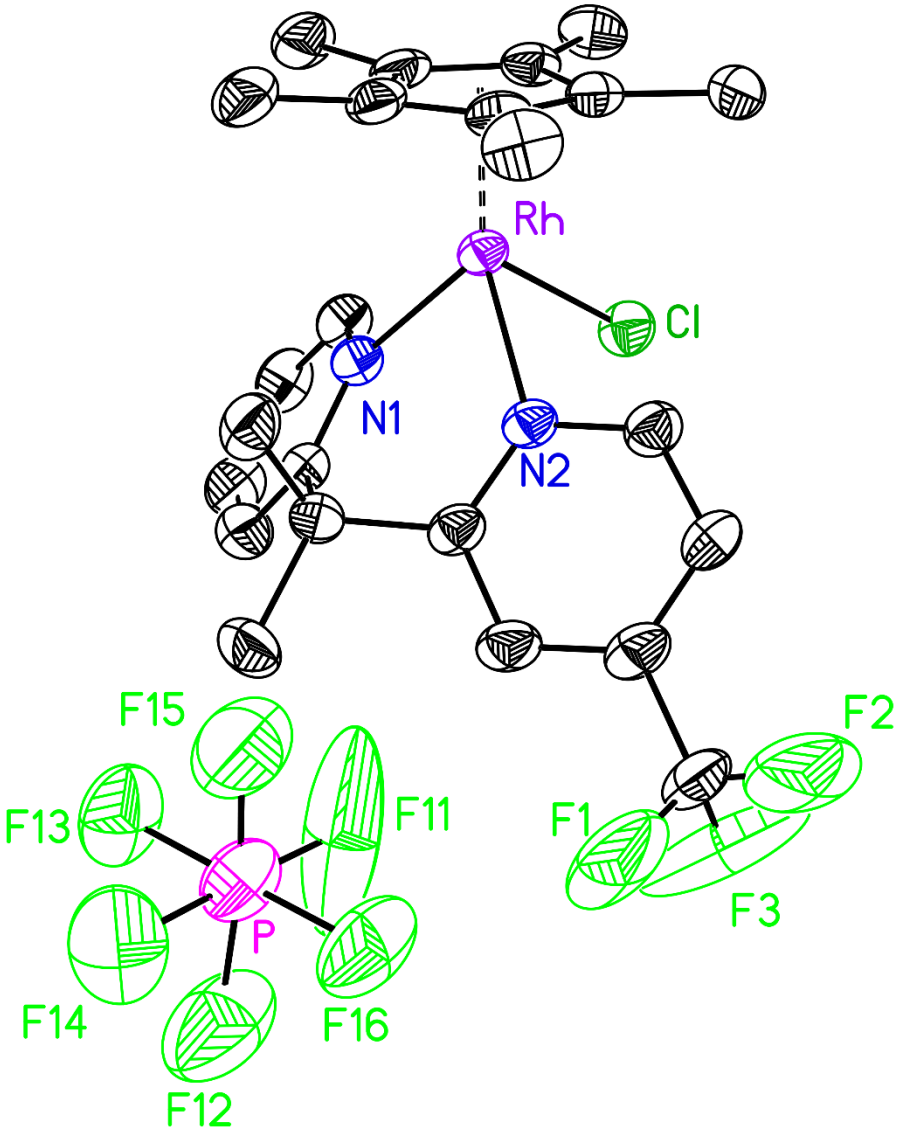

Figure D69. Full solid-state structure of $\mathbf{A}^{CF3}$. Hydrogen atoms omitted for clarity. Displacement ellipsoids shown at the 50% probability level.

Special Refinement Details for A^{OMe}

No special refinement was required.

Solid-State Structure of A^{OMe}

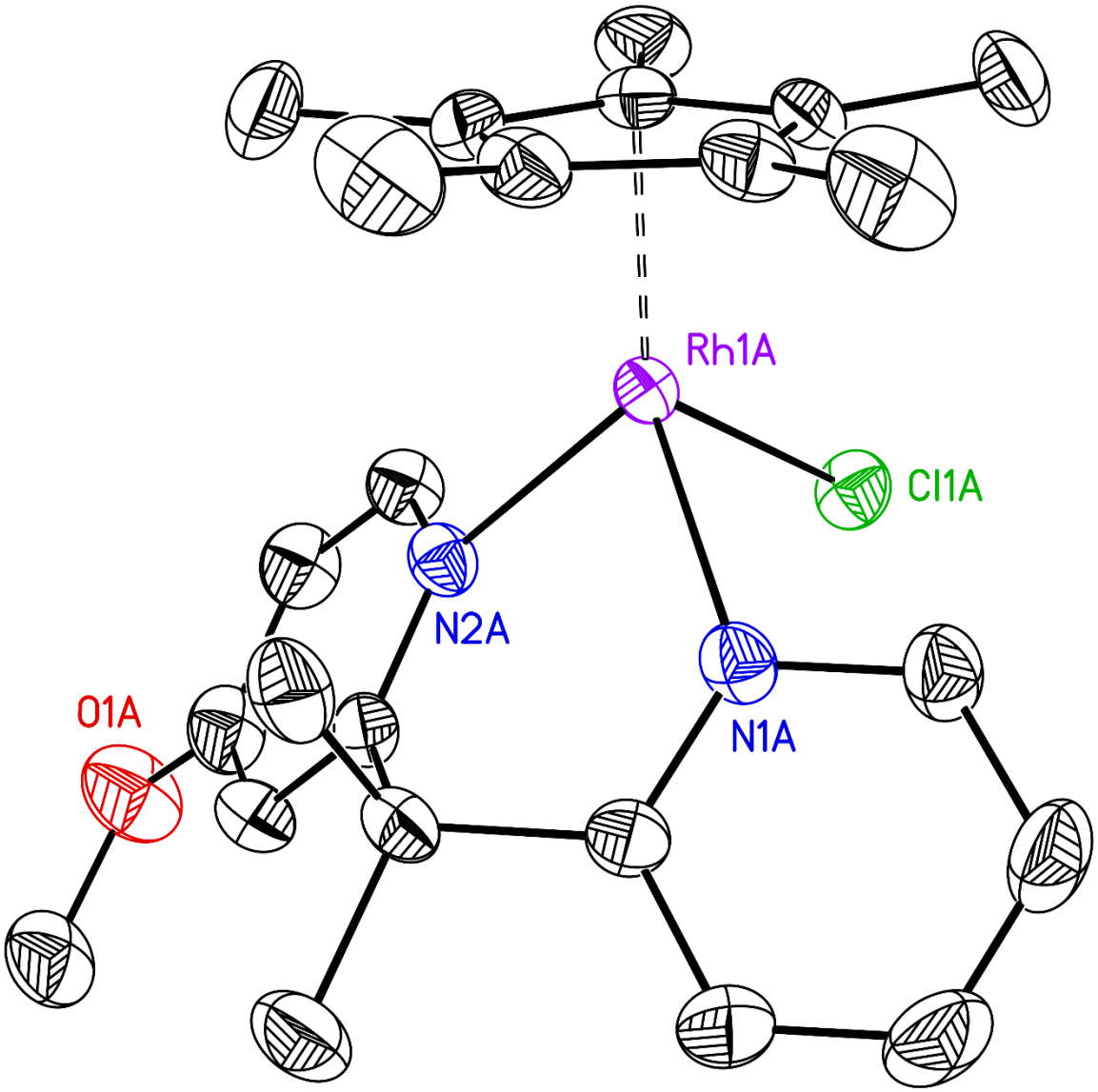

Figure D70. Solid-state structure of $\mathbf{A^{OMe}}$ (XRD). Hydrogen atoms, outer-sphere solvent molecules and counteranion molecules in the unit cell are omitted for clarity. Displacement ellipsoids are shown at the 50% probability level. One of two independent molecules observed in the asymmetric unit cell shown.

Solid-State Structure of A^{OMe}

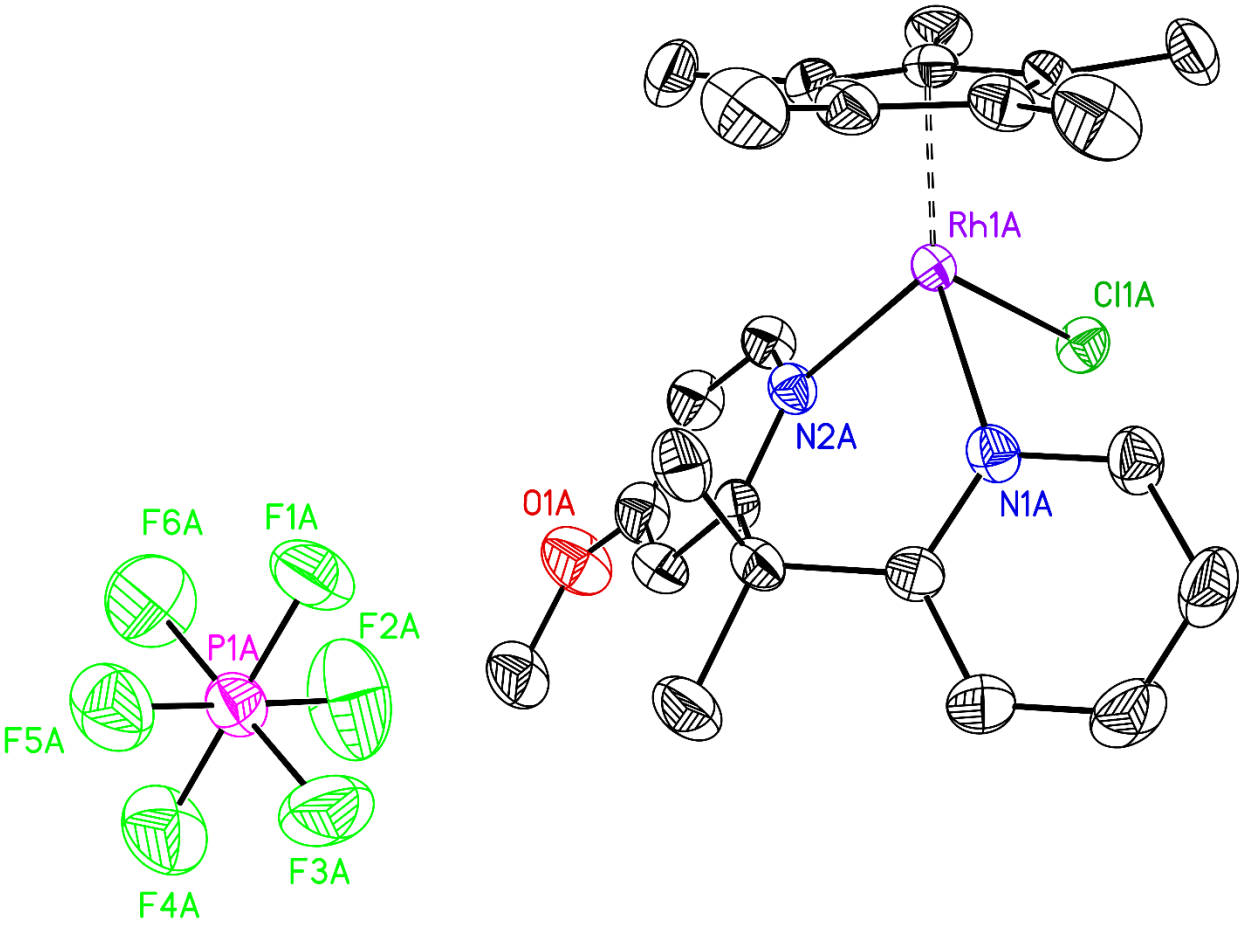

Figure D71. Solid-state structure of $\mathbf{A^{OMe}}$ (XRD). Hydrogen atoms, outer-sphere solvent molecules in the unit cell are omitted for clarity. Displacement ellipsoids are shown at the 50% probability level. One of two independent molecules observed in the asymmetric unit cell shown.

Full Solid-State Structure of A^{OMe}

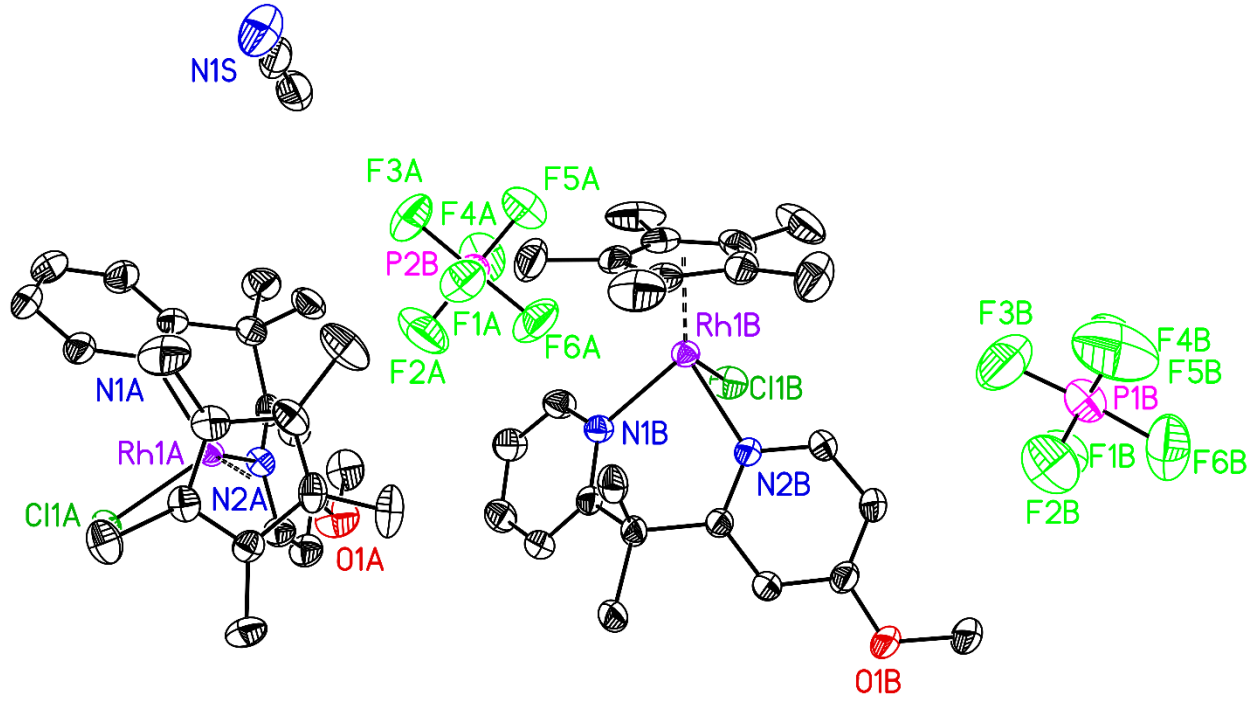

Figure D72. Full solid-state structure of $\mathbf{A}^{CF3}$. Hydrogen atoms omitted for clarity. Displacement ellipsoids shown at the 50% probability level.

Special Refinement Details for 3^{CF3}

No special refinement was required.

Full Solid-State Structure of 3^{CF3}

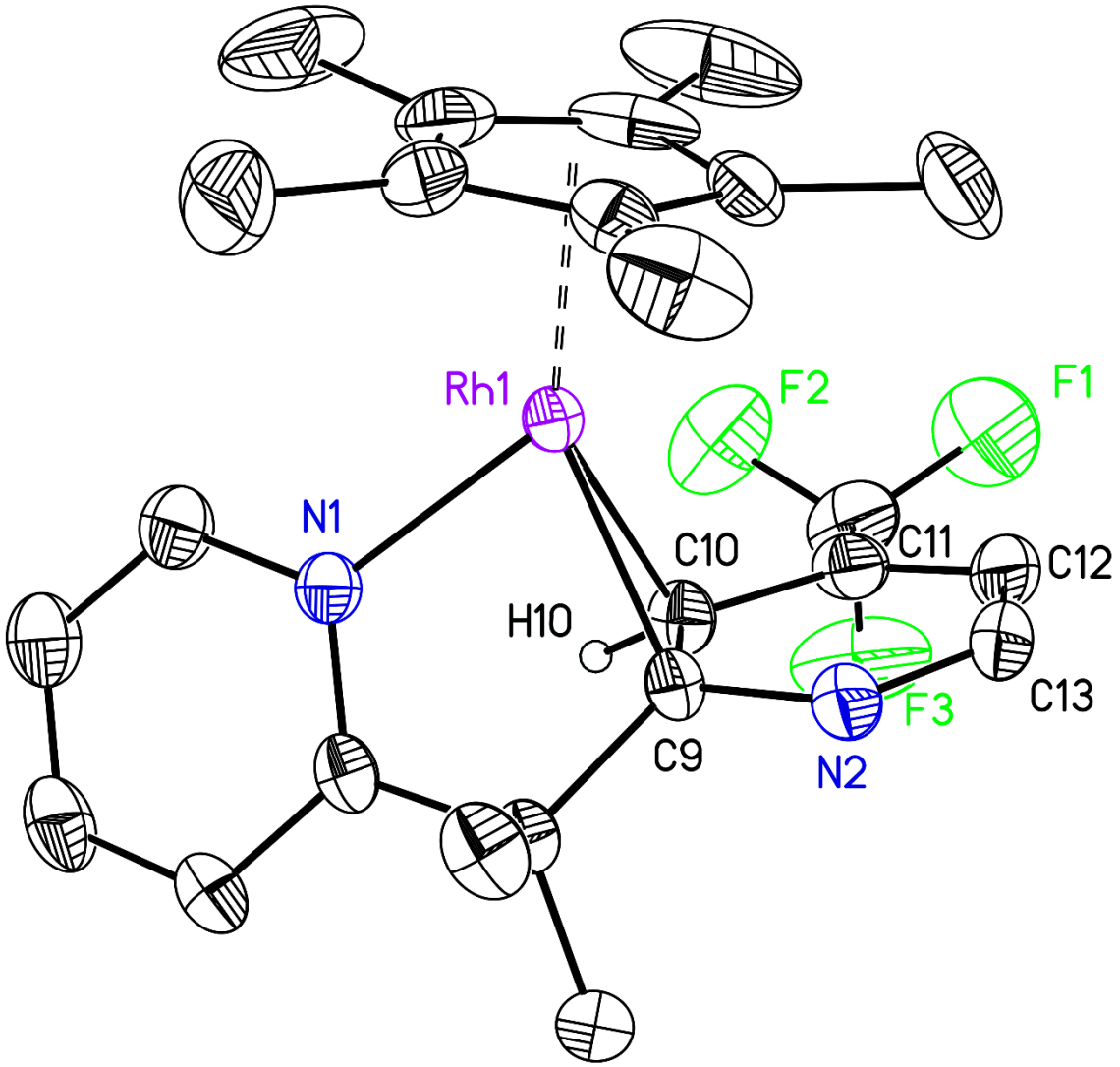

Figure D73. Full solid-state structure of $\mathbf{3^{CF3}}$. Hydrogen atoms omitted for clarity. Displacement ellipsoids shown at the 50% probability level.

Special Refinement Details for 3^{OMe}

No special refinement was required.

Solid-State Structure of 3^{OMe}

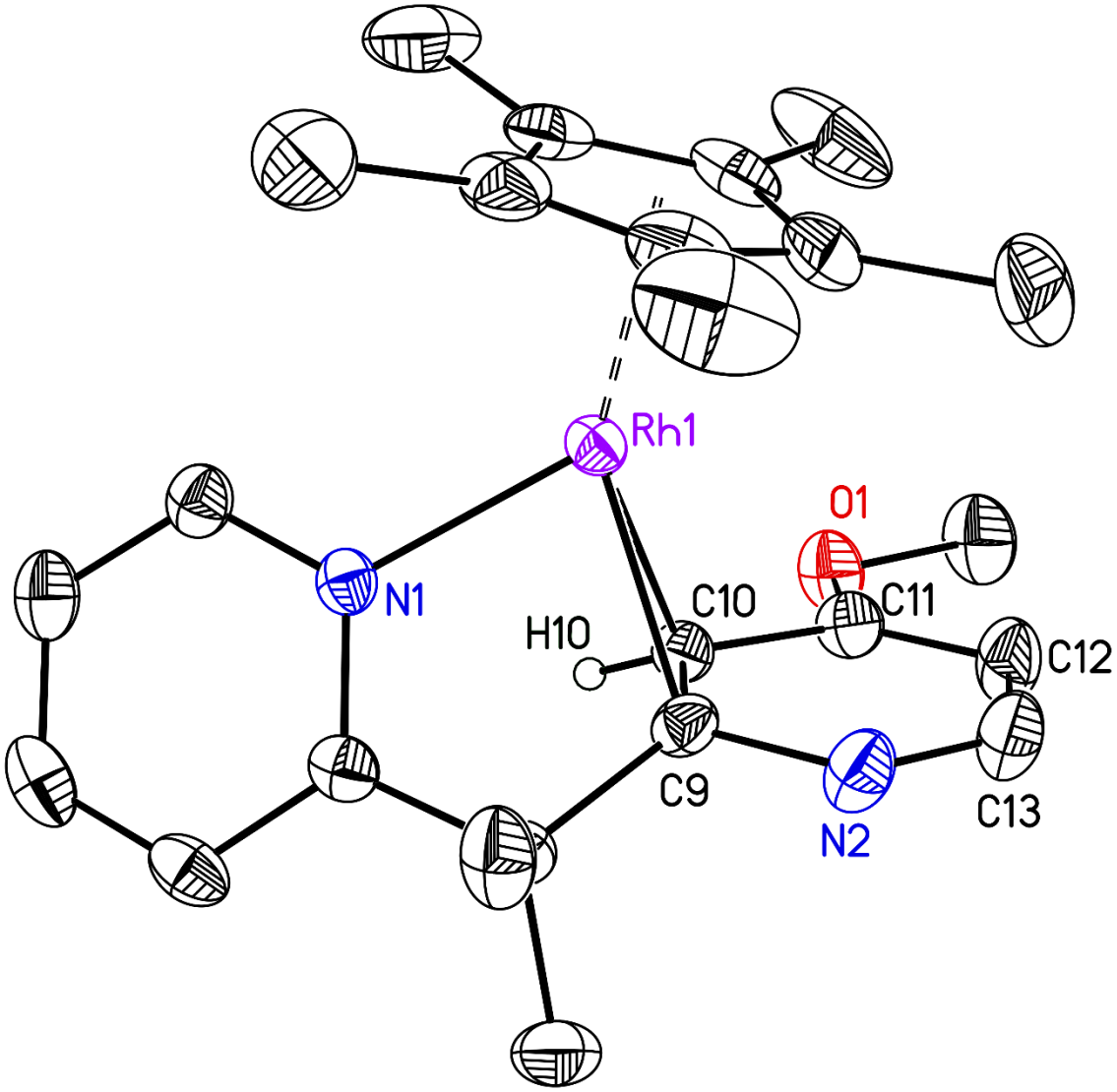

Figure D74. Full solid-state structure of $\mathbf{3^{OMe}}$. Hydrogen atoms omitted for clarity. Displacement ellipsoids shown at the 50% probability level.

Appendix E

Supplementary Information for Chapter 7

Electrochemistry

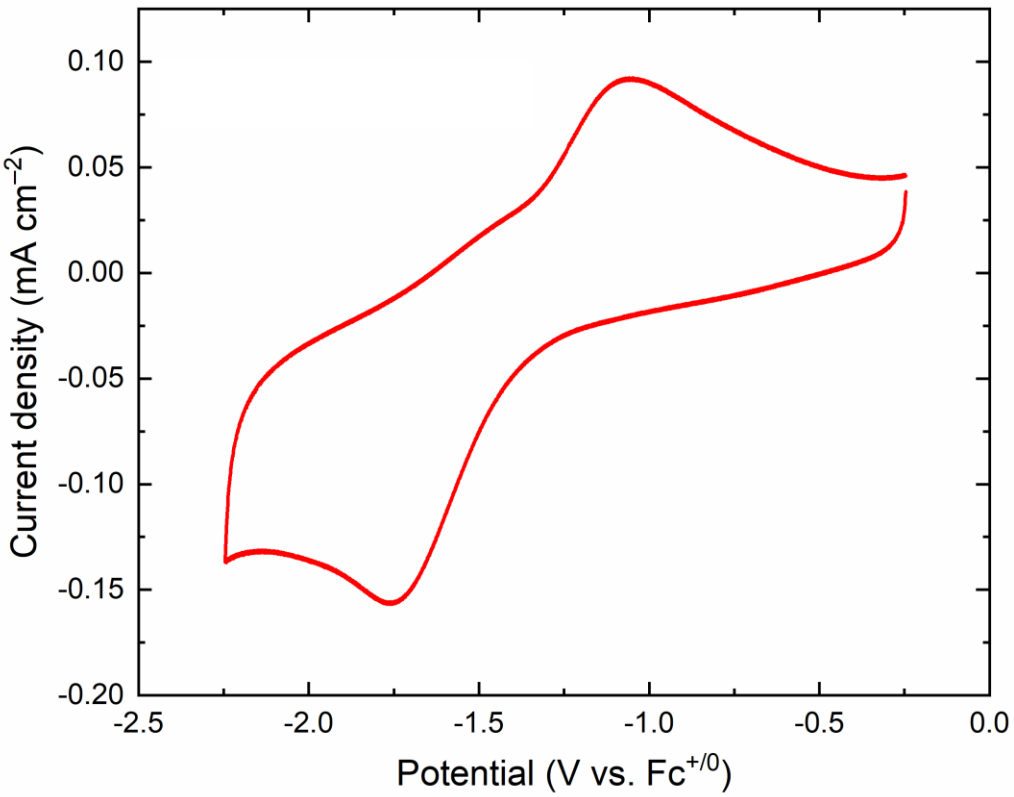

Figure E1. Cyclic voltammetry of **1** (THF, 0.1 M [^{n}Bu$_4$N][PF$_6$], 100 mV/s)

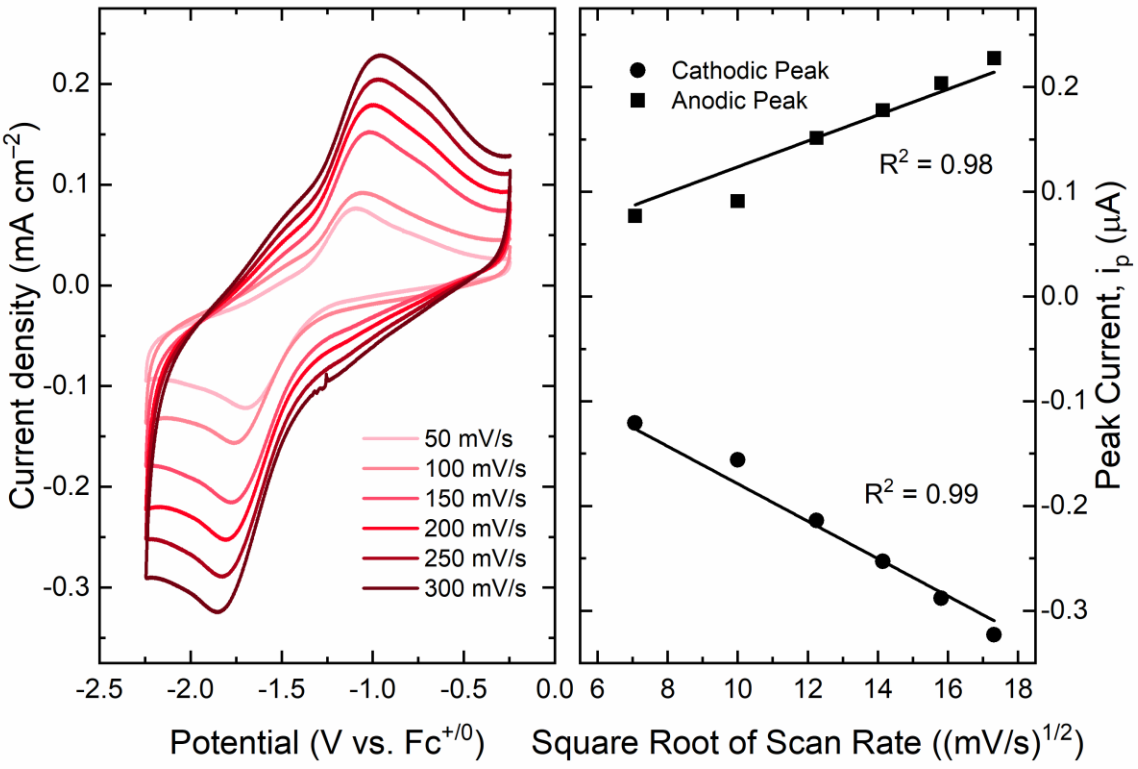

Figure E2. Left: Cyclic voltammetry of **1** at varying scan rate in CH_3CN (0.1 M [^{n}Bu$_4$N][PF_6]).Right: Linear dependence of peak cathodic current on square root of scan rate with the y-intercept set to 0.

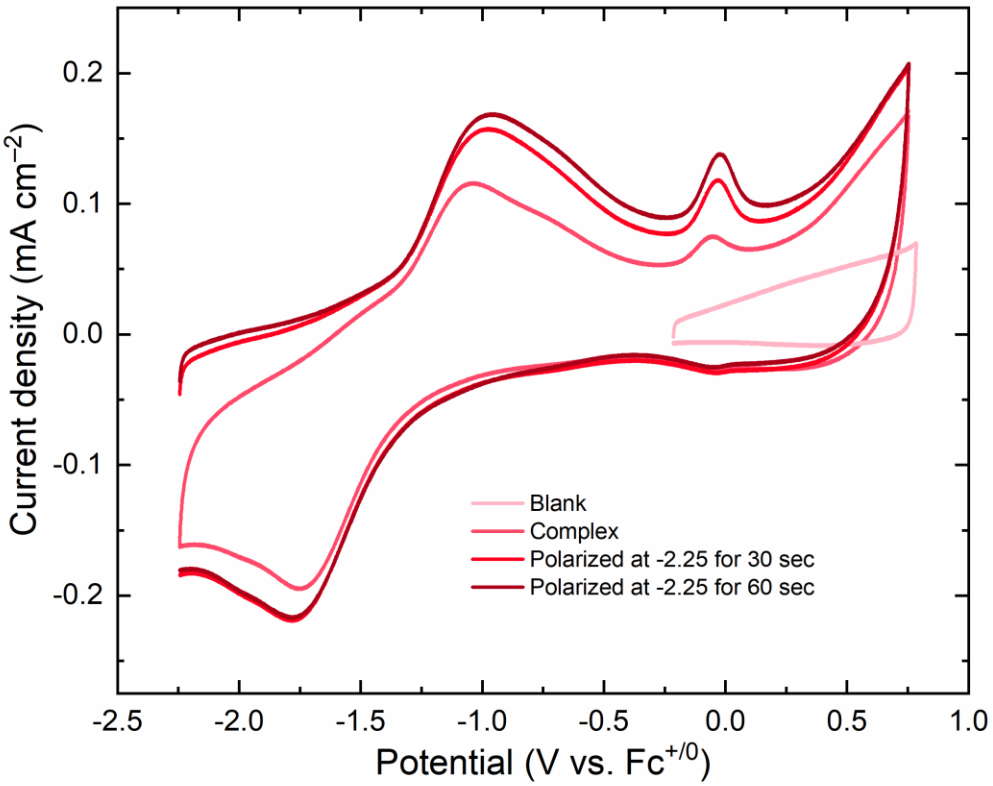

Figure E3. Cyclic voltammetry of **1** (THF, 0.1 M [^{n}Bu$_4$N][PF$_6$], 100 mV/s)

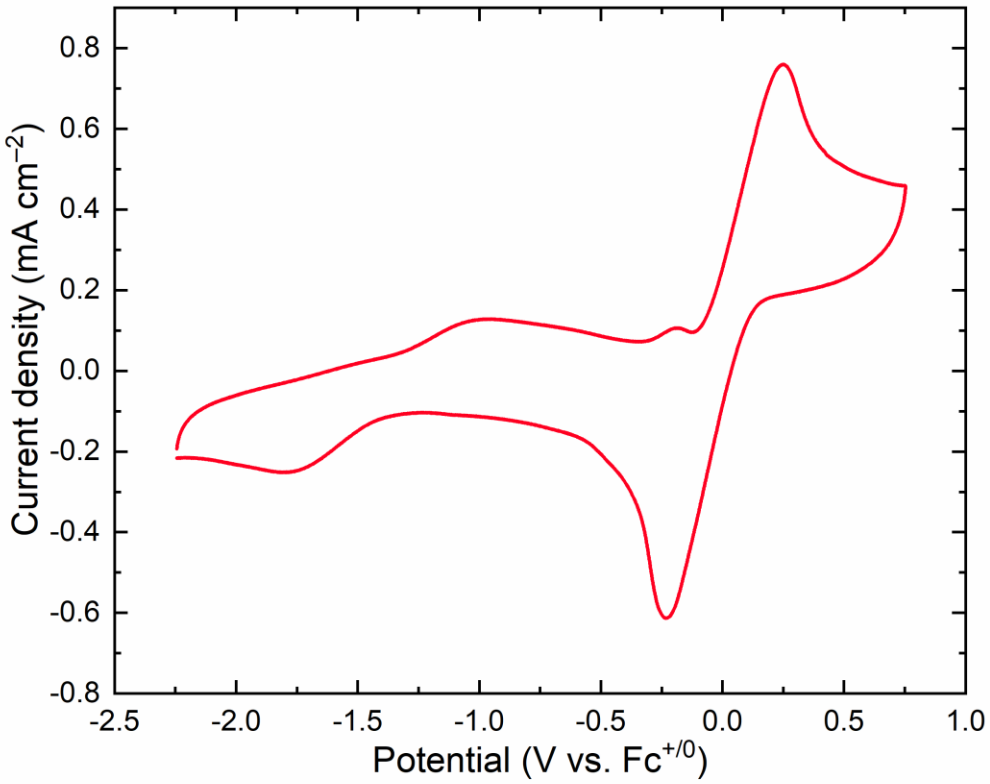

Figure E4. Cyclic voltammetry of **1** with a 1:1 ratio of ferrocene (THF, 0.1 M [^{n}Bu$_4$N][PF$_6$], 100 mV/s)

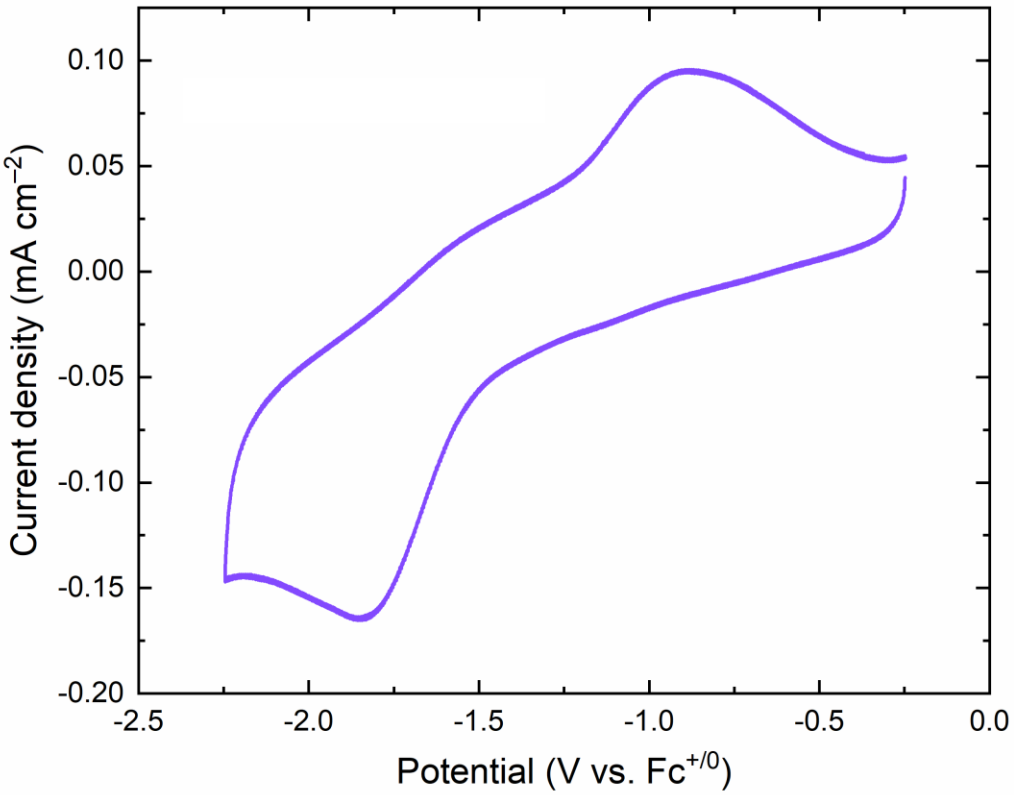

Figure E5. Cyclic voltammetry of **2** (THF, 0.1 M [^{n}Bu$_4$N][PF$_6$], 100 mV/s)

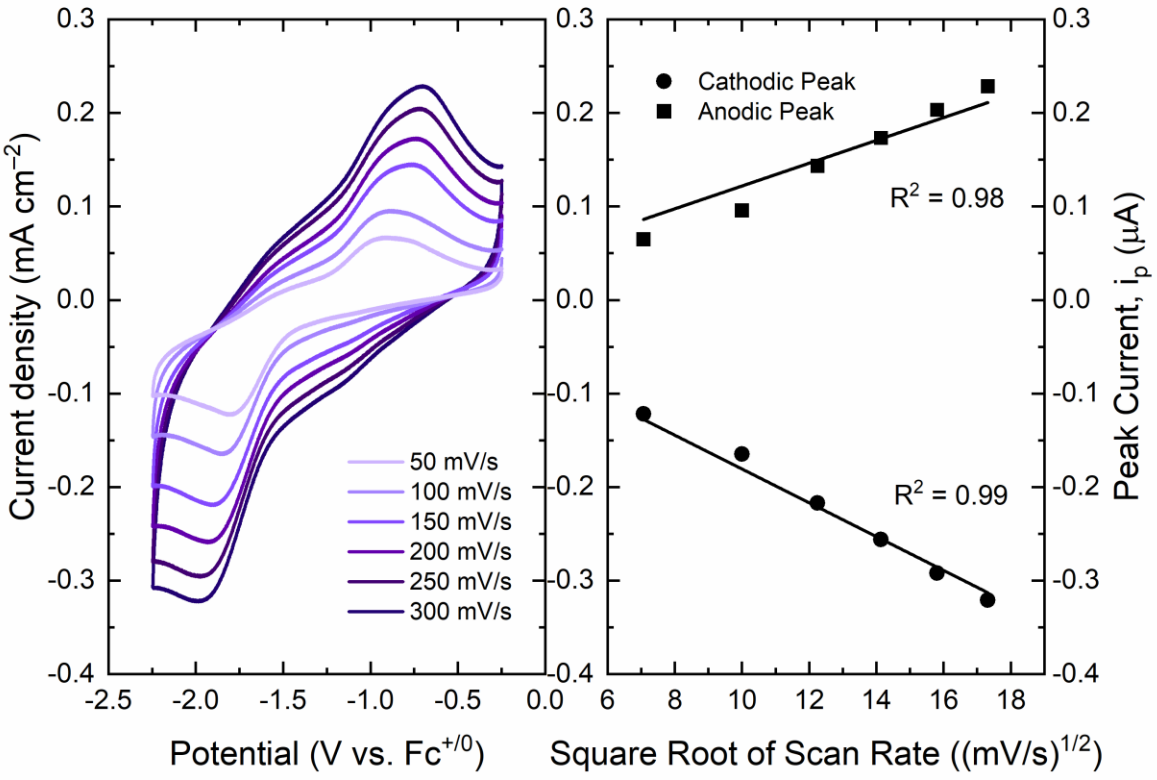

Figure E6. Left: Cyclic voltammetry of **2** at varying scan rate in CH_3CN (0.1 M [^{n}Bu$_4$N][PF_6]).Right: Linear dependence of peak cathodic current on square root of scan rate with the y-intercept set to 0.

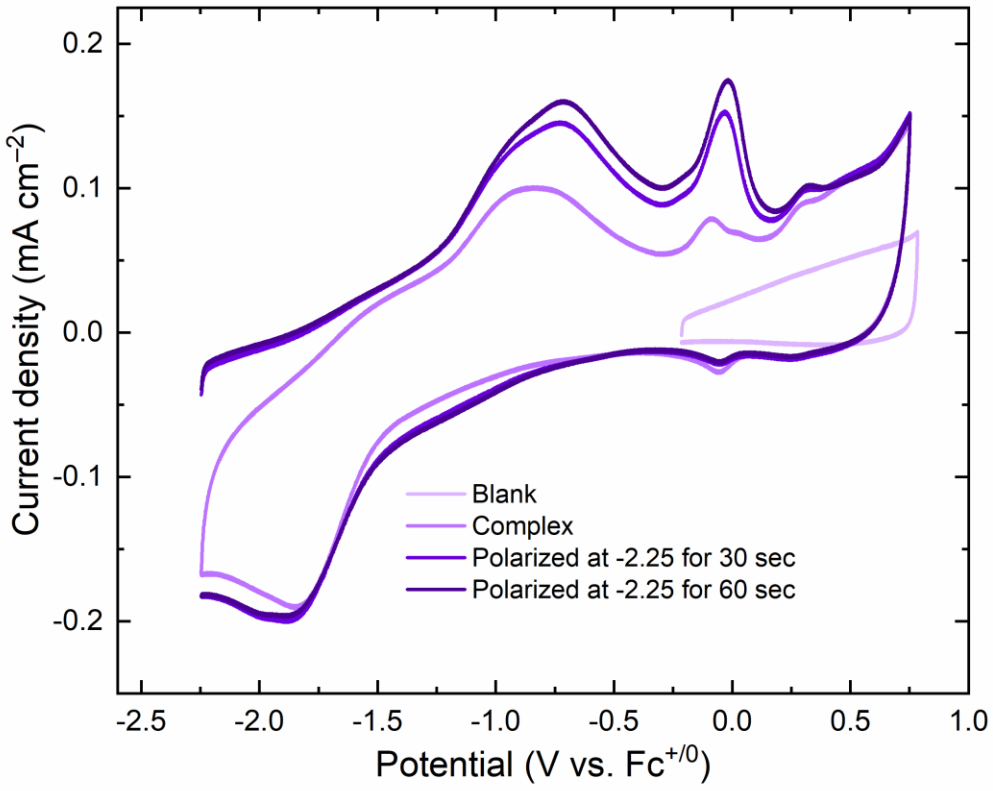

Figure E7. Cyclic voltammetry of **2** (THF, 0.1 M [^{n}Bu$_4$N][PF$_6$], 100 mV/s)

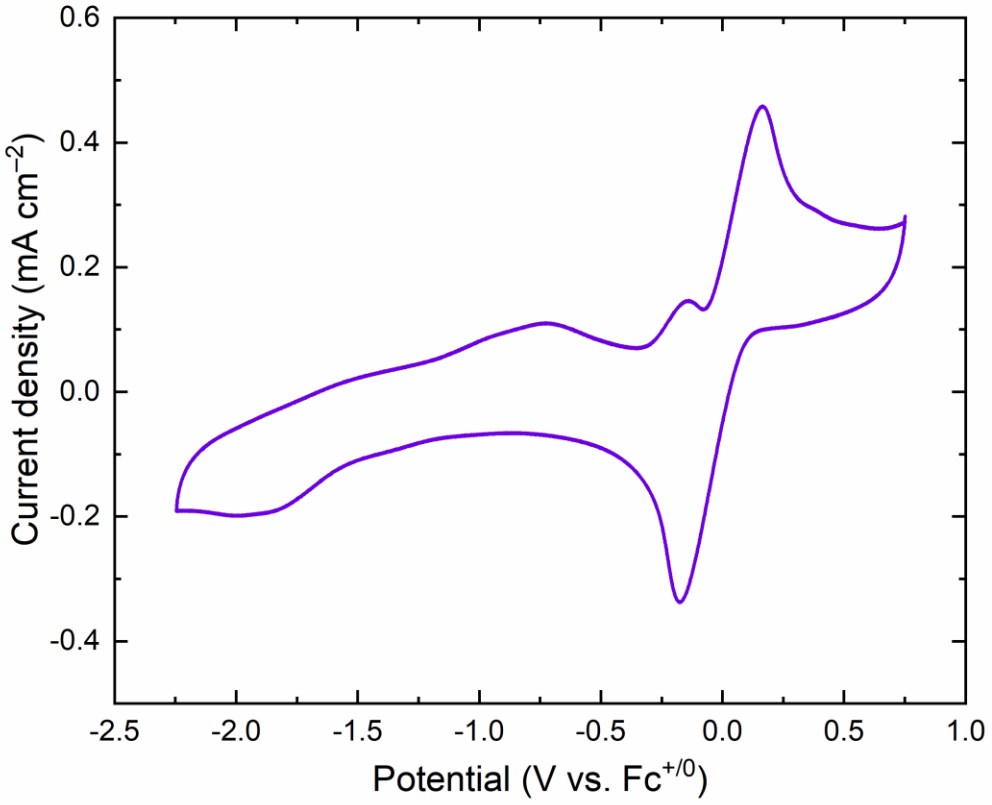

Figure E8. Cyclic voltammetry of **2** with a 1:1 ratio of ferrocene (THF, 0.1 M [^{n}Bu$_4$N][PF$_6$], 100 mV/s)

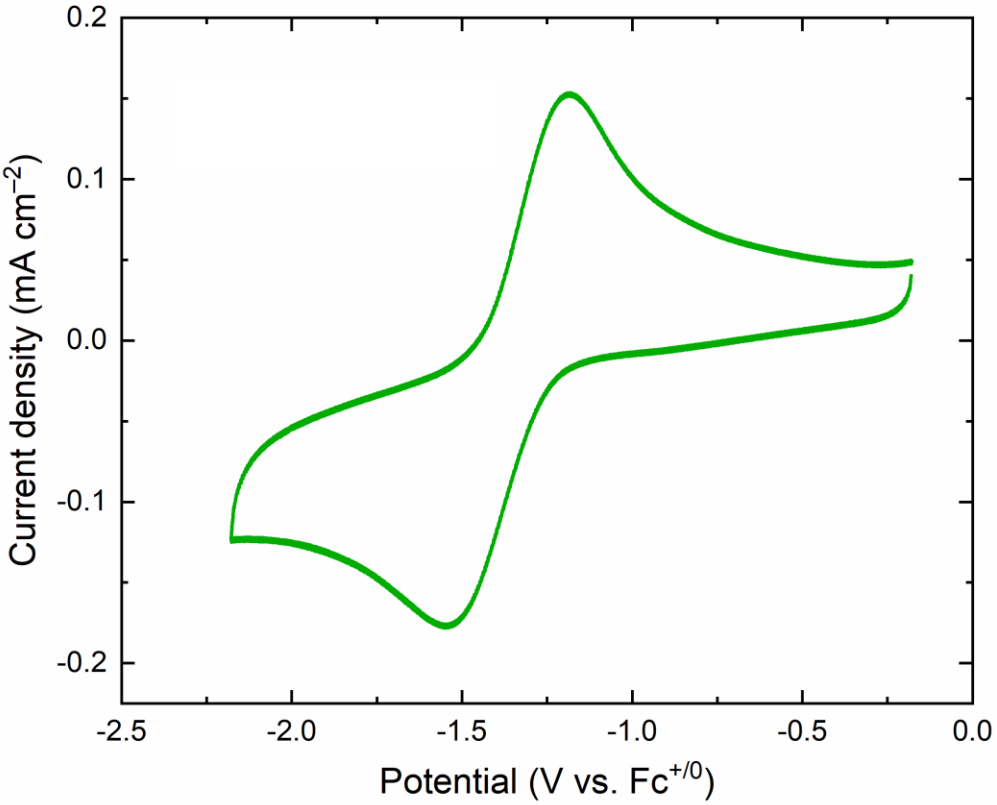

Figure E9. Cyclic voltammetry of **2** with a 1:1 ratio of ferrocene (THF, 0.1 M [^{n}Bu$_4$N][PF$_6$], 100 mV/s)

Figure E47. Cyclic voltammetry of **3** (THF, 0.1 M [^{n}Bu$_4$N][PF$_6$], 100 mV/s)

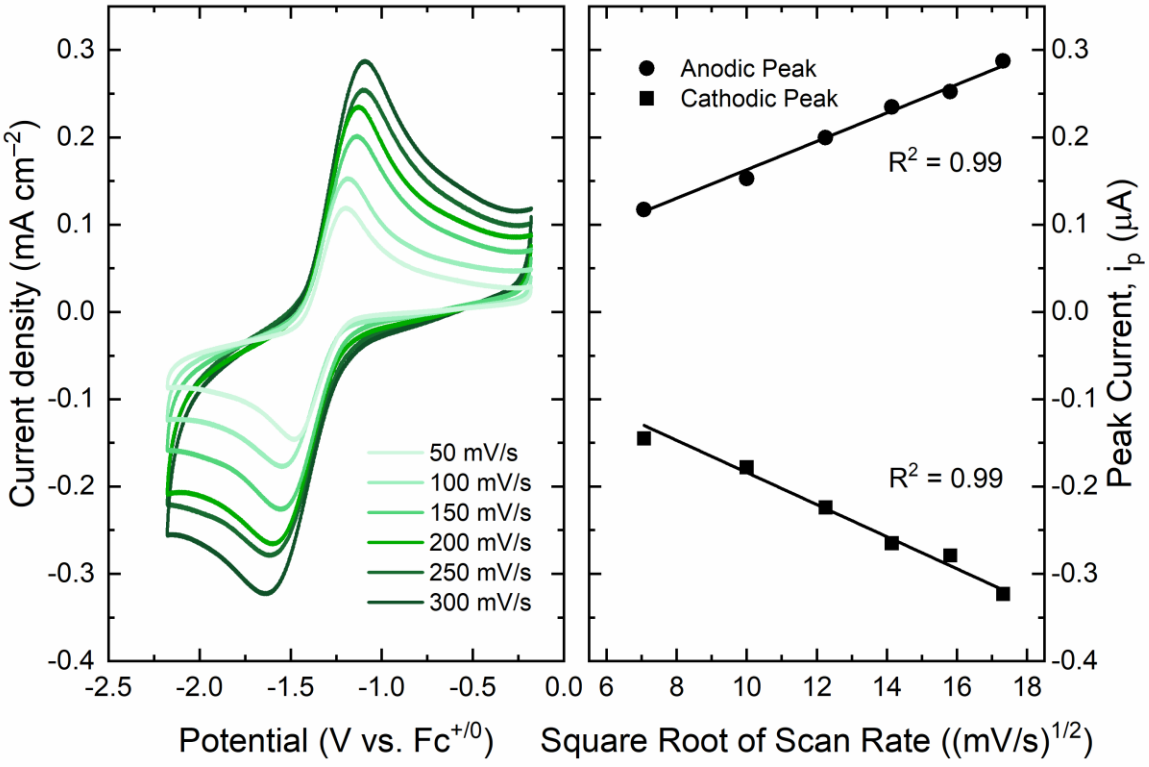

Figure E10. Left: Cyclic voltammetry of **3** at varying scan rate in CH_3CN (0.1 M [^{n}Bu$_4$N][PF_6]).Right: Linear dependence of peak cathodic current on square root of scan rate with the y-intercept set to 0.

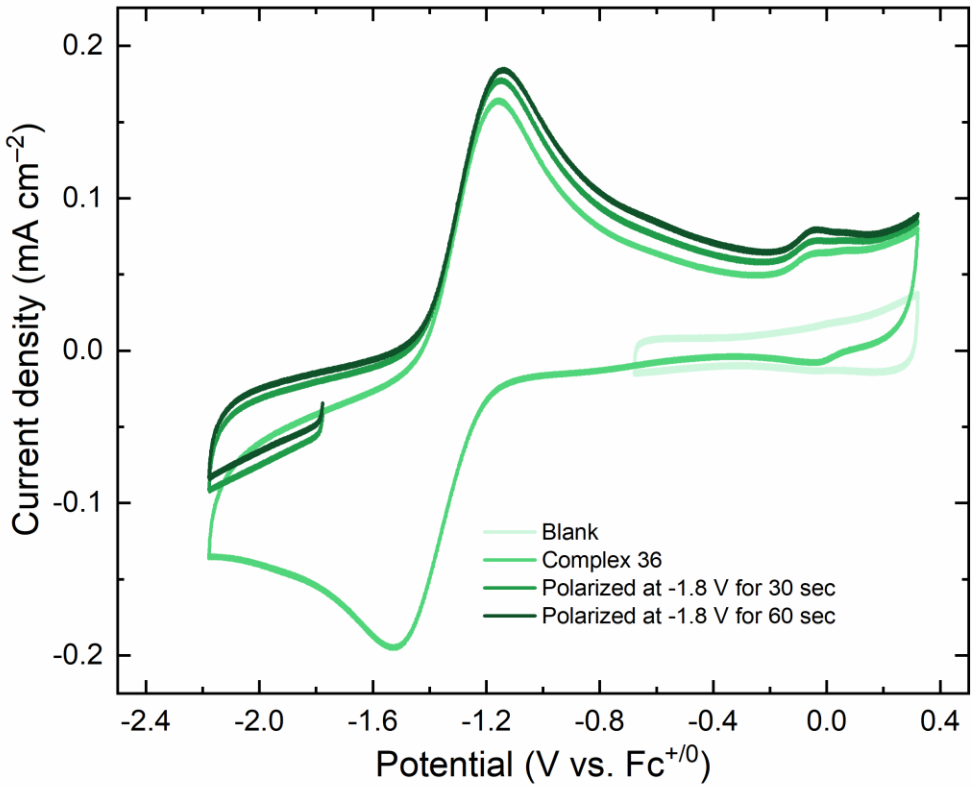

Figure E11. Cyclic voltammetry of **3** (THF, 0.1 M [^{n}Bu$_4$N][PF$_6$], 100 mV/s)

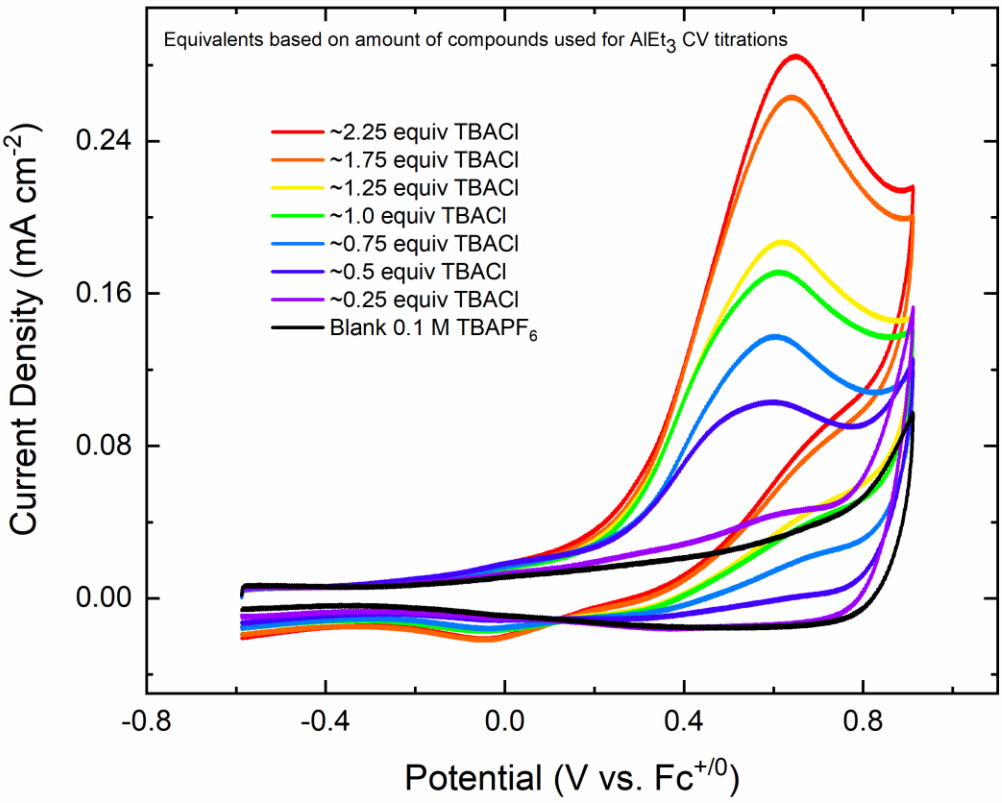

Figure E12. Titration of blank 0.1 M [nBu4N][PF6] solution with increasing equivalents of [nBu4N][Cl] (THF, 0.1 M [nBu_4N][PF_6], 100 mV/s).

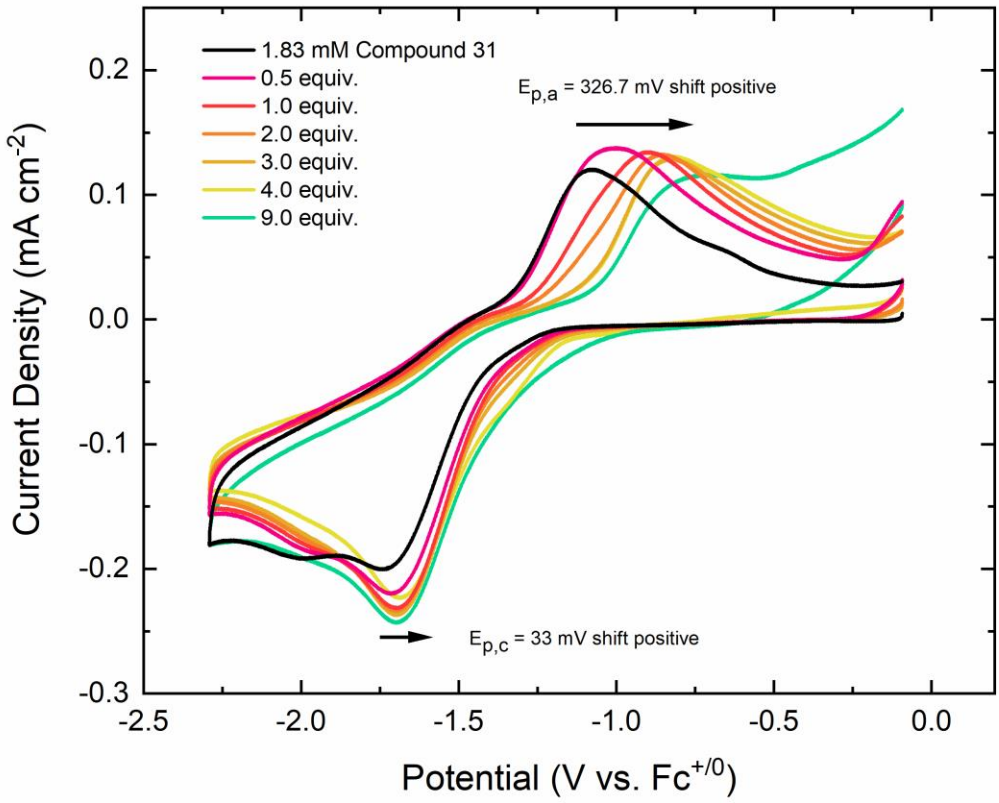

Figure E13. Titration of **1** solution with increasing equivalents of $AlEt_3$ (THF, 0.1 M $[nBu_4N][PF_6]$, 100 mV/s).

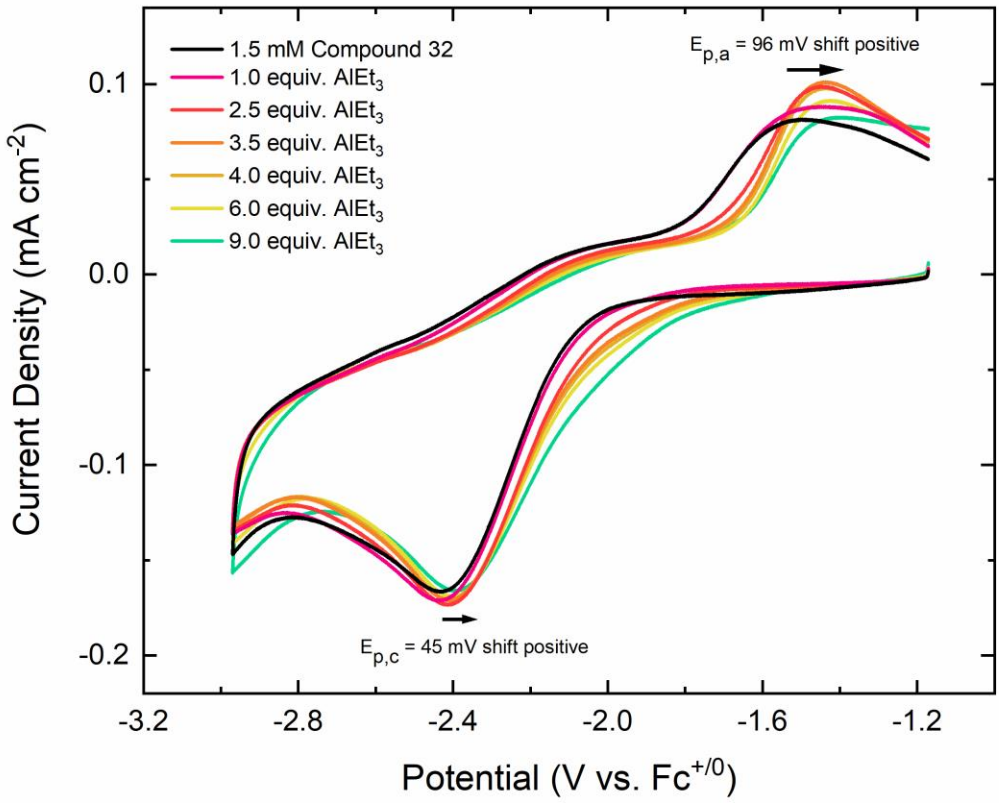

Figure E14. Titration of **2** solution with increasing equivalents of $AlEt_3$ (THF, 0.1 M $[nBu_4N][PF_6]$, 100 mV/s).

EQCM

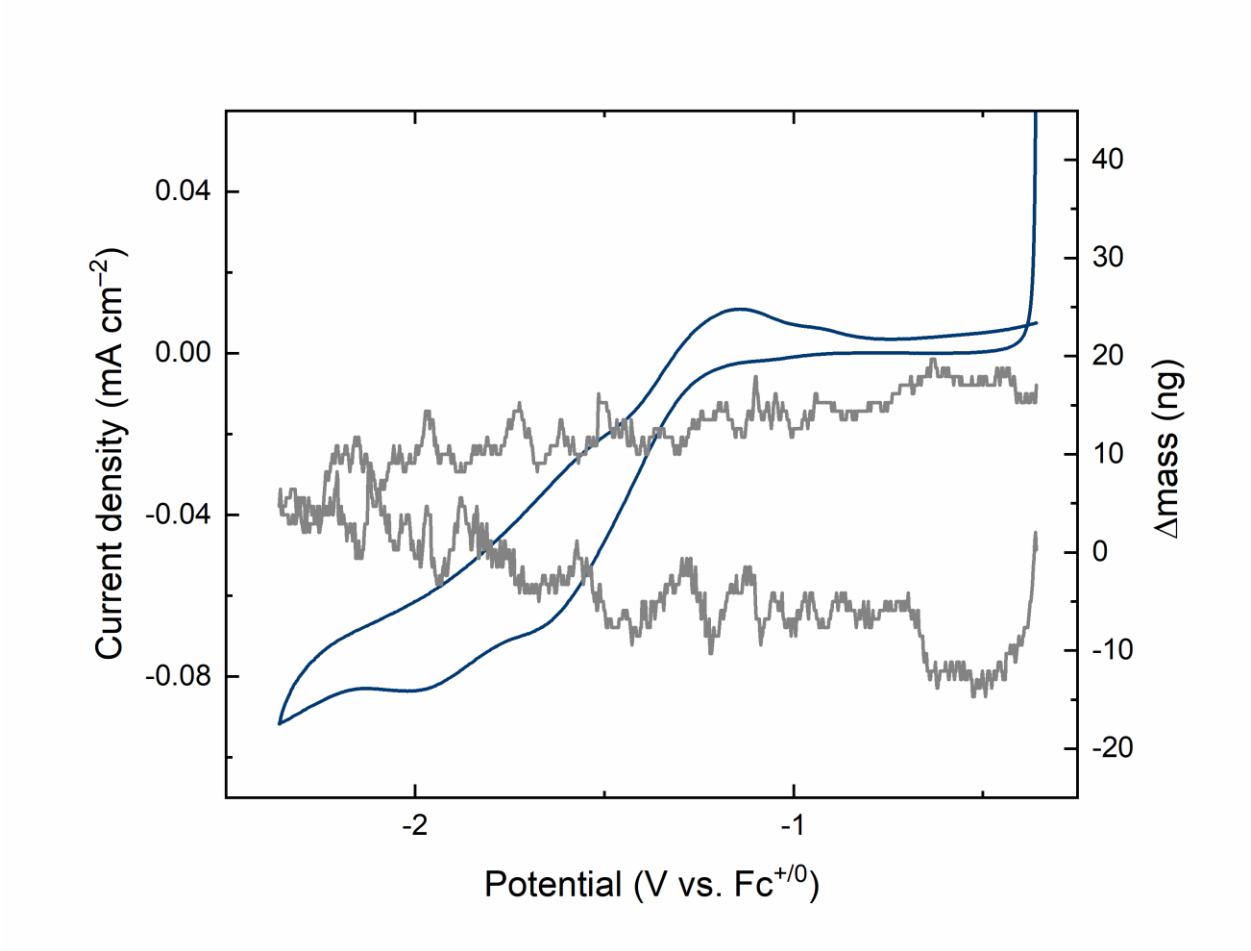

Figure E15. EQCM data of **1**. EQCM experiments with voltammetry (blue) and mass data (gray) for a solution containing **1**. Conditions: 1.5 mM **1** 0.1 M $TBAPF_6$, Au EQCM disk working electrode, Pt counter electrode, $Ag^{+/0}$ reference electrode. Scan rate: 20 mV/s.

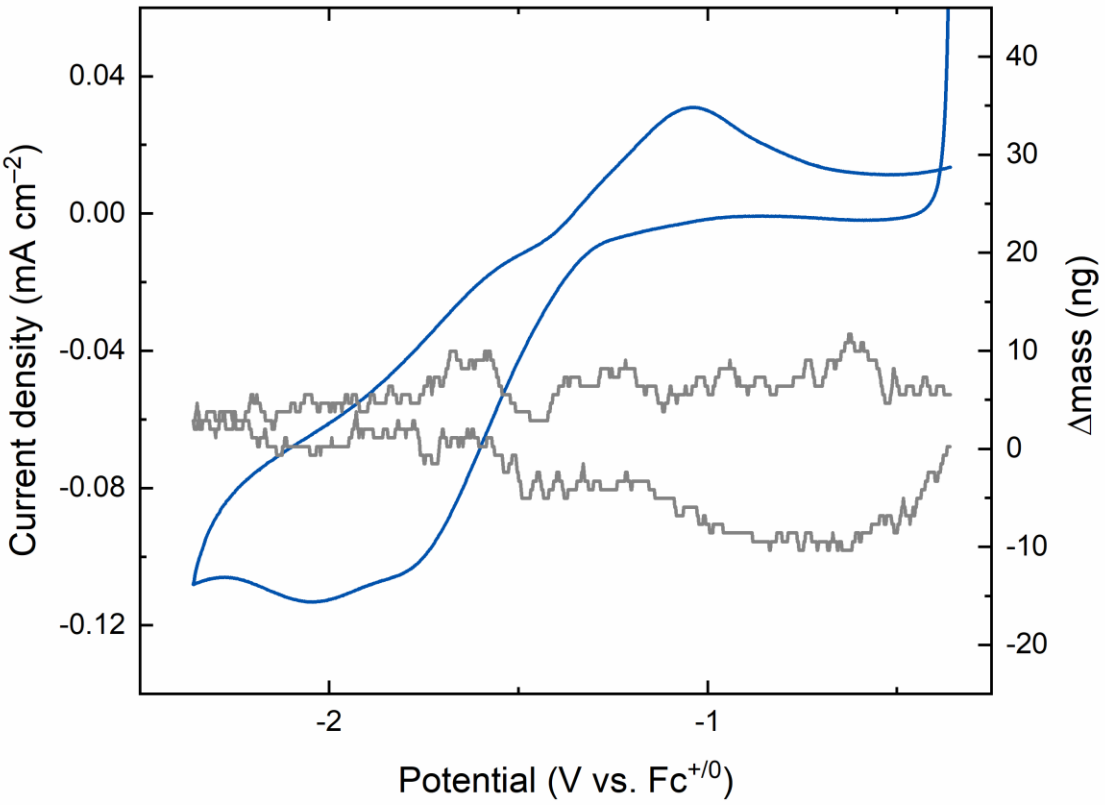

Figure E16. EQCM data of **1**. EQCM experiments with voltammetry (blue) and mass data (gray) for a solution containing **1**. Conditions: 1.5 mM **1** 0.1 M $TBAPF_6$, Au EQCM disk working electrode, Pt counter electrode, $Ag^{+/0}$ reference electrode. Scan rate: 50 mV/s

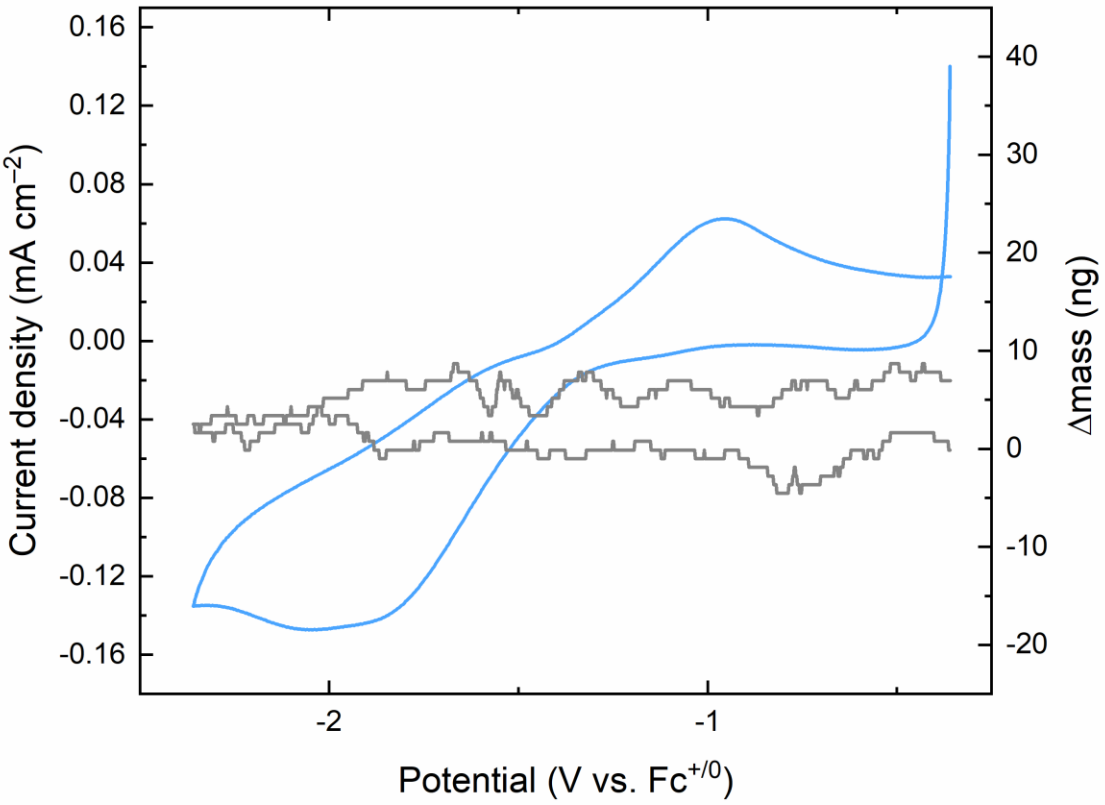

Figure E17. EQCM data of **1**. EQCM experiments with voltammetry (blue) and mass data (gray) for a solution containing **1**. Conditions: 1.5 mM **1** 0.1 M $TBAPF_6$, Au EQCM disk working electrode, Pt counter electrode, $Ag^{+/0}$ reference electrode. Scan rate: 100 mV/s

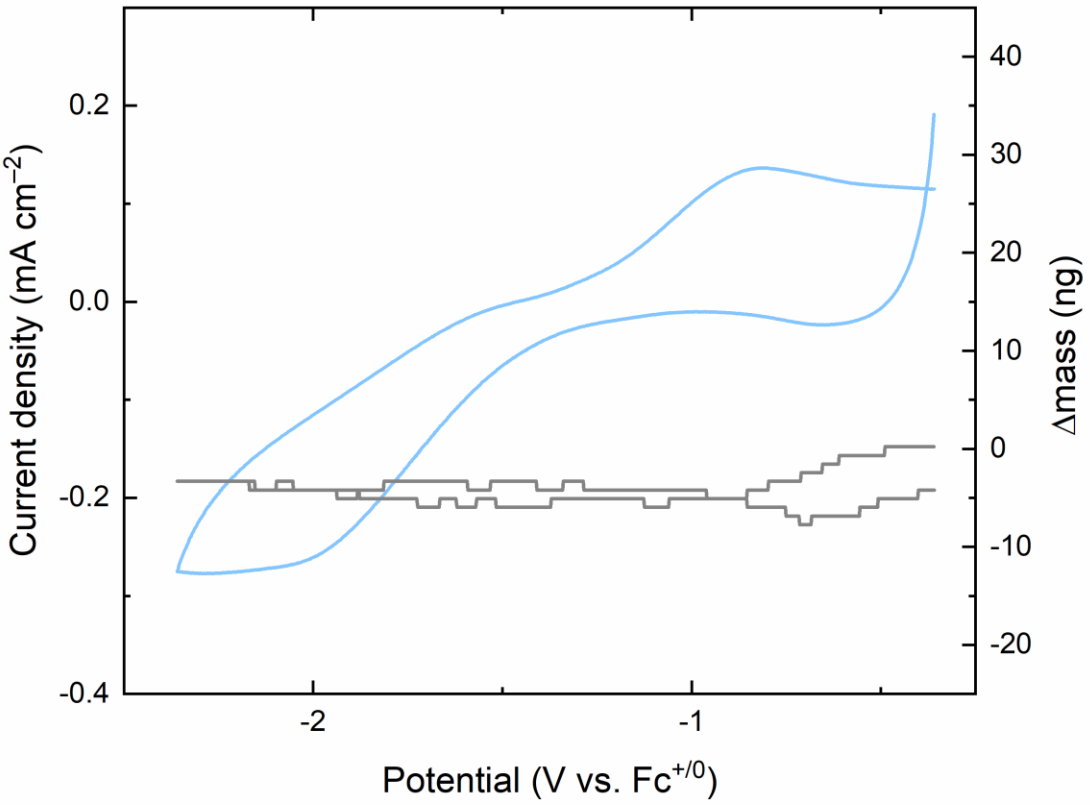

Figure E18. EQCM data of **1**. EQCM experiments with voltammetry (blue) and mass data (gray) for a solution containing **1**. Conditions: 1.5 mM **1** 0.1 M $TBAPF_6$, Au EQCM disk working electrode, Pt counter electrode, $Ag^{+/0}$ reference electrode. Scan rate: 400 mV/s

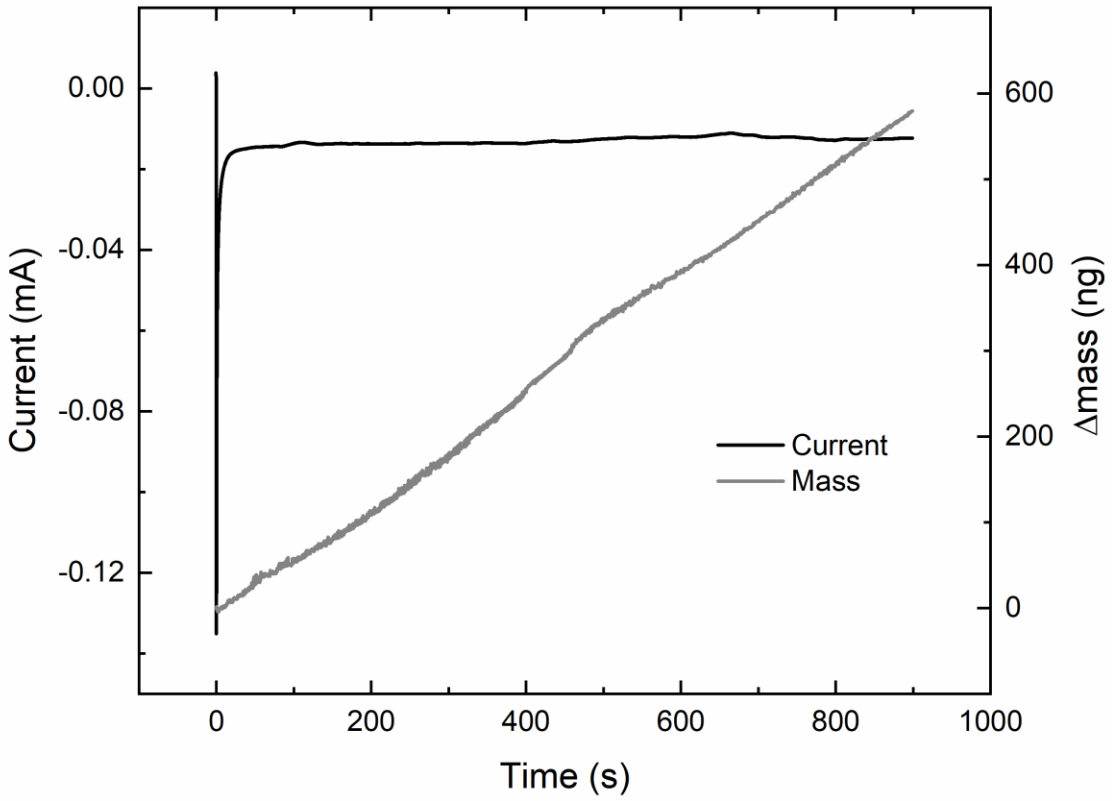

Figure E19. EQCM data of **1**. EQCM bulk electrolysis polarized –1.75 V vs. $Fc^{+/0}$ at experiments with voltammetry (black) and mass data (gray) for a solution containing **1**. Conditions: 1.5 mM Cr 0.1 M $TBAPF_6$, Au EQCM disk working electrode, Pt counter electrode, $Ag^{+/0}$ reference electrode.

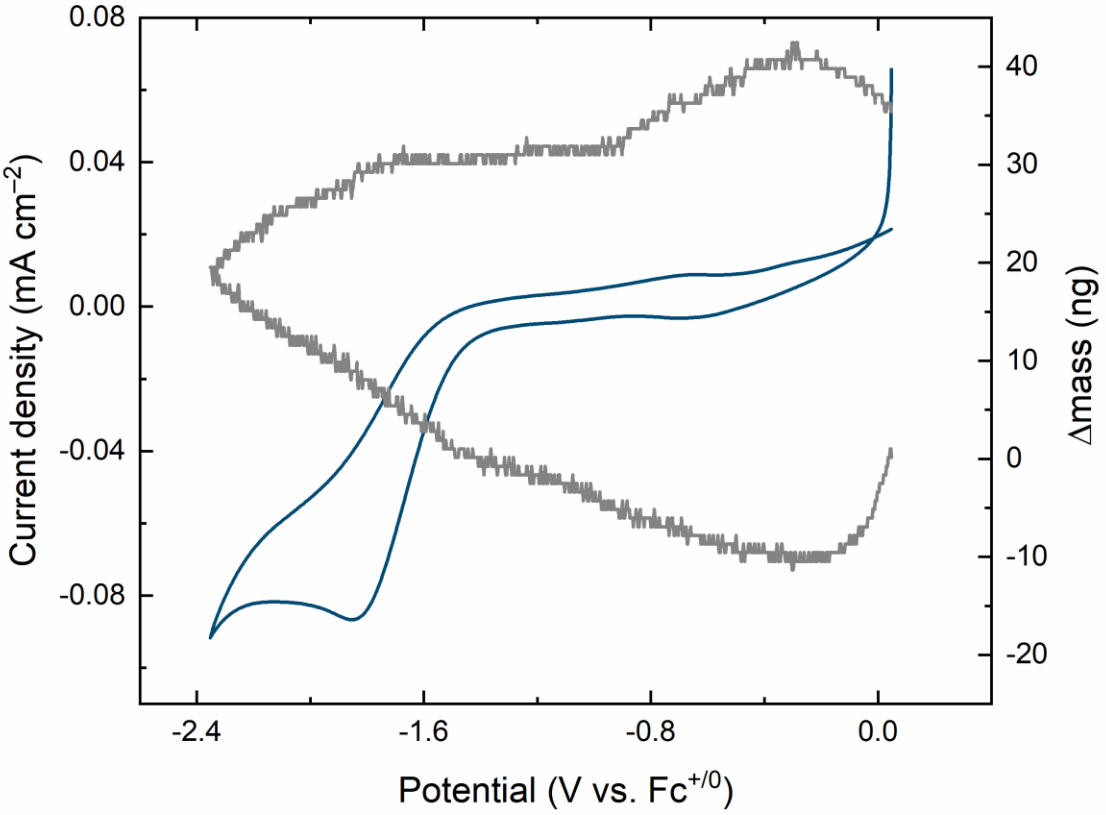

Figure E20. EQCM data of **2**. EQCM experiments with voltammetry (blue) and mass data (gray) for a solution containing **2**. Conditions: 1.5 mM **2** 0.1 M $TBAPF_6$, Au EQCM disk working electrode, Pt counter electrode, $Ag^{+/0}$ reference electrode. Scan rate: 20 mV/s

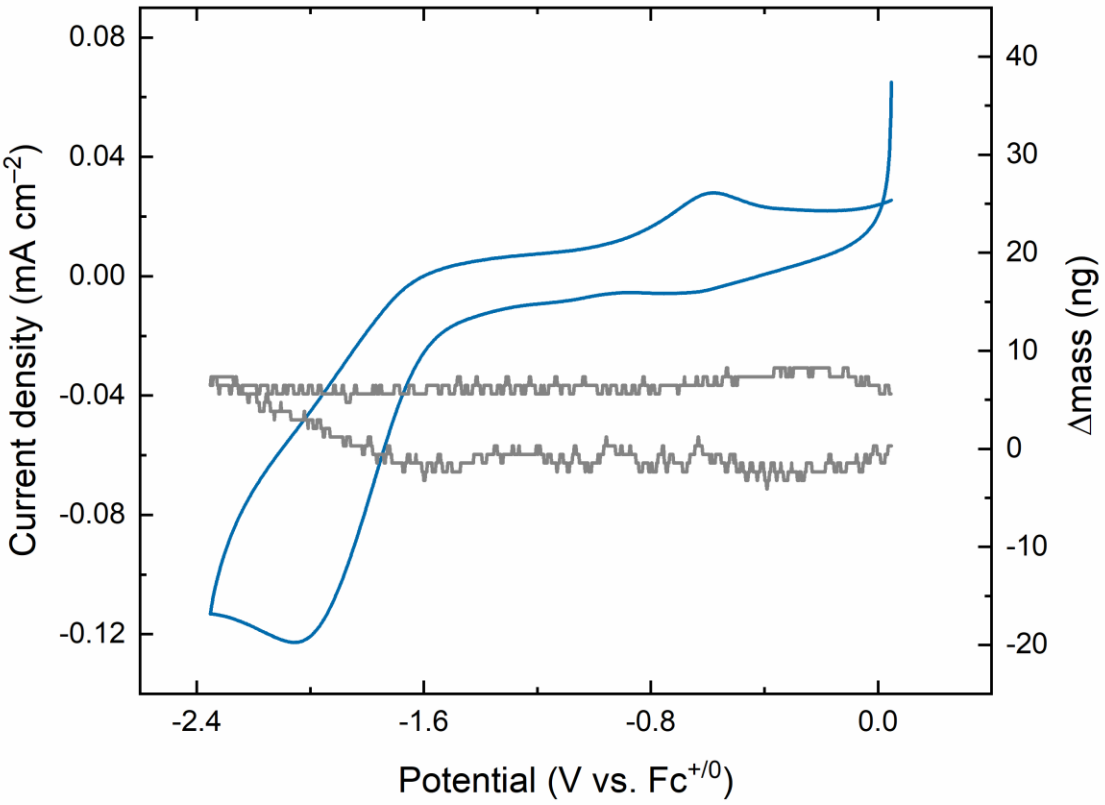

Figure E21. EQCM data of **2**. EQCM experiments with voltammetry (blue) and mass data (gray) for a solution containing **2**. Conditions: 1.5 mM **2** 0.1 M $TBAPF_6$, Au EQCM disk working electrode, Pt counter electrode, $Ag^{+/0}$ reference electrode. Scan rate: 50 mV/s

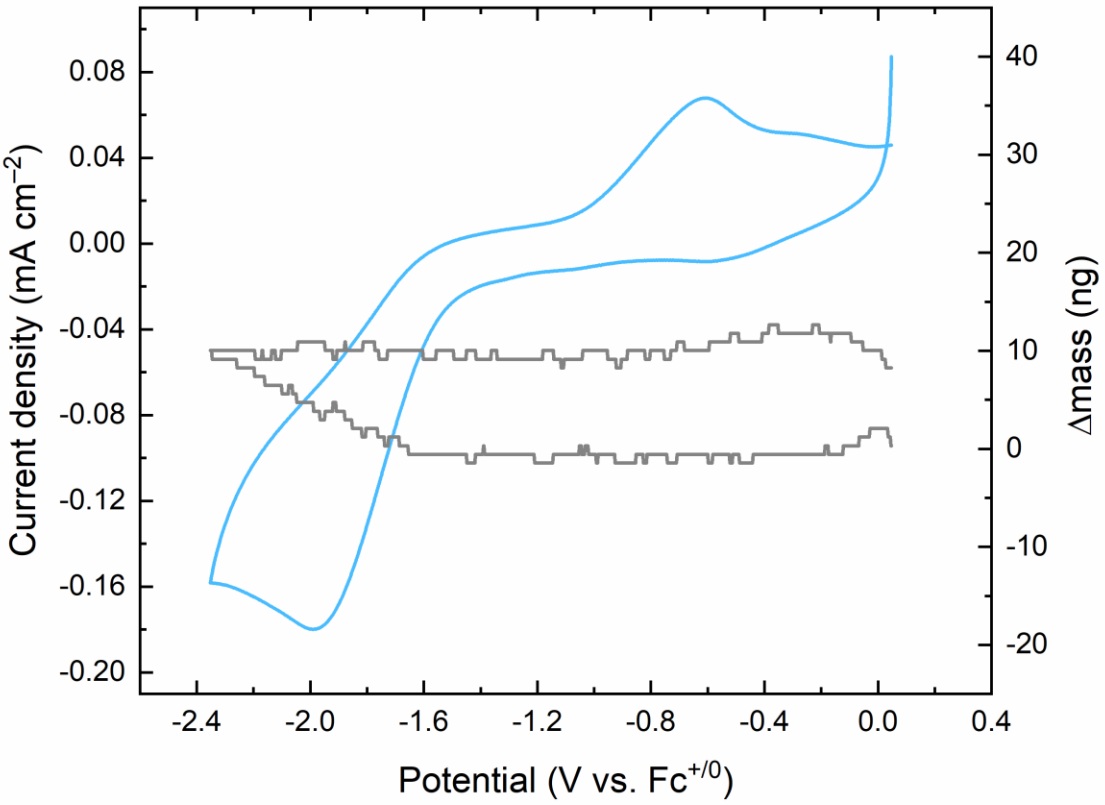

Figure E22. EQCM data of **2**. EQCM experiments with voltammetry (blue) and mass data (gray) for a solution containing **2**. Conditions: 1.5 mM **2** 0.1 M $TBAPF_6$, Au EQCM disk working electrode, Pt counter electrode, $Ag^{+/0}$ reference electrode. Scan rate: 100 mV/s

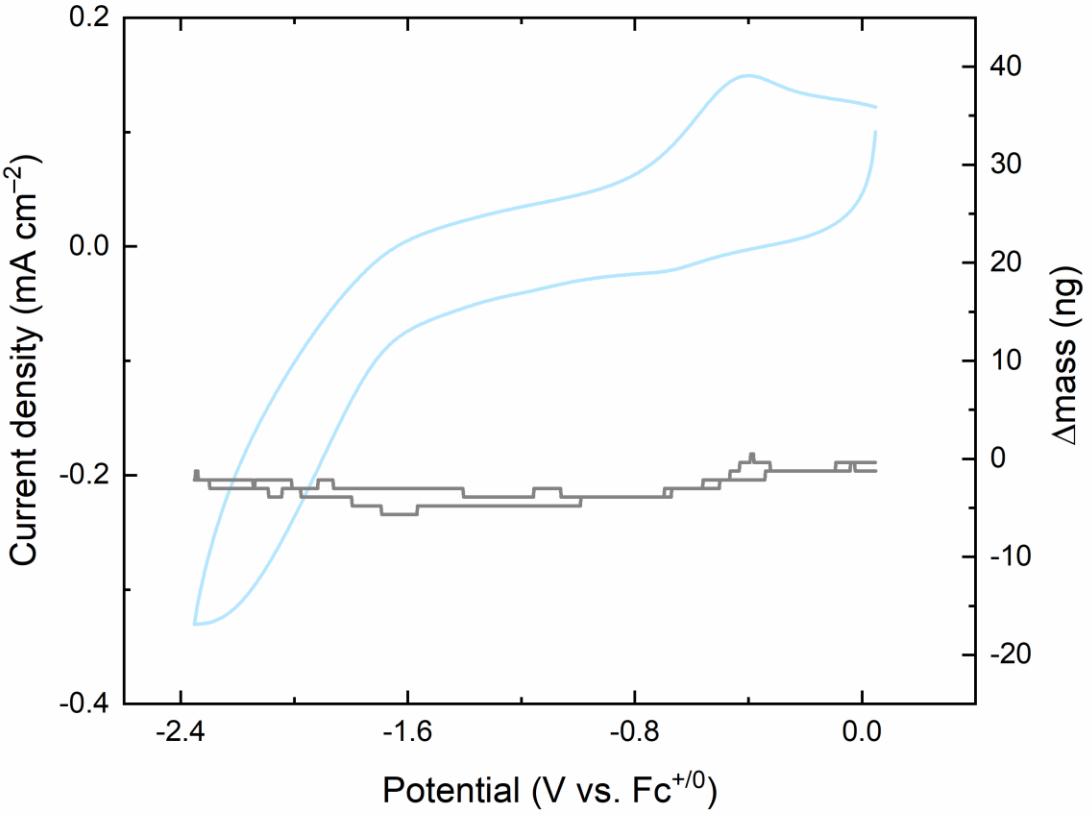

Figure E23. EQCM data of **2**. EQCM experiments with voltammetry (blue) and mass data (gray) for a solution containing **2**. Conditions: 1.5 mM **2** 0.1 M $TBAPF_6$, Au EQCM disk working electrode, Pt counter electrode, $Ag^{+/0}$ reference electrode. Scan rate: 20 mV/s

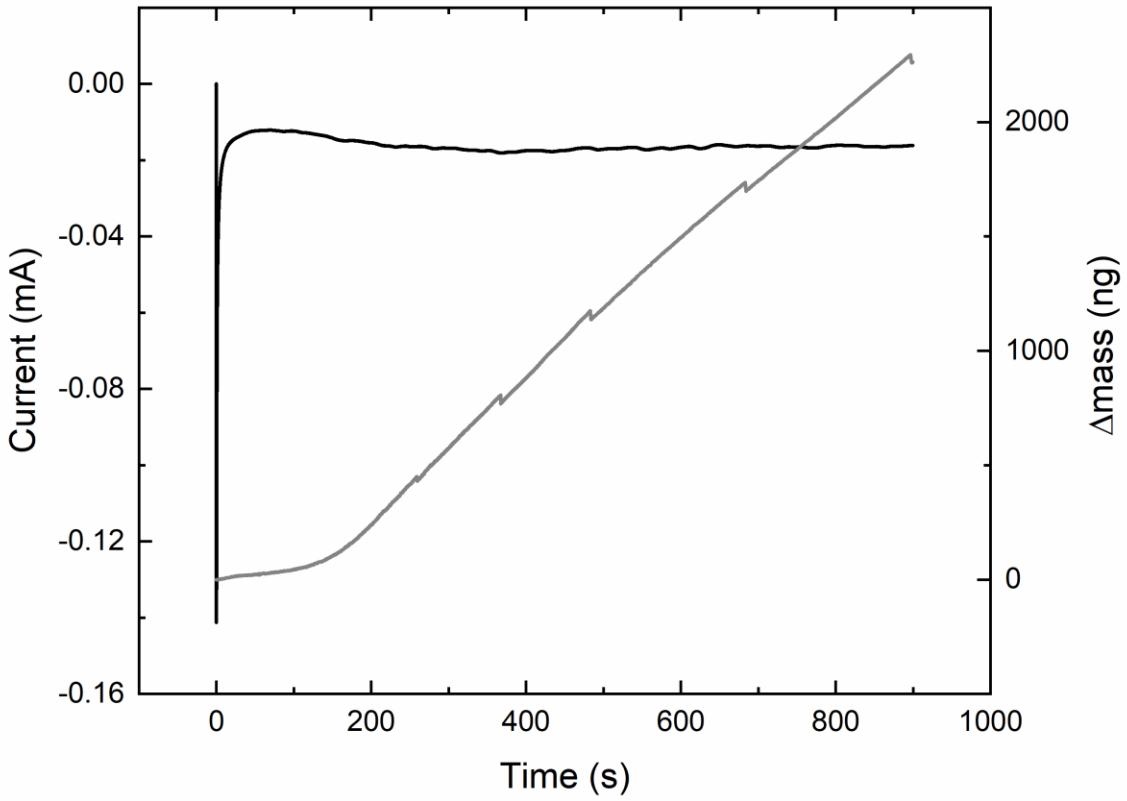

Figure E24. EQCM data of **2**. EQCM bulk electrolysis polarized –1.75 V vs. $Fc^{+/0}$ at experiments with voltammetry (black) and mass data (gray) for a solution containing **2**. Conditions: 1.5 mM Cr 0.1 M $TBAPF_6$, Au EQCM disk working electrode, Pt counter electrode, $Ag^{+/0}$ reference electrode.

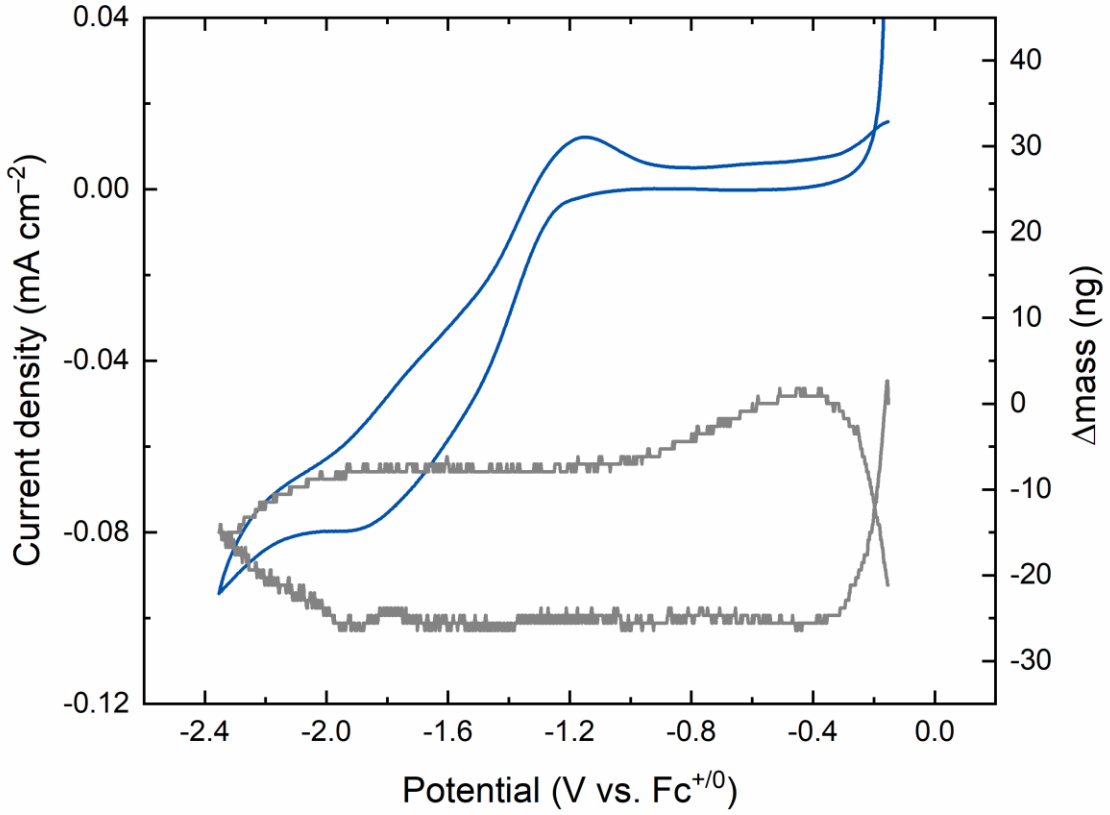

Figure E25. EQCM data of **3**. EQCM experiments with voltammetry (blue) and mass data (gray) for a solution containing **3**. Conditions: 1.5 mM **3** 0.1 M $TBAPF_6$, Au EQCM disk working electrode, Pt counter electrode, $Ag^{+/0}$ reference electrode. Scan rate: 20 mV/s

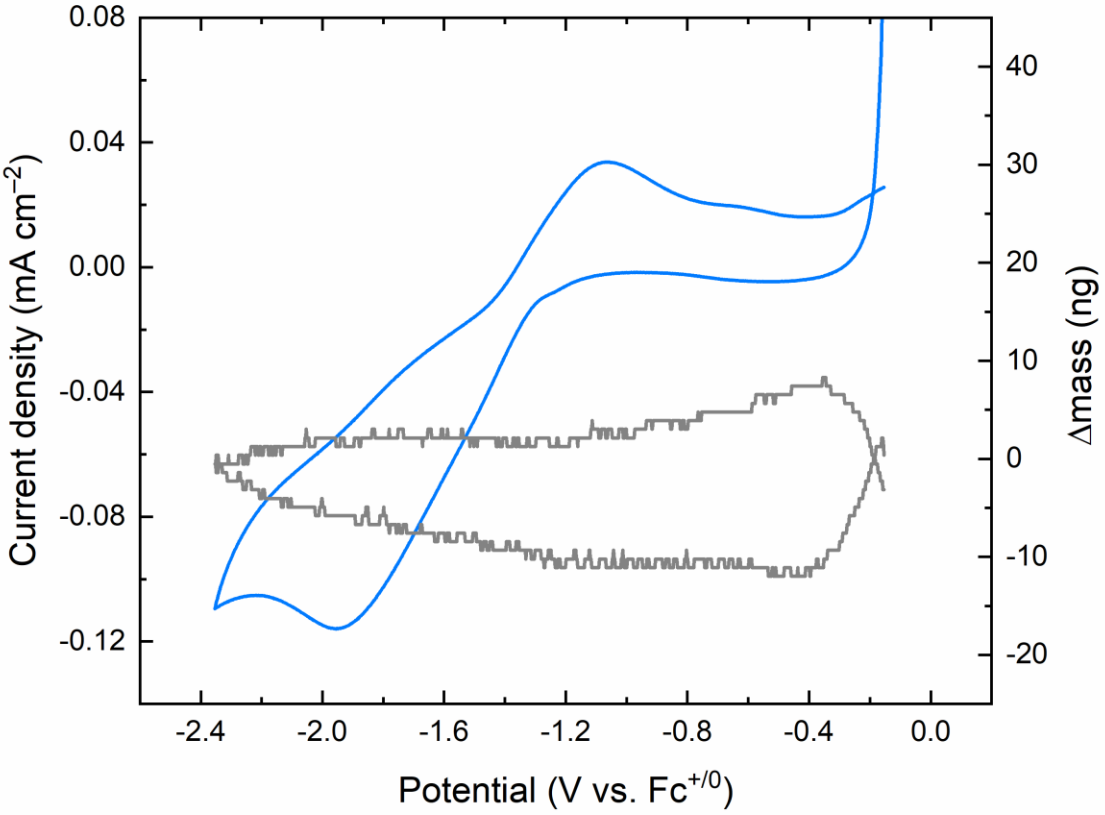

Figure E26. EQCM data of **3**. EQCM experiments with voltammetry (blue) and mass data (gray) for a solution containing **3**. Conditions: 1.5 mM **3** 0.1 M $TBAPF_6$, Au EQCM disk working electrode, Pt counter electrode, $Ag^{+/0}$ reference electrode. Scan rate: 50 mV/s

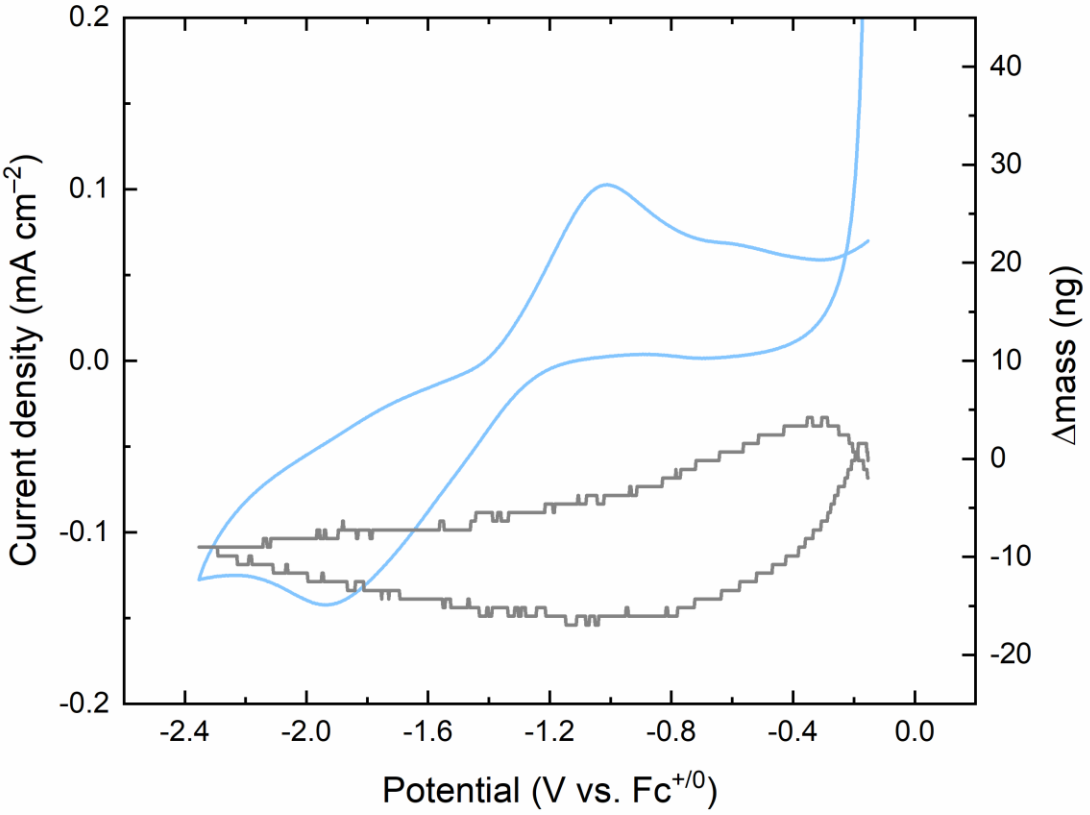

Figure E27. EQCM data of **3**. EQCM experiments with voltammetry (blue) and mass data (gray) for a solution containing **3**. Conditions: 1.5 mM **3** 0.1 M $TBAPF_6$, Au EQCM disk working electrode, Pt counter electrode, $Ag^{+/0}$ reference electrode. Scan rate: 100 mV/s

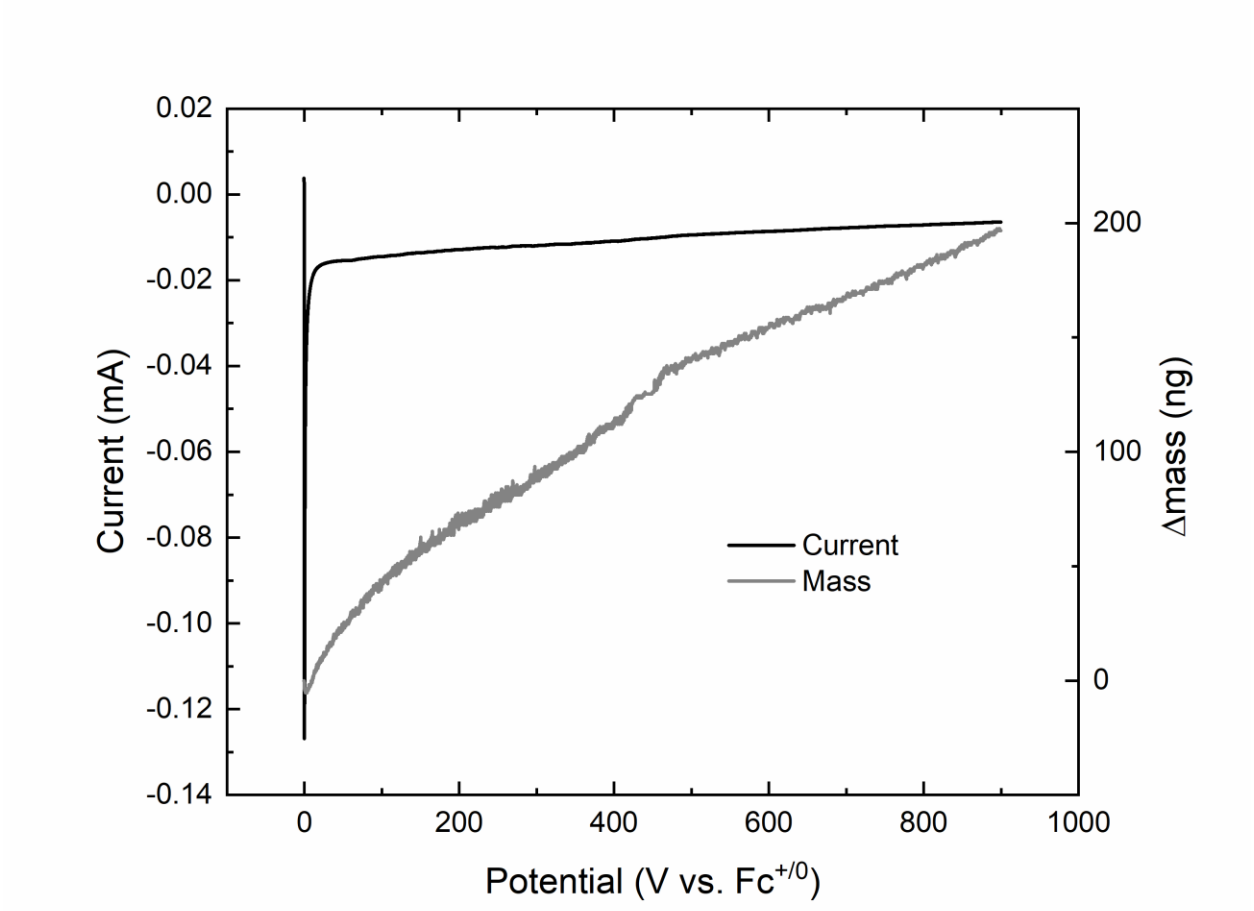

Figure E28. EQCM data of **3**. EQCM bulk electrolysis polarized –1.75 V vs. $Fc^{+/0}$ at experiments with voltammetry (black) and mass data (gray) for a solution containing **3**. Conditions: 1.5 mM Cr 0.1 M $TBAPF_6$, Au EQCM disk working electrode, Pt counter electrode, $Ag^{+/0}$ reference electrode.

Equation E1. The Sauerbrey equation.[1]
$\Delta f = -2f_o^2 \Delta m / A(\mu_q \rho_q)^{1/2}$

f_o = Resonant frequency (Hz)
Δm = Mass change (g)
A = Piezoelectrically active area (cm^2)
μ_q = Shear Modulus of quartz (2.947×10^{11} g cm^{-1} s^{-2})
ρ_q = Density of quartz (2.648 g/cm^3)

X-ray Photoelectron (XP) Spectra

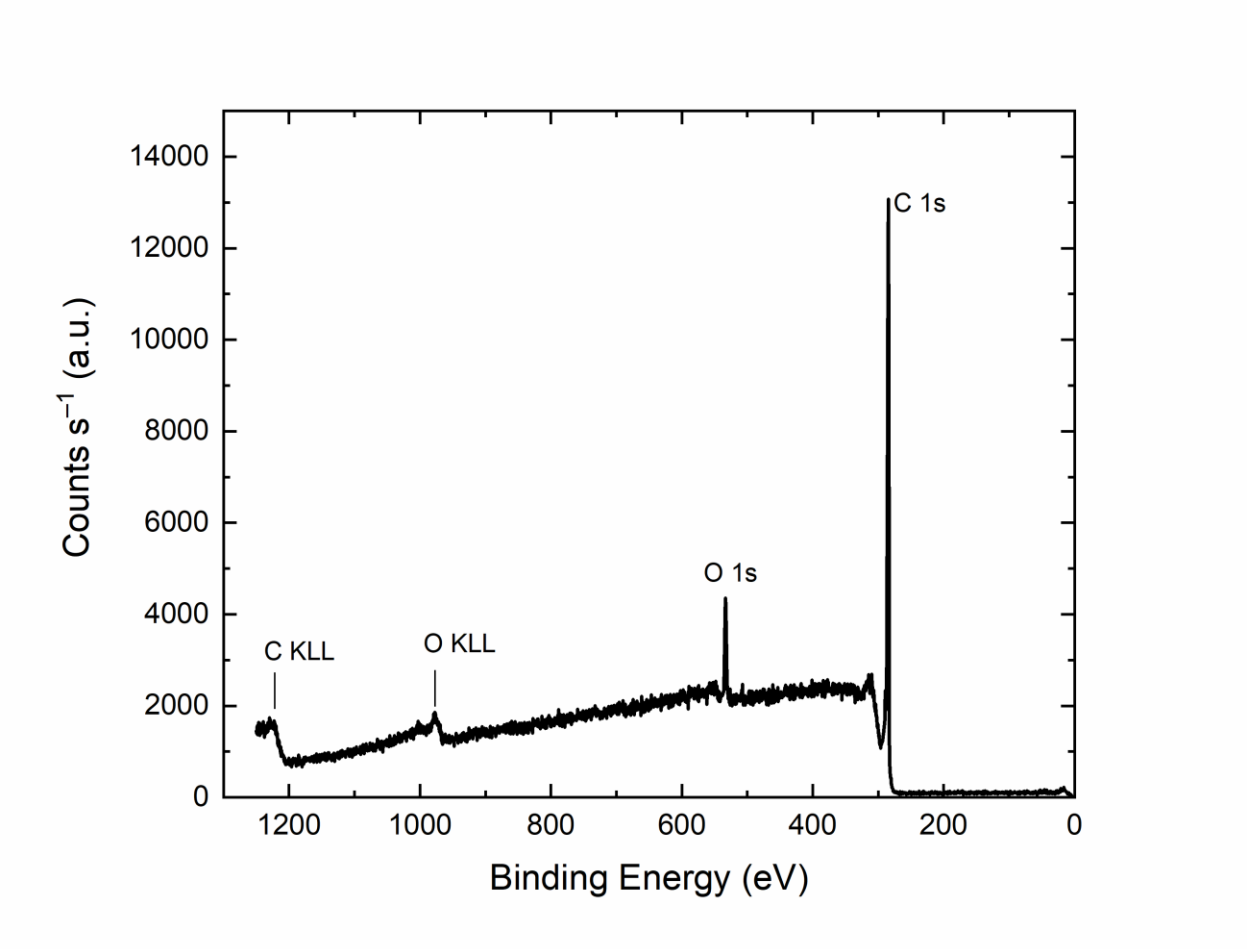

Figure E29. Survey XP spectrum of bare HOPG electrode. Survey X-ray photoelectron spectrum for a blank electrode, showing signals only for carbon (C 1s) and adventitious oxygen (O 1s, O KLL) present as a result of either trace water during handling in ambient conditions or partial oxidation of the electrode material

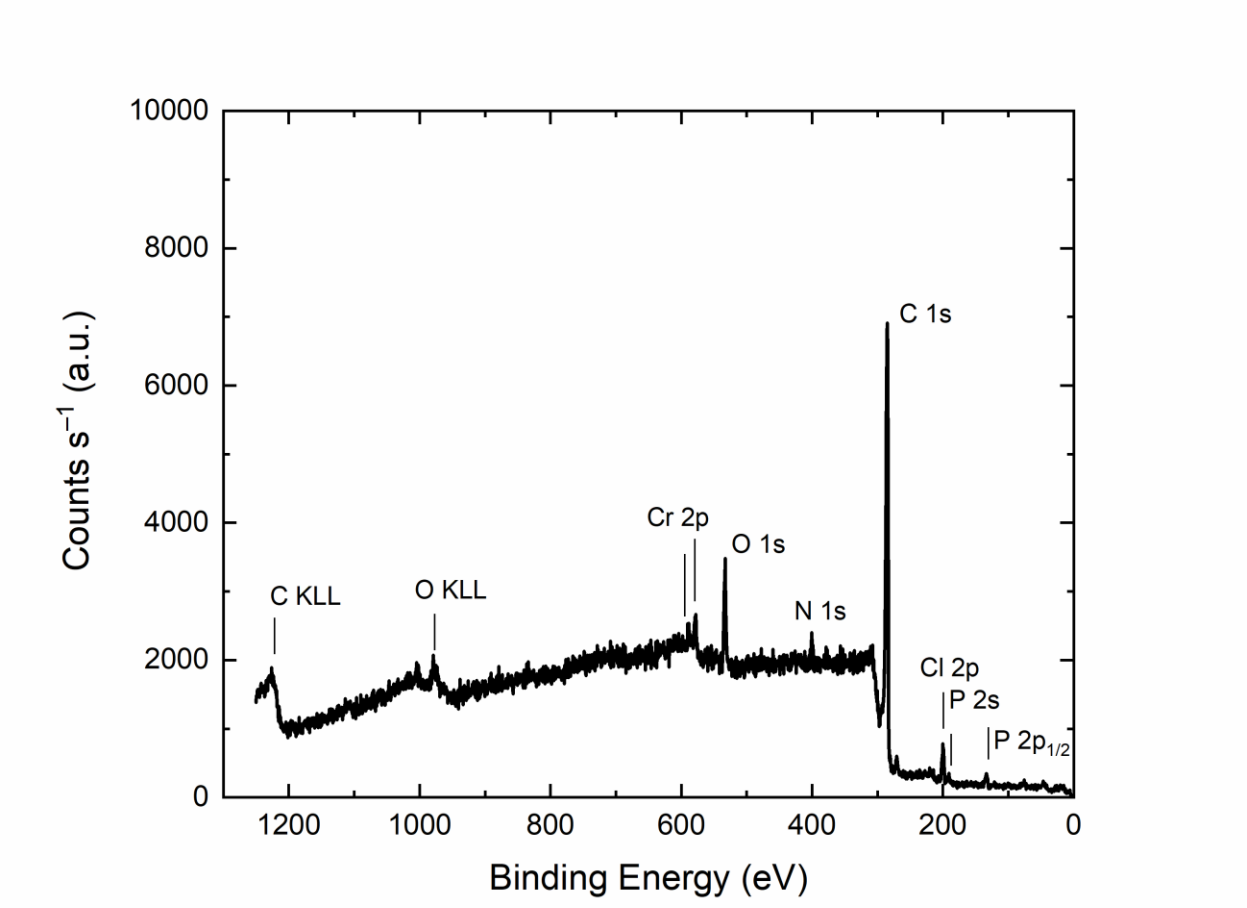

Figure E30. Survey XP spectrum of Drop Cast **2** HOPG electrode. Survey X-ray photoelectron spectrum for drop cast **2** on a blank electrode, showing signals only for carbon (C 1s) and adventitious oxygen (O 1s, O KLL) present as a result of either trace water during handling in ambient conditions or partial oxidation of the electrode material. Signals for chromium (Cr 2p), chlorine (Cl 2p), and phosphorus (P 2s and P 2p) that correspond to products related to complex **2** are clearly observable.

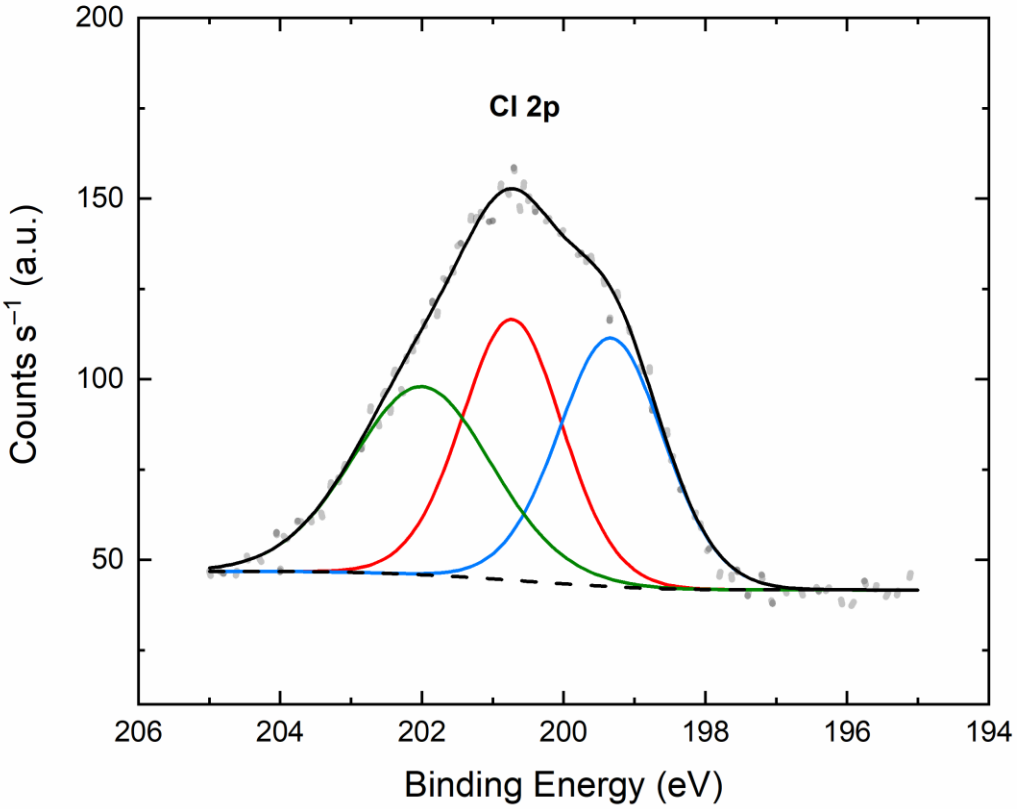

Figure E31. High resolution spectrum of Cl 2p Drop Cast **2** HOPG electrode. X-ray photoelectron spectrum in the Cl 2p region for drop cast **2**. Cl 2p peaks are labelled. Legend: gray dots: data; dashed black line: fitting background; blue line: Cl 2p peak fit; red line: Cl 2p peak fit; green line: Cl 2p peak fit (constrained to 1:1:1 area with respect to each fit); continuous black line: overall fit.

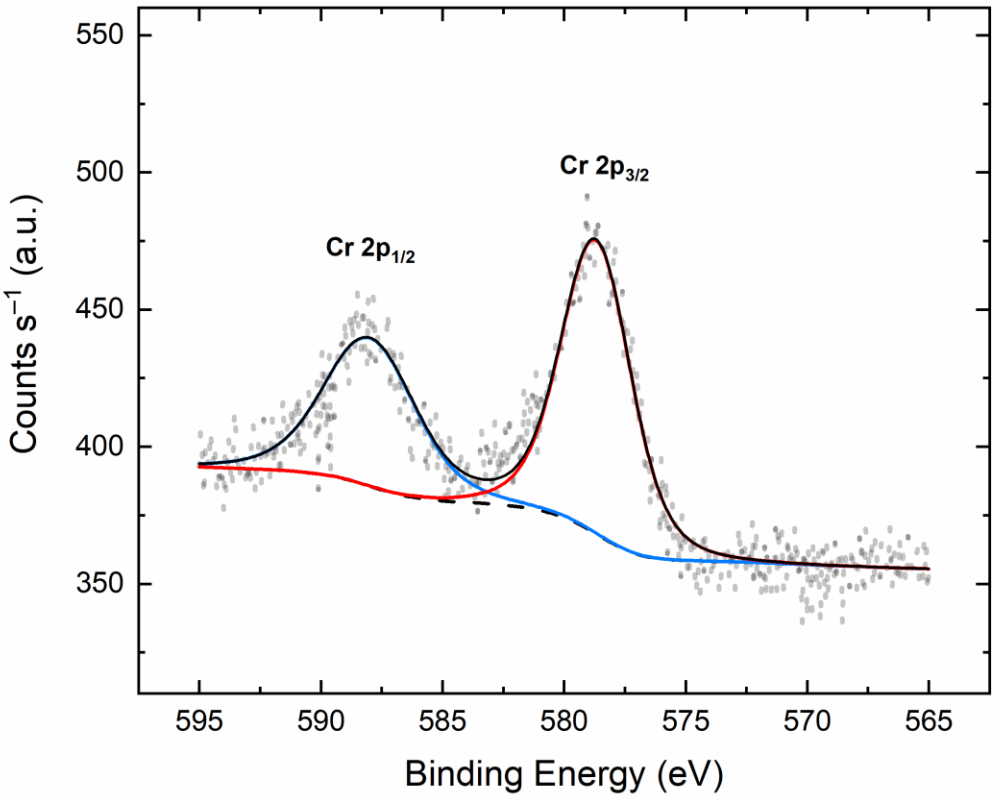

Figure E32. High resolution spectrum of Cr 2p Drop Cast **2** HOPG electrode. X-ray photoelectron spectrum in the Cr 2p regions for drop cast **2**. Cr $2p_{3/2}$ and $2p_{1/2}$ peaks are labelled. Legend: gray dots: data; dashed black line: fitting background; blue line: Cr $2p_{1/2}$ peak fit; red line: Cr $2p_{3/2}$ peak fit (constrained to 2/3 area with respect to Cr $2p_{3/2}$); continuous black line: overall fit.

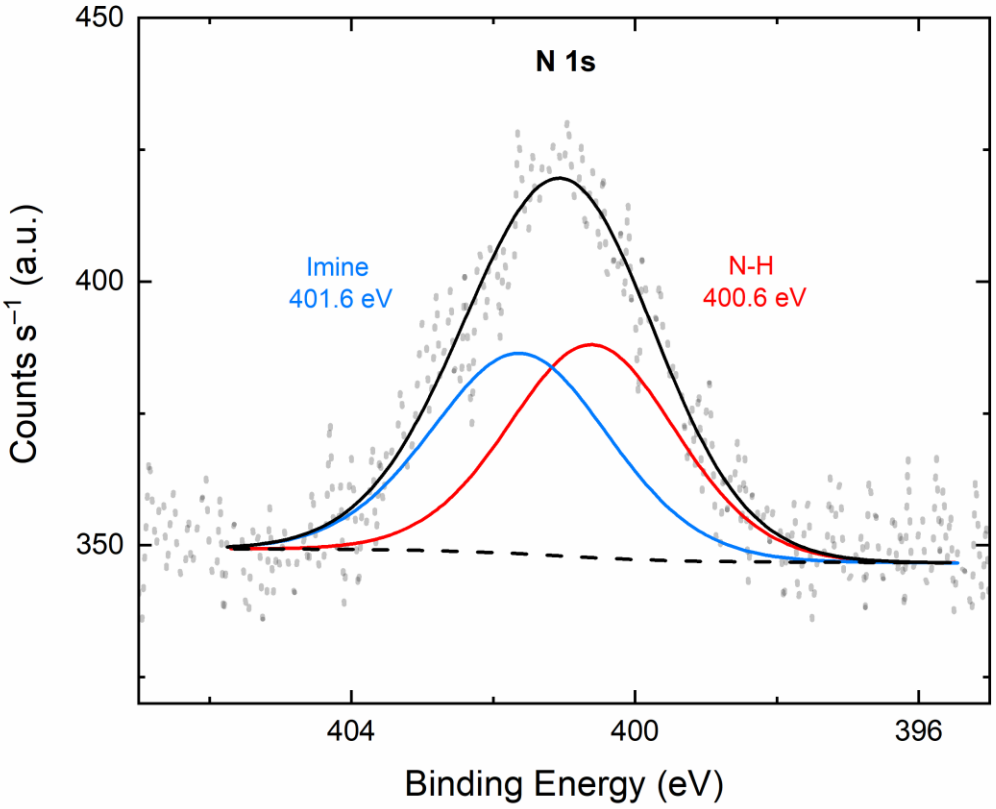

Figure E33. High resolution spectrum of N 1s region Drop Cast **2** HOPG electrode. X-ray photoelectron spectrum in the N 1s region for drop cast **2**. N 1s peaks are labelled. Legend: gray dots: data; dashed black line: fitting background; blue line: N 1s peak fit assigned to imine nitrogen; red line: N 1s peak fit assigned to amine nitrogen (constrained to 1:1 area with respect to each fit); continuous black line: overall fit.

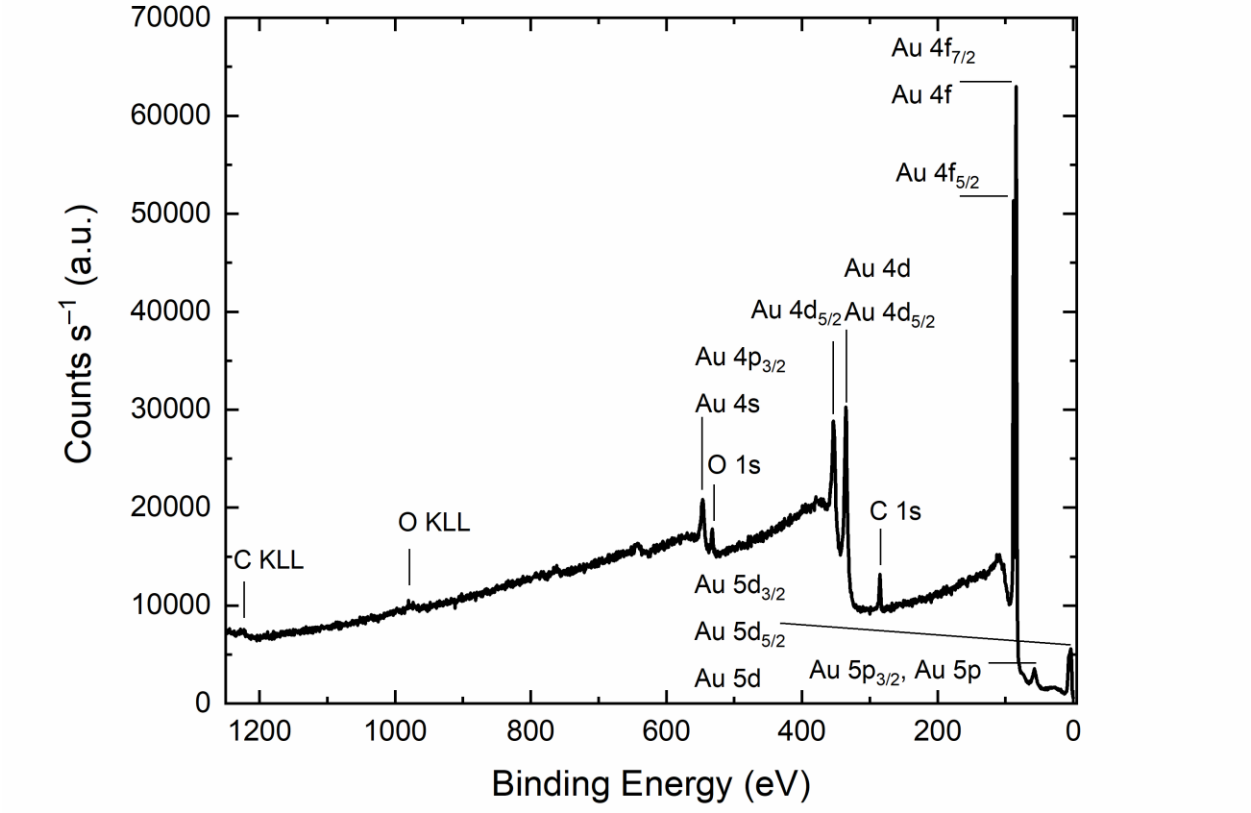

Figure E34. Survey XP spectrum of Blank Au electrode. Survey X-ray photoelectron spectrum for a blank electrode, showing signals only for gold (Au 4s, Au 4p, Au 4d and Au 4f) carbon (C 1s) and adventitious oxygen (O 1s, O KLL) present as a result of either trace water during handling in ambient conditions or partial oxidation of the electrode material.

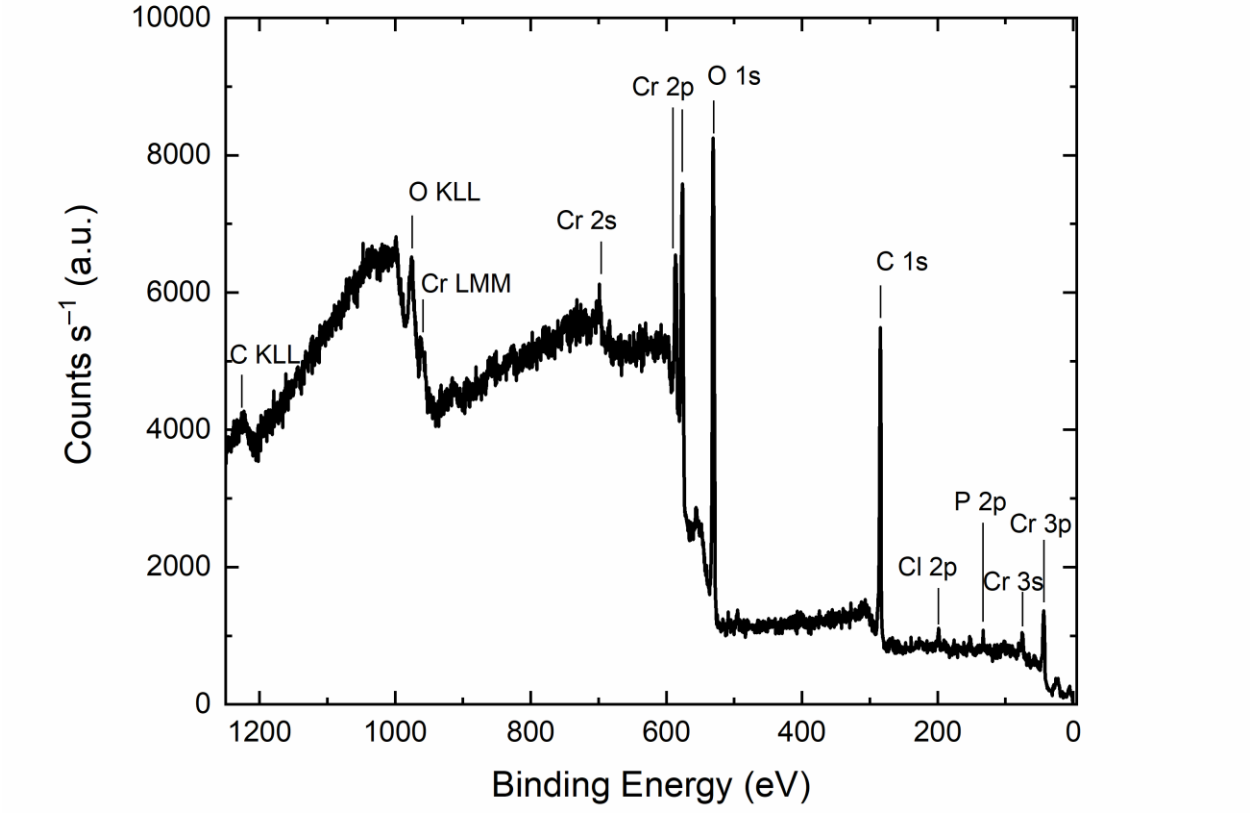

Figure E35. Survey XP spectrum of Electrolysis **2** Au electrode. Survey X-ray photoelectron spectrum for a blank electrode, showing signals only for gold (Au 4s, Au 4p, Au 4d and Au 4f) carbon (C 1s) and adventitious oxygen (O 1s, O KLL) present as a result of either trace water during handling in ambient conditions or partial oxidation of the electrode material. Signals for chromium (Cr 2p), chlorine (Cl 2p), and phosphorus (P 2s and P 2p) that correspond to products related to complex **2** are clearly observable.

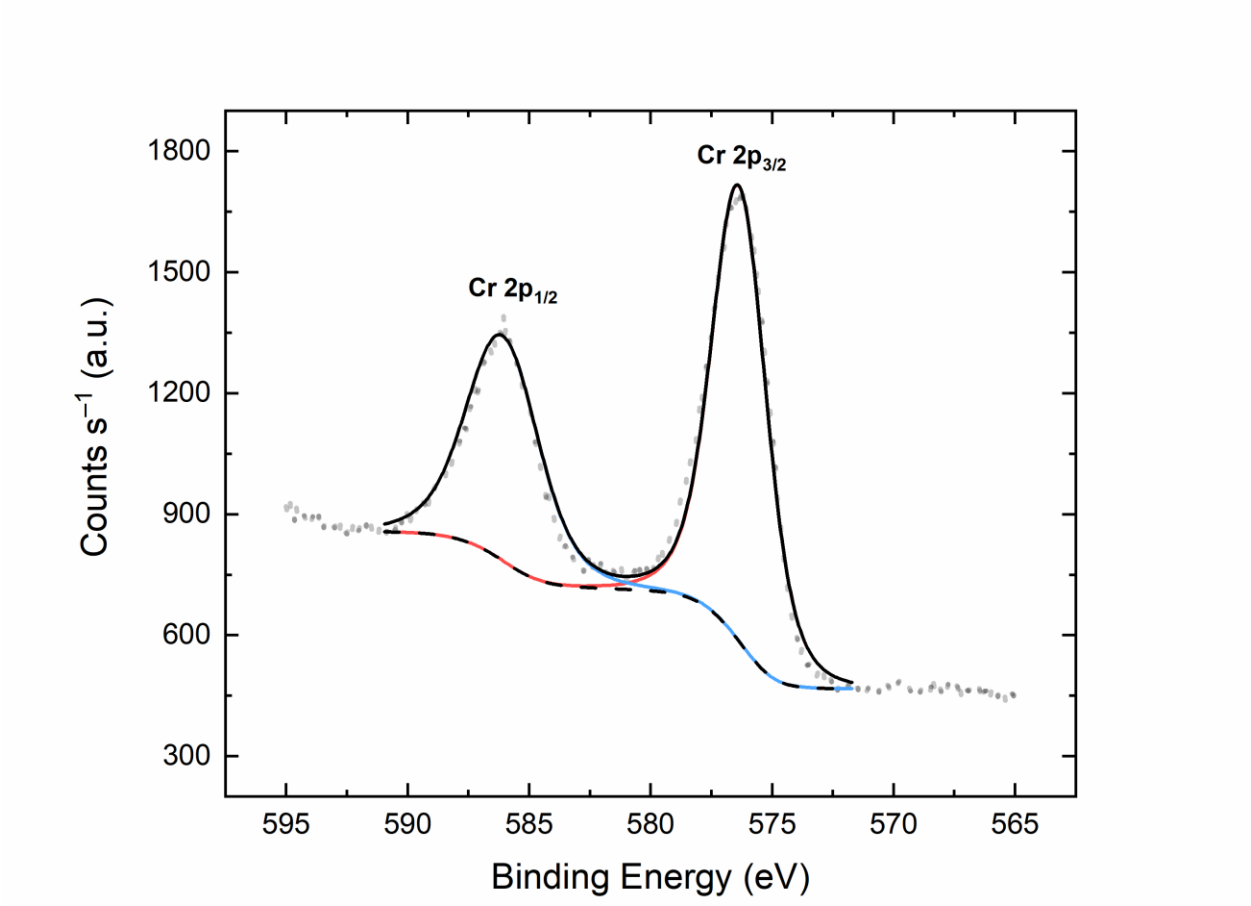

Figure E36. High resolution spectrum of Cr 2p region Electrolysis **2** Au electrode. X-ray photoelectron spectrum in the Cr 2p regions for electrolyzed **2**. Cr $2p_{3/2}$ and $2p_{1/2}$ peaks are labelled. Legend: gray dots: data; dashed black line: fitting background; blue line: Cr $2p_{1/2}$ peak fit; red line: Cr $2p_{3/2}$ peak fit (constrained to 2/3 area with respect to Cr $2p_{3/2}$); continuous black line: overall fit.

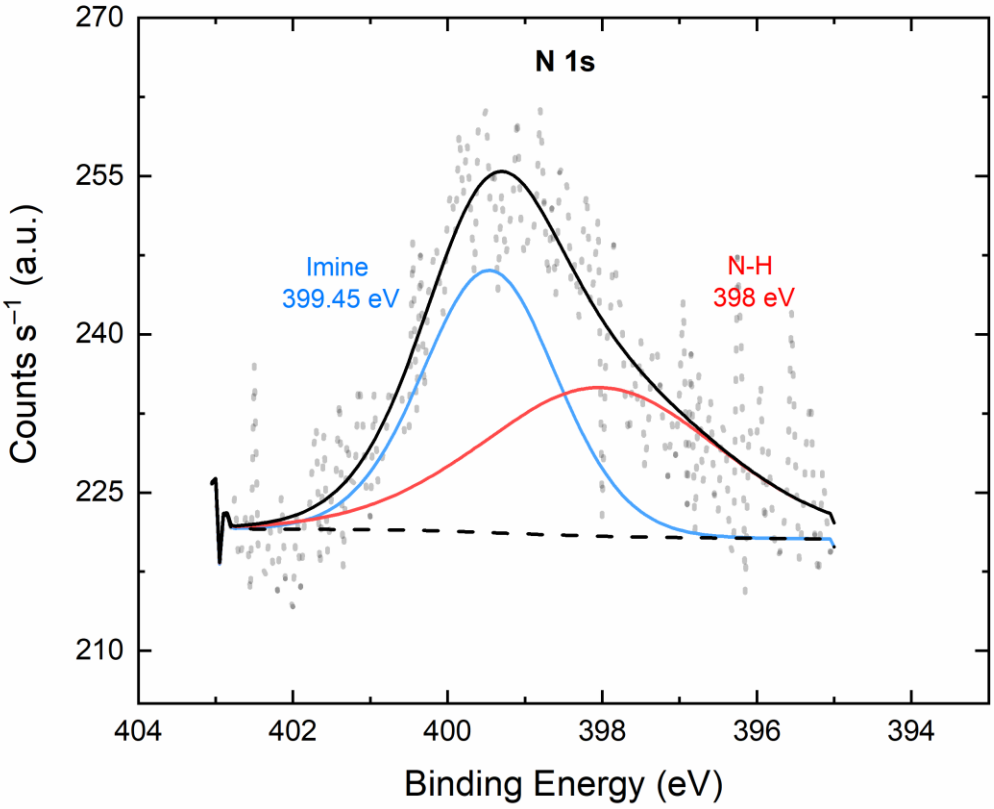

Figure E37. High resolution spectrum of N 1s region Electrolysis **2** Au electrode. X-ray photoelectron spectrum in the N 1s region for electrolyzed **2**. N 1s peaks are labelled. Legend: gray dots: data; dashed black line: fitting background; blue line: N 1s peak fit assigned to imine nitrogen; red line: N 1s peak fit assigned to amine nitrogen (constrained to 1:1 area with respect to each fit); continuous black line: overall fit.

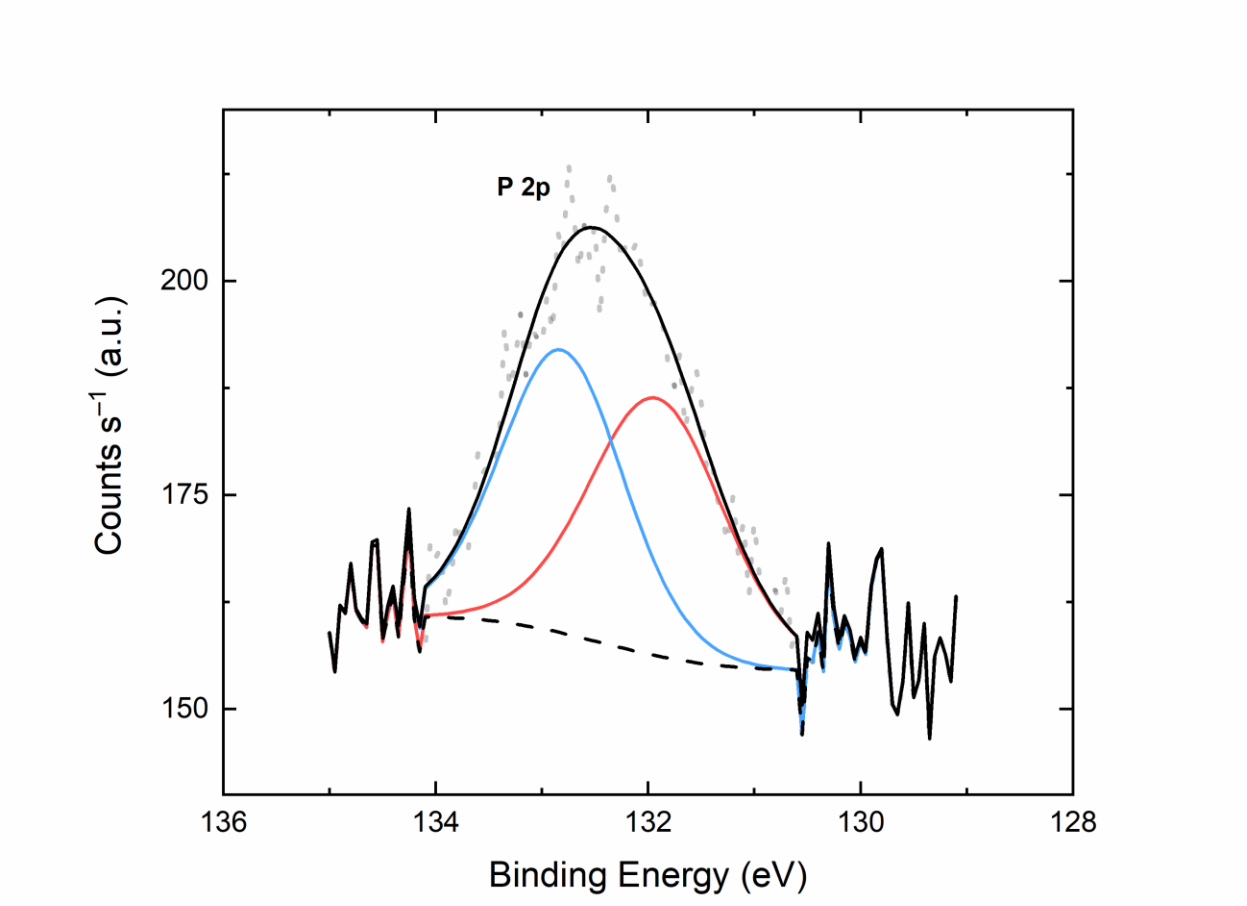

Figure E38. High resolution spectrum of P 2s region Electrolysis **2** Au electrode. X-ray photoelectron spectrum in the P 2p region for electrolyzed **2**. P 2p peaks are labelled. Legend: gray dots: data; dashed black line: fitting background; blue line: P 2p peak fit; red line: N 2p peak fit (constrained to 1:1 area with respect to each fit); continuous black line: overall fit.

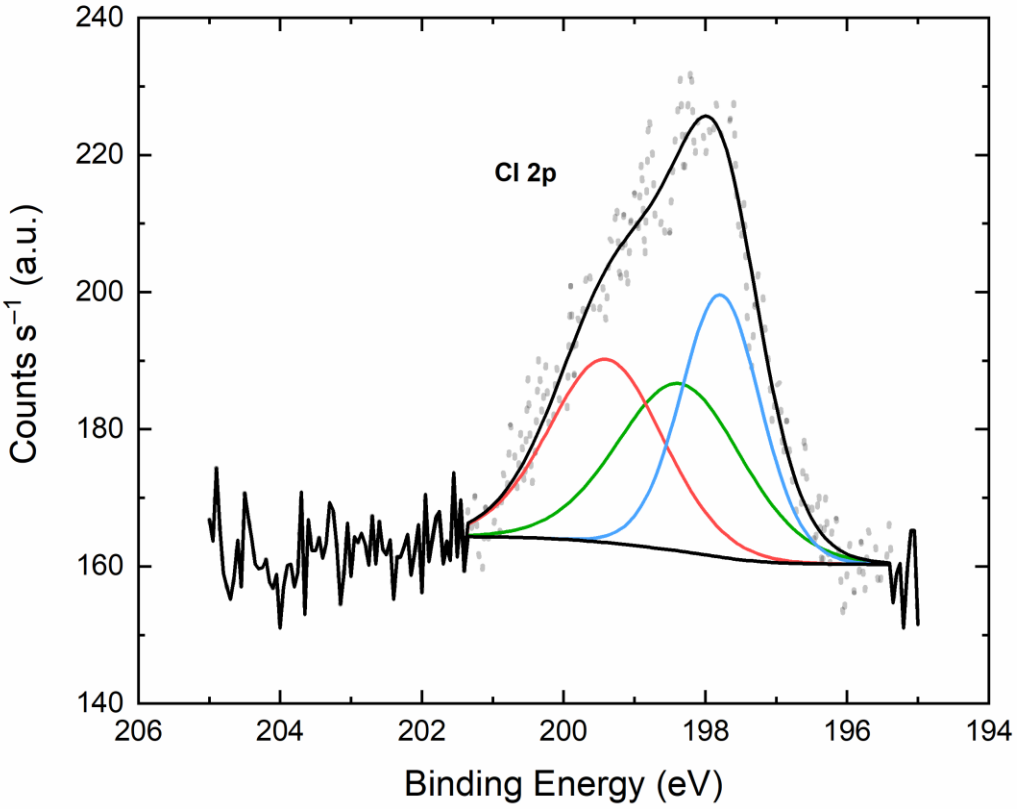

Figure E39. High resolution spectrum of Cl 2p region Electrolysis **2** Au electrode. X-ray photoelectron spectrum in the Cl 2p region for drop cast **2**. Cl 2p peaks are labelled. Legend: gray dots: data; dashed black line: fitting background; blue line: Cl 2p peak fit; red line: Cl 2p peak fit; green line: Cl 2p peak fit (constrained to 1:1:1 area with respect to each fit); continuous black line: overall fit.

Table E1. Ratios of elements in Drop Cast **2** on HOPG. High resolution data fitted using CasaXPS software.

Drop Cast **2**						
Element	Area	Scofield Sensitivity Factor	Relative Area	Total Relative Area	Ratio Based on Relative Areas	Binding Energies (eV)
Cr $2p_{3/2}$	416.0	7.96	54.10	123.06	1	578.85
Cr $2p_{1/2}$	274.5	3.98	68.97			588.15
N 1s	354.42	1.80	196.9	196.9	1.60	401.6 & 400.6
Cl 2p	590.64	1.69	349.49	349.49	2.84	199.35 to 202

Table E2. Ratios of elements in electrolyzed **2** on an Au quartz disk. High resolution data fitted using CasaXPS software.

Electrolysis of **2**						
Element	Area	Scofield Sensitivity Factor	Relative Area	Total Relative Area	Ratio Based on Relative Areas	Binding Energies (eV)
Cr $2p_{3/2}$	3196.7	7.96	415.69	945.80	14.29	576.5
Cr $2p_{1/2}$	2109.8	3.98	530.10			586.3
N 1s	119.10	1.80	66.17	66.17	1	399.5 & 398.0
Cl 2p	109.64	1.69	64.88	64.88	0.98	197 to 199

EPR Spectra

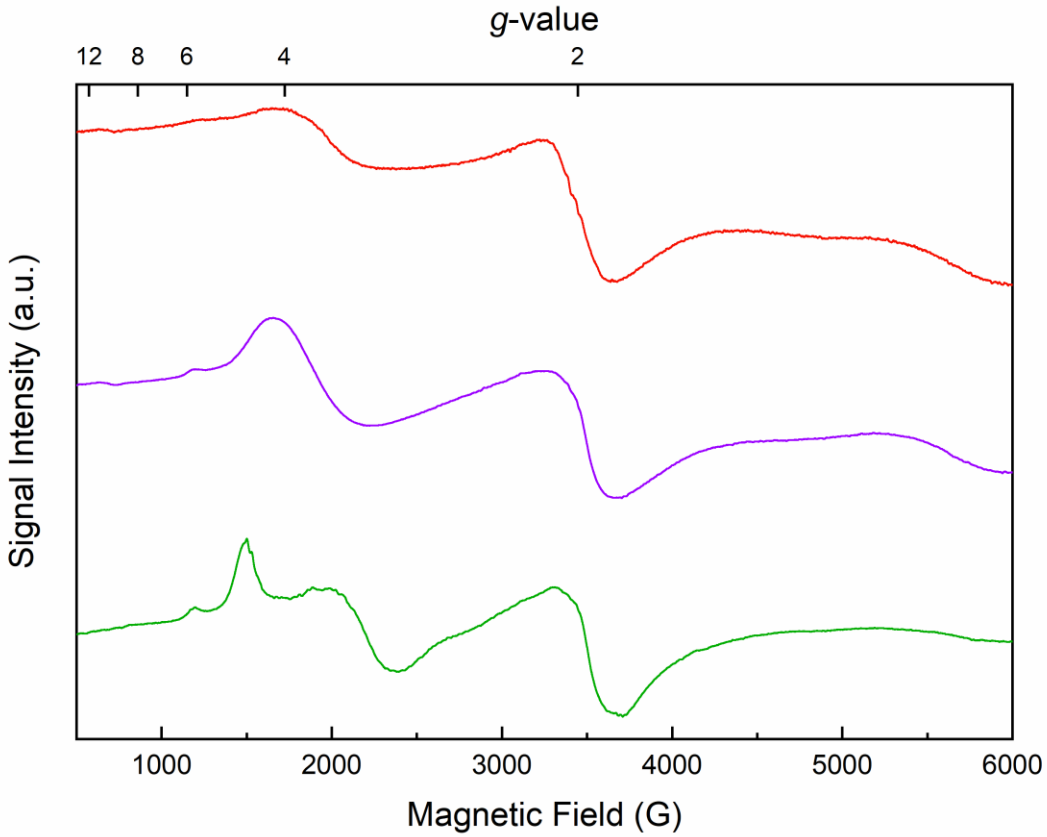

Figure E40. Stacked X-band continuous-wave EPR spectrum of **1** (red), **2** (purple), and **3** (green) in DCM. Conditions: T = 7 K; modulation amplitude = 4.0 G; time constant = 5 ms

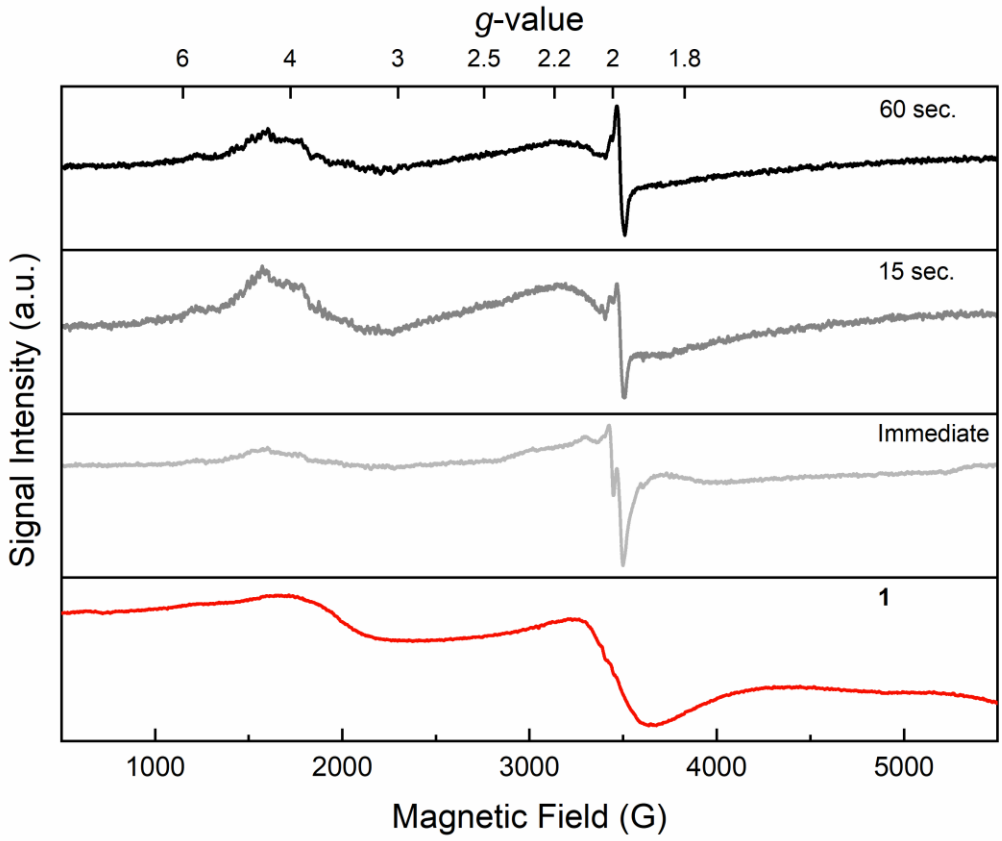

Figure E41. Stacked X-band continuous-wave EPR spectra from layering experiments of **1** plus Cp^*_2Co in THF, allowed to thaw and be mixed at increasing time intervals. Conditions: T = 7 K; modulation amplitude = 4.0 G; time constant = 5 ms

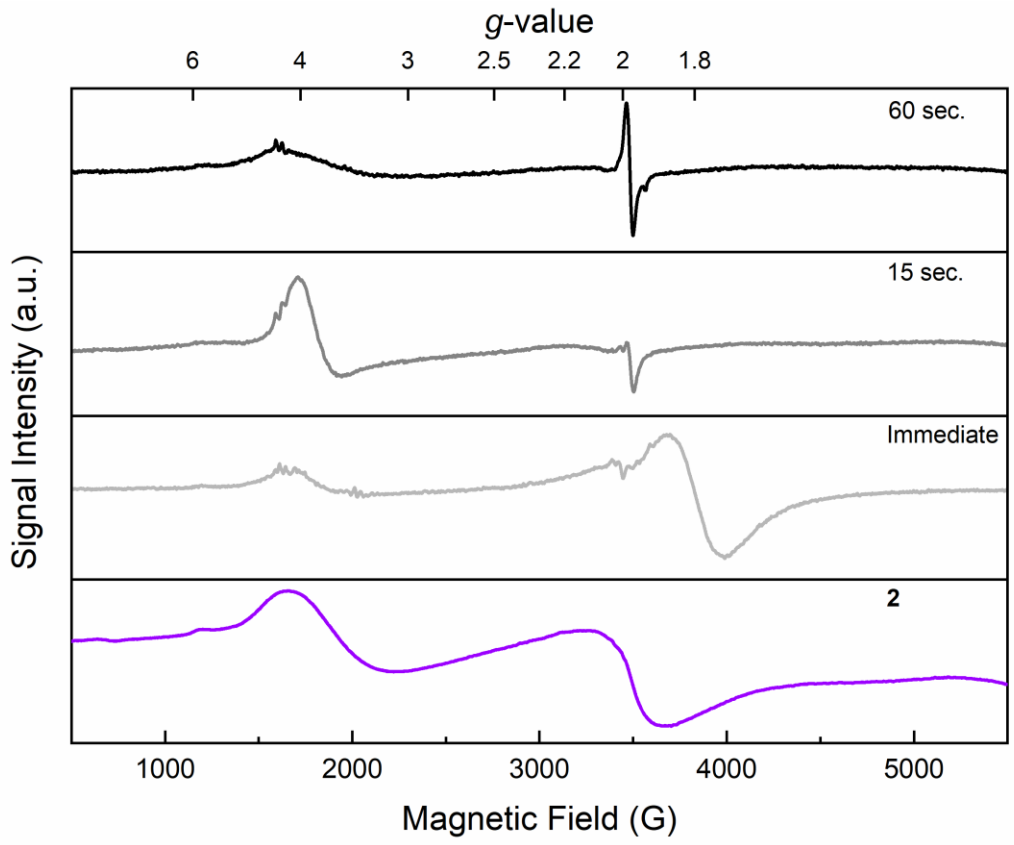

Figure E42. Stacked X-band continuous-wave EPR spectrum layering experiment of **2** plus Cp^*_2Co in THF, allowed to thaw and be mixed at increasing time intervals. Conditions: T = 7 K; modulation amplitude = 4.0 G; time constant = 5 ms

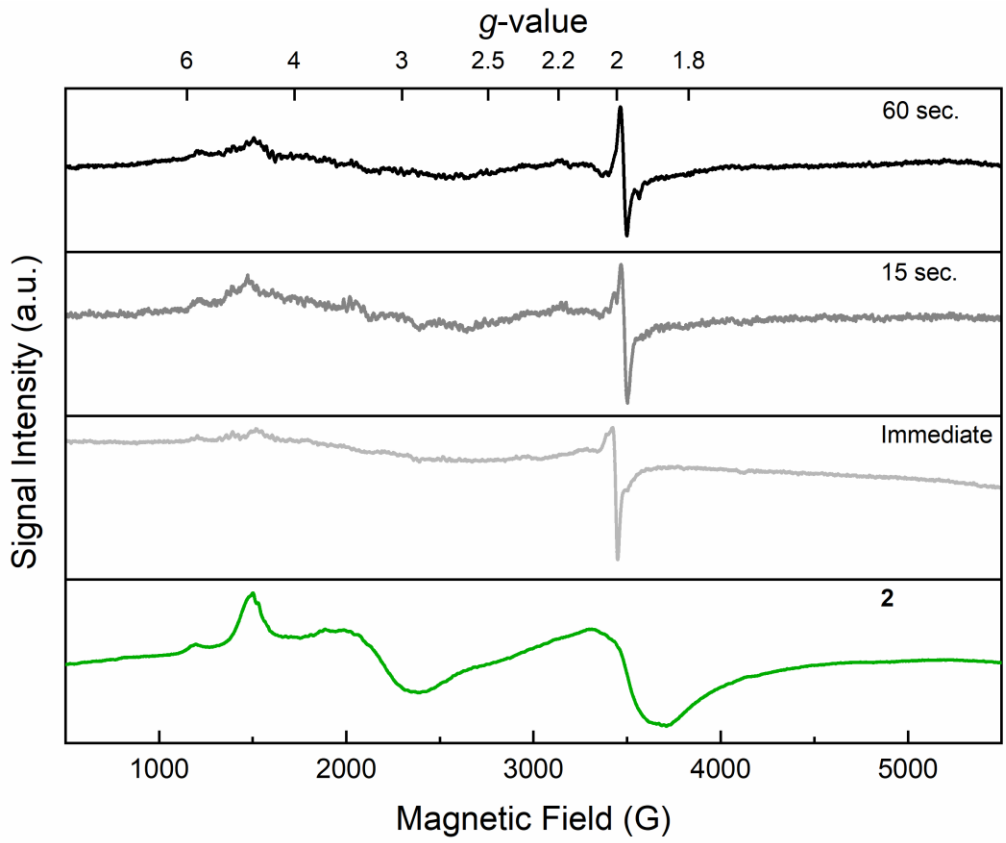

Figure E43. Stacked X-band continuous-wave EPR spectrum layering experiment of **3** plus Cp^*_2Co in THF, allowed to thaw and be mixed at increasing time intervals. Conditions: T = 7 K; modulation amplitude = 4.0 G; time constant = 5 ms

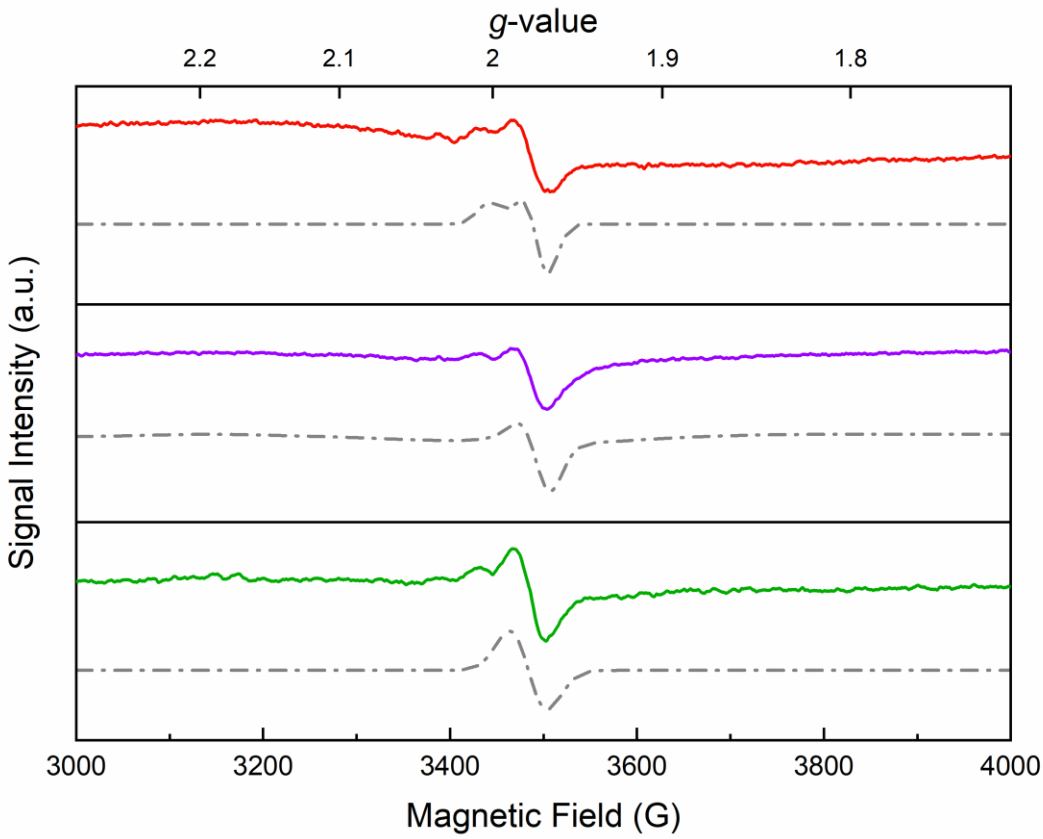

Figure E44. Stacked X-band continuous-wave EPR spectrum layering experiment of **1** (upper panel), **2** (middle panel), and **3** (lower panel) plus Cp^*_2Co in THF, allowed to thaw and be mixed for 15 seconds. Modeled data shown in gray dashed lines below experimental data. Conditions: T = 7 K; modulation amplitude = 4.0 G; time constant = 5 ms. Upper Gray trace: EasySpin simulation of EPR data; simulation parameters for component: S = 1/2, g = [2.3 2.13 2.13], nucleus: Cr, gstrain = [0.01 0.02 0.05], lwpp = 2. Middle Gray trace: EasySpin simulation of EPR data; simulation parameters for component: S = 1/2, g = [1.97 2 2], nucleus: Cr, A = [0 0 0], gStrain = [0.02 0.1], lw = 0. Lower Gray trace: EasySpin simulation of EPR data; simulation parameters for component: S = 1/2, g = [1.98 1.98 1.98], nucleus: Cr, gStrain = [0.01 0.01 0.01], lwpp = 10.

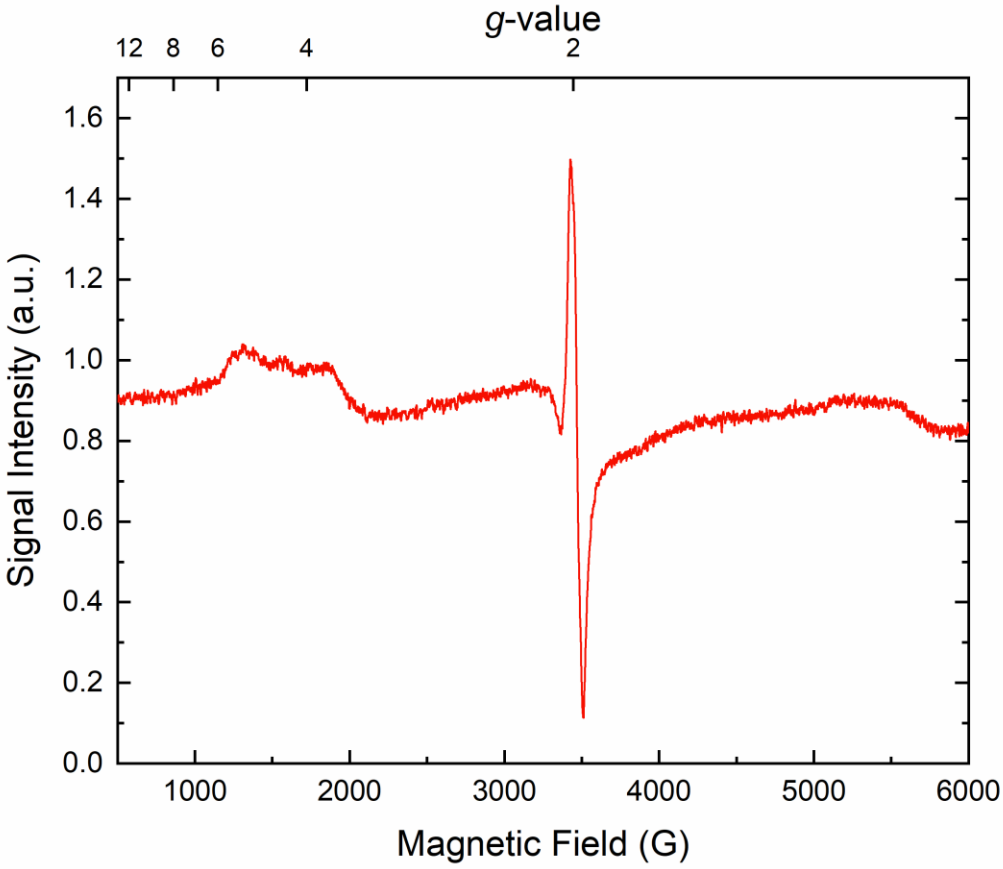

Figure E45. X-band continuous-wave EPR spectrum layering experiment of **1** plus $AlEt_3$ in THF, allowed to thaw and be mixed for 15 seconds and refrozen. Conditions: T = 7 K; modulation amplitude = 4.0 G; time constant = 5 ms.

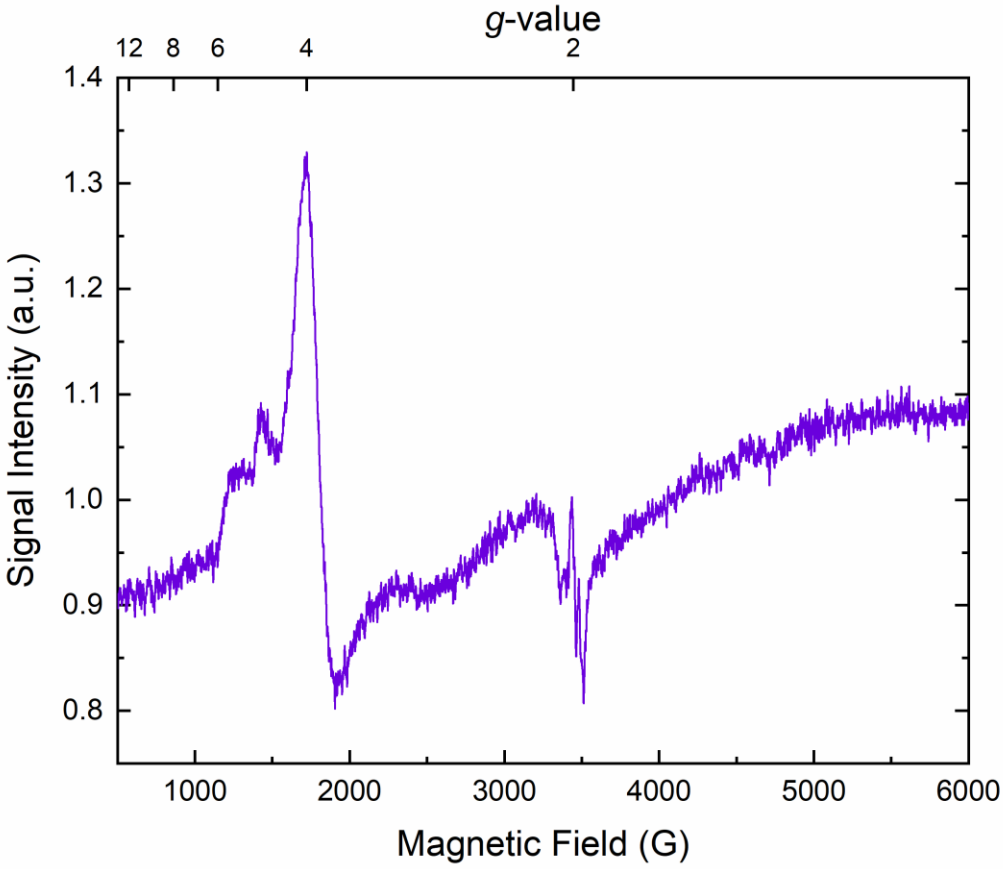

Figure E46. X-band continuous-wave EPR spectrum layering experiment of **2** plus MMAO in DCM, allowed to thaw and be mixed for 15 seconds and refrozen. Conditions: T = 7 K; modulation amplitude = 4.0 G; time constant = 5 ms.

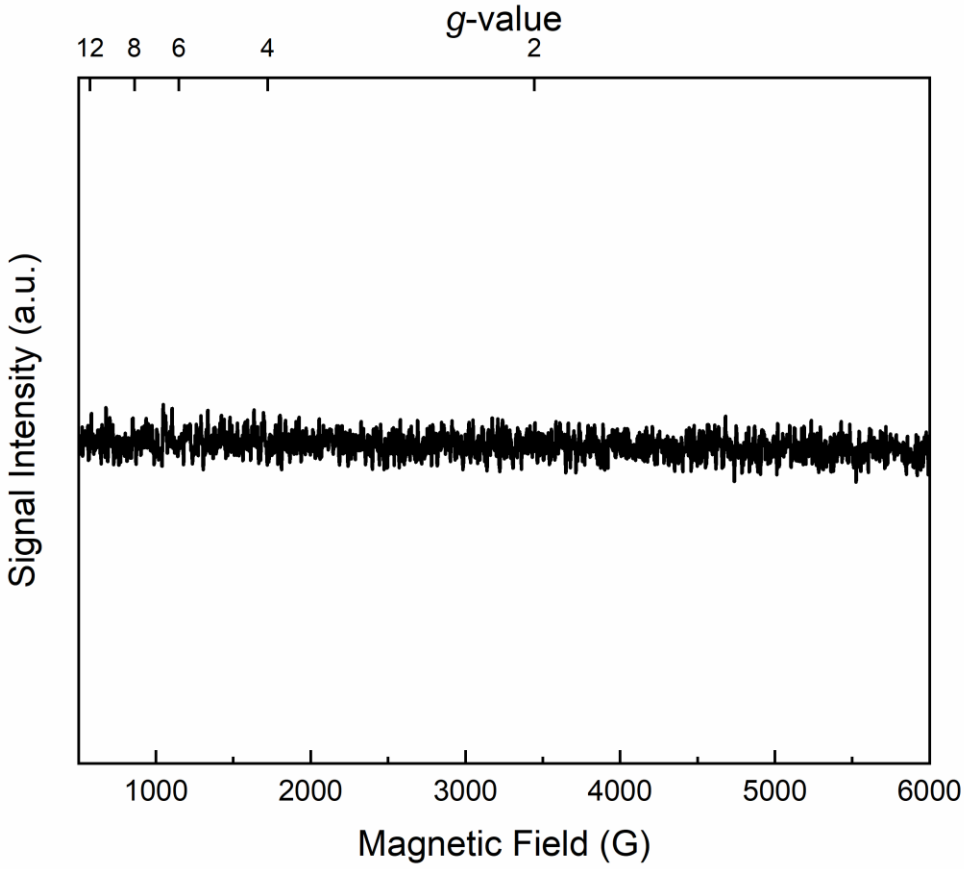

Figure E47. X-band continuous-wave EPR spectrum of **1-R** in MeCN. Conditions: T = 7 K; modulation amplitude = 4.0 G; time constant = 5 ms

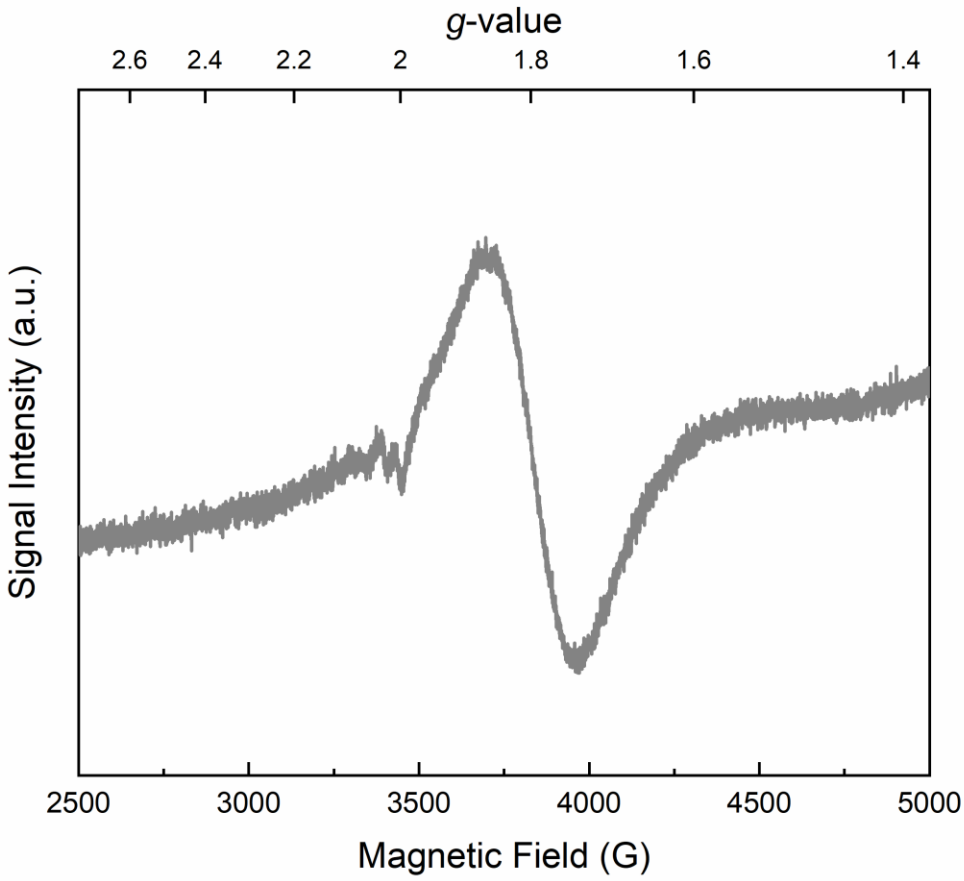

Figure E48. X-band continuous-wave EPR spectrum of Cp^*_2Co [2 mM]. Conditions: T = 7 K; modulation amplitude = 4.0 G; time constant = 5 ms

Quantitative EPR Studies

***QEPR Method and Validation*:**

Serial dilutions were carried out to prepare a series of samples of TEMPOL, $Cu(NO_3)_2$ and $MnCl_2$ at concentrations spanning the range from ca. 10 to 700 μM in 25% glycerol in H_2O. The concentration of the TEMPOL samples were validated using UV-vis of the stock solution (extinction coefficient of TEMPOL in water at 429 nm is 13.4 M^{-1} cm^{-1} from ref. 1), whereas the Cu^{2+} and Mn^{2+} samples were ICP standards (Sigma-Aldrich) and thus considered primary standards. For each sample, 300 μL in steps of 100 μL were pipeted into 4 mm EPR tubes (Wilmad Lab-Glass). These tubes were gently spun on a hand centrifuge to overcome capillary action/surface tension, then flash frozen in a dry ice-acetone bath and stored in liquid nitrogen. Temperature was equilibrated to the given set point. The spectral acquisition parameters were optimized to enable us to record a non-saturated spectrum with an acceptable signal-to-noise ratio for each analyte.

Data was processed using Origin to determine the double integral value. Because this value depends strongly on spectrometer settings, the double integral must be normalized by correcting for the relevant acquisition parameters using Equation E2[2]. The corrected double integral value for all samples in the validation dataset were plotted versus known concentration (Fig. E49). Linear regression was performed. The concentration of a paramagnetic species in a given sample can be determined using equation E3. For futher information on QEPR analysis methods please see *Quantitative EPR* by Eaton, Eaton, Barr and Weber.[2]

$$Corrected\ Double\ Integral = \frac{Double\ Integral}{\sqrt{P \cdot B_m \cdot Q \cdot g_{ave} \cdot n_B \cdot S \cdot (S+1)}}$$

Equation E2. Normalizing the response of the system. P, B_m, Q, g_{ave}, n_B, and S are the microwave power in Watts, the modulation amplitude in gauss, the Quality factor of the cavity plus sample, the average g value[3], the Boltzmann factor and the total electron spin, respectively.

$$C_{unknown} = \left(\frac{C_{Standard}}{Corrected\ Double\ Integral_{Standard}}\right) \cdot\ Corrected\ Double\ Integral_{Unknown}$$

Equation E3. The concentration of a paramagnetic species in a given sample equal the ration of the correction double integral (Equation E2) and the slope for the calibration curve, [2.77 ± 0.06] $x10^{-23}$ (see Figure E49).

Representative X-band continuous-wave EPR spectra, along with the integrated data, of TEMPOL, $Cu(NO_3)_2$ and $MnCl_2$ recorded under non-saturating conditions are shown in Figures E50-E52. Acquisition parameters are summarized in Table E3. The results of the QEPR analysis are summarized in Table E4.

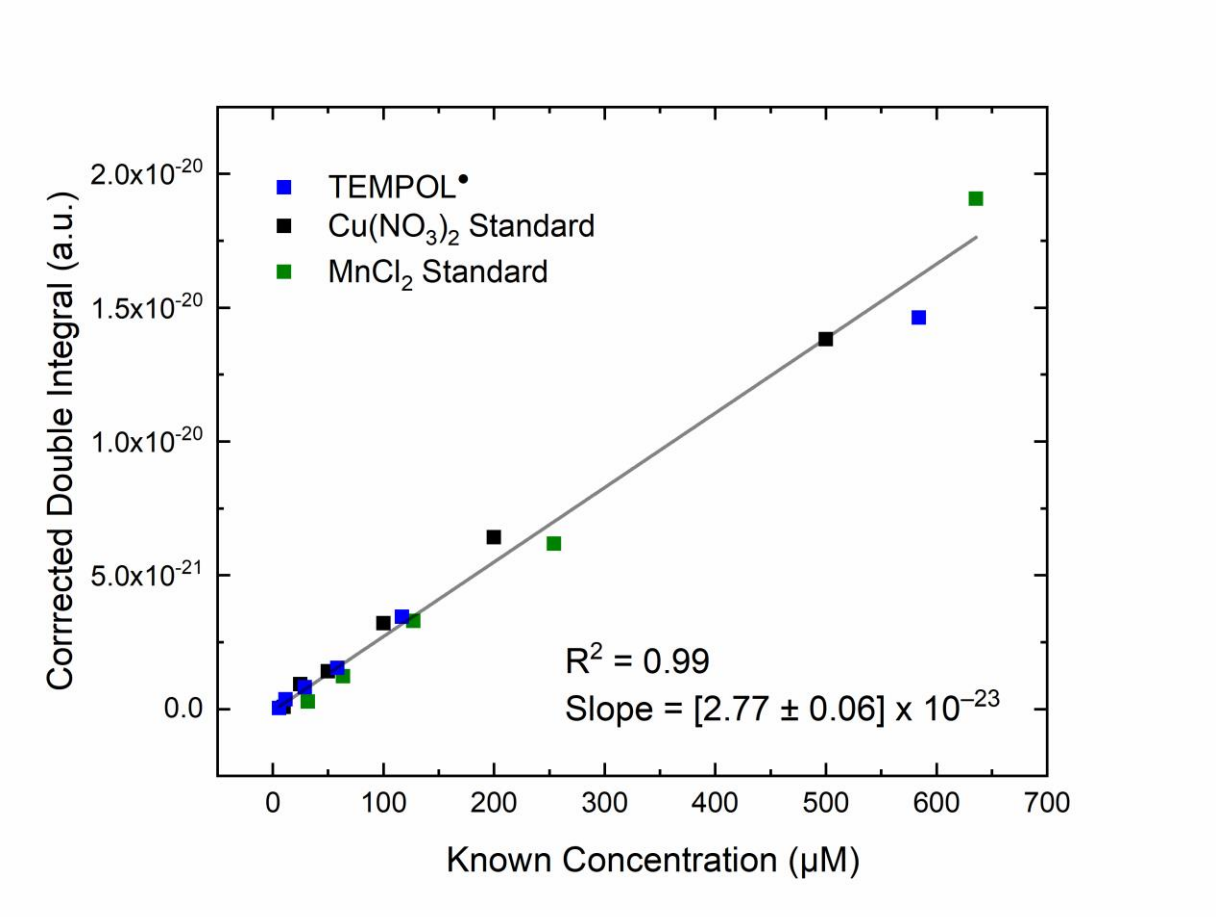

Figure E49. Calibration curve of the Corrected Double Integral of EPR Spectra versus concentration (μM). Multiple concentrations of Tempol, $Cu(NO_3)_2$, and $MnCl_2$ at multiple concentrations from 10 μM, to 635 μM. Slope of this line was used to determine concentrations of unknown Cr^I samples.

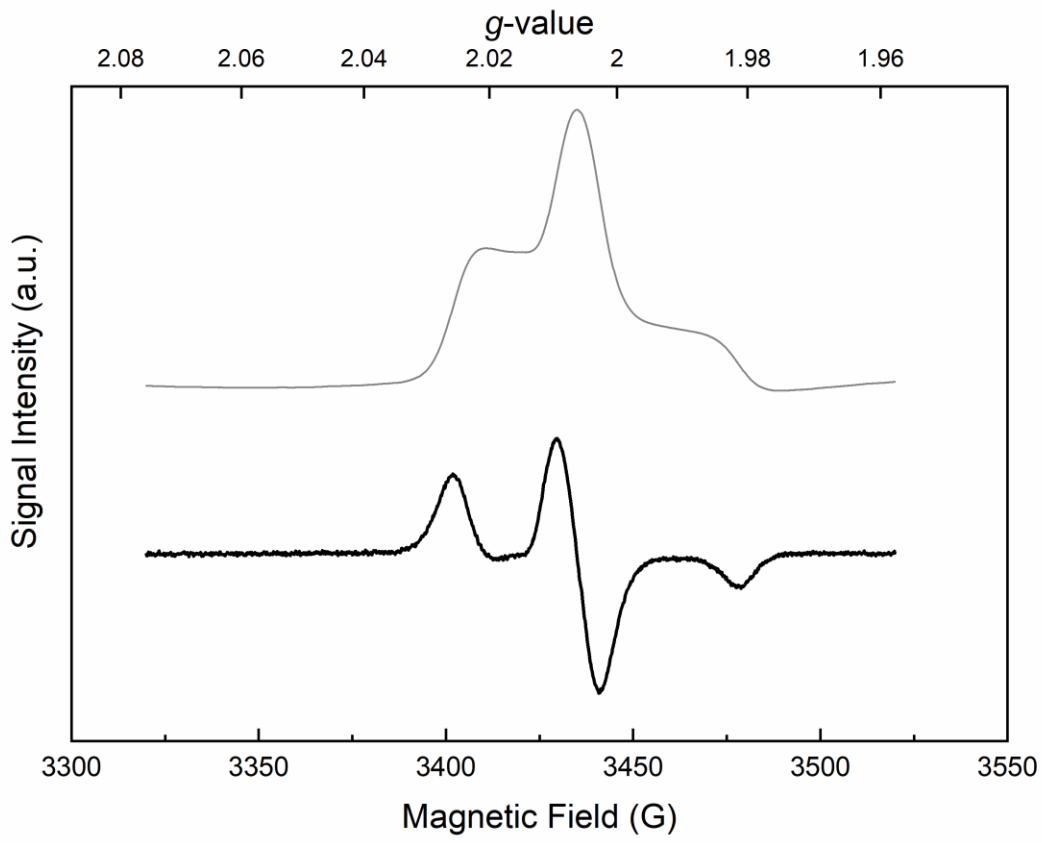

Figure E50. Stacked X-band continuous-wave EPR spectrum of TEMPOL standard 559 μM Water / 25% Glycerol (black trace). Gray trace: integrated data, double integral values determined using Origin. Conditions: T = 25 K; modulation amplitude = 4.0 G; time constant = 5 ms, Double integral = 160.093, P = 31.7 μW, B_{mod} = 8 G, Q = 5600, g_{avg} = 2.17, S = 1/2, Corrected Double integral = 4.26 x 10^{-24}

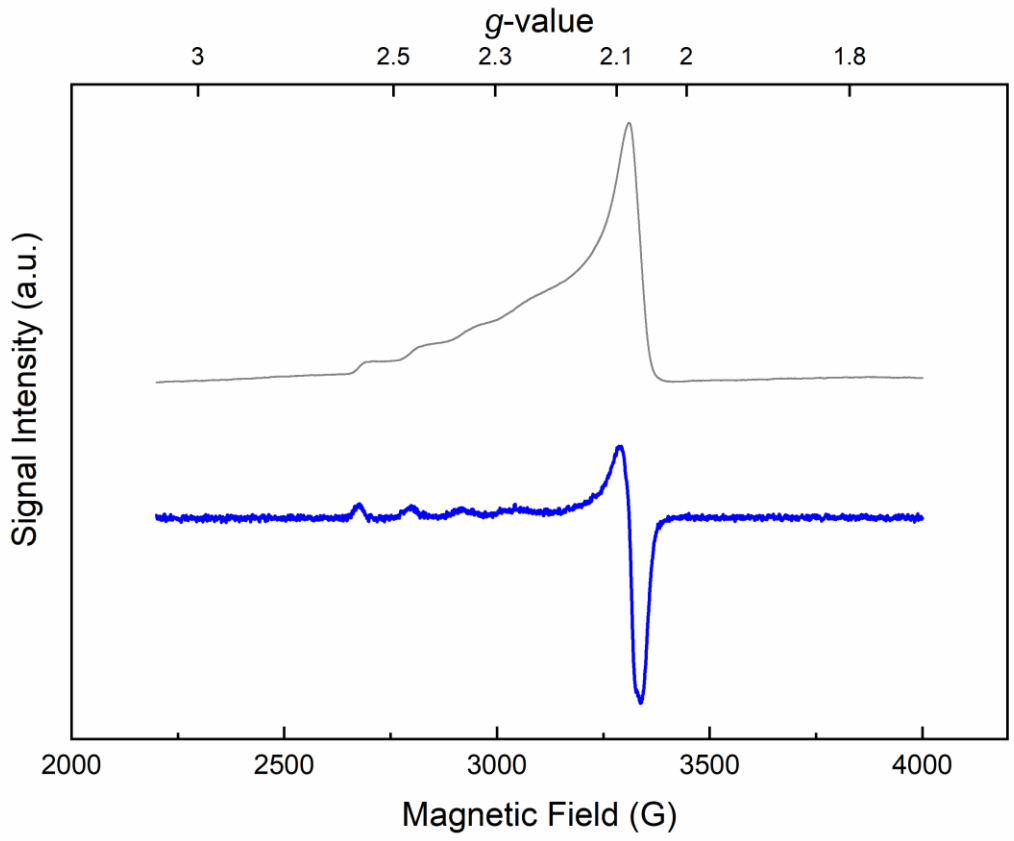

Figure E51. Stacked X-band continuous-wave EPR spectrum of $Cu(NO_3)_2$ standard 500 μM Water / 25% Glycerol (blue trace). Gray trace: integrated data, double integral values determined using Origin. Conditions: T = 80 K; modulation amplitude = 4.0 G; time constant = 5 ms, Double integral = 9.123, P = 2 μW, B = 6 G, Q = 5200, g_{avg} = 2.02, S = 1/2, Corrected Double integral = 4.76 x 10^{-24}.

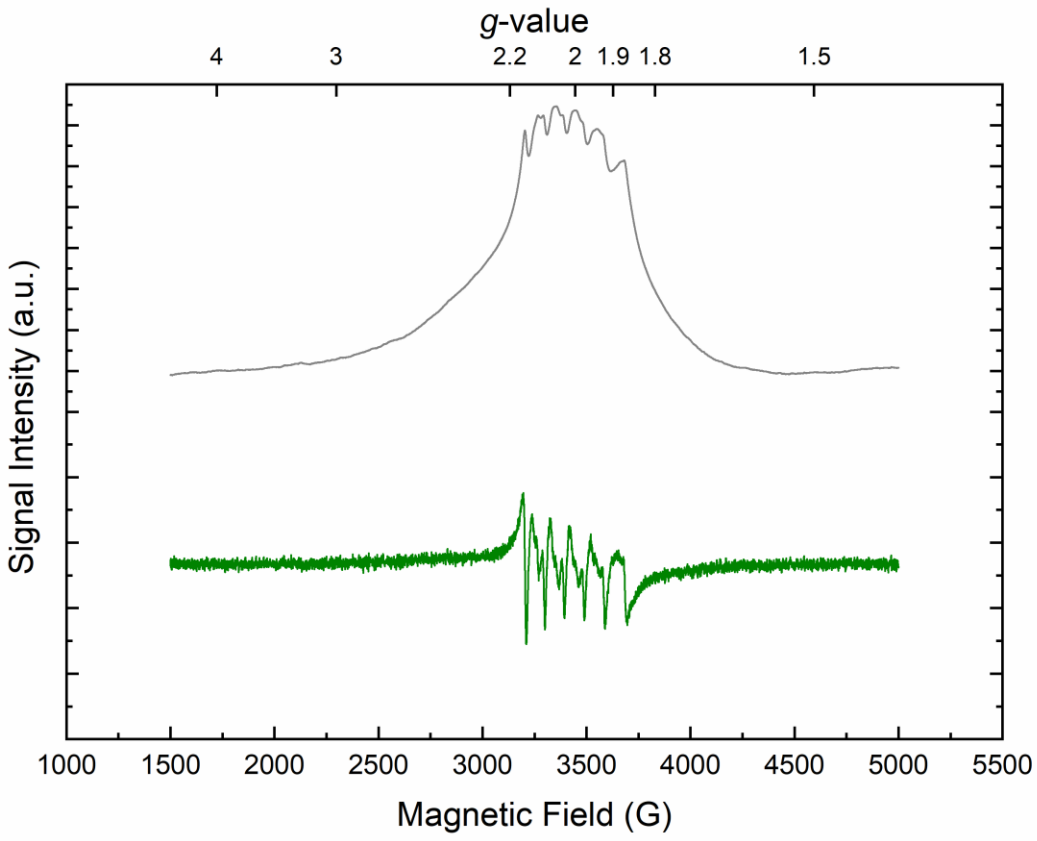

Figure E52. Stacked X-band continuous-wave EPR spectrum of $MnCl_2$ standard 635 μM Water / 25% Glycerol (green trace). Gray trace: integrated data, double integral values determined using Origin. Conditions: T = 25 K; modulation amplitude = 4.0 G; time constant = 5 ms, Double integral = 518.99, P = 2 μW, B = 7 G, Q = 5700, g_{avg} = 2.02, S = 5/2, Corrected Double integral = 5.68 x 10^{-24}.

Table E3. Conditions of Calibration curves for QEPR analysis.

	TEMPOL	**Cu**	**Mn**
Frequency	9.64 GHz	9.64 GHz	9.64 GHz
Temperature	80 K	25 K	25 K
Attenuation	50 dB	38 dB	50dB
Power	0.002 mW	0.0317 mW	0.002 mW
Solvent	Water (18.2 MΩ)/ 25% Glycerol	Water (18.2 MΩ)/ 25% Glycerol	Water (18.2 MΩ)/ 25% Glycerol
Atmosphere/ Preparation	Ambient/Frozen in dry ice/acetone	Ambient/Frozen in dry ice/acetone	Ambient/Frozen in dry ice/acetone

Table E4. Results of QEPR analysis.

		Concentration Determined by QEPR		
	Concentration Prepared	Pdt of Treatment w/ 1 equiv. Cp^*_2Co (THF)	Pdt of Treatment w/ 100 equiv. $AlEt_3$ (THF)	Pdt of Treatment w/ MMAO (DCM)
1	2.0 mM	2.44 μM (0.12%)	0.12.9 μM (0.64%)	5.54 μM (0.28%)
2	2.0 mM	2.97 μM (0.15%)	5.26 μM (0.26%)	0.70 μM (0.03%)
3	2.0 mM	2.23 μM (0.11%)	14.43 μM (0.72%)	6.55 μM (0.33%)

Conditions: 2 mM Cr^{III} solutions, all layered reduction spectra collected following 15 s of mixing.

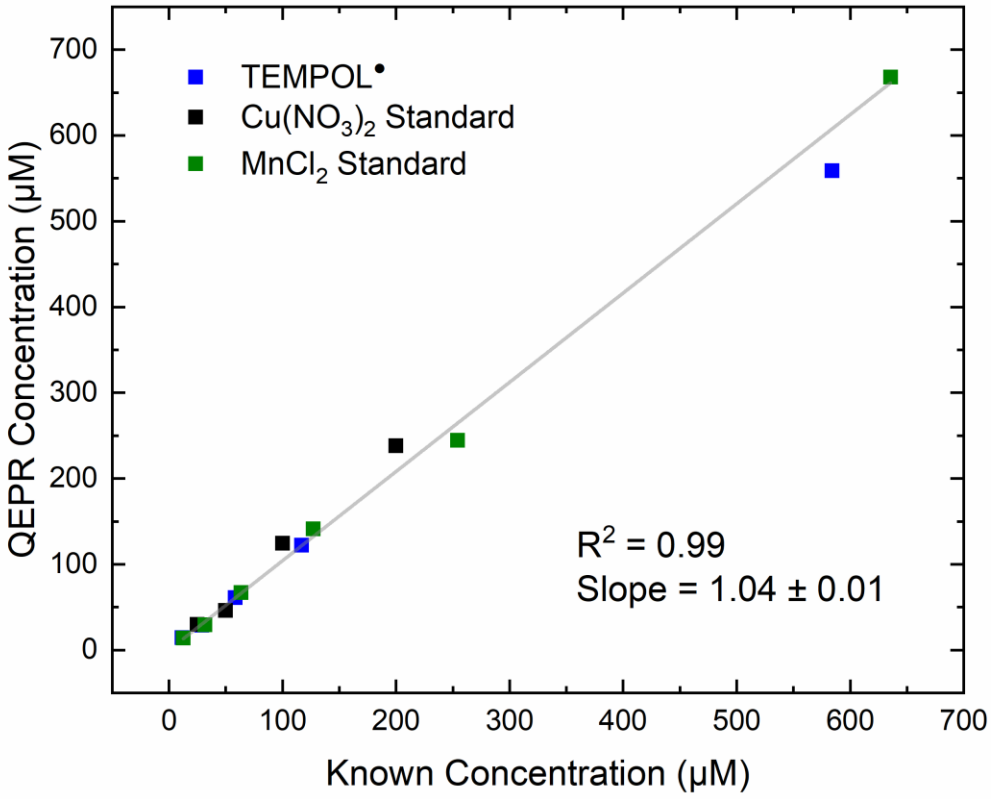

Figure E53. Plot of QEPR determined concentration versus known concentration (μM). Multiple concentrations of Tempol, $Cu(NO_3)_2$, and $MnCl_2$ at multiple concentrations from 10 μM, to 635 μM.

Electronic absorption spectrum

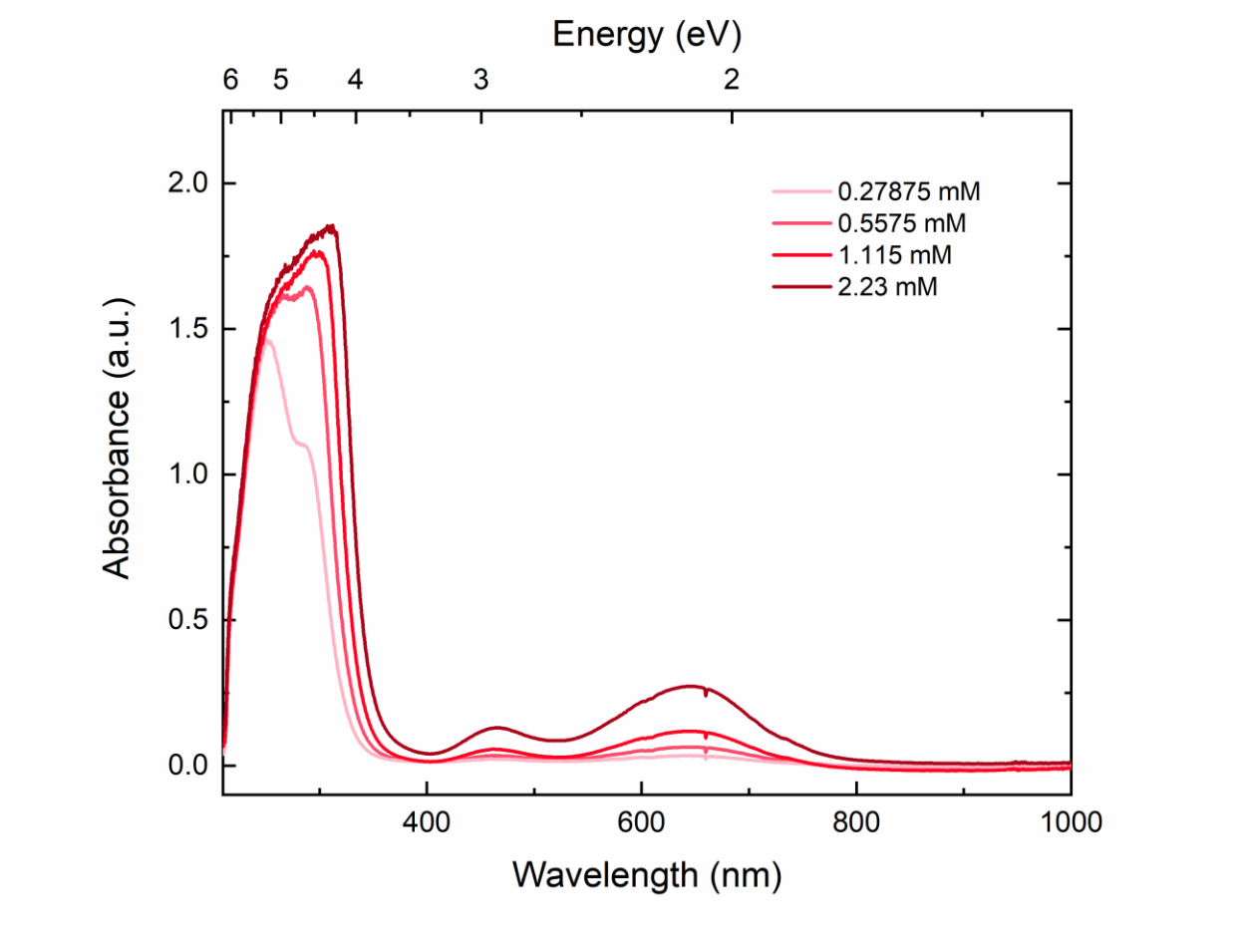

Figure E54. Electronic absorption spectrum of **1** at multiple concentrations.

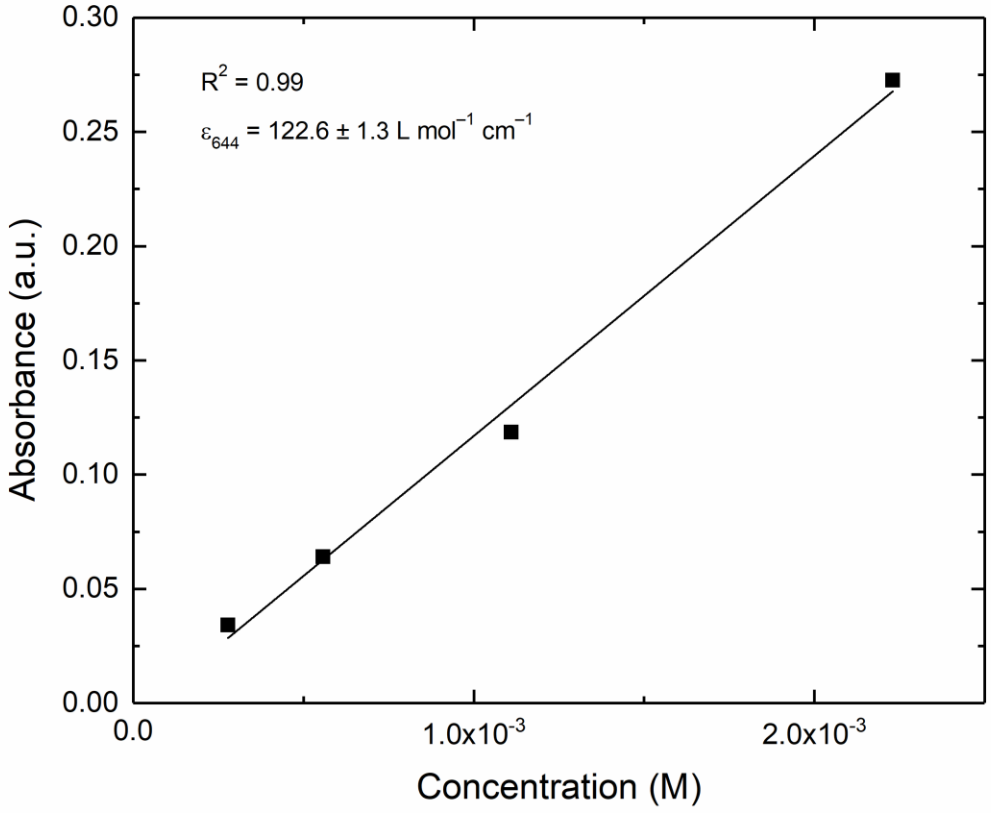

Figure E55. Molar Absorptivity of **1** at multiple concentrations.

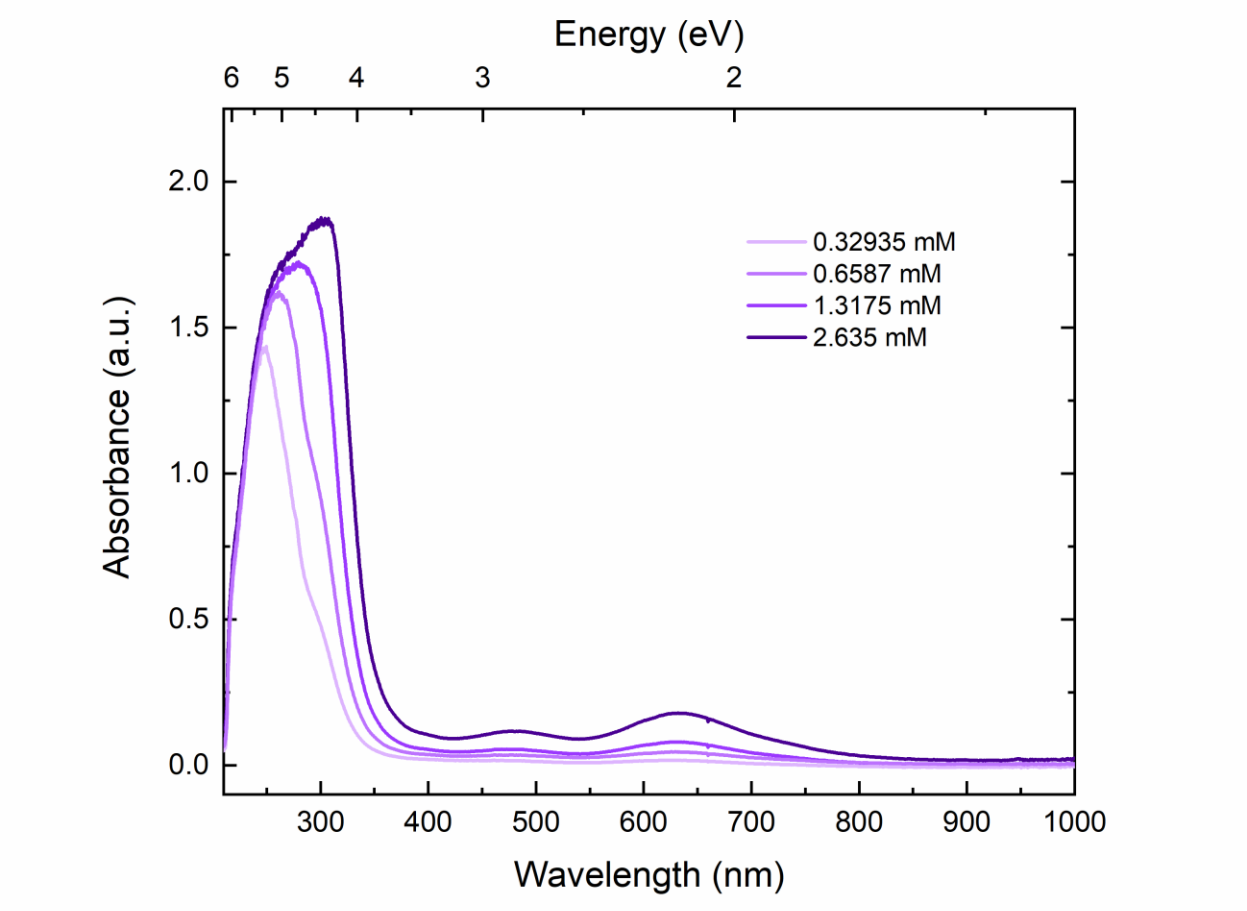

Figure E56. Electronic absorption spectrum of **2** at multiple concentrations.

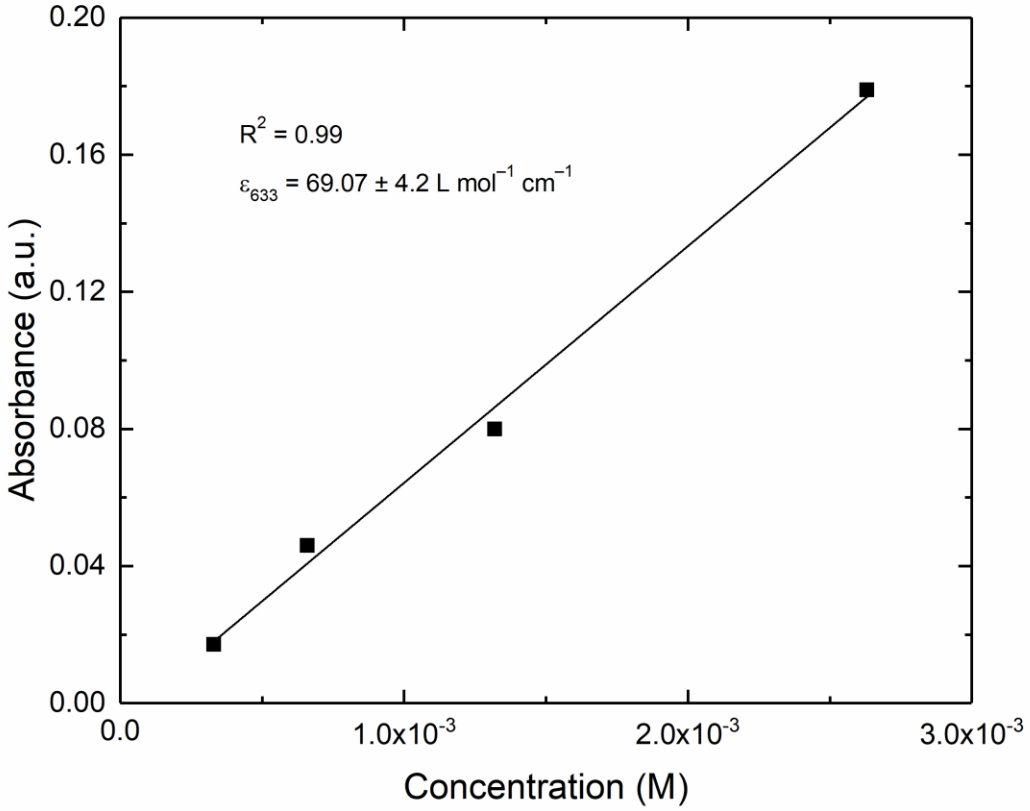

Figure E57. Molar Absorptivity of **2** at multiple concentrations.

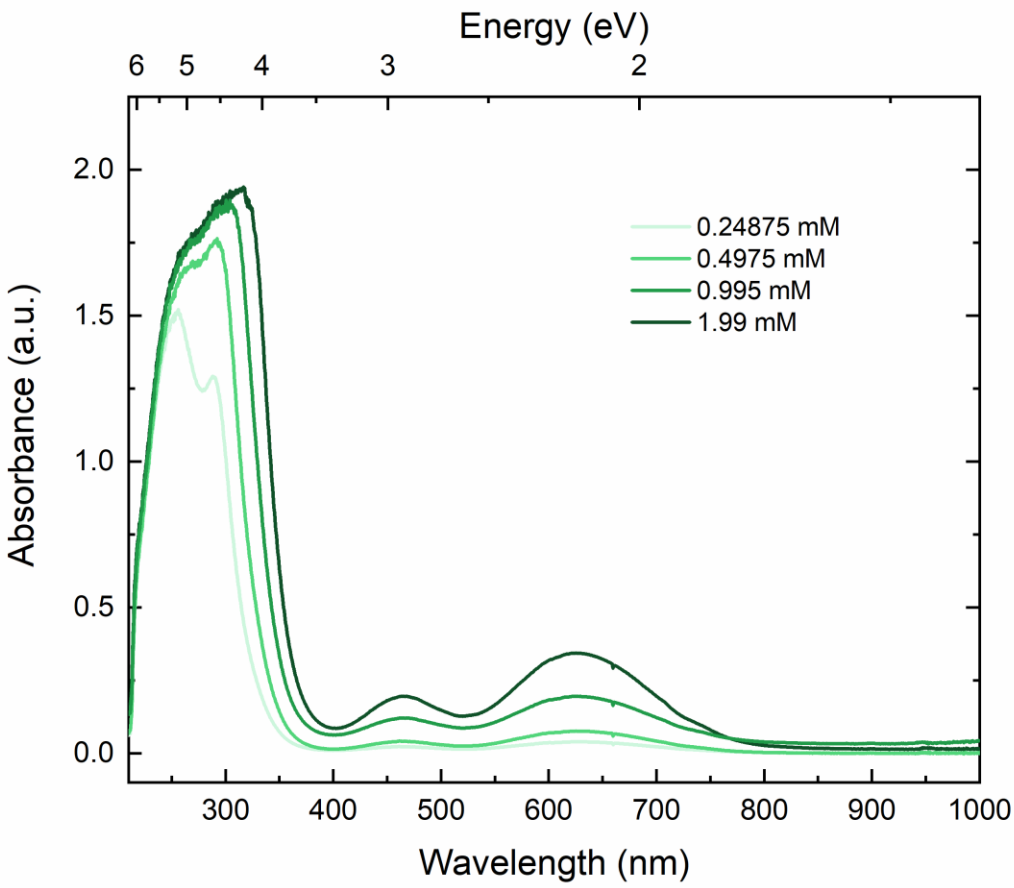

Figure E58. Electronic absorption spectrum of **3** at multiple concentrations.

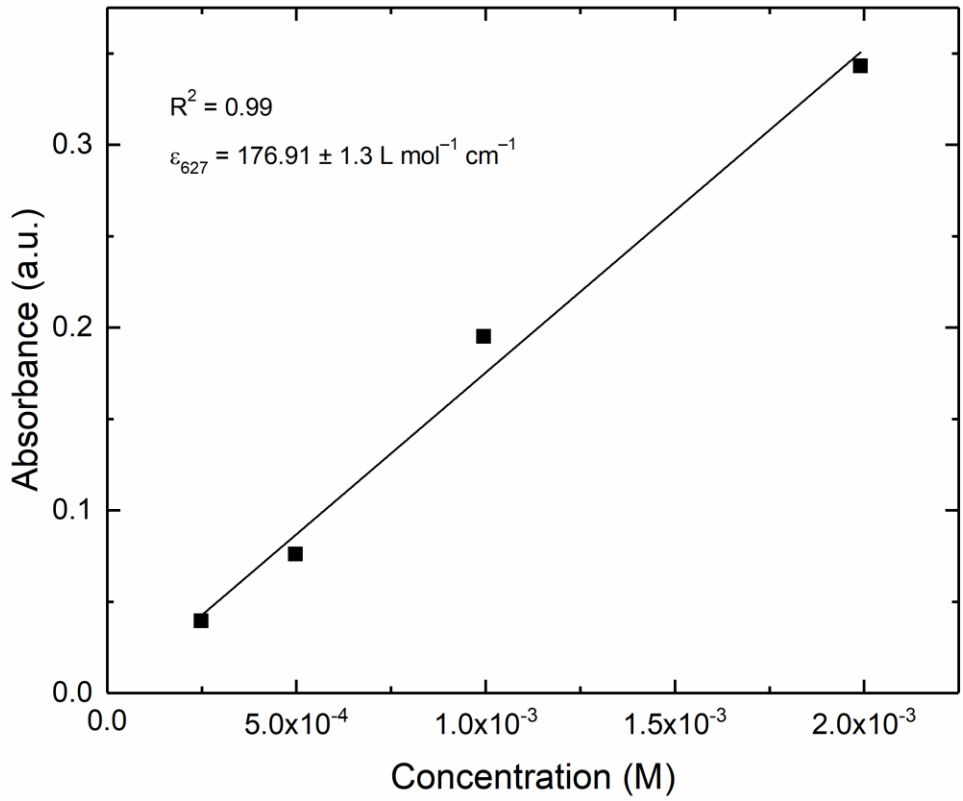

Figure E59. Molar Absorptivity of **3** at multiple concentrations.

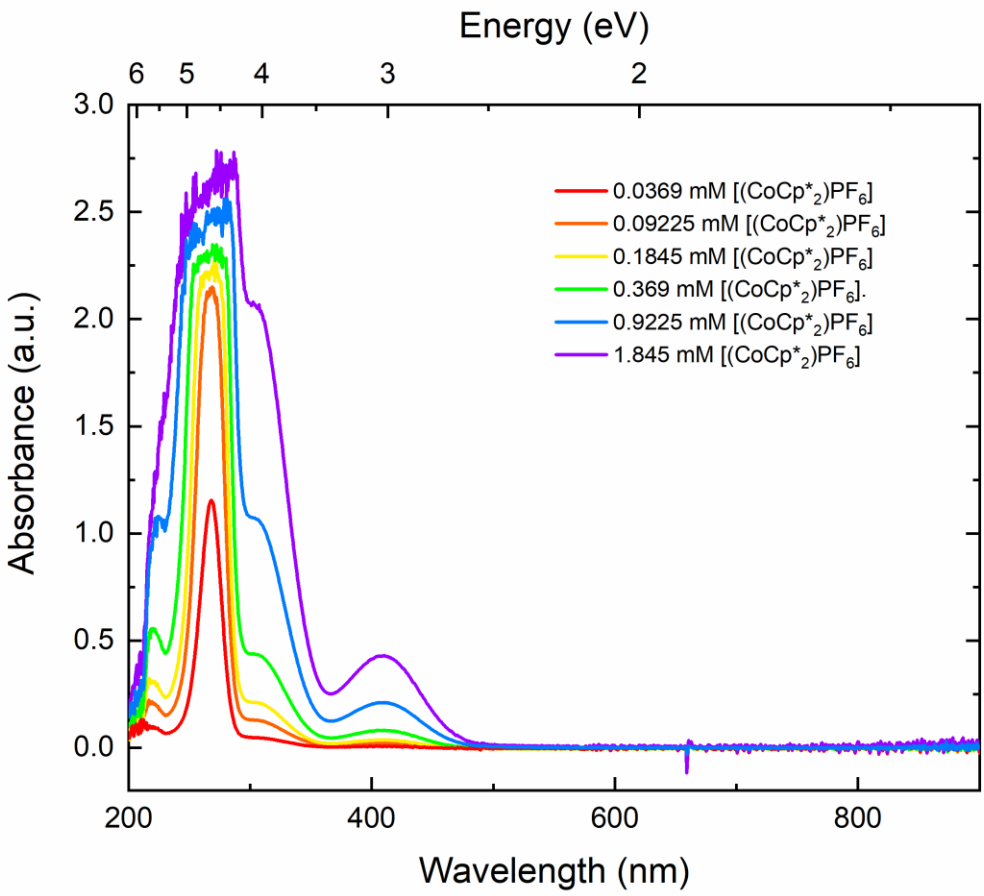

Figure E60. Electronic absorption spectrum of $[Cp^*_2Co][PF_6]$ at multiple concentrations.

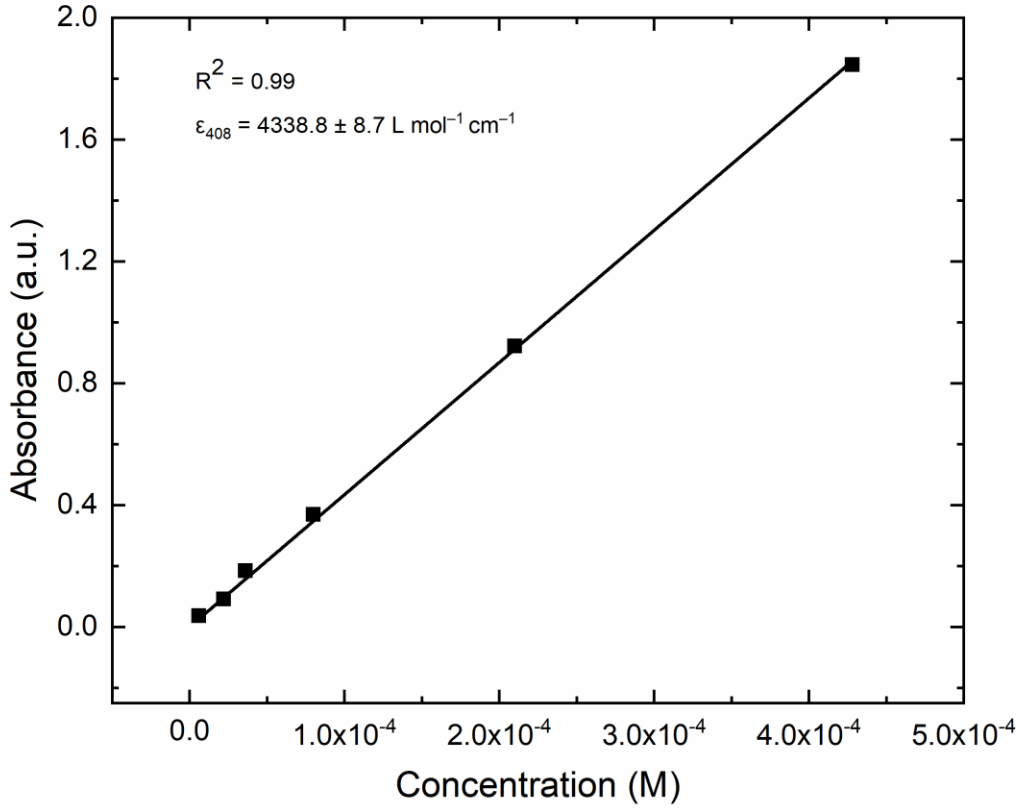

Figure E61. Molar Absorptivity of $[Cp^*_2Co][PF_6]$ at multiple concentrations.

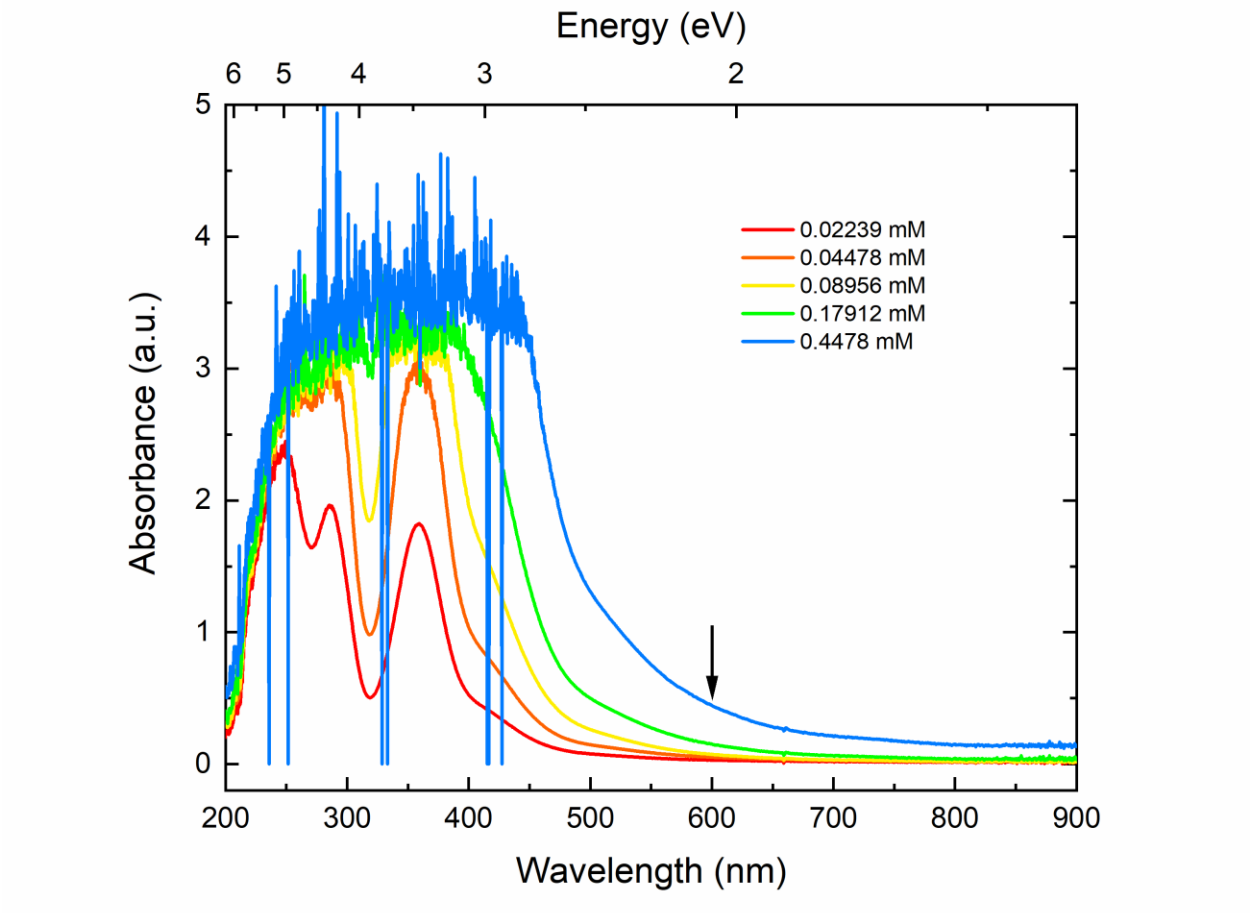

Figure E62. Electronic absorption spectrum of Cp^*_2Co at high concentrations.

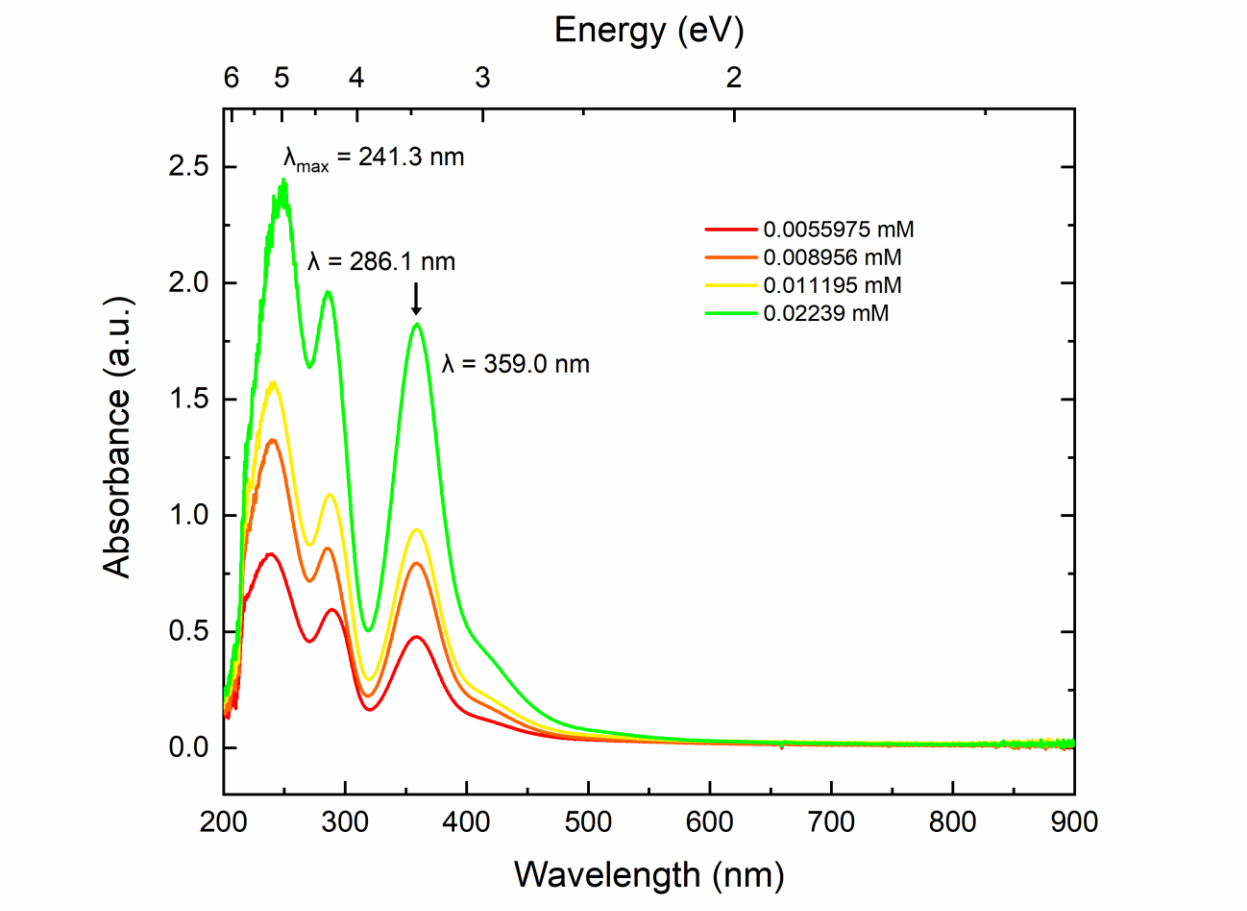

Figure E63. Electronic absorption spectrum of Cp^*_2Co at low concentrations.

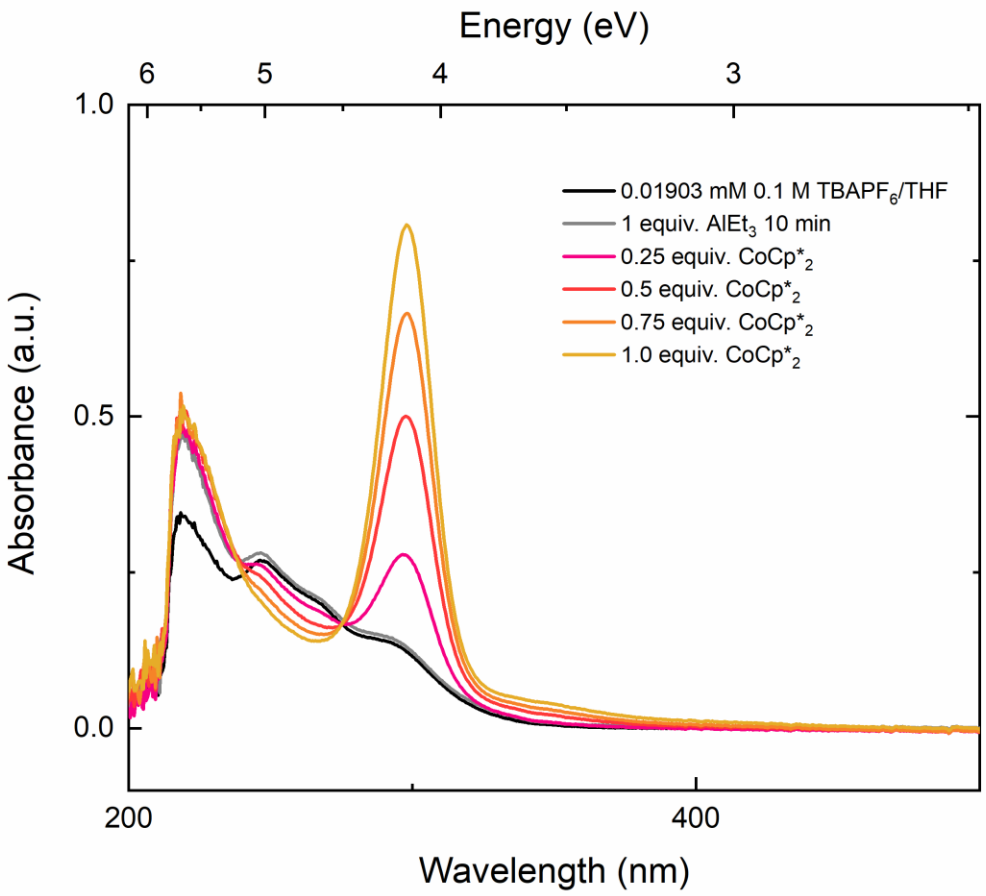

Figure E64. Electronic absorption spectrum titration of **1** and $AlEt_3$, 0.1 M $TBAPF_6$ with increasing amounts totaling to 1 equiv. of Cp^*_2Co (200 – 450 nm).

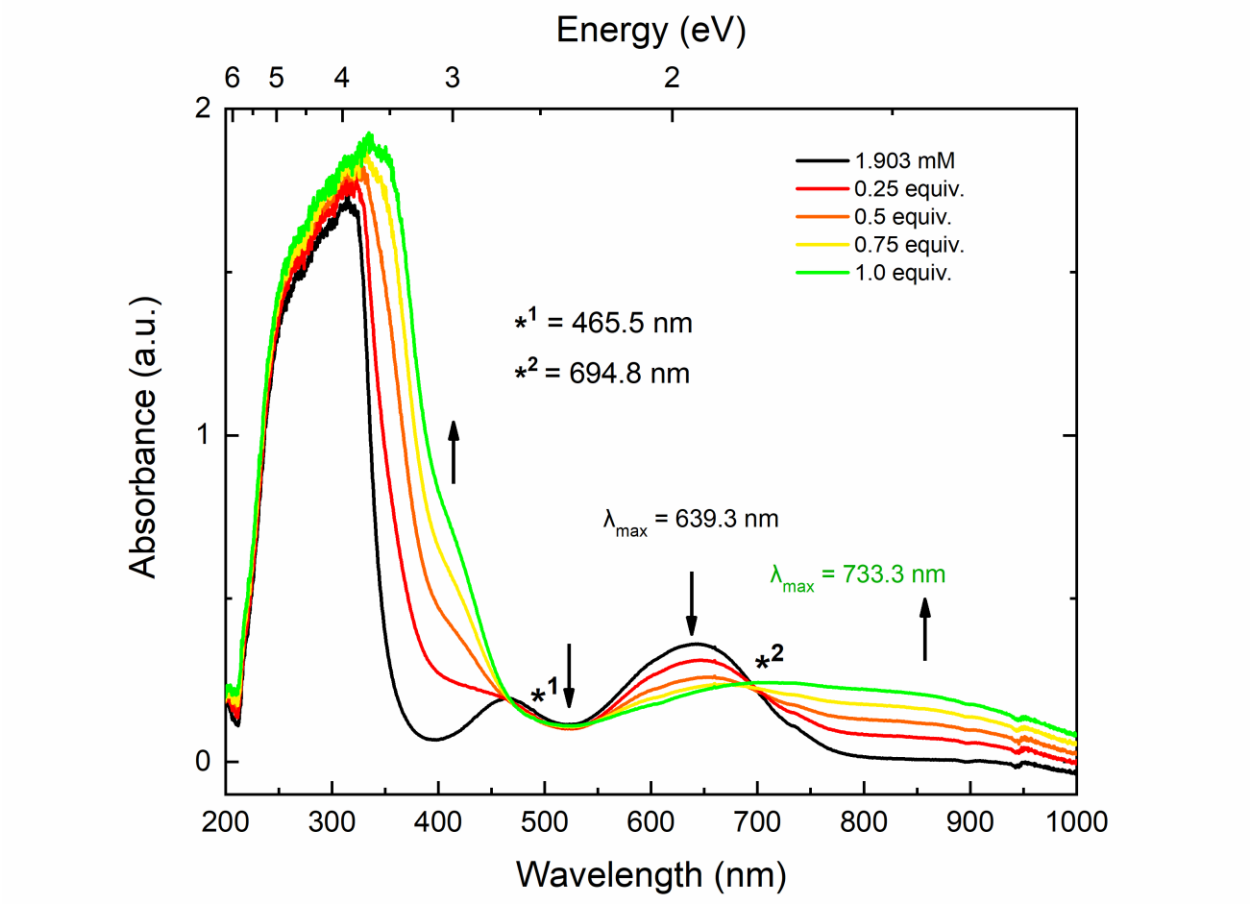

Figure E65. Electronic absorption spectrum titration of **1** with increasing amounts totaling to 1 equiv. of Cp^*_2Co.

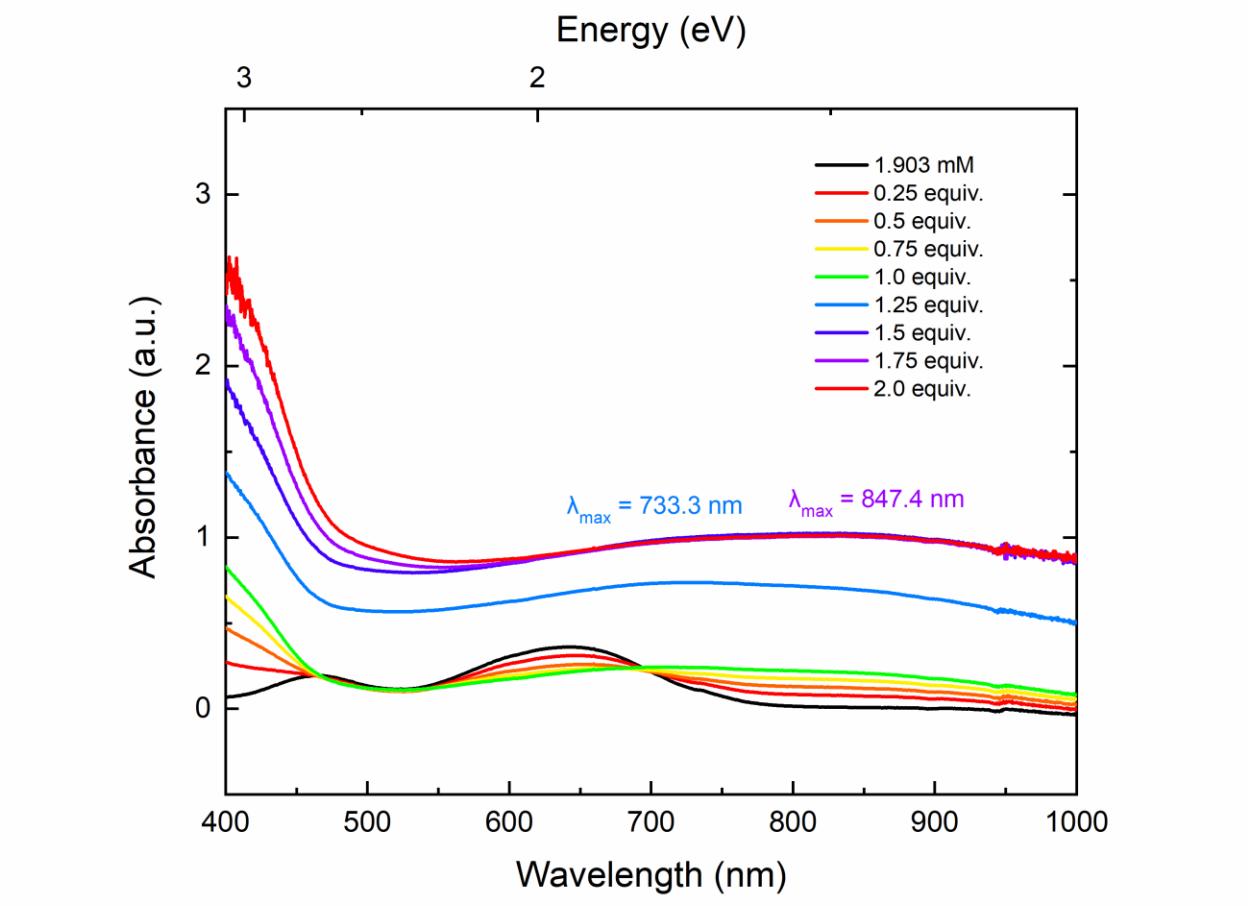

Figure E66. Electronic absorption spectrum titration of **1** with increasing amounts totaling to **2** equiv. of Cp^*_2Co (400 – 1000 nm).

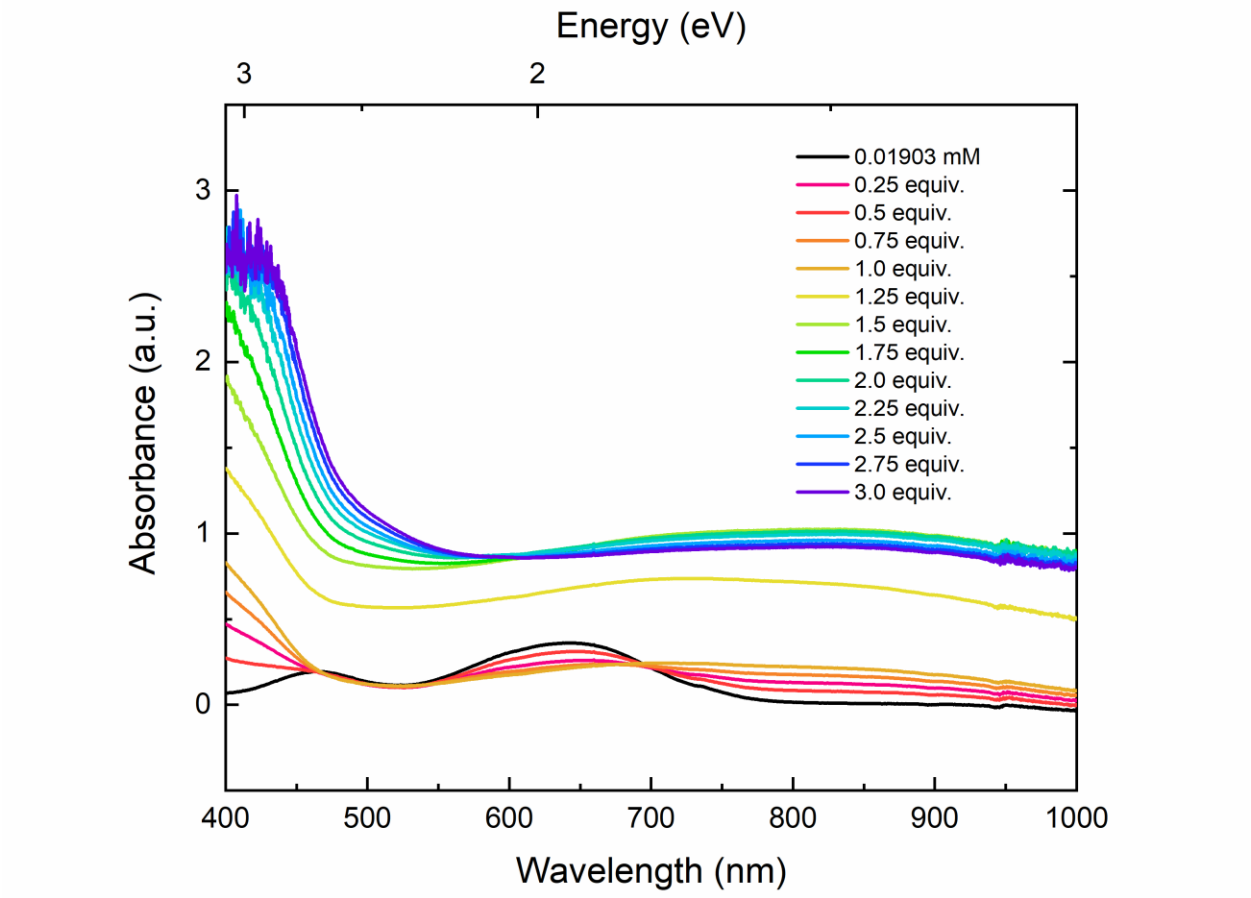

Figure E67. Electronic absorption spectrum titration of **1** with increasing amounts totaling to 3 equiv. of Cp^*_2Co (400 – 1000 nm).

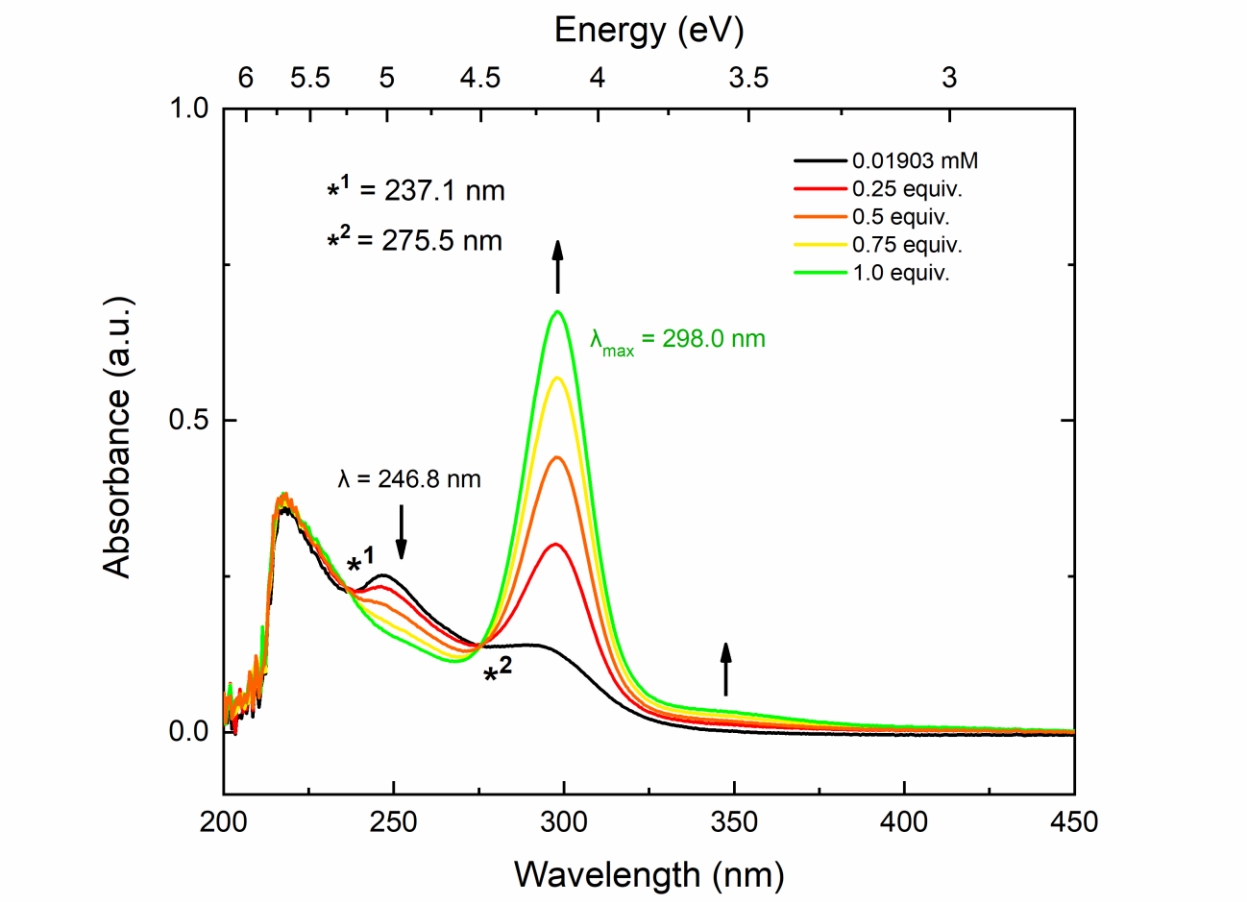

Figure E68. Electronic absorption spectrum titration of **1** with increasing amounts totaling to 1 equiv. of Cp^*_2Co (200 – 450 nm).

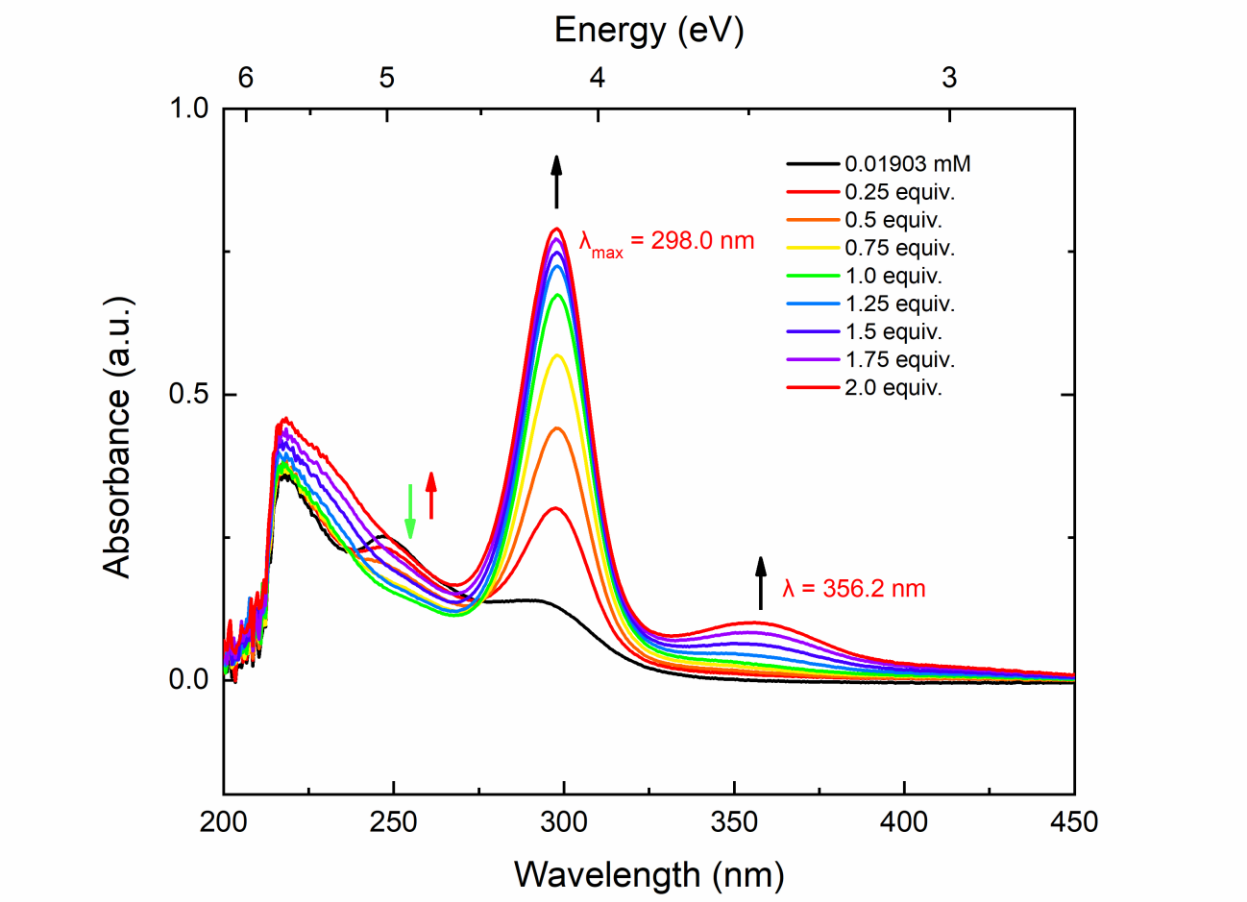

Figure E69. Electronic absorption spectrum titration of **1** with increasing amounts totaling to 2 equiv. of Cp^*_2Co (200 – 450 nm).

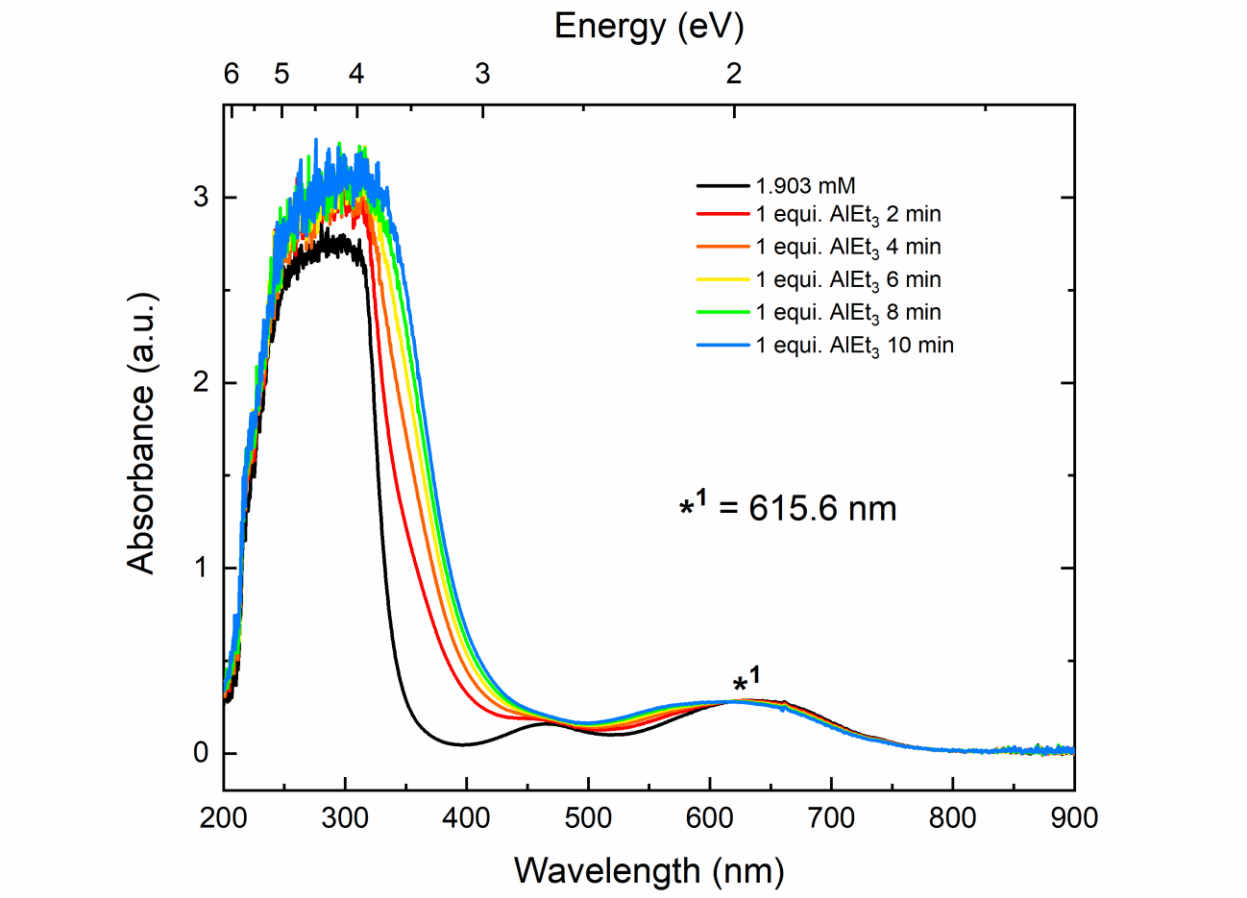

Figure E70. Electronic absorption spectrum **1** with $AlEt_3$.

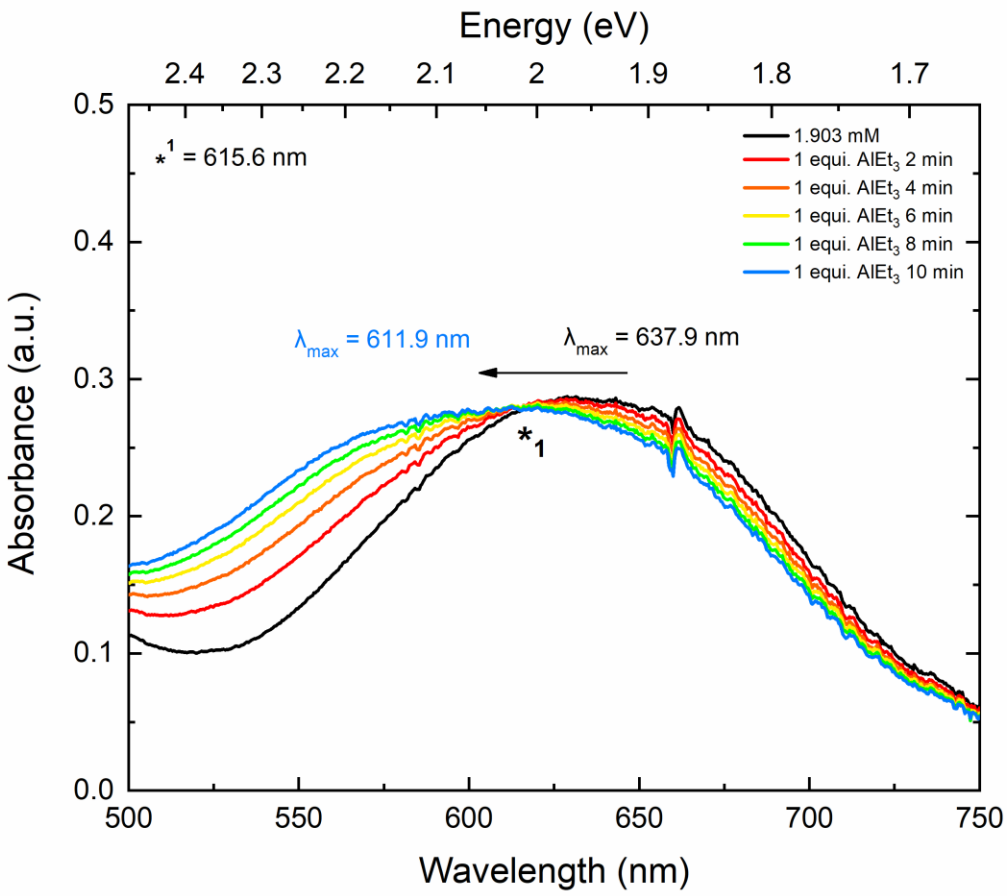

Figure E71. Electronic absorption spectrum **1** with $AlEt_3$ (500 – 750 nm).

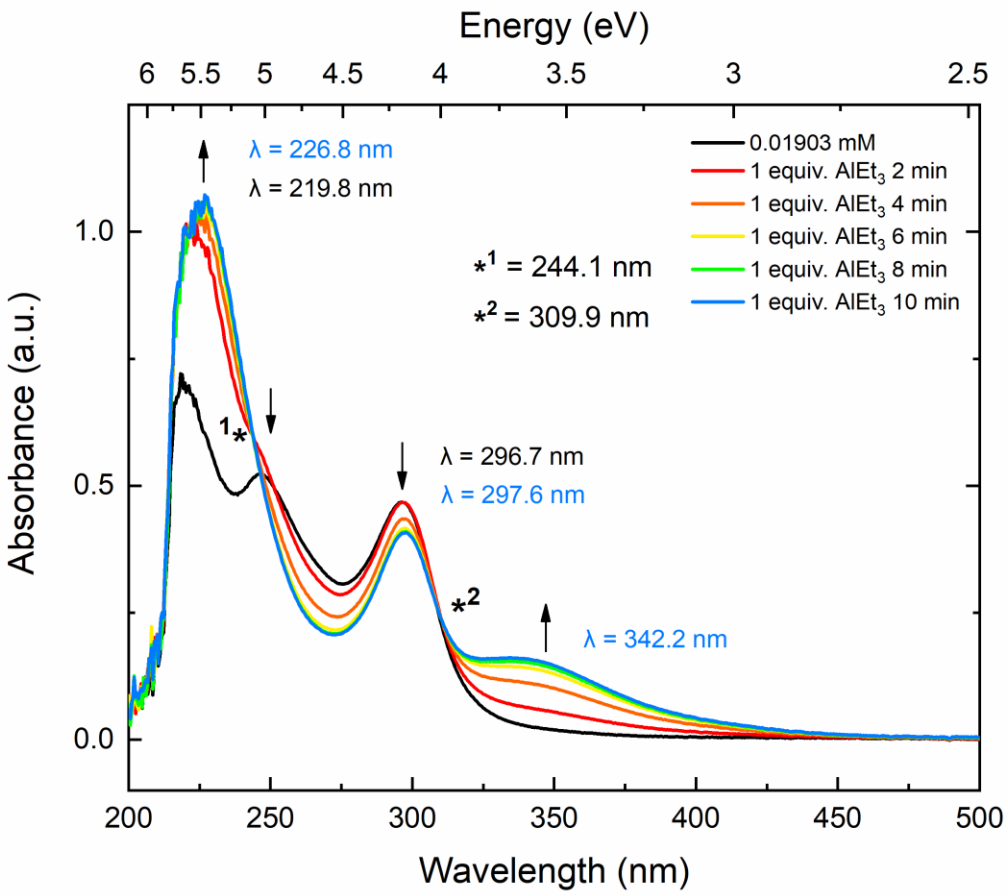

Figure E72. Electronic absorption spectrum **1** with $AlEt_3$ low concentration (200 – 500 nm).

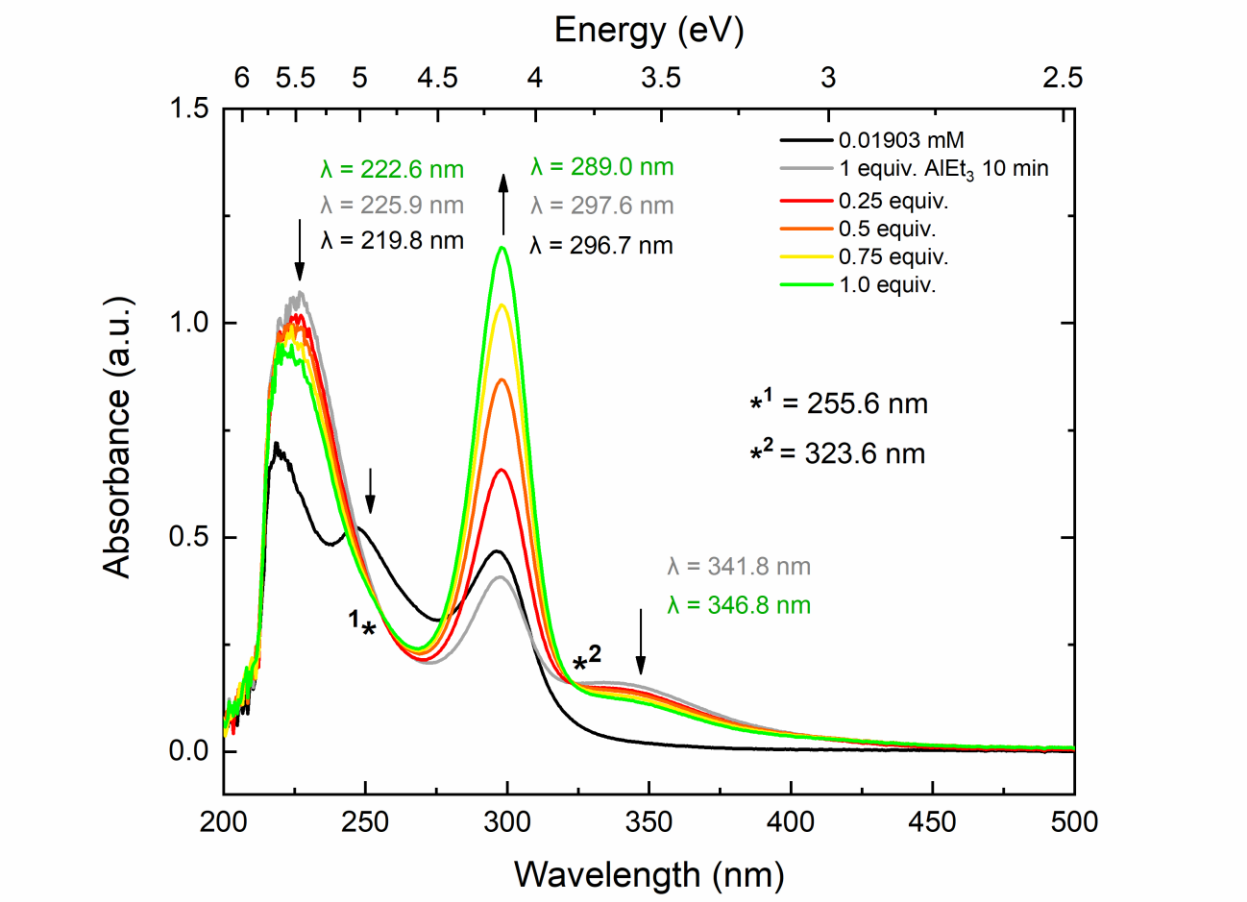

Figure E73. Electronic absorption spectrum titration of **1** and $AlEt_3$ with increasing amounts totaling to 1 equiv. of Cp^*_2Co (200 – 500 nm).

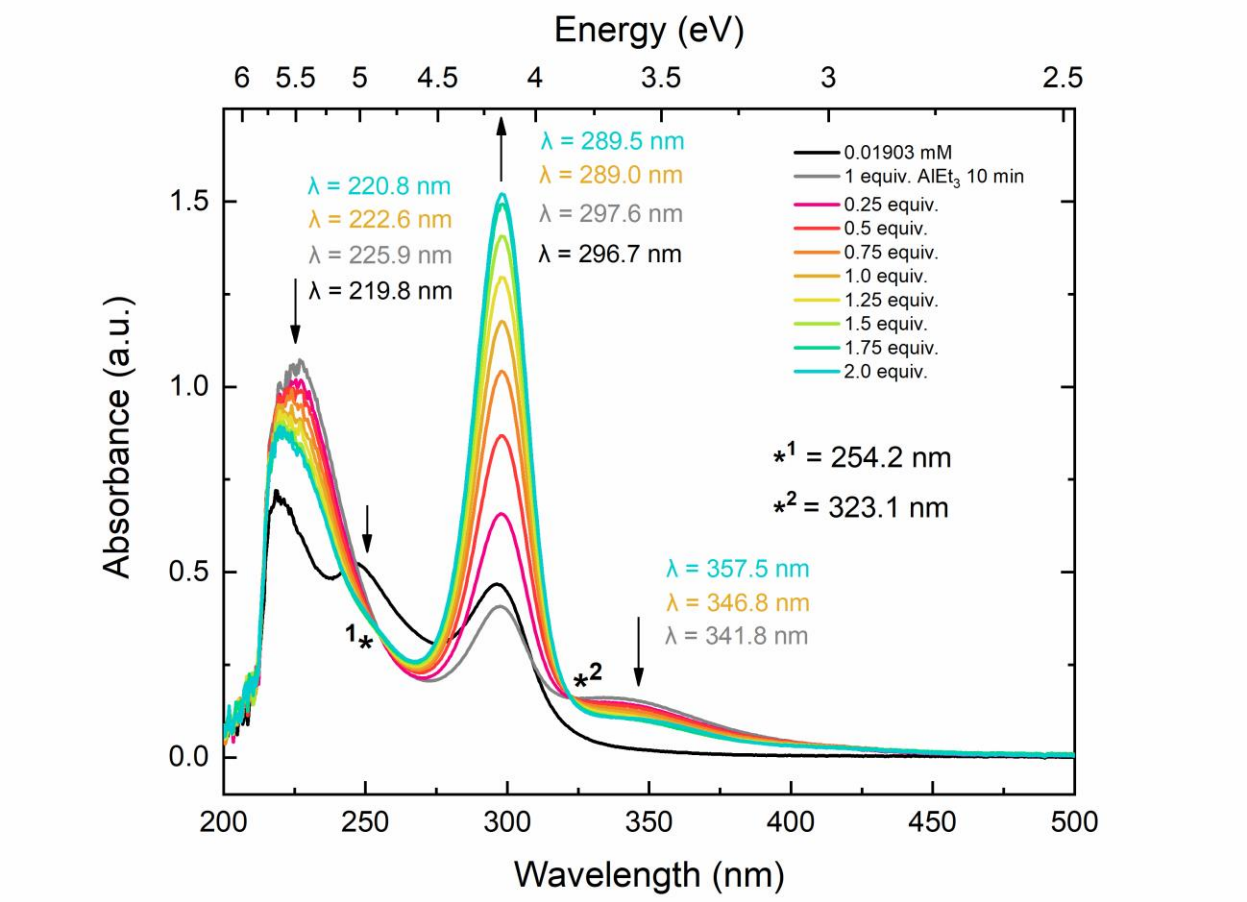

Figure E74. Electronic absorption spectrum titration of **1** and $AlEt_3$ with increasing amounts totaling to 2 equiv. of Cp^*_2Co (200 – 500 nm).

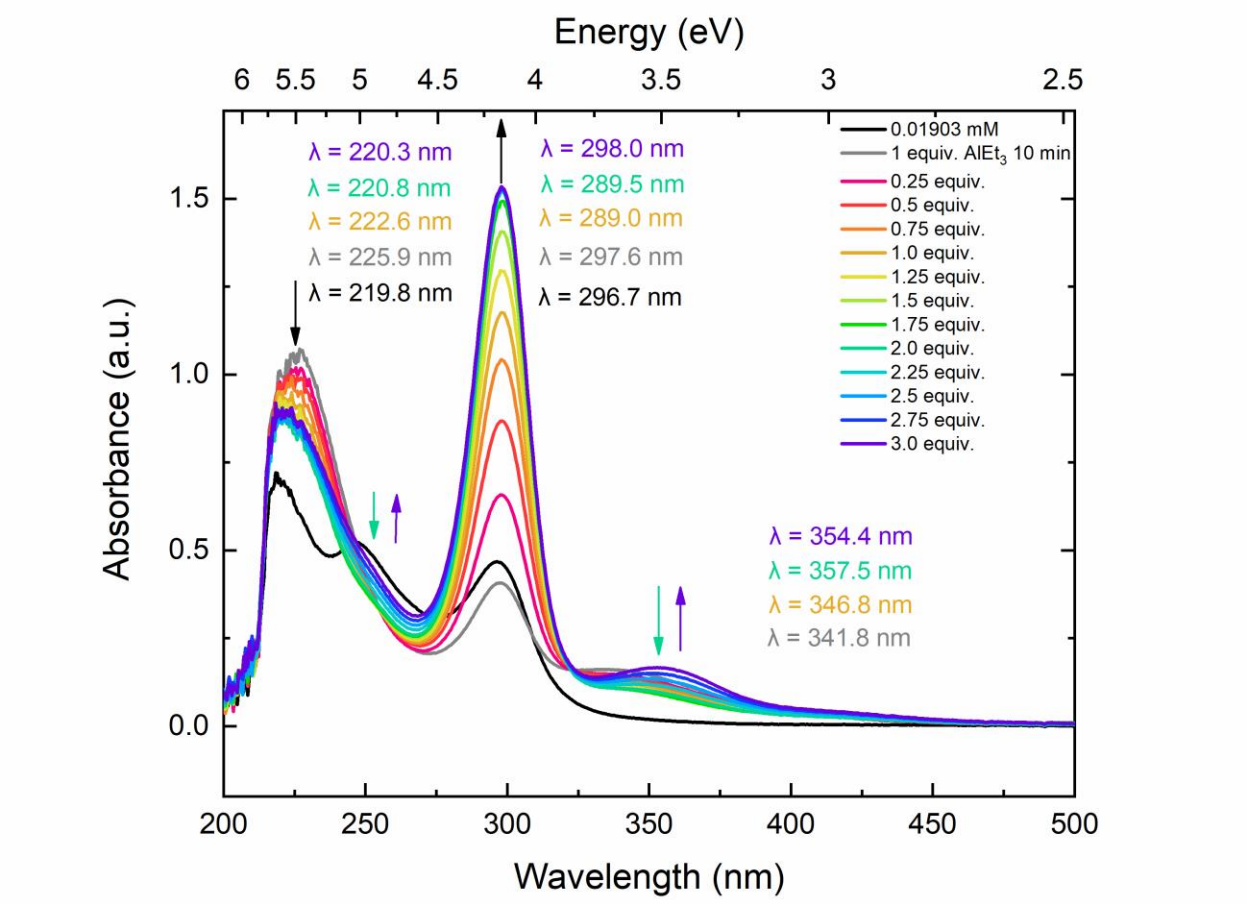

Figure E75. Electronic absorption spectrum titration of **1** and $AlEt_3$ with increasing amounts totaling to 1 equiv. of Cp^*_2Co (200 – 500 nm).

Infrared Spectra

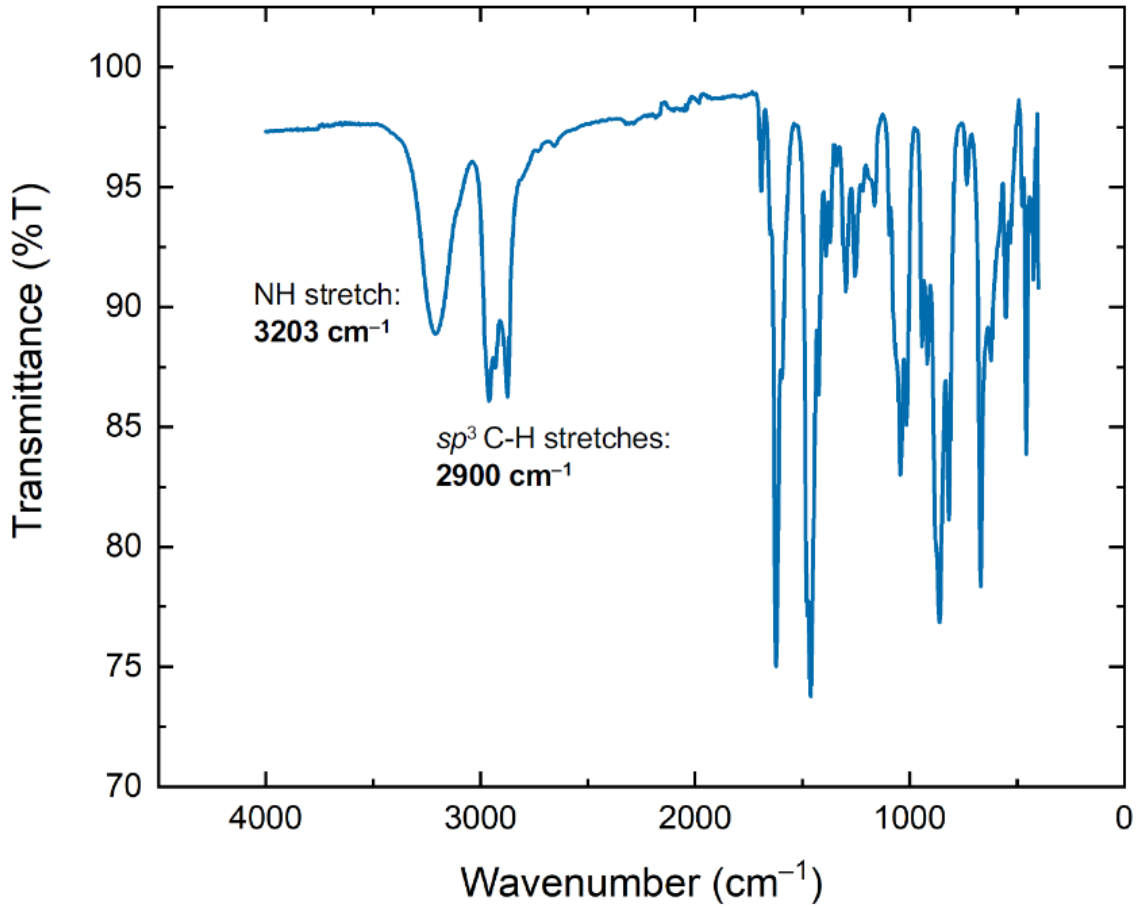

Figure E76. Solid state IR spectrum of **1**.

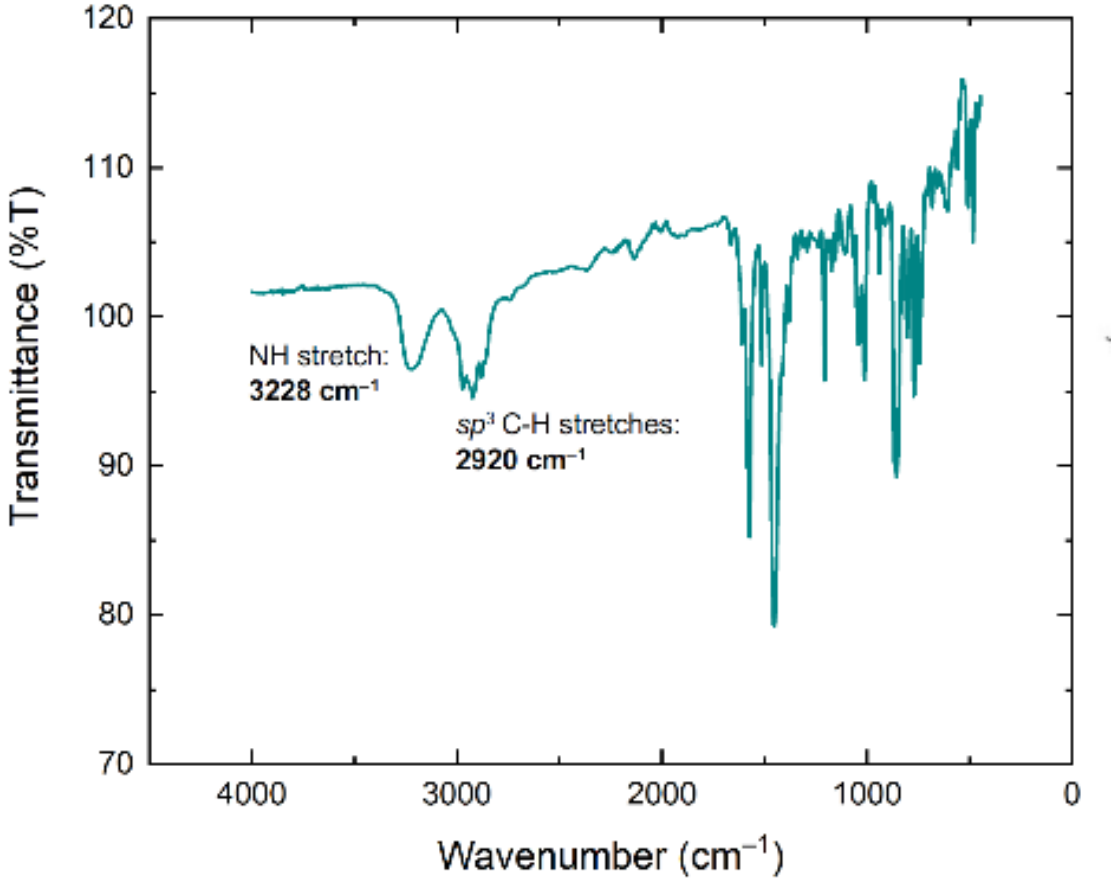

Figure E77. Solid state IR spectrum of **2**.

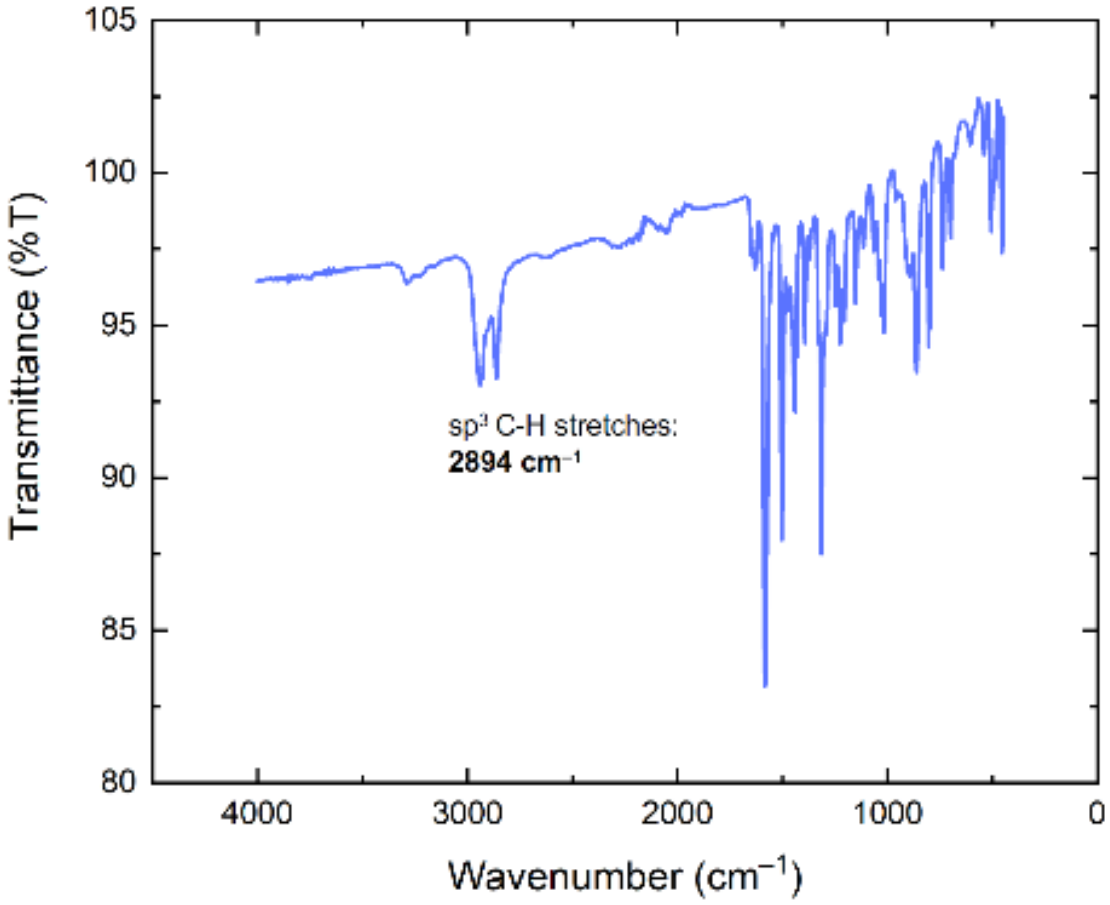

Figure E78. Solid state IR spectrum of **3**.

Infrared spectroscopy studies to interrogate the ligand environment upon reactivity indicate that the secondary amine (secondary amine observed for **1** and **2** at ca. 3390 cm^{-1}, see Figures E76 and E77) stays intact upon titration with modified MAO. The titration of **1** and **2** with modified MAO engenders a shift in vibrational energy of ca. 25 cm^{-1} (see Figures E79 and E80). This observation is consistent with a change in the environment of the secondary imine.

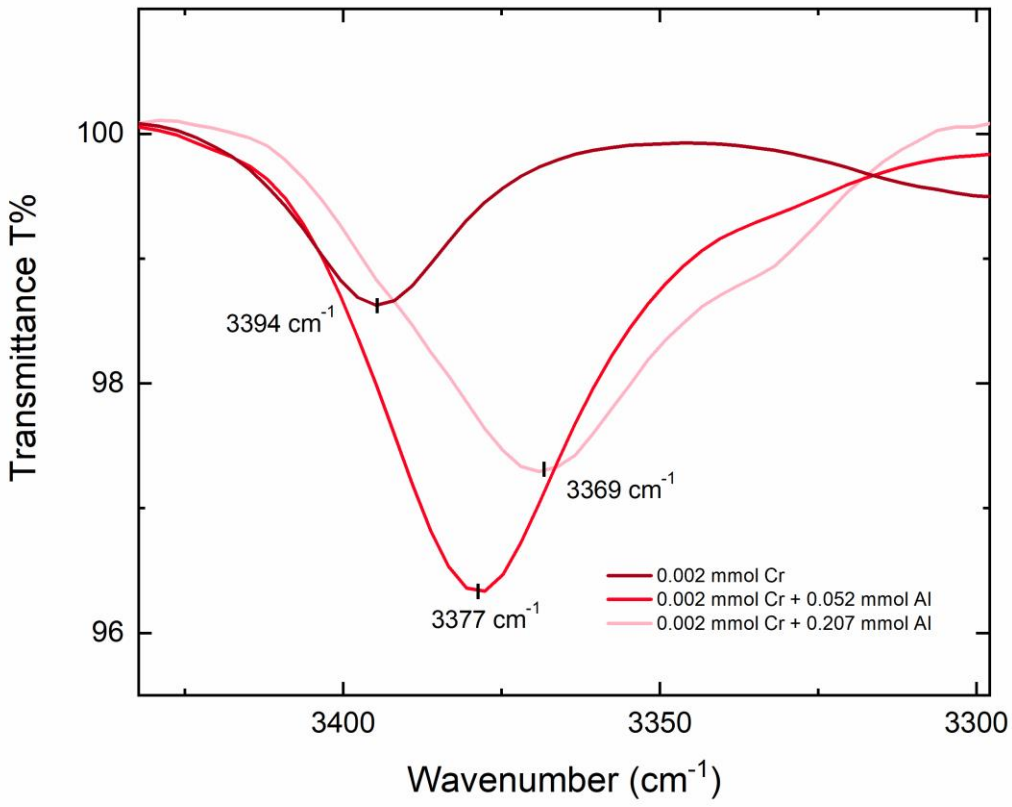

Figure E79. IR spectra of **1** DCM with MMAO.

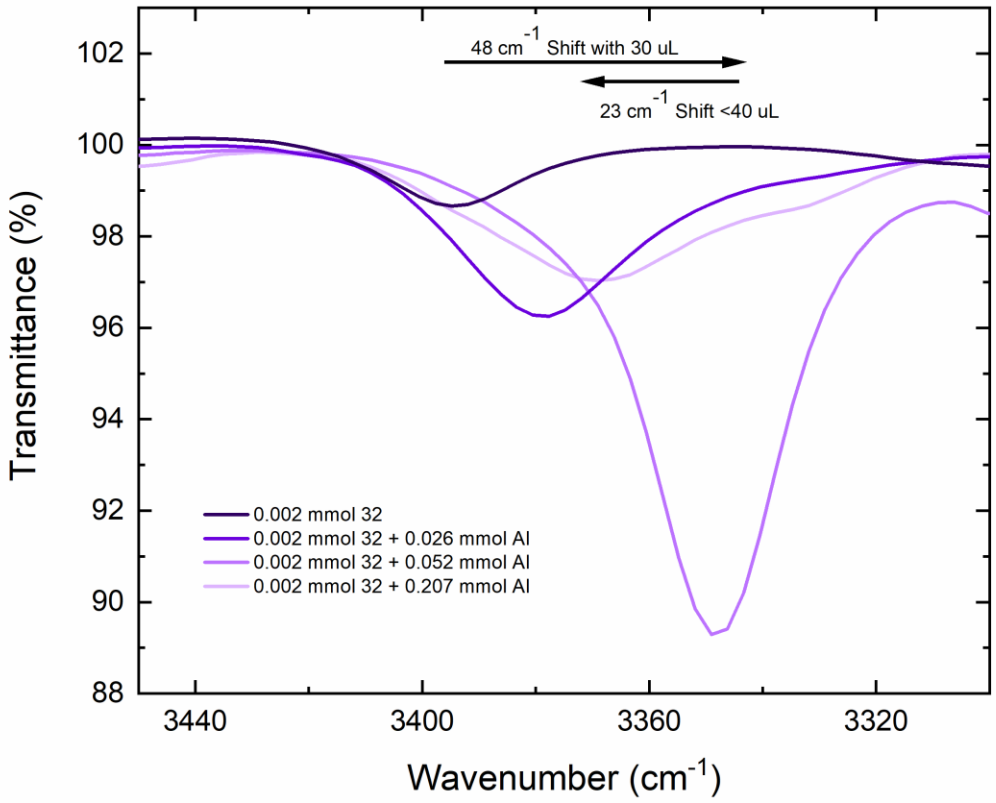

Figure E80. IR spectra of **2** DCM with MMAO

X-ray crystallography

*Refinement Details for **1-R**.*

The sample was interrogated by X-ray diffraction analysis, crystals were mounted on a goniometer head using Paratone oil with MiTeGen MicroMounts and placed in a cold nitrogen stream. Complete sets of low-temperature (200 K) diffraction data frames were collected for crystal sample using 1.0°-wide w- and/or f-scans.

X-rays for **1-R** were provided by a Bruker generator using a fine-focus Mo sealed tube running at 35 mA and 50 kV (Mo Kα = 0.71073.) and equipped with Bruker TRIUMPH curved-graphite optics. Data were collected with a Bruker PHOTON-II detector.

A total of of 4178 scans were taken with 1.0°-wide wand/or f-scan frames with counting times of 4-6 seconds were collected on the Bruker PHOTON-II detector. All diffractometer manipulations, including data collection, integration and scaling were carried out using the SAINT in the Bruker Apex2 Software Suite.[4] The data was corrected empirically for variable absorption effects with SADABS[5] using equivalent reflections. Probable space groups were determined on the basis of systematic absences and intensity statistics and the structures were solved by direct methods using The Bruker software package SHELXTL[6]. Final stages of weighted full-matrix least-squares refinement were conducted using F_o^2 data with SHELXTL or the Olex software package[7] equipped with XL[8]. The relevant crystallographic and structure refinement data for all four structures are given in Table S-6.

The final structural model for each structure incorporated anisotropic thermal parameters for all nonhydrogen atoms. Isotropic thermal parameters were used for all hydrogen atoms. The THF ligand is 55/45 disordered with two orientations about the Cr–O linkage.

Table E5. Crystal and Refinement Data for [Cr(PNN)Cl_2THF]

	1-R
CCDC number	2150976
Empirical formula	$C_{14}H_{29}Cl_2CrN_2OP$
Formula weight	395.26
Temperature	120.0 K
Wavelength	0.71073 Å
Crystal system	monoclinic
Space group	$P2_1/n$
a	7.9254(4) Å
b	16.9216(8) Å
c	14.2373(7) Å
α	90°
β	97.498(2)°
γ	90°
Volume	1893.04(16) $Å^3$
Z	4
Density (calculated)	1.387 g/cm^3
Absorption coefficient	0.971 mm^{-1}
F(000)	832.0
Crystal size	0.15 × 0.073 × 0.07 mm^3
Theta range	3.758 to 54.22 °
Index ranges	$-10 \le h \le 10$, $-21 \le k \le 21$, $-18 \le l \le 18$
Reflections collected	33114
Independent reflections	4178 [R_{int} = 0.0899, R_{sigma} = 0.0519]
Absorption correction	Numerical
Max. and min. transmission	0.918 and 0.934
Refinement method	Full-matrix least-squares on F^2
Data / restraints / parameters	4178/0/243
Goodness-of-fit on F^2	1.034
Final R indices [I>2σ(I)]	R_1 = 0.0464, wR_2 = 0.0895
R indices (all data)	R_1 = 0.0762, wR_2 = 0.1002
Largest diff. peak and hole	0.45/-0.74 e/$Å^{-3}$

[a] $R_1 = \Sigma||F_o|-|F_c|| / \Sigma|F_o|$ [b] $wR_2 = [\ \Sigma\ [w(F_o^2-F_c^2)^2] / \Sigma\ [w(F_o^2)^2]\ ]^{1/2}$

Table E6. Selected Bond Lengths for **1-R**.

Bond	**1-R** (Å)
Cr–P	2.4847(9)
Cr–N	2.079(2)
Cr–Cl1	2.3663(9)
Cr–Cl2	2.3378(9)
Cr–O	2.318(5)
Cr–O’	2.371(5)

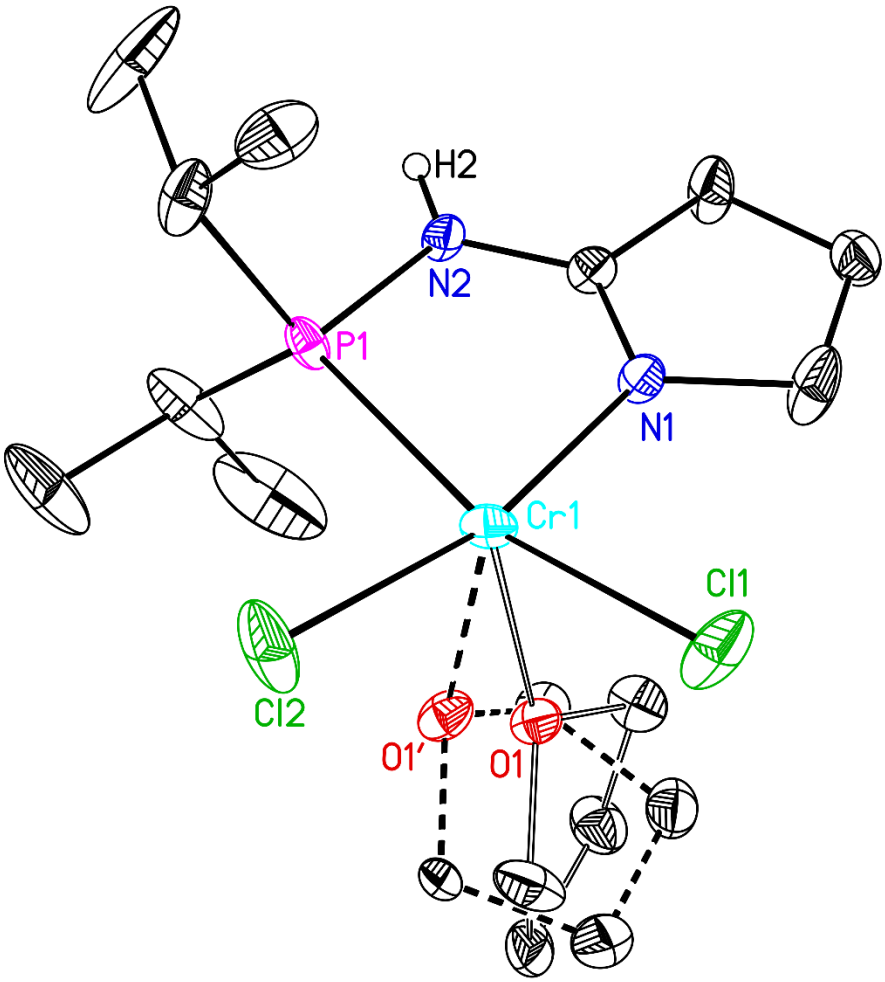

Figure E81. Full solid-state structure of **1-R**. All hydrogen atoms except H2 omitted for clarity. Displacement ellipsoids shown at the 50% probability level.

References

[1] Sauerbrey, G., Verwendung von Schwingquarzen zur Wägung dünner Schichten und zur Mikrowägung. *Zeitschrift für Physik* **1959,** *155*, 206-222.

[2] Eaton, G. R.; Eaton, S. S.; Barr, D. P.; Weber, R. T.; Eaton, S. R., *Quantitative EPR*. Wien New York : Springer: Wien New York, 2010. (adapted from Fig 11.1)

[3] Aasa, R.; Vänngård, t., EPR signal intensity and powder shapes: A reexamination. *J. Magnetic Resonance* **1975,** *19*, 308-315.

[4] *APEX2, Version 2 User Manual, M86-E01078*. Bruker Analytical X-ray Systems: Madison, WI, June 2006.

[5] Sheldrick, G. M. *SADABS (version 2008/1): Program for Absorption Correction for Data from Area Detector Frames*, University of Göttingen 2008.

[6] Sheldrick, G., SHELXT - Integrated space-group and crystal-structure determination. *Acta Crystallogr., Sect. A: Found. Crystallogr.* **2015,** *71*, 3-8.

[7] Dolomanov, O. V.; Bourhis, L. J.; Gildea, R. J.; Howard, J. A. K.; Puschmann, H., OLEX2: a complete structure solution, refinement and analysis program. *J. Appl. Crystallogr.* **2009,** *42*, 339-341.

[8] Sheldrick, G., Crystal structure refinement with SHELXL. *Acta Crystallogr., Sect. C: Cryst. Struct. Commun.* **2015,** *71*, 3-8.

Appendix F

Supplementary Information for Chapter 8

Section F1

NMR Spectra

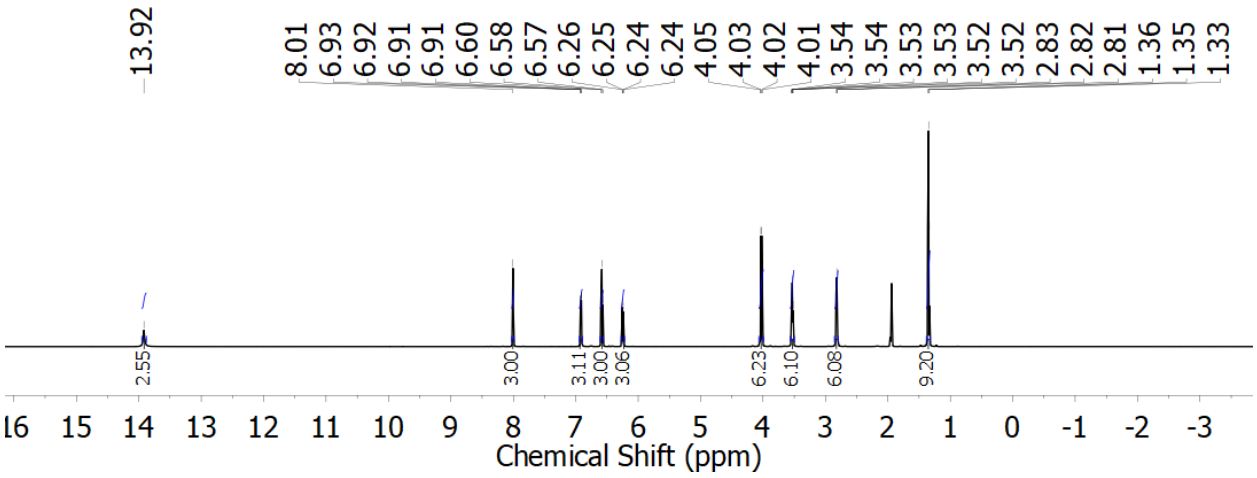

Figure F1. ^{1}H NMR spectrum (500 MHz, CD_3CN) of $\mathbf{L^{OEt}H_3}$.

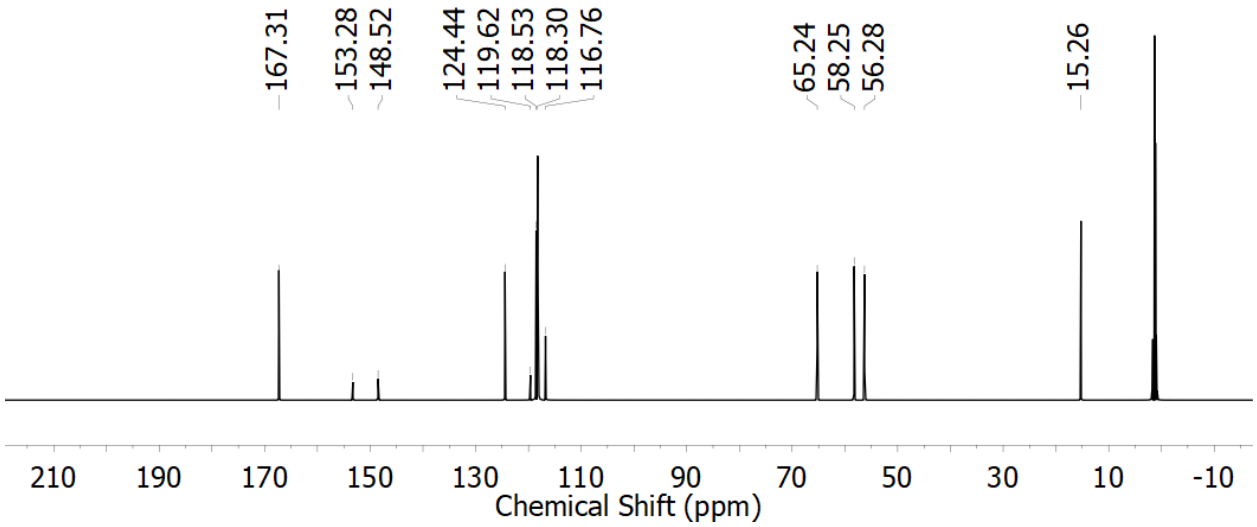

Figure F2. $^{13}C\{^{1}H\}$ NMR spectrum (126 MHz, CD_3CN) of $\mathbf{L^{OEt}H_3}$.

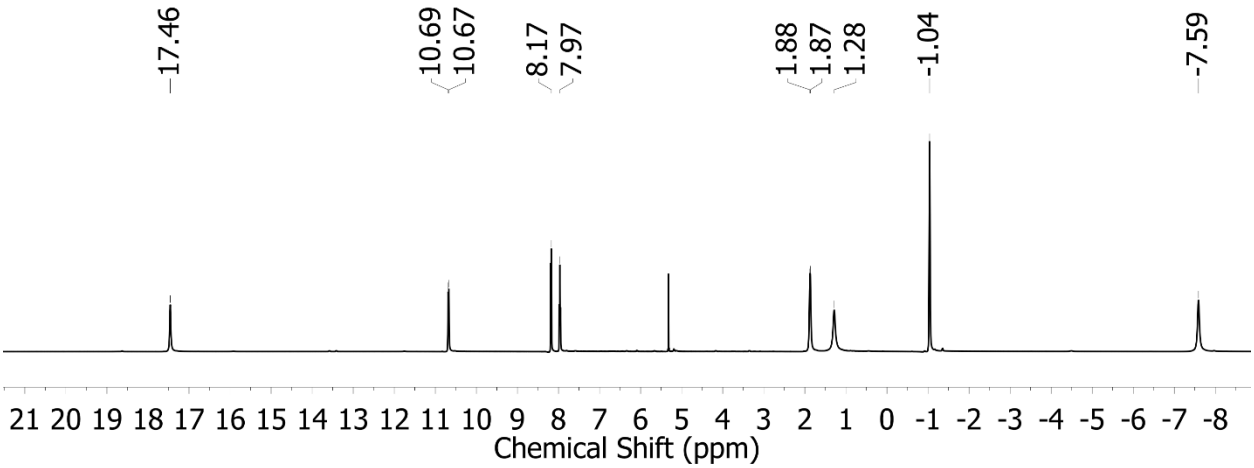

Figure F3. ^{1}H NMR spectrum (500 MHz, CD_3CN) of **1**.

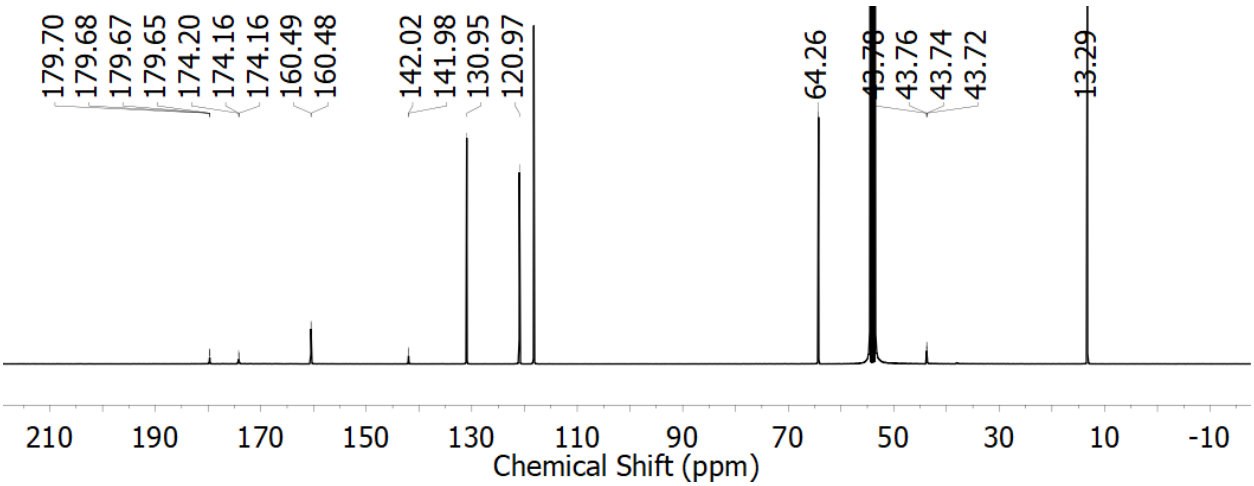

Figure F4. $^{13}C\{^{1}H\}$ NMR spectrum (126 MHz, CD_3CN) of **1**.

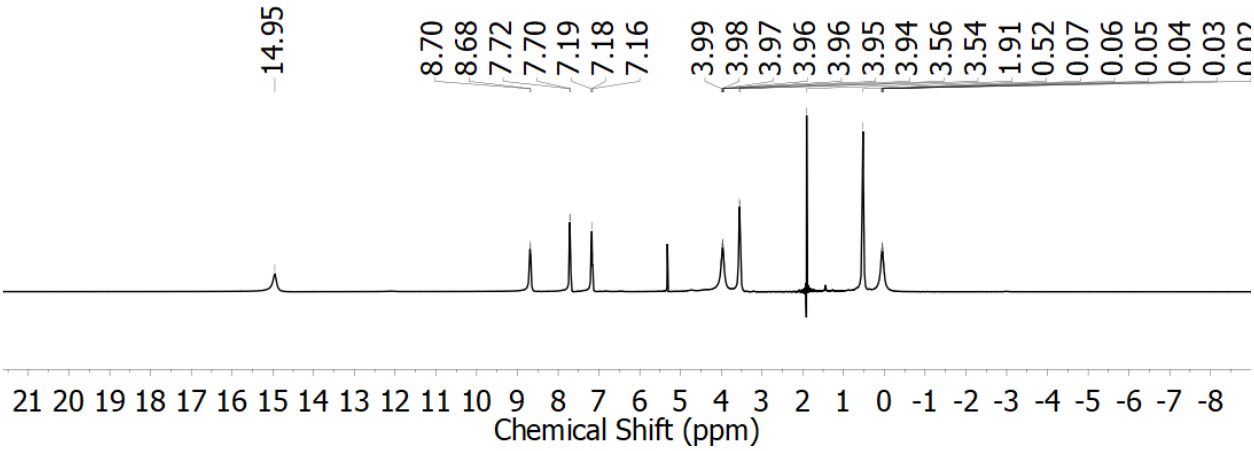

Figure F5. ^{1}H NMR spectrum (500 MHz, CD_3CN) of **1-K**.

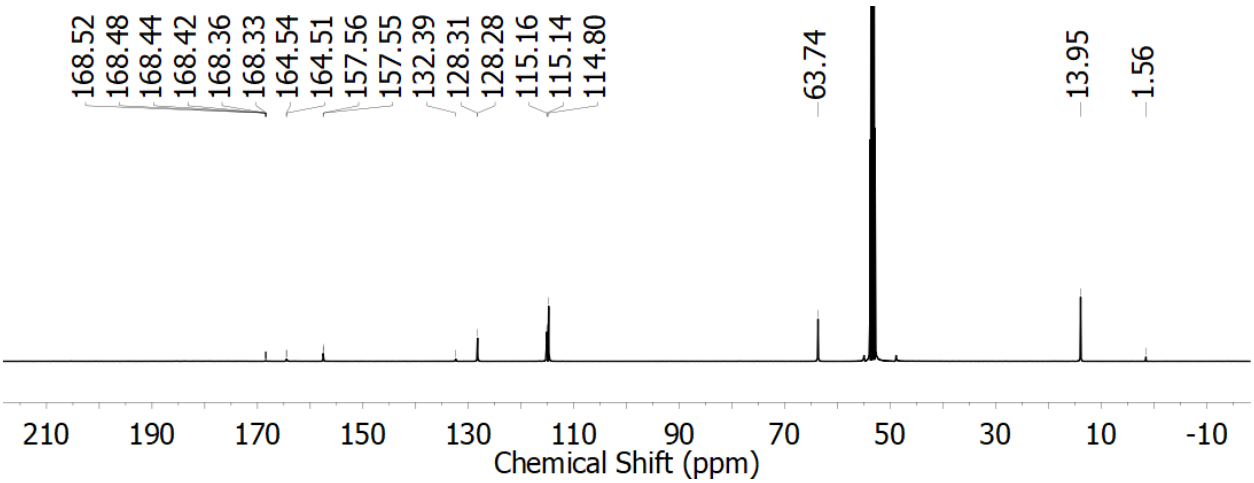

Figure F6. $^{13}C\{^{1}H\}$ NMR spectrum (126 MHz, CD_3CN) of **1-K**.

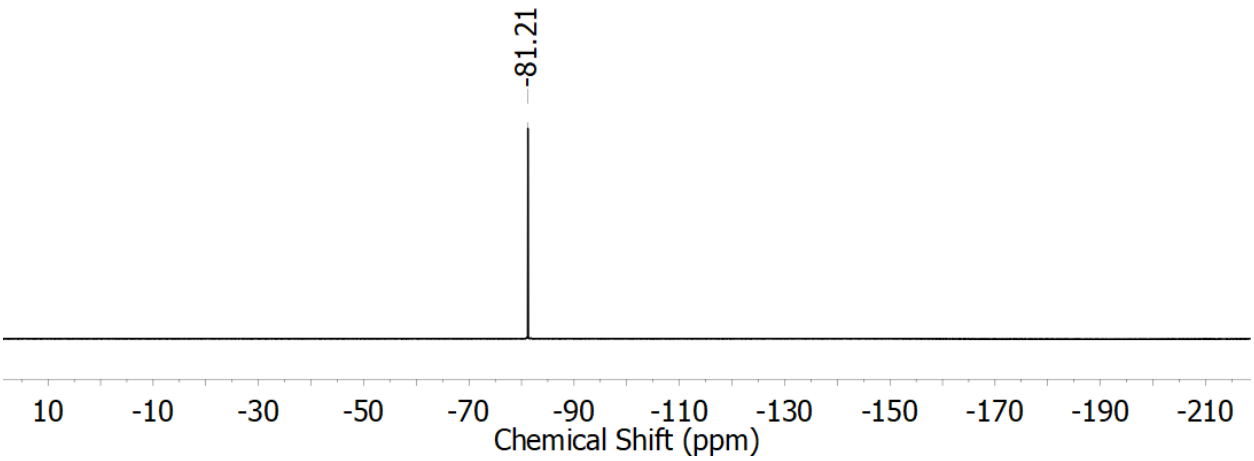

Figure F7. ^{19}F NMR spectrum (376 MHz, CD3CN) of **1-K**.

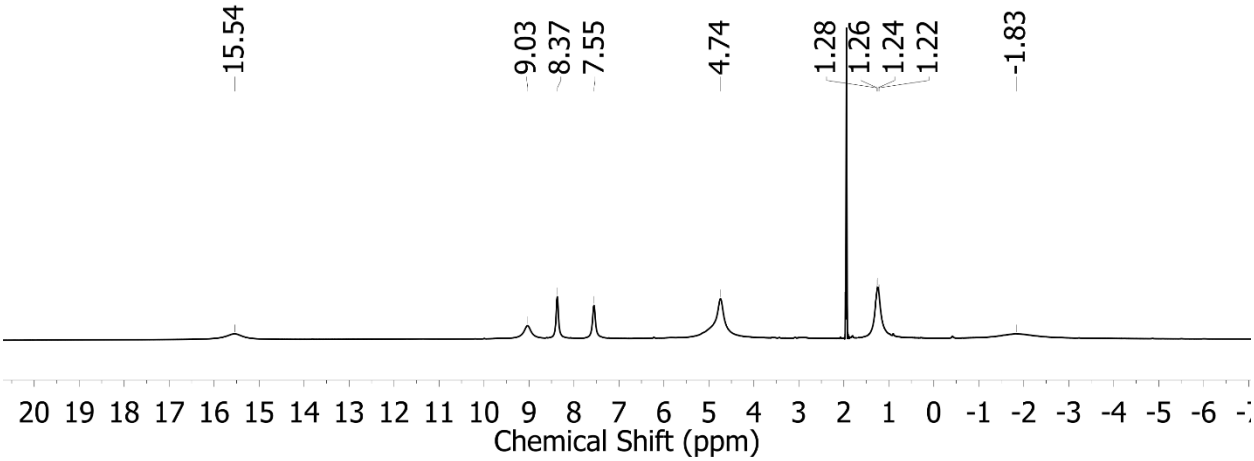

Figure F8. ^{1}H NMR spectrum (500 MHz, CD_3CN) of **1-Li**.

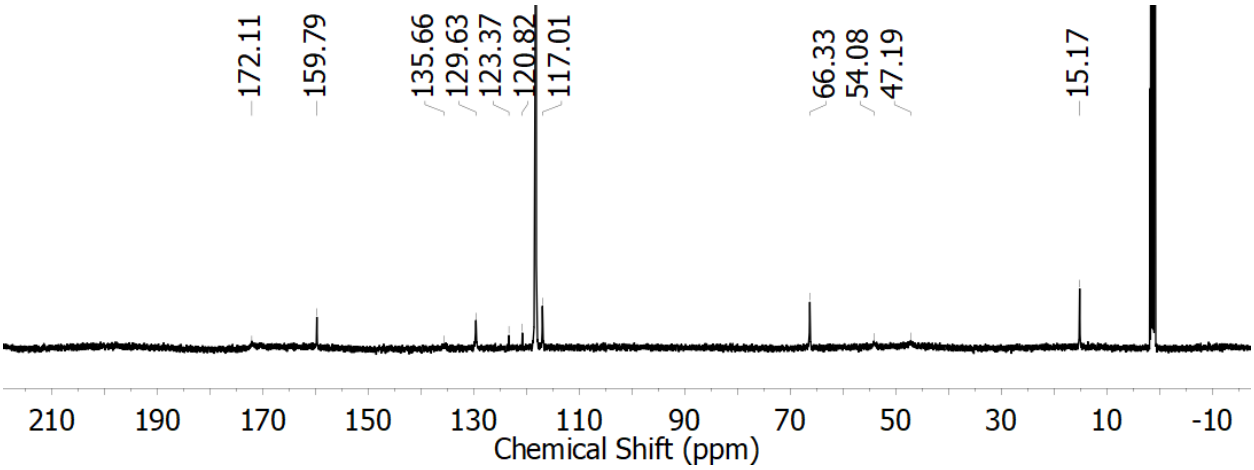

Figure F9. $^{13}C\{^{1}H\}$ NMR spectrum (126 MHz, CD_3CN) of **1-Li**.

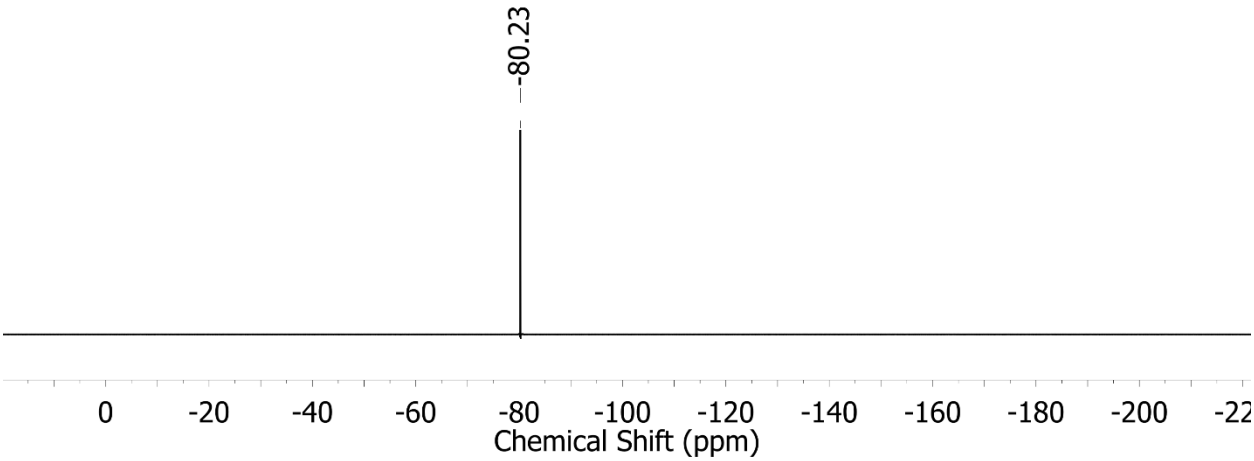

Figure F10. ^{19}F NMR spectrum (376 MHz, CD3CN) of **1-Li**.

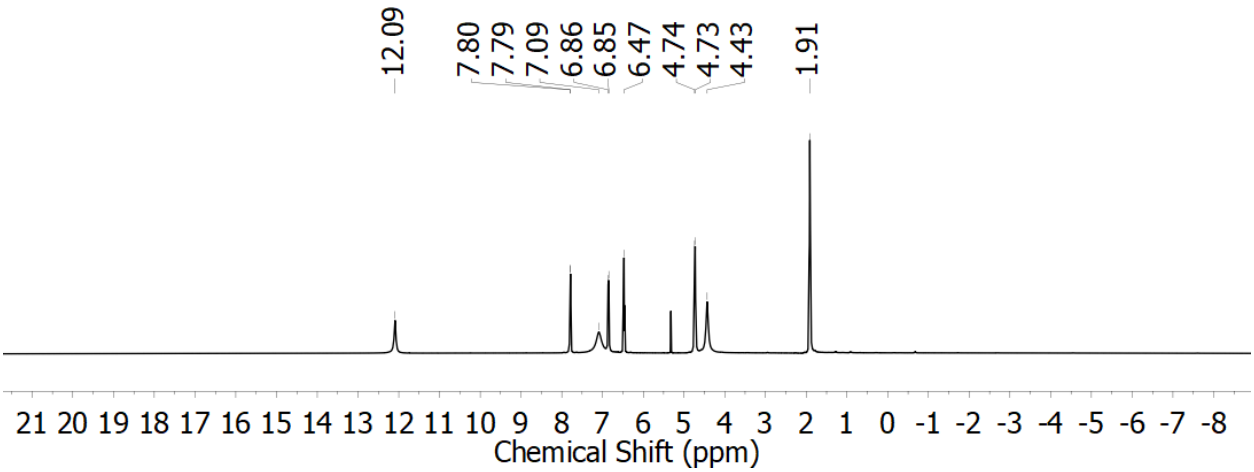

Figure F11. ^{1}H NMR spectrum (500 MHz, CD_3CN) of **1-Na**.

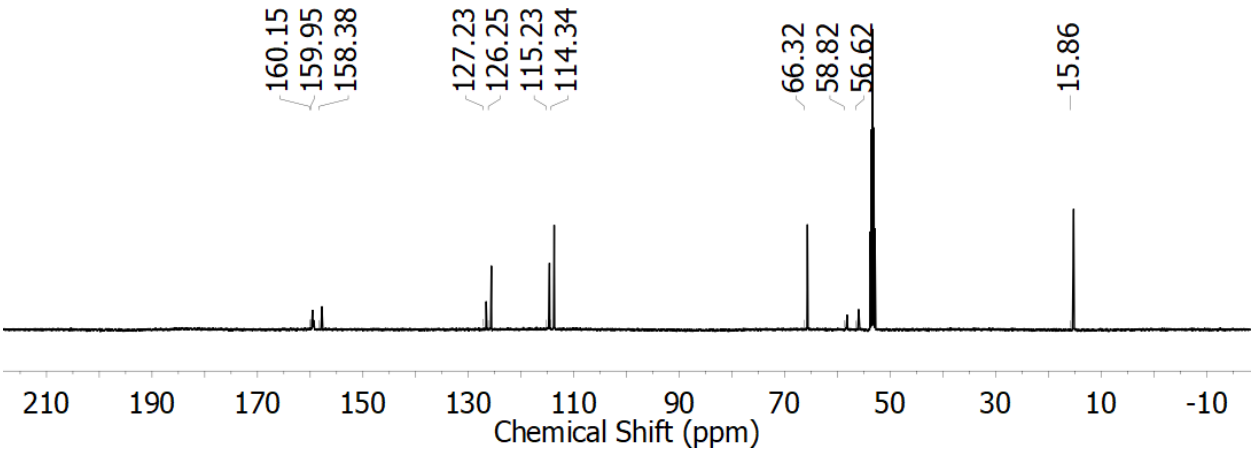

Figure F12. $^{13}C\{^{1}H\}$ NMR spectrum (126 MHz, CD_3CN) of **1-Na**.

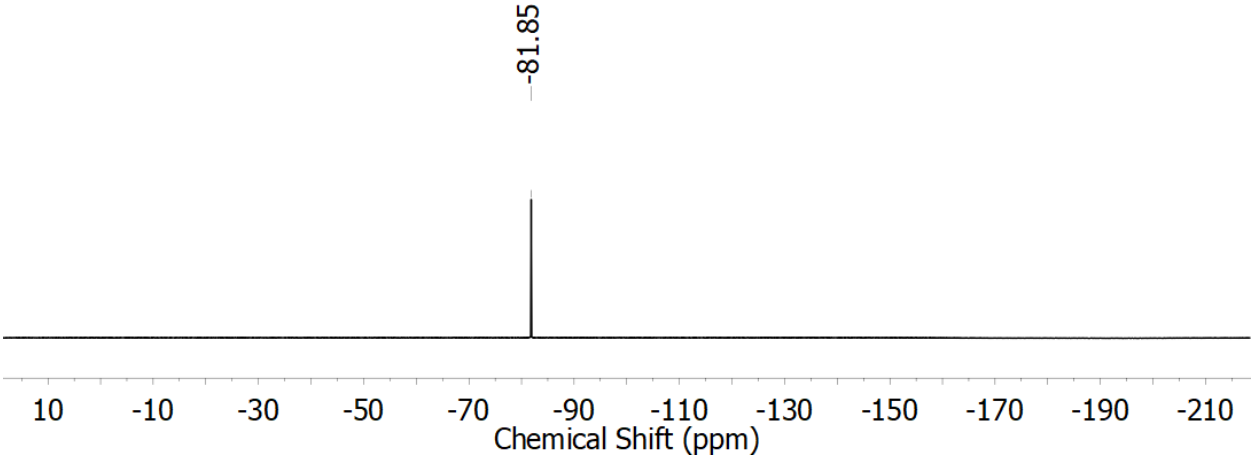

Figure F13. ^{19}F NMR spectrum (376 MHz, CD3CN) of **1-Na**.

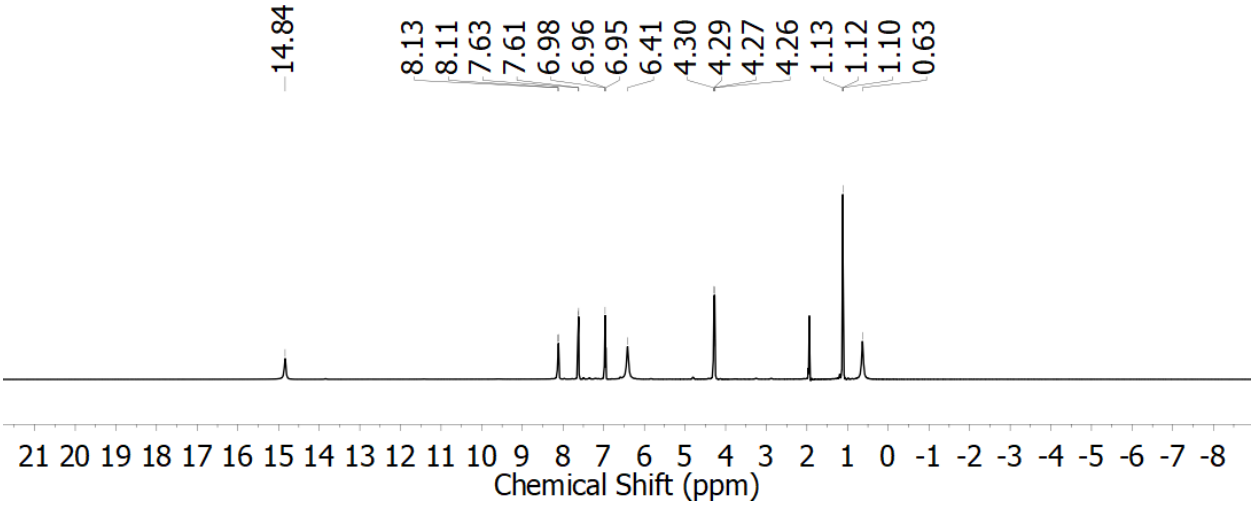

Figure F14. ^{1}H NMR spectrum (500 MHz, CD_3CN) of **1-Ba**.

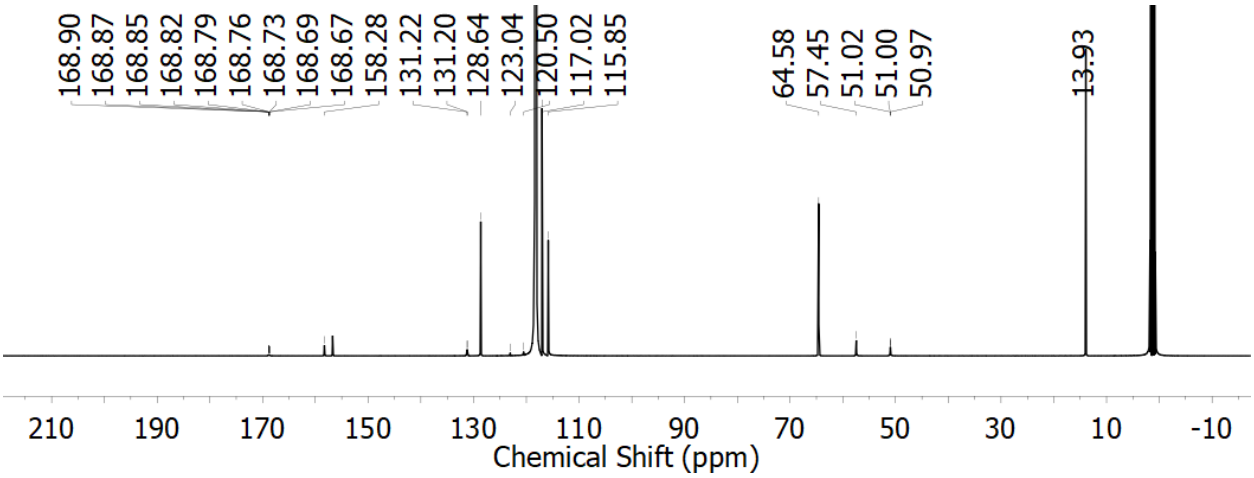

Figure F15. $^{13}C\{^{1}H\}$ NMR spectrum (126 MHz, CD_3CN) of **1-Ba**.

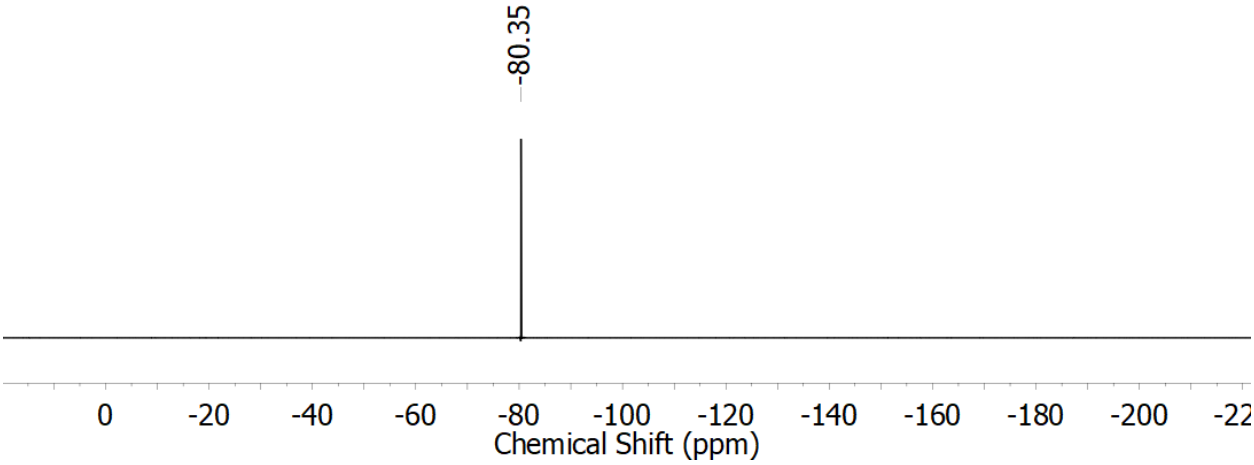

Figure F16. ^{19}F NMR spectrum (376 MHz, CD3CN) of **1-Ba**.

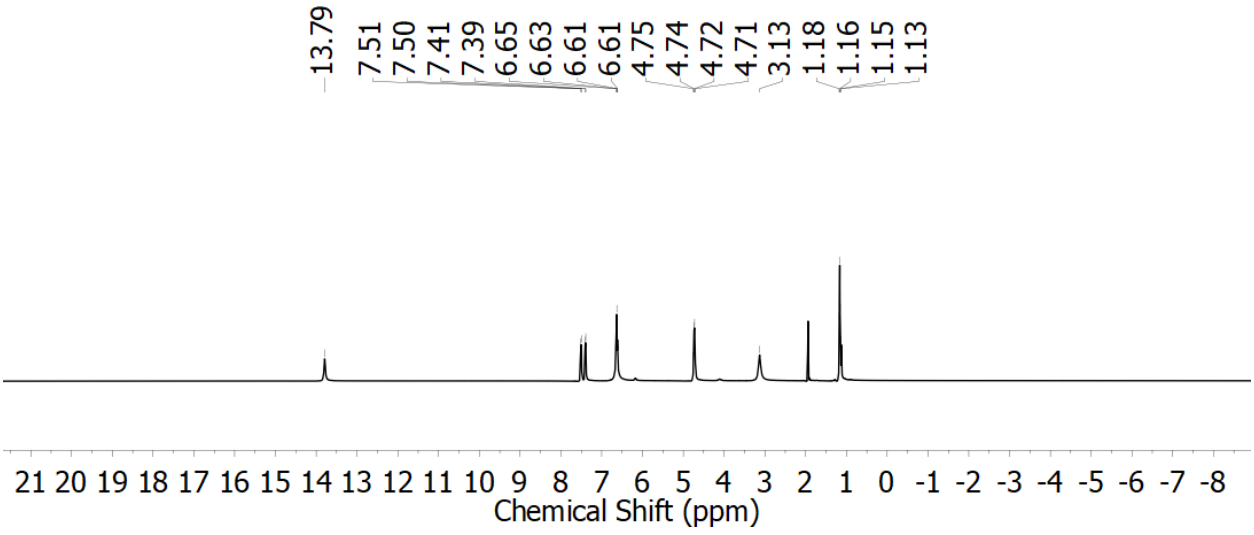

Figure F17. ^{1}H NMR spectrum (500 MHz, CD_3CN) of **1-Sr**.

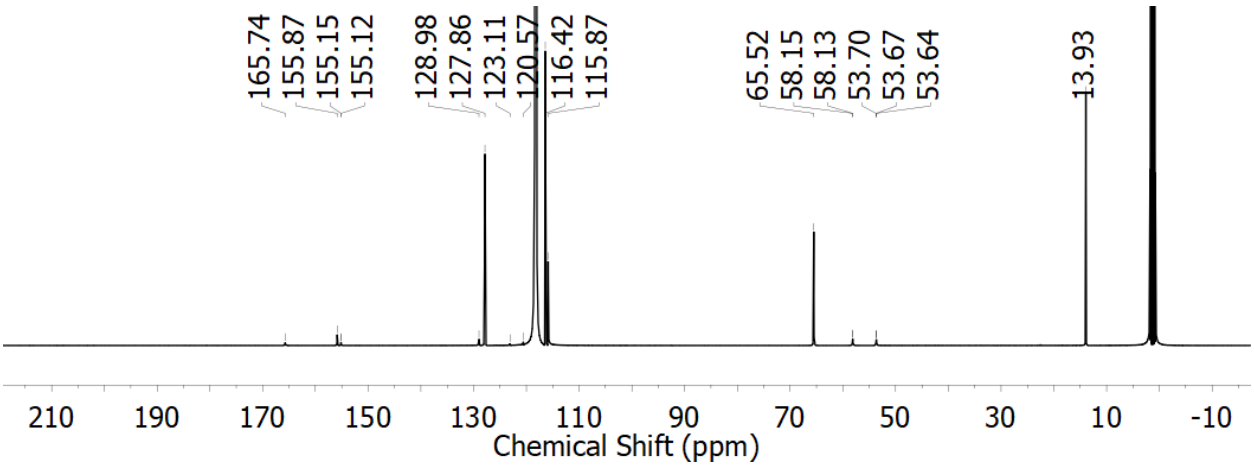

Figure F18. $^{13}C\{^{1}H\}$ NMR spectrum (126 MHz, CD_3CN) of **1-Sr**.

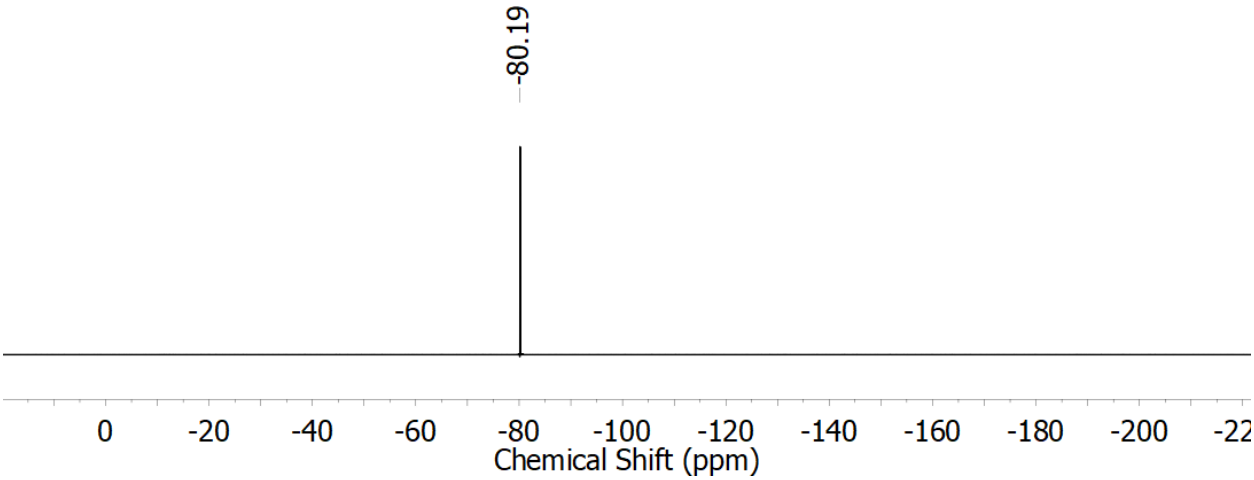

Figure F19. ^{19}F NMR spectrum (376 MHz, CD3CN) of **1-Sr**.

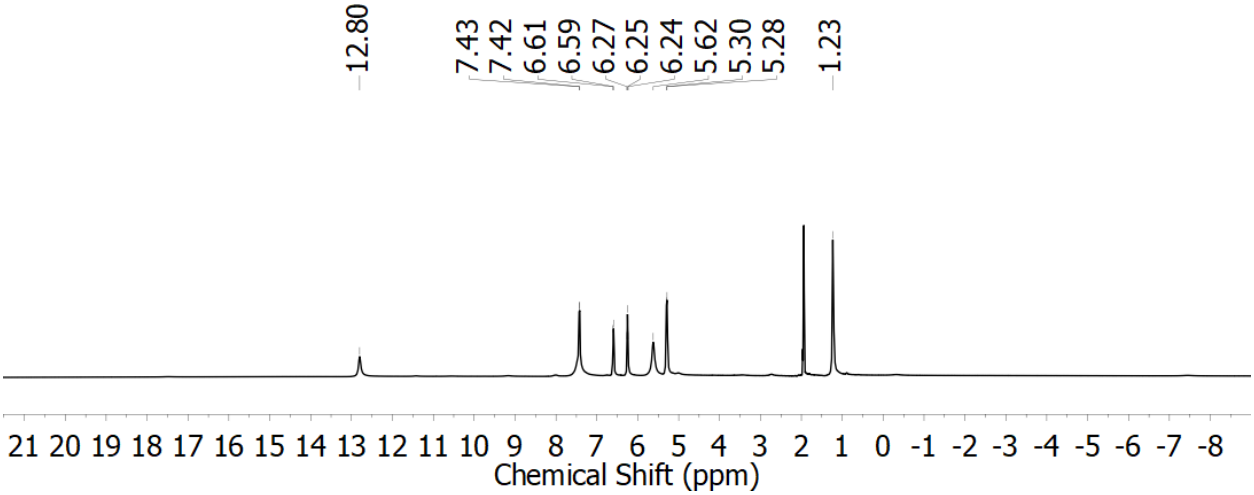

Figure F20. ^{1}H NMR spectrum (500 MHz, CD_3CN) of **1-Ca**.

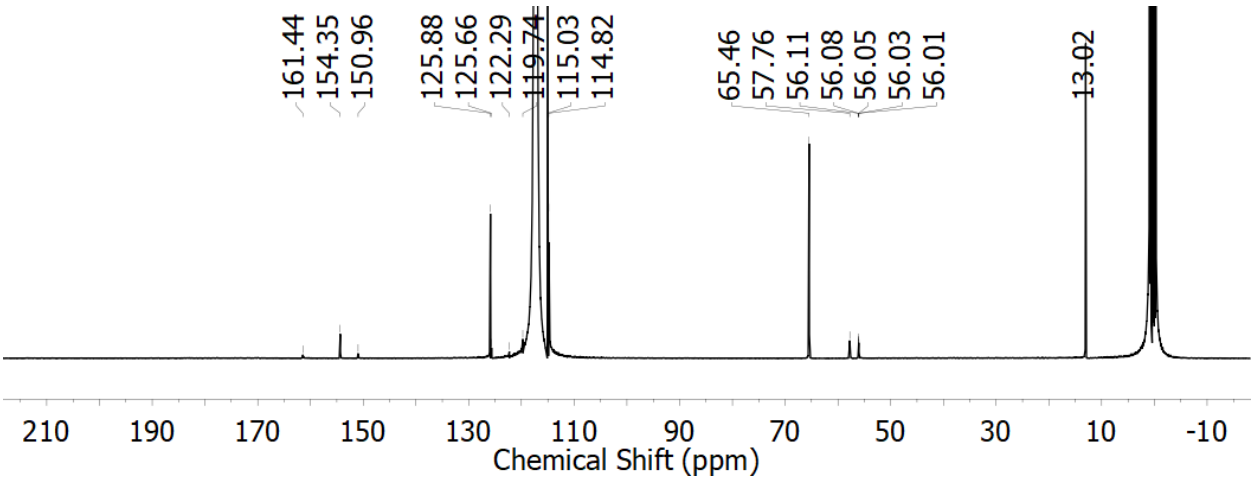

Figure F21. $^{13}C\{^{1}H\}$ NMR spectrum (126 MHz, CD_3CN) of **1-Ca**.

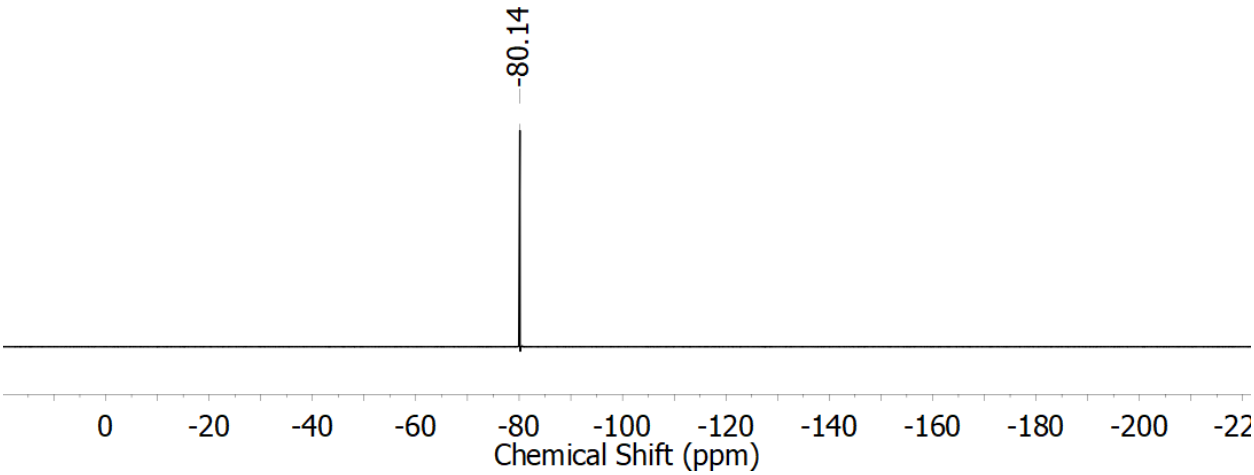

Figure F22. ^{19}F NMR spectrum (376 MHz, CD3CN) of **1-Ca**.

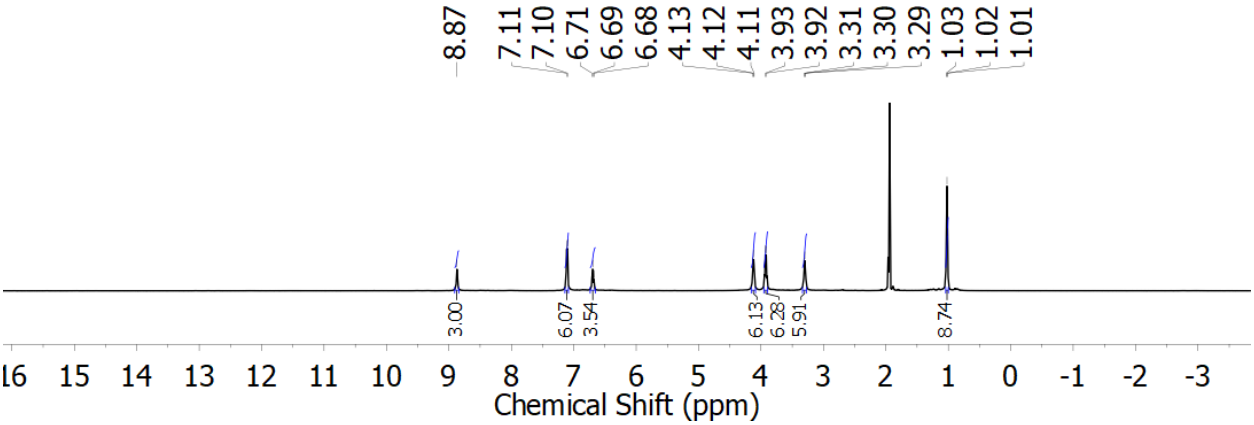

Figure F23. ^{1}H NMR spectrum (500 MHz, CD_3CN) of $\mathbf{2^{PF6}}$

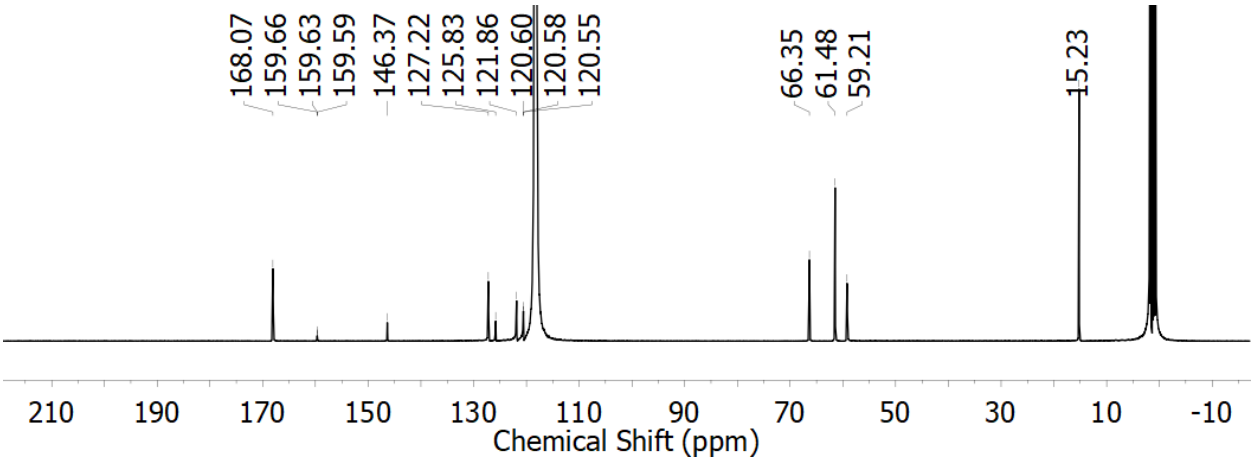

Figure F24. $^{13}C\{^{1}H\}$ NMR spectrum (126 MHz, CD_3CN) of **2**^{PF6}

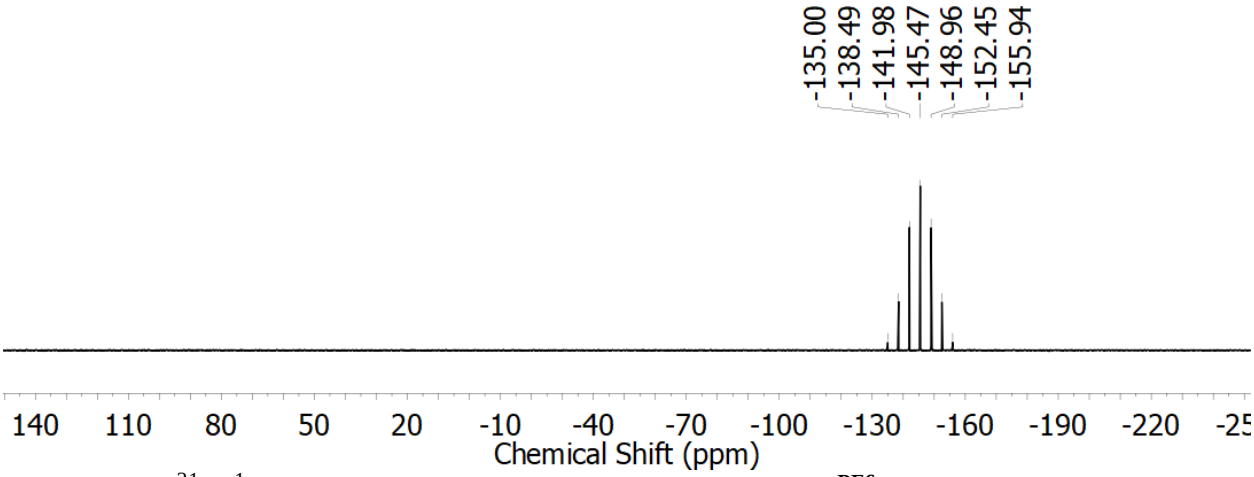

Figure F25. $^{31}P\{^{1}H\}$NMR spectrum (162 MHz, CD_3CN) of **2** ^{PF6}

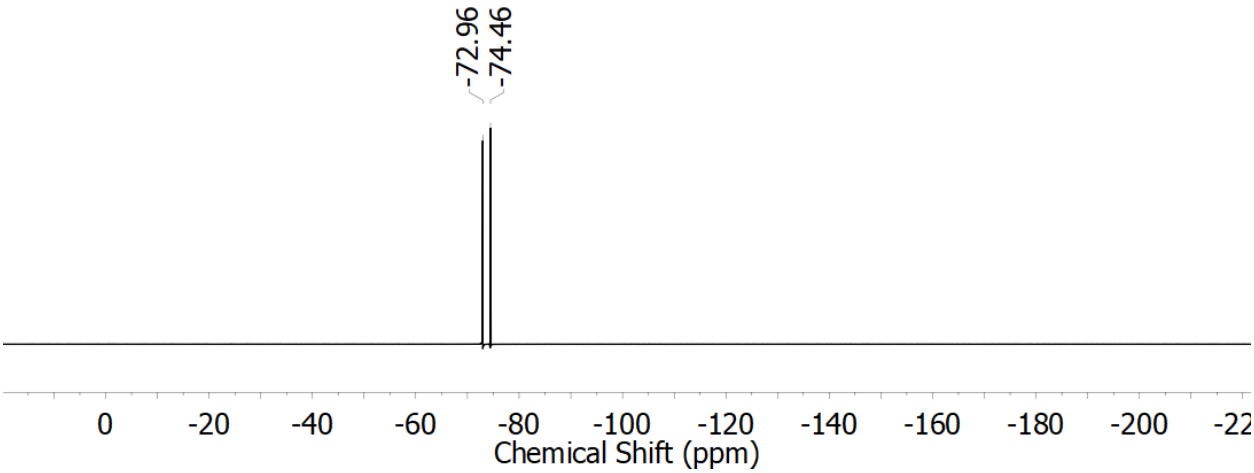

Figure F26. ^{19}F NMR spectrum (376 MHz, CD3CN) of **2** ^{PF6}

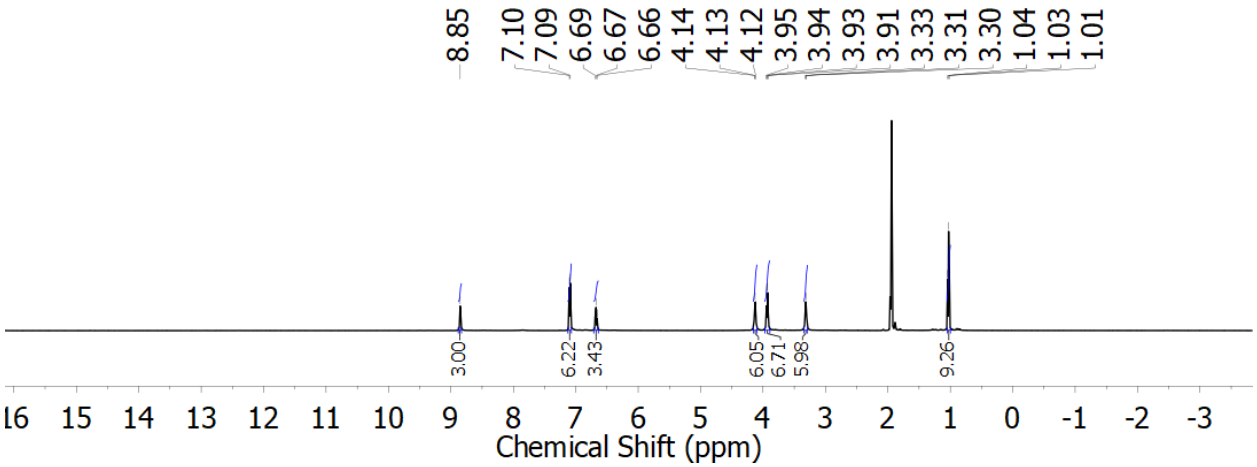

Figure F27. ^{1}H NMR spectrum (500 MHz, CD_3CN) of **2^{OTf}**

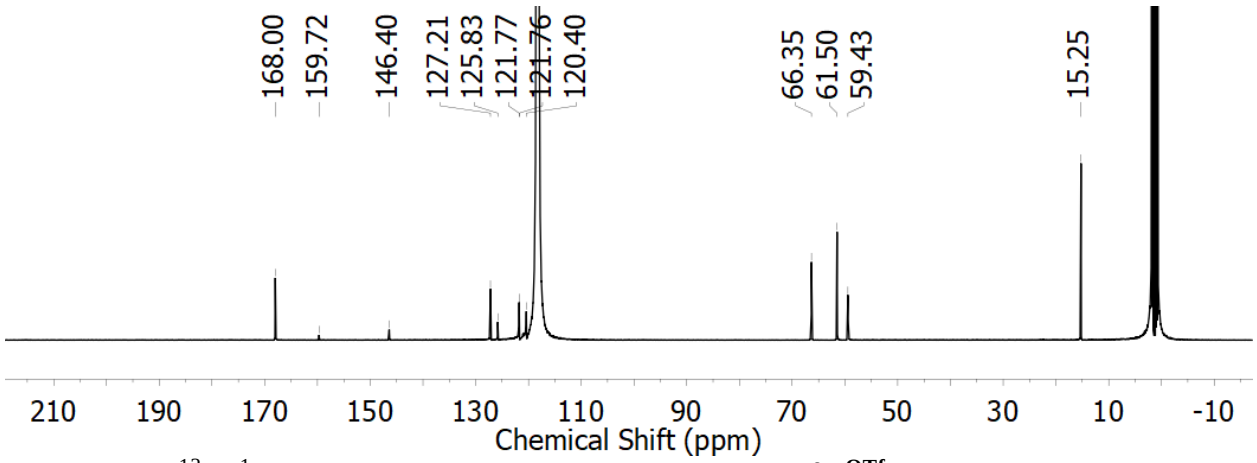

Figure F28. $^{13}C\{^{1}H\}$ NMR spectrum (126 MHz, CD_3CN) of **2^{OTf}**

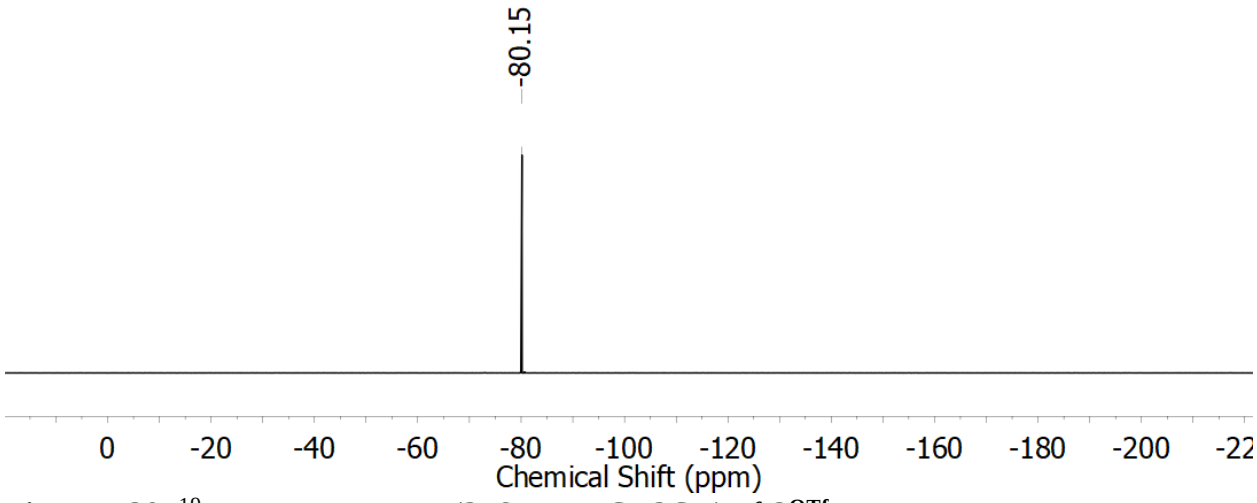

Figure F29. ^{19}F NMR spectrum (376 MHz, CD3CN) of **2^{OTf}**

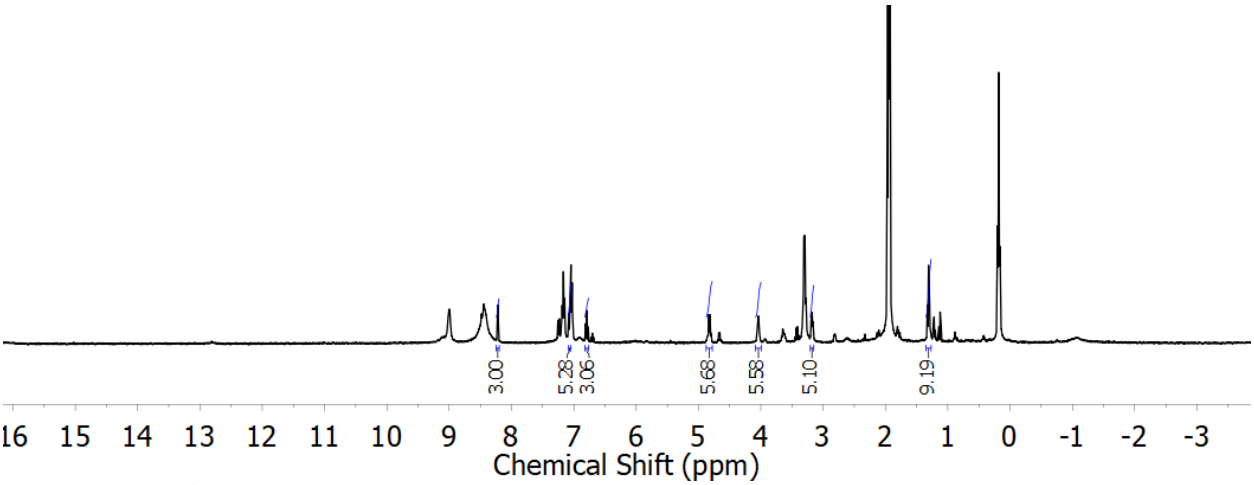

Figure F30. ^{1}H NMR spectrum (500 MHz, CD_3CN) of **1-La**. Integrations correspond to diamagnetic monometallic La^{3+} bound $\mathbf{L^{OEt}H_3}$ species.

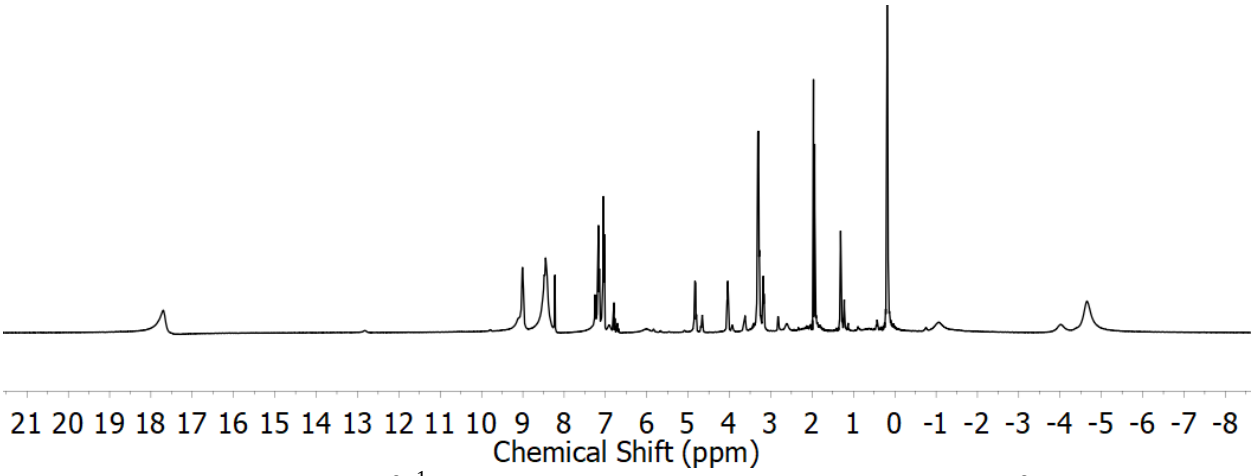

Figure F31. Wide range of ^{1}H NMR spectrum (500 MHz, CD_3CN) of **1-La**. Multiple paramagnetic and diamagnetic species observed.

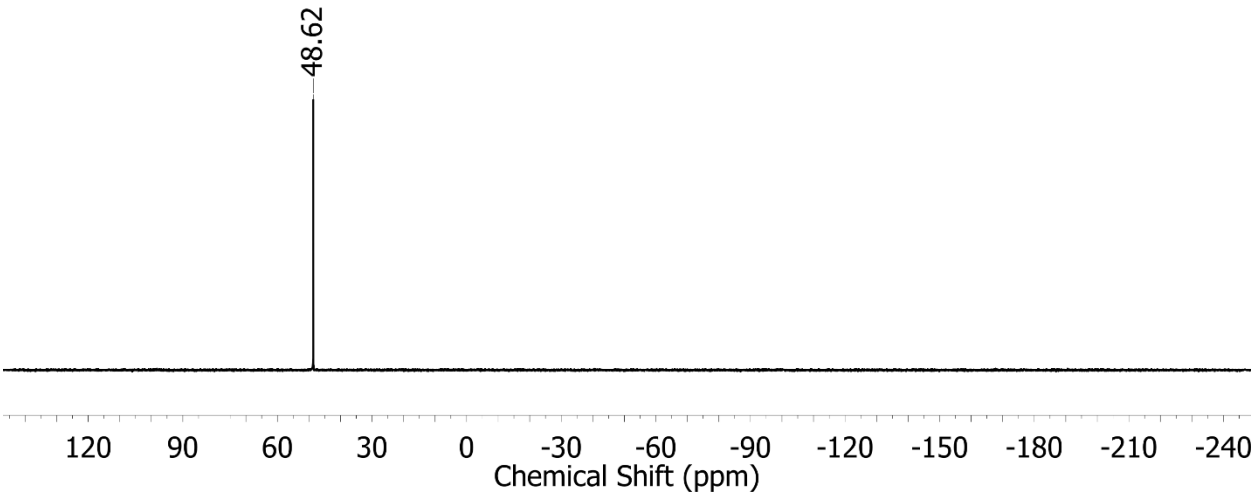

Figure F32. $^{31}P\{^{1}H\}$ NMR spectrum (162 MHz, CD_3CN) of TEPO (Triethyl phosphine oxide).

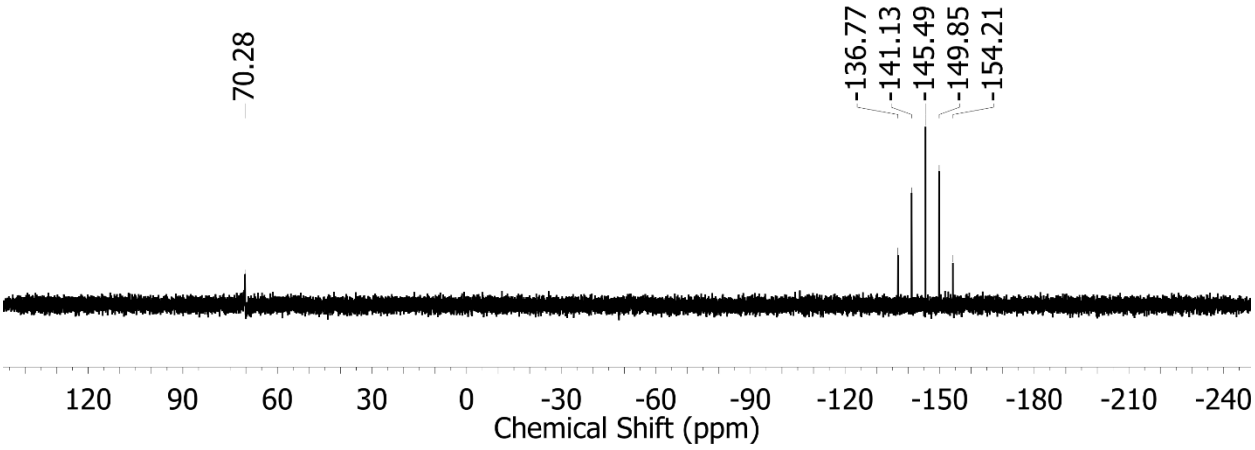

Figure F33. $^{31}P\{^{1}H\}$ NMR spectrum (162 MHz, CD_3CN) of $\mathbf{2^{PF6}}$:1 **1**:TEPO (Triethyl phosphine oxide).

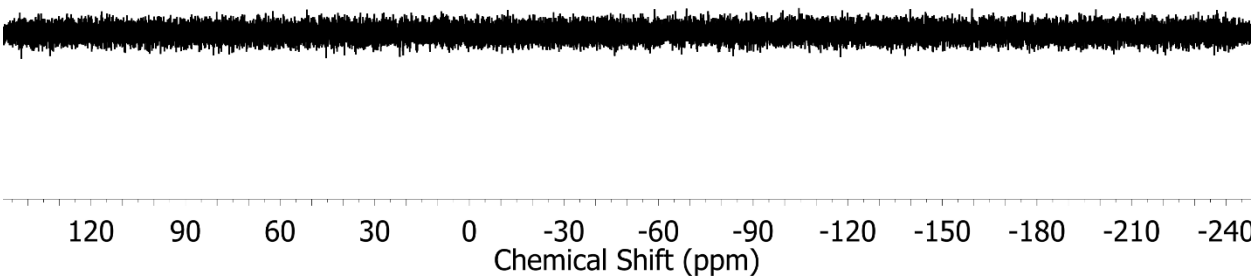

Figure F34. $^{31}P\{^{1}H\}$ NMR spectrum (162 MHz, CD_3CN) of 1:1 **1**:TEPO (Triethyl phosphine oxide).

Infrared Spectroscopy

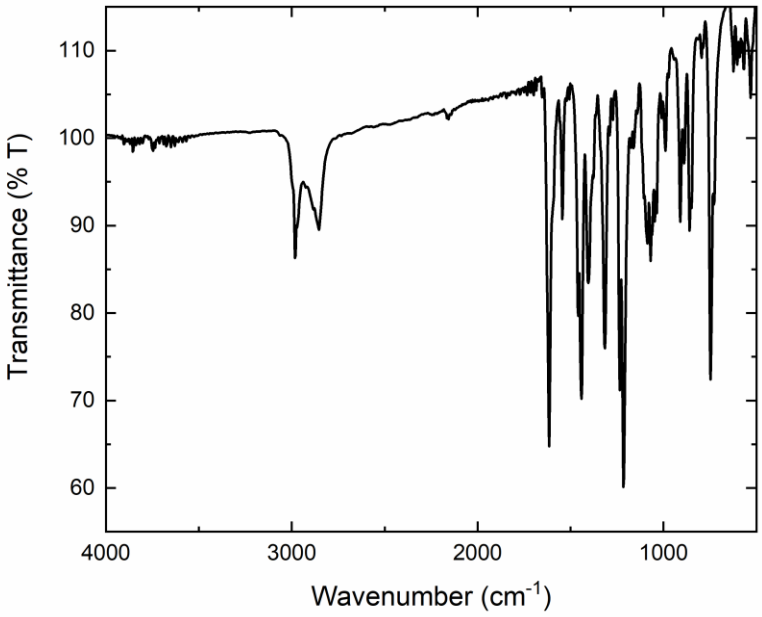

Figure F35. Solid-state IR spectrum of **1**

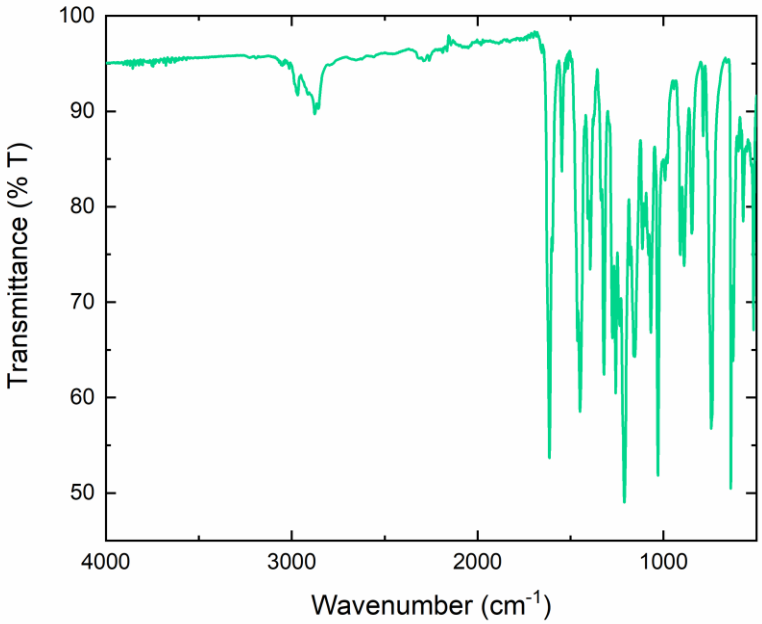

Figure F36. Solid-state IR spectrum of **1-K**

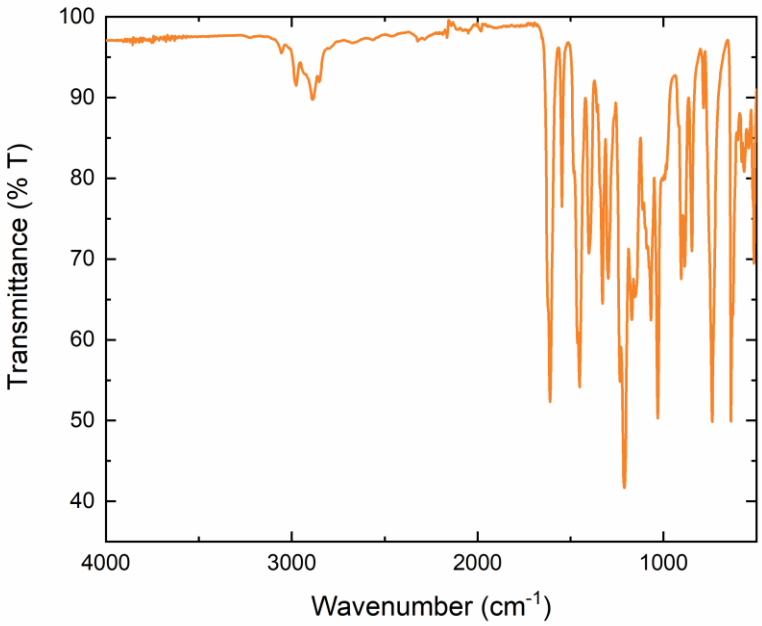

Figure F37. Solid-state IR spectrum of **1-Na**

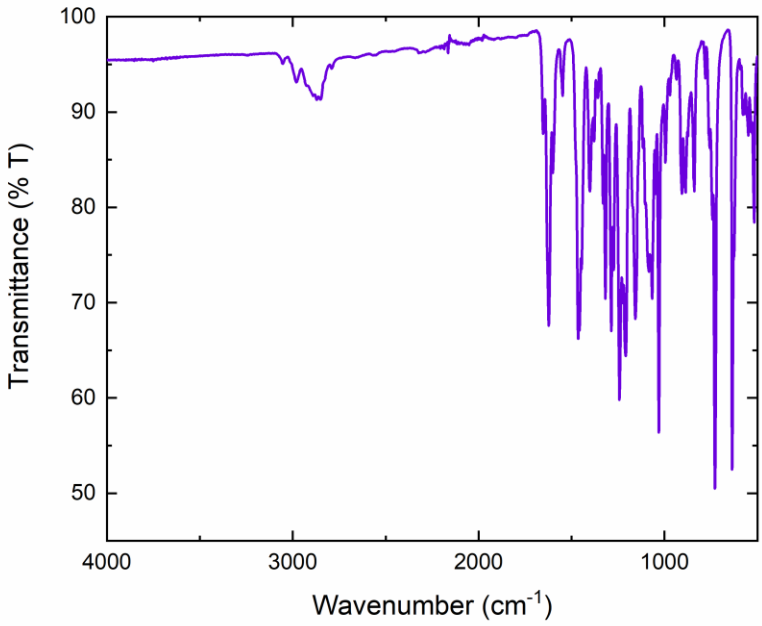

Figure F38. Solid-state IR spectrum of **1-Li**

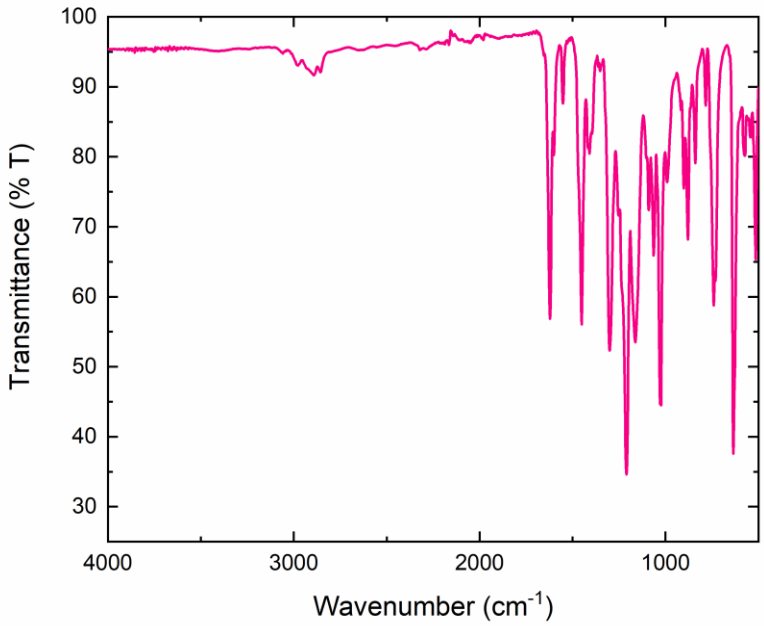

Figure F39. Solid-state IR spectrum of **1-Ba**

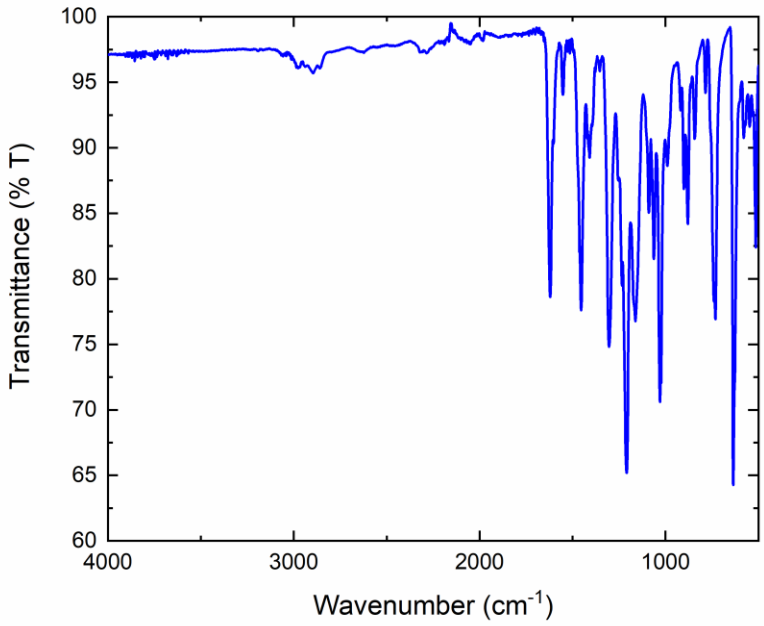

Figure F40. Solid-state IR spectrum of **1-Sr**

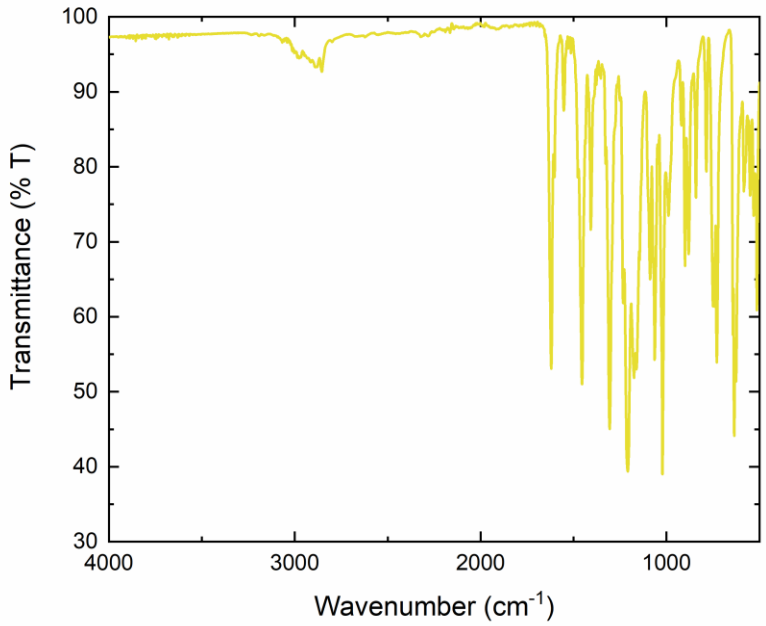

Figure F41. Solid-state IR spectrum of **1-Ca**

UV-Visible Spectroscopy

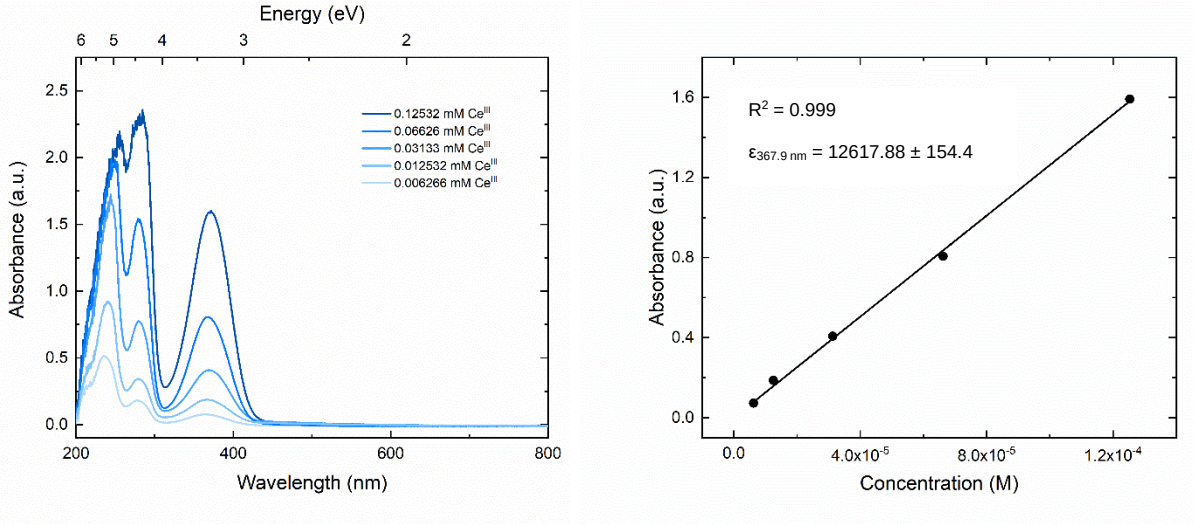

Figure F42. Electronic absorption spectra of **1** in CH_3CN.

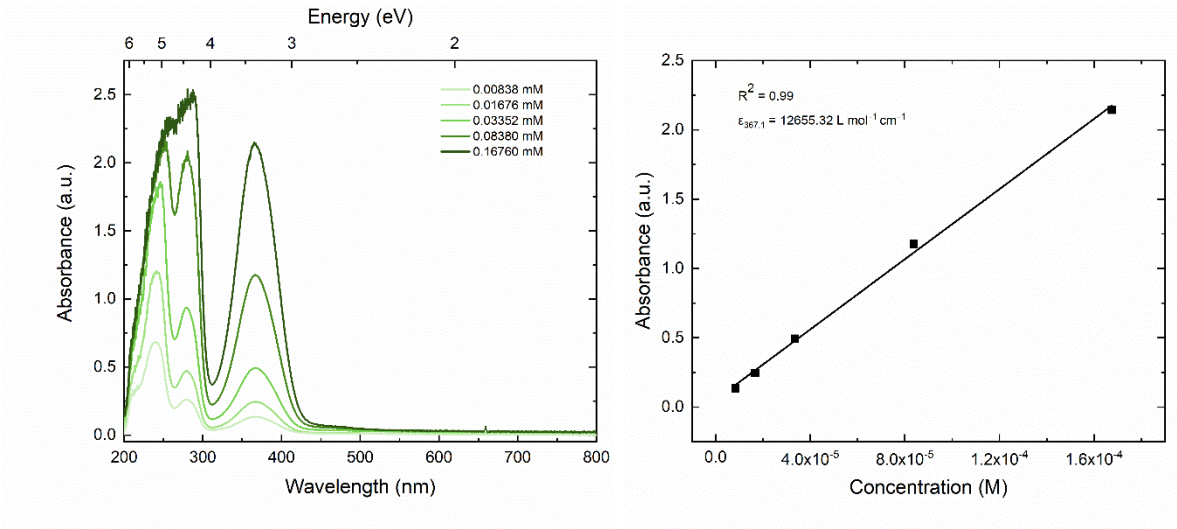

Figure F43. Electronic absorption spectra of **1-K** in CH_3CN.

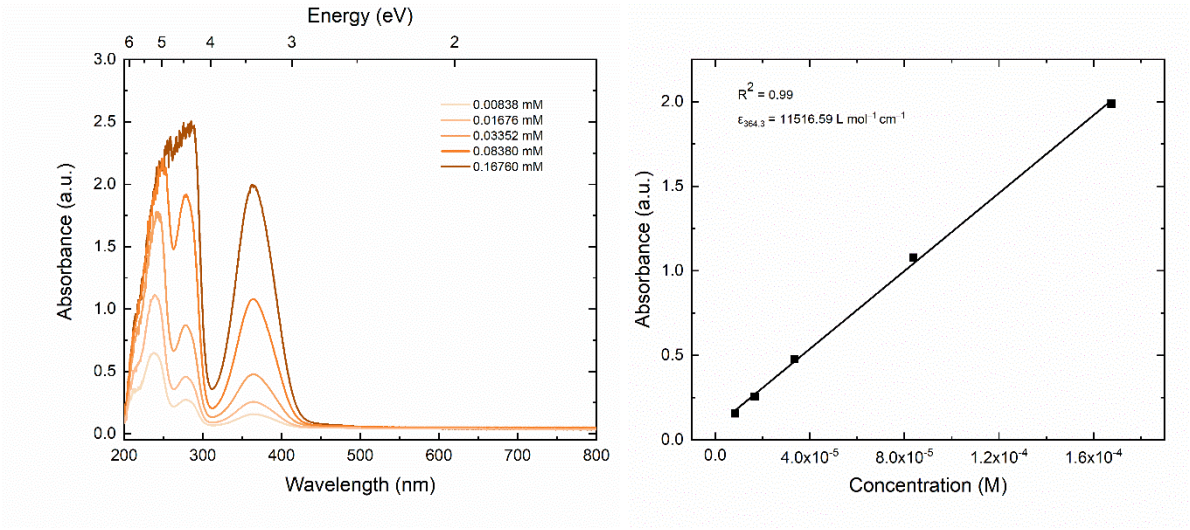

Figure F44. Electronic absorption spectra of **1-Na** in CH_3CN.

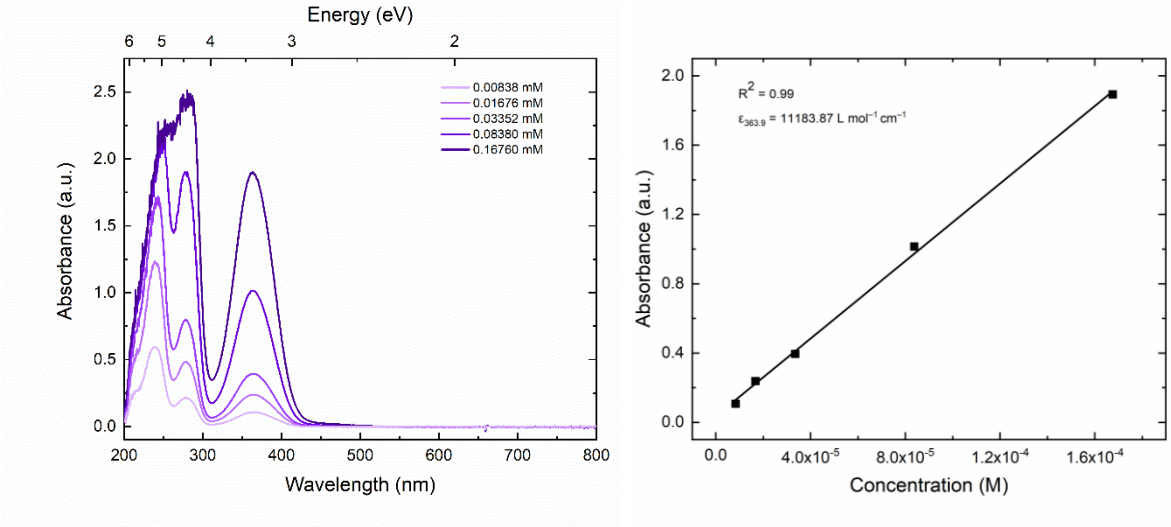

Figure F45. Electronic absorption spectra of **1-Li** in CH_3CN.

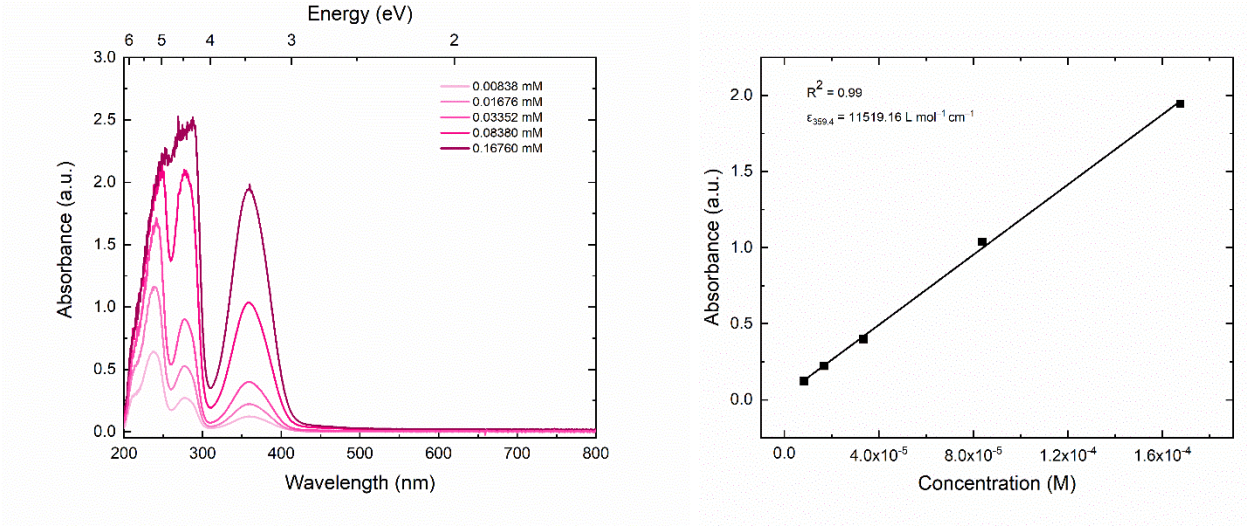

Figure F46. Electronic absorption spectra of **1-Ba** in CH_3CN.

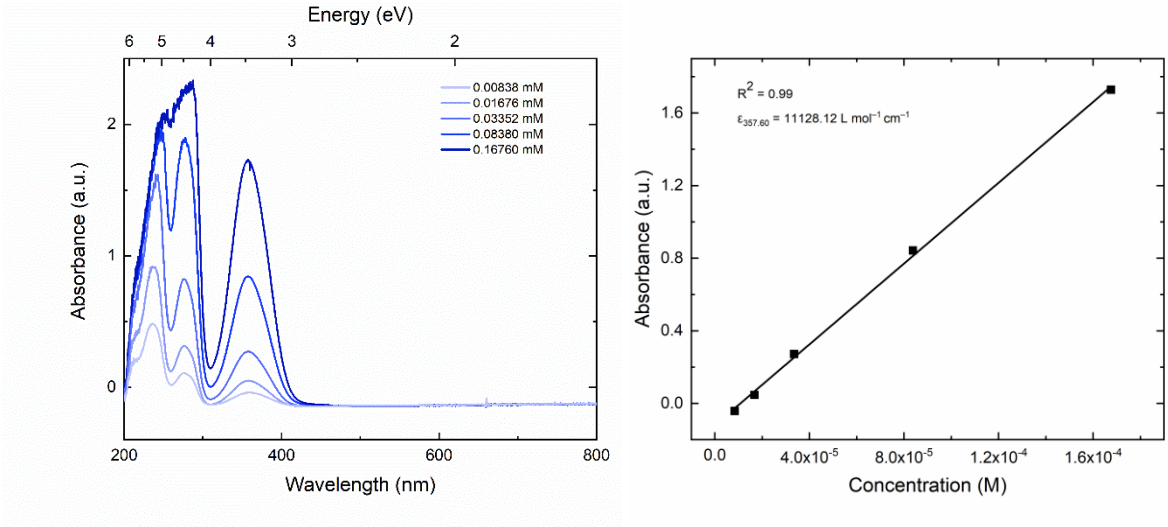

Figure F47. Electronic absorption spectra of **1-Sr** in CH_3CN.

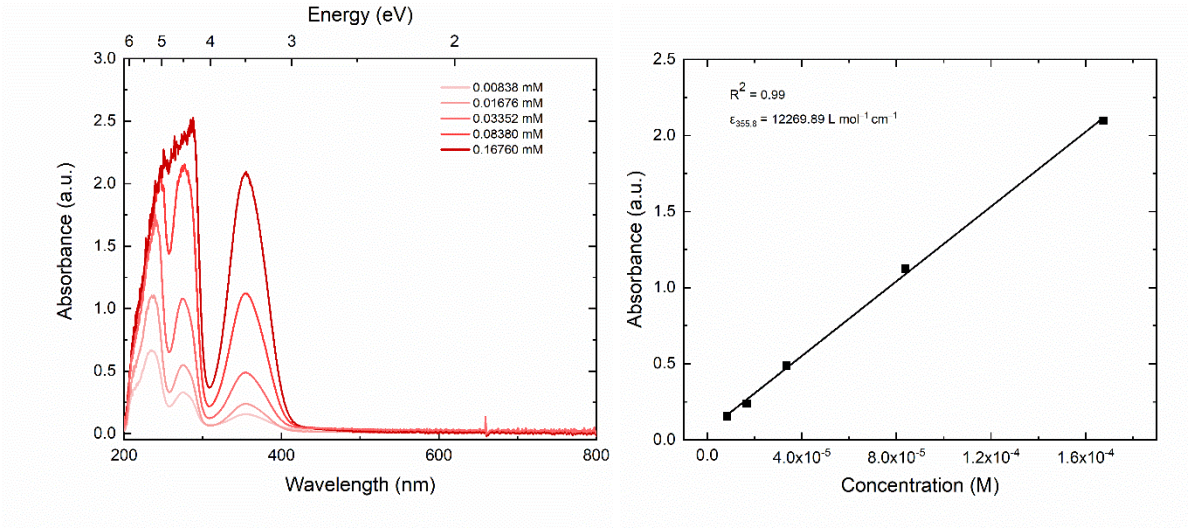

Figure F48. Electronic absorption spectra of **1-Ca** in CH_3CN.

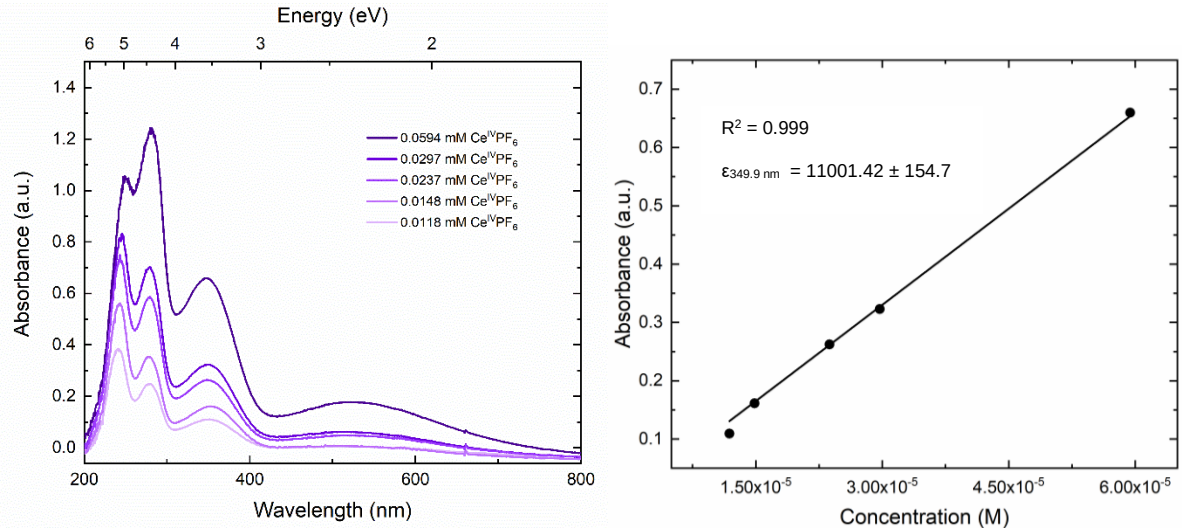

Figure F49. Electronic absorption spectra of $\mathbf{2^{PF6}}$ in CH_3CN.

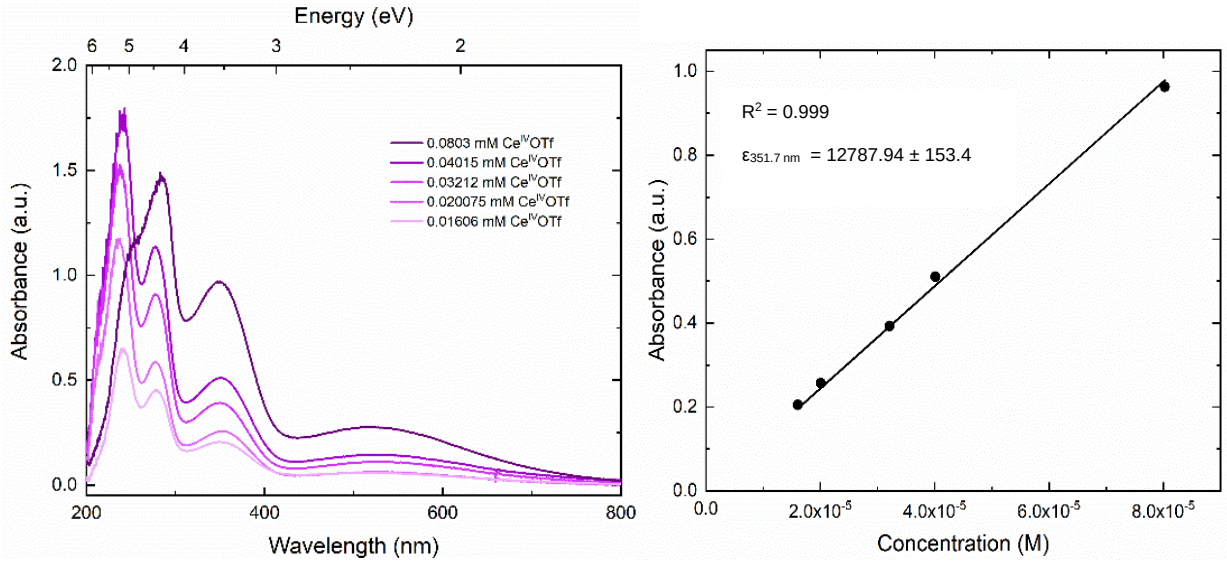

Figure F50. Electronic absorption spectra of $\mathbf{2^{OTf}}$ in CH_3CN.

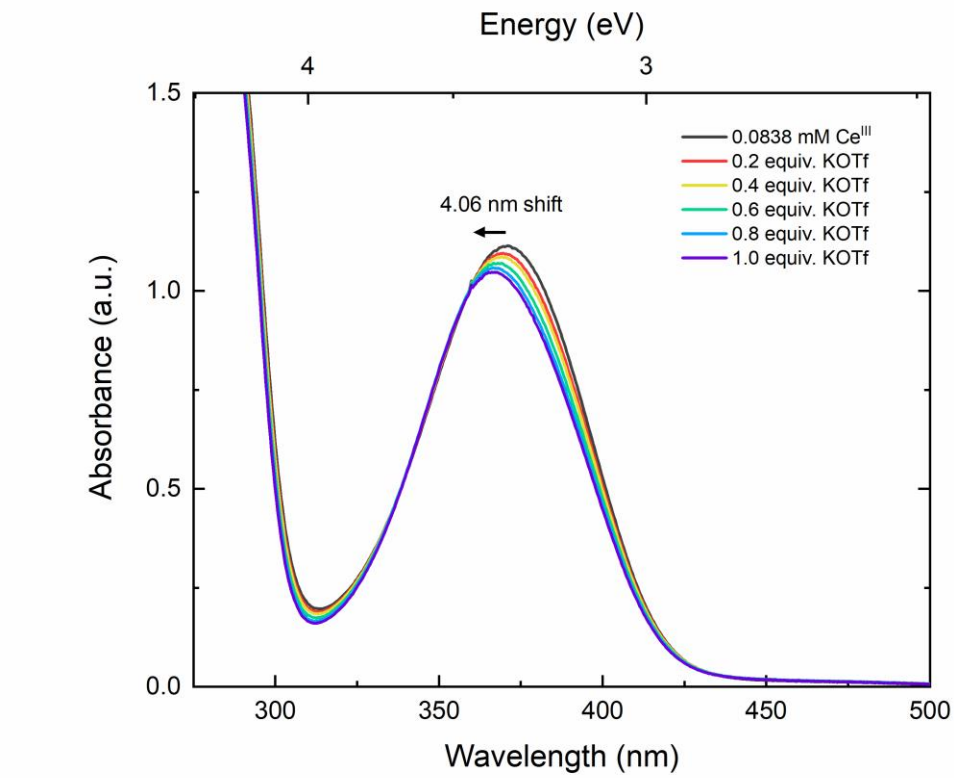

Figure F51. Electronic absorption spectra of **1** with KOTf in CH_3CN.

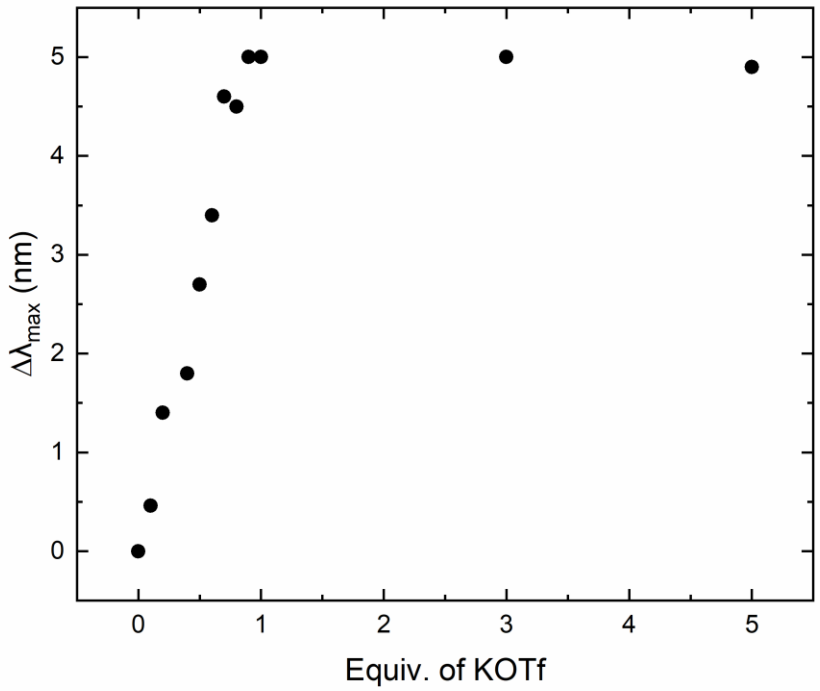

Figure F52. Plot of change of λ_{max} for titration of **1** with KOTf in CH_3CN.

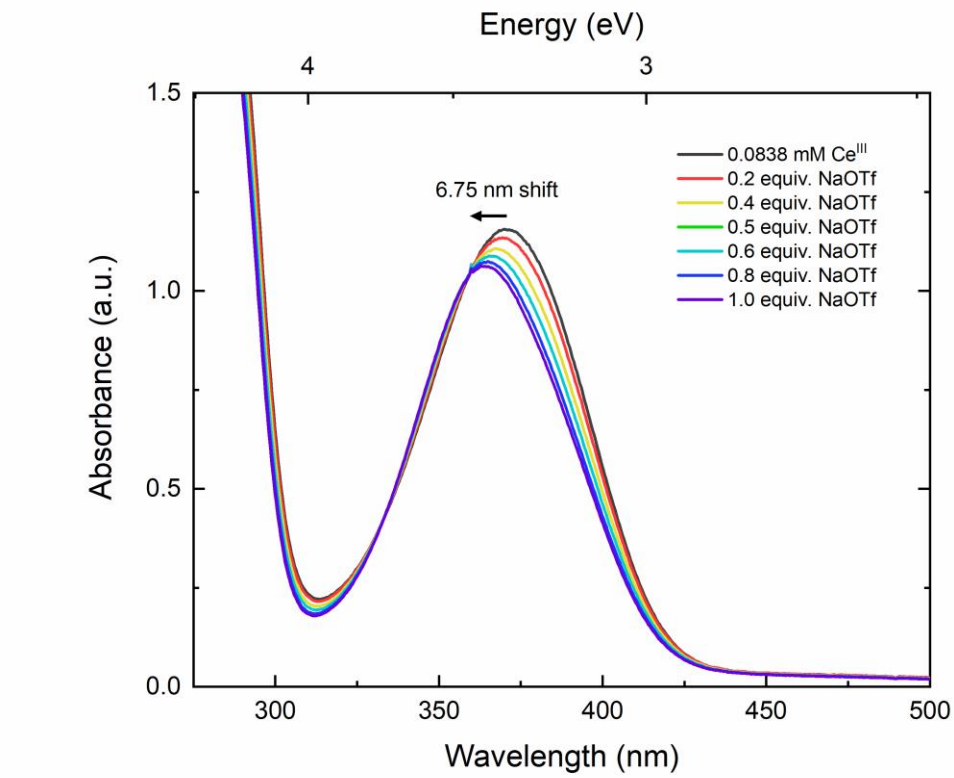

Figure F53. Electronic absorption spectra of **1** with NaOTf in CH_3CN.

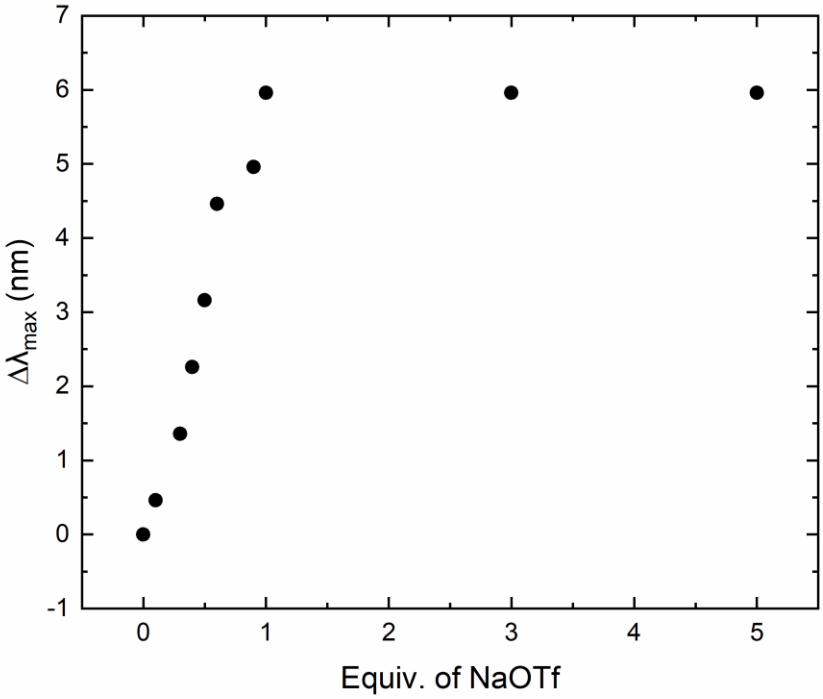

Figure F54. Plot of change of λ_{max} for titration of **1** with NaOTf in CH_3CN..

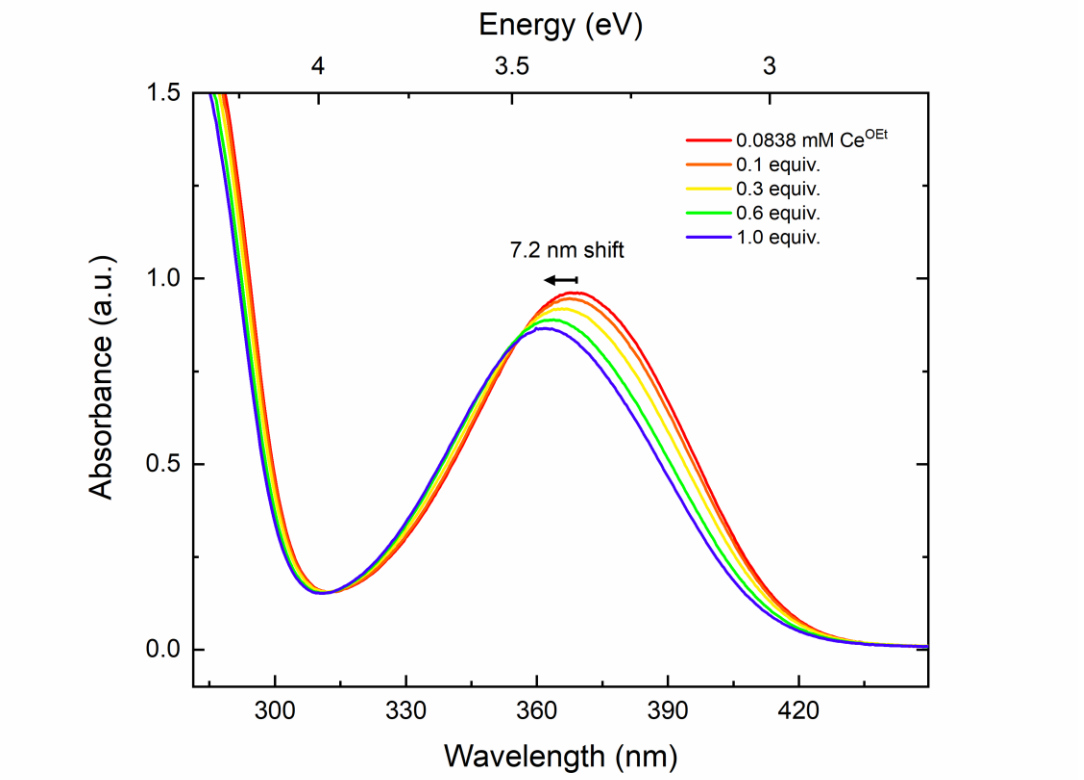

Figure F55. Electronic absorption spectra of **1** with LiOTf in CH_3CN.

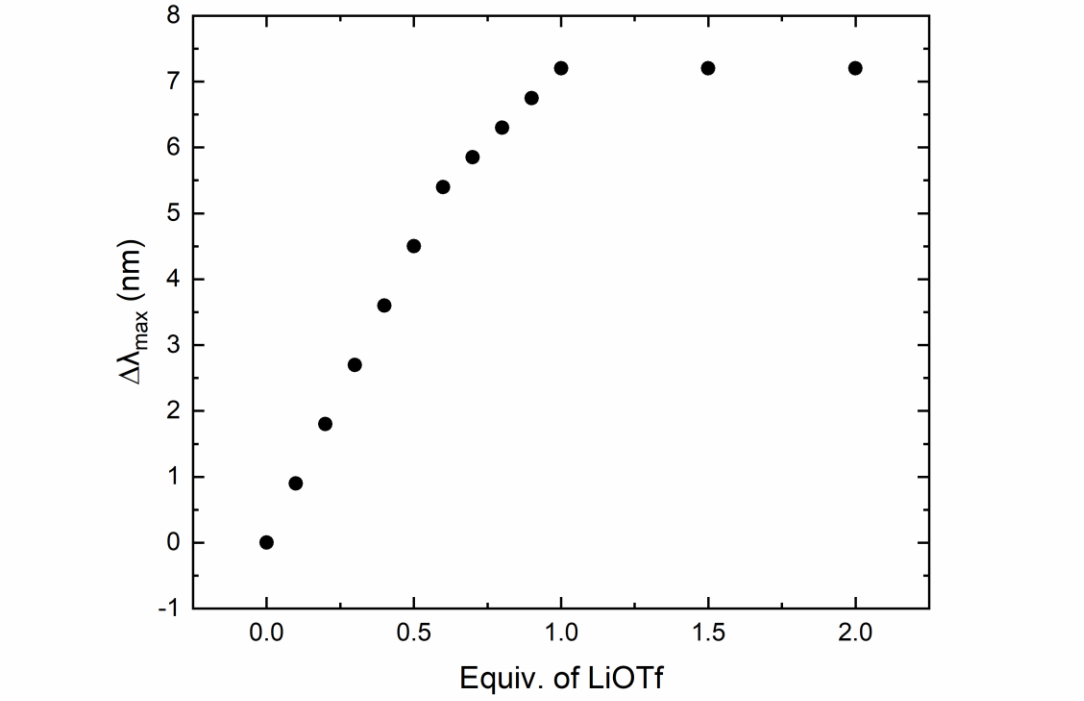

Figure F56. Plot of change of λ_{max} for titration of **1** with LiOTf in CH_3CN.

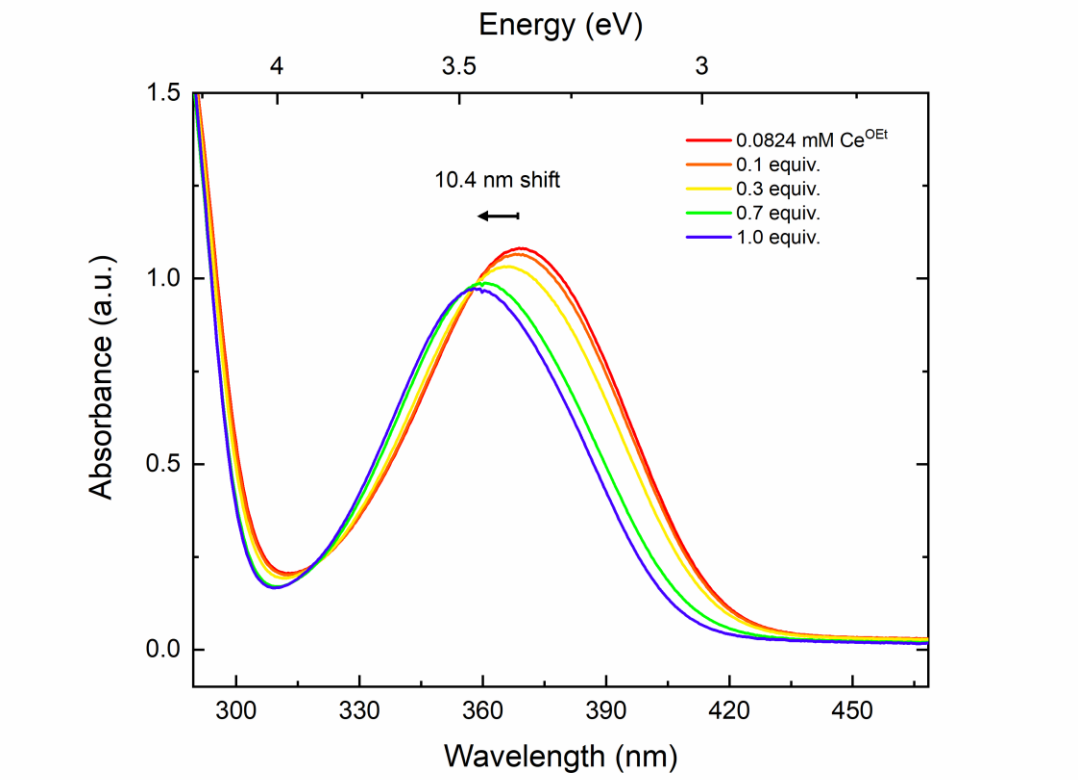

Figure F57. Electronic absorption spectra of **1** with $Ba(OTf)_2$ in CH_3CN.

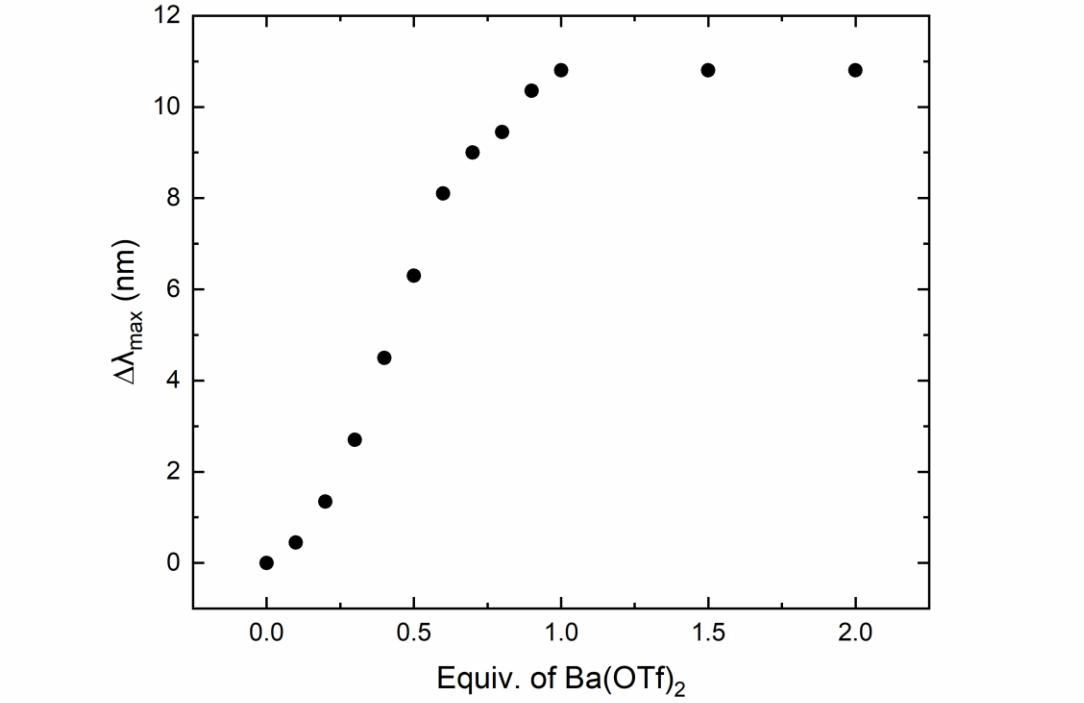

Figure F58. Plot of change of λ_{max} for titration of **1** with $Ba(OTf)_2$ in CH_3CN.

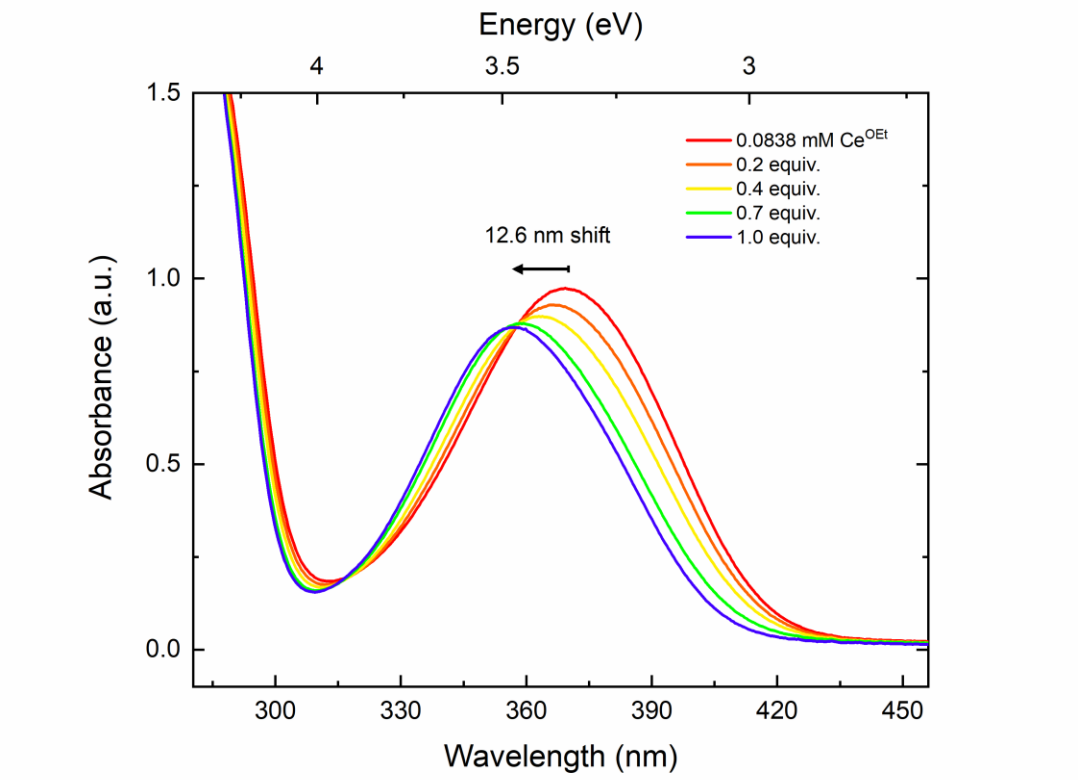

Figure F59. Electronic absorption spectra of **1** with $Sr(OTf)_2$ in CH_3CN.

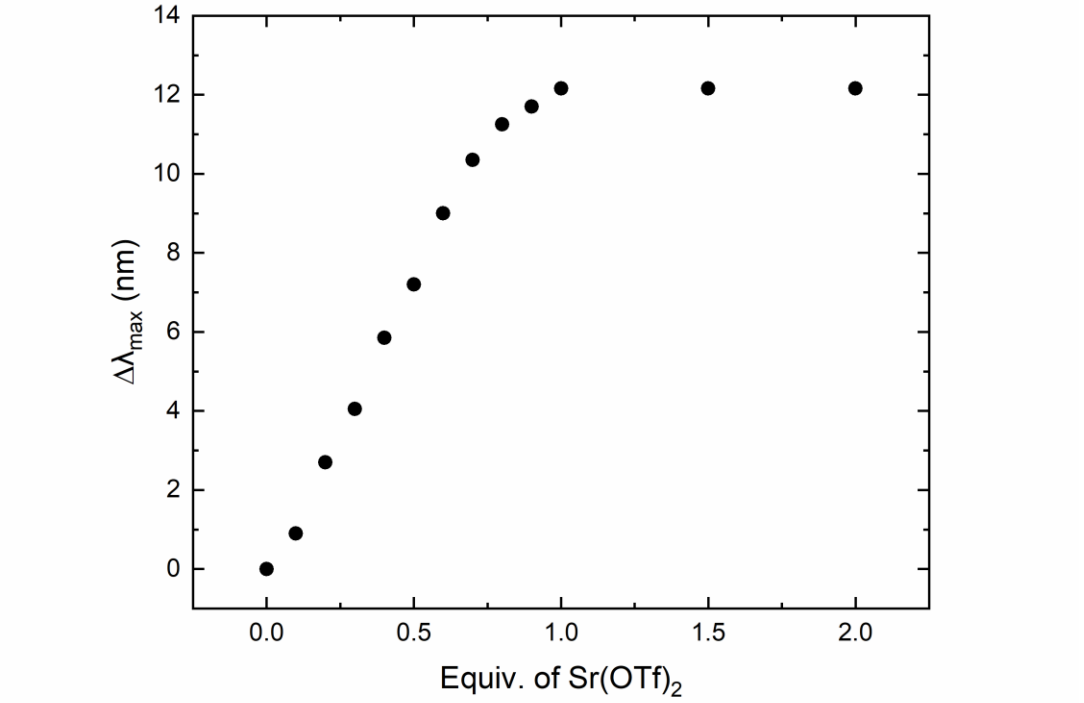

Figure F60. Plot of change of λ_{max} for titration of **1** with $Sr(OTf)_2$ in CH_3CN.

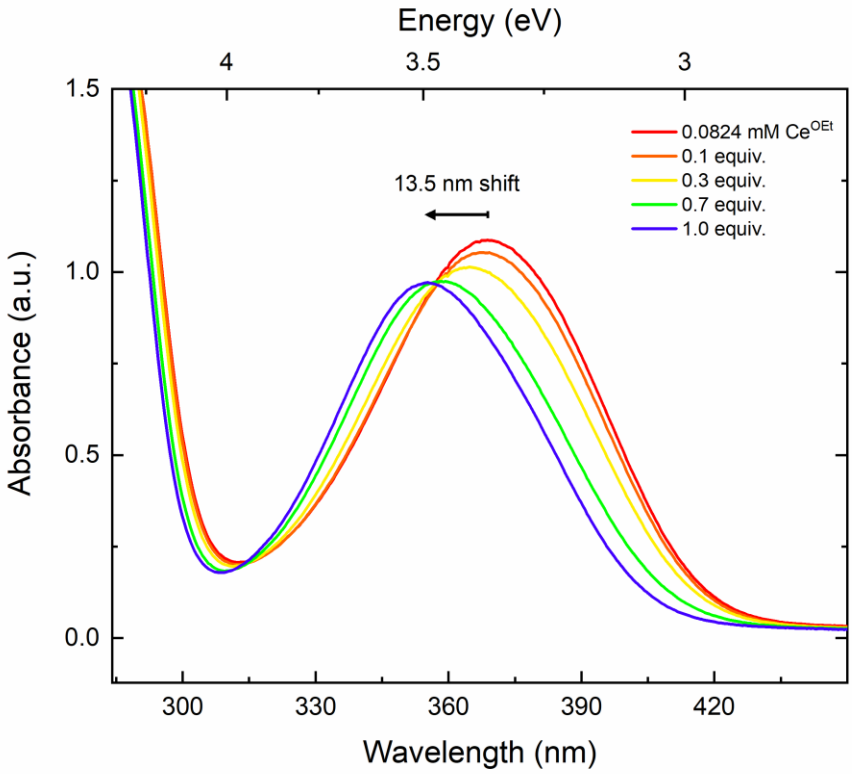

Figure F61. Electronic absorption spectra of **1** with $Ca(OTf)_2$ in CH_3CN.

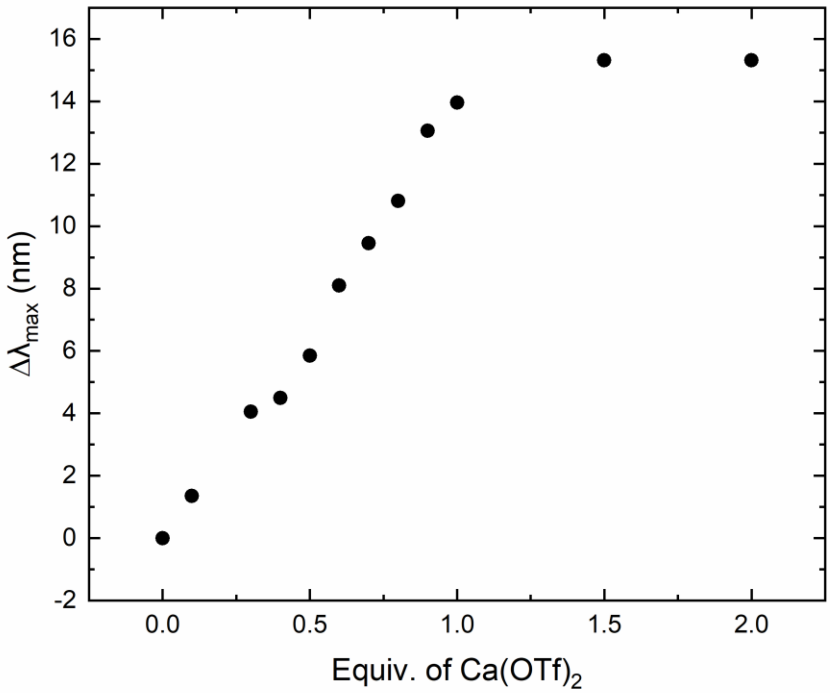

Figure F62. Plot of change of λ_{max} for titration of **1** with $Ca(OTf)_2$ in CH_3CN.

Electrochemistry

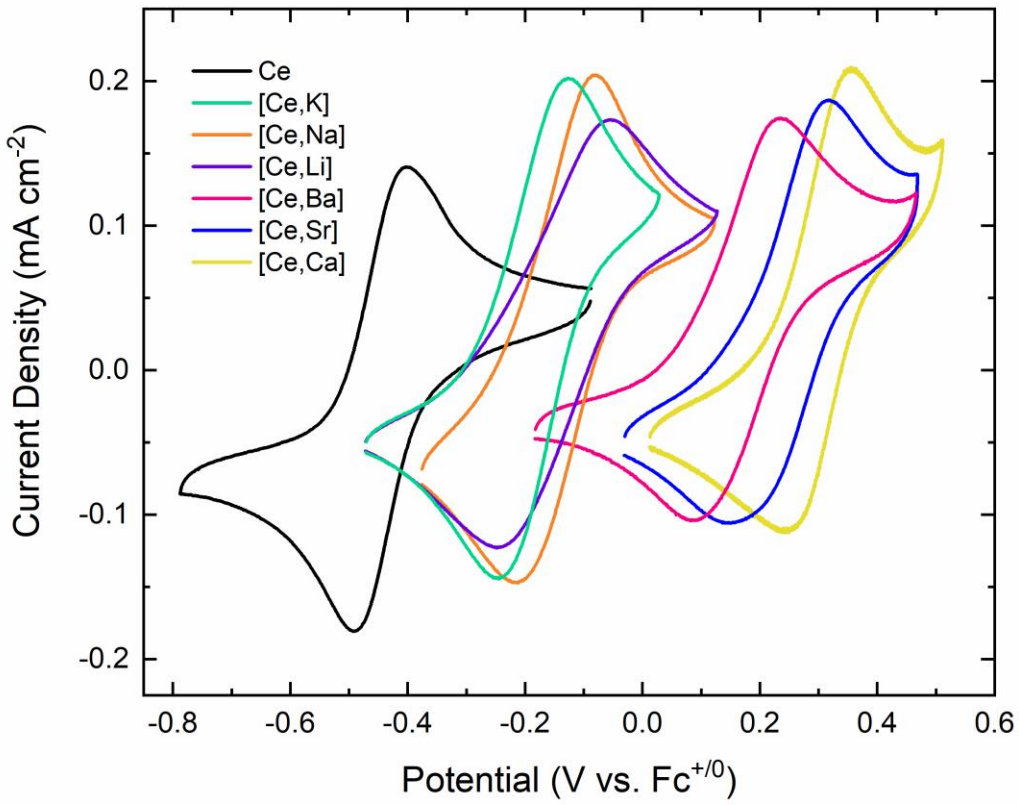

Figure F63. Cyclic voltammetry of overlayed **1** and **1-M** (CH_3CN, 0.1 M [$^nBu_4N$][PF_6], 100 mV/s)

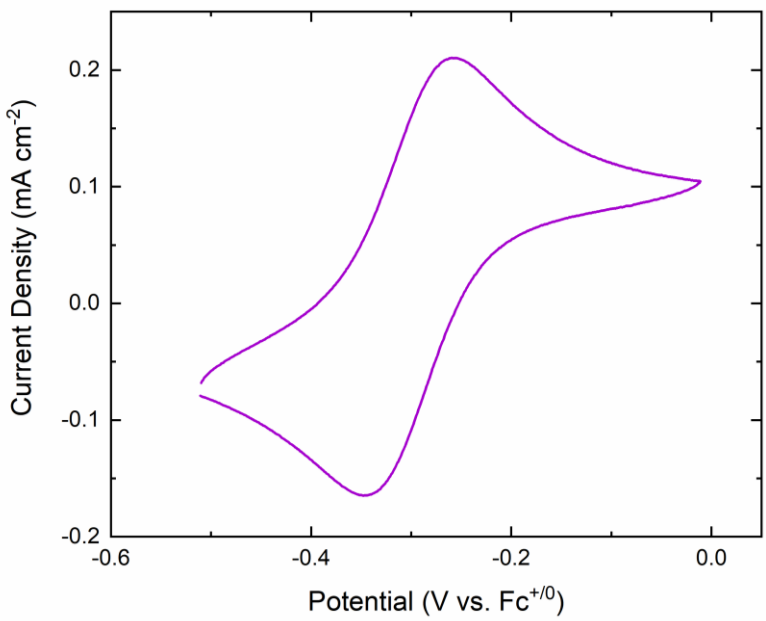

Figure F64. Cyclic voltammetry of **1** (CH_3CN, 0.1 M [$^nBu_4N$][PF_6], 100 mV/s)

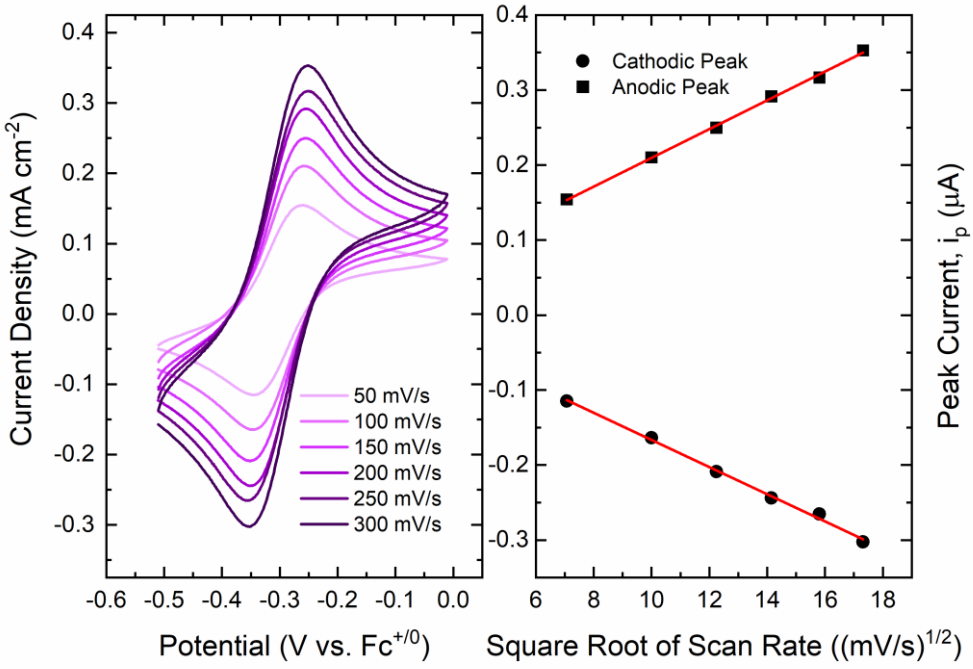

Figure F65. Left: cyclic voltammetry of first reduction event **1** at varying scan rate in CH_3CN (0.1 M [$^nBu_4N$][PF_6]). Right: linear dependence of peak cathodic current on square root of scan rate with the y-intercept set to 0.

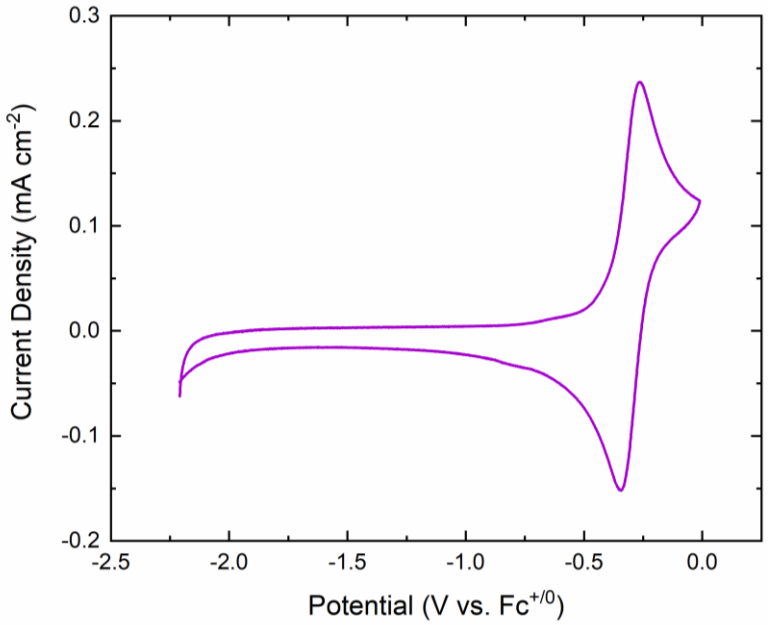

Figure F66. Cyclic voltammetry of **1** (CH_3CN, 0.1 M [$^nBu_4N$][PF_6], 100 mV/s)

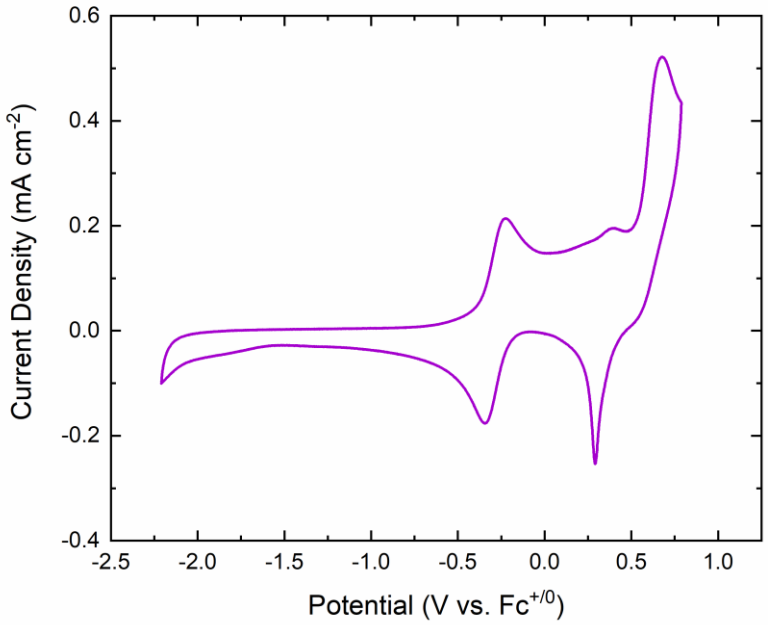

Figure F67. Cyclic voltammetry of **1** shows full scan including ligand oxidation (CH_3CN, 0.1 M [$^nBu_4N$][PF_6], 100 mV/s)

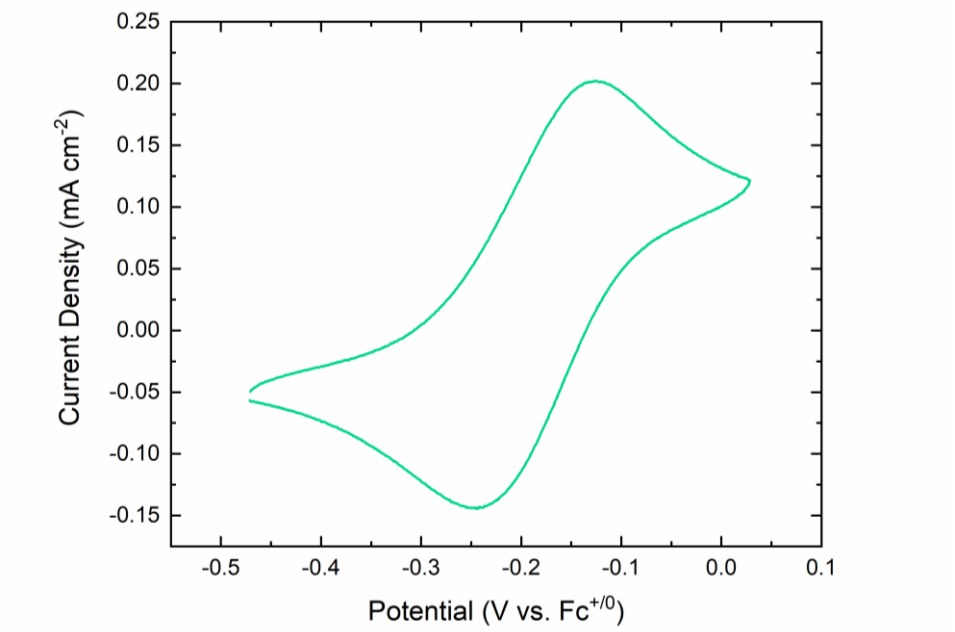

Figure F68. Cyclic voltammetry of **1-K** (CH_3CN, 0.1 M [$^nBu_4N$][PF_6], 100 mV/s)

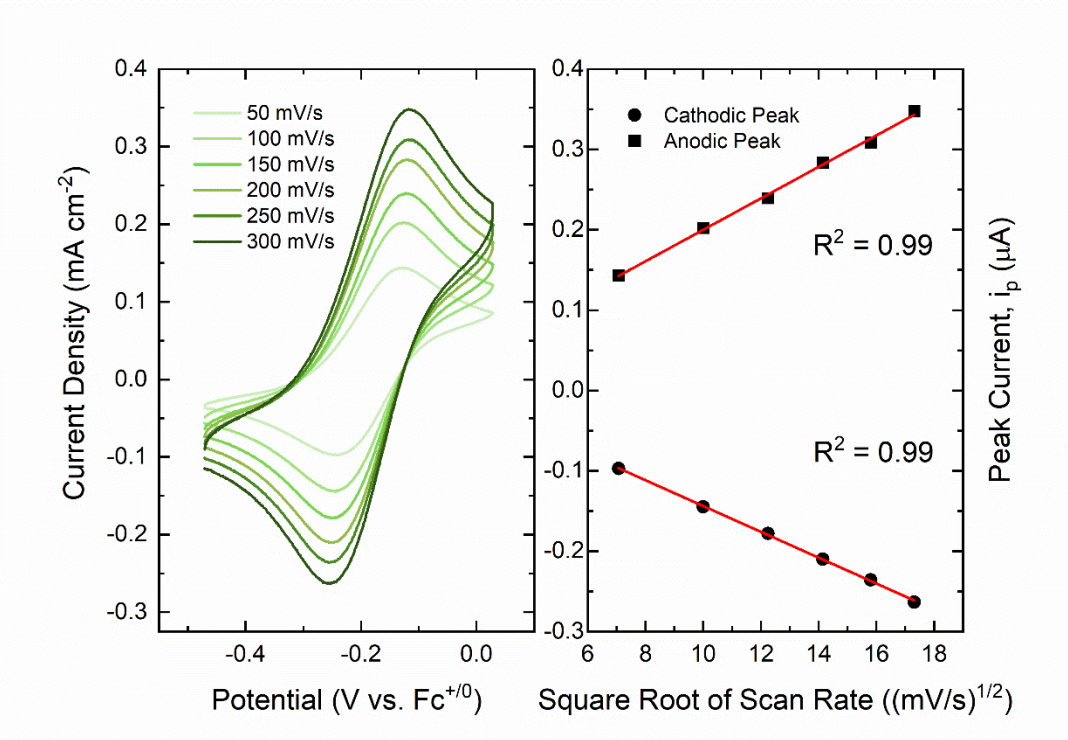

Figure F69. Left: cyclic voltammetry of first reduction event **1-K** at varying scan rate in CH_3CN (0.1 M [$^nBu_4N$][PF_6]). Right: linear dependence of peak cathodic current on square root of scan rate with the y-intercept set to 0.

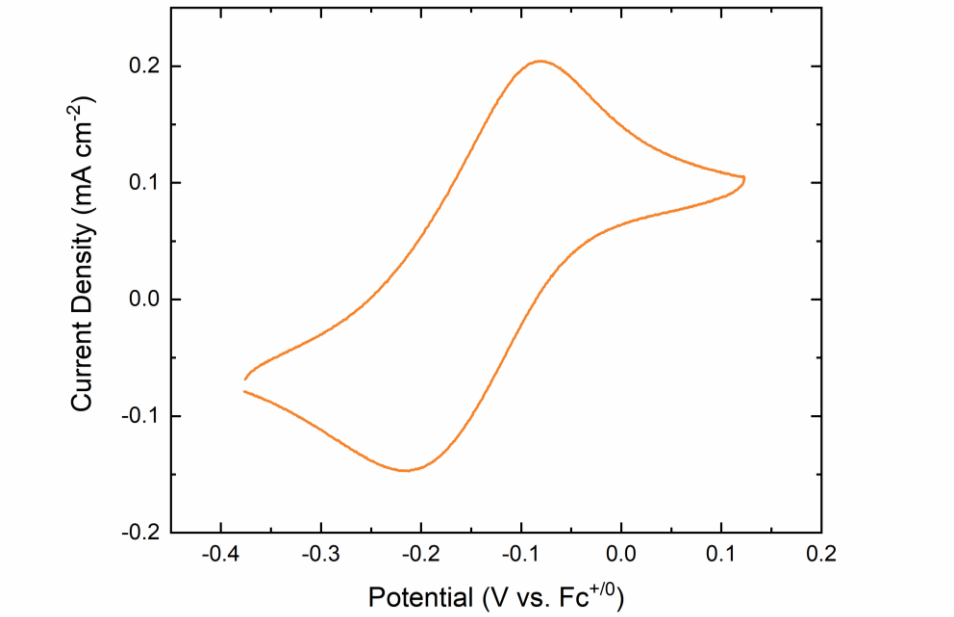

Figure F70. Cyclic voltammetry of **1-Na** (CH_3CN, 0.1 M [$^nBu_4N$][PF_6], 100 mV/s)

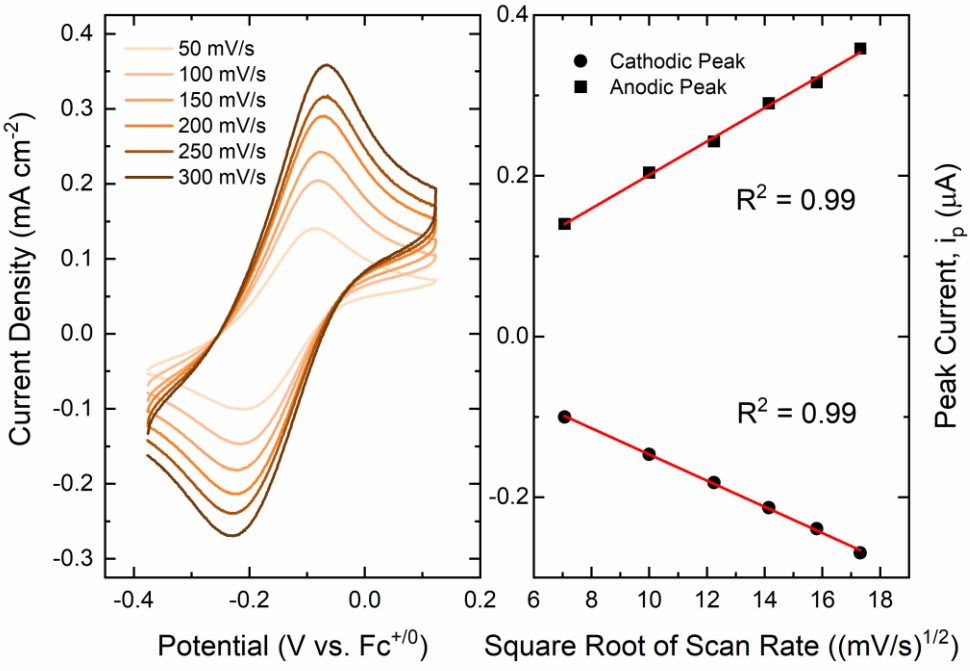

Figure F71. Left: cyclic voltammetry of first reduction event **1-Na** at varying scan rate in CH_3CN (0.1 M [$^nBu_4N$][PF_6]). Right: linear dependence of peak cathodic current on square root of scan rate with the y-intercept set to 0.

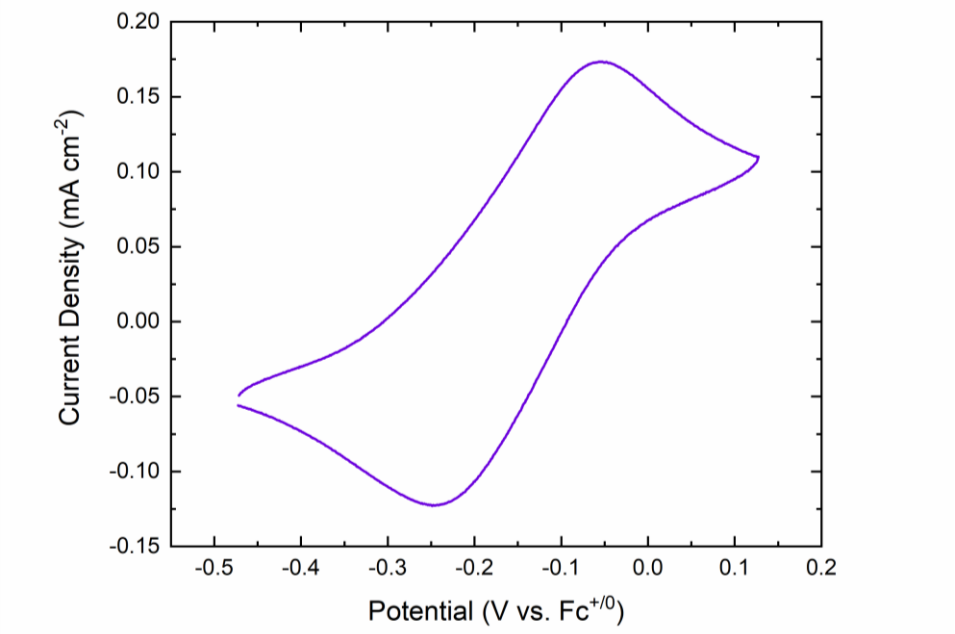

Figure F72. Cyclic voltammetry of **1-Li** (CH_3CN, 0.1 M [$^nBu_4N$][PF_6], 100 mV/s)

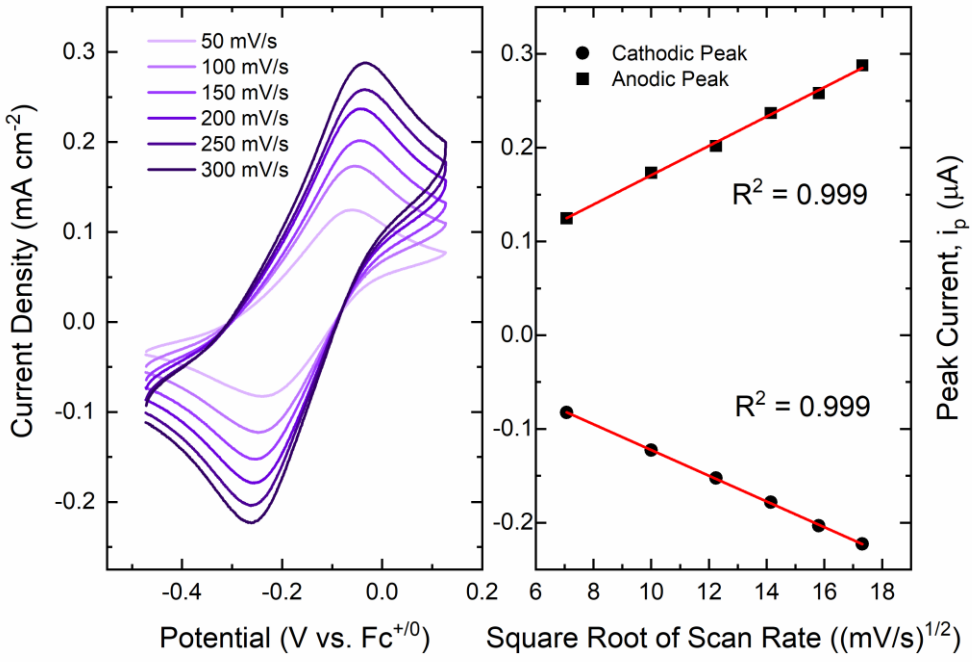

Figure F73. Left: cyclic voltammetry of first reduction event **1-Li** at varying scan rate in CH_3CN (0.1 M [$^nBu_4N$][PF_6]). Right: linear dependence of peak cathodic current on square root of scan rate with the y-intercept set to 0.

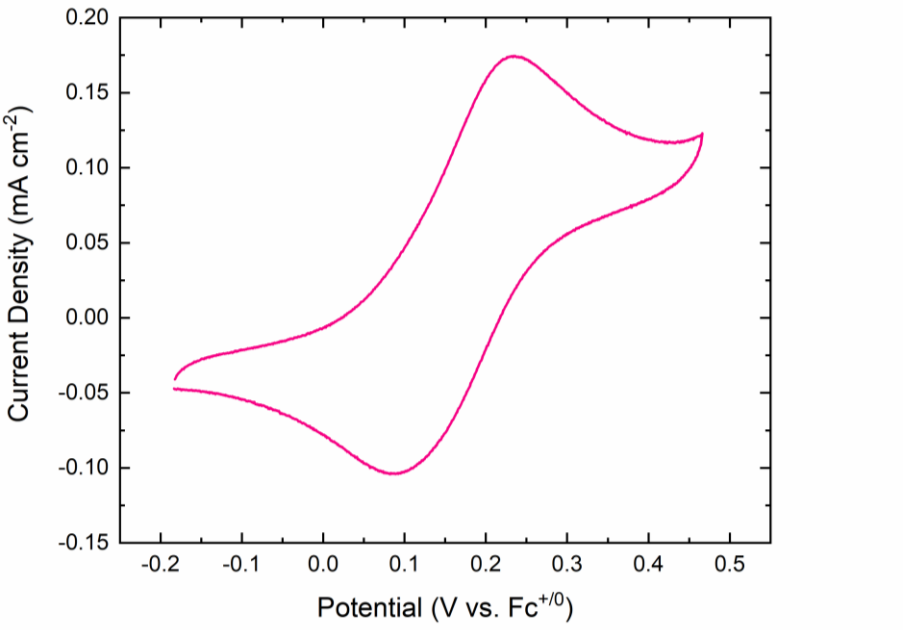

Figure F74. Cyclic voltammetry of **1-Ba** (CH_3CN, 0.1 M [$^nBu_4N$][PF_6], 100 mV/s)

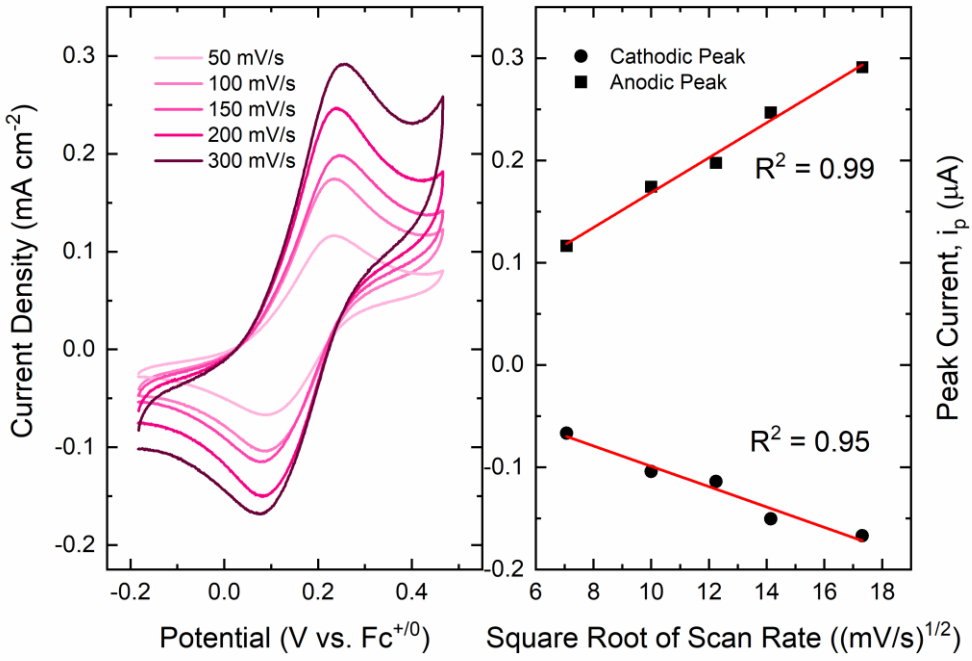

Figure F75. Left: cyclic voltammetry of first reduction event **1-Ba** at varying scan rate in CH_3CN (0.1 M [$^nBu_4N$][PF_6]). Right: linear dependence of peak cathodic current on square root of scan rate with the y-intercept set to 0.

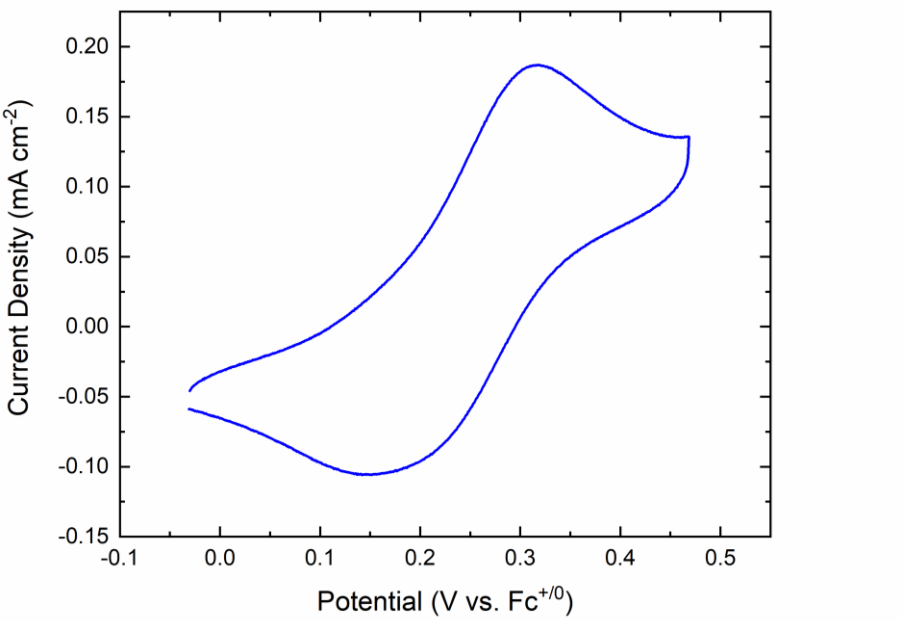

Figure F76. Cyclic voltammetry of **1-Sr** (CH_3CN, 0.1 M [$^nBu_4N$][PF_6], 100 mV/s)

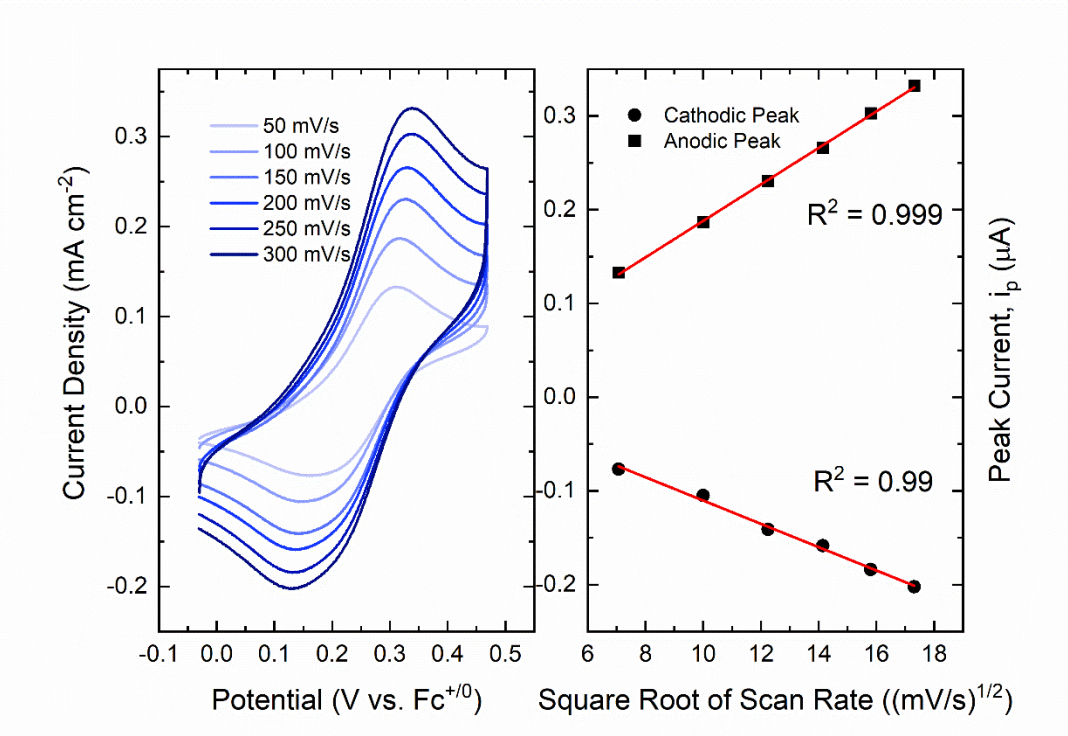

Figure F77. Left: cyclic voltammetry of first reduction event **1-Sr** at varying scan rate in CH_3CN (0.1 M [$^nBu_4N$][PF_6]). Right: linear dependence of peak cathodic current on square root of scan rate with the y-intercept set to 0.

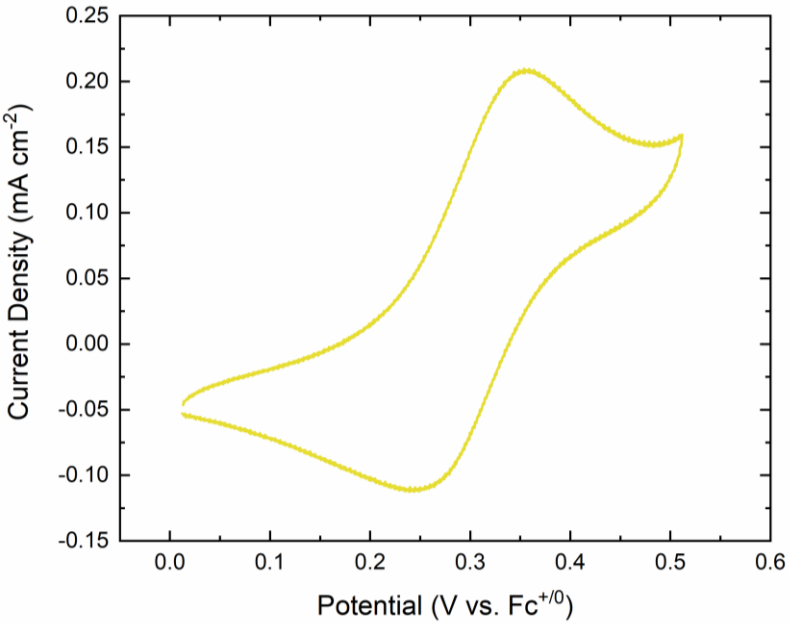

Figure F78. Cyclic voltammetry of **1-Ca** (CH_3CN, 0.1 M [$^nBu_4N$][PF_6], 100 mV/s)

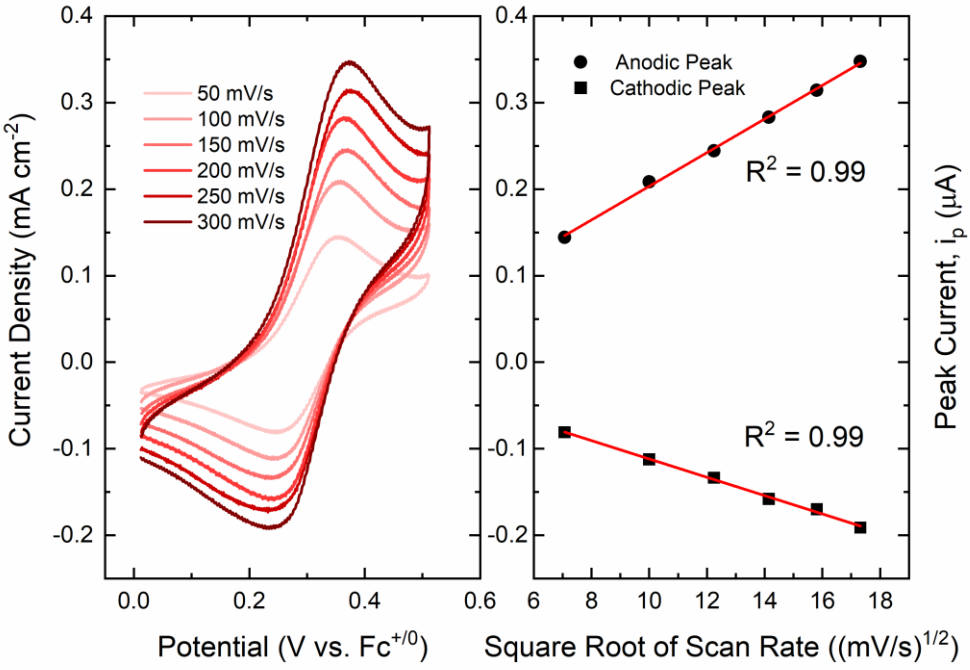

Figure F79. Left: cyclic voltammetry of first reduction event **1-Ca** at varying scan rate in CH_3CN (0.1 M [$^nBu_4N$][PF_6]). Right: linear dependence of peak cathodic current on square root of scan rate with the y-intercept set to 0.

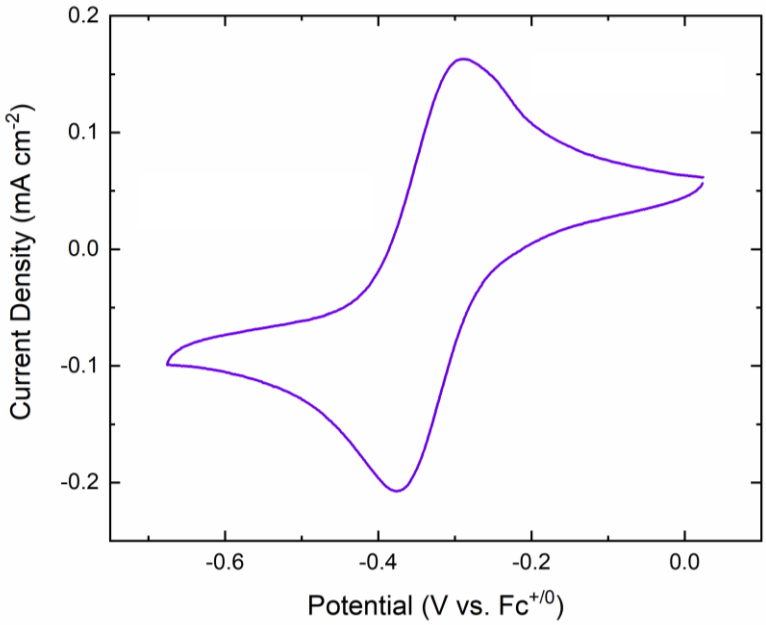

Figure F80. Cyclic voltammetry of $\mathbf{2^{PF6}}$ (CH_3CN, 0.1 M [$^nBu_4N$][PF_6], 100 mV/s)

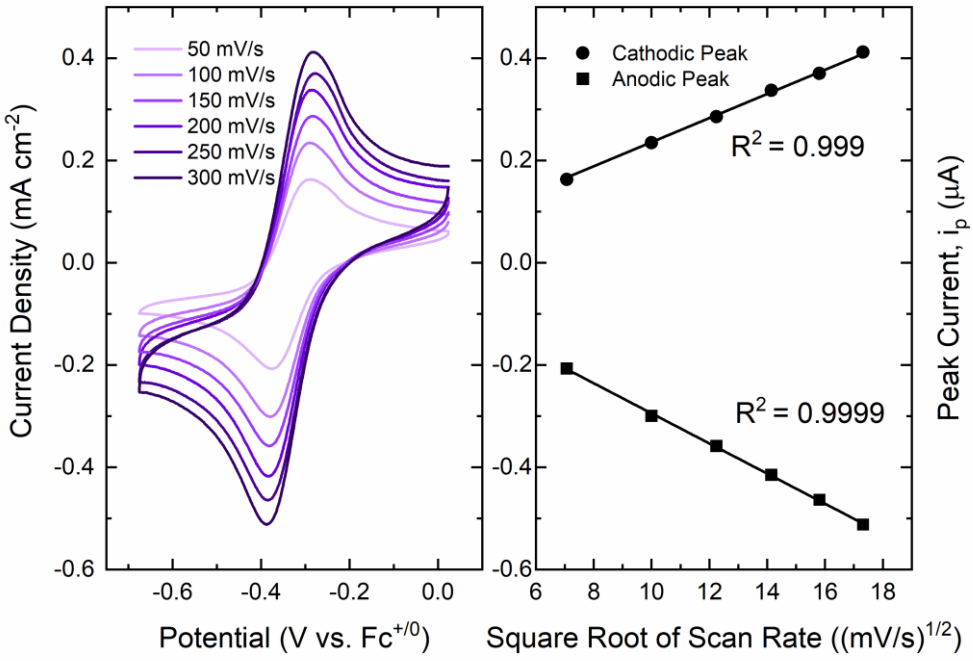

Figure F81. Left: cyclic voltammetry of $\mathbf{2^{PF6}}$ at varying scan rate in CH_3CN (0.1 M [$^nBu_4N$][PF_6]). Right: linear dependence of peak cathodic current on square root of scan rate with the y-intercept set to 0.

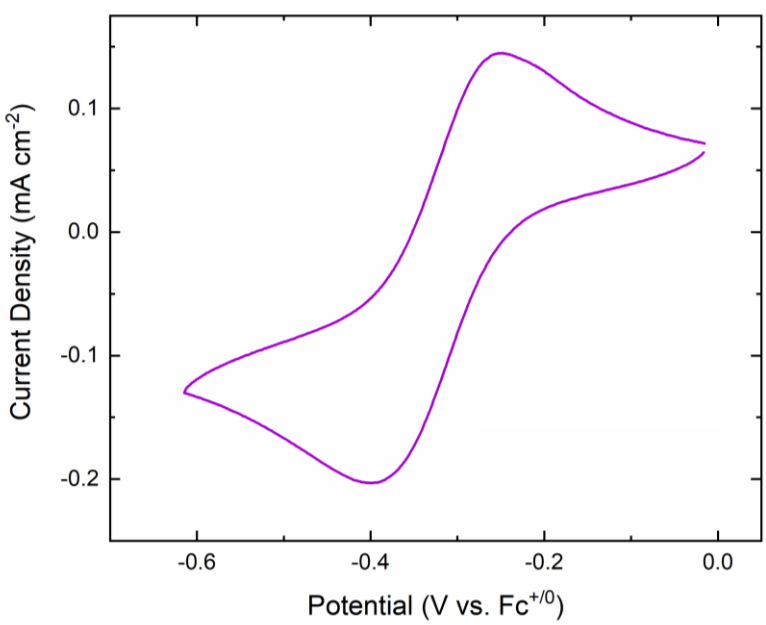

Figure F82. Cyclic voltammetry of **2^{OTf}** (CH_3CN, 0.1 M [$^nBu_4N$][PF_6], 100 mV/s)

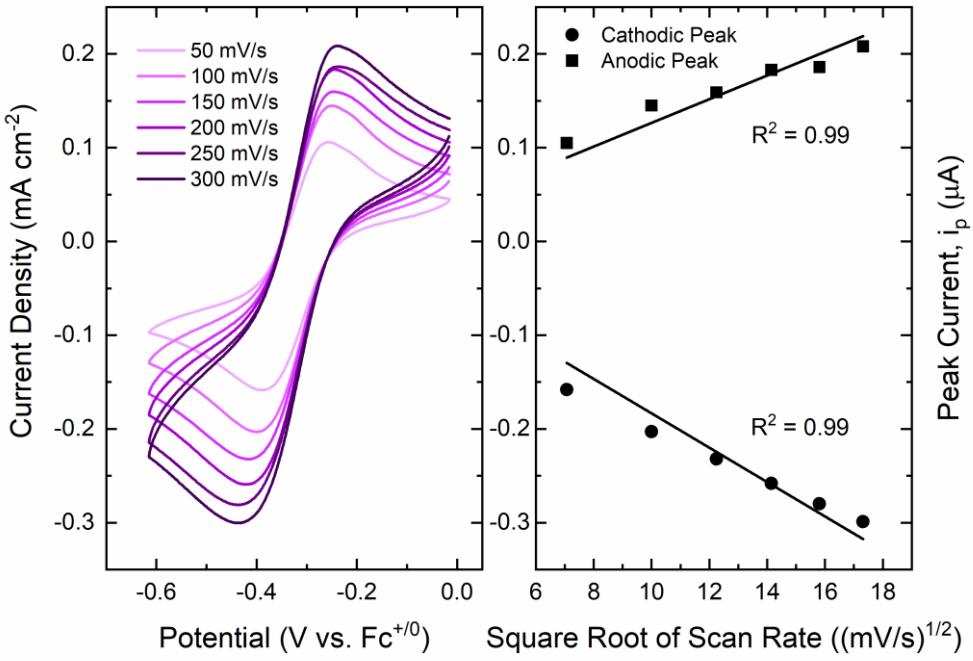

Figure F83. Left: cyclic voltammetry of **2^{OTf}** at varying scan rate in CH_3CN (0.1 M [$^nBu_4N$][PF_6]). Right: linear dependence of peak cathodic current on square root of scan rate with the y-intercept set to 0.

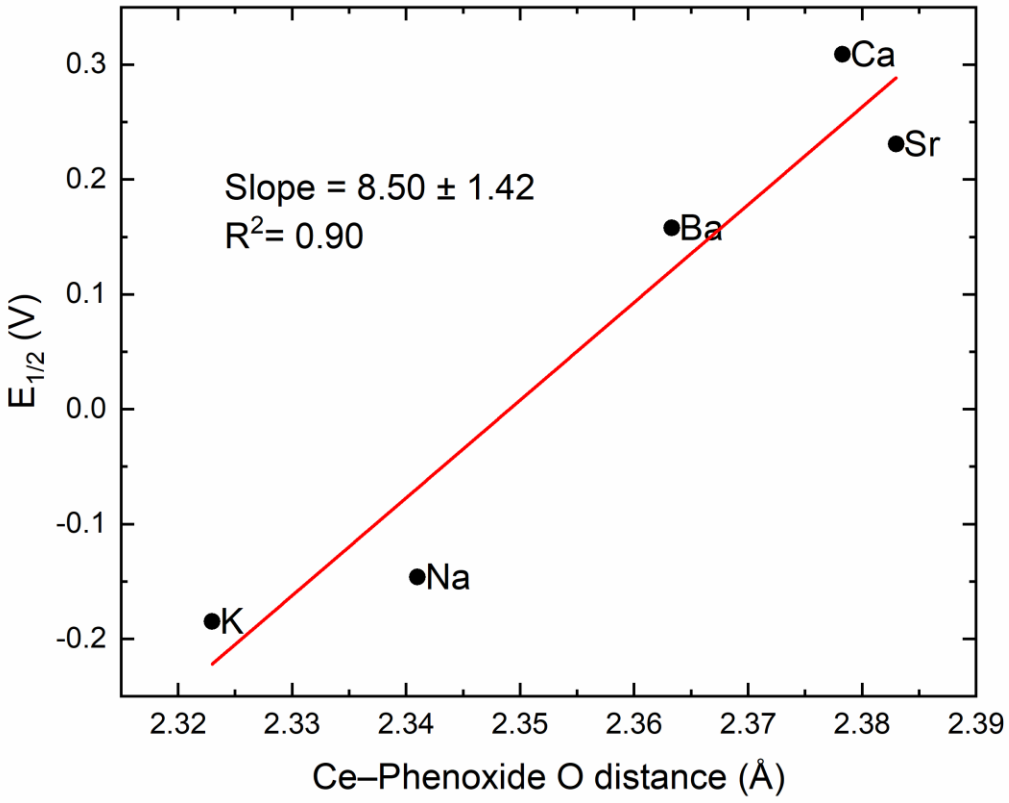

Figure F85. Dependence on average Ce–O_{Ar} distance on the reduction potential ($E_{1/2}$) of **1-**M (Excluding 1-Li).

Section F2

Table F1. Crystal and Refinement Data for ***1, 1-K, and 1-Na.***

	1 (q161)	**1-K (JH3099)**	**1-Na (q27l)**
CCDC number	2154613	2154614	2154612
Empirical formula	$C_{33}H_{39}CeN_4O_6$	$C_{36}H_{42}CeF_3KN_5O_9S$	$C_{34.67}H_{40}CeF_3N_{4.33}NaO_9S$
Formula weight	727.80	957.02	913.54
Temperature (K)	200.0	120.0	200.0
Wavelength (Å)	1.54178	0.71073	1.54178
Crystal system	Monoclinic	Triclinic	Triclinic
Space group	$P2_1/c$ - C_{2h}^5 (No. 14)	P-1- C_i^1 (No. 2)	P-1- C_i^1 (No. 2)
***a* (Å)**	11.8883(3) Å	11.8793(6)	11.6003(2)
***b* (Å)**	12.9424(4) Å	12.4898(6)	17.6407(3)
***c* (Å)**	21.3850(6) Å	15.3612(8)	29.3211(4)
***α* (º)**	90	101.9850(10)	106.2010(10)
***β* (º)**	96.6280(10)	109.7010(10)	92.3070(10)
***γ* (º)**	90	106.1510(10)	93.7250(10)
Volume	3268.4(2) $Å^3$	1943.2(2) $Å^3$	5739.1(2) $Å^3$
Z	4	2	6
Density (calculated)	1.479 g/cm^3	1.636 g/cm^3	1.586 g/cm^3
Absorption coefficient	11.16 mm^{-1}	1.41 mm^{-1}	10.45 mm^{-1}
F(000)	1484.0	970.0	2774.0
Crystal size	0.246 × 0.03 × 0.02 mm^3	0.261 × 0.169 × 0.119 mm^3	0.327 × 0.30 × 0.06 mm^3
2-Theta range (º)	7.49 to 140.36	2.99 to 56.54	3.14 to 140.26
Index ranges	$-12 \le h \le 14$, $-15 \le k \le 13$, $-25 \le l \le 24$	$-15 \le h \le 15$, $-16 \le k \le 16$, $-20 \le l \le 20$	$-14 \le h \le 13$, $-21 \le k \le 19$, $-34 \le l \le 34$
Reflections collected	21984	65749	72378
Independent reflections	5931 [R_{int}= 0.032, R_{sigma}= 0.029]	9639 [R_{int}= 0.036, R_{sigma}= 0.023]	20137 [R_{int} = 0.085, R_{sigma} = 0.078]
Absorption correction	Empirical	Numerical	Empirical
Ratio of Min. and max. transmission	0.488	0.848	0.566
Refinement method	Full-matrix least squares on F^2	Full-matrix least squares on F^2	Full-matrix least squares on F^2
Data / restraints / parameters	5931/0/434	9639/0/509	20137/0/1469
Goodness-of-fit on F^2	1.054	1.107	1.020
Final R indices [I>2σ(I)]	R_1= 0.029, wR_2 =0.074	R_1= 0.025, wR_2=0.057	R_1 = 0.044, wR_2 = 0.108
R indices (all data)	R_1= 0.038, wR_2 = 0.079	R_1= 0.028, wR_2=0.058	R_1 = 0.055, wR_2 = 0.115
Largest diff. peak and hole	1.50/-0.42 e/$Å^{-3}$	1.62/-1.07 e/$Å^{-3}$	1.56/-1.08 e/$Å^{-3}$

[a] $R_1 = \Sigma||F_o|-|F_c|| / \Sigma|F_o|$ [b] $wR_2 = [\ \Sigma\ [w(F_o^2-F_c^2)^2] / \Sigma\ [w(F_o^2)^2]\ ]^{1/2}$

Table F2. Crystal and Refinement Data for ***1-Ba, 1-Sr, and 1-Ca.***

	1-Ba (q25l)	**1-Sr (v51f)**	**1-Ca (JH3029)**
CCDC number	2154608	2154615	2154616
Empirical formula	$C_{39}H_{45}BaCeF_6N_6O_{12}S_2$	$C_{38}H_{45}CeF_6N_4O_{13}S_2Sr$	$C_{39}H_{53}CaCeF_6N_4O_{15}S_2$
Formula weight	1245.39	1171.64	1176.17
Temperature (K)	200.0	200.0	120.0
Wavelength (Å)	1.54178	1.54178	0.71073
Crystal system	Monoclinic	Triclinic	Monoclinic
Space group	$P2_1/c$ - C_{2h}^5 (No. 14)	P-1- C_i^1 (No. 2)	$P2_1/c$ - C_{2h}^5 (No. 14)
***a* (Å)**	13.3421(5)	10.4032(7)	18.1931(6)
***b* (Å)**	17.3731(7)	13.2713(9)	10.7821(4)
***c* (Å)**	21.0514(9)	17.3726(12)	24.0906(8)
***α* (º)**	90	97.1592(12)	90
***β* (º)**	93.097(3)	92.7299(13)	92.0300(10)
***γ* (º)**	90	106.6765(12)	90
Volume	4872.5(3) Å^3	2270.9(3) Å^3	4722.6(3) Å^3
Z	4	2	4
Density (calculated)	1.698 g/cm^3	1.713 g/cm^3	1.654 g/cm^3
Absorption coefficient	14.93 mm^{-1}	10.85 mm^{-1}	1.254 mm^{-1}
F(000)	2468.0	1174.0	2396
Crystal size	0.31 × 0.25 × 0.085 mm^3	0.358 × 0.355 × 0.131 mm^3	0.331 × 0.205 × 0.124 mm^3
2-Theta range (º)	6.60 to 140.89	5.15 to 137.43	3.38 to 56.63
Index ranges	$-15 \le h \le 16$, $-21 \le k \le 18$, $-25 \le l \le 25$	$-12 \le h \le 12$, $-15 \le k \le 15$, $-20 \le l \le 16$	$-24 \le h \le 24$, $-14 \le k \le 14$, $-32 \le l \le 32$
Reflections collected	32032	22195	155728
Independent reflections	8763 [R_{int}= 0.115, R_{sigma}= 0.151]	8006 [R_{int}= 0.057, R_{sigma}= 0.055]	11756 [R_{int}= 0.039, R_{sigma}= 0.017]
Absorption correction	Empirical	Numerical	Numerical
Ratio of Min. and max. transmission	0.498	0.131	0.890
Refinement method	Full-matrix least squares on F^2	Full-matrix least squares on F^2	Full-matrix least squares on F^2
Data / restraints / parameters	8763/26/652	8006/0/591	11756/0/634
Goodness-of-fit on F^2	1.065	1.048	1.114
Final R indices [I>2σ(I)]	R_1= 0.099, wR_2=0.244	R_1= 0.053, wR_2=0.144	R_1= 0.028, wR_2=0.063
R indices (all data)	R_1= 0.131, wR_2=0.267	R1= 0.053, wR2=0.145	R_1= 0.031, wR_2=0.064
Largest diff. peak and hole	2.09/-1.75 e/Å^{-3}	1.45/-1.33 e/Å^{-3}	0.93/-1.16 e/Å^{-3}

[a] $R_1\ \Sigma||F_o|-|F_c|| / \Sigma|F_o|$ [b] $wR_2 = [\ \Sigma\ [w(F_o^2-F_c^2)^2] / \Sigma\ [w(F_o^2)^2]\ ]^{1/2}$

Table F3. Crystal and Refinement Data for ***1-Li, 2^{PF6} and 2^{OTf}*.**

	1-Li (JH3100)	***2^{PF6}* (q21l)**	***2^{OTf}* (JH3145a)**
CCDC number	2154610	2154609	2154611
Empirical formula	$C_{35}H_{39}CeF_3LiN_{4.5}O_9S$	$C_{33}H_{39}CeF_6N_4O_6P$	$C_{34}H_{39}CeF_3N_4O_9S$
Formula weight	902.82	872.77	876.94
Temperature (K)	120.0	200.0	120.0
Wavelength (Å)	0.71073	1.54178	0.71073
Crystal system	Triclinic	Monoclinic	Monoclinic
Space group	P-1- C_i^1 (No. 2)	C2/c - C_{2h}^6 (No. 15)	$P2_1/c$ - C_{2h}^5 (No. 14)
***a* (Å)**	12.3228(7)	27.2706(8)	16.0967(14)
***B* (Å)**	13.1684(7)	18.7513(5)	18.9860(19)
***C* (Å)**	13.4918(7)	16.2129(5)	23.651(2)
***α* (º)**	105.3030(10)	90	90
***β* (º)**	116.8320(10)	121.0759(12)	96.796(3)
***γ* (º)**	93.450(2)	90	90
Volume	1843.0 (2) $Å^3$	7100.8(4)	7177.3(11) $Å^3$
Z	2	8	8
Density (calculated)	1.627 g/cm^3	1.633 g/cm^3	1.624 g/cm^3
Absorption coefficient	1.37 mm^{-1}	11.050 mm-1	1.402 mm^{-1}
F(000)	913.0	3520	3552
Crystal size	0.206 × 0.127 × 0.083 mm^3	0.113 x 0.073 x 0.049 mm3	0.150 × 0.148 × 0.115 mm^3
2-Theta range (º)	3.28 to 56.60	7.22 to 140.71	3.33 to 56.63
Index ranges	$-16 \le h \le 16$, $-17 \le k \le 17$, $-17 \le l \le 17$	$-31 \le h \le 30$, $-21 \le k \le 22$, $-18 \le l \le 19$	$-21 \le h \le 21$, $-25 \le k \le 25$, $-31 \le l \le 28$
Reflections collected	40951	31341	208677
Independent reflections	9135 [R_{int} = 0.021, R_{sigma} = 0.018]	6555 [R_{int} = 0.048, R_{sigma} = 0.042]	17857 [R_{int} =0.062, R_{sigma} =0.029]
Absorption correction	Empirical	Numerical	Numerical
Ratio of Min. and max. transmission	0.902	0.616	0.924
Refinement method	Full-matrix least squares on F^2	Full-matrix least squares on F^2	Full-matrix least squares on F^2
Data / restraints / parameters	9135/0/515	6555 / 21 / 521	17857/32/1081
Goodness-of-fit on F^2	1.055	1.119	1.118
Final R indices [I>2σ(I)]	R_1= 0.021, wR_2=0.050	R_1 = 0.048, wR_2=0.126	R_1 = 0.045, wR_2=0.073
R indices (all data)	R_1 = 0.024, wR_2 = 0.051	R_1 = 0.051, wR_2=0.129	R_1 = 0.060, wR_2=0.077
Largest diff. peak and hole	1.02/-0.75 e/$Å^{-3}$	2.27/-2.07 e/$Å^{-3}$	1.24/-1.81 e/$Å^{-3}$

[a] $R_1 \Sigma||F_o|-|F_c|| / \Sigma|F_o|$ [b] $wR_2 = [\Sigma [w(F_o^2-F_c^2)^2] / \Sigma [w(F_o^2)^2]]^{1/2}$

Table F4. Selected Bond Lengths for **1** and **1-M.**

	1	**1-K**	**1-Na**	**1-Li**	**1-Ba**	**1-Sr**	**1-Ca**
Ce–M	-	3.705	3.359	3.363	3.797	3.673	3.550
Ce–O1	2.285(2)	2.3028(14)	2.375(3)	2.3701(14)	2.378(10)	2.383(3)	2.3652(14)
Ce–O2	2.287(2)	2.3195(14)	2.330(4)	2.5223(15)	2.370(8)	2.380(3)	2.4100(14)
Ce–O3	2.289(2)	2.3452(13)	2.332(3)	2.3866(14)	2.347(10)	2.386(3)	2.3652(14)
Ce–N1	2.801(3)	2.7523(17)	2.709(4)	2.8504(17)	2.736(14)	2.758(4)	2.7349(17)
Ce–N2	2.629(3)	2.6161(17)	2.668(4)	2.6877(17)	2.612(15)	2.611(4)	2.6059(17)
Ce–N3	2.605(3)	2.6309(17)	2.684(4)	2.6264(18)	2.581(12)	2.619(4)	2.6187(18)
Ce–N4	2.625(3)	2.6984(16)	2.638(4)	2.6841(17)	2.656(13)	2.628(4)	2.5987(17)
LA–O1	-	2.8863(14)	2.386(4)	1.945(4)	2.703(11)	2.549(3)	2.4141(14)
LA–O2	-	2.6863(15)	2.342(4)	–	2.750(8)	2.531(3)	2.4105(14)
LA–O3	-	2.7255(14)	2.395(4)	1.975(4)	2.769(12)	2.610(3)	2.4235(14)
LA–O4	-	2.7506(14)	2.523(4)	2.195(4)	2.784(14)	2.771(4)	2.5612(15)
LA–O5	-	2.8485(15)	2.570(4)	–	3.00(2)	2.624(3)	2.4821(15)
LA–O6	-	2.7383(16)	2.557(4)	2.128(4)	2.926(16)	2.587(3)	2.6081(15)

Table F5. Selected Average Angles and Lengths for **1** and **1-M**

	1	**1-K**	**1-Na**	**1-Ba**	**1-Sr**	**1-Ca**
N_{imine} –N4 (Å)	2.935	2.941	2.947	2.906	2.948	2.942
O_{Ar}•••N4 (Å)	4.459	4.628	4.685	4.689	4.768	4.760
O_{Ar}•••N_{imine} (Å)	2.822	2.845	2.869	2.878	2.908	2.905
O_{Ar}•••O_{ether} (Å)	2.737	2.621	2.629	2.623	2.628	2.609
N_{imine} plane–O_{Ar} planes (Å)	2.413	3.092	3.542	3.551	2.850	2.802
∠N_{imine} plane–O_{Ar} planes (°)	1.40	2.00	5.40	4.50	1.60	1.90
O_{Ar} plane•••O_{ether} planes (Å)	2.031	2.718	3.061	3.369	2.290	1.851
∠O_{Ar} plane–O_{ether} planes (°)	1.70	4.90	1.40	5.70	0.50	1.70
∠M–Ce–N4 (°)	-	172.83	176.92	174.21	176.92	176.01

Table F6. Selected Average Angles and Lengths for **1** and **1-M**

	1	**1-K**	**1-Na**	**1-Ba**	**1-Sr**	**1-Ca**
pK_a of $[M(H_2O)_m]^{n+}$	-	16.0	14.8	13.4	13.2	12.6
Shannon Ionic Radius of M (Å)[a]	-	1.46	1.02	1.47	1.21	1.12
Ce•••N_{imine} plane (Å)	1.084	1.079	1.046	1.070	1.031	1.008
Ce•••O_{Ar} plane (Å)	1.194	1.543	1.662	1.644	1.716	1.749
M•••O_{Ar} plane (Å)	-	2.156	1.703	2.152	1.956	1.801
M•••O_{ether} plane (Å)	-	0.154	0.754	0.107	0.363	0.436
∠N_{imine} –Ce–N4 (°)	65.36	65.96	66.54	65.68	66.44	66.79
∠O_{Ar}–Ce–N_{imine} (°)	69.77	71.35	69.85	71.72	71.51	71.39
∠O_{Ar}–M–O_{ether} (°)	-	57.64	64.40	56.30	57.52	62.21

[a] Average radii observed for cation-anion distances in most oxide and fluoride crystal structures (Ref 1).

Table F7. Selected Average Angles and Lengths for **1**, **2^{PF6} and 2^{OTf}**

	1	**2^{PF6}**	**2^{OTf}**
Ce–N_{imine} (Å)	2.68(3)	2.53(3)	2.53(3)
Ce–O_{Ar} (Å)	2.29(2)	2.14(3)	2.14(3)
Ce–N4 (Å)	2.63(3)	2.73(3)	2.72(3)
N_{imine}•••N_{imine} (Å) [a]	4.11	4.01	4.03
O_{Ar}•••O_{Ar} (Å) [b]	3.39	3.16	3.14
O_{Ar}•••N4 (Å)	4.46	4.26	4.26
N_{imine}–N4 (Å)	2.93	2.88	2.89
O_{Ar}•••N_{imine} (Å)	2.82	2.74	2.74
O_{ether}•••O_{ether} (Å) [c]	5.51	5.22	5.23
O_{Ar}•••O_{ether} (Å) [d]	2.74	2.66	2.73
∠N_{imine} –Ce–N4 (°)	65.36	64.19	66.47
∠O_{Ar}–Ce– N_{imine} (°)	69.50	71.32	71.01

[a] Average distance between the N1, N2 and N3 atoms in the plane defined by the N_{imine} moieties. [b] Average distance between the O1, O2 and O3 atoms in the plane defined by the O_{Ar} moieties. [c] Average distance between the O4, O5 and O6 atoms in the plane defined by the O_{ether} moieties. [d] Average distance between the O4–O1, O5–O2, and O6–O3 atoms in the plane defined by the O_{ether} moieties.

Table F8. Bond lengths of molecules in the unit cell of **1-Na**. Average, standard deviation and percent error of bond lengths of the three structures.

Bond lengths of 1-Na												
Molecule A (Å)		**Molecule B (Å)**		**Molecule C (Å)**		**Average (Å)**		**Standard Deviation (Å)**		**Percent Error (%)**	
Ce1A O1A	2.332	Ce1B O1B	2.330	Ce1C O1C	2.333	**Ce O1**	**2.332**	Ce O1	0.0015	Ce O1	0.07
Ce1A O2A	2.375	Ce1B O2B	2.341	Ce1C O2C	2.361	**Ce O2**	**2.359**	Ce O2	0.0171	Ce O2	0.72
Ce1A O3A	2.330	Ce1B O3B	2.326	Ce1C O3C	2.339	**Ce O3**	**2.332**	Ce O3	0.0067	Ce O3	0.29
Ce1A N1A	2.668	Ce1B N1B	2.656	Ce1C N1C	2.636	**Ce N1**	**2.653**	Ce N1	0.0162	Ce N1	0.61
Ce1A N2A	2.684	Ce1B N2B	2.660	Ce1C N2C	2.662	**Ce N2**	**2.669**	Ce N2	0.0133	Ce N2	0.50
Ce1A N3A	2.638	Ce1B N3B	2.614	Ce1C N3C	2.622	**Ce N3**	**2.625**	Ce N3	0.0122	Ce N3	0.47
Ce1A N4A	2.709	Ce1B N4B	2.681	Ce1C N4C	2.712	**Ce N4**	**2.701**	Ce N4	0.0171	Ce N4	0.63
Na1A O1A	2.395	Na1B O1B	2.382	Na1C O1C	2.37	**Na O1**	**2.382**	Na O1	0.0125	Na O1	0.52
Na1A O2A	2.386	Na1B O2B	2.395	Na1C O2C	2.386	**Na O2**	**2.389**	Na O2	0.0052	Na O2	0.22
Na1A O3A	2.342	Na1B O3B	2.402	Na1C O3C	2.416	**Na O3**	**2.387**	Na O3	0.0393	Na O3	1.65
Na1A O4A	2.523	Na1B O4B	2.57	Na1C O4C	2.529	**Na O4**	**2.541**	Na O4	0.0256	Na O4	1.01
Na1A O5A	2.557	Na1B O5B	2.48	Na1C O5C	2.532	**Na O5**	**2.523**	Na O5	0.0393	Na O5	1.56
Na1A O6A	2.57	Na1B O6B	2.526	Na1C O6C	2.453	**Na O6**	**2.516**	Na O6	0.0591	Na O6	2.35

Table F9. Bond lengths of molecules in the unit cell of $\mathbf{2^{OTf}}$. Average, standard deviation and percent error of bond lengths of the two structures.

Bond lengths of 2^{OTf}									
Molecule A (Å)		**Molecule B (Å)**		**Average (Å)**		**Standard Deviation (Å)**		**Percent Error (%)**	
Ce1A O1A	2.142(2)	Ce1B O1B	2.125(2)	**Ce O1**	**2.134**	Ce O1	0.012	Ce O1	0.56
Ce1A O2A	2.131(2)	Ce1B O2B	2.147(2)	**Ce O2**	**2.139**	Ce O2	0.011	Ce O2	0.53
Ce1A O3A	2.139(2)	Ce1B O3B	2.141(2)	**Ce O3**	**2.140**	Ce O3	0.001	Ce O3	0.07
Ce1A N1A	2.545(3)	Ce1B N1B	2.517(3)	**Ce N1**	**2.531**	Ce N1	0.020	Ce N1	0.78
Ce1A N2A	2.537(3)	Ce1B N2B	2.528(3)	**Ce N2**	**2.533**	Ce N2	0.006	Ce N2	0.25
Ce1A N3A	2.531(3)	Ce1B N3B	2.528(3)	**Ce N3**	**2.530**	Ce N3	0.002	Ce N3	0.08
Ce1A N4A	2.723(3)	Ce1B N4B	2.716(3)	**Ce N4**	**2.720**	Ce N4	0.005	Ce N4	0.18

Special Refinement Details for 1

Two of the ligand ethoxy arms are disordered over two sites. The C32-C33 pair are 53/47 disordered with the C32′-C33′ pair and the O5-C30 pair is 74/26 disordered with the O5′-C30′ pair. Minor occupancy carbon atom C30′ was included in the structural model as an isotropic atom whose thermal parameter was allowed to refine.

Solid-State Structure of 1

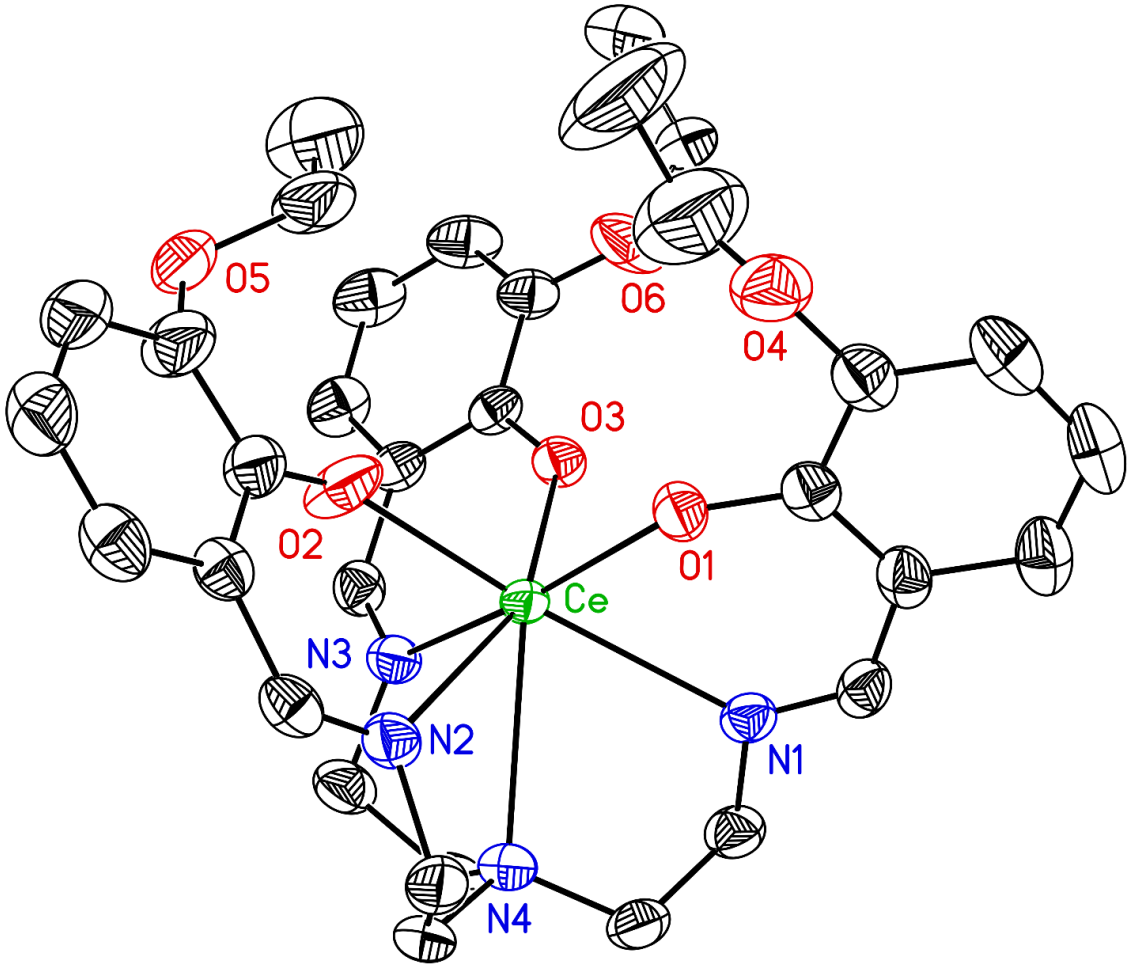

Figure F86. Solid-state structure of **1**. Hydrogen atoms and disordered atoms omitted for clarity. Displacement ellipsoids shown at the 50% probability level.

Full Solid-State Structure of 1

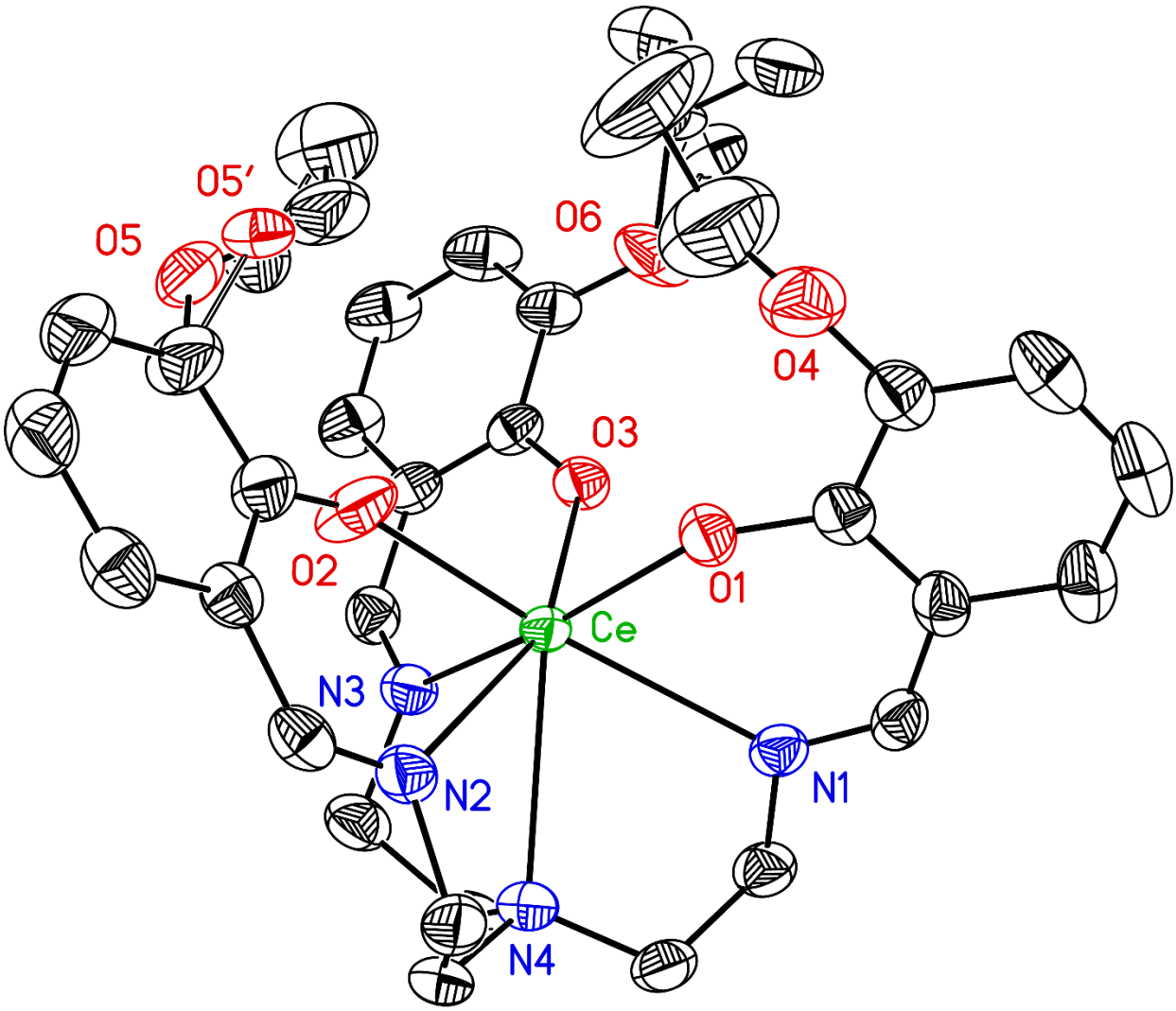

Figure F87. Full solid-state structure for non-hydrogen atoms of **1**. Two of the ligand ethoxy arms are disordered over two sites (hollow bonds for minor site). The C32-C33 pair are 53/47 disordered with the C32′-C33′ pair and the O5-C30 pair is 74/26 disordered with the O5′-C30′ pair. Hydrogen atoms omitted for clarity. Displacement ellipsoids shown at the 50% probability level.

Special Refinement Details for 1-K

No special refinement was required.

Solid-State Structure of 1-K

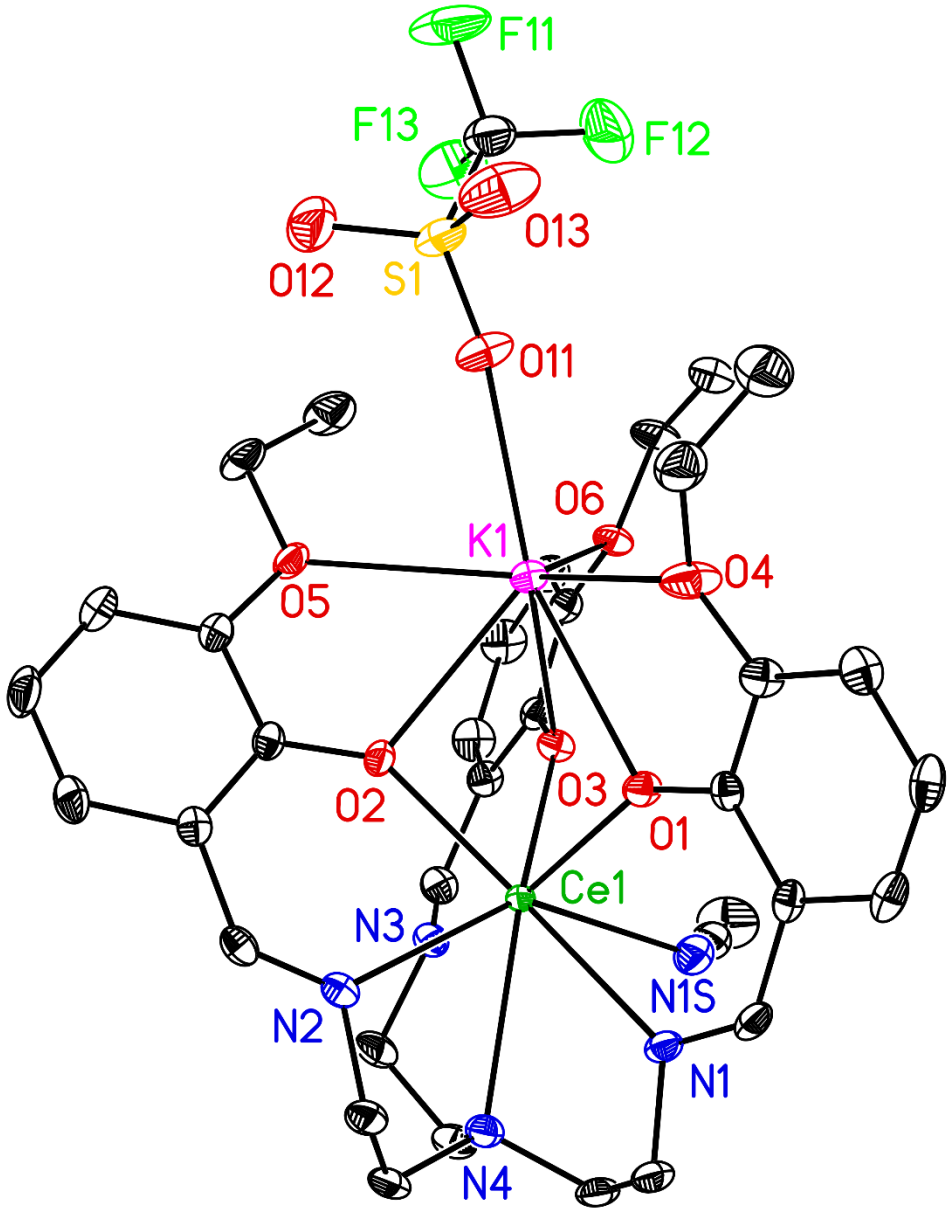

Figure F88. Full solid-state structure of **1-K**. Hydrogen atoms omitted for clarity. Displacement ellipsoids shown at the 50% probability level.

Special Refinement Details for 1-Na

No special refinement was required.

Solid-State Structure of 1-Na

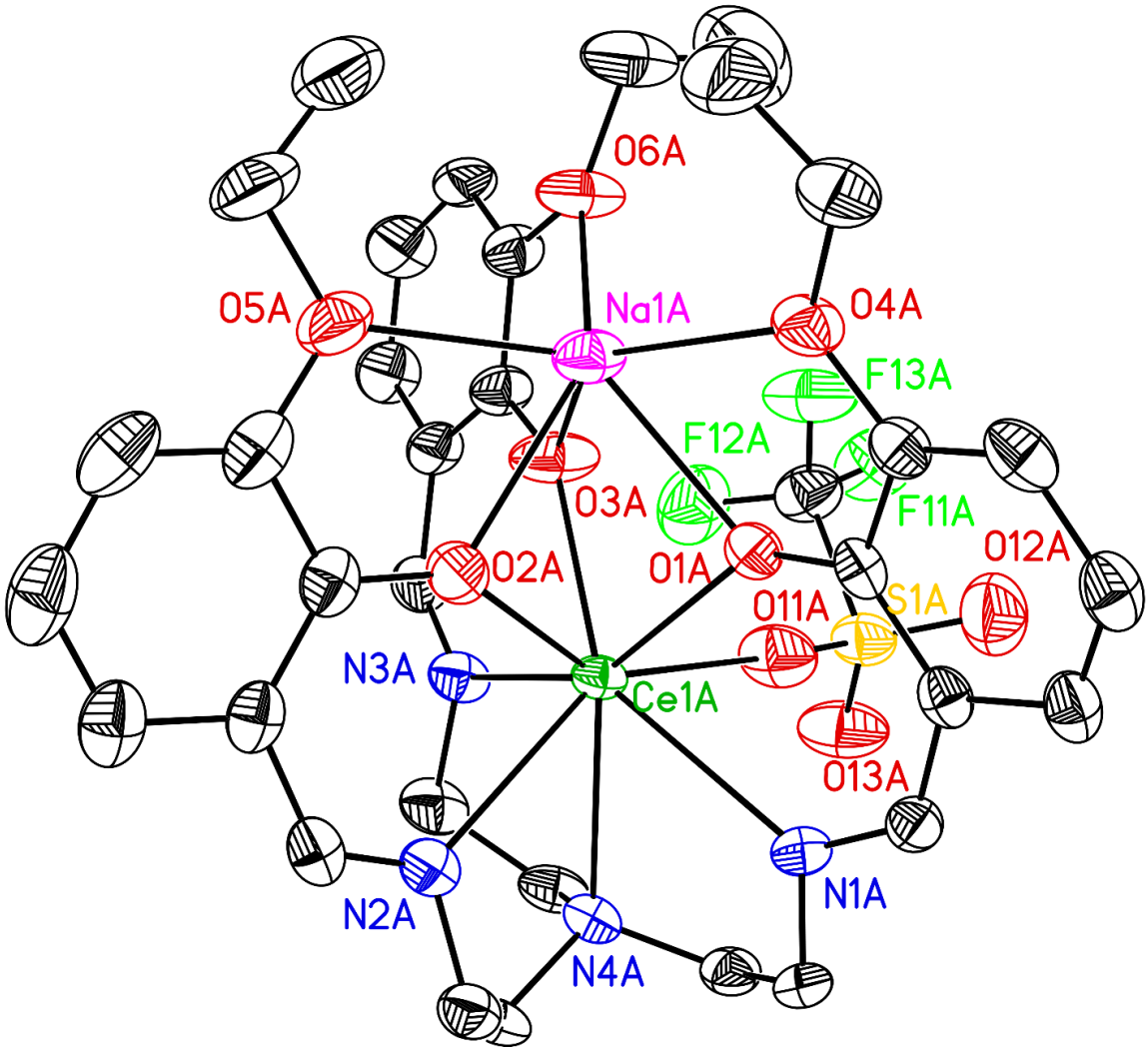

Figure F89. Structure for the first (A) of of three (A-C) virtually identical and crystallographically-independent [**1-Na]** molecules in the asymmetric unit of its solid-state structure. Hydrogen atoms, outer-sphere solvent molecules and additional molecules in the unit cell are omitted for clarity. Displacement ellipsoids are shown at the 50% probability level.

Full Solid-State Structure of 1-Na

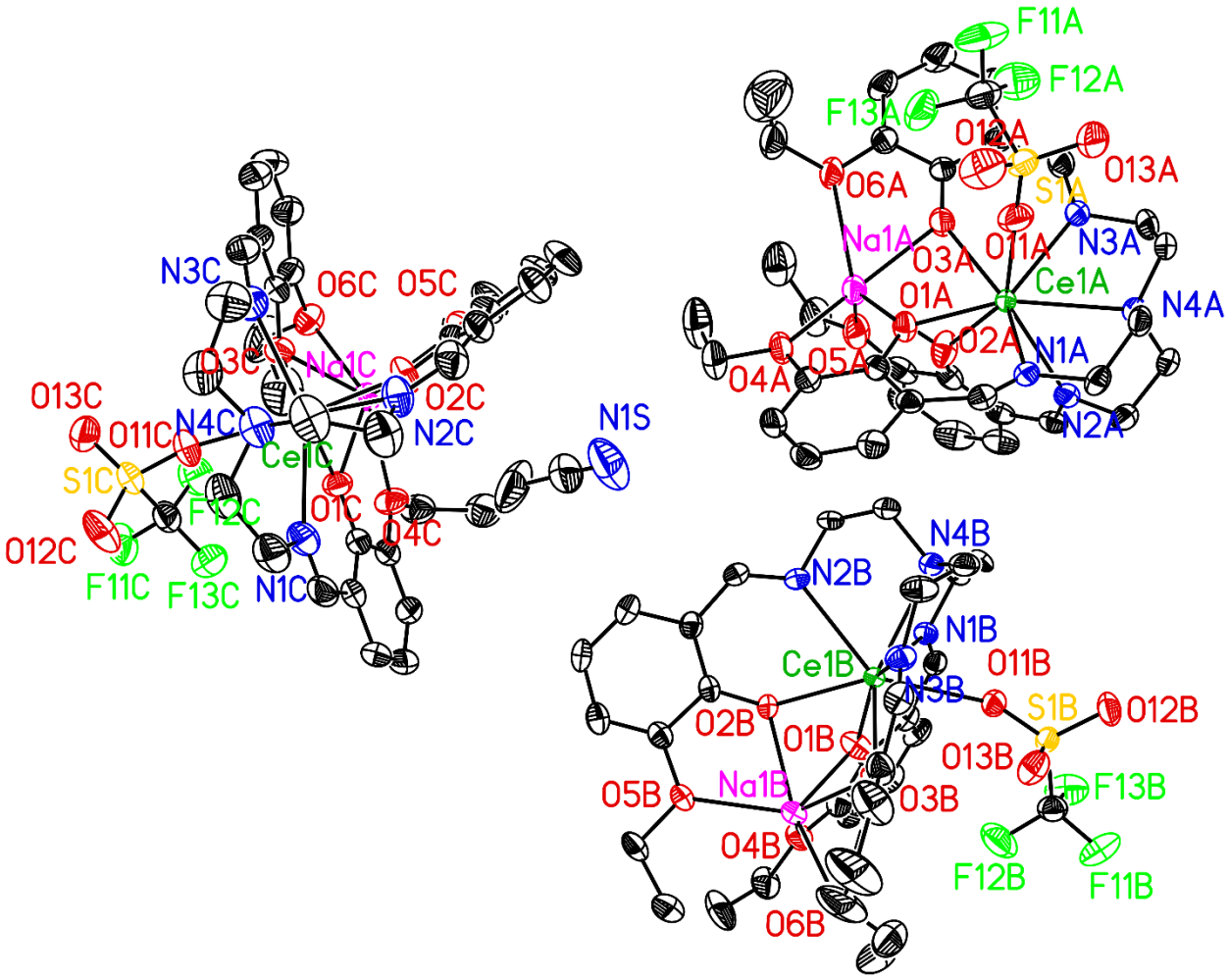

Figure F90. Full solid-state asymmetric unit of **1-Na** (XRD). Hydrogen atoms are omitted for clarity. Displacement ellipsoids are shown at the 50% probability level.

Special Refinement Details for 1-Ba

The first triflate is 68/32 disordered with two orientations about the Ce-O11 bond. All atoms for the minor (32%) occupancy triflate were refined with isotropic thermal parameters. C31 is 68/32 disordered between two positions by rotation about the O5-C30 bond.

Solid-State Structure of 1-Ba

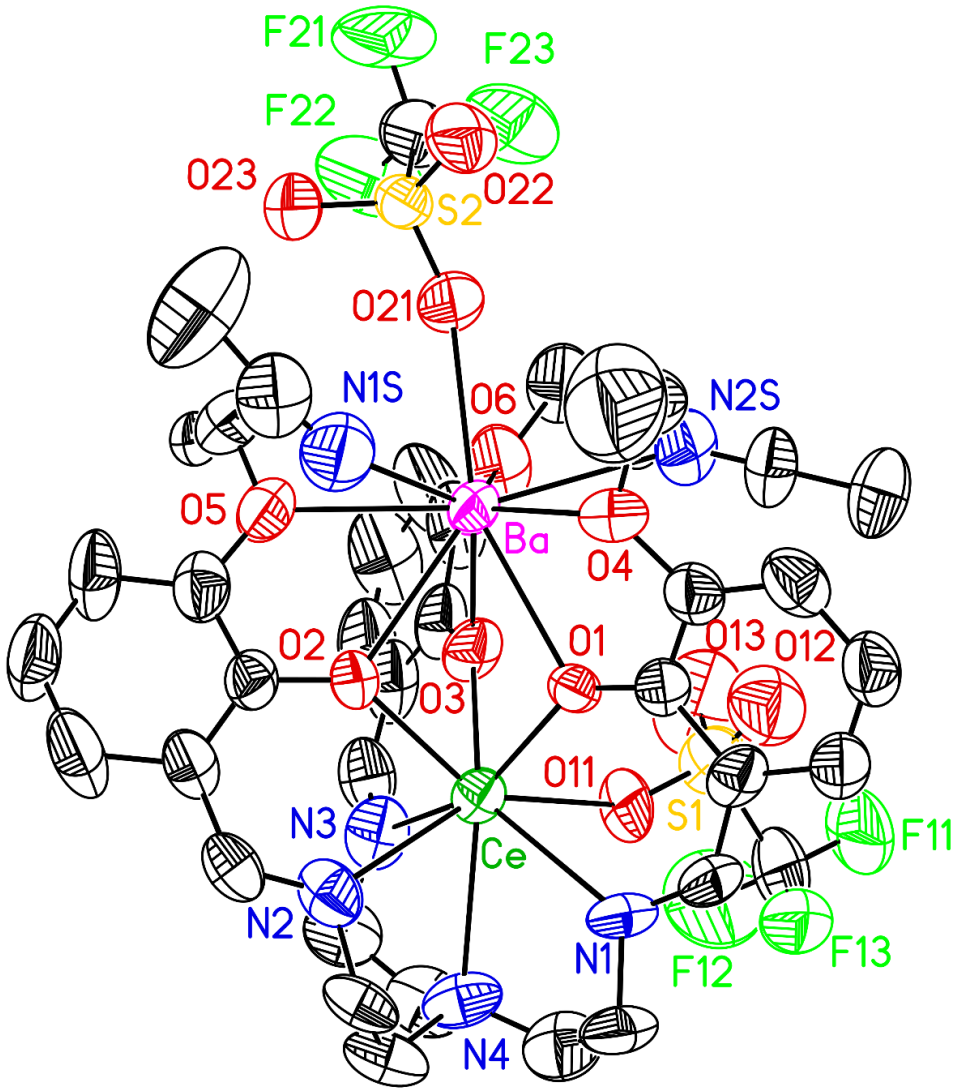

Figure F91. Solid-state structure of **1-Ba**. Hydrogen atoms and disordered atoms omitted for clarity. Displacement ellipsoids shown at the 50% probability level.

Full Solid-State Structure of 1-Ba

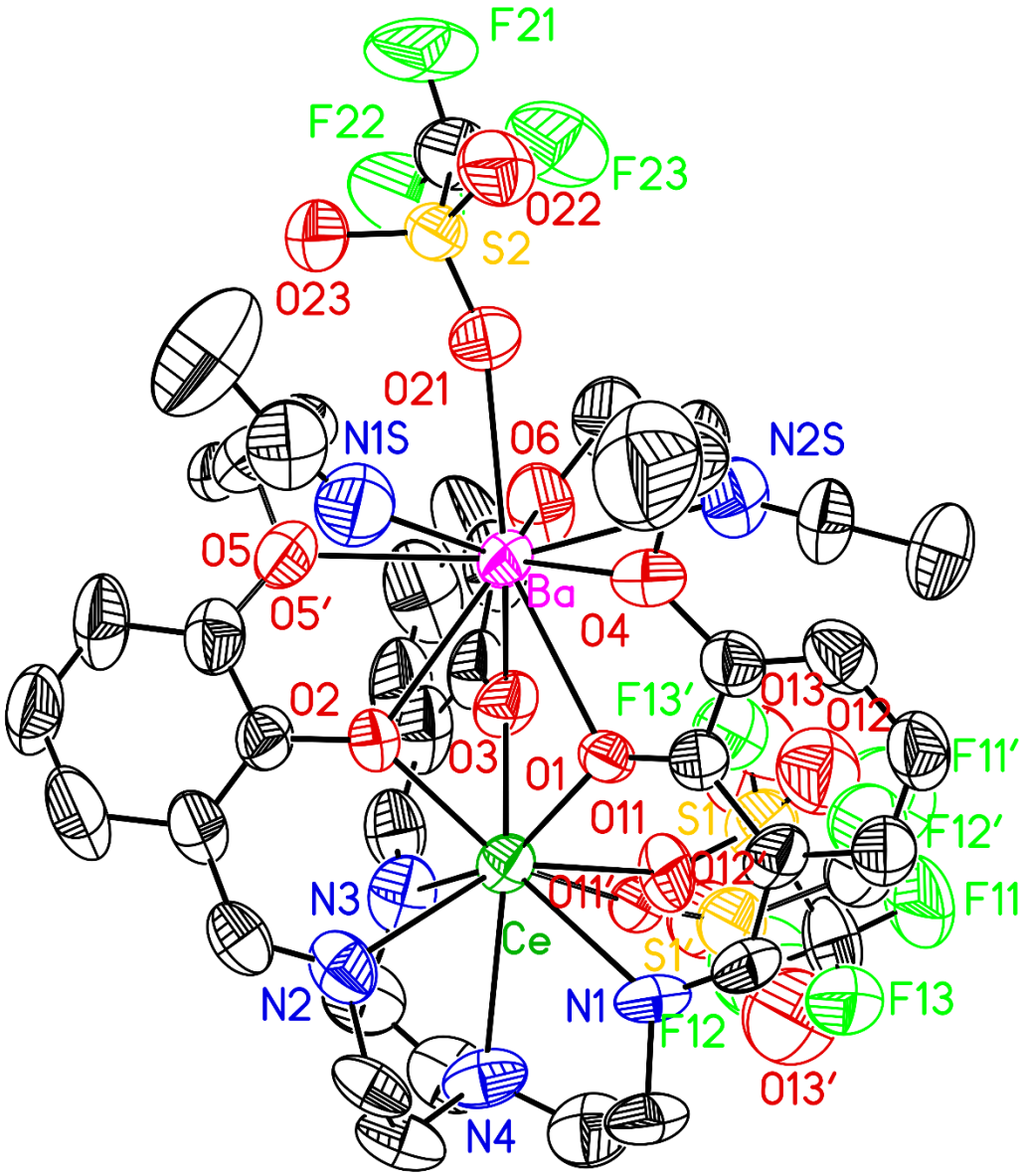

Figure F92. Full asymmetric unit for solid-state structure of **1-Ba**. Hydrogen atoms omitted for clarity. Displacement ellipsoids shown at the 50% probability level.

Special Refinement Details for 1-Sr

No special refinement was required.

Full Solid-State Structure of 1-Sr

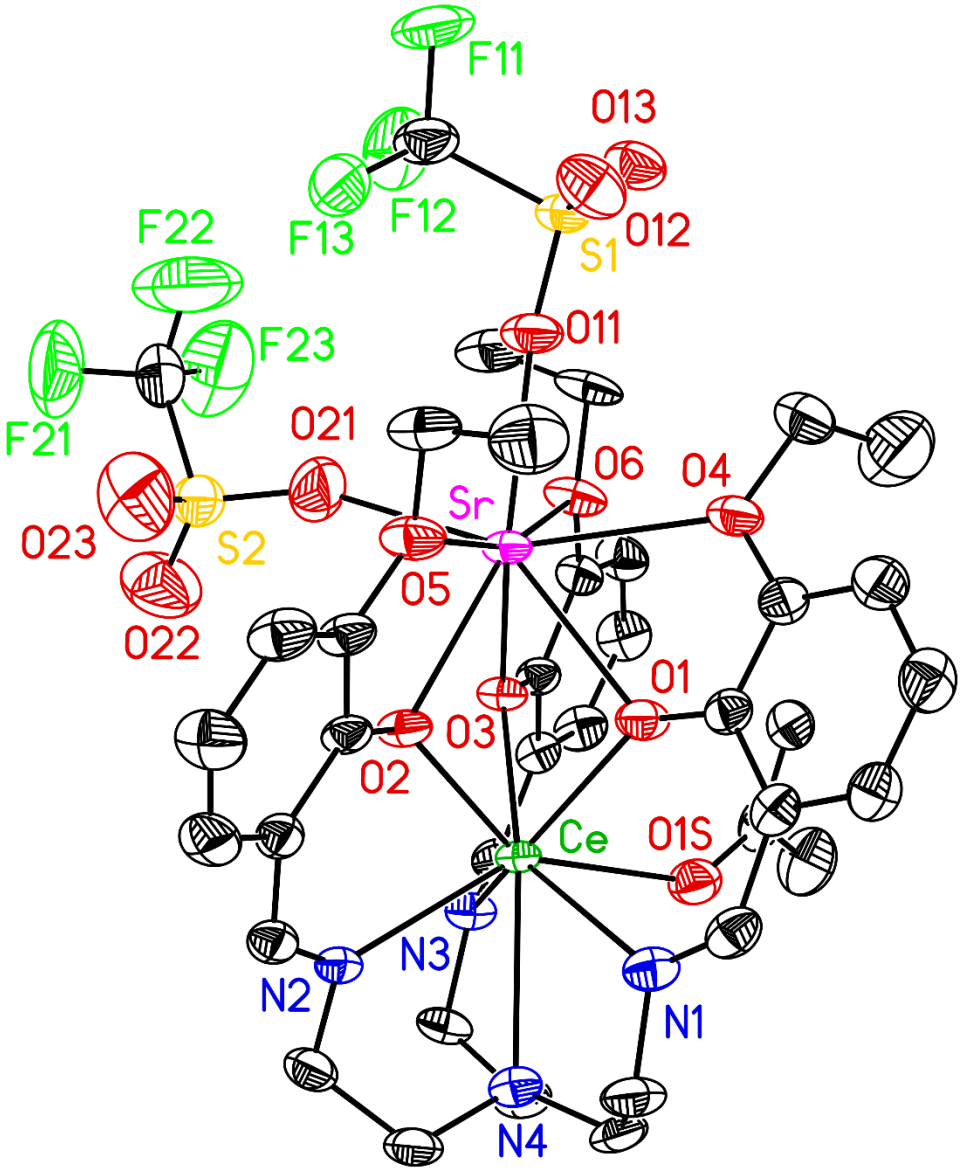

Figure F93. Solid-state structure for the asymmetric unit of **1-Sr**. Hydrogen atoms omitted for clarity. Displacement ellipsoids shown at the 50% probability level.

Special Refinement Details for 1-Ca

The four hydrogen atoms on the two coordinated water molecules were located from a difference Fourier and included in the structural model as independent isotropic atoms whose parameters were refined.

Solid-State Structure of 1-Ca

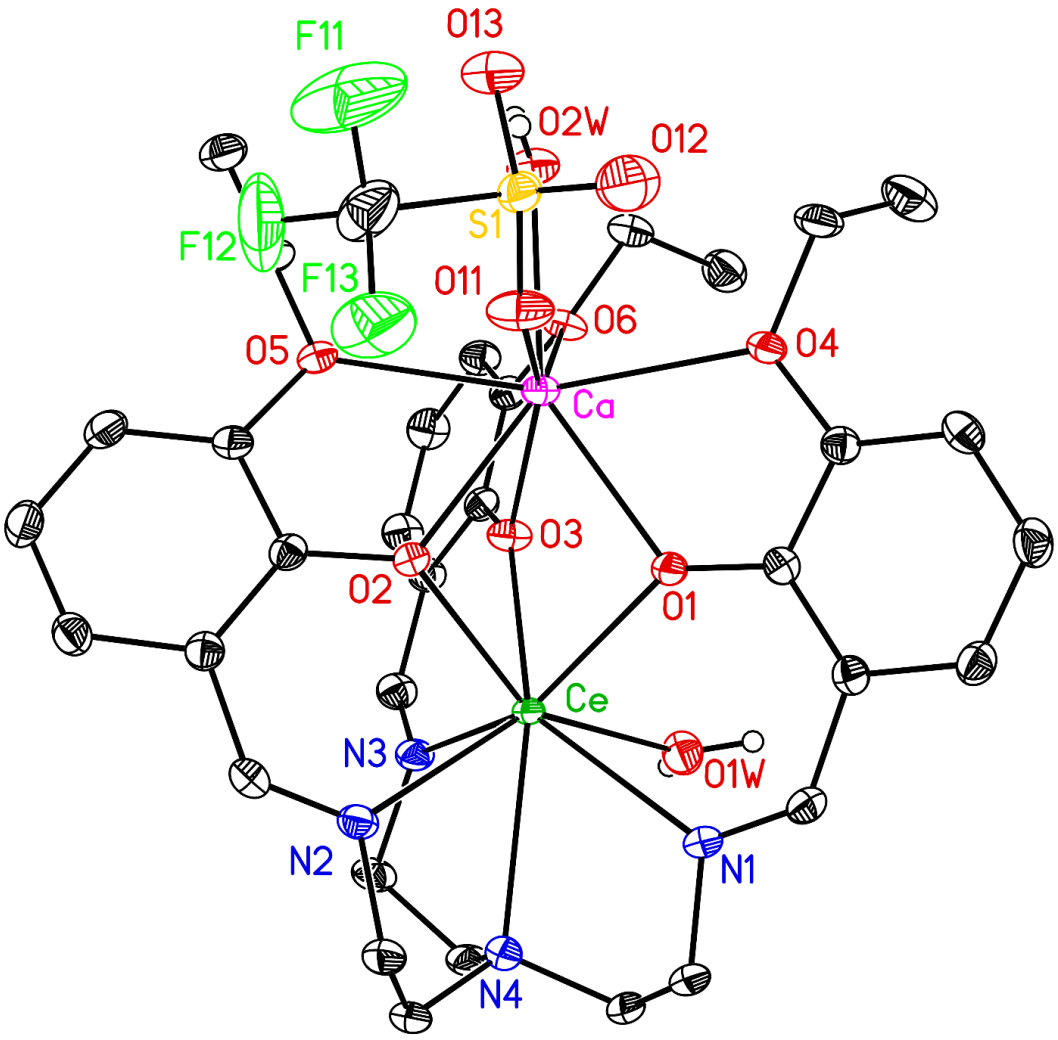

Figure F94. Solid-state structure of **1-Ca**. Hydrogen atoms not bonded to water, the outer-sphere triflate and ether solvent molecules in the asymmetric unit are omitted for clarity Displacement ellipsoids shown at the 50% probability level.

Full Solid-State Structure of 1-Ca

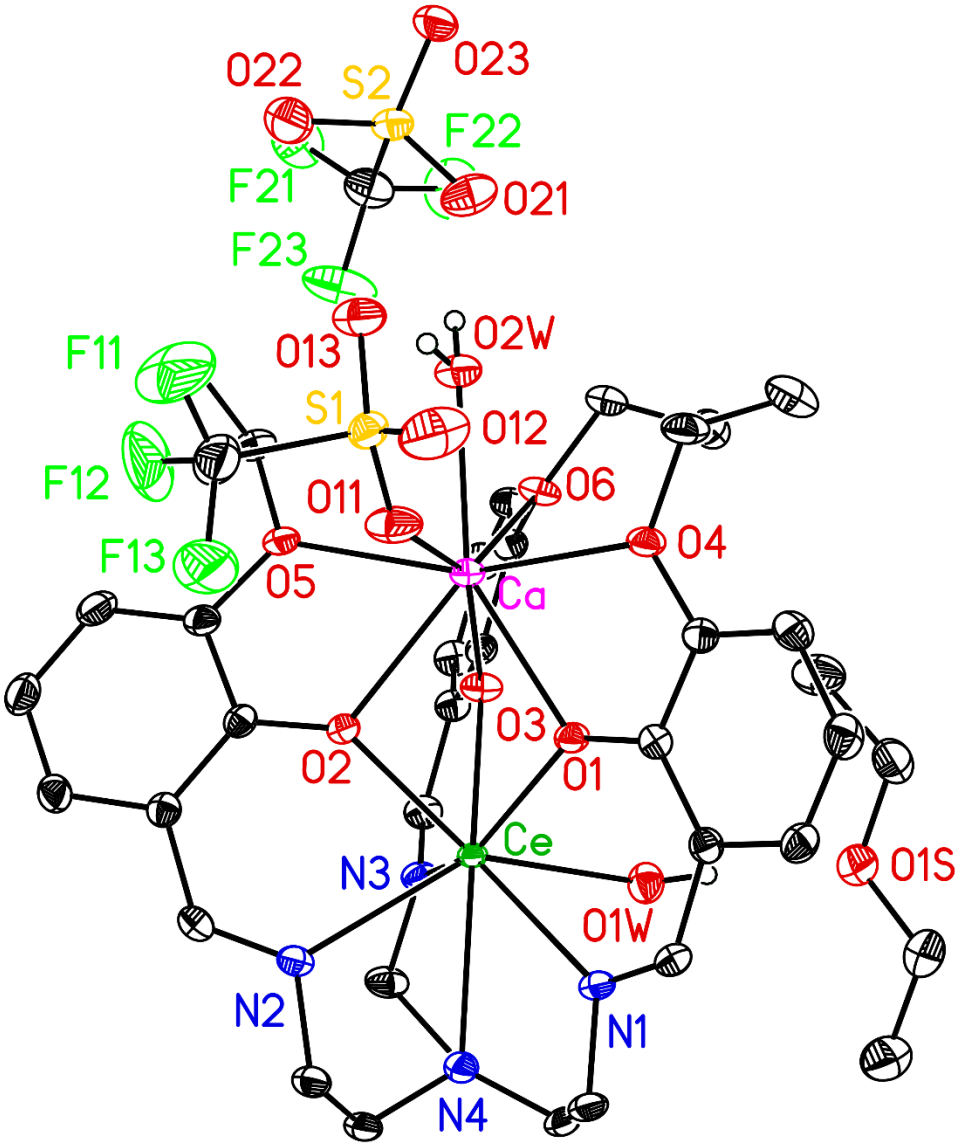

Figure F95. Full asymmetric unit for solid-state structure of **1-Ca**. Hydrogen atoms not bonded to water omitted for clarity. Displacement ellipsoids shown at the 50% probability level.

Special Refinement Details for 1-Li

The O4-C28-C29 ethoxy arm is 72/28 disordered over two sites by rotation about the O4-C28 bond. The acetonitrile molecule is 50/50 disordered about the inversion center at (½, ½, 0) with the C2S methyl carbon occupying the inversion center. Acetonitrile hydrogen atoms were not included in the structural model and all acetonitrile non-hydrogen atoms were included in the structural model with occupancy factors of 0.50.

Solid-State Structure of 1-Li

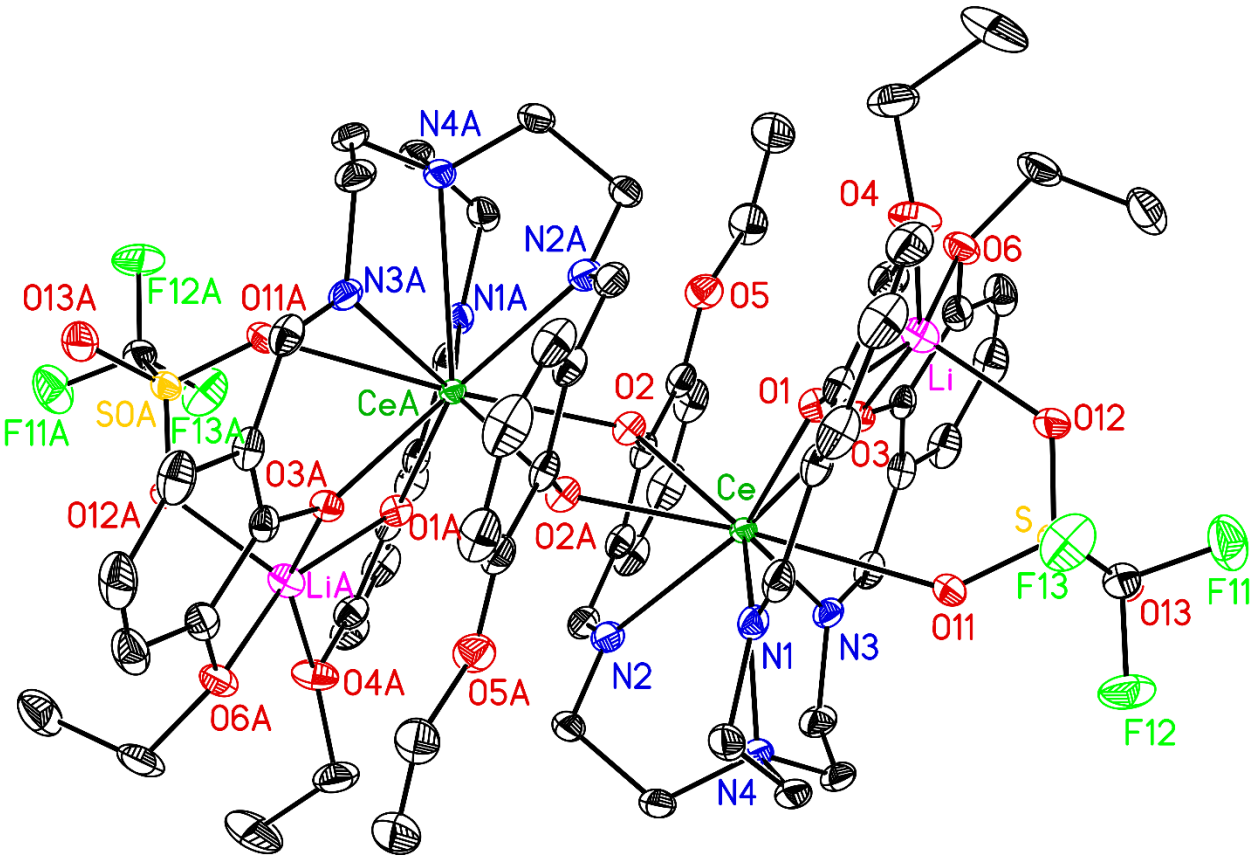

Figure F96. Centrosymmetric dimeric moiety formed in the solid-state structure of **1-Li**. Hydrogen atoms and acetonitrile solvent molecule of crystallization omitted for clarity. Displacement ellipsoids shown at the 50% probability level.

Monomeric Half of Dimer in the Asymmetric Unit of 1-Li

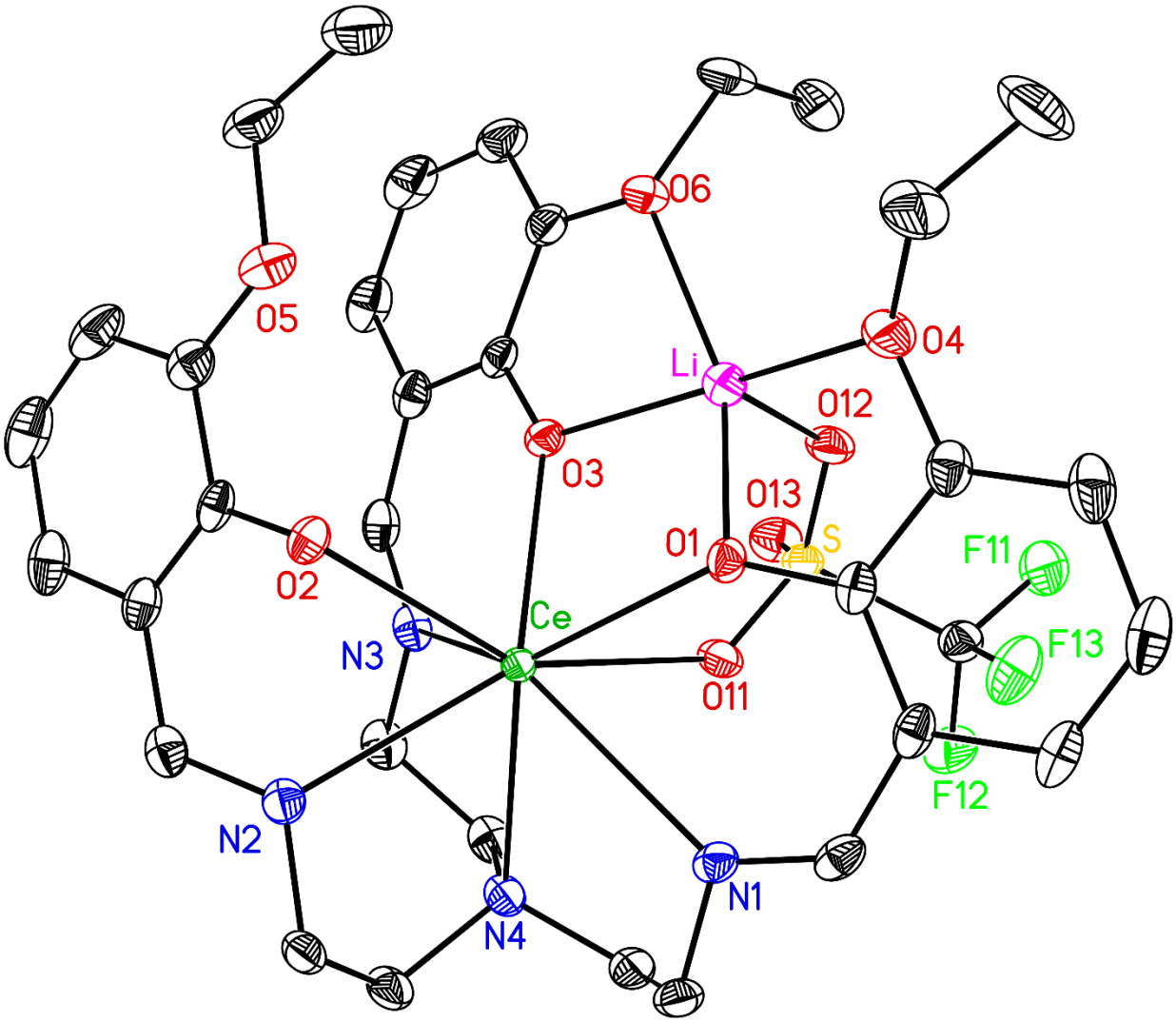

Figure F97. Monomeric half of the dimer present in the solid-state asymmetric unit of **1-Li**. The dimer is generated by a crystallographic inversion center at the origin of the unit cell. Hydrogen atoms and the other half of dimer are omitted for clarity. Displacement ellipsoids shown at the 50% probability level.

Full Solid-State Structure of 1-Li

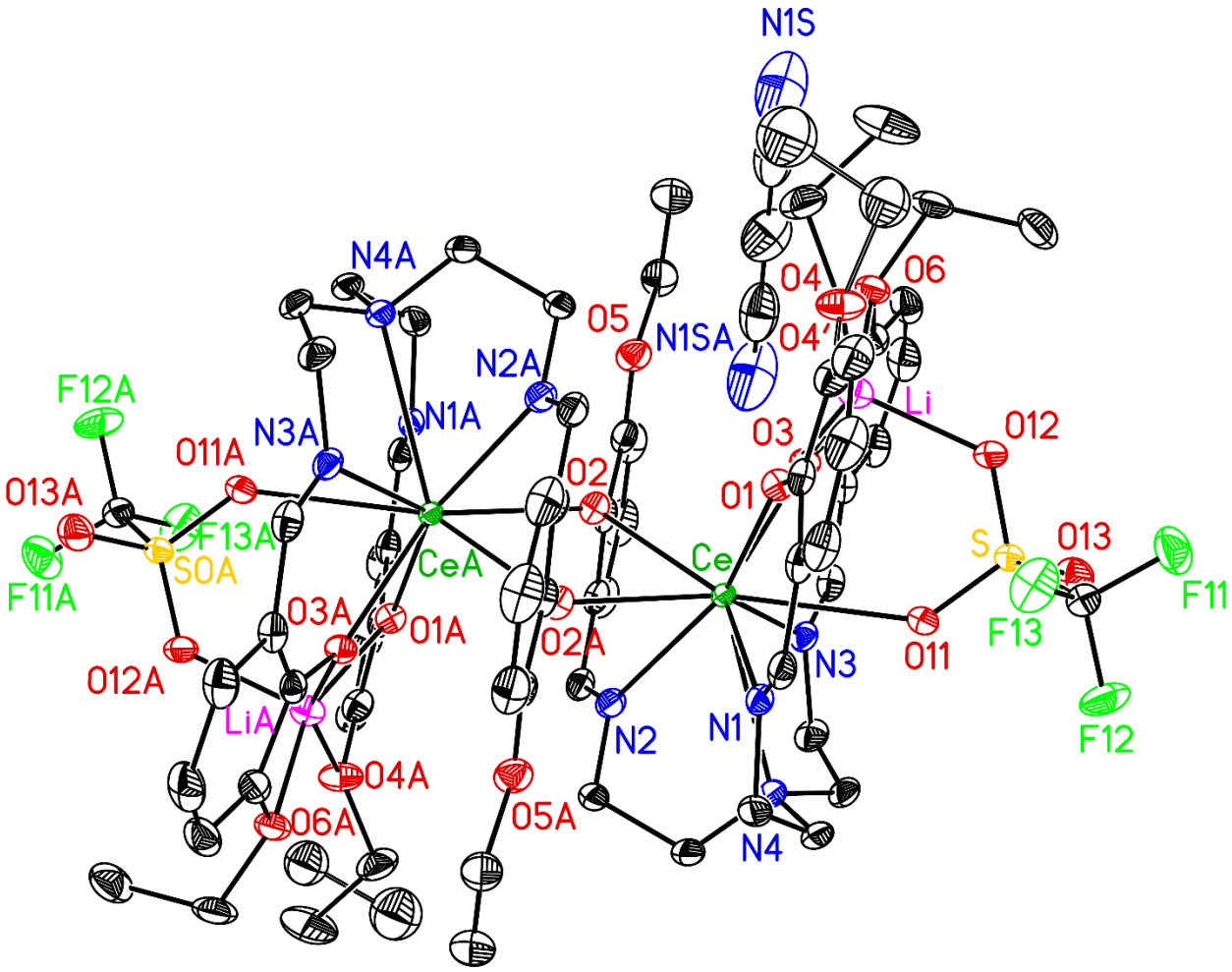

Figure F98. Solid-state structure of **1-Li showing two asymmetric units**. The O4-C28-C29 ethoxy arm is 72/28 disordered over two sites (minor site shown with hollow bond) by rotation about the O4-C28 bond. The acetonitrile molecule is 50/50 disordered about the inversion center at (½, ½, 0) with the methyl carbon occupying the inversion center. Hydrogen atoms omitted for clarity. Displacement ellipsoids shown at the 50% probability level.

Special Refinement Details for 2^{PF6}

The O6-C32-C33 ethoxy arm is 56/44 disordered over two sites. The second special-position (both occupy crystallographic C_2 axes) half occupancy $[PF_6]^-$ counteranion is 49/51 rotationally disordered about the phosphorus atom.

Solid-State Structure of 2^{PF6}

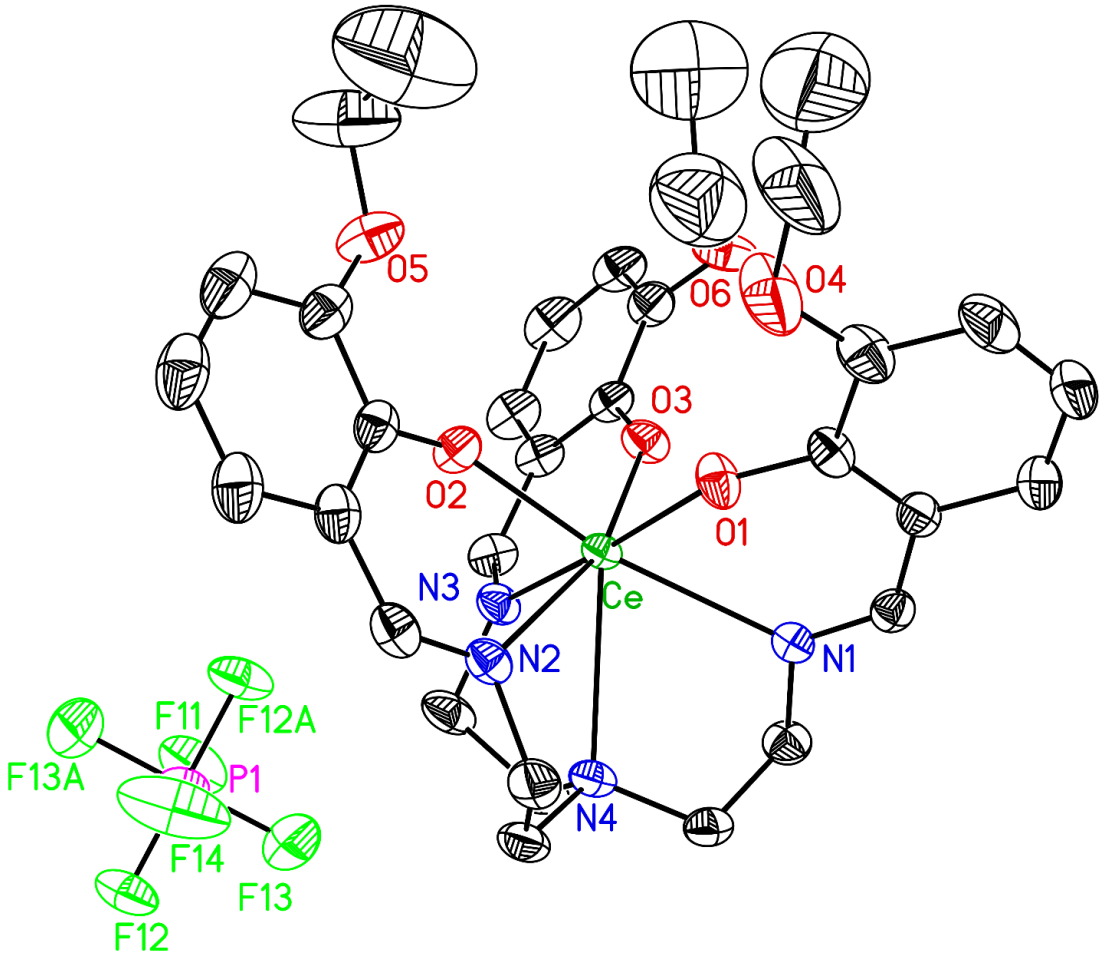

Figure F99. Solid-state structure of **2^{PF6}** showing one complete ordered special-position $[PF_6]^-$ counteranion Hydrogen atoms, disordered ethoxy arm and disordered second special-position $[PF_6]^-$ counteranion omitted for clarity. Displacement ellipsoids shown at the 50% probability level.

Solid-State Asymmetric Unit for 2^{PF6}

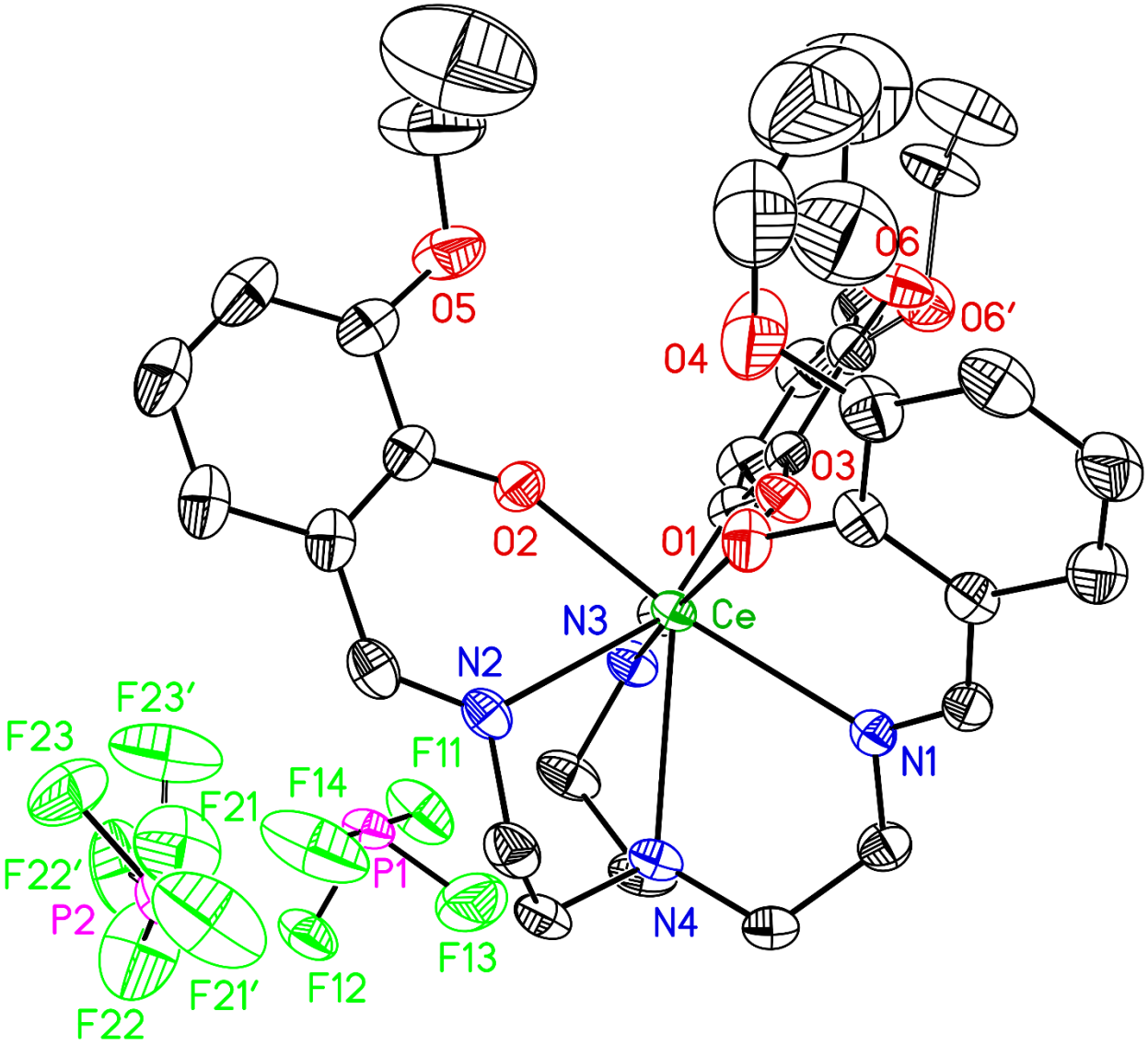

Figure F100. Full solid-state asymmetric unit for $\mathbf{2^{PF6}}$. Hydrogen atoms are omitted for clarity. Displacement ellipsoids shown at the 50% probability level.

Solid-State Structure of 2^{PF6}

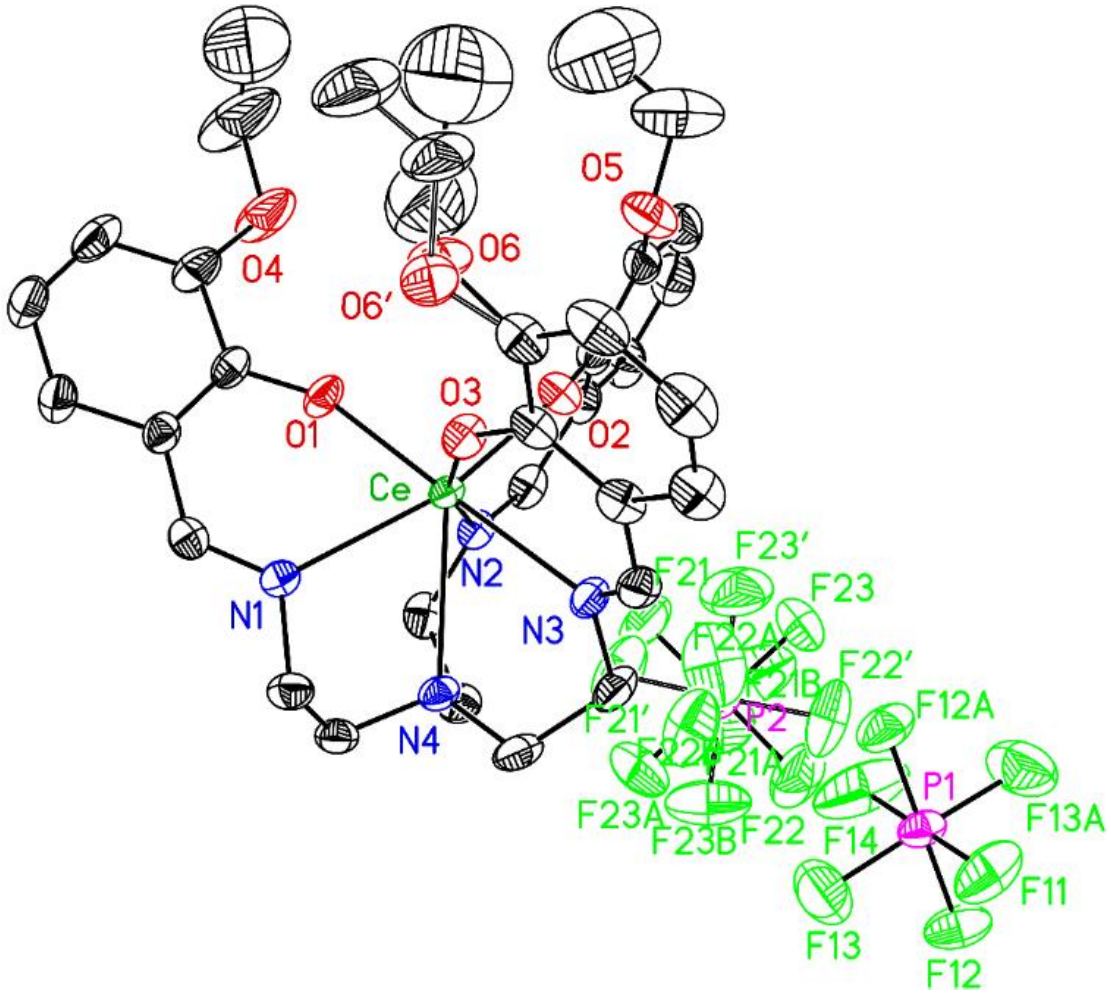

Figure F102. Solid-state structure of $\mathbf{2}^{PF6}$ showing disorder and two symmetry-expanded counteranions whose phosphorus atoms lie on the crystallographic C2 axis at (½ , y, ¾) in the unit cell. Each anion therefore account for a formal charge of (-½) for the asymmetric unit. The O6-C32-C33 ethoxy arm is 56/44 disordered over two sites and the minor occupancy site is shown with hollow bonds. Hydrogen atoms omitted for clarity. Displacement ellipsoids shown at the 50% probability level.

Special Refinement Details for 2^{OTf}

The second triflate occupies a disordered region of the asymmetric unit where the disorder involving this triflate and ethoxy arms of the second (B) Ce-containing molecule appear to be correlated. This triflate is 57/43 disordered with two closely separated orientations and a contiguous ethoxy C30B-C31B ethyl group is 58/42 disordered between two (B and C) sites. The nearby O4B-C32B-C33B ethoxy arm is 69/31 disordered over two sites and the C28B-C29B ethoxy ethyl group is 53/47 disordered over two sites. Atom names of the minor sites for this disorder have a C instead of a B.

Solid-State Structure of 2^{OTf}

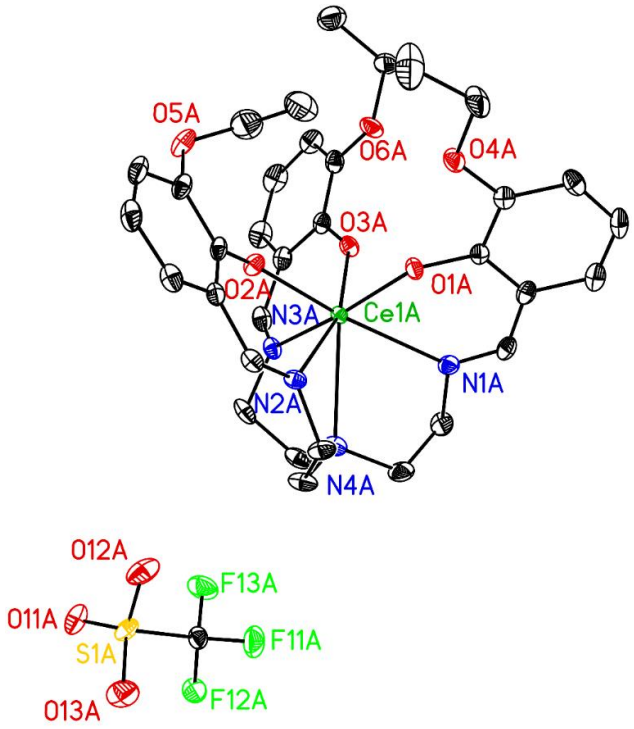

Figure F103. Solid-state structure for the first (A) anion/cation pair in the asymmetric unit of $\mathbf{2}^{OTf}$ (XRD). Hydrogen atoms, disordered atoms and the second (B) crystallographically-independent anion/cation pair in the asymmetric unit are omitted for clarity. Displacement ellipsoids are shown at the 50% probability level.

Full Solid-State Structure of 2^{OTf}

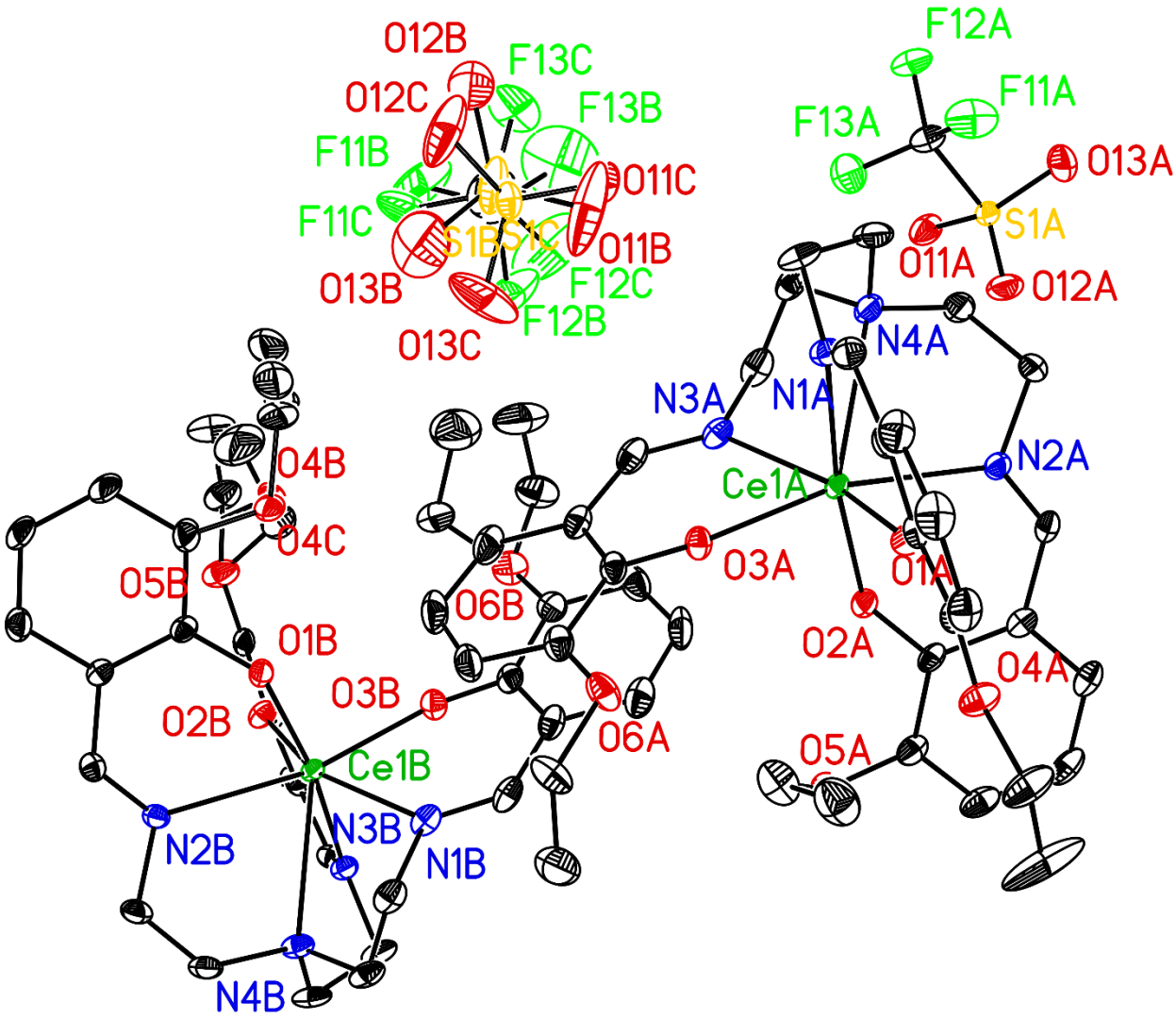

Figure F104. Full solid-state asymmetric unit of $\mathbf{2^{OTf}}$. Hydrogen atoms are omitted for clarity. Displacement ellipsoids shown at the 50% probability level. I think this one might need to be redrawn using the final coordinate file with the second triflate symmetry-transformed to be near the B/C cation.

Section F2.1 Effects of additional solvent and triflate ligands in 1-M

The identity of external ligands and coordination number of each secondary metal varies amongst each **1-M** complex; the differing steric influences and coordination number (Table E4-E6) gives rise to variability in direct comparison of properties and influences amongst the heterobimetallic complexes. In particular, this variability is exemplified in the scattering observed in comparison properties of the O_{Ar} plane and O_{ether} plane; in which there is no direct trend observed, steric or otherwise, for the distance or angle between these planes (see Appendix F, Figures F128 and F129). The bulkier triflate ligands featured in **1-Na**, **1-Ba** (Figure 8.3 and 8.4) markedly increase the N_{imine}•••O_{Ar} plane distance as compared to the smaller solvent ligands in **1-Sr**, **1-Ca**, and **1-K** (Figure 8.1, 8.4, and 8.5) by ca. 0.67 Å (see Appendix F, Figure F115). The angle between the N_{imine} plane and O_{Ar} plane are essentially parallel to one another, with small deviations from 0° (see Appendix F, Figure F114). Additionally, the core linearity of the **M**–Ce–N4 of the **1-M** complexes is observed to depend on the Shannon ionic radius[1] of the **M** secondary metal. We observe that metals with smaller ionic radius have a larger angle associated with the core linearity (closer to 180°) but binding of larger metal ions there is a smaller **M**–Ce–N4 angle (farther from 180°) (see Appendix F, Figure F124). This trend indicates that there is a dependency of ionic radius with the core linearity of the **1-M**, however, the deviation from 180° is minimal ranging c.a. 6.5° for **1-K**.

Section F2.2 Structural effects on ligand framework upon binding of M

The average distance of the aryl either O4, O5, O6 atoms range from 4.74 Å for **1-K** to 4.12 Å for **1-Ca**, for which there is a clear trend amongst the **1-M** complexes where the average O_{ether} distance increases with increasing ionic radius.[1] The average distance of the O_{Ar} O1, O2, O3 atoms range from 3.00 Å for **1-K** to 2.79 Å for **1-Ca** (Table F1). The observed

average O_{Ar} atom distances increase with increasing ionic radius and decreasing Lewis acidity (see Appendix F, Figure F105). However, there is a small observed trend amongst the **1-M** complexes in which the average N_{imine} atom distance varies with the Shannon ionic radius[1] and the Lewis acidity of the secondary metal. The observed average N_{imine} atom distances decrease with increasing ionic radius and decreasing Lewis acidity (see Appendix F, Figure F104).

Notably, we observe an inverse trend for the N_{imine} (N1, N2, and N3) distances compared to that of the O_{Ar} (O1, O2, and O3) and O_{ether} (O4, O5, and O6) moieties. The O_{ether} distances are most effected by the binding of the secondary ion, ranging 1.39 Å from **1** to **1-Ca**. This is ascribable to the labile nature of the ethoxy substituents. Comparatively, the O_{Ar} distances are less effected by the complexation of the secondary ion, ranging 0.60 Å from **1** to **1-Ca**. The O_{Ar} moieties have more inherent structural constraint because of the inflexible nature of the aryl backbone in the ligand framework. However, inspection of the N_{imine} distances reveal that they are the least impacted in terms of a change in distance to one another, 0.18 Å from **1** to **1-Na** (Table F4-F6). The N_{imine} moieties are the most inflexible due rigidity of the lower portion of the ligand framework. Importantly, this inverse trend for the O atom moieties and N_{imine} moieties indicates that upon binding a secondary metal the O atoms move outwards to accommodate the size of the secondary metal. Conversely, the binding of secondary metals with a larger ionic radius contract the N_{imine} thus moving inward as a result of the expansion of the O moieties on the ligand backbone within the **1-M** series.

Section F2.3 Structural trends of hexadentate site

There is more steric encumbrance for the larger ions to fit in the binding site and therefore sit higher in the upper site, the smaller ions are more sterically able to sit lower in the site.

The is supported by the inverse relationship between the Lewis acidic metal and O_{Ar} (O1-O3) plane distance and Lewis acidic metal and O_{ether} (O4-O6) plane distance with the secondary metal's Shannon ionic radius.[1] This behavior is reflected in the average bond angle between the O_{Ar} atoms-**M**-O_{ether} atoms (see Appendix F, Figure F121). The average bond angle decreases as the ionic radius of the secondary metal increases; thus, the higher position of the ion in the pocket consequently makes the angle smaller. The average distance of the O_{Ar} and O_{ether} moieties are independent ionic radius due to the rigidity of the 5-member metallocycle containing the aryl backbone (see Appendix F, Figure F120).

Section F2.4 Structural trends of heptadentate site

Examination of average O_{Ar} moieties (O1, O2, O3) to apical N4 distance, (O_{Ar}–N4) which illustrates that as the Lewis acidity increases, the average distance of the O_{Ar} to the apical N4 increases (see Appendix F, Figure F107). This trend further illustrates the phenomenon that the increasing Lewis acidity of **M** pulls the electron density of the O_{Ar} moieties towards the Lewis acidic metal. Additionally, the average Ce–O_{Ar} (O1-O3) distances reveals a direct trend with pKa of the Lewis acidic ion. The distance between the Ce center and O_{Ar} (O1-O3) plane reflects this relationship as well, it is observed that as the Lewis acidity of the secondary metal increases the Ce center and O_{Ar} (O1-O3) plane distance increases (see Appendix F, Figure F118). The inverse trend is observed for Ce center and N_{imine} (N1-N3) plane, as the Lewis acidity increases the N_{imine} (N1-N3) plane distance decreases (see Appendix F, Figure F112). Similarly, the distance between the O_{Ar} and N_{imine} moieties in the 6-membered metallocycle trend with Lewis acidity of the secondary metal, in which the distance of the N_{imine} and O_{Ar} moieties increase with increasing Lewis acidity of the secondary metal (see Appendix F, Figure F108). However, the apical Ce–N4 distance are essentially invariant with Lewis acidity

or ionic radius due to the distal placement (see Appendix F, Figure F111). A similar invariance is observed with the N_{imine} (N1-N3) distance to the apical N atom due to the rigid nature of the 4-member metallocycle containing the N_{imine} (N1-N3) Ce metal and apical N4 (see Appendix F, Figure F106).

Section F2.5 Further Discussion of the Structure of 1-Li

In the **1-Li** structure the Li^+ (Coordination Number (CN) 4: 0.73 Å, CN 6: 0.90 Å)[1] ion binds in a κ^2-fashion to the O_{Ar} and O_{ether} moieties of two of the ligands. Instead of binding to the third ligand arm, Li^+ binds in a κ^1-fashion to the oxygen of triflate. The triflate is bound to Li^+ ion and the Ce center, this binding for triflate is unique amongst the **1-M** series. Consequently, the O_{Ar} moiety of the unbound ligand arm forms a dimeric form of the complex in which there is a diamond core formed by CeA-O2A-O2-Ce (see Appendix F, Figure F96). In the **1-Li** structure the Li^+ ion binds in a κ^2-fashion to the O_{Ar} and O_{ether} moieties of two of the ligands. Instead of binding to the third ligand arm, Li^+ binds in a κ^1-fashion to the oxygen of triflate. The triflate is bound to Li^+ ion and the Ce center, this binding for triflate is unique amongst the **1-M** series. The average Ce–O2 bonds in the diamond core are significantly elongated (2.5205 (12) Å) compared to that of the Ce–O1 and Ce–O3 bonds bound to Li^+ (2.3863(12) Å and 2.3699(12) Å, respectively) (Table F4).

Section F2.6 Structural details of Ce(IV) complexes

As previously observed, there is an observed tendency for the heterobimetallic complexes to bind a triflate or solvent molecule to the Ce(III) center. It is expected that in the $\mathbf{2^{PF6}}$ complex does not in fact bind the hexafluorophosphate counteranion due to its non-coordinating nature. However, it is notable that the $\mathbf{2^{OTf}}$ complex does not bind the triflate counteranion in the solid-state even though binding of triflate to the Ce center is observed in

three of the heterobimetallic complexes. Additionally, this observation is interesting because the ^{31}P NMR studies with triethylphosphine oxide (TEPO) suggest that the Ce(III) and Ce(IV) monometallic complexes are capable of binding an eighth ligand in the solution state (see Appendix F, Figures F32-F34). In these experiments one equivalent of TEPO was added to **1** and $\mathbf{2^{PF6}}$ in CD_3CN. The ^{31}P NMR resonance for TEPO is observed at 48.62 ppm in CD_3CN. Addition of TEPO to the diamagnetic $\mathbf{2^{PF6}}$ complex results in a downfield shift to 75.44 ppm, indicating that the TEPO is bound to the cerium(IV) complex. Upon addition of TEPO to **1** upon we observe the disappearance of the resonance corresponding to TEPO, indicating that TEPO is bound to the paramagnetic cerium(III) complex. However, interestingly neither **1** nor $\mathbf{2^{PF6}}$ binds an eighth ligand in the solid-state.

Similar to the Ce(III) complex **1** (*vide supra*), the geometry about the Ce(IV) site is found to be mono-capped pseudo-octahedral as evidenced by XRD. The average "twist" angles of the N_{imine} and O_{Ar} moieties for $\mathbf{2^{PF6}}$ and $\mathbf{2^{OTf}}$ are 47.23° and 46.17° respectively and are larger in comparison to that of **1** (43.23°). The second hexadentate site presents a pseudo-trigonal prism geometry observable via XRD (see Appendix F, Figures F138 and F139). The average "twist" angles for the O_{Ar} and O_{ether} moieties of $\mathbf{2^{PF6}}$ and $\mathbf{2^{OTf}}$ are 9.97° and 9.83° respectively and very similar in comparison to that of **1** (10.10°) (Table F7). The enlargement of the "twist" angles of the N_{imine} and O_{Ar} moieties for $\mathbf{2^{PF6}}$ and $\mathbf{2^{OTf}}$ compared to **1** and the lack of variation "twist" angles for the O_{Ar} and O_{ether} moieties between **1** and $\mathbf{2^{X}}$ is attributed to the larger Shannon ionic radius[1] of the Ce(III) ion, 1.01 Å, and smaller radius of the Ce(IV) ion, 0.87 Å, and lack of secondary metal ion to influence the O_{Ar}, O_{ether} moieties. The angles between the planes defined by N_{imine} and O_{Ar} as well as the angles between the planes defined by the O_{Ar} and O_{ether} atoms are essentially parallel and show no large deviation between Ce(III) and

Ce(IV). The more electronegative Ce(IV) has a greater capacity to pull electron density towards itself than the Ce(III) ion, which results in a marked shortening of bonds in the comparison of **1** and $\mathbf{2^X}$ (Table F7). The only exception to this shortening of bond distances is the Ce–N4 bond in which there is a slight lengthening in the case of $\mathbf{2^X}$ and **1**. Notably, there is no great deviation between the Ce(III) and Ce(IV) complexes in the backbone of the ligand. There is not a notable difference in the N_{imine} –Ce–N4 nor the O_{Ar}–Ce– N_{imine} angle. Additionally, there is large deviation in the values of the O_{Ar}•••O_{ether} average distance due to the rigid aryl backbone.

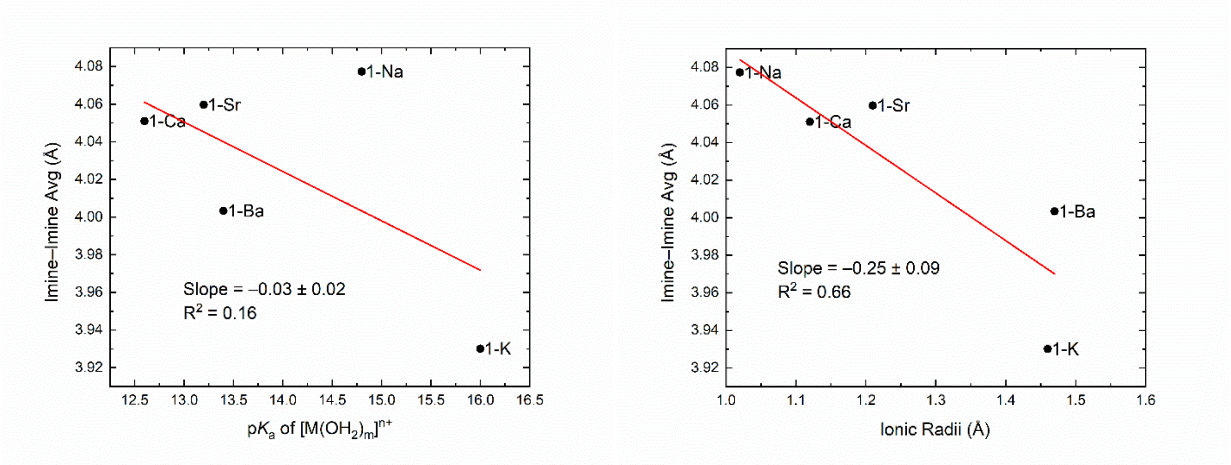

Figure F104. Dependence on average N_{imine}•••N_{imine} atom (N1, N2 and N3) distance on the pK_a of $[\mathbf{M}(H_2O)_m]^{n+}$ (left) and Shannon Ionic Radius (right) of 1-**M** (Excluding 1-Li).

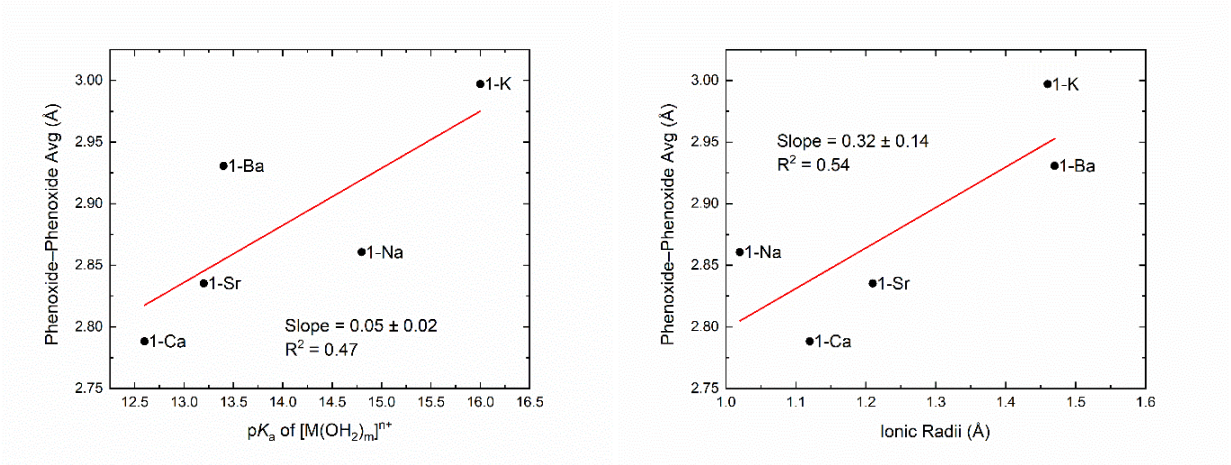

Figure F105. Dependence on average O_{Ar}•••O_{Ar} atom (O1, O2 and O3) distance on the pK_a of $[\mathbf{M}(H_2O)_m]^{n+}$ (left) and Shannon Ionic Radius (right) of 1-**M** (Excluding 1-Li).

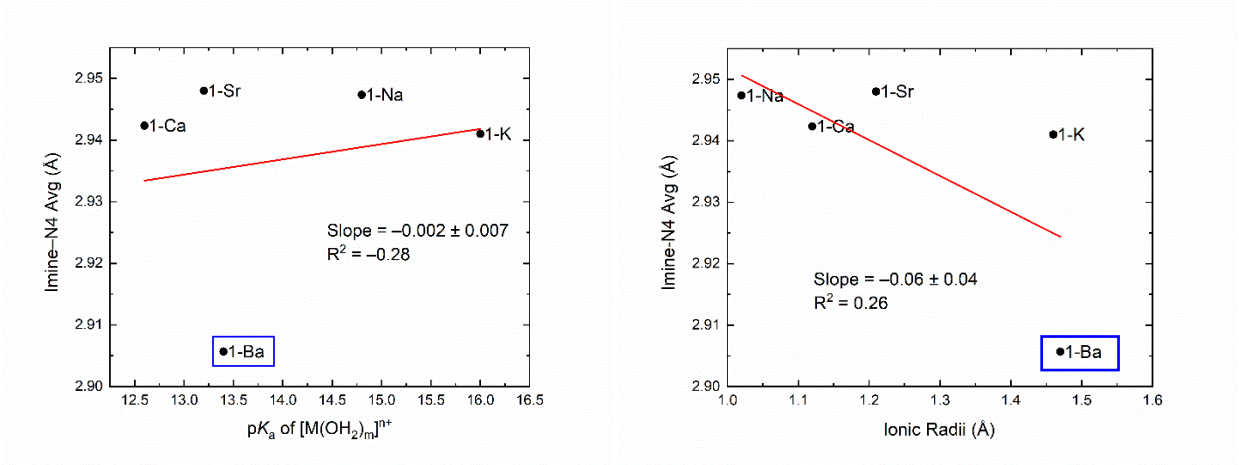

Figure F106. Dependence on average N_{imine}–N4 distance on the pK_a of $[\mathbf{M}(H_2O)_m]^{n+}$ (left) and Shannon Ionic Radius (right) of 1-**M** (Excluding 1-Li). 1-Ba complex is an outlier.

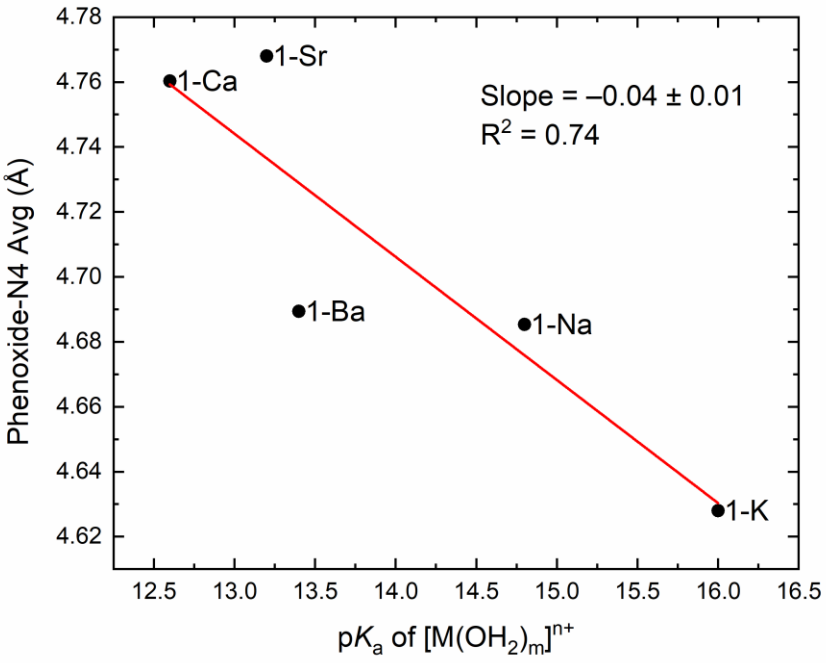

Figure F107. Dependence on average O_{Ar}•••N4 distance on the pK_a of $[\mathbf{M}(H_2O)_m]^{n+}$ (Excluding **1-Li**).

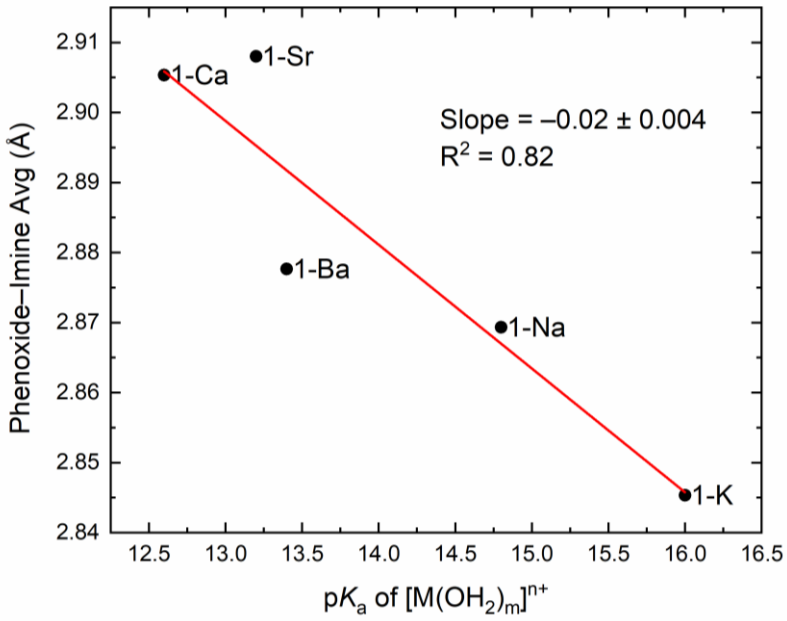

Figure F108. Dependence on average O_{Ar}•••N_{imine} distance on the pK_a of [**M**$(H_2O)_m]^{n+}$ (Excluding **1-Li**).

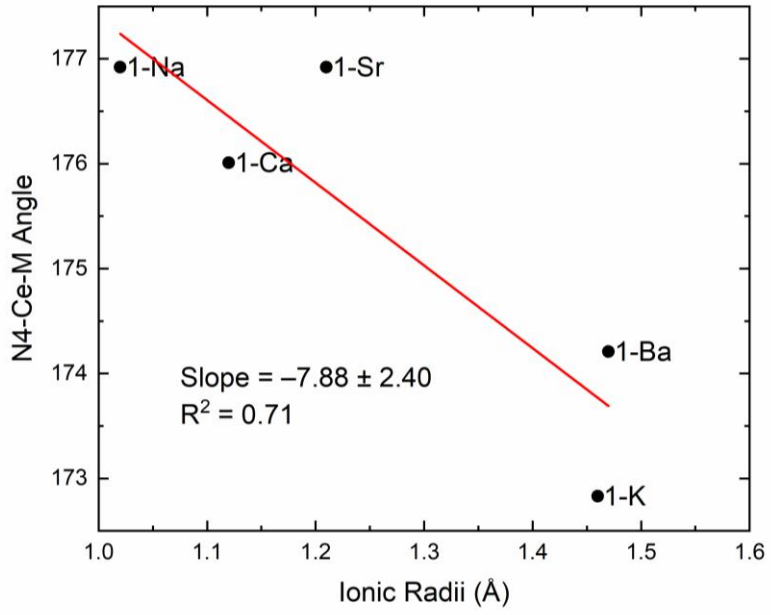

Figure F109. Dependence on average N_{imine}-Ce-N4 angle on the pK_a of [**M**$(H_2O)_m]^{n+}$ (Excluding **1-Li**).

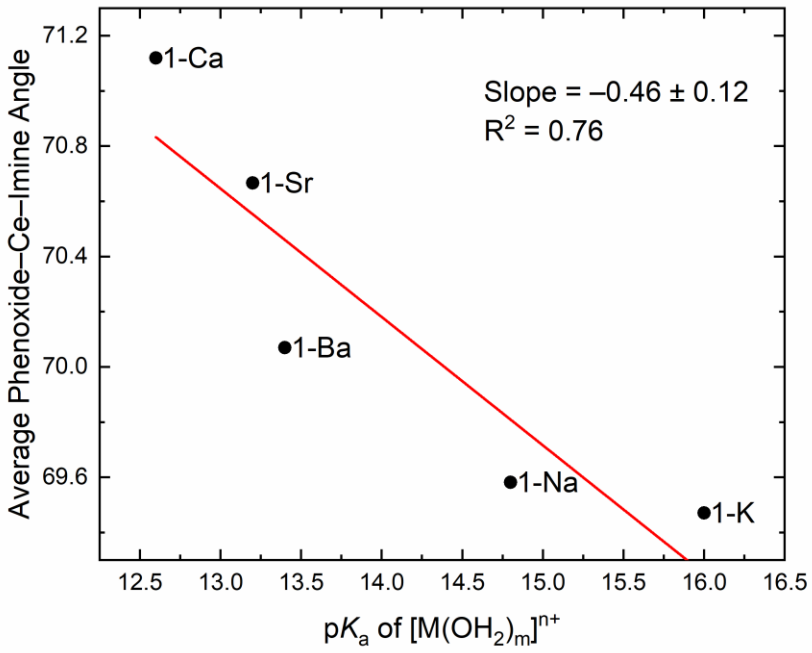

Figure F110. Dependence on average O_{Ar}-Ce-N_{imine} angle on the Shannon Ionic Radius (Excluding **1-Li**).

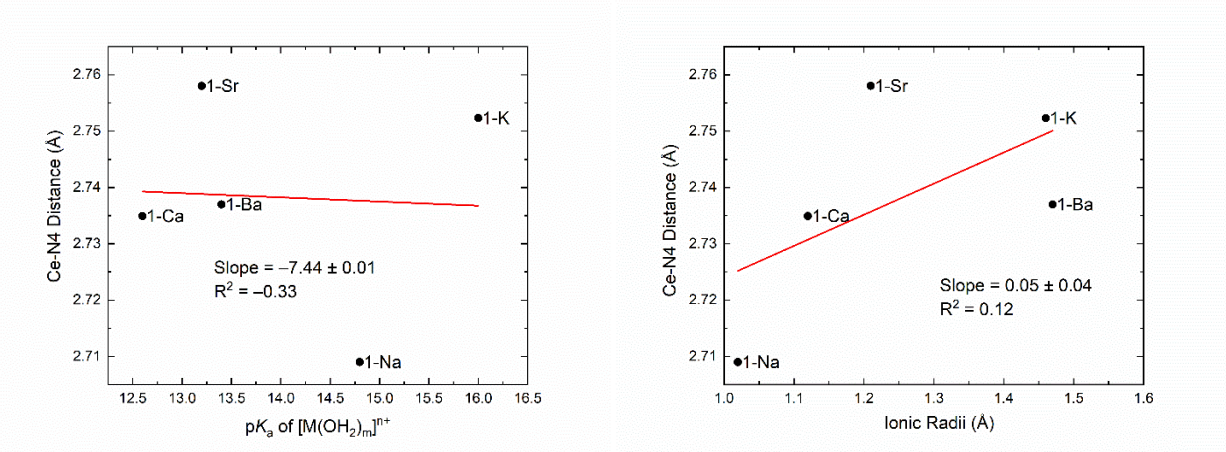

Figure F111. Dependence on average Ce–N4 distance on the pK_a of $[\mathbf{M}(H_2O)_m]^{n+}$ (left) and Shannon Ionic Radius (right) of **1-M** (Excluding **1-Li**).

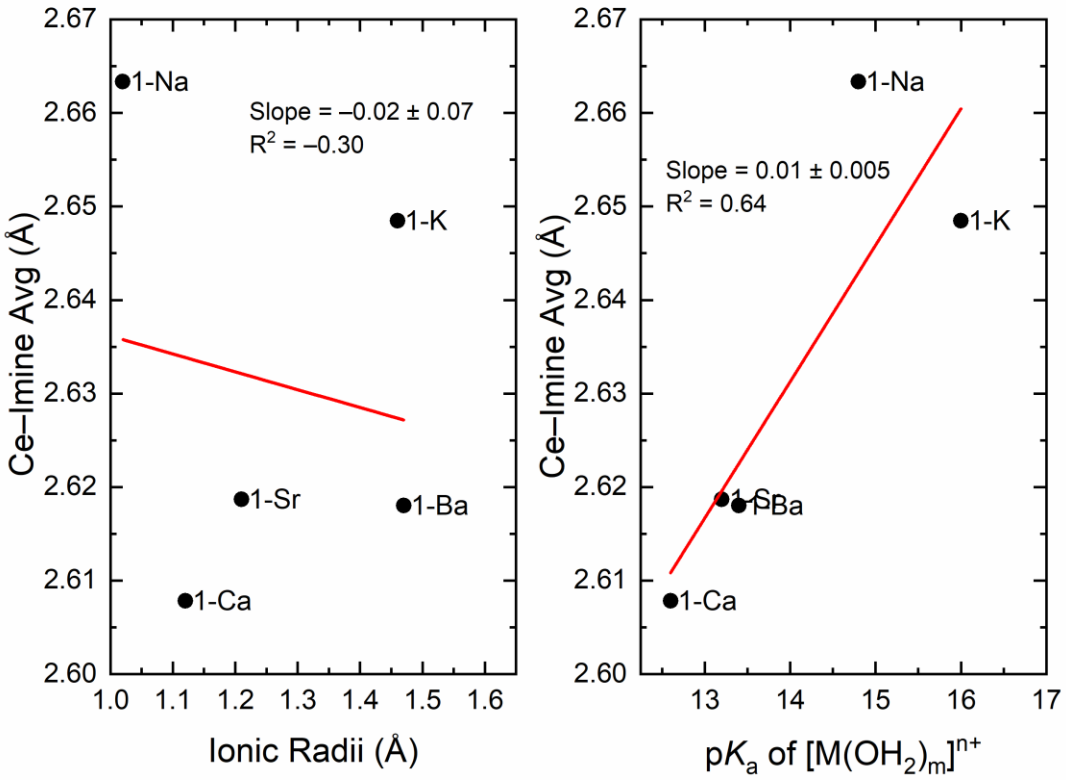

Figure F112. Dependence on average Ce–N_{imine} distance on the pK_a of [**M**$(H_2O)_m]^{n+}$ (right) and Shannon Ionic Radius (left) of **1-M** (Excluding **1-Li**).

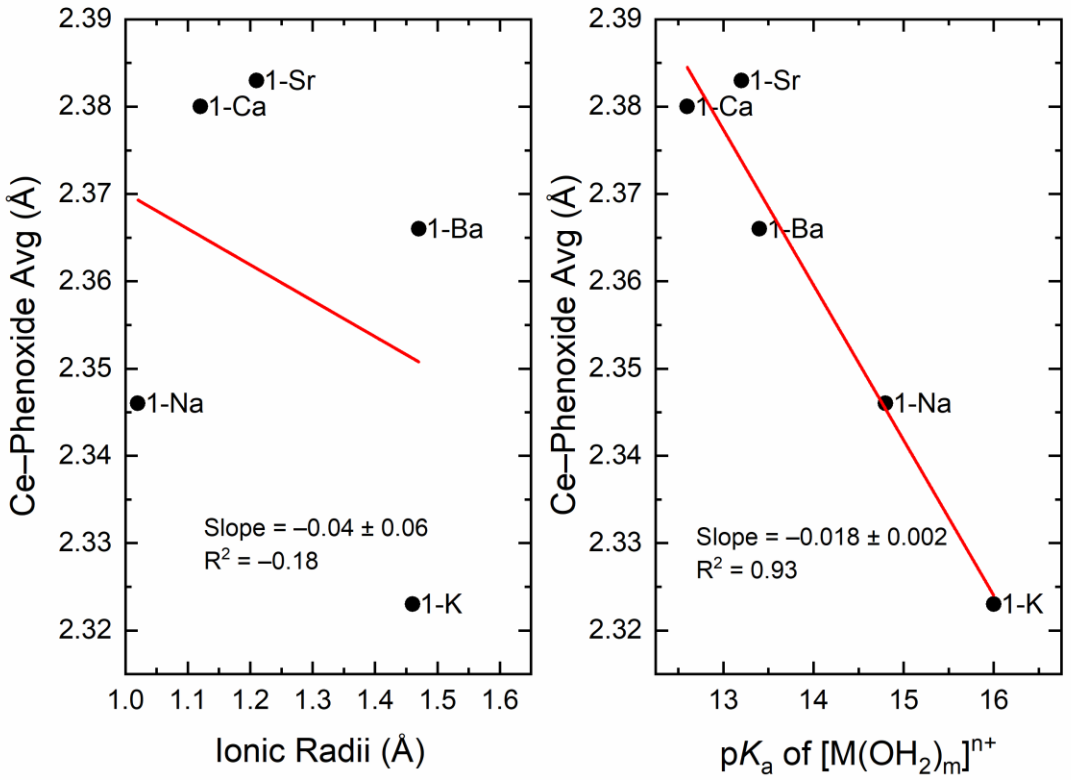

Figure F113. Dependence on average Ce–O_{Ar} distance on the pK_a of $[\mathbf{M}(H_2O)_m]^{n+}$ (right) and Shannon Ionic Radius (left) of **1-M** (Excluding **1-Li**).

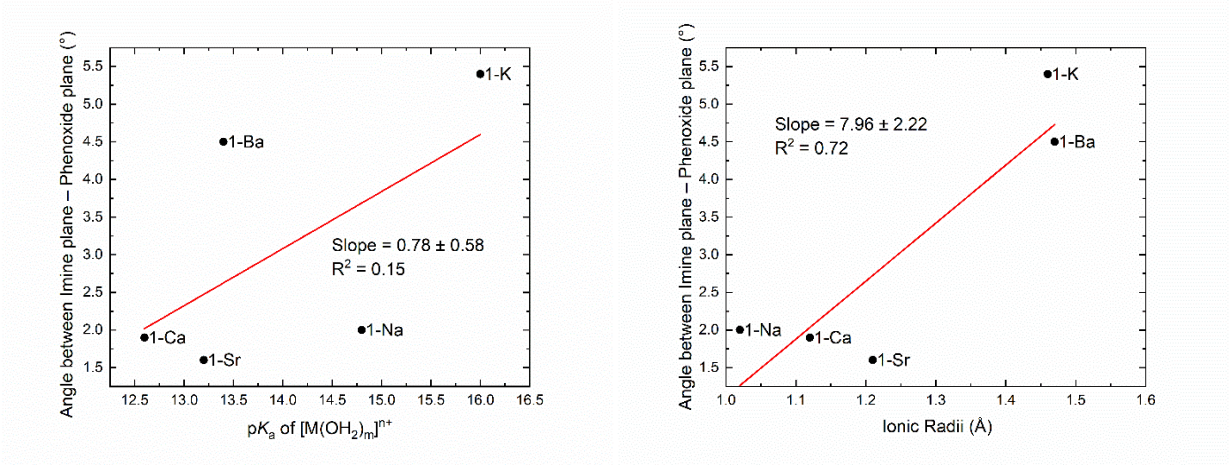

Figure F114. Dependence on angle of plane defined by N_{imine} atoms (N1, N2, and N3) and plane defined by O_{Ar} atoms (O1, O2, and O3) on the pK_a of $[\mathbf{M}(H_2O)_m]^{n+}$ (left) and Shannon Ionic Radius (right) of **1-M** (Excluding **1-Li**).

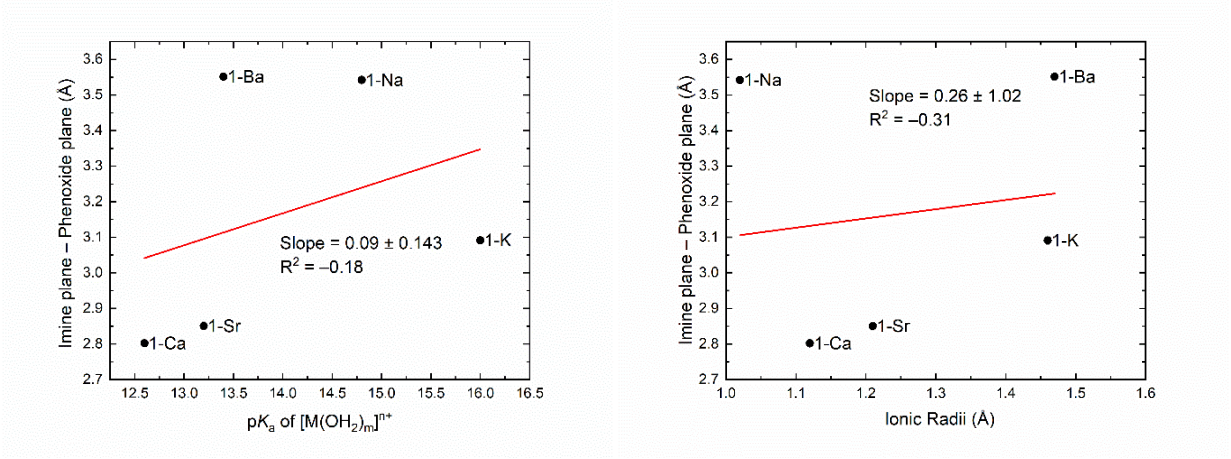

Figure F115. Dependence on distance of plane defined by N_{imine} atoms (N1, N2, and N3) and plane defined by O_{Ar} atoms (O1, O2, and O3) on the pK_a of $[\mathbf{M}(H_2O)_m]^{n+}$ (left) and Shannon Ionic Radius (right) of **1-M** (Excluding **1-Li**).

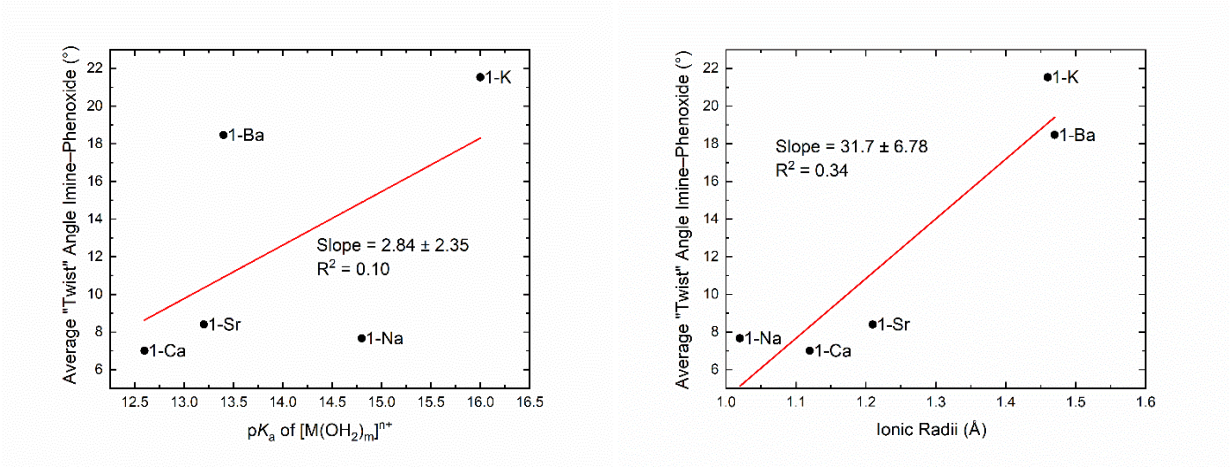

Figure F116. Dependence on "twist" angle N_{imine} and O_{Ar} on the pK_a of [**M**$(H2O)_m]^{n+}$ (left) and Shannon Ionic Radius (right) of **1-M** (Excluding **1-Li**).

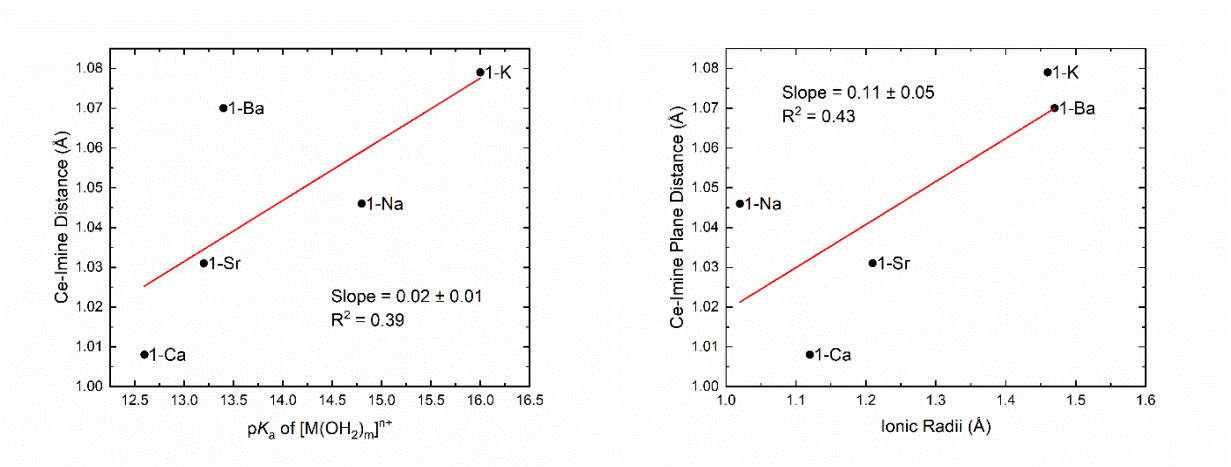

Figure F117. Dependence on distance of Ce and the plane defined by the N_{imine} atoms (N1, N2, and N3) on the pK_a of [**M**$(H_2O)_m]^{n+}$ (left) and Shannon Ionic Radius (right) of **1-M** (Excluding **1-Li**).

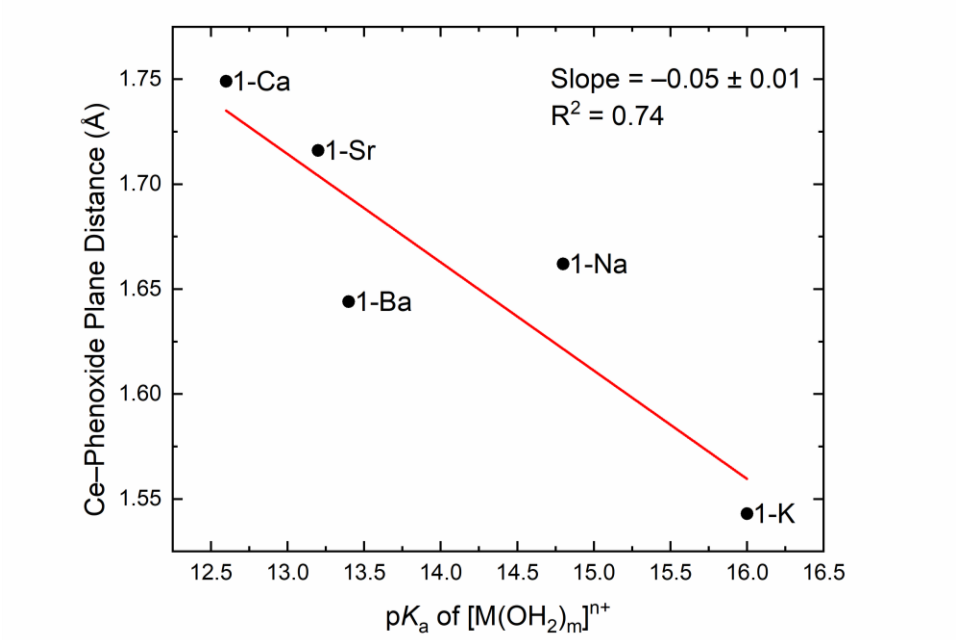

Figure F118. Dependence on distance of Ce and the plane defined by the O_{Ar} atoms (O1, O2, and O3) on the pK_a of [**M**$(H_2O)_m]^{n+}$ of **1-M** (Excluding **1-Li**).

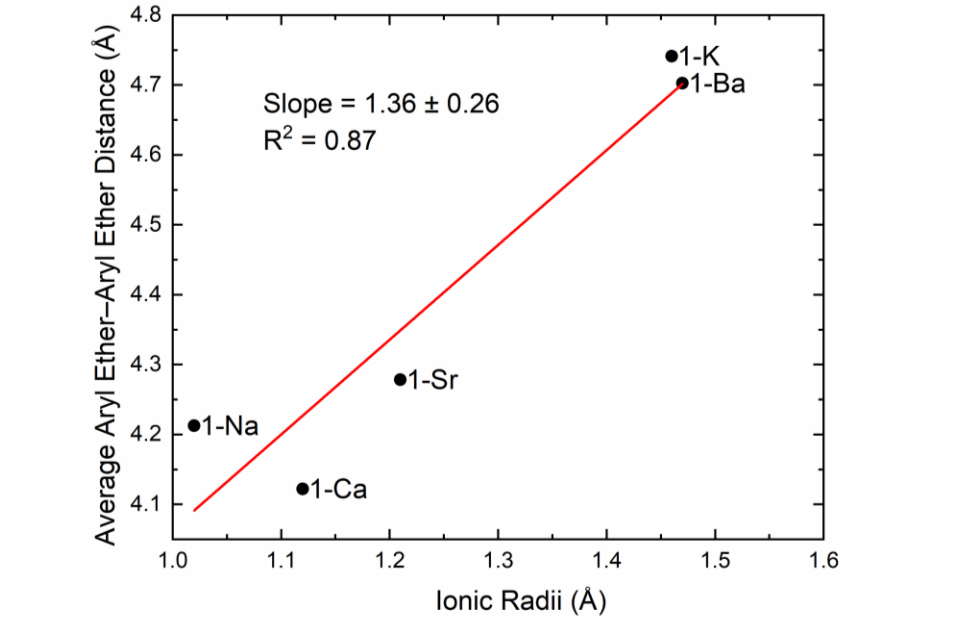

Figure F119. Dependence on average O_{ether}•••O_{ether} atom (O4, O5 and O6) distance on the Shannon Ionic Radius of **1-M** (Excluding **1-Li**).

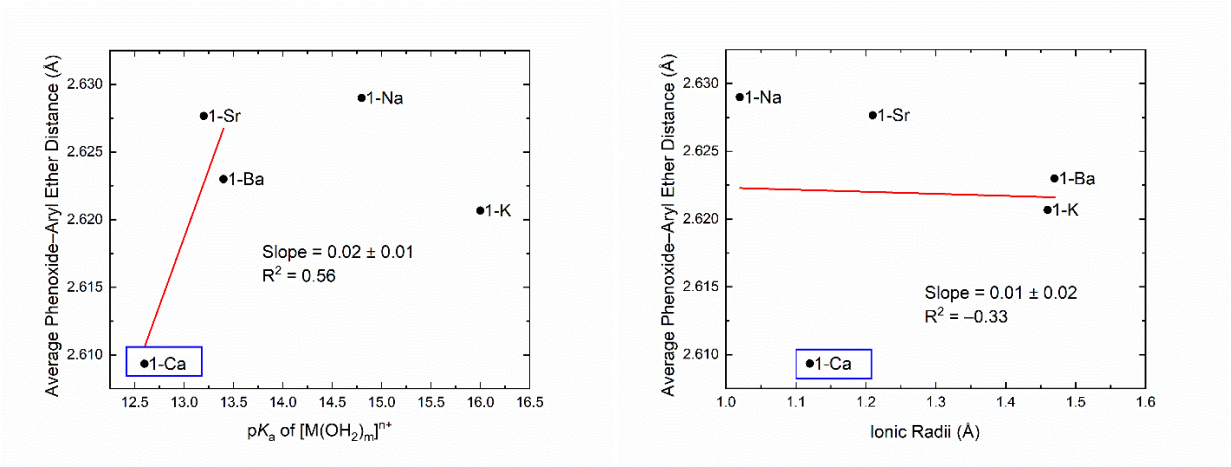

Figure F120. Dependence on average O_{Ar}•••O_{ether} distance on the pK_a of $[\mathbf{M}(H_2O)_m]^{n+}$ (left) and Shannon Ionic Radius (right) of **1-M** (Excluding **1-Li**). **1-Ca** complex is an outlier.

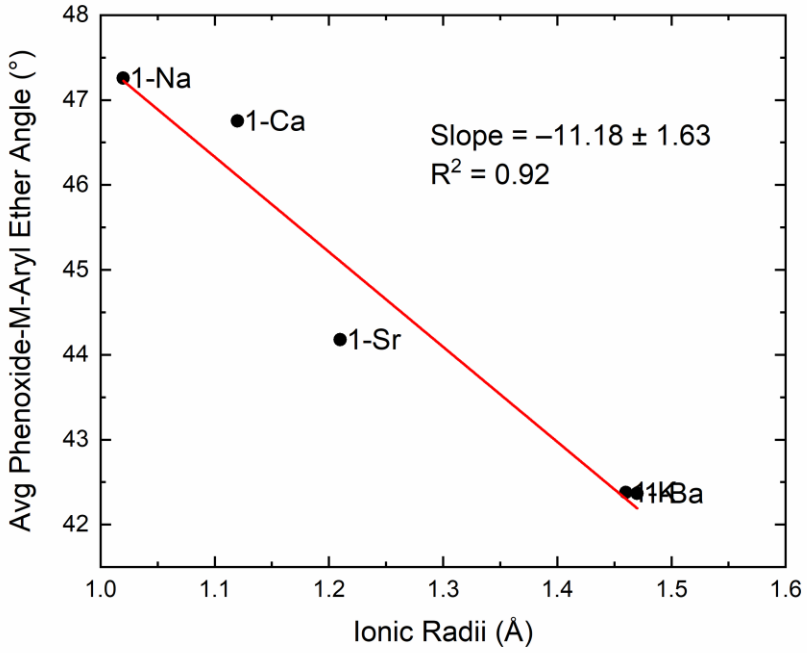

Figure F121. Dependence on average O_{Ar}-**M**-O_{ether} angle on the Shannon Ionic Radius of **1-M** (Excluding **1-Li**).

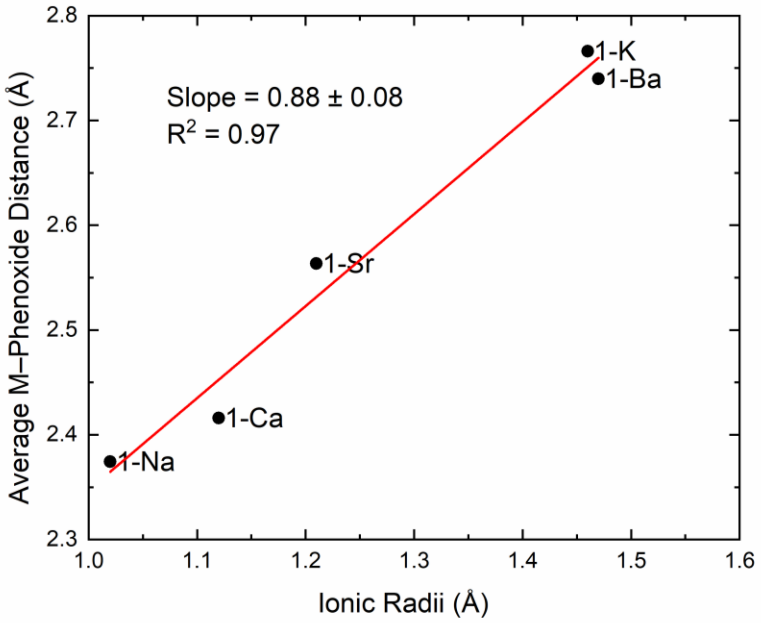

Figure F122. Dependence on average **M**–O_{Ar} atoms (O1, O2, and O3) distance on the Shannon Ionic Radius of **1-M** (Excluding **1-Li**).

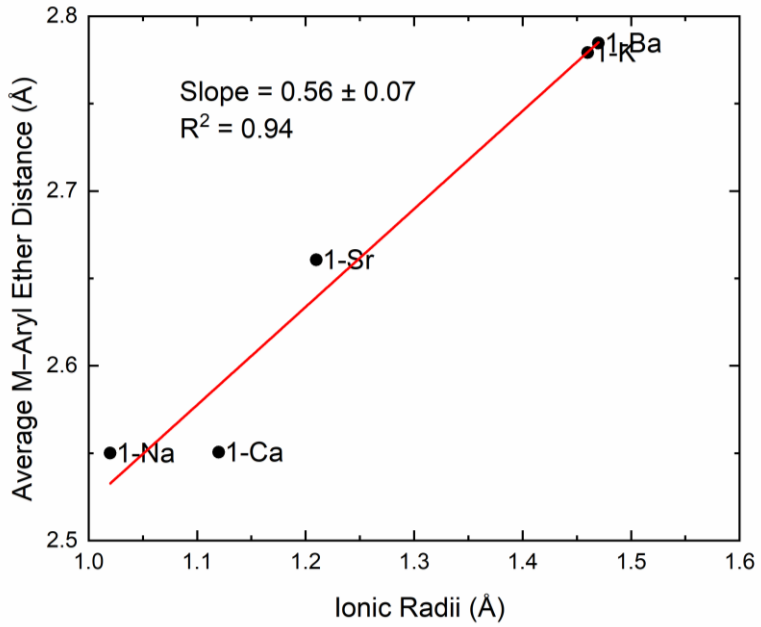

Figure F123. Dependence on average **M**–O_{ether} atoms (O4, O5, and O6) distance on the Shannon Ionic Radius of **1-M** (Excluding **1-Li**).

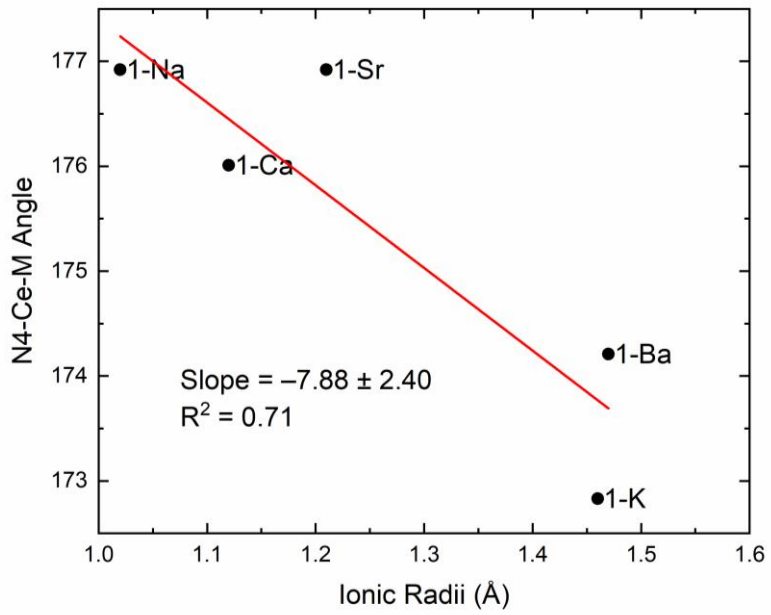

Figure F124. Dependence on **M**-Ce-N4 angle on the Shannon Ionic Radius of **1-M** (Excluding **1-Li**).

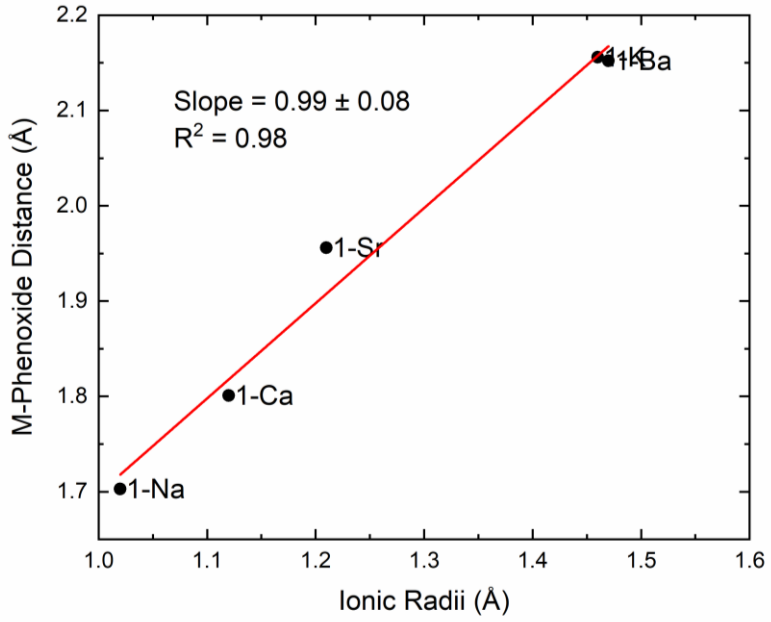

Figure F125. Dependence on distance of **M** and the plane defined by the O_{Ar} atoms (O1, O2, and O3) on the Shannon Ionic Radius of **1-M** (Excluding **1-Li**).

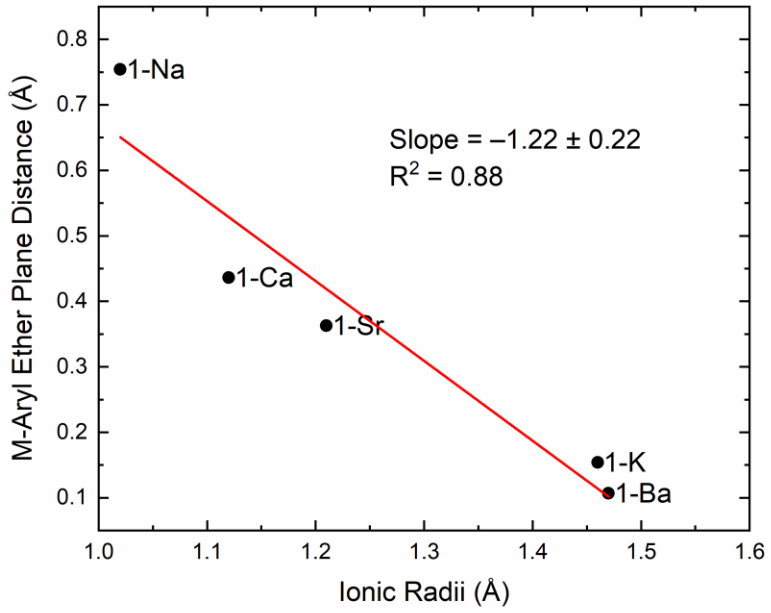

Figure F126. Dependence on distance of **M** and the plane defined by the O_{ether} atoms (O4, O5, and O6) on the Shannon Ionic Radius of **1-M** (Excluding **1-Li**).

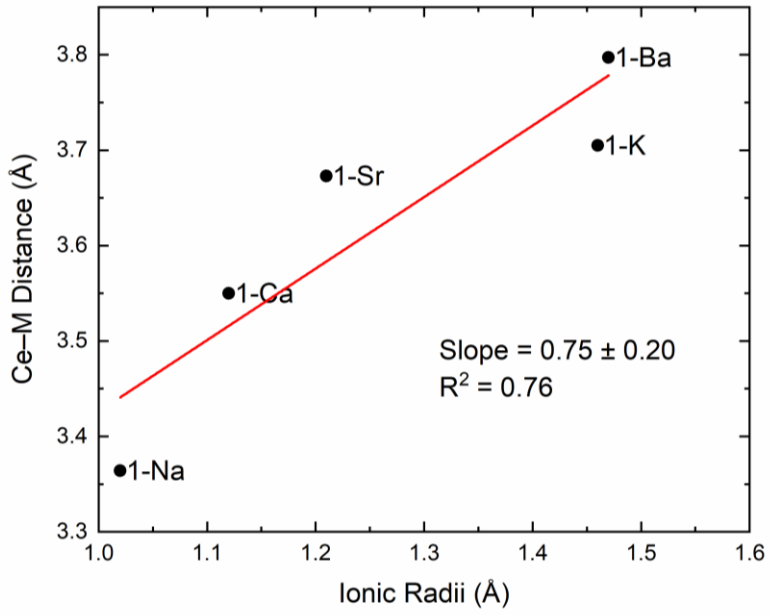

Figure F127. Dependence on distance of Ce•••**M** on the Shannon Ionic Radius of **1-M** (Excluding **1-Li**).

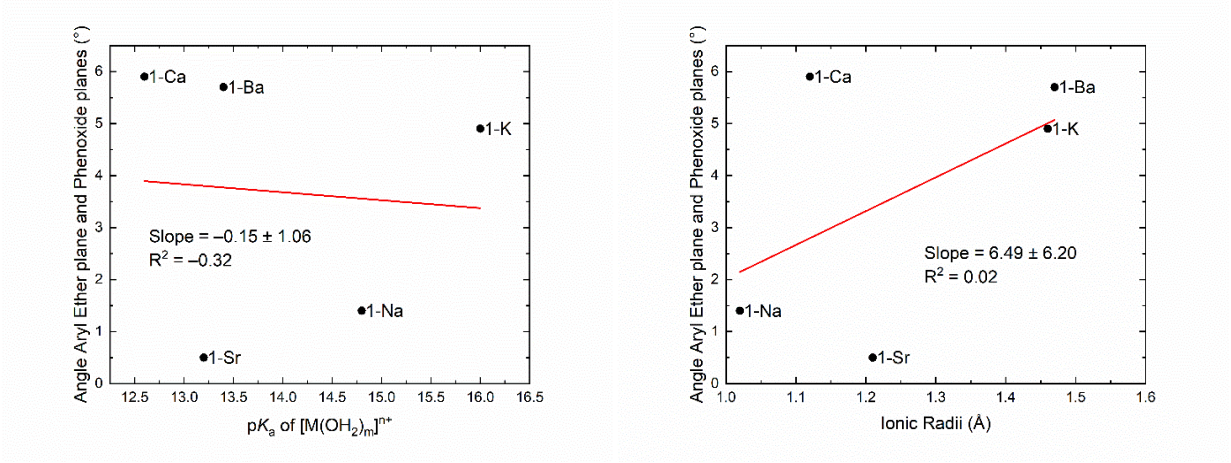

Figure F128. Dependence on angle of plane defined by O_{Ar} atoms (O1, O2, and O3) and plane defined by O_{ether} atoms (O4, O5, and O6) on the pK_a of $[\mathbf{M}(H_2O)_m]^{n+}$ (left) and Shannon Ionic Radius (right) of **1-M** (Excluding **1-Li**).

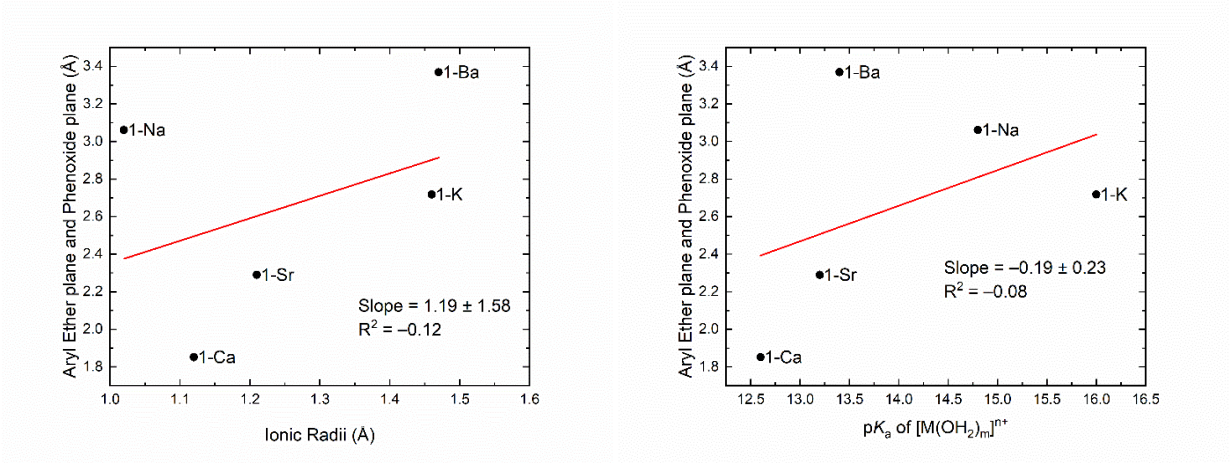

Figure F129. Dependence on distance of plane defined by O_{Ar} atoms (O1, O2, and O3) and plane defined by O_{ether} atoms (O4, O5, and O6) on the pK_a of $[\mathbf{M}(H_2O)_m]^{n+}$ (left) and Shannon Ionic Radius (right) of **1-M** (Excluding **1-Li**).

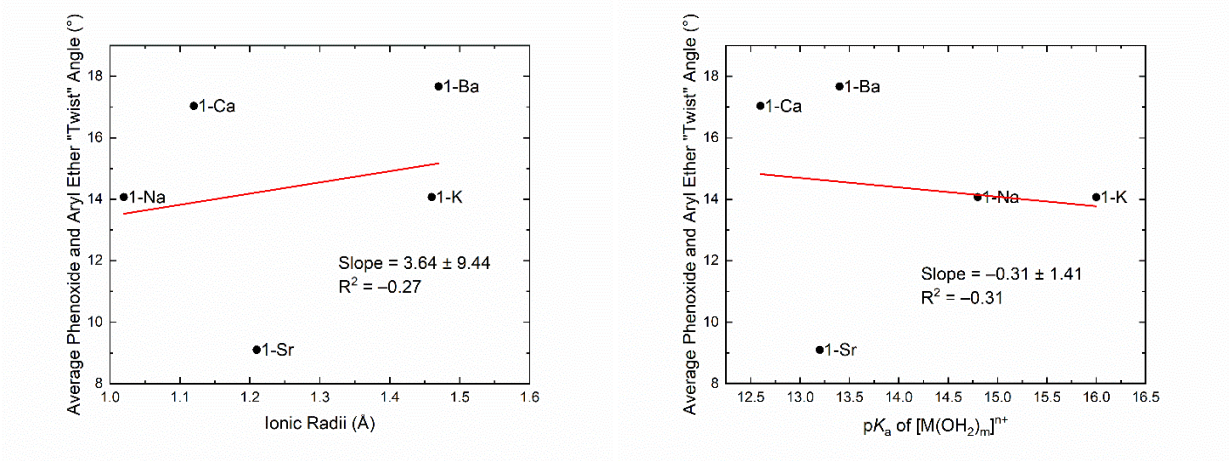

Figure F130. Dependence on "twist" angle of the O_{Ar} and O_{ether} on the pK_a of $[\mathbf{M}(H_2O)_m]^{n+}$ (left) and Shannon Ionic Radius (right) of **1-M** (Excluding **1-Li**).

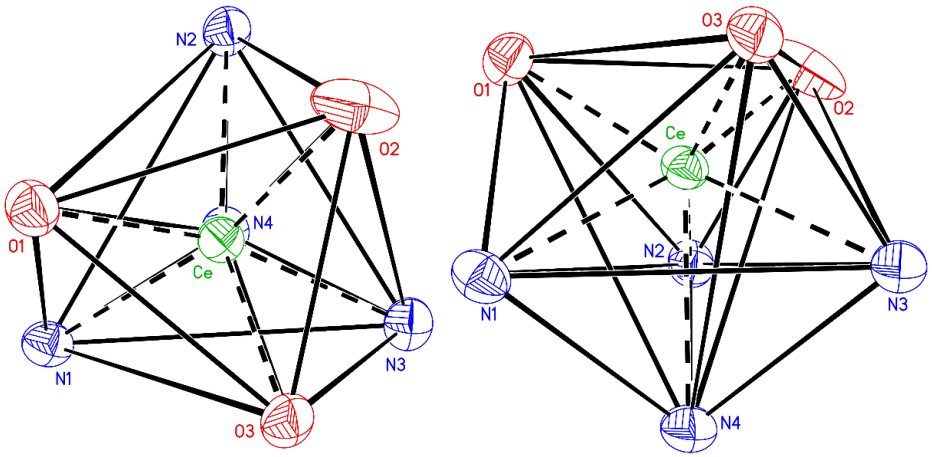

Figure F131. Polyhedron representation of Ce site of **1** (Left: Top view, Right: Side view). This figure is designed to give view of the twist angle (denoted as θ), which is defined as the as the average dihedral angle of each of the ligand "arms"; this quantity is defined by the angle between the N atom, the center-of-gravity of the imine nitrogen plane, the center-of-gravity of the phenoxide oxygen plane, and phenoxide O atom for each arm. All carbon and hydrogen atoms and associated solvent molecule omitted for clarity. Displacement ellipsoids shown at the 50% probability level.

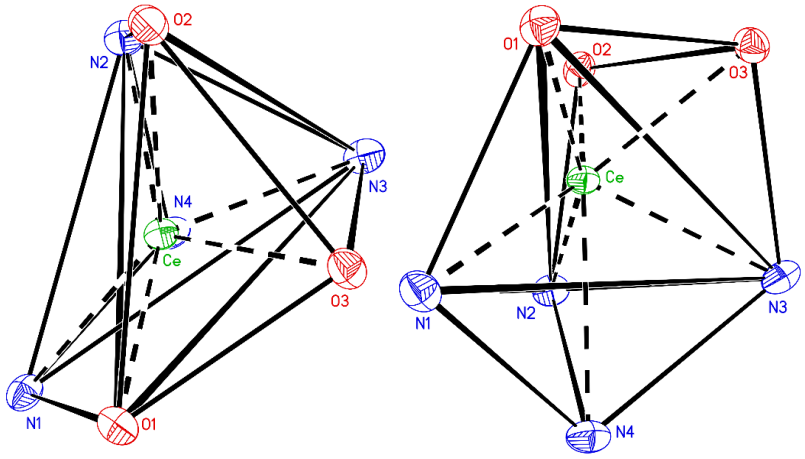

Figure F132. Polyhedron representation of Ce site of **1-Li** (Left: Top view, Right: Side view). This figure is designed to give view of the twist angle (denoted as θ), which is defined as the as the average dihedral angle of each of the ligand "arms"; this quantity is defined by the angle between the N atom, the center-of-gravity of the imine nitrogen plane, the center-of-gravity of the phenoxide oxygen plane, and phenoxide O atom for each arm All carbon and hydrogen atoms and associated solvent molecule omitted for clarity. Displacement ellipsoids shown at the 50% probability level.

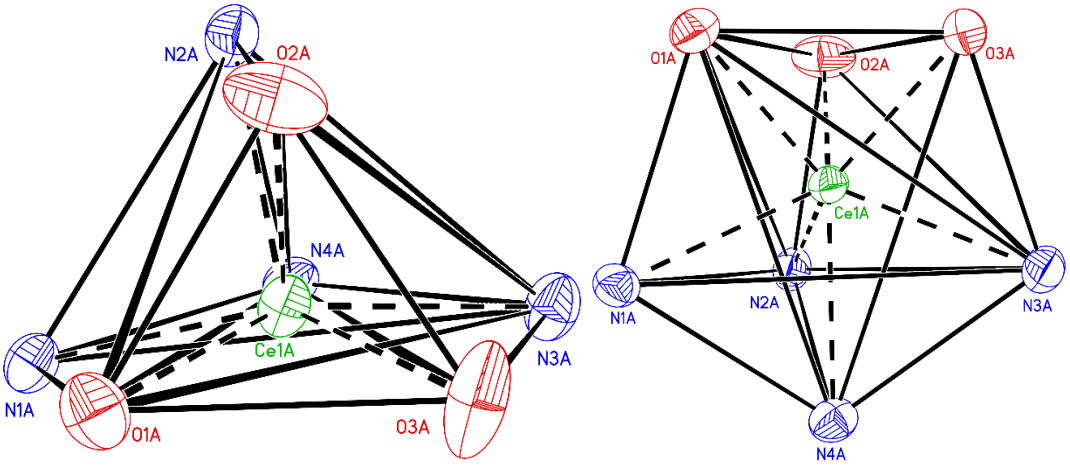

Figure F133. Polyhedron representation of Ce site of **1-Na** (Left: Top view, Right: Side view). This figure is designed to give view of the twist angle (denoted as θ), which is defined as the as the average dihedral angle of each of the ligand "arms"; this quantity is defined by the angle between the N atom, the center-of-gravity of the imine nitrogen plane, the center-of-gravity of the phenoxide oxygen plane, and phenoxide O atom for each arm. All carbon and hydrogen atoms and associated solvent molecule omitted for clarity. Displacement ellipsoids shown at the 50% probability level.

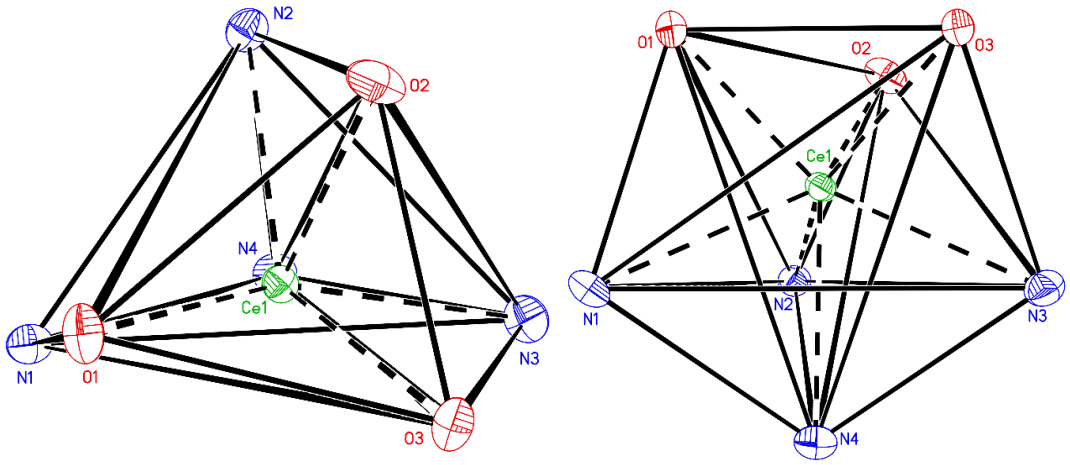

Figure F134. Polyhedron representation of Ce site of **1-K** (Left: Top view, Right: Side view). This figure is designed to give view of the twist angle (denoted as θ), which is defined as the as the average dihedral angle of each of the ligand "arms"; this quantity is defined by the angle between the N atom, the center-of-gravity of the imine nitrogen plane, the center-of-gravity of the phenoxide oxygen plane, and phenoxide O atom for each arm. All carbon and hydrogen atoms and associated solvent molecule omitted for clarity. Displacement ellipsoids shown at the 50% probability level.

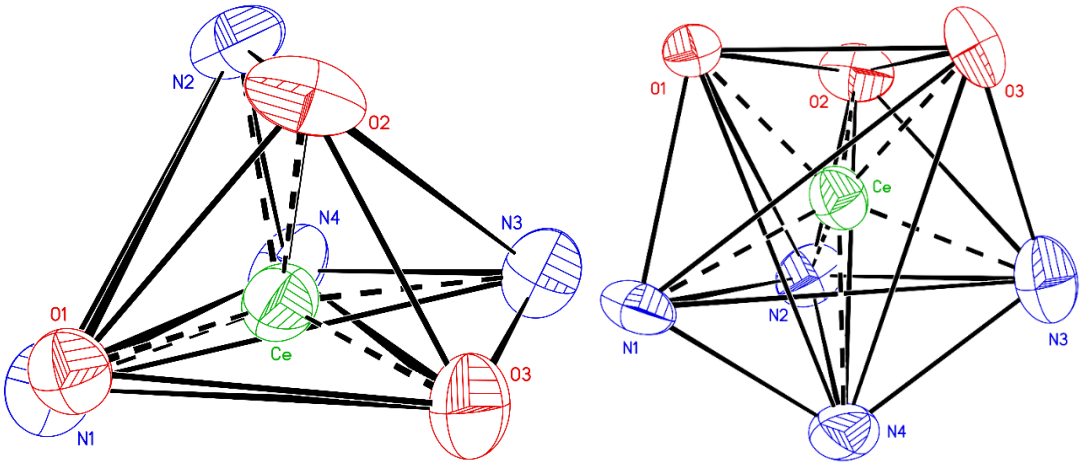

Figure F135. Polyhedron representation of Ce site of **1-Ba** (Left: Top view, Right: Side view). This figure is designed to give view of the twist angle (denoted as θ), which is defined as the as the average dihedral angle of each of the ligand "arms"; this quantity is defined by the angle between the N atom, the center-of-gravity of the imine nitrogen plane, the center-of-gravity of the phenoxide oxygen plane, and phenoxide O atom for each arm. All carbon and hydrogen atoms and associated solvent molecule omitted for clarity. Displacement ellipsoids shown at the 50% probability level.

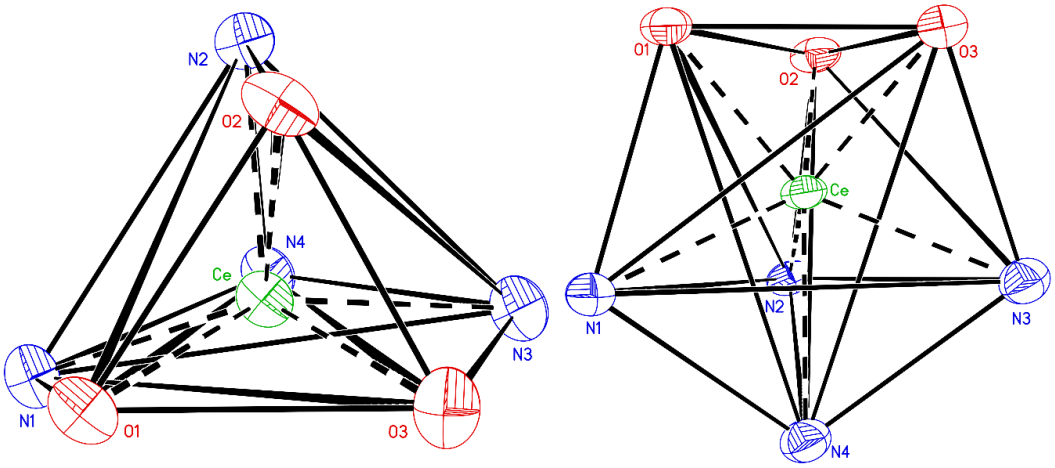

Figure F136. Polyhedron representation of Ce site of **1-Sr** (Left: Top view, Right: Side view). This figure is designed to give view of the twist angle (denoted as θ), which is defined as the as the average dihedral angle of each of the ligand "arms"; this quantity is defined by the angle between the N atom, the center-of-gravity of the imine nitrogen plane, the center-of-gravity of the phenoxide oxygen plane, and phenoxide O atom for each arm. All carbon and hydrogen atoms and associated solvent molecule omitted for clarity. Displacement ellipsoids shown at the 50% probability level.

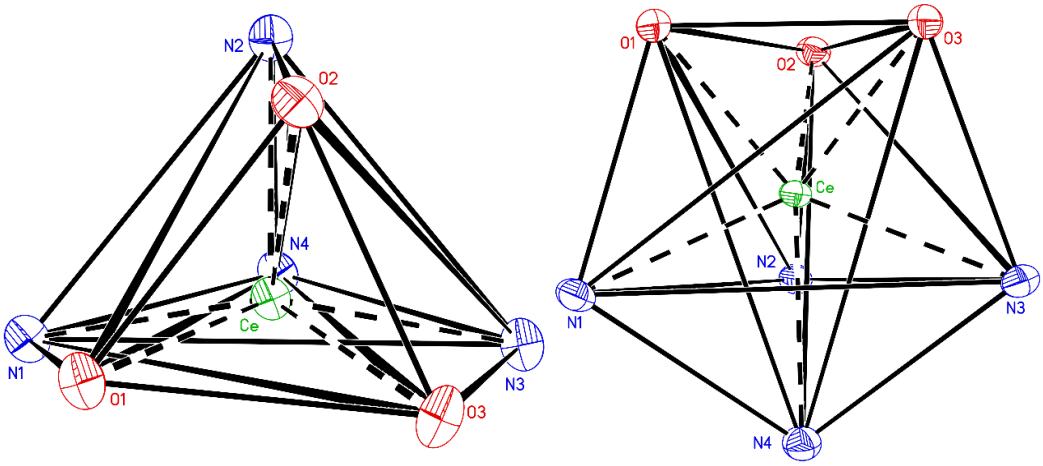

Figure F137. Polyhedron representation of Ce site of **1-Ca** (Left: Top view, Right: Side view). This figure is designed to give view of the twist angle (denoted as θ), which is defined as the as the average dihedral angle of each of the ligand "arms"; this quantity is defined by the angle between the N atom, the center-of-gravity of the imine nitrogen plane, the center-of-gravity of the phenoxide oxygen plane, and phenoxide O atom for each arm. All carbon and hydrogen atoms and associated solvent molecule omitted for clarity. Displacement ellipsoids shown at the 50% probability level.

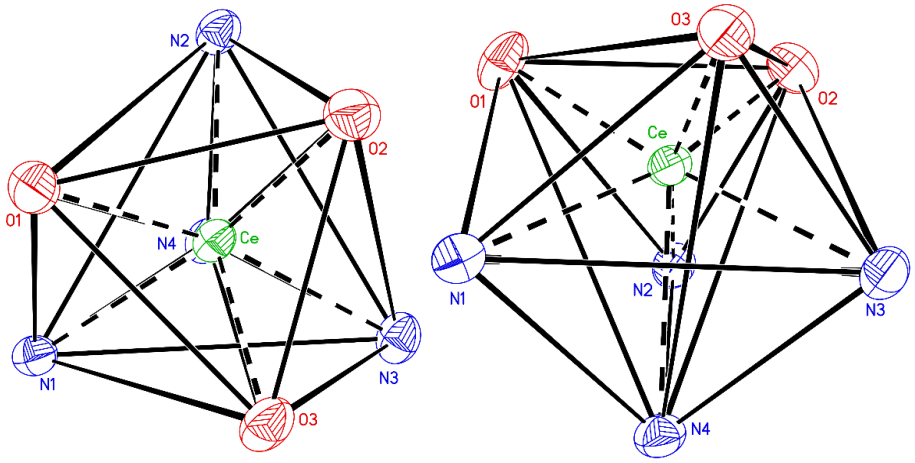

Figure F138. Polyhedron representation of Ce site of $\mathbf{2^{PF6}}$ (Left: Top view, Right: Side view). This figure is designed to give view of the twist angle (denoted as θ), which is defined as the as the average dihedral angle of each of the ligand "arms"; this quantity is defined by the angle between the N atom, the center-of-gravity of the imine nitrogen plane, the center-of-gravity of the phenoxide oxygen plane, and phenoxide O atom for each arm. All carbon and hydrogen atoms and associated solvent molecule omitted for clarity. Displacement ellipsoids shown at the 50% probability level.

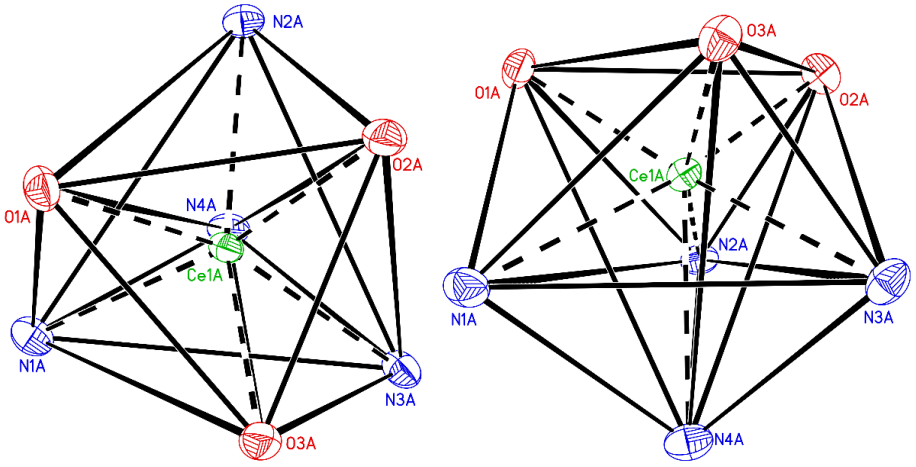

Figure F139. Polyhedron representation of Ce site of $\mathbf{2}^{\mathbf{OFT}}$ (Left: Top view, Right: Side view). This figure is designed to give view of the twist angle (denoted as θ), which is defined as the as the average dihedral angle of each of the ligand "arms"; this quantity is defined by the angle between the N atom, the center-of-gravity of the imine nitrogen plane, the center-of-gravity of the phenoxide oxygen plane, and phenoxide O atom for each arm. All carbon and hydrogen atoms and associated solvent molecule omitted for clarity. Displacement ellipsoids shown at the 50% probability level.

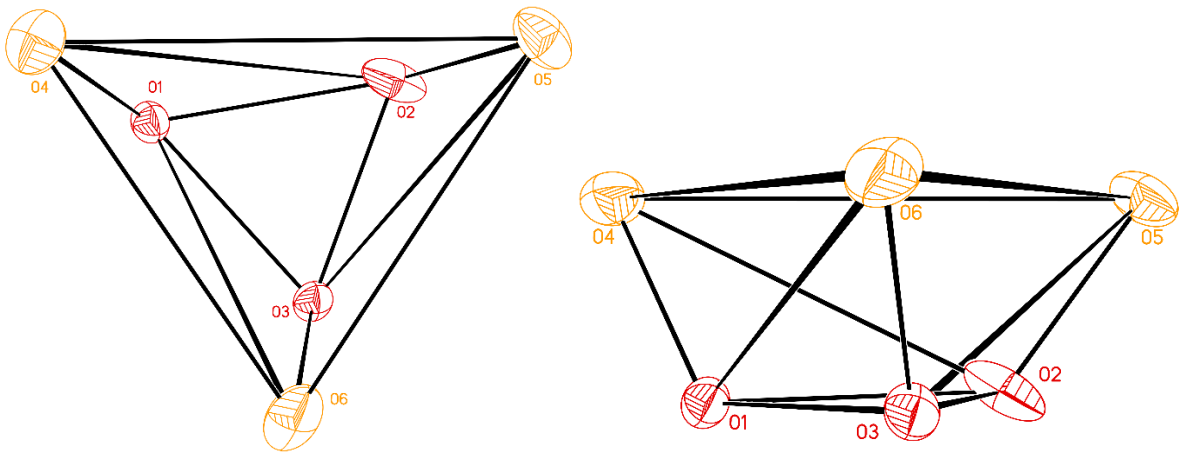

Figure F140. Polyhedron representation of secondary metal site of **1** (Left: Top view, Right: Side view). This figure is designed to give view of the twist angle (denoted as θ′), which is defined as the as the average dihedral angle defined by the phenoxide O atom, the center-of-gravity of the phenoxide oxygen plane, the center-of-gravity of the aryl ether oxygen plane, and aryl ether O atom for each arm of the structure. All carbon and hydrogen atoms and associated solvent molecule omitted for clarity. Displacement ellipsoids shown at the 50% probability level.

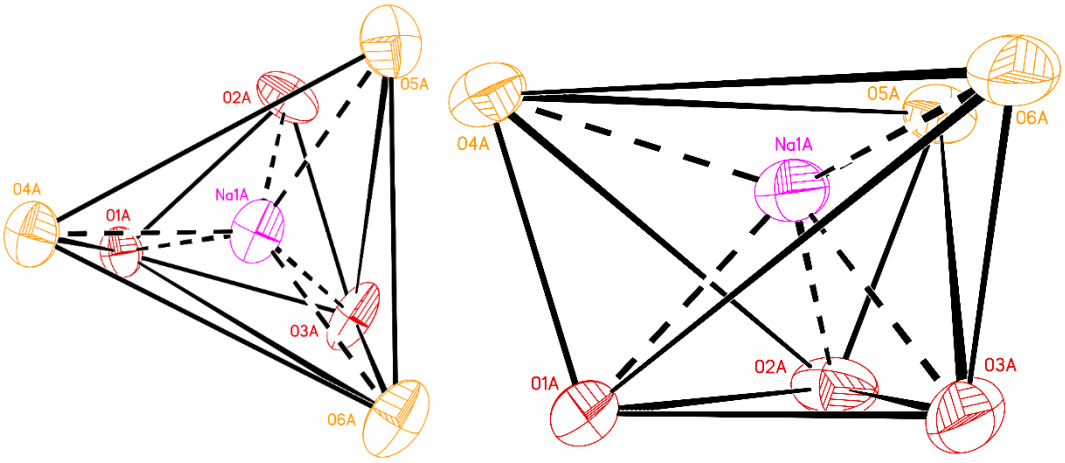

Figure F141. Polyhedron representation of secondary metal site of **1-Na** (Left: Top view, Right: Side view). This figure is designed to give view of the twist angle (denoted as θ′), which is defined as the as the average dihedral angle defined by the phenoxide O atom, the center-of-gravity of the phenoxide oxygen plane, the center-of-gravity of the aryl ether oxygen plane, and aryl ether O atom for each arm of the structure. All carbon and hydrogen atoms and associated solvent molecule omitted for clarity. Displacement ellipsoids shown at the 50% probability level.

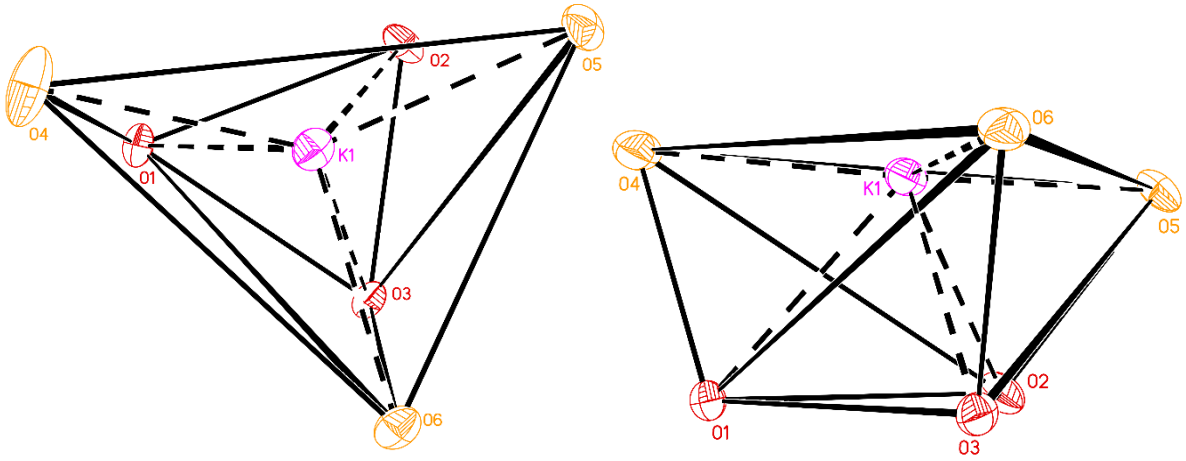

Figure F142. Polyhedron representation of secondary metal site of **1-K** (Left: Top view, Right: Side view). This figure is designed to give view of the twist angle (denoted as θ′), which is defined as the as the average dihedral angle defined by the phenoxide O atom, the center-of-gravity of the phenoxide oxygen plane, the center-of-gravity of the aryl ether oxygen plane, and aryl ether O atom for each arm of the structure. All carbon and hydrogen atoms and associated solvent molecule omitted for clarity. Displacement ellipsoids shown at the 50% probability level.

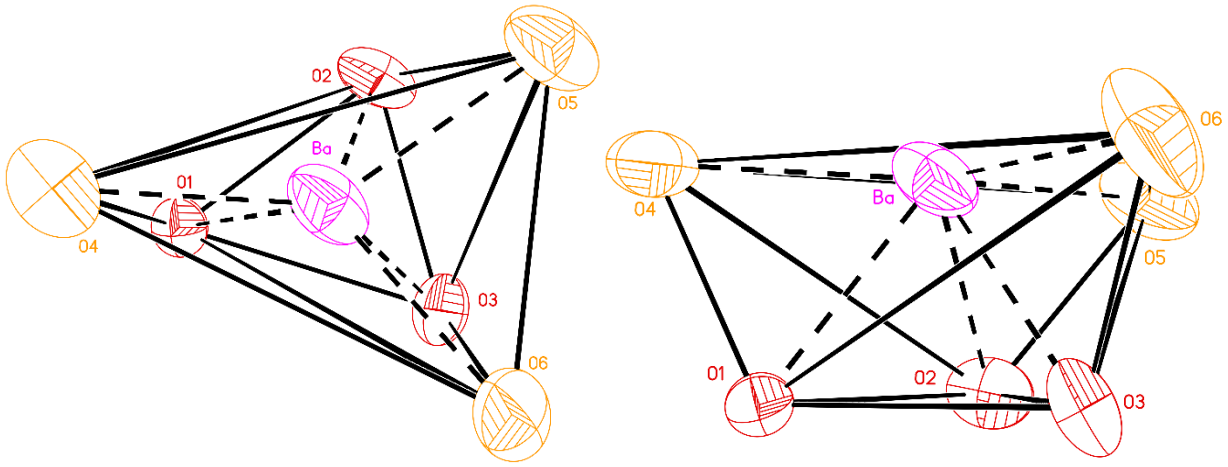

Figure F143. Polyhedron representation of secondary metal site of **1-Ba** (Left: Top view, Right: Side view). This figure is designed to give view of the twist angle (denoted as θ′), which is defined as the as the average dihedral angle defined by the phenoxide O atom, the center-of-gravity of the phenoxide oxygen plane, the center-of-gravity of the aryl ether oxygen plane, and aryl ether O atom for each arm of the structure. All carbon and hydrogen atoms and associated solvent molecule omitted for clarity. Displacement ellipsoids shown at the 50% probability level.

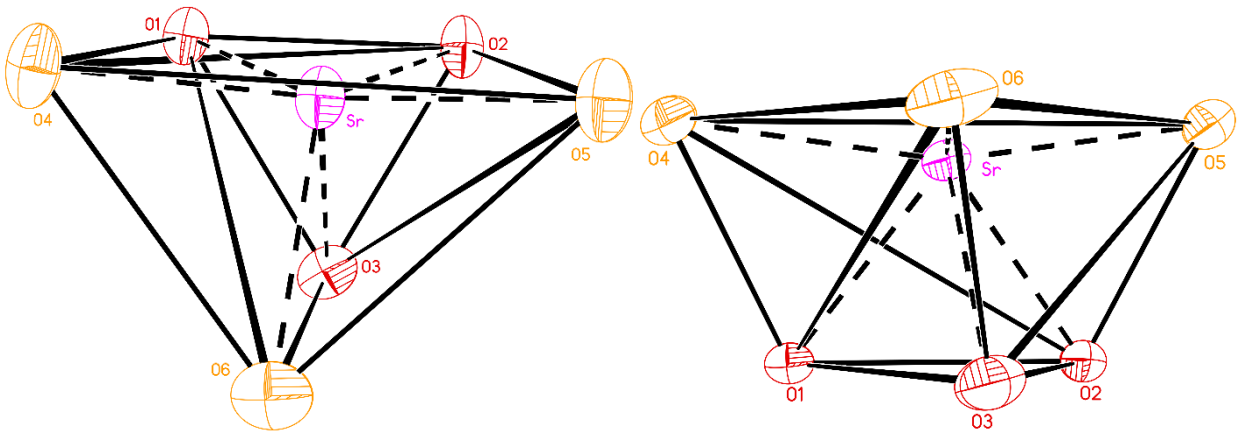

Figure F144. Polyhedron representation of secondary metal site of **1-Sr** (Left: Top view, Right: Side view). This figure is designed to give view of the twist angle (denoted as θ′), which is defined as the as the average dihedral angle defined by the phenoxide O atom, the center-of-gravity of the phenoxide oxygen plane, the center-of-gravity of the aryl ether oxygen plane, and aryl ether O atom for each arm of the structure. All carbon and hydrogen atoms and associated solvent molecule omitted for clarity. Displacement ellipsoids shown at the 50% probability level.

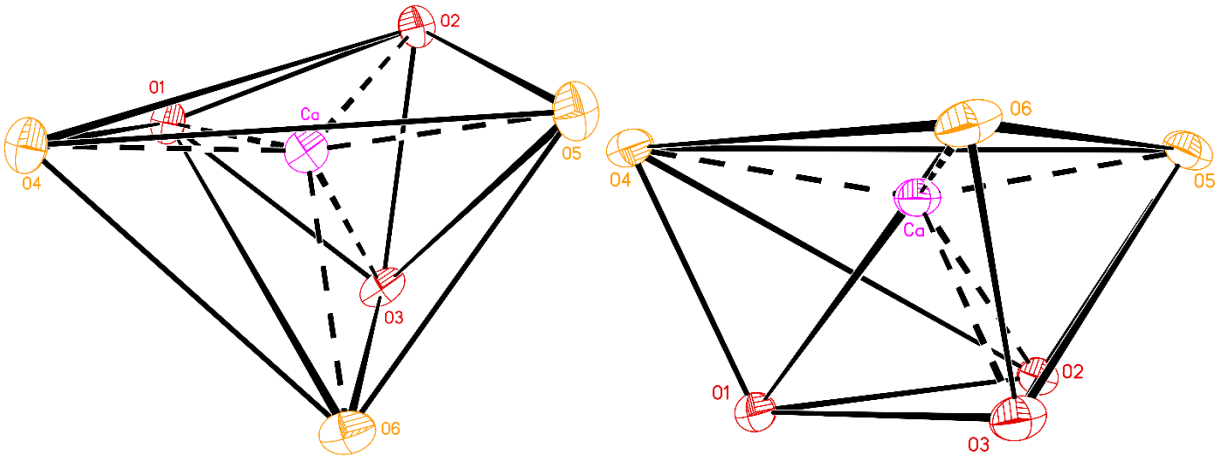

Figure F145. Polyhedron representation of secondary metal site of **1-Ca** (Left: Top view, Right: Side view). This figure is designed to give view of the twist angle (denoted as θ′), which is defined as the as the average dihedral angle defined by the phenoxide O atom, the center-of-gravity of the phenoxide oxygen plane, the center-of-gravity of the aryl ether oxygen plane, and aryl ether O atom for each arm of the structure. All carbon and hydrogen atoms and associated solvent molecule omitted for clarity. Displacement ellipsoids shown at the 50% probability level.

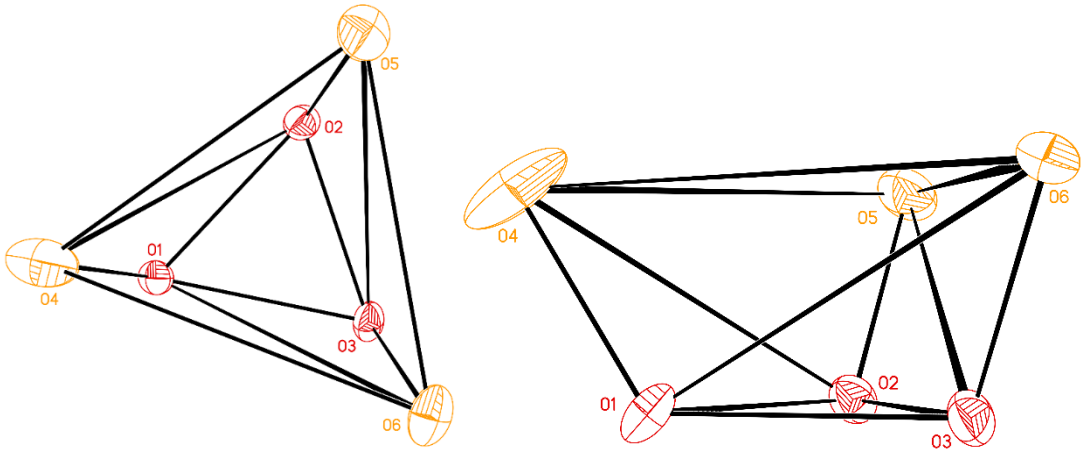

Figure F146. Polyhedron representation of secondary metal site of $\mathbf{2^{PF6}}$ (Left: Top view, Right: Side view). This figure is designed to give view of the twist angle (denoted as θ′), which is defined as the as the average dihedral angle defined by the phenoxide O atom, the center-of-gravity of the phenoxide oxygen plane, the center-of-gravity of the aryl ether oxygen plane, and aryl ether O atom for each arm of the structure. All carbon and hydrogen atoms and associated solvent molecule omitted for clarity. Displacement ellipsoids shown at the 50% probability level.

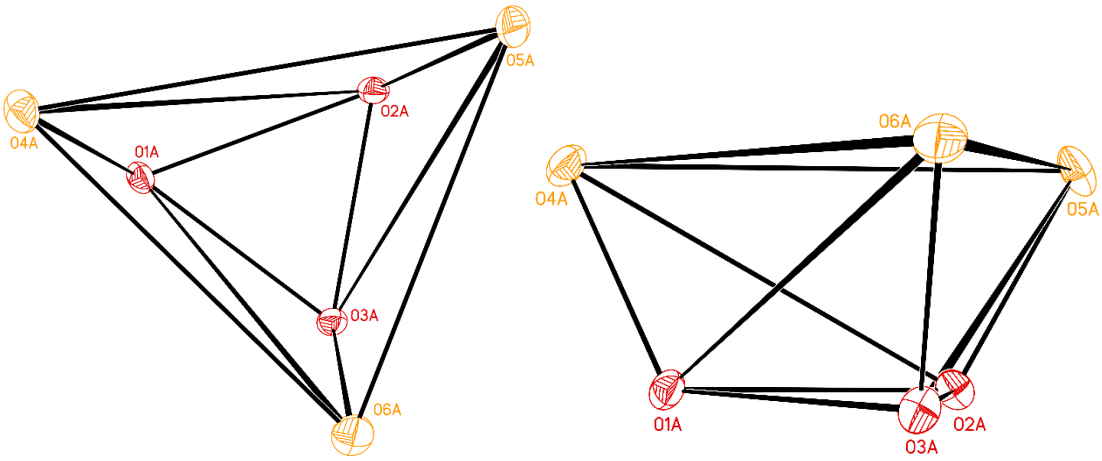

Figure F147. Polyhedron representation of secondary metal site (θ′) of $\mathbf{2}^{\mathbf{OTf}}$ (Left: Top view, Right: Side view). This figure is designed to give view of the twist angle (denoted as θ′), which is defined as the as the average dihedral angle defined by the phenoxide O atom, the center-of-gravity of the phenoxide oxygen plane, the center-of-gravity of the aryl ether oxygen plane, and aryl ether O atom for each arm of the structure. All carbon and hydrogen atoms and associated solvent molecule omitted for clarity. Displacement ellipsoids shown at the 50% probability level.

Section F3
X-ray Absorption Spectroscopy

Section F3.1 Detailed XAS analysis of 1, 1-Na and 1-Ca

The values measured for **1**, **1-Na** and **1-Ca** can be used to benchmark relative effective nuclear charge to other trivalent cerium complexes. These values are higher than those present for cerium complexes featuring imidophosphorane ligand systems, whose inflection points are at 5722.7 eV.[2,3] On the other hand, these values are lower than that of $[CeCl_6]^{3-}$, whose inflection point is at 5724.5 eV.[4] This indicates that this ligand system's charge donation to the metal center can be qualitatively bound between that for imidophosphorane ligand systems and that for the hexahalides. These compounds' spectra also contain very weak pre-edge feature that is attributable to a quadrupole-allowed $2p_{3/2} \rightarrow 4f$ transition, which is not completely excluded in this symmetry.

Section F3.2 Detailed XAS analysis of 2^{PF6}

For $\mathbf{2^{PF6}}$ the open-shell singlet ground state shields the core hole, in a similar fashion as formally trivalent cerium complexes, which results in a shift in peak energy to a lower energy than that of the close-shell singlet.[5,6,7] There is also a very weak pre-edge feature that is attributable to a quadrupole-allowed $2p_{3/2} \rightarrow 4f$ transition. With these features in mind, the $\mathbf{2^{PF6}}$ absorption edge is fit with three Voigt functions and one step function. Within the restrictions of this two-peak model, the relative proportion of f^1 character (n_f) can be determined by the weighted relative intensity of this feature to the total weight of both features ($n_f = A_{p2}/(A_{p2} + A_{p3})$, where A is the intensity of the peak). The value of n_f is sensitive to the curve-fit methodology and utilization of a step function at the rising edge of the edge provides a lower limit to the n_f value of $\mathbf{2^{PF6}}$, 0.57(1). This value is in in a similar range as ceria and cerium hexachloride, with values of 0.58(3) and 0.51(5), respectively.[4,8]

Table F10. Curve-Fit Parameters for **1**

	Peak 1 (Blue)	*Peak 2 (Pink)*
Energy (eV)	5719.2 ± 0.132	5726.2 ± 0.0161
Height	0.076149 ± 0.00913	2.141 ± 0.00619
Width	2.5061 ± 0.17	3.2396 ± 0.0213
Curve area	0.25152544	9.14162638
% Error	8.580	0.7182

Table F11. Curve-Fit Parameters for **1-Na**

	Peak 1 (Blue)	*Peak 2 (Pink)*
Energy (eV)	5718.8 ± 0.0666	5726.0 ± 0.006
Height	0.080057 ± 0.00166	2.2609 ± 0.00324
Width	2.293 ± 0.0794	2.9189 ± 0.00637
Curve area	0.24195	8.69793
% Error	4.037	0.2611

Table F12. Curve-fit Parameters for **1-Ca**

	Peak 1 (Blue)	*Peak 2 (Pink)*
Energy (eV)	5718.8 ± 0.124	5726.0 ± 0.00476
Height	0.083775 ± 0.00481	2.4612 ± 0.00418
Width	2.1473 ± 0.159	2.8069 ± 0.00616
Curve area	0.2370951	9.1051
% Error	9.370	0.2775

Table F13. Curve-fit Parameters for $\mathbf{2^{PF6}}$

	Peak 1 (blue)	*Peak 2 (pink)*	*Peak 3 (green)*
Energy (eV)	5719.7 ± 0.146	5728.8 ± 0.258	5737.6 ± 0.0201
Height	0.033468 ± 0.00417	0.81797 ± 0.00239	0.80861 ± 0.00445
Width	1.3305 ± 0.211	4.8181 ± 0.0591	3.5974 ± 0.0265
Curve area	0.0587	5.19432	3.8339
% Error	20.17	1.26	0.92

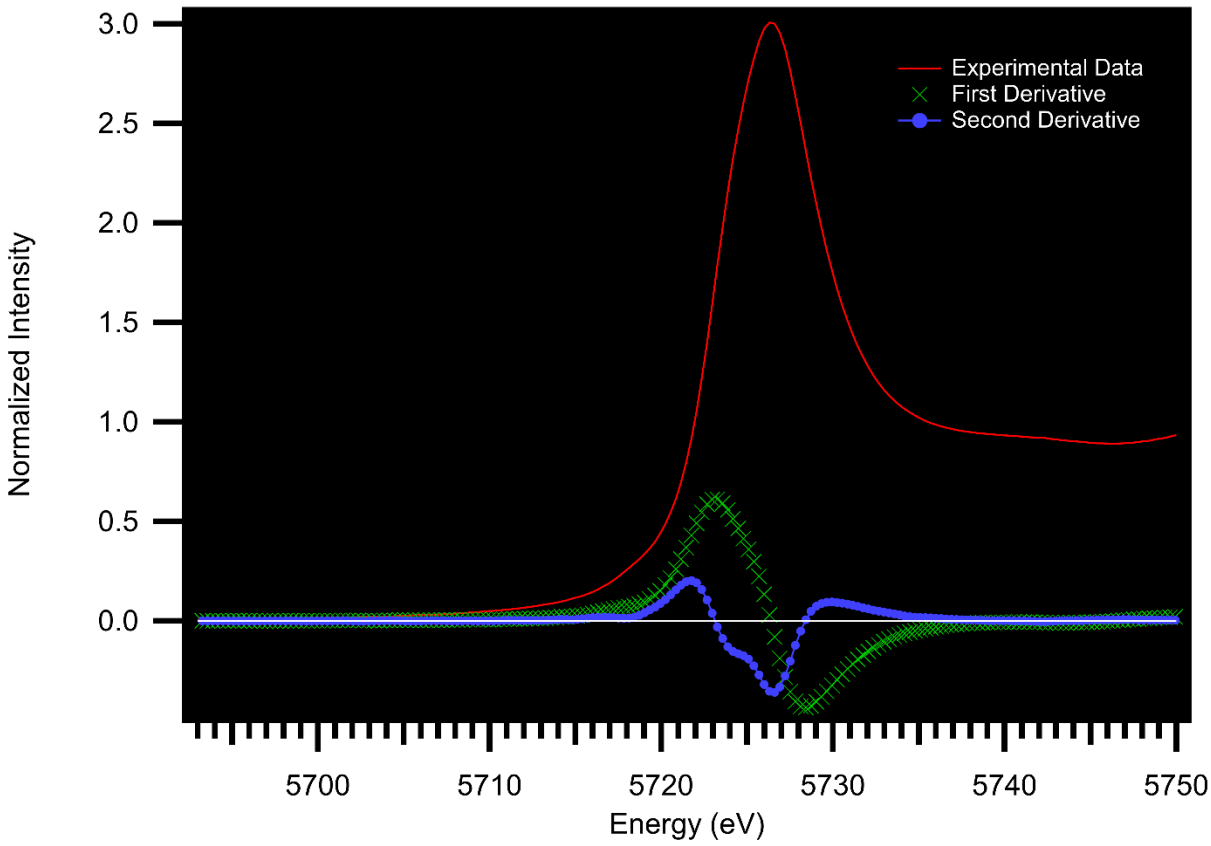

Figure F148. Ce L_3-edge XAS experimental data (red) obtained for **1**. The first and second derivative of the experimental data are shown in green and blue, respectively.

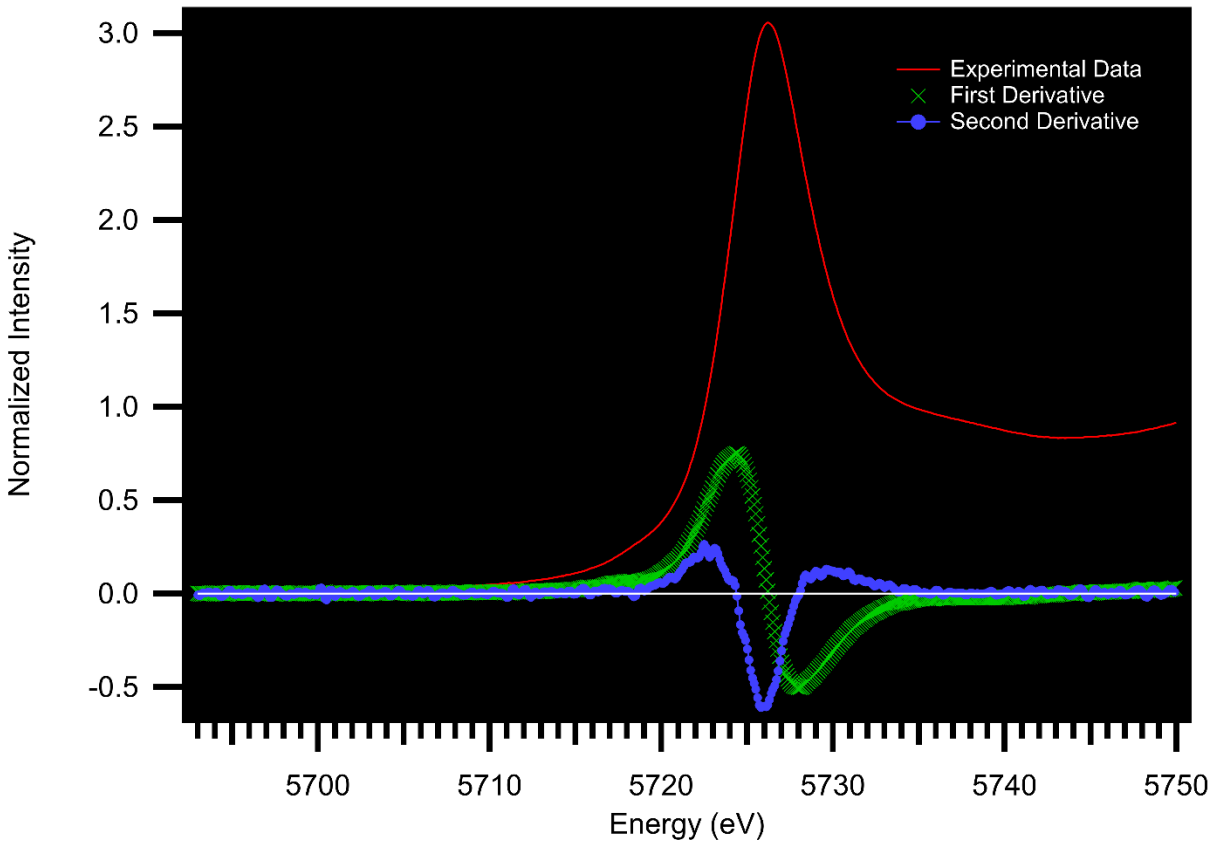

Figure F149. Ce L_3-edge XAS experimental data (red) obtained for **1-Na**. The first and second derivative of the experimental data are shown in green and blue, respectively.

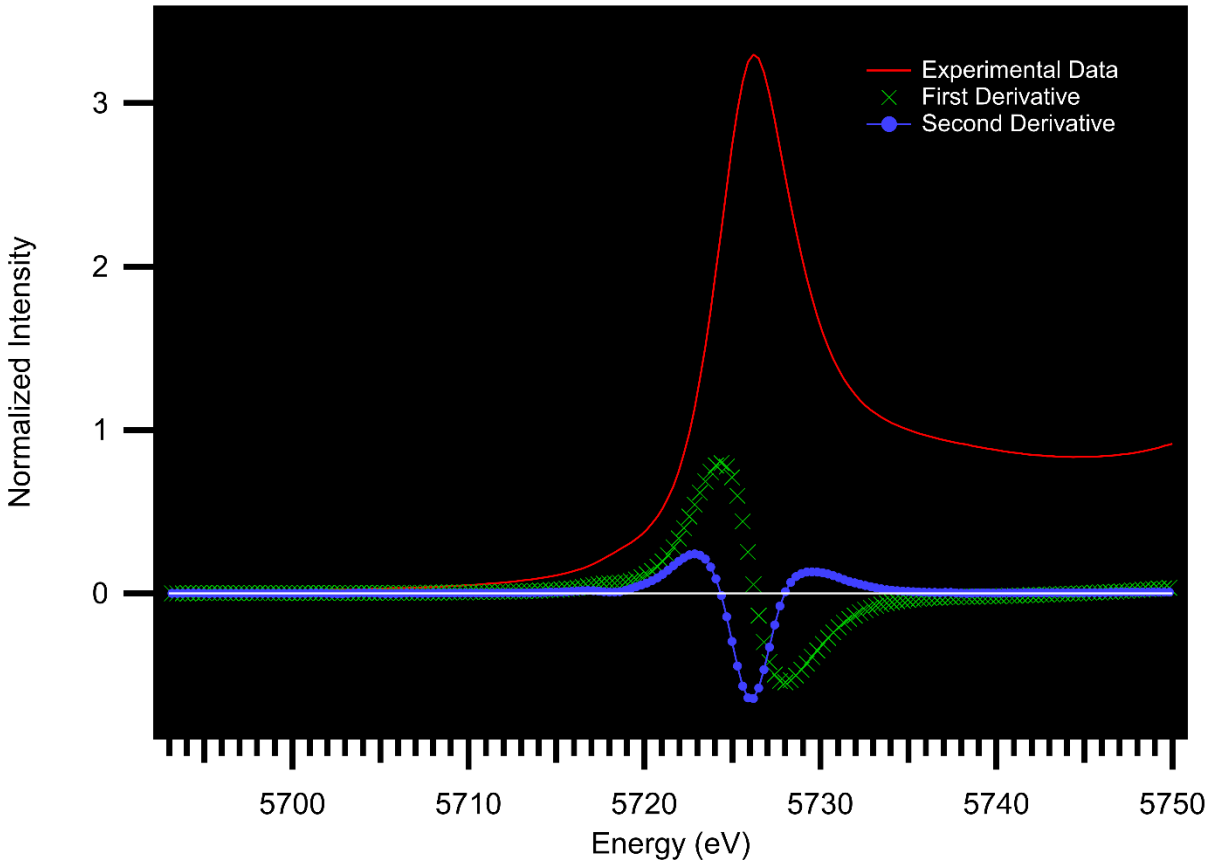

Figure F150. Ce L_3-edge XAS experimental data (red) obtained for **1-Ca**. The first and second derivative of the experimental data are shown in green and blue, respectively.

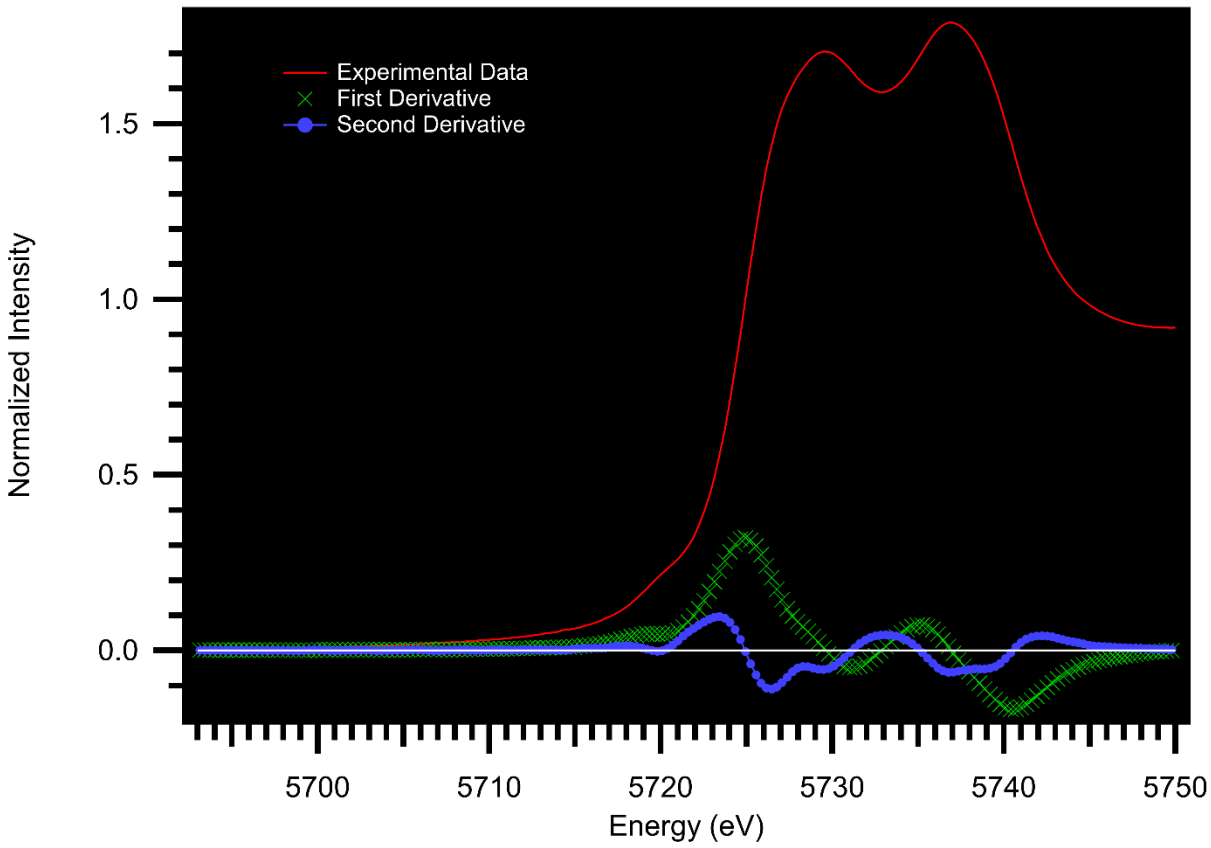

Figure F151. Ce L_3-edge XAS experimental data (red) obtained for $\mathbf{2^{PF6}}$. The first and second derivative of the experimental data are shown in green and blue, respectively.

References

[1] Shannon, R. D., Revised effective ionic radii and systematic studies of interatomic distances in halides and chalcogenides. *Acta Cryst. A.* **1976,** *32*, 751-767.

[2] Rice, N. T.; Popov, I. A.; Russo, D. R.; Bacsa, J.; Batista, E. R.; Yang, P.; Telser, J.; La Pierre, H. S., Design, Isolation, and Spectroscopic Analysis of a Tetravalent Terbium Complex. *J. Am. Chem. Soc.* **2019,** *141*, 13222-13233.

[3] Rice, N. T.; Su, J.; Gompa, T. P.; Russo, D. R.; Telser, J.; Palatinus, L.; Bacsa, J.; Yang, P.; Batista, E. R.; La Pierre, H. S., Homoleptic Imidophosphorane Stabilization of Tetravalent Cerium. *Inorg. Chem.* **2019,** *58*, 5289-5304.

[4] Löble, M. W.; Keith, J. M.; Altman, A. B.; Stieber, S. C. E.; Batista, E. R.; Boland, K. S.; Conradson, S. D.; Clark, D. L.; Lezama Pacheco, J.; Kozimor, S. A.; Martin, R. L.; Minasian, S. G.; Olson, A. C.; Scott, B. L.; Shuh, D. K.; Tyliszczak, T.; Wilkerson, M. P.; Zehnder, R. A., Covalency in Lanthanides. An X-ray Absorption Spectroscopy and Density Functional Theory Study of $LnCl_6^{x-}$ (x = 3, 2). *J. Am. Chem. Soc.* **2015,** *137*, 2506-2523.

[5] Booth, C. H.; Walter, M. D.; Daniel, M.; Lukens, W. W.; Andersen, R. A., Self-Contained Kondo Effect in Single Molecules. *Phys. Rev. Lett.* **2005,** *95*, 267202.

[6] Halbach, R. L.; Nocton, G.; Booth, C. H.; Maron, L.; Andersen, R. A., Cerium Tetrakis(tropolonate) and Cerium Tetrakis(acetylacetonate) Are Not Diamagnetic but Temperature-Independent Paramagnets. *Inorg. Chem.* **2018,** *57*, 7290-7298.

[7] Bogart, J. A.; Lewis, A. J.; Medling, S. A.; Piro, N. A.; Carroll, P. J.; Booth, C. H.; Schelter, E. J., Homoleptic Cerium(III) and Cerium(IV) Nitroxide Complexes: Significant Stabilization of the 4+ Oxidation State. *Inorg. Chem.* **2013,** *52*, 11600-11607.

[8] Minasian, S. G.; Batista, E. R.; Booth, C. H.; Clark, D. L.; Keith, J. M.; Kozimor, S. A.; Lukens, W. W.; Martin, R. L.; Shuh, D. K.; Stieber, S. C. E.; Tylisczcak, T.; Wen, X.-d., Quantitative Evidence for

Lanthanide-Oxygen Orbital Mixing in CeO_2, PrO_2, and TbO_2. *J. Am. Chem. Soc.* **2017,** *139*, 18052-18064.